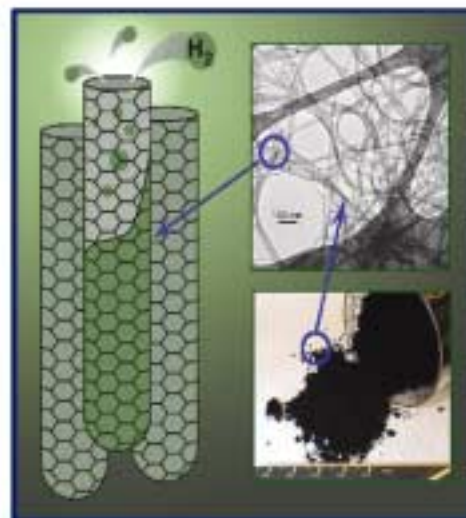


Proceedings of the 2001 U.S. DOE Hydrogen Program Review

Sponsored by the Office of Hydrogen and
Superconductivity Technologies,
Office of Power Technologies,
U.S. Department of Energy

*Presented at the 2001 U.S. DOE
Hydrogen Program Review
Baltimore, Maryland
April 17–19, 2001*



NREL

National Renewable Energy Laboratory

1617 Cole Boulevard
Golden, Colorado 80401-3393

NREL is a U.S. Department of Energy Laboratory
Operated by Midwest Research Institute • Battelle • Bechtel

Contract No. DE-AC36-99-GO10337

NOTICE

This report was prepared as an account of work sponsored by an agency of the United States government. Neither the United States government nor any agency thereof, nor any of their employees, makes any warranty, express or implied, or assumes any legal liability or responsibility for the accuracy, completeness, or usefulness of any information, apparatus, product, or process disclosed, or represents that its use would not infringe privately owned rights. Reference herein to any specific commercial product, process, or service by trade name, trademark, manufacturer, or otherwise does not necessarily constitute or imply its endorsement, recommendation, or favoring by the United States government or any agency thereof. The views and opinions of authors expressed herein do not necessarily state or reflect those of the United States government or any agency thereof.



Proceedings of the 2001 U.S. DOE Hydrogen Program Review

TABLE OF CONTENTS

Biological Hydrogen Production

<u>Biological H₂ from Fuel Gases and from Water</u>	1
P.-C. Maness and P.F. Weaver, National Renewable Energy Laboratory	
<u>Bioreactor Design Studies for a Novel Hydrogen-Producing Bacterium</u>	11
E.J. Wolfrum and A.S. Watt, National Renewable Energy Laboratory	
<u>Development of an Efficient Algal H₂-Production System</u>	23
M. Seibert, M. Forestier, L. Zhang, and M. Ghirardi, National Renewable Energy Laboratory	
<u>Discovery of an Alternative Oxygen Sensitivity and its Potential Application in Photosynthetic H₂ Production</u>	31
J. Lee and E. Greenbaum, Oak Ridge National Laboratory	
<u>Absence of the Pigments Lutein, Violaxanthin and Neoxanthin Affects the Functional Chlorophyll Antenna Size of Photosystem-II But Not That of Photosystem-I in the Green Alga Chlamydomonas ReinhardtII</u>	45
J.E.W. Polle, K.K. Niyogi, and A. Melis, University of California, Berkeley	
<u>Cyclic Photobiological Algal H₂-Production System</u>	67
M.L. Ghirardi, S. Kosourov, and M. Seibert, National Renewable Energy Laboratory	
<u>Efficient Hydrogen Production Using Enzymes of the Pentose Phosphate Cycle</u>	77
N.I. Heyer and J. Woodward, Oak Ridge National Laboratory	
<u>Hydrogen Production by the Thermophilic Bacterium, Thermotoga neapolitana</u>	103
S.A. Van Ooteghem, S.K. Beer, and P.C. Yue, National Energy Technology Center	

Biomass-Based Hydrogen Production

<u><i>Production of Hydrogen from Biomass-Derived Liquids</i></u>	115
S. Czernik, R. French, C. Feik, and E. Chornet, National Renewable Energy Laboratory	
<u><i>Modeling of Biomass Pyrolysis for Hydrogen Production: The Fluidized Bed Reactor</i></u>	125
D. Lathouwers and J. Bellan, Jet Propulsion Laboratory	
<u><i>An Integrated Approach to Hydrogen Production from Agricultural Residues for Use in Urban Transportation</i></u>	160
J. Abedi, Y.D. Yeboah, and K.B. Bota, Clark Atlanta University, M. Realff, Georgia Institute of Technology, D. McGee, Enviro-Tech Enterprises, Inc., and J. Howard, Scientific Carbons Inc.	
<u><i>Engineering Scale Up of Renewable Hydrogen Production by Catalytic Steam Reforming of Peanut Shells Pyrolysis Products</i></u>	187
R. Evans, S. Czernik, E. Chornet, C. Feik, and S. Phillips, National Renewable Energy Laboratory	
<u><i>Supercritical Water Partial Oxidation</i></u>	197
N.W. Johanson, M.H. Spritzer, G.T. Hong, and W.S. Rickman, General Atomics	
<u><i>Role of Initial Sucrose and pH Levels on Natural, Hydrogen-Producing, Anaerobe Germination</i></u>	213
S. Van Ginkel, S. Sung, and L. Li, Iowa State University, J.-J. Lay, National Kaohsiung First University of Science and Technology	

Fossil-Based Hydrogen Production

<u>Thermal Dissociation of Methane Using a Solar Coupled Aerosol Flow Reactor</u>	228
A.W. Weimer, J. Dahl, and K. Buechler, University of Colorado, A. Lewandowski, R. Pitts, and C. Bingham, National Renewable Energy Laboratory	
<u>Thermocatalytic CO₂-free Production of Hydrogen from Hydrocarbon Fuels</u>	271
N. Muradov, Florida Solar Energy Center	
<u>Novel Catalytic Fuel Reforming with Advanced Membrane Technology</u>	297
P. Irving, W.L. Allen, Q. Ming, and T. Healey, InnovaTek, Inc.	
<u>ITM Syngas and ITM H₂ Engineering Development of Ceramic Membrane Reactor Systems for Converting Natural Gas to Hydrogen and Synthesis Gas for Liquid Transportation Fuels</u>	306
P.N. Dyer and C.M. Chen, Air Products and Chemicals Inc.	
<u>Technoeconomic Feasibility Analysis of Hydrogen Production by Integrated Ceramic Membrane System</u>	316
M.M. Shah and R.F. Drnevich, Praxair, Inc., U. Balachandran, S.E. Dorris, and T.H. Lee, Argonne National Laboratory	
<u>Production of Hydrobromic Acid from Bromine and Methane for Hydrogen Production</u>	330
R. Bradshaw, Sandia National Laboratories	

Renewable Production Electrolytic Processes

<u>Solar Photocatalytic H₂ Production from Water Using a Dual Bed Photosystem</u>	339
C.A. Linkous and D.K. Slattery, Florida Solar Energy Center	
<u>Photoelectrochemical Systems for Hydrogen Production</u>	347
J. Turner, National Renewable Energy Laboratory	
<u>Photoelectrochemical Hydrogen Production</u>	359
E. Miller and R. Rocheleau, University of Hawaii	

Technology Validation

<u>Hydrogen Production through Electrolysis</u>	382
R.J. Friedland and A.J. Speranza, Proton Energy Systems, Inc.	
<u>Renewable Hydrogen Systems Integration and Performance Modeling</u>	392
R. Jacobson, R. Purcell, D. Wermers, Desert Research Institute, B. Wood, D. Donovan, D. Lane, M. Matheus, University of Nevada, Reno	
<u>Ovonic Metal Hydride Based Hydrogen Ice Scooter</u>	404
K. Sapru, S. Ramachandran, Z. Tan, and E. Kurlonko, Energy Conversion Devices, Inc.	
<u>Research and Development of a PEM Fuel Cell, Hydrogen Reformer, and Vehicle Refueling Facility</u>	416
V. Raman, Air Products and Chemicals Inc.	
<u>The Rural Area Power Program Diesel Reformer Evaluation</u>	423
D. Witmer, T. Johnson, and R. Johnson, University of Alaska Fairbanks, J. Keller and A. Lutz, Sandia National Laboratories	
<u>Filling Up with Hydrogen 2000</u>	429
M. J. Fairlie and P. B. Scott, Stuart Energy USA	
<u>Light/Medium-Duty Fleet Applications</u>	435
K. Collier, NRG Tech	
<u>Hydrogen-Based Utility Energy Storage System</u>	439
R. Parker, SRT Group, Inc., and W. L. Clapper, Jr., SunLine Services Group	
<u>SunLine Transit Agency: Hydrogen Commercialization for the 21st Century</u>	446
W. Clapper, SunLine Services Group	

Separation and Purification

<u>Separation Using Encapsulated Metal Hydride</u>	453
L.K. Heung, Westinghouse Savannah River Technology	
<u>Defect-Free Thin Film Membranes for H₂ Separation and Isolation</u>	460
T.M. Nenoff, Sandia National Laboratories	

Storage

<u>Feasibility of Fullerene Hydride as a High Capacity Hydrogen Storage Material</u>	467
R.O. Loutfy and E. M. Wexler, Material and Electrochemical Research (MER) Corporation	
<u>Carbon Nanotube Materials for Hydrogen</u>	478
M. Heben, National Renewable Energy Laboratory	
<u>Doped Carbon Nanotubes for Hydrogen Storage</u>	495
R. Zidan, Savannah River Technology Center	
<u>Catalytically Enhanced Systems for Hydrogen Storage</u>	500
C.M. Jensen, D. Sun, B. Lewandowski, K.K. Kumashiro, W.P. Niemczura, D. Morales-Morales, and Z. Wang, University of Hawaii	
<u>Light-Weight Hydride Development</u>	509
K.J. Gross, G.J. Thomas, E. Majzoub, and G. Sandrock, Sandia National Laboratories	
<u>Hydrogen Storage in Polymer-Dispersed Metal Hydrides (PDMH)</u>	524
W.R. Schmidt, United Technologies Research Center	
<u>Next Generation Hydrogen Tankage</u>	538
A. Weisberg, Lawrence Livermore National Laboratory	
<u>Performance and Certification Testing of Insulated Pressure Vessels for Vehicular Hydrogen Storage</u>	549
S.M. Aceves and J. Martinez-Frias, Lawrence Livermore National Laboratory, O. Garcia-Villazana and F. Espinosa-Loza, FIMEE, Universidad de Guanajuato	
<u>Advanced Thermal Hydrogen Compression</u>	563
M. Golben and D.H. DaCosta, Ergenics, Inc.	

Hydrogen Utilization Research

<u>Small Battery – Fuel Cell Alternative Technology Development</u>	574
M.S. Wilson and C. Zawodzinski, Los Alamos National Laboratory, M. Daugherty, Enable Fuel Cell Corp. (DCH Technology, Inc.)	
<u>Low Cost, High Efficiency Reversible Fuel Cell (and Electrolyzer) Systems</u>	583
Technology Management Inc.	
<u>High-Efficiency Steam Electrolyzer</u>	591
A.-Q. Pham, Lawrence Livermore National Laboratory	
<u>Gallium Nitride Integrated Gas/Temperature Sensors for Fuel Cell System Monitoring for Hydrogen and Carbon Monoxide</u>	599
S.C. Pyke, Peterson Ridge, LLC, L. Sadwick, University of Utah	
<u>Design and Development of New Nano-Engineered Glass-Ceramic Proton Conducting Membranes</u>	614
S.W. Martin, R.C. Belin, and J.T. Sutherland, Iowa State University	
<u>Interfacial Stability of Thin Film Hydrogen Sensors</u>	624
R. Pitts, P. Liu, S.-H. Lee, and E. Tracy, National Renewable Energy Laboratory, R. D. Smith and C. Salter, DCH Technology	
<u>Codes and Standards Analysis</u>	636
M.R. Swain, E. Grilliot, P. Filoso, and M.N. Swain, University of Miami	
<u>Testing of High Pressure Hydrogen Composite Tanks</u>	666
B.C. Odegard, Jr. and G.J. Thomas, Sandia National Laboratories	
<u>Fuel Leak Simulation</u>	679
M. R. Swain, University of Miami	
<u>Advanced Internal Combustion Electrical Generator</u>	690
P. Van Blarigan, Sandia National Laboratories	
<u>Combustion of Hydrogen-Enriched Methane in a Lean Premixed Swirl Burner</u>	710
R. W. Schefer, Sandia National Laboratories	
<u>Hydrogen/Natural Gas Blends for Heavy-Duty Applications</u>	720
K. Collier, NRG Tech	

Analysis

<u>Process Analysis Work for the DOE Hydrogen Program – 2000</u>	724
W.A. Amos, M.K. Mann, P.L. Spath, and J.M. Lane, National Renewable Energy Laboratory	
<u>U.S. Department of Energy Hydrogen Program Infrastructure Activities</u>	735
C. J. Hammel and R. Hewett, National Renewable Energy Laboratory	
<u>Distributed Hydrogen Fueling Systems Analysis</u>	743
C.E. Thomas, J.P. Reardon, F.D. Lomax, Jr., J. Pinyan and I.F. Kuhn, Jr., Directed Technologies, Inc.	
<u>Enhancing Strategic Management of the Hydrogen Option: Scenario Planning by the DOE Hydrogen Technical Advisory Panel</u>	826
J. Ohi, National Renewable Energy Laboratory	
<u>Hydrogen Technical Analysis</u>	838
S. Lasher, M. Stratonova, and J. Thijssen, Arthur D. Little, Inc.	
<u>Commercial Applications for Stationary Fuel Cell Systems</u>	851
D. Stevenson, CTA Energy Solutions	
<u>Hydrogen Fuel Cell Bus Evaluation</u>	859
L. Eudy and R. Parish, National Renewable Energy Laboratory, J. Leonard, Arthur D. Little–Acurex Environmental	

Technology Transfer

<u>International Energy Agency Agreement on the Production and Utilization of Hydrogen</u>	870
C.C. Elam and C.E. Gregoire Padró, National Renewable Energy Laboratory	
<u>Technoeconomic Analysis of Area II Hydrogen Production – Part 1</u>	879
A. T-Raissi, Florida Solar Energy Center	
<u>IEA Hydrogen Annex 13 Transportation Applications Analysis</u>	906
S.M. Schoenung, Longitude 122 West, Inc.	
<u>Technical Evaluations of DOE Projects and Storage Database</u>	925
E.G. Skolnik, J. Miller, and C.Y. TerMaath, Energetics, Incorporated	
<u>Outreach Activities</u>	934
L.A. Kervitsky, SENTECH, Inc.	
<u>Inventory and Gap Analysis of Federally Funded Research and Development Activities</u>	941
C.C. Elam and H.L. Chum, National Renewable Energy Laboratory	
<u>NHA Hydrogen Safety Codes and Standards Activities</u>	949
K. Miller, The National Hydrogen Association	

BIOLOGICAL H₂ FROM FUEL GASES AND FROM WATER

Pin-Ching Maness and Paul F. Weaver
National Renewable Energy Laboratory
Golden, CO 80401

Abstract

When photosynthetic bacterium *Rubrivivax gelatinosus* CBS-2 was cultured under an atmosphere containing CO, a unique water-gas shift pathway is quickly induced. This bacterium is able to convert CO (and H₂O) into H₂ (and CO₂). The terminal step involves a CO-linked hydrogenase. This hydrogenase is unique in its tolerance to O₂, with a half-life of 21 hours when stirred in full air. By measuring H₂-D₂O (H-D) exchange reaction with a capillary mass spectrometer, we determined that this hydrogenase is also partially functional in an atmosphere containing up to 3% O₂, carrying out the H-D exchange reaction at a linear rate throughout the 10-min measurement. This level of tolerance renders this hydrogenase suitable for scale-up application in which O₂ is present simultaneously. In order to sustain long-term H₂ production, we need to further understand the components involved and rate-limiting steps of the bacterial water-gas shift pathway. To achieve this goal, we performed mutant isolation and obtained seven mutants with enhanced CO shift rates, which are worthy of further investigations. Using a different approach to elucidate the components involved in CO shift pathway, we determined that once photo-reduced, a soluble ferredoxin of both a bacterial and of a blue-green algal source can link to the bacterial hydrogenase from CBS-2 to support H₂ production. This finding strongly suggests that a ferredoxin could be involved in mediating H₂ production from CO oxidation in *Rx gelatinosus* CBS-2.

Introduction

Photosynthetic bacteria are versatile in their modes of H₂ metabolism. They have four terminal enzymes mediating the H₂ metabolism: nitrogenase; an uptake hydrogenase; a fermentative hydrogenase; and a CO-linked hydrogenase. Nitrogenase is derepressed under N-free condition and catalyzes H₂ production while an abundance of energy is available (Stewart, 1973). This enzyme system is light-dependent and consumes 4 moles of ATP per mole of H₂ produced. A classical uptake hydrogenase has been isolated from numerous photosynthetic microbes and its main function is to oxidize H₂ to support CO₂ fixation (Colbeau *et al.*, 1983). A hydrogenase linking to formate oxidation has also been identified and its main function is to dissipate excess reducing equivalents under fermentative dark growth mode (Gorrell and Uffen, 1977; Schultz and Weaver, 1982). This enzyme is extremely O₂ sensitive with a half-life of less than 1 min in full air; it equilibrates at 10% partial pressure of H₂ (Maness and Weaver, unpublished data), and is therefore not suitable for scale-up application.

The fourth enzyme, the CO-linked hydrogenase (refer to as “hydrogenase” for the rest of the document), is the most unique among all hydrogenases reported. It was first reported by Uffen in two strains of photosynthetic bacteria to shift CO (and H₂O) in darkness to H₂ (and CO₂) (Uffen, 1981). We have since isolated 450 strains of photosynthetic bacteria possessing this water-gas shift pathway. Among them, *Rubrivivax gelatinosus* CBS-2 is most unique in that its hydrogenase is highly resistant to O₂, with a half-life of 21 hours when whole cells were stirred in full air. When the membrane-free, partially purified hydrogenase was stirred in full air, a half-life of 4.5 hr was observed, clearly indicating that its O₂ tolerance lies in the intrinsic nature of the enzyme conformation, not owing to higher respiratory rates contributed by whole cells. This enzyme has a rate constant of over 60,000 and is energetically more favorable toward the H₂ evolution direction. Compared to most other hydrogenase systems, the CO-linked pathway is most robust and has great potential for commercial applications.

One requirement for economical H₂ production is to further characterize its O₂ tolerance. Although previous data reveal that the hydrogenase has a half-life of 21 hrs when stirred in full air, this experiment was conducted by pre-exposing whole cells in air, followed by assaying H₂ production anaerobically. Since O₂ was not present during the assay, the results only indicate that the hydrogenase is reversible with regards to O₂ inactivation. We need to determine whether hydrogenase can actually function with the simultaneous presence of O₂, which would provide insight as to the immediate impact upon O₂ addition, along with duration and rates of the enzyme in O₂. We have been using an assay method including a reducing agent and an electron mediator, both of which exclude the addition of O₂ during assays. To meet the requirement of including O₂ during the assay, we developed an H₂-D₂O (H-D) exchange assay. Hydrogenases from various sources have been reported to catalyze an H-D exchange reaction yielding HD without using a reducing agent, nor a mediator (San Pietro, 1957; Fauque *et al.*, 1988; Vignais *et al.*, 1997). This method is suitable to determine hydrogenase activity in the presence of O₂. Using this method, we found that the simultaneous presence of O₂ inhibited hydrogenase activity by 20% at 3.3% O₂ and 40% by 13% O₂. Yet, more than 90% of the original activity was restored when O₂ was removed subsequently. However, this batch assay does not yield kinetic information as to the immediate impact of O₂ on the enzyme activities and whether the loss was due to enzyme operating at a lower but constant level, or at a high initial rate which then fell off.

In this report, we document the development of a continuous sampling system using a capillary mass spectrometer that resolves these issues.

Another goal of this project is to gain a better understanding of the components involved in the overall water-gas shift reaction to identify the rate-limiting step(s) so the shift rates can be further enhanced. The biological water-gas shift pathway is a multi-step reaction involving at least two enzymes (CO dehydrogenase and hydrogenase) and four or more mediators shuffling electrons through the chain reaction (Ludden *et al.*, 1996). There are three approaches to study the components involved in the shift reaction. The first one is to biochemically purify all the components, and then, through reconstitution experiments, determine what role each component plays in re-establishing the overall reaction. This approach is time-consuming and requires extensive effort on purification of the membrane-bound proteins. The second approach is to genetically obtain mutants deficient in one or more of the intermediates and determine their ability to carry out the overall reaction. This report documents an ongoing effort in generating mutants to meet this goal. The third approach is the most easily attainable among the three in the near term. This method is to construct an *in vitro* assay containing photosynthetic membranes from spinach, bacterial hydrogenase from CBS-2, and any physiological electron mediators of interest that might link the reaction, assuming the mediator can be photo-reduced by the spinach membranes. Any evidence of linkage *in vitro* would suggest that the mediator could play a role *in vivo* also. We chose to examine ferredoxin from two sources as the candidate mediator since ferredoxin is known to serve as a natural electron mediator in many low-redox potential reactions including hydrogenase in all life forms. This paper details the construction of such an *in vitro* system and reports the successful linkage of ferredoxin in mediating the CO-linked hydrogenase from *Rx. gelatinosus* CBS-2.

Materials and Methods

Growth Condition

Rubrivivax (formerly *Rhodocyclus*) *gelatinosus* CBS-2 was cultivated in modified RCV medium (Weaver *et al.*, 1975) supplemented with Na-malate (28mM) and yeast extract (0.05%, w/v) (BG medium) along with 17% CO to fully induce the water-gas shift pathway. Photosynthetic cultures were illuminated with a band of 40W incandescent lamps with approximately 100W/m² of light intensity reaching the culture surface.

H₂-D₂O Exchange Reaction

Whole cells of CBS-2 (5 day old) cultured as above were spun down and suspended in 20 mM potassium phosphate buffer (pH 7.5) to a final concentration of 29.4 mg cell dry wt (cdw)/ml. A 15-ml aliquot of the cell suspension was placed inside a 100-ml Erlenmeyer flask. To collect signal, a capillary tube was inserted, through a 22G needle, into a neoprene stopper and positioned right above the culture surface. The headspace contains 3% H₂. Background levels of HD was recorded for 5 min, followed by the addition of 5 ml D₂O (Sigma-Aldrich) to initiate the H-D exchange reaction. Mass 3 for HD was continuously monitored for changes during the kinetic isotope exchange experiment, collected by a Balzers Quadstars data gathering software. The capillary mass spec (Balzers) was equipped with a Pfeiffer high vacuum system (TCP015).

Mutant Isolation

Log-phase CBS-2 culture was randomly mutagenized with N-methyl-N'-nitro-N-nitrosoguanidine (NTG, 20 μ g/ml) for 35 min to achieve 50% cell killing. The mutant was then inoculated into fresh RCV medium containing penicillin (150 μ g/ml) in the presence of 17% CO to kill only those cells capable of shifting CO. After 8-10 hrs of incubation in light, the culture was spun down (8,000 \times g, 15 min) to remove excess penicillin. The pellet was resuspended in 1-ml BG medium followed by adding penicillinase (one crystal, < 1 mg) to remove residual antibiotics. The suspension was inoculated into fresh BG medium for photosynthetic growth for the next round of penicillin killing. We repeated this penicillin killing/CO selection procedure three times to enrich for the population of CO⁻ species. This culture is now designated as CBS2NTG3P.

A log-phase CBS2NTG3P culture was serially diluted in PBS and spread onto nutrient agar surface containing malate to yield approximately 150 to 200 colonies per plate. These colonies were then picked onto two sets of agar plates (pH 8.0) for replica plating, with one set containing Na-acetate (40 mM) along with CO (17%) while the other set containing Na-acetate and Na-bicarbonate (0.1%). After one week of photosynthetic growth, the patterns of both sets were compared to look for colonies that grow well on acetate/NaHCO₃, but do not grow on acetate/CO, an indication of lacking the CO-shift pathway. Colonies fitting that criterion were then transferred to BG liquid medium for photosynthetic growth.

Photoreductant Linkage

Stored-bought spinach was deveined to yield ~ 200g of leaves. The leaves were blended in 500 ml of B1 buffer (0.4M NaCl, 2 mM MgCl₂, 0.2% BSA, and 20 mM Tricine, pH 7.5) for 10 seconds at low speed, then two times at full speed. The blended extract was filtered through 16 layers of cheesecloth to remove unbroken cells. The filtrate was centrifuged at 300 \times g for 1 min, followed by 4000 \times g for 10 min. The resulted precipitates containing thylakoid membranes were resuspended in ~10 ml of K4 buffer containing 400 mM sucrose, 15 mM NaCl, 5 mM MgCl₂ and 20 mM K-phosphate (pH 7.0). Chlorophyll was determined by extracting 10 μ l of the membranes into 10 ml 80% acetone and measuring absorption using the equation (8.02 \times A_{663nm}) + (20.21 \times A_{645nm}) yielding chlorophyll in mg per ml. Membranes prepared this way have very good water-splitting activity.

To prepare membranes containing hydrogenase activity, four-day old CBS-2 culture was resuspended in 50 mM HEPES buffer (pH 7.5) to approximately 10 mg cdw/ml. The suspension was subjected to sonication for 5 min at 80% output (model W 375, Heat Systems-Ultrasonics, Inc). Unbroken cells were removed by centrifugation at 35,000 \times g for 15 min and the supernatant was used for the linkage experiment.

Photoreductant linkage experiment was conducted according to Fry *et al.* (1977) and Rao *et al.* (1978) in a Clark-type O₂ electrode system (Yellow Spring, OH). The reaction mix contains, in final concentrations: 1.5 ml K4 buffer (pH 7.0), glucose (25 mM), glucose oxidase (5 units/ml), catalase (500 units/ml), ethanol (1%), thylakoid membranes (~ 20 μ g chlorophyll), and 0.3 ml hydrogenase extract. A baseline activity was recorded in light (5V output, Unitron, Inc.)

followed by additions of either methyl viologen (10 μM) or ferredoxins from *Clostridium pasteurianum* (8.5 μM) or from *Spirulina sp.* (5 μM), obtained from Sigma Chemical Co.

Results and Discussion

Effect of O_2 on the Kinetics of Hydrogenase Activity

After evaluating configurations of the various mass spectrometers at NREL, we concluded that a capillary mass spectrometer is most suited for kinetic measurements of low quantity of HD continuously. CO-linked hydrogenase has a very high forward/backward ratio (near 50) of reaction rates measured with methyl viologen for both directions, suggesting that the enzyme prefers H_2 production reaction versus H_2 oxidation reaction. However, the H-D exchange reaction is initiated by a heterolytic cleavage of H_2 molecule to a proton and a hydride prior to exchanging with the deuterium ions in the liquid medium. Based on these criteria, a capillary mass spectrometer would meet our needs since it provides continuous sampling of reactor headspace at near ambient pressure without requiring any carrier gas, which normally would dilute the HD signal significantly.

Figure 1 shows the kinetics of HD production when 3% H_2 was in the atmosphere. The exchange reaction occurred almost immediately upon the addition of D_2O to the bacterial suspension and it proceeded with a linear rate for at least 10 min. Prior measurements indicated that the exchange reaction reached equilibrium after 10-min period (data not shown). Therefore, to study O_2 inhibition, O_2 would have to be added at zero time so any decrease in rates can be attributed entirely to O_2 inactivation, not from reaction reaching equilibrium. Consequently, to quantify O_2 tolerance, we divided the same bacterial suspension into several aliquots and each received D_2O along with various amounts of O_2 to initiate the exchange reaction. Data from Fig. 1 indicate that even though the hydrogenase activity was inhibited with increased levels of O_2 , the H-D exchange reaction rate was linear with the simultaneous presence of various amounts of O_2 . This result clearly suggests that the hydrogenase was operational in O_2 . Most hydrogenases are inhibited irreversibly by even a trace amount of O_2 . Our results indicate that CO-linked hydrogenase is not only tolerant, it is also partially functional in the presence of O_2 , which has not been reported in literature. This unique feature allows for the genetic transfer of this hydrogenase into a cyanobacterium leading to H_2 production with the simultaneous production of O_2 derived from photosynthetic water-splitting reaction.

Isolation of mutants affected in the water-gas shift reaction

As discussed earlier, one approach to understanding the water-gas shift reaction is to generate mutants affected in the shift reaction and then study the impact on rates. Our strategy of mutant isolation is based on the fact that photosynthetic growth on Na-acetate requires exogenous CO_2 , which can be provided entirely via CO shift reaction. Any mutant deficient in the CO shift reaction therefore will not generate enough CO_2 to support growth in acetate with CO while the wild type would. Following the mutagenesis, selection and enrichment scheme according to Methods and after screening approximately 1400 colonies, we identified seven colonies that grew well in acetate/ CO_2 , but not in acetate/CO, indicating their CO shift pathway could be impaired. However, when these mutants were grown in liquid medium containing malate/yeast

extract/CO, GC analysis of the headspace revealed H₂ production. This conflicting finding prompted us to examine rates of H₂ production in two reactions using GC analysis. We first measured H₂ production from CO, a reaction that requires every component of the CO to H₂ pathway to function. We then measured H₂ production from Na-dithionite and methyl viologen, a reaction that requires only the terminal hydrogenase to be functional. Results are shown in Table 1. Unexpectedly, comparing with parent CBS-2, all mutants show enhanced rates of H₂ production from either CO or reduced methyl viologen. Three of them: E63, G42 and T21 had the most significant increase, presenting great values for enhanced H₂ production if incorporated in an applied system.

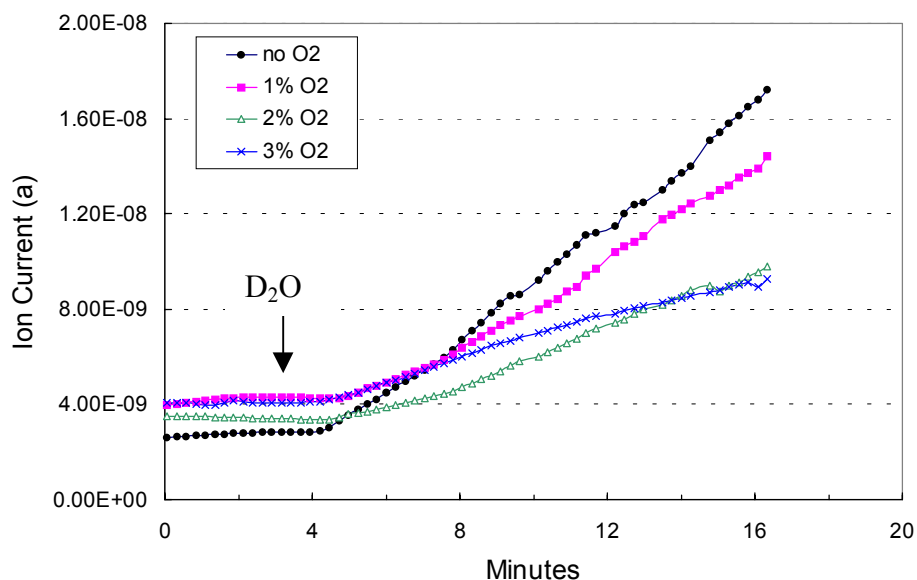


Figure 1. Effect of O₂ on kinetic exchange activity in whole cells of *Rx. gelatinosus* CBS-2

Linking bacterial hydrogenase with a photoreduced ferredoxin

To examine if ferredoxin indeed plays a role in our system, we constructed an *in vitro* assay according to Methods. We used a soluble ferredoxin from either *Clostridium pasteurianum* (bacterial source) or *Spirulina sp.* (blue-green algal source), since ferredoxin of prokaryotic source probably is most compatible with a photosynthetic bacterium.

Figure 2 shows that when an artificial electron mediator such as methyl viologen was used, H₂ production occurred almost immediately when light was turned on, yielding a rate of 1.4 μm H₂/hr/mg chl. When a physiological electron mediator such as *clostridial* ferredoxin was used instead, similar linkage was observed, although at a much lower rate (90 nm H₂/hr/mgchl). When ferredoxin from a blue-green algal source was used, a slightly higher rate was observed (135 nm H₂/hr/mgchl). The linkage is strictly light-dependent. No activity was detected when mediator was not included. These results clearly support our assumption that a ferredoxin-like protein is most likely involved in mediating electron transfer to CBS-2 hydrogenase, whether photoreduced by spinach photosystems or by the CO-oxidation reaction.

Table 1. Isolation of mutants with enhanced CO shift activities

	CO to H₂ (% Activity)	Hydrogenase (% Activity)
D44	134.1	210
D63	111.2	214
E63	160.7	253.2
F52	140	175.2
G42	168.1	273.8
K44	107.1	168.7
T21	156	211
CBS-2 (parent)	100	100

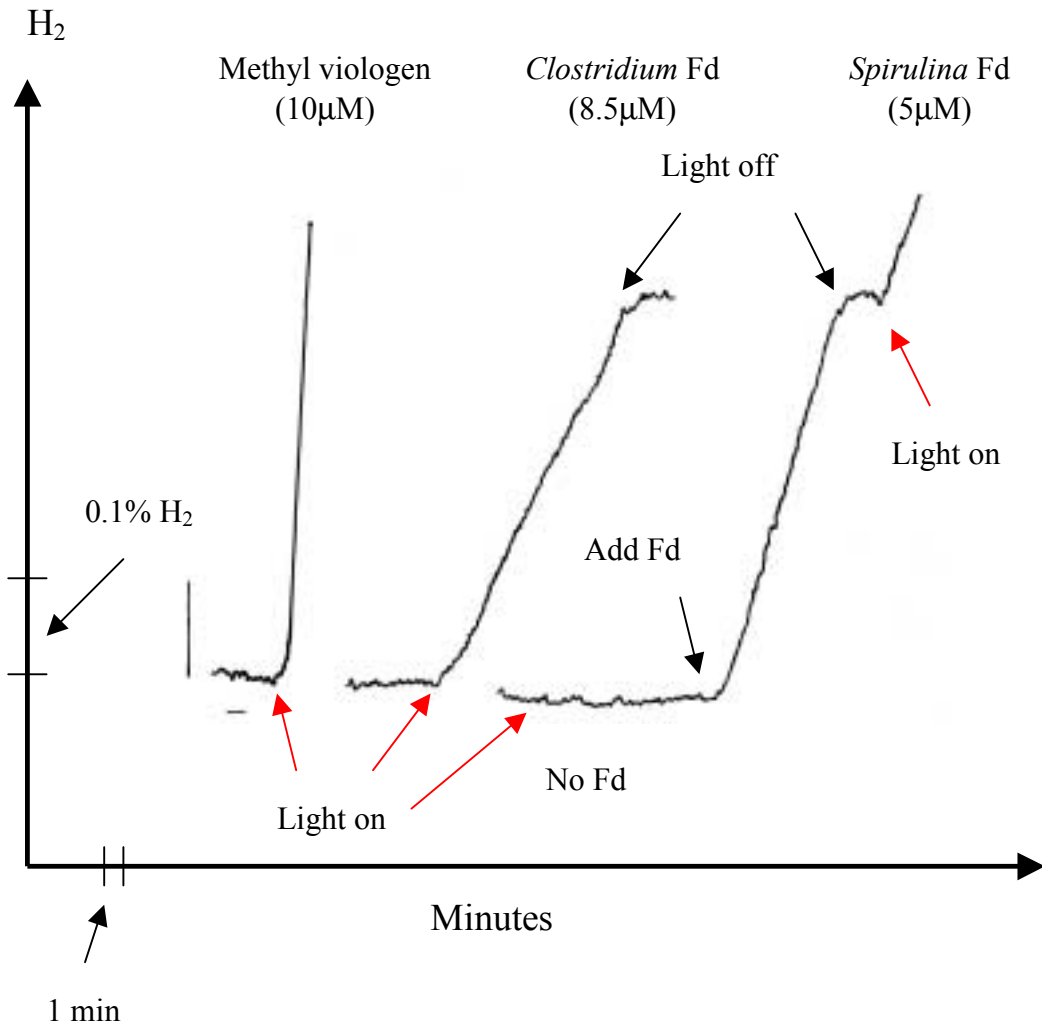


Figure 2. The photo-linkage of spinach thylakoids, CBS-2 hydrogenas, and various electron mediators. Fd: ferredoxin

We used a crude membrane fraction as the source of hydrogenase activity. These membranes presumably also contain other mediators native to the hydrogenase enzyme. Reduced methyl viologen is known to interact directly with the active site of the enzyme bypassing other native components, which explains its high linkage rate. On the other hand, reduced ferredoxin would still need to interact with other mediators before electrons are finally shuffled to the active site of the enzyme. This process will certainly account for the lower reaction rate.

We used a crude membrane fraction as the source of hydrogenase activity. These membranes presumably also contain other mediators native to the hydrogenase enzyme. Reduced methyl viologen is known to interact directly with the active site of the enzyme bypassing other native components, which explains its high linkage rate. On the other hand, reduced ferredoxin would still need to interact with other mediators before electrons are finally shuffled to the active site of the enzyme. This process will certainly account for the lower reaction rate.

Our result is supported by findings in the literature. Many evolving hydrogenases have been reported to accept electrons from reduced ferredoxin to mediate H₂ production (Adams *et al.*, 1981). Kemner and Zeikus (1994) reported the involvement of a ferredoxin in the CO-oxidizing: H₂ evolving activity in the acetotroph *Methanosarcina thermophila*. Based on genetics evidence, a ferredoxin-like protein has also been proposed by Ludden and his coworkers (1996) to be involved in CO shift reaction of another photosynthetic bacterium *Rhodospirillum rubrum*.

Conclusions

The thrust of this project is the demonstration of an O₂-tolerant hydrogenase from a novel photosynthetic bacterium *Rx. gelatinosus* CBS-2. Knowing that most hydrogenases are irreversibly inhibited even by a minute quantity of O₂, the CO-linked hydrogenase from CBS-2 is indeed unique with a half-life of 21 hours when stirred in full air. Using a very sensitive kinetic H-D sampling methodology, this report demonstrates that this hydrogenase is also partially functional in O₂. This phenomenon has not been reported in literature with other hydrogenases. H-D exchange reaction solely relies on the proton and deuterium ions interacting with the active site of the enzyme to carry out the H₂-oxidation and H₂-production reactions. Since no reductant nor mediator is involved in the H-D exchange reaction, the tolerance to O₂ is entirely contributed to the intrinsic nature of the active site of the enzyme itself, not owing to an activation of the enzyme by an added reductant or the reduced mediator interacting with O₂. The actual demonstration of a working hydrogenase in O₂ is a significant breakthrough.

The development of the methodology for continuous sampling of HD formation is also a valuable contribution. Operating at near ambient pressure, the capillary leak provides continuous sampling of the HD signal without using any carrier gas. This configuration renders this assay to be extremely sensitive and can be used to evaluate other hydrogenase enzyme for its functionality in the presence of O₂.

Using a scheme designed to isolate mutant with impaired CO shift rates, we acquired seven mutants with enhanced activities instead. We need to re-evaluate this selection/enrichment technique itself as to why the opposite of the concluded result was obtained. One possible

explanation is that the above procedure could have selected for mutants deficient in the CO₂-uptake pathway instead; therefore, cells would have to overly express their CO shift reaction to compensate. Even though we do not fully understand the nature of these mutants, their enhanced rates do present opportunity in an applied system to achieve elevated levels of H₂ production.

Our photoreductant linkage experiment clearly indicates that ferredoxin could play an important role in mediating H₂ production from CO oxidation. This finding is consistent with reports in the literature. The fact that the ferredoxin from a blue-green algal source is more effective than that of a bacterial source is encouraging. This finding makes it possible to transfer bacterial hydrogenase into a cyanobacterium in which the bacterial hydrogenase can then utilize the native ferredoxin of the host to mediate H₂ production reaction *in vivo*.

Future Work

The above kinetic HD determination was conducted with whole cells, which could respire and thus lower the O₂ tension. To complete the O₂-tolerance determinations without complications of cellular respiratory reaction, we need to measure kinetic HD production in O₂ with purified enzyme instead. This requires purified enzyme with sufficient quantity and improved purity. We will continue to develop various detergent extraction steps to improve yield by solubilizing more of the membrane-bound hydrogenase, and subjecting it to chromatography columns more specific to the hydrogenase itself to enhance purity. The purified enzyme can also be used in the photoreductant linkage experiment to further understand the electron mediator involved. Presently the crude membranes used also contain other cofactor besides the hydrogenase. Using a purified enzyme, we will test if it can couple directly with a photo-reduced ferredoxin without contributions from other cofactors. Having seven mutants with enhanced shift rates in our library of culture collection, we plan to determine their enzyme stability over repeated sub-culturing and against selection pressure. Only those stable mutants will have potential applications in an applied system. Once their stability is determined, it may be worthwhile to determine, at genetic levels, the nature of the genotype that accounts for the enhanced rates; namely whether the changes occur at regulation levels or in the hydrogenase gene itself. Eventually, we like to test these mutants in a bioreactor to examine if indeed they would produce elevated levels of H₂ for scale up application.

Acknowledgements

We thank Kim Magrini for developing methodology and carrying out the capillary mass spectrometer measurements, and Sharon Smolinski for preparing thylakoid membranes from spinach.

References

Adams, M.W.W., L.E. Mortenson, and J.-S. Chen. 1981. "Hydrogenase." *Biochem. Biophys. Acta.*, 594: 105-176.

- Colbeau, A., J. Chabert, and P.M. Vignais. 1983. "Purification, molecular properties and localization in the membrane of the hydrogenase of *Rhodobacter capsulata*." *Biochimica et Biophysica Acta*, 748: 116-127.
- Fauque G., H.D. Peck, J.J.G. Moura, B.H. Huynh, Y. Berlier, D.V. DerVartanian, M. Teixeira, A.E. Przybyla, P.A. Lespinat, I. Moura, and J. LeGall. 1988. "The three classes of hydrogenases from sulfate-reducing bacteria of the genus *Desulfovibrio*." *FEMS Microbiol. Rev*, 54: 299-344.
- Fry, I., G. Papageorgiou, E. Tel-Or, and L. Packer. 1977. "Reconstitution of a system for H₂ evolution with chloroplasts, ferredoxin, and a hydrogenase." *Z. Naturforsch* 32c: 110-117.
- Gorrell, T.E. and R.L. Uffen. 1977. "Fermentative metabolism of pyruvate by *Rhodospirillum rubrum* after anaerobic growth in darkness." *J. Bacteriol.*, 131: 533-543.
- Kemner, J.M. and J. G. Zeikus. 1994. "Purification and characterization of membrane-bound hydrogenase from *Methanosarcina thermophila*." *Arch. Microbiol.*, 161: 47-54.
- Ludden, P.W., G.P. Roberts, R.L. Kerby, N. Spangler, J. Fox, D. Shelver, Y. He, and R. Watt. 1996. "The biochemistry of CO dehydrogenase in *Rhodospirillum rubrum*." *Microbial Growth on C₁ Compounds*, 183-190. M.E. Lindstrom and F.R. Tabita (eds). Kluwer Academic Publishers. Netherlands.
- Rao, K.K., I.N. Gogotov, and D.O. Hall. 1978. "Hydrogen evolution by chloroplast-hydrogenase systems: improvement and additional observations." *Biochimie*. 60: 291-296.
- San Pietro, A., 1957. "The measurement of stable isotopes." In *Methods in Enzymology*, vol. IV, p. 473-488. Colowick, S. P. and N.O. Kaplan (eds.), Academic Press, Inc., N.Y.
- Schultz, J.E. and P.F. Weaver. 1982. "Fermentation and anaerobic respiration by *Rhodospirillum rubrum* and *Rhodopseudomonas capsulata*." *J. Bacteriol.*, 181-190.
- Stewart, W.D.P. 1973. "Nitrogen fixation by photosynthetic microorganisms." *Ann. Rev. Microbiol.*, p. 283-316.
- Uffen, R.L., 1981. "Metabolism of carbon monoxide." *Enzyme Micro. Technol.*, 3: 197-206.
- Vignais, P.M., B. Dimon, N.A. Zorin, A. Colbeau, and S. Elsen. 1997. "HupUV proteins of *Rhodobacter capsulatus* can bind H₂: evidence from the H-D exchange reaction." *J. Bacteriol.*, 179: 290-292.
- Weaver, P.F., J.D. Wall, and H. Guest. 1975. "Characterization of *Rhodopseudomonas capsulata*." *Arch. Microbiol.*, 105: 207-216.

BIOREACTOR DESIGN STUDIES FOR A NOVEL HYDROGEN-PRODUCING BACTERIUM

**Edward J. Wolfrum, Andrew S. Watt
National Renewable Energy Laboratory
1617 Cole Boulevard, Golden, CO 80401**

Abstract

Carbon monoxide (CO) can be metabolized by a number of naturally occurring microorganisms along with water to produce hydrogen (H₂) and carbon dioxide (CO₂). NREL researchers have isolated a number of bacteria that perform this so-called “water-gas shift” reaction at ambient temperatures. We have performed experiments to measure the rate of biological CO conversion and H₂ production in a trickle bed reactor (TBR). The reactor support material has a significant effect on the mass transfer coefficient, which in turn controls the overall reactor performance for this mass transfer-limited reaction. A simple reactor model taken from the literature is used to quantitatively compare the relative performance of the different support materials, including one support material tested at two different TBR sizes (1-L and 5-L). A TBR bioreactor was used to condition water-scrubbed synthesis gas from a biomass gasifier, and was unaffected by the presence of low concentrations of aromatic compounds over the course of the weeklong test.

Introduction

The biologically-mediated water-gas shift reaction may be a cost-effective technology for the conditioning of synthesis gas for storage or direct use within a hydrogen fuel cell, where the presence of even low concentrations of carbon monoxide are deleterious. NREL researchers have isolated a number of photosynthetic bacteria that can perform the water-gas shift reaction, in

which carbon monoxide is oxidized to carbon dioxide while simultaneously water is reduced to hydrogen (Weaver *et al.* 1980). The overall stoichiometry of this reversible reaction is:



One significant advantage to using bacteria to perform the water-gas shift reaction is their ability to operate at ambient temperature. Because the reaction occurs at ambient temperature, the reaction is not equilibrium-limited (at 25°C, $K_{EQ} \sim 5 \times 10^4$). The advantages of low operating temperature and lack of equilibrium limitation make the biological shift reaction a promising alternative to conventional shift technologies. Preliminary data already collected at NREL suggest that this reaction is far more rapid than the rate at which CO can be supplied to the bacterial culture (Markov *et al.* 1997). This is consistent with many other gas/liquid biological reaction systems, including most aerobic fermentations, where metabolic rates are commonly limited by the transfer rate of a gaseous substrate to the liquid media.

A number of researchers have investigated the biological conversion of gaseous substrates to produce fuels and chemicals. Vega and others (Vega *et al.* 1989a, et al. Vega 1989b) used batch (anaerobe bottles) and continuous (chemostat) experiments to investigate CO conversion to acetate using the bacterium *Peptostreptococcus productus*. The authors developed kinetic expressions for cell growth and CO utilization under mass transfer- and kinetics-limited operation in each reactor, but the resulting rate expressions predicted different levels of CO inhibition at higher substrate concentrations. Klasson *et al.* (1990) extended this work to investigate acetate production from CO by *P. productus* in a chemostat, a packed bubble column, and a trickle bed reactor. They developed a simple reactor model and used it to calculate mass transfer coefficients for each reactor tested. Kimmel *et al.* (1991) used a triculture of *Rhodospirillum rubrum*, *Methanosarcina barkeri*, and *Methanobacterium formicicum* to produce methane from synthesis gas using two different size trickle bed reactors. *R. rubrum* performed the water gas shift reaction to produce H₂ and CO₂, and the two methanogens subsequently converted these gases to CH₄. They compared the performance of the two reactors, but got considerably lower conversion rates in the larger column, even though they operated the larger column at slightly higher liquid velocities. The authors pointed to poor liquid distribution in the larger column as a likely cause of the differences between the two reactors.

In this work we use a monoculture of a unique photosynthetic bacterium, *Rubrivivax gelatinosus* CBS2, to carry out the water gas shift reaction (Eq. 1) and use a simple reactor model taken from the literature to analyze the mass transfer characteristics of a trickle bed bioreactor. We examine the influence of reactor support material on carbon monoxide conversion in a TBR, and then examine the relative performance of two different reactor reactors of identical geometry but different size. Finally, we present preliminary experimental data documenting the ability of *R. gelatinosus* CBS2 to condition biomass-derived synthesis gas streams.

Experimental

Materials

The reactor design used in this work was a trickle bed bioreactor (TBR), shown schematically in Figure 1. Both a 1-L and a 5-L TBR assembly were used. The 1-L TBR assembly consisted of a 2" ID (nominal) glass pipe 24" long. Rubber stoppers (#11 size) were inserted at each end of the glass pipe and acted as end caps. The reactor support rested on a stainless steel mesh approximately 3" above the bottom of the reactor. This space provided a sump area where the recirculating liquid collected and could be conveniently sampled for cell density and pH. The gas inlet and outlet fittings which passed through the rubber stopper end caps were 1/8" OD stainless steel tubing, and the liquid inlet and outlet fittings were 1/4" OD stainless steel tubing. The inlet fittings (gas and liquid) were located in the center of each end cap, with the corresponding outlet fittings offset slightly. The liquid drained into the reactor sump by gravity and was recirculated using a peristaltic pump and 1/4" ID flexible tubing (MasterFlex #24 Norprene tubing) back to the top of the TBR. The 5-L TBR assembly was conceptually similar to the 1-L assembly except that the reactor was composed of 3" diameter glass tubing, the rubber stoppers were larger (#14 size), and gas and liquid inlet and outlet fittings were 1/4" stainless steel.

Four different reactor supports were tested in the 1-L TBR assembly. Two nonporous glass beads (3mm and 6mm diameter) were tested. Two porous materials were also tested: a cellulosic sponge material, cut into approximately 1-cm cubes; and mixture of northeastern mixed hardwoods milled to approximately 1.5-cm pieces. The 6mm-diameter glass bead support was also tested in the 5-L TBR assembly.

The microorganism used in this work was *Rubrivivax gelatinosus* CBS2, isolated from the natural environment by the Weaver group at NREL (Maness and Weaver 1994). The minimal culture media (M-1 basal) had the following composition (amounts are for 1 L of final media preparation): basal salts (120 mg $\text{MgSO}_4 \cdot 7\text{H}_2\text{O}$, 75 mg $\text{CaCl}_2 \cdot 2\text{H}_2\text{O}$, 11.8 mg $\text{FeSO}_4 \cdot 7\text{H}_2\text{O}$, 20 mg EDTA); trace elements (2.8 mg H_3BO_3 , 1.6 mg $\text{MnSO}_4 \cdot \text{H}_2\text{O}$, 0.75 mg $\text{Na}_2\text{MoO}_4 \cdot 2\text{H}_2\text{O}$, 0.24 mg $\text{ZnSO}_4 \cdot 7\text{H}_2\text{O}$, 0.04 mg $\text{Cu}(\text{NO}_3)_2 \cdot 3\text{H}_2\text{O}$, 0.8 mg $\text{CoCl}_2 \cdot 6\text{H}_2\text{O}$, 0.8 mg $\text{NiCl}_2 \cdot 6\text{H}_2\text{O}$); phosphates (1.2 g KH_2PO_4 , 1.8 g K_2HPO_4); vitamins (1.0 mg thiamine HCl, 15 ug biotin, 1.0 mg nicotinic acid, 10 ug B-12, 0.1 mg p-aminobenzoic acid); and ammonia (1.5 g NH_4Cl). In addition, malate (5 g/L) and yeast extract (0.5 g/L) were added as carbon sources. The media was prepared using deionized water and stock solutions of basal salts, trace elements, vitamins, buffers, ammonia, and D,L-malic acid. Yeast extract was added as a powder immediately prior to sterilization. The stock solutions were in turn prepared using stock chemicals from various manufacturers, which were used as received.

Methods

Pure cultures of *Rx. gelatinosus* CBS2 were grown and periodically subcultured under sterile conditions using 20-mL screw-top test tubes and 200-mL serum flasks. These vessels were kept under incandescent illumination until used to inoculate the TBR assemblies. The microorganisms were not exposed to carbon monoxide during the growth/subculture process.

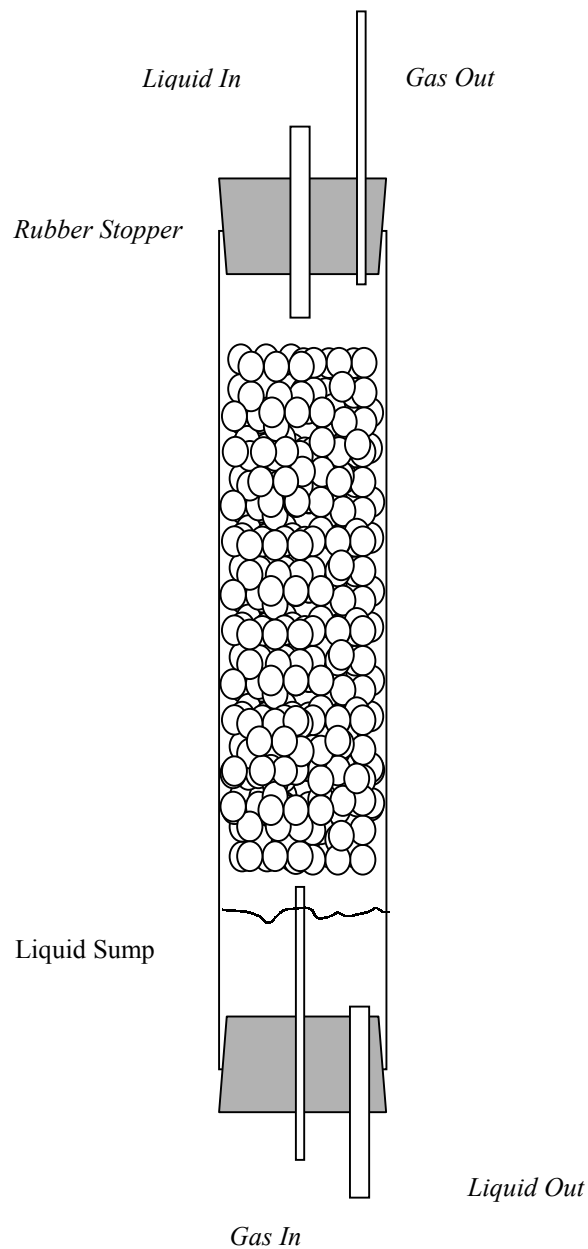


Figure 1. Schematic Diagram of countercurrent Trickle Bed Bioreactors (TBRs) used in the present work.

The 1-L TBR experiments proceeded as follows. The reactor, including the external liquid recirculation loop, was assembled, autoclave sterilized, and allowed to cool. The assembly was then installed in a canopy hood, and the gas inlet fitting connected to the source gas (20%CO, 0.5% He as tracer gas, balance N₂). The reactor was then rinsed with sterile M-1 media while gas flow was initiated. After several reactor volumes of gas were allowed to flow through the reactor, the reactor was drained of any remaining media and inoculated with one serum flask of

Rx. gelatinosus. Default gas and liquid flowrates were established (200mL/min liquid recirculation rate, 25 accm gas flowrate) and the reactor sump was illuminated with a 65W incandescent lamp for several days. CO uptake (and concomitant H₂ production) was induced within approximately 48 hours. Once H₂ production reached a steady state, the lamp was turned off and the reactor loosely covered with black cloth. The operating conditions of the reactor (gas and liquid flowrates) were periodically adjusted, and the outlet gas composition was monitored over time, using a portable gas chromatograph (Agilent Inc. P200). The reactor typically required 12 hours or more to reach steady state after a change in operating conditions. These steady state values were recorded, and then the operating conditions were changed. The total liquid volume in the reactors (including the reactor sump) was approximately 200mL. There was some liquid loss due to evaporation. Periodically, ~20mL aliquots of sterile M-1 media were added to the reactor to replenish the liquid. No effect on reactor productivity (CO shift rate) was seen as a result of these media additions.

The 5-L TBR experiments proceeded in a similar fashion, except the reactor was not autoclaved. Rather, it was washed with standard laboratory soap and rinsed thoroughly with deionized water passed through a sterile 0.2µm filter. Larger liquid inocula were used, typically 600 mL. The default gas and liquid flowrates for the 5-L TBR assembly were 65 accm and 500 mL/min, respectively.

As mentioned above, the inlet gas stream contained 0.5% He as an inert tracer to compensate for changes in the volumetric gas flowrate across the reactor. The water gas shift reaction causes an increase in the volumetric gas flow rate, since 2 moles of gas (H₂, CO₂) are produced for every mole of CO consumed (water is supplied by the media). This volume change would bias CO outlet concentrations low, since CO would not only be consumed by the microorganisms but also diluted by additional gas flowrate. Similarly, outlet hydrogen concentrations would be biased low due to dilution. Since helium is neither consumed nor produced in the reaction, its molar flowrate is constant. Thus, any change in helium concentration must correspond to a change in the overall gas flowrate. This correction factor was applied to all outlet concentration measurements.

Reactor Modeling

The performance of TBR reactor assembly can be modeled as simple plug-flow reactor, with the overall reaction rate controlled by a mass transfer coefficient. This model was developed by Gaddy et al. for a number of different reactor geometries, including CSTRs, packed bubble column reactors, and trickle bed reactors (Vega *et al.* 1989a, Vega *et al.* 1989b, Klasson *et al.* 1990). When the reaction rate is limited by the rate of mass transfer, the steady-state liquid concentration of reactant (in this case, carbon monoxide) can be assumed to be zero, and the controlling equation for an ideal trickle bed reactor is:

$$v_z \frac{dC}{dz} = -\frac{k_L a}{H} C \quad (2)$$

where v_z is the axial gas velocity, C is the gas-phase concentration of reactant, $k_L a$ is the overall mass transfer coefficient (based on empty bed reactor volume) and H is the Henry's Law coefficient of the reactant, a measure of its solubility in the liquid phase. Often the mass transfer coefficient is based on the liquid holdup volume, and the term $k_L a$ in the Eq. 2 is replaced by $k_L a \cdot e_L$, where e_L is the liquid porosity (the ratio of the liquid holdup volume to the empty bed reactor volume). In this work we base the mass transfer coefficient on the overall reactor volume, so no such correction is necessary. Eq. 2 can be integrated to give:

$$C_o = C_i \exp\left(-\frac{k_L a}{H} t_{EBCT}\right) \quad (3)$$

where C_o and C_i are the outlet and inlet reactant concentrations, and t_{EBCT} is the empty bed contact time of the reactant in the reactor, calculated as the empty bed volume of the reactor divided by the volumetric gas flowrate. By using an overall mass transfer coefficient in Eqs. 2 and 3, we treat the reactor system as a "black box," a view reinforced by the use of t_{EBCT} as the independent variable. Thus, reactors with variable geometries, capacities, and support materials can be directly compared using this equation.

Conditioning Biomass-Derived Syngas

The longer-term goal of this project is to use the biological water gas shift reaction to condition biomass-derived synthesis gas. One concern with this process is the presence of organic compounds in the synthesis gas that may be toxic to microorganisms. These organic compounds are generally referred to as "tars," and have a broad range of molecular weights and chemical structures. To test this, we operated a bioshift reactor on a slipstream of biomass-derived synthesis produced at NREL's Thermochemical User Facility (TCUF).

Biomass-derived synthesis gas was produced by feeding an 8-inch diameter fluid bed reactor at the TCUF with a mixture of hard and soft woods at 12 kg/h, with superheated steam providing the fluidization at 25 kg/h. The bed temperature was approximately 580°C, sufficient to generate both pyrolysis gas and vapors. Thermal (steam) cracking of the vapors in the secondary thermal cracker (780-800°C) converted the vapors to syngas. Cyclones and wet scrubbing cleaned the syngas of char/ash and high molecular weight tars. A slipstream of this gas was taken directly downstream of the wet scrubber.

A 1-L reactor containing *R.gelatinosis* CBS2 immobilized on knife milled (sieved to 10-12 mesh) northeastern mixed hardwoods was fed synthesis gas for a total of 29 hours over four days. Since the TCUF operates only during the day, at night the bioreactor was fed a synthetic syngas mixture. The water scrubbing removed most of the high molecular weight and the most polar "tars." However, GC data indicated the presence of both acetylene and ethylene, and mass spectroscopy indicated the presence of both benzene and toluene in the feed to the bioreactor at approximately 5000 and 3000 ppmv, respectively.

Results and Discussion

The results of a typical experiment (a 1-L TBR reactor with cellulose support) are shown in Figure 2. This figure shows the variation in conversion, mass balance and ratio of hydrogen

produced to carbon monoxide consumed ($H_2/(CO_{in}-CO_{out})$) vary with time. The mass balance data were very stable at 98.0% +/- 0.8% over the entire course of the experiment, which lasted about 25 days. The H_2/CO ratio is also quite stable at 101.4 +/- 3.6%, and is in agreement with theoretical stoichiometry. The conversion goes from zero to approximately 60% over the first four days of the experiment. This represents the induction period of a non-induced culture; the time necessary for the microorganisms to activate the necessary enzyme pathways to metabolize CO. Once this steady-state value is reached, the reactor conditions (gas and liquid flowrates) are systematically varied, causing dramatic changes in CO conversion. During these rapid fluctuations in CO conversion, the mass balance and H_2/CO ratio values remain essentially constant, giving us confidence that our analytical system is functioning well and that the bioreactor system as a whole is performing properly. The data in Figure 2 are reduced to yield approximately 12 discrete conversion versus gas flowrate data points.

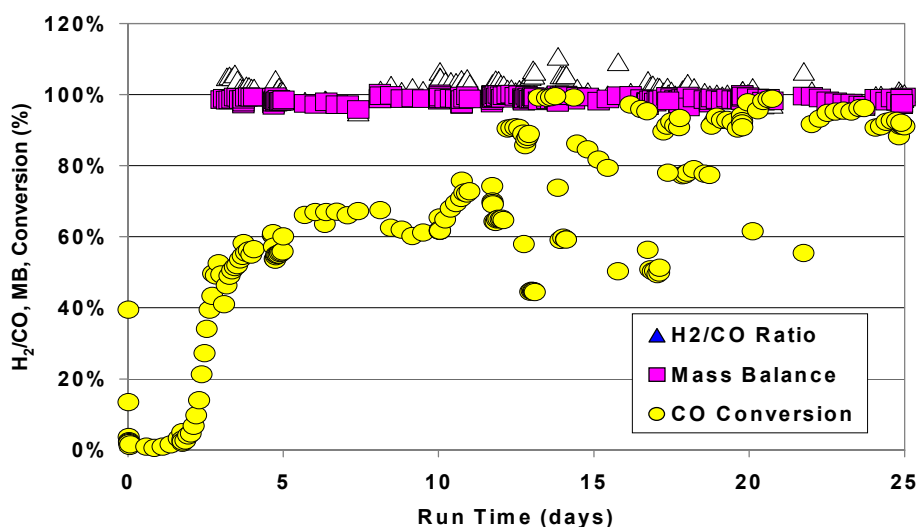


Figure 2. Typical performance of the 1-L TBR assembly. The liquid recirculation rate was 200 mL/min and the gas flowrate was 25 accm.

Influence of Reactor Support

Figure 3 shows the effect of the four reactor support materials on CO conversion in the 1-L TBR assembly. The abscissa in this figure is the space velocity, which is the ratio of the volumetric gas flowrate to the empty bed reactor volume, the inverse of the empty bed contact time. The nature of the reactor support clearly has a profound influence on the performance of the TBR. The same data are replotted according to Eq. 3 in Figure 4. The slopes of these lines are the quantity $k_L a/H$ (the solid lines in Figure 3 are the model fits of Eq. 3). Since the Henry's Law coefficient for carbon monoxide (at 25°C) is 57,800 atm (mole fraction)⁻¹ or 42.3 (unitless) (Foust 1980), the overall mass transfer coefficients for the four supports are: 0.85 min⁻¹ (hardwood), 0.72 min⁻¹ (cellulose), 0.38 min⁻¹ (3mm glass beads) and 0.19 min⁻¹ (6mm glass beads). Thus, by varying the reactor support material, the performance of the reactor can be altered by over a factor of 4.

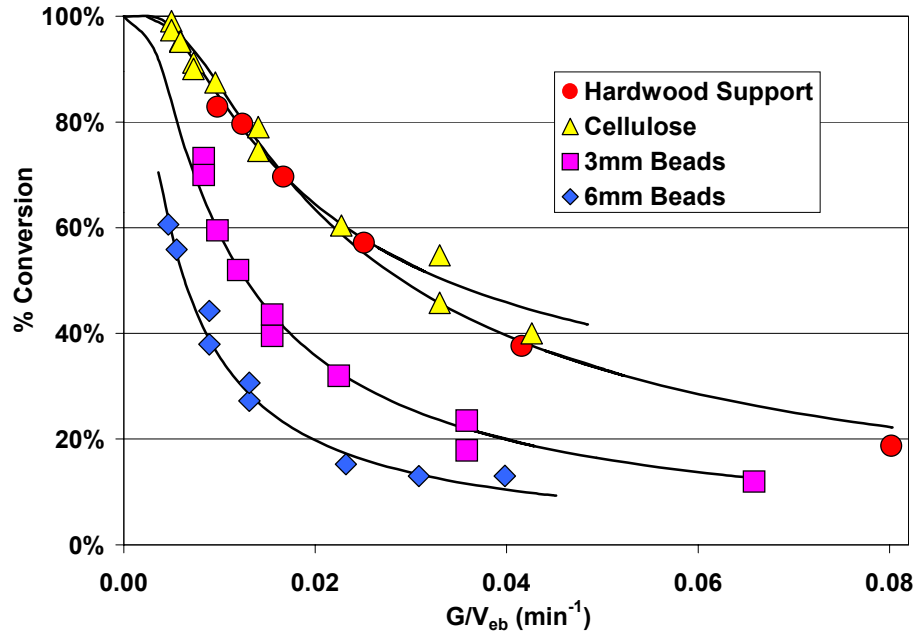


Figure 3. Comparison of CO conversion vs. space velocity in the 1-L TBR assembly using different support materials.

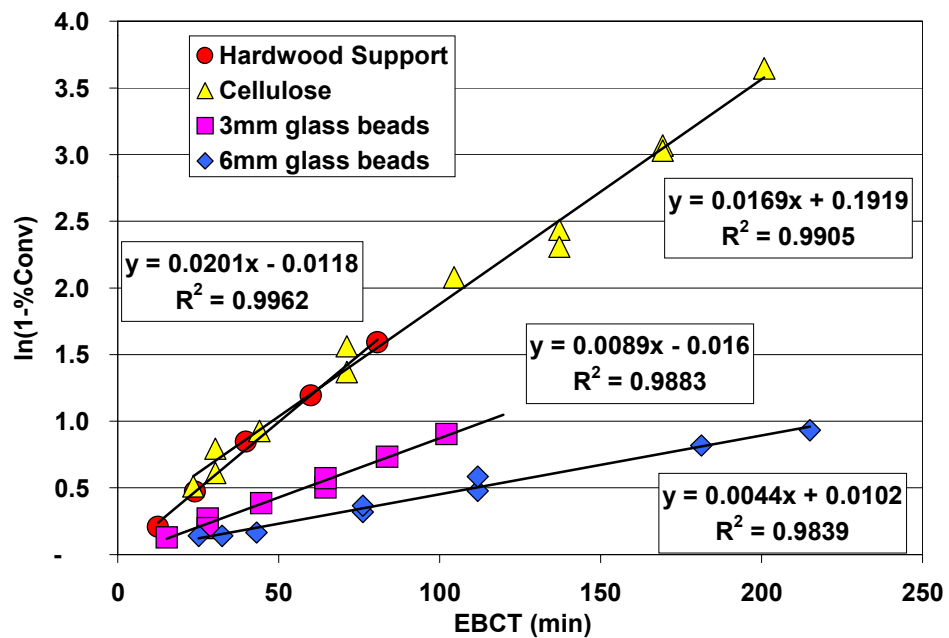


Figure 4. $\ln(C_o/C_i)$ vs. EBCT for the 1-L TBTR experiments. The liquid recirculation rate was 200 mL/min.

Reactor Scaling

The ability of this simple model to predict reactor performance at different scales is tested in Figures 5 and 6, where the influence of the same reactor support (6mm-diameter glass beads) in the 1-L and 5-L TBR assemblies are compared. The performance of the two reactors is essentially identical. Note that the superficial liquid phase velocities were slightly different: 1.06 cm s^{-1} and 1.18 cm s^{-1} in the 1-L and 5-L TBR assemblies, respectively. Since the liquid velocity in the larger reactor was slightly higher, we would expect slightly better performance in this reactor. Nonetheless, these results give us considerable confidence in our understanding of the reactor dynamics, and in our ability to accurately predict the performance of larger reactors from the performance of smaller ones.

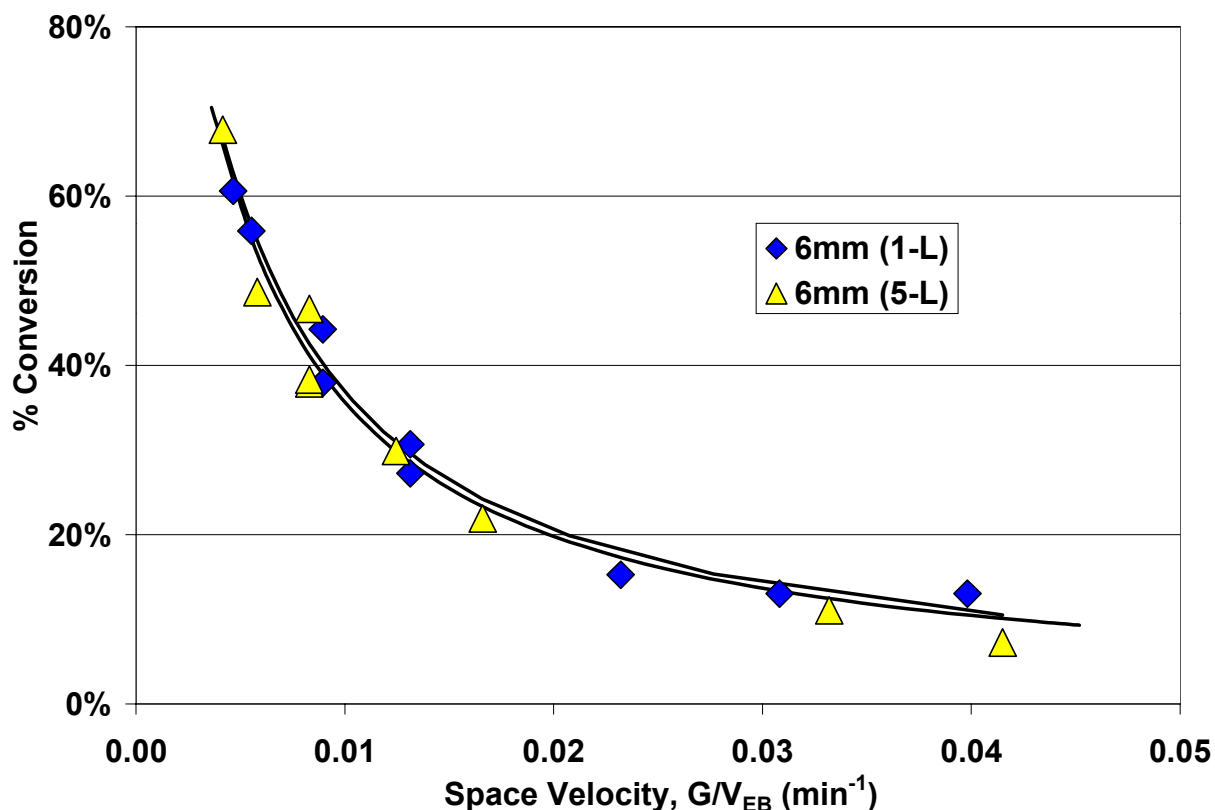


Figure 5. Comparison of CO conversion vs. space velocity using a 6mm-diameter glass bead support in the 1-L and 5-L TBR assemblies. The liquid recirculation rate was 200 mL/min for the 1-L TBR and 500 mL/min in the 5-L TBR, giving similar superficial liquid velocities.

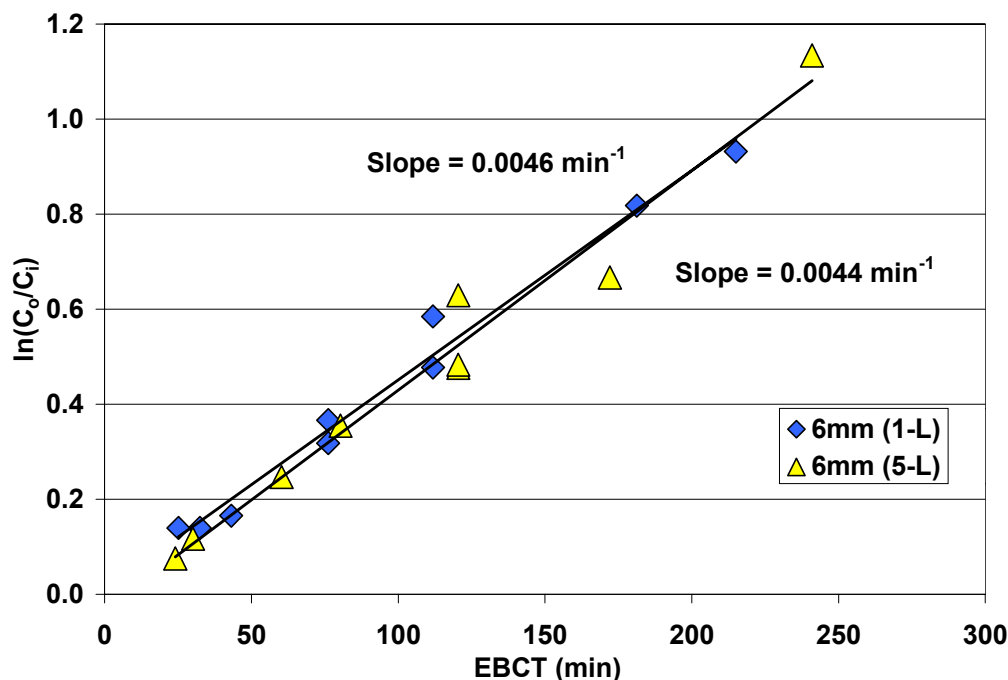


Figure 6. $\ln(C_o/C_i)$ vs. EBCT for the 6mm diameter glass bead support in the 1-L and 5-L TBR assemblies. Superficial liquid velocities were 1.06 cm s^{-1} and 1.18 cm s^{-1} in the 1-L and 5-L TBR assemblies, respectively.

Conditioning Biomass-Derived Syngas

Figure 7 shows the results of the biomass-derived syngas conditioning experiment performed at the NREL TCUF. A 1-L bioreactor conditioned the water-scrubbed synthesis gas during the day for four consecutive days, running with bottled synthesis gas overnight. Over the course of this experiment, the conversion efficiency was essentially constant at 25%, and the carbon mass balance was substantially closed. The variation in the outlet concentrations of both carbon monoxide and hydrogen at the beginning of days 2-4 is an artifact of the switch between bottled gas and process gas. This was the first test of the bioreactor using biomass-derived syngas, rather than synthetic carbon monoxide mixtures, and the overall performance was encouraging. Concerns that tar components of syngas (and permanent gases including ethylene and acetylene) may be toxic or inhibitory to *R. gelatinosus* were unsubstantiated by this experiment. We are presently performing rigorous toxicity experiments in the laboratory to further investigate this important issue.

Conclusions

A trickle bed reactor was used to examine the influence of reactor support material on the conversion of carbon monoxide to hydrogen by a novel photosynthetic bacterium in a trickle bed bioreactor. A simple reactor model taken from the literature was used to quantitatively compare the performance of the different supports, and to compare the performance of a single support in two different reactor sizes. The nature of the support affects the mass transfer coefficient, which

in turn controls the overall reactor performance. The two reactor sizes performed approximately the same, giving us confidence in the scale-up of this reaction.

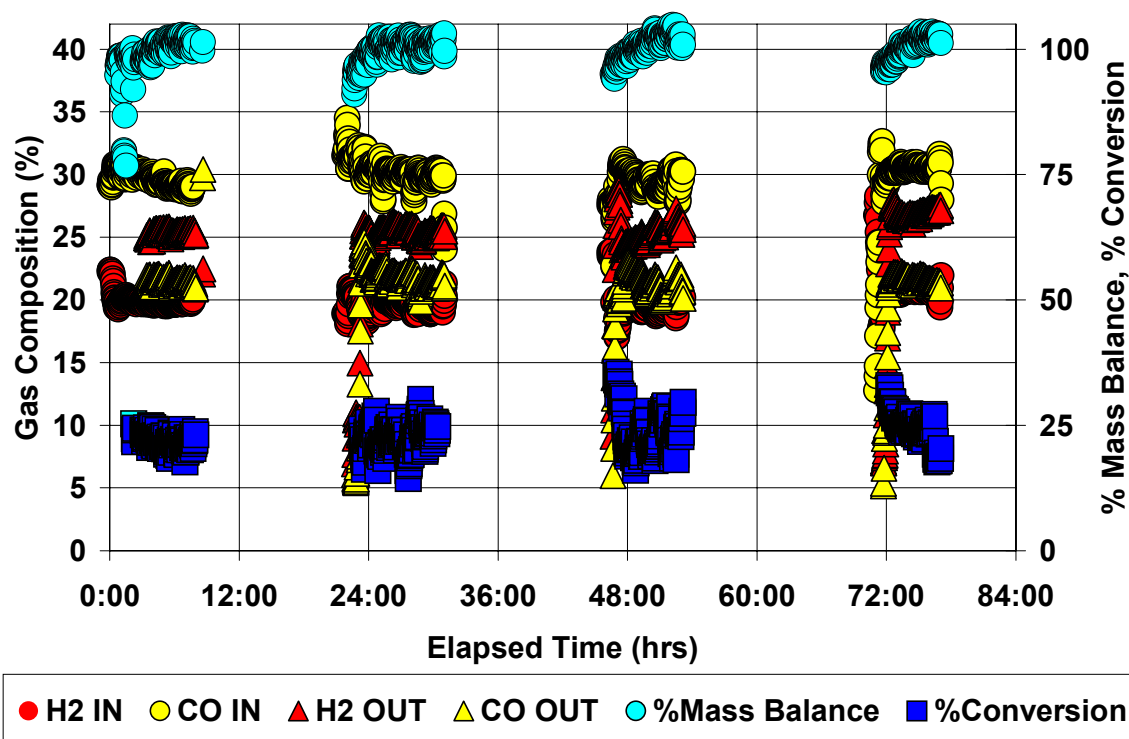


Figure 7. Results from four-day experiment using *Rx. gelatinosus* CBS2 to condition biomass-derived synthesis gas.

Acknowledgments

The authors would like to acknowledge Pin-Ching Maness and Paul F. Weaver of the NREL Basic Sciences Center, who provided guidance and advice throughout the course of this work. Mr. Christopher Doelling performed a number of preliminary experiments.

References

- A.R. Pedersen and E. Arven. "Removal of Toluene in Waste Gases Using a Biological Tricking Filter," 1995. *Biodegradations*. 6:109-118.
- A.S. Foust; L.A. Wenzel; C.W. Clump; L. Maus, and L.B. Anderson. 1980. *Principles of Unit Operations, 2nd Edition*. New York: John Wiley & Sons.

Kimmel, D. E.; Klasson, K. T.; Clausen, E. C., and Gaddy, J. L. 1991. "Performance of trickle-bed bioreactors for converting synthesis gas to methane." *Applied Biochemistry and Biotechnology*, 28/29:457-469.

Klasson, K. T.; Elmore, B. B.; Vega, J. L.; Ackerson, M. D.; Clausen, E. C., and Gaddy, J. L. 1990. "Biological Production of Liquid and Gaseous Fuels from Synthesis Gas." *Applied Biochemistry and Biotechnology*, 24/25:857-873.

Maness, P.-C. and Weaver, P. F. 1994. "Production of poly-3-hydroxyalkanoates from CO and H₂ by a novel photosynthetic bacterium." *Applied Biochemistry and Biotechnology*, 45/46:395-406.

Markov, S.; Weaver, P. F., and Seibert, M. 1997. "Spiral tubular bioreactors for hydrogen production by photosynthetic microorganisms: design and operation." *Applied Biochemistry and Biotechnology*, 63/65:577-584.

Vega, J. L.; Clausen, E. C., and Gaddy, J. L. 1989a. "Study of Gaseous Substrate Fermentations: Carbon Monoxide Conversion to Acetate. 1: Batch Culture." *Biotechnology and Bioengineering*. 34:774-784.

Vega, J. L.; Antorrena, G. M.; Clausen, E. C., and Gaddy, J. L. 1989b. "Study of Gaseous Substrate Fermentations: Carbon Monoxide Conversion to Acetate: 2. Continuous Culture." *Biotechnology and Bioengineering*. 34:785-793.

Weaver, P. F.; Lien, S., and Seibert, M. 1980. "Photobiological production of hydrogen." *Solar Energy*, 24(1):3-45.

DEVELOPMENT OF AN EFFICIENT ALGAL H₂-PRODUCTION SYSTEM

Michael Seibert, Marc Forestier, Liping Zhang and Maria Ghirardi
National Renewable Energy Laboratory
Golden, CO 80401

Abstract

The ultimate goal of our research is to generate *Chlamydomonas reinhardtii* mutants that are sufficiently tolerant to O₂ to produce H₂ under aerobic conditions. We have been addressing this goal by means of both classical genetic and molecular biology approaches. Two generations of algal mutants were produced by application of chemical mutagenesis, selection, and screening to a wild-type algal strain. The H₂ production activity of the mutants showed up to 9 times higher tolerance to O₂ when compared to the parental strain. However, since the algal hydrogenase gene sequence was not known, it was not possible to determine whether the chemical mutagenesis that gave rise to the O₂ tolerant phenotypes was due to a single-point mutation affecting the hydrogenase gene or whether it was due to a secondary mutation in another gene.

We have concomitantly pursued a molecular biology approach, in order to enhance the probability of ultimately obtaining a commercially-viable organism. Our purpose was to first clone the hydrogenase gene and then to use molecular genetic means to generate random mutations in the hydrogenase gene. The transformed genes would be used in the future to re-transform wild-type *C. reinhardtii*, and O₂-tolerance of the resulting transformants would be determined by chemochromic screening, as was done for the classical mutants.

Current results include the successful cloning and sequencing of not only the Fe-only reversible hydrogenase gene but also a second Fe-only hydrogenase gene in *C. reinhardtii*. Preliminary studies suggesting differences in the expression of the two genes are also reported. The cloning of the algal hydrogenase will also allow us to re-analyze our mutants obtained previously by the classical mutagenesis approach. This will determine the specific locus of each genotype and may help guide us in possible future site-directed mutagenesis approaches to improving O₂ tolerance

Introduction

Mutant bacterial organisms containing hydrogenases that are able to operate at higher O₂ concentrations have been described (Gogotov 1986, McTavish *et al.* 1995, Maness *et al.* 1999), suggesting that the enzyme is amenable to manipulations that may affect its O₂ tolerance. These observations led us initially to investigate several classical genetic approaches to generate and isolate *C. reinhardtii* mutants that can produce H₂ in the presence of O₂. They involved using random chemical mutagenesis of the organism, followed by the application of selective pressures under gradually increasing O₂ concentrations. The two selective pressures (McBride *et al.* 1977; Ghirardi *et al.* 1996, 1997a, 1997b; Flynn *et al.* 1999) were based on the reversible activity of the algal hydrogenase, e.g., H₂-production and H₂-uptake. A chemochromic sensor was also developed to allow us to quickly screen the survivors of the selective pressures for H₂-producing clones. Using this combination of mutagenesis, selection and screening, we isolated two generations of H₂-production mutants, 76D4 and 141F2, with, respectively, 4 and 9 times higher tolerance to O₂ compared to the WT parental strain (Flynn *et al.* 1999; Ghirardi *et al.*, 1999; Seibert *et al.* 2000). We also isolated two generations of H₂-uptake mutants, 104G5 and 155G6, with, respectively, 2 and 3 times higher tolerance to O₂ (Ghirardi *et al.* 1999; Seibert *et al.* 2000). The latter were also more quickly reactivated upon removal of O₂ from the medium.

The classical genetic approach described above is a good choice if one is interested in isolating an O₂-tolerant, H₂-producing *organism*, independent of whether the mutation affects the hydrogenase gene or some other gene that confer the same phenotype in the organism. Indeed, genetic crosses involving our different O₂-tolerant mutants in the future will indicate whether more than one locus is involved in the isolated phenotypes. However, if one proposes to generate an O₂-tolerant *hydrogenase* (instead of an O₂-tolerant, H₂-producing *organism*), the preferable approach is random error-prone polymerase chain reaction (PCR) mutagenesis of the cloned gene. This technique will generate random mutants of the cloned hydrogenase gene, which then will be re-introduced back into the wild-type organism for expression.

The *C. reinhardtii* hydrogenase, an Fe-only enzyme has been isolated to purity by Happe and Naber (1993), who also sequenced 24 amino acid residues from the N-terminal portion of the enzyme. However, until recently, no further information on its amino acid or nucleotide sequence was available. Iron-only hydrogenases are a class of enzymes that catalyze either H₂ production or H₂ uptake. These enzymes have been found in anaerobic bacteria or in green algae, and contain two or three 4Fe4S centers and one 2Fe2S center (Adams 1990). The catalytic site of the enzyme consists of a 4Fe4S and a 2Fe2S and is called the H-cluster. Iron-only hydrogenases usually have high specific activity but are very easily inactivated by O₂ and CO. Two different approaches were used to clone the *C. reinhardtii* enzyme, using the polymerase chain reaction to amplify selected mRNA sequences following their conversion into cDNA by the reverse transcriptase (RT-PCR). In the first approach, degenerate primers were designed based on the N-terminal amino acid sequence of the enzyme (Happe and Naber 1993), and they were used in 5' rapid amplification of cDNA ends (RACE) reactions to partially amplify the corresponding mRNA (Ghirardi *et al.* 1998). Many clones

were obtained, but none succeeded in further amplification of the 3' end of the mRNA. In the end, we were unable to clone and sequence the complete gene by this approach. In this paper, we describe a second approach that turned out to be successful. It was based on the high degree of homology between bacterial and algal Fe-only hydrogenases, which was used to guide the design of gene-specific 5' and 3'-end primers used to amplify the catalytic region of the hydrogenase gene from a pool of algal mRNA. The amplified product was then used as a probe to isolate the complete gene from a cDNA algal library.

Materials and Methods

Cell growth, anaerobic induction, mRNA extraction, reverse transcription and RT-PCR

Chlamydomonas reinhardtii cell wall-less strain cw15 (currently identified as cc125) was grown in the light in 15 mM potassium phosphate, 10 mM NH₄Cl, 1 mM MgSO₄, 1.5 mM Na₃ citrate, 0.5 mM CaCl₂, 0.5 mM FeCl₃ and 1 x Hutner's trace elements (Harris 1989) to an OD₇₅₀ of ~1. Harvested cells were anaerobically induced as previously described (Ghirardi *et al.* 1997) and immediately lysed using binding buffer (S.N.A.P kit, Invitrogen Inc.). The pooled total RNA was further enriched for poly-A⁺ RNA using the FastTrack 2.0 kit by the same manufacturer. The resulting mRNA was reverse transcribed at 50°C using poly-dT₁₅ primers and random hexamers according to the Superscript II kit by Life Technologies Inc. An aliquot of the cDNA was PCR amplified in 30 mM Tricine, pH 8.4 (at 20 °C), 3.5 mM MgCl₂, 5 mM β-mercapto-ethanol, 0.01% gelatin and 0.01% Igepal CA-630, 1.2 mM dNTPs, 1.5 μM primers with annealing at 58 °C for 30 cycles.

cDNA library screening and lambda phage plasmid excision

The amplified products were cloned onto the cloning vector pUC19. An amplification product generated from clone RC53_43 was non-isotopically labeled using digoxigenin-11-dUTP (Roche Molecular Biology) and used to screen a lambda ZAP II *C. reinhardtii* cDNA library (kindly provided by John Davies, Exelixis Inc.). Positive plaques were purified by replating and rescreening and the cDNA inserts retrieved as pBluescript SK(-) plasmids using the Rapid Excision kit by Stratagene Inc, with modifications. The cDNA clone containing the amplified product was designated Hyd A.

Expressed sequence tag (EST) amplification and cDNA library screening

Two specific primers, BE5P1 and BE3P1 were used to amplify an EST (shown to have a high degree of homology to other Fe-only hydrogenases in the GenBank database) from a sample of the cDNA library (see above), using the Failsafe PCR kit (Epicentre Inc.). Clone EST_26, which contained the amplified nucleotide sequence of the EST was used to generate digoxigenin-labelled probes for cDNA library screening. A strongly hybridizing clone, designated Hyd B, was obtained, retrieved in pBluescript SK (-) and shown to be derived from the EST.

DNA sequencing and assembly of Fe-only hydrogenase clones Hyd A and Hyd B

Cesium chloride density gradient purified plasmid DNA was submitted to the primer walk service at the Iowa State University Sequencing and DNA Synthesis Facility. Sequence reads were evaluated based on the chromatograms and assembled using the Wisconsin Package V. 10 software by Genetics Computer Group, Inc. Both strands of the DNA were sequenced independently.

Northern blot analysis

Five μg of total RNA was fractionated by electrophoresis on 1.2% formaldehyde agarose gels and transferred to Nytran N⁺ membranes by capillary blotting. The nucleic acid was fixed by UV cross-linking and baking for 2 h at 80 °C. Membranes were prehybridized in 6 x SSC buffer, 10% dextran sulfate, 50% formamide, 1 x Denhardt's solution, 0.1% SDS and 100 $\mu\text{g}/\text{mL}$ denatured salmon sperm DNA at 42 °C for ≥ 1 h. Denatured ³²P labelled probe was added and the blots were washed at medium stringency (0.5 x SSC, 0.5% SDS at 58 °C) after overnight hybridization. Membranes were exposed to storage phosphor screens (Kodak Inc.) and scanned with a STORM 860 PhosphorImager (Molecular Dynamics Inc.). Quantitation was performed with the ImageQuant software provided. Nytran membranes were stripped in hot 0.5% SDS and rehybridized as needed.

H₂-Evolution Assay

MOPS buffer (50 mM, pH 6.8) was added into a water-jacketed chamber (a 2.5 ml volume held at 25 °C) and equipped with two Clark electrodes (YSI 5331, Yellow Springs, OH), one poised for the measurement of H₂ and the other for O₂ production (Ghirardi *et al.* 1997b). The O₂ concentration in the cuvette was set close to zero with Ar, and 200 μl of anaerobically induced cell suspension were injected into the buffer. The cell suspension was illuminated (320 $\mu\text{E m}^{-2} \text{s}^{-1}$, PAR incandescent light filtered through 1% CuSO₄) for three minutes. The initial rates of H₂ production were estimated from the initial slope of the curves.

Results and Discussion

RT-PCR amplification of the hydrogenase active site

A multiple sequence alignment of Fe-only hydrogenases from *Clostridium pasteurianum*, *Trichomonas vaginalis* and *Desulfovibrio vulgaris* was obtained and used as input to the CODEHOP algorithm (<http://www.blocks.fhcrc.org/codehop.html>) to generate potential primers for the PCR amplification reaction. The chosen primers, RC5 and RC3, had 64 and 32 degeneracies, respectively. An anaerobically induced sample of *C. reinhardtii* provided the source mRNA material for direct RT-PCR amplification. A double-band centered around 800 basepairs was evident in the lanes originating from induced mRNA but not in the controls (not shown). The band was excised and blunt-end cloned into the vector pUC19. One of the resulting clones, RC53_43 showed all four strictly conserved cysteines that are involved in binding the catalytic 4Fe-4S cluster bridged to a 2Fe-

2S cluster, also termed the H-cluster (the active site of the reversible hydrogenase enzyme). It contained a 43 amino acid insertion between H-cluster motif 2 and 3, similar to a 28 amino acid insertion at the same location in a putative Fe-only hydrogenase clone from *Scenedesmus obliquus* (Wunschiers *et al.* 2001). Figure 1 shows that the expression of this active site sequence is dependent upon anaerobiosis, supporting its possible role as a hydrogenase.

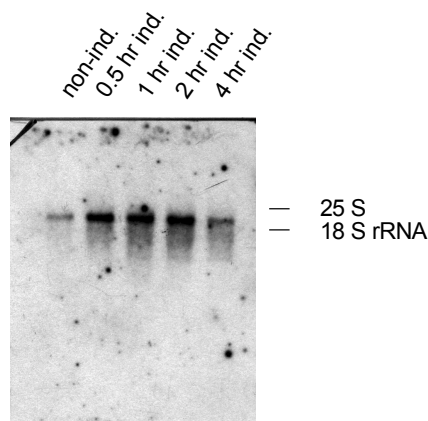


Figure 1. Northern blot of mRNA isolated from non-induced and anaerobically-induced *C. reinhardtii* cells and probed with RC53_43.

Retrieval of full-length Hyd A and Hyd B clones

The active site clone RC53_43 was used as a probe to retrieve a full-length cDNA clone from the cDNA library. From 30,000 lambda plaques plated, 40 hybridized to the active site probe. The lambda plaques were subject to an *in-vivo* excision procedure to obtain the cDNAs as pBluescript SK (-) plasmids. Restriction site analysis and DNA sequencing proved one of our clones, denoted Hyd A, to be 100% identical in the first 1,83 kb to an unpublished clone in GenBank, denoted hyd1 (Accession no. AF 289201). Hyd A was retrieved as a 2.45 kilobase cDNA exhibiting an open reading frame (ORF) encoding 498 amino acids. It also contains the previously reported 24 amino acid N-terminus (Happe and Naber 1993), preceded by a 56 residue leader peptide that directs the protein to the chloroplast stroma.

The deduced amino acid sequence of clone RC53_43 also revealed another close match in a BLAST search to an expressed sequence tag (EST) from *C. reinhardtii*. We designed primers for the amplification of this EST from the cDNA library. The resulting clone EST_26 was identical in nucleotide sequence to the EST, as revealed by DNA sequencing. It was also distinctively different from the active site clone RC53_43 in that it contained a unique restriction site not found in the latter. Clone EST_26 was used as probe to screen a cDNA library, which led to the retrieval of a full-length clone, Hyd B. The Hyd B cDNA is slightly larger in size than Hyd A and is predicted to encode a 505 residue enzyme. An online service (<http://www.cbs.dtu.dk/services/ChloroP-1.0.html>) predicted the presence of a chloroplast sequence with a cleavage site after 16 amino acids from the start of the ORF.

Table 1 shows that a comparison of our newly isolated clones to Hydrogenase I from *Clostridium pasteurianum* (Meyer and Gagnon 1991) and Hyd A from *Scenedesmus obliquus* (Florin *et al.* 2001), as expected, places them in closer relationship with the latter (Accession no. AJ271546, Table 1). *Scenedesmus* and *Chlamydomonas* Fe-only hydrogenases share a number of characteristic features only found in the green algal enzymes: a short (*Scenedesmus*) to intermediate (*Chlamydomonas*) insertion in-between H-cluster motifs 2 and 3 and the lack of the more distal 4Fe-4S clusters normally found in all bacterial and protozoan Fe-only hydrogenases (Cammack 1999). The biological implications of these unique features are not known at present.

Table 1. Comparison of amino acid sequences of different cloned Fe-only hydrogenases.

<i>C. reinhardtii</i> hydrogenase clone	<i>C. pasteurianum</i> Cp 1H	<i>S. obliquus</i> Hyd A
Hyd A	47 % similar, 40 % identical	69 % similar, 63 % identical
Hyd B	48 % similar, 42 % identical	71 % similar, 63 % identical

Analysis of Hyd A and Hyd B mRNA levels upon anaerobic induction

The expression of the two hydrogenase clones was studied by Northern blot analyses, and compared to the expression of the enzyme activity by incubation under anaerobic conditions. Figure 2 (left panel) shows that a small amount of Hyd A mRNA is detected under aerobic conditions (0 h) and that it increases about 4-fold during a 4-h anaerobic incubation period. These data are in agreement with measurements of light-dependent hydrogenase activity (Fig. 2, right panel). The levels of Hyd B mRNA, on the other hand, seem to change little during the anaerobic induction treatment, and do not correlate with enzyme activity. The results suggest that Hyd A encodes the chloroplast reversible Fe-only hydrogenase linked to photosynthetic electron transport through ferredoxin. The nature of the hydrogenase encoded by Hyd B is not known at present. It is possibly a second chloroplast protein, and its physiological role will be the focus of future research.

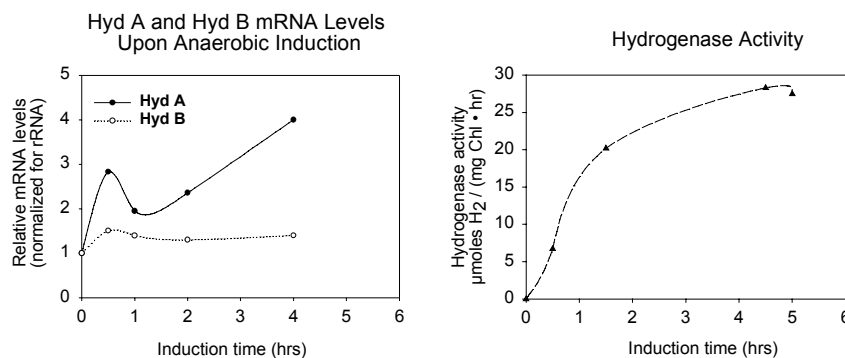


Figure 2. Quantitation of mRNA levels of Hyd A and Hyd B upon anaerobic induction of *C. reinhardtii* cells (A) and overall hydrogenase activity as judged by amperometric measurement of H₂ evolution (B).

Acknowledgements

We thank the Molecular Cellular and Developmental Biology Department at the University of Colorado in Boulder, for allowing us to use their PhosphorImager, and Dr. John Davis from Exelixis Inc., CA for the cDNA library.

References

- Adams, MWW. 1990. The Structure and Mechanism of Iron-Hydrogenases. *Biochim. Biophys. Acta* 1020: 115-145.
- Cammack, R. 1999. Hydrogenase Sophistication. *Nature* 397: 214-215.
- Florin, L, Tsokoglou, A and Happe. 2001. A Novel Type of Fe-Hydrogenase in the Green Alga *Scenedesmus obliquus* is Linked to the Photosynthetic Electron Transport Chain. *J. Biol. Chem.* 276: 6125-6132.
- Flynn, T, Ghirardi, ML and Seibert, M. 1999. Isolation of *Chlamydomonas* Mutants with Improved Oxygen-Tolerance. In *Division of Fuel Chemistry, 1999 ACS Meeting, New Orleans, LA*, vol. 44: 846-850.
- Ghirardi, ML, Markov, S and Seibert, M. 1996. Development of an Efficient Algal H₂-Producing System. In *Proceedings of the 1996 U.S. DOE Hydrogen Program Review*, 285-302, NREL/CP-430-21968.
- Ghirardi, ML, Flynn, T, Markov, S and Seibert, M. 1997a. Development of an Efficient Algal H₂-Producing System. In *Proceedings of the 1997 U.S. DOE Hydrogen Program Review*, 11-24, NREL/CP-430-23722.
- Ghirardi, ML, Togasaki, RK and Seibert, M. 1997b. Oxygen Sensitivity of Algal H₂-Production. *Appl. Biochem. Biophys.* 63-65:141-151.
- Ghirardi, ML, Flynn, T, Forestier, M, Iyer, A, Melis, A, Danielson, P and Seibert, M. 1998. Generation of *C. reinhardtii* Mutants that Photoproduce H₂ from H₂O in the Presence of O₂. In *Photosynthesis: Mechanisms and Effects* (G. Garab, ed.), Kluwer Academic Publishers, The Netherlands, Vol. III, 1959-1962.
- Ghirardi, ML, Flynn, T, Forestier, M and Seibert, M. 1999. Development of an Efficient Algal H₂-Producing System. In *Proceedings of the 1999 U.S. DOE Hydrogen Program Review*, 16-29, NREL/CP-570-26938.
- Gogotov, IN 1986. Hydrogenases of Phototrophic Microorganisms. *Biochimie* 68:181-187.

- Happe, T and Naber, JD. 1993. Isolation, Characterization and N-terminal Amino Acid Sequence of Hydrogenase from the Green Alga *Chlamydomonas reinhardtii*. Eur. J. Biochem. 214:475-481.
- Harris, EH 1989. *The Chlamydomonas Sourcebook*, Academic Press, New York.
- Maness, P-C and Weaver, PF. 1999. Biological H₂ from Fuel Gases and from H₂O. In *Proceedings of the 1999 U.S. DOE Hydrogen Program Review*, 111-124, NREL/CP-570-26938.
- McBride, AC, Lien, S, Togasaki, RK and San Pietro, A 1977. Mutational Analysis of *Chlamydomonas reinhardtii*: Application to Biological Solar Energy Conversion. In *Biological Solar Energy Conversion* (A. Mitsui *et al.*, eds.), Academic Press, New York.
- McTavish, H, Sayavedra-Soto, LA and Arp, DJ. 1995. Substitutions of *Azotobacter vinelandii* Hydrogenase Small-Subunit Cysteines by Serines Can Create Insensitivity to Inhibition by O₂ and Preferentially Damages H₂ Oxidation over H₂ Evolution. J. Bacteriol. 177:3960-3964.
- Meyer, J and Gagnon, J. 1991. Primary Structure of Hydrogenase I from *Clostridium pasteurianum*. Biochem. 30: 9697-9704.
- Seibert, M, Flynn, T and Ghirardi, M. 2000. Strategies for Improving Oxygen Tolerance of Algal Hydrogen Production". In *Biohydrogen II* (Miyake, J., T. Matsunaga and A. San Pietro, eds). Elsevier, pp. 65-75.
- Wünschiers R, Senger H, Schulz R. 2001. Electron pathways involved in H₂-metabolism in the green alga *Scenedesmus obliquus*. Biochim Biophys Acta 1503:271-278.

DISCOVERY OF AN ALTERNATIVE O₂ SENSITIVITY AND ITS POTENTIAL APPLICATION IN PHOTOSYNTHETIC H₂ PRODUCTION

**James Lee and Elias Greenbaum
Chemical Technology Division
Oak Ridge National Laboratory
Oak Ridge, TN 37831-6194**

Abstract

We have discovered a new O₂ sensitivity in algal H₂ production that represents an alternative to the O₂ sensitivity of the hydrogenase per se. The principal findings serving as evidences of this alternative O₂ sensitivity are as follows: (1) the unexpected surge of H₂ photoevolution immediately after the onset of actinic illumination in the continued presence of low concentrations of O₂; (2) the relief effect of FCCP on O₂ inhibition of H₂ photoevolution; (3) the absence of tolerance to the continued presence of the background O₂ in National Renewable Energy Laboratory's O₂-tolerant mutants; and (4) the observation of residual hydrogenase activity at O₂ concentrations as high as 5000 ppm, where the steady-state H₂ photoevolution was inhibited almost completely.

The reported O₂ sensitivity is apparently linked to the photosynthetic H₂ production pathway that is coupled with proton translocation across the thylakoid membrane. Addition of the proton uncoupler (FCCP) can eliminate this mode of O₂ inhibition on H₂ photoevolution. This mode of inhibition is likely due to the background O₂ which apparently can serve as a terminal electron acceptor in competition with the H₂ production pathway for the photosynthetically generated electrons from water splitting. This O₂-sensitive H₂-production electron transport pathway can be inhibited by DCMU. Our experiments demonstrated that this alternative pathway is more sensitive to O₂ than the traditionally known O₂ sensitivity of the hydrogenase. These findings clarify the meaning of "oxygen tolerance" in algal H₂ production by demonstrating the two modes in which atmospheric oxygen interacts with the hydrogen evolution process. Future work will focus on mapping this alternative electron transport pathway and on applying it to enhancing the production of H₂.

Introduction

Algal photosynthetic hydrogen (H_2) production is a potential clean energy resource. In green algae, photoevolution of H_2 and O_2 occurs in the same cell, where the photosynthetically produced O_2 can inhibit the production of H_2 .¹ Therefore, the application of green algae for H_2 production must address the problem of O_2 sensitivity. In the past, this O_2 -sensitive phenomenon was generally interpreted as the direct O_2 -inhibition effect on hydrogenase activity.² In the course of our investigations, we discovered that the classic interpretation of O_2 sensitivity needs to be revised. In recent experiments that characterized O_2 tolerance in H_2 -producing wild-type *Chlamydomonas reinhardtii*, we observed a new O_2 sensitivity that is clearly distinct from that of the hydrogenase. This O_2 sensitivity indicates that there is an alternative electron transport pathway that can redirect electrons from the hydrogenase-catalyzed H_2 -production pathway to O_2 . Our experiments demonstrated that the alternative mechanism is more sensitive to O_2 than the classic O_2 sensitivity of hydrogenase. It is felt that these findings represent a significant progress in algal H_2 production studies. This paper reports the detailed experimental results.

Materials and Methods

Chlamydomonas reinhardtii wild-type strain 137c and O_2 -tolerant mutants 155G6, 141F2, 76D4, and 104G5 were grown under light intensity of about $20 \text{ F E m}^{-2} \text{ s}^{-1}$ in minimal-plus-acetate medium. When the culture grew to a cell density of about 10^6 cells/ml, the algal cells were harvested by gentle centrifugation (3000 RPM). The algal cells were then washed and re-suspended in fresh minimal medium for O_2 -tolerance hydrogen-production assays. The O_2 -tolerance assays were performed under atmospheres of research-grade helium (purity >99.9999%, zero oxygen) and a series of O_2 concentrations [10, 100, 300, 1000 (0.1000%), 5000, and 10,000 ppm O_2] in helium using our unique dual-reactor-flow detection system. The 10, 100, 300, 1000, 5000, and 10,000 ppm O_2 in helium were primary standards purchased from Matheson Gas and Equipment, Inc.

As illustrated in Fig. 1, the assays were conducted using a laboratory-built dual-reactor flow detection system.³ For each assay, 35 ml of algal sample (3 Fg Chl/ml) was placed and sealed in each of the two reactors that are water-jacketed and held at 20°C with a temperature-controlled water bath (Lauda RM6, Brinkmann Instruments, Germany). The algal sample was then purged by helium flow (50 ml gas/min) through the liquid reaction medium. The helium flow serves two purposes: (1) to remove O_2 from the algal sample to establish and maintain anaerobic conditions that are necessary for induction of the algal hydrogenase synthesis and production of H_2 and (2) to carry any H_2 gas product to the hydrogen sensors. After induction of hydrogenase and establishment of steady-state photoevolution of H_2 under the helium atmosphere (which normally required about 8 h or more), the primary standards 10, 100, 300, 1000, 5000, and 10,000 ppm O_2 in helium were introduced into the reactors by replacing the pure helium at the same flow rate (50 ml/min) to characterize the oxygen sensitivity of photoevolution of H_2 . The actinic illumination at $100 \text{ u E m}^{-2} \text{ s}^{-1}$ (about 5% of the full LED intensity) for the H_2 photoevolution assay was provided by an electronically controlled LED light source with its full (100%) intensity of about 2000

$uE_{670}^{1.2 \times 10^{11}}$ at 670 nm. The actinic intensity was measured with an IL-1700 light meter. Both the rate of H_2 production and the actinic intensity were recorded simultaneously by a PC computer.

For the chemical inhibitor studies, 3-(3,4-dichlorophenyl)-1,1-dimethyl-urea (DCMU) and carbonyl cyanide *p*-(trifluoromethoxy) phenylhydrazone (FCCP) were purchased from Sigma Chemical Company. Stock (500 μM) solutions of these chemicals were made. Then, small aliquots of the stock solutions were injected into the reactors to give the final concentrations of 10 μM DCMU and 5 μM FCCP in the reaction medium as specified in the particular experiments.

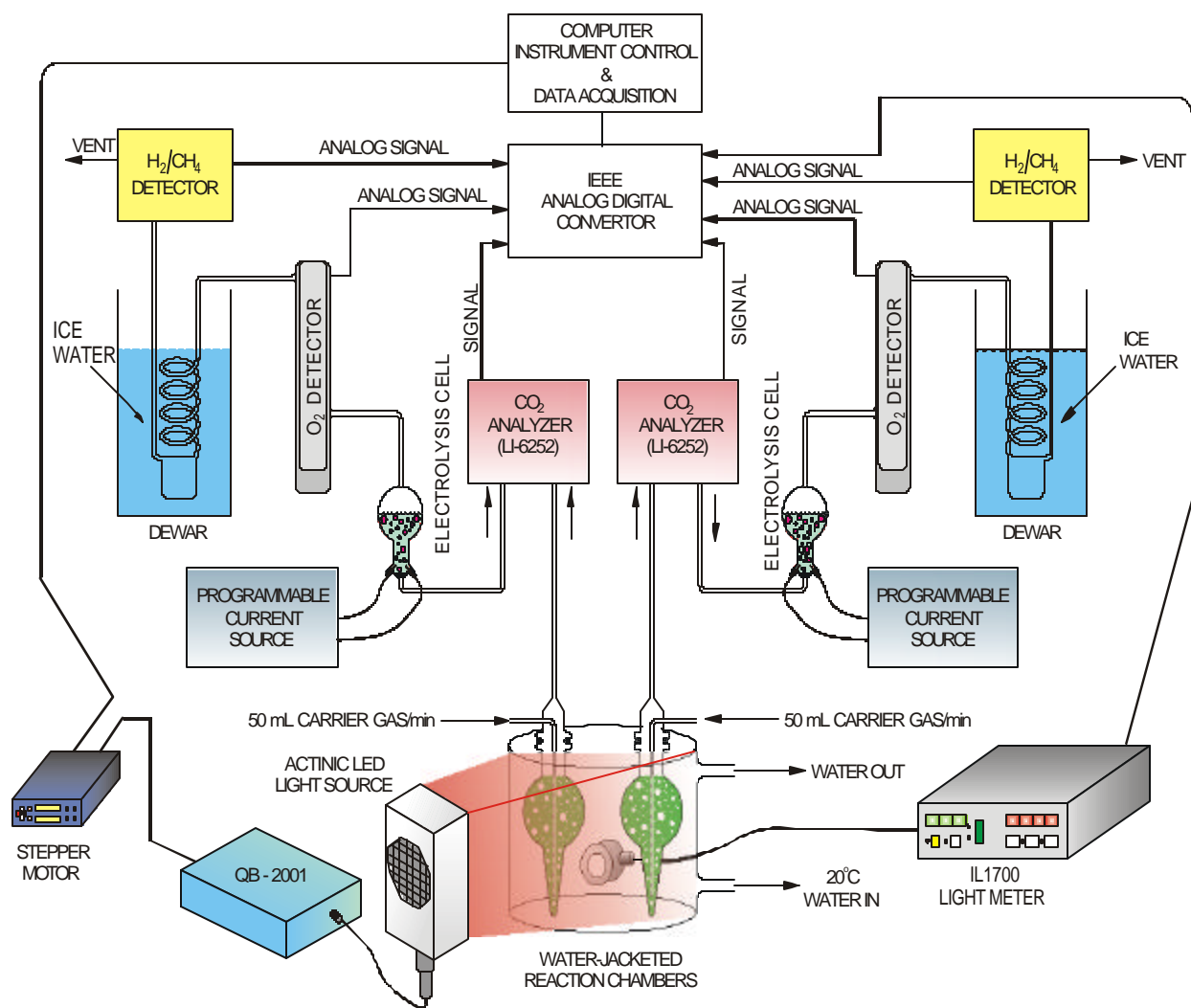


Figure 1. Schematic of a dual-reactor flow detection system for simultaneous detection of CO_2 , H_2 , and O_2 .

Results and Discussion

First Evidence of a New O₂ Sensitivity in Algal H₂ Production

The results of the assays are very intriguing. As illustrated in Fig. 2, introduction of 0.1000% (1000 ppm) O₂ dramatically reduced the rate of algal H₂ photoevolution. The steady-state H₂ production rate in the presence of 0.1000% O₂ was 0.33 μmol H₂/mg Chl^l·h^l which is only about 2.8% of the full steady-state rate (12 μmol H₂/mg Chl^l·h^l) before the introduction of the 0.1000% O₂. In the past, this type of H₂ production decay was commonly interpreted as the inhibition of O₂ on hydrogenase activity. Our experimental results have now proved that this classic interpretation of oxygen sensitivity on algal H₂ production is not consistent with the data. According to the classic interpretation, the reduction of H₂ production after the introduction of 0.1000% O₂ is due to O₂ inhibition on hydrogenase per se: that is, hydrogenase activity would be the limiting factor for the rate of H₂ photoevolution. If this interpretation were correct, one would expect the rate of H₂ photoevolution to be no higher than the inhibited rate (0.33 μmol H₂/mg chl^l·h^l) after a brief dark period in the presence of 0.1000% O₂. However, the experimental data turned out to be very different from the classic expectation. As shown in Fig. 2, there was a

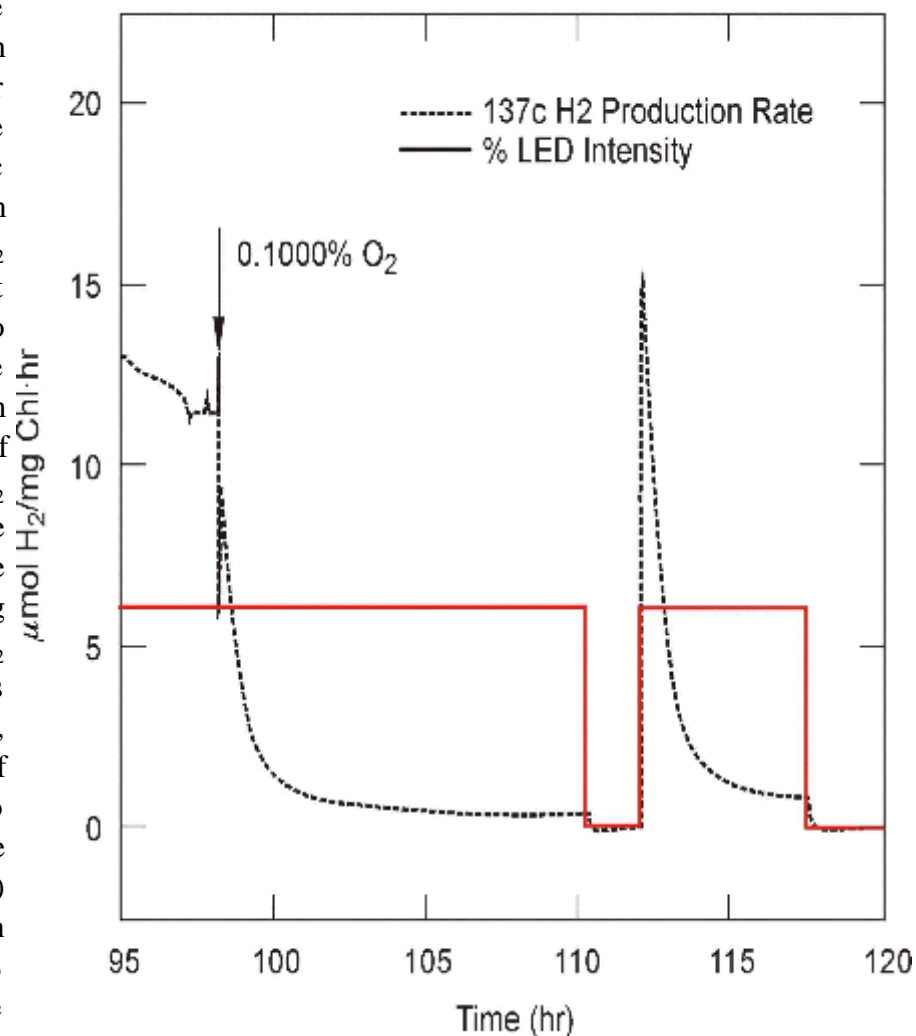


Figure 2. Observation of a new O₂ sensitivity to algal H₂ production in *Chlamydomonas reinhardtii*.

surge of H₂ photoevolution after a 2-h dark period *in the continued presence of 0.1000% O₂*. The peak rate of H₂ photoevolution was about 15 μmol H₂@mg Chl¹·h¹ which is about 45 times higher than the classically predicted rate (0.33 μmol H₂@mg Chl¹·h¹). This assay has now been repeated for more than 6 times and all the results were consistent with the observation presented in Fig. 2.

This observation clearly indicated that hydrogenase activity was not the limiting factor for H₂ photoevolution at this level of O₂. There must be an alternative electron transport pathway that takes the photogenerated electrons away from ferredoxin (Fd) to O₂. The observed reduction of H₂ production after the introduction of 0.1000% O₂ can be explained by such a pathway that competes for electrons with the Fd/hydrogenase-catalyzed H₂-production pathway. This is an important discovery since it fundamentally redefines the meaning of “oxygen tolerance” in algal H₂ production.

Evidence for a New O₂ Sensitivity from Studies with DCMU and FCCP

Our studies with the chemical inhibitor (DCMU) and proton uncoupler (FCCP) have yielded additional evidence for the new O₂ sensitivity.

FCCP is a proton uncoupler that can dissipate the proton gradient across the thylakoid membrane in algal cells. As illustrated in Fig. 3, in the presence of 1000-ppm O₂ after the induction of the hydrogenase enzyme, the steady-state photoevolution of H₂ around the time of 20:00 hours was slightly less than 1 μmol H₂@mg Chl¹·h¹. After a brief dark period (from 20:20 to 22:20), a burst of H₂ photoevolution appeared, followed by an oscillation in the decay curve. Since both the actinic intensity and the background O₂ concentration (1000 ppm) remained the same, this oscillation also indicated that the decay (inhibition) in the rate of H₂

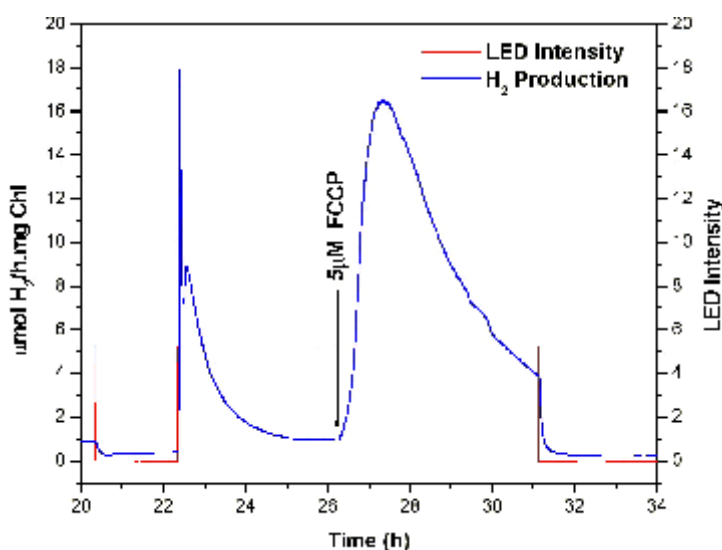


Figure 3. Evidence of a new O₂ sensitivity from H₂ production assays with proton uncoupler FCCP under continued presence of 1000-ppm O₂ in *C. reinhardtii* 137c.

photoevolution resulted not from O₂ inhibition of the hydrogenase enzyme per se but from a kinetic effect of O₂ on the electron transport that is related to the H₂-production process. Addition of 5 μM FCCP produced a dramatic reversal of the O₂ inhibition on H₂ photoevolution. The rate of H₂ production rose to about 16 μmol@mg Chl¹·h¹. This FCCP-stimulated H₂ production is clearly photo-dependent. As soon as the actinic light was turned off, the H₂ production stopped. The data (Fig. 3) also demonstrated that the FCCP-enhanced photoevolution of H₂ can last for more 4 hours with somewhat decay. The decay is due to a side effect of FCCP known as the ADRY effect in which FCCP gradually inhibits PSII activity

by deactivation of the photosynthetic water-splitting complex in the S_2 and S_3 states.⁴ However, FCCP does not have any known effect on the hydrogenase enzyme per se. Therefore, the observed stimulation of H_2 photoevolution by FCCP in the presence of 1000 ppm O_2 is additional evidence for a new O_2 sensitivity in algal H_2 production that is alternative to the oxygen sensitivity to hydrogenase per se. The result clearly demonstrated that the newly discovered O_2 -sensitive electron transport pathway requires the presence of a proton gradient (or ATP) to operate.

DCMU is a chemical inhibitor that binds at the Q_B site of photosystem II (PSII) and thus blocks the transport of electrons acquired from PSII water splitting to photosystem I (PSI). The experimental data (Fig. 4) showed that addition of DCMU inhibited the burst of H_2 photoevolution after a dark period in the presence of 1000-ppm background O_2 . This result indicated that over 90% of the electrons that are used in the photoproduction of H_2 are derived from PSII water splitting. Therefore, water is the main source of electrons for H_2 production even after the dark period in the presence of 1000 ppm O_2 . Organic reserves are not the main source of electrons in this mode of H_2 production.

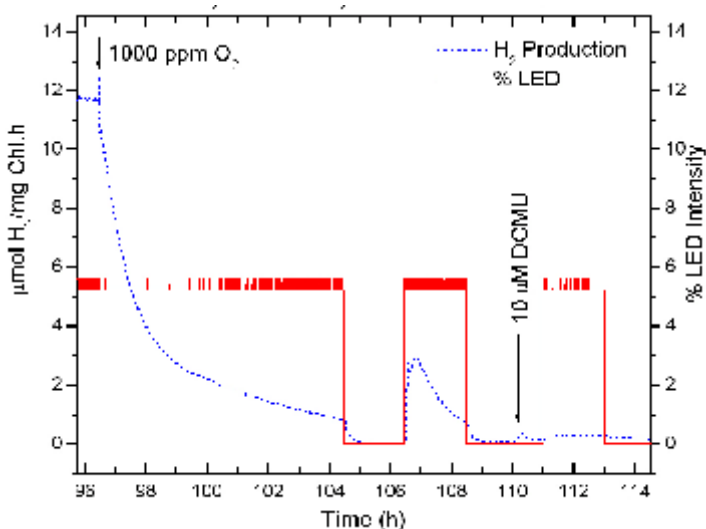


Figure 4. O_2 -tolerance assay in algal H_2 production with DCMU.

Evidence for a New O_2 Sensitivity from Studies with O_2 -Tolerant Mutants

There is an active DOE research effort to produce H_2 -producing, O_2 -tolerant mutants of green algae *Chlamydomonas reinhardtii*.^{5, 6} Using classical chemical mutagenesis and metronidazole-selection techniques, a number of H_2 -producing O_2 -tolerant mutants of *Chlamydomonas reinhardtii* (e.g., 155G6, 141F2, 76D4, and 104G5) have been recently generated at National Renewable Energy Laboratory (NREL). According to the short-term O_2 -tolerance assays that were conducted at NREL, mutants 76D4 and 141F2, respectively, had 4 and 9 times higher O_2 tolerance than did the wild-type parental strain. Mutant strains 104G5 and 155G6 reportedly have an O_2 tolerance 13 times higher than that of the wild-type parental strain.⁷ In a collaborative effort with Drs. M. Seibert and M. Ghirardi of NREL, all of these mutants were sent to our Oak Ridge National Laboratory (ORNL) for O_2 -tolerance assays with continuous exposure to low concentrations of O_2 . The experimental results showed that none of the mutants possess any sustained O_2 tolerance under the steady-state assay conditions. A typical experimental result is presented in Fig. 5 for mutant strain 155G5 and its wild-type parent 137c. When the carrier gas was

shifted from pure helium to 1000-ppm O₂ in helium, H₂ photoevolution decayed at essentially the same rate—from about 13 to 1 μmol H₂/mg Chl/h— in both mutant 155G6 and the wild type 137c. This result indicates that mutant 155G6 does not possess improved O₂-tolerant properties under these steady-state conditions. However, the spike (the initial rate) of H₂ production immediately followed the onset of the actinic illumination after a 2-h dark period was higher in 155G6 than in 137c. The observed higher initial rate in 155G6 compared with that of 137c seems consistent with results of NREL's short-term O₂-tolerance assays, which

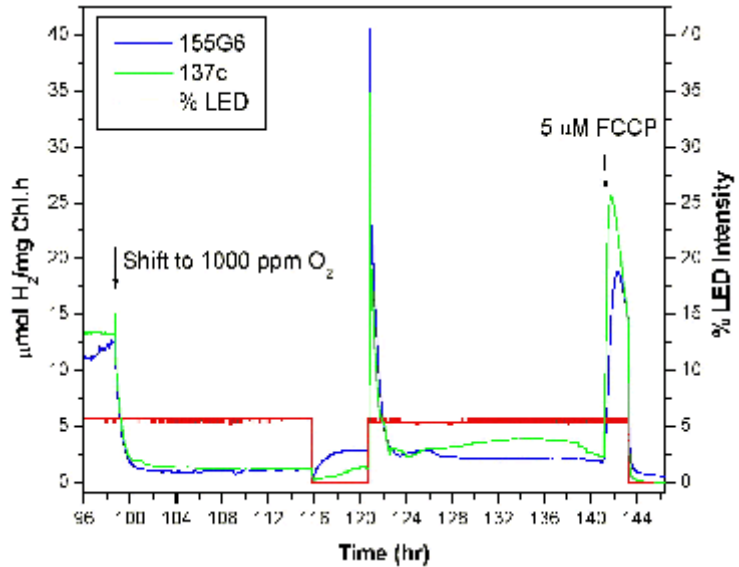


Figure 5. O₂-tolerance assay with NREL mutant 155G6 and the wild-type parental strain 137c.

may reflect the O₂ tolerance of the hydrogenase per se. The H₂ photoevolution (Fig. 5) showed that the spike was followed by a quick oscillation and then a quite steady decay in the rate of H₂ production in both 155G6 and 137c. Also, both of the strains responded to the addition of 5 μM FCCCP and resulted in dramatic relief of O₂ inhibition on the H₂ photoevolution. These similarities between 155G6 and 137c in the response to the presence of the continuous background (1000-ppm) O₂ and to the addition of FCCCP also suggested that the observed inhibition in the steady-state H₂ photoevolution was due to the newly discovered oxygen sensitivity that is alternative to the O₂ sensitivity to the hydrogenase per se.

Kinetic Characterization of the New O₂ Sensitivity

This newly discovered O₂ sensitivity was further characterized by using a series of different O₂ concentrations. The experimental results showed that introduction of 100-ppm O₂ had no significant effect on the steady-state rate of H₂ photoevolution in 137c (Fig. 6). However, addition of 300-ppm O₂ began to show some inhibitory effect on H₂ production (Fig. 7). When the O₂ concentration was raised to 5000 ppm, the inhibition on H₂ production was dramatic and the rate H₂ photoevolution decreased to nearly zero (Fig. 8). However, the

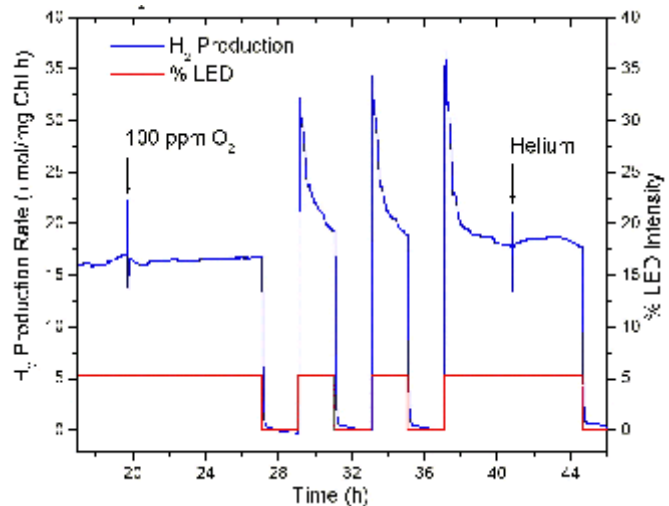


Figure 6. Wild-type algal H₂ production can tolerate 100-ppm O₂.

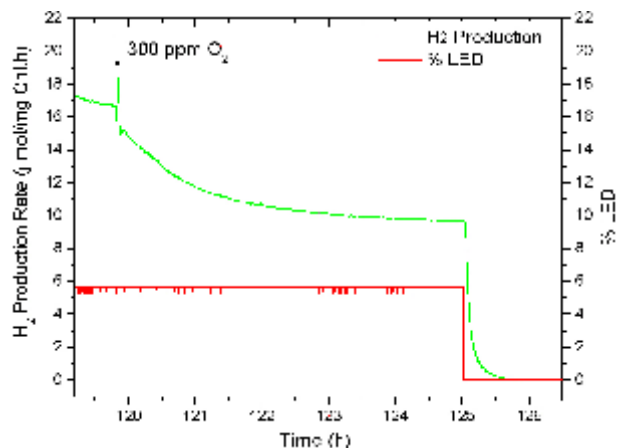


Figure 7. Introduction of 300-ppm O₂ leads to partial inhibition of algal H₂ production.

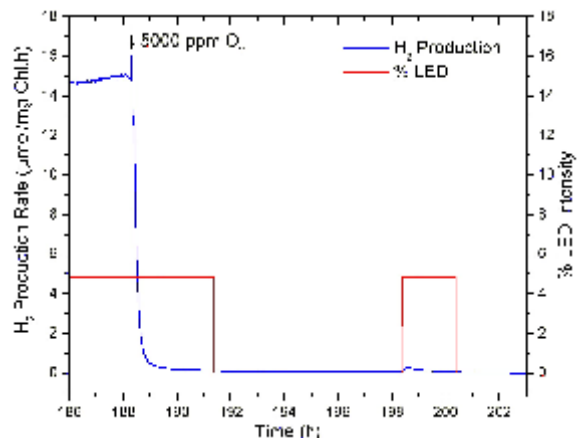


Figure 8. Introduction of 5000-ppm O₂ has dramatic inhibition of H₂ production, but the hydrogenase remains active.

hydrogenase in the algal cells was still active even after the continued presence of 5000 ppm O₂ for more than 10 h. When the actinic was turned on again after hour 198, a small peak of H₂ photoproduction was observed. As illustrated in the expanded scale (Fig. 9), this H₂ photoproduction peak was clearly above the background noise and/or dark-H₂ signal, indicating the presence of active hydrogenase in the algal cells. Therefore, the hydrogenase in the wild-type cells can tolerate up to 5000 ppm of O₂.

Figure 10 plots percentage of steady-state H₂-production rate against the background O₂ concentrations in the mutant 141F2 and the wild-type 137c. This result indicates that compared with the wild type, mutant 141F2 does not possess improved O₂-tolerant properties under these steady-state conditions. Thus, with respect to this newly discovered O₂ sensitivity, mutant 141F2 showed no more tolerance to O₂ than its wild-type parental strain 137c. The O₂ concentration that gave 50% inhibition of H₂ photoevolution was about 500 ppm for both the mutant and the wild type.

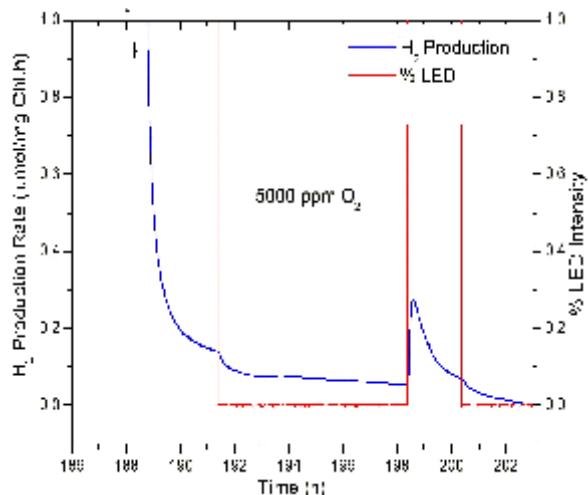


Figure 9. Expanded scale of Fig. 8, showing a clear peak of H₂ photoevolution after 10 h of continued presence of 5000-ppm O₂.

Conclusions

We have discovered a new O₂ sensitivity in algal H₂ production that is different from the O₂ sensitivity of the hydrogenase. The principal findings serving as evidence of this new O₂ sensitivity are as follows: (1)

the unexpected surge of H₂ photoevolution immediately after the onset of actinic illumination in the continued presence of low concentration of O₂; (2) the relief effect of FCCP on O₂ inhibition of H₂ photoevolution; (3) the absence of tolerance to the continued presence of the background O₂ in NREL's O₂-tolerant mutants; and (4) the observation of hydrogenase activity at O₂ concentrations as high as 5000 ppm, where the steady-state H₂ photoevolution was inhibited almost completely.

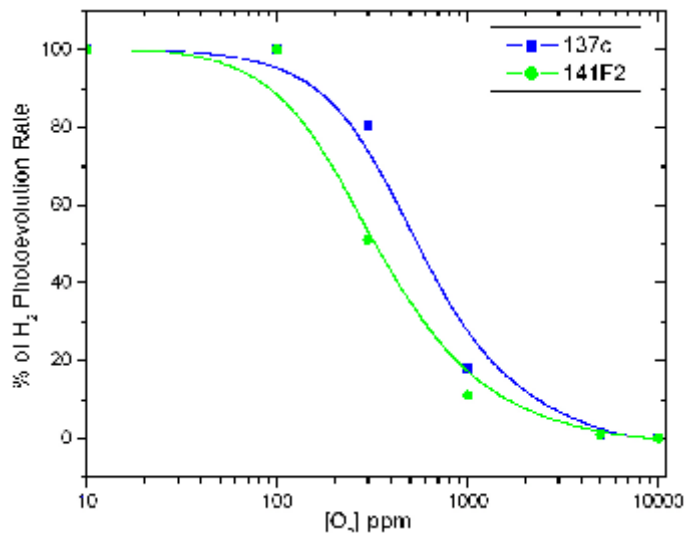


Figure 10. Effect of background O₂ concentrations on steady-state H₂ photoevolution.

This newly discovered O₂ sensitivity is apparently linked to the photosynthetic H₂ production pathway that is coupled with proton translocation across the thylakoid membrane. Addition of the proton uncoupler

(FCCP) can eliminate this mode of O₂ inhibition on H₂ photoevolution. This mode of O₂ inhibition on H₂ production is likely due to the background O₂, which apparently can serve as a terminal electron acceptor in competition with the H₂ production pathway for the photosynthetically generated electrons from water splitting. This O₂-sensitive H₂-production electron transport pathway can be inhibited by DCMU. Our experiments demonstrated that this alternative mechanism is more sensitive to O₂ than the O₂ sensitivity of the hydrogenase. These findings redefine oxygen tolerance in algal H₂ production. Future work should focus on mapping this alternative electron transport pathway and on developing a technique to control this pathway to enhance the production of H₂.

Future Work

Our future work will focus on mapping this alternative electron transport pathway and on developing a new approach to enhance the production of H₂ based on the new findings.

Mapping Out the Pathway

As discussed previously, this newly discovered O₂ sensitivity apparently represents a new pathway in the photosynthetic H₂ production that is coupled with proton translocation across the thylakoid membrane. As illustrated in Fig. 11, the site for the reduction of O₂ could be at the RuBisCo enzyme, which can serve as both a RuDP carboxylase and/or a RuDP oxygenase in the Calvin cycle. Under the conditions for H₂ photoevolution where CO₂ is not present and ATP is abundant owing to the associated photophosphorylation, the Calvin-cycle enzymes are fully activated and RuBisCo could act as a strong oxygenase. This hypothesis can explain how FCCP mitigates the O₂ inhibition of H₂ photoevolution, since

the operation of the Calvin cycle requires formation of ATP using the proton gradient across the thylakoid membrane. Another possible site for the O₂ interaction could be at Ferredoxin (Fd), which could also serve as the electron donor to O₂ (as in the classic Mehler reaction). More experimental studies are needed to completely elucidate the O₂-sensitive H₂-production electron transport pathway. We plan to elucidate this pathway by using more chemical inhibitors and a RuBisco-deficient mutant of *Chlamydomonas reinhardtii* in our experimental studies. RuBisco-deficient mutants, such as strain 76-5EN, which was generated by chemical mutagenesis, are now available. We will obtain RuBisco-deficient mutant 76-5EN from the *Chlamydomonas*

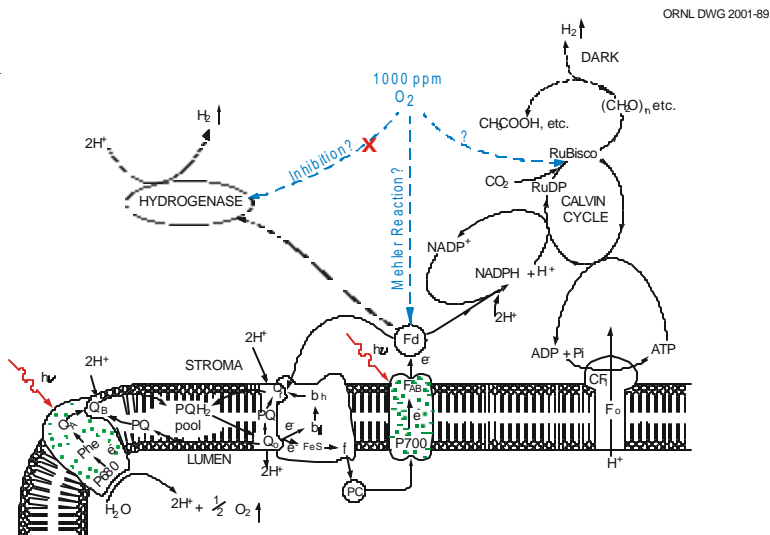


Figure 11. The newly discovered O₂ sensitivity is likely due to the background O₂ (at about 1000 ppm levels) acting as a terminal sink, in competition with the Fd/hydrogenase H₂ production pathway, for photosynthetically generated electrons.

Genetic Center at Duke University. Use of this mutant in our future assays should make it possible to confirm whether RuBisco is indeed the site where the background O₂ could act as a terminal sink for the photosynthetically generated electrons and thus reduce H₂ production because of the nonproductive drainage of the reducing power (electrons). If RuBisco is indeed the site where the background O₂ enters the pathway, the H₂ photoevolution in a RuBisco-deficient mutant is expected to have a sustained tolerance to the background O₂.

Developing a New Approach to Enhance H₂ Production

Our experimental studies have demonstrated that addition of the proton uncoupler FCCP can enhance H₂ photoevolution by eliminating or reducing the activity of the newly discovered O₂ sensitivity. If the site of O₂ entry is indeed at the RuBisco enzyme, then a RuBisco-deficient mutant could, theoretically, also be free of this O₂ sensitivity for H₂ production. However, a RuBisco-deficient mutant cannot grow photoautotrophically and requires organic substrate for its photoheterotrophic growth. Moreover, it lacks the ability to overcome the problem of proton-gradient buildup that impedes the linear electron transport from PSII water splitting to the Fd/hydrogenase in H₂ photoevolution.⁸ Therefore, it is probably impractical to use such a RuBisco-deficient mutant for large-scale H₂ production.

Addition of proton uncouplers such as FCCP could eliminate both the problems of back-proton accumulation and the newly discovered O₂ sensitivity. However, most of these chemical proton uncouplers, such as FCCP, carbonyl cyanide *m*-chlorophenylhydrazone (CCCP), and anilinothiophene,

have undesirable side effects such as the ADRY effect that can damage the photosynthetic activity in algal cells. Also, these chemicals are hazardous materials that are environmentally unacceptable for large-scale applications. Therefore, we propose a technique to overcome these problems in a more effective way.

This new approach is to insert a piece of DNA that contains a hydrogenase promoter and a CF1 suppressor (or a proton-channel gene) into a host alga as illustrated in Fig. 12.

This DNA insertion can be achieved by using the techniques of gene transformation. The CF1-suppressor or proton-channel gene will not be expressed under aerobic conditions since the hydrogenase promoter is activated only under anaerobic conditions. Therefore, the transformed alga should be able to perform autotrophic photosynthesis using ambient air CO₂ as the carbon source and grow normally under aerobic conditions such as in an open pond. When the algal culture is grown and ready for H₂ production, the CF1-suppressor or proton-channel gene can then be expressed simultaneously with the induction of the hydrogenase enzyme under anaerobic conditions. The expression of the CF1 suppressor should create CFo, which could act as a free proton channel without the CF1 cap, thus dissipating the proton gradient across the thylakoid membrane without ATP formation (Fig. 13).

The effect of the free CFo channel on H₂ photoevolution could be twofold. (1) The accumulation of proton gradient that impedes the photosynthetic electron transport from water to Fd/hydrogenase could be prevented; and (2) The newly discovered O₂ sensitivity could be avoided by

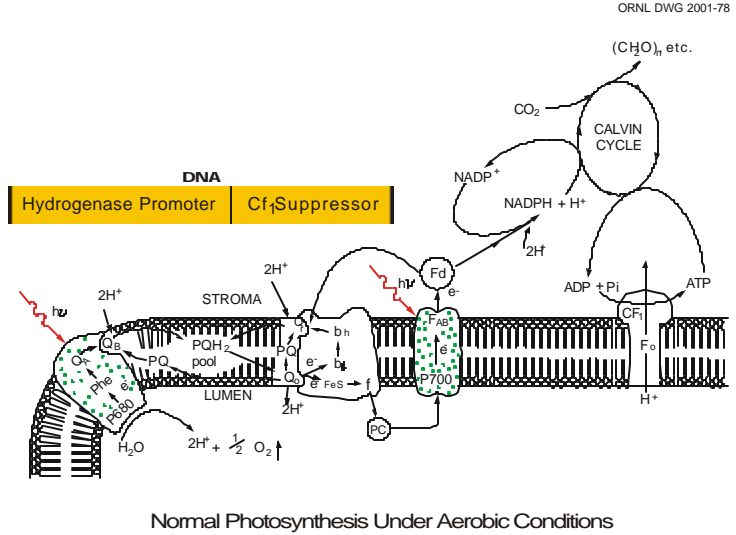


Figure 12. A transformed alga that contains the DNA of a hydrogenase promoter and a CF1 suppressor could grow photoautotrophically using ambient air CO₂.

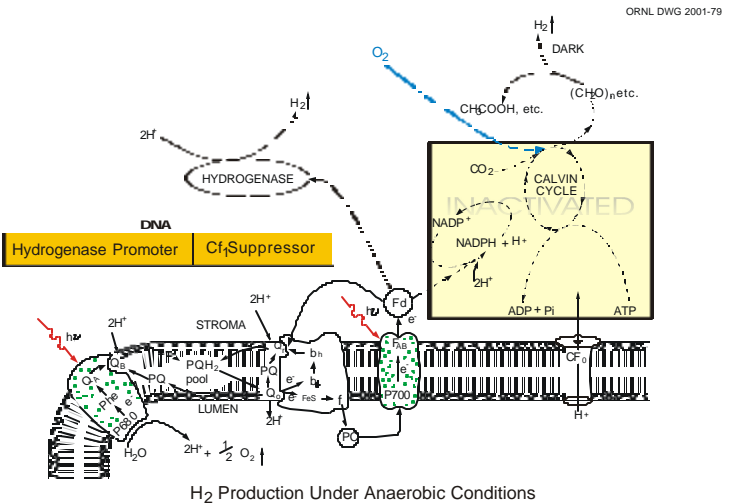


Figure 13. Expression of the CF1 suppressor to create free CFo (without CF1 cap) simultaneously with induction of the hydrogenase in the transformed alga. CFo could serve as a proton channel to dissipate the proton gradient to enhance H₂ production.

(2) The newly discovered O₂ sensitivity could be avoided by

eliminating the photophosphorylation that is required for the activation of the Calvin cycle and the RuDP-oxygenase activity of the RuBisCo enzyme (assuming that the entry of the background O_2 is indeed at the RuBisCo).

Membrane proton channels made of synthetic polypeptides have already been demonstrated. From the known polypeptide sequence, a corresponding DNA sequence for a polypeptide proton channel can now be constructed. Therefore, construction and transformation of a vector that contains the hydrogenase promoter and a synthetic DNA sequence for the polypeptide proton channel are probably more achievable. Expression of such a polypeptide proton channel (Fig. 14) should provide the same benefits to enhance H_2 photoevolution as those from the free CFo channels (Fig. 13). Our collaborator, Prof. Laurie Mets of the University of

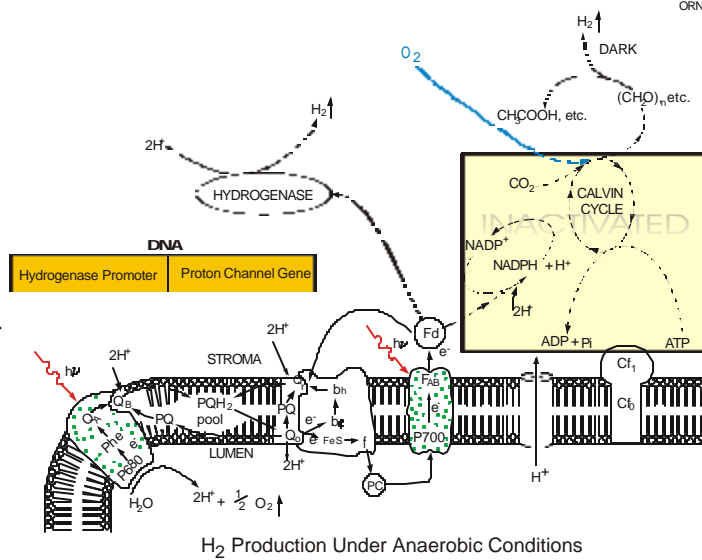


Figure 14. Development of an efficient algal H_2 -production system by construction and transformation of a vector that contains the hydrogenase promoter and a piece of synthetic DNA for a polypeptide proton channel. The transformed alga could grow normally using ambient air CO_2 under aerobic conditions without the polypeptide proton channel, which could be expressed only with the induction of the hydrogenase under anaerobic conditions when its function is needed for enhanced H_2 production.

Chicago, has already cloned a hydrogenase promoter. In our future work, we will focus on the construction and transformation of a vector that contains the hydrogenase promoter and a synthetic DNA sequence for the polypeptide proton channel into *Chlamydomonas reinhardtii* DSP521. DSP521 is a genetically modified strain for which we have experimentally demonstrated the higher overall photon-utilization efficiency which is attributed to its smaller chlorophyll-antenna size in comparison with that of its wild-type parental strain DES15.⁹ Coordinated expression of the polypeptide proton channel (or CF1 suppressor) simultaneously with the induction of the hydrogenase would transform algal cells into inexpensive, effective, and environmentally friendly machines for production of H_2 by photosynthetic water splitting.

Acknowledgments

The authors thank C. A. Woodward, B. Forbes, and B. Kusiak for culture media preparation; A. Jones for secretarial support; M. K. Savage for editorial assistance; and C. D. King and V. W. Purdue for

technical illustrations. We are grateful to Drs. M. Seibert and M. L. Ghirardi of National Renewable Energy Laboratory for their O₂-tolerant mutants and stimulating discussions. This research was supported by the U.S. Department of Energy Hydrogen Program and the DOE Office of Science Young Scientist Award (to J. W. Lee). Oak Ridge National Laboratory is managed by UT-Battelle, LLC, for the U.S. Department of Energy under contract DE-AC05-00OR22725.

References

1. Greenbaum, E., and J. W. Lee 1998. "Photosynthetic hydrogen and oxygen production by green algae." In *BioHydrogen*, O. R. Zaborsky ed., pp. 235–241. New York, Plenum Press.
2. Ghirardi, M. L., R. K. Togasaki, and M. Seibert 1997. "Oxygen sensitivity of algal H₂-production" *Applied Biochemistry and Biotechnology*, 63-65:141–151.
3. Lee, J. W., S. L. Blankinship, and E. Greenbaum 1995. "Temperature effect on production of hydrogen and oxygen by *Chlamydomonas* cold strain CCMP1619 and wild-type 137c" *Applied Biochemistry and Biotechnology*, 51/52:379–385.
4. Samuilov, V. D., E. L. Barsky, and A. V. Kitashov 1995. "ADRY agent-induced cyclic and non-cyclic electron transfer around photosystem II" *Photosynthesis: from Light to Biosphere*, P. Mathis (ed.), Vol. II, 267–270. The Netherlands, Kluwer Academic Publishers.
5. Ghirardi, M. L., S. Markov, and M., Seibert 1996. "Development of an efficient algal H₂-producing system," in Proceeding of the 1996 U.S. Department of Energy Hydrogen Program Review, vol. I, NREL/CP-21908430, pp. 285–302.
6. Seibert, M., T. Flynn, D. Benson, E. Tracy, and M. Ghirardi 1998. "Development of selection and screening procedures for rapid identification of H₂-producing algal mutants with increased O₂ tolerance," In *Biohydrogen*, O. R. Zaborsky, ed., pp. 227-234. New York, Plenum Press.
7. Ghirardi, M. L., Z. Huang, M. Forestier, S. Smolinski, M. Posewitz, and M. Seibert 1999. "Development of an efficient algal H₂-production." in *Proceeding of the 1999 U.S. Department of Energy Hydrogen Program Review*.
8. Lee, J. W. and E. Greenbaum 1997. "A new perspective on hydrogen production by photosynthetic water splitting." ACS Symposium Series 666, *Fuels and Chemicals from Biomass*, B. C. Saha and J. Woodward, eds. Chapter 11, pp. 209–222.

- 9 . Lee, J. W. , L. Mets, and E. Greenbaum 2001. “Improvement of photosynthetic CO₂ fixation at high light through reduction of chlorophyll antenna size.” *Applied Biochemistry and Biotechnology*, submitted.

**ABSENCE OF THE PIGMENTS LUTEIN, VIOLAXANTHIN
AND NEOXANTHIN AFFECTS THE FUNCTIONAL
CHLOROPHYLL ANTENNA SIZE OF PHOTOSYSTEM-II
BUT NOT THAT OF PHOTOSYSTEM-I IN THE
GREEN ALGA *CHLAMYDOMONAS REINHARDTII***

**Juergen E. W. Polle, Krishna K. Niyogi, Anastasios Melis
University of California, Berkeley
Department of Plant and Microbial Biology
411 Koshland Hall
Berkeley, CA 94720-3102, U.S.A.**

Abstract

Chlamydomonas reinhardtii double mutant *npq2 lor1* lacks the β,ϵ -carotenoids lutein and loroxanthin as well as all β,β -epoxycarotenoids derived from zeaxanthin (e.g. violaxanthin and neoxanthin). Thus, the only carotenoids present in the thylakoid membranes of the *npq2 lor1* cells are β -carotene and zeaxanthin. The effect of these mutations on the photochemical apparatus assembly and function was investigated. In cells of the mutant strain, the content of photosystem-II (PSII) and PSI was similar to that of the wild type, but *npq2 lor1* had a significantly smaller PSII light-harvesting Chl antenna size. In contrast, the Chl antenna size of PSI was not truncated in the mutant. SDS-PAGE and Western blot analysis qualitatively revealed the presence of all LHCII and LHCI apoproteins in the thylakoid membrane of the mutant. The results showed that some of the LHCII and most of the LHCI were assembled and functionally connected with PSII and PSI, respectively. Photon conversion efficiency measurements, based on the initial slope of the light-saturation curve of photosynthesis and on the yield of Chl *a* fluorescence *in vivo*, showed similar efficiencies. However, a significantly greater light-intensity was required for the saturation of photosynthesis in the mutant than in the wild type. It is concluded that zeaxanthin can successfully replace lutein and violaxanthin in the functional light-harvesting antenna of the *npq2 lor1* mutant.

Introduction

Higher plants and green algae collect light energy for photosynthesis by an antenna system consisting of pigment-protein complexes. These complexes contain Chl and a variety of carotenoids (Car) with different cyclic end-groups (Cunningham and Gantt 1998). The various Car are distributed among the photosynthetic complexes in the thylakoid membrane and play multiple roles in photosynthesis. They contribute to light harvesting, maintain structure and function of the photosynthetic complexes, quench Chl triplet states, scavenge reactive oxygen species, and dissipate excess energy (Demmig-Adams et al. 1996, Niyogi 1999).

The most abundant carotenoids in higher plants and green algae are the β,ϵ -carotenoid lutein and the β,β -carotenoid violaxanthin. They are associated with the light-harvesting complexes of PSI (LHCI) and PSII (LHCII). LHCII comprises several different Chl *a/b*-binding proteins, which are distinguished according to their abundance in the thylakoid membrane into major LHCII and minor LHCII. The minor LHCII are also termed CP29, CP26, and CP24 (Jansson 1994). It is generally accepted that assembly of the major LHCII requires approximately 7 Chl *a* molecules, 6 Chl *b* molecules, two lutein molecules and one neoxanthin molecule (Kuhlbrandt et al. 1994, Croce et al. 1999a, Hobe et al. 2000). In contrast to the major LHCII, the minor LHCII bind fewer Chl molecules, have a higher Chl *a*/Chl *b* ratio and are enriched in violaxanthin (Bassi et al. 1993, Ruban et al. 1994, Green and Durnford 1996, Sandona et al. 1998). Although less is known about the carotenoid composition of light-harvesting proteins associated with PSI (LHCI), all LHC proteins are believed to contain at least 3 carotenoid binding sites that show preferential binding for the xanthophylls lutein, violaxanthin and neoxanthin (Lee and Thornber 1995, Croce et al. 1999b).

Under physiological conditions *in vivo*, the carotenoid zeaxanthin occurs only in trace amounts within the LHC (Ruban et al. 1994, Lee and Thornber 1995, Verhoeven et al. 1999). However, during high-light exposure of photosynthetic tissue, zeaxanthin is formed upon de-epoxidation of violaxanthin through operation of the reversible xanthophyll cycle (Yamamoto 1979, 1985). Although zeaxanthin binds to the LHC during irradiance stress, such association is usually only transient. Upon recovery under low-light or in darkness, zeaxanthin is replaced by violaxanthin (Yamamoto 1985). Because zeaxanthin is present only under irradiance stress conditions, and even then in relatively small amounts, its specific association with the LHC proteins is difficult to establish. Nevertheless, it was concluded from recent *in vitro* studies (Croce et al. 1999b, Hobe et al. 2000), upon analysis of zeaxanthin accumulating *Arabidopsis thaliana* mutants (Pogson et al. 1996, Pogson et al. 1998, Tardy and Havaux 1996), and from the green alga *Scenedesmus obliquus* (Heinze et al. 1997, Bishop et al. 1998), that zeaxanthin could replace lutein and violaxanthin in the LHC of the photosynthetic apparatus.

Although the carotenoid composition of the LHC in lutein and violaxanthin lacking mutants has been investigated before, the photosynthetic apparatus organization of such carotenoid mutants has not been determined. It is still unclear whether zeaxanthin can functionally replace lutein and violaxanthin *in vivo*. In this work, we characterized the photosynthetic apparatus organization and function of a mutant (*npq2 lor1*) of the green alga *Chlamydomonas reinhardtii* with specific deletions in carotenoid biosynthesis. The size of the light-harvesting Chl antenna, the stoichiometry of the photosystems and the functionality of the photosynthetic apparatus in the

absence of lutein, loroxanthin, violaxanthin and neoxanthin are questions that have been addressed in this work. We present evidence that when zeaxanthin is the sole xanthophyll present, LHC complexes are assembled and functionally connected with the reaction center complexes of PSII and PSI. Contrary to results reported for *Scenedesmus obliquus* (Bishop et al. 1998), absence of lutein and violaxanthin did not appear to compromise the photon conversion efficiency of photosynthesis in *Chlamydomonas reinhardtii*. However, lack of these xanthophylls specifically resulted in a truncated light-harvesting Chl antenna size for PSII in the *npq2 lor1* mutant.

Materials and Methods

Organisms, Maintenance and Growth

Cells of *Chlamydomonas reinhardtii* wild type strain CC125 and of the *npq2 lor1* mutant were cultivated photoautotrophically on HS (Harris 1989) agar plates either under 5 $\mu\text{mol photons m}^{-2} \text{s}^{-1}$ or 400 $\mu\text{mol photons m}^{-2} \text{s}^{-1}$ continuous light (cool-white fluorescent). For measurements cells were grown in liquid culture at 200 $\mu\text{mol photons m}^{-2} \text{s}^{-1}$ at 22°C in flat 1 L Roux bottles in bicarbonate enriched medium (Polle et al. 2000). Stirring of the cultures prevented cell settling and ensured uniform illumination.

Cell count and Pigment Analysis

Cell density was monitored by counting the number of cells per milliliter of culture using a Neubauer ultraplane hemacytometer. The absorbance of light $\lambda > 640 \text{ nm}$ of the cell culture was measured using a Klett-Summerson photoelectric colorimeter (Sumner and Somers 1944). For growth curves the logarithm of the reading (*Ln Growth*) was plotted as a function of time.

For pigment determination cells or thylakoid membranes were extracted in 80% acetone and debris was removed by centrifugation at 10,000g for 5 min. The absorbance of the supernatant was measured with a Shimadzu UV-160U spectrophotometer. The Chl (*a* and *b*) concentration of the samples was determined according to Arnon (1949), with equations corrected as in Melis et al. (1987).

For HPLC analysis the HPLC model Hewlett Packard Series 1100 equipped with a Waters Spherisorb S5 ODS1 4.6 X 250 mm cartridge column was used. 1 ml algal suspension was centrifuged at 14,000 RPM for 2 min. The pigments were extracted from algal cells by adding 200 μl 100% acetone to the pellet and vortexing at maximum speed for 1 min. The extract was centrifuged in an Eppendorf centrifuge at 14,000 RPM and 15 μl of the filtered supernatant (0.2 μm nylon filter) subjected to HPLC. HPLC analysis was performed using a modification of the method of Garcia-Plazaola and Becerril (1999). Pigments were eluted with a linear gradient from 100% solvent A (acetonitrile:methanol:[0.1 M Tris-HCl pH 8.0]; 84:2:14) to 100% solvent B (methanol:ethyl acetate; 68:32) for 15 min, followed by 3 min of solvent B. The solvent flow rate was 1.2 mL/min. Pigments were detected by absorbance at 445 nm with a reference at 550 nm, and concentrations of individual pigments were determined using standard curves of purified pigments (VKI, Hørsholm, Denmark) at known concentrations.

Isolation and Separation of Thylakoid Membrane Proteins

Cells were harvested by centrifugation at 1,000g for 4 min at 4°C. The resulting pellets were resuspended in 1-2 ml buffer containing 50 mM Tricine (pH 7.8), 10 mM NaCl, 5 mM MgCl₂ and stored frozen at -80°C. Samples were thawed on ice and diluted with ice-cold sonication buffer containing 50 mM Tricine (pH 7.8), 10 mM NaCl, 5 mM MgCl₂, 0.2% polyvinylpyrrolidone 40, 0.2% sodium ascorbate, 1 mM aminocaproic acid, 1 mM aminobenzamide and 100 µM phenylmethylsulfonylfluoride (PMSF). Cells were broken by sonication with a Branson 250 Cell Disrupter operated at 4°C for 30 s (pulse mode, 50% duty cycle, output power 5). This process was repeated three times with 30 s interval. Unbroken cells and starch grains were removed by centrifugation at 3,000 g for 4 min at 4°C. These crude thylakoid membranes were collected by centrifugation of the supernatant at 100,000 g for 25 min at 4°C.

For protein analysis of crude thylakoid membranes the pellet was solubilized in 250 mM Tris-HCl (pH 6.8), 20% glycerol, 7% SDS and 2 M urea. Solubilization of thylakoid membrane proteins was carried out for 30 min at room temperature (a procedure designed to prevent the formation of protein aggregates during denaturation) and was followed by centrifugation of the samples in a microfuge for 4 min to remove unsolubilized material. Aliquots for Chl determination were taken and samples diluted accordingly to yield equal Chl concentrations before the samples were stored at -80°C.

SDS-PAGE and Immunoblot Analysis

Prior to loading for electrophoresis, samples were brought to room temperature. Gel lanes were loaded with an equal amount of Chl (4 nmol Chl per lane). SDS-PAGE analysis was carried out according to Laemmli (1970), with resolving gels containing 12.5% acrylamide. Gels were first run for 30 min at a constant current of 16 mA until the samples migrated into the gels and then for 16 h at a constant current of 9 mA. For protein visualization, gels were stained with 1% Coomassie brilliant blue R. Electrophoretic transfer of the SDS-PAGE resolved proteins onto nitrocellulose was carried out for 3 h at a constant current of 800 mA, in transfer buffer containing 50 mM Tris, 380 mM glycine (pH 8.5), 20% methanol and 1% SDS. Identification of LHC proteins of the thylakoid membrane was accomplished with polyclonal antibodies raised against the LHC complex of *Zea mays*, kindly provided by Dr. R. Bassi (Di Paolo et al. 1990, Bassi et al. 1992) and polyclonal antibodies raised against a polypeptide of CP26. For determination of the level of reaction center core complex proteins polyclonal antibodies against the D1 protein (Kim et al. 1993) or the *psaA/psaB* gene products (Kashino et al. 1990) were used. Cross-reaction with the antibodies was visualized by a chromogenic reaction with anti Ig-G secondary antibodies conjugated with alkaline phosphatase (BioRad, Hercules, CA). Immunoblots were scanned with a HP Scanjet 5300C optical scanner connected to a MacIntosh/G3 computer and the NIH Image version 1.6 program was used for deconvolution of the bands.

Chlorophyll Fluorescence

The initial (F_0), variable (F_v) and maximum (F_{max}) Chl fluorescence yield of intact cells was measured upon excitation of the cultures with green light (CS 4-96 and CS 3-69 Corning Filters, actinic light intensity of $75 \mu\text{mol photons m}^{-2} \text{s}^{-1}$). An aliquot from the culture was incubated in the dark for 10 min prior to the measurement and the Chl fluorescence was recorded in the absence or presence of DCMU ($2.5 \mu\text{M}$ final concentration).

A fluorescence video imaging apparatus (Niyogi et al. 1997a, Niyogi et al. 1998) was utilized to visualize the Chl fluorescence of algal cultures grown on agar plates. Prior to the measurement the plates were dark incubated for at least 5 min. Actinic illumination of $\sim 2,000 \mu\text{mol photons m}^{-2} \text{s}^{-1}$, sufficient to induce the F_{max} emission from the algal colonies, was employed in this fluorescence video imaging analysis. The actinic illumination was administered for a period of 1 s and the resulting fluorescence images were captured by the digital video camera of the apparatus.

Spectrophotometric Analyses

For spectrophotometric measurements the thylakoid membrane pellet was resuspended in a buffer containing 50 mM Tricine (pH 7.8), 10 mM NaCl, 5 mM MgCl_2 . The concentration of the photosystems in the thylakoid membranes was estimated spectrophotometrically from the amplitude of the light *minus* dark absorbance difference signal at 700 nm (P700) for PSI, and 320 nm (Q_A) for PSII (Melis and Brown 1980). The functional light-harvesting Chl antenna size of PSI and PSII was measured from the kinetics of P700 photo-oxidation and Q_A photoreduction, respectively (Melis 1989).

Oxygen Evolution Measurements

Oxygen evolution activity of the cultures was measured at 22°C with a Clark-type oxygen electrode illuminated with a slide projector lamp. Yellow actinic excitation light was provided by a CS 3-69 Corning cut-off filter in combination with an Ealing 35-5453 VIQ5-8 filter. An aliquot of 5 ml cell suspension ($2 \mu\text{M}$ Chl) was transferred to the oxygen electrode chamber. To ensure that oxygen evolution was not limited by the carbon source available to the cells, $100 \mu\text{l}$ of 0.5 M sodium bicarbonate solution (pH 7.4) was added to the suspension prior to the oxygen evolution measurements. The measurement of the light-saturation curve of photosynthesis was implemented with the oxygen electrode, beginning with the registration of dark respiration in the cell suspension, and followed by measurements of the rate of oxygen evolution at 30, 70, 125, 240, 375, 525, 700, 1150, 1500, 2250, and $3200 \mu\text{mol photons m}^{-2} \text{s}^{-1}$. Registration of the rate (slope) of oxygen evolution at each light intensity step was recorded for about 2.0 min. The photosynthetic efficiency of the cells was calculated from the initial slope of the light-saturated curve of photosynthesis.

Results

Isolation and Pigment Analysis of a Secondary Pigment Mutant

From the background of the β,ϵ -carotenoid-less strain *lor1* of *Chlamydomonas reinhardtii* (Chunaev et al. 1991, Niyogi et al. 1997a, b), we isolated a spontaneous *npq2* mutation, resulting in the absence of the β,β -epoxycarotenoids antheraxanthin, violaxanthin and neoxanthin (Cunningham and Gantt 1998). Lack of xanthophylls derived from zeaxanthin was due to a defect in the activity of the zeaxanthin epoxidase enzyme (Niyogi et al. 1997a). Based on the results of the HPLC analysis (Figure 1), showing that zeaxanthin was the only xanthophyll present, we termed this new carotenoid mutant as *npq2 lor1*.

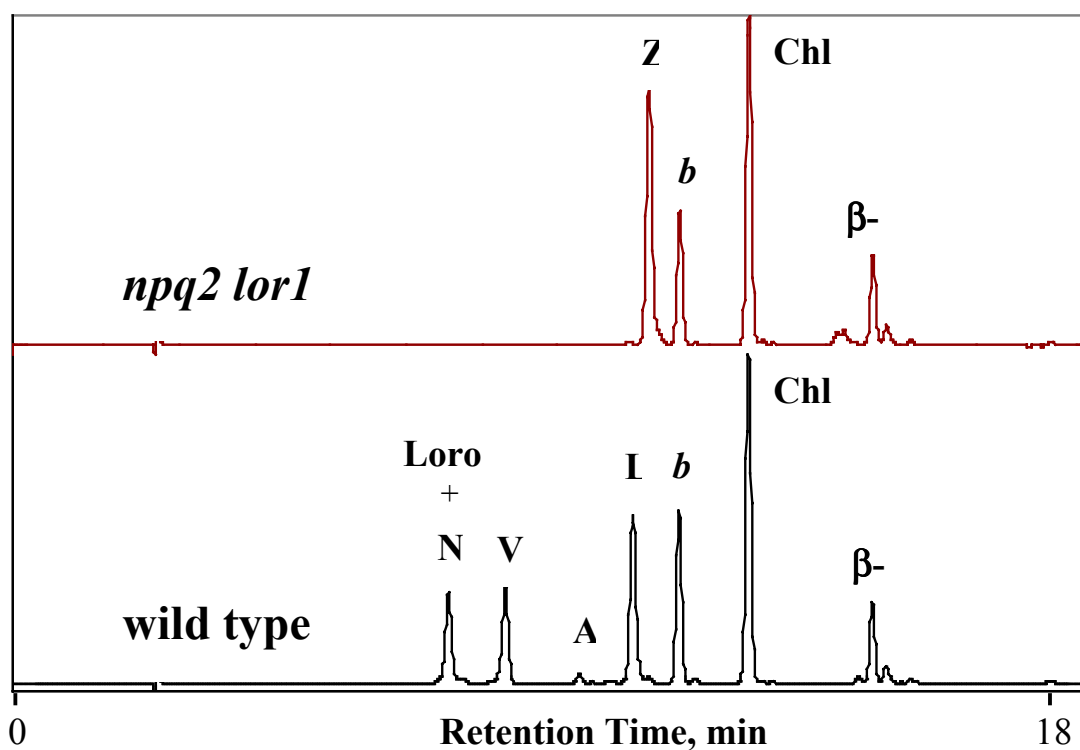


Figure 1 HPLC elution profile of total pigment extract from *Chlamydomonas reinhardtii* wild type and *npq2 lor1* mutant. Traces were normalized to the peak of Chl *a*. Identification of lettered peaks is as follows: Loro, Loroxanthin; N, neoxanthin; V, violaxanthin; A, antheraxanthin; L, lutein; Z, zeaxanthin; b, Chl *b*; Chl *a*, Chl *a*; β-Car, β-carotene.

Table 1 Pigment content of wild type and a mutant of *Chlamydomonas reinhardtii* (*npq2 lor1*) lacking lutein, loroxanthin, violaxanthin and neoxanthin. Values represent means \pm SD.

Parameter	wild type	mutant
Chl <i>a</i> / Chl <i>b</i>	2.9 \pm 0.2	4.1 \pm 0.4
mol x10 ⁻¹⁵ Chl/cell	4.4 \pm 0.7	3.1 \pm 0.33
mol x10 ⁻¹⁵ Carotenoids/cell	1.7 \pm 0.2	1.2 \pm 0.2
Car/Chl (mol:mol)	0.39	0.39

Table 1 shows that the Chl *a*/Chl *b* ratio (=4.1) of the *npq2 lor1* mutant, like its *lor1* parent (Niyogi et al. 1997b), was significantly higher than that of the wild type (=2.9). This result suggested a different photosynthetic apparatus organization for the mutant than for the wild type (Anderson 1986, Melis 1991). Table 1 also shows that the total amounts of Chl and Car per cell in the mutant were slightly lower than that of the wild type. However, the total Car to Chl mol:mol ratio was the same in the two strains. Taken together, these results (Fig. 1 and Tab. 1) suggest that, in the *npq2 lor1* mutant, zeaxanthin has replaced and least lutein and violaxanthin in the two of the three xanthophyll-binding sites of the LHCII. The third, neoxanthin-binding site in the LHCII is reported to be highly specific for this xanthophyll species (Croce et al. 1999a,b; Connelly et al. 1997) and, therefore, it is possible that this binding site remains empty in the absence of neoxanthin in the *npq2 lor1* mutant.

Photosynthetic Apparatus Organization

Figure 2 shows growth curves of wild type and *npq2 lor1* mutant in a liquid Tris-Bicarbonate medium (see Materials and Methods) under a light intensity of 200 μ mol photons $m^{-2} s^{-1}$. Wild type and *npq2 lor1* mutant cells had similar growth rates indicating that lack of lutein, loroxanthin, violaxanthin and neoxanthin did not compromise the photosynthetic and growth abilities of the *npq2 lor1* mutant.

In order to investigate the photosynthetic apparatus organization of the *npq2 lor1* mutant, we measured, spectrophotometrically, the amounts of photochemically active primary quinone acceptor Q_A of PSII and the reaction center P700 of PSI.

Table 2 shows that, on a Chl basis, the *npq2 lor1* mutant (4.5 mmol Q_A per mol Chl) had about 50% more photochemically competent PSII centers than the wild type (2.9 mmol Q_A per mol Chl). The amount of P700 per Chl in the mutant (1.74 mmol:mol) was only slightly higher than that of the wild type (1.4 mmol:mol). When compared on a per cell basis, mutant and wild type had similar amounts of Q_A (Table 2). In contrast, the amount of P700 per cell in the mutant was slightly lower than that in the wild type (Table 2). In consequence, the PSII/PSI molar ratio in the mutant (2.6:1) was slightly higher than that in the wild type (2.1:1).

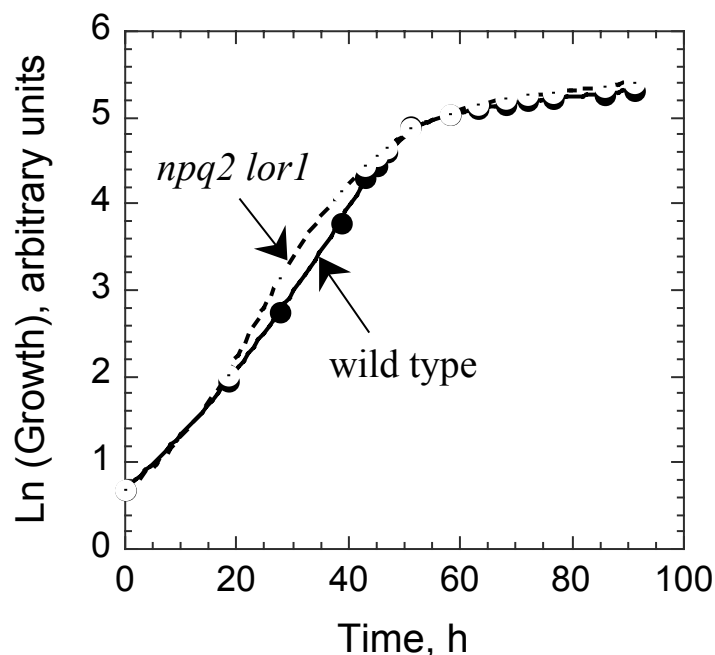


Figure 2 Growth curve of wild type (●) and *npq2 lor1* (○) mutant of *Chlamydomonas reinhardtii*. The logarithm of a photoelectric calorimeter reading of the cultures is plotted as a function of time during cell growth. Cells were cultivated photoautotrophically on a bicarbonate enriched medium under $200 \mu\text{mol photons m}^{-2} \text{s}^{-1}$.

Table 2 Photochemical apparatus characteristics of wild type and *npq2 lor1* mutant of *Chlamydomonas reinhardtii*.

Parameters	wild type	mutant
$Q_A / \text{total Chl (mmol:mol)}$	2.9 ± 0.18	4.5 ± 0.4
$P700 / \text{total Chl (mmol:mol)}$	1.4 ± 0.1	1.74 ± 0.05
$*10^{-18} \text{ mol } Q_A / \text{cell}$	13.0	13.9
$*10^{-18} \text{ mol P700} / \text{cell}$	6.3	5.4
PSII / PSI	2.1	2.6

The lower Chl per cell content and the elevated Chl *a*/Chl *b* ratio in *npq2 lor1* indicated a truncated Chl antenna size of the photosystems in the mutant relative to that in the wild type. In order to address this point in detail, we performed measurements of the functional Chl antenna size of the photosystems with the “kinetic/spectrophotometric” method (Melis and Anderson 1983, Melis 1989). In this approach, functional Chl molecules are assigned to each photosystem in direct proportion to the rate of light absorption/utilization by PSI and PSII. The rates for PSI and PSII were measured in isolated and DCMU poisoned thylakoids from the kinetics of P700 photooxidation and Q_A photoreduction, respectively (Melis 1989).

Results, summarized in Table 3, showed that thylakoid membranes of wild type contain approximately equal amounts of the two types of PSII, PSII α and PSII β (Melis and Duysens 1979). This distribution is similar to that reported for the *Chlamydomonas reinhardtii* strain *cw15* (Polle et al. 2000). However, in the *npq2 lor1* mutant, PSII α accounted for only about 23% and PSII β for 77% of the total PSII. Further, Table 3 provides values for the functional Chl antenna size (N) of PSII α , PSII β and PSI in the thylakoid membrane of wild type and *npq2 lor1* mutant. In the wild type, PSII α contained about 300 Chl *a* and Chl *b* molecules and PSII β contained 135 Chl molecules. The Chl antenna size of PSI contained about 240 Chl *a* and Chl *b* molecules.

Table 3 Chl antenna sizes of PSII and PSI in wild type and *npq2 lor1* mutant. The concentration of the various forms of PSII is given as a % of total PSII in the thylakoid membrane. The antenna size of PSII and PSI is given as the number of Chl molecules functionally associated with a photosystem. Values represent the average of two experiments.

Parameter	wild type	mutant	Minimum Chl antenna size
PSII α	55 %	23 %	
PSII β	45 %	77 %	
N _{PSIIα}	301	171	
N _{PSIIβ}	135	90	37
N _{PSI}	242	294	95

In the *npq2 lor1* mutant, the functional Chl antenna size of PSII α (170 Chl molecules) and PSII β (90 Chl molecules) were substantially smaller than those of the wild type (Table 3). Taking into consideration the smaller functional Chl antenna in both PSII α and PSII β and the lowered PSII α /PSII β ratio in the mutant, we estimated that PSII in the mutant contained only about 60% of the Chl compared to that in the wild type (not shown). It is evident that absence of lutein, loroxanthin, violaxanthin and neoxanthin resulted in a significantly truncated PSII Chl antenna size. Nevertheless, this functional Chl antenna size was still larger than that of the PSII-core (N_{PSII_{core}} = 37 Chl molecules, Manodori et al. 1984, Glick and Melis 1988), suggesting that zeaxanthin alone is sufficient to facilitate the assembly of a significant portion of the auxiliary LHCII. Moreover, the occurrence of PSII α centers with a relative large Chl antenna size (N_{PSII α} = 171 Chl molecules) suggested that both major and minor components of the LHCII are assembled and functionally associated with PSII in the *npq2 lor1* mutant. Surprisingly, and in contrast to PSII, the functional Chl antenna size of PSI in the *npq2 lor1* (N_I = 294 Chl molecules) was slightly larger than that of the wild type (N_I = 242 Chl molecules). This result suggests that absence of lutein, loroxanthin, violaxanthin and neoxanthin does not bring about an adverse effect on the functional Chl antenna size of PSI.

SDS-PAGE and Western Blot Analysis of Thylakoid Membrane Proteins

The results presented above provide evidence for an altered photosynthetic apparatus organization of the *npq2 lor1* mutant. To probe further the effect of the mutation on the Chl antenna size, we qualitatively and quantitatively compared profiles of thylakoid membrane proteins from wild type and *npq2 lor1* mutant.

Figure 3 shows SDS-PAGE analysis of isolated thylakoid membrane proteins of wild type and *npq2 lor1*. Comparison of wild type (wt) and mutant (mt) lanes in Figure 3 shows quantitative, but not qualitative changes in the polypeptide composition between wild type and mutant, mainly occurring in the 31 kDa electrophoretic migration region. It is suggested that, on a per Chl basis, some of the LHCII proteins are depleted in the *npq2 lor1* mutant whereas LHCI proteins are more abundant when compared to that of the wild type level.

The assessment was further tested by Western blot analysis. Figure 4 shows an immunoblot of thylakoid membrane proteins isolated from wild type and *npq2 lor1* mutant, probed with antibodies against the PsaA/PsaB proteins of PSI (Kashino et al. 1990) and the D1 protein of PSII (Kim et al. 1993). On a per Chl basis, the mutant contained slightly more D1 than the wild type. This is consistent with the results of the spectrophotometric analysis (Table 2), in which the Q_A content was about 50% greater in the *npq2 lor1* than that in the wild type. Figure 4 also shows that the level of PsaA/PsaB proteins is very similar in wild type and *npq2 lor1* mutant indicating that, on a per Chl basis, both strains have approximately the same amount of PSI (Table 2).

Figure 5 shows a Western blot analysis of thylakoid membrane proteins probed with antibodies that recognize most LHC proteins of *Chlamydomonas reinhardtii* (Bassi et al. 1992, Polle et al. 2000). It is evident from the results in Fig. 5 that, on a per Chl basis, wild type and *npq2 lor1* mutant qualitatively contain the same LHC proteins in their thylakoid membranes. However, absence of lutein, linoxanthin, violaxanthin and neoxanthin brought about changes in the quantity of the various LHC proteins in the thylakoid membrane of the mutant. Specifically, loss of these xanthophylls resulted in significantly lower levels of CP26 whereas levels of CP29 and CP24 were higher in the *npq2 lor1* than in the wild type. The level of the major LHCII at 29 kDa was lower in the mutant than in the wild type. However, levels of the LHCII subunit migrating at ~33kDa did not seem to be affected by the mutation. In contrast to this differential effect on LHCII, levels of the various LHCI were uniformly higher in the mutant than in the wild type.

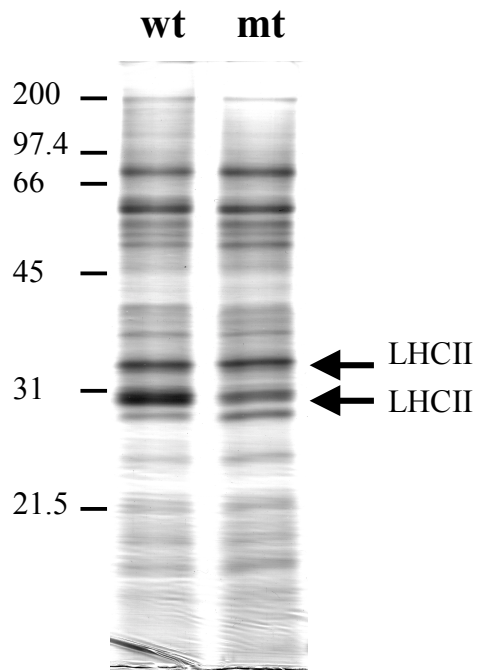
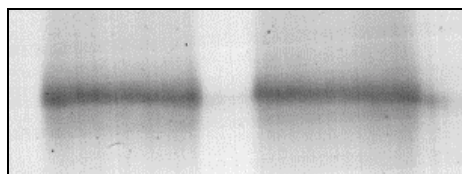
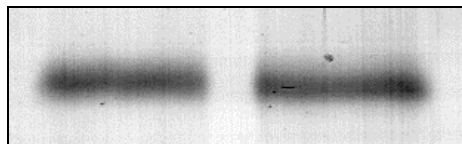


Figure 3 Thylakoid membrane protein profile from wild type (wt) and *npq2 lor1* mutant (mt) of *Chlamydomonas reinhardtii*. Proteins were separated by SDS-PAGE and visualized by Coomassie staining. The lanes were loaded on an equal Chl basis (4 nmol Chl/lane). The electrophoretic mobility of molecular-weight markers is indicated in kDa.

wild type *npq2 lor1*



PsaA/PsaB



D1

Figure 4 Western blot analysis of thylakoid membrane proteins of wild type and *npq2 lor1*, probed with specific polyclonal antibodies against the PsaA/PsaB (PSI) or D1 (PSII) reaction center proteins.

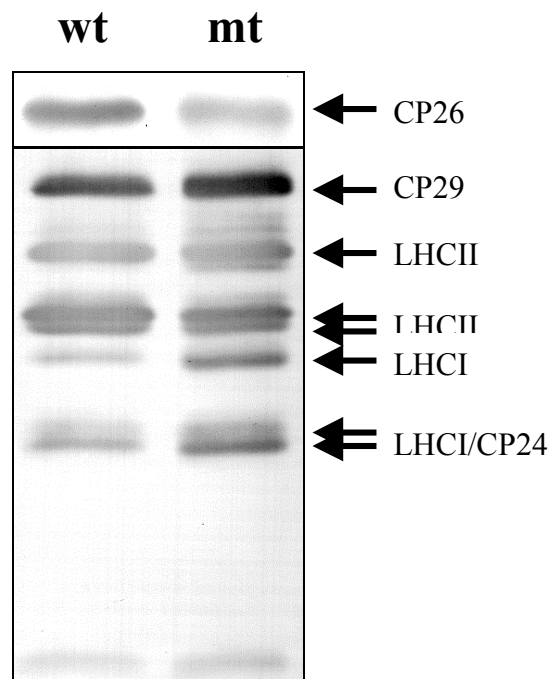


Figure 5 Western blot analysis of thylakoid membrane proteins of wild type and *npq2 lor1*, probed with specific polyclonal antibodies against the LHC proteins of PSII and PSI. Proteins were loaded on a Chl basis. The position of various LHC proteins is indicated. Asterisk denotes a possible degradation product of the LHC.

Since we determined the amount of Q_A , P700 and the LHC proteins on a per Chl basis, it was possible to normalize the level of the LHC proteins to that of PSII or PSI in the cells. The result of such analysis, shown in Figure 6, allows quantitative comparison of the LHC proteins content in the thylakoid membrane of wild type and mutant on a per PSII or PSI basis.

Figure 6A shows a comparison on the basis of Q_A . It is evident from Fig. 6A that the amounts of CP29 and LHCII per PSII in the *npq2 lor1* mutant were lowered to about 60% of that seen in the wild type. The amount of CP26 per PSII was drastically reduced to about 25% of that in the wild type. Figure 6B shows a comparison on the basis of P700. In this case, it is evident that the level of LHCI per PSI in the *npq2 lor1* mutant was significantly higher than that of the wild type.

It is noteworthy that all LHC proteins detected in association with the *npq2 lor1* mutant were fully integrated into the lipid bilayer of the corresponding thylakoid membrane. Treatment of thylakoids with 1 M Tris-HCl pH 9.0, a procedure designed to remove extrinsic proteins from the thylakoid membrane, did not result in loss of any LHC polypeptides associated with this mutant strain (data not shown).

Efficiency and Rate of Photosynthesis

Recently, Bishop et al. (1998) reported that a carotenoid double mutant of the green alga *Scenedesmus obliquus* with a phenotype similar to that of the *npq2 lor1* mutant in *Chlamydomonas reinhardtii* had a slightly increased photosynthetic capacity, but significantly reduced photosynthetic efficiency. To assess the photosynthetic capacity and efficiency of the

npq2 lor1 mutant, the rate of O₂ evolution was measured and plotted as a function of light intensity, thus obtaining the *photosynthesis versus irradiance* curve (light-saturation curve). From the slope of the initial linear portion of the light-saturation curve of photosynthesis, information was obtained about the relative efficiency of photosynthesis (Φ) in wild type and mutant (Björkman and Demmig 1987, Neale et al. 1993). The rate of oxygen evolution under light-saturation conditions provided information about P_{max}, the capacity of photosynthesis in the two strains (Powles and Critchley 1980).

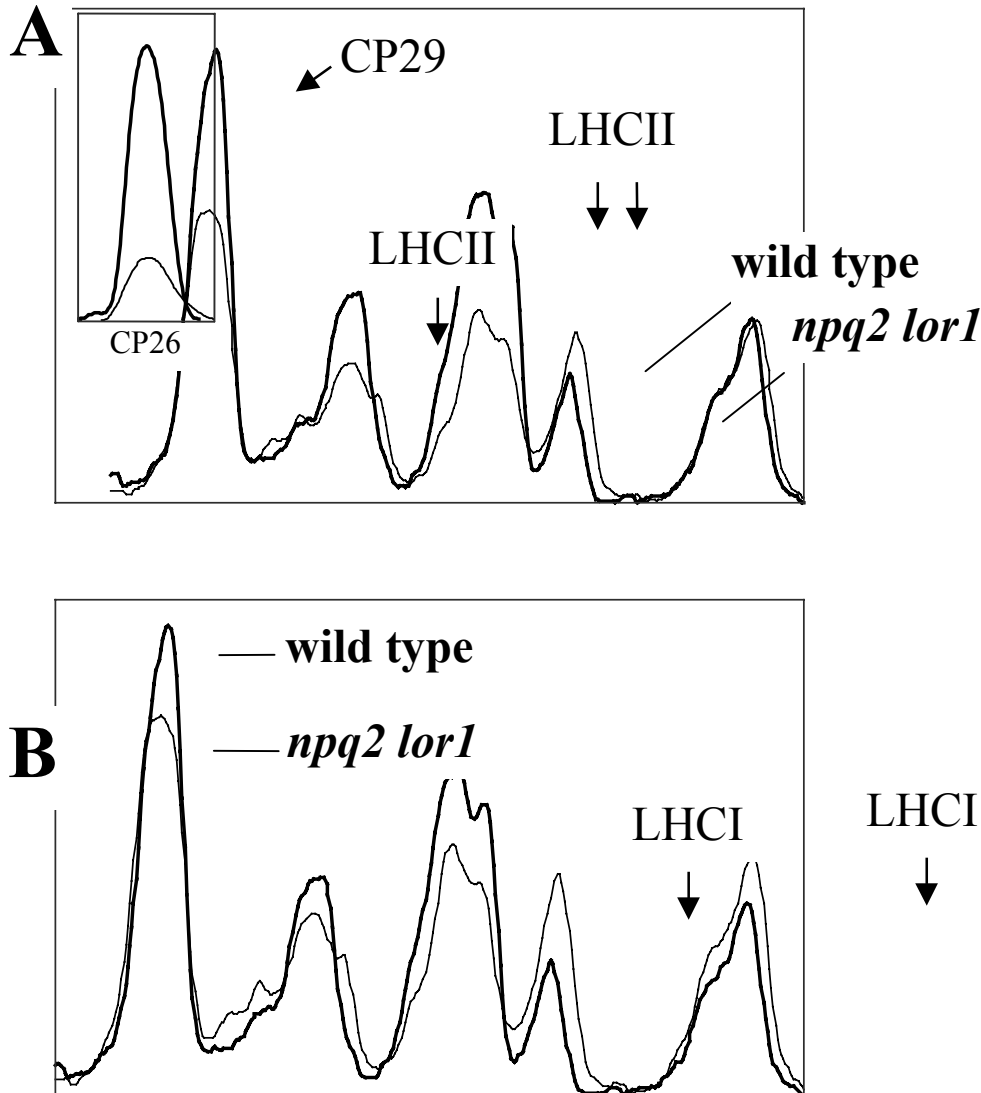


Figure 6 Densitometric scan of Western-blot lanes from Fig. 5, normalized on the basis of PSII/Q_A (A) or PSI-P700 (B). Superimposed scans were normalized on the basis of equal Q_A loading. Arrows indicate the position of the various LHC forms. Note that amounts of CP26, CP29 and LHCII per PSII/Q_A are lower in the *npq2 lor1* mutant compared to wild type (A). Conversely, levels of the LHCI per P700 are greater in the mutant when compared to wild type (B).

Figure 7 shows the light-saturation curve of photosynthesis for wild type and *npq2 lor1* mutant.

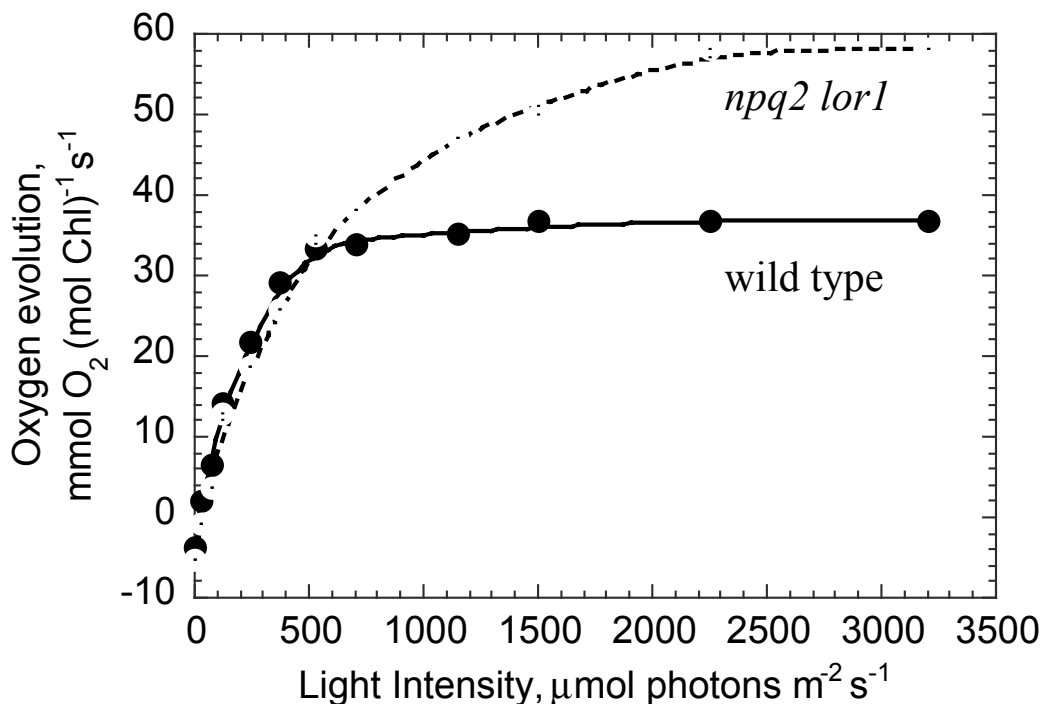


Figure 7 The light-saturation curve of photosynthesis in wild type and *npq2 lor1* mutant.

As summarized in Table 4, wild type ($\Phi=0.14\pm0.02$) and mutant ($\Phi=0.125\pm0.03$) had similar photosynthetic efficiencies. The photosynthetic capacity of the *npq2 lor1* mutant ($P_{\text{max}}=59 \text{ mmol O}_2 [\text{mol Chl}]^{-1} \text{ s}^{-1}$) was about 50% greater than that of the wild type ($P_{\text{max}}=36 \text{ mmol O}_2 [\text{mol Chl}]^{-1} \text{ s}^{-1}$).

Table 4 Gas exchange and PSII efficiency of wild type and a zeaxanthin accumulating *npq2 lor1* mutant of *Chlamydomonas reinhardtii* expressed on a per Chl basis. Values are means \pm SD.

Parameter	wild type	mutant
Respiration ($\text{mmol O}_2 (\text{mol Chl})^{-1} \text{ s}^{-1}$)	4.0 ± 0.04	5.1 ± 1.2
Photosynthesis ($\text{mmol O}_2 (\text{mol Chl})^{-1} \text{ s}^{-1}$)	36.5 ± 1.8	59.0 ± 12.7
Photosynthetic efficiency (relative values)	0.14 ± 0.02	0.125 ± 0.03
PSII efficiency (F_v/F_{max})	0.69 ± 0.04	0.60 ± 0.03

Table 4 also compares the photochemical conversion efficiency at PSII, measured from the F_v/F_{max} fluorescence ratio in wild type ($F_v/F_{\text{max}}=0.69$) and *npq2 lor1* mutant ($F_v/F_{\text{max}}=0.60$). The similar F_v/F_{max} ratios in wild type and *npq2 lor1* validate the similar photosynthetic efficiencies as measured from the light-saturation curve of photosynthesis. Taken together, these results suggested that replacement of lutein, loroxanthin and violaxanthin by zeaxanthin, as it

occurred in the *npq2 lor1* mutant, did not bring about a significantly adverse effect on light absorption and utilization in the photochemical apparatus of the mutant. This is clearly evidenced by the similar photon conversion efficiencies observed in the photochemical apparatus of the two strains and ultimately by their similar growth rates.

Discussion

We isolated a carotenoid double mutant of *Chlamydomonas reinhardtii* that lacks not only all α -carotenoids (*lor1*) but is also unable to synthesize violaxanthin and neoxanthin from zeaxanthin (*npq2*). These lesions in carotenoid biosynthesis did not impair photoautotrophic growth of the *npq2 lor1* double mutant. Such observation is consistent with findings in *Scenedesmus obliquus* (Bishop 1996) and *Arabidopsis thaliana* (Pogson et al. 1998). Interestingly, in contrast to reduced virescence and seedling lethality of the analogous *aba1 lut2* mutant of *Arabidopsis* (Pogson et al. 1998), the growth rate of the *npq2 lor1 Chlamydomonas reinhardtii* mutant was not compromised. Accumulation of zeaxanthin in the *npq2 lor1* occurred concomitant with a lowering in the cellular Chl and Car content, by about one-third as compared to that of the wild type. However, levels of PSII per cell were similar and levels of PSI per cell were only slightly lower in the *npq2 lor1* when compared to that of the wild type. Therefore, it is concluded that a reduction in the level of Chl and Car per cell in the *npq2 lor1* mutant is mainly due to a reduction in the amount of LHC proteins.

Previous work with carotenoid mutants of green algae (Chunaev et al. 1991, Bishop et al. 1995, Bishop et al. 1998, Niyogi et al. 1997a,b) and higher plants (Pogson et al. 1996, Tardy and Havaux 1996) showed that loss of lutein and/or violaxanthin was accompanied by alterations in the profile of the LHC proteins in the photosynthetic apparatus. In agreement with these reports, we demonstrated in this work that lack of xanthophylls that are derived from α -carotene, as well as lack of xanthophylls derived from zeaxanthin, resulted in an altered LHC composition in the *npq2 lor1* mutant (Fig. 5). Since all LHC polypeptides are present in the thylakoid membranes of *npq2 lor1* (Fig. 5) and washing of thylakoid membranes did not remove any LHC (data not shown), we conclude that zeaxanthin can successfully substitute for other xanthophylls in the LHC in *Chlamydomonas reinhardtii*. The successful substitution of other xanthophylls by zeaxanthin in the LHCII was also demonstrated *in vitro* when zeaxanthin was used as the only xanthophyll in reconstitution experiments (Croce et al. 1999b, Hobe et al. 2000). Interestingly, the *in vitro* studies revealed that LHCII containing only zeaxanthin were not as efficient in energy transfer as control LHCII (Croce et al. 1999b). Our *in vivo* results, however, showed that *npq2 lor1* had a PSII and overall photon conversion efficiency similar to that of the wild type. These findings are in agreement with results reported for the higher plant *Arabidopsis thaliana* (Hurry et al. 1997). In contrast, stable assembly of the major LHCII was not observed in lutein-lacking mutants of the green alga *Scenedesmus obliquus* (Bishop 1996, Bishop et al. 1998, Heinze et al. 1997). Obviously, absence of specific xanthophylls may have a variable effect on the assembly of the major LHCII in different organisms.

Quantitative LHC polypeptide analysis revealed that PSII units in the *npq2 lor1* mutant contained lower levels of CP26 (25% of the wt) and CP29 (60% of the wt). They also contained a lower level of the major LHCII (60% of the wt). Consistent with the above-described biochemical analysis, the spectrophotometric/kinetic analysis showed that the functional light-

harvesting Chl antenna size of the *npq2 lor1* is only about 60% of that in the wild type. Taken together, this rigorous analysis suggests that many PSII units in the *npq2 lor1* mutant do not contain a copy of CP26 and/or CP29. In addition, they may lack some of the peripheral components of the trimeric LHCII. In contrast, the level of CP24 per PSII was not affected in the *npq2 lor1*, indicating that every PSII unit in the mutant has a copy of CP24.

Figure 8 shows, as a working hypothesis, the organization and size of the Chl antenna of PSII α and PSII β units in wild type and *npq2 lor1* mutant. This model is consistent with the results presented in this work and also consistent with the analyses presented by other authors (Hankamer et al. 1997, Melis 1998, Nield et al. 2000). The Chl antenna model of PSII, shown in Fig. 8, is based on the assumption of three levels of organization for the Chl-proteins in PSII:

- The PSII-core complex is the first level consisting of D1, D2, CP43, and CP47. This is the minimum PSII configuration that can be stably assembled *in vivo*. The PSII-core contains about 37 Chl *a* molecules (Manodori et al. 1984, Glick and Melis 1988).
- The second level of organization contains, in addition to the PSII-core, one copy of CP29, CP26, CP24, two LHCII monomers and one LHCII trimer. This PSII complex is defined as PSII β and contains about 130 Chl *a* and Chl *b* molecules (Melis 1991).
- Further step-wise addition of trimeric LHCII to PSII β results in the formation of the PSII α units (Melis 1998).

On the basis of the quantitative data presented in this work, we estimated that only about 25% of PSII units in the *npq2 lor1* mutant contain CP26. It is thought that CP26 serves as an intermediary in the supramolecular structure of the LHCII by serving to connect peripheral LHCII trimers to the PSII-core. In the absence of CP26 from 75% of the PSII units in the *npq2 lor1* mutant, it follows that an equivalent number of PSII might not be able to bind trimeric LHCII, a prerequisite for the development of the mature PSII α type of Chl antenna. Therefore, PSII units without a copy of CP26 should have a Chl antenna size that is slightly smaller than that of PSII β , owing to the lack of the trimeric LHCII and lack of CP26. This is actually observed in the Chl antenna size of PSII β in the *npq2 lor1*, which contains 90 Chl molecules instead of the 135 Chl molecules detected in PSII β of the wild type. The difference in Chl antenna size between PSII β in wild type and *npq2 lor1* mutant (about 45 Chl molecules) is consistent with the number of Chl molecules predicted to be in association with one LHCII trimer *plus* one copy of CP26. Therefore, we conclude that only monomeric LHCII are structurally associated with PSII in the antenna of the mutant, having an antenna size of 90 Chl molecules (Fig. 8). Since the PSII-core complex contains about 37 Chl *a* molecules, and a LHCII monomer is believed to contain 8-12 Chl molecules (Sandona et al. 1998), it follows that the remaining ~50 Chl *a* and Chl *b* molecules in PSII β of the mutant would occupy binding sites in about 4 LHCII monomers.

It is noteworthy that a permanently truncated PSII Chl antenna size has taken place due to alterations in the carotenoid biosynthetic pathway. This truncated Chl antenna mutant exhibited essentially the same photon conversion efficiency as the wild type and had a 50% greater photosynthetic capacity. In contrast to these results with the *npq2 lor1* mutant of *Chlamydomonas reinhardtii*, Bishop et al. (1998) showed that an analogous double mutant of the green alga *Scenedesmus obliquus* had a significantly lower photosynthetic efficiency and a photosynthetic capacity of only about 20% greater than that of the wild type. The difference

between these results could be explained by the fact that *Scenedesmus obliquus* was cultivated under heterotrophic growth conditions and only shifted to photoautotrophy prior to the measurements, whereas *Chlamydomonas* in this study was grown entirely under photoautotrophic conditions. Heterotrophy is known to affect the efficiency and capacity of the photosynthetic apparatus (Polle et al. 2000) and this consideration may be sufficient to explain differences between the *Scenedesmus* and *Chlamydomonas* results.

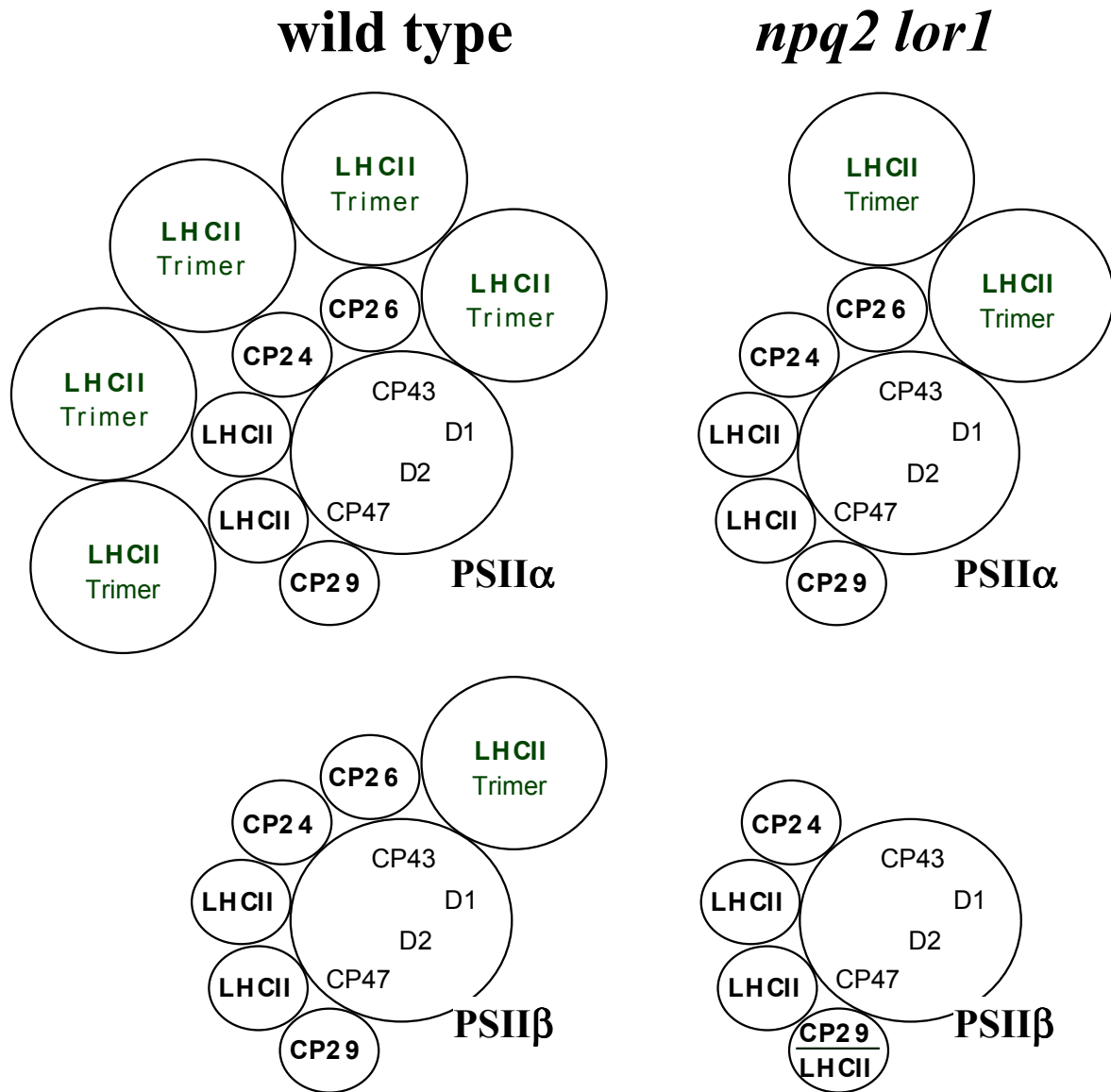


Figure 8 Model of the *Chlamydomonas reinhardtii* PSII light-harvesting antenna organization in wild type and *npq2 lor1* mutant .

In summary, the present work establishes that lutein, loroxanthin, violaxanthin and neoxanthin are not essential for the assembly and function of the LHCII and LHCI in the photosynthetic apparatus. With the possible exception of neoxanthin, these xanthophylls can be successfully substituted by zeaxanthin, resulting in the stable assembly of most, but all, Chl *a/b* LHCs. In consequence, the *npq2 lor1* mutant displayed a truncated PSII Chl antenna size but had a normal PSI Chl antenna size.

Acknowledgements

The work was produced under a DOE-UCB Cooperative Agreement Number DE-FC36-00GO10536 to A.M. Also supported (partially) by NIH grant number GM5879901 to K.K.N. We thank Ms. S.A. Chou for assistance with the preparation of the CP26 antibody, Dr. R. Bassi for providing the LHC antibodies and Dr. I. Enami for the PSI antibody, respectively.

References

- Anderson, J.M. 1986. Photoregulation of the composition, function, and structure of thylakoid membranes. *Ann. Rev. Plant Physiol.* 37: 93-136
- Arnon, D.I. 1949. Copper enzymes in isolated chloroplasts. Polyphenoxidase in *Beta vulgaris*. *Plant Physiol.* 24: 1-15
- Bassi, R., Soen, S.Y., Frank, G., Zuber, H. and Rochaix, J.-D. 1992. Characterization of chlorophyll *a/b* proteins of photosystem I from *Chlamydomonas reinhardtii*. *J. Biol. Chem.* 267: 25714-25721
- Bassi, R., Pineau, B., Dainese, P. and Marquardt, J. 1993. Carotenoid-binding proteins of photosystem II. *Eur. J. Biochem.* 212: 297-303
- Bishop, N.I. 1996. The β,ϵ -carotenoid, lutein, is specifically required for the formation of the oligomeric forms of the light harvesting complex in the green alga, *Scenedesmus obliquus*. *J. Photochem. Photobiol. B* 36: 279-283
- Bishop, N.I., Urbig, T. and Senger, H. 1995. Complete separation of the β,ϵ - and β,β -carotenoid biosynthetic pathways by a unique mutation of the lycopene cyclase in the green alga, *Scenedesmus obliquus*. *FEBS Letters* 367: 158-162
- Bishop, N.I., Bulga, B. and Senger, H. 1998. Photosynthetic capacity and quantum requirement of three secondary mutants of *Scenedesmus obliquus* with deletions in carotenoid biosynthesis. *Bot. Acta* 111: 231-235
- Björkman, O. and Demmig, B. 1987. Photon yield of O₂ evolution and chlorophyll fluorescence characteristics at 77K among vascular plants of diverse origins. *Planta* 170: 489-504

- Chunaev, A.S., Mirnaya, O.N., Maslov, V.G. and Boschetti, A. 1991. Chlorophyll *b*- and loroxanthin-deficient mutants of *Chlamydomonas reinhardtii*. *Photosynthetica* 25: 291-301
- Connelly, J.P., Müller, M.G., Basi, R., Croce, R. and Holzwarth, A.R. 1997. Femtosecond transient absorption study of carotenoid to chlorophyll energy transfer in the light-harvesting complex II of photosystem II. *Biochemistry* 36: 281-287
- Croce, R., Remelli, R., Varotto, C., Breton, J. and Bassi, R. 1999a. The neoxanthin binding site of the major light harvesting complex (LHCII) from higher plants. *FEBS Letters* 456: 1-6
- Croce, R., Weiss, S. and Bassi, R. 1999b. Carotenoid-binding sites of the major light-harvesting complex II of higher plants. *J. Biol. Chem.* 274: 29613-29623
- Cunningham FX and Gantt E 1998. Genes and enzymes of carotenoid biosynthesis in plants. *Ann. Rev. Plant Physiol. And Plant Mol. Biol.* 49: 557-583
- Demmig-Adams, B., Gilmore, A.M. and Adams, W.W. .1996. Carotenoids 3: *In vivo* function of carotenoids in higher plants. *FASEB Journal* 10: 403-412
- Di Paolo, M.L., Dal Belin Peruffo, A. and Bassi, R. 1990. Immunological studies on chlorophyll-*a/b* proteins and their distribution in thylakoid membrane domains. *Planta* 181: 275-286
- Garcia-Plazaola, J.I. and Becerril, J.M. 1999. A rapid high-performance liquid chromatography method to measure lipophilic antioxidants in stressed plants: Simultaneous determination of carotenoids and tocopherols. *Phytochem. Anal.* 10: 307-313
- Glick, R.E. and Melis, A. 1988. Minimum photosynthetic unit size in System-I and System-II of barley chloroplasts. *Biochim. Biophys. Acta* 934: 151-155
- Green, B.R. and Durnford, D.G. 1996. The chlorophyll-carotenoid proteins of oxygenic photosynthesis. *Rev. Plant Physiol. Plant Mol. Biol.* 47: 685-714
- Hankamer, B., Barber, J. and Boekema, E.J. 1997. Structure and membrane organization of PSII in green plants. *Annu. Rev. Plant Physiol. Plant Mol. Biol.* 48: 641-671
- Harris, E.H. 1989. *The Chlamydomonas Sourcebook. A comprehensive guide to biology and laboratory use.* Edited by Harris, E.H. pp. 25-29. Acad. Press, Inc., San Diego
- Heinze, I., Pfündel, E., Hühn, M. and Dau, H. 1997. Assembly of light harvesting complexes II (LHC-II) in the absence of lutein. A study on the α -carotenoid-free mutant C-2A`-34 of the green alga *Scenedesmus obliquus*. *Biochim. Biophys. Acta* 1320: 188-194
- Hobe, S., Niemeier, H., Bender, A. and Paulsen, H. 2000. Carotenoid binding sites in LHCIIb. Relative affinities towards major xanthophylls of higher plants. *Eur. J. Biochem.* 267: 616-624

- Hurry, V., Andersson, J.M., Chow, W.S. and Osmond, C.B. 1997. Accumulation of zeaxanthin in abscisic acid-deficient mutants of *Arabidopsis* does not affect chlorophyll quenching or sensitivity to photoinhibition *in vivo*. *Plant Physiol.* 113: 639-648
- Jansson, S. 1994. The light-harvesting chlorophyll *a/b*-binding proteins. *Biochim. Biophys. Acta* 1184: 1-19
- Kashino, Y., Enami, I., Satoh, K. and Katoh, S. 1990. Immunological cross-reactivity among corresponding proteins of photosystems I and II from widely divergent photosynthetic organisms. *Plant Cell Physiol.* 31: 479-488
- Kim, J.H., Nemson, J.A. and Melis, A. 1993. Photosystem II reaction center damage and repair in *D. salina* green alga. Analysis under physiological and irradiance-stress conditions. *Plant Physiol.* 103: 181-189
- Kuhlbrandt, W., Wang, D.N. and Fujiyoshi, Y. 1994. Atomic model of plant light-harvesting complex by electron crystallography. *Nature* 367: 614-621
- Laemmli, U.K. 1970. Cleavage of structural proteins during the assembly of the head of bacteriophage T4. *Nature* 227: 680-685
- Lee, A. I.-C. and Thornber, J.P. 1995. Analysis of the pigment stoichiometry of pigment-protein complexes from barley (*Hordeum vulgare*). *Plant Physiol.* 107: 565-574
- Manodori, A., Alhadeff, M., Glazer, A.N. and Melis, A. 1984. Photochemical apparatus organization in *Synechococcus* 6301 (*Anacystis nidulans*). Effect of phycobilisome mutation. *Arch. Microbiol.* 139: 117-123
- Melis, A. 1989. Spectroscopic methods in photosynthesis: photosystem stoichiometry and chlorophyll antenna size. *Phil. Trans. R. Soc. Lond. B* 323: 397-409
- Melis, A. 1991. Dynamics of photosynthetic membrane composition and function. *Biochim. Biophys. Acta* 1058: 87-106
- Melis, A. 1998. Photostasis in plants. Mechanism and regulation. *In* Photostasis and Related Phenomena. Edited by Williams and Thistle pp. 207-221. Plenum Press, New York
- Melis, A. and Duysens, L.N.M. 1979. Biphasic energy conversion kinetics and absorbance difference spectra of PS II of chloroplasts. Evidence for two different PS II reaction centers. *Photochem. Photobiol.* 29: 373-382
- Melis, A. and Brown, J.S. 1980. Stoichiometry of system I and system II reaction centers and of plastoquinone in different photosynthetic membranes. *Proc. Natl. Acad. Sci. USA* 77: 4712-4716
- Melis, A. and Anderson, J.M. 1983. Structural and functional organization of the photosystems in spinach chloroplasts: Antenna size, relative electron transport capacity, and chlorophyll composition. *Biochim. Biophys. Acta* 724: 473-484

- Melis, A., Spangfort, M. and Andersson, B. 1987. Light-absorption and electron-transport balance between photosystem II and photosystem I in spinach chloroplasts. *Photochem. Photobiol.* 45: 129-136
- Neale, P.J., Cullen, J.J., Lesser, M.P. and Melis, A. 1993. Physiological bases for detecting and predicting photoinhibition of aquatic photosynthesis by PAR and UV radiation. *Photosynthetic responses to the environment*. Current Topics in Plant Physiology. Edited by Yamamoto, H.Y. and Smith, C.M., American Society of Plant Physiologists Publication Series, Vol. 8: 61-77
- Nield, J., Orlova, E.V., Morris, E.P., Gowen, B., Van Heel, M. and Barber, J. 2000. 3D map of the plant photosystem II supercomplex obtained by cryoelectron microscopy and single particle analysis. *Nature* 7: 44-47
- Niyogi, K.K. 1999. Photoprotection revisited: Genetic and molecular approaches. *Annu. Rev. Plant Physiol. Plant Mol. Biol.* 50: 333-359
- Niyogi, K.K., Björkman, O. and Grossman, A.R. 1997a. *Chlamydomonas* xanthophyll cycle mutants identified by video imaging of chlorophyll fluorescence quenching. *Plant Cell* 9: 1369-1380
- Niyogi, K.K., Björkman, O., Grossman, A.R. 1997b. The roles of specific xanthophylls in photoprotection. *Proc. Natl. Acad. Sci. USA* 94: 14162-14167
- Niyogi, K.K., Grossman, A.R. and Björkman, O. 1998 Arabidopsis mutants define a central role for the xanthophyll cycle in the regulation of photosynthetic energy conversion. *Plant Cell* 10: 1121-1134
- Pogson, B.J., McDonald, K.A., Truong, M., Britton, G. and DellaPenna, D. 1996. Arabidopsis carotenoid mutants demonstrate that lutein is not essential for photosynthesis in higher plants. *Plant Cell* 8: 1627-1639
- Pogson, B.J., Niyogi, K.K., Björkman, O. and DellaPenna, D. 1998. Altered xanthophyll compositions adversely affect chlorophyll accumulation and nonphotochemical quenching in *Arabidopsis* mutants. *Proc. Natl. Acad. Sci. USA* 95: 13324-13329
- Polle, J.E.W., Benemann, J.R., Tanaka, A. and Melis, A. 2000. Photosynthetic apparatus organization and function in the wild type and a chlorophyll *b*-less mutant of *Chlamydomonas reinhardtii*. Dependence on carbon source. *Planta* 211: 335-344
- Powles, S.B. and Critchley, C. 1980. Effect of light intensity during growth on photoinhibition of intact attached bean leaflets. *Plant. Physiol.* 65:1181-1187
- Ruban, A.V., Young, A.J., Pascal, A.A. and Horton, P. 1994). The effects of illumination on the xanthophyll composition of the photosystem II light-harvesting complex of spinach thylakoid membranes. *Plant Physiol.* 104: 227-234

Sandona, S., Croce, R., Pagano, A., Crimi, M. and Bassi, R. 1998. Higher plants light harvesting proteins. Structure and function as revealed by mutation analysis of either protein or chromophore moieties. *Biochim. Biophys. Acta* 1365: 207-214

Sumner, J.B. and Somers, G.F. 1944. Laboratory experiments in biological chemistry. pp. 69-75. Academic Press Inc., New York

Tardy, F. and Havaux, M. 1996. Photosynthesis, chlorophyll fluorescence, light-harvesting system and photoinhibition resistance of a zeaxanthin-accumulating mutant of *Arabidopsis thaliana*. *J. Photochem. Photobiol.* 34: 87-94

Verhoeven, A.S., Adams III, W.W., Demmig-Adams, B., Croce, R. and Bassi, R. 1999. Xanthophyll cycle pigment localization and dynamics during exposure to low temperatures and light stress in *Vinca major*. *Plant Physiol.* 120: 727-737

Yamamoto, H.Y. 1979. Biochemistry of the violaxanthin cycle in higher plants. *Pure Appl. Chem.* 51: 639-648

Yamamoto, H.Y. 1985. Xanthophyll cycles. *Methods in Enzymology* 110: 303-312

CYCLIC PHOTOBIOLOGICAL ALGAL H₂-PRODUCTION

Maria L. Ghirardi, Sergey Kosourov and Michael Seibert
National Renewable Energy Laboratory
1617 Cole Blvd.
Golden, CO 80401

Abstract

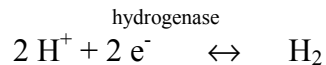
We have achieved continuous photoproduction of large volumes of H₂ by down-regulating O₂ evolution activity in algal cells (Ghirardi, *et al.* 2000a). Trends in Biotechnol. 18: 506-511). This was accomplished by temporarily depleting the cells of sulfur (Melis, *et al.* 2000). Investigations are underway to simplify the system, accelerate the transition to the H₂-production mode upon sulfur depletion, and to determine the metabolic pathways involved in the process.

Current year results include the observations that: (i) the rates of H₂ production are not limited by the level of enzyme activity nor by the residual *capacity* of the algal cells to extract reductants from H₂O but are directly related to the steady-state rate of photosynthetic electron transport, (ii) synchronization of the cultures by light/dark phases results in a higher total output of H₂ but lower specific activity; and (iii) rigorous sulfur depletion and controlled sulfur re-addition increase the total amount of H₂ produced, increase the specific rate of H₂ production, and shorten the transition from the aerobic to the anaerobic, H₂-production phase.

We conclude that the used of light/dark growth cycles, as required for cultivation of algal cells under outdoor conditions does not have any adverse effects on subsequent H₂ photoproduction (under continuous illumination) when the cultures are re-supplemented with low concentrations of sulfate. In fact, some results indicate increased yields of H₂ gas upon re-addition of sulfate.

Introduction

Photosynthetic production of H₂ from water is a biological process that can convert sunlight into useful, stored chemical energy. The basic phenomenon has been known for 60 years (Gaffron 1940; Gaffron and Rubin 1942), but little progress has been reported on the biotechnology of the process. Hydrogen production is a property of many phototrophic organisms (Weaver *et al.* 1980; Appel and Schulz 1998; Asada and Miyake 1999; Boichenko *et al.* 2001), and the list of H₂ producers includes several hundred species from different genera of both prokaryotes and eukaryotes (Boichenko and Hoffmann 1994). The enzyme mediating H₂ production in green algae is the reversible (or bidirectional) hydrogenase that catalyzes the following ferredoxin (Fd)-linked reaction in the absence of ATP input (Boichenko and Hoffman, 1994):



Hydrogenase activity appears after several hours of anaerobic induction in the dark (Gaffron and Rubin 1942; Roessler and Lien 1984; Happe *et al.* 1994), and H₂-photoproduction depends on low potential electrons supplied to ferredoxin by the photosynthetic electron-transport chain (Appel and Schulz 1998; Wünschiers *et al.* 2001). Unfortunately, the reversible hydrogenase in green algae is highly sensitive to O₂, which irreversibly inactivates the enzyme's activity within minutes (Ghirardi *et al.* 1997). As a consequence, the direct photoproduction of H₂ from water in algal cultures is difficult to sustain. The sensitivity of hydrogenase to O₂ generated by normal photosynthesis has until now precluded consideration of green algae for possible use in applied H₂-producing systems.

Both chemical and mechanical methods have been developed to remove O₂ produced by the photosynthetic activity of the algal cells. These have included the addition of O₂ scavengers (Healey 1970; Randt and Senger 1985), the use of added reductants (Randt and Senger 1985), and the purging the cultures with inert gases (Greenbaum 1982; Gfeller and Gibbs 1984). However, all these methods are expensive upon scale-up and realistically may not be applicable to applied systems. To keep the cost of H₂ production low, applied systems will have to operate under ambient outdoor conditions (Borodin *et al.* 2000). In attempting to achieve continuous H₂ production in green algae under these conditions, we subjected the cultures to sulfur (in the form of sulfate) depleted conditions (Melis *et al.* 2000). In the absence of sulfur but in the presence of light, *C. reinhardtii* cells lose PSII activity reversibly. After about 20 – 24 hours, the rate of O₂ evolution by PSII decreases to the rate of O₂ uptake by respiration. After this point, the algae respire all remaining dissolved O₂, rapidly making their environment anaerobic. Under these conditions, the cells induce the reversible hydrogenase and produce H₂ for up to 4 days (Melis *et al.* 2000; Ghirardi *et al.* 2000a). Subsequently, if sulfate is re-added to the spent cultures at high concentration, addition cycles of cell growth and H₂ production can be observed (Ghirardi *et al.* 2000a).

The rates of H₂ production by sulfur-depleted algal cells are still too low at this time to warrant the development of commercial systems. To address this issue, we have investigated biochemical factors that might limit the rates. We have also studied the effects of

synchronization of cell division and re-addition of micromolar concentrations of sulfur to sulfur-depleted medium on H₂ photoproduction by *C. reinhardtii* cells.

Materials and Methods

Cell growth

Chlamydomonas reinhardtii, strain cc124, was grown photoheterotrophically on Tris-acetate-phosphate (TAP) medium, pH = 7.2, in flat glass bottles with stirring at about 25°C. During growth, the cultures were continuously illuminated with cool-white fluorescent light (~ 200 $\mu\text{E}\cdot\text{m}^{-2}\cdot\text{s}^{-1}$) and bubbled with 3% CO₂ in air. The gas mixture was sterilized using membrane filters with a 0.2 μm pore size (Acro 37 TF, Gelman Sciences, Inc., Ann Arbor, MI). Algal cells were grown to the mid-logarithmic phase ($2 - 5 \times 10^6$ cells $\cdot\text{ml}^{-1}$), harvested by centrifugation at 2000 g for 5 min, washed five times in TAP-minus-sulfur medium, and resuspended in the same medium to a final concentration of about 9 – 12 $\mu\text{g Chl}\cdot\text{ml}^{-1}$ ($4-5 \times 10^6$ cells $\cdot\text{ml}^{-1}$).

The synchronous division of *C. reinhardtii* cells was achieved by alternating light and dark (14-h light: 10-h dark) periods and maintained by daily dilution of the cultures to a starting density of about $0.5 - 1 \times 10^6$ cells $\cdot\text{ml}^{-1}$. In this study, the synchronized cultures were harvested 4 h after the beginning of light cycle, washed and re-suspended in TAP-minus-sulfur medium as described above. This particular time in the cell cycle was chosen based on preliminary experiments indicating higher rates of H₂ evolution following sulfur deprivation at this point.

Bioreactor system

Both synchronized and unsynchronized sulfur-deprived cell suspensions were placed in each of four specially fabricated, glass photobioreactors (4-cm optical path, 1.2 L culture volume; Ghirardi *et al.* 2000b). The algal cells were cultured under continuous two-sided illumination of ~300 $\mu\text{E}\cdot\text{m}^{-2}\cdot\text{s}^{-1}$ (twelve 40-W cool-white fluorescent lamps) at $28 \pm 1.5^\circ\text{C}$ for up to 140 h. Four biophysical and electrochemical parameters in addition to the volume of H₂ gas produced were monitored simultaneously and independently in each of the four photobioreactors: dissolved O₂ (pO₂), redox (eH), pH, and temperature. The quantity of gas produced by algal cultures was measured by the displacement of water from a gas-to-liquid conversion vessel to a liquid-accumulating bottle. The latter was weighed to determine the amount of gas produced. Finally, an integrated microprocessor system, consisting of two computers, was used for data accumulation, storage and processing. Before each experiment, the photobioreactors (with the electrodes in place) were washed several times with deionized double-distilled water and sterilized in an autoclave. The specific rates of H₂ production were calculated at the beginning of the H₂-production phase (during the first 10–15 h) and expressed on the basis of chlorophyll content measured in the cultures at that time.

Biochemical assays

Hydrogenase activity was assayed amperometrically by measuring the initial rate of light-induced H₂ production (Ghirardi *et al.* 1997), or chemically using reduced methyl viologen as the electron donor. Sealed 13.5 ml glass vials, containing 1 ml of 10 mM oxidized methyl viologen

in 50 mM potassium-phosphate buffer (pH = 6.9) and 0.2% w/v Triton X 100, were flushed for 20 min with ultra pure Ar gas. Then, 100 μ L of anaerobic 100 mM Na dithionite solution was added to the vials to reduce the methyl viologen. The reaction was performed at 37°C in the dark and started by the injection of 1 ml of anaerobic cell suspension taken directly from the bioreactor. The rate of H₂ production was measured with a Hewlett Packard gas chromatograph (Model 1050, Hewlett-Packard, Palo Alto, CA) and expressed on the basis of the sample chlorophyll content.

Photosynthetic O₂ evolution and dark respiration were measured at 25°C with a Clark-type O₂ electrode as described previously (Melis *et al.* 2000). The chlorophyll *a* + *b* content was assayed spectrophotometrically in 95 % ethanol extracts by the method of Spreitzer (Harris 1989). The protein concentration in the cells on a ml of culture basis was determined according to the method of Lowry *et al.* (1951). Light intensities on the surfaces of growth bottles and photobioreactors were measured with a Li-Cor quantum photometer (Model LI-250, Lincoln, NE).

Results

Biochemical factors limiting algal H₂ photoproduction during sulfur depletion

The production of H₂ by sulfur-depleted cells occurs at fairly high steady-state rates in the early stages of sulfur depletion (Ghirardi *et al.* 2000b), but halts after about 3-4 days. In order to study factors that might limit the rates of H₂ production, we measured the hydrogenase activity of the organism following incubation for different periods of time in sulfur-depleted medium and compared it to the rate of H₂ gas collection. Two assays were used to determine enzyme activity. The first used a Clark electrode to amperometrically measure the amount of H₂ released by the cells upon illumination (electrode). The second measured the dark enzymatic reduction of protons by dithionite-reduced methyl viologen. Trixon X-100 was added to facilitate the penetration of the reductant into the cells, and the amount of H₂ produced was measured by gas chromatography (GC). Figure 1 shows the changes in hydrogenase activity, measured by the two assays (closed and open circles, respectively) as a function of the incubation time in sulfur-depleted medium. For comparison, the open triangles show the rate of H₂ collection in the same units. The capacity for hydrogenase activity measured with either of the two assays is substantially higher than the rate of actual gas collection at every time point, suggesting that factors other than enzyme activity are involved in limiting the reaction.

Earlier work (Ghirardi *et al.* 2000b) suggested that at least 80% of the reductant used for H₂ production by sulfur-depleted cells originated from the oxidation of H₂O (with concomitant O₂ evolution) by Photosystem II (PSII). We then investigated the possibility that the rate of PSII-catalyzed O₂ evolution limited H₂ production. Figure 1 (closed inverted triangles) also shows that the residual capacity of the cells for photosynthetic O₂ evolution (a 4-electron reaction) is about twice as high as the rate of H₂ production (a 2-electron reaction) and decreases as a function of incubation time in sulfur-depleted medium. These data further confirm the close link between photosynthetic electron transport and H₂ production in sulfur-depleted cells. They also suggest that steady-state H₂ evolution is possibly limited by factors that lower the effective capacity of photosynthetic electron transport under steady-state conditions.

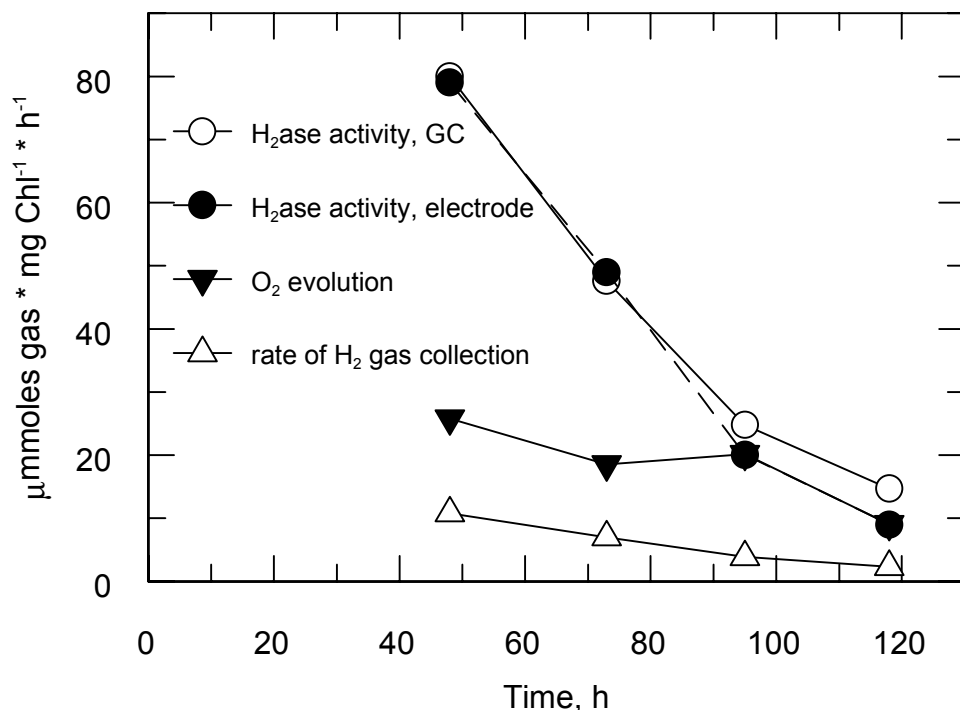


Figure 1. Measurements of hydrogenase activity, capacity for photosynthetic O₂ evolution and the rate of H₂ gas collection by algal cells as a function of incubation time under sulfur-depleted conditions.

Effects of synchronization of growth prior to removal of sulfur from the culture medium on H₂ photoproduction

The simultaneous and continuous monitoring of a number of biophysical and electrochemical parameters in *C. reinhardtii* cultures shows that the algae exhibit dramatic changes in dissolved oxygen (pO₂), pH and redox potential (eH) during adaptation to sulfur-deprived conditions (Kosourov *et al.* submitted). Light/dark synchronized, sulfur-deprived *Chlamydomonas* cultures transition first from an aerobic to an anaerobic phase and then start to produce H₂. Unsynchronized cultures exhibit similar behavior.

The kinetic parameters of the response to sulfur depletion by the two types of cultures, however, show significant differences, as seen in Table 1. Synchronized cells become anaerobic earlier and thus begin producing H₂ earlier. We also observed that the specific rate of H₂ production, calculated at the beginning of H₂ production phase was lower in synchronized cells compared to unsynchronized cells (3.27 ± 0.83 vs. 5.74 ± 0.30 µmoles H₂•mg Chl⁻¹•h⁻¹, respectively). On the other hand, the final yields of H₂ collected over the 140-h experiment were similar in both types of cultures (about 80–86 ml).

In summary, during adaptation to sulfur-depletion conditions, synchronized cells transition from one phase to the next earlier than unsynchronized cells, and thus start producing H₂ sooner, but with a lower specific rate.

Table 1. Kinetic Parameters for H₂ Photoproduction by Sulfur-Depleted Algal Cells

Sulfur concentration, μM	Start of the anaerobic phase, h	Start of H ₂ photoproduction, h	Specific initial rate of H ₂ photoproduction ¹	Total yield of H ₂ at 140 h
Synchronized cultures				
0	25-27	39-43	3.27 ± 0.83^2	80 ± 31
12.5	33-36	38-39	5.15 ± 0.26	219 ± 43
25	35-38	38-41	5.94 ± 0.56	241 ± 56
50	35-37	39-40	3.96 ± 0.30	109 ± 9
100	-	68 ³	-	56 ³
Unsynchronized cultures				
0	31-40	41-49	5.74 ± 0.30	86 ± 19
12.5	30-37	39-47	6.40 ± 0.39	127 ± 14
25	35-37	44-47	5.31 ± 0.16	152 ± 11
50	32-38	43-49	3.99 ± 0.26	191 ± 27
100	-	144 ³	-	43 ³

¹ $\mu\text{moles H}_2 \cdot \text{mg Chl}^{-1} \cdot \text{h}^{-1}$

²Values are means \pm standard deviations of three to five independent experiments

³One experiment

Effects of addition of micromolar concentrations of sulfur on H₂ photoproduction by sulfur-depleted cells

Preliminary experiments showed that the total yield of H₂ produced by sulfur-deprived algal cultures depends on the stringency of the sulfur-deprivation procedure. We suspected that small quantities of sulfur remaining in the medium after incomplete washing might still affect the metabolic pathways responsible for H₂ evolution. Therefore, we studied the effect of re-adding micromolar concentrations of sulfur to algal cultures that had been rigorously depleted of sulfur. In these experiments, *C. reinhardtii* cells were washed five times in TAP-minus-sulfur medium, resuspended in the same medium, and then placed into the photobioreactors.

Additions of small quantities of sulfate (12.5–50 μM MgSO₄ final concentrations) to sulfur-depleted cell suspensions resulted in an initial increase in the culture density, measured on the basis of both cellular chlorophyll and protein contents (not shown). These increases were accompanied by only slight initial increases in the cell number, suggesting that re-addition of sulfate to the growth medium affects culture density mainly through an acceleration of cell growth, but not of cell division. As a result of increases in culture density (to a limited point), we also observed increases in the total H₂ output in both synchronized and unsynchronized algal cultures (Table 1).

The maximum effect of sulfur re-addition on H₂ production was observed in synchronized cell suspensions supplemented with about 25 μM sulfate. The length of the H₂-production phase increases to above 100 h (the cells still produced H₂ by the end of the 140-h experiment), and the final yield of H₂ gas produced per liter of culture increased from about 80 ml to 241 ml (more than 3 times) compared to cells without added sulfate. Re-addition of sulfate at 100 μM results in a significant delay in the start of the H₂-photoproduction phase and in a decrease in the H₂ output in both synchronized and unsynchronized cells.

The specific rates of H₂ photoproduction calculated at the beginning of the H₂-production phase vary, as a function of added sulfate concentration. Re-addition of small quantities of sulfate (12.5 – 25 μM) to the sulfur-depleted cultures resulted in an increase in the initial specific rates of H₂ photoproduction in both synchronized and unsynchronized cell cultures. However, the relative effect of sulfur re-addition was also greater in synchronized cells, particularly in the concentration range below 25 μM. Further increases in the initial sulfate concentration have a clearly negative effect on the specific rates as mentioned before. The decrease in the specific rate of H₂ production at above 25 μM was shown to be most likely the result of increased light limitations (not shown), since the addition of inorganic sulfur at these levels leads to a significant increase in the optical density of the cultures.

Effects of re-addition of sulfur on residual water-oxidation capacity

Since we have shown above that the rate of H₂ photoproduction by sulfur-depleted cells is dependent on the capacity of the culture for photosynthetic electron transport, we hypothesized that the increase in the specific rates of H₂ production observed upon re-addition of sulfate could be due to a specific effect of sulfur on the residual activity of PSII. We measured O₂-evolution and respiratory capacity of the cells directly with a Clark-type O₂ electrode. Table 2 shows that re-addition of sulfate at the beginning of the experiment indeed increases the residual O₂ evolution capacity, but it also increases the respiratory activities of the cells measured at the start of the H₂-production phase. These results suggest that addition of controlled concentrations of sulfate to sulfur-depleted cells protects the residual PSII activity against inactivation.

Table II. Effect of sulfur addition on rates of photosynthetic and respiratory electron transport by sulfur-depleted synchronized algal cultures

Sulfur concentration, μM	Rate of Photosynthetic O ₂ Evolution ¹	Rate Respiration ¹
0	1.5	19
12.5	12	24
25	15	31
50	20	34

¹μmoles O₂•mg Chl⁻¹•h⁻¹

Discussion

The algal reversible hydrogenase is extremely sensitive to O₂, and H₂ production does not occur in this class of organism under normal photosynthetic conditions. Recently, we reported a new physiological approach that enables sustained H₂ photoproduction with the green alga, *C. reinhardtii*, based on the removal of inorganic sulfur from the culture medium (Melis *et al.* 2000; Ghirardi *et al.* 2000a). Under sulfur-deprived conditions, algae lose photosynthetic O₂-evolution activity with time, transition to an anaerobic phase as the result of respiratory activity, and then start to produce H₂ for up to 4 days.

We have investigated H₂ photoproduction by both synchronized and unsynchronized cultures of *C. reinhardtii* under sulfur-deprived conditions. Oxygen consumption and the establishment of anaerobiosis is critical for subsequent H₂ production, because a delay in the transition from an aerobic to an anaerobic phase also results in a delay in the onset of H₂ evolution (Table 1). The use of synchronized cell suspensions, which are induced by light/dark cycles simulating natural photoperiodic conditions outdoors, decreases the time until the start of H₂ production by about 4 hours compared to unsynchronized cultures, and thus promote earlier onset of H₂ photoproduction (Table 1). At the same time, in the absence of inorganic sulfur in the medium, both types of cultures demonstrate similar total amounts of H₂ output (Table 2) over the 140 hours of the experiment (but synchronized cells show lower initial specific activity). These findings demonstrate that, in principle, synchronized cell suspensions generated by light/dark cycles could be used in an outdoor H₂-production system.

Moreover, we also found that re-addition of micromolar quantities of inorganic sulfur as magnesium sulfate to the sulfur-deprived cell suspension significantly affects both the initial specific rate of H₂ evolution and the total output of H₂. These data raise the question as to why the re-addition of sulfate affects H₂ production in sulfur-deprived cultures. We checked the influence of re-added sulfur on both the residual O₂-evolving activity of PSII and the rate of respiration measured at the start of the H₂-photoproduction phase. Based on these data we conclude that sulfur does indeed affect H₂ production in this system by increasing the residual activity of PSII.

In conclusion, optimization of H₂ photoproduction in this system can be achieved by carefully controlling the amount of sulfur in the medium at the time of sulfur deprivation. On the one hand, the presence of micromolar concentrations of inorganic sulfur stimulates the residual activity of PSII upon which most of the electrons for H₂ production depend. But on the other, the addition of too much sulfur (above 50 μM) results in the over-expression of this activity, which in turn delays the onset of H₂ production and lowers the final yield of H₂ produced. Cell synchronization is also an important parameter. In this context, it is clear that additional experiments are necessary in order to determine if there are other physical and biochemical parameters that might be manipulated to increase the yield of H₂ produced.

References

- Appel J, Schulz R. 1998. Hydrogen metabolism in organisms with oxygenic photosynthesis: hydrogenases as important regulatory devices for a proper redox poising? *J Photochem Photobiol* 47:1-11.
- Asada Y, Miyake J. 1999. Photobiological hydrogen production. *J Biosci Bioeng* 88:1-6.
- Boichenko VA, Hoffmann P. 1994. Photosynthetic hydrogen-production in prokaryotes and eukaryotes: occurrence, mechanism, and functions. *Photosynthetica* 30:527-552.
- Boichenko VA, Greenbaum E, Seibert M. 2001. Hydrogen production by photosynthetic microorganisms. *In* Photoconversion of Solar Energy: Molecular to Global Photosynthesis (M.D. Archer and J. Barber, eds) vol. 2, Imperial College Press, London, in press.
- Borodin VB, Tsygankov AA, Rao KK, Hall DO. 2000. Hydrogen production by *Anabaena variabilis* PK84 under simulated outdoor conditions. *Biotech Bioeng* 69:478-485.
- Gaffron H. 1940. Carbon dioxide reduction with molecular hydrogen in green algae. *Am J Bot* 27:273-283.
- Gaffron H, Rubin J. 1942. Fermentative and photochemical production of hydrogen in algae. *J Gen Physiol* 26:219-240.
- Gfeller RP, Gibbs M. 1984. Fermentative metabolism of *Chlamydomonas reinhardtii*, I: Analysis of fermentative products from starch in dark and light. *Plant Physiol* 75:212-218.
- Ghirardi ML, Togasaki RK, Seibert M. 1997. Oxygen sensitivity of algal H₂-production. *Appl Biochem Biotech* 63:141-151.
- Ghirardi ML, Zhang L, Lee JW, Flynn T, Seibert M, Greenbaum E, Melis A. 2000a. Microalgae: a green source of renewable H₂. *Trends Biotechnol* 18:506-511.
- Ghirardi ML, Kosourov S, Tsygankov A, Seibert M. 2000b. Two-phase photobiological algal H₂-production system. Proceedings of the 2000 DOE Hydrogen Program Review. NREL/CP-570-28890.
- Greenbaum E. 1982. Photosynthetic hydrogen and oxygen production: kinetic studies. *Science* 196:879-880.
- Happe T, Mosler B, Naber JD. 1994. Induction, localization and metal content of hydrogenase in the green-alga *Chlamydomonas reinhardtii*. *Eur J Biochem* 222: 769-774.
- Harris EH. 1989. The *Chlamydomonas* sourcebook: a comprehensive guide to biology and laboratory use. San Diego: Academic Press. 780 p.

Healey FP. 1970. The mechanism of hydrogen evolution by *Chlamydomonas moewusii*. Plant Physiol 45:153-159.

Kosourov S, Tsygankov, A, Seibert and Ghirardi ML. Sustained Hydrogen Photoproduction by *Chlamydomonas reinhardtii*—Effects of Culture Parameters. submitted.

Lowry OH, Rosebrough NJ, Farr AL, Randall RJ. 1951. Protein measurement with the Folin phenol reagent. J Biol Chem 193: 265-275.

Melis A, Zhang L, Forestier M, Ghirardi ML, Seibert M. 2000. Sustained photobiological hydrogen gas production upon reversible inactivation of oxygen evolution in the green alga *Chlamydomonas reinhardtii*. Plant Physiol 122:127-136.

Randt C, Senger H. 1985. Participation of the two photosystems in light dependent hydrogen evolution in *Scenedesmus obliquus*. Photochem Photobiol 42:553-557.

Roessler PG, Lien S. 1984. Activation and *de novo* synthesis of hydrogenase in *Chlamydomonas*. Plant Physiol 76:1086-1089.

Weaver PF, Lien S, Seibert M. 1980. Photobiological production of hydrogen. Solar Energy 24:3-45.

Wünschiers R, Senger H, Schulz R. 2001. Electron pathways involved in H₂-metabolism in the green alga *Scenedesmus obliquus*. Biochim Biophys Acta 1503:271-278.

EFFICIENT HYDROGEN PRODUCTION USING ENZYMES OF THE PENTOSE PHOSPHATE CYCLE

Narinder I. Heyer and Jonathan Woodward
Oak Ridge National Laboratory
Oak Ridge, TN 37831-6194

Abstract

Increase in the production of hydrogen from biomass-derived glucose and attainment of the maximum molar yield of H₂, can be achieved through the enzymes of the pentose phosphate cycle in conjunction with a hyperthermophilic hydrogenase. This process centers on three NADP⁺ dependent enzymes, glucose-6 phosphate dehydrogenase (G6PDH), 6-phosphogluconate dehydrogenase (6PGDH) and hydrogenase from *Pyrococcus furiosus*. The dehydrogenases are currently obtained from mesophilic sources. However, in order to increase the rates and sustainability of hydrogen production, work has been carried out to isolate the genes for these enzymes from thermophilic sources. Success has been achieved through the isolation and cloning of both genes from the bacterial species *Thermotoga maritima*.

Individual characterization of both mesophilic enzymes has revealed that the first enzyme G6PDH, has a 20-fold greater turnover number than that of the second enzyme. However, the second enzyme 6PGDH, is far more thermostable, possessing a t_{50%} of 130 mins at 60°C. The maximum yield of hydrogen from glucose using only the oxidative portion of the pentose phosphate pathway (two moles per mole of glucose 6-phosphate) has been achieved using mesophilic sources of these enzymes in conjunction with a hyperthermophilic hydrogenase at 40°C. Additional monitoring of CO₂ evolution confirmed the stoichiometry of H₂ to CO₂ to be 2:1. Variation of the components and conditions of the system show that 6-PGDH is the rate-limiting step in the pathway and is required in over 20-fold greater amounts to prevent the build up of the intermediate 6-phosphogluconic acid.

Introduction

Significance and Background

The inevitable consumption of all our supplies of fossil fuels requires the development of alternative sources of energy for the future. Introduction of a hydrogen economy will gain greater importance due to the promise of using hydrogen over fossil fuels. These advantages include its limitless abundance and also its ability to burn without generating any toxic by-products, where the only by-product of hydrogen combustion is water.

At present hydrogen is widely used in petroleum refining and chemical processes, metal processing operation, in the electronics industry and more famously as rocket fuel. In addition, it is now gaining more acclaim as an alternative fuel for transportation (Leslie, 1997).

Hydrogen is currently produced by several methods, including steam/methane reforming (Wilson and Newall, 1970), dissociation of ammonia, and by-product streams from chemical manufacturing and petroleum reforming. However, despite all the promise of this potential new fuel, much controversy is being made about these methods of manufacturing hydrogen. This is due to the absence of a practical natural source of hydrogen. Therefore, it must be made by transforming some other energy source at a cost. Even electrolysis of sea water, a vast reserve of hydrogen, would require the use of electricity. Additionally, the manufacture of hydrogen from petroleum and methane eventually leads to the release of carbon dioxide, thus creating a cost to the environment. Consequently this has led to the discovery of hydrogen manufacture from renewable, less costly and non-polluting sources.

Alternative method of hydrogen production

The enzymatic conversion of cellulosic waste to H_2 via an *in vitro* enzymatic pathway (Woodward *et al.*, 1996; Woodward and Orr, 1998; Inoue *et al.*, 1999; Woodward *et al.*, 2000) involves the conversion of potential glucose sources such as cellulose by cellulases, and plant sap (i.e. sucrose) by invertase and glucose isomerase to glucose. Glucose, the sugar produced by photosynthesis, is also renewable, unlike fossil fuels such as oil. The glucose substrate is then oxidized and the cofactor, $NADP^+$ is simultaneously reduced. The presence of a pyridine-dependent-hydrogenase in this system (Egerer *et al.*, 1982; Bryant and Adams, 1989), causes the regeneration and recycling of $NAD(P)^+$ with the concomitant production of molecular hydrogen.

Pentose Phosphate Pathway (PPP)

The pentose phosphate pathway is primarily an anabolic pathway that utilizes the 6 carbons of glucose to generate 5 carbon sugars and reducing equivalents (Fig. 1). However, this pathway does oxidize glucose and under certain conditions can completely oxidize glucose to CO_2 and water. The pentose phosphate pathway has both an oxidative and non-oxidative arm.

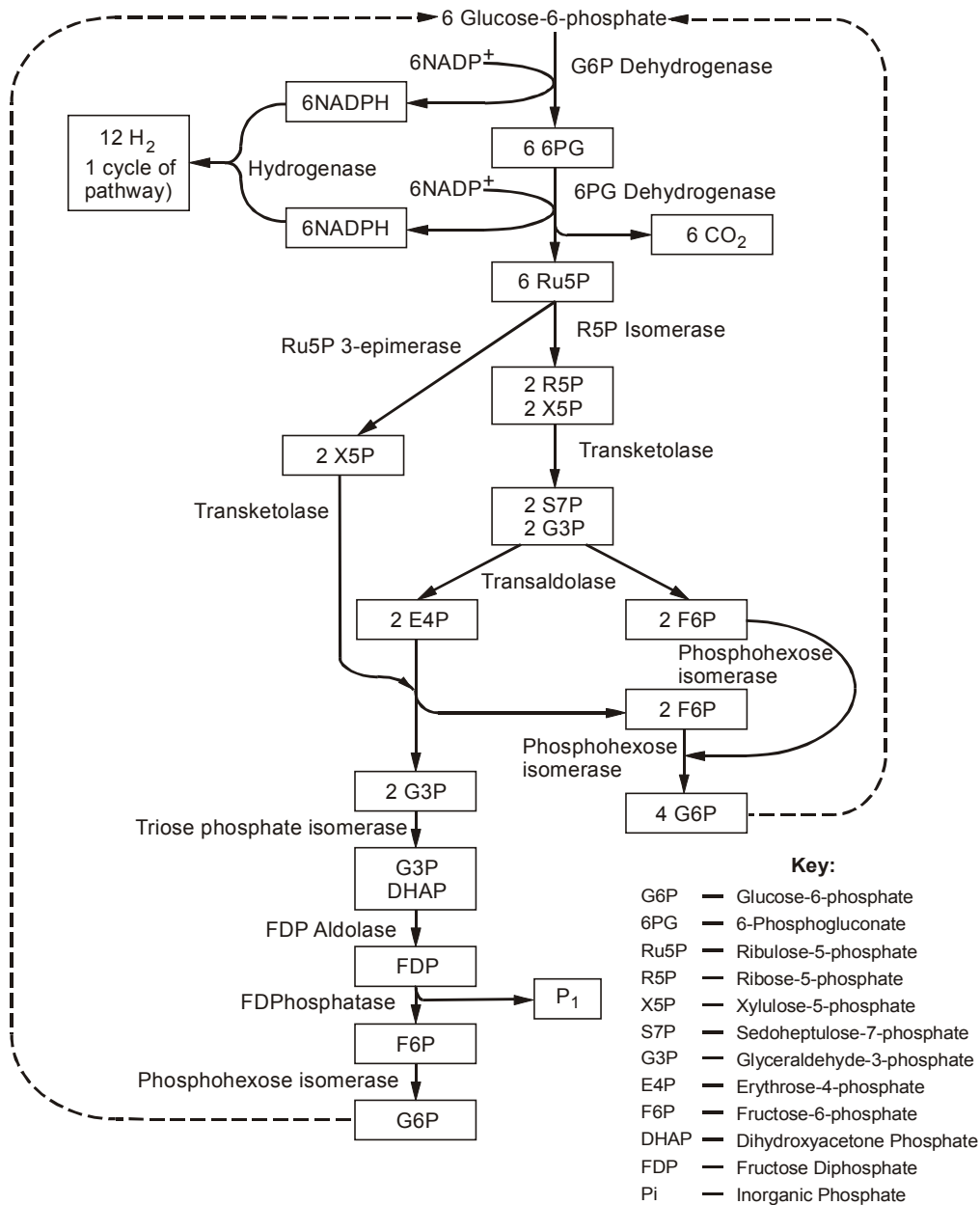


Fig. 1 The pentose phosphate pathway

Oxidative Branch of the Pentose Phosphate Pathway

The oxidation steps, utilizing glucose-6-phosphate (G6P) as the substrate, occur at the beginning of the pathway and are the reactions that generate NADPH. The reactions catalyzed by glucose-6-phosphate dehydrogenase and 6-phosphogluconate dehydrogenase generate two moles of NADPH for every mole of glucose-6-phosphate (G6P) that enters the PPP. The first step is rate-limiting and is essentially irreversible due to the spontaneous hydrolysis of the intermediate 6-

phosphogluconolactone into 6-phosphogluconic acid. It is regulated by the $\text{NADP}^+/\text{NADPH}$ ratio through substrate competition.

Non-oxidative Branch of the Pentose Phosphate Pathway

The non-oxidative reactions of the PPP are primarily designed to generate ribose-5-phosphate (R5P) for the synthesis of nucleotides and nucleic acids. Equally important reactions of the PPP are the conversion of dietary 5 carbon sugars into both 6- (fructose-6-phosphate) and 3- (glyceraldehyde-3-phosphate) carbon sugars, which can then be utilized by the pathways of glycolysis. The 6-carbon sugars can be recycled into the pathway in the form of G6P, generating more NADPH.

Thermostable Enzymes

With the exclusion of phylogenetic variations, thermostable enzymes are found to be very similar to their mesophilic counterparts in terms of their amino acid sequence (Vielle *et al.*, 1995; Burdette *et al.*, 1996) and three-dimensional structures and catalytic mechanisms (Fujinaga *et al.*, 1993; Russel *et al.*, 1997). In addition to enhanced stability at elevated temperatures, thermophilic enzymes also possess a greater resistance to chemical denaturation than their mesophilic counterparts (Lebbink *et al.*, 1995).

Three Domains of Life

The evolutionary history of life is provided by sequence comparisons of small subunit rRNA due to its strictly conserved function and its non-transfer between species. Comparison of these sequences proposes a tripartite division of the living world into the following domains, Eukarya, Eubacteria and Archaea (Fig. 2) (Woese and Fox, 1977; Woese *et al.*, 1990).

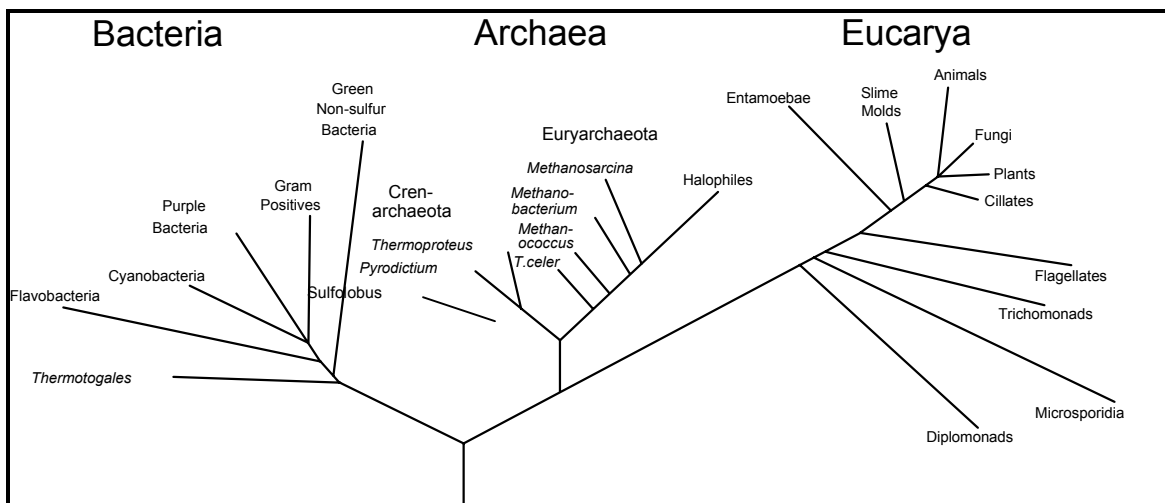


Fig. 2 The Universal phylogenetic tree, constructed from rRNA sequence comparisons, according to Woese *et al.* (1990).

Sulfolobus solfataricus

Sulfolobus solfataricus is an aerobic hyperthermophilic archaeobacteria able to grow at 87°C and pH 3.5 (Zillig et al., 1980). *Sulfolobus solfataricus* belongs to the kingdom of Crenarchaeota within the domain of Archaea (Fig. 2). Various strains of *Sulfolobus solfataricus* have been isolated from a number of geographically distant, aquatic and terrestrial solfatara fields (Brock et al., 1972; De Rosa et al., 1974; De Rosa et al., 1975; Zillig et al., 1980; Segerer and Stetter, 1991; Zillig et al., 1994). It is able to grow on various complex organic substrates, as well as simple sugars and amino acids (Brock et al., 1972; Segerer and Stetter, 1991). Its central metabolism is thought to occur via non-phosphorylated intermediates through a pathway called the non-phosphorylated Entner-Doudoroff (ED) pathway. However, further analysis by Selig et al. (1997) revealed that a variety of hyperthermophiles, and particularly the anaerobic archaea, were able to degrade sugar to pyruvate using modified Embden-Meyerhof (EM) and ED pathways or a combination of both.

Thermotoga maritima

Thermotoga maritima is an anaerobic hyperthermophilic eubacterium with an optimum growth temperature of 80°C, that has been isolated from geothermally-heated sea floors in Italy and the Azores (Huber et al., 1986). *T. maritima* is able to grow on many simple and complex carbohydrates including glucose, sucrose, starch, cellulose and xylan (Huber et al., 1986; Huber et al., 1992).

T. maritima type strain, MSB8 was cloned, sequenced and assembled by The Institute for Genomic Research (TIGR) from a culture derived from a single cell provided by R. Huber (Nelson et al., 1999). Small subunit ribosomal RNA (SSU rRNA) phylogeny places this bacterium as one of the deepest and most slowly evolving lineages in the Eubacteria (Achenbach-Richter et al., 1987). In addition, conservation of gene order between *T. maritima* and the Archaea in many of the clustered regions suggests that lateral gene transfer may have occurred between thermophilic Eubacteria and Archaea. Complete genome sequencing revealed the presence of the enzymes constituting the pentose phosphate pathway. However, initial investigations did not find all the expected enzyme activities for this pathway (Nelson et al., 1999). Metabolism of sugar in *T. maritima* is thought to occur via the EM, ED and the pentose phosphate pathways (Nelson et al., 1999; Selig et al., 1997).

Oxidative pentose phosphate enzymes from T. maritima genome project

The gene coding for G6PDH is located at 1,170,072 – 1,168,555 bp at locus TM1155 and codes for a protein 496 amino acids in length (Fig. 3). At a remote location in the *T. maritima* genome of 459,482 – 460,888 bp, locus TM04308 is the gene coding for 6PGDH. This gene codes for a protein of length 469 aa (Fig. 3).

```

1  MKCSLGLEKC . PDDLRLCFPK . IEQPFQIVIF . GASGDLTKRK . LIPALNRLF . AGILPERFFV
61  GAARTKMDD . KKFRSRFDAN . PDFLEHCSYI . SVDYQDPESF . KQLKNTIETL . IKRIDSSNLV
121  FYLAVPPDLY IPILENLSKT  GLNEKPARVV  IEKPFQKDL  SARRLEDTLQ  KYFQEDQIFR
181  IDHYLGKETV  QNILVFRFAN  FIFEEIWNK  FVDHVQITMA  EDIGVEHRAG  YFENVGLLRD
241  IFQNHMLQIL  ALIAMEPPSS  FNGENFRNER  VKLLRSIRPF  PVEELESWIV  RGQYGRGVVN
301  GKEVPAYREE  PGVAKDSNVE  TFMVAKLFD  NWRWSGVVFPY  LRSRKRLPKK  ITEVAVVFKK
361  IPHSIFAGVP  SDELEPNTIV  FTLQPNEGIS  LEFQVQRPCP  GMFPQLLSMD  FRYEDYFGVK
421  LPDAYERLLL  DVILGDPTLF  MRRDDLEVSW  ELLDPVLKAW  ENDPVRFSPY  VYPAGTWGPR
481  EADLLIERDG  RKWRKL

```

```

1  MKSHIGLIGL  AVMGQNLALN  IARKGYKVS  YNRTAQRTEE  FVKNRVTNEE  IEPHYDIESF
61  VKSLERPRKI  ILMVKAGKPV  DDTISQLLPH  LEPGDLIIDG  GNSHYMDTER  RFKELSEKGI
121  LFLGMGVSGG  EYGALHGPSL  MPGGSREAYN  LVEEILLEIA  AKTEDGPCCT  YVGERSAGHF
181  VKMVHNGIEY  AIMQAIAEVY  HIMRDVLSLS  SEEMSSIFEE  WNRGELSSFL  VEITYKILRK
241  KDEETGKPMV  DVILDKAEQK  GTGKWSQAA  LDLGIPTPSI  NLAVVERVIS  HFKDIRTRLS
301  KLYNKRRSAT  QGSEEFRLDL  RNSLFFAMFM  AFSQGMWLIA  EASKEFGYGV  SLSEVLRIWK
361  GGCIIRAKLI  DTLRRYISNE  NAYLLENEEV  MNLLKKGKIDS  LKNILKASIE  NEIPVPLVSS
421  SYNFMFLTE  ERLPANLIQA  QRDFFGAHTF  ERVDREGVVFH  INWEEGEIG

```

Fig. 3. Amino acid sequences of G6PDH and 6PGDH from *T. martima*, respectively.

Aim

The overall aim is to increase the production of hydrogen from biomass-derived glucose and achieve the maximum molar yield of H₂ by employing the enzymes of the pentose phosphate pathway in conjunction with the hydrogenase from *Pyrococcus furiosus*. This will also require the future development of an immobilized enzyme bioreactor for efficient hydrogen production at high theoretical yields. If this could be achieved practically, this would represent a major innovation that would advance our abilities to develop an efficient and practical system for bio-hydrogen production. The main advantage over hydrogen production by fermentation is that close-to-theoretical yields of hydrogen from sugar would be possible.

The initial objective is to characterize the mesophilic enzymes of the oxidative branch of the pentose phosphate pathway, with a view to identifying the rate-limiting steps and optimizing the system. This process centers on three NADP⁺ dependent enzymes, glucose-6-phosphate dehydrogenase (G6PDH), 6-phosphogluconate dehydrogenase (6PGDH) and hydrogenase (Fig. 4). The dehydrogenases are currently obtained from commercial mesophilic sources, from *Leuconostoc mesenteroides* and *Torula* yeast, respectively. However, in order to increase the rate of hydrogen production, it is necessary to isolate the genes coding for G6PDH and 6PGDH from *Thermotoga maritima*. The final objective is to express these genes as recombinant enzymes in a mesophilic host and incorporate them into an entirely hyperthermophilic *in vitro* enzymatic H₂ production system.

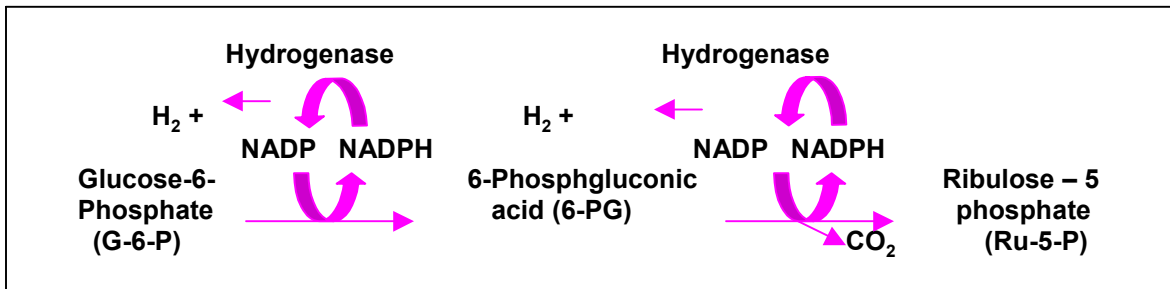


Fig. 4 *In vitro* enzymatic pathway to produce molecular hydrogen

Results

Characterization of the Mesophilic Oxidative Branch of the Pentose Phosphate Pathway

Characterization Studies

Temperature and pH optima

The optimal temperature and pH for the G6PDH from *Leuconostoc mesenteroides* are 30°C and pH 7.8, and for 6PGDH from *Torula* yeast are pH 7.6 and 50°C. The optimal pH of the two-enzyme pathway was also determined to be approximately pH 8 (Fig.5).

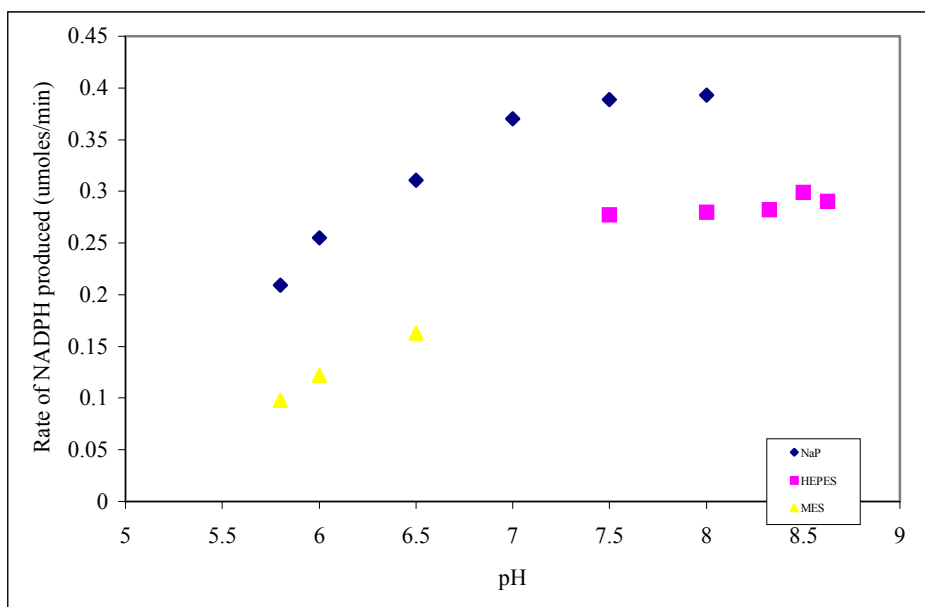


Figure 5. The effect of pH on the activity of the mesophilic oxidative branch of the pentose phosphate pathway.

Thermal inactivation

Thermal inactivation studies of the mesophilic enzymes (Fig. 6) have revealed that G6PDH and 6PGDH possess $t_{50\%}$ at 60°C of 2.88 min and 126.8 min, respectively. Co-incubation of both of the enzymes at a final concentration of 1 mg/mL reveals that the higher protein concentration of the 6PGDH enzyme has not influenced its thermal stability in comparison to the G6PDH enzyme.

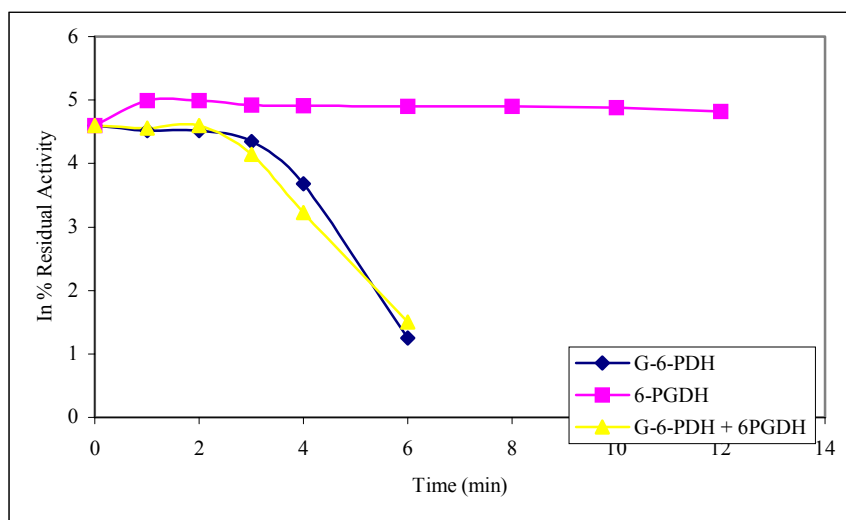


Figure 6. Thermal inactivation studies of 6PGDH and G6PDH at 60°C. Protein concentrations of incubation reactions were the following: 6PGDH at 2 mg/mL, G6PDH at 0.045mg/mL and mixture at 1 mg/mL.

Kinetic parameters

The two individual enzymes were characterized to determine their kinetic parameters (Table 1).

Table 1. Kinetic data for mesophilic pentose phosphate enzyme

Glucose 6-phosphate dehydrogenase enzyme from <i>Leuconstoc mesenteroides</i>			
Substrate	Km (mM)	Vmax (μmoles/min)	Turnover number (min ⁻¹)
glucose 6-phosphate	1.15	0.415	4 x 10 ⁴
NADP ⁺	0.060	0.35	
6-Phosphogluconate dehydrogenase Type IV from <i>Torula Yeast</i>			
Substrate	Km (mM)	Vmax (μmoles/min)	Turnover number (min ⁻¹)
6-phosphogluconic acid	1.65	0.22	1.9 x 10 ³
NADP ⁺	0.12	0.23	

Product inhibition

6-Phosphogluconic acid inhibition assays These were carried out at 40°C in 0.2 M sodium phosphate buffer, pH 7.5 using 0.1U of G6PDH, 1 mM of NADP⁺ and 5 mM of Glucose-6-phosphate. No inhibition was observed at 10 mM concentrations of 6-phosphogluconic acid.

Ribulose-5-phosphate inhibition assays These were carried out at 40°C in 0.2 M sodium phosphate buffer, pH 7.5 using 0.1U of each enzyme, 1 mM of NADP⁺ and 5 mM of Glucose-6-phosphate and 6-phosphogluconic acid, respectively (Table 2).

Table 2. Effect of Ru5P concentration on G6PDH and 6PGDH activity

Concentration of Ribulose-5-Phosphate (mM)	0	2.5	10
Glucose-6-phosphate dehydrogenase activity (Units)	2.02	2.1	1.754
6-Phosphogluconate dehydrogenase activity (Units)	0.41	0.39	0.28

In Vitro Hydrogen Production Studies

A continuous flow system was constructed to measure hydrogen and carbon dioxide production based on the system as shown and described in Woodward *et al.* (1996) and Greenbaum, (1984). A modification was made with the inclusion of a CO₂ analyzer in-line prior to the H₂ sensor. The maximum yield of hydrogen from glucose using only the oxidative portion of the pentose phosphate pathway (two moles per mole of glucose 6-phosphate) has been achieved using mesophilic sources of these enzymes at 1 unit concentrations in conjunction with 68 units of hyperthermophilic hydrogenase, at 40°C with 2.5 mM initial glucose 6-phosphate concentration.

Effect of pH

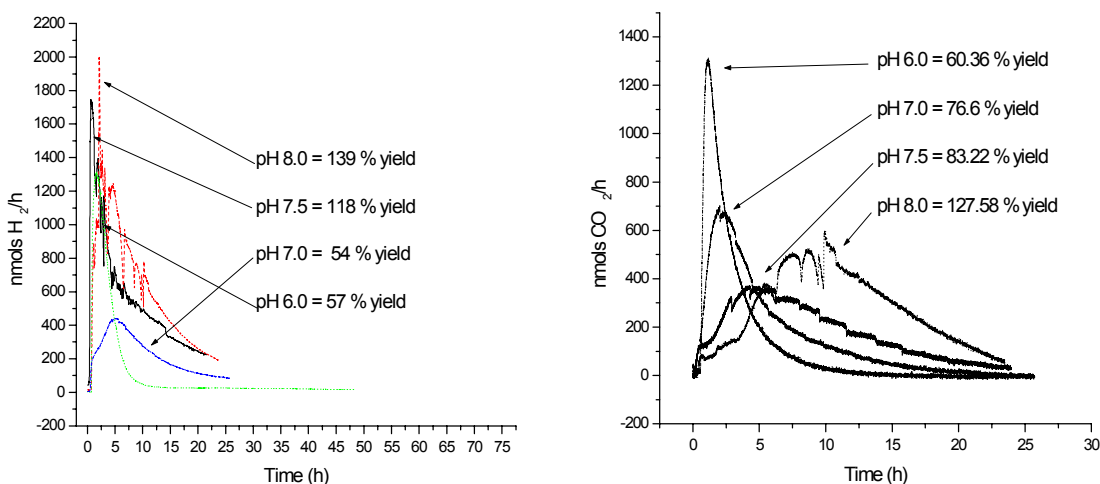


Fig. 7. Effect of pH on the rate and yield of H₂ and CO₂ production. Using 2.5 mM G6P initial concentration, 2.0 mM NADP⁺, 1 Unit of each PPP enzyme, 68U Hydrogenase in 0.2 M Sodium phosphate buffer at 40°C.

Subjecting the complete hydrogen system to pH values of pH 7.5 and 8.0 have also resulted in the maximal percentage yields of H₂ and CO₂ from 2.5 mM G6P.

Effect of Temperature

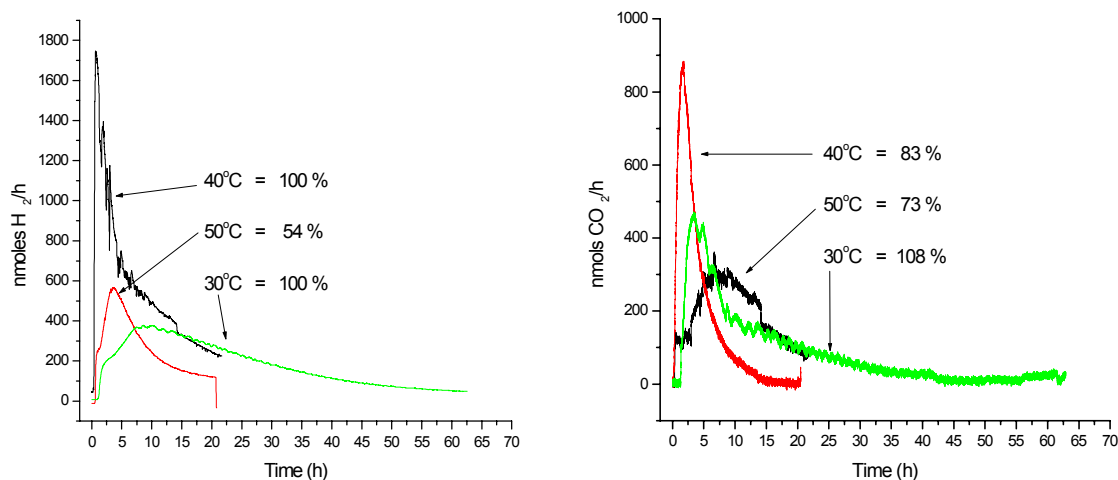


Fig. 8. Effect of temperature on the rate and yield of H₂ and CO₂ production. Using 2.5 mM G6P initial concentration, 2.0 mM NADP⁺ 1 Unit of each PPP enzyme, 68 U Hydrogenase in 0.2 M Sodium phosphate buffer pH 7.5

Maximal theoretical yields of H₂ and CO₂ were achieved at 30 and 40°C. However, increasing the temperature to 50°C led to the decrease in the yields of these two gases.

Effect of NADPH Concentration

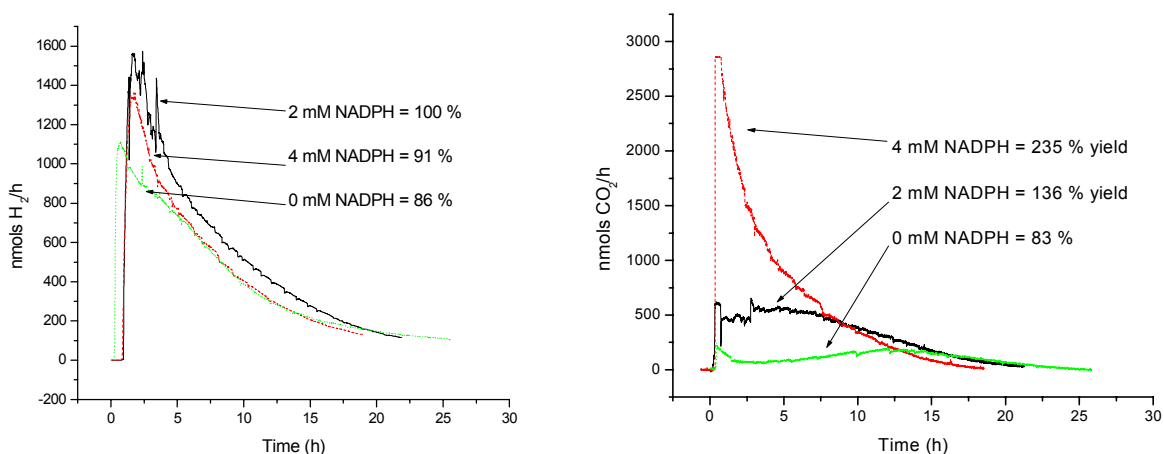


Fig. 9. Effect of NADPH on the rate and yield of H₂ and CO₂ production. Using 2.5 mM G6P initial concentration, 1 Unit of each PPP enzyme, 68 U Hydrogenase in 0.2 M Sodium phosphate buffer, pH 7.5 at 40°C

Supplementing the reaction with additional reduced cofactor led to the expected increase in H₂ and CO₂ production.

Adding increasing amounts of 6PGa from 0 – 10 mM, to the reaction system resulted in the reduction of H₂ and CO₂ that can be obtained from G6P at an initial concentration of 2.5 mM.

Effect of 6-Phosphogluconic Acid Concentration

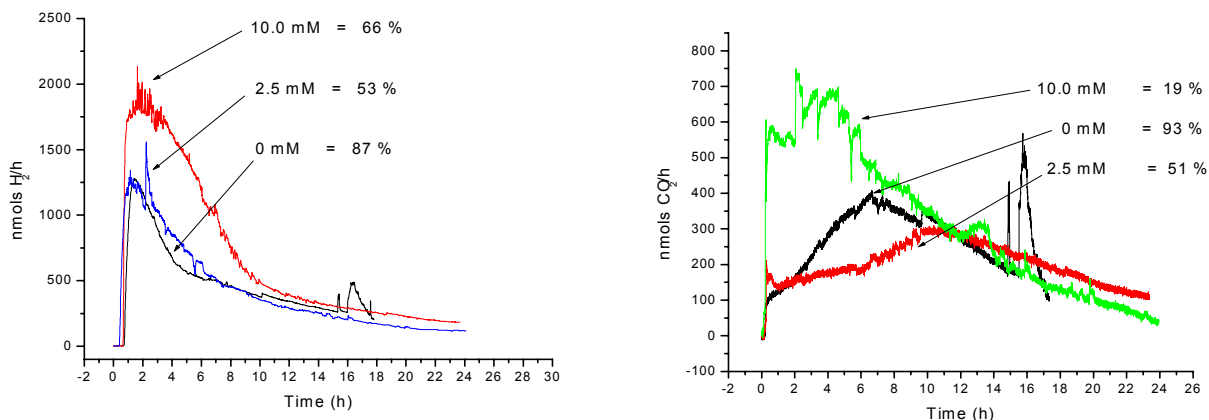


Fig.10. Effect of 6-phosphogluconic acid on rate & yield of H₂ and CO₂ production. Using 2.5 mM G6P initial concentration, 2.0 mM NADP⁺ 1 Unit of each PPP enzyme, 68 U Hydrogenase in 0.2 M Sodium phosphate buffer, pH 7.5 at 40°C.

A 20-fold increase in the concentration of 6PGDH has brought about the increase in yields of H₂ and CO₂ from an initial concentration of 10 mM G6P.

Effect of Ratio of the Two Pentose Phosphate Enzymes

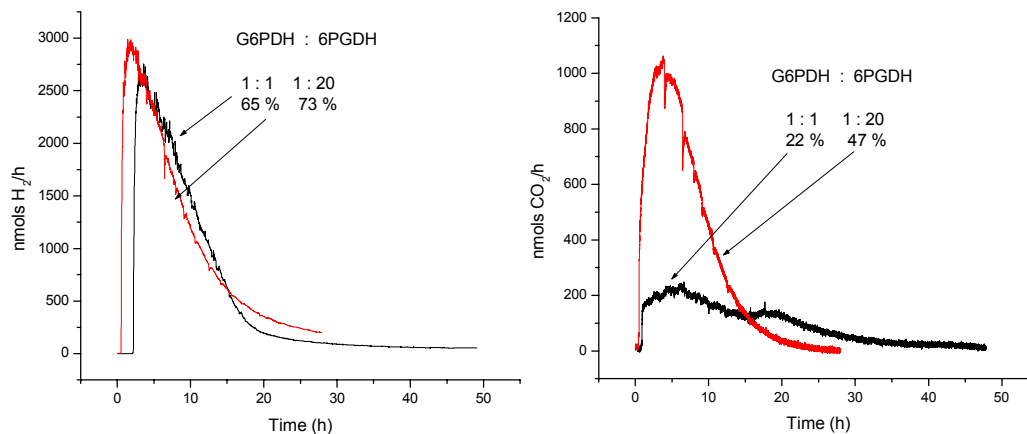


Fig. 11. Effect of enzyme ratio on the rate and yield of H₂ and CO₂ production. Using 10.0 mM G6P initial concentration, 2 mM NADP⁺, 68 U Hydrogenase in 0.2 M Sodium phosphate buffer, pH 7.5 at 40°C.

Isolation of a Thermophilic Oxidative Branch of the Pentose Phosphate Pathway

Approach with *Sulfolobus solfataricus*

Growth of *Sulfolobus solfataricus*

The hyperthermophilic counterpart of this system was being established using enzymes isolated from the Archaeon *Sulfolobus solfataricus*. The culture was grown in ATCC medium #1304 at 70°C for approximately 2 days. Cultures were grown as 5 mL cultures statically in test tubes or as 500 mL cultures in specifically designed vessels that allow continuous aeration (Fig. 12). After this time the cells were harvested and cell pellets were stored at -20°C. Genomic DNA was isolated according to “Current Protocols in Molecular Biology” (1990).

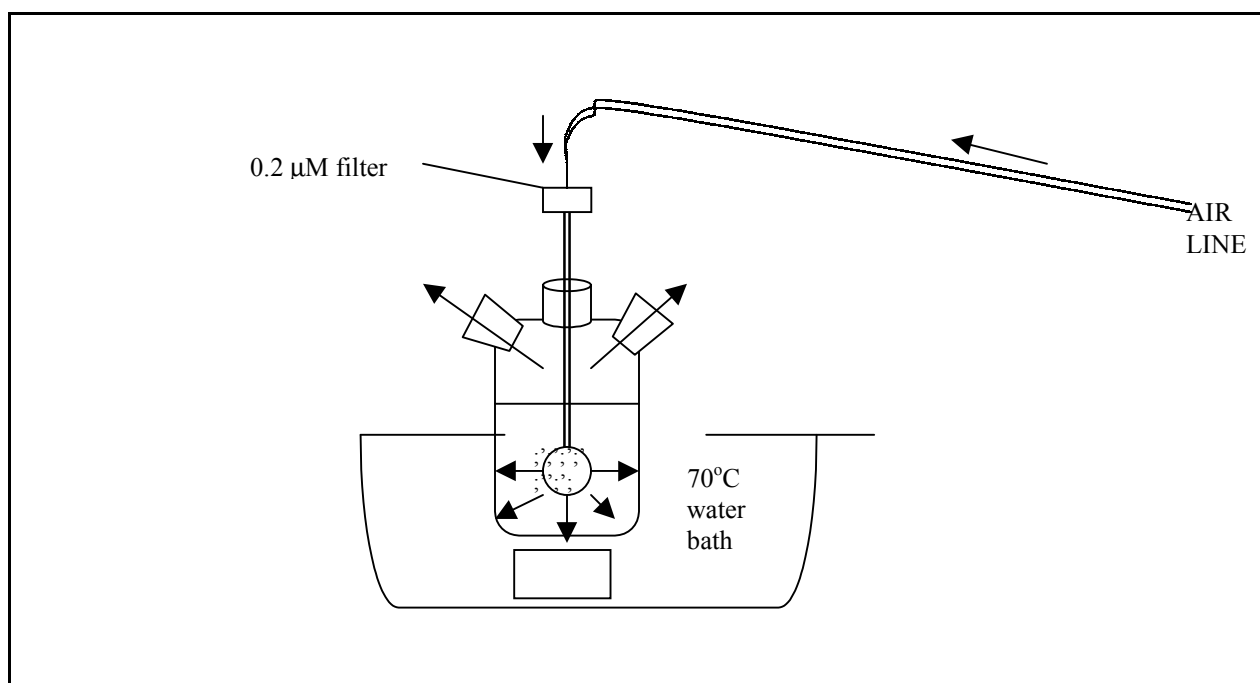


Fig. 12. Diagrammatic depiction of vessel used for large scale culturing of *S. solfataricus*.

Large Scale Growth of *Sulfolobus solfataricus* culture 500 mL of aerated cultures were grown in medium A - standard ATCC Medium (# 1304) with 0.1% Casamino acids and 0.2% yeast extract as the carbon sources - and in medium B, with the addition of 0.5% Glucose and 0.5% Casamino acids and 1.0% yeast extract (Table 3).

Cell breakage Cell pellets were lysed in detergent (0.1% Triton-X100), lysozyme and DNase at 37°C for 60 min

Cell Activity Assays These were carried out with lysed cell extracts at 70°C in sodium phosphate buffer, pH 7.5 with 1 mM NADP⁺, 10 mM glucose, 1 mM glucose-6-phosphate and 2.5 mM 6-

phosphogluconic acid. The enzyme activities of glucose dehydrogenase, G6PDH and 6PGDH were determined, respectively (Table 4).

Table 3. *S. solfataricus* cell culture growth measured as absorbance at 600 nm

Time (hr)	Cell density – measured as absorbance at OD ₆₀₀	
	Standard medium	Enhanced medium
0	0	0
7.5	0.035	0.009
8.5	0.03	0.008
24	0.19	0.15

Table 4. Determination of enzyme activities from *S. sulfolobus* cell extracts grown in standard and enhance media.

Enzyme activity	Medium type	Total Activity in 5 mL (Units)	Specific activity (U/mg of protein)	Specific activity (U/g of cells)
Glucose dehydrogenase	Standard	2.9	0.13	5.18
Glucose dehydrogenase	Enhanced	2.1	0.07	1.52
G6PDH	Standard	N.O.	-	-
G6PDH	Enhanced	0.4	0.013	0.29
6PGDH	Standard	N.O.	-	-
6PGDH	Enhanced	0.4	0.013	0.29

N.O. = no activity observed

Semi-purification of 6PGDH

Purification of the 6PGDH from *S. solfataricus* cell pastes revealed a protein with approximate molecular weight of 48 kDa. The following N-terminal sequence was obtained for this protein – MKIGLIGLGIMGYRIAANLAKANKLNLVYDRTQE. This sequence has been found to align with a number of 6PGDHs from other species as shown in Fig. 13, compiled according to Thompson *et al.*, (1994). This alignment also includes a putative 6PGDH from an alternative strain of *S. solfataricus*, P2, obtained from the P2 genome project (<http://www.cbr.nrc.ca/magpie/sulfolobus/sulfolobus.html>).

First PCR Approach

The first requirement was to create a suitably sized gene fragment to act as a probe for the 6PGDH gene in hybridization experiments with the *S. solfataricus* genome. An alignment of a variety of 6PGDHs from Eukarya and Eubacteria revealed a highly conserved region at approximately 175-200bp (Fig. 14). Therefore, on assuming the exact conservation of this

region in the 6PGDH from *S. solfataricus*, degenerate primers were designed with in the N-terminus and the highly conserved region that was expected to generate a PCR product of 125-175 bp in length. The PCR reaction was optimized in terms of template DNA concentration, primer concentration, MgCl₂ concentration and annealing temperature. Several PCR products were obtained at 3 mM MgCl₂ and 40°C annealing temperature. However, subsequent cloning, sequencing and database searching of those products revealed that they only gave matches with catalase and a SocE regulatory protein. Another alignment of 6PGDHs including the recently released putative 6PGDH sequence from *S. solfataricus* strain P2 (<http://www.cbr.nrc.ca/magpie/sulfolobus/sulfolobus.html>), revealed that the putative 6PGDH from *S. solfataricus* strain P2 does not possess the highly conserved region possessed by all the other enzymes (Fig. 14). Thus, this indicates that if the P2 sequence is in fact a 6PGDH then the highly conserved may also be absent from the 6PGDH present in the P1 strain being used in this work.

→ S.solf. P1	----MKIGLIGLGIMGYRIAANLAKANKLNLVYDRTQEKIER	33	%
S.solf. P2	----MKVGFIFGLGIMGFPMASNLLKAGYDLTVYNRTIEKAEK	34	58
E.coli	MS-KQQIGVVGMVAVMGRNLALNIESRGYTVSVFNRSREKTEE	40	38
S.typhimurium	MS-KQQIGVVGMVAVMGRNLALNIESRGYTVSVFNRSREKTEE	40	32
Synechococcus	MA-LQQFGLIGLAVMGENLALNIERNGFSLTVYNRTAEKTEA	40	44
T.maritima	-M-KSHIGLIGLAVMGQNLALNIARKGYKVSVINRTAQRTTE	39	45
D.melanogaster	MSGQADIALIGLAVMGQNLILNMDEKGFVVCAYNRTVAKVKE	42	31
S.cerevisiae	MS--ADFGLIGLAVMGQNLILNAADHGFTVCAYNRTQSKVDH	40	38
A.aeolicus	---MKTLFLIGLGRMGALAYRLKNRGWEIYGYSRTQTTRER	38	44
	. . : * : . ** : . . . : * :		

Fig. 13. N-terminal Alignment of 6-Phosphogluconate Dehydrogenases From All Three Domains of Life. Arrow indicates the N-terminal sequence of 6PGDH from *S. solfataricus*. Amino acid length and percentage identities to P1 N-terminal sequence are shown.

E.coli	175	ADGAGHYV KMVHNG IEYGDMLIAEA	200
S.typhimurium	174	ADGAGHYV KMVHNG IEYGDMLIAEA	199
Synechococcus	175	PGGSGHYV KMVHNG IEYGDMLIAEA	200
D.melanogaster	172	DGGAGHFV KMVHNG IEYGDMLICEA	197
Homo sapien	176	DEGAGHFV KMVHNG IEYGDMLICEA	201
S.cerevisiae	174	PAGAGHYV KMVHNG IEYGDMLICEA	199
T.maritima	174	ERSAGHFV KMVHNG IEYAIMQAIIEV	199
A.aeolicus	164	SSGAGHFA KMVHNG IEYGIMEAIAEG	189
S. solf. P2	162	DVGSQALKLCNQVVVALNMVSVVEG	187
		. : * : * : : : * : *	

Fig. 14. Alignment of 6PGDH “conserved region” From All Three Domains of Life

Second PCR Approach

Degenerate primers were designed immediately within the N-terminal sequence. A PCR fragment of expected approximate length of 100bp from genomic DNA was generated. This was intended for use as a probe in hybridization experiments. The tandem positioning of the 6PGDH

and the G6PDH genes in the genome of the extremophilic and ancient eubacteria *Aquifex aeolicus* (Deckert *et al.*, 1998), it is expected that sequencing of the hybridized clone may reveal a glucose 6-phosphate dehydrogenase in its flanking regions. However, further searches of the DNA databases revealed the recent release of the sequence previously deemed to be the 6PGDH from *S. solfataricus* P2. However, it was now assigned the function of a 3-hydroxyisobutyrate dehydrogenase. Another alignment of the P1 N-terminal sequence with several 3-hydroxyisobutyrate dehydrogenases was compiled to compare the relative sequence identities (Fig. 15).

					%
S.solf.P1	-MK-IGLIGLGIMGYRIAANLAKANKLNLVYDRTQEKIER				
38S.solf.P2	-MK-VGFIGLIGMGFPMASNLLKAGYDLTVYNRTIEKAEK	38			
57E.coli	-MK-VGFIGLIGMGKPMKSNLLKAGYSLVVADRNPEAI	36			
52L.lactis	MSK-IAFIGTGVMGAAMAGHLM DAGHDLIVYNRTKSKTD	38			
41B.subtilis	MKKTIGFIGLIGVMGKSMASHILNDGHPVLVYTRTKEKAE	39	48	* : : : *	
	* : * * : : : : . . * * . .				

Fig. 15. N-terminal alignment of 3-hydroxyisobutyrate dehydrogenases from all three domains of life. Amino acid length and percentage identities to N-terminal sequence are shown.

Approach with Thermotoga maritima

100 mL cultures were grown in standard ATCC medium (#2114) under 100% N₂ atmosphere for approximately 2 days at 70°C. After this period the cells were harvested and stored as cell pellets at -20°C. Genomic DNA isolation from *T. maritima* was carried out according to “Current Protocols in Molecular Biology” (1990)

Design of PCR Primers

PCR is employed to amplify the gene fragments from genomic DNA (Fig.16). Each set of primers allowed for the incorporation of the ribosome binding sites (Shine-Delgarno sequences) (Shine and Delgarno, 1974, 1975), which may aid future expression work (Table 4).

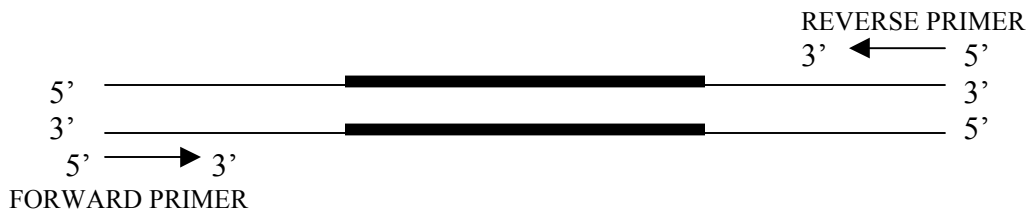


Fig. 16. Mechanism of PCR amplification

Table 4. Primer sets used to generate amplified genes of 6PGDH and G6PDH. Shine-Delgarno sequences are shown underlined.

Name	Sequence	Length (bp)	Melting temp. (T _m)
6PGDH-F	5' GCT TTA CAT <u>CGA AGG</u> TAA AGC TCT 3'	24	59.3
6PGDH-RA	5' GTA GAC CTT CGT TCT CAC GAG G 3'	22	62.1
G6PDH-F	5' CAA CGT ACC CAT <u>CTT CGA</u> GCA GG 3'	23	64.2
G6PDH-RA	5' GGC AGG TGA GAT CAT GAA GTG CAG TC 3'	26	66.4

PCR from T. maritima

Carried out using “hot-start” method to prevent non-specific binding, with 600 ng (template) gDNA, 1µM of primers, 1.5 - 2.5 mM MgCl₂ and at an annealing temperature of 55°C, 1.5 Kb PCR fragments were obtained for both reactions, which is the desired size of each gene product.

Cloning & Transformation

The generated PCR fragments were directly ligated to the cloning vector pCR2.1 using standard TA cloning sites. The recombinant vectors were subsequently transformed into *Escherichia coli* strain TOP10F' (non-expression host). Colonies were selected by ampicillin resistance and blue/white screening (successful insertion into the multiple cloning site of pCR2.1 causes the interruption of the lacZ gene coding for the α peptide of β-galactosidase and results in the failure to convert substrates such as X-Gal to a colored product and produce blue colonies). Plasmid mini preps were employed to extract the recombinant plasmid DNA from selected cultures. Restriction digests were then carried out to excise the 1.5 Kb gene inserts using restriction enzyme EcoRI. This would confirm the successfulness of the cloning procedure. Both sets of vectors contained the 1.5 Kb inserts.

Sequencing

Partial sequence of the gene coding for G6PDH was obtained (Fig. 17). This sequence included the downstream primer and 1/3 of the gene sequence in the reverse orientation. Partial sequence was also obtained of the gene coding for 6PGDH (Fig. 18). This sequence included the upstream primer and 1/3 of the gene sequence in the correct orientation.

Confirmatory restriction digest

To confirm the initial restriction digest and sequence data, both gene-containing vectors were digested with EcoRI and HindIII to produce fragments of specific sizes (Table 5).

All the expected fragments were obtained on digestion, thus confirming the presence of the gene inserts.

GTGCTTCCATGTNNGNCGAATAAGGGCCCTCTANATGCATGCTCGAGCGGCCGCCAGTGTGATGGATATTTGCAGAA
 TTCNGCTT**GCTTTACATCCGAAGGTAAGC**TNTGCTGAANTAAAATANGGAGGTGACNCCG**GTG**AAATCTCATATTG
 GTCTCATCGGTCTTGCTGTGATGGGTGAGAATCTTGCNCTGAACATTGCGAGGAAAGGCTACAAAGTTTCGGTTTAC
 AACAGAACAGCACATANAACGGAGGAATTTGTGAAAAATCGTGTAAGTGAATGAAGAGATAGAACCCTCATTNCCGAT
 ATCCNAANGCTTCNTGAAGTCTCTCGANAGACCAANAAAGATAATCTTAATGGTAAAGGCANGAAAACCCGTGGATG
 ATNCNATTTCTCAGCTTCTTCTCACCTCGAACANGTGATTTGATAATAGACGGTGGTNATTCCCNTTACATGGAT
 ACCGANAGACGCTNCNAGGAAGTCTCTTGANAAGGAATACTTTTCTCCGTATGGNNAGTAATTGGTGGTGNGTAC
 NGGGCTCTTACGGGCCTTCTNTCCTGCCTGGGGANNTANNNACGCGTNTAACCTGGTTGNGGANANCCTTTTGGN
 AAATCCCAGCCNNACCCAGNATGNGNCCCTTCTGNCATACNTTTGGTNAACCGATCINNCTGNCCNCTTTTTNNCCAT
 GGNTCACACCNGCATTTNGAANCCNCTTTNTGNMNGCCCAAACCGGAANTTATCCNCATCINNNTNNANGNTGTCCCTG
 CGCCCATCNTNTGNAANAAAATTGTCCCNTNTCTTCTCAACCNNGGGGCNCTNNNNGAACAACCTTTCNCTTAGCTCC
 CTTGGTGNGNGANCCCCCTNCCCACNATTTTGGCAGACACCAGCTNNTNCACCCCTCCGCTTACCTGNTGGNNACTAT
 GTGTNCNCNTCTTGGCANANNGTNTGGAAACACNNAGGGNGATCTCGGTAAACNTGCCACANTCNCNACNNTCGCTN
 CATNNTNNCATCCGTANANTCTTAAACCTTTTCTGTAAANTNTCTNCGCCTNCGCNCATTNACAAGGGNGNCAACA
 TGTCCNTTTTCTCANACACANNANNCAAAAACCTCGGGNTNTTCTCCNCGCCCCTCTCNTCNANACGNANATACACNC
 TCCTCACTCTCGCGGTCTCNCNCGCNNTCANTCNCTCGCG

Fig. 17. Partial gene sequence of 6PGDH in vector pCR2.1. Sequenced using T7 promoter primer. EcoRI site is underlined. Forward PCR primer (6PGDH-F) is in bold and gene start codon is underlined and in bold.

CNCACNNCACNTCTNNCCNGCTATNTNNNTTNNTAANNANNNATNGNCCGGNNNCGACNTANNCTNNTNATAACN
 NNCGTNCCNNNGCTTGCCTTNTTAATNCACCCCNCTNNTCGTTNTCTACCCNTNTNANANNNNCTNNNCACTNTC
 NCNNCCCNCNCCCCTGTGGTTTTNCNTATTNGTACGGCGANNAGGGCCNCTAGCANGCATGCTCGAGCGGNCNCC
 AGTGTGATGGATNTTTCAGAAATTCNGCTT**GGCNGGTGACATTCATGATGTGC**ACNNTGGGATNGGAGAAANGTCCA
 GATGATACNTCCGGTGTATCCAAAGATCGNACNACCTTTTNGAATTGNGATCTTNNCGCTTTCNTGGTGACCTNA
 CAAAAGAAAGCTNATTCCCCTTTTGAACAGGATGNTACGAGGCAGGANAAAACAAGCCCGAACGCTTTANCNNGT
 TCGGCGCGGCACNAACGAAAATGGACTNTNANAAATCTCANATGCCACATTNCANGCCAACCCCTGNTTTTTTTGNA
 CATTGCAGTTACATACACCGNGGATCTATCNGGNTCCTGATAGCTTCNANCANACANAAAAACACTCNTCNANACNT
 CNCATAACAACGGATCTNANTCCNGCAATCGTGGTCTTTCATNTNAAACNNTGNNACCNTCCCGGANTCNTNCCACNN
 CCCTCTTCTTNTGNAANAANCANCNNTNANACTGNNNTTGAACAAANNACCTGCTGNACTGNTNATNANNCAANA
 NCCANNTNGNAAAANAANCATNNAATTTCTGCCAGANNTANCTGNCANCACTCTTTCACNAAATANTTANTCCG
 GAAATGCATCCNCTCTCCNNGANNNTNACCATTTCCNTTNGGCNAAGCAAACCNATCCGANNCATTACNTGGGTGN
 TTTTATGNNNNCCACCATCCGTTANCTCCCGGNAANACCTGCGACCNCGCNNGTTCNTGTGGGATTNCTANACA
 AAANTNCACAACGGGNCGTNNNCNCTTTTNCGCCGNACCCCTGGNCGTGGNTNTTNTCTAAANCCNNTGCATCNCN
 CAGGNGTNCCTTTCTACAANTACNNTNCTNNTTCTCCNNTNACANNTGANCCCATCNTTANTTTTCTG
 TCAAAAANTANNCAAGCNGTNGNTNANNNTTATAAANAACAGNNCGTTACNTGCNGCNNTATNTCANACTACANGT
 CNCNNGNCCCTNNGNAGGGACATNACNNANACANGTGCNCGCNCTNNATAAANACTANTNNGNNNCCGTNCCCT
 GCANCTNTCATCGNACNTANATCNNTCNCN

Fig. 18. Partial gene sequence of G6PDH in vector pCR2.1 in reverse orientation. Sequenced using M13 reverse primer. EcoRI site is underlined. Forward PCR primer (6PGDH-F) is in bold and gene start codon is underlined and in bold.

Table 5. Restriction digestion of cloned PCR gene fragments to confirm the inclusion of the complete fragments.

Recombinant vector	Expected fragment sizes
pCR2.1 + G-6-PDH	3.9, 824 and 683 bp
pCR2.1 + 6-PGDH	3.9, 1231, 184 bp

Growth of non-expression host

Cultures of *E. coli* strain TOP 10F' transformed with the recombinant vector pCR2.1 containing their respective PPP gene, were grown. The inclusion of ribosome binding sites upstream of the gene inserts would allow for expression to take place. 250 mL cultures were grown in Luria broth media with 100µg/mL ampicillin at 37°C until they reached a cell density of OD₆₀₀ = 0.5. 0.4 mM of the inducing agent IPTG was then added and the cells were grown for a further 20 hours. Cell breakage was carried out with detergent 0.1% Triton X-100, DNase and lysozyme and followed by a 25-min heat step at 80°C. The resulting cell extracts were then analysed for PPP enzyme activity (Table 6).

Table 6. PPP enzyme activities from non-expression transformed *E. coli* cultures.

Sample	Weight of cells (g)	Volume (mL)	Total Activity (U)	Total Protein (mg)	Specific Activity	
					Per mg of protein	Per g of cells
G6PDH	0.9	12	2.4	48	0.05	2.6
6PGDH	0.7	12	4.8	72	0.067	6.86

As can be seen from the level of enzymic activity for G6PDH and 6PGDH, the expression levels are very low and will require further cloning into an expression vector.

PCR to introduce restriction sites for cloning into an expression vector

Primers were designed to introduce suitable restriction sites on either side of the PPP genes to facilitate their cloning in the correct orientation into the cloning vector pET-15b (Table 7). The genes were initially analyzed using a restriction enzyme analysis program, (<http://darwin.bio.geneseo.edu/~yin/WebGene/RE.html>) to determine all the restriction sites that do not cut within the gene sequence.

Restriction digestion of PPP genes and pET-15b.

Following PCR, the completed reactions were precipitated with ethanol in order to denature the DNA polymerase. The reactions were then resuspended in 100 µL of nanopure water. Restriction digestion of the PCR fragments and also the expression vector pET-15b were then carried out using the respective restriction enzymes at 37°C for 4 – 16 h. All the digested fragments were

separated by agarose gel electrophoresis in order to prevent re-ligation in subsequent steps. All the restricted fragments were purified to remove the agarose.

Table 7. Primers including the site mutations used to incorporate the desired restrictions sites.

	Restriction site	Restriction Site Sequence	Primer sequence
G6PDH Upstream	Nde I	CATATG	5' GGC AGG TGA GCA TAT GAA GTG CAG TC 3'
G6PDH Downstream	Bam H I	GGATCC	5' CGA CTA CAA AAT CAA GGA TCC CAT C 3'
6PGDH Upstream	Nco I	CCATGG	5 ' GGT GAC GCC CAT GGA ATC TC 3'
6PGDH Downstream	Bam H I	GGATCC	5' CTC ACG GGA TCC ACT TCG 3'

Ligation and transformation of PPP genes and pET-15b

The purified PCR and vector fragments were ligated together. The resulting recombinant vectors were transformed into *E.coli* strain JM109. Colonies were selected by ampicillin resistance. No colonies were obtained for the 6PGDH gene insert indicating the failure of the ligation reaction. Plasmid mini preps were employed to extract the recombinant plasmid DNA from cultures grown from single selected colonies. Restriction digests were then carried out to excise the 1.5 Kb gene inserts using restriction enzymes indicated in Table 9. This would confirm the success of the cloning procedure. However, none of the plasmids from the selected colonies appear to possess the 1.5 Kb gene inserts.

Discussion

Characterization of the Mesophilic Oxidative Branch of the Pentose Phosphate Pathway

Assay characterization

The rate of turnover of the final products, H₂ and CO₂, shows that 6PGDH is the rate-limiting step in the pathway. In terms of the life-time of the mesophilic pathway, the first enzyme G6PDH is rate-limiting and possesses a t_{50%} of only 3 min at 60°C. However, the t_{50%} possessed by both of the mesophilic enzymes is far inferior to that of the hydrogenase from *P. furiosus*, which has a t_{50%} of 21 h at 80°C (Bryant and Adams, 1989). The pH optima of the mesophilic pathway enzymes are in agreement with that of the hydrogenase and the components of the H₂ production system.

In vitro hydrogen production studies

Monitoring of the system at different temperatures (Fig. 7) revealed that the optimal temperature for this set of enzymes is 40°C. 100% of the expected yield was achieved at this temperature as with an experiment carried out at 30°C. However, that maximal rate of H₂ and CO₂ production was decreased by approximately 78% at 30°C. Raising the temperature to 50°C produced a slightly higher rate but only resulted in approximately half the maximal yield of H₂ and 73% of the CO₂ that could be expected. The ratio of H₂:CO₂ obtained from the oxidative portion of the pentose phosphate pathway should be 2:1. However, at the higher temperatures, the cofactor NAD⁺(H) is very thermolabile (Zatman *et al.*, 1953; Wu *et al.*, 1986; Daniel and Danson, 1994) and therefore may result in the observing less H₂ than could actually be produced. Additionally, the greater thermostability of the second enzyme (6PGDH) causes it to keep catalyzing the production of CO₂ using the excess intermediate (6PGa) that is produced due to the greater turnover number of the first enzyme, G6PDH.

Alteration of the pH in the H₂ production system agrees with the results obtained for the optimal pH of the individual PPP enzymes (Fig. 5). However, this is also aided by the fact that the optimal pH for the hydrogenase for oxidizing reactions is also pH 8 (the hydrogenase from *P. furiosus* is a “bifunctional” sulfhydrogenase possessing H₂-oxidizing and S⁰-reduction activities that respond differently to pH, temperature and inhibitors (Ma *et al.*, 1993)). The level of activity of the hydrogenase at the temperatures used in this study is much reduced (optimal temperature of hydrogenase is over 95°C in H₂-oxidizing activities (Fiala and Stetter, 1986) and 85°C with NADP⁺ as a cofactor (Ma *et al.*, 1994). Despite the inclusion of excess amounts of hydrogenase, the build-up of NADPH may still occur. Therefore, the higher pH values may also be advantageous for the NADP⁺/NADPH ratio due to the increased stability of NADPH in dilute alkali (Wong and Whitesides, 1981; Chenault and Whitesides, 1987; Woodward and Orr, 1998). The addition of excess NADPH (Fig. 9) does not decrease the rate and yield of H₂ and CO₂ and leads to expected increases in H₂ production, which may also be due to the favorable pH of the reaction buffer.

The effect of including excess amounts of 6-phosphogluconic acid (6PGa) (Fig. 10) indicates that the second enzyme in the pathway (6PGDH) is indeed being overwhelmed by the concentration of the intermediate. An addition of 2.5 mM 6PGa, which is only 3 times the K_m for 6PGDH, leads to a 50% reduction in the maximal H₂ and CO₂ that can be obtained. This inhibition is even more evident when 10 mM 6PGa is added, which results in 66% and 19% final yields of H₂ and CO₂, respectively. The maximal theoretical yield also includes the amount of H₂ and CO₂ that can be obtained from the added 6PGa, which is also a substrate. The loss of the 2:1 ratio is caused by the addition of extra 6PGa, which produces one mole of H₂ and CO₂ per mole of 6PGa. The limitation of the second enzyme (6PGDH) is confirmed by the addition of more 6PGDH to the system containing 10 mM initial concentration of glucose-6-phosphate (G6P) (Fig. 11), where the rates and yields of CO₂ production are dramatically increased. The ratio of 1:20 was used to reflect that ratio of the turnover numbers of these enzymes and was expected to prevent the build up of the intermediate, 6PGa. In the case of the 1:1 and the 1:20 (G6PDG:6PGDH) ratios, the G6PDH enzyme appears to be capable of converting all the available G6P to 6PGa and NADPH, and is not inhibited by the high concentration of G6P. Therefore, the majority of the H₂ produced in the 1:1 ratio is due to the NADPH produced by

G6PDH. Increasing the concentration of 6PGDH leads to a 10% increase in the yield of H₂ that can be obtained from 10 mM G6P, but also causes a 25% increase in the theoretical yield of CO₂. The rate of CO₂ production is also increased by 80% on increasing the level of 6PGDH in the reaction system. Despite the observed improvement of H₂ and CO₂ yields, the ratio did not lead to the maximal yields of gases expected from the use of this ratio.

Isolation of a Thermophilic Oxidative Branch of the Pentose Phosphate Pathway

Approach with Sulfolobus solfataricus

The N-terminus MKIGLIGLGIMGYRIAANLAKANKLNLVYDRTQE was obtained for a 48 kDa protein partially purified using affinity chromatography along with the enzyme glucose dehydrogenase (GDH) (41 kDa). Sequence comparison analysis revealed this protein N-terminus to match with a variety of 6-phosphogluconate dehydrogenases. Despite the reported absence of central metabolic pathways employing phosphorylated intermediates in this species (De Rosa *et al.*, 1984), very low levels of activity for both the PPP enzymes could be detected in cell cultures grown in enhanced media. The enhanced media contained higher concentrations of carbon sources and this may have influenced the expression of these enzymes. However, the far greater specific activity obtained for the GDH suggests that this is the dominant pathway for the degradation of glucose in *S. solfataricus*.

Despite originating from the same species, the sequences of the 6PGDHs from the two strains of *S. solfataricus* P1 and P2, surprisingly only share 57% sequence identity and 72% sequence similarity. However, the assigning of a function for the P2 gene appears to be based purely on sequence identity and may, in fact, be incorrect. This has since been established by the assigning of a new function of a 3-hydroxybutyrate dehydrogenase.

Approach with Thermotoga maritima

Both genes coding for the enzymes of the oxidative branch of the pentose phosphate pathway have been successfully isolated and cloned from the species *T. maritima* into the cloning vector pCR2.1. However, the failure to obtain fully transformed colonies of JM109 cells i.e. those containing recombinant PPP genes, has required that several trouble-shooting procedures be put in place to determine the specific step that led to the failure of successful ligation. The restriction enzymes are required to be tested to determine their efficiency for excising the DNA at the correct sites. Therefore, the colonies observed growing on ampicillin-containing plates could contain fully-functional non-recombinant pET-15b plasmids. Or it may be possible that the initial restriction digest (and subsequent ligation) were successful and that the resulting plasmids obtained from the *E. coli* strain JM109 colonies do contain the gene inserts, but that the second restriction digest to determine this has not been successful. This work is still in progress.

Conclusions

Characterization of the Mesophilic Oxidative Branch of the Pentose Phosphate Pathway

The system has been optimized in terms of the reaction buffer, pH and temperature. The ratio of G6PDH:6PGDH of 1:20, which reflects the respective turnover numbers of these enzymes, still does not result in the complete conversion of 10 mM G6P to H₂ and CO₂.

Isolation of a Thermophilic Oxidative Branch of the Pentose Phosphate Pathway

Even with the less complex method of growing *S. solfataricus*, the N-terminus that gives 31 – 58% matches with other 6PGDHs, and the observation of low level activity for the PPP enzymes, it appears that it may not be a suitable host for obtaining all the enzymes of the complete pentose phosphate pathway. Both genes coding for the enzymes of the oxidative branch of the pentose phosphate pathway have been successfully isolated and cloned from the species *T. maritima* and expression work is still in progress.

Future Work

- Optimize the expression and purification of recombinant thermophilic oxidative Pentose Phosphate enzymes.
- Purify and characterize the native wild-type enzymes from *T. maritima*.
- Compare hydrogen production by mesophilic and thermophilic G6PDH and 6PGDH.
- Establish that thermophilic enzymes will offer advantage over mesophilic enzymes for H₂ production.

This work will result in new knowledge showing the advantage of using thermophilic enzymes for the generation of molecular hydrogen from renewable energy.

Acknowledgements

I would like to thank Dr. Hugh O'Neill, Dr. Barbara Evans, Dr. Steve Blankinship and Dr. Elias Greenbaum from our group at ORNL for help and advice in carrying out the research. Dr. Frank Larimer and Mrs. Shen Lu at ORNL for carrying out the sequencing and also Prof. Michael Danson and Dr. David Hough for providing the N-terminal sequence. I would also like to thank the Hydrogen Program of the U.S. Department of Energy for funding this work. Oak Ridge National Laboratory is managed by UT-Battelle, LLC for the U.S. Department of Energy under contract DE-ACO5-00OR22725.

References

- Aachenbach-Richter, L., Gupta, R., Stetter, K. O. and Woese, C. R. (1987) *Syst. Appl. Microbiol.* **9**, 34 – 39.
- Ausubel, F. M. (1990) *Current Protocols in Molecular Biology*. Published by Greene Pub. Associates and Wiley-Interscience : J. Wiley, New York.
- Brock, T.D., Brock, K.M., Belly, R.T., & Weiss, R.L. (1972) *Arch. Microbiol.* **84**, 54 – 68. *Sulfolobus* – A New Genus of Sulfur-Oxidizing Bacteria Living at Low pH and High Temperature.
- Bryant, F. O. & Adams, M.W.W. (1989) *J. Biol. Chem.* **264**, 9, 5070 - -5079. Characterization of Hydrogenase from the hyperthermophilic Archaeobacterium, *Pyrococcus furiosus*.
- Burdette, D.S., Vielle, C., & Zeikus, J.S. (1996) *Biochem. J.* **316**, 115 - 122. Cloning and expression of the gene encoding the Thermoanaerobacter ethanolicus 39E secondary-alcohol dehydrogenase and biochemical characterization of the enzyme.
- Chenault, H.K. & Whitesides, G.M. (1987) *Appl. Biochem. Biotech.* **14**, 2, 147 – 197. Regeneration of nicotinamide cofactors for use in organic synthesis.
- Daniel, R.M. & Danson, M.J. (1995) *J. Mol. Evol.* **40**, 559 - 563. Did primitive micro-organisms use nonhem iron proteins in place of NAD/P?
- Deckert, G., Warren, P. V., Gaasterland, T., Young, W. G. Lenox, A. L. Graham, D. E., Overbeek, R., Snead, M. A., Keller, M., Aujay, M., Hubert, R., Feldman, R. A., Short, J. A., Olsen, G. J. and Swanson, R. V. (1998) *Nature* **222**, 392 (6674) 353 – 358. The complete genome of the hyperthermophilic bacterium *Aquifex aeolicus*.
- De Rosa, M., Gambacorta, A., Millonig, G., & Bu'Lock, J.D. (1974) *Experientia* **30**, 866 - 868. Convergent characters of extremely thermophilic acidophilic bacteria.
- De Rosa, M., Gambacorta, A., & Bu'Lock, J.D. (1975) *J. Gen. Microbiol.* **86**, 156 – 164. Extremely Thermophilic Acidophilic Bacteria Convergent with *Sulfolobus acidocaldarius*.
- De Rosa, M., Gambacorta, A., Nicolaus, B., Giardina, P., Poerio, E., & Buonocore, V. (1984) *Biochem. J.* **224**, 407 – 414. Glucose metabolism in the extreme thermoacidophilic archaeobacterium *Sulfolobus solfataricus*.
- Egerer, P., Günter, H., & Simon, H. (1982) *Biochim. Biophys Acta* **703**, 149 - 157. On the hydrogen-deuterium exchange reaction catalyzed by the soluble hydrogenase from *Alcaligenes eutrophus* H16 in the free and immobilized state.
- Entner, N.& Doudoroff, M. (1951) *J. Biol. Chem.* **196**, 853 – 863. Glucose and gluconic acid oxidation of *Pseudomonas saccharophila*.

Fiala, G. & Stetter, K.O. (1986) *Arch. Microbiol.* **145**, 56 - 61. *Pyrococcus furiosus* sp. nov. represents a novel genus of marine heterotrophic archaeobacteria growing optimally at 100°C.

Fujinaga, M., Berthet-Colominas, C., Yaremchuk, A.D., Tukalo, M.A., & Cusack, S. (1993) *J. Mol. Biol.* **234**, 222 - 233. Refined crystal structure of the seryl-tRNA synthetase from *Thermus thermophilus* at 2.5 Å resolution.

Greenbaum, E. (1984) *Photobiochem. Photophys.* **8**, 323 - 332. Biophotolysis of water: the light saturation curves.

Huber, R., Langworthy, T. A., König, H., Thomm, M., Woese, C. R., Sleytyr, U. B. and Stetter, K. O. (1986) *Arch. Microbiol.* **144**, 324 – 333. *Thermotoga maritima* sp. nov. represents a new genus of unique extremely thermophilic eubacteria growing up to 90°C.

Huber, R., and Stetter, K. O. (1992) in *The Prokaryotes* (eds Balows, A., et al.) 3809 – 3815. Springer, Berlin, Heidelberg, New York.

Inoue, T., Kumar, S.N., Kamachi, T., & Okura, I. (1999) *Chem. Lett.* **2**, 147 - 148. Hydrogen evolution from glucose with the combination of Glucose dehydrogenase and Hydrogenase from *A. eutrophus* H16.

Lebbink, J.H.G., Eggen, R.I.L., Geerling, A.C.M., Consalvi, V., Chiaraluce, R., Scandurra, R., & DeVos, W.M. (1995) *Prot. Eng.* **8**, 1287 - 1994. Exchange of domains of glutamate dehydrogenase from the hyperthermophilic archaeon *Pyrococcus furiosus* and the mesophilic bacterium *Clostridium difficile* : effects on catalysis, thermoactivity and stability.

Leslie, J. (1997) *Wired* **Oct.**, 1 -2. Dawn of the hydrogen age. (see appendices)

Ma, K., Schicho, R.N., Kelley, R.M. & Adams, M.W.W. (1993) *Proc. Natl. Acad. Sci. USA* **90**, 5341 - 5344. Hydrogenase of the hyperthermophile *Pyrococcus furiosus* is an elemental sulfur reductase or sulfhydrogenase: Evidence for a sulfur-reducing hydrogenase ancestor.

Ma, K., Zhou, Z. H., & Adams, M.W.W. (1994) *FEMS Microbiol. Lett.* **122**, 245 - 250. Hydrogen production from pyruvate by enzymes purified from the hyperthermophilic archaeon, *Pyrococcus furiosus*: A key role for NADPH.

Nelson, K. E., Clayton, R. A., Gill, S. R., Gwinn, M. L., Dodson, R. J., Haft, D. H., Hickey, E. K., Peterson, J. D., Nelson, W. C., Ketchum, K. A., McDonald, L., Utterback, T. R., Malek, J. A., Linher, K. D., Garrett, M. M., Stewart, A. M., Cotton, M. D., Pratt, M. S., Phillips, C. A., Richardson, D., Heidelberg, J., Sutton, G. G., Fleischman, R. D., Eisen, J. A., White, O., Salzberg, S. L., Smith, H. O., Venter, C. J. and Fraser, C. M. (1999) *Nature* **399**, 323 – 329. Evidence for lateral gene transfer between Archaea and Bacteria from genome sequence of *Thermotoga maritima*.

Pearson, W.R. & Lipman, D.J. (1988) *Proc. Natl. Acad. Sci. USA* **85**, 2444 - 2448. Improved tools for biological sequence comparison.

Russel, R.J.M., Ferguson, J. M.C., Hough, D.W., Danson, M.J., & Taylor, G.L. (1997) *Biochemistry* **36**, 9983 – 9994. The Crystal Structure of Citrate Synthase from the Hyperthermophilic Archaeon *Pyrococcus furiosus* at 1.9 Å Resolution.

Segerer, A.H. & Stetter, K.O. (1991) *The Prokaryotes*, **1**, 2nd. edn., Springer Verlag, Ed. Belows, A. The Order Sulfolobales.

Selig, M., Xavier, K.B., Santos, H., & Schönheit, P. (1997) *Arch. Microbiol.* **167**, 217 – 232. Comparative analysis of Embden-Meyerhof and Entner-Doudoroff glycolytic pathways in hyperthermophilic archaea and the bacterium *Thermotoga*.

Shine, J. & Delgarno, L. (1974) *Proc. Natl. Acad. Sci. USA* **71**, 4, 1342 - 1346. The 3'-Terminal Sequence of *Escherichia coli* 16S Ribosomal RNA: Complementarity to Nonsense Triplets and Ribosome Binding Sites.

Shine, J. & Delgarno, L. (1975) *Nature* **254**, 34 - 37. Determinant of cistron specificity in bacterial ribosomes.

Stetter, K.O., Segerer, A., Zillig, W., Huber, G., Fiala, G., Huber, R., & König, H. (1986) *System. Appl. Microbiol.* **7**, 393 - 397. Extremely thermophilic sulfur-metabolizing Archaeobacteria.

Vielle, C., Hess, J.M., Kelly, R.M., & Zeikus, J.G. (1995) *Appl. Environ. Microbiol.* **61**, 1867 - 1875. xylA cloning and sequencing and biochemical characterization of xylose isomerase from *Thermotoga neapolitana*.

Wilson, J.G. & Newall, A.B. (1970) *General and inorganic chemistry*, second ed., Cambridge-Uni. Press, Cambridge.

Woodward, J., Mattingly, S.M., Danson, M., Hough, D., Ward, N., & Adams, M. (1996) *Nature Biotech.* **14**, 872 – 874. *In vitro* hydrogen production by glucose dehydrogenase and hydrogenase.

Woodward, J. & Orr, M. (1998) *Biotechnol. Prog.* **14**, 897 – 902. Enzymatic Conversion of Sucrose to Hydrogen.

Woodward, J., Orr, M., Cordray, K. and Greenbaum, E. (2000) *Nature* **405**, 1014 – 1015. Enzymatic production of biohydrogen.

Wong, C-H. & Whitesides, G.M. (1981) *J. Amer. Chem.Soc.* **103**, 4890 - 4899. Enzyme-catalyzed organic-synthesis - NAD(P)H cofactor regeneration by using glucose-6-phosphate and the glucose-6-phosphate dehydrogenase from *Leuconostoc mesenteroides*.

Woese, C.R & Fox, G.E. (1977) *Proc. Natl. Acad. Sci. USA* **74**, 11, 5088 - 5090. Phylogenetic structure of the prokaryotic domain: the primary kingdoms.

Woese, C.R., Pace, N.P., & Olsen, G.J. (1986) *Nature* **320**, 401 - 402. Are arguments against archaeobacteria valid?

Woese, C.R., Kandler, O., & Wheelis, M.L. (1990) *Proc. Natl. Acad. Sci. USA* **87**, 4576 - 4579. Towards a natural system of organisms: Proposal for the domains Archaea, Bacteria, and Eukarya

Wu, J.T., Wu, L.H., & Knight, J.A. (1986) *Clin. Chem.* **32**, 2, 314 - 319. Stability of NADPH: effect of various factors on the kinetics of degradation.

Zatman, L.J., Kaplan, N.O., & Colowick, S.P. (1953) *J. Biol. Chem.* **200**, 127 - 212. Inhibition of spleen Diphosphopyridine nucleotidase by Nicotinamide, an exchange reaction.

Zillig, W., Stetter, K.O., Wunderl, S., Schulz, W., Prier, H. and Scholz, I. (1980) *Arch. Microbiol.* **125**, 259 -269 .

Zillig, W., Kletzin, A., Schleper, C., Holz, I., Janekovic, D., Hain, J., Lanzendörfer, M., & Kristjansson, J.B. (1994) *System. Appl. Microbiol.* **16**, 609 - 628. Screening for *Sulfolobales*, their plasmids and their viruses in Icelandic Solfataras.

Hydrogen Production by the Thermophilic Bacterium, *Thermotoga neapolitana*

Suellen A. Van Ooteghem

with

Stephen K. Beer

Paul C. Yue

National Energy Technology Center, U.S. Department of Energy

3610 Collins Ferry Rd., Morgantown WV 26507

304-285-5443, 304-285-4403 Fax

svanoo@netl.doe.gov

Abstract

Virtually all members of the order *Thermotogales* have demonstrated the ability to produce hydrogen and some members of this order produce considerably greater quantities than the rest. With one representative of this order, *Thermotoga neapolitana*, we have consistently obtained accumulations of 25-30% hydrogen with carbon dioxide as the only other prominent byproduct of the batch reaction (12-15%). In contradistinction to information widely disseminated in the literature, we have also found that most members of this order tolerate and appear to utilize moderate amounts of oxygen in the gaseous phase of the batch reactor (6-12%), with no apparent decrease in hydrogen production. Hydrogen accumulation has been widely reported to inhibit growth of members of the *Thermotogales*. While this may be true at very high hydrogen tensions, we have noted hydrogen generation during both the log and stationary phase. To maximize hydrogen production and minimize production of hydrogen sulfide, inorganic sulfur donors are avoided and the cysteine concentration in the medium is increased. Different members of the order *Thermotogales* have been demonstrated by the authors and by others to utilize a wide variety of feedstocks, including complex carbohydrates and proteins. Our results suggest that organisms within this order have the potential to utilize a variety of organic wastes and to cost-effectively generate significant quantities of hydrogen gas.

Introduction

The U.S. currently consumes approximately 3.6 trillion cubic feet of hydrogen annually, while the worldwide consumption is about three times that amount (Heydorn *et al* 1998, Padro *et al* 1999). The U.S. demand for hydrogen is expected to grow by 40% within the next five years. According to recent DOE hydrogen program overviews, most of this hydrogen gas is currently made from synthesis gas that comes either from the reformation of natural gas or from the gasification of coal. These processes are costly and environmentally problematic. Therefore, society must develop economical, continuous, environmentally friendly methods of production. Biological production of hydrogen as an endproduct or byproduct of the metabolism of biological organisms has been proposed as one means of producing needed hydrogen (Zaborsky 1997).

Investigators have attempted to produce bio-hydrogen for many years, generally using one of three different types of metabolic processes: (1) photosynthetic unicellular organisms that utilize either nitrogenase or hydrogenase reactions to produce hydrogen, (2) fermentative bacteria that produce hydrogen anaerobically, and (3) various stepwise processes in which a combination of bacteria of one population predigests more complex organic molecules to make a less complex feedstock of simple organic molecules that can be subsequently used by hydrogen-producing organisms (Kaplan *et al.* 1998, Vatsala 1990, Weaver 1990, Melis *et al.* 2000). Only modest success has been achieved so far because: (1) organism growth is end-product (or byproduct) inhibited by catabolites produced in the medium, (2) hydrogen gas production is inhibited because growth slows with increasing hydrogen concentrations, (3) the range of feedstocks the organisms can use is prohibitively narrow, (4) the concomitant production of undesirable gases is high, or (5) the rate of hydrogen gas production is endogenously low (Kaplan *et al.* 1998).

Building on information obtained by earlier investigators, we have taken a different approach to the biogenesis of hydrogen, and have tested the hydrogen generation capability of fifteen different strains of extremophilic bacteria of the order *Thermotogales*. *Thermotogales* is an order composed of rod-shaped, gram-negative, non-sporulating bacteria that have a loose surrounding membrane or “toga.” Huber *et al.* (1986) identified the first member of this order, *Thermotoga maritima* (DSM 3109), in 1986. At about the same time, a second extremophilic bacterium, *Thermotoga neapolitana* (DSM 4359, ATCC 49049), was identified by Belkin *et al.* (1986), and later expanded upon and classified as a member of the *Thermotogales* by Jannasch *et al.* (1988.) More than twenty different members in more than five different genera (Huber and Stetter 1992) are currently known. These organisms have been isolated from a variety of environments; freshwater and marine hot springs, hot sulfur springs, near the mouth of marine black smokers, and hot oil wells. All of these organisms have been isolated from environments where the temperature is significantly elevated. Most of the *Thermotogales* can withstand elevated pressures as well; however, our laboratory studies confirm earlier reports (10-14) that they grow quite readily at atmospheric pressure as long as the temperature is elevated. Most species, including *Thermotoga neapolitana*, are reported in the literature to be obligate anaerobes (10-14); however, we present evidence to indicate that they can also grow in the presence of low concentrations of headspace oxygen. Many species of the *Thermotogales* appear to reduce S^0 or other sulfur compounds, although sulfur reduction does not appear to be required for the growth of *T. neapolitana*. In any event, the relationship between growth and sulfur utilization by the *Thermotogales* is currently unclear (Adams 1994).

We cultured and tested fifteen different species in the order *Thermotogales* and confirmed literature results indicating that during bacterial metabolism these species characteristically produce hydrogen. Most reports in the literature do not give a clear indication of the amount of hydrogen produced, or the potential utility of these organisms for commercial hydrogen production. We have found that the amount of hydrogen generated can be highly variable, depending upon the *Thermotogales* species used and the degree of optimization of the organisms for hydrogen production. However, we observed that under microaerophilic conditions, most species of the *Thermotogales* produce significant amounts of hydrogen during incubation.

Our studies concentrated on optimization of hydrogen production using *Thermotoga neapolitana* because this organism appears to be particularly robust and adaptable to varying conditions and to utilization of different primary carbon sources. Earlier workers showed that *T. neapolitana* is the only member of this order that can grow on a medium that does not contain proteins or other substances which are poorly defined (Childers *et al.* 1992), and that it can utilize a wide variety of substrates.

Preserved cultures were purchased from either DSMZ or ATCC. Prior to inoculation of a new batch culture vessel, a sample of the stock culture was grown on a medium that did not contain a carbon source other than the yeast and trypticase that was part of the medium formulation. In this way, we ensured that carbohydrate levels were not artificially elevated by inoculation of the new batch culture vessel with a carbon-rich medium. Serum bottles with rubber septa sealed with crimped lids were used for batch reactors.

Materials and Methods

The following medium (modified from ATCC 1977 medium recommended for *T. elfeii*) was used to prepare the batch reactors for culture of *T. neapolitana*: NH₄ Cl, 1.0 gm; K₂ HPO₄, 0.3 gm; KH₂PO₄, 0.3 gm; MgCl₂ x 6 H₂O, 0.2 gm; CaCl₂ x 2 H₂O, 0.1 gm; NaCl, 10.0 gm; KCl, 0.1 gm; Cysteine HCl, 1.0 gm; Yeast Extract, 2.0 gm; Trypticase, 2.0 gm; Vitamin Solution (DSMZ medium 141), 10.0 ml; Trace Element Solution (DSMZ medium 141), 10.0 ml; H₂O, 1.0 L. The initial pH of the medium was adjusted to 8.5 @ 20°C with NaOH. Trizma base (1.0E-04M) can be added to help maintain pH in an optimal range for longer periods of time during incubation. A primary carbon source (0.25 g/50 ml cellulose, cellobiose, starches, or glucose) was also added.

The medium was always prepared aerobically. Fifty ml. of the above medium was aliquoted into serum bottles, allowing 110 ml. headspace for gas accumulation. Excess oxygen was removed by heating the batch reactors containing medium and substrate to 100°C while sparging its contents (2-10 min) with nitrogen gas. Sparging time was varied to achieve predetermined concentrations of oxygen of between 1 and 12% in the headspace and then the actual oxygen concentration in the bottle was tested using a gas chromatograph. (The effects of different oxygen concentrations are shown below). Serum bottles were then sealed, capped and sterilized.

The headspace was routinely sampled using gas-tight syringes during the course of the experiment using a Hewlett-Packard Gas Chromatograph (GC). One ml of a stock bacterial inoculum solution

was transferred to the fresh medium using tuberculin syringes. The serum bottle reactors were then incubated at 70°C. All gas measurements were made at room temperature using the GC. Glucose measurements were made with a hand-held glucometer produced by Bayer and confirmed with a glucometer produced by Nova Biomedicals. Cell counts were done using a counting chamber in association with Sigma counting software, and confirmed using a Beckmann-Coulter counter. Optical density was also measured on the same samples for which actual cell counts were obtained.

Results

As noted above, we have tested several different carbon sources for their ability to support production of hydrogen gas. Figure 1 shows an example of the variable hydrogen generation results obtained with different primary carbon sources. For our more complete analysis (below), only the results obtained when glucose was the primary carbon source will be examined since growth on glucose is widely reported in the literature. This allows our results to be readily compared with those reported by other investigators.

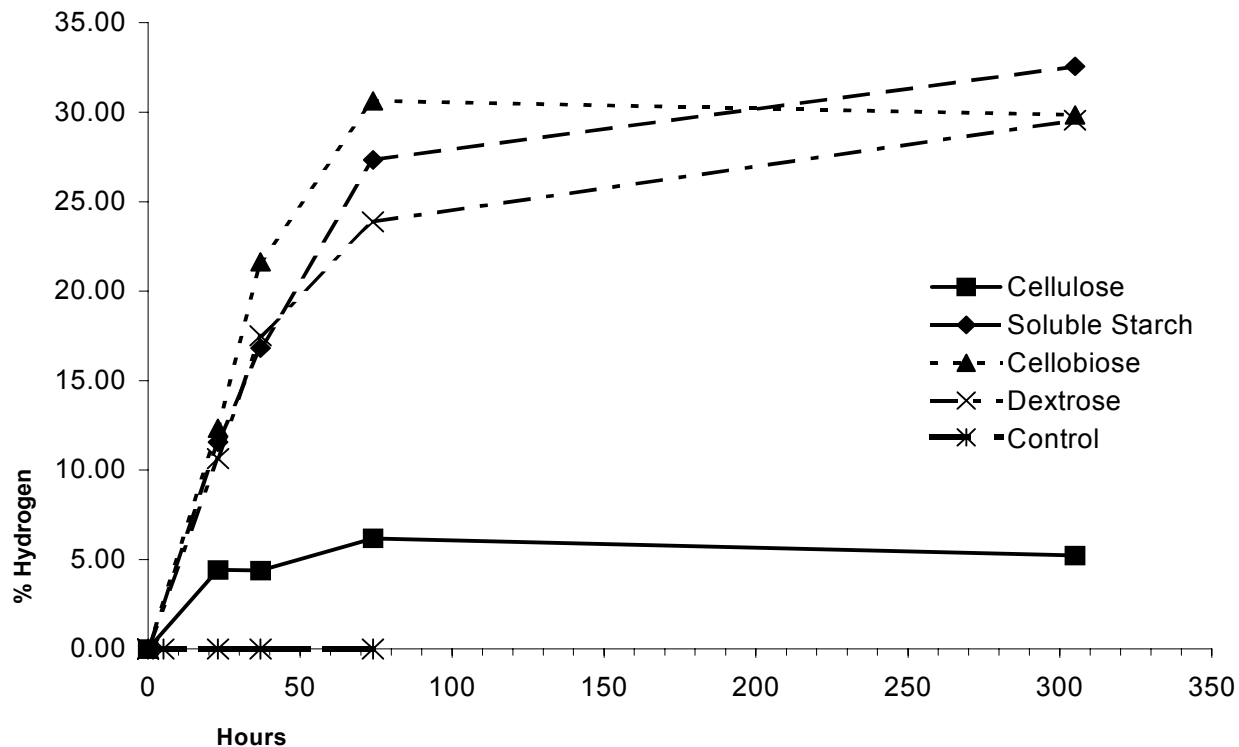


Figure 1: Hydrogen generation from various carbon sources

A comparison between the hydrogen generation seen when the oxygen concentration is slightly elevated and when the oxygen is very low can be found in Fig. 2 a & b. In Fig. 2a, the average (n=6) initial oxygen level in the headspace was greater than 11%, and the average concentration of hydrogen in the headspace after the experiment exceeded 28%. In a similar set of experiments (n=3), where the initial oxygen levels in the headspace was quite low, hydrogen generation was also low (12%). In fact, oxygen concentrations in the headspace appeared to rise modestly over time when the initial oxygen level in the headspace was very low (Fig.2b).

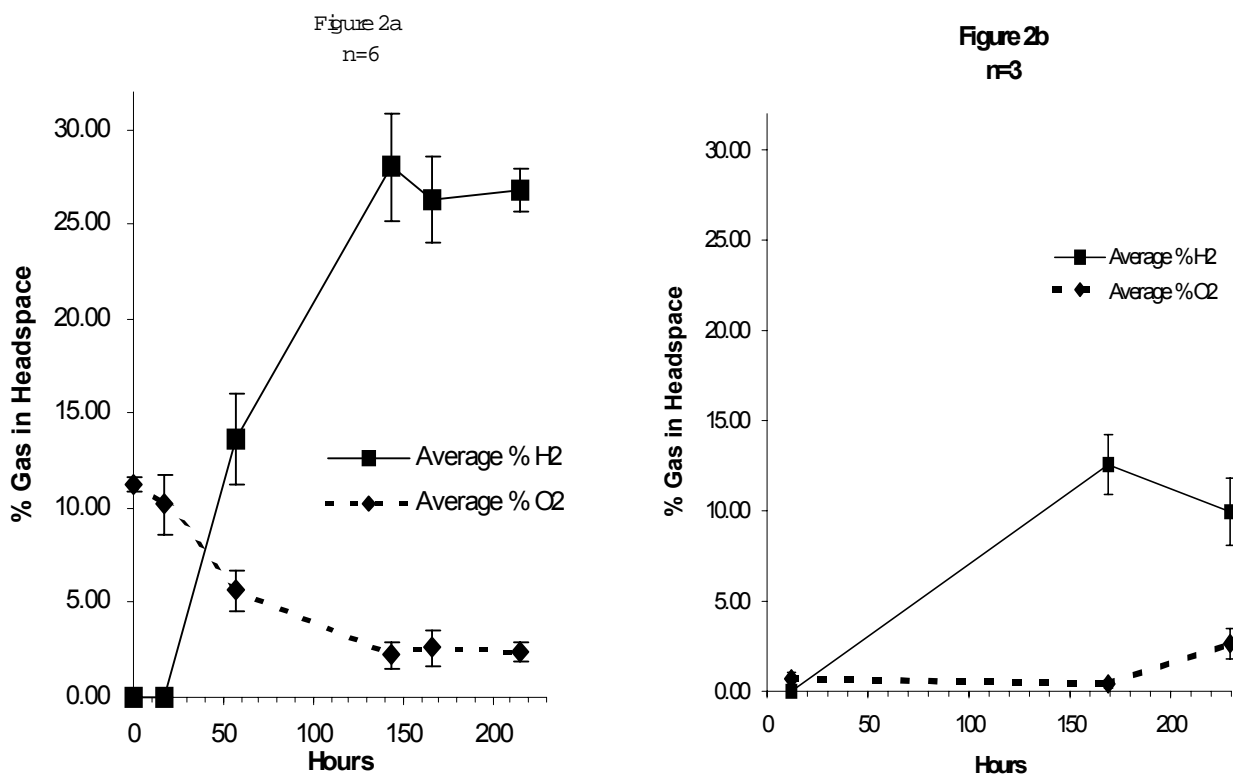


Figure 2a: Relationship of headspace hydrogen and oxygen concentrations vs time when the initial oxygen concentration was high. The percent hydrogen (■) increased to an average of 28.05% while the percent oxygen (◆) decreased from greater than 11% to less than 3% over the same period of time(n=6).

Figure 2b: Percent hydrogen and oxygen concentrations vs time when the initial headspace oxygen concentration was low. The maximum hydrogen (■) increased to an average of less than half of that seen in Fig. 2a, while the initial average percent oxygen (◆) was less than 1 initially and actually increased slightly over time.

Our experiments indicate that not all of the initial oxygen decrease in the headspace of the batch reactor can be related directly to utilization by microorganisms. Figure 3 a-c shows the relationship of oxygen depletion to hydrogen and carbon dioxide generation. Figure 3a shows the results of control experiments, indicating oxygen levels (\square), accumulation of hydrogen (clear column), and carbon dioxide (shaded column) for uninoculated batch reactors containing a glucose substrate. No hydrogen and very little carbon dioxide were produced. Overall, an oxygen decrease of about 3% (n=5) in the batch reactor headspace was seen. A similar response (about 2% oxygen (\square) decrease, n=3) was observed when the inoculated batch reactor contained no glucose as a substrate but did contain trypticase and yeast extract as a carbon source (Fig. 3b). Note that under these circumstances, a small amount of hydrogen and carbon dioxide were produced. However, in inoculated batch reactors (n=6) containing glucose (Fig. 3c) and oxygen (\square) levels of about 6% in the head space at the start of the batch reactor, oxygen depletion was nearly complete over the course of the experiment. In addition, after 62 hours, the hydrogen concentration averaged over 23% and the carbon dioxide level also increased. The ratio of hydrogen to carbon dioxide approached a ratio of 2:1. It is unlikely that this oxygen depletion results from leakage of the septum because hydrogen is a much smaller molecule and it remained contained within the headspace while the oxygen concentration decreased.

In order to determine if these organisms might be capable of catabolic processes requiring (and possibly utilizing) oxygen, we tested the ability of malonate, a competitive inhibitor of the TCA enzyme succinic dehydrogenase, to block the catabolic processes that are associated with hydrogen production.

The results of those tests are shown above (Fig. 4a-b). In the presence of 0.104 g/50 ml malonate hydrogen generation was completely inhibited for over 40 hours. After that time, it is postulated that free malonate is no longer available to block catabolism, and thus rapid hydrogen generation ensues. It should also be noted that oxygen depletion does not begin in malonate treated samples until hydrogen generation begins, and that oxygen concentration continues to decrease when hydrogen generation is ongoing.

Discussion

The rates and maximal concentrations of hydrogen generated can vary greatly depending on the primary carbon source and the initial oxygen concentration in the headspace. The maximum hydrogen generation rate we have recorded for any one specific batch experiment to date is shown in Table 1 below. In a single experiment using *T. neapolitana* grown on soluble starch, 28.47 ml of hydrogen gas was produced in 39 hours. Using the ideal gas laws to calculate the production rate yields 6.63E+00 ml/l headspace/hr, 2.98E-05 mol/hr or 5.97E-04 mol/l fluid/hr. Because this was a batch experiment of short duration, the bacteria were still in the log phase of growth, so this tells us little about what to expect from these bacteria in the stationary growth phase.

Figure 3a
n=6

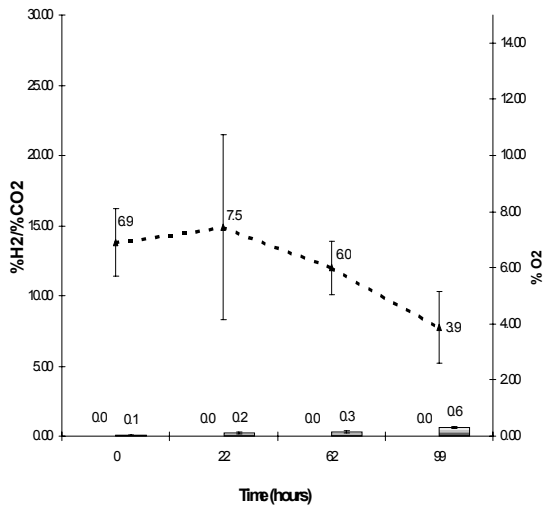


Figure 3b
n=3

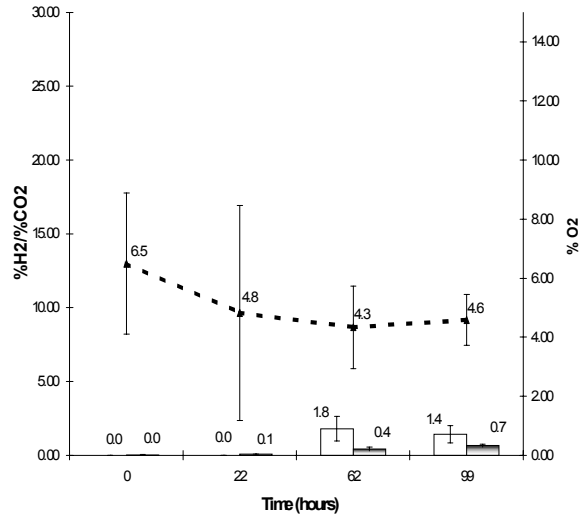


Figure 3c
n=6

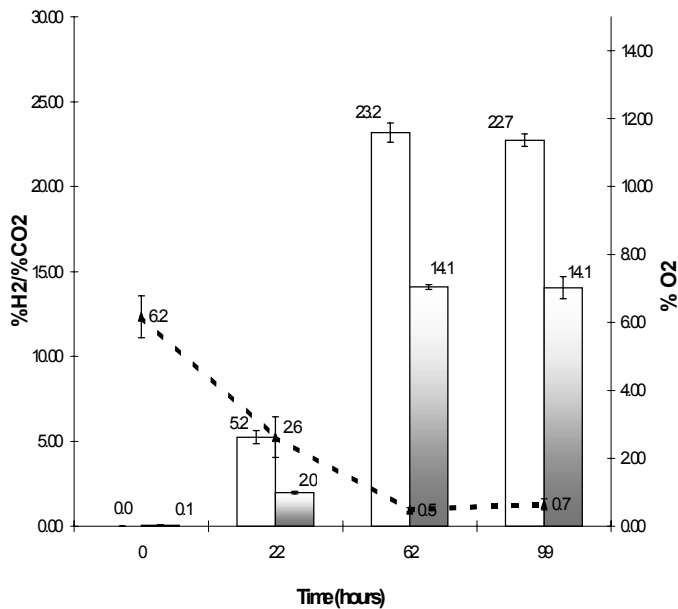


Figure 3a: Relationship of average percent hydrogen (clear bar), carbon dioxide (shaded bar), and oxygen (□) with respect to time when no inoculum was added to the batch reactor. Some oxygen depletion occurred in the absence of metabolizing cells; however, no hydrogen and very little carbon dioxide was produced without inoculation and incubation of the medium.

Figure 3b: Relationship of average percent hydrogen (clear bar), carbon dioxide (shaded bar), and oxygen (□) with respect to time when no glucose was added to the batch reactor. Some of the yeast and trypticase added to the batch reactor were capable of generating modest amounts of hydrogen and carbon dioxide. However, no hydrogen and very little carbon dioxide was produced without inoculation and incubation of the medium.

Figure 3c: Relationship of average percent hydrogen (clear bar), carbon dioxide (shaded bar), and oxygen (□) when the batch reactor both contained glucose and was inoculated with bacteria.

Fig 4a: No Malonate
(n=7)

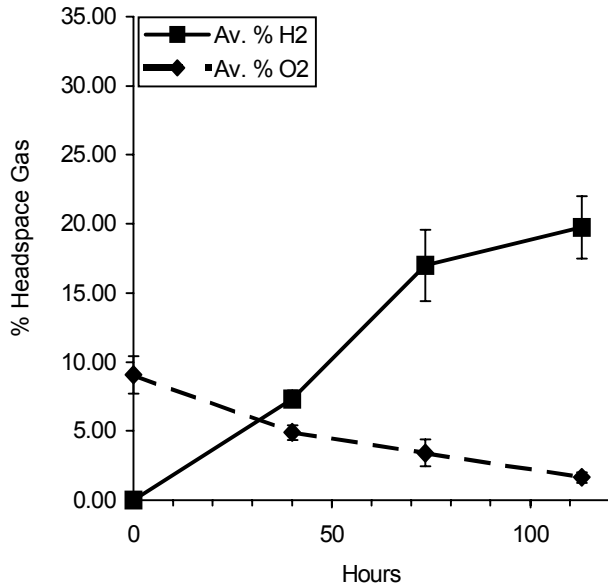


Fig 4b: 0.104 g/l Malonate
(n=7)

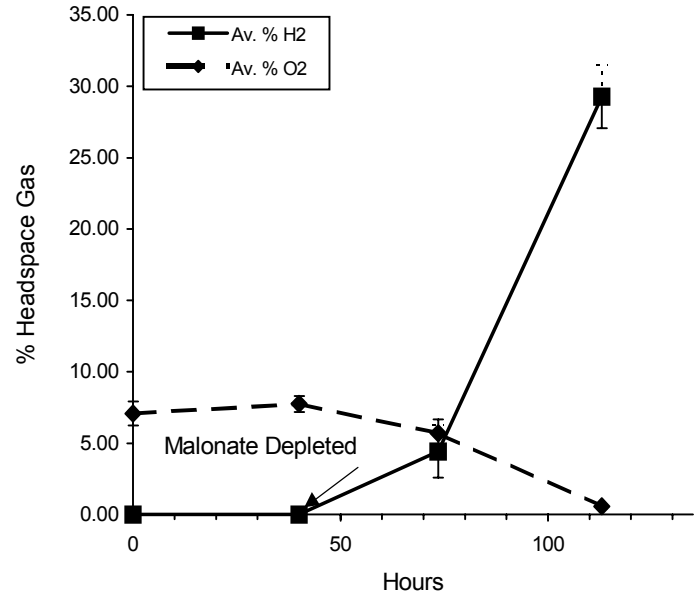


Figure 4. Effect of malonate on hydrogen gas generation and oxygen depletion.

Figure 4a shows hydrogen generation in the absence of malonate.

Figure 4b shows hydrogen generation in the presence of 0.104g/50 ml malonate. Oxygen depletion pattern is also affected by malonate block of hydrogen generation

The greatest rate of hydrogen output produced to date during a batch experiment is shown below in Table 1. Elapsed time reflects the time from the start of inoculation and incubation at 70°C. These calculations utilize the ideal gas laws and assume that the initial pressure in the batch experiment was one atmosphere and that the temperature of measurement was 25°C. The initial H₂ concentration was measured to be zero. Soluble starch was the primary carbon source.

Table 1: Rates of Hydrogen Output

Final % H ₂	Elapsed Time (hrs)	Head-space Volume (ml)	Fluid Volume (ml)	H ₂ Partial Pressure (atm)	Final Vol H ₂ (ml)	Moles H ₂ Product	H ₂ Production Rate (ml/l head-space/hr)	H ₂ Production Rate (mol/hr)	H ₂ Production Rate (mol/l fluid/hr)
25.86	39	110	50	.259	28.47	1.16E-03	6.63E+00	2.98E-05	5.97E-04

In Table 2 we have shown a test of potential efficiency. We obtained hydrogen gas accumulations in the headspace of up to 28.51% in 50 ml batch experiments incubated for periods of six days (144 hours). The calculated hydrogen production in the 110 ml headspace was 1.28E-03 moles with a calculated rate of production of 1.98E+00 ml/l headspace/hour, or 8.9E-06 mol/hour. Based on the amount of glucose present before and after the experiment, and the amount of hydrogen produced, the calculated efficiency of this process was estimated to be $71 \pm 24\%$ or greater, thus exceeding the Thauer limit anticipated for fermentations (Thauer *et al.* 1977). Because *T. neapolitana* has the ability to grow using only proteins as a carbon source, the endproduct hydrogen gas produced in the absence of glucose as a substrate was subtracted from the total hydrogen output prior to calculation of efficiency. We also counted the number of cells at the start and end of the experiment and found the increase in cell number to be greater than 35.4 ± 3.1 times. This increase was correlated with absorbance changes and measured glucose concentrations before and after the batch reactor experiment (Table 3). Thus, calculated efficiency values do not include increases in bacterial cell number.

Hydrogen production by *T. neapolitana* sample used to determine cell counts, absorbance measurements and efficiency shown in Table 2b. The first line of this table shows the total hydrogen gas generated while the second row shows the values obtained when the % hydrogen generated by utilization of the trypticase and yeast added to the media have been subtracted. Rates were calculated using the ideal gas laws and assuming initial pressure is one atmosphere and the temperature at which gases were assayed was 25°C. Bacteria were grown with glucose as the primary carbon source.

Table 2: Potential Efficiency

Final % H ₂	Elapsed Time (hrs)	Head-space Volume (ml)	Fluid Volume (ml)	H ₂ Partial Pressure (atm)	Final Vol H ₂ (ml)	Moles H ₂ Product	H ₂ Production Rate (ml/l head-space/hr)	H ₂ Production Rate (mol/hr)	H ₂ Production Rate (mol/l fluid/hr)
31.05	144	110	50	.311	34.16	1.40E-03	2.16E+00	9.71E-06	1.94E-04
28.51	144	110	50	.285	31.36	1.28E-03	1.98E+00	8.91E-06	1.78E-04

Estimated *T. neapolitana* hydrogen gas generation and biomass increase in 144 hours, shown in Table 3. Comparison of direct cell counts using a newly developed computerized direct counting technique, and measurements of absorbance for comparison. The standard deviations obtained using the direct counting technique are higher than desirable; however, these numbers are considered to be conservative since it is likely that some of the bacteria were distributed out of the plane of focus and not counted. Similarly, the calculated hydrogen production efficiency represents a very conservative estimate. Absorbance was measured using a Perkin/Elmer Lambda 3b spectrophotometer.

Table 3: Calculated Production Efficiency

Glucose Used (mg/50 ml)	Initial Count (cells/ml)	Initial Abs ₄₂₀	Final Count (cells/ml)	Final Abs ₄₂₀	Cell Count (Final/Initial)	Calc. % H ₂ Prod.Eff.
27 ± 9	7.293E+08± 3.8 %	.013±.002	2.58E+10± 8.2%	.320±.002	35.4± 3.1	71± 24



- Moles glucose = 2.7E-02g glucose/1.802E+02 g glucose/mole;
- Efficiency = Moles H₂ / (12 x Moles glucose) = 1.498E-04 moles glucose = 71%;
- ** Error reflects uncertainty of glucose measurements.

Most investigators have studied these organisms as strict anaerobes, and have developed elaborate methods to remove all oxygen from the environment, forcing only fermentative catabolism. While *T. neapolitana* does grow anaerobically, it also appears to be able to grow and produce significant amounts of hydrogen when provided low levels of oxygen. Based on our results, *T. neapolitana*, appears to be a microaerophile, capable of utilizing reduced levels of oxygen and generating hydrogen as an endproduct. A finding of oxygen tolerance/utilization is not unprecedented since the only other thermophilic bacterial order that has been identified as phylogenetically closely related to *Thermotogales*, the *Aquifex-Hydrogenobacter* group, includes more than one microaerophile (Kelly and Adams 1994, Shiba 1985). Beh *et al.* (1993) has shown that *Aquifex pyrophilus* (a microaerophile) is capable of shifting its metabolic behavior depending on oxygen availability. With oxygen availability and utilization, *T. neapolitana* metabolic behavior might also be predicted to shift to a more energy efficient catabolic pattern resulting in elevated hydrogen production and greater metabolic efficiency. Thus, oxygen removal may be responsible for a failure of earlier investigators to obtain high rates of hydrogen production. One avenue of future work will be to determine to what extent other facets of the metabolic behavior of *T. neapolitana* also vary with increased oxygen availability.

Given the findings presented above, a remaining factor that needs to be accounted for is the fate of the excess oxygen generated by this process. The original media contains a considerable amount of ammonium chloride, and when the media is used by the bacteria the solution turns a bright yellow color. The possibility exists that nitrate and/or nitrite ions that were not present in the initial media may be produced, and that nitrogen may accept the oxygen generated. This possibility is one major focus for our further research and clarification.

Hydrogen generation rates can vary greatly for a variety of reasons other than varying oxygen levels in the headspace. Factors such as sampling time, pH, buffering capability of the medium, and genetic heterogeneity also contribute to variable hydrogen generation rates. These confounding factors (pH, buffers, media components, etc.) have been thoroughly examined and will be considered in a separate publication (in preparation). Even with confounding factors present, the effects of differing oxygen concentrations clearly affect hydrogen generation most dramatically. Future work will continue to decipher the roles of the various factors and optimize both rates and efficiency.

Meeting the future worldwide demand for hydrogen will require development of continuous processes for hydrogen generation and efficient use of inexpensive waste materials as primary carbon sources. We are currently developing such a process. Preliminary experiments, using a continuous stirred tank reactor (CSTR) in batch mode, indicate that after six weeks of growth at constant temperature and pH, the organisms are still capable of producing significant amounts of hydrogen.

Acknowledgements

The authors thank Dr. Robert Romanosky and Dr. Neil Rossmeissl of the Department of Energy (FE and EE respectively) for funding this work. We wish to also thank Dr. Robert Kleinmann, Dr. Michael Eastman and Mark McKoy for their encouragement, Tom Simonyi for his excellent and tireless GC analyses, and Richard Pineault for his technical assistance.

References

- Adams, M.W.W. 1994. "Biochemical diversity among sulfur-dependent, hyperthermophilic microorganisms." *FEMS Microbiol. Rev.* 15:261-277.
- Beh, M., G. Strauss, R. Huber, K.O. Stetter, G. Fuchs. 1993. "Enzymes of the reductive citric acid cycle in the autotrophic eubacterium *Aquifex pyrophilus* and in the archaebacterium *Thermoproteus neutrophilus*." *Archives of Microbiology* 60(4):306-311.
- Belkin, S., C.O. Wirsen and H. W. Jannasch. 1986. "A new sulfur-reducing, extremely thermophilic eubacterium from a submarine thermal vent." *Appl. Env. Microbiol.*, 51(6),1180-1185.
- Childers, S.E., M. Vargas, and K.M. Noll. 1992. "Improved methods for cultivation of the extremely thermophilic bacterium *Thermotoga neapolitana*." *Appl. Environ. Microbiol.* 58:3949-3953).
- DOE Hydrogen Program Strategic Plan-Twenty-Year Vision (DEO/GO-10098-532) 1998.
- Heydorn, B., H. Schwendener, S. Mori. 1998. Hydrogen Product Review *Chemical Economics Handbook*.
- Huber, R., K.O. Stetter. 1992. "The order Thermotogales." *In: Balows, A., H. G. Truper, M. Dworkin, W. Harder, K.H. Schleifer (eds) The prokaryotes. 2nd edn. Springer, Berlin Heidelberg New York.* pp 3809-3815.
- Huber, R., T.A. Langworthy, H. Konig, M. Thomm, C. R. Woese, U.B. Sleytr, K.O. Stetter. 1986. "*Thermotoga maritima* sp. nov. represents a new genus of unique extremely thermophilic eubacteria growing up to 90°C." *Arch. Microbiol.* 144:324-333.

Hydrogen Program Overview Produced by the National Renewable Energy Laboratory for the DOE (DOE/GO 10095-088) 1995.

Jannasch, H.W., R. Huber, S. Belkin, K. O. Stetter. 1988. “*Thermotoga neapolitana* sp. nov. of the extremely thermophilic eubacterial genus *Thermotoga*.” *Arch. Microbiol.*, 150,103-104.

Kaplan, S., M. D. Moore. 1998. Process for the production of hydrogen using photosynthetic proteobacteria. *U.S. Patent 5,804,424*.

Kelly, R.M., M.W.W. Adams. 1994. “Metabolism in hyperthermophilic microorganisms.” *Antonie van Leeuwenhoek* 66:247.

Melis, A.L., M. Zhang, M. Foredtier, M. L. Ghirardi, M. Seibert. 2000. “Sustained photobiological hydrogen gas production upon reversible inactivation of oxygen evolution in the green alga *Chlamydomonas reinhardtii*.” *Plant Physiol.*, 122,127-136.

Padró, C.E.G., V. Putche. Survey of the Economics of Hydrogen Technologies (NREL/TP-570-27079) 1999.

Shiba, H., T. Kawasumi, Y. Igarashi, T. Kodama, Y. Minoda. 1985. “The CO₂ assimilation via the reductive tricarboxylic-acid cycle in an obligately autotrophic, aerobic hydrogen-oxidizing bacterium, *Hydrogenobacter thermophilus*.” *Arch. Microbiol.* 141,198.

Thauer, R.K., K. Jungerman, K. Decker. 1977. “Energy conservation in chemotrophic anaerobic bacteria.” *Bacteriol. Rev.* 41:100-180.

Vatsala, T.M. 1990. Microbial process for photohydrogen production from cellulose in high saline water medium. *U. S. Patent 4,921,800*.

P. F. Weaver. 1990. Photoenhanced anaerobic digestion of organic acids. *U.S. Patent 4,919,813*.

Zaborsky, O.R. 1997. (Ed.), *BioHydrogen* (Plenum Press, New York).

PRODUCTION OF HYDROGEN FROM BIOMASS-DERIVED LIQUIDS

Stefan Czernik, Richard French, Calvin Feik, and Esteban Chornet
National Bioenergy Center
National Renewable Energy Laboratory
Golden, Colorado, USA 80401

Abstract

Biomass as a product of photosynthesis is a renewable resource that can be used for sustainable production of hydrogen. Direct production of hydrogen from biomass by gasification/water-gas shift technology is economically unfavorable, except for very low cost feedstocks and very large plants. An alternative strategy, with potentially better economics, results from the combined production of hydrogen with valuable co-products. The concept is based on a two-stage process: fast pyrolysis of biomass to generate bio-oil, followed by catalytic steam reforming of the oil or its fractions to produce hydrogen. The preferred option is to separate bio-oil into a lignin-derived fraction that could be used for producing phenolic resins or fuel additives, and a carbohydrate-derived material that would be steam reformed to produce hydrogen. In order to increase the hydrogen production in a biomass-based plant, co-reforming of the bio-oil fraction and natural gas has also been considered. The co-product strategy can also be applied to residual fractions derived from pulping operations and from ethanol production. Effluents from other biomass conversion technologies such as transesterification of vegetable oils and food processing residues (“trap grease”) can also be attractive low-cost feedstocks for the production of hydrogen. This work focused on catalytic steam co-reforming of (a) carbohydrate-derived fraction of bio-oil and natural gas and (b) “trap grease.” We employed a fluidized bed reactor configuration with commercial nickel catalysts developed for processing natural gas and naphtha. The hydrogen yields obtained were 80-90% of the potential values for stoichiometric conversion of feed to CO₂ and H₂.

Introduction

At present, hydrogen is produced commercially from fossil fuels such as natural gas, naphtha, and coal. In such a case, the same amount of CO₂ as that formed from combustion of those fuels is released during hydrogen production stage. Renewable biomass is an attractive alternative to fossil feedstocks because of essentially zero net CO₂ impact. However, the hydrogen content in lignocellulosic biomass is only 6-6.5%, compared to almost 25% in natural gas. Consequently, the yield of hydrogen from biomass is relatively low, 12-14% based on the dry feedstock weight. Vegetable oils have a better potential for producing hydrogen than lignocellulosic materials but their high costs make the process economically non-viable. Only an integrated process, in which biomass is partly used to produce valuable materials (such as fibers) or chemicals (such as phenolics) while the residual fractions are utilized for generation of hydrogen, can be an economically viable option.

Our approach to the production of hydrogen from biomass is depicted in Figure 1. In earlier papers (Wang et al. 1997 and 1998, Czernik et al. 1999) we proposed a method that combines fast pyrolysis of biomass to generate bio-oil and catalytic steam reforming of the bio-oil to hydrogen and carbon dioxide. A significant advantage of this method is its potential for production and recovery of higher-value co-products from bio-oil, which would help to improve the economics of the entire process. The lignin-derived fraction can be separated from bio-oil and used as a phenol substitute in phenol-formaldehyde adhesives (Kelley et al. 1997) or converted to cyclohexyl ethers fuel additives (Shabtai et al. 1997) while the carbohydrate-derived fraction is catalytically steam reformed to produce hydrogen.

The carbohydrate-derived bio-oil fraction includes non-volatile compounds (sugars, oligomers) that do not evaporate and tend to decompose thermally, forming carbonaceous deposits in the reactor freeboard before contacting the steam reforming catalyst. Because of this, a fixed-bed catalytic reactor configuration used for steam reforming natural gas did not prove to be efficient for processing pyrolysis liquids. Therefore, we decided to employ a fluidized bed reactor that can overcome the limitations of the fixed beds. Though carbonization cannot be completely avoided, the bulk of the fluidizing catalyst remains in contact with the liquid droplets fed to the reactor. Catalyst regeneration can be done by steam or carbon dioxide gasification of carbonaceous residues in a second fluidized bed reactor.

In previous years we demonstrated that bio-oil carbohydrate-derived fraction could be efficiently converted to hydrogen. The hydrogen yields approached or exceeded 90% of theoretical (defined as the stoichiometric conversion of this fraction to CO₂ and H₂) when using commercial nickel-based catalysts. The proposed strategy improves the process economics but reduces the amount of hydrogen that can be produced from biomass to about 6% based on the initial weight of the feedstock.

A viable way to increase the production of hydrogen in a biomass-based plant could be co-reforming of pyrolysis liquid with natural gas. This approach, similar to co-firing of biomass with coal for power generation, would add environmental benefits to the traditionally fossil-based technology. The objective of this work was twofold: (a) to validate the co-reforming approach; (b) to determine the feasibility of producing hydrogen from “trap grease.” The latter is

a widely available low-cost waste material recovered from restaurants, food processing plants, and water treatment facilities. The estimated amount of 13 lbs/person/year of “trap grease” (Wiltsee, 1998) translates into a potential source of 1 billion pounds (0.5 Mt/year) of hydrogen.

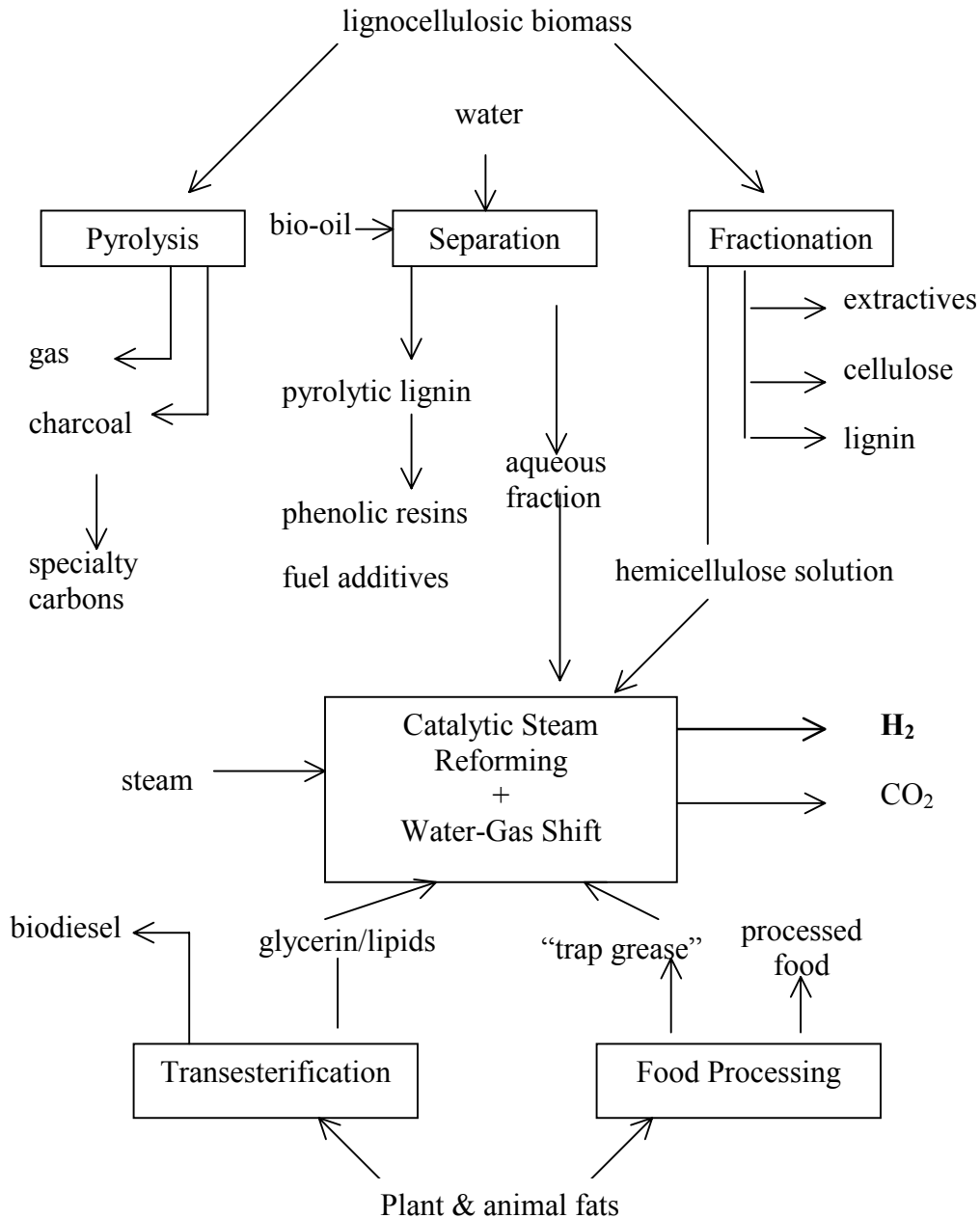


Figure 1. Biomass to hydrogen – Process concept

Experimental

Materials

Bio-oil used for this study was generated from pine sawdust using the NREL fast pyrolysis vortex reactor system (Diebold and Scahill, 1988). The oil composition (wt%, dry basis) was 47.7% carbon, 7.4% hydrogen, and 44.8% oxygen. Water content was 26.7%. It was separated into aqueous (carbohydrate-derived) and organic (lignin-derived) fractions by adding water to the oil in a weight ratio of 1.5:1. The aqueous fraction contained 20.0 wt.% organics and 80.0% water and consisted of 11.8% carbon, 9.6% hydrogen, and 78.6% oxygen.

Natural gas from the public utility had the following composition: 82.4% CH₄, 6.6% C₂H₆, 2.6% CO₂, and 8.4% N₂ (by volume.)

“Trap grease” was obtained from Pacific Bio-Diesel, a company collaborating with the DOE Bio-Diesel Program. The raw “trap grease” was filtered (at Pacific Bio-Diesel) to remove solid impurities. The grease was a dark-colored liquid of very high viscosity at room temperature. However, at 45°C its viscosity decreased to ca. 80 cP, which made it easy to pump. The grease mainly consisted of fatty acids and their mono-, di-, and triglycerides. The overall elemental analysis of the grease showed 75.5% carbon, 11.8% hydrogen, and 12.7% oxygen.

C11-NK, a commercial nickel-based catalyst used for steam reforming of natural gas and naphtha, was obtained from Süd-Chemie (formerly United Catalysts) and ground to a particle size of 300-500 μ .

Fluidized bed reformer

The bench-scale fluidized bed reactor is shown in Figure 2. A two-inch-diameter Inconel reactor having a porous metal fluidizing gas distribution plate was placed inside a three-zone electric furnace. The reactor contained 250-300g of commercial nickel-based catalyst ground to the particle size of 300-500 μ . The catalyst was fluidized using superheated steam, which is also a reactant in the reforming process. Steam was generated in a boiler and superheated to 750°C before entering the reactor at a flow rate of 2-4 g/min. In the co-reforming experiments, natural gas was compressed and fed to the reactor at a rate of 0.75 L (standard)/min. Liquids were fed at a rate of 2 g/min using a diaphragm pump. In the case of “trap grease,” the feed was preheated and the feeding lines were heat-traced and maintained at 60-80°C to facilitate liquid flow and atomization. A specially designed injection nozzle supplied with a cooling jacket was used to spray liquids into the catalyst bed. The temperature in the injector was controlled by coolant flow and maintained below the feed boiling point to prevent evaporation of volatile and deposition of nonvolatile components. The product gas passed through a cyclone and hot-gas filter that captured fine catalyst particles and, possibly, char generated in the reactor, then through two heat exchangers that removed excess steam. The condensate was collected in a vessel whose weight was continuously monitored.

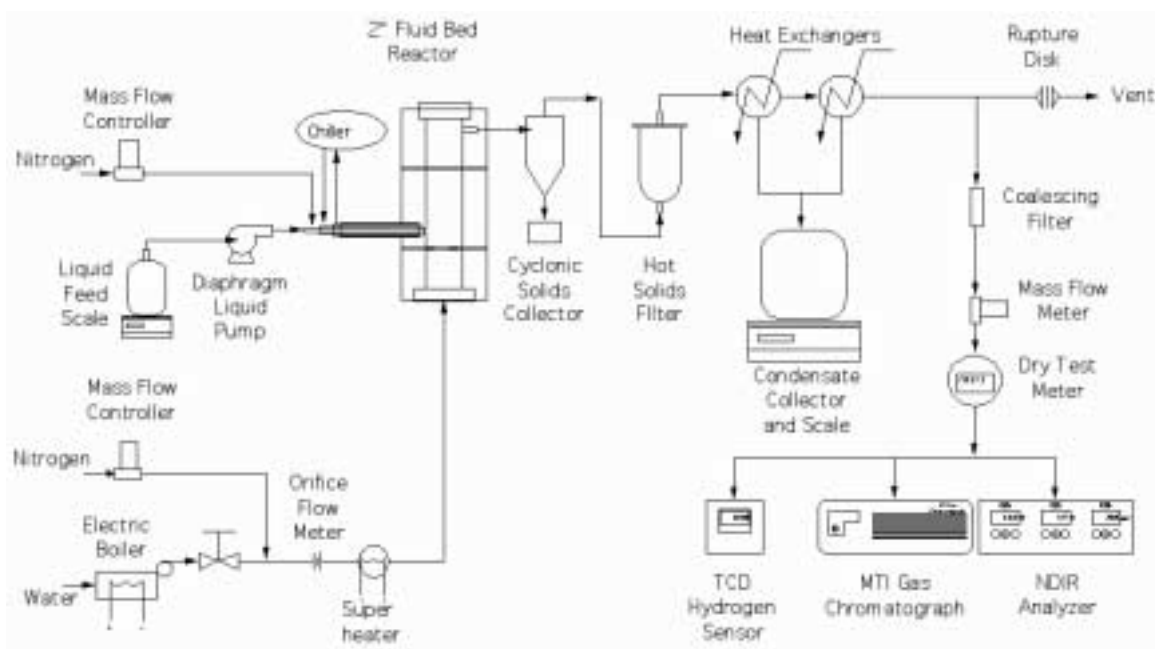


Figure 2. Fluidized bed reformer system

The flow rate of the outlet gas was measured using a mass flow meter and a dry test meter. The concentrations of CO₂, CO, and CH₄ in the reforming gas composition were monitored by a non-dispersive infra-red analyzer (NDIR Model 300) and that of hydrogen by a thermal conductivity monitor (TCM4). In addition, the gas was analyzed every 5 minutes by an on-line MTI gas chromatograph that provided concentrations of hydrogen, carbon monoxide, carbon dioxide, methane, ethylene, and nitrogen as a function of time. The temperatures and flows in the system the flows were recorded and controlled by the OPTO data acquisition and control system. Total and elemental balances were calculated as well as the yield of hydrogen generated from the feed.

Results and Discussion

Co-reforming of bio-oil and natural gas

The reactor operated at 850°C with a methane-equivalent gas hourly space velocity G_{C_1HSV} of ca. 1000 h⁻¹ and a molar steam-to-carbon ratio of 4.6. The test was carried out without interruption for 56 hours alternating between co-reforming and bio-oil-only reforming. The operation was smooth, especially during the co-reforming cycles. Co-feeding of natural gas helped maintain and restore the catalyst activity. The concentration of major product gas components as a function of time is shown in Figure 3.

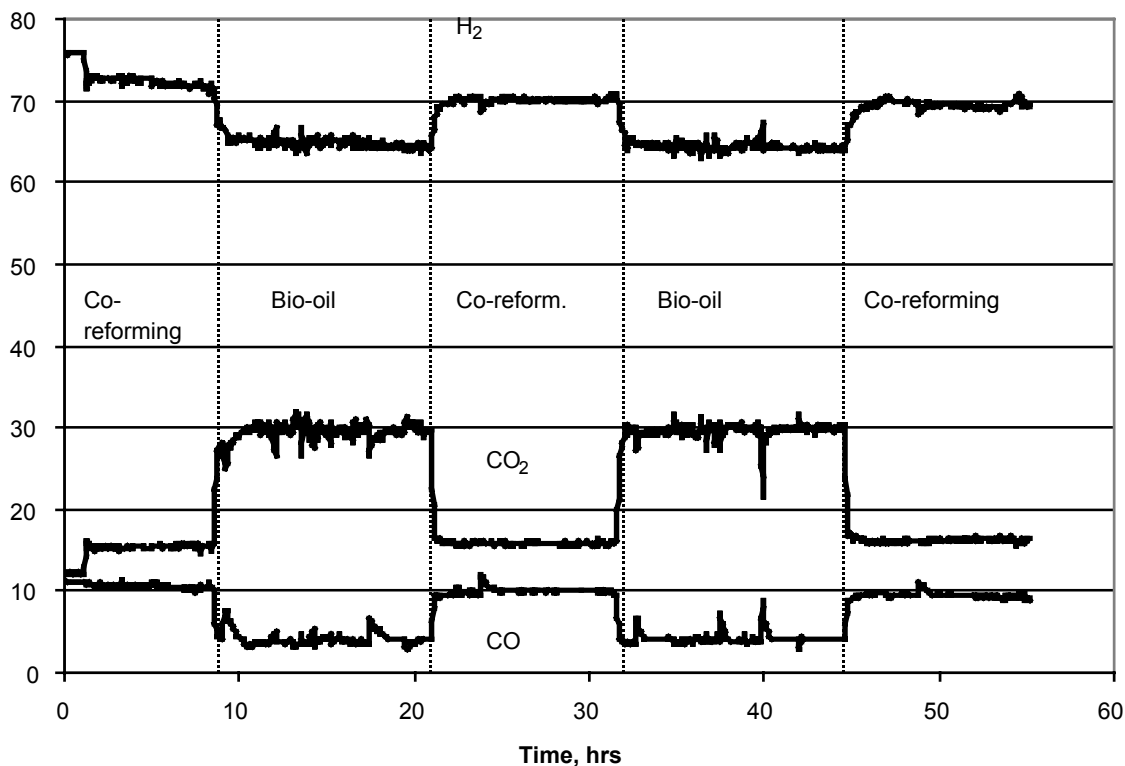


Figure 3. Reforming gas composition (vol %) as a function of run time

The gas composition was almost constant during the reforming phase and the co-reforming phase, though a small decrease in hydrogen and increase in methane concentration were observed between the first and the second co-reforming cycle. Methane conversion was initially 92.5% but decreased to 80% by the end of the test. A sharp increase in methane concentration at the reactor outlet was observed at the beginning of the second and third cycles of co-reforming but CH_4 significantly decreased after 30 minutes (Figure 4). The hydrogen yield was initially 80% then decreased to 75% of the theoretical (stoichiometric) potential (amount of hydrogen that would be obtained when total organic carbon converts to CO_2) via reforming + water gas shift, WGS) as shown in Figure 5. During co-reforming, 23-26% of the hydrogen was generated from bio-oil and 73-77% from natural gas.

Reforming of “trap grease”

“Trap grease” reforming was carried out at 850°C with a methane-equivalent gas space velocity ($G_{\text{Cl}}\text{VHSV}$) of 950 h^{-1} and a molar steam to carbon ratio of 5. The experiments proceeded very smoothly and the concentration of the major gas products was constant during the whole run of 17 hours as shown in Figure 6.

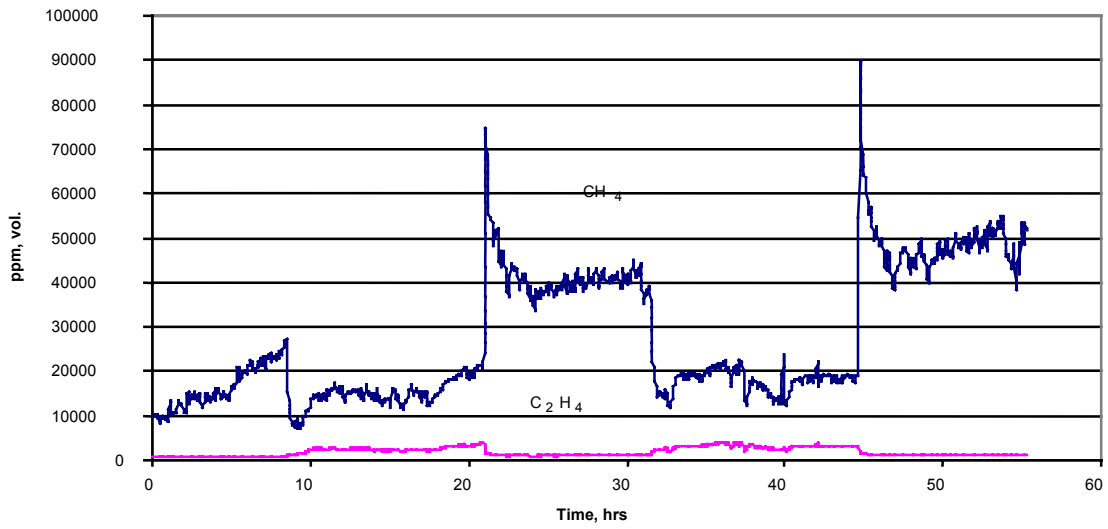


Figure 4. Concentration of hydrocarbons in the co-reforming gas

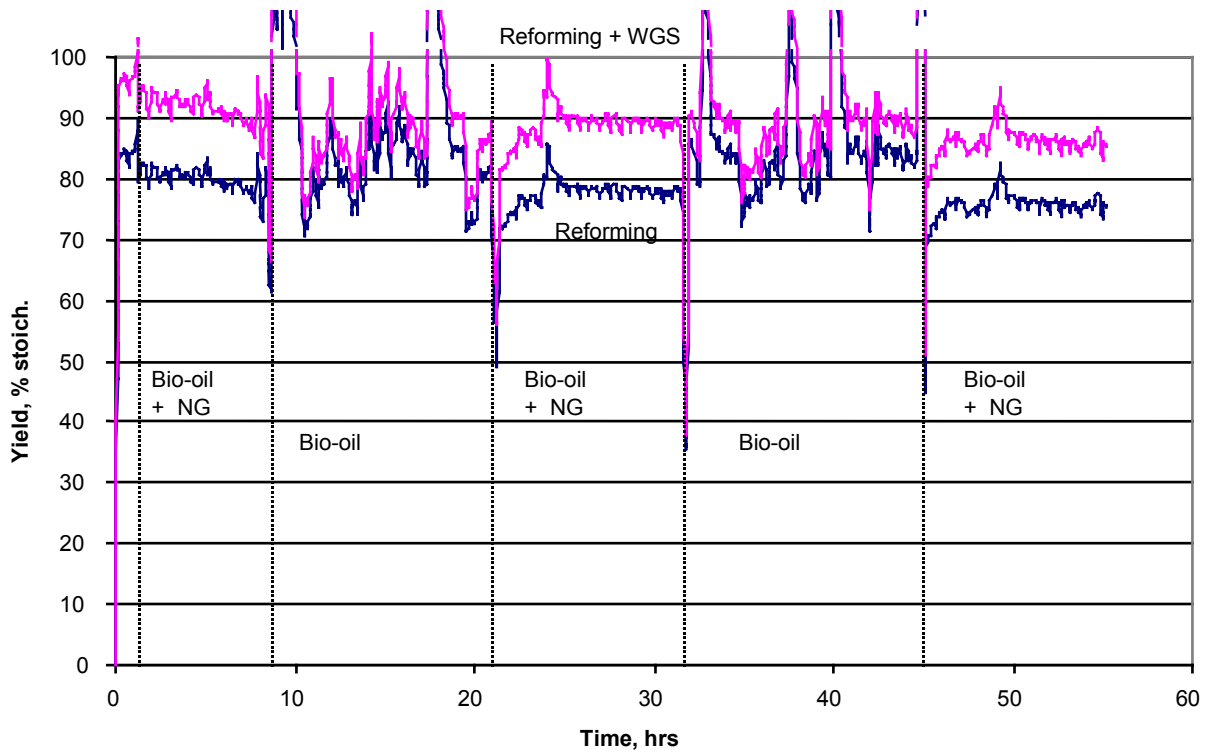


Figure 5. Yield of hydrogen from co-reforming of bio-oil and natural gas

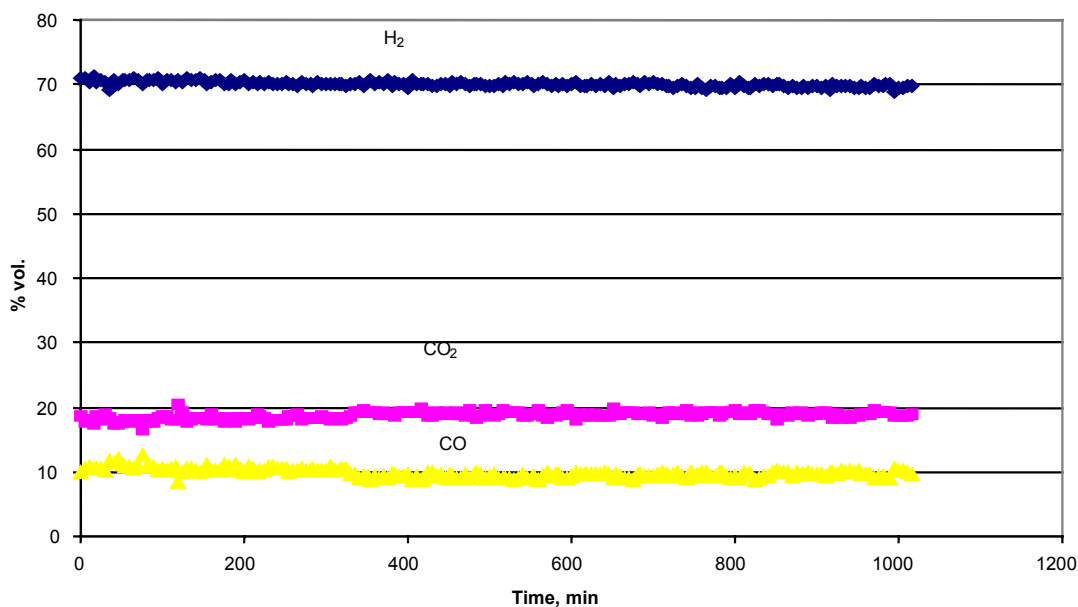


Figure 6. Product gas composition obtained by reforming of “trap grease”

The concentrations of minor products, methane and ethylene (Figure 7), increased during the first ten hours of the experiment, which could be due to a decreasing catalyst activity. However, they leveled off in the second half of the test.

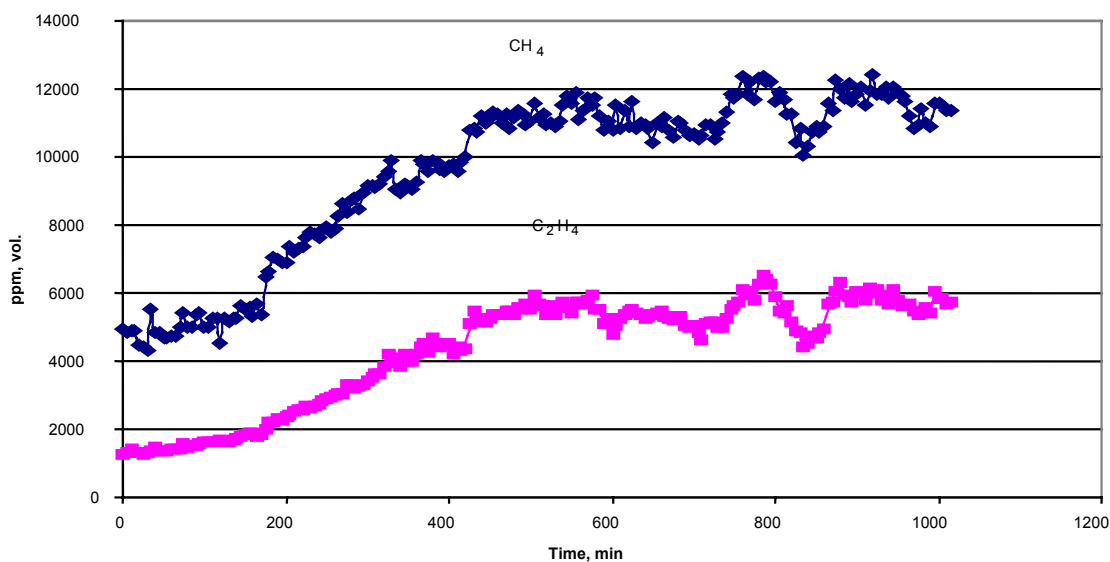


Figure 7. Concentration of hydrocarbons during steam reforming of “trap grease”

The hydrogen yield that was initially 31.1 g per 100 g of “trap grease” decreased to 28.7 g after 17 hours of operation. This corresponds respectively to 88% and 81% of the amount that could be achieved if total organic carbon were converted to CO₂ (Figure 8). These yields could be 10% higher if the reforming were followed by water-gas shift to convert CO to CO₂ (upper curve). The overall mass balance closure was essentially 100% throughout the duration of the test. Closures were also observed for elemental balances of carbon, hydrogen and oxygen, indicating that all the carbon from “trap grease” was converted to gases.

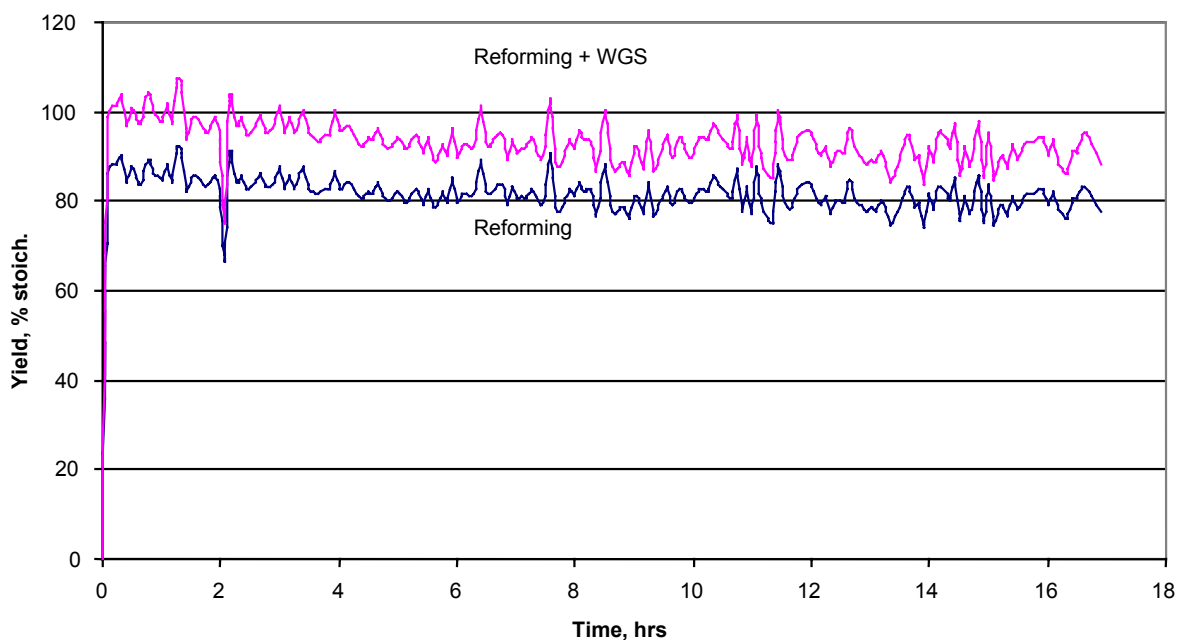


Figure 8. Hydrogen yield obtained from reforming of “trap grease”

The above results indicate that “trap grease” can be a convenient feedstock for producing hydrogen. It is available at a price of 2-4¢/lb. Since over 30 kg of hydrogen can be obtained from 100 kg of “trap grease,” the feedstock costs contributes only \$1-2/GJ to the total cost of hydrogen. With current market prices for hydrogen in the \$6-9/GJ range, “trap grease,” which can be processed directly without any expensive pretreatment, offers an opportunity for further development. The technology needs to be further studied to determine the catalyst time on stream and the efficiency of regeneration. Also effects of possible contaminants in “trap grease,” especially inorganics, should be thoroughly investigated.

Summary and Conclusions

1. Biomass can be a valuable resource for producing hydrogen if used in an integrated process that also generates higher value co-products. Following this strategy we have presented two process options: fast pyrolysis/steam reforming (extended to co-reforming bio-oil and natural gas) and steam reforming of biomass residues (“trap grease” in this study).

2. We have demonstrated feasibility of co-reforming the aqueous fraction of bio-oil and natural gas. The hydrogen yield obtained in a fluidized bed reactor using a commercial catalyst was about 80% of the stoichiometric value. This yield would increase by 10% if CO present in the gas were further converted by water-gas shift. In our tests, about 75% of the hydrogen was obtained from natural gas while 25% was from bio-oil.
3. We have successfully proven the concept of using a fluidized bed catalytic steam reforming process for the production of hydrogen from “trap grease,” a low-cost feedstock available at food processing and sewage treatment plants. The hydrogen yield was about 30 g per 100 g of feed, which is above 81% of theoretical (stoichiometric conversion), for 17 hours of catalyst time on stream. This yield could increase by 10% if a secondary water-gas shift reactor followed the reformer.
4. The catalytic fluidized bed process should be further studied to determine the catalyst time on stream and efficiency of regeneration. The effect of possible inorganic impurities on the catalyst needs to be determined.

References

- Czernik, S., French, R., Feik, C, and Chornet, E. 1999. “Fluidized bed catalytic reforming of pyrolysis oils for production of hydrogen.” In *Proceedings of the Fourth Biomass Conference of the Americas*, (Ed. by Overend, R. and Chornet, E.), pp. 827-832. Elsevier Science Ltd., Oxford.
- Diebold, J. and Scahill, J. 1988. “Production of primary pyrolysis oils in a vortex reactor.” In *Pyrolysis Oils from Biomass: Producing, Analyzing and Upgrading*, (Ed. by Soltes, E. J. and Milne, T. A.), pp. 31-40. American Chemical Society, Washington, D.C.
- Kelley, S. S., Wang, X.-M., Myers, M. D., Johnson, D. K., Scahill, J. W. 1997. “Use of biomass pyrolysis oils for preparation of modified phenol formaldehyde resins.” In *Development in Thermochemical Biomass Conversion*, (Ed. by Bridgwater, A.V. and Boocock, D.G.B.), pp. 557-572. Blackie Academic & Professional, London.
- Shabtai, J.S., Zmierczak, W., and Chornet, E. 1997. “Conversion of lignin to reformulated gasoline compositions.” In *Proceedings of the Third Biomass Conference of the Americas*, (Ed. by Overend, R.P. and Chornet, E.), pp. 1037-1040. Elsevier Science Ltd., Oxford.
- Wang, D., Czernik, S., Montané, D., Mann, M., and Chornet, E. 1997. “Biomass to hydrogen via pyrolysis and catalytic steam reforming of the pyrolysis oil and its fractions.” *I&EC Research*, **36**, 1507-1518.
- Wang, D.; Czernik, S., and Chornet, E. 1998. “Production of hydrogen from biomass by catalytic steam reforming of fast pyrolysis oils.” *Energy & Fuels*, **12**, 19-24.
- Wiltsee, G. 1998. *Urban Waste Grease Resource Assessment*, Report prepared by Appel Consultants, Inc., for NREL, subcontract No. ACG-7-17090-01.

MODELING OF BIOMASS PYROLYSIS FOR HYDROGEN PRODUCTION: THE FLUIDIZED BED REACTOR

**Danny Lathouwers and Josette Bellan
Jet Propulsion Laboratory
California Institute of Technology
Pasadena, CA 91108-8099**

Abstract

A numerical study is performed in order to evaluate the performance and optimal operating conditions of fluidized bed pyrolysis reactors used for condensable tar production from biomass. For this purpose, a previously validated biomass particle pyrolysis model is coupled with a detailed hydrodynamic model for the binary gas particle mixture. The kinetics scheme is based on superimposed cellulose, hemicellulose, and lignin reactions. Any biomass feedstock can be simulated through knowledge of its initial mass composition with respect to these three primary components. The separately validated hydrodynamic model is based on a three fluid model (gas, sand, and biomass) derived from the kinetic theory of granular flows. Separate transport equations are constructed for each particle class, allowing for the description of such phenomena as particle segregation and for separate temperatures for each particle class. The model is employed to investigate the effect of various operating conditions on the efficiency of tar collection in fluidized bed reactors. Results indicate that, at fixed particle size, the operating temperature is the foremost parameter influencing tar yield. The biomass feed temperature, the feedstock, and fluidization velocity magnitude, all have minor impact on the yield. The particle diameter has a considerable influence on the short-time tar yield, but it is inferred that it may have a more moderate influence on the steady-state tar yield.

For the range of fluidizing gas temperatures investigated, optimum steady-state tar collection is obtained for 750 K under the assumption that the pyrolysis rate is faster than the feed rate; the predicted optimum temperature is only slightly higher if this assumption is not satisfied. Finally, scale up of the reactor is addressed and is found to have a small negative effect on tar collection at the optimal operating temperature. It is also found that slightly better scaling is obtained by using shallow fluidized beds with higher fluidization velocity.

Introduction

The interest in clean hydrogen fuel production has triggered substantial activity in high temperature biomass pyrolysis in many countries. The aim of these activities is to obtain a process that maximizes tar yield while simultaneously minimizing char formation. Biomass pyrolysis involves the heating of raw biomass in the absence of an oxidizer in order to extract reaction products for subsequent processing. Among several reactor geometries, the vortex reactor and the fluidized bed reactor were the subject of research activities at the National Renewable Energy Laboratory (NREL), being potentially attractive as commercial pyrolysis devices. The vortex reactor was the subject of an earlier study (Miller and Bellan 1998) accomplished by coupling a detailed model for pyrolysis to a fundamental fluid dynamics model of the vortex reactor. A similarly fundamental and detailed study of the pyrolysis conditions in a bubbling fluidized bed is not available in the literature.

The fluidized bed reactor consists of a cylindrical vessel partially filled with sand. The sand's main purpose is to provide a large heat reservoir to keep the mean temperature of the bed constant. In turn, heat has to be provided to the biomass, as the pyrolysis is an endothermic process. This is achieved by heating the walls of the reactor and by injecting hot steam or nitrogen which is further used to fluidize the mixture, while also preheating it. The fluidizing gas induces a violent gas and solid flow pattern in the reactor, with both locally dense and void particle regions. An overall circulative complex flow occurs, explaining the excellent mixing behavior of fluidized bed reactors. Fresh, relatively cool, biomass is injected into the reactor through a feeding mechanism in the wall, or directly into the bed using an injection 'rod'. After the biomass is fed into the reactor, it partially mixes with the sand and heats up. As heating progresses, the particles pyrolyze and eject product gases (tar and gas; gas denotes here the collection of gaseous products complementary to tar) while at the same time forming char which maintains the particle matrix. Product gases mix up with the fluidizing gas and are transported towards the reactor exit after which they are cooled to prevent product degradation, making collection of the condensable tars possible. To prevent degradation of product tars within the reactor it is important to achieve small residence times for the gaseous pyrolysis products. Finally, remaining particles containing char erode to smaller size grains and are carried out of the reactor by the gas flow. This self cleaning feature makes fluidized bed reactors especially suited to continuous operation.

In spite of the attractive simplicity of the reactor design, no thorough analyses are available of fluidized pyrolysis reactors addressing issues such as efficiency, optimal operating conditions and scale up for commercial use. Although the literature addressing the modeling of the biomass fluidized bed reactor is virtually absent, experimental studies (Scott and Piskorz 1982, 1984) have shown its potential for condensable tar production. These studies, however, have primarily focussed on bench and pilot scale setups, not focusing on commercial size operation.

In this paper, we present quantitative results from numerical simulations of both pilot scale and commercial scale fluidized bed reactors under viable operating conditions. These simulations are obtained from the coupling of a realistic biomass kinetics model with a detailed hydrodynamic model for the gas/particle mixture. Of particular interest are a quantitative assessment of parametric effects, optimal conditions, and scaling potential. The individual submodels, i.e. kinetics and hydrodynamics, have been appropriately validated against experimental data in previous publications (Miller and Bellan 1997; Lathouwers and Bellan 2000). Favorable comparisons for these submodels lends support to confidence and validity of the overall model.

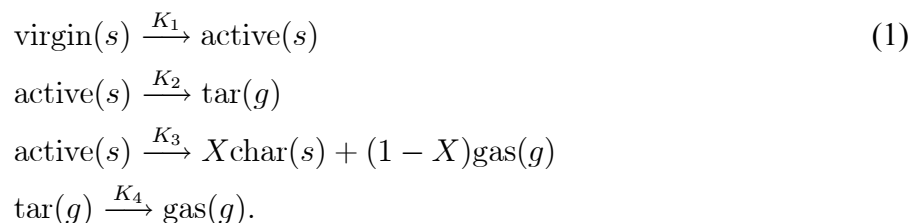
The paper is organized as follows: A summarized description of the kinetics and hydrodynamic submodels is given in Section 2; more details are available elsewhere (Lathouwers and Bellan 2000, 2001). Section 3 describes the specifics of the fluidized bed reactor under consideration and contains the reactor simulation results and parametric studies. The parameters studied are the fluidizing gas temperature, initial biomass particle temperature, feed stock, fluidization velocity magnitude, particle size and reactor scaling. A summary and conclusions are provided in Section 4.

Model formulation

As previously stated, the model developed by Lathouwers and Bellan 2001, consists of coupled submodels of the biomass kinetics and of the hydrodynamics of the gas particle mixture. The succinct description of these submodels is addressed below.

Single particle biomass pyrolysis model

The particle pyrolysis model employed here is that of the detailed kinetics derived by Miller and Bellan 1997, based on superimposed cellulose, hemicellulose, and lignin reactions. This enables the simulation of different biomass feedstock through knowledge of the initial mass composition with respect to these three primary components; biomass impurities are lumped with the hemicellulose as this model correlated best with the experimental data. Each of the virgin components undergoes the same generic competitive reaction scheme:



As indicated in the above kinetic scheme, the virgin components, the active intermediates and the char are solid phase species, while tar and gas are vapor products; these species are not pure chemical species but instead represent groups of compounds. All reactions are modelled with first order Arrhenius kinetics; $K_i = A_i \exp(-E_i/RT)$, where the rate constants, A_i , activation energies, E_i for reactions K_1, K_2, K_3 and the mass ratio X are dependent on the particular component, whereas all heats of reaction and secondary tar decomposition parameters (K_4) are independent of the source component.

This kinetic model combined with a porous particle flow dynamics model yielded validated predictions on tar/char yields ranging from the kinetically controlled regime (micro particles) to the

diffusion controlled limit (macro particles), c.f. Miller and Bellan 1997. In the present paper, for simplicity, the biomass pyrolysis is assumed kinetically controlled. This assumption may be justified in the dense particulate regime where contact between particles may induce fragmentation (see Miller and Bellan 1998 for a fragmentation model) and reduce the size of the particles to the point where the internal temperature equilibrates rapidly. Thus, the particle temperature, its mass and composition (global solid mass fractions) completely describe the state of the particle.

The sand and biomass particles are both solid and hence thermodynamically belong to the same phase. They, however, have different physical properties and different temperatures, etc. In particular, the biomass particles are porous whereas the sand particles are not. Therefore we solve separate equations for these particle classes.

Hydrodynamic model

The hydrodynamic model describing the dynamics of the gas particle mixture is that derived by Lathouwers and Bellan.2000 In previous papers (Lathouwers and Bellan 2000, 2001), the model was applied to a variety of test cases in order to quantify its predictive capabilities. These included (i) comparison of the stresses generated by the shearing of a homogeneous particle mixture, (ii) comparison of the particle pressure generated along the wall of a bubbling fluidized bed, (iii) the characteristic behavior of monodisperse and binary homogeneously fluidized beds, and (iv) biomass particle pyrolysis in a fluidized bed reactor. Here, we give a brief description of the model, referring the reader for full details to the derivation of Lathouwers and Bellan 2001.

The hydrodynamic model is based on a three fluid model description where macroscopic transport equations are derived from the kinetic theory of granular flows using inelastic sphere models, thereby accounting for collisional transfer in high density regions. Separate transport equations are constructed for each of the particle classes, allowing for the independent acceleration of the particles in each class and the interaction between size classes, as well as for the interaction processes whereby momentum and energy are exchanged between the respective classes and the carrier gas.

Definitions and averaging

The continuum model was derived by Lathouwers and Bellan 2001 applying separate averaging procedures to both the carrier gas and solid phases. A phase ensemble average was used for the carrier phase, combined with a particle ensemble average where particle properties, such as velocity, are directly averaged. This procedure is attractive when resolution of the detailed degrees of freedom of the particles (e.g. internal temperature profiles or profiles of the internal chemical composition) is undesirable or unnecessary.

The general ensemble average of a field quantity $\Psi(\mathbf{x}, t)$, (\mathbf{x}, t denoting space and time coordinates) is

$$\langle \Psi(\mathbf{x}, t) \rangle = \int \Psi(\mathbf{x}, t) P(\Pi) d\Pi \quad (2)$$

where $P(\Pi)$ is the probability that a specific realization Π is encountered in the ensemble. The gas-phase ensemble average and its density-weighted counterpart are defined (Drew 1983) as $\bar{\Psi} \equiv \langle \chi_g \Psi(\mathbf{x}, t) \rangle / \alpha_g$ and $\tilde{\Psi} \equiv \langle \chi_g \rho_g \Psi(\mathbf{x}, t) \rangle / \alpha_g \bar{\rho}_g$, where ρ_g is the gas density, χ_g denotes the phase indicator of the gas phase which is unity in the gas phase and zero otherwise, and the gas

phase fraction, α_g , is defined as the ensemble average of the indicator function, i.e. $\alpha_g = \langle \chi_g \rangle$. Average transport equations for the gas phase then follow by multiplying the local instantaneous equations (the Navier Stokes set supplemented with energy and species equations) by the phase indicator and ensemble averaging.

The transport equations for the solids were derived similarly to those for dense gases, using kinetic theory concepts. Important differences from classical kinetic theory are the inelasticity of collisions between macroscopic particles leading to dissipation, and the presence of an interstitial gas exerting drag on the particles, which leads to interaction terms in the averaged transport equations.

Let $f_i^{(1)}(\mathbf{x}, \mathbf{c}, Y_\xi, T, m, t)$ denote the single particle distribution function of particle class i such that $f_i^{(1)}$ is the probable number of particles of class i having their center of mass in the region $[\mathbf{x}, \mathbf{x} + d\mathbf{x}]$, a velocity in the region $[\mathbf{c}, \mathbf{c} + d\mathbf{c}]$, mass in the region $[m, m + dm]$, mass fractions in $[Y_\xi, Y_\xi + dY_\xi]$, and temperature in $[T, T + dT]$. With this distribution function, a particle average is introduced as an integration over the phase space

$$\bar{\Psi}_i(\mathbf{x}, t) = \frac{1}{n_i} \int \Psi_i f_i d\mathbf{c} dY_\xi dT dm. \quad (3)$$

Here n_i denotes the number density of the solid class i , and is defined as

$$n_i(\mathbf{x}, t) = \int f_i d\mathbf{c} dY_\xi dT dm. \quad (4)$$

It is also convenient to introduce mass weighted averages

$$\tilde{\Psi}_i(\mathbf{x}, t) = \frac{1}{\alpha_i \bar{\rho}_i} \int m_i \Psi_i f_i d\mathbf{c} dY_\xi dT dm \quad (5)$$

where $\alpha_i \bar{\rho}_i = n_i \bar{m}_i = \int m_i f_i d\mathbf{c} dY_\xi dT dm$. This definition of the mass-weighted particle average is completely comparable to that used for the carrier phase and leads to more convenient forms of the macroscopic equations (see below).

Here, α_i denotes the local phase fraction of class i (where pores are excluded, i.e. are counted as part of the gas phase) and $\bar{\rho}_i$ its corresponding average particle density. We also introduce equivalent definitions for $\hat{\alpha}_i$ and $\hat{\rho}_i$ where the pores of the particles are counted as volume belonging to the particle. Note that $\alpha_i \bar{\rho}_i = \hat{\alpha}_i \hat{\rho}_i$. Mass weighted averages are also denoted by brackets, i.e. $\langle \Psi \rangle_i \equiv \tilde{\Psi}_i$ in the equations below. Using the above definitions we define the average velocity $\mathbf{u}_i = \langle \mathbf{c}_i \rangle$, the fluctuation velocity component, $\mathbf{C}_i = \mathbf{c}_i - \mathbf{u}_i$, and the granular temperature, $\Theta_i = \frac{1}{3} \langle C_i^2 \rangle$. The granular temperature plays a crucial role in the determination of the transport properties of granular flows and may be interpreted similarly to the temperature of a normal gas (see e.g. Campbell 1990).

The solidity of a particle, $\eta = 1 - \epsilon$, where ϵ is the porosity of a particle, is defined as the ratio of the volume displaced by the particle and the volume displaced by the particle had its pores been closed. The solidity is then easily shown to equal

$$\eta_i = \frac{m_i}{V_i} \sum \frac{Y_\xi}{\rho_\xi} \quad (6)$$

where V_i is the total volume of a particle (including its pores). In the present case of biomass pyrolysis, we assume that the particle diameter stays constant throughout the pyrolysis, and that

the porosity of the particle simply increases in time (Miller and Bellan 1997). This assumption is correct when the particle does not break or erodes.

Macroscopic equations

Mass

The mass conservation equation for the gas phase is

$$\frac{\partial(\alpha\bar{\rho})_g}{\partial t} + \nabla \cdot (\alpha\bar{\rho}\tilde{\mathbf{u}})_g = \Gamma_g \quad (7)$$

where α , ρ , and \mathbf{u} denote the volume fraction, density and velocity respectively. The term on the right hand side, Γ_g , represents the mass transfer rate originating from pyrolysis.

Similar equations can be derived for each solid class i through the formalism stated earlier:

$$\frac{\partial(\alpha\bar{\rho})_i}{\partial t} + \nabla \cdot (\alpha\bar{\rho}\tilde{\mathbf{u}})_i = \Gamma_i \quad (8)$$

where the mass transfer rate for each solid class is related to the average mass reduction of all particles in the specific class, $\Gamma_i = \alpha_i\bar{\rho}_i \langle \frac{1}{m_i} \frac{dm_i}{dt} \rangle$, which may in turn be related to the average conversion rate of solid to gas-phase reactions $\Gamma_i = \alpha_i\bar{\rho}_i \sum_{\xi} \langle R_{i,\xi} \rangle$, with $R_{i,\xi}$ denoting the total reaction rate for particle class i and species ξ . For inert particles, this term is absent. For consistency we require $\Gamma_g + \sum_i \Gamma_i = 0$.

Momentum:

After some mathematical manipulations and modeling (see Lathouwers and Bellan, 2001), the gas phase momentum equation can be written as

$$\frac{\partial(\alpha\bar{\rho}\tilde{\mathbf{u}})_g}{\partial t} + \nabla \cdot (\alpha\bar{\rho}\tilde{\mathbf{u}}\tilde{\mathbf{u}})_g = -\alpha_g \nabla \bar{p}_g + \nabla \cdot 2\alpha_g \mu_g \mathbf{S}_g + \alpha_g \bar{\rho}_g \mathbf{f}_g + \sum_i \frac{\alpha_i \bar{\rho}_i}{\tau_{i,12}} (\mathbf{u}_i - \tilde{\mathbf{u}}_g) - \sum_i \Gamma_i \mathbf{u}_i \quad (9)$$

where p_g is the thermodynamic pressure, \mathbf{S}_g denotes the strain rate tensor $\mathbf{S}_g = (\nabla \tilde{\mathbf{u}}_g + \nabla \tilde{\mathbf{u}}_g^T)/2 - (\nabla \cdot \tilde{\mathbf{u}}_g)/3$, μ_g is the shear viscosity, \mathbf{f}_g is the gravitational acceleration and $\tau_{i,12}$ is the fluid particle interaction time scale. The terms on the right hand side denote the pressure gradient force, shear stresses, gravitational body force, the force exerted on the gas phase by drag on the particles and finally, the effect of mass transfer on the momentum of the carrier gas.

The thermodynamic pressure, p_g , is related to the gas phase temperature, T_g , and density, $\bar{\rho}_g$, through the average equation of state

$$\bar{p}_g = R_u \bar{\rho}_g \sum_{\xi} \frac{\tilde{Y}_{\xi}}{W_{\xi}} \tilde{T}_g \quad (10)$$

where R_u denotes the universal gas constant, and W_{ξ} is the molecular weight of species ξ .

The gas-particle interaction time scale, $\tau_{i,12}$, depends strongly on the flow regime; in the dilute regime it is derived from the drag coefficient, C_d , of a single particle in an infinite medium, empirically corrected for the presence of other surrounding particles by a function $f(\alpha_g) = \hat{\alpha}_g^{-1.7}$

(e.g. Gidaspow 1986) whereas in the dense regime the classical Ergun relation is used. To avoid discontinuous behavior, a weighted average of the two time scales is introduced

$$\frac{1}{\tau_{i,12}} = W \frac{3\bar{\rho}_g C_d(Re_i)}{4\bar{\rho}_i d_i} |\mathbf{u}_i - \tilde{\mathbf{u}}_g| f(\hat{\alpha}_g) + (1 - W) \frac{\bar{\rho}_g}{\bar{\rho}_i} \left[(1 - \hat{\alpha}_g) \frac{150}{Re_i} + 1.75 \right] \frac{|\mathbf{u}_i - \tilde{\mathbf{u}}_g|}{d_i} \quad (11)$$

where the present switch function, $W(\hat{\alpha}_g) = \arctan(150(\hat{\alpha}_g - 0.8))/\pi + 1/2$, gives a rapid transition from one regime to the other. d_i is the diameter of the particle and Re_i is the Reynolds number based on the relative velocity with the gas, $Re_i = \hat{\alpha}_g \rho_g |\mathbf{u}_i - \tilde{\mathbf{u}}_g| d_i / \mu_g$. The single particle drag coefficient C_d is determined from the well-known correlation (Schiller and Nauman 1935)

$$C_d = \frac{24}{Re_i} (1 + 0.15 Re_i^{0.687}). \quad (12)$$

In the modeling of the momentum transfer associated with mass transfer from solid to gas phase, it has been assumed that fluctuations in the particle velocity are negligible.

The averaged momentum equation for each solids class is

$$\frac{\partial(\alpha \bar{\rho} \tilde{\mathbf{u}})_i}{\partial t} + \nabla \cdot (\alpha \bar{\rho} \tilde{\mathbf{u}} \tilde{\mathbf{u}})_i = -\hat{\alpha}_i \nabla \bar{p}_g - \nabla \cdot (\boldsymbol{\Sigma}_i + \boldsymbol{\Sigma}_i^f) + \alpha_i \bar{\rho}_i \mathbf{f}_g + \frac{\alpha_i \bar{p}_i}{\tau_{i,12}} (\tilde{\mathbf{u}}_g - \mathbf{u}_i) + \phi_i + \Gamma_i \mathbf{u}_i. \quad (13)$$

This equation contains similar terms when compared to its gas phase counterpart, i.e. a mean pressure gradient, a drag term having the reverse sign compared to that in the gas phase equation, and a mass transfer related term. Terms unique to the solid's equation are the solid stress tensors, $\boldsymbol{\Sigma}_i$ and $\boldsymbol{\Sigma}_i^f$, and a collisional source term, ϕ_i which represents the momentum exchange among the various solid classes due to collisions. Note, however, that both collisions between particles from the same class and collisions between particles from different classes contribute to $\boldsymbol{\Sigma}_i$, while ϕ_i only contains contributions from collisions between unlike particles. Closure relations for these terms, derived by Lathouwers and Bellan 2001, are provided below.

Collisional models determining $\boldsymbol{\Sigma}_i$ are restricted to the region where particles interact exclusively through slightly inelastic, short duration, collisions. However, as the volumetric fraction approaches the maximum packing volume fraction (i.e. in the dense particle packing regime), α_{max} , particles will, increasingly, be in simultaneous contact with several neighbors and stresses will be transmitted at points of sustained sliding or rolling contact. Considering the high particle volume fraction in a bubbling fluidized bed, the solid's momentum equations include a specific frictional stress term, $\boldsymbol{\Sigma}_i^f$, that prevents the particles from overpacking even when collisions are absent (for vanishingly low granular temperature). The proposed model consists of a simple relationship between stresses and strains: $\boldsymbol{\Sigma}_i^f = -p_i^f \mathbf{I} + 2\mu_i^f \mathbf{S}_i$ for $\alpha > \alpha_{min}$ where α_{min} is the minimum solids fraction at which frictional transfer becomes influential. Experimental observations indicate that the frictional normal stress increases rapidly with bulk density and diverges as α_{max} is approached. A simple algebraic representation of this behavior is (c.f. Anderson and Jackson 1992)

$$p_i^f = \frac{\alpha_i \rho_i}{\sum \alpha_i \rho_i} Fr \frac{(\hat{\alpha} - \alpha_{min})^p}{(\alpha_{max} - \hat{\alpha})^n} \quad (14)$$

where Fr is a material constant. The frictional viscosity, μ_i^f , is related to the frictional pressure and the angle of internal friction, ϕ , as $\mu_i^f = p_i^f \sin(\phi) / 2\sqrt{I_2}$ where I_2 denotes the second invariant of the strain rate tensor. The following values for the parameters have been used in the present work:

$p = 2$, $n = 5$, $Fr = 0.005$, $\alpha_{min} = 0.6$, $\alpha_{max} = 0.64$, and $\phi = 25$ degrees (see Lathouwers and Bellan 2000).

Species:

Applying the averaging formalism to the gas phase species equations, one obtains

$$\frac{\partial(\alpha\bar{\rho}\tilde{Y}_\xi)_g}{\partial t} + \nabla \cdot (\alpha\bar{\rho}\mathbf{u}\tilde{Y}_\xi)_g = \nabla \cdot \alpha_g\bar{\rho}_g\mathcal{D}_\xi\nabla\tilde{Y}_{g\xi} + \alpha_g\bar{\rho}_g\tilde{R}_{g\xi} + \sum_i \alpha_i\bar{\rho}_i \langle R_{i,\xi}^{s \rightarrow g} \rangle \quad (15)$$

Here, we have neglected turbulent transport in the gas phase (see Lathouwers and Bellan, 1999 for an outline of a turbulence model). The first term on the right hand side represents molecular diffusion and \mathcal{D}_ξ is the diffusion coefficient (multicomponent fluxes are neglected); the second term is the average production rate of specie ξ due to gas phase reaction; whereas the final term denotes the mass source for a particular component due to solid's reactions, converting solids to gas.

For the species in each solid class, a similar equation is obtained

$$\frac{\partial(\alpha\bar{\rho}\tilde{Y}_\xi)_i}{\partial t} + \nabla \cdot (\alpha\bar{\rho}\mathbf{u}\tilde{Y}_\xi)_i = \nabla \cdot (\alpha_i\bar{\rho}_i\mathcal{D}_{ii}\nabla\tilde{Y}_{i\xi}) + \Gamma_{i\xi}. \quad (16)$$

The first term on the right hand side denotes the diffusion of species due to fluctuations in the velocity of the solids. \mathcal{D}_{ii} is calculated as the self diffusion coefficient which is directly derived from the velocity distribution of the particles (see Lathouwers and Bellan 2001 for a detailed derivation). The second term, $\Gamma_{i\xi} = \alpha_i\bar{\rho}_i \langle R_{i,\xi} \rangle$ is the average mass source arising from the pyrolysis reactions.

Thermal energy:

The thermal energy equation for the gas phase is

$$\begin{aligned} (\alpha\bar{\rho}C_p)_g \frac{D_g\tilde{T}_g}{Dt} = & \nabla \cdot \alpha_g\lambda_g\nabla\tilde{T}_g + \sum_i \frac{6\hat{\alpha}_i\lambda_g}{d_i^2} Nu_i(\tilde{T}_i - \tilde{T}_g) + \\ & \sum_i \left\{ \Gamma_{tar}^{s \rightarrow g} (C_p^{tar}\tilde{T}_b - C_{p,g}\tilde{T}_g) + \Gamma_{gas}^{s \rightarrow g} (C_p^{gas}\tilde{T}_i - C_{p,g}\tilde{T}_g) \right\}. \end{aligned} \quad (17)$$

The first term on the right hand side is the thermal conductive flux where λ_g is the thermal conductivity. The second term represents the heat exchange with the particles by conduction and convection; Nu_i denotes the effective Nusselt number associated with this transfer. The final collection of terms is the excess enthalpy flux entering the gas phase carried by the gaseous products leaving the particles, where it is assumed that the vapor products leave the particle at its mean temperature. $\Gamma_{tar}^{s \rightarrow g}$, and $\Gamma_{gas}^{s \rightarrow g}$ denote the averaged mass transfer rates of respectively, tar and gas. More details concerning the derivation of the latter term are given in Lathouwers and Bellan 2001.

In obtaining relevant Nusselt relations for this situation, it is assumed that the particle temperature is uniform, i.e. the resistance to heat transfer is mainly in the gas-phase. This assumption is consistent with those used to derive the continuum theory, as the state variables of the particles include their mean temperature only, i.e. no information on the internal temperature distribution

is available. Implicitly, the Biot numbers are assumed small ($Bi = h_i d_i / \lambda_i$, where h_i is the gas-particle heat transfer coefficient). In the present case, the Nusselt number is given by the single particle Nusselt relation, multiplied by a correction factor, F_{bl} , accounting for the effect of mass transfer on the heat transfer rate, i.e.

$$Nu = Nu_0 F_{bl}(Re_{bl}, Pr_g). \quad (18)$$

The formulation used here for the blowing factor is that taken from Miller et al. 1999 and was also given by Gyarmathy 1982 where the factor depends on the ‘blowing Reynolds number’, $Re_{bl} = \dot{m} / \pi d_i \mu_g$,

$$F_{bl} = \frac{Pr_g Re_{bl} / 2}{e^{Pr_g Re_{bl} / 2} - 1}. \quad (19)$$

To calculate Nu_0 , we use the standard Ranz correlation

$$Nu_0 = 2 + 0.66 Re_i^{1/2} Pr_g^{1/3}. \quad (20)$$

The final enthalpy equation for each solid class is

$$(\alpha_i \bar{\rho} C_p)_i \frac{D_i \tilde{T}_i}{Dt} = \nabla \cdot (\alpha_i \bar{\rho}_i C_{p,i} \mathcal{D}_{ii} \nabla \tilde{T}_i) + \frac{6 \hat{\alpha}_i \lambda_g}{d_i^2} Nu_i (\tilde{T}_g - \tilde{T}_i) + \alpha_i \bar{\rho}_i \left\langle \frac{Q_{r,i}}{m_i} \right\rangle + \alpha_i \bar{\rho}_i \left\langle \frac{dm_i}{dt} \frac{(h_v - \tilde{h}_i)}{m_i} \right\rangle. \quad (21)$$

As in the case of the solid species equations, the diffusive transport of heat has been modeled through a self-diffusion coefficient. The second term on the right hand side is also present in the gas phase equation, and was discussed above. The term $\alpha_i \bar{\rho}_i \langle Q_{r,i} / m_i \rangle$ denotes the source due to thermal radiation processes. A similar term is not present in the gas phase equation because at the temperatures of interest, the gas may be considered transparent. This radiative source is modeled through knowledge of the absorptivity, κ_{ai} , and of the radiation intensity within the domain. In the present model, the radiation intensity is calculated on the basis of a six-flux method; more details may be found in Lathouwers and Bellan.2001 With the calculated radiative intensities, the sources in the thermal energy equations of the solids are given by

$$\alpha_i \bar{\rho}_i \left\langle \frac{Q_{r,i}}{m_i} \right\rangle = -4\pi \kappa_{ai} \left(I_{bbi} - \frac{I_x + I_y + I_z}{3} \right) \quad (22)$$

with the black body intensity for class i given by $I_{bbi} = \sigma_B T_i^4 / \pi$ where σ_B is the Stefan Boltzmann constant. The absorption and scattering coefficients (required within the six-flux method) are calculated in the optical limit where the efficiency factors for absorption and scattering equal unity, i.e.

$$\kappa_{ai} = \kappa_{si} = \frac{3 \hat{\alpha}_i}{2 d_i}. \quad (23)$$

The final term on the right hand side of eq. 21 is exactly equal to the total average heat of reaction of all reactions taking place in the particle (both solid to solid and solid to gas).

Granular kinetic energy:

The transport equation for the granular temperature of each particle class is

$$\frac{3}{2} \left[\frac{\partial (\alpha \bar{\rho} \Theta)_i}{\partial t} + \nabla \cdot (\alpha \bar{\rho} \tilde{\mathbf{u}} \Theta)_i \right] = -\Sigma_i : \nabla \tilde{\mathbf{u}}_i - \nabla \cdot \mathbf{q}_i + \gamma_i + \frac{3}{2} \Gamma_i \Theta_i. \quad (24)$$

The first term on the right hand side of eq. 24 is the production of kinetic energy of the fluctuations due to shearing of the solid phase. Note however, that only collisional stresses contribute to this term whereas frictional terms are deleted, inherently assuming that the frictional work is directly converted to thermal internal energy. \mathbf{q}_i is the average ‘heat flux’ both due fluctuations in the velocity of the particles and through collisions. Both like and unlike particle collisions contribute to this flux. The source term, γ_i , represents the effects of energy redistribution among particle classes and the dissipative effect of inelastic collisions. This term is also composed of contributions between like and unlike particles. The effect of mass transfer is contained in the last term of eq. 24. The effects of the carrier gas have been neglected in this equation, which is warranted by the fact that the particles of interest are relatively heavy. That is, velocity fluctuations in the gas phase do not affect the particle velocity too strongly. Furthermore, in the dense systems here of interest, the fluid mechanics is dominated by collisional effects, not by the turbulence of the carrier gas. Closure for the collisional source and flux are provided below.

Collisional and kinetic contributions

The above model describes a particle mixture in a gaseous carrier using conservation equations for mass, momentum energy and granular temperature of each solid class. These multiple-class equations describe the independent accelerations of the species, as well as momentum and energy exchange between solid classes. Several terms in the transport equations have already been modeled, such as transfer related terms. We have purposely left other terms in the equations so far unspecified in order to discuss their origin and closure. Specifically, collisional and kinetic sources and fluxes and their related transport properties are discussed in the present section.

In principle, the single particle distribution functions are solutions of Boltzmann type equations, however, they are difficult to obtain in situations when the phase space includes many variables (mass fractions, temperature, etc.). Therefore, it has been assumed that the velocity distribution function for solution of the hydrodynamic problem can be obtained without incorporating the explicit effect of the thermochemistry. The hydrodynamic problem is then basically decoupled from the thermochemistry as far as the velocity distribution is concerned, and the velocity distributions may be obtained by similar techniques as are used in a non-reactive flow, taking into account the mean evolution of, for instance, the particle mass.

Therefore, the single particle distribution function is assumed to be Maxwellian, i.e. the lowest order approximation to the Boltzmann equation in the absence of dissipative effects

$$f_i^{(1)}(\mathbf{x}, \mathbf{c}_i, t) = \frac{n_i}{(2\pi\Theta_i)^{3/2}} \exp\left[-\frac{(\mathbf{c}_i - \tilde{\mathbf{u}}_i)^2}{2\Theta_i}\right]. \quad (25)$$

This is a good approximation when the flow has small spatial gradients, the collisions are nearly elastic and the particles are sufficiently heavy (i.e. the time between collisions is much smaller than the particle relaxation time; the particle-fluid correlation is small). The integrals require specification of the radial distribution function at contact, $h_{ik}(\mathbf{r})$, accounting for the effects of excluded area and particle shielding on the spatial distribution of colliding pairs. The form of the radial distribution function is taken from Jenkins and Mancini 1987, slightly adjusted to prevent overpacking of the solids, α_{max} being the maximum allowable solids volume fraction.

$$h_{ik} = \frac{1}{1 - \hat{\alpha}/\alpha_{max}} + 6 \frac{\sigma_i \sigma_k}{\sigma_i + \sigma_k} \frac{\xi}{(1 - \hat{\alpha}/\alpha_{max})^2} + 8 \left(\frac{\sigma_i \sigma_k}{\sigma_i + \sigma_k} \right)^2 \frac{\xi}{(1 - \hat{\alpha}/\alpha_{max})^3}. \quad (26)$$

Here $\xi = 2\pi/3 \sum n_i \sigma_i^2$ where σ_i denotes the radius of a particle of class i .

The present study is targeted towards dense systems where the drift between particle classes is small. Therefore, the collision integrals are approximated by assuming that the relative velocity $\Delta \mathbf{u}_{ik} = \mathbf{u}_i - \mathbf{u}_k$, is small compared to the square root of the sum of the granular temperatures, $(\Theta_i + \Theta_k)^{1/2}$. This significantly simplifies the calculation of the required integrals, and furthermore should not affect the applicability of the equations for our purposes. A more detailed discussion may be found in Lathouwers and Bellan 2001.

Using the above distributions and neglecting products of the spatial gradients, products of $(1 - e_{ik})$ with spatial gradients, and products of $\Delta \mathbf{u}_{ik}$ with the spatial gradients, yields the following constitutive equations for ϕ_i , Σ_i , \mathbf{q}_i , and γ_i

$$\phi_i = \sum_k F_{ik} \left\{ \frac{4}{3} \sqrt{2\pi} (\Theta_i + \Theta_k)^{1/2} (\tilde{\mathbf{u}}_k - \tilde{\mathbf{u}}_i) + \frac{\pi}{3} \sigma_{ik} (\Theta_i + \Theta_k) \nabla \ln \frac{n_i}{n_k} \right\} \quad (27)$$

$$\Sigma_i = n_i m_i \Theta_i \mathbf{I} + \sum_k \left\{ p_{ik} \mathbf{I} - \mu_i^{ik} [2\mathbf{S}_i + \frac{5}{3} \nabla \cdot \tilde{\mathbf{u}}_i] - \mu_i^{kk} [2\mathbf{S}_k + \frac{5}{3} \nabla \cdot \tilde{\mathbf{u}}_k] \right\} \quad (28)$$

$$\mathbf{q}_i = \sum_k \left\{ \kappa_i^{ik} \nabla \Theta_i + \kappa_i^{kk} \nabla \Theta_k \right\} \quad (29)$$

$$\gamma_i = \sum_k -2\sqrt{2\pi} F_{ik} (\Theta_i + \Theta_k)^{1/2} \left\{ 2(M_i \Theta_i - M_k \Theta_k) + M_k (1 - e_{ik}) (\Theta_i + \Theta_k) \right\} \quad (30)$$

where $F_{ik} = n_i n_k m_i M_k (1 + e_{ik}) h_{ik} \sigma_{ik}^2$. The indices on the viscosities and conductivities are arranged as follows, the subscript i indicates the relevance for class i , the first superscript labels the pertinent velocity gradient, and the k superscript denotes the collisions with particles from class k . The pressure and transport coefficients are

$$p_{ik} = \frac{1}{3} \pi n_i n_k m_i M_k (1 + e_{ik}) h_{ik} \sigma_{ik}^3 (\Theta_i + \Theta_k) \quad (31)$$

$$\mu_i^{ik} = \frac{1}{15} \sqrt{2\pi} n_i n_k m_i M_k^2 (1 + e_{ik}) h_{ik} \sigma_{ik}^4 (\Theta_i + \Theta_k)^{3/2} / \Theta_i \quad (32)$$

$$\mu_i^{kk} = \frac{1}{15} \sqrt{2\pi} n_i n_k m_k M_i^2 (1 + e_{ik}) h_{ik} \sigma_{ik}^4 (\Theta_i + \Theta_k)^{3/2} / \Theta_k \quad (33)$$

$$\kappa_i^{ik} = \frac{1}{3} \sqrt{2\pi} n_i n_k m_i M_k (1 + e_{ik}) h_{ik} \sigma_{ik}^4 (\Theta_i + \Theta_k)^{1/2} (M_k \Theta_k / \Theta_i) \quad (34)$$

$$\kappa_i^{kk} = \frac{1}{3} \sqrt{2\pi} n_i n_k m_i M_k (1 + e_{ik}) h_{ik} \sigma_{ik}^4 (\Theta_i + \Theta_k)^{1/2} (M_i \Theta_i / \Theta_k). \quad (35)$$

The terms in ϕ_i represent solid-solid drag and ordinary diffusion, respectively (thermal diffusion has been neglected). The stress tensor depends on the shear rates of all solid classes where the shear viscosities arise entirely from collisions, not from streaming; this is a result of the Gaussian approximation. Similar remarks hold for the heat flux vector. Recently, Manger 1986 has presented similar closure relations for binary mixtures. For coding purposes, the shear rates of both phases are assumed equal (small drift) so that the actually used viscosity equals the sum of several contributions: $\mu_i = \sum_k \mu_i^{ik} + \mu_i^{kk}$. A similar procedure has been used for the conductivity. This procedure renders the resulting equations coupled only through algebraic, rather than also differential, terms and thus makes the code more computationally efficient.

Auxiliary relations

The hydrodynamics of the system strongly depends on the mass of the particles in each class. Very light particles, for example, tend to be blown out of the bed by the carrier gas while heavier particles are more difficult to fluidize. Due to solid conversion to gaseous products, the mass of biomass particles decreases as time progresses. Therefore, one must simultaneously consider both freshly fed biomass as well as fully converted, nonreactive waste particles. To account for this spatial-temporal effect, the following transport equation for the mean particle mass of each reactive solid is solved:

$$\frac{\partial(\alpha\bar{\rho}\bar{m})_i}{\partial t} + \nabla \cdot (\alpha\bar{\rho}\tilde{\mathbf{u}}\bar{m})_i = \nabla \cdot \alpha_i\bar{\rho}_i\mathcal{D}_{ii}\nabla\bar{m}_i - 2\Gamma_i\bar{m}_i. \quad (36)$$

This equation states that mass is convected along the mean velocity while mass transfer effects portrayed by the final term in the equation, cause a reduction in the mass. The diffusion term is analogous to those already encountered in the species and energy equations and reflects the effect of velocity fluctuation on the mixing of the solids.

In the above model, conversion of α_i to $\hat{\alpha}_i$ and vice versa is performed through knowledge of the solidity of the porous particles which can be related to the average species mass, \bar{m}_i , the particle volume, V_i (considered constant), and its composition

$$\bar{\eta}_i = \frac{\bar{m}_i}{V_i} \sum_{\xi} \frac{\tilde{Y}_{\xi}}{\rho_{\xi}}. \quad (37)$$

The model contains many average reactive sources. These averages are all evaluated at the average temperature and mass fractions. For example, the mass exchange rate is evaluated as

$$\Gamma_i = \alpha_i\bar{\rho}_i \sum_{\xi} \tilde{R}_{i,\xi}^{s \rightarrow g} = \alpha_i\bar{\rho}_i \sum_{\xi} R_{i,\xi}(\{\tilde{Y}\}, \tilde{T}_i) \quad (38)$$

where $\{\tilde{Y}\}$ denotes any pertinent combination of the set of species mass fractions and where only solid to gas reactions need to be considered. Although this procedure neglects correlations between particle temperature and the mass fractions, these approximations are not very restrictive since the reaction rates are first order with respect to the species, and therefore do not exhibit the stronger nonlinearity normally associated with second or higher order reaction rates.

Finally, transport properties are required, such as the specific heats (both gas and solids) and thermal conductivities (gas only). These are calculated from a mass-weighted average of the individual species properties. Considering ϕ to be one such general property, its average is then computed from $\bar{\phi} = \sum_{\xi} Y_{\xi}\phi_{\xi}$. An exception to this procedure is in the calculation of the average particle density, $1/\bar{\rho}_i = \sum_{\xi} Y_{i,\xi}\rho_{\xi}$.

Initial and boundary conditions

Initial conditions are specified corresponding to the standard fluid bed shown in Fig. 1. The fluid bed is initially at rest, having specified the velocities of all phases to be null; the granular energy is set to a small number, typically $10^{-7} \text{ m}^2/\text{s}^2$. To induce bubbling, several void areas are created at the bottom of the bed by setting the void fraction to unity in specified computational cells.

Practically, there are three such regions distributed on the x axis, at locations corresponding to cells 5-7, 18-20 and 30-32. Areas are then created by making these regions 5 computational cells high in the y direction. The effects of the initial conditions survive a minute fraction of the total physical time and do not affect the statistical behavior of the fluid flow.

Inflow conditions are specified to reflect realistic conditions corresponding to bubbling fluidization; at inlet sections, the volume fractions and velocities are specified together with the temperatures of all phases and the composition of the gas phase and biomass particles, depending on the pertinent feedstock used. The initial temperature of both sand and gas in the domain is set equal to the inlet temperature of the fluidization gas. Hence, it is assumed that the fluidization gas has preheated the sand, even though initially the sand bed is stationary. This does not affect the calculation of product yield, as we are interested in the asymptotic (i.e. long time) behavior of the reactor; that is, long after which a statistically steady flow field has emerged.

Along solid walls, no-slip conditions are applied for the gas phase ($\tilde{\mathbf{u}}_g = 0$), whereas the solids are allowed to slip freely ($\partial\tilde{\mathbf{u}}_{i,t}/\partial n = 0$, where n is a unit normal and the subscript t denotes tangential). Zero-flux boundary conditions are imposed for the solids thermal energy equations, consistent with the energy transfer in particle wall collisions being negligible. As the thermal boundary layers along the wall are not resolved, a similar condition is imposed for the gas phase. Boundary conditions for the thermal radiation model have been detailed by Zaichik et al. 1997 and have been stated in Lathouwers and Bellan 2001 for the specific application of the fluidized bed reactor.

At outlets, Neumann conditions are specified for all variables except for the velocity component normal to the outlet plane which is calculated using a prescribed atmospheric pressure at that plane. Solids are inhibited to exit the domain, simulating a fine solids-filtering grid.

Numerical procedure

Spatial discretization of the governing equations is based on a finite volume technique using a staggered grid. All convective fluxes are approximated with a second-order accurate bounded TVD-scheme avoiding the excessive numerical diffusion associated with the first-order accurate upwind scheme. The time discretization is based on a backward Euler scheme in combination with a pressure-correction technique with a time step adjustment procedure. The momentum equations of all phases are solved in a coupled manner, though separately for each velocity direction. Compared with the well-known Partial Elimination Algorithm (PEA), the present approach is more general (see Lathouwers 1999 for more details on full-field coupling and multiphase pressure correction algorithms). The species and energy equations constitute a strongly coupled, stiff system of equations. To avoid very large linear systems arising from (the necessarily) implicit discretization, a time splitting is used (Strang 1968) for the combined species and energy system consisting of three steps: (i) performance of a half convection-diffusion time step, (ii) time integration of the equations over a full time step with only the source terms present (reaction terms, radiation, etc.), (iii) performance of another half convection-diffusion time step. The advantage of this split scheme is that during steps (i) and (iii), the equations are decoupled into standard convection-diffusion systems which are easily handled, whereas in step (ii) there is no spatial coupling. The stiff integration in step (ii) is performed by using either the well-known stiff integrator VODE (Brown et al. 1989). All sparse linear systems arising from the discretization of convection-diffusion systems are solved

Reaction	$A(1/s)$	$E(J/kmol)$
K_1^c	$2.8 \cdot 10^{19}$	$242.4 \cdot 10^6$
K_2^c	$3.28 \cdot 10^{14}$	$196.5 \cdot 10^6$
K_3^c	$1.30 \cdot 10^{10}$	$150.5 \cdot 10^6$
K_1^h	$2.10 \cdot 10^{16}$	$186.7 \cdot 10^6$
K_2^h	$8.75 \cdot 10^{15}$	$202.4 \cdot 10^6$
K_3^h	$2.60 \cdot 10^{11}$	$145.7 \cdot 10^6$
K_1^l	$9.60 \cdot 10^8$	$107.6 \cdot 10^6$
K_2^l	$1.50 \cdot 10^9$	$143.8 \cdot 10^6$
K_3^l	$7.70 \cdot 10^6$	$111.4 \cdot 10^6$
K_4	$4.28 \cdot 10^6$	$108 \cdot 10^6$

Table 1: **Rate constants and activation energy for the biomass pyrolysis kinetics scheme. The char formation ratios for reaction K_3 are: $X^c = 0.35$, $X^h = 0.60$, and $X^l = 0.75$.**

with preconditioned Krylov methods (Conjugate Gradient (CG) for the pressure Poisson equation and Generalized Minimum RESidual (GMRES) for the other transport equations; see e.g. Barrett et al. 1994).

All computations have been performed on a 40×148 uniform grid (x and y directions respectively). Runs have been performed in parallel (although the code is serial) on a SGI Origin 2000 supercomputer. Simulation of 5 seconds of physical time requires approximately 250 hours of CPU time per run.

Biomass particle pyrolysis in a fluidized bed reactor

Among the pyrolysis reactor designs investigated for commercial production of condensable tars from biomass, the fluidized bed reactor is potentially efficient due to the high particle heating rates that can be achieved (e.g. Scott et al. 1999) and its excellent mixing properties, assuring a reasonably uniform product quality. As stated above, a further interesting feature of this type of reactor is that char does not accumulate in the bed, but is elutriated with the gas flow instead, after which it may be filtered out, making the reactor very suitable for continuous operation.

Although the process has received considerable attention experimentally (e.g. Scott and Piskorz 1982, 1984), currently there are no fundamental theoretical analyses available, addressing simultaneously all physico-chemical processes in the reactor. Most of the work to date related to fluidized bed reactors has focused on single-particle pyrolysis in a gas stream which requires *a priori* knowledge of ambient gas flow parameters, its temperature in particular (Miller and Bellan 1997, Di Felice et al. 1999).

Below, we present quantitative results from numerical simulations based on the detailed mathematical model above, and we address the issues of tar collection efficiency and the potential for scale-up of the process.

Detailed physico-chemical parameters of biomass pyrolysis

The kinetics scheme of the present biomass pyrolysis model was already presented in Section 2. All of the pre-exponential constants A , and the reaction's activation energy, E , are tabulated in

Specie	$W(kg/kmol)$	$C_p(J/kgK)$	$\lambda(J/msK)$	$\mu(kg/ms)$	$D(m^2/s)$
N_2	28.013	1120.91	$5.63 \cdot 10^{-2}$	$3.58 \cdot 10^{-5}$	$8.52 \cdot 10^{-4}$
Gas	30	1100	$2.577 \cdot 10^{-2}$	$3.0 \cdot 10^{-5}$	$1.1 \cdot 10^{-4}$
Tar	100	2500	$2.577 \cdot 10^{-2}$	$3.0 \cdot 10^{-5}$	$1.1 \cdot 10^{-4}$

Table 2: **Property values for the gas phase species. The properties for nitrogen are taken at $T = 800K$ and $p = 100kPa$.**

Species	$C_p(J/kgK)$	$\rho(kg/m^3)$
Biomass	2300	2167
Char	1100	2333
Sand	800	2600

Table 3: **Specific heat and densities for solid species. Biomass refers to both virgin species and active species.**

Table 1 (c.f. Miller and Bellan 1997) and are dependent of the source component.

Due to a lack of more detailed knowledge, the heats of reaction are taken as independent of the source component. The depolymerization reaction K_1 has $\Delta h_1 = 0 kJ/kg$, reaction K_2 is endothermic with $\Delta h_2 = 255 kJ/kg$, and both the char formation and the secondary tar reactions are exothermic with $\Delta h_2 = -20 kJ/kg$ and $\Delta h_2 = -42 kJ/kg$. All other properties of gaseous and solid species are listed in Tables 2 and 3, respectively.

Simulation details

A sketch of the simulated geometry and the standard dimensions employed is given in Fig. 1. The reactor standard size is $0.1m \times 0.55m$, and it is filled with sand only up to a height of $0.163 m$ at a volume fraction of 0.6 which corresponds to dense packing. The geometry has been chosen to resemble that used in experiments by Scott and Piskorz 1982, 1984, among others. Although the real fluidized bed is a cylindrical vessel, for computational simplicity, the present computational domain is approximated to be rectangular. In the simulations, the biomass is fed through an inlet section in one of the side walls, together with an amount of gas, which preheats the biomass during the feeding process. The center of feed point 1 is located $4.6 cm$ from the bottom of the bed and has a height (area) of $1.86 cm$; feeder no. 2 has the same height (area) and is located $12.1 cm$ from the bottom. In the present simulations, the temperature of the gas used for fluidization, T_g , is equal to that fed through the biomass feed section; the inlet temperature of the biomass, T_b , however is assumed to vary to investigate the effect of biomass preheating. Note that, regardless of the biomass feed temperature, the biomass compositions used at the inlet correspond to those of biomass that has not pyrolyzed, i.e. it is assumed that the residence time in the feeder is short (no appreciable biomass conversion) while the effective heating of the particles is as efficient as required (by specifying the required temperature). To vary the cellulose/hemicellulose/lignin proportions of the feedstock, bagasse, olive husk, maple, and oak are used in the simulations. The initial biomass composition of these biomass types are given in Table 4.

To investigate scale-up of the system, both proportional scaling and non-proportionally scaled fluidized beds have been explored. A summary of all simulations performed is listed in Table 5.

Feed	cellulose	hemicellulose	lignin
bagasse	0.36	0.47	0.17
maple	0.40	0.38	0.22
olive husk	0.22	0.33	0.45
oak	0.35	0.40	0.25

Table 4: **Initial biomass composition by mass fractions (see Miller and Bellan, 1997).**

The diameter of the sand and biomass particles is varied from 0.5 to 1.0 mm , which are common values in practical operation. Biomass particles are assumed to have an initial porosity of 0.7 (c.f. Miller and Bellan 1997) and the biomass feed flux is constant and has a value of 0.5 kg/m^2s (when two feed points are used, the flow is equally split between feed points). The gas velocity through the feeder is 0.5 m/s , while the gas flow used for fluidization of the mixture is varied from 0.5 to 0.7 m/s and is uniform over the bottom of the domain.

Tar collection efficiency parameters

The true measure of the reactor efficiency for the tar production can be quantitatively determined by comparing global quantities such as the actual mass of tar exiting the reactor (Ω_{tar}) and the amount still present in its interior (M_{tar}) to the biomass feed flow (M_{feed}):

$$\Omega_{tar} = \int_0^t \int_{outlet} (\alpha_g \rho_g \mathbf{u}_g Y_{tar}) \cdot d\mathbf{A} dt' \quad (39)$$

$$M_{tar} = \int_{reactor} (\alpha_g \rho_g Y_{tar}) dV \quad (40)$$

$$M_{feed} = \int_0^t \int_{inlet} (\alpha_b \rho_b \mathbf{u}_b) \cdot d\mathbf{A} dt' \quad (41)$$

where the subscript b denotes biomass. With these definitions, two measures for reactor performance are the yield (η) and the differential reactor efficiency (DRE), ϑ , c.f. Miller and Bellan 1998:

$$\eta_{tar}(t) = \frac{\Omega_{tar} + M_{tar}}{M_{feed}} \quad (42)$$

$$\vartheta_{tar}(t) = \frac{\Omega_{tar} + M_{tar}}{\sum_{\xi} (\Omega_{\xi} + M_{\xi})} \quad (43)$$

where the summation is over the species tar, gas and char. These measures quantify the relative efficiency of reactor tar production relative to the biomass feed flow, and the relative proportion of tar produced compared to gas and char. Similar definitions are used for the reactor performance with respect to gas and char production.

The above two definitions of tar collection are strongly related in that their values converge at steady-state conditions (i.e. states reached at sufficiently long time after reactor start-up) under certain circumstances. If conditions in the reactor are such that the pyrolysis reaction rate is at least equal to the feed rate of biomass into the reactor (i.e. sufficiently high temperature), then both definitions lead to the same steady-state value. This can easily be shown by considering the denominators of eqs. 42 and 43, M_{feed} and $\sum_{\xi} (\Omega_{\xi} + M_{\xi})$, respectively. In the limit, $t \rightarrow \infty$, the two terms can only differ by a small amount corresponding to the unreacted biomass, and hence

Run No	$T_g(K)$	$T_b(K)$	Feedpoint	Feedstock	Feedrate	$V_g(m/s)$	$d_p(mm)$	Scale-factor	Radiation
0	750	400	1	bagasse	1	0.5	0.5	1	excl.
1	600	400	1	bagasse	1	0.5	0.5	1	incl.
2	700	400	1	bagasse	1	0.5	0.5	1	incl.
3*	750	400	1	bagasse	1	0.5	0.5	1	incl.
4	800	400	1	bagasse	1	0.5	0.5	1	incl.
5	850	400	1	bagasse	1	0.5	0.5	1	incl.
6	950	400	1	bagasse	1	0.5	0.5	1	incl.
7	750	450	1	bagasse	1	0.5	0.5	1	incl.
8	750	500	1	bagasse	1	0.5	0.5	1	incl.
9	750	400	1	bagasse	1	0.6	0.5	1	incl.
10	750	400	1	bagasse	1	0.7	0.5	1	incl.
11	750	400	1	olive husk	1	0.5	0.5	1	incl.
12	750	400	1	maple	1	0.5	0.5	1	incl.
13	750	400	1	oak	1	0.5	0.5	1	incl.
14	750	400	2	bagasse	1	0.5	0.5	1	incl.
15	750	400	1+2	bagasse	1	0.5	0.5	1	incl.
16	750	400	1	bagasse	1	0.5	0.75	1	incl.
17	750	400	1	bagasse	1	0.5	1.0	1	incl.
18	750	400	1	bagasse	2	0.5	0.5	1	incl.
19	750	400	1	bagasse	3	0.5	0.5	1	incl.
20	750	400	1	bagasse	1	0.5	0.5	2 (pr.)	incl.
21	750	400	1	bagasse	1	0.5	0.5	3 (pr.)	incl.
22	750	400	1	bagasse	1	0.6	0.5	2 (pr.)	incl.
23	750	400	1	bagasse	1	0.7	0.5	2 (pr.)	incl.
24	750	400	1	bagasse	1	0.5	0.5	2 (non-pr.)	incl.
25	750	400	1	bagasse	1	0.5	0.5	3 (non-pr.)	incl.

Table 5: Summary of operating parameters in the simulations performed. The standard conditions are those of Run 3, denoted by a star.

the yield and DRE will have approximately the same value since the unreacted amount of biomass is negligible. However, if the pyrolysis rate is lower than the biomass feed rate (under sufficiently low operating temperatures), then the yield will be lower than the obtained DRE. Thus, the DRE is an upper limit for the yield obtained at complete steady-state. This relation between the two collection parameters is noteworthy as it turns out that the DRE reaches a steady-state value earlier than the corresponding yield parameter.

Results

The model presented in Section 2 is quite complex, and as stated in Section 3, computationally intensive. It is therefore of interest to examine the effect of simplifications that may be possible, thereby reducing the CPU time. Lathouwers and Bellan 2000 have already determined that the collisional and friction models are essential for quantitative predictions of the fluidized bed hydrodynamics. Miller and Bellan 1997 have determined that the biomass kinetics presented in Section 2.1 is the only one capable of accurate predictions for a wide range of operating conditions. The only model whose importance has not yet been evaluated in the context of fluidized bed reactors is that of the multi-particle radiation. Thus, we first assess here the difference between results of simulations with and without radiation. Once this issue is settled, we present a quantitative study of

various effects on tar collection, focusing on the prediction of the steady-state yield. In particular, we investigate how the different operating parameters affect it, and whether scale up has a negative influence on tar collection thus inhibiting commercial viability.

Effects of thermal radiation

As outlined in the modeling section, the mathematical model contains a description of thermal radiative transfer between the hot sand and the cooler biomass particles. Single biomass particle simulations present in the literature always take gas-particle radiation into account, although compared to the particle-particle radiation heat transfer one may doubt its importance at the relatively low reactor temperatures used in biomass pyrolysis. At these relatively low temperatures, neither the rotational nor the vibrational gas modes are excited, and the gas is basically transparent for thermal radiation.

In order to quantify the effects of including the particle-particle radiation model on the obtained tar collection, simulations have been performed with and without this model and the results are presented in Fig. 2. Conditions of these simulations pertain to the standard Run 3. The indication from Fig. 2a illustrating the tar yield is that there is a distinctive effect on the prediction of this important quantity. Although the results have not reached their steady-state values, considerable difference is expected in the predicted values. To further investigate this effect, Figs. 2b and 2c show the distribution of the biomass temperature at 2.5 s after start-up plotted for the same contour levels. Although the differences are hard to quantify, in general the contours in Fig. 2c are more confined to the inlet region, indicating shorter heat up times due to additional heat transfer from the sand to the biomass. The conclusion is that the particle-particle radiation model must be included for accurate tar yield prediction.

Steady-state tar yield prediction

In a commercial reactor operation, the main interest is in steady-state values of the tar collection parameters. As already explained, if the pyrolysis rate is high enough to keep up with the feed rate (as it does in all but the low temperature cases), there is a correspondence between the steady-state yield and the steady-state DRE. It is, however, difficult to determine *a priori* whether for given conditions the DRE is an accurate representation of the tar yield. On the other hand, the present detailed simulations being computationally intensive, it is important to develop a strategy for predicting steady-state tar yield from short-time simulations. The idea here is to extrapolate the yield data in a meaningful manner. In fact, in cases where the temperature of the system is too low, and hence the reaction rate is slower than the feed rate, this is the only manner to obtain the steady-state values, as the DRE will constitute an over prediction in those situations, as discussed above. Notably, the yields approach their steady-state value approximately in an exponential way (see Lathouwers and Bellan 2001). Therefore, the yield data have been here fitted with an exponential function:

$$Y = Y_{\infty}(1 - e^{-\Psi}) \quad (44)$$

$$\Psi = \left(\frac{t - t_0}{\tau}\right)^s$$

where the parameters Y_{∞} , t_0 , τ , and s are to be determined by the fitting procedure, and Y_{∞} represents the steady-state yield whose prediction is the present goal. The yield data are fitted over

a time range, from the start time, t_s to the final 5 s. The start time is varied from 1 s to 2.2 s, between which the yield starts to rise significantly. For each choice of start time, an optimal set of fit parameters is obtained (for Y_∞ , t_0 , τ , and s). However, there are two primary uncertainties associated with this extrapolation process: (i) the yield may not be completely exponential, and (ii) the variation of the Y_∞ for different choices of the start time, t_s may introduce uncertainties in the prediction. To illustrate the effect of a different choice of t_s , Fig. 3 shows the tar yield as a function of time obtained from the standard simulation (Run 3) and 2 exponential fits with different t_s . Although both fits appear to fit the data well in the intended region, their values of the steady-state tar yield differ significantly (fit1: $Y_\infty = 0.585$; fit 2 $Y_\infty = 0.705$). In the subsequent parametric study, these uncertainties are denoted with error bars. We, however, emphasize that the existing uncertainty is not a major issue, as in most cases the DRE at 5 s may be approximately equated to the steady-state yield (except for the lower gas temperatures, or large particles).

Parametric study

The effect of the most important process parameters determining the obtainable tar collection is here evaluated.

Displayed in Fig. 4a is the yield at 5 s, the extrapolated yield and the DRE, all for the tar, as a function of the gas temperature. Clearly there is an optimum in all curves at around 750 K. This temperature is in accordance with experimental data (e.g. Scott et al. 1999) but the exact value of the optimum will depend on the type of biomass used. Noteworthy is the coincidence of the yield, extrapolated yield and the DRE at the highest temperatures, which is consistent with the fact that for these conditions the yield at 5 s appears to be almost steady (see Lathouwers and Bellan 2001). This coincidence gives confidence that the fitting procedure is valid. For the lower temperatures, the correspondence between the extrapolated yield and the DRE is still good, indicating that the extrapolation process is reasonable. Figure 4b shows similar results for char collection parameters. The general trend is that char collection decreases as the operating temperature increases. At lower temperatures the correspondence between the extrapolated char yield and the corresponding DRE is flawed. This may be due to the fact that in this case the char yield is not exponential as a function of time, with accompanying uncertainties in the fitting process. Figure 4c shows that, as the temperature is increased, the gas formation becomes dominant (c.f. Miller and Bellan 1998; Di Felice 1999).

Figures 5a, 5b, and 5c show the effect of the biomass feed temperature, the fluidization velocity, and the biomass feed rate, respectively. The effects of these parameters on tar collection are found to be relatively mild, as the slowest time is that of tar formation, which therefore governs the process. The figures do again indicate that in general the extrapolated yields are underpredicted compared to the DRE. The insensitivity of the short-time tar yield and the DRE to the feed rate, combined with the timewise evolution up to 5 s shown by Lathouwers and Bellan 2001 represents strong evidence that at these conditions the tar reactions keep up with the feed rate, and therefore that the DRE is a good estimate of the steady-state tar yield. This observation is particularly important when discussing reactor scale-up.

The effect of biomass particle diameter variation is illustrated in Fig. 5d. Note that no extrapolated values are shown as the curves were found to be far from steady-state (even the DRE values are not steady). The tar collection decreases strongly with the particle diameter due to a strong increase in

the heat-up time of the particles. However, at steady-state it is expected that the weaker dependence displayed by the DRE will prevail. Nevertheless, for commercial operation, the particle diameter should be small so as to reduce heat-up times.

In Fig. 5e the tar collection is depicted as function of the cellulose content of the biomass feed. The simulations exhibit a slight trend showing that tar collection increases with the cellulose percentage, similarly to the previous results of Miller and Bellan 1997. Lathouwers and Bellan 2000 found that contrary to the accepted notion that the tar yield correlates positively with the percent cellulose, it seems to better correlate negatively with the percent lignin, indicating the importance of char formation reactions.

The relationship between biomass lignin content and char yield is displayed in Fig. 6 showing both the char yield and DRE as function of the biomass lignin percentage for the four feedstocks used. The slight reduction for maple indicates that char formation is not only the result of lignin content, but is also intimately related to the process parameters, notably the gas temperature and heat up time. However, the general idea that char formation increases with lignin content seems to be confirmed.

Scale-up

As discussed above, tar collection can be maximized through appropriate choices of the reactor temperature, and biomass species, amongst others. Once the operating parameters are optimized, it is of considerable interest to examine whether the fluidized bed has the potential of reaching similar tar collection values when operated at a larger scale. However, theoretical/numerical studies with respect to scale up of fluidized bed pyrolysis reactors are virtually absent in the literature. A notable exception is a similar investigation for maximizing tar collection in vortex pyrolysis reactors by Miller and Bellan 1998. Herein, the effects of reactor geometry and scaling are addressed in order to assess the industrial viability of the process.

Figure 7a shows the obtained tar yield at 5 s, the DRE at 5 s and the extrapolated tar yield as function of a proportional scaling factor. Because, as discussed above, the reactor operation is a very weak function of the biomass feed rate, the pertinent quantity indicating the steady-state tar yield is the DRE. Basically, both the short-time and DRE tar collection are weak functions of the scaling factor, confirming the ideas outlined above regarding secondary tar decomposition. To further confirm this idea, a non-proportionally scaled fluidized bed has also been investigated, where the scaling in the x-direction is the same, but where the vertical size of the bed remains unchanged. Figure 7b illustrates the results of this comparison, and it can be concluded that similar results are obtained as for the proportional scaling. Only marginally better scaling is obtained in Fig. 7b than in Fig. 7a.

Since reactor scaling for pyrolysis applications is particularly inhibited by the associated increase in gas residence time, τ_R , and the accompanying tar-to-gas conversion mechanism, τ_{tar} , it is therefore important to minimize τ_R in order to reduce secondary production of gas. To evaluate the possibility of minimizing τ_R , with respect to τ_{tar} one may estimate their ratio defined as

$$\frac{\tau_R}{\tau_{tar}} = \frac{L_y}{V_g} A_{tar} \exp(-E_{tar}/R_u T_g) \quad (45)$$

where the kinetic parameters are those of reaction K_4 (tar-to-gas conversion), L_y is the height of the domain, and V_g is the fluidization velocity. To prevent secondary gas formation, the goal is to have $\tau_R/\tau_{tar} \ll 1$. Depicted in Fig. 8 is such an estimate for several proportional scale-up factors as a function of T_g . The curves were obtained from eq. 45 by fixing $V_g = 0.5$ m/s and proportionally varying L_y . If one considers that $\tau_R/\tau_{tar} \sim 0.1$ represents a threshold above which tar-to-gas conversion is important, it is clear that only the standard scale reactor can operate close to the optimal temperature found from the detailed simulations; the larger scale reactors must operate at a temperature below the optimal one, or incur tar losses before collection. We note that this standard scale reactor is laboratory, rather than industrial scale.

Finally, two detailed simulations were performed with a higher V_g in a proportionally scaled bed to explicitly decrease the residence time of the gas while keeping other parameters constant. Only slight improvements in tar collection were obtained (of the order of 1%), and thus the results are not shown. This result agrees with the simple estimate provided by eq. 45 where it is clear that V_g must be proportionally increased with L_y to maintain τ_R/τ_{tar} constant. Therefore, to optimize tar collection in industrial scale reactors, it is proposed that the gas fluidization velocity should be increased with the reactor height.

Conclusions

A comprehensive mathematical model of fluidized bed reactors used for harvesting tar from biomass has been presented. The model is based on detailed submodels for the hydrodynamics of the gas-solid mixture and the biomass kinetics. The submodels were chosen for their ability to capture the relevant physics. The separately validated biomass pyrolysis kinetics model of Miller and Bellan 1997 was chosen for its ability to differentiate between the various biomass feeds available through the use of a superimposed cellulose, hemicellulose and lignin kinetics scheme. The hydrodynamics model is based on the detailed multiphase model of Lathouwers and Bellan 2001 which is able to describe the dynamics and heat transfer of dense, reactive gas-solid mixtures. The multiphase flow mathematical description is obtained from systematic averaging of the local instantaneous equations using the kinetic theory of granular flows in combination with rigid sphere interaction models explicitly accounting for collisional transfer between the particles. This model avoids as much as possible heuristic extensions from monodisperse results which are common throughout the literature. The model was previously qualitatively and quantitatively validated against experimental data of bubbling fluidized beds. The combined submodels have been used herein to investigate the efficiency of bubbling fluidized bed reactors for condensable tar production from biomass particles by means of pyrolysis. A series of simulations has been performed in order to assess the influence of process parameters on the efficiency of the reactor, and to investigate the potential for scale up. The present study appears to be the first in literature where such a detailed computational study is reported in the context of biomass particle pyrolysis using bubbling fluidized bed reactors.

Results indicate that the optimum temperature for a biomass feed consisting of bagasse particles is around 750 K. The obtained tar collection at this temperature is about 0.7 which is in accordance with experimental data for various bubbling bed geometries. Higher temperatures give rise to increasing gas collection at the expense of tar. At fixed particle size, the fluidizing gas temperature is the most important process parameter. Results concerning the variation of other major process parameters, such as the biomass temperature on entering the reactor, feedstock, fluidization ve-

locity magnitude and the biomass feed rate, indicate that tar collection displays a low sensitivity with respect to these parameters. To assess the commercial viability of the bubbling fluidized bed for pyrolysis applications, scale up of the system has also been investigated. Scaling is found to have a small adverse effect on the tar collection capabilities at the optimal operating temperature. Shallow beds scale slightly better than those having large aspect ratios (height/width length ratio). Using a simple estimate of characteristic times, it is proposed that the fluidization velocity should be proportionally increased with reactor height to maintain minimal tar-to-gas conversion at high reactor temperatures beneficial to tar production from biomass.

Nomenclature

A	Rate constant	$1/s$
Bi	Biot number	—
C	Particle velocity fluctuation	m/s
C_d	Drag coefficient	—
C_p	Heat capacity at constant pressure	J/kgK
c	Particle velocity	m/s
D_{ii}	Self diffusion coefficient	m^2/s
D_ξ	Gas species diffusion coefficient	m^2/s
d_i	Particle diameter	m
E^a	Activation energy	$J/kmol$
e_{ik}	Restitution coefficient	—
F_{bl}	Blowing correction factor	—
F_{ik}	Multiplication factor	kg/m^7
Fr	Frictional stress model constant	Pa
f	Correction factor for drag coefficient	—
f_g	Gravitational acceleration	m/s^2
$f^{(1)}$	Single particle distribution function	$s^3/m^6 kgK$
h	Specific enthalpy	J/kg
h_{ik}	Radial distribution function	—

I	Radiation intensity	W/m^2
I_2	Second invariant of strain rate tensor	$1/s^2$
K	Reaction rate	$1/s$
L	Macroscopic length scale	m
M_i	Reduced particle mass	—
M_ξ	Total mass of species ξ in reactor	kg
m_i	Particle mass	kg
Nu	Nusselt number	—
n	Frictional stress model constant	—
n_i	Number density	$1/m^3$
$P(\Pi)$	Probability of encountering realization Π	—
Pr_g	Gas phase Prandtl number	—
p	Frictional stress model constant	—
p_s	Scattering phase function	—
p_g	Thermodynamic pressure	Pa
Q_r	Radiative component of particle heat transfer	W
\mathbf{q}	Heat flux vector	J/m^2s
\mathbf{q}_i	Collisional flux in granular energy equation	kg/s^2
$R_{i,\xi}$	Reaction rate for phase i for species ξ	$1/s$
R_u	Universal gas constant	$J/kmolK$
Re	Particle Reynolds number	—
\mathbf{S}	Strain rate tensor	$1/s$
T	Temperature	K
t	Time	s
t_s	Start time	s

\mathbf{u}	Velocity vector	m/s	
V_i	Particle volume, including pores	m^3	
X^c, X^h, X^l	Char ratio formed through reaction of cellulose, etc.		—
\mathbf{x}	Spatial coordinate	m	
Y	Species mass fraction		—
W	Weight function for gas-particle drag		—
W_ξ	Molecular weight of species ξ	$kg/kmol$	

Greek symbols

α	Phase fraction with pores included in gas phase		—
$\hat{\alpha}$	Phase fraction with pores included in particle phase		—
Γ	Mass transfer rate	kg/m^3s	
γ_i	Collisional source in granular energy equation	kg/ms^2	
Δh	Reaction enthalpy	J/kg	
ϵ_i	Particle porosity		—
η_i	Particle solidity		—
η	Yield parameter		—
ϑ	Differential reactor efficiency		—
Θ_i	Granular temperature	m^2/s^2	
κ	Absorption or scattering coefficient		$1/m$
λ	Thermal conductivity	W/mK	
μ	Viscosity	kg/ms	
ρ	Density	kg/m^3	
Σ	Stress tensor	kg/ms^2	
σ_i	Particle radius	m	
σ_B	Stefan Boltzmann constant	W/m^2K^4	

τ_R	Mean gas residence time	s
$\tau_{i,12}$	Fluid particle drag time scale	s
τ_{tar}	Secondary tar conversion time scale	s
ϕ	Angle of internal friction	deg.
ϕ_i	Collisional source in momentum equation	kg/m^2s^2
χ	Phase indicator	–
Ψ	General variable	consistent units
Ω_ξ	Total mass of species ξ convected out the reactor	kg

Subscripts

a	Absorption
b	Black body
bl	Blowing
g	Gas phase
i	Phase index
max	Maximum value
min	Minimum value
s	Scattering
v	Vapor
ξ	Species index

Superscripts

f	Frictional
-----	------------

- [1] Miller, R. S. and J. Bellan. 1998. "Numerical simulation of vortex pyrolysis reactors for condensable tar production from biomass." *Energy and Fuels* 12(1), 25-40.
- [2] Scott, D. S. and J. Piskorz. 1982. "The flash pyrolysis of Aspen-polar wood." *Can. Journal Chem Eng.* 60, 666-674.
- [3] Scott, D. S. and J. Piskorz. 1984. "The continuous pyrolysis of biomass." *Can. Journal Chem*

Eng 62, 404-412.

- [4] Miller, R. S. and J. Bellan. 1997. "A generalized biomass pyrolysis model based on superimposed cellulose, hemicellulose and lignin kinetics." *Combust. Sci. and Tech* 126, 97-137.
- [5] Lathouwers, D. and J. Bellan. 2000. "Modeling and simulation of bubbling fluidized beds containing particle mixtures." *Proc. of the Comb. Inst.* Vol. 28, 2297-2304
- [6] Lathouwers, D. and J. Bellan. . 2001. "Modeling of dense gas-solid reactive mixtures applied to biomass pyrolysis in a fluidized bed." *Int. J. Multiphase Flow* submitted
- [7] Drew, D. A. 1983. "Mathematical modeling of two-phase flow." *Ann. Rev. Fluid Mech* 15, 261-291.
- [8] Campbell, C. S. 1990. "Rapid granular flows." *Ann. Rev. Fluid Mech* 22, 57-92.
- [9] Gidaspow, D. 1986. "Hydrodynamics of fluidization and heat transfer: supercomputer modelling." *Appl. Mech. Rev* 39, 1-22.
- [10] Schiller, L. and A. Nauman. 1935. "A drag coefficient correlation." *V.D.I. Zeitung* 77, 318-320.
- [11] Anderson, K. G. and R. J. Jackson. 1992. "A comparison of the solutions of some proposed equations of motion of granular materials for fully developed flow down inclined planes." *J. Fluid Mech.* 241, 145-168.
- [12] Lathouwers, D. and J. Bellan. 1999. "Multiphase flow equations for modeling tar production from biomass particle pyrolysis in a fluidized bed reactor." *Proceedings of the Fall Technical Meeting of the Western States Section of the Combustion Institute*, Irvine, October 25-26.
- [13] Miller, R. S., K. Harstad and J. Bellan. 1999. "Evaluation of equilibrium and non-equilibrium evaporation models for many-droplet gas-liquid flow simulations." *Int. J. Multiphase Flow* 24(6), 1025-1055.
- [14] Gyarmathy, G. 1982. "The spherical droplet in gaseous carrier streams: review and synthesis." *Multiphase Science and Technology* Vol. 1. Eds. Hewitt, G. F., Delhay, J. M., and Zuber, N. McGraw Hill, 99-279.
- [15] Jenkins, J. T. and F. Mancini. 1987. "Balance laws and constitutive relations for plane flows of a dense, binary mixture of smooth, nearly elastic, circular disks." *J. Appl. Mech.* 54, 27-34.
- [16] Manger, E. 1996 "Modelling and simulation of gas/solids flow in curvilinear coordinates." PhD thesis, Telemark College, Norway.
- [17] Zaichik, L. I., V. A. Pershukov, M. V. Kozelev and A. A. Vinberg. 1997. "Modeling of dynamics, heat transfer, and combustion in two-phase turbulent flows: 2. Flows with heat transfer and combustion." *Exp. Thermal Fluid Sci.* 15, 311-322.

- [18] Lathouwers, D. 1999. Modelling and Simulation of Turbulent Bubbly Flows. PhD thesis, Delft University of Technology, The Netherlands.
- [19] Strang, G. 1968. "On the construction and comparison of difference schemes." *SIAM J. of Numer. Anal.* 5(3), 506-517
- [20] Brown, P. N., G. D. Byrne and A. C. Hindmarsh. 1989. "VODE: A Variable-coefficient ODE solver." *SIAM J. Sci. Stat. Comput* 10(5), 1038-1051.
- [21] Barrett, R., M. Berry, T. F. Chan, J. Demmel, J. Donato, J. Dongarra, V. Eijkhout, R. Pozo, C. Romine and H. Van der Vorst. 1994. "Templates for the solution of linear systems: building blocks for iterative methods." *SIAM*, Philadelphia.
- [22] Scott, D. S., P. Majerski, J. Piskorz and D. Radlein. 1999. "A second look at fast pyrolysis of biomass - the RTI process." *J. Anal. Appl. Pyrolysis* 51, 23-37.
- [23] Di Felice, R., G. Coppola, S. Rapagna, and N. Jand. 1999. "Modeling of biomass devolatilization in a fluidized bed reactor." *The Can. J. Chem. Eng.* 77, 325-332.

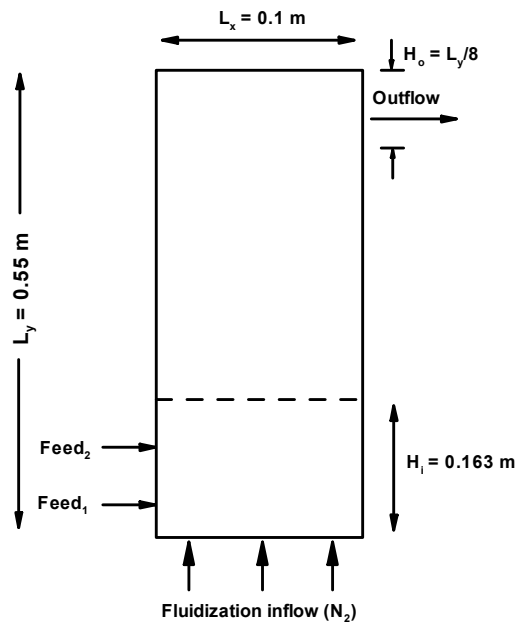


Figure 1. Schematic of the fluidized bed.

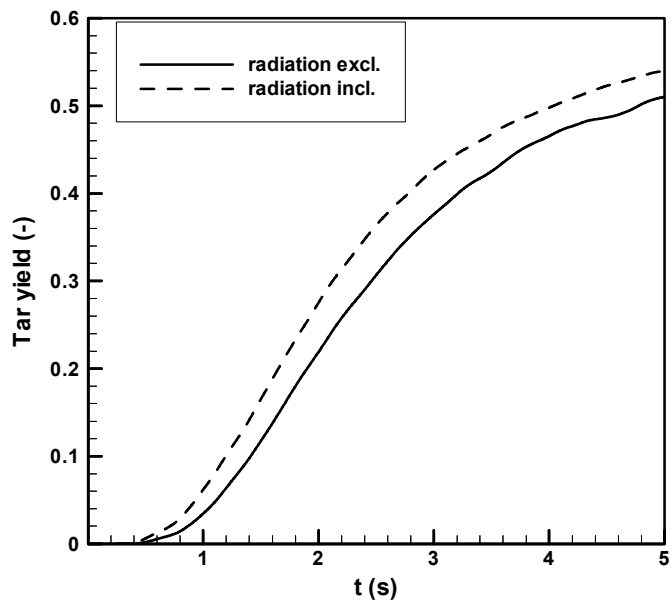


Figure 2a. Tar yield obtained from simulations with and without the radiation model, respectively.

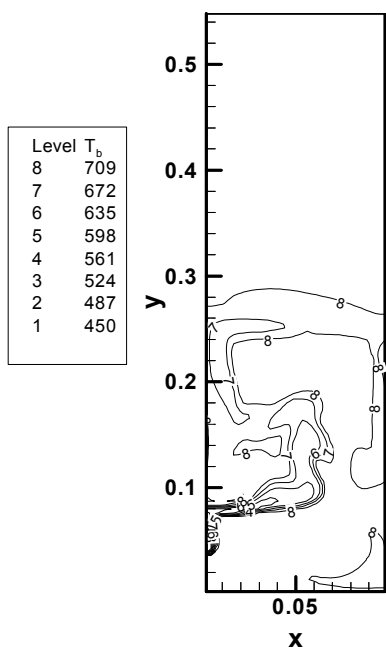


Figure 2b. Biomass particle temperature at 2.5 s from a simulation without radiation taken into account.

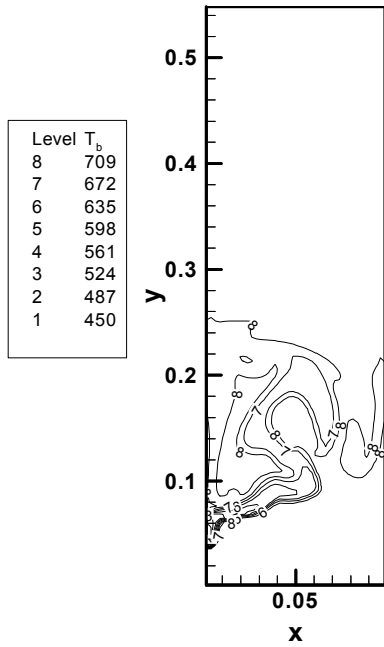


Figure 2c. Biomass particle temperature at 2.5 s taking radiation into account.

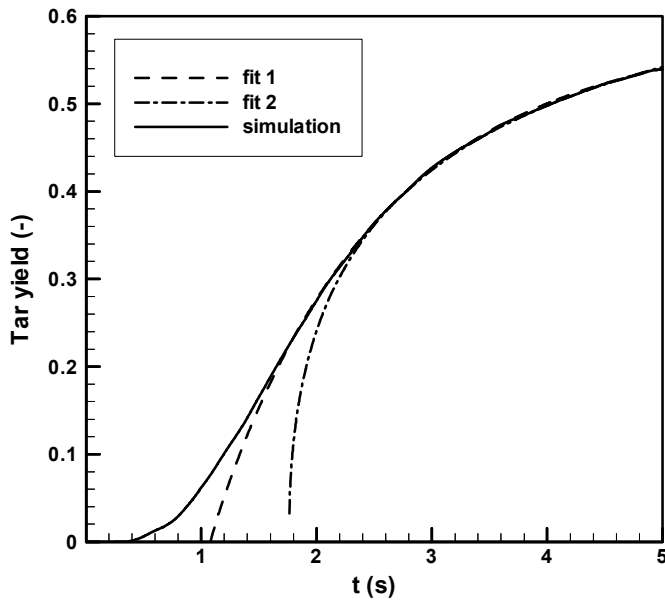


Figure 3. Example of the short-time tar-yield solution fits to obtain the steady state tar yield. This tar yield solution was obtained for following initial conditions: $T_g = 750$ K, $T_b = 400$ K, $V_g = 0.5$ m/s, biomass particle diameter of 0.5 mm, and bagasse feed stock.

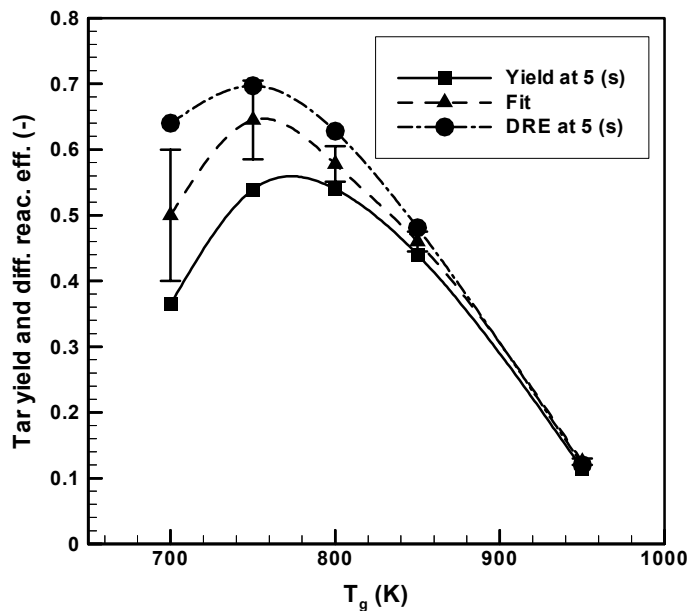


Figure 4a. Tar DRE, yield at 5 s, and predicted steady state tar yield as a function of the fluidization gas temperature.

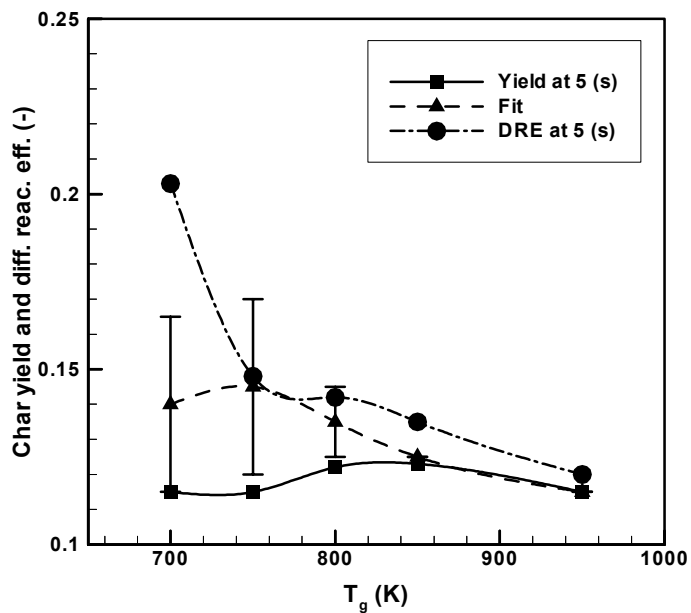


Figure 4b. Tar DRE, yield at 5 s, and predicted steady state tar yield as a function of fluidization fluxes.

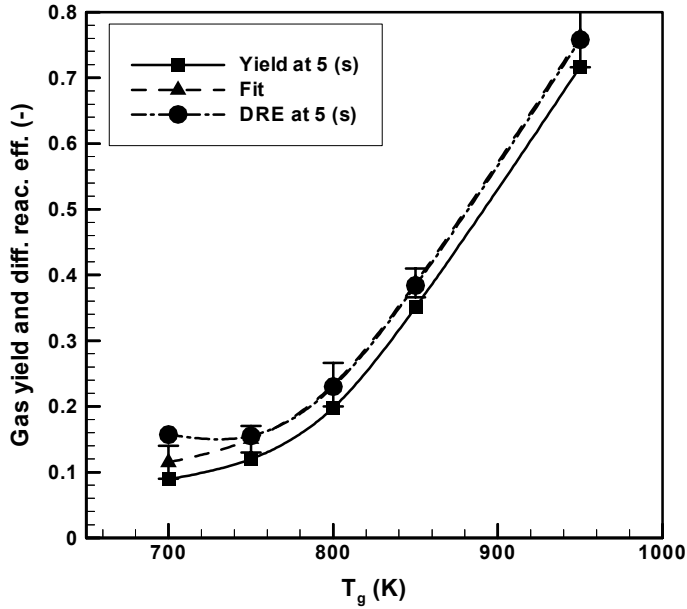


Figure 4c. Gas DER, yield at 5s, and predicted steady state gas yield as a function of the fluidization gas temperature.

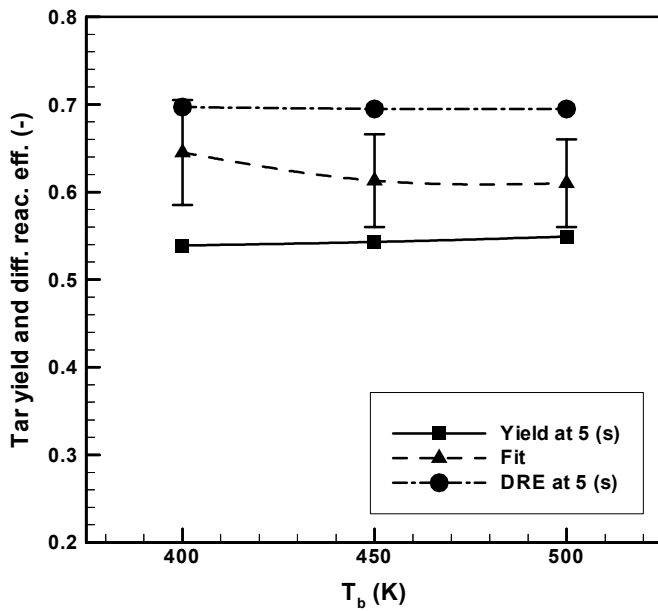


Figure 5a. Tar DRE, yield at 5 s, and predicted steady state tar yield as a function of biomass injection temperatures.

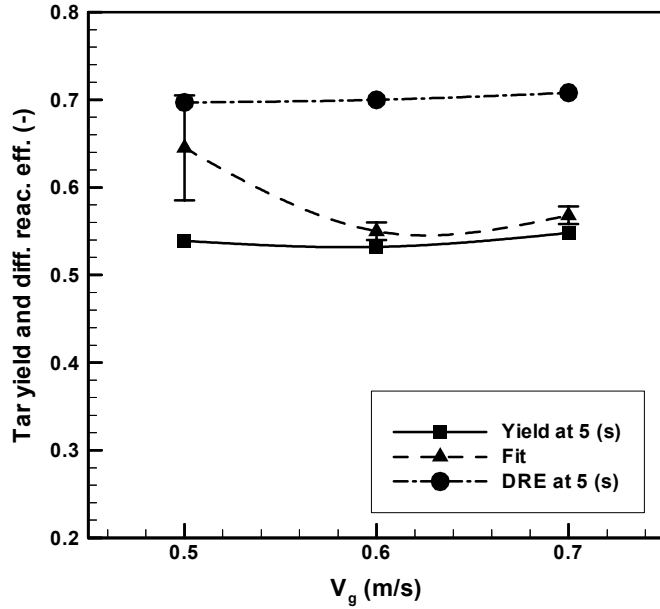


Figure 5b. Tar DRE, yield at 5 s, and predicted steady state tar yield as a function of fluidization fluxes.

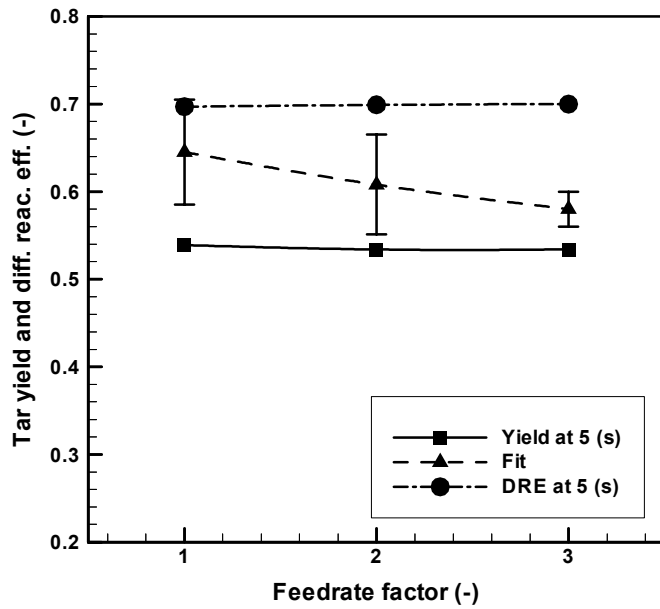


Figure 5c. Tar DRE, yield at 5 s, and predicted steady state tar yield as a function of biomass feed rate.

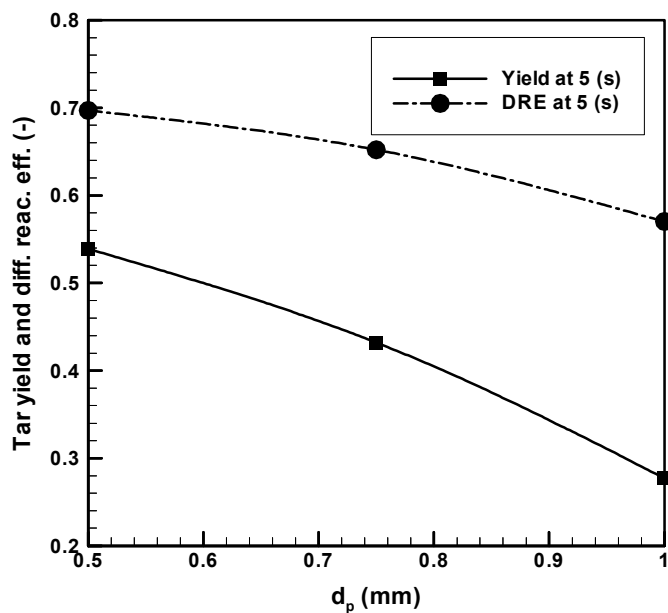


Figure 5d. Tar DRE and yield at 5 s as a function of biomass particle size.

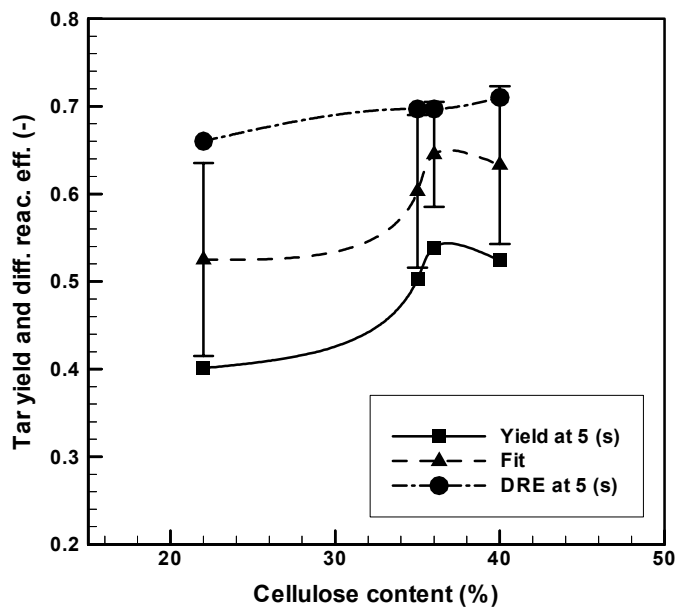


Figure 5e. Tar DRE, yield at 5 s, and predicted steady state tar yield as a function of biomass feedstock % cellulose.

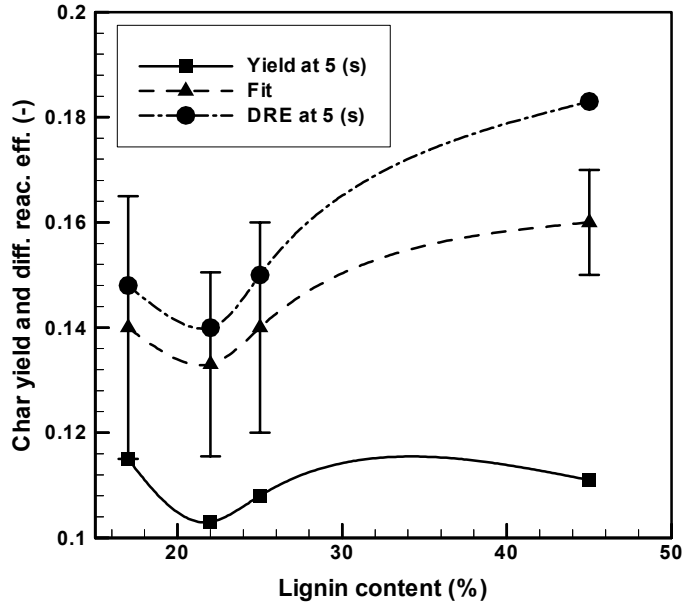


Figure 6. Char DRE, yield at 5 s, and predicted steady state char yield as a function of biomass feedstock % lignin.

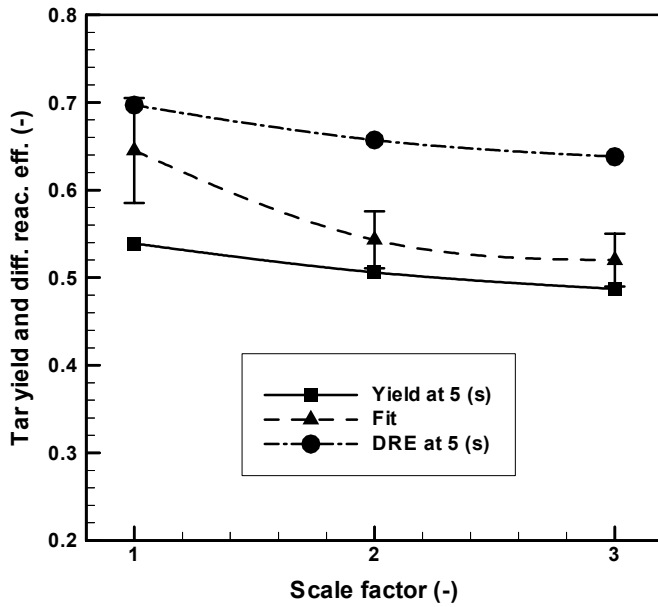


Figure 7a. Tar DRE, yield at 5 s, and predicted steady state tar yield versus scale factor (1,2 and 3) for proportional scaling.

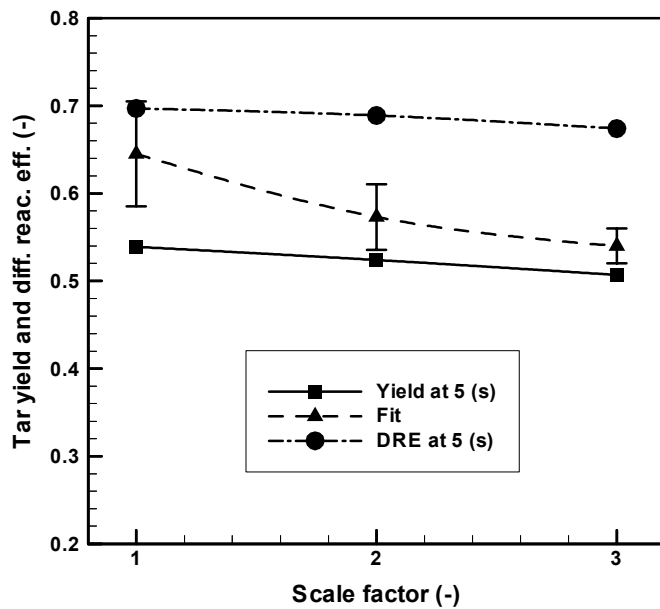


Figure 7b. Tar DRE, yield at 5 s, and predicted steady state tar yield versus scale factor (1,2 and 3) for shallow bed scaling.

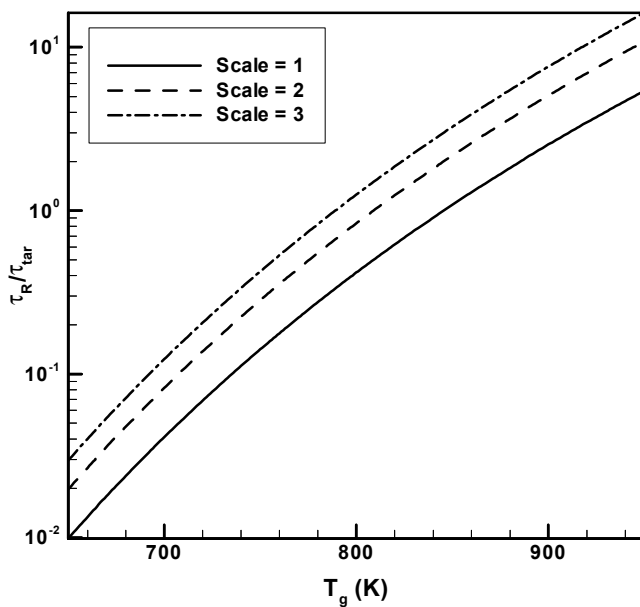


Figure 8. Ratio of the mean tar residence time to the tar-to-gas conversion kinetic time for proportional scaling.

AN INTEGRATED APPROACH TO HYDROGEN PRODUCTION FROM AGRICULTURAL RESIDUES FOR USE IN URBAN TRANSPORTATION

**Jalal Abedi¹, Yaw D. Yeboah¹, Matthew Realff², Denis McGee³, Jan Howard⁴, and
Kofi B. Bota¹**

1- Clark Atlanta University, 223 James Brawley Dr., Atlanta, GA 30314

2- Georgia Institute of Technology, Atlanta, Georgia 30332

3- Enviro-Tech Enterprises Inc., 10555 Paces Ave. #415, Matthews, NC 28105

4- Scientific Carbons Inc., 253 North Bay, Blakely, GA 31723

Abstract

This project focuses on the use of agricultural residues such as peanut shells to produce hydrogen for urban transportation. Specifically, a side stream of the pyrolysis products of a process for making activated carbon from densified peanut shells at Scientific Carbons Inc. in Southwest Georgia will be used to test the concept. The primary focus of this work was to undertake process development studies in the use of the large quantities of peanut shells produced in Georgia as feedstock for the pyrolysis-steam reforming process. The method combines two stages: slow pyrolysis of biomass to generate charcoal and catalytic steam reforming of the pyrolysis vapors to hydrogen and carbon dioxide. Scientific Carbons Inc. is currently operating a pilot facility in Blakely, GA to convert 24 tons/day of pelletized peanut shells to activated carbon. Scientific Carbons' facility will be used to perform a scaled-up demonstration of a steam reforming process to convert the off-gas of the peanut shell carbonization process to hydrogen. As a small company with the demonstrated ability to build modular systems, their current processes could be modified and expanded to run a variety of other feedstocks and to make a range of alternative products. This year we focused on development of decision models for selecting feedstock, process and alternatives, and the design and management of the construction of a 7-kg/hr fluidized-bed catalytic reactor system. The catalytic reactor system was successfully constructed and shipped to NREL. Shakedown runs of the system are expected to be completed in summer 2001.

Introduction

Background

Hydrogen is the most environmentally friendly fuel and can be efficiently used for stationary power and mobile applications. When burned or oxidized, it generates water as the only emission (small amounts of NO_x are generated during the combustion process but can be controlled to very low levels). At present, hydrogen is produced almost entirely from fossil fuels such as natural gas, naphtha, and coal. During these hydrogen production processes, large amounts of fossil-derived CO₂ are released to the atmosphere. Renewable biomass is an attractive alternative to fossil feedstocks because of essentially zero net CO₂ impact [1].

Biomass is defined as a material that has participated in the “growing cycle.” Agriculture waste, forest residue, urban wood waste, and trees and grasses grown as energy crops are materials commonly referred to as biomass. Because biomass consumes as much CO₂ in the growing cycle as is produced when it is transformed into energy, the net CO₂ contribution from biomass-derived fuels is considerably less than from fossil-derived fuels. In addition, producing biomass on a sustainable basis by growing energy crops will support Georgia’s agricultural sector, an important part of the state’s economy. Successful commercialization of this technology will also reduce oil and gas imports of the U.S. [1].

Agriculture is Georgia’s largest industry and contributes over \$46 billion to the state’s annual economic output. One in six Georgians work in an agriculture-related sector. Georgia ranks as the number one state in the U.S. in peanut production, producing about 45% of all peanuts grown in the U.S. Georgia farmers grew about 1.5 billion pounds of peanut in 79 counties in 1999. Disposal of the large quantity of peanut shells in an environmentally acceptable manner is a significant challenge for the peanut industry. Hence peanut shells have been targeted as a feedstock for conversion to hydrogen.

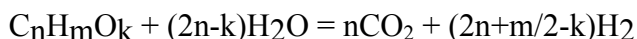
The National Renewable Energy Laboratory (NREL) in Golden, CO has developed the basis of a technology for the generation of hydrogen from biomass and agricultural residue [2,3]. Biomass can be converted to hydrogen by two distinct strategies: 1) gasification followed by shift conversion and 2) pyrolysis of biomass to form a bio-oil that can be subsequently converted to hydrogen via catalytic steam reforming and shift conversion. The NREL technology uses the latter approach, which has the potential to be cost competitive with current commercial processes for hydrogen production [4]. The process has been demonstrated at the bench scale using model compounds and the carbohydrate-derived fraction of bio-oil [2,3]. This concept has several advantages over the traditional gasification technology. Bio-oil is easily transportable so the second step (steam reforming) can be carried out at a different location, close to the existing infrastructure for hydrogen use or distribution. The second advantage is the potential for production and recovery of higher-value co-products from bio-oil that could significantly impact the economics of the entire process.

The bio-oil produced from fast pyrolysis of biomass contains about 75-85 wt% organics and 15-25% water [2,3]. The latter is the result of the moisture content in the biomass feed and dehydration reactions which proceed in parallel with the thermal depolymerization reaction. The

organics are generally a mixture of aldehydes, alcohols and acids derived from the carbohydrate fraction of biomass, and phenolics derived from the lignin fraction. Fast pyrolysis produces a bio-oil made up of two distinct fractions: a monomer-rich aqueous fraction (containing typically 20 wt% organics) and a hydrophobic fraction composed mainly of oligomers derived from lignin. Steam reforming can be used to convert the entire bio-oil or each of the fractions of the oil.

The hydrogen content in biomass is relatively low (6-6.5%), compared to almost 25% in natural gas. For this reason, producing hydrogen via the biomass gasification/water-gas shift process cannot compete on a cost basis with the well-developed commercial technology for steam reforming of natural gas. However, an integrated process, in which part of the biomass is used to produce more valuable materials or chemicals and the residual fractions are used to generate hydrogen, can be an economically viable option.

The overall steam reforming reaction of bio-oil or any oxygenated organic compound with a chemical formula of $C_nH_mO_k$ can be represented as:



The stoichiometric yield of hydrogen is $2+m/2n-k/n$ moles per mole of carbon in feed. A mass balance of the NREL approach using fast pyrolysis is shown in Figure 1.

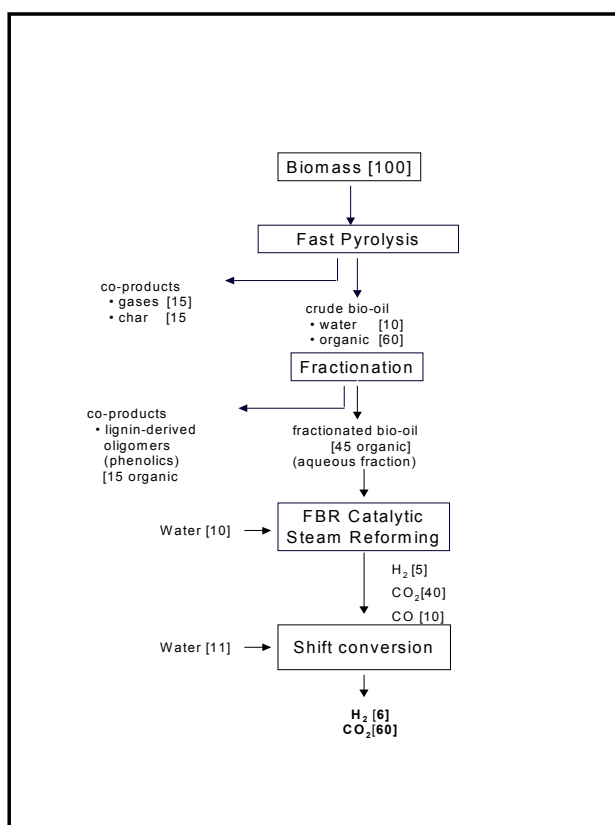


Figure 1. NREL Biomass to Hydrogen Process based on fast pyrolysis with phenolic coproducts.

Prior Work

In previous years it was demonstrated, initially through micro-scale tests then in the bench-scale fixed-bed reactor experiments [2,5,6], that bio-oil model compounds as well as the carbohydrate-derived fraction of bio-oil can be efficiently converted to hydrogen. Using commercial nickel catalysts the hydrogen yields obtained approached or exceeded 90% of those possible for stoichiometric conversion. The carbohydrate-derived bio-oil fraction contains a substantial amount of non-volatile compounds (sugars, oligomers) which tend to decompose thermally and carbonize before contacting the steam reforming catalyst. Prior studies managed to reduce these undesired reactions by injecting the oil fraction to the reactor in a form of a fine mist. However, the carbonaceous deposits on the catalyst and in the reactor freeboard made most of the catalyst inaccessible to contact with the oil, limiting the reforming time to 3-4 hours. For the above reasons, NREL decided to employ a different reactor configuration, a fluidized bed, to overcome at least some limitations of the fixed-bed unit. This greatly increased the reforming efficiency and extended the catalyst time-on-stream. Catalyst regeneration was done by steam or carbon dioxide gasification of carbonaceous residues providing additional amounts of hydrogen.

Experiments at NREL

Pelletized peanut shells were obtained from Scientific Carbons Inc. in Georgia. These materials were pyrolyzed at the NREL Thermochemical Users Facility (TCUF) using the fast ablative pyrolysis system (vortex reactor). The reactor wall temperature was maintained within the range of 600-625°C, which has been proven to provide the highest bio-oil yield. Nitrogen at a flow rate of 15 kg/h was used as the carrier gas for the biomass particles in the pyrolysis reactor. The tests proceeded smoothly at the rate of 10 kg/h. Eventually, 200-300 kg of pyrolysis oil was generated from feedstock. Peanut shell oil was collected in the scrubber of the pyrolysis system as a two-phase liquid (water was used for scrubbing pyrolysis vapors), with the top fraction containing 32.3% organics (6% are lignin-derived oligomers) and 67.7% water. Water content of the liquids was determined by Karl-Fisher titration method using a Metrohm 701 KF Titrino analyzer. Elemental composition, including the carbon, hydrogen, and oxygen content of these liquids was analyzed by a commercial laboratory (Huffman Laboratories, Golden, CO). The aqueous solutions were then used in reforming tests to produce hydrogen.

Fluidized Bed Reforming System

The experiments were carried out using a bench-scale fluidized-bed steam reformer. The schematic of the fluidized bed system is shown in Figure 2. The two-inch-diameter Inconel reactor supplied with a porous metal distribution plate was placed inside a three-zone electric furnace. The reactor contained 150-200g of commercial nickel-based catalyst from UCI (C11-NK) ground to the particle size of 300-500 μ m. The catalyst was fluidized using superheated steam, which was also a reactant in the reforming process. Steam was generated in a boiler and superheated to 750°C before entering the reactor at a flow rate of 2-4 g/min. Liquids were fed at a rate of 2-5 g/min using a diaphragm pump. A specially designed oil injection nozzle supplied with a cooling jacket was used to spray liquids into the catalyst bed. The oil temperature in the injector was controlled by a coolant flow and maintained below boiling point to prevent premature evaporation of volatiles and consequent deposition of nonvolatiles. The condensate was collected in a vessel whose weight was continuously monitored. The outlet gas flow rate

was measured by a mass flow meter and by a dry test meter. The gas composition was analyzed every 5 minutes by an MTI gas chromatograph. The analysis provided concentrations of hydrogen, carbon monoxide, carbon dioxide, methane, ethylene, and nitrogen in the outlet gas stream as a function of time. The temperatures in the system as well as the flows were recorded and controlled by the OPTO data acquisition and control system.

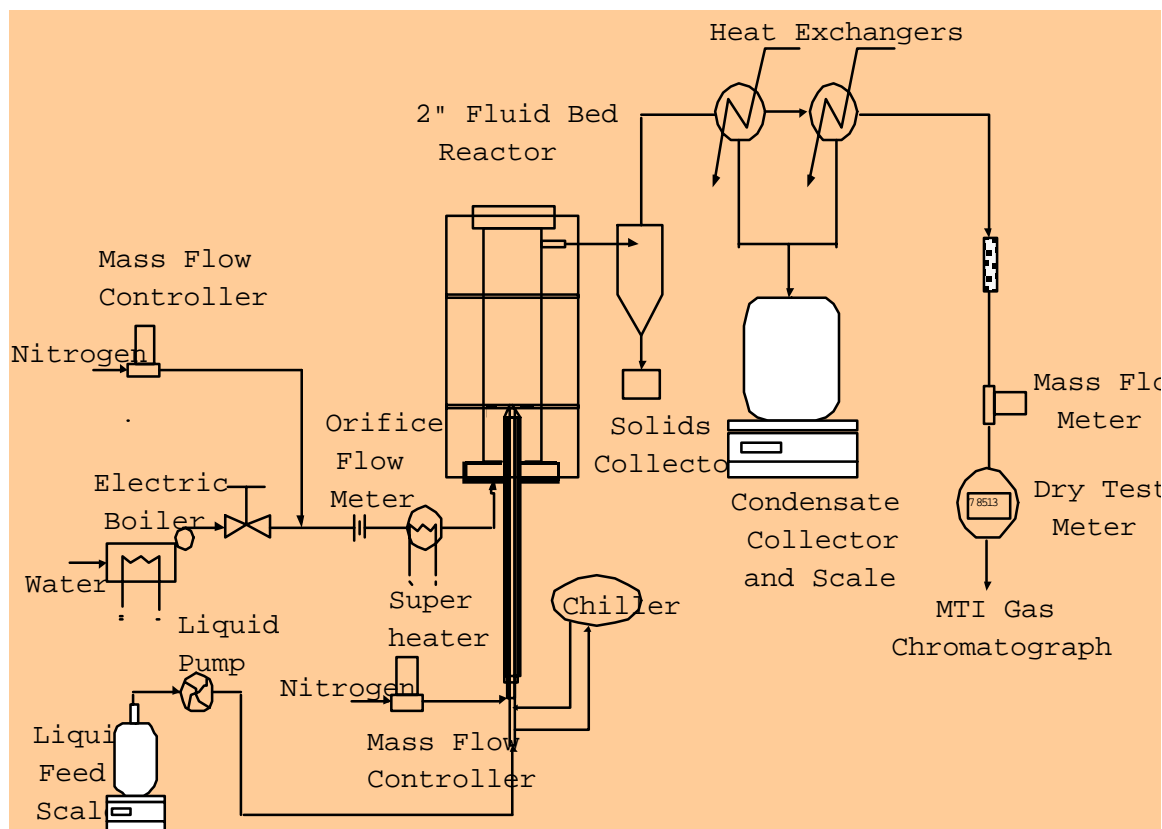


Figure 2. Schematic of the fluidized bed reforming system.

The measurements allowed determination of the total and elemental balances for the reforming tests as well as the calculation of the yield of hydrogen generated from the biomass-derived liquid feed. The maximum (stoichiometric) yield of hydrogen was $2 + \frac{m}{2n - k/n}$ moles per mole of carbon in feed. Therefore, 63 g of hydrogen could be theoretically obtained from 1 L of peanut shell oil extract. The steam reforming experiments in the fluidized bed reactor were carried out at the temperature of 800°C and 850°C. The steam to carbon ratio varied from 7 to 13, while the methane-equivalent gas hourly space velocity $G_{C1}HSV$ was in the range of 1200-1500 h^{-1} . Gas composition (on nitrogen free basis) obtained from the peanut shell pyrolysis oil is shown in Figure 3. During eight hours of the experiment, the gas composition was very stable and only a small decrease in the concentration of hydrogen and an increase in methane were observed.

Methane concentration, though it grew to 3000-4000 ppm, still remained an order of magnitude smaller than that of the three major gas components and, therefore, is not shown in Figure 3. More fluctuation was observed in the amount of gas produced and, consequently, in the yield of hydrogen from the peanut bio-oil fraction, which is presented in Figure 4. The hydrogen yield

was still at the level of 80% of the stoichiometric potential after eight hours on stream. Peanut shell liquid had a higher concentration of the organic compounds, especially of lignin oligomers than the wood oil fractions. Large molecules of lignin compounds are less reactive and probably required a longer contact time with the catalyst than the smaller carbohydrate-derived fragments. They are also more likely to form carbon deposits on the catalyst surface. However, at 850°C, these deposits were removed and converted to hydrogen and carbon oxides by steam processing with the same efficiency as that observed for wood-derived liquids (carbon to gas conversion of 92%). This resulted in hydrogen yields greater than 80% of the stoichiometric potential during eight-hour catalyst time on stream.

The yields of hydrogen would be 5-7% higher if the reforming was followed by water-gas shift processing of carbon monoxide in the product gas. The global mass balance closure for the whole experiment was 94%, and 88-91% of bio-oil carbon was converted to gases. Both the decrease in the hydrogen production and the missing carbon in the mass balance suggest that a small part of the carbon from bio-oil formed deposits on the catalyst surface. Steam treatment of the used catalyst performed at 850°C resulted in the release of hydrogen and CO₂ in the amount corresponding to 4-5% of the carbon fed (about half of the missing carbon). The other part of carbon unaccounted for was probably entrained by product gases together with the catalyst fines and collected in the cyclone and condensers. The steam treatment - by removing deposits from the surface - also regenerated the catalyst, which performed during the following test at the same level of activity as the fresh catalyst.

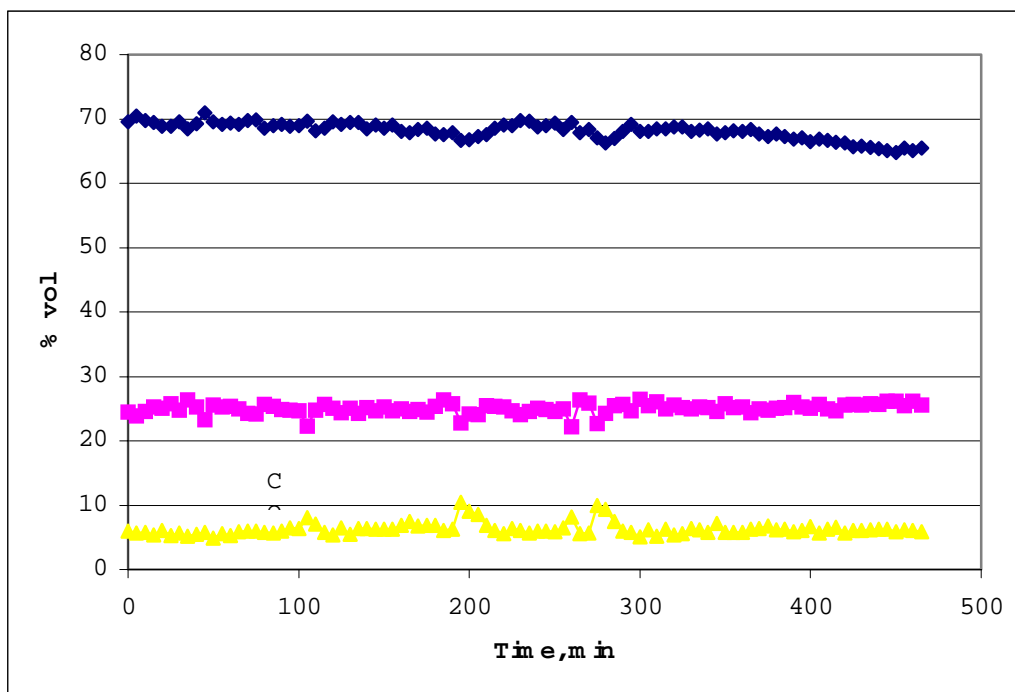


Figure 3. Composition of the gas produced during steam reforming of peanut shell bio-oil carbohydrate-derived fraction at 850°C and S/C=9 [3].

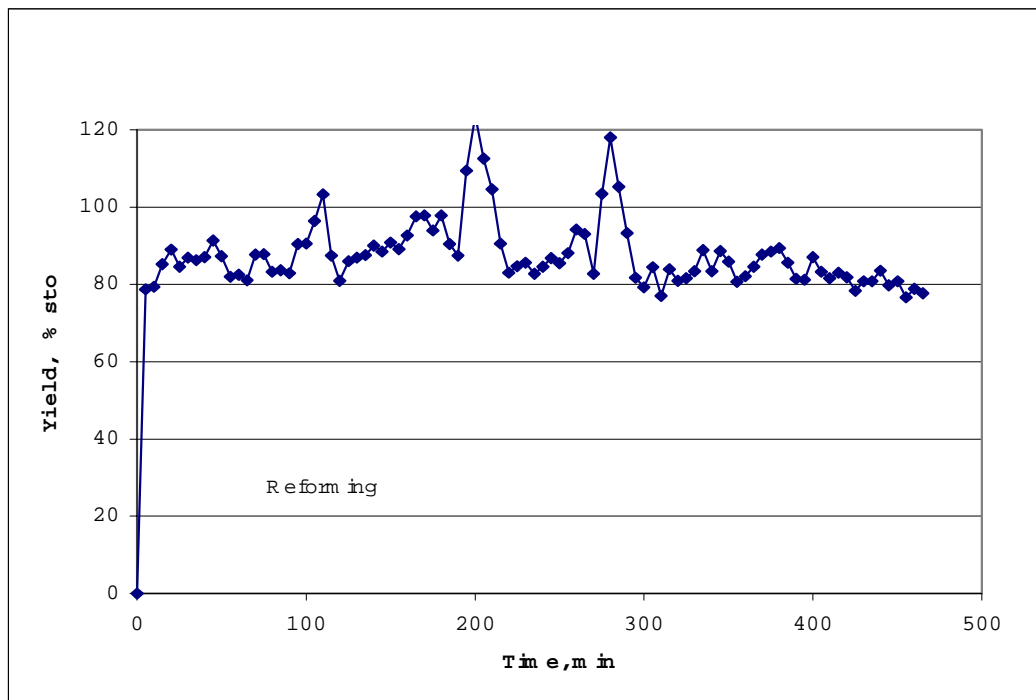


Figure 4. Yield of hydrogen obtained during reforming of peanut shell bio-oil carbohydrate-derived fraction at 850°C and S/C=9 [3].

Process Economics

The work performed at NREL to date has focused on the scenario shown in Figure 1 for fast pyrolysis. The economics of this approach has been assessed with an adhesive coproduct and the selling price of hydrogen is estimated in the range of \$6-8/MBTU [4]. This study addresses another process option based on slow pyrolysis, which is currently practiced to produce charcoal for conversion to activated carbon. A modification of this approach to convert the by-products to hydrogen is shown in Figure 5. A preliminary economic analysis of the steam reforming of the bio-oil produced from the activated carbon process has been performed by NREL [5,6]. The process examined included steam reforming of the slow pyrolysis vapors, followed by further hydrogen production in shift reactors and hydrogen purification in a conventional pressure swing adsorption (PSA) system. The base case process assumes utilization of all of the 225 kg of pyrolysis vapors/hr (the current scale of the Scientific Carbons process). At this utilization rate, it appears that the carbon process is still slightly positive with respect to energy, although this will depend on heat losses. In other words, the process produces enough energy to sustain the system without requiring additional fuel.

The yield of hydrogen from the slow pyrolysis bio-oil is significantly higher (~70%) on a mass basis than that from the fast pyrolysis bio-oil. When looking at the total process (i.e., biomass to bio-oil to hydrogen), however, the yield from the slow pyrolysis process is lower than that from the fast pyrolysis process. Table 1 compares the yields from both processes. As shown in Table 1, the yield of hydrogen from bio-oil in the fast pyrolysis system is roughly 11%, but in the slow

pyrolysis case, it is almost 19%. However, the yield on a total dry biomass basis is 4.5% for slow pyrolysis and 7.3% for fast pyrolysis. The primary reasons for these differences are variations in the bio-oil composition, yield of other products, and process assumptions.

Also shown in Table 1 are estimates of the composition of the bio-oil from both processes. In the fast pyrolysis process, the bio-oil has a composition that is < 50% carbon, but that from the slow pyrolysis process has a carbon composition of almost 73% [5]. Thus, for the same steam addition rate (i.e., lb H₂O/lb C), more hydrogen will be produced per pound of bio-oil in the slow pyrolysis process.

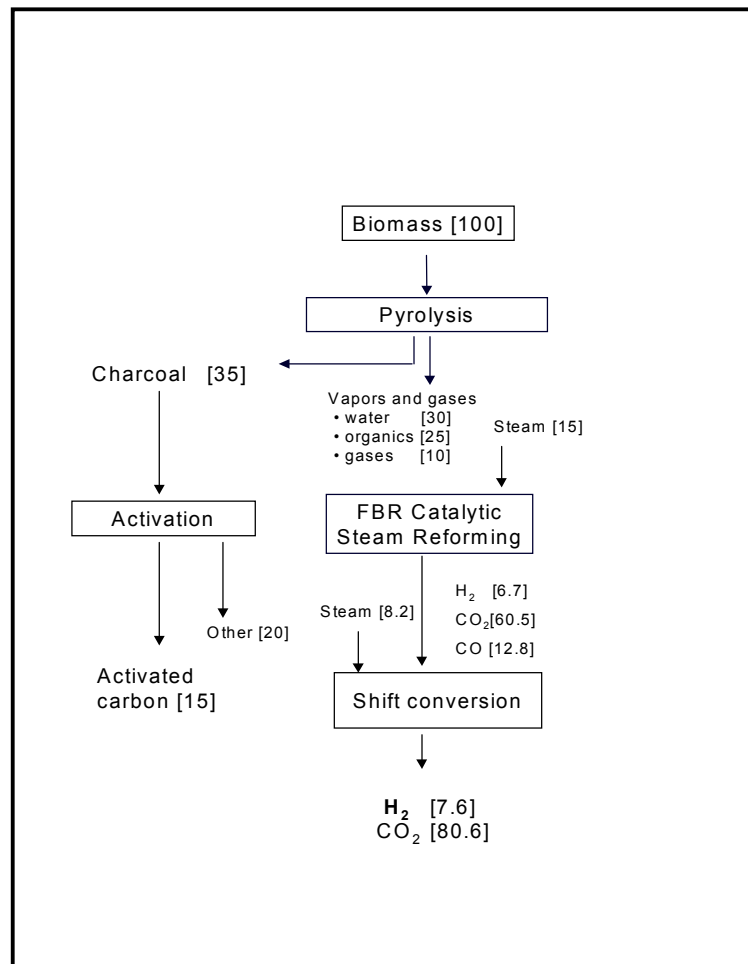


Figure 5. Proposed process based on reforming of slow pyrolysis oils.

The economic feasibility determination was based on a discounted-cash-flow rate of return (DCFRROR) analysis using a 10% rate of return. All parameters for the study were taken from the standardized hydrogen economic analysis [6]. Table 2 summarizes the important economic parameters.

Table 1. Yield Comparison for Slow and Fast Pyrolysis

Process	Slow Pyrolysis	Fast Pyrolysis
Bio-oil Yield (kg/kg dry feed)	0.239	0.657
Hydrogen Yield (kg/kg dry feed)	0.045	0.073
(kg/kg bio-oil)	0.189	0.111
(kg/kg vapor)	0.063	NA
(kg/kg dry vapor)	0.113	NA
Bio-Oil Ultimate Analysis (wt%)		
Carbon	72.50	48.71
Hydrogen	5.13	6.61
Nitrogen	1.2	0.0
Sulfur	0.04	0.0
Oxygen	21.13	44.68

NA – Not applicable; the vapors are not processed in the fast pyrolysis process

Table 2. Standard Economic Parameters

Economic Parameter	Value
Discount rate	10%
Plant life	20 years
Depreciation	None
Construction Period	3 years
On-stream time	Year 1 45% Year 2+ 90%

Capital costs were scaled from Mann [4] using a 0.84 exponent. This exponent was derived from the three cases presented in the paper [4]. Fixed operating costs and working capital were also based on the paper. Variable operating costs were determined from the material balance. The pyrolysis vapor was assumed to be available at \$2.56/GJ, a value that is roughly 90% of its fuel value (assuming an energy equivalence to natural gas at \$2.50/GJ). The analysis also assumed that steam would be produced in the reforming operation. A credit based on \$3.50/1000 lbs of steam was assumed.

Using the above assumptions, the total capital investment for the additional equipment to modify the existing facility to produce hydrogen from the pyrolysis off-gas is estimated at \$1.4 million. For an annual hydrogen production rate of 4.4 million Nm³, the selling price of hydrogen is estimated to be \$9.51/GJ. The hydrogen-selling price for a fuel cost of \$1.28/GJ (i.e., 45% fuel value) is \$7.78/GJ. Using a no-cost bio-oil the selling price for the hydrogen is \$6.05/GJ. These price ranges are very promising considering that the economics were performed for a very small-scale operation.

Advantages and Potential Impact

The proposed method combines two stages: pyrolysis of biomass to generate bio-oil and catalytic steam reforming of the bio-oil to hydrogen and carbon dioxide. This concept has several

advantages over traditional gasification technology. First, bio-oil is much easier to transport than solid biomass and therefore, pyrolysis and reforming can be carried out at different locations to improve the economics. For instance, a series of small size pyrolysis units could be constructed at sites where low cost feedstock is available. The oil would then be transported to a central reforming plant located at a site with an existing hydrogen storage and distribution infrastructure. A second advantage is the potential production and recovery of higher value added co-products from bio-oil that could significantly impact the economics of the entire process. In the original NREL concept, the preferred route leads to co-products hydrogen and partly "depolymerized lignin." Lignin-derived oligomer-rich fraction can be used as a feedstock for the production of resins with formaldehyde. Such resins can become valuable co-products (a substitute for phenol-formaldehyde), which will lower the production costs of hydrogen from the aqueous fraction as demonstrated in related technoeconomic studies [4]. Other viable application of the lignin-derived fraction is the production of "oxyaromatic ethers," a new class of high-octane fuel additive. The economics of the whole bio-oil reforming are less favorable than for the co-product strategy. However, the hydrogen yields obtained from the whole oil are higher than in the case when only the aqueous, carbohydrate-derived fraction is processed. In addition, since hydrogen is the only product, this option is independent of co-product markets.

A key partnership that will be fostered in this project is with the Federation of Southern Cooperatives, an organization of southern family farmers that represent 25,000 farmers in a 13-state region. As part of the assessment for expanded application of this technology, we will develop a database of the biomass and agricultural residues (and their volumes) that may be used as potential feedstocks in the proposed conversion scheme. The information from the database will be used to assess the economic and environmental impact of the proposed work on the state of Georgia.

The anticipated potential benefits or impact on the Georgia economy include:

- Use of biomass will support and further expand the agriculture-related sector, which is the largest industry in Georgia; employing one in six Georgians and producing 45% of the U.S. peanut production.
- Application of the proposed technology will provide an economical and environmentally acceptable means of disposing of the large quantity of peanut shells that result from the 1.5 billion pounds (768,500 tons) of peanut produced each year in Georgia. The demand for peanut shells as feedstock of the proposed technology will improve the economic competitiveness of the peanut industry in Georgia and secure its long-term future.
- Widespread use of renewable hydrogen, the cleanest fuel for power generation and for transportation applications, will reduce oil and gas imports and will have significant environmental and health benefits for the major cities in the state of Georgia.
- The proposed process will produce co-products in addition to hydrogen. Alternative co-products that may be obtained from different bio-oil fractions include phenol (for phenol-formaldehyde resins) and fuel oxygenates. Similar to petroleum crude oil, biomass pyrolysis oil can be used for the production of a multitude of fuel and chemical products, in addition to hydrogen.
- The development of new agro-industrial infrastructure options that could result in sustainable and equitable growth. The inclusion of small farms and the attention to the appropriate scale

of production technology will ensure the ability to distribute the benefits of enhanced materials along the value chain to the communities involved in generating the wealth.

Approach and Accomplishments

Feedstock Supply, Process Economics, and Deployment Strategy

The ultimate impact of the biomass-to-hydrogen process depends on overall economics. Feedstock issues, such as supply, cost and logistics are major factors in cost-effectiveness of the hydrogen production process. This task is developing decision models for selecting among feedstock, process, and deployment alternatives. Of particular interest in Phase 1 on this project are peanut shells supply and cost projections and the evaluation of other agricultural residue feedstocks available in the same geographical area. Process economics are being developed for the major process options and used to construct a process options database. Different network options are developed to determine optimum subdivision of tasks among potential sites and to develop criteria for location of new processing sites. The evaluation of other coproducts are also included. This work is utilizing Geographical Information Systems (GIS) databases for constructing various scenarios relative to feedstock location, plant location and hydrogen and co-product markets.

Process Modeling

The current process converts peanut hulls into activated carbon and derives a bio-oil for fuel via pyrolysis. The process modeling effort is directed towards evaluating the enhancement of this basic process with options to recover a phenolic fraction for further processing into adhesives and steam reforming and hydrogen purification for a transportation fuel. The main unit operations that can achieve this separation and further refining are liquid-liquid extraction (LLE), steam reforming and pressure swing absorption (PSA). Three alternative flowsheets for the process are shown in Figures 6, 7 and 8. To model the LLE process it is necessary to establish the solubility of various components of the bio-oil in water and organic solvents. To achieve this goal it is necessary to characterize and model the bio-oil that is generated from the pyrolysis process and to ensure that the phase behavior of the components is adequately described in the process simulator. The description of the bio-oil components has been the main focus of the effort in process modeling at this stage. We have tried to identify key component classes, and representative components within these classes that can be used to test the ability of the process simulator to match the phase behavior of the components.

Prior to developing a model for simulating the processing of biomass derived pyrolysis oils, an attempt to characterize these oils was undertaken. This course of action involved both a survey of the existing literature to identify compounds prevalent in pyrolysis oils, as well as an attempt to use HYSYS, a process simulator package from Hyprotech, to simulate a typical process oil with a few representative compounds for further analysis.

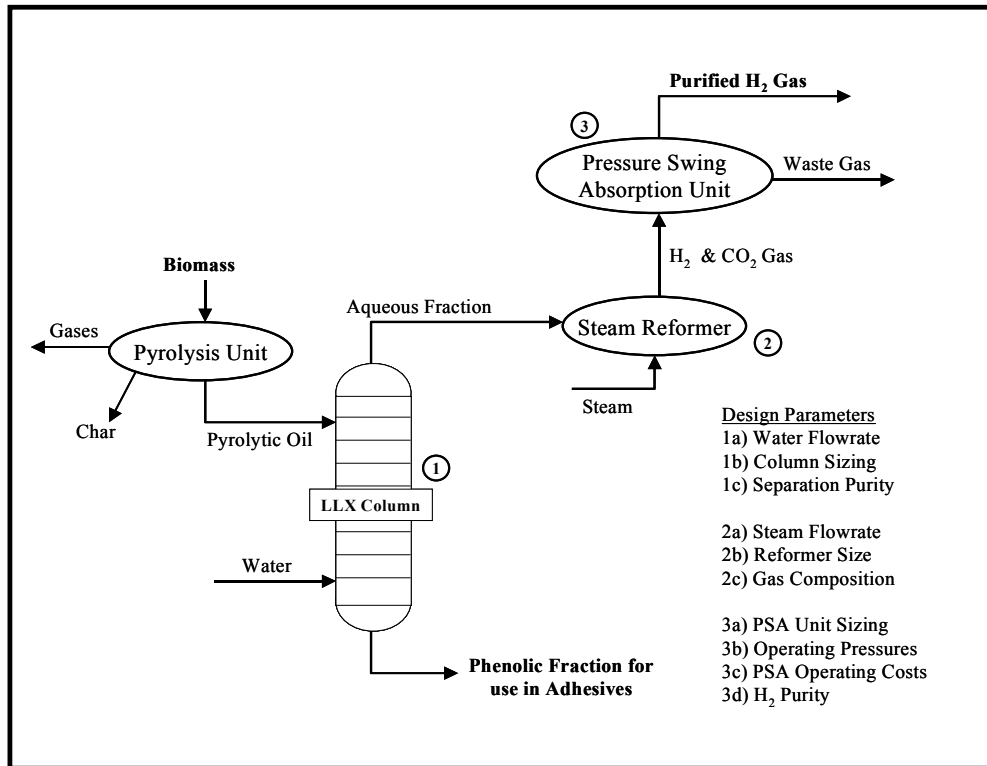


Figure 6. Stage Aqueous Extraction

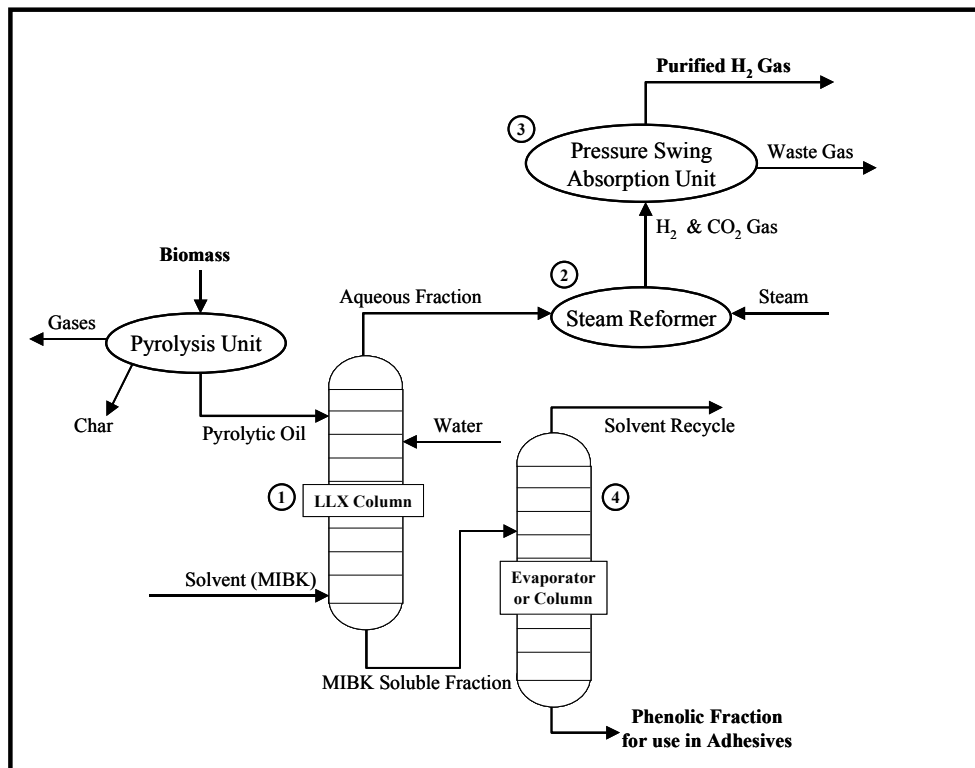


Figure 7. Stage Simultaneous Extraction

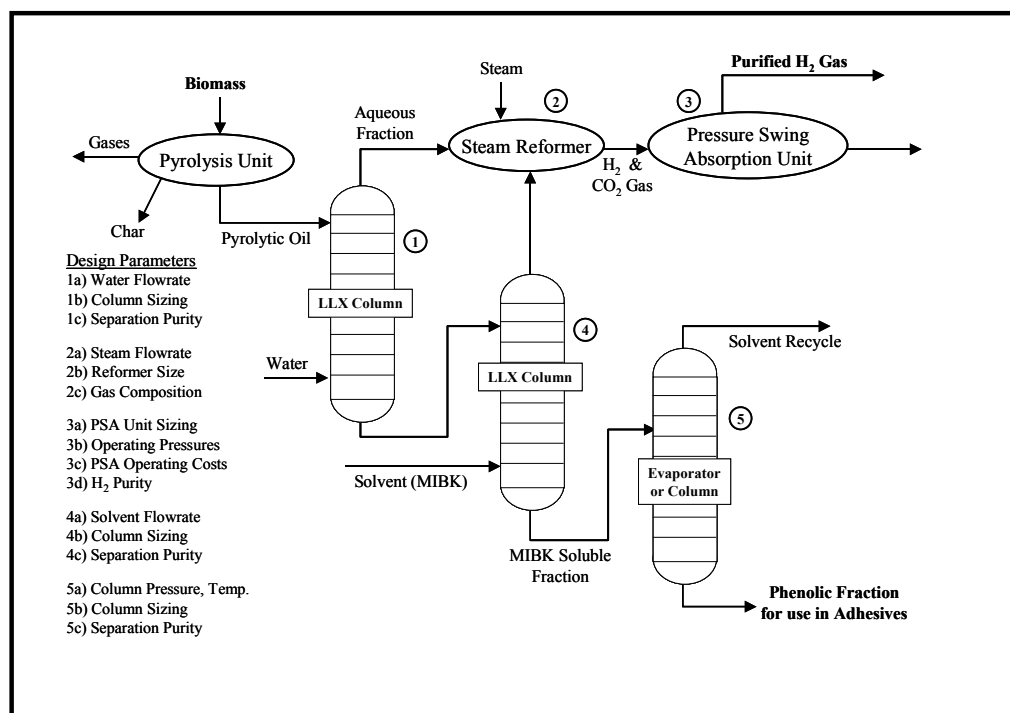


Figure 8. Stage Extraction

In general, the range and variety of chemicals found in pyrolysis oils shown in Table 3, far exceed that of crude oil to which analogies are often drawn. The key difference between bio-oil and crude oil is the prevalence of oxygenated compounds in bio-oil as opposed to fully reduced hydrocarbons in crude oil. However, some trends can still be noted due to the shared biological components common to the majority of plant life from which many pyrolysis oils are derived. In particular, the presence of cellulose and other polysaccharides causes the formation of various carbohydrates in the oils. Similarly, the several types of lignin found in “woody” biomass sources form the basis for most phenolic and aromatic compounds found in pyrolytic liquids [7]. The phenolic compounds are of particular interest and present one of the more feasible economic opportunities for development in the form of phenol based-adhesives. Developing a realistic process model hinges not only on the composition of the phenols present but also on the other various carbohydrates, acids, alcohols and other compounds present in large quantity which must be separated out and directed to the highest value end uses.

In general, the distribution of chemicals in the oil depends not only on the compounds found in the biomass but also on the pyrolysis operating conditions (residence time, temperature, pressure, and type of reactor). To date, no systematic compositional analysis has been undertaken for a large number of compounds at reproducible operating conditions. This situation can be attributed to the large number of possible feedstocks, the interest in particular feedstocks to the exclusion of others being influenced strongly by geographic region and industry, and the early stage of development that exists for bio-oil processing. Development that has been done to date has focused heavily on the processing of wastes associated with the forestry industry [8]. An attempt

has been made to compile a list of compounds common to pyrolysis oils from varying sources in order to create a characteristic bio-oil of “typical” composition.

Table 3. Pyrolysis Oil Composition [8-10]

Acids	Aldehydes	Syringols
formic (methanoic)	methanal (formaldehyde)	syringol (2,6-dimethoxy phenol)
acetic (ethanoic)	ethanal (acetaldehyde)	methyl syringol
propanoic	2-methyl-2-butenal	4-ethyl syringol
hydroxyacetic	Phenols	syringaldehyde
butanoic	phenol	4-propenyl syringol
pentanoic	2-methyl phenol o (o-cresol)	4-hydroxy-3,5-dimethoxyphenylethanone
4-oxopentanoic	3-methyl phenol m (m-cresol)	Mixed Oxygenates
hexanoic	4-methyl phenol p (p-cresol)	glyoxal
benzoic	2,3-dimethylphenol (2,3-xilenol)	Methylglyoxal
heptanoic	2,4-dimethylphenol (2,4-xilenol)	hydroxyethanal
dodecanoic acid	2,5-dimethylphenol (2,5-xilenol)	1,2-dihydroxyethane
Sugars	2,6-dimethylphenol (2,6-xilenol)	propanal-2-one
o-xylose	2-ethylphenol	1-hydroxy-2-propanone
1,6-anhydroglucofuranose	2,3,5-trimethylphenol	2-hydroxypropanal
levoglucosan	Guaiacols	butyrolactone
alpha-D-glucose	guaiacol (2-methoxyphenol)	2,3-pentenedione
fructose	4-methyl guaiacol	1,2-dihydroxybenzene
cellobiosan	4-ethyl guaiacol	1,3-dihydroxybenzene (rescorcinol)
glucose	4-propenyl guaiacol	1,4-dihydroxybenzene
mother oligosaccharides	eugenol	2-hydroxy-3-methyl-2-cyclopentene-1-one
Alcohols	isopugenol	methylcyclopentenone
methanol	4-propyl guaiacol	2-methyl-3-hydroxy-2-pyrone
ethanol	Ketones	hydroxyacetaldehyde
cyclohexanol	2-butanone	4-hydroxy-3-methoxybenzaldehyde
Furans	2-butanone (MEK)	Testosterone
furan	cyclopentanone	Methyl Salicate
2-methylfuran	3-methyl-2-cyclopenten-1-one	Ethylene glycol
2-furanone	2-ethylcyclopentanone	Acetol
furfural (2-furaldehyde)	dimethylcyclopentanone	Acetoin
3-methyl-2(3H) furanone	trimethylcyclopentanone	pyrolytic lignin (water insoluble)
6-methyl furfural		Various tannins
6-hydroxymethyl-2-furaldehyde		Various flavonoids
1,6 anhydroglucofuranose		

From this table of compounds, a select list was developed and is shown in Table 4, that represents both the major classes of compounds, present in typical ratios as well as C/H/O molecule ratios desired for the subsequent process model that will be developed. At this time, the select list of compounds contains the following chemicals:

Table 4. Representative Compounds of Bio-oil for Process Simulation

Representative Compounds	
water	phenol
ethanol	2-methyl phenol (o-cresol)
methanol	2-butanone
cyclohexanol	dodecanoic acid
formic Acid	hypothetical steroid
acetic Acid	hypothetical flavonoid
glucose	hypothetical tannin

The distributions of the compounds are varied based upon the predicted C/H/O ratios for a particular situation within the constraint of reported compound distributions from literature sources. Additionally, total phenolic content is varied but kept near or below the composition of 55 wt%, an achievable value with modern pyrolysis techniques focused specifically on phenolic specific liquid production [9].

Logistics & Overall System Design

The basic goal of this part of the project is to determine the overall system information for evaluating widespread adoption of peanut or other sources of biomass for value-added processing. This required two subtasks. The first is finding specific information for peanut hulls, some of which is summarized below, and some of which is provided in the form of maps showing the distribution of peanut production in southeastern USA. The second is to develop a more generic analysis of the interaction of collection of biomass and the scaling of process cost.

Our current understanding of the southeast region peanut hull market is summarized as follows. Peanut hulls are not traded as a commodity as are peanuts. Hull prices are not reported publicly and are set by the few players (primarily Birdsong and Golden's hull marketing arm). Moreover, these sellers have a large storage capacity so the price and supply of hulls are neither highly seasonal, nor highly correlated with the price or supply of peanuts. There are two major sellers in the southeast, Golden (#1) and Birdsong (#2) and this industry is quite concentrated. Birdsong has 5 plants in the southeast (not including Virginia).

Peanuts are about 20% hulls by weight, and this is a little variable, maybe ranging from 20-22%. Hull density is ~9-10 lb/ft³. Shells are sold in three major forms: loose (unprocessed), ground, and ground then pelletized. Current prices are about \$10-20/ton loose and \$40/ton pelletized, with purchasers generally paying for transport. The hull market is relatively new. New uses for hulls are continuing to arise, causing the price to trend upward. Uses for hulls include: livestock feed, chicken litter, insulation board, metal casting, a medium for pesticides, as well as activated carbon.

While projecting hull prices is difficult due to the market structure, the overall supply of peanuts can be projected based on projections for peanut supply---hulls comprise about 20% by weight of unshelled peanuts. Future prices will likely depend on the development of new uses for hulls and the prices of substitutes for the various uses. Prices are trending up due to increasing demand, as more new uses for hulls are developed. This is a bad combination with the prices for activated carbon possibly trending down, though none of the uses is very high-value, and most have other relatively cheap substitutes. A ceiling on the long-term price of hulls is probably low, but not yet determined.

Facility Location/Allocation Models for Process Scale & Transportation Tradeoffs

The most economically efficient sizing and location for biomass processing facility depend in large part on the geographic availability of the feedstock and raises important issues in the trade-offs between economies of scale to be gained from large processing facilities and the diseconomies of scale for agricultural inputs.

These issues are not yet well addressed in the literature. We are working to understand the relationship between the geographic availability of feedstocks (perhaps peanut hulls) and the optimal number and size of processing facilities, to narrow the parameters for facility location and process design.

Biomass processing is for the moment a low-revenue business. To be economically feasible, it must also be low-cost. Its cost structure is unusual in a few specific ways, most notably, because the overall costs must be low. Additionally, because the inputs to the process are agricultural products, they arise from highly distributed sources, and so the material transportation costs contribute significantly to overall costs. This cost structure can also occur in distribution systems to customers and in reverse logistics systems, e.g. for collecting end-of-life products for recycling or remanufacture.

The literature on facility sizing does not usually account for input transportation costs---the unit prices of inputs are usually assumed to be constant regardless of the quantity demanded by each facility. This does not hold true, however, when additional units of inputs must be transported from larger and larger distances.

The literature on facility location and allocation of capacity, on the other hand, does not usually include explicit consideration of facility costs as a function of either capacity or throughput. Perhaps because sizing decisions are made upstream, without reference to input transportation costs, the facility location/allocation problem is often to locate a given number of new facilities, among existing facilities. Using assumptions that are unrealistic for our application, Love et al [11], shows curves similar to those shown for the “elegant” model, for finding the optimal number of facilities. It is also usually assumed that input sources and output sinks are fixed points. Moreover, the models used in transportation are usually very detail-heavy and specific, making it hard to draw any general conclusions about optimal facility sizing, for example.

When the models in the existing literature on the economics of biomass processing do attempt to quantify transportation costs, they use very location- and application-specific models, often using GIS models, taking destinations as given (does not optimize with respect to location) and their results cannot be generalized. While many of the economic models for biomass processing do not take transportation into account at all, those that do often find it to be a significant contributor to total costs:

- Angus-Hankin et al [12] 20-40% delivered input cost
- Nilsson [13] ~30%
- Gomes et al [14]\$.14-.21/km-ton vs. total delivered price \$18.04-38.23/ton

Figures 9 and 10 show some of the model/simulation predictions.

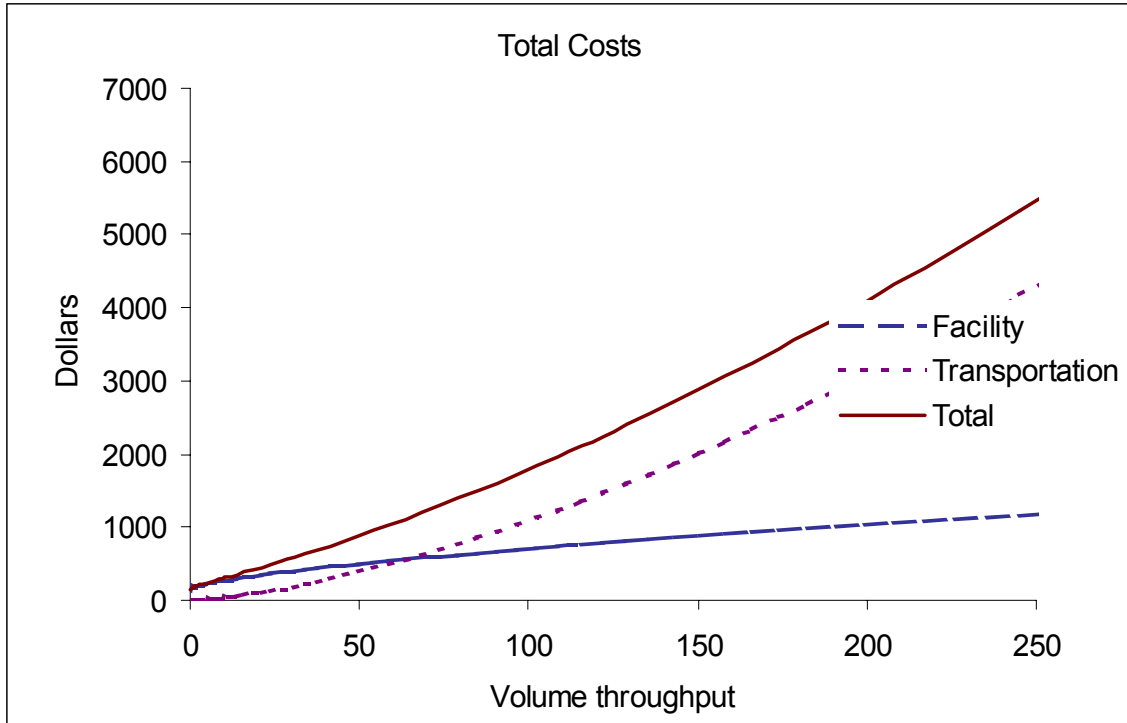


Figure 9. Sample model/simulation prediction of total cost vs. volume throughput.

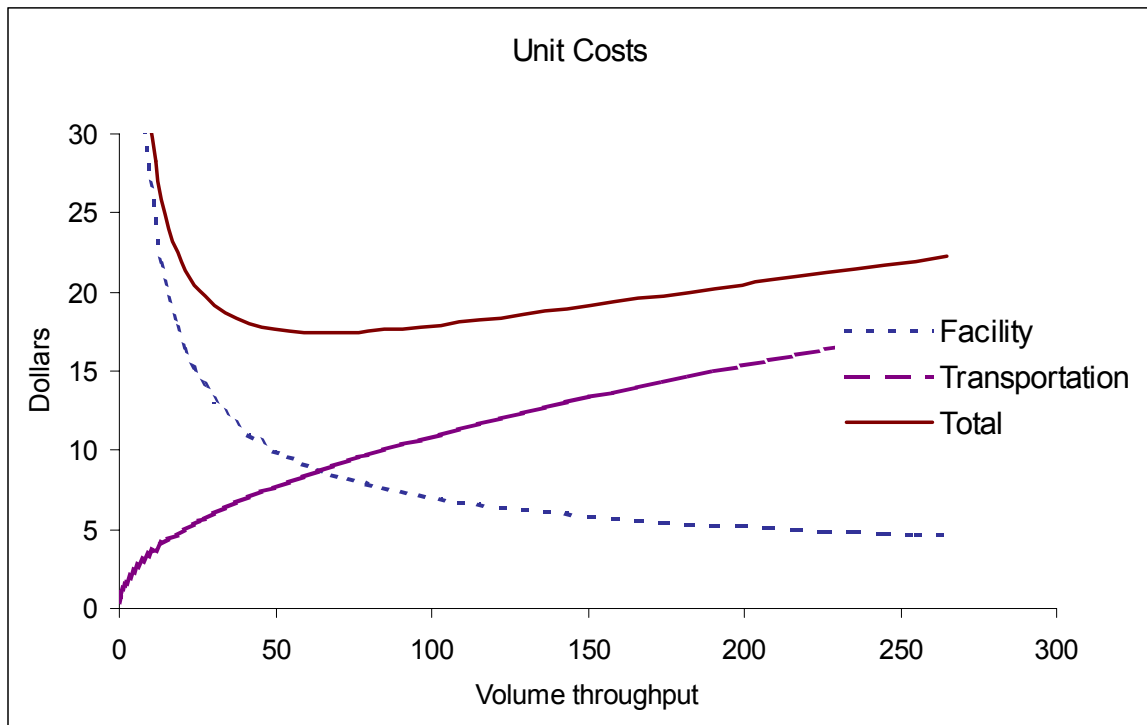


Figure 10. Sample model/simulation prediction of total cost vs. volume throughput.

Reactor Development and Commissioning: Design, Construction and Shake Down of a Catalytic Fluid Bed Reformer Capable of Processing 10-20 kg/h of Pyrolysis Vapors.

The catalytic fluid bed reformer was designed and constructed based on past results with the bench-scale, fluid-bed reactor. The schematic of the reformer is shown in Figure 11. The reactor can process 7-10 kg/h of pyrolysis vapor. The maximum allowable operating temperature and pressure are 900° C and 140 kPa, respectively. The reformer is equipped with fluid bed reactor, vapor and liquid injection, steam (and O₂) injection, internal and external cyclones for disengaging catalyst particles, heat exchanger to recover heat and condense the water vapor, instrumentation, data acquisition, and safety features (alarms, etc.). The product collection line includes a cyclone that captures fine catalyst particles and possibly, char generated in the process and two heat exchangers to condense excess steam. The Inconel reactor with a porous material distribution plate is placed inside a three zone electric furnace. Commercial nickel-based catalyst ground to particle size 300-500 μ is used in the reactor. The catalyst is fluidized using superheated steam, which is also a reactant in the reforming process. The initial shakedown of the reactor is being performed at NREL's TCUF.

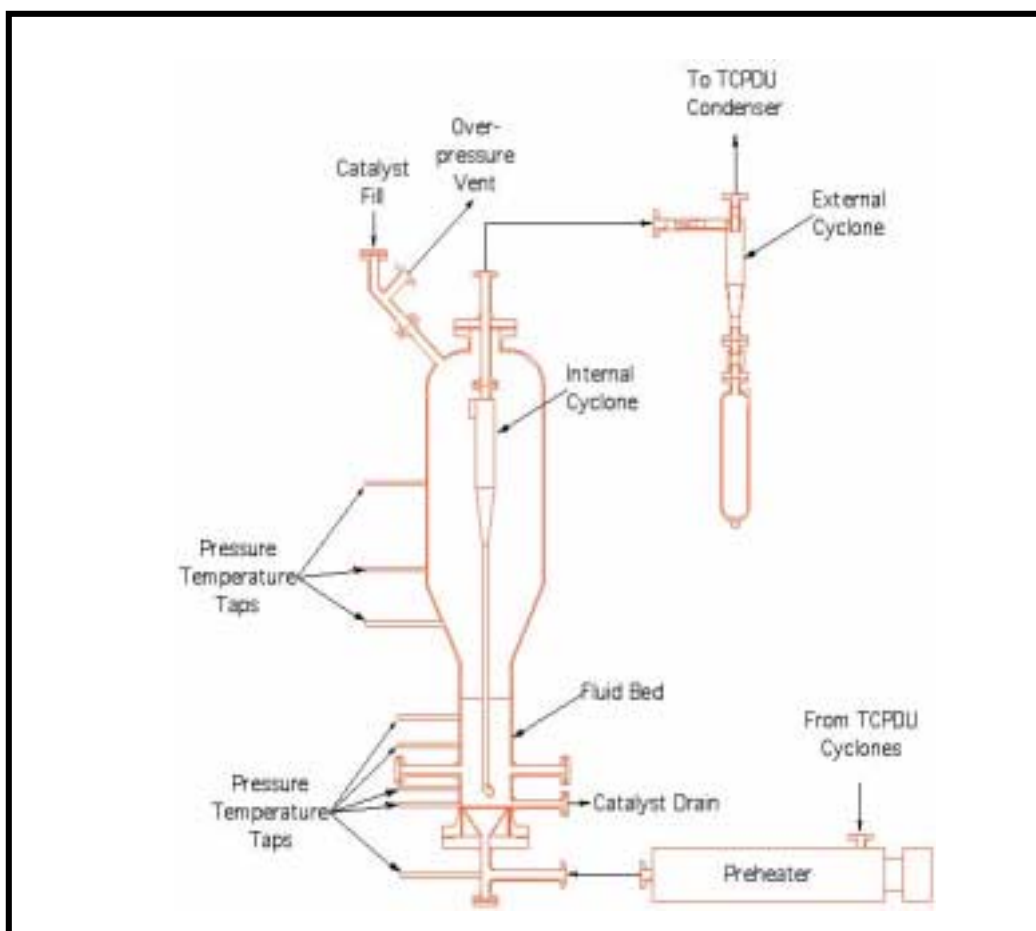


Figure 11. Schematic of the fluid bed reformer

For the initial runs, a commercial nickel-based catalysts from UCI is being fluidized using superheated steam which serves as a reactant in the reforming process. A 10-20 kg/hr fluid bed pyrolysis unit at TCUF is able to feed the steam-reforming unit for the shakedown. The steam reforming reactor system was shipped to NREL in March 2001 and installed in April 2001. Two tons of pelletized peanut shells were shipped from Scientific Carbons to NREL for the tests. The catalyst, in a form suitable for fluid bed, is not commercially available and hence has been purchased from United Catalysts. Initial tests are monitoring catalyst fluidization and attrition under simulated conditions. Methane reforming is being used to verify catalyst performance. Subsequent runs with pyrolysis vapors will be performed until performance matches previous work at the bench scale.

The process conditions and description for the hydrogen reformer system are as follows:

Process Conditions

Maximum Temp: 900° C (1650° F)

Maximum Pressure: 140 kPa (20 psig)

Process Gas Composition

Steam: 16 kg/hr (35 lb/hr)

Hydrogen: 1.2 kg/hr (2.6 lb/hr)

CO₂: 14 kg/hr (31 lb/hr)

CO: 1 kg/hr (2.2 lb/hr)

Description of Reformer Vessel

Vertical Reformer Vessel (Figures 12 and 13)

- Constructed entirely of Alloy 800 except for the exterior flanges.
- Exterior flanges N1 and the bottom closure is 316 stainless overlaid with Alloy 800. Other exterior flanges are 316 stainless steel.
- A Carbon steel support structure with the approximate dimensions of 52” wide and long and 64” tall and painted with a high temp coating system.
- External cyclone and the catch vessel are also constructed as the same materials as the reformer vessel and includes:
- A high temp ball valve is located between the external cyclone and the collection vessel.

The reformer vessel, the external cyclone and its catch vessel are designed, fabricated, inspected, tested and stamped in accordance with the *ASME Boiler and Pressure Vessel Code, Section VIII, Division 1, 1198 Edition*, for 20 psig at 1650°F with no corrosion allowance.

Preheater Vessel

- 3” pipe size x 59” overall length circulation preheater with 1.5” class 300 flanged inlet and outlet connections and mounting supports for horizontal mounting
- Vessel fabrication of 316H stainless steel.
- Three tubular heating elements sheathed in Inconel 600 and designed for operation at 240 volts a.c, 4 kW maximum.
- NEMA 4 terminal housing

- Hi-Limit type K thermocouple is attached to the vessel shell and Process type K thermocouple is located near the outlet.
- The preheater vessel is thermally insulated with 2” TR-19 insulation and two 2” layers of Calcium Silicate insulation
- The preheater vessel was designed, fabricated, inspected, tested and stamped in accordance with the *ASME Boiler and Pressure Vessel Code, Section VIII, Division 1, 1198 Edition*, for 50 psig at 1450°F with no corrosion allowance.

Thermal Contact Protection

- The preheater vessel, reformer vessel, external cyclone (Figure 14) and the catch vessel are provided with insulation and/or external guarding to prevent accidental human contact with surfaces having a temperature greater than 150° F during normal operation.
- The carbon steel support structure for the vessel provides support for the preheater vessel and ceramic wool insulation with a further covering of expanded metal.

Reactor Vessel Heaters for Section 1, 2, and 3

- 2-piece, semi-cone shaped ceramic fiber heater
- Dimensions are 26” inside diameter x 36” section 1; 18” inside diameter x 14.25” long for section 2, and 12” inside diameter x 27.5” long for section 3
- Designed for operation at 240 volts a.c.

Control Panel for Preheater and Reformer Heaters

- As designed and built by Watlow Heaters
- 56 kW, three phase
- Four Watlow Din-A-Mite power controllers
- Four Watlow Series F4 Process Controls with cascade software
- Four Watlow Series 146 Hi-Limit Devices for over temperature protection
- On / Off / Set up Control selector switch with pilot light
- Hi-limit pilot lights with common reset pushbutton
- Mounted in a 36” high x 24” wide x 10” deep NEMA 12 electrical enclosure with filtered cooling fans
- Controls wired and tested at Watlow factory

The above reformer system, designed by the project team, was constructed by an outside professional firm through subcontracting. A photograph of the final product is shown in Figure 15.

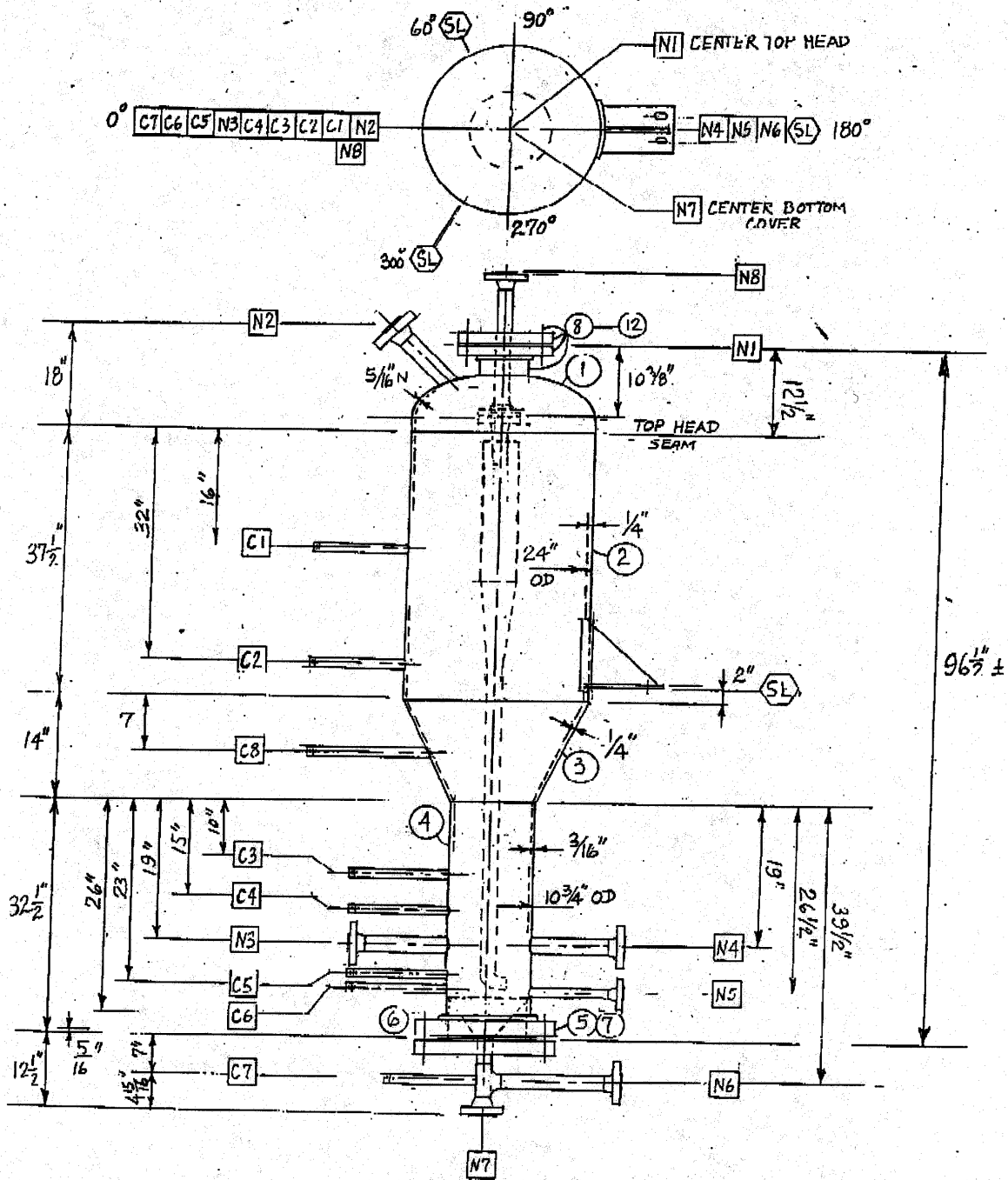


Figure 12. Vertical Reformer Vessel

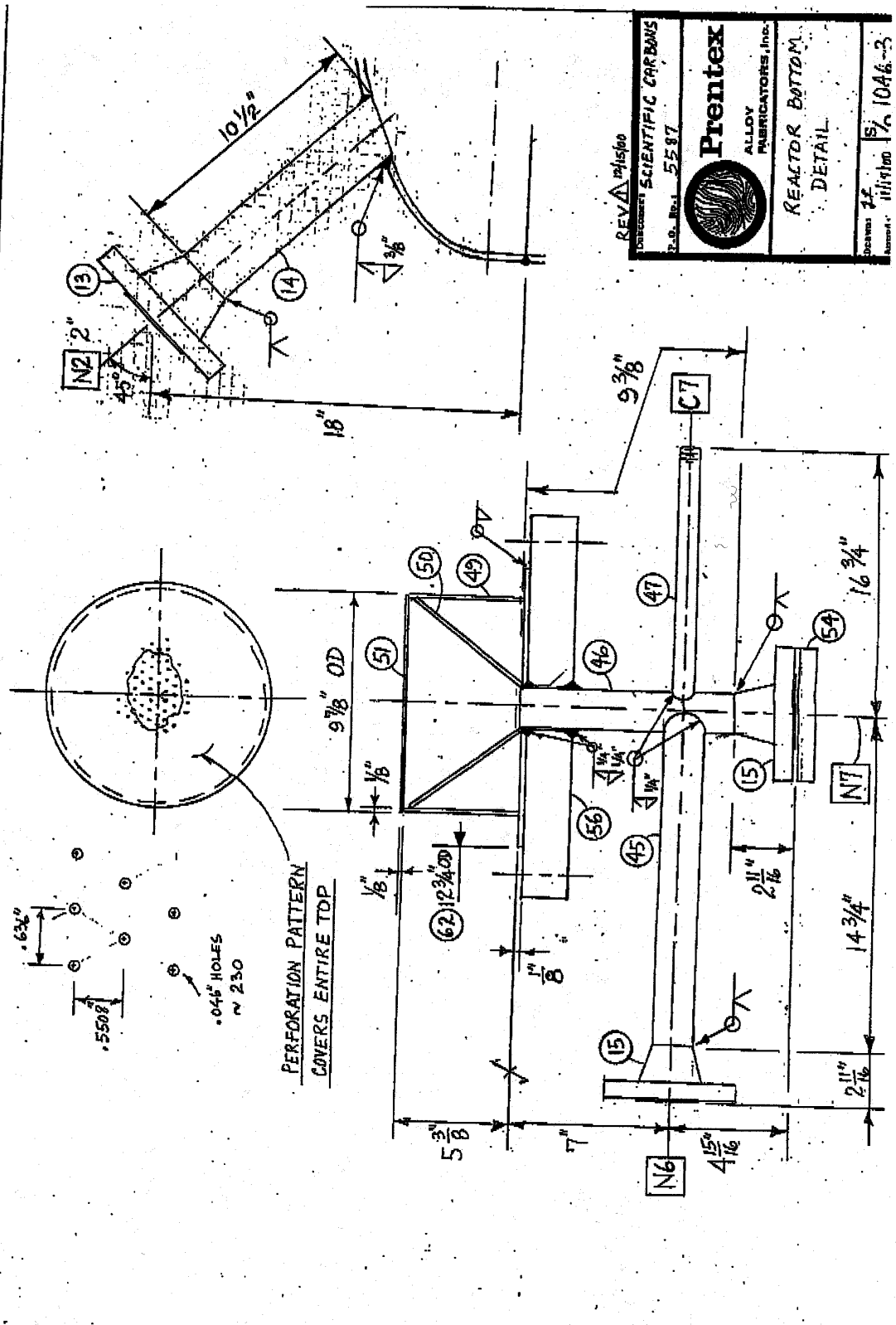


Figure 13. Reactor Bottom Detail

Figure 14. Internal Cyclone Detail



Figure 15. Fluidized-bed catalytic reactor

Preparation for long-term testing at Scientific Carbons.

Work has begun on the location of the interface and the operating conditions. An assessment is being made of the impact of the long-term steam reforming tests on the mass and energy balance of the current Scientific Carbons operation. The existing pyrolysis facility owned and operated by Scientific Carbons, will be modified as follows:

- Design, construction and addition of a slip stream capable of withdrawing 10-20 kg/h of pyrolysis vapors
- Installation of instrumentation and on-line monitoring and data acquisition for the above system for product stream analysis, and process mass and energy balance.

The operation of the system at the Scientific Carbons Inc. site will not occur in Phase 1, but would begin in the second year under a Phase 2 project. We have prepared the necessary analytical systems to monitor the transportation system performance.

Preparation for Hydrogen Storage and Utilization

We have begun analysis of how storage will be accomplished on the Scientific Carbons site. Past approaches to the storage of hydrogen in mixtures with compressed natural gas are being reviewed and calculation of mixture limits are being made. Other storage options are being explored that will meet the needs of the planned demonstration. Model system testing will be performed. The design of a storage system is being done and include:

- Pressure Swing Absorption (PSA) system for the purification of hydrogen and the separation of CO₂
- Holding tank (or another device) for H₂ storage
- Compression station to charge the H₂ into blends with CNG
- Instrumentation and on-line monitoring and data acquisition for the above system

In preparation for hydrogen utilization, our activities in Phase 1 have included identifying the community partner and working with that partner to define the transportation fleet application. The utilization system design will then occur including modification to a refueling station and the vehicle(s). Up to 30% of hydrogen by volume could be stored in this way and hence the blend would enable the hydrogen produced to be used in a convectional CNG bus without major modifications. To simplify the start up of the project, the system would begin with commercial sources of hydrogen.

Environmental and Technical Evaluation

An important part of the decision to implement a hydrogen transportation technology will be documentation and evaluation of benefits and system performance. We have begun this evaluation in conjunction with the planning of the bus demonstration.

Partnership Building and Outreach

We coordinated the fuel utilization demonstration by working with a local municipality to operate a vehicle, such as a transit bus, under normal operation. Work has begun with local parties to participate in the transportation demonstration. We have received a letter of interest in accepting partnership role from Albany State University (ASU) to host the hydrogen bus demonstration in the city of Albany Georgia. Albany Water, Gas & Light Commission, a municipally owned utility, has expressed interest in the use of renewable hydrogen for power generation. Initial meetings with Dougherty County officials to propose a non-operational role were held and they are interested in participating. Collaboration with researchers and modelers at JPL was initiated. In addition, close cooperation with other related projects at NREL and JPL is constantly maintained. A special interest among the partners is the identification of other co-product options for expanded deployment opportunities. Emissions monitoring will be performed to assess the environmental impact of the hydrogen blend. A social acceptability study will be

performed to assess how the community views the benefits and risks of this new technology.

Future Work

The approach for the next stage is to address the remaining engineering research and development questions related to the conversion of pyrolysis vapors and/or bio-oil to hydrogen, so that a demonstration of the overall concept of biomass to hydrogen can be successful. The use of bio-oils derived from slow pyrolysis of biomass in a reforming operation and the direct coupling of vapors from pyrolysis to steam reforming have not been previously attempted. Process research is required to identify the best operating conditions. Catalyst performance and lifetime will be assessed and data collected on catalyst regeneration. This information will be used in the development of the catalyst regenerator. The other tasks will continue to focus on feedstocks, hydrogen storage options, fuel utilization and partnership development, and are essential to the development of a demonstration of the technology. This will allow commercial evaluations of the concept to be made.

Specific future work and milestones include: gather data for estimating model parameters and run logistical model for Georgia with peanuts as feedstock; quantify importance of transportation costs in biomass processing and identify other biomass feedstocks available in Georgia; perform experiments of liquid-liquid equilibrium on representative compounds found in bio-oils; setup, shakedown and operate continuously reactor at Scientific Carbons site; design hydrogen storage and utilization system for transportation demonstration; cost-effective local bus demonstration on hydrogen utilization; develop a fuel cell based hydrogen utilization effort with the Albany Water, Gas & Light Commission; establish additional non-operational partners in Y2 (2001/2002) & Y3 (2002/2003); and incorporate hydrogen technology in student training and education at Clark Atlanta University.

Conclusions

Biomass as a product of photosynthesis is a renewable resource that can be used for sustainable production of hydrogen. However, direct production of hydrogen from biomass by gasification/water-gas shift technology is unfavorable economically, except for very low cost feedstocks and very large plants. Our approach proposes an alternative strategy with potentially better economics resulting from combined production of hydrogen with valuable co-products. The concept is based on a two-stage process: slow pyrolysis of biomass to generate activated carbon and bio-oil, and catalytic steam reforming of the oil or its fractions to produce hydrogen. The design and utilization of the fluid-bed reformer was completed and shakedown of the reactor is to be completed by Summer 2001. Phase 2 of the project will focus on the long term catalyst testing at Scientific Carbons.

References

1. The Green Hydrogen Report: The 1995 Progress Report of the Secretary of Energy's Hydrogen Technical Advisory Panel, May 1995, DOE/GO-10095-179 DE95009213.
2. Wang, D., S. Czernik, D. Montané, M. Mann, and E. Chornet, 1997, I&EC Research, 36, 1507-1518.

3. Wang, D., S. Czernik, and E. Chornet, 1998, "Production of Hydrogen from Biomass by Catalytic Steam Reforming of Fast Pyrolysis Oil", *Energy&Fuels*, 12, 19-24.
4. Mann, M.K. 1995. "Technical and economic analyses of hydrogen production via indirectly heated gasification and pyrolysis," in *Proceedings of the 1995 Hydrogen Program Review*, Vol. 1, NREL/CP-430-20036-Vol. 1, pp. 205-236.
5. Wang, D., D. Montané, E. Chornet, 1996, "Catalytic Steam Reforming of Biomass-Derived Oxygenates: Acetic Acid and Hydroxyacetaldehyde", *J. Appl. Catal. A: General*, 143, 245-270.
6. Czernik, S., D. Wang, D. Montané, E. Chornet, 1997, "Catalytic Steam Reforming of Biomass-Derived Fractions from Pyrolysis Processes. *Developments in Thermochemical Biomass Conversion*", Eds. Bridgwater, A.V. and Boocock, D.G.B., Blackie Academic & Professional, pp.672-686.
7. Goldstein, Irving S., 2000, "Composition of Biomass." *Organic Chemicals from Biomass*. Boca Raton: CRC Press.
8. Milne, T., et al. "A Review of the Chemical Composition of Fast-Pyrolysis Oils from Biomass." Notes from the NREL, Center for Renewable Chemical Technologies and Materials.
9. Roy, et al. U.S. Patent 6,143,856., 2000, "Process for the production of phenolic-rich pyrolysis oils for use in making phenol-formaldehyde resole resins." .
10. Piskorz, J., et al., 1998, "Composition of Oils Obtained by Fast Pyrolysis of Different Woods." *Pyrolysis Oils from Biomass: Producing, Analyzing, and Upgrading*. Washington, D.C.: American Chemical Society.
11. Packdel, H. & Roy, Christian., 1998, "Chemical Characterization of Wood Pyrolysis Oils Obtained in a Vacuum-Pyrolysis Multiple-Hearth Reactor." *Pyrolysis Oils from Biomass: Producing, Analyzing, and Upgrading*. Washington, D.C.: American Chemical Society.
12. Love, Robert F., Morris, James G., and Wesolowsky, George O., 1988, *Facilities Location: Models & Methods*, North Holland, New York.
13. Angus-Hankin, C., Stokes, B., and Twaddle, A., 1995, "The Transportation of Fuel Wood from Forest to Facility," *Biomass and Bioenergy* v. 9(1-5) p. 191-203.
14. Nilsson, D., 1999, "SHAM---a simulation model for designing straw fuel delivery systems. Part 2: model applications," *Biomass and Bioenergy* v.16, p. 39-50.
15. Gomes, Raquel S., Wilson, Paul N., Coates Wayne E., and Fox, Roger W., 1997, "Cotton (Gossypium) plant residue for industrial fuel. An economic assessment," *Industrial Crops and Products* v. 7, p. 1-8.

ENGINEERING SCALE UP OF RENEWABLE HYDROGEN PRODUCTION BY CATALYTIC STEAM REFORMING OF PEANUT SHELLS PYROLYSIS PRODUCTS

**Robert Evans, Stefan Czernik, Esteban Chornet, Calvin Feik, Steven Phillips
National Renewable Energy Laboratory
Golden, CO 80401**

Abstract

Renewable hydrogen may be produced in the near term at a cost competitive with natural gas reforming by integrating hydrogen production with existing industrial utilization of agricultural residues. Researchers at NREL are assisting a team of industrial and academic organizations from Georgia in adapting NREL's steam reforming process to a process for making activated carbon from densified peanut shells.

The thermochemical user's facility (TCUF) at NREL is the site for the initial shakedown of the scaled-up reactor. It will be interfaced with the 10-20 kg/hour fluidized-bed fast pyrolysis system and take advantage of NREL's process chemical analysis and computer control and monitoring capabilities. Working with the Georgia team, the scaled-up reactor was designed, built and shipped to TCUF for installation and initial operation before being shipped to the industrial site in Georgia for Phase 2 testing.

The hydrogen produced will be blended with CNG and used to power a bus in the nearby city of Albany, GA in Phase 3 of this project. This integrated strategy will demonstrate the potential impact of hydrogen and bioenergy on the economic development and diversification of rural areas.

Introduction

Near-term production of renewable hydrogen from biomass requires a co-product strategy to compete with conventional production of hydrogen from the steam reforming of natural gas (Chornet et al. 1994; Spath and Mann 1998). The production of hydrogen by the processing of pyrolysis products that are produced as a by-product of activated carbon is one path that is possible to demonstrate in the near term. NREL is supporting a team of organizations that are carrying on the demonstration of the NREL-developed technology. The research team includes:

- **Clark Atlanta University** – capabilities in steam reforming, combustion science, and environmental science.
- **Scientific Carbons Inc.** – a company developing innovative processes to make activated carbon from agricultural residues.
- **Enviro-Tech Enterprises, Inc.** - a technology transfer company whose goal it is to establish public/private partnerships to create jobs via sustainable technology.
- **Georgia Institute of Technology** – involving faculty with capabilities in systems analysis, and environmental and energy technologies.

Objectives

This project has these specific objectives in support of the subsequent demonstration of the reformer technology in Georgia.

- To lead the design of the 10 kg/hour fluid bed catalytic steam reformer system.
- To conduct the system shakedown at NREL by interfacing with the Thermochemical Process Development Unit (TCPDU) in the TCUF. NREL's experience with the development of the technology at the bench scale and the available analytical capabilities of the TCUF will allow the reactor to be characterized for the subsequent operation on a slipstream of the Scientific Carbons pyrolysis products.
- To participate in the design of the process modifications that will be necessary to integrate the reactor safely and efficiently in the existing Scientific Carbons process in Phase 2.
- To support the partnership development that will be necessary for the bus demonstration.
- To identify, with the Georgia Institute of Technology, other biomass resources in the region that could be used to produce hydrogen in conjunction with the Scientific Carbons process or by other integrated biomaterial processing technologies.

Catalytic Steam Reforming Development Status

NREL began the development of the catalytic steam reforming process in December 1993 (Chornet et al. 1994). The strategy is based on producing hydrogen from biomass pyrolysis oils in conjunction with other products that have greater value and can reduce the cost of hydrogen. The original concept was that the pyrolysis oil could be fractionated into two fractions based on water solubility. The water-soluble fraction is to be used for hydrogen production and the water insoluble fraction could be used in adhesive formulations (Kelley et al. 1997). Although this option remains viable, commercial deployment opportunities for hydrogen linked to the adhesives co-products are still not near-term. Hence, other opportunities had to be developed based on the co-product strategy.

The conversion of biomass to activated carbon is an alternative route to hydrogen with a valuable co-product. Slow pyrolysis is used in the first step of the activated carbon process to maximize the yield of charcoal and organic vapors are produced as a by-product in 30 to 50% yield. Southwest Georgia was identified as an excellent opportunity because of the importance of agriculture, the forest product industry and the need for zero-emission transportation fuels in the Atlanta area. Scientific Carbons Inc. in Blakely GA uses pelletized peanut shells as the feed material for the production of activated carbon. They feed up to 1000 kg/hour of the densified peanut shells to a two-stage process producing charcoal that is further processed in a kiln to produce activated carbon. The vapor by-products are currently used for boiler feed. The team submitted a successful proposal to the U.S. DOE's Hydrogen Program to demonstrate the steam reforming process over a three-year period. Scientific Carbons Inc. facility in Blakely, Georgia will be used as the development site. A slipstream of pyrolysis vapors produced in the 1000 kg of feed/h continuous pyrolysis unit will be used for the long-duration steam reforming tests.

Conversion Technology

Over the past four years, NREL has developed the technology for the generation of hydrogen from biomass and agricultural residue based on the pyrolysis of biomass to form a bio-oil that can be subsequently converted to hydrogen via catalytic steam reforming and shift conversion. The NREL approach has the potential to be cost-competitive with current commercial processes for hydrogen production. The process has been demonstrated at the bench scale using model compounds and the carbohydrate-derived fraction of bio-oil (see Chornet et al. 1994, 2001).

Recent laboratory work has demonstrated the feedstock flexibility with the processing of pyrolysis oil fractions from different feedstocks as well as other aqueous biomass streams such as glycerine from biodiesel production, trap grease, and wood hydrolysis effluents (Czernik et al. 2001).

Catalyst life is promising with run times in a two-inch fluid bed reactor of over 100 hours. Systematic studies of variation in catalyst composition have shown that commercial steam reforming catalysts perform optimally for the conversion (Garcia et al. 2000). However, physical attrition is a problem since these catalysts are not manufactured for fluid bed operation. The catalyst is prepared by grinding and sieving to the required particle size for fluidization. Losses of approximately 5% per day of operation have been reported in the small reactor (Chornet et al. 2001).

Results

Design and Construction of Catalytic Fluid Bed Steam Reforming Reactor

Based on the results from the 5-cm bench scale fluid bed catalytic steam reformer reactor, NREL researchers worked with the Clark Atlanta team (Abedi et al. 2001) to design a reactor that would process 10-20 kg/ hour of pyrolysis products. A schematic of the reactor is shown in Figure 1. The construction was completed in March 2001. The reactor will be operated with the NREL Thermochemical Users Facility (TCUF) pyrolysis unit in the summer of 2001. In Phase 2 of the project, the unit will be shipped to Blakely, Georgia and run on a slipstream of the Scientific Carbons process stream.

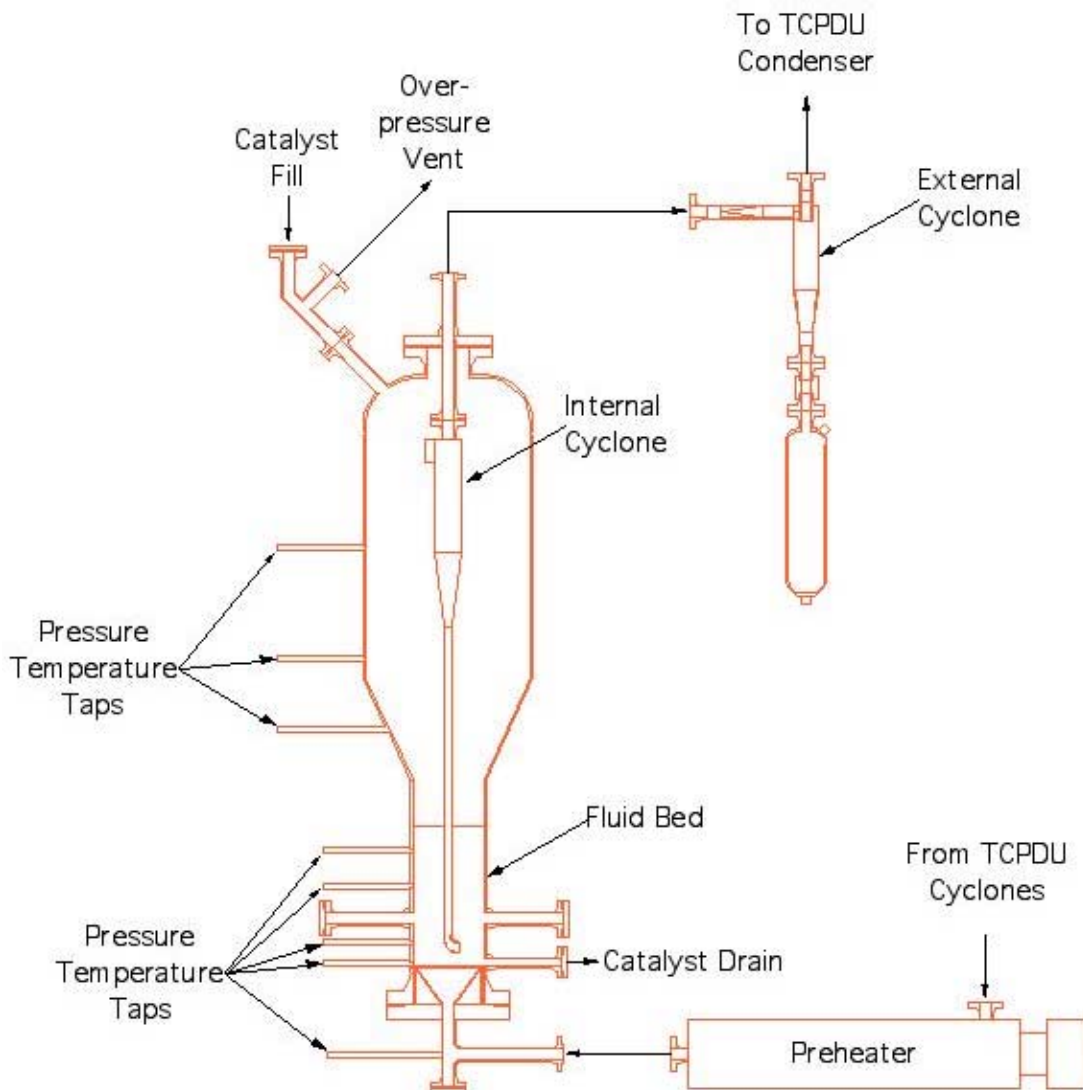


Figure 1. The Catalytic Fluid Bed Steam Reforming Reactor. Installation and Shakedown of the Reactor at NREL

The TCUF at NREL is designed to assist bioenergy technology developers in the testing of thermochemical process concepts by interfacing key unit operations in the existing TCUF facility. This approach minimizes risk and disruption by taking advantage of NREL's process control systems and analytical capabilities, which would not be available for shakedown or proof of concept in an industrial environment. By performing the initial system tests at NREL, the expertise of the NREL researchers and the state-of-the-art analytical equipment of TCUF can be used to monitor and optimize the system performance. The 20-kg/hr fluid bed pyrolysis unit at TCUF will be used to feed the steam reforming unit for the shakedown. A photo of the fluid bed unit is shown in Figure 2.



Figure 2. The Fluid Bed Pyrolysis Reactor.

A schematic of the unit operations that will be used is shown in Figure 3. Preheated steam is used to fluidize the sand bed and ground peanut shell pellets are metered into the bed with a screw feeder. An internal cyclone (not shown in Figure 3) removes most of the sand and large

char particles before the gases are transported through a thermal cracker, which can be used for two-stage gasification. In this work the thermal cracker and all down stream operations before the reformer will be kept at 400°C to prevent physical condensation of the vapor and minimize thermal cracking. However, some tests will be done in the reforming work to determine how vapor-phase composition affects steam reforming efficiency. Char is separated in the two cyclones. The steam/vapor stream then enters a preheater that raises the temperature to the desired reforming temperature. The reformer is equipped with external electrical heaters to maintain the reactor at temperature during the endothermic steam reforming operation. The reformer also has an internal cyclone as well as an external cyclone. The reformed products are next passed to the spray scrubbers and a cold wall condenser before passing through a coalescing filter to remove aerosols. The condensable effluents will be analyzed and related to operating conditions and time on stream. This will be important in determining the operating procedures that will be used in Phase 2 operation.

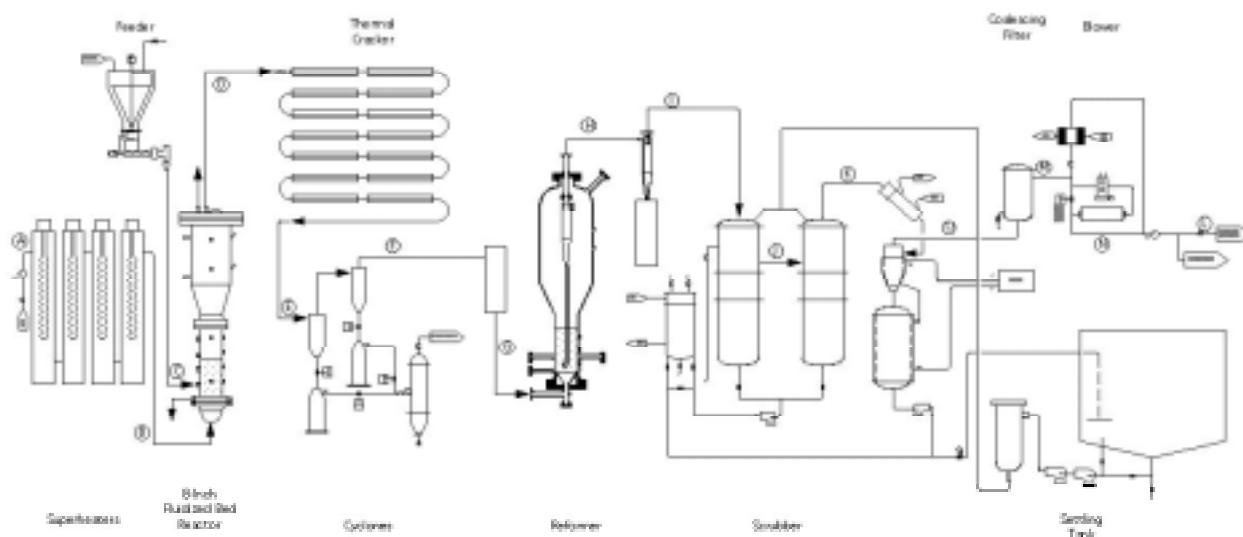


Figure 3. Process Flow Sheet for the Shakedown of the Steam Reforming Reactor in the Thermochemical Process Development Unit.

The system will be run in three modes: catalyst activation, reforming, and catalyst regeneration. In the initial activation mode, hydrogen and steam will be used to reduce the catalyst. The catalyst will then be first tested with methane to verify activity and to shake down the physical operation of the bed.

The estimated process conditions and compositions are shown for four key positions (refer to Figure 3) in the reforming mode in Table 1: D, after the pyrolysis unit; G, after the preheater and before the reformer; H, after the reformer; and M, after the scrubbing system. The molar gas composition is also shown for position M.

Table 1. Process Mass Flows at Several Key Positions in the Reforming Process. (Refer to Figure 3)

Process Site	D	G	H	M	M
Temperature, C	500	800	850	12	12
Pressure, psig	10	8.25	7	5.5	5.5
Flow Rate	Kg/hr	Kg/hr	Kg/hr	Kg/hr	Mol/hr
Biomass	0	0	0	0	0.0
Steam or water	30.9	30.9	27.2	0.0	0.0
Nitrogen	0.1	0.1	0.1	0.1	0.0
Hydrogen	0.0	0.0	0.7	0.7	0.4
Carbon Monoxide	0.3	0.3	0.8	0.8	0.0
Carbon Dioxide	0.7	0.7	6.2	6.2	0.1
Methane	0.0	0.0	0.5	0.5	0.0
Pyrolysis Vapors	3.4	3.4	0.0	0.0	0.0
Char/Ash	1.8	0.1	0.1	0.0	0.0
Total	37.2	35.5	35.6	8.3	0.6

The catalyst is not commercially available in a form suitable for a fluid bed, so it was commissioned from Süd-Chemie (formerly United Catalysts) who prepared the required size fraction by grinding a catalyst used for packed bed methane steam reforming.

Preparation for Installation at the Scientific Carbons Site in Phase 2

NREL is supporting the work on the preparation for the testing that will occur in the second year at the industrial site. The existing pyrolysis facility owned and operated by Scientific Carbons, will be modified as follows:

- Design, construction, and addition of a slip stream system capable of withdrawing 10-20 kg/h of pyrolysis vapors
- Installation of instrumentation and on-line monitoring and data acquisition for the above system for product stream analysis, and process mass and energy balance.

In preparation for this task NREL researchers have designed a probe that will be installed on the Scientific Carbons pyrolysis reactor at the site for the interface to monitor product composition over time. Samples of condensate will be taken for chemical analysis and could be used for bench-scale steam reforming tests. The objective is to better understand the range of composition that will be experienced due to variation in process parameters, such as temperature and pressure. Installation and operation of the probe will occur during the next production run at the Blakely facility.

Cost Analysis for Hydrogen Production from Alternative Biomass Feedstocks

Feedstock issues, such as supply, cost, logistics and the value of coproducts, are major factors in the cost-effectiveness of the hydrogen production process. In this task, NREL is working with the project partners to develop decision models for selecting among feedstock, process, and deployment alternatives. Of particular interest are peanut shells supply and cost projections and the evaluation of other agricultural residue feedstocks available in the same geographical area.

In order for biomass-to-hydrogen to make a significant energy impact, multiple feedstocks will have to be used in combination with realistic markets for co-products. Activated carbon from peanuts is an excellent starting point. Approximately 750 million pounds of shells are produced in the United States with 45% of these produced in southwest Georgia. Using the yields for the activated carbon by-product scenario, this represents a hydrogen yield of approximately 5 trillion BTUs. If this were to be compared to the transportation use in the Atlanta area it would represent about 1% of the total. Therefore, for hydrogen from biomass to make a significant impact, other feedstocks will have to be developed in time. In the southwest Georgia region the list includes cotton gin trash, peach pits and pecan shells, all of which could be used for activated carbon production. Other feedstocks could be developed in other region of the state, such as wood wastes and residues from the textile industry. Ozyurt and Realff (1999) have addressed the logistics of deployment considering volume and distribution of feedstocks.

The development of new crops is an important part of the bioenergy and biomaterials initiative (Biomass R&D Board, 2001). The project team met with representatives from the Federation of Southern Cooperatives, Albany State University, Fort Valley State University, and the Albany Public Utility Commission to discuss the project and the participation of these local groups. The Federation represents 25,000 African-American farmers in the southern states. They are interested in developing new crops and new uses for crop residues. Fort Valley, a land grant HBCU (Historically Black College and University), is also interested in the same topic. Albany State will participate in the project by providing students and faculty to assist in the Phase 2 operation of the reformer in nearby Blakely and by hosting the utilization of the hydrogen in their campus transportation system. Albany Power will explore ways that they may participate in the demonstration. NREL is arranging to have students from Clark Atlanta, Fort Valley, and Albany State participate in the shakedown of the reactor at NREL this summer.

The economics of hydrogen and co-product production from fast pyrolysis liquids have been assessed for an adhesive co-product, resulting in a selling price of hydrogen in the range of \$6-8/MBTU (Spath and Mann 1998). For this slow pyrolysis process used to produce charcoal for conversion to activated carbon, a preliminary economic analysis (Putshe 1999) on the base case process assumes utilization of all of the pyrolysis vapors (225kg/hr) at the current scale of the Scientific Carbons process. The pyrolysis vapor was assumed to be available at \$2.56/GJ, a value that is roughly 90% of its fuel value (assuming an energy equivalence to natural gas at \$2.50/GJ). The analysis also assumed that steam would be produced in the reforming operation. A credit based on \$3.50/1000 lbs. of steam was assumed. Using the above assumptions, the total capital investment for the additional equipment to modify the existing facility to produce hydrogen from the pyrolysis off-gas is estimated at \$1.4 million. For an annual hydrogen production rate of 4.4 million Nm³, the selling price of hydrogen is estimated to be \$9.51/GJ.

The hydrogen selling price for a fuel cost of \$1.28/GJ (i.e., 45% fuel value) is \$7.78/GJ. Using a no-cost bio-oil, the selling price for the hydrogen is \$6.05/GJ. These price ranges are very promising considering that the economics were performed for a very small-scale operation.

Summary and Future Work

The Steam Reforming of Biomass Pyrolysis oil, when integrated with the production of high value products, is a promising near-term approach to the production of renewable hydrogen. Based on bench-scale work at NREL, a team from Georgia is utilizing the NREL TCUF and its staff to develop a 10-20 kg/hr scale reactor that will be operated at NREL this year before being run at the production site in Georgia on densified peanut shells. The application in Georgia is at a plant that makes activated carbon from peanut shells and has pyrolysis by-products available for conversion. The key technical goals for the shakedown at NREL are to ensure the safety of the reactor and obtain preliminary performance data on the catalyst, especially physical attrition and deactivation.

In Phase 2, the reactor will be tested on the pyrolysis vapors produced in the first step of the activated carbon process. An interface system is being designed this year for construction and operation in Phase 2. In Phase 3, the hydrogen produced will be purified by converting residual CO to H₂ over a shift catalyst and separating hydrogen from CO₂ using pressure swing adsorption. The purified hydrogen will be mixed with natural gas and used in a transportation demo. Working with the team from Georgia, other agricultural residues are being evaluated for cost and co-product potential.

References

Abedi, J., Y. D. Yeboah, M. Realf, D. McGee, J. Howard, and J. B. Bota, "An Integrated Approach to Hydrogen Production from Agricultural Residues for Use in Urban Transportation," *Proceedings of the 2001 DOE/NREL Hydrogen Program Review*, Baltimore, MD.

Biomass Research and Development Board, *Fostering the Bioeconomic Revolution in Biobased Products and Bioenergy*. See: <http://www.Bioproducts-bioenergy.gov>.

Chornet, E., S. Czernik, D. Wang, C. Gregoire, and M. Mann, "Biomass to Hydrogen via Pyrolysis and Reforming," *Proceedings of the 1994 DOE/NREL Hydrogen Program Review*, 407-432. Livermore, California, NREL/CP-470-6431; CONF-9404194.

Chornet, E., S. Czernik, C. Feik, R. French, "Biomass-to Hydrogen via Fast Pyrolysis and Catalytic Steam Reforming," *Proceedings of the 2001 DOE/NREL Hydrogen Program Review*, Baltimore, MD.

Czernik, S., R. French, C. Feik, E. Chornet, "Hydrogen form Biomass-Derived Liquids," *Progress in Thermochemical Biomass Conversion*, A. V. Bridgwater, Ed. In press.

Kelley, S.S., X.-M. Wang, M. D. Myers, D. K. Johnson, and J. W. Scahill, "Use of Biomass Pyrolysis Oils for Preparation of Modified Phenol Formaldehyde Resins," *Developments in Thermochemical Biomass Conversion*, 557-572. A. V. Bridgwater and D. G. B. Boocock, Editors. London: Blackie Academic & Professional.

Ozyurt, B. D., M. J. Realf, "Synthesis of a Food Processing-Agriculture Based Industrial Complex," *AIChE National Meeting Special Symposium*, Dallas, TX.

Putsche, V., "Preliminary Analysis of Peanut Shell Pyrolysis/Activated Carbon Process," Personal Communications.

Spath, P. L., M. K. Mann, "Technoeconomic Assessment of Four Biomass-to-Hydrogen Conversion Technologies," *Hydrogen Energy Progress XII. Proceedings of the 12th World Hydrogen Energy Conference*, 2057-2067. Buenos Aires, Argentina. Eds. J. C. Bolcich and T. N. Veziroglu. Vol 3.

SUPERCRITICAL WATER PARTIAL OXIDATION

**N.W. Johanson, M.H. Spritzer, G.T. Hong, W.S. Rickman
General Atomics
San Diego, CA 92121-1122**

Abstract

In 2000, General Atomics was selected by DOE's Hydrogen Program to perform cooperatively-funded research on supercritical water partial oxidation (SWPO) of biomass, municipal solid waste (MSW), and high-sulfur coal to generate hydrogen. Phase I of this research is being performed in GA's privately-funded supercritical water (SCW) pilot plant at its San Diego, CA facilities.

This pilot plant is a logical next step from both the sewage sludge supercritical water gasification (SCWG) test program conducted by GA for the DOE Hydrogen Program in 1997 and the SCWG test program conducted in 1999 by GA for Environmental Energy Systems Inc. (EESI) in a cooperative program with the California Energy Commission's Public Interest Energy Research (PIER) program to successfully gasify slurries containing 40 wt% composted biomass and MSW under supercritical conditions.

SWPO involves carrying out oxidative reactions in the SCW environment – akin to high-pressure steam – in the presence of sub-stoichiometric quantities of an oxidant, typically pure oxygen or air. The key advantage of the SWPO process is the use of partial oxidation in-situ to flash heat the gasification medium through the sensitive temperature range, resulting in less char formation and improved hydrogen yields. A second advantage of the SCW process is the negligible emission of criteria pollutants, including particulates, NO_x, SO_x, and hazardous air pollutants. A third advantage is the high-pressure, high-density aqueous environment that is ideal for reacting and gasifying organics. The high density also allows utilization of compact equipment that minimizes capital cost and footprint requirements.

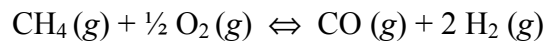
This paper provides background, describes the Phase I objectives, and discusses current status and future work.

Introduction

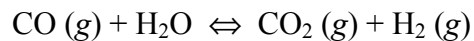
GA was awarded a development contract from DOE's Hydrogen Program to (a) perform a series of bench-scale Supercritical Water Partial Oxidation (SWPO) tests using cornstarch, biomass fuels, and coal, (b) perform pilot-scale design and analysis of a SWPO system concept for Phase-II development, and (c) prepare a development plan identifying cost, schedule and market potential and outlining the path forward to an integrated SWPO demonstration system.

Background

Several thermal processes exist for producing hydrogen from organic compounds. These include catalytic steam reforming, pyrolysis, plasma catalytic reforming, and supercritical water pyrolysis of wet biomass. Another thermal process for producing hydrogen is partial oxidation, whereby an organic compound is oxidized with less than stoichiometric quantities of oxygen to produce hydrogen and carbon monoxide, which then undergoes a further shift reaction with steam to convert the carbon monoxide to carbon dioxide and additional hydrogen from steam. The overall chemical reaction for the partial oxidation of methane is given by the following formula:



The shift reaction is given by the formula:



All of these processes rely on high-temperature reactions between the organic compounds and water to produce hydrogen, carbon monoxide, carbon dioxide and methane. With the exception of the partial oxidation process, the thermal processes all require the addition of an external source of heat to drive the chemistry. The partial oxidation process gets its heat from the in-situ exothermic oxidation reactions.

Many of these processes have been adapted to the production of hydrogen from biomass with the advantage that the carbon dioxide produced will have a net zero effect on the carbon dioxide concentration in the atmosphere.

Scientific Principles of SCW Processes

SCW processes are based on the unique properties of water at conditions near and beyond its thermodynamic critical point of 705°F and 3206 psia. At typical SCW reactor conditions of 1200°F and 3400 psi, densities are only one tenth that of normal liquid water. Hydrogen bonding is almost entirely disrupted, so that the water molecules lose the ordering responsible for many of liquid water's characteristic properties. In particular, solubility behavior is closer to that of high-pressure steam than to liquid water. The loss of bulk polarity by the water phase has

striking effects on normally water-soluble salts. No longer readily solvated by water molecules, they frequently precipitate out as solids.

Small polar and nonpolar organic compounds, with relatively high volatility, will exist as vapors at typical SCW conditions, and hence will be completely miscible with supercritical water. Gases such as N_2 , O_2 , and CO_2 show similar complete miscibility. Larger organic compounds and polymers will hydrolyze to smaller molecules at typical SCW conditions, thus resulting in solubilization via chemical reaction. Figure 1 summarizes the density and typical solubility behavior of water at 3400 psi as a function of temperature. Figures 1a and 1b show the rapid drop in density in the vicinity of the critical temperature, with a concomitant increase in the solubility of nonpolar organics and gases. As shown in Figure 1c, high-salt solutions may persist well beyond the critical temperature.

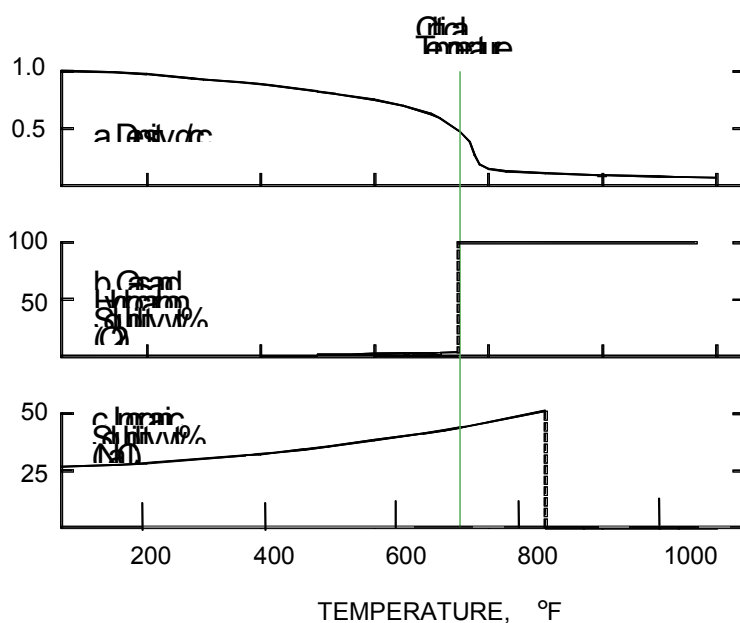


Figure 1. Characteristic of water at 3400 psi as a function of temperature.

The molecular dispersion of the organic and oxidant reactants within a single phase, in conjunction with the high diffusivity, low viscosity, and relatively dense SCW reaction medium, is conducive to rapid reactions. Furthermore, the temperature is sufficiently high that reaction completion is usually attained within seconds to tens of seconds. Rapid reaction rates have been demonstrated for virtually all types of organic materials, including solids.

Theoretical SWPO Calculations

For the proposed SWPO process, the feed slurry can be preheated to about 752°F by heat exchange with the product stream. A mixture containing about 11% wood in water has sufficient chemical heat to raise the mixture's temperature from 752°F to 1292°F at 3400 psi, assuming all carbon converts to CO and fuel-bound hydrogen converts to water. At this temperature, the thermodynamic equilibrium for the water/CO mixture produced by the partial oxidation reaction

will produce a dry gas that has about 94% hydrogen, 5% CO₂, 0.3% CO, and 0.6% methane by volume after separation from the water. At 1292°F, the theoretical equilibrium yield of hydrogen in the wood to hydrogen gas is about 80%. For a 14% wood-in-water mixture at 1472°F the theoretical yield increases to 87%. These calculations assume that the quantity of wood fed to the reactor is only that required to raise the feed temperature from 752°F to the reaction temperature.

These calculations demonstrate the theoretical feasibility of producing a hydrogen-rich gas stream by utilizing partial oxidation of biomass in supercritical water. The calculations above assume all fuel-bound hydrogen converted to water. However, if the partial oxidation reaction liberates free hydrogen, as shown in first equation above, then even higher yields of hydrogen may be possible. This could be the case for an excess of fuel over the amount needed to heat the mixture to reaction temperature. This raises the first of several important technical questions that need to be resolved:

- What is the fate of fuel-bound hydrogen during partial oxidation?
- How will the actual hydrogen yield compare with theoretical calculations and does it hold promise for a commercially-viable hydrogen generation process?
- Will the oxidative “flash” heating of the feed through the char-forming temperature range suppress formation of char to acceptable levels?

Clearly, the answers will have important ramifications for the efficacy of the partial oxidation process.

Another issue is whether oxygen or air is more effective as the oxidizing agent. At SWPO reaction temperatures, the presence of nitrogen may result in ammonia formation that, if formed in sufficient quantity, could adversely impact hydrogen yield. This latter question is not one to be answered in the Phase I testing described here but should be explored during an expanded Phase II testing. Use of air will also impede the liquifaction and collection of CO₂. For the present test program the only oxidant used will be O₂.

Prior Work

There is little, if any, published data for the SWPO process in the open literature. There are a number of patents that describe partial oxidation in high-pressure steam environments. The readily-available, relevant background information and data relate to the two precursor technologies – SCWG and SCWO.

Supercritical Water Gasification (SCWG)

The earliest tests on gasification in supercritical water were carried out by Modell and coworkers at the Massachusetts Institute of Technology (MIT) in the late 1970’s (Modell, et al., 1978). See Table 1, Summary of SCWG Test Results, below. These tests utilized residence times of at least 30 minutes with temperature and pressure conditions essentially at water’s critical point. Various metallic catalysts were employed. In later tests, dramatically improved results were

achieved through the use of higher temperatures with reactor residence times of less than a minute. Recently, a number of results have been reported in which the yield of gas is actually higher than the mass of organic feed. This situation arises when water is consumed in gas-forming reactions.

In 1997, under sponsorship of the DOE Hydrogen Program, GA performed SCWG studies with thickened sewage sludge. At 1200°F and 2 minutes residence time, GA achieved up to 94% conversion of the sludge carbon to gas, with a small amount of char (General Atomics, 1997). In 1999, under sponsorship of the California Energy Commission's Innovations Small Grant Program, GA conducted SCWG studies for EESI using biomass comprised of sewage sludge and composted MSW (EESI/General Atomics, 2001). The primary objective was to determine the product spectrum and conversion efficiency for gasification at 3400 psig and 1200°F. Operation of the system also provided information about char formation, corrosion, and salts/solids handling. GA was able to formulate and pump heavy slurries of up to 40 wt% solids, and achieved 98% conversion of the organic carbon to gas with no char or tar formation.

Table 1. Summary of SCWG Test Results

Reference	Feedstock	%C Gasified	% H ₂ Yield	Temp °F	Pressure psi	Catalyst	Reaction Time, min	Char	Scale
Modell et al., 1978	Glucose Cellulose	23	5	705	3200	Mixed metallic	30	None	Lab
		18	0.2						
Woerner, 1976	Maple sawdust	88	21	705	3200	None	30	None	Lab
Whitlock, 1978	Glucose	36	12	716	4750	Mixed metallic	13	None	Lab
Sealock and Elliott, 1991	Cellulose	79	NA	752	4000	Ni/Cs ₂ CO ₃	15	None	Lab
Yu et al., 1993	Glucose	86	128	1112	5140	None	0.5	None	Lab
Xu et al., 1996	Glucose Bagasse Glycerol	99	64	1112	5140	Activated carbon	0.3	None	Lab
		100	56				1.4		
		100	88				0.75		
Antal, 1996	Cellobiose Water hyacinth	100	47 31	1112	5140	Activated carbon	0.3	None	Lab
General Atomics, 1997	Sewage sludge	94	29	1200	3425	Activated carbon	2	Yes	Pilot
Antal and Xu, 1998	Corn starch (CS) Sewage sludge + CS Sawdust + CS	100	161	1200	4170	Activated carbon	0.25	None	Lab
		94	139						
		100	199						
EESI/General Atomics, 2001	Sewage Sludge + MSW	98		1200	3400	None		None	Bench

Supercritical Water Oxidation (SCWO)

SCWO has proven to be a robust method for the complete oxidation and mineralization of a wide spectrum of materials. It is particularly suited to feedstocks with a high water content, such as biomass-derived materials, as well as dirty fuels such as high-sulfur coal. It is a natural

complement to the process of SCWG, with the matched pressures of the processes facilitating heat interchange.

SCWO arose as an outgrowth of the gasification work at MIT in combination with the well-known process of wet oxidation. The key concepts were formulated by Modell (1982) in the early 1980s. Experimentation quickly established that temperatures considerably higher than the critical temperature of water (705°F), in the range of 1100°F, were desirable to achieve rapid and complete oxidation. In contrast, the pressure functionality was more ambiguous, with good oxidation result being reported at pressures both considerably below and above the critical pressure of 3206 psi (Hong, 1992; Buelow, et al., 1990). (For simplicity, the process is still referred to as SCWO, even though the operating pressure may be somewhat subcritical.)

The low temperature of SCWO in comparison to normal combustion has the advantage of reducing NO_x and SO_x formation. Typical effluent levels for these gases, even with nitrogen-containing feeds and air oxidant, is less than 1 ppm. Residence times for complete oxidation are typically less than a minute and can be as little as several seconds for liquid or gaseous feeds. The short reaction time and relatively dense process medium results in reactors that are highly compact as compared to conventional combustors.

The effectiveness of SCWO has been demonstrated at the laboratory and pilot scale on hundreds of feedstocks. Of particular interest is sewage sludge, for which GA has carried out pilot plant development for a commercial client. The as-received sludge had a solids content of 4 to 5 wt%. Prior to SCWO treatment the sludge was treated with a thickening/dewatering agent to yield a sludge solids content up to 10.7 wt%. Processing through the SCWO unit gave organic destruction efficiencies in excess of 99%, with nondetectable SO_x and NO_x (less than 20 ppm). The solid byproduct consisted primarily of metal oxides that were shown to pass the EPA TCLP, allowing disposal in a sanitary landfill.

Other feedstocks of interest that have been treated by SCWO include coal slurry (Modar, Inc. unpublished results), pig manure (Rulkens, et al., 1989), various biomass slurries including pulp mill sludge (Modell, 1990), pulverized wood with ground plastic, rubber, and charcoal (General Atomics, 1999), fermentation waste (Johnston, et al., 1988) and ground cereal (Hong, et al., 1996). Complete oxidation of virtually any organic material, including highly refractory hazardous wastes such as hexachlorobenzene, has been demonstrated. Regardless of the particular feedstock, the heat of combustion is captured directly within the high-pressure aqueous stream without the need for intervening heat transfer surfaces.

Power recovery from SCWO has been a facet of interest from the very beginning of the technology (Modell, 1982). For a period of about 5 years starting in 1988, a DOE-sponsored program was carried out at Modar, Inc., with one of its goals being to evaluate the feasibility of power recovery as a byproduct from the treatment of industrial waste streams (Bettinger, 1993). The effluent gas stream was cleaned through the use of ceramic filters. A conclusion of the study was that a prototype turbine would be required to test the feasibility of operating the turbine on the cleaned supercritical stream (Stone & Webster, 1989).

Supercritical Water Partial Oxidation (SWPO)

SWPO combines elements of both fully-oxidizing SCWO (heat generation via oxidation) and fully-reducing SCWG (gas production via heat absorption). In SWPO, partial oxidation is used for rapidly heating the slurry through the transition temperature to improve the yield of hydrogen and to reduce char.

Discussion of Current Status

Phase I of the SWPO project has three major objectives:

- Bench-scale testing with heavy slurries of coal/biomass
- Pilot-scale concept design for Phase II development
- Development plan defining market fit, finance/schedule needs and the path forward to a demonstration plant

Bench-scale Tests

The start of the SWPO project was delayed to December 2000 and refocused to take advantage of the larger-scale GA-SCW pilot plant being constructed.

The SCW Pilot Plant Test Facility

The throughput of the bench-scale apparatus used for prior SCWG work was about 15 gm/min. The throughput for the SWPO test matrix in the new pilot-plant downflow reactor will in the range of 0.38 to 1.00 kg/min, a scale-up of 25 to 66 over the prior bench-top apparatus. The new pilot plant is capable of testing various process configurations and feed mixtures. Both downflow vessel and tubular reactors are installed. Feedstocks can be prepared and pumped at up to 40 wt% solids using in-line grinders/macerators and GA-developed high-pressure slurry feed pumps. Another advantage is that gaseous effluents are continuously monitored for O₂, CO₂, CO, H₂, and total HCs with an on-line gas analysis system. Figure 2 shows photographs of the general arrangement of equipment on the three major equipment skids: (1) feed skid, (2) pump skid, and (3) reactor skid.

To provide oxygen, a high-pressure oxygen supply system has been acquired and installed in an available space on the pump skid. Although air will not be tested as an oxidant for SWPO in Phase I, high-pressure air compressors are available as needed for future tests.

Figure 3 illustrates a simplified process flow diagram for the SWPO pilot plant.



Figure 2. GA SCW Test Facility

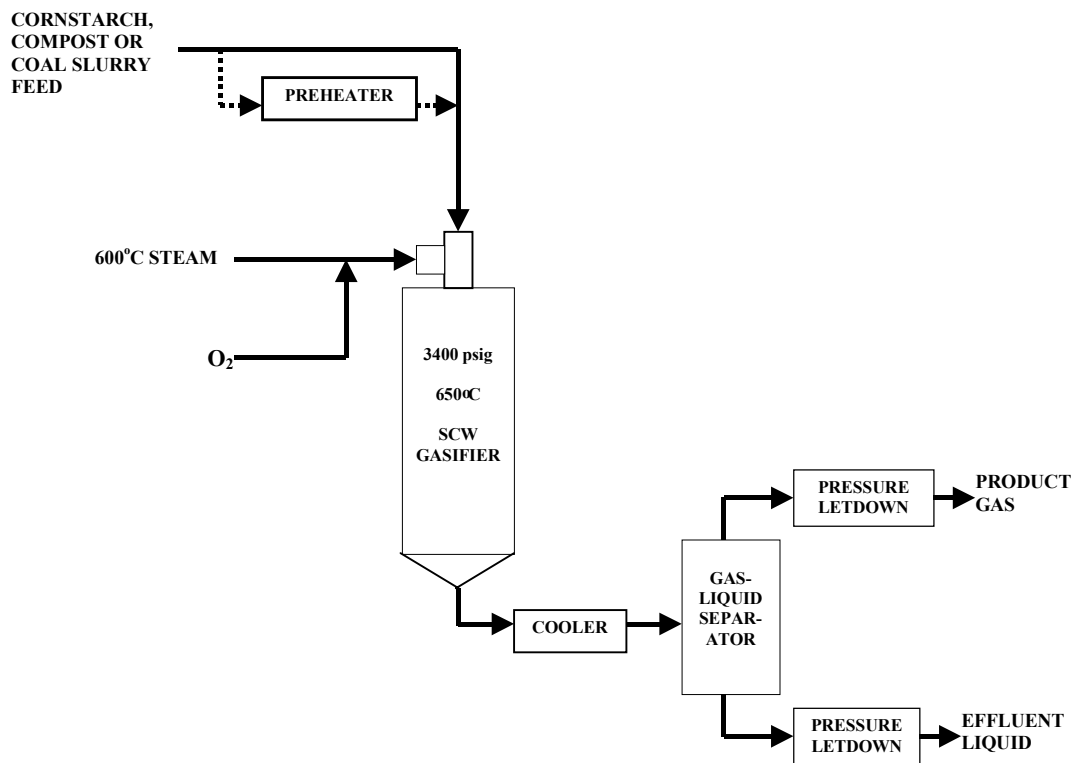


Figure 3. Simplified Process Flow Diagram for SWPO Pilot Plant

SWPO Test Plan

This Phase I test program has been structured to emphasize those feeds that have high probability of yielding significant data for evaluation of the basic partial oxidation process while requiring minimal preparation and pumping technique development. While a number of feeds were considered, it was decided to focus on those for which a high level of confidence existed that heavy slurries could be successfully prepared and fed with minimal problems. This would reduce the chance of expending effort on issues secondary to obtaining data on the core SWPO process. The three feeds selected for testing are cornstarch, composted biomass and coal.

A detailed test plan was completed including operating conditions, process measurements and instrumentation for tests of SWPO with various feedstocks. A summary of the test matrix is presented in Table 2. All tests will be conducted using the new pilot plant, which has just become available following completion of extended startup testing under General Atomics funding.

Within the budgeted time and funding we have realistically planned a total of five test series, each containing three separate test runs for a total of fifteen data points. Total test duration will be about one month.

Table 2. Test Plan Summary^(a)

Test Seq. No.	Test Series ^(b) Ident.	Type of Fuel to be Fed	Feed Temp. (°F)	Solids Conc. (%)	Type Reactor Used	Status
-3	Start-up	Ethanol	77	0	Downflow	Complete
-2	Systemization	Cornstarch (CS)	77	0	Downflow	In Progress
-1	Systemization	Raw compost (RC)	77	0	Downflow	In Progress
1	1	CS	77	10.4 - 13.3	Downflow	Pending
2	2	CS	572	10.4 - 13.3	Downflow	Pending
3	3	Bituminous coal (BC)	77	8.0 - 13.1	Downflow	Pending
4	4	RC	77	8.0 - 13.1	Downflow	Pending
5	5	RC	572	8.0 - 13.1	Downflow	Pending
6	Optional	RC+BC (50/50)	TBD	8.0 - 13.1	Downflow	Pending
7	Optional	CS	77	10.4 - 16.5	Tubular	Pending

NOTE: (a) All tests at 1155-1200°F reactor temperature.

(b) Each test series consists of a minimum of three runs and an optional fourth run if time permits.

Each test series also allows for a fourth (optional) run should the first three runs proceed more rapidly than we expect. In addition, two additional (optional) tests series (6 and 7) are defined to be conducted only as available time permits. Under the most optimistic outcome, a total of twenty-eight data points might be obtained.

Testing will begin with SWPO tests on cornstarch. Cornstarch tests will provide a baseline for comparison to prior published data. These tests will be followed by tests with composted biomass and coal. The automated data acquisition system will record pressures, temperatures, flows, and on-line gas analyses as shown in Figure 4. Sampling and analysis will also be performed to characterize the liquid, gaseous, and solid effluents from the tests. The following test sequence will be used:

- Test Series 1 and 2 will be conducted using the model compound cornstarch in the down-flow reactor and using the quench system to study the reaction kinetics. The conditions for these two test series will be nearly identical, the only difference being that, in Series 2, the cornstarch paste feed will be heated to 572°F prior to entering the mixing nozzle to minimize the use of oxygen and to improve the yield of hydrogen. These tests will provide SWPO data for a fuel with a relatively low C/H ratio for direct comparison to other published supercritical water gasification data.
- Test Series 3 will be conducted using coal water slurry as the feed to the down-flow reactor. These tests will provide SWPO data on fuels with very high C/H ratios.

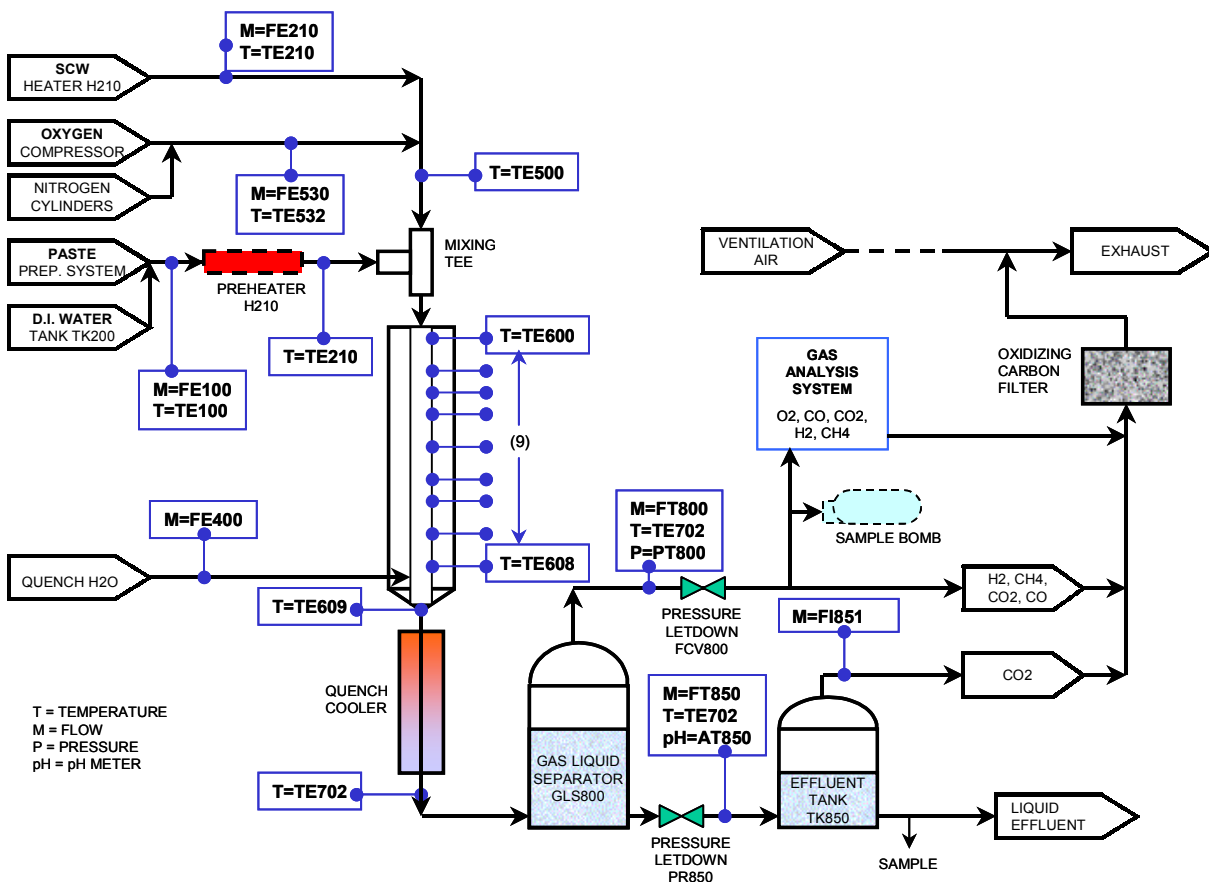


Figure 4. SWPO On-line Data Acquisition and Sampling Points

- Test Series 4 and 5 will be conducted using the raw compost in the down-flow reactor with the raw compost being heated to 572°F prior to the mixing tee in Series 5. These tests will provide SWPO data for typical biomass fuels with intermediate C/H ratios.
- If time permits, Test Series 6-TP will be conducted using a mixture of 50% raw compost and 50% coal in a feed concentration of 40% by weight of dry solids. These tests will provide SWPO data for blended fuels with relatively high C/H ratios.
- Finally, if time permits, Test Series 7-TP will be conducted using cornstarch and the tubular reactor, at the same test conditions as Series 1. These tests will provide SWPO data for a characteristically different gasifier geometry with a relatively long residence time.

Test Progress to Date

Inventories of the three test feeds (cornstarch, composted MW/sewage sludge, and bituminous coal) were procured and are onsite. Modifications to the SCW pilot plant required for SWPO testing were completed. The high-pressure oxygen system was acquired, installed and checked out. Startup testing with ethanol was completed, but it has taken longer than originally planned to debug the system. Systemization of the pilot plant is currently underway, with integrated runs using compost slurry and cornstarch. These tests will complete the startup/systemization phase and confirm pilot-plant readiness for the SWPO test plan matrix.

Pilot-scale Design/Analysis

This task has two main subtasks: Conceptual Design and System Engineering Analysis.

Pilot-scale Conceptual Design

Considerable progress has been made on the conceptual design of the SWPO pilot-scale system. A detailed six-sheet P&ID has been prepared for the SWPO configuration of the new pilot plant that incorporates most of the expected features of the SWPO process for Phase II development.

System Engineering Evaluation

The preliminary integrated SWPO system design is being evaluated to identify potential interface components through literature reviews, survey of equipment vendors, as well as a review of prior gasification work and system integration studies performed by GA. Review of the most recent developments forthcoming from the DOE Hydrogen Program are also being factored into this evaluation.

The block flow diagram, Figure 5, defines the key steps in an overall process of converting biomass or low-grade fuels into hydrogen suitable for a variety of end-uses. Emphasis is on the SWPO core technologies that the subject of development for this multi-phase project (see Future Work). Feed preparation and gas cleanup and separation requirements remain to be defined.

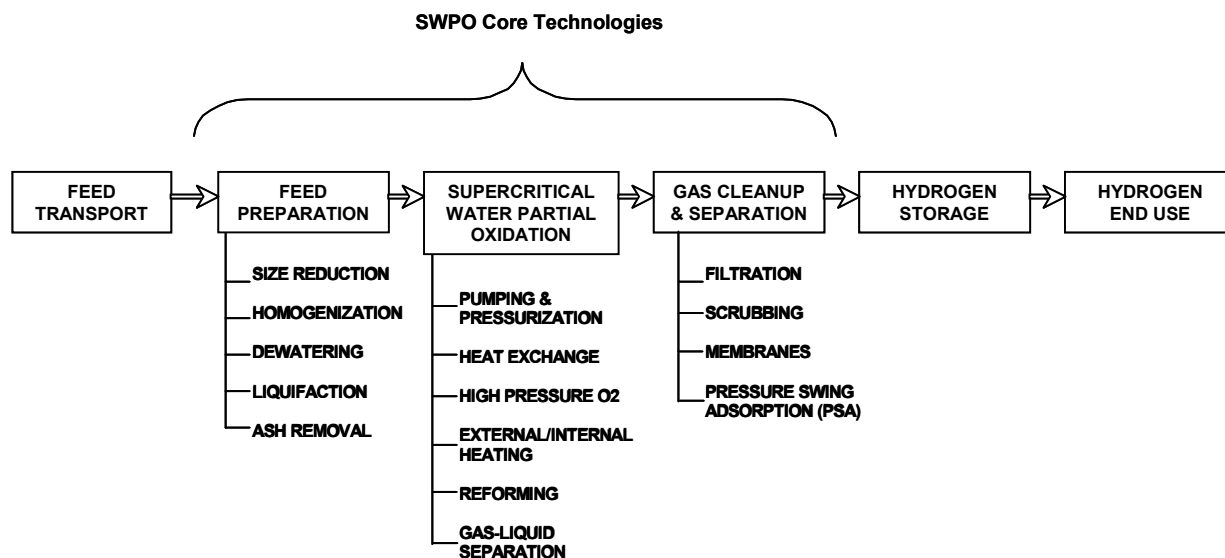


Figure 5. Block Flow Diagram for an Integrated SWPO Hydrogen System

A preliminary review of the technology associated with each of the major components and subsystems for the steps identified in Figure 5 is underway. Based on this preliminary review, the principal development requirements are summarized in Table 3. The items requiring substantial further development are shown in bold-face type. This evaluation is continuing and will likely change as the SWPO data becomes available.

Table 3. Summary of Development Requirements for Component Technologies

Component Technology	Status
Feed particle size reduction	Commercially available with minor modifications
Sludge Pretreatment	Unnecessary for many feeds, more development required for others
High pressure slurry pumping	Commercially available
Heat exchange/recovery	Some testing at lab and pilot scale; more development needed
Pure O ₂ or high O ₂ content oxidant	Commercially available
SCWO and SCWG Reactors	Some testing at lab and pilot scale; more development needed
Gas-liquid separation	Development essentially complete
Gas cleanup/separation	Some commercially available, others tested at lab and pilot scale; more development needed

SWPO Development Plan

A development plan is being prepared for the commercialization of SWPO for the production of hydrogen/hydrogen-rich fuel gases from biomass and low-grade fuel. This task encompasses three subtasks: Cost and Schedule Estimate, a Business Plan identifying SWPO/H₂ market potential, and Definition of Follow-on Activities leading to an integrated SWPO demonstration system.

The commercial software BizPlan Builder is being used to create the plan for commercializing the integrated SWPO pilot-scale demonstration system. BizPlan incorporates a series of central topic templates that include Product Strategy, Market Analysis, Marketing Plan and Financial Plan. The templates may be tailored to the specific needs of the development plan for the SWPO technology.

The SWPO plan will be developed along parallel lines used by Mann (1995) to evaluate the BCL gasifier and will make use of prior analysis of a SCWG system for gasification of biomass (General Atomics, 1997).

Development Cost/Schedule

The development plan incorporates specific plans for the pilot-scale development effort, including the detailed design and fabrication of the SWPO unit operation as well as slurry feed preparation and pumping equipment, heat exchange equipment and gas conditioning equipment. Cost and schedule estimates will be prepared for pilot-scale demonstration and follow-on phases of development.

Business Plan Identifying SWPO Market Potential

A business plan is also in preparation. The business plan evaluates the market potential for the SWPO technology including economic analysis to provide comparisons with other conventional or advanced hydrogen generation methods. Elements being considered in the market analysis are market definition, customer profiles, competition for feed stocks, financial risk, promotion and sales strategy.

Ongoing market explorations include discussions with municipal authorities to determine the generation rates, characteristics and variability of potential biomass feed stocks and to determine the incentives that will create interest in cooperative partnerships. One local authority, the San Diego Municipal Waste Water Department (MWWD) and the Environmental Services Department (ESD) have expressed interest in the possibility of being a host site for a demonstration pilot-scale SWPO plant. The MWWD and ESD have co-located facilities for sewage sludge collection and municipal solid waste sorting, recycle, and landfill. These are the targeted feedstock for GA's SWPO technology, and a summary of the available feedstock quantities for San Diego is provided in Table 4. The items in bold-face type are the most likely sources of SWPO biomass feedstocks. These categories total about 500,000 tons of moisture-containing biomass, or about 250,000 dry tons per year.

Follow-on Activities Leading to Pilot-Scale Demonstration of Integrated SWPO System

Detailed activities that must be implemented in order to move the SWPO technology forward from bench-scale testing to an operational integrated demonstration plant will be laid out in the development plan. The required steps to mature the technology will be structured into a multi-phased, multi-year schedule with well-defined critical progress milestones.

A proposal for the Phase II follow-on work is underway for submittal in June 2001.

Table 4. San Diego Annual Materials Disposed by Major Sectors^(a)

Material Type	Residential Waste Generated In-City		Commercial Waste Generated In-City		In-City Military Facilities		City Departments	
	Est. Pct.	Est. Tons	Est. Pct.	Est. Tons	Est. Pct.	Est. Tons	Est. Pct.	Est. Tons
Recyclable Paper	23.0%	137,099	15.0%	115,976	10.6%	10,793		
Rock, Soil and Fines			8.0%	62,291	29.7%	30,310	25.6%	53,553
Food	13.9%	82,911	6.6%	51,379	5.4%	5,465		
Sewage Solids							57.7%	120,560
Recyclable Yard Waste	13.4%	79,934	4.7%	36,194				
Treated Lumber	3.2%	18,852	7.0%	53,888	16.4%	16,695		
Remainder/Composite Paper	6.8%	40,243	5.2%	39,913				
Concrete	3.0%	17,633	5.5%	42,964	3.1%	3,157		
Non-Treated Lumber			6.5%	50,455	4.1%	4,218		
Film Plastic	3.5%	20,945	3.1%	24,238				
Carpet & Carpet Padding			5.3%	41,087				
Gypsum Board			4.7%	36,240				
Asphalt Roofing			4.3%	33,570				
Other Ferrous Metal			3.8%	29,642	3.5%	3,537		
Remainder/Composite Construction and Demolition			3.9%	29,888				
Contaminated soil, street sweepings, drain cleanings					3.6%	3,689	6.9%	14,380
Asphalt Paving							3.3%	6,836
Subtotal	66.8%	397,617	83.7%	647,724	76.3%	77,865	93.4%	195,329
All Other Waste Types	33.2%	197,212	16.3%	126,571	23.7%	24,187	6.6%	13,706
Total Disposed	100.0%	594,829	100.0%	774,295	100.0%	102,052	100.0%	209,035

^(a)(City of San Diego, 2000)

Concurrent and Related Activities

Efforts in addition to Phase I objectives include actively pursuing related programs with both NETL and with the California Energy Commission's P.I.E.R. program to broaden the funding base for development of SWPO and related SCW technologies.

GA is actively pursuing strategic partnerships, contracts with related programs, and other opportunities to advance the technology. In March, GA presented a technical paper on supercritical water cycles at the 26th International Technical Conference on Coal Utilization & Fuel Systems. (March 5-8, 2001 in Clearwater, FL). In May, GA submitted a Memorandum of Understanding to the City of San Diego to form an alliance directed toward the joint development of biomass power generation based on municipal wastes.

Future Work

The future path beyond Phase-I and the probable time-line leading to a SWPO demonstration plant is outlined below in the following phases.

- Phase II: Technology Development: (1/02 to 12/03)
 - Design, fabricate and test pilot-scale SWPO reactor
 - Optimize SWPO operating parameters and hydrogen yields
 - Demonstrate feasibility; provide data for evaluation and scale-up
- Phase III: System Integration and Design: (1/04 to 12/04)
 - Safety, reliability and maintainability analyses
 - Life-cycle cost analyses
 - Process design and long-lead procurement for Phase IV
- Phase IV: Demonstration Plant: (1/05 to 12/07)
 - Implement requirements defined during Phase III studies
 - Match pilot-scale SWPO to industrial hydrogen separation and storage systems

Each of these future phases will be expanded and detailed as a part of the development plan being prepared in Phase I.

References

- Antal, M.J., Jr. 1996. "Catalytic Supercritical Gasification of Wet Biomass." International Patent Publication No. WO 96/30464.
- Antal, M.J., Jr., and X. Xu. 1998. "Total, Catalytic, Supercritical Steam Reforming of Biomass." Unpublished manuscript, University of Hawaii at Manoa.
- Bettinger, J.A. and W.R. Killilea. 1993. "Development and Demonstration of Supercritical Water Oxidation." Federal Environmental Restoration Conference Technical Paper 93-31.
- Buelow, S.J., R.B. Dyer, C.K. Rofer, J.H. Atencio and J.D. Wander. 1990. "Destruction of Propellant Components in Supercritical Water." Los Alamos National Laboratory paper no. LA-UR-90-1338.
- City of San Diego, Environmental Services Department. 2000. "Waste Composition Study 1999–2000." Final Report.
- EESI/General Atomics. 2001. "Process For Converting Sewage Sludge and Municipal Wastes to Clean Fuels." EISG Final Report, California Energy Commission, Public Interest Energy Resesarch Grant 99-04, 2001.
- General Atomics. 1997. "Sewage Sludge Gasification in Supercritical Water." Final Report, U.S. DOE Cooperative Agreement No. DE-FC36-97GO10216.

General Atomics. 1999. "Assembled Chemical Weapons Assessment (ACWA), Test Technical Report."

Hong, G.T. 1992. "Process for Oxidation of Materials in Water at Supercritical Temperatures and Subcritical Pressures." U.S. Pat. No. 5,106,513.

Hong, G.T., B. Borchers, S. Pisharody and J. Fisher. 1996. "A Supercritical Water Oxidation Unit for Treating Waste Biomass." Paper No. 961560, Society of Automotive Engineers, *26th International Conference on Environmental Systems*.

Johnston, J.B., R.E. Hannah, V.L. Cunningham, B.P. Dagy, F.J. Sturm and R.M. Kelly. 1988. "Destruction of Pharmaceutical and Biopharmaceutical Wastes by the Modar Supercritical Water Oxidation Process." *Biotechnology*, 6:1423-1427.

Mann, M.K. 1995. "Technical and Economic Assessment of Producing hydrogen by Reforming Syngas from the Battelle Indirectly Heated Biomass Gasifier." NREL/TP-431-8143.

Modell, M., R.C. Reid and S.I. Amin. 1978. "Gasification Process." U.S. Pat. No. 4,113,446.

Modell, M. 1982. "Processing Methods for the Oxidation of Organics in Supercritical Water." U.S. Pat. No. 4,338,199.

Modell, M. 1990. "Treatment of Pulp Mill Sludges by Supercritical Water Oxidation." Paper No. DOE/CE/40914-T1.

Rulkens, W.H. et al.. 1989. "Feasibility Study of Wet Oxidation Processes for Treatment of Six Selected Waste Streams." Dutch Rijkswaterstaat Report No. DBW/RIZA 89-079.

Sealock, L.J.Jr., D.C. Elliot. 1991. "Method for Catalytic Conversion of Lignocellulosic Materials." U.S. Pat. No. 5,019,135.

Stone & Webster. 1989. "Assessment and Development of an Industrial Wet Oxidation System for Burning Wastes and Low-Grade Fuels." U.S. DOE Report DE-FC07-88ID127111.

Woerner, G.A. 1976. "Thermal Decomposition and Reforming of Glucose and Wood at the Critical Conditions of Water." M.S. Thesis, Massachusetts Institute of Technology.

Whitlock, D.R. 1978. "Organic Reactions in Supercritical Water." M.S. Thesis, Massachusetts Institute of Technology.

Xu, X., Y. Matsumura, J. Stenberg and M.J. Antal, Jr. 1996. "Carbon-Catalyzed Gasification of Organic Feedstocks in Supercritical Water." *Ind. Eng. Chem. Res.*, 35:2522-2530.

Yu, D., M. Aihara and M.J. Antal, Jr. 1993. "Hydrogen Production by Steam Reforming Glucose in Supercritical Water." *Energy and Fuels*, 7:574-577.

ROLE OF INITIAL SUCROSE AND PH LEVELS ON NATURAL, HYDROGEN-PRODUCING, ANAEROBE GERMINATION

**Steven Van Ginkel, ShihWu Sung, Ling Li
Department of Civil & Construction Engineering,
Iowa State University,
Town Engineering Building,
Ames, Iowa 50011-3232, U.S.A.**

**Jiunn-Jyi Lay
Department of Safety, Health, and Environmental Engineering,
National Kaohsiung First University of Science and Technology,
1 University Road,
Yanchau, Kaohsiung,
Taiwan, R.O.C.**

Abstract

Anaerobic batch cultures were established to assess natural anaerobic sporulation, germination, and hydrogen production. Heat-shocked soil inocula obtained from a potato field was cultured using sucrose as the substrate. Eleven batch experimental results suggested that baking was an excellent heat-shock treatment to select for spore forming hydrogen-producing bacteria i.e. clostridia from the soil. Sucrose could induce clostridial spore germination and subsequent hydrogen production. Hydrogen production potential and rate were selected for monitoring clostridial spore germination and vegetative cell activity, and could be systematically estimated using a modified Gompertz equation. Multivariate analysis (i.e., polynomial regression with stepwise) and response surface plots performed with a central composite design (sucrose: 15 – 45 g COD/L; pH: 4.5 – 6.5) demonstrated that the constant hydrogen production rate increased and

the potential decreased with a decrease in the sucrose concentration from 45 to 15 g COD/L. The results indicate that substrate deprivation was more important than initial pH on hydrogen-production/clostridial germination. Based on the results of this study, at a substrate concentration of 15 g COD/L, the pH value of 5.5 might be a trigger for clostridial germination and a pH of 5.5 or greater may shift the dynamic metabolic balance from solventogenesis to hydrogenesis.

Introduction

Hydrogen is an excellent alternative energy candidate for the future. It has a high calorific value and water is the only by-product resulting from the combustion of hydrogen. It can also easily be stored as a metal hydride (Billings, 1991). While hydrogen can be easily produced by water electrolysis, thermochemical, and radiolytic processes, these processes are not very economical owing to intensive energy consumption and are viable only in areas where cheap electricity is readily available (Rajeshwar *et al.*, 1994). From the perspective of global environmental impacts, such as the greenhouse effect and resource recovery, microbial hydrogen production from renewable biomass reduces dependence on fossil fuel, decreases carbon dioxide emission, and recovers bioenergy (Gray and Gest, 1965; Borkris, 1973).

The microbial conversion of agricultural and industrial wastes and residues into hydrogen is attracting increasing interest. Apart from surplus agricultural products, suitable source materials are now readily available in the form of wastes from the sugar producing and processing industry and fruit processing factories (Afschar and Schaller, 1991). Hydrogen is a major intermediate in organic matter degradation in the digested sludge ecosystem. It is produced by fibrolytic and fermentative microorganisms and could be potentially re-utilized by the hydrogenotrophic bacteria (Giallo *et al.*, 1985). Interspecies hydrogen transfer between hydrogen-producing and hydrogen-utilizing microorganisms allows growth and activity of fermentative and hydrolytic microorganisms. Several studies have been carried out using pure cultures of anaerobic bacteria, such as *Clostridium* sp., to study the conversion of carbohydrates (e.g., glucose) to hydrogen gas (Zeikus, 1980; Miyake *et al.*, 1984; Taguchi *et al.*, 1992). Recently, some investigators have used anaerobic microorganisms, taken from sludge compost, to generate hydrogen from sugary wastewater in a chemostat culture (Ueno *et al.*, 1996). However, only traces of hydrogen are usually evolved with continuous flow digesters due to the ubiquitous nature of hydrogen consumers (Kibdy and Nedwell, 1991). If the activity of hydrogenotrophic bacteria contained in anaerobic cultures is inhibited, the culture possesses significant capacity for the transformation of sugary processing wastes into hydrogen gas. The review by Zajic and coworkers (Zajic *et al.*, 1978) indicates that anaerobic spore-forming bacteria form an important part of the acidogenic bacterial population performing acetate/butyrate fermentation and the main anaerobic hydrogen-producing sporeformers are *Clostridium* sp. The clostridial bacteria could be enriched from soil, cracked cereals and comparable sources using a heat-shock treatment to inactivate non-spore-formers (Biebl, 1999). Preliminary experiments have successfully used a heat-shock digested sludge to convert the organic fraction of municipal solid wastes into hydrogen gas and demonstrated that the sludge possessed clostridial characteristics and no methanogenesis occurred (Lay *et al.*, 1999).

Starting a bioprocess with a spore-soil mixture to generate hydrogen, the spores germinate to vegetative cells in a triggering stage. Proper pH control and substrate concentration are key factors improving the germination of the clostridia, as well as in operating a hydrogen-producing bioprocess (Craven, 1998). This is due to the fact that bacterial germination/sporulation involves several metabolic pathways associated with morphological, physiological, and chemical changes and can affect end products associated with energy metabolism (Labbé and Shih, 1997). Specific carbohydrate composition of the growth media also affects the ability of the culture to germinate. Rapidly metabolizable carbohydrates such as glucose are generally avoided in germination media because they are vigorously fermented by certain saccharolytic species of *Clostridium*, resulting in considerable acid production (Labbé and Rey, 1979).

The objective of this study was to investigate the role of the environmental factors of initial pH and carbohydrate concentration on clostridia-rich, natural anaerobe germination for hydrogen production. For these purposes, the experiments in this paper were performed with heat-shock treatment on small batch reactors using sucrose and an undefined bacterial consortium derived from potato soil as inocula. A fractional factorial central composite design was employed in planning experiments for learning the effects of these environmental factors on clostridial germination using hydrogen production potential and rate as indicators summarized with a predictive polynomial quadratic equation incorporating stepwise regression and response surface methodology (Box *et al.*, 1978).

Materials and Methods

Seed Microorganisms

In most natural environments, clostridia have significant ability to transform organics to acids, alcohols, and hydrogen. They are easily obtained from soil, roots (especially of leguminous plants), cracked cereals, and comparable sources using starchy mashes or media containing sugar (Biebl, 1999). In this study, the natural anaerobes were taken from the Iowa State University Student Farms in Ames, Iowa and respectively brought to a two-hour bake and a fifteen-minute boil to inhibit the bioactivity of hydrogen consumers and to harvest hydrogen-producing spore-forming anaerobes (i.e., clostridia). This soil was obtained in February and potatoes were grown the previous year.

Experimental Design

To assess the soil having the capability of biohydrogen production, two sets of experiments were conducted with 250-mL bottles with two grams of sucrose added, while the pH varied from 4.0 to 8.0 in increments of 0.5. The boiling and the baking heat-shock treatments were used for the first and the second experiments, respectively. Additionally, experiments were run with and without sucrose added in the 250-mL bottles containing the same quantity of soil and nutrients in order to observe no hydrogen production resulting from degradation of organic matter contained in the soil.

To evaluate the characteristics of clostridial germination for hydrogen production, a fractional factorial central composite experimental design of key variables of initial pH and sucrose concentration was performed by measuring their hydrogen-producing rate and potential. This design (Table 1) used a central value consisting of four grams of sucrose and an initial pH of 5.5. This central value was replicated three times. The variables, sucrose and pH, were coded by the following equation in order to be used in a regression equation.

$$x_i = (X_i - X_i^*)/\Delta X_i \quad (1)$$

where x_i is the coded value of the i th test variable, X_i is an uncoded value of the i th test variable, X_i^* is an uncoded value of the i th test variable at the center point and ΔX_i is the step change value. Response Surface Methodology (Box *et al.*, 1978) is a statistical technique involving the solution of multivariate polynomial regression equation (refer to Eq. 3) simultaneously. The visual evaluation of these graphs can give insight to the main effects and the mutual interactions of the variables used in the design.

Table 1. Full factorial central composite design variables in coded and natural units.

Sucrose (g/L)	pH Range and Levels				
	4.5 (-2)	5.0 (-1)	5.5 (0)	6.0 (1)	6.5 (2)
2 (-2)			+		
3 (-1)		+		+	
4 (0)	+		+		+
5 (1)		+		+	
6 (2)			+		

* Numbers in parentheses are x_i .

* Central value (5.5, 4) was replicated three times.

Experimental Apparatus and Procedures

The experiment was conducted at random in 250 mL batch serum bottles filled to 150 mL with 30 grams of the soil, varying amounts of initial sucrose and initial pH values (Table 1), and 0.5 mL of nutrient stock solution. Each liter of nutrient stock solution contained 200 g of NH_4HCO_3 , 100g of KH_2PO_4 , 10g $\text{MgSO}_4 \cdot 7\text{H}_2\text{O}$, 1.0 g of NaCl , 1.0 g of $\text{Na}_2\text{MoO}_4 \cdot 2\text{H}_2\text{O}$, 1.0 g of $\text{CaCl}_2 \cdot 2\text{H}_2\text{O}$, 1.5g of $\text{MnSO}_4 \cdot 7\text{H}_2\text{O}$ and 0.278g of FeCl_2 . After addition of substrate and nutrients, the bottles were flushed for 15 seconds with nitrogen gas. The optimal temperature for vegetative clostridia is between 35 and 40°C although a few strains of this species can also sporulate at the same temperature range (Garcia-Alvarado *et al.*, 1992). The bottles were then incubated at 37°C in an orbital shaker at a rotational speed of 150 rpm. The volumes of the biogas collected were measured using 2 to 50 mL syringes as described by Owen *et al.* (1979).

Analytical Methods

The hydrogen gas percentage was calculated by comparing the sample biogas with a standard of pure hydrogen using a GOW-MAC Series 350 GC equipped with a thermal conductivity detector. The column was an 8' by 1" SS 350A Molesieve 13X 80/100. The operational temperatures of the injection port, the oven and the detector were 100, 50, and 100°C, respectively. Nitrogen was used as the carrier gas with a flow rate of 40 mL/min. The concentrations of total solids (TS) and volatile solids (VS) were determined by placing a 10 mL sample in 105 and 550°C ovens, respectively, according to the procedures described in APHA *et al.* (1995).

Data Analysis

A modified Gompertz equation was used to fit the experimental data to estimate the hydrogen production potential, P (mL) and the maximum hydrogen production rate, R (mL/h).

$$H = P \cdot \exp\left\{-\exp\left[\frac{R \cdot e}{P}(\lambda - t) + 1\right]\right\} \quad (2)$$

where λ is lag phase time (h) and e is 2.718. The specific hydrogen production potential (mL/g sucrose), P_s was calculated by dividing P by the appropriate grams of sucrose. The specific hydrogen production rate, R_s was calculated by dividing R by the Δ VS (the difference of final and initial VS in each individual bottle) because VS contained biomass and organics in the soil. The parameters of Eq. (2) were estimated using the function of "Solver" in Microsoft Excel version 5.0 (Microsoft, Inc., 1985 - 1995). This program uses a Newton algorithm. Up to 100 iterations were used to converge the ratio of sum of square error (SSE) to correlation coefficient (R^2) between the experiment and the estimate to a minimum. Starting parameter values were estimated using a built-in visual procedure based on a limited fit algorithm (Lay *et al.*, 1998).

The influences of pH and sucrose concentration on clostridial germination corresponding to P_s and R_s were obtained by solving the second order polynomial regression equation according to the least squares approach.

$$y = a_0 + a_1x_1 + a_2x_2 + a_{11}x_1^2 + a_{22}x_2^2 + a_{12}x_1x_2 \quad (3)$$

where y represents Ps and Rs , x_1 is pH, x_2 is sucrose (g), and a_{xx} are the coefficients of the equation. All coefficients were diagnosed by: sum of the square errors (SSE), correlation coefficient (R^2), standard errors (SE), 95% confidence limits, and F-test. Here, Statistica V.5.5 was employed for polynomial regression and response surface contour plots.

Results and Discussions

Feasibility of Natural Anaerobes Converting Sucrose to Hydrogen

Table 2 lists the biohydrogen potential of heat-shocked anaerobes consuming sucrose under a pH range from 4.0 to 8.0. In Table 2, the range of biohydrogen potential of the anaerobes consuming sucrose was from 62 to 185 mL, while the potential increased and decreased with increasing pH for the baking and boiling methods, respectively. It is obvious that the cultures contained a significant population of hydrogen-producing clostridia although a high variation in potential occurred. This variation resulted mainly from poor mixing and poor soil sample homogeneity among the batch bottles. Experience learned from soil inoculum preparation indicated that the baked soil grinded into meal easily obtained homogeneous soil samples. Additionally, experiments were run with and without added sucrose to confirm that no hydrogen production resulted from degradation of soil organic matter. As shown in curve “D” of Figure 1, no significant hydrogen production occurred from the bottle without added sucrose, indicating that soil organic matter was not converted to hydrogen.

Table 2. Biohydrogen potential of natural anaerobes using sucrose with various pH and pretreatment approaches.

Pretreatment Approach	pH Value								
	4.0	4.5	5.0	5.5	6.0	6.5	7.0	7.5	8.0
Baking	97 (14%)	82 (11%)	80 (8%)	120 (50%)	78 (6%)	165 (7%)	116 (36%)	134 (63%)	185 (6%)
Boiling	138 (19%)	118 (4%)	110 (30%)	157 (60%)	86 (41%)	164 (20%)	118 (53%)	62 (45%)	89 (7%)

* Numbers in parentheses are relative standard errors.

* Unit of potential is mL

* Data are the mean of two replicate cultures.

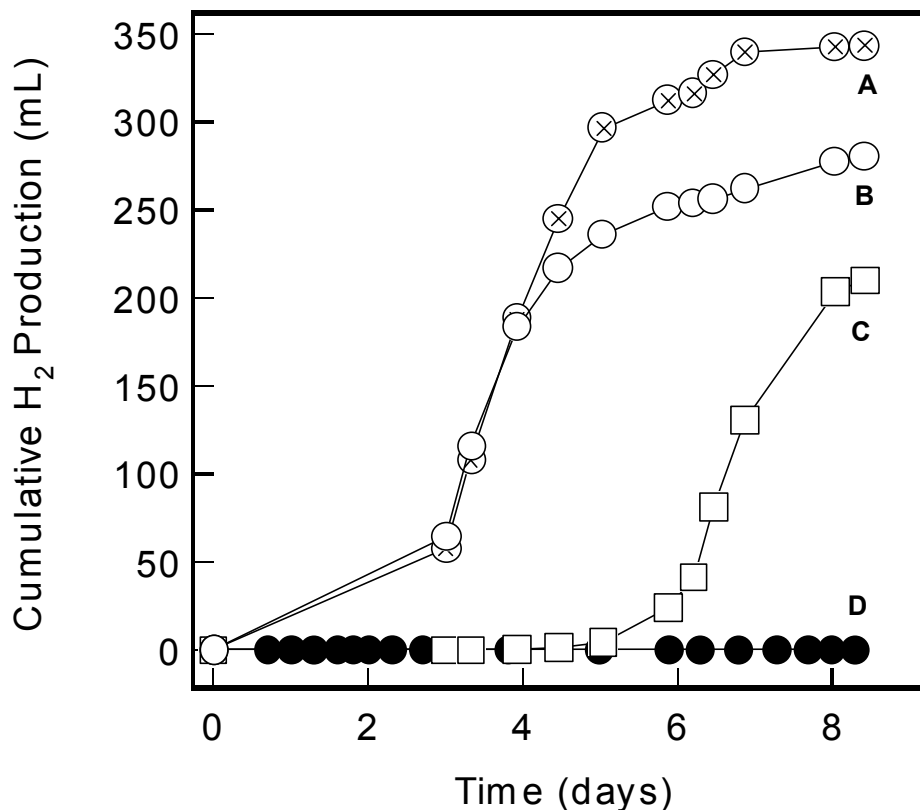


Figure 1. Feasibility of the natural anaerobes converting sucrose into hydrogen. “A” and “B” are 250-mL bottle adding with 2 and 4 grams of sucrose, respectively. “C” is 250-mL bottle adding with 2 grams of sucrose but delay 2 days. “D” is without adding sucrose.

To ensure hydrogen-producing sporeformers (i.e. clostridia) in the soil inocula consumed sucrose, two bottles containing the same soil and nutrients as described previously were individually charged with 2 and 4 grams of sucrose, which are respectively shown in curves “A” and “B” of Figure 1. Moreover, two grams of sucrose was anaerobically injected into a bottle after a 2-day incubation period (“C” curve of Figure 1). Graphically, in Figure 1, the hydrogen production shows a phase in which the production rate started at a value of zero and accelerated to a maximal value after a certain period of time (lag phase, λ). In addition, the curves contain a final phase in which the rate decreased and finally reached zero, (i.e. an asymptote or potential, P, was reached). In Figure 1, the lag-periods of curves “A” and “B” (approximately 3 days) were significantly less than that of curve “C” (approximately 5 days), indicating that the sucrose addition significantly affected the hydrogen-producing anaerobes.

Comparison of Boiling and Baking Heat Shock Treatments on Hydrogen-producing Spore Germination

Preliminary experimental experience (Lay, 2000a) indicates that if a culture of clostridia were regularly transferred as vegetative cells, the ability to form hydrogen may be permanently lost. This unusual property is named degeneration and has been circumvented by inoculating with only dry spores which were heat-shocked before incubation to eliminate the “weak” spore. In order to avoid degeneration of the culture, the spores can be activated by heat shock (Biebl, 1999). This phenomena is due to a set of so-called heat shock proteins that are clearly induced when the clostridial cells are suddenly exposed to a higher temperature (Bahl *et al.*, 1995). These proteins may play a role in the complex cycle of metabolic and morphological differentiation of clostridial bacteria. Especially, the baked soil could be ground to provide a homogeneous spore-soil mixture for initiating hydrogen-producing batch experiments. Hydrogen production potential was, therefore, introduced to monitor the effect of heat-shock treatment on clostridial germination and the transformation of sucrose into hydrogen. An eleven-repetition average indicates that the hydrogen production potential and rate of the boiling experiments (137 mL and 2.9 mL/hr, respectively) was less than that of the baking experiments (189 mL and 4.1 mL/hr, respectively), implying that the latter was superior to the former on clostridial germination. In addition, an eighteen repetition average of the batch experiments conducted with 2 grams of sucrose with a pH range of 4 to 8 indicates that the hydrogen production potential and rate of the boiling experiments (165 mL and 3.9 mL/hr, respectively) was less than that of the baking experiments (210 mL and 5.1 mL/hr, respectively), implying that the latter was superior to the former on clostridial germination. Interestingly, the environments triggering the initiation of clostridial germination still play key roles in affecting their metabolic characteristics, including hydrogen-producing activity and ability. As a result, the baking heat shock treatment might be a good candidate to induce sporulation of hydrogen-producing clostridial spores subsequently providing stable hydrogen production in addition to inhibiting hydrogenotrophic bacterial activity contained in the natural anaerobic culture.

Indicators of Hydrogen-producing Spore Germination

The cultures of hydrogen-producing anaerobes (i.e. clostridia) obtained from natural inocula typically displayed a lag-period (Figure 1). During this period, the spore suspensions transform into vegetative cells. Biosystems created with these cells initially transform sucrose into hydrogen with an exponential phase (R) and a final saturation phase (P) obtained throughout the whole culture history. Dividing the R and the P by the ΔVS and the amount of sucrose could correspond to the hydrogen-producing activity (R_s) and the specific potential (P_s) of the sucrose converted into hydrogen, respectively (Lay *et al.*, 1999).

The P_s and the R_s were, therefore, selected as indicators for monitoring spore germination. A set of batch experiments were performed by changing the initial sucrose concentrations from 13 to 40 g/L (corresponding to 15 to 45 gCOD/L) and initial pH from 4.5 to 6.5 in order to examine the effects of these environmental factors on spore germination for generating hydrogen. Equation (2) was then used to fit the experimental data of each cumulative hydrogen production curve. Typical results are plotted in Figure 2. Table 2 summaries the design matrix of the

variables in both coded and natural units along with the best values of the parameters. The diagnosis results presented that all of the correlation coefficients, R^2 , and the statistics test, $F_{0.05}$, were larger than 0.90 and the tabulated value, respectively. The F is defined as MSR/MSE , where MSR is the mean square of regression, obtained by dividing the sum of squares of regression by the degrees of freedom. MSE is the mean squares of error from the analysis of variance. If the calculated value of F exceeds that in the F table at a specified probability level (i.e., $F(P-1, v, 1-\alpha)$), then a “statistically significant” regression model is obtained, where v is the degree of freedom of error and P is the number of parameters. $F(P-1, v, 1-\alpha)$ is the F value at the α probability level. This means that a perfect fit to the experimental data and the evaluated parameters were taken to be statistically significant at a confidence interval of 95% (Box *et al.*, 1978). Moreover, both the curve fitting and statistical analysis demonstrated that Equation (2) was suitable for estimating the hydrogen production lag-period, rate, and potential of the clostridia in converting sucrose to hydrogen.

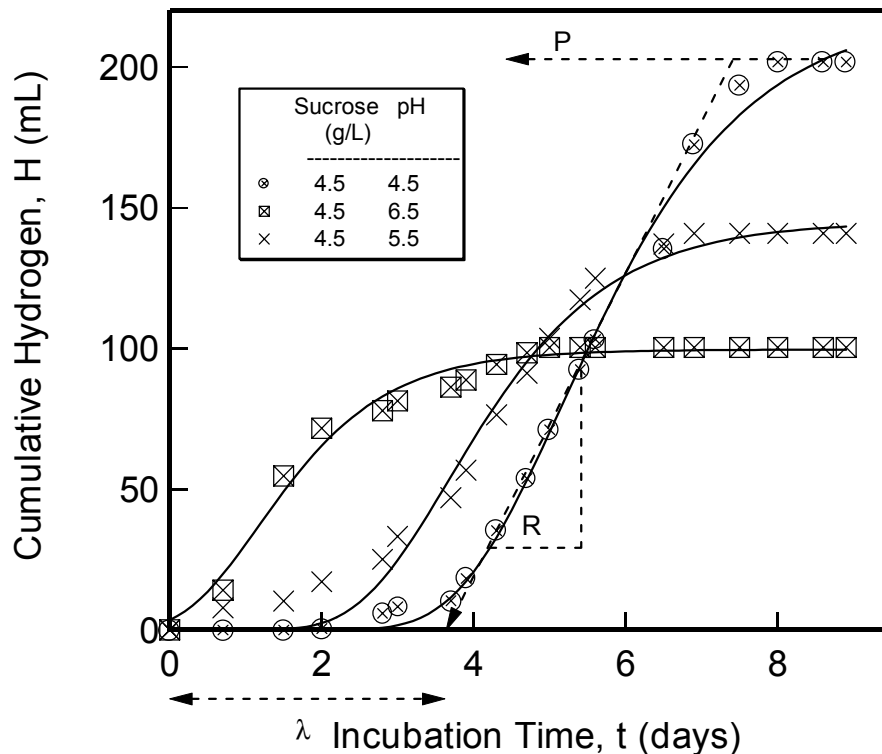


Figure 2. A typical cumulative hydrogen production curve in batch experiments (markers are experimental data; lines are nonlinearly estimated using Eq. 2; and the variables R , λ , and P are defined as in Eq. 2).

Specific Hydrogen Production Potential and Rate

To depict the relationships between pH (x_1) and sucrose concentration (x_2) on specific hydrogen production potential (Ps) and rate (Rs), the design matrix with corresponding results listed in Table 3 was subjected to multivariate analysis; that is, multiple regression with stepwise method, depending on the quadratic polynomial model used (refer to Equation (3)). The following equations could arrange the rank of linear, squared, and interaction effects between pH and sucrose concentration on spore germination for hydrogen production.

$$Ps = 13.57 - 0.45767x_2 + 0.00552x_2^2 + 0.00727x_1x_2 - 0.46523x_1 \quad (4)$$

(F = 43.9, df = 4, 6, $R^2 = 0.9670$)

$$Rs = 3.16 - 0.19165x_2 + 0.002268x_2^2 + 0.332233x_1 - 0.002538x_1x_2 \quad (5)$$

(F = 20.6, df = 4, 6, $R^2 = 0.9320$)

The significance of Equations (4) and (5) was estimated using the same statistical approach that was used for Equation (2) and the values of R^2 and F were larger than 0.90 and the tabulated

Table 3. Full factorial central composite design matrix of two variables in coded and natural units along with the observed responses.

x_1	x_2	pH	Sucrose (g)	Sucrose (gCOD/L)	Baking Experiments	
					Ps (mL/gCOD _{sucrose})	Rs (mL/TVS/hr)
-1	-1	5.0	3.0	22.5	3.9	1.0
1	-1	6.0	3.0	22.5	4.8	1.5
-1	1	5.0	5.0	37.5	2.4	0.6
1	1	6.0	5.0	37.5	2.3	0.5
0	0	5.5	4.0	30.0	3.3	0.9
-2	0	4.5	4.0	30.0	3.3	0.8
2	0	6.5	4.0	30.0	3.5	0.9
0	-2	5.5	2.0	15.0	6.7	2.3
0	2	5.5	6.0	45.0	2.2	0.5
0	0	5.5	4.0	30.0	3.2	1.0
0	0	5.5	4.0	30.0	3.4	0.8

*Data are the mean of two replicate cultures.

value, respectively, indicating that the models were suitable for accurately representing the experimental results. Examining the terms listed in Equations (4) and (5), sucrose concentration played a more important role than the pH value on specific hydrogen production rate and potential. For the examination of the dependence of the potential and rate on both factors, the contour plots (Figure 3) were constructed using Equations (4) and (5). Consider the fitted equations (Equations (4) and (5)) graphed in Figure 3. The constant potential and rate curves have the shape commonly referred to as a “ridge” system. The constant rate and potential increased with a decrease in the sucrose concentration from 45 to 15 gCOD/L. This phenomena appears to be correlated with the anaerobic biohydrogenization of microcrystalline cellulose (Lay, 2000b). The low initial ratio of substrate concentration (S_0) to sludge density (X_0) corresponding to low S_0 and constant X_0 accompanied high-level hydrogen production. It was also tempting to consider a high concentration of organic acids produced by the hydrogen-producing clostridia consuming high levels of sucrose to cause the internal pH to decrease to below critical values, resulting in the cessation of growth and the loss of viability (Gottwald and Gottschalk, 1985).

Compared to sucrose concentration, there was very little increase in hydrogen production potential and rate in the pH range of 4.5 to 6.5 (Figure 3). To assess the role of pH on hydrogen-producing spore germination, consider the hydrogen production potential and rate graphed in Figure 3 using Equations (4) and (5), respectively, while the sucrose concentration was 15 g COD/L. As shown in Figure 4, the relative hydrogen production potential decreased and the rate

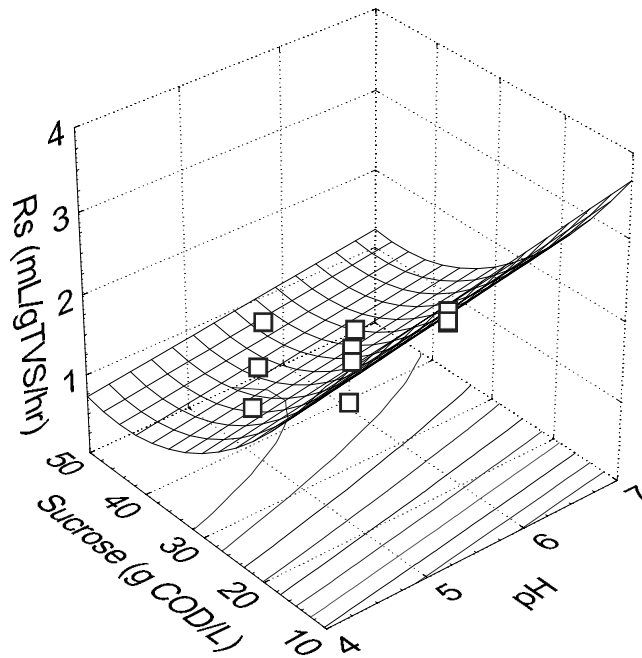


Figure 3. Constant specific hydrogen-producing potential (P_s , mL H_2 /gCOD_{sucrose}) and rate (R_s , mL H_2 / Δ gVS/hr) contour lines of baking soil against initial pH and sucrose concentration.

increased with increase in initial pH. Although no significant evidence could explain this phenomena, on the examination of the two lines plotted in Figure 4, the rate increased 50% and the potential decreased 50% at a pH of 5.5. Furthermore, the pH value of 5.2 was the optimum pH for controlling a chemostat reactor using heat-shocked anaerobic digested sludge to transform starch into hydrogen (Lay, 2000a). Similarly, the experimental results of Bahl and coworkers demonstrated that an acidic pH below 5.0 was found optimal for butanol-producing clostridia (Bahl et al., 1982). However, what is the optimal pH for hydrogen-producing clostridial spore germination or hydrogen formation is still an open question. According to the description in Figure 4, the pH of 5.5 might be a trigger for hydrogen-producing clostridial germination and for the dynamic metabolic balance between hydrogenesis and solventogenesis. Nevertheless, according to multivariate analysis (refer to Eq. (4) and (5)) and contour plots (Figure 3), substrate deprivation was more important than initial pH value on spore germination for generating hydrogen although very little has been done to clarify the mechanisms of hydrogen-producing spore germination associated with metabolites.

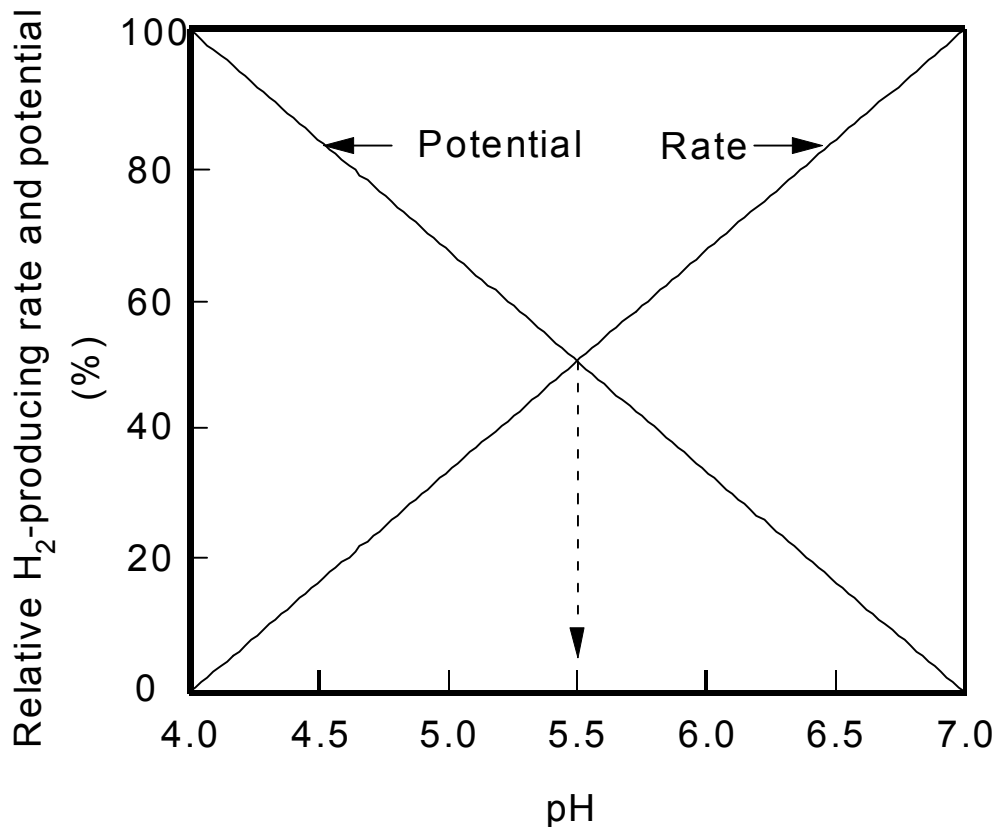


Figure 4. Relationship between initial pH and relative hydrogen-producing potential and rate under sucrose concentration of 15 gCOD/L using Eqs. (4) and (5), respectively.

Conclusions

Naturally obtained, sporeforming, hydrogen producing anaerobic bacteria (i.e. clostridia) have considerable potential in the transformation of carbohydrates into hydrogen. As of yet, there is no selective enrichment procedure for hydrogen-producing spores. Nevertheless, they are easily obtained from soil and the samples can easily be heat-shocked to exclude non-spore-forming, hydrogen-consuming anaerobes. However, obtaining an appropriate approach for hydrogen-producing clostridial germination is complicated by the fact that the genus *Clostridium* and their germination-associated metabolites have yet to be clarified. To overcome this problem, cultures with boiling- and baking-shock treatments were performed to measure the stability of natural anaerobes to form hydrogen, indicating the latter was easier than the former in finding a stable hydrogen-production potential. Experimental observations may indicate that the soil contained a high proportion of hydrogen-producing spore-forming clostridia, however their germination was significantly affected by sucrose addition. Statistical experimental strategies were adopted to systematically collect clostridial hydrogen-producing data sets from batch cultures by varying initial pH and sucrose concentrations from 4.5 to 6.5 and 15 to 45 gCOD/L, respectively. Although what controls the mechanisms of clostridial hydrogen-producing germination has not been determined in detail, substrate deprivation was suggested to be more important than the initial pH value on clostridial germination according to multivariate analysis (i.e., polynomial regression with stepwise) and response surface plots. Correlations between the relative hydrogen production rate and potential plotted against their respective pH value demonstrates clearly that the pH value of 5.5 might be a trigger for clostridial germination and might shift the metabolic balance from hydrogen to solvent formation.

References

- APHA, AWWA, WPCF. 1995. Standard methods for the examination of water and wastewater, 19th ed. American Public Health Association, Washington, DC, USA.
- Afschar, A. S., Schaller, K. 1991. Production of acetone and butanol from starch by continuous bioprocess. *J. Biotechnol.* **18**: 255-264.
- Bahl, H., Andersch, W., Braun, K., Gottschalk, G. 1982. Effect of pH and butyrate concentration on the production of acetone and butanol by *Clostridium acetobutylicum* grown in continuous culture. *European J. Appl. Microbiol. Biotechnol.* **14**:17-20.
- Bahl, H., Muller H., Behrens, S., Joseph, H., Narberhaus, F. 1995. Expression of heat shock genes in *Clostridium acetobutylicum*. *FEMS Microbiol. Rev.* **17**: 341-348.
- Biebl, H. 1999. *Clostridium acetobutylicum*. In: Robinson, R., Batt, C. and Patel, P., editors. *Encyclopedia of Food Microbiology*, pp. 445 – 451. Academic Press.

- Billings, R. E. 1991. The hydrogen world view, pp. 66 – 76, American Academy of Science.
- Borkris, J. O'M. 1973. A hydrogen economy. *Science* **178**: 1323-1323.
- Box, G. E. P., Hunter, W. G., Hunter, J. S. 1978. Statistics for experimenters. An introduction to design, data analysis, and model building, Wiley, New York.
- Craven, S. E. 1988. Increased sporulation of *Clostridium perfringens* in a medium prepared with the prereduced anaerobically sterilized technique or with carbon dioxide or carbonate. *J. Food Prot.* **51**: 700-706.
- Garcia-Alvarado, J. S., Rodriguez, M. A. and Labbé, R. G. 1992. Sporulation and enterotoxin production by *Clostridium perfringens* Type A. *Appl. Environ. Microbiol.* **58**: 1411-1414.
- Giallo, J., Gaudin, C. and Belaich, J.-P. 1985. Metabolism and solubilization of cellulose by *Clostridium cellulolyticum* H10. *Appl. Environ. Microbiol.* **49**(5): 1216-1221.
- Gottwald, M. and Gottschalk, G. 1985. The internal pH of *Clostridium acetobutylicum* and its effect on the shift from acid to solvent formation. *Arch. Microbiol.* **143**: 42-46.
- Gray, C. T., Gest, H. 1965. Biological formation of molecular hydrogen. *Science* **148**: 186-191.
- Kidby, D. W. and Nedwell, D. B. 1991. An investigation into suitability of biogas hydrogen concentration as performance monitor for anaerobic sewage sludge digesters. *Water Res.* **25**(8): 1007-1012.
- Labbé, R. G. and Rey, D. K. 1979. Raffinose increases sporulation and enterotoxin production by *Clostridium perfringens* Type A. *Appl. Environ. Microbiol.* **37**: 1196-1200.
- Labbé, R. G. and Shih, N.-J. 1997. Physiology of sporulation of clostridia. *In* The clostridia: molecular and pathogenesis, p 21-32, Rood, J. I., McClane, B. A., Songer, J. G., Titball, R. W. (eds), Academic Press, New York.
- Lay, J. J., Li, Y. Y., Noike, T. 1998. A mathematical model for methane production from a landfill bioreactor. *J. Envir. Engrg., ASCE*, **124**(8): 730-736.
- Lay, J. J., Lee, Y. J, Noike, T. 1999. Feasibility of biological hydrogen production from organic fraction of municipal solid waste. *Water Res.* **33**(11): 2579-2586.
- Lay, J. J. 2000a. Modeling and optimization of anaerobic digested sludge converting starch to hydrogen. *Biotechnol. Bioeng.* **68**(3): 269-278.
- Lay, J. J. 2000b. Biohydrogen generation by mesophilic anaerobic fermentation of microcrystalline cellulose. Submitted for publication.
- Microsoft Excel User Guide; version 5.0. 1994. Microsoft Corporation.

- Miyake, J., Mao, X.-Y., Kawashima, S. 1984. Photoproduction of hydrogen from glucose by a co-culture of photosynthetic bacterium and *Clostridium butyricum*. J. Ferment. Technol. **62**: 531-535.
- Owen, W. F., Stuckey, D. C., Healy Jr., J. B., Young, L. Y., McCarty, P. L. 1979. Bioassay for monitoring biochemical methane potential and anaerobic toxicity. Water Res. **13**: 485-493.
- Rajeshwar, K., Ibanez, J. G., Swain, G. M. 1994. Electrochemistry and the environment. J. Appl. Electrochem. **24**: 1077-1091.
- Sauer, U., Santangelo, J. D., Treuner, A., Buchholz, M., Durre, P. 1995. Sigma factor and sporulation genes in *Clostridium*. FEMS Microbiol. Rev. **17**: 331-340.
- Taguchi, F., Chang, J. D., Takiguchi, S., Morimoto, M. 1992. Efficient hydrogen production from starch by a bacterium isolated from termites. J. Ferment. Technol. **73**: 244-245.
- Ueno, Y., Kawai, T., Sato, S., Otsuka, S., Morimoto, M. 1995. Biological production of hydrogen from cellulose by natural anaerobic microflora. J. Ferment. Technol. **79**(4): 395 - 397.
- Woods, D. R. and Jones, D. T. (1986) Physiological responses of *Bacteroides* and *Clostridium* strains to environmental stress factors. Adv. Microb. Physiol. **28**: 1-64.
- Zajic, J. E., Kosaric, N. and Brosseau, J. D. 1978. Microbial production of hydrogen. Adv. Biochem. Eng. **7**: 57-109.
- Zeikus, J. G. 1980. Chemical and fuel production by anaerobic bacteria. Ann. Rev. Microbiol. **34**: 423-464.

THERMAL DISSOCIATION OF METHANE USING A SOLAR COUPLED AEROSOL FLOW REACTOR

**Alan W. Weimer, Jaimee Dahl, and Karen Buechler
University of Colorado, Department of Chemical Engineering
Boulder, CO 80309-0424**

**Allan Lewandowski, Roland Pitts, and Carl Bingham
National Renewable Energy Laboratory
Golden, CO 80401-3393**

**Gregory C. Glatzmaier
Peak Design
Evergreen, CO 80439**

Abstract

A solar-thermal aerosol flow reactor has been constructed, installed and tested at the High-Flux Solar Furnace (HFSF) at the National Renewable Energy Laboratory (NREL). “Proof-of-concept” experiments were successfully carried out for the dissociation and the dry reforming (with CO₂) of methane to produce hydrogen and carbon black, and syngas, respectively. Approximately 90% dissociation of methane was achieved in a 25-mm diameter quartz reaction tube illuminated with a solar flux of 2400 kW/m² (or suns). An improved reactor has been designed and is being constructed to obtain more complete kinetic and process data for scale-up. Preliminary economics for a 5,000,000 kg/yr solar-thermal hydrogen plant were evaluated using a discount cash flow analysis that required a 15% internal rate of return (IRR). If either product is the sole source of revenue, the required selling price for hydrogen was \$23/MBtu and for carbon black it was \$0.48/lb. If both products are sold, and carbon black is sold for \$0.20/lb (typical tire applications), the required selling price for hydrogen was \$13/MBtu. If carbon black is sold at the current market price for typical chemical/battery applications (\$0.35/lb), the price for hydrogen is a very attractive \$6/MBtu. Both the experimental and economic results are very encouraging and support further work to address the technical issues and to develop the process.

Introduction

The primary driver for the development of renewable energy strategies is current concern over the potential, irreversible environmental damage that may occur with the continued or accelerated use of fossil fuels. Movement toward a hydrogen (H₂) based economy is an essential component of an international program to address that concern and will, in addition, address concerns over pollution in cities and associated health costs. However, current methods for producing H₂ incur a large environmental liability because fossil fuels are burned to supply the energy to reform methane (CH₄). We propose an alternate strategy using highly-concentrated sunlight as the energy source that does not result in an increase of environmental liability. Indeed, it represents a route for utilizing current natural gas reserves that fixes carbon as well as increasing the energy content of the fuel. The research presented here is oriented at developing a cost-effective, solar-thermal method of deriving H₂ from natural gas.

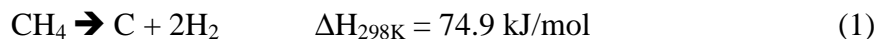
Objectives

The long-term objectives of the project are (1) to develop a technical and economic understanding of the benign synthesis of hydrogen using solar-thermal driven aerosol processing of natural gas; and (2) if technically and economically feasible, to develop the process with industrial partners.

Shorter-term objectives include (1) preliminary “proof-of-concept” experiments; (2) the design, fabrication, installation, and evaluation of an improved reactor system with in-line analytical characterization of the produced hydrogen-rich gas and measured flows allowing material balance closure – the design incorporating a secondary solar concentrator to increase solar efficiency and to increase attainable system temperatures; (3) an improved understanding of the process through preliminary math model development/experimental validation and economic/environmental impact analysis; (4) analytical characterization to assess the value of the produced carbon black under varying processing conditions (solar intensities, flow rates, etc.); and (5) dissemination of information via oral presentations at technical meetings and publications in peer-reviewed research journals.

Background

Steinberg [1986, 1987, 1994, 1995, 1998, 1999] and Steinberg and co-workers [Steinberg and Cheng, 1989] have been major proponents of the thermal decomposition of CH₄ process for H₂ production. Methane (CH₄) is dissociated to carbon (C) black and H₂ according to:



Methane (CH₄) is a preferred choice for the production of H₂ from a hydrocarbon because of its high H to C ratio (H/C = 4), availability, and low cost. Furthermore, the C produced can be sold as a co-product into the carbon black market (inks, paints, tires, batteries, etc.) or sequestered,

stored, and used as a clean fuel for electrical power generation. The sequestering or storing of solid C requires much less development than sequestering gaseous CO₂.

Gibbs free energy minimization calculations have been carried out ($P = 0.1$ MPa; $873 \text{ K} \leq T \leq 2273 \text{ K}$) for the CH₄ dissociation system (i.e. CH₄ + heat → equilibrium products) to determine equilibrium products. The concentrations of chemical species reaching a state of chemical equilibrium from reaction or partial reaction at atmospheric pressure for various reaction temperatures have been calculated using the F*A*C*T equilibrium code EQUILIB [Thompson et al., 1985]. Thermodynamically favored products (Figure 1) indicate dissociation above 600 K and that temperatures $T > 1600 \text{ K}$ are required to achieve nearly complete dissociation. Although not shown, trace products at 1600 K include C₂H₂, C₂H₄, C₄H₈, C₃H₆, C₂H₆, and other species at concentrations < 40 ppm.

There are several alternatives to supply the energy required to drive reaction (1). In the commercial “Thermal Black Process” [Donnet, 1976], the energy is provided by burning CH₄ with air to heat a fire brick furnace to temperatures as high as 1673K. Once hot, the air is shut off

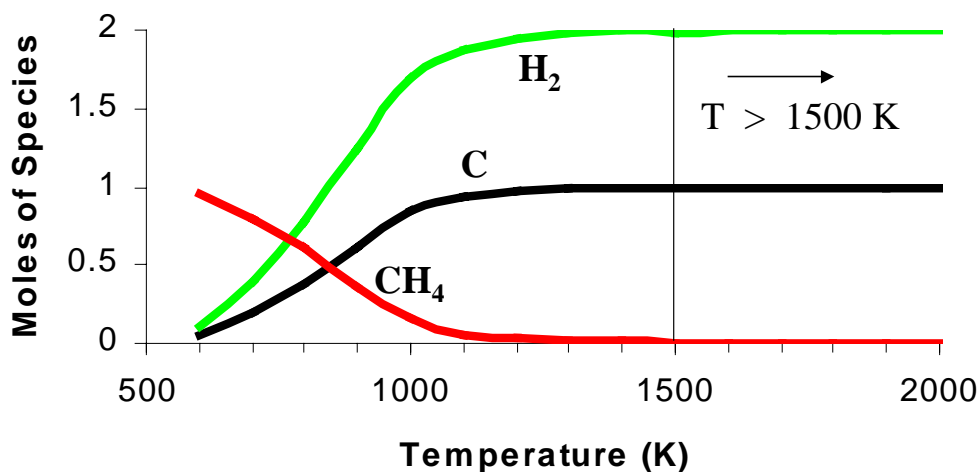


Figure 1. Primary Methane Decomposition Equilibrium Products $P = 0.1$ MPa

and the CH₄ decomposes according to reaction (1) until the wall temperature drops to below 1073 K. The system is operated semi-continuously with CH₄ burned in one sequence of the cycle to supply the heat necessary to carry out the decomposition in the second sequence. This process has been practiced for many years for the production of carbon black. The H₂ produced is used as a fuel to heat the furnace and the CH₄ feedstock.

Pohleny and Scott (1962) used a fluidized bed/riser thermal decomposition reactor process that uses iron oxide for heat transfer and as a catalyst. Carbon collected on the iron oxide particles in the fluidized bed is burned off in the riser reactor for reheating the iron oxide particles that are

recirculated to the endothermic fluidized bed reactor. Hydrogen is produced continuously by the decomposition occurring in the fluidized bed.

Gaudernack and Lynum (1996) and Bromberg et al. (1998) used a plasma torch to supply the necessary energy to decompose CH_4 and produce a continuous stream of H_2 . The plasma gas is H_2 that is recirculated from the process. Although no CO_2 is liberated from the process reactor itself, electricity is required to produce the plasma. When the electrical power is produced from natural gas fuel combustion, even in an efficient combined cycle plant, the overall thermal efficiency is significantly reduced and the CO_2 emission per unit energy is significantly increased.

In another process [Steinberg, 1995a], a molten metal bath reactor (such as tin or copper) is used to transfer heat to CH_4 that is bubbled through the molten metal. The reactor is heated by combustion products (CH_4 or H_2 burned with air) that flow through an internal heat exchanger. In this process, it is proposed to capture carbon in the liquid metal and to separate it from the metal by density difference, skimming the carbon off from the surface much as slag is skimmed off the surface of molten iron in a conventional blast furnace.

Although thermodynamics can predict when a reaction will not occur, it cannot predict whether a reaction will indeed occur in practice. Activation energies, transport processes (e.g. heating rate), and other reaction kinetic considerations are needed in order to determine if a reaction can be completed for a given amount of time in a chemical reactor design. Such kinetic data have been reported for reaction (1) using electrically-heated pilot-scale aerosol flow reactors [Matovich, 1977].

Matovich (1977) showed that the decomposition of CH_4 could be carried to completion in a short residence time aerosol reaction tube at temperatures $T > 2088$ K. The reactor consisted of a 0.0762-m diameter x 0.914-m long (3 inch ID x 3 ft long) graphite aerosol reaction tube heated indirectly by radiation from external electrodes heated directly by electrical resistance. Later studies included work carried out in 0.305-m ID x 3.66-m long (1 ft ID x 12 ft long) reaction tubes [Lee et al., 1984]. A small amount of carbon black was introduced in the CH_4 feed stream to serve as a radiation-absorbing target to initiate the pyrolytic reaction. Due to the high temperatures involved and the difficulty in heating a gas to those temperatures (by convection from the reactor walls), the carbon particles are the key to this process.

Reactions were carried out in the temperature range of $1533 < T < 2144$ K with residence times between approximately 0.1 and 1.5 seconds. The fraction of CH_4 dissociated was determined by measuring the thermal conductivity of the effluent gas after filtering the carbon black particles from the sample. Hydrogen (H_2) flowed radially through a porous reaction tube, providing a fluid-wall to prevent carbon black from depositing on the wall. The residence time in the reactor was controlled by the inlet flow of CH_4 , the radial flow of H_2 , and the reactor temperature. Some reported results [Matovich, 1977] where data were available for both a minimum residence time ($t_{r(\min)}$) of 0.2 s and a maximum residence time ($t_{r(\max)}$) of 1 s are summarized in Figure 2. It is clear from these results that residence time has little effect on dissociation for temperatures $T > 1900$ K and that complete dissociation can be achieved in aerosol flow reactors for temperatures greater than approximately 2100 K for reaction times of $t = 0.2$ s.

The process investigated here is the high-temperature thermal dissociation of CH_4 using a solar-thermal aerosol flow reactor. The energy required to drive reaction (1) is supplied by concentrated sunlight. An experimental reactor apparatus was constructed and interfaced to NREL's HFSF [Jenkins et al., 1996; Lewandowski, 1993; Lewandowski et al., 1991; and Pitts et al., 1993]. There is no need for auxiliary cooling at the optical source. The reactor is operated as a cold wall process, because the beam is delivered directly on target. In addition, the control of solar radiation (on/off) is almost instantaneous. Absorbing surfaces exposed to concentrated solar radiation can reach temperatures of between 1000 K and 3000 K in fractions of a second. The process produces H_2 using high-efficiency direct solar-thermal heating with no associated CO_2 generation.

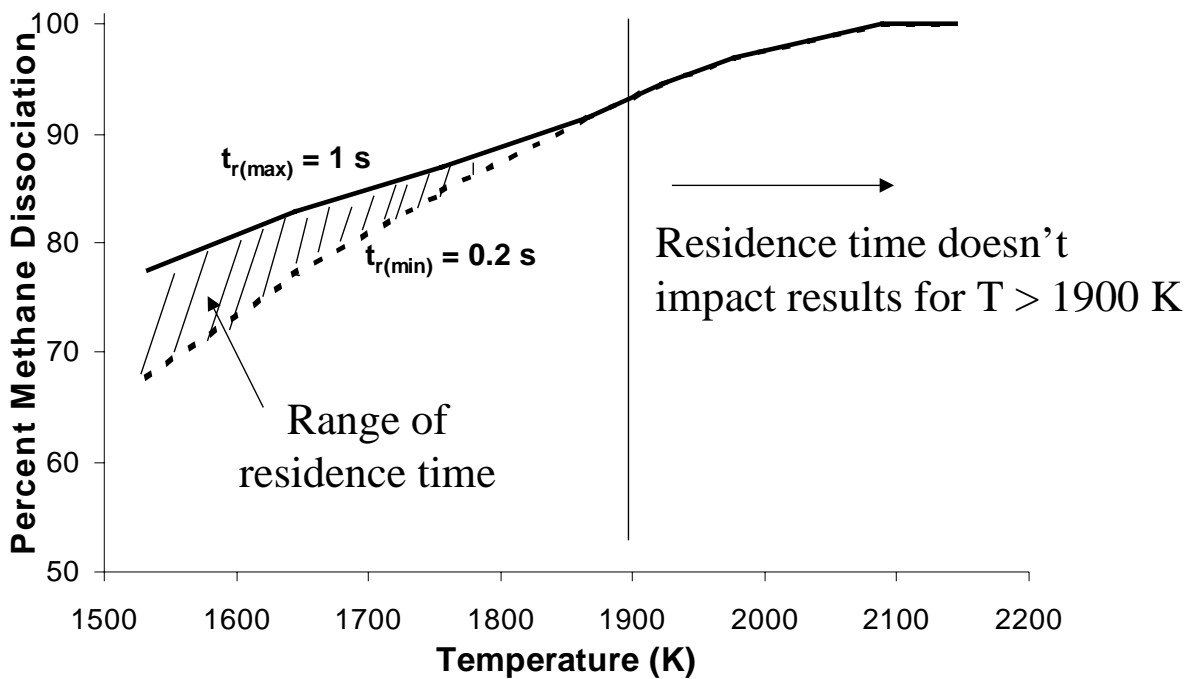


Figure 2. Effect of Residence Time & Temperature

Theoretical Work

In order to gain a better understanding of the reaction kinetics in the solar-thermal reactor, a model was developed to describe the reactor developed by Matovich (1977). The data obtained by Matovich (1977) are the only known data for complete dissociation of methane to carbon and hydrogen at high temperatures. The model incorporates a kinetic model to describe the rate of conversion as well as a gas phase energy balance and a carbon particle energy balance. The following assumptions are made: (1) both the carbon particle and the gas temperature vary only

in the axial direction; (2) all gases are transparent to radiation [Kreith and Black, 1980]; (3) radiative emissivities and absorptivities are equal for the carbon particles [Kreith and Black, 1980]; (4) the carbon particles and the gas stream are moving at the same velocity; (5) the reactor operates at steady state; and (6) the feed gas is pure methane. The nomenclature for the next sections is located at the end of this document.

Kinetic Model

A typical rate expression for decomposition was used to model kinetics [Weimer, 1997]:

$$\frac{dX}{dt} = k(1-X)^a \quad (2)$$

Using the chain rule,

$$\frac{dX}{dz} = \frac{k(1-X)^a}{v_g} \quad (3)$$

where the reaction rate, k , is defined by the Arrhenius expression:

$$k = k_o \exp\left(\frac{-E_a}{RT_g}\right) \quad (4)$$

Due to the nonlinearity of the Arrhenius expression, an interaction between k_o and E_a arises. This interaction is reduced by a transformation of T_g in the expression [Himmelblau, 1970]:

$$k = k_o^* \exp\left[\frac{-E_a^*}{R} \left(\frac{1}{T_g} - \frac{1}{T_o}\right)\right] \quad (5)$$

where $T_o = 1200K$. T_o is an arbitrarily chosen temperature that is within the range of temperatures occurring in the reactor. The resulting kinetic expression is

$$\frac{dX}{dz} = \frac{k_o^* \exp\left[\frac{-E_a^*}{R} \left(\frac{1}{T_g} - \frac{1}{T_o}\right)\right] (1-X)^a}{v_g} \quad (6)$$

Carbon Particle and Gas Phase Thermal Energy Balances

An energy balance around an arbitrary volume element of the gas phase was made. The gas phase is heated by the reactor wall, the hydrogen gas introduced through the porous reactor wall,

and the carbon particles. The sources of the energy generated and consumed are shown in Figure 3.

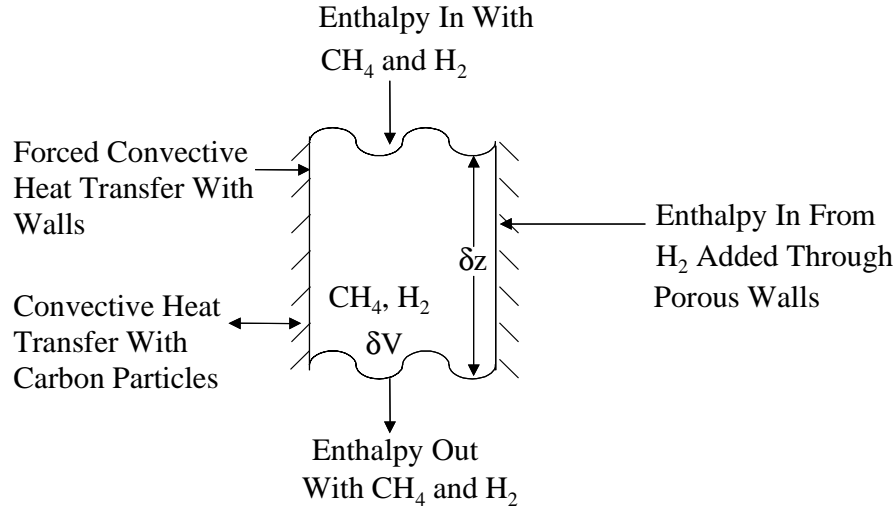


Figure 3. Schematic of Heat Transfer in Gas Phase

By combining these sources of energy one can develop an expression that describes the change in gas temperature along the distance down the reactor:

$$\frac{dT_g}{dz} = \frac{F_{CH_4}^0 [H_{CH_4}(@T_g) - 2H_{H_2}(@T_g)] \frac{dX}{dz} + g \int_{T_g}^{T_w} C_{pH_2} dT + h_w \pi d_i (T_w - T_g) + h_p \frac{a_c F_c M_{wc}}{v_g V_c \rho_c} (T_c - T_g)}{F_{CH_4} C_{pCH_4} + F_{H_2} C_{pH_2}} \quad (7)$$

The first term in the numerator of the right hand side accounts for the hydrogen formed by reaction, the second term describes the energy brought in with the hydrogen added through the walls, the third term accounts for the convective heat transfer between the walls and the gas stream, and the last term describes the convective heat transfer between the particles and the gas phase.

A similar balance was conducted for a cloud of carbon particles. The particles absorb heat from the walls and transfer that energy to the gas stream. The components of the energy balance are shown in a schematic diagram in Fig. 4.

A description of the change in carbon particle temperature over the distance of the reactor is given by:

$$\frac{dT_c}{dz} = \frac{-F_{CH_4}^0 H_c(@T_c)}{F_c C_{pc}} \frac{dX}{dz} + \frac{-h_{pac} A_{inc} (T_c - T_g) + \epsilon_c \sigma a_c A_{inc} (T_w^4 - T_c^4)}{F_c C_{pc}} \quad (8)$$

The first term on the right hand side of equation (8) describes heat generated by the carbon formed by reaction. The second term on the right hand side accounts for the convective heat

transfer between the particles and the gas, and also the radiative heat transfer between the reactor walls and the particles.

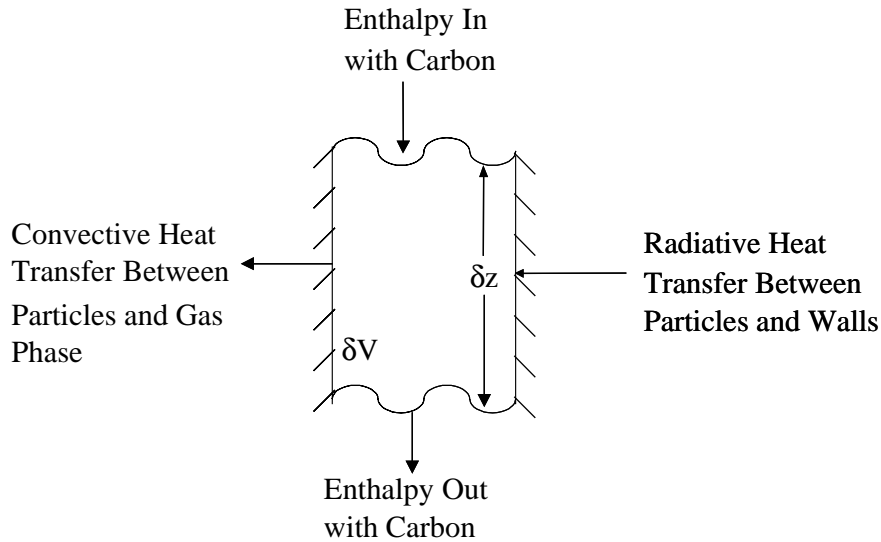


Figure 4. Schematic of Heat Transfer in a Cloud of Carbon Particles

Supporting Equations

Several equations were used to define the variables in the ordinary differential equations. The heat transfer coefficient between the gas phase and the carbon particles is defined as:

$$h_p = \frac{k_g}{R_o} \quad (9)$$

where k_g is the thermal conductivity of the gas and R_o is the radius of a carbon particle.

For surface temperatures from 1173 K to 2473 K, the convective coefficient between the gas phase and the reactor walls is [Roberts et al., 1971]:

$$h_w = 0.034 \left[\frac{k_g(@T_f)}{d_i} \right] \left[\frac{F_g M_{w_g} d_i}{A_i \mu_g(@T_f)} \right]^{0.8} \left(\frac{T_g}{T_f} \right)^{0.8} \left[\frac{C_{p_g}(@T_f) \mu_g(@T_f)}{k_g(@T_f) M_{w_g}} \right]^{0.4} \left(\frac{L}{d_i} \right)^{0.1} \quad (10)$$

where T_f is the film temperature (arithmetic average of the gas temperature and wall temperature), F_g is the molar flow rate of the gas, M_{w_g} is the molecular weight of the gas, μ_g is the viscosity of the gas, and C_{p_g} is the heat capacity of the gas.

The molar flow rates for each species are as follows:

$$F_{CH_4} = F^0_{CH_4}(1 - X) \quad (11a)$$

$$F_c = XF^o_{CH_4} + 0.1 \text{ mol/s} \quad (11b)$$

$$F_{H_2} = 2XF^o_{CH_4} + fz \quad (11c)$$

The second term on the right hand side of Equation (11b) is an estimate of the amount of carbon added to the system initially to initiate the reaction. The second right-hand-side term of Equation (11c) accounts for the hydrogen added through the porous walls. It was assumed that the quantity of hydrogen entering the reactor was evenly distributed over the length of the reactor tube.

The molecular weight of the gas phase can be calculated as follows:

$$M_{wg} = \frac{\sum_{\text{gas}(i)} F_i M_{wi}}{\sum_{\text{gas}(i)} F_i} \quad (12)$$

Similarly, the specific heat capacity of the gas phase can be calculated as:

$$C_{Pg} = \frac{\sum_{\text{gas}(i)} F_i C_{pi}}{\sum_{\text{gas}(i)} F_i} \quad (13)$$

The thermal conductivity of the gas phase can be calculated by:

$$k_g = \frac{\sum_{\text{gas}(i)} F_i k_i M_{wi}^{1/3}}{\sum_{\text{gas}(i)} F_i M_{wi}^{1/3}} \quad (14)$$

The viscosity of the gas phase can be calculated as:

$$\mu_g = \frac{\sum_{\text{gas}(i)} F_i \mu_i M_{wi}^{1/3}}{\sum_{\text{gas}(i)} F_i M_{wi}^{1/3}} \quad (15)$$

The velocity of the gas phase can be calculated by:

$$v_g = \frac{\sum_{\text{gas}(i)} \frac{F_i}{\rho_i}}{A_i} \quad (16)$$

Data found in Yaws (1999), Touloukian (1970, 1975), and FACT (1999) are used to calculate the viscosities, heat capacities, and thermal conductivities of hydrogen and methane.

Simulations

The parameters used for simulating the reactor are listed in Table 1. These parameters, as well as the experimental conditions, such as furnace wall temperature (T_w), feed gas flow rate ($F_{CH_4}^o$), and flow rate of H_2 added through the reactor walls (f), are used with equations 6, 7, and 8 and the supporting equations to form a system of coupled ordinary differential equations and algebraic equations that are solved simultaneously. A best-fit model is obtained by varying the kinetic constants (a , k_o^* , and E_a^*). The Gauss-Newton method [Chapra and Canale, 1988] is used, which minimizes the sum of the squares of the residuals between the conversions reported by Matovich (1977) and the conversions calculated by equation (6). A constraint was placed in the model requiring approximately 100% conversion for wall temperatures at or above 2089K for methane feed flow rate of 0.0189 mol/s. In addition to conversion profiles, the simulation outputs gas phase and carbon particle temperature profiles.

Results and Discussion

Intrinsic Kinetics

All data with a conversion of 90% or less were fit. This resulted in fitting 22 data points in the wall temperature range of 1533-1977 K as well as forcing the model to predict approximately 100% conversion at the point corresponding to a wall temperature of 2089 K and an initial methane flow rate of 0.0189 mol/s. A comparison between the conversions determined experimentally by Matovich and the conversions calculated theoretically using the model is shown in Figure 5.

These conversions were calculated using the following best-fit kinetic parameters: $a=4.4$, $k_o=6 \times 10^{11} \text{ s}^{-1}$, and $E_a=208 \pm 65 \text{ kJ/mol}$. These three parameters had the best fit to the experimental data, but there were several other points with comparable fits. The activation energy predicted by this model is lower than that reported in the literature. The fine carbon particles that are fed into the reactor and are formed by reaction have a significant amount of surface area. They catalyze the reaction and thus decrease the activation energy [Steinberg, 1998].

Using these parameters, the model was run for various reactor wall temperatures and initial methane molar flow rates. A plot of feed methane molar flow rate versus final conversion for several wall temperatures is shown in Figure 6.

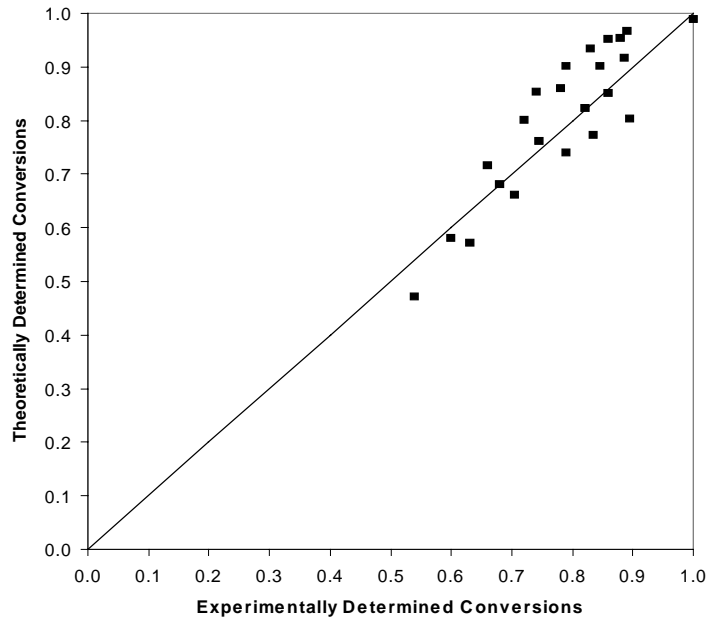
Due to the large number of data points, profiles from only a selection of points will be presented. The conversion profiles for an initial methane molar flow rate of 0.0566 mol/s are shown in Figure 7. The wall temperature was varied between 1533 and 1922 K. Conversion profiles for a wall temperature of 1644 K, with the initial methane molar flow rate varying from 0.0189 to 0.0944 mol/s, are portrayed in Figure 8.

Table 1. Parameters Used in Reactor Simulation

Parameter	Value	
a	4.4	
a _c	3.14x10 ⁻⁸	m ²
A _i	4.56x10 ⁻³	m ²
d _i	0.076	m
E _a	208	kJ/mol
F	2.36x10 ⁻³	m ³ /s
F ^o _{CH4}	0.0189 - 0.0944	mol/s
K _o	6x10 ¹¹	s ⁻¹
L	0.914	m
M _{wc}	0.012	kg/mol
R	8.314	J/mol K
R _o	5x10 ⁻⁵	m
T _w	1533 - 2144	K
V _c	5.24x10 ⁻¹³	m ³
ε _c	1	
ρ _c	2270	Kg/m ³
σ	5.67x10 ⁻⁸	W/m ² K ⁴

Initial Conditions for Ordinary Differential Equations

T _g	298	K
T _c	298	K
X	0	

**Figure 5.** Comparison of Theoretically and Experimentally Determined Conversions

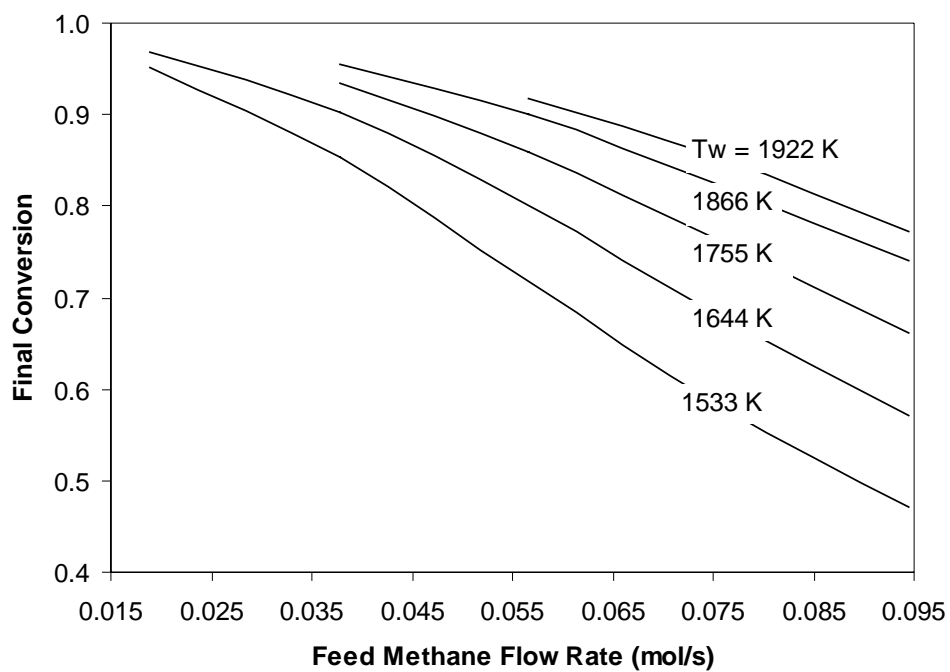


Figure 6. Feed Methane Flow Rate Versus Final Conversion for Various Wall Temperatures

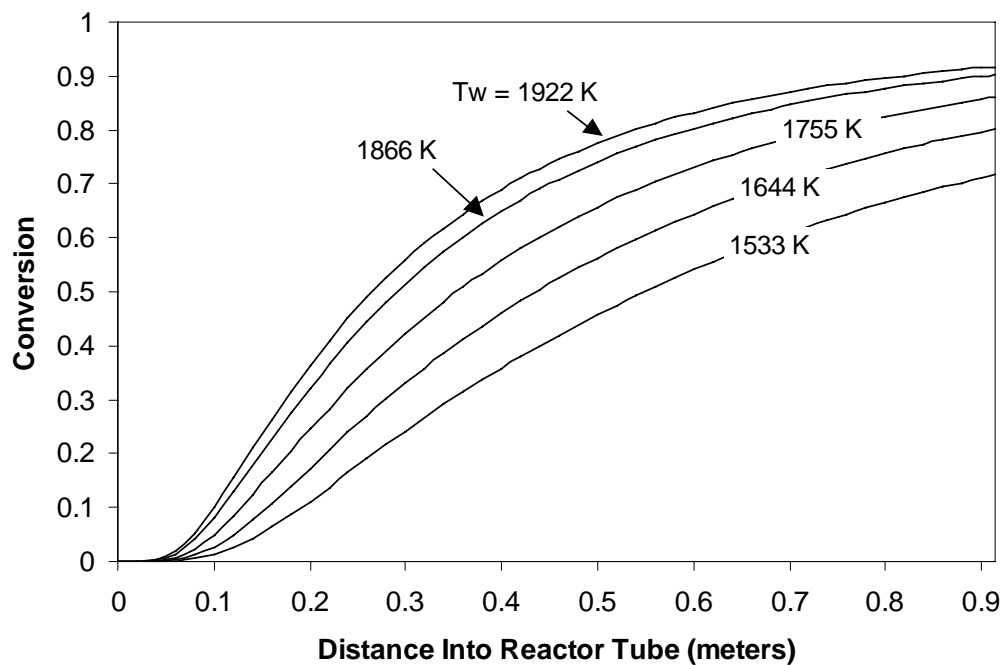


Figure 7. Conversion Profiles for $F_{\text{CH}_4}^0 = 0.0566 \text{ mol/s}$

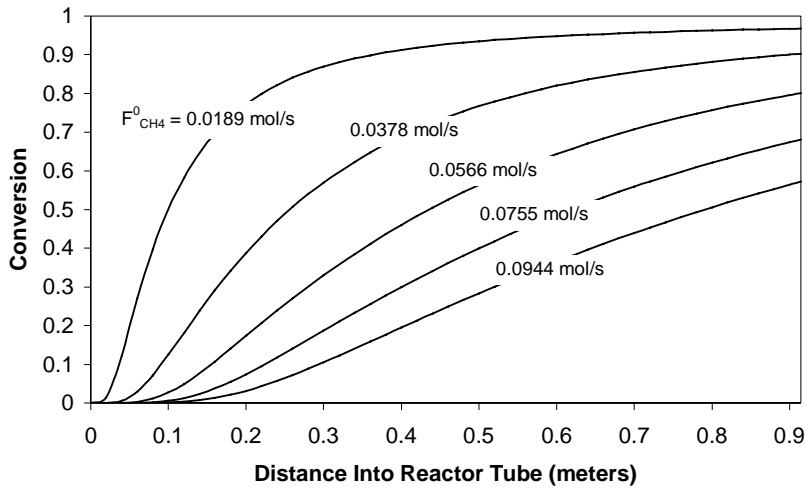


Figure 8. Conversion Profiles for $T_w = 1644$ K

Temperature Profiles

The best-fit kinetic constants ($a=4.4$, $k_0=6 \times 10^{11} \text{ s}^{-1}$, and $E_a=208 \text{ kJ/mol}$) were used to find temperature profiles for various reactor wall temperatures and initial methane molar flow rates. The gas temperature profiles and carbon particle temperature profiles for wall temperatures of 1533 and 2144 K and initial methane molar flow rate of 0.0566 mol/s are shown in Figure 9.

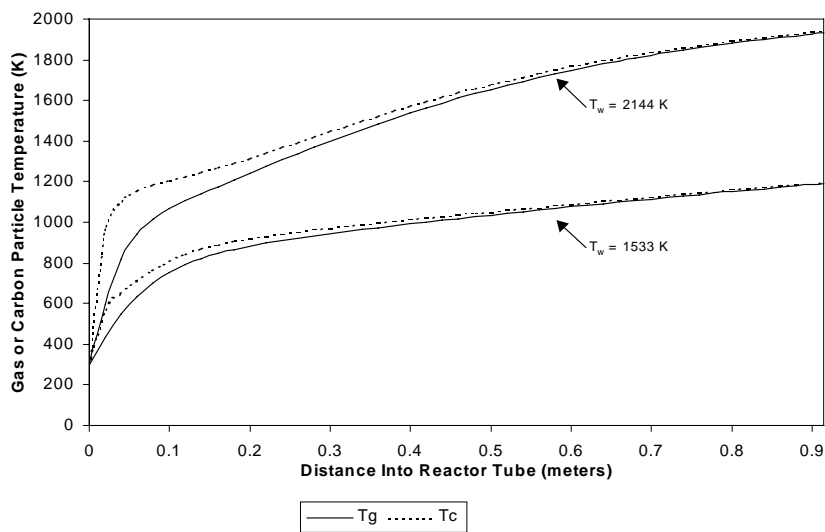


Figure 9. Gas and Carbon Particle Temperature Profiles for $F_{\text{CH}_4}^0 = 0.0566 \text{ mol/s}$

It is evident from these profiles that the temperature of the gas stream very closely follows the temperature of the carbon particles. The heating rate for both the gas stream and the carbon particles is extremely fast for the first 0.1 m of the reactor tube. The heating rate then slows as the streams move through the remainder of the reactor until both streams reach approximately the same temperature at the end of the reactor. The final temperature of both the gas stream and the carbon particles is slightly lower than the wall temperature.

Experimental Work

High-Flux Solar Furnace

The HFSF facility (Figure 10) at NREL in Golden, CO was used for this research. NREL is the primary national laboratory in the United States for renewable energy research. The HFSF uses a series of mirrors that concentrate sunlight to a focused beam at maximum power levels of 10 kW into an approximate diameter of 10 cm. The solar furnace's long focal length and its off-axis design give researchers flexibility and control over the delivered flux. It operates with a heliostat that has an area of 31.8 m² and a 92% solar-weighted reflectivity. The heliostat reflects sunlight to a primary concentrator consisting of 25 hexagonal facets that are spherical mirrors ground to a 14.6-m radius of curvature. The total surface area of the primary concentrator is 12.5 m² and it reflects radiation from the entire solar spectrum (300 nm to 2500 nm). Under optimal conditions, the primary concentrator can achieve maximum flux intensities of 2,500 suns. Secondary concentrators that achieve intensities of more than 20,000 suns and refractive designs approaching 50,000 suns can be installed at the primary concentrator's focal point to increase the intensity further. The furnace is easily capable of delivering flux densities on the order of 100-1000 W/cm². No secondary solar concentration was used in these studies.

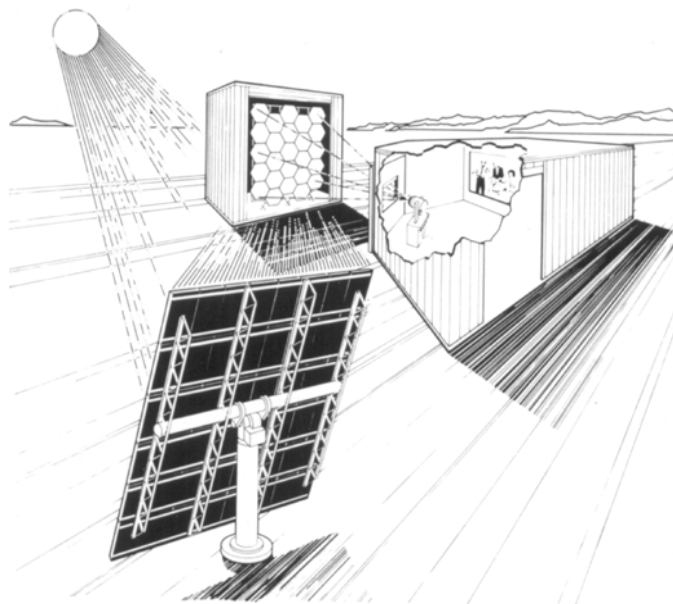


Figure 10. High-Flux Solar Furnace Schematic

Reactor System

Proof-of-concept experiments were carried out using a modified reactor system originally built for previous experiments in fullerene production [Mischler et al., 1997]. The reactor consists of a particle and gas feed mechanism, quartz reactor tube, an internal graphite “target” feed tube, and a filter housing. The reactor operates at atmospheric pressure with gas flow driven and controlled through a series of mass flow controllers. An in-line Horiba model TCA-300 H₂ detector was inserted downstream of the particle filter. This detector is based on thermal conductivity measurements and was calibrated for 5 % H₂ in argon (Ar). Gas samples were also taken and analyzed using an off-line gas chromatograph (GC). CH₄ and produced H₂ were kept outside flammability limits by operating with a dilute 5% CH₄ in Ar feed gas mixture and a pure Ar purge stream. The temperature inside the quartz tube reactor is exceedingly difficult to determine. However, the temperature of the quartz tube is carefully monitored using an infrared camera positioned on the side of the reactor. The quartz temperature is monitored to avoid warping or even melting the reactor wall with concentrated sunlight. A schematic of the reactor system is shown in Figure 11.

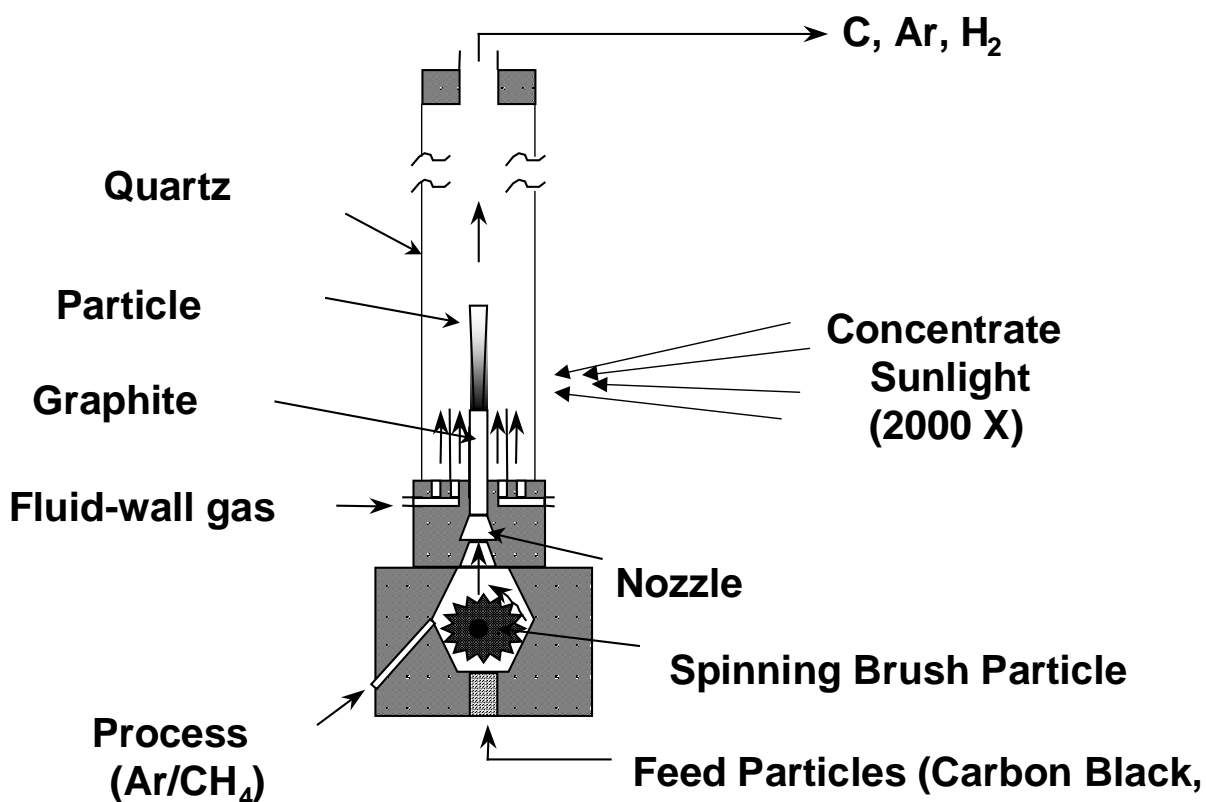


Figure 11. Schematic of Solar-Thermal Aerosol Flow Reactor

A key aspect of the reactor operation is the heating means for the feed CH_4 . The reactor has been designed for three alternative heating methods: (1) heating a 6 mm OD x 3 mm thick “target” graphite tube with concentrated sunlight, the heated target then heating the CH_4 -containing feed gas by conduction; (2) heating the “target” graphite tube, but with radiation absorbing fine carbon black particles suspended in the CH_4 -containing feed gas stream so the inside wall of the “target” radiates to the flowing particles that subsequently heat the flowing feed gas by particle surface conduction in addition to the wall conduction; and (3) heating the suspended carbon black particles directly with concentrated sunlight, the sunlight directed above the top of the graphite tube. Alternatives (2) and (3) involve volumetric absorption of light by a gas-solid suspension. The graphite tube can be seen contained within the quartz tube reactor assembly as shown in Figure 12. The quartz tube extends beyond the limits of the concentrated solar flux provided by the HFSF. The quartz tube was positioned at the nominal focus along the optical axis of the HFSF with its axis “vertical”.

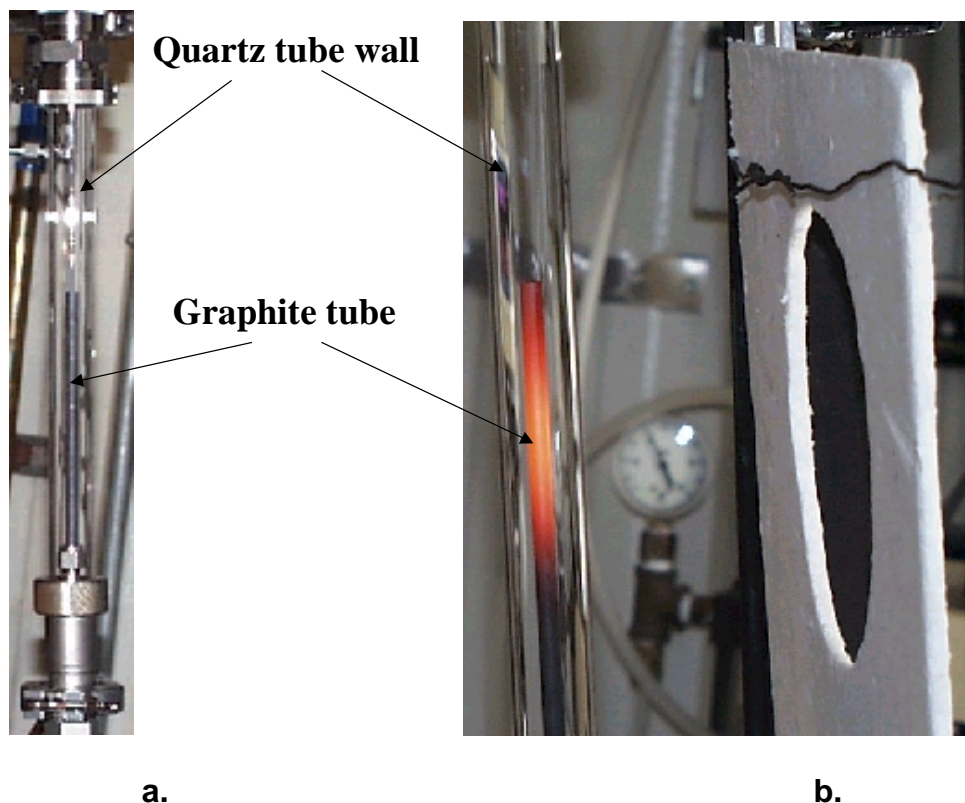


Figure 12. Reactor Tube Assembly: a. before heating, b. immediately after heating (shutter closed)

The particle suspension is generated in a feed mechanism located below the quartz tube (see Figure 13). Lightly compacted carbon black particles (“ShawiniganTM,” acetylene carbon black; product of Chevron Chemical Co., Houston, TX) are fed against a rotating steel brush that conveys the particles to a space where they are mixed with the 5% CH_4/Ar feed gas. The suspension then flows through a set of nozzles that destroy any particle agglomerates. The nozzle size varies between 0.33 mm and 0.64 mm. Before the particle cloud passes through the focal

area, two streams of “sweep” Ar gas are “wrapped” around the gas-solid suspension. This “fluid-wall” is designed to prevent particles from reaching the quartz glass in locations where heating by the highly concentrated sunlight might soften or melt the tube. The gas and particles are fed from bottom to top of the quartz reactor. With the ratio of “sweep” Ar to feed 5% CH₄/Ar on the order of 10:1, the overall percentage of CH₄ or H₂ was relatively low for these proof-of-concept experiments. These low concentrations are used as a safety precaution for initial studies. A side view of the reactor assembly above the particle feeding system is shown in Figure 14.



Figure 13. Particle Feeding System (below reactor assembly)

During one set of experiments, the reactant gas was fed at a rate of 0.2 standard liters per minute (SLM) into the graphite reaction tube while the annular argon “purge” gas flowed at a rate of 2 SLM. The adjusted molar concentration of inlet CH₄ accounting for a combined reactant “purge” gas stream near the exit of the graphite reaction tube was 0.45%. The estimated flux of concentrated sunlight heating the graphite reaction tube target was 1200 kW/m². A temperature of 1550 K was measured inside the graphite tube using a Type C thermocouple positioned in the center of the hot zone. The length of the hot zone was 50 mm long. The residence time of the methane in the hot zone of the reactor tube was 0.019 seconds. Any fed and synthesized carbon black were separated downstream of the reactor using a HEPA filter. A calibrated thermal conductivity detector located downstream of the filter indicated a hydrogen concentration of 0.27 mole% H₂ in argon. This corresponded to a methane conversion to carbon and hydrogen of 30% according to reaction (1).

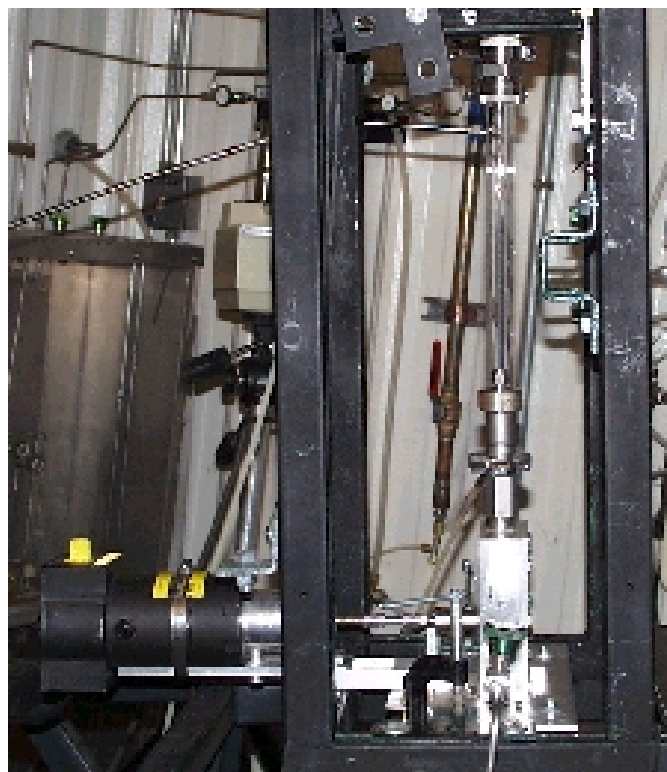


Figure 14. Reactor Assembly (above particle feeding system)

Proof-of-concept Results and Discussion

The process parameters described above were repeated with the exception that no carbon particles were fed in the process. The product gas was measured by the calibrated thermal conductivity detector to have a hydrogen content of 0.16% H₂, corresponding to a reduced methane conversion of 18%. Carbon black produced according to reaction (1) was collected in a downstream filter and analyzed by transmission electron microscopy (TEM). The carbon black was amorphous and was comprised of carbon particles having a size in the range of 20 to 40 nanometers. These results indicated that the feeding of fine carbon black particles to the process increases the conversion of the thermal dissociation of methane for low temperatures. These results also indicate that amorphous fine carbon black powder is produced in the process and the process provides an in-situ method of generating carbon black radiation absorbers in the reactor (without having to feed it).

The next set of experiments was performed to determine the effect of varying the solar flux. The reactant gas flowed at a rate of 0.2 SLM and had a composition of 10 mole% CH₄ in argon. The annular “purge” argon flow rate was 1 SLM and no carbon particles were fed. The adjusted molar concentration of CH₄ accounting for a combined reactant “purge” gas stream near the exit of the graphite reaction tube was 1.67%. The estimated flux of concentrated sunlight heating the graphite reaction tube target was varied as 1170 kW/m², 1780 kW/m², 2060 kW/m², and

2350 kW/m². The corresponding temperatures in the reaction tube were 1550, 1730, 1820, and 1900 K, respectively. The residence time varied in the range of 0.019 to 0.015 seconds, respectively. The response of the hydrogen content in the flowing product gas stream resulting from the solar flux changes is shown in Figure 15. The conversion of methane according to reaction (1) was calculated from the measured concentration of H₂ and was 7%, 38%, 43%, and 47%, respectively. These results indicate that an increase in the solar flux results in an increase in the thermal dissociation (conversion) of methane to H₂ and carbon black.

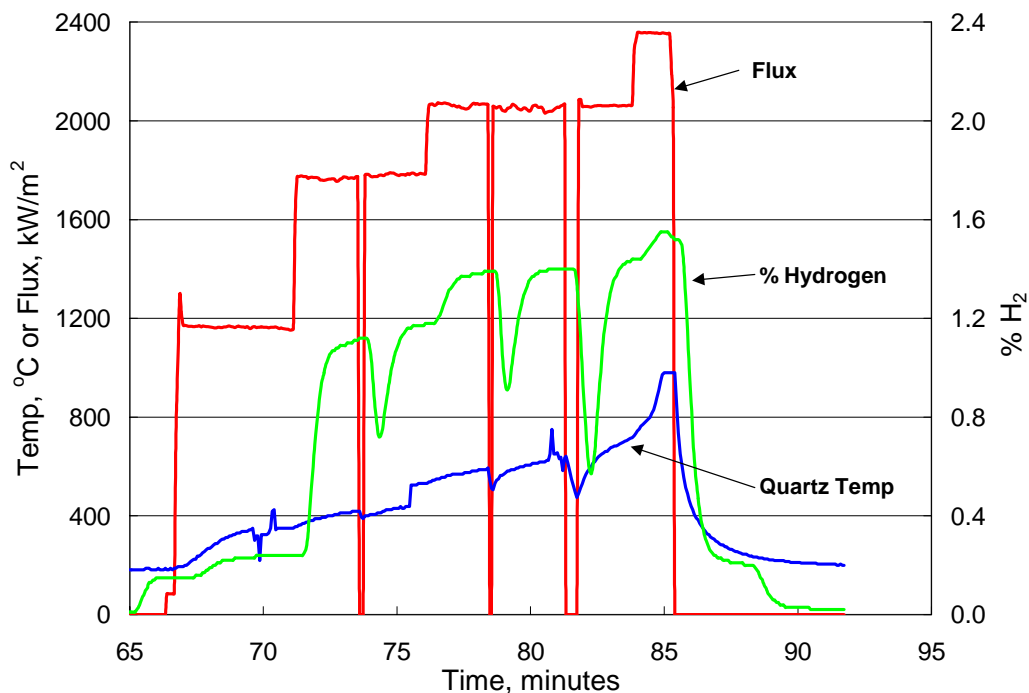


Figure 15. Signal Response to Solar Flux (1.7% CH₄ and no particle feed)

Once again, the reactant gas was fed at a rate of 0.2 standard liters per minute (SLM) into the graphite reaction tube while the annular argon “purge” gas flowed at a rate of 2 SLM. However, in this set of experiments, the solar flux was increased from 1200 kW/m² (described previously) to 2430 kW/m². The temperature in the hot zone was measured to be 1915 K compared to 1550 K (described previously). The resulting concentration of H₂ (0.55 mole%) indicated a methane dissociation of 61% according to reaction (1). This result indicates that the higher solar flux results in a higher degree of dissociation (conversion) of methane.

The same process conditions were repeated, except that no carbon particles were fed to the reactor. The concentration of H₂ indicated that the dissociation of CH₄ was 36%. This illustrates that a decrease in dissociation results when carbon particles are not co-fed in the process to improve heat transfer.

The process conditions were repeated except reactant gas flow was decreased to 0.1 SLM, resulting in an adjusted molar concentration of CH₄ accounting for a combined reactant “purge”

gas stream near the exit of the graphite reaction tube of 0.24 mole%. A calculated residence time of 0.03 seconds resulted in a measured outlet hydrogen concentration of 0.4 mole% H₂ for a degree of dissociation of 84%. This experiment shows that high conversions (extents of dissociation) can be achieved in hundredths of a second for high reactor temperatures (1915 K) obtained using concentrated solar-thermal heating.

This set of experiments was run to determine the effect of using larger graphite tube sizes. Particles were fed and the reactant gas was fed at a rate of 0.2 standard liters per minute (SLM) into the graphite reaction tube while the annular argon “purge” gas flowed at a rate of 3 SLM. A 10 mm outside diameter graphite tube was used. An adjusted molar concentration of CH₄ accounting for a combined reactant “purge” gas stream near the exit of the graphite reaction tube was 0.91 mole%. The solar flux was 1523 kW/m², 1700 kW/m², and 1900 kW/m². The measured temperatures in the graphite reaction tube were 1650 K, 1710 K, and 1770 K and the corresponding reaction residence times were 0.064, 0.061, and 0.059 seconds, respectively. The concentrations of hydrogen determined from the thermal conductivity detector were 0.54 mole%, 0.83 mole%, and 1.14 mole%, respectively. During the course of the experiments, gas samples were taken in the outlet line and analyzed using an off-line gas chromatograph (GC). The following chemical compositions were determined, respectively: 0.65 mole%, 0.85 mole%, and 1.25 mole%. The GC results corresponded to a methane dissociation of 35%, 48%, and 70% conversion. This set of experiments indicated that different sizes of graphite reaction tubes could be used and that the experimental results using the thermal conductivity analysis were validated with the off-line GC.

The processing conditions described in the previous paragraph were repeated with the exception that a 76 mm outside diameter external quartz tube was used, the graphite reaction tube was 6 mm outer diameter, the reactant gas composition was 5 mole % methane, and the annular argon “purge” flow was 1.2 SLM. The adjusted molar concentration of CH₄ accounting for a combined reactant “purge” gas stream near the exit of the graphite reaction tube was 1 mole%. The solar flux was varied at seven different intensities between 1000 and 2540 kW/m², with corresponding temperatures in the range of 1480 to 1955 K. The measured hydrogen content in the product gas for each of these conditions showed an increase in methane dissociation over a range of 6% to 43% for a solar flux of 1480 kW/m² to 1955 kW/m². This set of experiments indicated that different sizes of outer quartz protection tubes could be used and that the extent of dissociation increased with an increase in the solar-flux to the reaction tube.

The reactor apparatus was modified so the graphite reaction tube extended over the entire length of the surrounding protective quartz tube. This design modification kept the reaction contents inside the graphite reaction tube and isolated the graphite reactor contents from the annular space between the graphite tube and the quartz protection tube. A non-oxidizing argon gas flowed in the annular space between the graphite reaction tube and the quartz protection tube to prevent oxidation of the graphite tube. The flow of this non-oxidizing gas also prevented any volatile species emanating from the graphite tube upon heating from depositing on the inside surface of the quartz protection tube. This design also prevented any deposition of carbon particles on the inside surface of the quartz protection tube. The concentrated sunlight passed through the protective quartz wall to the graphite tube outside wall where it heated the graphite tube to reaction temperature.

The outside quartz protection tube had an outside diameter of 25 mm and was 305 mm long. The inside graphite reaction tube had an outside diameter of 10 mm and was also 305 mm long. Inert argon gas flowed through the annular gas flow space at a rate of 3 SLM. Reactant gas comprising 10 mole% methane in argon flowed through the graphite reaction tube at a flow rate of 0.3 SLM. No carbon particles were fed during the run, but, instead were formed during the reaction and provided an in-situ method for providing radiation coupling to heat reactant gas during the processing. A solar flux of 2140 kW/m^2 was used to heat the graphite reaction tube to a temperature of 1835 K. The downstream thermal conductivity detector measured the concentration of hydrogen in the combined reaction product gas/annular “purge” gas stream to be 1.04 mole% H_2 . The residence time in the hot zone of the reaction tube was 0.06 seconds. A 58% conversion of CH_4 to carbon black and H_2 was obtained. Inspection of the quartz wall after the run indicated no deposition of carbon black or other species. This example indicates that the surface of the protective quartz wall can be kept clean by extending the graphite reaction tube along the entire length of the surrounding protective tube and isolating the reactor contents from the annular space between the concentric tubes.

The apparatus described above (a graphite tube that extended the length of the quartz tube) was used for this set of experiments. This experiment was run on a very clear day with direct normal irradiance at approximately 1000 W/m^2 . As used herein, “irradiance” is defined as the quantity of sunlight coming directly from the sun disk, measured within a cone angle of 5 degrees by a Normal Incidence Pyrheliometer. The estimated flux on the target was about 2400 kW/m^2 or 2400 suns. The graphite reaction tube temperature was 1910 K.

The flow of annular “purge” argon gas was initiated at 2 SLM, then the particle feed and a 5 mole% methane-in-argon mixture (at a flow rate of 0.1 SLM) were started at about 4 minutes. The time delay for the flow to reach the hydrogen detector was about 20 – 30 seconds. The thermal conductivity of methane is higher than that of argon, indicated by a change in the apparent H_2 mole% trace. When the signal became steady, concentrated sunlight was introduced by opening a fast-acting shutter. A nearly immediate increase can be seen in the percent H_2 trace. The shutter was closed at about 11 minutes, corresponding to a decrease in the H_2 signal at about 11 minutes. At 16 minutes of elapsed time, the flow of methane-in-argon was stopped, then restarted, stopped again, and restarted at 0.2 SLM at 18 minutes elapsed time. The changes in H_2 signal clearly indicate that the hydrogen production is following these flow manipulations. A sample bag was filled for subsequent analysis during the interval between about 20 and 25 minutes. The shutter was closed at about 27 minutes.

The gas sample was analyzed by GC and found to be comprised of 0.813 mole% H_2 , 183 parts per million (ppm) CH_4 , 523 ppm C_2H_4 , 183 ppm C_2H_2 , and the balance (99.4 mole%) argon. For the flow rates of methane and argon in this experiment, complete conversion of methane to hydrogen would have resulted in 0.91 mole% H_2 . Thus, the measured conversion of methane was about 88%. Inspection of the quartz tube wall indicated that no deposition of carbon black or volatile species occurred. This example demonstrates that high reaction temperatures and reaction conversions can be achieved using concentrated sunlight while preventing wall deposition on the protective quartz tube.

The apparatus described above was also used in the study of the dry reforming of methane and carbon dioxide (CO₂) to form hydrogen and carbon monoxide (CO). Like reaction (1), this is a highly endothermic reaction that requires high temperatures to achieve high conversions. During this experiment, the annular argon “purge” flow rate was 2 SLM. The reactant gas was comprised of 0.90 mole% CH₄ (0.2 SLM of 10 mole% CH₄ in argon) and 0.45 mole% carbon dioxide (0.01 SLM of dry CO₂). A gas sample was taken downstream prior to solar-thermal heating and analyzed using a GC. The measured composition of 0.45 mole% CO₂ and 0.84 mole% CH₄ with the balance argon indicated a feed molar composition of CH₄ to CO₂ in the ratio 1.87 / 1. The reactor was heated to a temperature of 1645 K using a solar-flux of 1500 kW/m². Carbon black was collected downstream after the run indicating that reaction (1) took place. The downstream product gas (analyzed by GC) was comprised of 0.23 mole% CO₂, 0.20 mole% CH₄, 0.35 mole% CO, and 1.55 mole% H₂, corresponding to a CO₂ conversion to CO of approximately 49%. The experiments were repeated, but with a solar-flux of 2000 kW/m² heating the reaction tube to a temperature of 1795 K. A GC analysis of the collected product gas indicated a composition of 0.11 mole% CO₂, 0.07 mole% CH₄, 0.62 mole% CO, and 1.60 mole% H₂, corresponding to a CO₂ conversion to CO of approximately 76%. The fact that large concentrations of H₂ were measured indicates that a significant amount of the excess CH₄ fed according to the dry reforming reaction dissociated according to reaction (1). Carbon black was found in the collection dust filter to further substantiate this observation. This set of examples illustrates that concentrated sunlight can be used to carry out dry CO₂ reforming of CH₄ reactions in short-residence-time (fractions of a second) solar-thermally heated transport graphite reaction tubes.

Improved Experimental Reactor Design

The reactor system is currently being modification and re-designed to eliminate some of the experimental limitations inherent in the proof-of-concept design. The new reactor system will allow us to perform experiments at high concentration of methane. This should allow us to get better kinetic expression results. We will also be constructing a new feeder mechanism in order to provide smoother consistent feeding of particles. The current particle feed system is extremely limited in capacity of feed. The new particle feeder will be capable of continuous operation. There is also a secondary concentrator, which will increase the solar radiation incident upon the graphite tube. The current design only allows at most a 10% solar efficiency. The addition of the secondary concentrator will increase the solar efficiency to 74%. This should increase the temperature that the reactor is capable of achieving.

A process schematic is shown in Figure 16. The particle feeder is a conical screw feeder. The feed particles drop into a jetted stream of process gases. The jets should entrain the small graphite powders into a fine aerosol of powders. This aerosol flows into the top of the graphite tube. The graphite will heat with the solar radiation and this will in turn heat the graphite powders. The fine aerosol of powders will in turn heat the gases. Methane will crack into H₂ and C. The C will be removed in a filter housing. The product gases will be analyzed for composition by an in-line GC/MS. A dry test meter will measure the volume of product gases. This will allow quantification of reaction conversion. Outside the graphite tube, a quartz tube contains a cooling

gas. This gas is inert for safety reasons. The inert annular gas will not mix with the process gases.

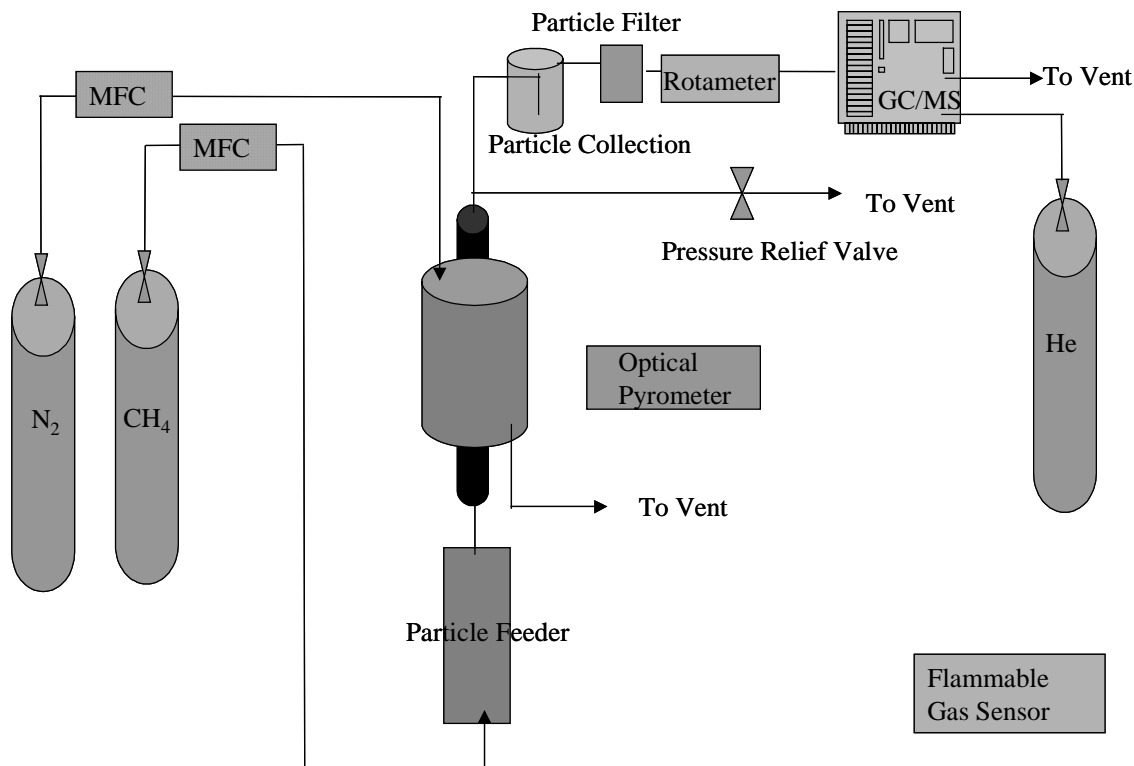


Figure 16. Process Flow Schematic of Improved Experimental Reactor

The reactor itself (Figure 17) consists of a glassy carbon graphite tube inside a quartz tube. The two tubes are sealed at the ends with custom fittings designed to have small clearance in order to reduce the excess length of the reactor. Two sizes of graphite tubes will be investigated, 2.4 cm and 1.2 cm outer diameter with a wall thickness of 3 mm. The total length of the reactor is 15 inches. There are four silicone O-ring seals on each end of the reactor that prevent leaking of gases into the atmosphere as well as mixing of the two gas streams. The gas inlets and outlets will be fitted with VCR-type fittings. These connections will have to be opened frequently and the VCR fittings provide positive seal when a new gasket is used each time the fitting is closed.

Rudimentary heat transfer modeling of the proposed reactor design was performed in order to determine if the selected materials were appropriate for construction. It was assumed that the graphite tube was $2000^{\circ}C$ at the center portion while the gases entered that portion at room temperature. The outlet temperature of the graphite and the quartz were predicted based on co-current plug flow of gases, uniform radial temperature through the quartz and graphite, and no radiative heat losses. This model predicted that the process gases would quickly reach the temperatures we desire for reaction ($\sim 2000^{\circ}C$). The ends of the graphite tube reach about $300^{\circ}C$, which is below the maximum operating temperature of the silicone O-rings of $370^{\circ}C$. The model

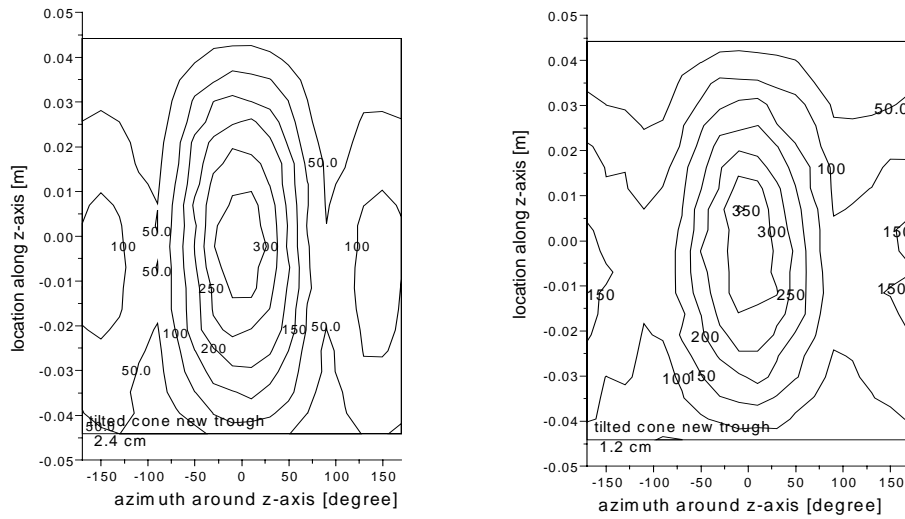


Figure 18. Distribution and Intensity of Solar Radiation on Graphite Tubes

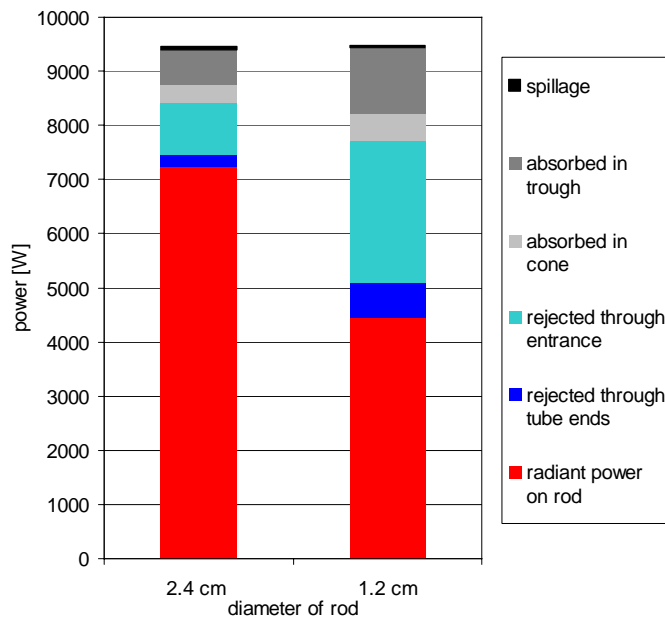


Figure 19. Predicted Energy Distribution Through Improved Experimental Reactor

A schematic of the secondary concentrator is shown in Figure 20. The secondary concentrator will be constructed out of aluminum plates. Final polishing of the surfaces will create an optically smooth surface. Denton Vacuum will coat the plates in a vacuum deposition process. Each individual plate will have cooling channels cut into the back side, with a cooling water inlet and outlet. This will prevent heat from building up in the reflector and damaging the coating on the inside.

The particle collection container is a micro filter that collects all of the powders while allowing the gases to pass through. This is a large-surface-area filter, which should not clog except under very high particle loading. The filters can be easily changed between runs so that particle morphology can be studied as a function of reaction conditions.

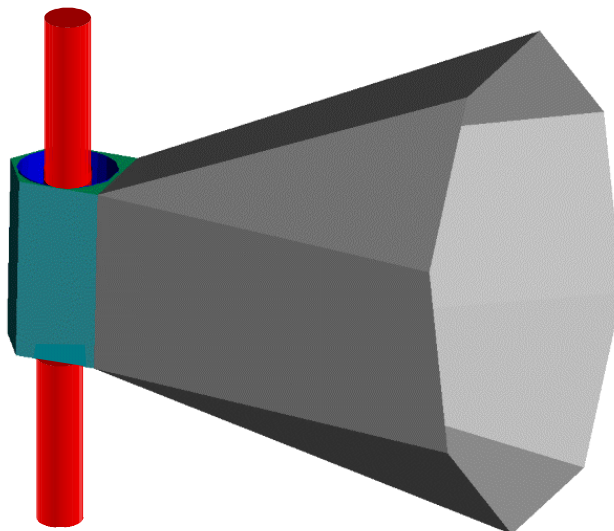


Figure 20. Schematic of Secondary Solar Concentrator

An Inficon (East Syracuse, NY) Hapsite GC/MS system will be used to measure the concentration of different gases in the reagent and product streams. The GC will be equipped with a 27 m x 0.32 mm Carboxen 1010 capillary column (Supelco, Bellefonte, PA). This will allow for separation of the light gas compounds. Helium will be used as the carrier gas. This prevents interference of N_2 (normally used with the Hapsite for portability) with CO during the MS analysis. The quadrupole mass spectrometer should be capable of measuring ppm levels of light gases in the samples. Concentrations much higher than that are anticipated in the product stream. The Hapsite was chosen for these studies due to its stability. It was designed to be used as a portable GC/MS unit. While this application does not require a portable field unit, it does require a low-drift instrument.

This new design addresses all of the experimental deficiencies in the previous design. Since the flammable gas stream was only contained in glass, safety concerns prevented study of high concentration of reactant. The new design separates the flammable gas from the glass with a glassy carbon tube, which is completely sealed from the inert gas passing between the quartz and graphite. The old reactor did not allow for in-line quantification of the product gases. The GC/MS will allow semi-continuous and quantitative monitoring of the product stream composition. Volumetric flow rate measurements of the product stream will allow a mass balance to be closed.

Process Design and Cost Analysis

A preliminary plant design was developed for a solar-coupled process for the thermal decomposition of methane to hydrogen and carbon black. The process economics were evaluated using discount cash flow analysis. Cash flow analysis determines the required selling prices of the hydrogen and carbon black products. The sales price of these products must generate sufficient revenue to pay for annual operating expenses and the initial capital investment, and provide an acceptable internal rate of return over the lifetime of the process.

Since some of the specific design factors and process costs were not known exactly, these factors and costs were treated as parameters in the analysis. This approach provides insight into how the process economics depend on the values of these factors and costs, and determines which factors and costs are most important in determining the overall process economics.

A preliminary evaluation of the current carbon black commercial market was also performed to determine current market sizes for the various grades of carbon black products and their corresponding selling prices. Results from the process design, economic analysis, and market evaluation were used to draw conclusions and make recommendations for future research and process development.

Process Plant Design

The solar-coupled plant is envisioned to have many of the same unit operations as those of a current commercial carbon black plant [Wang, 1993]. A schematic of the plant is shown in Fig. 21. The reactor is mounted on top of the tower that receives concentrated solar from a field of tracking mirrors or heliostats. The concentrated solar energy provides the energy needs for the process and eliminates the need for partial combustion of the feed. The feed for this process is natural gas, which is preheated in the heat exchanger by the product stream. Natural gas, recycled hydrogen and carbon particles enter the top of the reactor and flow downward where they are heated directly with solar flux. Decomposition of the natural gas results in a product stream consisting of carbon black and hydrogen.

A water quench is not used in this design to maintain a pure stream of carbon black and hydrogen. The product stream flows through the tube side of the heat exchanger and is cooled to about 200°C (473 K) before entering the bag houses. The carbon black is separated in the bag houses and transferred to the storage tanks in the same manner as that of the commercial carbon black process. Hydrogen gas exits the top of the bag houses at near-ambient temperature and pressure. A portion of the hydrogen gas is recycled back to the reactor and fed separately to flow past the reactor window and prevent deposition of carbon black. This process design and analysis does not include unit operations for the compression and storage of the hydrogen gas product.

Operation of a solar-coupled plant will be continuous but will only operate when sufficient solar irradiance is available. This fraction of time is referred to as the solar capacity factor and varies with geographic location. Capacity factors for locations that are favorable for solar processes, such as the desert southwest portion of the United States, have been measured to be as high as 0.41. For this work, the capacity factor was varied from 0.28 to 0.41. Limited operation of the

solar-coupled plant results in higher capital costs as compared to a continuous operation plant with the same annual production capacity.

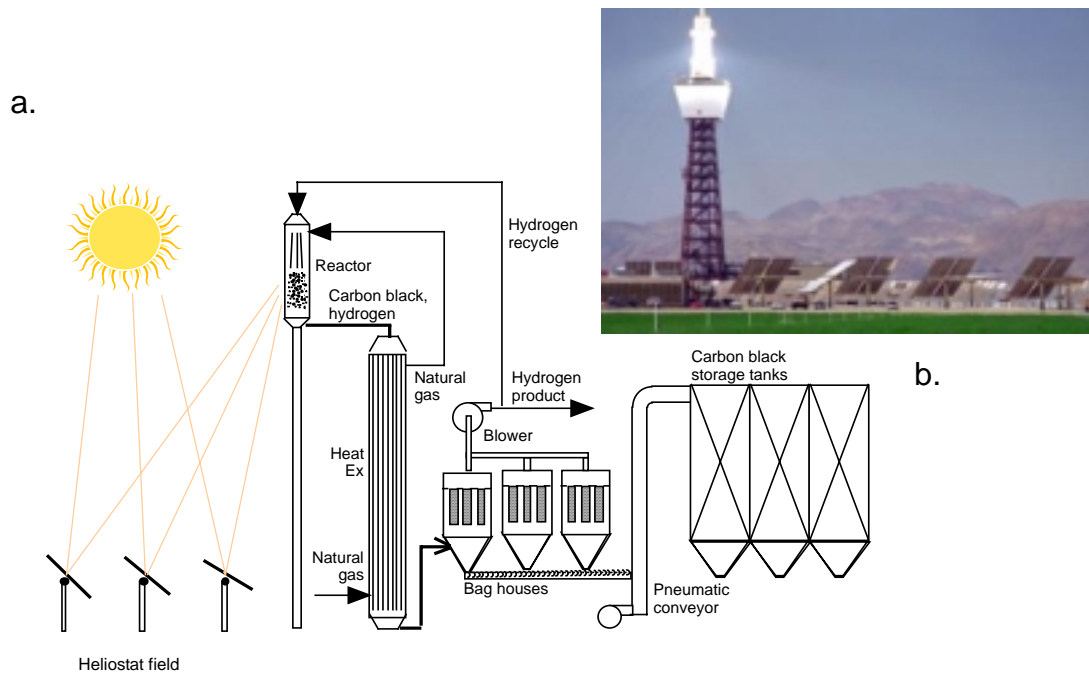


Figure 21. Solar-Thermal Processing: a. schematic of aerosol CH₄ dissociation process, b. photograph of 10 MW Barstow, CA facility

Cash Flow Analysis

Cash flow analysis was performed to determine process economics for the solar-coupled process. The analysis consisted of determining the fixed capital and annual operating costs for the process as a function of several cost parameters. These parameters included heliostat cost, reactor thermal efficiency, and the cost of natural gas. The methods for determining capital and operating costs are described previously [Weimer, et.al., 2000]. Capital and operating costs for each case were used in the cash flow analysis to determine the required selling price for hydrogen.

All material & energy balances and cost calculations were performed using a Microsoft Excel® spreadsheet. The spreadsheet that was developed previously included calculations for discount cash flow over the lifetime of the process. These calculations were used to determine the required selling price for hydrogen for a given set of parameter values. The spreadsheet was structured such that values of the hydrogen price had to be assigned in the spreadsheet until the correct value produced the proper cumulative discount cash flow. This “trial & error” method was replaced by restructuring the spreadsheet so that the required price for the hydrogen product is calculated explicitly. User-defined functions were written to perform the search for the correct hydrogen price value for a given set of parameter values.

The current cash flow analysis has the assumptions listed in Table 2.

Table 2. Economic Assumptions for the Discount Cash Flow Analysis

Economic Factor	Value
Internal Rate of Return	15%
Depreciation	see Table 3
Recovery Period	11 years
Plant Life	21 years
Construction Period	1 year
Working Capital	18% of Fixed
State Tax	5% of net income
Federal Tax	see Table 3
Salvage Value	10% of Fixed
Debt/Equity Ratio	0/100
Cost of Labor	\$34/hr (loaded)
Reference Year for Costs	2000

Depreciation occurred over the first 11 years of plant operation according to Table 3 [Seider et al., 1999].

Table 3. Depreciation Schedule

Year	Percent of Capital Depreciated
1	10.00
2	18.00
3	14.40
4	11.52
5	9.22
6	7.37
7	6.55
8	6.55
9	6.56
10	6.55
11	3.28

Federal tax for the net income was calculated according to the schedule in Table 4. The total tax was determined by applying the appropriate tax rate to each range of income. For example, to determine the tax on a net income on \$120,000, the first \$50,000 is taxed at 15%, the next \$25,000 is taxed at 25%, the next \$25,000 is taxed at 34%, and the last \$20,000 is taxed at 39%.

Table 4. Federal Tax Schedule

Net Income (K\$)	Tax Rate (%)
< 50	15
50 to 75	25
75 to 100	34
100 to 335	39
335 to 10,000	34
10,000 to 15,000	35
15,000 to 18,300	38
> 18,300	35

Cash flow analysis determined the required selling prices of hydrogen and carbon black to achieve a net present value of zero at the end of the lifetime of the process. This approach is consistent with the method used by the Hydrogen Program to assess the economics of hydrogen production processes [Mann, 1995]. For all cases, the hydrogen that was produced was assumed to have an energy content of 39.4 kWhr/kg (0.0611 MBtu/lb), which corresponds to its higher heating value (HHV). The final hydrogen product was at ambient temperature and pressure.

Capital Cost Estimation

The capital equipment items for the process included the land, heliostats and tower, reactor, heat exchanger, bag houses, pneumatic conveyor, blower, and storage tanks. For each item, a purchase cost was determined. Methods for calculating purchase costs for each item have been described previously [Weimer, et.al., 2000]. The purchase cost included shipping and sales taxes. The fixed capital cost for each item was determined by multiplying the purchase cost by an inflation factor, a set of direct and indirect cost factors, and a contingency and fee. The only change to the methods for calculating equipment purchase costs was for the solar reactor.

The reactor was assumed to be a vertical cylindrical design consisting of a graphite cylinder enclosed within an outer quartz cylinder. The quartz cylinder is supported inside a steel housing. A portion of the length would not have the steel housing and would function as the window. Reactant flow is through the graphite cylinder. The quartz outer cylinder is included to thermally shield the graphite reactor and to prevent oxidation of the graphite during operation. The graphite cylinder volume is determined from the volumetric flow rate at reaction temperature and pressure and the required residence time. Since the molar and volumetric flow rates increase as the decomposition of methane proceeds, these flow rates were based on product flow rates. The quartz volume was determined assuming a gap between the graphite and quartz cylinders was 0.13 meters.

The purchase cost was based on cost estimates obtained from a local vender for quartz tubing having diameters of 1, 2, 2.5, 3, and 3.5 ft. For all sizes, the cost of the quartz tubing, on a volume basis, varied from \$900/ft³ to \$1,200/ft³. The purchase cost of the reactor was chosen to be \$1,100/ft³ or \$38,870/m³. The purchase cost of the reactor was assumed to be linear with reactor volume. The purchase cost of the graphite cylinder was assumed to be \$300/ft³. An additional factor was included for the cost of the steel housing.

The estimated cost for heliostats varies widely depending on the size of the plant and state of maturity of the solar industry. For this reason, heliostat cost was made a parameter in this analysis. The overall heliostat field efficiency accounts for reflectivity losses (about 5%), projected area losses due to the angle between the incident sunlight and the target reactor and soiling due to dust and dirt. Values for this efficiency vary depending on the location of the heliostat and tower relative to the position of the sun in the sky. An average value for all of the heliostats was assumed to be 0.69. Resource is the average solar resource that is available when the plant is operating. For this analysis, the solar resource was assumed to be 0.75 kW/m².

The operating and maintenance (O&M) costs were determined for the process. The process was assumed to require a staff of 3 operators during operation. In addition, several labor hours were included for each process item for maintenance and repair. For each item, the number of labor hours per day or per some measure of equipment size or production capacity was estimated. The fully-burdened rate for all labor was \$34/hour. Supervision labor was estimated at 15% of the total O&M labor. Since the price of natural gas has varied dramatically in the past year, the cost of natural gas was evaluated as a parameter.

Base Case

A base case for the process was developed in which the most likely values for the parameters were used. A production capacity of 5,000,000 kg/yr was chosen because this capacity requires about 16 MW of power to be delivered to the reactor. This corresponds to about half the power that is delivered to the receiver at the solar thermal electric power plant in Barstow, California. Cash flow analysis determined the required selling prices of hydrogen and carbon black to achieve a net present value of zero at the end of the process lifetime. The parameter values for the base case are given in Table 5.

Table 5. Parameter Values for the Base Case

Parameter	Value
Annual hydrogen production	5,000,000 kg/yr
Heliostat cost	\$200/m ²
Fraction of hydrogen recycled	0.2
Reactor temperature	2,000°C (2273 K)
Reactor residence time	0.1 second
Reactor thermal efficiency	0.5
Solar capacity factor	0.28
Cost of natural gas	\$3/1000 scf

A summary of the equipment size and equipment fixed capital cost according to equation for each piece of equipment is included in Table 6 for the base case of 5,000,000 kg H₂/yr. The total equipment fixed capital investment is \$26,300,000 and total capital required is \$31,000,000.

Table 6. Summary of Fixed Capital Equipment Cost (Base Case)

Equipment	Size*	Purchase Cost*
Land:	370,000 m ²	\$185,000
Heliostat:	61,700 m ²	\$12,300,000 (installed)
Tower:	79 m	\$590,000 (installed)
Reactor:	16 MW _{th}	\$460,000
Heat Exchanger:	5,200 m ²	\$360,000
Baghouse Filter:	590 m ²	\$69,000
Other Equipment		
Pneumatic Conveyer:	1000 kg/hr	Other Equipment Total: \$686,000
Storage Tanks:	115 m ³	
Blower:	2.4 m ³ /s (5,000 scfm)	
Total Equipment:		\$14,700,000
Installation:	Direct + Indirect	<u>\$11,600,000</u> **
Fixed Capital Investment		\$26,300,000
Working Capital	18%	<u>\$4,700,000</u>
Total Capital		\$31,000,000

* Rounded for clarity ** other than heliostat and tower

Cash flow analysis determined the required selling prices of hydrogen and carbon black to achieve a net present value of zero at the end of the lifetime of the plant.

Various price combinations for hydrogen and carbon black were determined. The extreme cases are hydrogen sales only where the price of carbon black is \$0/kg and carbon black sales only where the hydrogen price is \$0/kWhr. For the intermediate cases, the price for carbon black was set and the required price for hydrogen was then determined. A summary of these results is presented in Table 7.

Table 7. Required Sales Prices for Hydrogen and Carbon Black for Base Case.

Carbon Black Price (\$/lb)	Hydrogen Price (\$/MBtu)
0.00	23.26
0.10	18.35
0.20	13.44
0.30	8.53
0.40	3.62
0.48	0

Results show that if only hydrogen is sold, the price must be \$23/Mbtu. If only carbon black is sold, the price must be about \$0.48/lb.

Parametric Analysis

The selling prices for hydrogen and carbon black were determined for variations of the base case in which the parameter values were varied one at a time. Each of the following parameter variations assumes a different fixed price for the carbon black. As a result the relative impacts of the parameter are the important result rather than the absolute values.

Increasing the reactor temperature also increases total gas volumetric flow through the reactor. When the reactor temperature is changed from 1500°C to 2200°C, the hydrogen price ranged from \$2.3-4.2/MBtu at a carbon black price of \$0.40/lb. Decreasing the reactor residence time appears to be practical based on the reaction kinetics. When residence time ranges from 0.05 to 1 second, the hydrogen sales price ranges from \$17.7-26.5/MBtu at a carbon black sales price of \$0.10/lb.

When the size of the plant was increased from 1,000,000 kg/yr to 10,000,000 kg/yr, the required sales price of hydrogen went from 17.9/MBtu to 15.4/MBtu at a fixed cost of carbon black of \$0.15/lb.

The cost of heliostats is uncertain because the technology and the market are still developing. This cost was varied from \$100/m² to \$500/m² with a resulting price of hydrogen of \$10-23/MBtu at fixed cost of carbon black of \$0.20/lb.

Decreasing the reactor thermal efficiency increases the thermal energy requirement for the reaction, and therefore, the size of the heliostat field. Decreasing this efficiency from 0.7 to 0.2 increased the sales price of hydrogen from \$5.5-\$24.7/MBtu at a sales price of carbon black of \$0.30/lb.

The cost of natural gas is increasing in the current market. At a fixed cost of carbon black of \$0.40/lb increasing natural gas cost from \$3/1000scf to \$10/1000scf results in an increase in the price of hydrogen from \$3.6/MBtu (base case) to \$14.9/MBtu.

The profitability analysis is summarized in Figure 22. The effect of residence time, plant size, heliostat cost, reactor efficiency and natural gas cost on required hydrogen selling price is shown at arbitrary, fixed values of carbon black selling price.

Clearly, reactor efficiency is an important parameter in achieving overall system performance and acceptable hydrogen selling prices. This is also an engineering parameter that should be, and is, the focus of the technology development within this project. Tied to reactor efficiency is the residence time. Although driven primarily by the attractive kinetics of this reaction, the reactor must be designed to allow effective heat transfer to the reactants for the kinetics to take place.

In the range of reasonable solar thermal plant sizes, it appears that there is relatively little economy-of-scale. Starting with a smaller plant size in the development phase of the project will have small impact on the price of hydrogen. As solar thermal technology for other applications (power plants, etc.) grows, the cost of heliostats will be reduced. This cost is mostly driven by

outside influences and will be tracked as the technology develops. This is also true for the cost of natural gas.

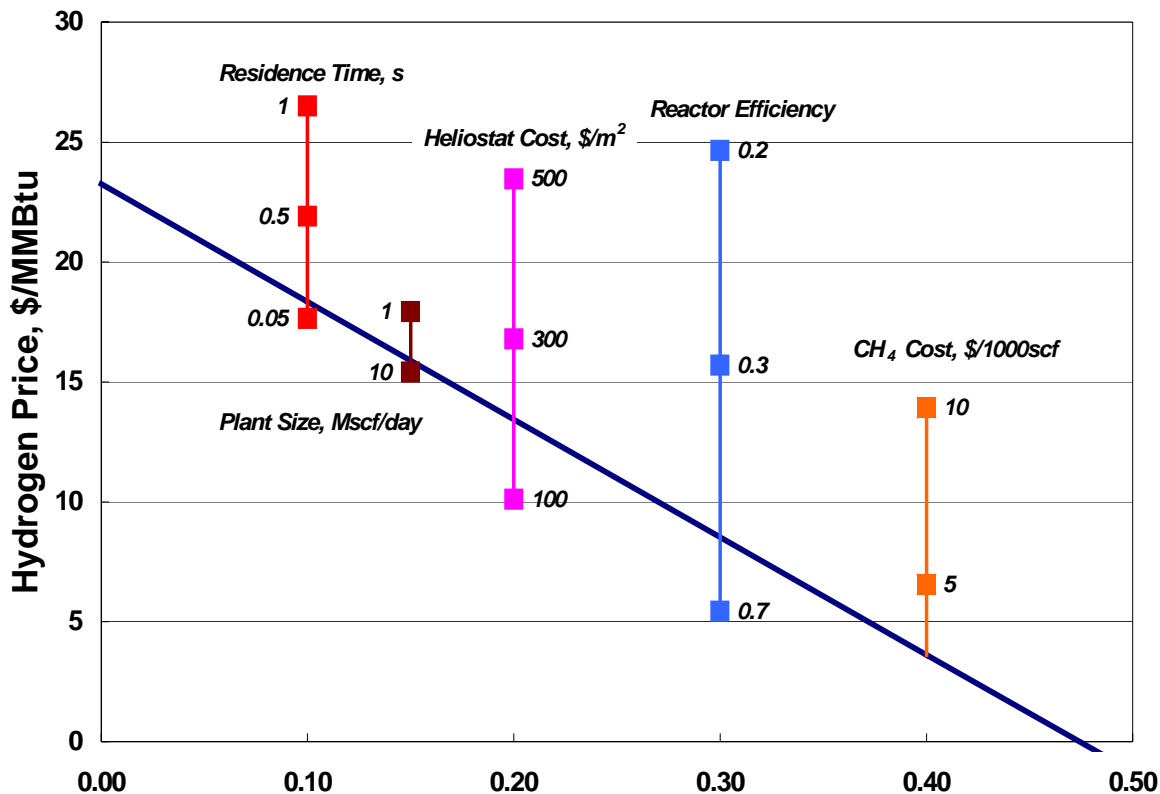


Figure 22: Profitability Analysis

By far the largest influence on the price of hydrogen is the sale of the second reaction product, carbon black (see Figure 23). If high quality carbon black from this process can be sold for significantly more than the current market price for bulk carbon black for the tire market, then this dominates the overall economics and hydrogen almost becomes irrelevant. However, if hydrogen is sold for the current market value (based on other production technologies) then the profitability of this process can be significantly increased (i.e., higher IRR).

Energy Efficiency

An overall energy efficiency was determined for the process. The efficiency is defined as the quantity of energy captured by the methane decomposition reaction due to the heat of reaction divided by the quantity of energy incident on the heliostat field. The efficiency accounts for optical losses of the heliostat field and the thermal efficiency of the reactor. It also accounts for the fact that a portion of the energy delivered to the reactor is use to heat the reactants to the

reaction temperature. Overall efficiencies were determined for the base case with reactor thermal efficiencies of 0.3, 0.5, & 0.7. One can also determine the ratio of the quantity of energy available in the hydrogen product divided by the quantity of energy required to make the hydrogen from methane. Results are presented in Table 8.

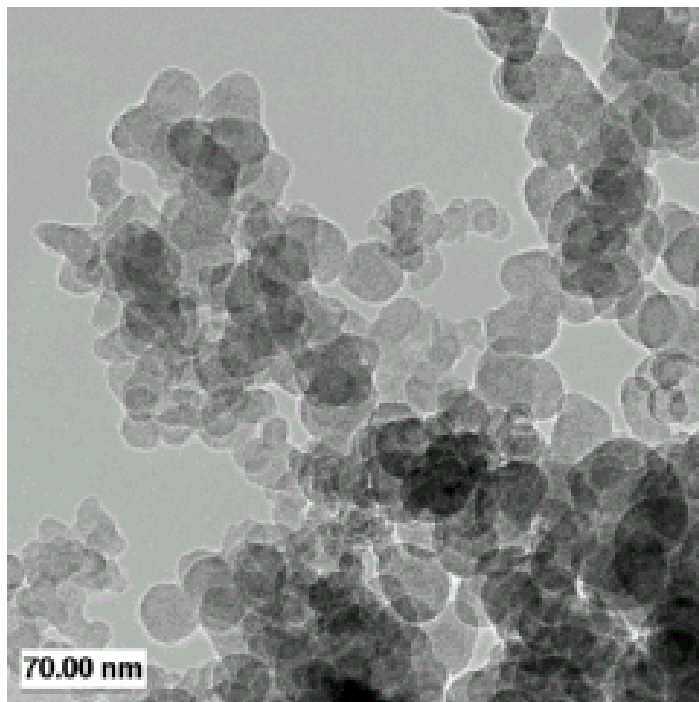


Figure 23. 20 to 40 nm Sized Amorphous Carbon Black Formed By Methane Solar-thermal Decomposition

Table 8. Energy Efficiencies and Available Product Energies

Reactor Thermal Efficiency	Process Energy Efficiency	Ratio of Energy Available to Energy Used
0.3	0.170	1.04
0.5	0.283	1.74
0.7	0.396	2.43

Market Analysis for Carbon Black

A preliminary evaluation of the current carbon black commercial market was also performed to determine current market sizes for the various grades of carbon black products and their

corresponding selling prices. Applications for carbon black include the reinforcement of rubber, use as black pigment, and as a conductive additive to rubber and plastic products [Kirk Othmer, 1991]. World production of carbon black in 1989 was greater than 6 million metric tons. United States production was about 1.6 million metric tons. About 70% of the carbon black that is produced is used in the reinforcement of rubber for tires, 20% is used in other rubber products, and the remaining 10% in non-rubber products. Carbon black used for rubber reinforcement sells for about \$0.30/lb to \$0.35/lb [Chemical Marketing Reporter, 2000].

The non-rubber applications include additives to plastics, printing inks, paint, and paper. A special electrically conductive grade of carbon black sells for prices that are considerably higher than those that are used in rubber reinforcement. Electrically conductive grades are used to produce conductive and antistatic polymer composites. Applications include antistatic carpeting, floor tile, heating elements, videotapes and disks, and electrical shielding. Markets for these applications are increasing faster, on a percentage basis, than those for conventional uses. The current price for a higher grade of carbon black (Thermax) is \$0.78/lb [Canadian Carbon Company, 2000]. An even higher grade of carbon black produced from acetylene sells for \$1.40/lb [Chevron Chemical Company, 2000].

In 1989, the total market for specialty-grade carbon blacks was 126,000 metric tons or 126,000,000 kg. A solar-coupled hydrogen production plant that produces 5,000,000 kg/yr of hydrogen will produce 3,000,000 kg/yr of carbon black. This represents about 10% of the current United States market for higher-grade carbon blacks. The addition of this production capacity to the current market would not have a significant impact on the price of higher-grade carbon blacks and as this market is increasing faster than other carbon black markets, demand for the additional production capacity should be easy to identify.

Life Cycle Assessment

To evaluate the environmental impact of the solar thermal methane dissociation plant, we performed a preliminary life cycle assessment (LCA), on a limited number of process blocks within the system. Life cycle assessment (LCA) is an analysis that provides an evaluation of the environmental impacts associated with a product, process, or activity. This assessment identifies material and energy consumption, as well as pollutants released to the environment because of the process [www.life-cycle.org/]. Although hydrogen is a clean fuel and the process of solar thermal dissociation of methane itself is also a clean process, there are various polluting processes that are associated with a real-life implementation of the process. An LCA provides a cradle-to-grave perspective on the system that incorporates the environmental impacts of the associated processes. While this preliminary LCA provided us a framework for evaluating the environmental benefits of this process, a more detailed assessment is required for determining actual impacts. Results to-date indicates that significant reductions in greenhouse gas emissions and system energy consumption are possible. Future studies will expand the boundaries to include all operations required for the solar-thermal driven aerosol reactor to operate. Additionally, a more complete LCA study will allow us to compare this system with steam methane reforming.

Summary and Conclusions

The objectives of this work were to carry out “proof-of-concept” experiments at the NREL HFSS, develop a fundamental understanding of methane thermal dissociation kinetics, develop an improved process design for a solar-thermal process, evaluate the process economics using discount cash flow analysis, and carry out a life cycle assessment of the process compared to conventional steam reforming to produce hydrogen. The initial results are encouraging and have demonstrated that the process works in principle.

High methane dissociation conversions have been achieved using a solar-thermal reactor not designed for the specific process and using only modest solar concentration levels. In addition, solar-thermal dry reforming has been demonstrated for the conversion of contaminated with CO₂ natural gas sources to produce useful syngas. The Phase 2 experimental system has been designed and is being constructed. It eliminates the deficiencies that are inherent in the current reactor system (low solar efficiency and low feed concentrations) and allows for more complete quantification of products. A secondary solar concentrator having solar-thermal efficiencies approaching 75% with an in-line GC/MS and volumetric flow rate measurements will allow material balance closure and better definition of the overall process that are needed for scale-up. Reactor temperatures of 2000°C can be obtained and pure methane and natural gas can be decomposed.

The conceptualized plant design includes the same major equipment components as current commercial carbon black production plants. These components include a high-temperature reactor, heat exchanger, bag house filters, pneumatic conveyor, blower, and storage tanks. In addition, the process includes a solar heliostat field and tower to provide the thermal energy needs of the process. The process design and economic analysis contain enough refinement to determine how the price of hydrogen and carbon black vary with the values of several key process parameters and costs. Parametric analysis provides insight into how the process economics depends on the values of these factors and costs and determines which factors and costs are most important in determining the overall process economics.

Results of the discount cash flow analysis show that the required single-product selling price for hydrogen for the base case 5,000,000 kg/yr hydrogen plant is \$23/MBtu and for carbon black is \$0.48/lb. These prices assume that only one product is sold. If both products are sold, then the selling price for each decreases. For example, selling prices of \$13.4/MBtu for hydrogen and \$0.20/lb for carbon black meet the discounted cash flow requirements (15% IRR).

The selling prices were determined as a function of several parameters that are not well established at this point in the development of this process. Some are technical in nature and can be influenced by the results of this project (residence time and reactor efficiency) and others are influenced more by outside markets (heliostat cost and natural gas cost). Clearly, the reactor efficiency is the most significant parameter and designing an effective and efficient reactor should be a primary activity within this project.

A preliminary evaluation of the current carbon black commercial market was also performed to determine current market sizes for the various grades of carbon black products and their corresponding selling prices. About 90% of the carbon black that is produced worldwide is used for rubber reinforcement. About 10% is considered specialty-grade carbon black and is used as additives in plastics, printing inks, paint, and paper. The current price for a higher grade of carbon black is about \$0.78/lb (\$1.72/kg). A solar-coupled hydrogen production plant that produces 1,000,000 kg/yr of hydrogen, will produce about 2.4% of the current United States market for higher-grade carbon black. Since this market is increasing faster than other carbon black markets, demand for the additional production capacity should be easy to identify.

Alternatively, a fine carbon black boiler could be interfaced to the process to burn produced carbon black to generate electricity. Although it is more desirable to sell the carbon black into the carbon black market, it may be feasible to take advantage of the fact that the solar-thermal process increases the energy content of the fuel (resulting C and H₂ heating values relative to starting CH₄ heating value) by about 10%. The fine, high-purity carbon black could be produced at fast rates and stock-piled when the solar-thermal process is operating. A carbon black boiler process with minimal air pollution equipment could then be used to burn carbon black on a continuous basis while hydrogen is supplied intermittently to an on-site fuel cell process for generating electricity and/or sent by pipeline or tube trailers to transportation centers for use.

The encouraging experimental results, attractive economic analysis, and benign processing indicate that this process warrants further investigation. The sensitivity of the hydrogen selling price to reactor efficiency and heliostat cost points out the need to focus on reactor/secondary concentrator design and performance in the next stages of the project.

Acknowledgements

The authors want to thank the DOE Hydrogen Program and The University of Colorado for financially supporting this work under Grants DE-FC36-99GO10454 and DE-PS36-99GO10383.

References

Bale, C.W., A.D. Pelton, W.T. Thompson, J. Melançon, S. Degterov, and G. Eriksson. 1999. Facility for the Analysis of Chemical Thermodynamics.

Bromberg, L., D. Cohn, and A. Rabinovich. 1998. "Plasma Reforming of Methane," *Energy & Fuels*, 12, 11-18.

Canadian Carbon Company. 2000. Personal Communication. Cancarb Limited, 1702 Brier Park Crescent NW, Medicine Hat, Alberta, Canada T1A 7G1 (www.CanCarb.com).

Chapra, S.C. and R.P. Canale. 1988. *Numerical Methods for Engineers*. New York; McGraw Hill.

- Chemical Engineering*. 2000. McGraw-Hill Publishing Co. (New York).
- Chemical Marketing Reporter*. 2000.
- Chevron Chemical Company. 2000, Personal Communication, Houston, TX
- Donnet, J.B. 1976. Carbon Black, 16-18, Marcel Dekker, New York.
- Gaudernack, B. and S. Lynam. 1996. "Hydrogen Production from Natural Gas Without Release of CO₂ to the Atmosphere," *Proceedings of the 11th World Hydrogen Energy Conference*, 511-523, Coco Beach, Florida (June, 1996).
- Himmelblau, D.M. 1970. *Process Analysis by Statistical Methods*. New York; John Wiley & Sons.
- Jenkins, D., R. Winston, J. O'Gallagher, C. Bingham, A. Lewandowski, R. Pitts, and K. Scholl. 1996. "Recent Testing of Secondary Concentrators at NREL's High-Flux Solar Furnace," *ASME J. of Solar Energy Engineering*, 29-33.
- Kirk-Othmer Encyclopedia of Chemical Technologies. 1991. 4th ed., 4, 1037-1072, John Wiley & Sons.
- Kreith, F. and W.Z. Black. 1980. *Basic Heat Transfer*. New York; Harper and Row.
- Lee, K.W., W.R. Schofield, and D. Scott Lewis. 1984. "Mobile Reactor Destroys Toxic Wastes in Space," *Chemical Engineering*, 46 – 47, April 2, 1984.
- Lewandowski, A. 1993. "Deposition of Diamond-Like Carbon Films and Other Materials Processes Using a Solar Furnace," *Mat. Tech.*, 8, 237-249.
- Lewandowski, A., C. Bingham, J. O'Gallagher, R. Winston, and D. Sagie. 1991. "Performance Characteristics of the SERI High-Flux Solar Furnace," *Solar Energy Materials*, 24, 550-563.
- Mann, M.K. 1995. "Technical and Economic Assessment of Producing Hydrogen by Reforming Syngas from the Battelle Indirectly Heated Biomass Gasifier," *NREL/TP-431-8143*, 10-13.
- Matovich, E. 1977. "High Temperature Chemical Reaction Processes Utilizing Fluid-Wall Reactors," *U.S. Patent 4056602* (Nov. 1, 1977).
- Mischler, D., R. Pitts, C. Fields, C. Bingham, M. Heben, and A. Lewandowski. 1997. "Solar Production of Fullerenes from a Powdered Graphite Source," *presented at the International Symposium on Solar Chemistry*, Villigen, Switzerland, October 6-7.
- Peters, M.S. and K.D. Timmerhaus. 1991. Plant Design & Economics for Chemical Engineers, 4th ed. McGraw-Hill, Inc. (New York).
- Pohleny, J.B. and N.H. Scott. 1962. "Method of Hydrogen Production by Catalytic Decomposition of a Gaseous Hydrogen Stream," Chemical Engineering, 69, 90-91.

Pitts, J.R., E. Tracy, Y. Shinton, and C.L. Fields. 1993. "Application of Solar Energy to Surface Modification Processes," *Critical Reviews in Surface Chemistry*, 2 (4), 247.

Roberts, F., R.F. Taylor, and T.R. Jenkins, ed. 1971. *High Temperature Chemical Reaction Engineering*. London; The Institute of Chemical Engineers.

Roine, A. 1997. *Outokumpu HSC Chemistry for Windows Version 3.0*.

Spath, P.L. and M.K. Mann. 2000. "Life-cycle Assessment of Hydrogen Production via Natural Gas Steam Reforming," NREL/TP-570-27637 (Revised November 2000).

Steinberg, M. 1986. "The Direct Use of Natural Gas for Conversion of Carbonaceous Raw Materials to Fuels and Chemical Feedstocks," *Int. J. Hydrogen Energy*, 11, 715-720.

Steinberg, M. 1987. "A Low Cost High Energy Density Carbon Black Fuel Mix for Heat Engines," *Energy Sources*, 9, 161-171.

Steinberg, M. 1994. "Fossil Fuel and Greenhouse Gas Mitigation Technologies," *Int. J. Hydrogen Energy*, 19, 659-665.

Steinberg, M. 1995a. "The Carnol Process for CO₂ Mitigation from Power Plants and the Transportation Sector," *Brookhaven National Laboratory Report BNL 62835*, Upton, NY.

Steinberg, M. 1995b. "The Hy-C Process (Thermal Decomposition of Natural Gas) Potentially the Lowest Cost source of Hydrogen with the Least CO₂ Emission," *Energy Convers. Mgmt.*, 36 (6-9), 791-796.

Steinberg, M. 1998. "Production of Hydrogen and Methanol from Natural Gas with Reduced CO₂ Emission," *Int. J. Hydrogen Energy*, 23, 419-425.

Steinberg, M. 1999. "Fossil Fuel Decarbonization Technology for Mitigating Global Warming," *Int. J. Hydrogen Energy*, 24, 771-777.

Steinberg, M. and H.C. Cheng. 1989. "Modern and Prospective Technologies for Hydrogen Production from Fossil Fuels," *Int. J. Hydrogen Energy*, 14, 797-820.

Touloukian, Y.S., P.E. Liley, and S.C. Saxena. 1970. *Thermal Conductivity*. New York; IFI/Plenum.

Touloukian, Y.S., S.C. Saxena, and P. Hestermans. 1975. *Viscosity*. New York; IFI/Plenum.

Turner, J.H., A.S. Viner, J.D. McKenna, R.E. Jenkins, and W.M. Vatauvuk. 1987a. "Sizing and Costing of Fabric Filters, Part 1: Sizing Considerations," *JAPCA*, 37 (6), 749-759.

Turner, J.H., A.S. Viner, J.D. McKenna, R.E. Jenkins, and W.M. Vatauvuk. 1987b. "Sizing and Costing of Fabric Filters, Part 1: Costing Considerations," *JAPCA*, 37 (9), 1105-1112.

Wang, J. 1993. Carbon Black (2nd ed.), Marcel Dekker.

Weimer, A.W., ed. 1997. Carbide, Nitride, and Boride Materials Synthesis and Processing. London; Chapman & Hall.

Weimer, A., J. Dahl, J. Tamburini, A. Lewandowski, R. Pitts, C. Bingham, G. Glatzmaier. 2000. "Thermal Dissociation Of Methane Using A Solar Coupled Aerosol Flow Reactor", Proceedings of the 2000 DOE Hydrogen Program Review, NREL/CP-570-28890

Warren, D. S., Seader, J. D., Lewin, D. R., *Process Design Principles, Synthesis, Analysis, and Evaluation*, John Wiley & Sons, 392-393 (1999).

Yaws, C.L. 1999. *Chemical Properties Handbook*. New York; McGraw-Hill.

Nomenclature

Variable	Description	Value/Equation	
a	Arbitrary kinetic constant	Eqn. 6	
a _c	Surface area of carbon particle	3.14x10 ⁻⁸	m ²
A _i	Cross sectional area of reactor	4.56x10 ⁻³	m ²
C _{pC}	Heat capacity of carbon	FACT (1999)	J/mol K
C _{pCH4}	Heat capacity of methane	FACT (1999)	J/mol K
C _{pg}	Heat capacity of gas phase	Eqn. 13	J/mol K
C _{pH2}	Heat capacity of hydrogen	FACT (1999)	J/mol K
d _i	Inside diameter of reactor tube	0.076	m
E _a	Reaction activation energy	Eqn. 4	kJ/mol
E _a [*]	Transformed reaction activation energy	Eqn. 5	kJ/mol
f	Flow rate of H ₂ added through porous walls	2.36x10 ⁻³	m ³ /s (@STP)
F _C	Molar flow rate of carbon	Eqn. 11b	mol/s
F _{CH4}	Molar flow rate of methane	Eqn. 11a	mol/s
F _{CH4} ^o	Initial molar flow rate of methane	Varies	mol/s
F _g	Total molar flow rate of gas	F _{H2} +F _{CH4}	mol/s
F _{H2}	Molar flow rate of hydrogen	Eqn. 11c	mol/s
g	Multiplying factor times f	43.74f	mol/m s
H _C	Molar enthalpy of carbon	FACT (1999)	J/mol
H _{CH4}	Molar enthalpy of methane	FACT (1999)	J/mol
H _{H2}	Molar enthalpy of hydrogen	FACT (1999)	J/mol
h _p	Convective coefficient between gas phase and carbon particles	Eqn. 9	W/m ² K
h _w	Convective coefficient between gas phase and reactor walls	Eqn. 10	W/m ² K
k	Reaction rate	Eqn. 5	s ⁻¹
k _g	Thermal conductivity of gas	Eqn. 14	W/m K
k _o	Pre-exponential factor	Eqn. 4	s ⁻¹
k _o [*]	Transformed pre-exponential factor	Eqn. 5	s ⁻¹
L	Length of reactor tube	0.914	m
M _{wC}	Molecular weight of carbon	0.012	kg/mol
M _{wg}	Molecular weight of the gas phase	Eqn. 12	kg/mol
n _c	Number of carbon particles per volume	$\frac{F_c M_{wc}}{v_g A_i V_c \rho_c}$	m ⁻³
R	Gas constant	8.314	J/mol K
R _o	Carbon particle radius	5x10 ⁻⁵	m
t	Time	Varies	s
T _C	Temperature of carbon particles	Eqn. 8	K

T_f	Film temperature	$\frac{T_g + T_w}{2}$	K
T_g	Temperature of gas phase	Eqn. 7	K
T_o	Transformation temperature	1200	K
T_w	Reactor wall temperature	Varies	K
V_C	Volume of carbon particle	5.24×10^{-13}	m^3
v_g	Velocity of gas phase	Eqn. 16	m/s
X	Conversion	Eqn. 6	
z	Axial distance through reactor	$0 < z < L$	m

Greek Symbols:

Variable	Description	Value/Equation	
ϵ_C	Radiative emissivity coefficient for carbon	1	
μ_g	Viscosity of gas	Eqn. 15	Pa s
ρ_C	Density of carbon	2270	kg/m^3
σ	Stefan-Boltzman constant	5.67×10^{-8}	$W/m^2 K^4$

THERMOCATALYTIC CO₂-FREE PRODUCTION OF HYDROGEN FROM HYDROCARBON FUELS

Nazim Muradov
Florida Solar Energy Center
1679 Clearlake Road, Cocoa, FL 32922

Abstract

The main goal of this project is the development of an economically viable process for production of hydrogen and elemental carbon via thermocatalytic decomposition (TCD) of natural gas or other hydrocarbon fuels. The technical approach is based on a single-step decomposition (pyrolysis) of methane and other hydrocarbons over carbon-based catalysts in an air/water-free environment. This approach eliminates the concurrent production of carbon oxides and, therefore, obviates the need for water-gas shift and CO₂ removal stages, required by conventional processes (e.g., methane steam reforming and partial oxidation), which significantly simplifies the process. Considerable reductions in overall greenhouse gas emissions, compared to conventional processes, could also be expected from the TCD process. Clean carbon (free of sulfur, ash and metals) is produced as a valuable byproduct of the process. The experimental data on the catalytic activity of different carbon-based catalysts for the methane decomposition reaction are presented in this work. The paper also discusses factors affecting long-term stability of the carbon catalysts and the sustainability of the catalytic process. It was found that the process sustainability can be improved via in-situ generation of catalytically active carbon particles. Various conceptual designs for the reactor suitable for decomposition of methane with production of hydrogen-rich gas and continuous withdrawal of elemental carbon were considered; a fluidized bed reactor was selected as the most suitable for this purpose. The reactors for small-scale production of hydrogen (10 W and 1 kW range) have been designed, fabricated and tested. A wide range of hydrocarbon fuels, including methane, propane, gasoline and diesel fuel were converted into a hydrogen-rich gas with H₂ concentration up to 80 v.%, the balance being methane. The gas produced did not contain carbon oxides or other reactive

impurities, therefore, it could be directly fed to a fuel cell without need for the additional gas conditioning and purification stages. Techno-economic analysis conducted by NREL showed that the TCD process would be economically advantageous if credits for the carbon product and avoided CO₂ emissions were applied.

Introduction

Background and Overall Approach

Fossil fuels are likely to play a major role in hydrogen production in the near- to medium-term future. On the other hand, fossil fuels are major source of anthropogenic CO₂ emissions into the atmosphere. There are several possible ways to mitigate CO₂ emission problem. Among them are traditional (e.g. use of non-fossil and renewable energy resources), as well as novel technological approaches pertaining to fossil fuel decarbonization concept. Two fossil fuel decarbonization strategies are actively discussed in the literature: (i) hydrogen production by methane steam reforming coupled with CO₂ sequestration (fuel gas decarbonization), and (ii) hydrogen production via thermal decomposition (pyrolysis) of hydrocarbons with co-production of solid carbon (direct decarbonization of fuels). The following is a brief discussion of “fuel gas” and “direct” decarbonization strategies.

Figure 1 depicts the schematic diagram of fuel gas decarbonization (FGD) concept using natural gas (NG) as a feedstock. FGD system includes a methane steam reforming (SR) hydrogen production plant and a CO₂ sequestration subsystem.

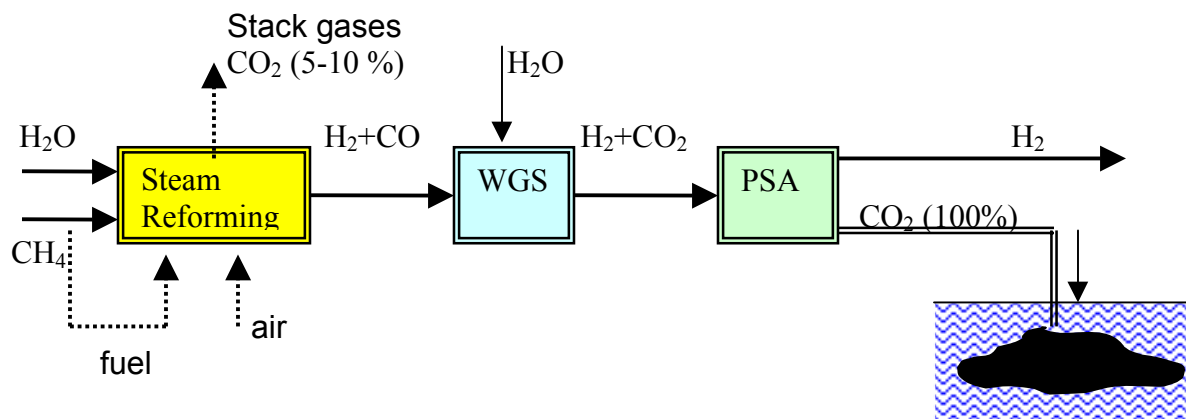


Figure 1. Schematic Diagram of a Fuel Gas Decarbonization Concept

The SR process consists of several stages: (i) highly endothermic catalytic steam reforming of methane ($\Delta H^{\circ}=206$ kJ/mol), (ii) water-gas shift reaction (WGS), and (iii) separation of the H₂/CO₂ mixture (preferably, using a pressure swing adsorption unit, PSA). Other energy-intensive stages of SR process include: feedstock desulfurization and the production of steam

(average steam/carbon ratio of 3-5). As a result, a considerable part of NG (up to 30-35% of the total amount) is used as a process fuel, thus, producing significant amounts of stack gases with CO₂ concentration in the range of 5-10 v.%. Thus, SR process produces two streams of CO₂-containing gases: the concentrated stream after PSA (70% of the total) and diluted (stack gases) stream (30% of total) (Blok et. al 1997). The total CO₂ emissions (including stack gases) from SR process could reach up to 0.3-0.4 m³ CO₂ per m³ of hydrogen produced.

CO₂ sequestration involves the capture, pressurization, transportation and injection of liquid CO₂ under the ocean (at depths of more than 2 km) or underground (e.g. depleted NG wells, or geologic formations). All the operations associated with CO₂ sequestration are energy intensive and costly. There have been some estimates reported in the literature on the economics of CO₂ sequestration associated with hydrogen production from fossil fuels. Thus, according to the authors (Audus et.al. 1996), the capture and disposal of CO₂ add about 25-30% to the cost of hydrogen produced by SR. Furthermore, because of large energy consumption during CO₂ sequestration, additional amounts CO₂ will be emitted (0.25 kg CO₂ per kg of sequestered CO₂, assuming world average energy production scenario). The key risk factor of FGD approach results from uncertain long-term ecological consequences of CO₂ sequestration. Many questions with regard to the duration and extent of CO₂ retention (underground or under the ocean) still remain unanswered. There have been concerns expressed in the literature on possible hazardous environmental effects of CO₂ sequestration, e.g. the harmful effect of local decrease in pH on marine life (when disposing CO₂ in the ocean), or underground structural damage with catastrophic release of CO₂ (Steinberg 1999). Recent studies indicated that stockpiling CO₂ in plants and soil may be effective only for the short term, if at all (Perkins 2000).

Direct decarbonization (DD) strategy (see Figure 2) involves thermal decomposition (TD) (or cracking, pyrolysis) of methane and other hydrocarbons in air- and/or water-free environment with production of hydrogen and elemental carbon:



Methane decomposition reaction is moderately endothermic process. The energy requirement per mole of hydrogen produced (37.8 kJ/mole H₂) is somewhat less than that for the SR process. Due to a relatively low endothermicity of the process, less than 10% of the heat of methane combustion is needed to drive the process. Unlike FGD, the DD approach does not include WGS and CO₂ removal stages, which significantly simplifies the process. In addition to hydrogen as a major product, the process produces a very important byproduct: clean carbon. Carbon can be used as a commodity product or sequestered (or stored) for future use.

Kvaerner company of Norway has developed and operated plasma-assisted decomposition of methane into hydrogen and carbon black (Gaudernack et al. 1996). Although technologically simple, the process is energy-intensive: it was estimated that up to 1.9 kWh of electrical energy is consumed per one normal cubic meter of hydrogen produced (Fulcheri et al. 1995). Since 80% of the world electric energy supply is based on fossil fuels, electricity-driven hydrogen production processes (including electrolysis) generate large amounts of CO₂, and potentially would require its disposal.

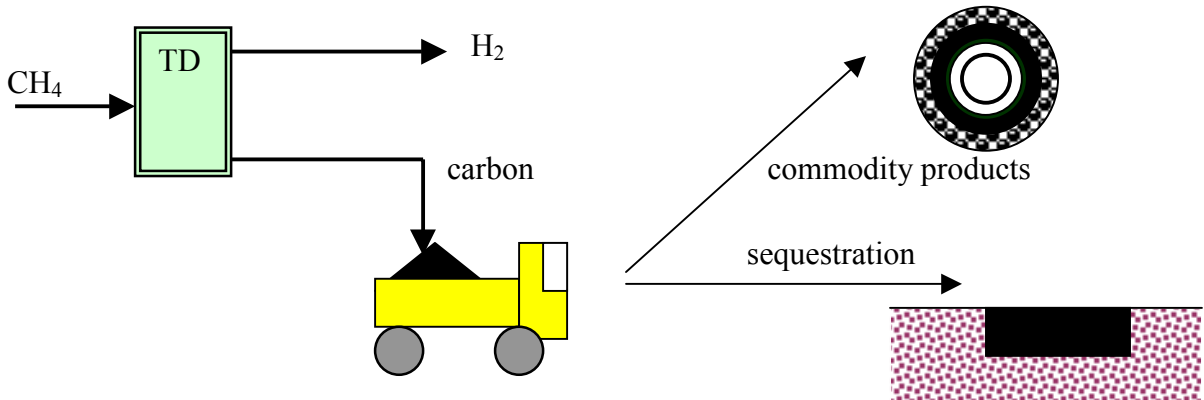


Figure 2. Schematic Diagram of a Direct Decarbonization Concept

There have been attempts to use different catalysts to reduce the maximum temperature of TD of methane. Metal catalysts, including Ni, Fe, Co and others, have been most commonly used for methane decomposition (Calahan 1974, Muradov 1993). However, there was a catalyst deactivation problem associated with the carbon buildup on the catalyst surface. In the vast majority of related publications (e.g., Calahan 1974, Pourier 1997) carbon produced was burned off the catalyst surface in order to remove it from the reactor and regenerate the original activity of the metal catalyst. As a result, the amount of CO₂ produced is comparable with that of the conventional processes (e.g., SR or partial oxidation). Another serious problem arising from the oxidative regeneration of metal catalysts relates to unavoidable contamination of hydrogen with carbon oxides, which would require an additional purification step.

Our technical approach is based on the use of carbon-based catalysts for hydrocarbon decomposition in an oxidant-free environment. Use of carbon catalysts offers the following advantages over metal catalysts: (i) no need for the regeneration of the catalyst by burning product carbon, (ii) no contamination of hydrogen with carbon oxides and, consequently, no need for the additional gas purification, and (iii) production of a valuable byproduct carbon. In Phase I work we demonstrated the technical feasibility of methane decomposition over carbon catalysts at moderate temperatures (<850°C) with simultaneous production of hydrogen-rich gas and elemental carbon. Phase II work focuses on the improvement of long-term catalyst stability and process sustainability, and other technological aspects of the thermocatalytic process.

Experimental

Reagents

Methane (99.99 v.%, Air Products and Chemicals, Inc.) and propane (99.0 v.%, Praxair) were used without further purification. Samples of commercial gasoline and diesel fuel were purchased at a gas-filling station and dried over Drierite for two days before the experiments.

Samples of activated carbons were obtained from Barneby Sutcliffe Corp., NORIT Americas and Kanzai Coke & Chemicals. Cabot Corp. provided different samples of carbon black. Graphites, glassy carbon and acetylene black were obtained from Alfa Aesar and used without further purification. All carbon samples were used in the form of fine powder (<100 μ m). Table 1 summarizes the information on the carbon samples tested for catalytic activity in methane decomposition reaction.

Table 1. Carbon Catalysts Tested for Catalytic Activity in Methane Decomposition Reaction

Manufacturer (brand name) of carbon catalyst	Origin of carbon	Surface area, m ² /g	Method of activation of AC
NORIT Americas (Darco KB-B)	hardwood	1500	steam/chemical
NORIT Americas (Darco 20-40)	lignite coal	650	steam
NORIT Americas (Norit RO 0.8)	peat	900	steam
NORIT Americas (G-60)	proprietary	900	steam
Barnebey Sutcliff Corp. (CL-20)	coconut shell	1500	steam
Barnebey Sutcliff Corp. (KE)	coconut shell	1150	steam
Barnebey Sutcliff Corp. (GI)	coconut shell	1300	steam
Kanzai Coke & Chemicals (KCC) (MAXSORB MSP-15)	carbonized phenol resin	1980	KOH
KCC (MAXSORB MSP-20)	phenol resin	2260	KOH
KCC (MAXSORB MSC-25)	petroleum coke	2570	KOH
KCC (MAXSORB MSC-30)	petroleum coke	3370	KOH
Cabot (CB Black Pearls 2000)	petroleum	1500	
Cabot (CB Black Pearls 120)	petroleum	25	
Cabot (Vulcan XC72)	petroleum	254	
Cabot (Regal 330)	petroleum	94	
Acetylene Black	acetylene	80	
Diamond powder synthetic		7.9	
Graphite crystalline	petroleum coke	3-10	
Graphite microcrystalline	coke	10-12	
Graphite natural	graphite	4-6	
Glassy carbon			

Apparatus

The experimental set-up for hydrocarbon fuel decomposition consisted of 3 main subsystems: (1) a thermocatalytic reactor (with temperature-controlled electric heater and pre-heater), (2) a hydrocarbon metering and delivery sub-system, and (3) an analytical sub-system. All catalytic reactors were made out of fused quartz or ceramic (alumina) in order to reduce the effect of the reactor material on the rate of hydrocarbon decomposition. The reactor was maintained at a constant temperature via a type K thermocouple and Love Controls microprocessor. The amount of carbon catalyst used in the catalyst screening experiments varied in the range of 0.03-2.0 g. Hydrocarbon flow rates were metered by Gilmont flow meters and varied from 5 ml/min to 2

l/min (depending on the reactor used). Fused quartz tubings with the O.D.=10-24 mm were used for fabrication of spouted and fluidized bed reactors. Gaseous products of hydrocarbon decomposition passed through a ceramic filter (for the separation of airborne carbon particles and aerosols) and were directed to a flow meter and GC.

Analysis

The analysis of the products of hydrocarbon decomposition was performed gas chromatographically: SRI-8610A (a thermal conductivity detector, Ar carrier gas, a silica gel column, temperature programming from 25 to 180°C), and Varian-3400, flame ionization detector, He-carrier gas, stationary phase-Hysep D_B. Polynuclear aromatic byproducts were analyzed spectrophotometrically (Shimadzu UV-2401PC). Characterization of carbon products was conducted at Universal Oil Products using SEM, XRD and XPS methods.

Results and Discussion

Decomposition of Hydrocarbons over Carbon Catalysts

This year we continued screening carbon materials of different origin and structure (e.g., activated carbons, carbon blacks, graphites, nanostructured carbons and others) for catalytic activity toward methane decomposition reaction (see Table 1). Testing of all the carbon samples was conducted in the identical experimental conditions (temperature 850°C, methane flow rate 5.0±0.2 ml/min and the amount of carbon sample 0.03±0.001g). This corresponds to a residence time of approximately 1 s in the carbon sample bed. No methane decomposition products other than hydrogen and carbon and very small amounts of C₂ hydrocarbons ($\Sigma C_2 < 0.1$ v.%) were detected in the effluent gas during the experiments. The amount of carbon produced corresponded to the volume of hydrogen within the experimental margin of error (5%). In this paper, all references to the catalytic activity of carbon samples relate to the methane decomposition rate per unit of carbon weight (in mmole/min-g). The control experiments using an inert contact (silica gel with surface area of 600 m²/g) demonstrated that no appreciable thermal decomposition of methane occurred at these conditions.

Activated carbons (AC) demonstrated the highest initial activity among all of the carbon samples tested. A high initial decomposition rate was followed by a rapid drop in catalytic activity, and, finally, by a quasi-steady reaction rate (in most cases over period of 1-1.5 hours). It is noteworthy that the kinetic curves of methane decomposition over AC samples are quite close to each other despite of the differences in their origin, surface area and method of activation. The initial methane decomposition rates for all the AC samples tested were in the range of 1.63-2.04 mmole/min-g (for the comparison, their surface areas were in much wider range of 650-3370 m²/g). Experimental data showed no apparent correlation between surface area and the catalytic activity of ACs. Likewise, the origin and method of AC activation had no significant effect on AC catalytic activity in methane decomposition reaction. The initial hydrogen concentration in the effluent gas of AC-catalyzed reaction was in the range of 40-46 v.%. It should be noted, however, that at relatively high residence times (e.g. 10 s in the carbon bed) AC catalysts produced H₂/CH₄ mixtures with the initial hydrogen concentrations reaching up to 90 v.%, which

is an indication of fairly high catalytic activity (comparable with that of Ni- and Fe-based catalysts measured at the identical conditions). The initial rate of methane decomposition over amorphous carbons, e.g. carbon blacks (CB) and acetylene black (AB), was somewhat lower than that of AC samples. CB-catalyzed methane decomposition quickly reached a quasi-steady state rate (over 10-20 min) and remained practically stable for several hours, followed by the gradual decline in the reaction rate. There is a linear dependence between surface area of amorphous carbons (CB and AB) and their relative catalytic activity toward methane decomposition (Figure 3). It is noteworthy that CB and AB were manufactured by different processes (partial oxidation and decomposition, respectively) and from different feedstocks (residual aromatic hydrocarbons and acetylene, respectively).

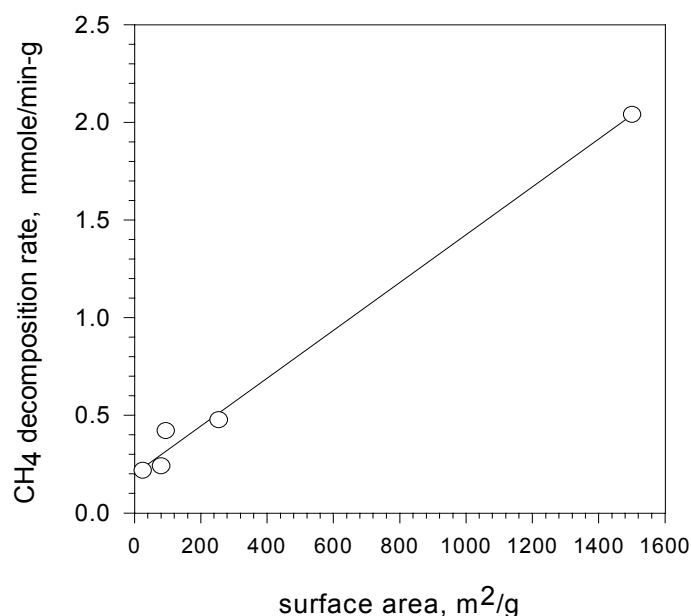


Figure 3. Effect of Surface Area on Methane Decomposition Rate

The above experimental results can be explained as follows. The total rate of the methane decomposition reaction is the sum of the rates of carbon nuclei formation and carbon crystallites growth. The rate of carbon nuclei formation is proportional to the substrate surface area: carbons with high surface area (e.g. ACs and some CBs) tend to have high initial catalytic activity. It was determined that the activation energy of the carbon nuclei formation during methane thermal decomposition (316.8 kJ/mole) is much higher than the activation energy of the carbon crystallites growth (227.1 kJ/mole) (Tesner 1987). Thus, in general, the rate of carbon crystallites growth tends to be higher than the rate of carbon nuclei generation. Rapid deactivation of AC catalysts can be explained by blocking of AC pores by growing carbon crystallites that hinder the internal diffusion of methane molecules. The pore diffusion-controlled reaction could also be responsible for the insensitivity of methane decomposition rate to the origin and surface area of ACs. In contrast, most of the CB surface is relatively easily

accessible to methane molecules during decomposition reaction. CBs differ in particle size, average aggregate mass, morphology, etc. (e.g. the oil furnace process produces CBs with particle diameters in the range of 10-250 nm, and surface area of 25-1500 m²/g). CBs with high external surface area (e.g. CB BP-2000) result in relatively high steady-state methane decomposition rates. The process could go on for several hours until most of the surface is covered by carbon crystallites produced from methane. It was estimated that it would take almost three hours to cover the surface of CB (BP-2000) with carbon species produced from methane (which is in acceptable agreement with the experiment). After 3-4 hours we observed gradual decrease in methane decomposition rate, due to rapid carbon crystallite growth and reduction in the catalytic surface. Sharp drop in activity of glassy carbon can be explained by the relatively large (comparing to CB) size of particles (3-12 micron), and the lack of open porosity.

In the case of carbon samples with low surface area (graphites, diamond powder, some CBs), the rates of carbon nuclei formation and crystallite growth are likely to become comparable. Low initial methane decomposition rate over natural graphite surface is due to high activation energy of nuclei formation over this material. The increase in hydrogen production rate after the short induction period can be explained by the gradual increase in the surface concentration of catalytically active carbon species produced from methane. It is noteworthy that after 30 minutes the methane decomposition rates over glassy carbon, graphites and synthetic diamond become fairly close. Most likely, from this moment on, the methane decomposition rate is controlled by the catalytic activity of carbon crystallites produced from methane.

Thermocatalytic decomposition of propane over CB catalyst at relatively low residence times (<1s) resulted in pyrolysis gas with relatively high concentrations of ethylene. This can be explained by the thermodynamically favorable reaction ($\Delta H^{\circ} = 81.3$ kJ/mol) of the thermal cracking of propane into methane and ethylene. For example, at 800°C and a residence time of approximately 1 s, propane pyrolysis over carbon black CB2000 catalyst resulted in the production of a gaseous mixture with the following composition (vol.%): 52.1% H₂, 38.2% CH₄, 8.5% C₂H₄ and 1.2% C₂H₆. We also conducted a series of experiments on catalytic pyrolysis of a wide range of liquid hydrocarbons (hexane, octane, gasoline and diesel fuel) using different carbon-based catalysts. The quasi steady-state production of the pyrolysis products was achieved over periods of 10-20 min. During gasoline pyrolysis, the gas production yield reached 700 mL per mL of gasoline with an average steady-state hydrogen concentration of approximately 50 v.%.

X-ray diffraction (XRD) studies of the original carbon catalysts and carbon samples produced during propane and methane decomposition were conducted. Carbon black (BP-2000) and activated carbon with the surface area of 1500 m²/g were used. It was found that the original sample of CB catalyst had one- or, possibly, some two-dimensional ordering, whereas, sample produced from hydrocarbon decomposition had graphite-like ordering in the “columnar” or stacking (003) direction (Figure 4).

The d-spacing (lattice spacing) or spacing between plates is practically uniform, so that the (003) columnar reflection is clearly present. Thus, carbon produced during propane pyrolysis clearly has a typical graphite a-b-c-a type stacking of the carbon ring plates. The actual d-spacing (d = 3.4948 Å) of this (003) peak is somewhat larger than that of the standard graphite structure (d =

3.3480 Å), which indicates that the plates are slightly further apart in the columnar stacking direction.

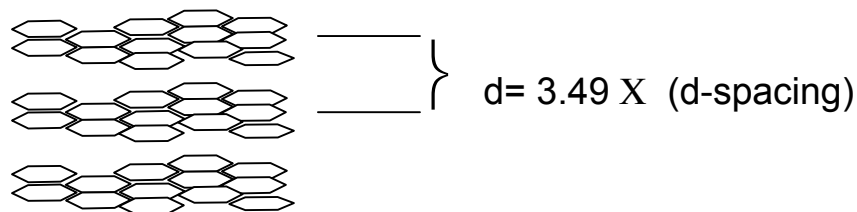


Figure 4. Graphical Representation of Carbon Ring Plates Stacking

Catalyst Stability and Process Sustainability

The development of carbon catalysts featuring long-term stability is one of the major aspects of this work. The experimental results indicated that catalyst deactivation during methane decomposition is common for all types of carbon-based catalysts (although CB is deactivated much slower than AC). It was determined that three chief factors contribute to carbon catalyst deactivation:

- 1) blocking of catalytically active sites by carbon deposits,
- 2) surface deposition of catalytically inactive carbon particulates, and
- 3) reduction in catalytic surface area

Our approach to solving the catalyst deactivation problem is based on an in-situ generation of carbon species catalytically active in the methane decomposition reaction. It is known that the catalytic activity of carbons in methane decomposition is determined by the size of the carbon crystallite and its structure (Tesner 1987). Potentially, the size of carbon crystallites can be affected by the reaction temperature and the presence of other hydrocarbons. The size of the carbon crystallite produced during thermal decomposition of methane is an inverse function of the reaction temperature: the higher the temperature, the smaller the carbon crystallite (Tesner 1987). Figure 5 depicts the correlation between the size of carbon crystallite produced by methane decomposition and the reaction temperature. It is clear that an increase in temperature from 800 to 1100°C would result in only a three-fold reduction in carbon crystallite size. Thus, improvement in catalytic activity of carbon particles via temperature-induced reduction of their crystallite size would require significant increase in methane decomposition temperature (several hundred degrees), which may not be desirable.

We explored the accelerating effect of certain hydrocarbons on the methane decomposition rate as the means of improving long-term stability of carbon catalysts and the sustainability of the process as a whole. It was found that the improvement in the process sustainability can be achieved via in-situ generation of catalytically active carbon particles produced by co-decomposition of hydrocarbons other than methane. We determined the relative catalytic activity of carbons produced by decomposition of hydrocarbons of different classes, e.g. alkanes, unsaturated and aromatic hydrocarbons. Particularly, it was found that carbon produced by

decomposition of unsaturated and aromatic hydrocarbons is catalytically more active than one produced from methane, or other alkanes. Figure 6 demonstrates the accelerating effect of ethylene on the methane decomposition rate.

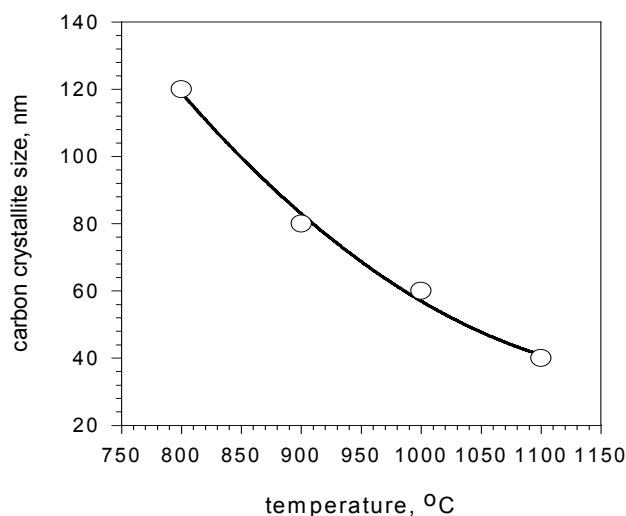


Figure 5. Carbon Crystallite Size as a Function of Temperature

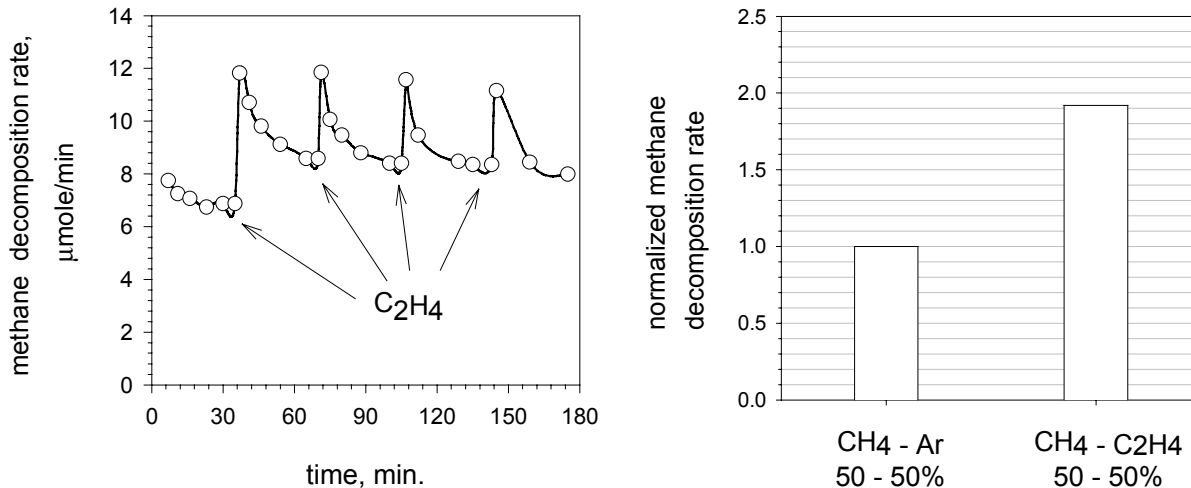


Figure 6. Effect of Ethylene on Methane Decomposition Rate at 850°C

The experiment started with thermal decomposition (850°C) of methane over the surface of activated alumina until quasi steady-state was established (approx. 0.5 h). A pulse of ethylene was introduced into the reactor, followed by rapid purging of the reactor with an inert gas (to remove products of ethylene decomposition), and the introduction of methane into the reactor. We observed a sharp increase (spike) in methane decomposition rate during the first seconds

after methane introduction, followed by its gradual decline to a steady-state level. This procedure was repeated several times, and every time we observed a surge in methane decomposition rate after ethylene pulse (see Figure 6, left). Thus, this experiment proved that carbon produced from ethylene is catalytically more active in methane decomposition than one produced from methane. The accelerating effect of ethylene on the methane decomposition reaction was also demonstrated in a continuous flow experiment using binary $\text{CH}_4\text{-C}_2\text{H}_4$ (50-50 v.%) mixtures. Particularly, we observed that the rate of methane decomposition over the surface of silica gel at 850°C almost doubles in the presence of ethylene (Figure 6, right). Thus, decomposition of a hydrocarbon with low activation energy (ethylene) induces the decomposition of hydrocarbon with high activation energy (methane).

A similar, even more pronounced effect, was observed when benzene pulses were introduced into the reactor where methane decomposition took place (see Figure 7, left). It was found that the yield of hydrogen produced by the decomposition of methane in a binary mixture with benzene vapor (5 v.%) at 850°C increased almost 8 fold compared to pure methane (after adjusting for the amount of hydrogen produced by benzene) (Figure 7, right).

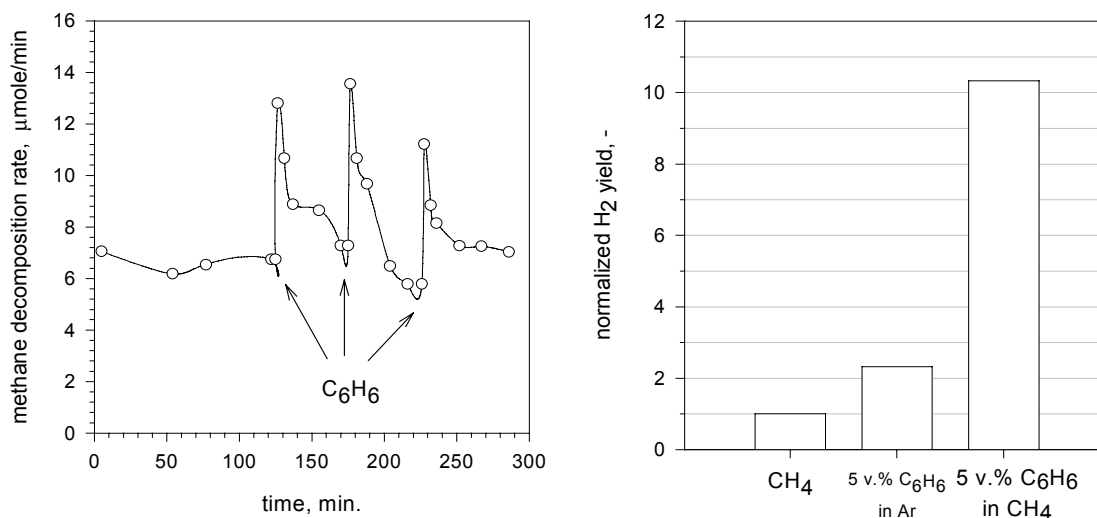


Figure 7. Effect of Benzene Vapors on Methane Decomposition at 850°C

Figure 8 summarizes the relative activity of carbons produced by decomposition of different hydrocarbons in the methane decomposition reaction (normalized against catalytic activity of carbon produced from methane). It was concluded that among all the hydrocarbons tested, carbon produced from aromatics (benzene and naphthalene) exhibited the highest catalytic activity toward methane decomposition.

The relative activity of carbons produced from methane, ethylene and benzene is a linear function of carbon crystallite size in semi-log coordinates (Figure 9).

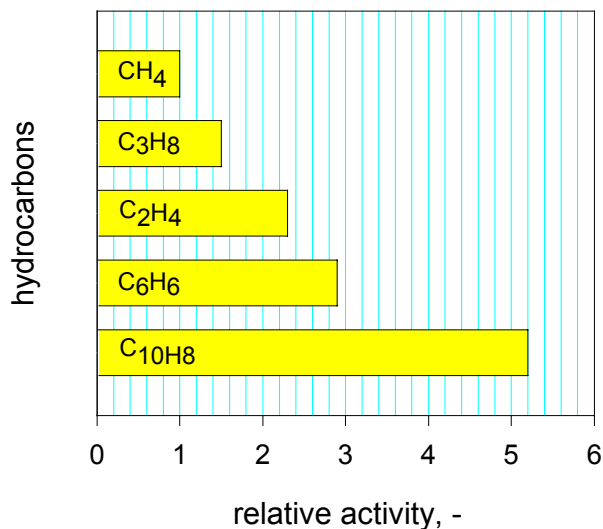


Figure 8. Relative Activity of Carbons Produced from Different Hydrocarbons in Methane Decomposition Reaction at 850°C

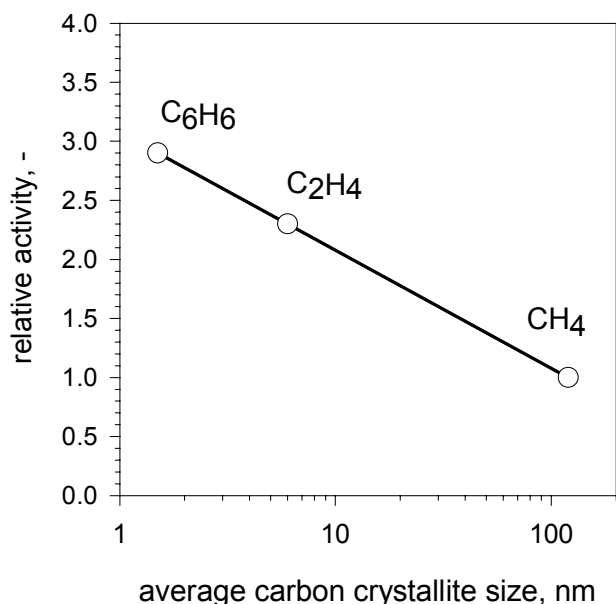


Figure 9. Relative Activity of Carbons Produced from Methane, Ethylene and Benzene as a Function of Carbon Crystallite Size

These data have important implications on improvement of the process sustainability of the hydrocarbon decomposition process. At relatively high space velocities, noticeable amounts of ethylene and aromatics are present in the gases of propane and methane-propane pyrolysis. Thus, recycling pyrolysis gas (with olefins and aromatics) back to the reactor after separation of hydrogen could significantly improve the long-term stability of carbon catalyst and the process sustainability.

Catalytic Reactors for Decomposition of Hydrocarbons

The selection of a catalytic reactor suitable for the efficient decomposition of methane (or other hydrocarbons) with continuous withdrawal of the product carbon from the reactor is another important aspect of the process development. During Phase I work, we looked upon several types of reactors potentially suitable for the production of hydrogen and continuous withdrawal of carbon, such as a tubular, a fluid wall, and a free-volume reactor. Unfortunately, these reactors featured very high temperatures (in excess of 1000°C) and low methane conversions. Fixed (or packed) bed catalytic reactors were used in our studies to rapidly screen the catalytic activity of carbon samples. However, continuous adding to or withdrawal of carbon from a fixed bed reactor could present a daunting technical problem. This year we continued studies on the development (or selection) of reactors suitable for the production of hydrogen-rich gas with simultaneous withdrawal of carbon from the reactor at moderate temperatures (< 900°C). The reactors under consideration were spouted and fluidized bed catalytic reactors. We fabricated micro-reactors of each type and tested them for the simultaneous production of hydrogen and carbon using methane and propane as feedstocks.

Spouted bed reactor

In a spouted bed reactor (SPR) hydrocarbon feedstock enters from the small nozzle at the base of the catalytic bed at high velocity, creating a central dilute phase core (Figure 10). The carbon particulates rise inside the core forming a fountain. Hydrocarbon flows mainly inside the core, although some percentage of the flow might be distributed to the peripheral annular region (annulus). We fabricated a small-size SBR and tested it for methane decomposition in the presence of carbon black (BP-2000) in temperature ranges of 800-1000°C.

Before the actual methane decomposition experiments we ran “cold” experiments to visually determine the optimum gas velocity for carbon particles spouting. It was found that an adequate spouting of carbon black particles by the stream of methane could be achieved at the superficial gas velocity of 2 cm/s and a bed depth to a reactor diameter ratio of 5-6. At higher values of superficial gas velocities and depth-to-diameter ratios, we observed a non-homogeneous fluidization of carbon particles. Applying the above conditions to the methane decomposition experiments (at 900°C) we observed fairly poor conversion of methane (7%). This could be attributed to very short contact time between carbon particles and hydrocarbon within the spouting region. The contact time in the spout was estimated by calculating mean spout diameter according to the following equation (Mathur 1974):

$$D_s = \frac{0.118G^{0.48} D_c^{0.68}}{\rho_b^{0.41}}$$

where: D_s is the spout diameter (cm), G is the methane mass flow rate per unit of reactor cross section (g/sec-cm²), D_c is the reactor diameter (cm), and ρ_b is the carbon bulk density (g/cm³).

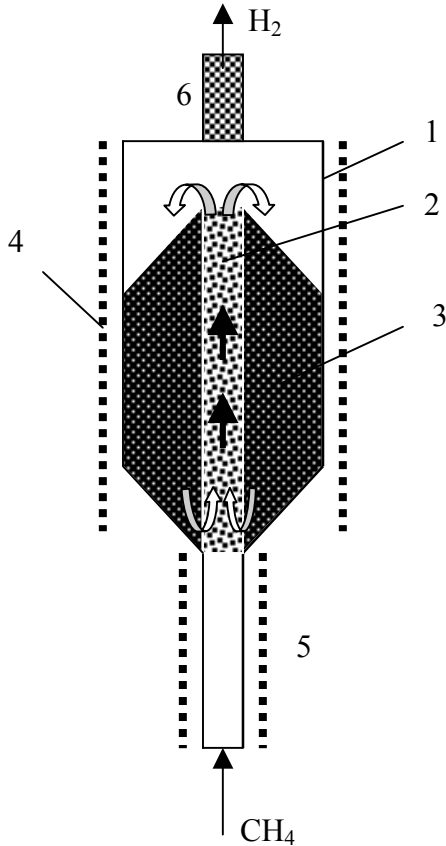


Figure 10. Spouted Bed Reactor

- 1- external wall of the reactor
- 2- spouting zone
- 3- catalyst
- 4- electric heater
- 5- pre-heater
- 6- filter

The calculation yielded a residence time of approximately 0.1 s within the spouting region. Although intense turbulence makes for high coefficients of heat and mass transfer, the effect would be minimal due to the very small residence time in the reaction zone (which would be very difficult to control). Thus, very short contact times intrinsic in the operation of SBRs could result in relatively low methane conversion rates. It should be noted that due to inequality of contact times in the spout and annulus of the SBR, the extent of the reaction taking place in these regions would also be unequal, which might present a problem with modeling the reactor.

Another potential problem is associated with the size of carbon particles. According to (Mathur 1974), the minimum particle diameter for which spouting appears to be practical is about 1 mm, which by far exceeds the expected range of carbon particle sizes in our process (estimated at 10-100 microns). These considerations weigh heavily against the use of SBR for NG decomposition in a large scale units.

Fluidized Bed Reactor

Fluidized bed reactors (FBR) have been widely used in the chemical, metallurgical and petroleum industries. A fluidized bed system does provide constant flow of solids through the reaction zone, which makes it particularly suitable for the continuous addition and withdrawal of carbon particles from the reactor (similar to fluid catalytic cracking process). In an FBR, the bed of fine carbon particles behaves like a well-mixed body of liquid giving rise to high particle-to-gas heat and mass transfer rates. During fluidization, carbon particles are allowed to spend a certain time in the reaction zone, which could be easily controlled by adjusting the ratio between the feed rate and the weight of the bed. The bed could also buffer any instabilities that arise during continuous operation.

A schematic diagram of FBR used in our experiments is shown in Figure 11. Preheated to 400°C a stream of methane (or propane, or methane-propane mixture) entered the FBR from the bottom, and contacted with the fluidized bed of carbon particles (carbon black BP-2000) at 800-950°C in the reaction zone, where pyrolysis of hydrocarbons occurred.

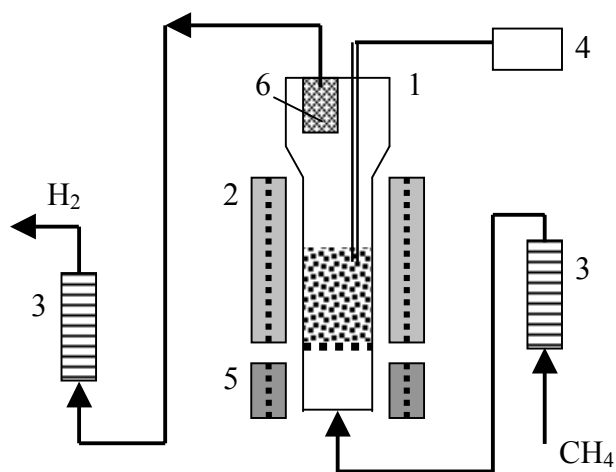


Figure 11. Fluidized Bed Reactor

- 1- fluidized bed reactor
- 2- electric heater
- 3- flow meter
- 4- temperature controller
- 5- pre-heater
- 6- filter

The minimum methane flow rate necessary for fluidization of carbon particles was found from the following equation (Othmer 1956):

$$G = \frac{0.005d_p^2 \varepsilon^3 (\rho_p - \rho_f) \rho_f g}{\psi^2 (1 - \varepsilon) \mu}$$

where: G is the mass flow rate necessary to initiate fluidization, d_p is the diameter of the particle (cm), ε is the fraction voids, ρ_p is the density of particle (g/cm^3), ρ_f is the density of methane (g/cm^3), g is the acceleration gravity (cm/s^2), ψ is the shape factor, μ is the viscosity ($\text{g}/\text{cm}\cdot\text{s}$)

The flow of hydrogen-containing gas exited from the top of the reactor through a ceramic filter and was directed to a gas chromatograph.

Figure 12 depicts the kinetic curves of decomposition of methane, propane and their mixtures (3:1 by volume) over CB catalyst at 850 and 950°C. Propane was almost quantitatively converted into hydrogen-rich gas, whereas, methane decomposition yields were somewhat lower. The propane pyrolysis gas was rich in ethylene and other heavier hydrocarbons. Thus, the experimental results indicated that a gas with the hydrogen concentration in the range of 40-50 v.% could be produced from methane and methane-propane mixtures in a quasi steady-state regime using fluidized bed of BP-2000 particles.

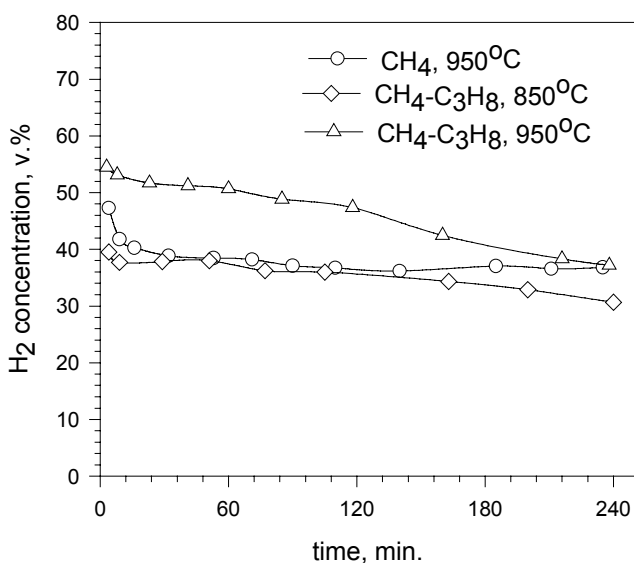


Figure 12. Methane and propane decomposition over CB (BP2000) using fluidized bed reactor

It can be seen from the Figure 12 that after 1.5-2 hours, hydrocarbon decomposition rates started to drop, which could be explained by the decrease in the catalytic surface area. Indeed, at the end of experiment we observed the accumulation of coarse (0.1-1 mm in diameter) carbon particles in the bottom section of the reaction zone.

Technological Scheme of Thermocatalytic Process

Based on the above experimental data, we proposed the following technological scheme for the thermocatalytic decomposition (TCD) process. Figure 13 shows the simplified schematic diagram of the TCD process. A fluidized bed catalytic reactor (1) and a fluidized bed heater (2) are the two main pieces of equipment in the process. For the sake of simplicity, auxiliary equipment such as compressors, cyclones, and others are not shown in the figure. A preheated stream of a hydrocarbon feedstock enters the reactor (1) where it is decomposed (pyrolyzed) at temperatures of 850-900°C, and pressure of 100-500 kPa over the fluidized bed of catalytically active carbon particulates. The resulting hydrogen-containing gas is directed to a cyclone, a heat exchanger (3), and, finally, to a gas separation unit (4), where a stream of hydrogen with the purity of >99.0 v.% is separated from the gaseous stream. The gas separation unit could be a membrane or pressure-swing adsorption (PSA) unit. The concentration of hydrogen in the effluent gas after the reactor (1) depends on the hydrocarbon feedstock, the temperature and the residence time in the reactor and varies in the range of 40-60 v.%, with the balance being methane and higher hydrocarbons (C₂+, including ethylene and other unsaturated and aromatic hydrocarbons). The non-permeate gas (or PSA off-gas), consisting of CH₄ and C₂+ hydrocarbons, is recycled to the catalytic reactor. The concentration of gaseous olefins in the non-permeate gas (or off-gas) depends on the feedstock and could reach up to 20 v.%. As discussed earlier, decomposition of unsaturated and aromatic hydrocarbons produce carbon species catalytically active in the methane decomposition reaction. Thus, recycling the non-permeate gas (or PSA off-gas) containing olefins and aromatic hydrocarbons back to the reactor allows one to sustain the thermocatalytic process via in-situ generation of catalytically active carbon species.

Product carbon (coke) is withdrawn from the bottom of the fluidized bed reactor in the form of carbon particulates with the size of >100 microns. Approximately half of carbon is ground into fine (<100 microns) powder in a grinder (5), and directed to a heater (2) where it is heated to 900-1000°C. The hot carbon particles from the heater flow down to the top of the reactor bed. A jet attrition system in the reactor provides additional seed carbon particles to maintain a constant particle size within the system (approximately 100 micron). The heat input necessary to drive the endothermic process could be provided by burning a portion of carbon with air in a heater. Alternatively, heat could be provided by combusting either a part of the hydrocarbon feedstock, or a portion of the recycle. Ash-, sulfur- and metal-free carbon is a valuable byproduct of the process that could significantly reduce the cost of hydrogen production by TCD process. Thus, in general, the technological chain of the process is similar to that of the fluid coking process, which has been successfully operated since 1950's.

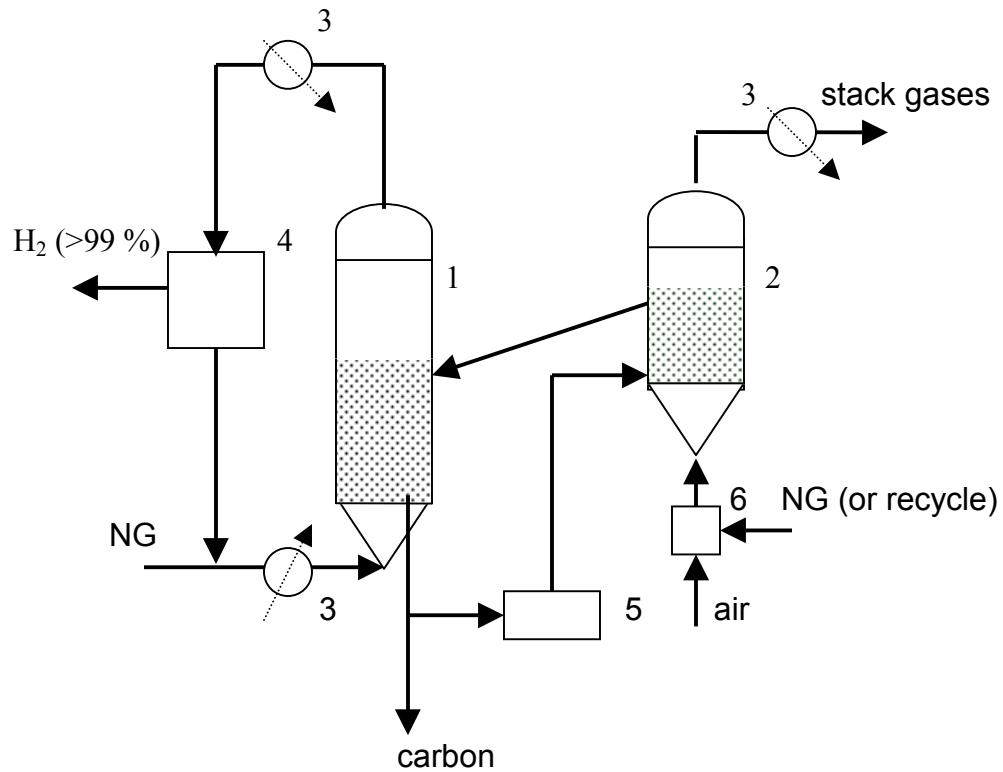


Figure 13. Simplified Schematic Diagram of Thermocatalytic Process
 1- reactor, 2- heater, 3- heat exchanger, 4- gas separation unit,
 5- grinder, 6- combustor

Reactors for Small Scale Hydrogen Production

Miniature (10 W) Hydrogen Generator

We have been working on the development of the reactors for small-scale hydrogen production. The concept is based on the catalytic decomposition of liquefied or liquid hydrocarbon fuels that act as irreversible chemical “hydrides.” For example, gravimetric densities of hydrogen in propane and gasoline are equal to 18.2 and 13.4 w.%, respectively, which by far exceed that of all known metal hydrides and nano-carbon systems. Furthermore, the reactor does not produce CO, which obviates the need for WGS and other gas conditioning stages. This may potentially result in a compact hydrogen generator operating on a wide range of hydrocarbon fuels, e.g. LPG, gasoline, kerosene and diesel fuel. To demonstrate the technical feasibility of this concept we designed and fabricated a 10 W_{th} hydrogen generator (Figure 14).



Figure 14. A 10 W Hydrogen Generator

The hydrogen generator has a tubular design (OD=2.5 cm and length of 15 cm) (the design of the generator is proprietary; a patent application has been filed with U.S. PTO). It has been tested using commercial gasoline and diesel fuel as feedstocks (the fuels were pre-dried before the experiments). The hydrogen generator produced a gaseous stream consisting of hydrogen and methane as a major and a minor component, respectively. No CO or CO₂ were detected in the gas produced by the hydrogen generator. In the case of gasoline, the hydrogen-rich gas was produced at the average production rate of 10 ml/min and the following composition (v.%): 76.3% H₂, 23.7% CH₄, with trace amounts of C₂⁺ hydrocarbons. Based on the hydrogen yield, the specific energy (SE) achieved in this system was estimated at 2.3 kW_{th}h per kg of fuel (the external source of energy for the heating is not included). Coupling of this reactor with a PEM FC (at PEM efficiency of 50%) would result in SE of the entire power system close to 1 kW_{el}h per kg of fuel. This value of SE is three times higher than that of the advanced methanol/water reformer (300 Wh per kg of fuel) reported in the literature (Fuel Cell Industry Report 2000). The portable power systems (10-50 W range) based on the combination of a compact hydrogen generator with a fuel cell can find important applications in many areas, particularly in “soldier power” systems, as it lacks acoustic and chemical “signatures.”

1 kW Hydrogen Generator

We have designed and fabricated a 1 kW_{th} hydrogen generator. Similar to the 10 W hydrogen generator, its operation is based on thermocatalytic pyrolysis of hydrocarbon fuels over carbon-based catalysts. Since no carbon oxides are produced during catalytic decomposition of hydrocarbon fuels, the hydrogen gas can be directly fed into a polymer electrolyte membrane (PEM) fuel cell without need for water-gas shift, preferential oxidation and CO₂ separation stages. Figure 15 demonstrates the experimental set-up consisting of 1 kW hydrogen generator, a propane tank, a PEM fuel cell and testing equipment.

A PEM fuel cell has been provided by the Energy Partners, and the fuel cell testing equipment was purchased from Scribner Assoc. The results of the hydrogen generator testing (without connecting it to a fuel cell) are presented in Figure 16. In the first series of experiments, propane was introduced into the hydrogen generator at different flow rates. Figure 16 (left) demonstrates the distribution of propane pyrolysis products as a function of the effluent gas flow rate. Hydrogen concentration in the pyrolysis gas reached almost 80 v.% at lower flow rates, and it dropped to approximately 70 v.% as the effluent gas flow rate increased from 1.2 to 5.1 L/min. The balance was methane with the traces of ethane. No appreciable amounts of carbon oxides or other reactive gases were detected in the pyrolysis gas.



Figure 15. Hydrogen Generator Connected to Propane Tank, PEM Fuel Cell and Testing Equipment

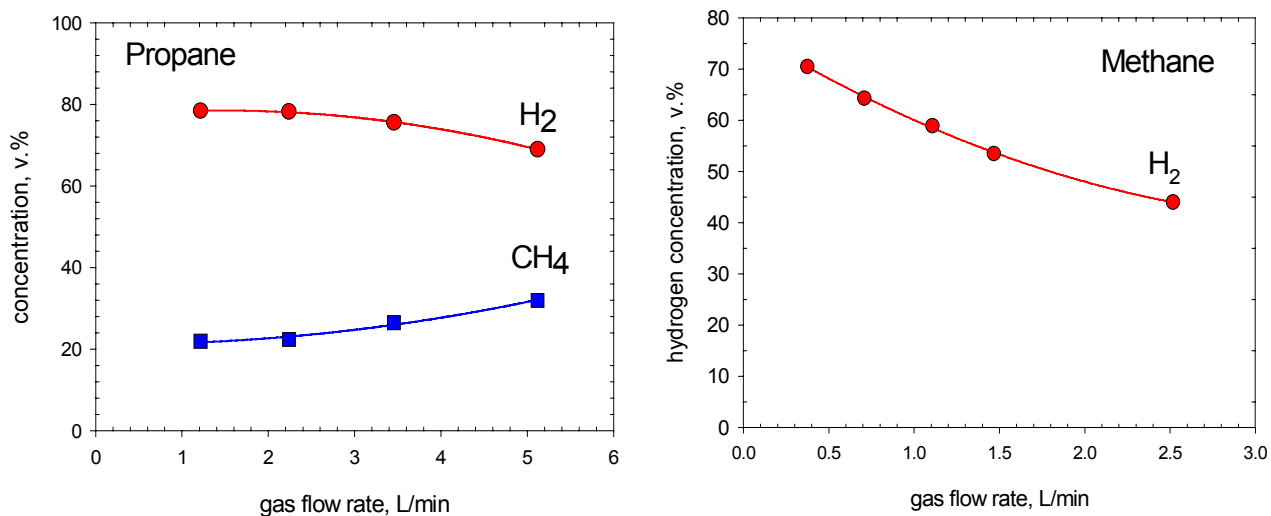


Figure 16. Production of Hydrogen-rich Gas from Propane (left) and Methane (right) Using 1 kW Hydrogen Generator

As expected, methane produced a gas with somewhat lower concentrations of hydrogen (Figure 16, right.) At low flow rates, the concentration of hydrogen in methane decomposition gas was 70 v.%; however, it dropped to 45 v.% at high flow rates (2.5 L/min) of the effluent gas. Again, no carbon oxides were detected in the gaseous stream exiting the hydrogen generator.

Status of Economics

Technoeconomic analysis of thermocatalytic decomposition of natural gas was conducted by NREL, based on the experimental data input provided by FSEC. The details of the analysis will be published in NREL's report (Lane and Spath 2001). Courtesy of NREL, we present selected results of the analysis related to one particular process design that included a fluidized bed catalytic reactor and a fluidized bed heater with carbon particles circulating between these two apparatuses (similar to the schematic presented in Figure 13). Process heat is provided by combusting part of the NG and carbon. A PSA unit was assumed for the production of high purity hydrogen (>99 v.%). Three plant sizes were analyzed (in MMscfd): small- 6, medium- 20 and large- 60. The analysis assumed the internal rate of return of 15%. Figure 17 demonstrates hydrogen selling price as a function of natural gas selling price for three hydrogen plants (assuming a carbon selling price of \$300/t).

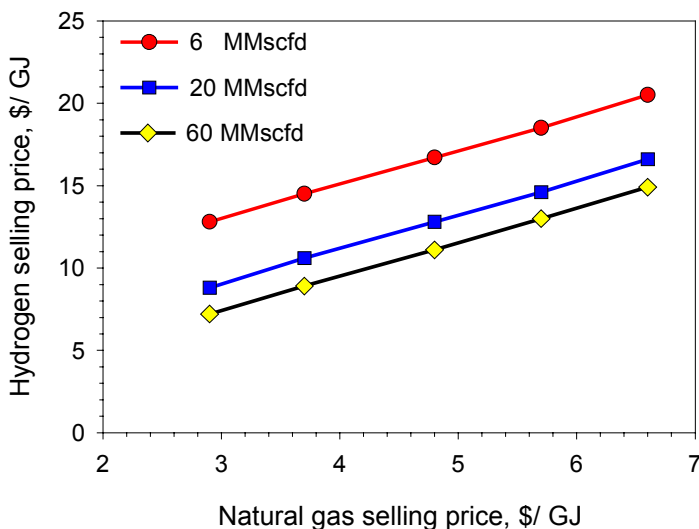


Figure 17. Hydrogen Selling Price vs Natural Gas Selling Price

At natural gas prices ranging from \$2.9 to 6.6 per GJ, the hydrogen selling price varied in the range of \$7.2-14.9 /GJ for a large plant, and \$12.8–20.5/ GJ for a small plant. It should be noted that hydrogen selling prices would be further reduced if a carbon credit for avoided CO₂ emissions were applied.

The sensitivity analysis on the effect of the carbon selling price on the hydrogen selling price was also conducted. Figure 18 shows the plots: hydrogen selling price vs carbon selling price for the small, medium and large hydrogen plants at a NG price of \$3.72 per GJ. It is evident that carbon credit significantly reduces the cost of hydrogen production. Particularly, at carbon selling prices ranging from \$0 to 500 per metric ton, the plant gate hydrogen selling price varies from \$13.8 to 5.7/GJ, for the large plant, and from \$19.4 to 11.2/GJ, for the small plant.

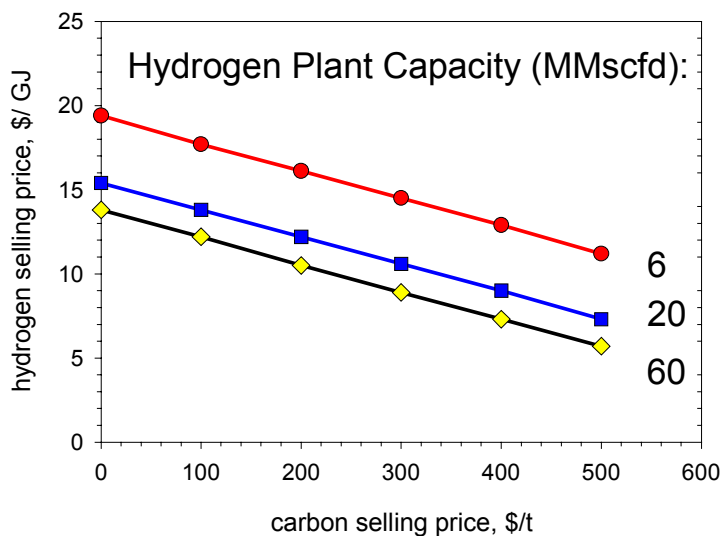


Figure 18. Hydrogen Selling Price vs Carbon Selling Price

Since carbon credit markedly affects the economics of the TCD process, a great deal of consideration was given to the characterization of the carbon product and estimation of its market value. This work was conducted in cooperation with the Universal Oil Products (UOP) (Des Plaines, IL). UOP has conducted SEM, XRD and XPS analysis of carbon produced by catalytic pyrolysis of propane and methane over carbon black catalyst. In general, the results of XRD analysis conducted by UOP were in an agreement with the results of the prior analysis of carbon samples, conducted by AMIA Laboratories (Rigaku) (see Phase I Report). It was inferred that the carbon produced by TCD process revealed a graphite-like structure. It was also concluded that carbon produced in the process could be suitable for the production of electrodes in the aluminum and ferro-alloy industries. Currently, the aluminum industry produces annually close to 4 mln tons of aluminum, with a carbon (coke) consumption rate of 0.4-0.5 kg of carbon per kg of Al (Kirk-Othmer 1992). Thus, the aluminum industry could be a very important market for sulfur- and metal-free carbon produced in TCD process with the selling prices of \$300 per ton and higher.

Comparative Assessment of TCD and SR Processes

We have conducted a comparative economic assessment of TCD (with and without carbon credit) and SR (with and without CO₂ sequestration) processes (Figure 19).

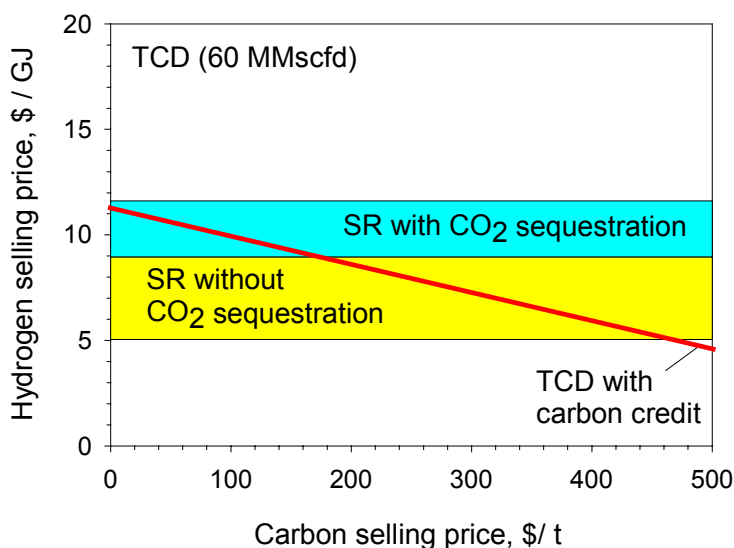


Figure 19. Comparative Economic Assessment of TCD and SR

The comparison is based on a large capacity hydrogen plant and a NG price of about \$3/GJ. The cost of hydrogen production by a large SR plant was estimated at \$5-9/GJ (Ogden et al. 1997). It was assumed that the total cost of hydrogen production by SR plant coupled with CO₂ sequestration would increase by 25-30% (Audus et al. 1996). For the purpose of this comparative assessment, sequestration of CO₂ from TCD process is not considered (it was assumed that upon the optimization of TCD process, CO₂ emissions from it would be minimal compared to those from SR). It is evident from the Figure 19 that the cost of hydrogen production by TCD process becomes comparable with that of SR process (without CO₂ sequestration) if carbon is sold at the price range of approximately \$160-460 per ton. However, if strict environmental restrictions on CO₂ emissions are imposed in future, and CO₂ sequestration from SR process becomes mandatory, hydrogen selling prices for SR and TCD will be comparable, even without carbon credit.

Conclusion

Thermocatalytic decomposition of NG (or other hydrocarbon fuels) as a viable technological approach to the production of hydrogen and solid carbon is discussed in this paper. Decomposition (or pyrolysis) of hydrocarbons occurs in the presence of catalytically active carbon particles at moderate temperatures (<900°C) in an air/water-free environment, which

eliminates the concurrent production of carbon oxides. The advantages of TCD process can be summarized as follows: (i) it is technologically simple (only one chemical stage); (ii) clean carbon is produced as a valuable byproduct; and (iii) CO₂ emissions from the process are significantly reduced. Phase II work focuses on the long-term catalyst stability and process sustainability, and other technological aspects of the TCD process development. Factors affecting carbon catalyst activity and stability were investigated. It was determined that the catalyst stability and process sustainability can be improved via in-situ generation of catalytically active carbon species. Several types of reactors, including spouted and fluidized bed reactors were evaluated for hydrocarbon decomposition process. A fluidized bed reactor was selected as the most suitable for the efficient decomposition of methane and propane with the production of hydrogen-rich gas and simultaneous withdrawal of carbon from the reactor. Reactors for small-scale production of hydrogen (at 10 W and 1 kW range) have been designed, fabricated and tested. It was found that a wide range of hydrocarbon fuels, including methane, propane, gasoline and diesel fuel could be efficiently converted into a gas with hydrogen concentration up to 80 v.%, with the balance being methane. Since this gas does not contain carbon oxides or other reactive impurities, it could be directly fed to any type of fuel cell, including CO-sensitive PEM fuel cells. The techno-economic analysis conducted by NREL demonstrated that the TCD process could be economically advantageous if credits for the product carbon and avoided CO₂ emissions were applied.

The ecological advantages of TCD over other processes become more appreciable if applied to small-scale hydrogen plants for on-site (or decentralized) production of hydrogen. It was concluded by the authors of recent technical reports that the sequestration of CO₂ produced by decentralized SR hydrogen plants would not be economical, since it would require building of an expensive CO₂ infrastructure (Ogden et al. 1997 and Sokolow, Ed. 1997). This implies that all the CO₂ produced at decentralized SR hydrogen plants will be vented into the atmosphere. In contrast to that, solid carbon produced by TCD process could be easily handled by means of truck shipping to an end-user or to a disposal site without the necessity of building a new infrastructure.

New markets for carbon-based products will most likely be developed in the near future. For example, it is conceivable that carbon-based materials would eventually replace (at least, partially) many major building and construction materials, and, most importantly, cement. This would result in even further reductions in overall CO₂ emissions due to phasing out of cement manufacturing plants, which are major industrial CO₂ producers. Although the market for carbon-based materials is continuously growing, it is possible that not all the carbon produced by TCD process will be absorbed by the traditional and perspective application areas. In this case all the remaining carbon would be sequestered or stored for the future use. Carbon is an inert material under ambient conditions, so it can be conveniently and safely stored for the extended periods of time (in landfills or depleted mines) with minimal ecological uncertainties.

Future Work

- Collaborate with industry to scale up and optimize the process with respect to throughput, hydrogen purity and reduced greenhouse gas emissions

- Design and fabricate a process development unit and evaluate its performance using technical-grade hydrocarbon fuels
- Demonstrate active operation of the thermocatalytic reactor coupled with a PEM fuel cell
- Address safety issues related to operation of the reactor and handling the carbon product
- Demonstrate tolerance to moisture, sulfur and other impurities present in commercial hydrocarbon fuels
- Increase specific energy of the thermocatalytic reactor
- Work with industry to identify the areas of applications for the carbon product; evaluate new markets for carbon

Acknowledgements

This work was supported by the U.S. Department of Energy under the contract No. DE-FC36-99GO10456 and the Florida Solar Energy Center (University of Central Florida). The author also acknowledges the contribution of the Universal Oil Products, National Renewable Energy Laboratory, Energy Partners, Florida Institute of Technology, and AMIA Laboratories (Rigaku).

References

- Audus, H., O. Kaarstad, and M. Kowal. 1996. "Decarbonization of Fossil Fuels: Hydrogen as an Energy Carrier". In *Proceedings of 11th World Hydrogen Energy Conference*, 525. Stuttgart, Germany.
- Blok, K., R. Williams, R. Katofsky, and C. Hendriks. 1997. "Hydrogen Production from Natural Gas, Sequestration of Recovered CO₂ in Depleted Gas Wells and Enhanced Natural Gas Recovery". *Energy*, 22: 161-168
- Calahan, M. 1974. "Catalytic Pyrolysis of Methane and other Hydrocarbons". In *Proceedings of Conference on Power Sources*. 181
- Fuel Cell Industry Report. 2000. 1: No.4
- Fulcheri, L., and Y. Schwob. 1995. "From Methane to Hydrogen, Carbon Black and Water". *Int. J. Hydrogen Energy*, 20: 197.
- Gaudernack, B., and Lynum S. 1996. "Hydrogen from Natural Gas without Release of CO₂ to the Atmosphere". In *Proceedings of 11th World Hydrogen Energy Conference*, 511-523. Stuttgart, Germany.
- Kirk-Othmer Encyclopedia of Chemical Technology*. 1992. New York, John Wiley & Sons
- Lane, J. and P.Spath. 2001. *Technoeconomic Analysis of the Thermocatalytic Decomposition of Natural Gas*, NREL Technical Report. Golden, CO.

Mathur, K. and N. Epstein. 1974. *Spouted Beds*, New York, Academic Press

Muradov, N. 1993. "How to Produce Hydrogen from Fossil Fuels without CO₂ Emission". *Int. J. Hydrogen Energy*, 18: 211

Ogden, J., M. Steinbugler and T. Kreutz. 1997. "Hydrogen as a Fuel for Fuel Cell Vehicles: a Technical and Economic Comparison". In *Proceedings of the 8th Annual U.S. Hydrogen Meeting*, Alexandria, 469. VA

Othmer, D. (Ed.). 1956. *Fluidization*. New York; Reinhold Publ.

Pourier, M. and C. Sapundzhiev. 1997. "Catalytic Decomposition of Natural Gas to Hydrogen for Fuel Cell Applications". *Int. J. Hydrogen Energy*, 22:429

Perkins, S. 2000. *Science News*, 158: 396.

Socolow, R. (Ed.). 1997. "Fuels Decarbonization and Carbon Sequestration". Report of a Workshop. PU/CEES Report No. 302, Princeton University

Steinberg, M. 1999. "Fossil Fuel Decarbonization Technology for Mitigating Global Warming". *Int. J. Hydrogen Energy*, 24: 771

Tesner, P. 1987. *Kinetics of Pyrocarbon Formation*. Moscow; VINITI.

Novel Catalytic Fuel Reforming with Advanced Membrane Technology

**P. Irving, W.L. Allen, Q. Ming, and T. Healey
InnovaTek, Inc.
350 Hills Street
Richland, WA 99352**

Abstract

InnovaTek is developing a hydrogen generator that processes multiple fuel types to create hydrogen directly for fuel cells or indirectly for refueling stations for fuel cell-powered vehicles.

Our ultimate goal is the development of a micro channel catalytic reactor that produces pure hydrogen through catalytic reforming of methanol, diesel fuel and natural gas. Advanced membrane technology is incorporated to remove carbon dioxide and detrimental co-products such as CO from the reformat stream. Our technology provides a pure output stream of hydrogen that can be used in a compatibly-sized PEM fuel cell for electrical generation or at refueling stations for vehicles equipped with hydrogen storage tanks.

A thermal and process system model that was developed as a system simulator was used to optimize the design of our micro channel reactor and heat exchangers. With iterative testing and further refinement, the model will be used to provide a sound basis for improved reactor design and process engineering.

On-going tests indicate that hydrogen production is maximized and CO production is minimized by proper selection of 1) temperature-dependent reaction equilibria, 2) ratio of fuel to steam, and 3) catalyst activity. The use of micro-reactor and micro-heat exchanger components helps optimize these processes. Milestones achieved include catalyst testing with sulfur present in the fuel and fabrication of a hydrogen-permeable membrane that is less than 10 micrometers thick. On-going work includes the development of a mini-plasmatron and a micro-fuel injection system.

Introduction

Although fuel cells have been around for years, it wasn't until recently that advances, such as those made in fuel processing technology, promise to make fuel cells economical and reliable enough for use in a multitude of commercial applications.

The InnovaTek H2GEN™ hydrogen production system, currently under development, uses advanced technology to provide a pure hydrogen stream to fuel cells for stationary, portable, and mobile applications. The technology conveniently uses today's standard fuels such as natural gas, gasoline or diesel to generate hydrogen for clean on-site electrical power production.

Our portable power reformer (Fig. 1) can generate enough hydrogen for a 100 Watt fuel cell. Our development plans include systems to generate hydrogen for equivalent sub-kW, kW, and multi-kW power production devices. We report here on our development and testing of the primary sub-components of the H2GEN™ system and results from testing.



Figure 1. Model of InnovaTek's H2GEN Fuel Processor

System Components

InnovaTek's fuel processor is based on catalytic steam-reforming coupled with hydrogen separation membrane technology, and incorporates various proprietary and licensed components. The technology can reform gasoline, diesel, methanol and natural gas. We are developing and integrating the following critical enabling technologies into components (Fig. 2) that create a system offering significant advantages over traditional reactors:

- Sulfur-tolerant reforming catalyst that eliminates the requirement for extra components for sulfur removal
- Sulfur-tolerant H-separation membrane that yields 100% hydrogen product (no CO, H₂S or CO₂ to poison fuel cell or dilute hydrogen) thereby producing higher fuel cell current densities
- Fuel Injector Micro-Nozzle that eliminates catalyst coking
- Micro-channel reactor and heat exchanger for compact high-efficiency system design
- Plasmatron for fast start-up and catalyst regeneration.

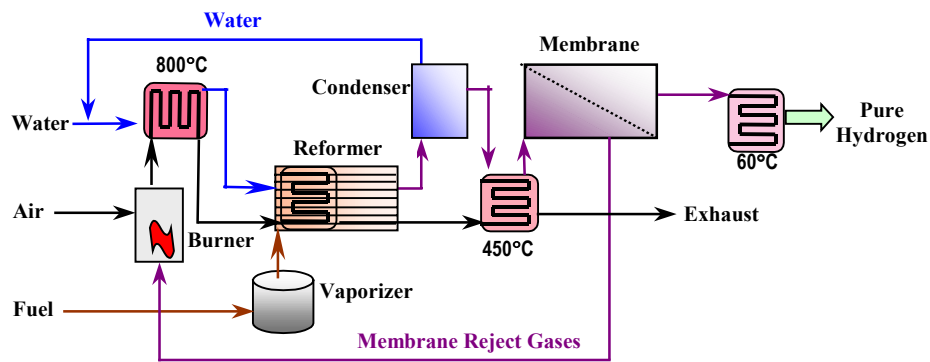


Figure 2. Process Flow Diagram For Hydrogen Generation System

A thermal and process system model that was developed as a system simulator was used to optimize the design of our micro-channel reactor. With iterative testing and further refinement, the model will be used to provide a sound basis for improved reactor and process engineering.

The process starts with water, air, and fuel, which are injected into two subcomponents – the burner unit and the vaporizer/fuel injector unit. The burner unit combusts the membrane reject gases to convert the water to steam and create enough heat for fuel vaporization and reforming processes.

Micro-channel heat exchangers transfer the energy to the catalytic micro-channels of the reformer where the vaporized fuel and steam are injected. The catalytic reaction occurs at about 800°C producing reformat that consists primarily of hydrogen (H₂), carbon monoxide (CO), and carbon dioxide (CO₂). Small amounts of hydrogen sulfide are produced from fuels with sulfur content.

The reformat is cooled through the use of microchannel heat exchangers and water is condensed and recycled. The dry reformat is heated to 450°C and then purified by the membrane component. Only hydrogen can pass through the membrane thereby producing a stream of pure hydrogen that is delivered to the fuel cell after additional cooling. The gas that does not pass through the membrane, known as the “reject stream” is sent back to the burner where the cycle continues.

Experimental Results

Catalyst Testing

The performance of InnovaTek’s catalyst ITC-3 for reforming commercial-grade “regular” gasoline was evaluated using a tube reactor. Gasoline normally contains some sulfur compounds in the concentration range between 50 and 300 ppm, The results (Figure 3) indicate that the catalyst maintains its activity with no deactivation for 50, hours at which time the experiment was terminated.

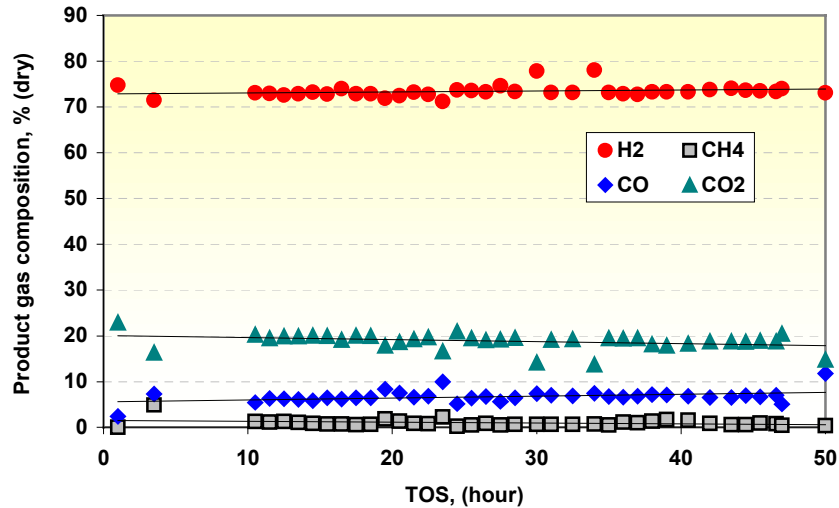


Figure 3. The product gas composition vs. the reforming time using InnovaTek catalyst ITC-3 for commercial gasoline; feed rate was about 0.1 g/minute; the ratio of steam:C varied from 5 to 8 and the temperature was 800°C.

Tests were also conducted using iso-octane feed containing 1000-ppm sulfur (Figure 4). The catalyst, ITC-3, has maintained its high activity and hydrogen selectivity for over 100 hours of testing; the reactor is still operating and data continues to be collected. The hydrogen concentration was maintained at about 70% during the testing period and no deactivation was observed. We believe the slight decrease (from 75% to 70%) after the first 30 hours was the result of some initial coking in our reactor that reduced the volume of active catalyst. The presence of H₂S in the reformat was detected (by lead acetate paper) shortly after the reaction started indicating that sulfur was reduced (and not absorbed by the catalyst bed, which would deactivate it).

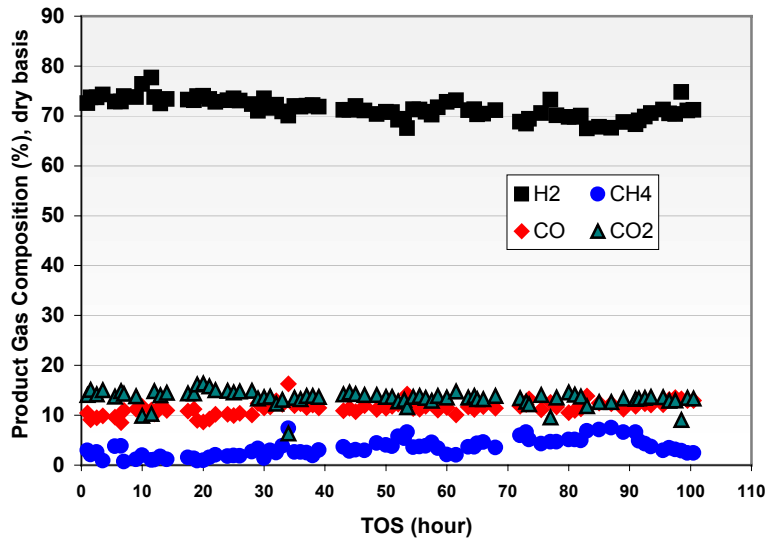


Figure 4. Product gas composition vs reforming time using InnovaTek catalyst ITC-3 for iso-octane with 1000 ppm sulfur; feed rate of iso-octane was about 0.1 gram/minute; steam/C ratio was about 4; and temperature was 800°C.

Microchannel Reactor Design and Fabrication

A micro-channel reactor was designed and fabricated from stainless steel and ceramic. The device consists of four layers performing separate functions: heat source (burner), fuel mixing, heat exchange, and catalytic reforming (Figure 5). The burner plate serves as the heat source for the reactor and the preheater for the fuel and water. The combustion of the fuel and air in the burner generates heat, a portion of which is transferred to the other plates by conductive heat transfer. Another portion of the heat is carried by the exhaust through micro channels generating convective heat transfer.

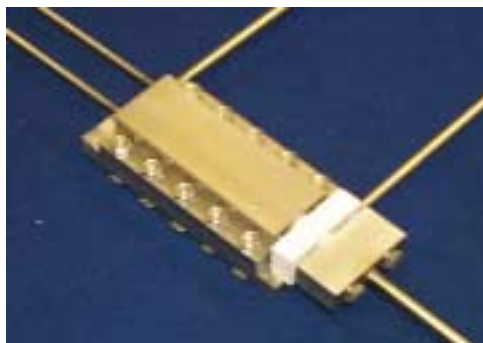


Figure 5. Integrated micro channel fuel reformer and burner 6"x 2.5"x 2".

Both mixing and reactor plates (Fig. 6) have micro channels on top and bottom. This provides advantages in reducing mass and blocking unnecessary heat transfer to other regions. The mixing plate sits directly on top of the burner and the reactor plate is separated from the mixing channel by a thin stainless steel foil and graphite sheet. The top side of the reactor plate is enclosed by the cover plate. The plates and burner are fastened by bolts that prevent leakage but are removable for inspection of components or to install new catalyst.

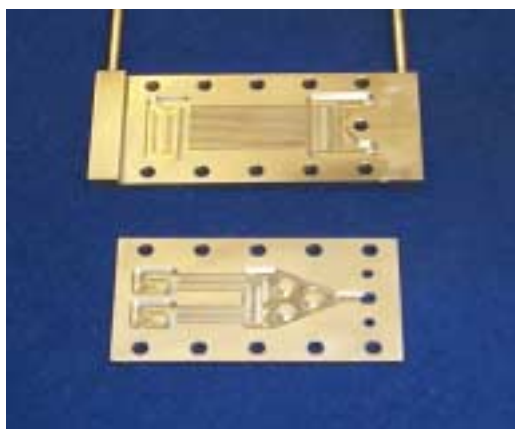


Figure 6. Catalytic reactor (top) and fuel mixer components (bottom).

Tests were conducted with the catalyst packed into the micro-channel reactor that had heat supplied to it by an integrated micro-burner. The burner supplied heat, steam and vaporized fuel

to the micro-channel reactor. A more complex fuel mixture consisting of isooctane, toluene, dodecane, and about 500 ppm sulfur was used to simulate gasoline. Our results for steam reforming indicate that the catalytic micro-reactor produced greater than 70% hydrogen at a constant level for 65 hours (Figure 7).

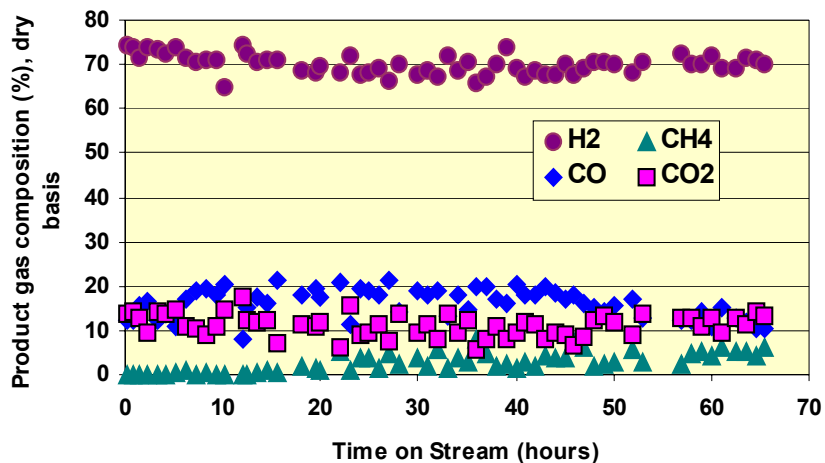


Figure 7. Steam reforming of simulated gasoline with about 500 ppm sulfur using InnovaTek’s proprietary catalyst ITC-2 at 800°C.

Heat Exchange

Counter-flow micro-channel heat exchangers made of 316 SS (Fig. 8) were tested to determine efficiency and effectiveness. Heat exchanger size for a gas flow rate up to 9 LPM is approximately 12.3 x 1.4 x 0.9 cm. Pressure drop at 5 LPM was 0.6 psi. The core volume of the device is approximately 12 cm³.



Figure 8. Micro-channel heat exchanger.

Results indicate that at 400°C heat exchange efficiency was greater than 80% and decreased to about 50% as flow rates were reduced to 2 LPM (Fig. 9). Room temperature (25°C) air was used for the counter-current side for these tests. Micro-channel heat exchangers will be used to maintain optimum temperature conditions for each stage of our fuel processing system (see Fig. 2). Tight temperature control is essential to maintaining maximum chemical conversion and thermal efficiencies in the system.

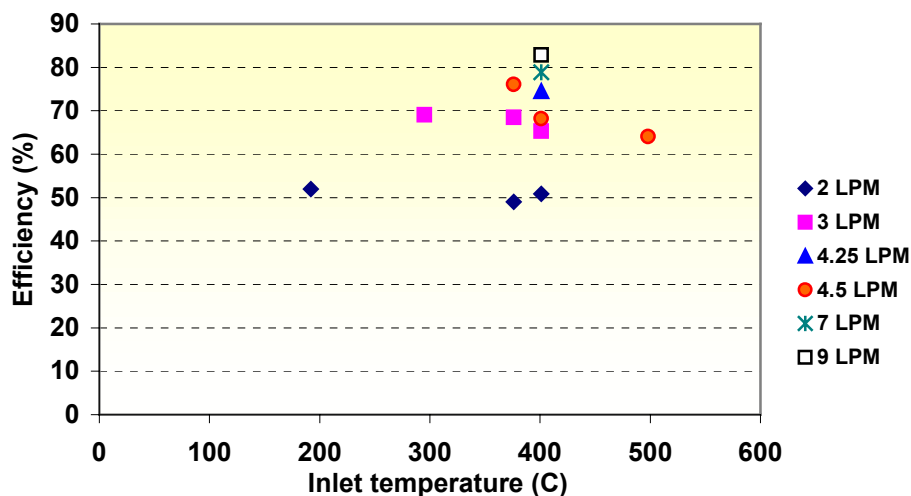


Figure 9. Heat Exchanger Efficiency as a Function of Inlet Temperature (hot side) and Flow Rate.

Hydrogen Separation

An apparatus to test the hydrogen membrane was constructed to measure performance under various temperature and pressure conditions. For simplicity a compressed cylinder of gas containing 65% H₂, 20% CO₂ and 15% CO (simulating our reformat composition) was used as the feed gas for separation tests. The membrane was fabricated on the inner surface of a support structure with 7 mm ID and 22 cm in length, with an effective surface of about 53 cm² and a membrane thickness of about 10 μm. Membrane development is continuing with the goal of further reducing membrane thickness and incorporating a composition that is sulfur tolerant.

Tests were conducted by changing the pressure (P₂) on the feed side of the membrane, while the pressure (P₁) at permeation side was at atmospheric pressure. As the pressure P₂ increases, the hydrogen permeation rate increases (Fig.10). Results are shown for varying pressures and temperatures.

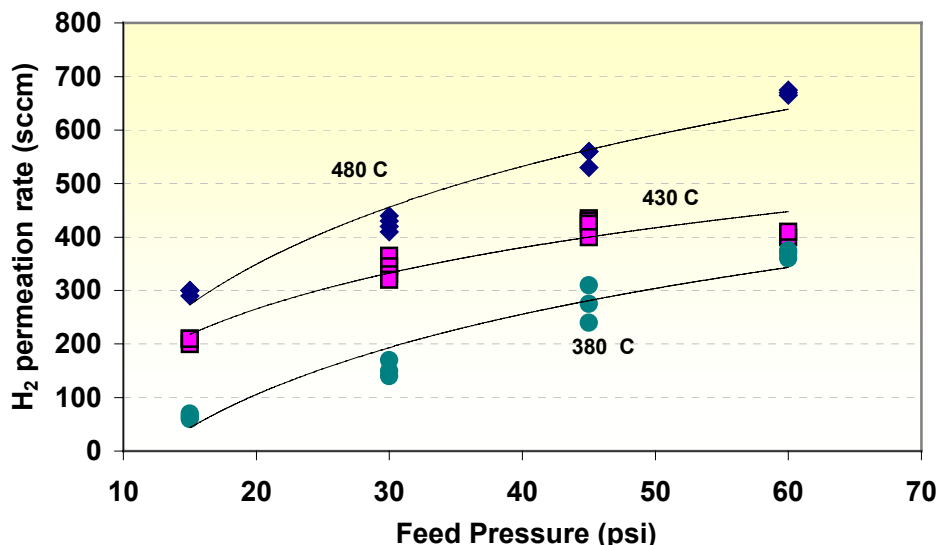


Figure 10. The hydrogen permeation rate vs. pressure of membrane feed gas at different testing temperatures; the pressure at permeate side (pure hydrogen) is atmospheric; the composition of feed gas is 65% H₂, 20% CO₂, and 15% CO.

Composition of the membrane permeate stream (which is the system output) is pure hydrogen with >80% recovery at a temperature of 450°C and pressure of 60 psi (Table 1). The reject gas stream is recycled to the system burner to vaporize fuel and water for the reformer and achieve the temperatures needed for catalytic reforming. This approach creates a very efficient system with little thermal and chemical losses.

Table 1. Composition and Flow Rate in Membrane Stream at 60 psi and 450 °C

Reformate Compound	% Composition Membrane Component		
	Feed	Reject	Permeate
Hydrogen	65	25	100
Carbon Dioxide	20	43	0
Carbon Monoxide	15	32	0
Hydrogen Recovery			82

Future Research

Further research is being conducted to develop additional micro components to optimize system design. These include micro-nozzles for fuel injection to reduce coking in diesel fuel systems and a micro-plasmatron for fast start-up and possible catalyst regeneration. System components will be integrated and tested.

Summary

We have successfully engineered novel micro-technologies in developing a fuel processor that offers the following competitive advantages:

- Reforms multiple fuel types without the need for prior sulfur removal. This greatly expands the market potential to include 1) military logistical fuel and 2) those areas of the world with high sulfur content fuels.
- Produces nearly pure hydrogen output thereby enabling higher fuel cell voltages and power densities with no potential for electrode poisoning.
- Utilizes a steam reforming process that yields higher hydrogen product per volume of fuel consumed.
- Incorporates micro-technology for reactor, heat exchanger, and fuel vaporizer components to improve system efficiency through optimized thermal management and fluid dynamics.

Acknowledgements

This work was funded by the U.S. Department of Energy Hydrogen Program under Contract DE-FC36-99GO. Funding under a complementary program was also received from the U. S. Army Communications-Electronics Command under Contract DAAD05-99-D-7014 DO 0007.

Several collaborators are funded as subcontractors on this project, including Washington State University for catalyst evaluation; the University of Washington for micro-nozzle development; and University collaborators for membrane development. Matching funds were provided by the Washington Technology Center for work performed at the University of Washington.

Papers in Proceedings

Irving, P.M., W. L. Allen, T. Healey, W.J. Thomson, "Catalytic Micro Reactor Systems for Hydrogen Generation", invited presentation at the 5th International Conference on Microreaction Technology, Strasbourg, May 2001.

Patricia M. Irving, W. Lloyd Allen, Quentin Ming, and Todd H. Healey, "The H2GENTTM gasoline/diesel processor for portable fuel cell hydrogen production." In: Proceedings of the 2001 Conference on Small Fuel Cells, April 2001, Washington DC, sponsored by The Knowledge Foundation, Brookline MA.

ITM SYNGAS AND ITM H2

ENGINEERING DEVELOPMENT OF CERAMIC MEMBRANE REACTOR SYSTEMS FOR CONVERTING NATURAL GAS TO HYDROGEN AND SYNTHESIS GAS FOR LIQUID TRANSPORTATION FUELS: DE-FC26-97FT96052

**Paul N. Dyer and Christopher M. Chen
Air Products and Chemicals Inc.
7201 Hamilton Boulevard
Allentown, PA 18195 - 1501**

Abstract

Air Products, in collaboration with the United States Department of Energy (DOE) and other members of the ITM Syngas Team, is developing Ion Transport Membrane (ITM) technology for the generation of hydrogen and synthesis gas. ITMs are ceramic membranes that are non-porous, multi-component metallic oxides. They operate at high temperatures and have exceptionally high oxygen flux and selectivity.

The ITM H2 process is a potential break-through technology that could have a major impact on the cost of distributed hydrogen, especially in the range of 0.1 to 1 MMSCFD. Initial estimates indicate the potential for a significant reduction in the cost of high-pressure hydrogen produced by this new route, compared with the cost of trucked-in liquid hydrogen. A successful development of the ITM technology could be important to emerging hydrogen markets such as hydrogen-based fuel cells for transportation.

The major goals of the ITM Syngas and ITM H2 development program are summarized in this paper, and the progress of the ITM Syngas Team in successfully meeting those goals and objectives is described. The current focus of the program is the construction and commissioning of a nominal 24 MSCFD Process Development Unit (PDU).

Introduction

Hydrogen is an important industrial gas with many existing and future applications. Current production technology is typically through the steam reforming of natural gas or, for lower requirements, the purification of off-gas from, for example, refineries. Purified hydrogen can be liquefied and transported to the point of use and vaporized. This is currently the most economic source for hydrogen when the requirement is modest. For larger supply requirements, for example greater than 1 to 10 MMSCFD, on-site steam reforming is typically more cost effective.

Air Products and Chemicals in collaboration with the DOE and others is developing a potential break-through technology that could have a significant impact on the cost of hydrogen, especially in the range of 0.1 to 1 MMSCFD. If successful, this technology could be important to emerging hydrogen markets such as hydrogen-based fuel cells for transportation [1].

The new technology utilizes non-porous ceramic ITM membranes, fabricated from multi-component metallic oxides that conduct both electrons and oxygen ions at high temperatures (greater than approximately 700°C). In operation, oxygen from a hot air stream is reduced at one surface of the ITM membrane to oxygen ions, which flow through the membrane under a chemical potential gradient. At the opposite surface, the oxygen ions partially oxidize a pre-reformed mixture of hot natural gas and steam to form syngas, a mixture of carbon monoxide and hydrogen. The ratio of hydrogen to carbon monoxide is in part dependent upon the amount of steam. The membrane material must show long-term stability in reducing and oxidizing atmospheres, and long-term compatibility with any oxygen reduction and reforming catalysts that are in contact with its surface.

The ITM H₂ and ITM Syngas technology is being developed in an eight-year, \$90MM development program supported by the DOE. The objective of the program is to research, develop and demonstrate a novel ceramic membrane reactor system for the low-cost conversion of natural gas to synthesis gas and hydrogen for liquid transportation fuels: the ITM Syngas and ITM H₂ processes [2-7].

ITM Syngas/ITM H₂ is a complex new technology whose successful development to a commercial process requires a closely integrated, cooperative team effort. The members of the ITM Syngas Team are shown in Figure 1. Working with Air Products, the team members contribute in all aspects of the development program.

The overall development schedule, from laboratory feasibility studies to commercialization, is aggressive and is illustrated in Figure 2. Phase 2 of the program was initiated in FY2000 and will extend for 3.5 years. The current focus of the program is the construction and commissioning of a nominal 24 MSCFD Process Development Unit (PDU).



Figure 1 – The ITM Syngas Team

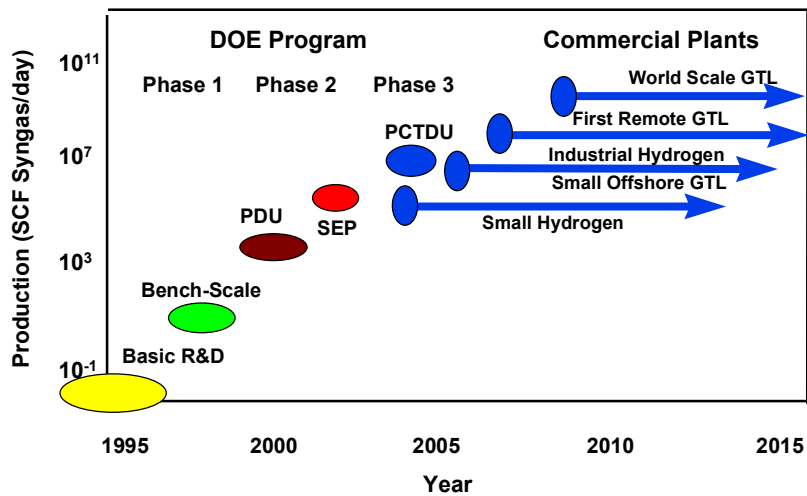


Figure 2 - The Development Schedule for ITM Syngas / ITM H2

Phase 2 - ITM Syngas / ITM H2 PDU and SEP

In Phase 2, the process concepts and performance are being validated in two stages of scale-up: the Process Development Unit (PDU), which will begin operation in 2001, and the Sub-scale Engineering Prototype (SEP), which will begin operation in 2003. An engineering, operating and economic database will be created based on the performance of these two units. The objectives of Phase 2 by Task are as follows:

Task 2.1 Commercial Plant Economic Evaluation

Air Products, Chevron, McDermott and Norsk Hydro will develop advanced ITM Syngas and ITM H2 processes, with input from the University of Alaska. The economics of operation at the commercial plant scale will be evaluated based on the results of the Phase 2 program.

Task 2.2 Materials and Seals Development and Evaluation

Air Products, Eltron Research and Penn State University will obtain laboratory-scale, statistical performance and lifetime data for membrane materials and seals under ITM Syngas and ITM H₂ process conditions, with input from Norsk Hydro, Pacific Northwest National Laboratory and the University of Pennsylvania. Ceramatec will fabricate the ITM membrane/seal samples for testing.

Task 2.3 ITM Syngas Membrane and Module Design and Fabrication

Air Products, Ceramatec and McDermott will design membrane reactors for the ITM Syngas/ITM H₂ processes at the PDU, SEP and commercial scales. Ceramatec will fabricate sub-scale membrane modules for testing in the PDU. Ceramatec will scale up the fabrication of the membrane reactor modules in a Production Development Facility (PDF) to supply the requirements of the SEP.

Task 2.4 Nominal 24 MSCFD ITM Syngas PDU

Air Products will demonstrate the components of the ITM Syngas/ITM H₂ technology in a laboratory PDU. This unit will operate at up to an equivalent of 24 MSCFD of syngas capacity, and will performance test sub-scale planar membranes under commercial process operating conditions.

Task 2.5 Nominal 500 MSCFD ITM Syngas SEP

An SEP unit will be built to demonstrate the ITM Syngas and H₂ technology using full-size membranes in sub-scale modules. The SEP will demonstrate the operation of the ITM Syngas and ITM H₂ processes at up to an equivalent of 500 MSCFD of syngas capacity.

Results

Phase 2 was initiated successfully, and all the milestones through April 2001 were completed on schedule.

Task 2.1 Commercial Plant Economic Evaluation

As reported previously [6], preliminary process design and economic evaluation for ITM H₂ in the “Distributed H₂” target range of 0.1 to 1.0 MMSCFD H₂ indicated the potential for up to 27% savings in production costs compared with trucked-in liquid hydrogen for 5000 psig fuel cell vehicle refueling applications. A nominal capacity of 0.5 MMSCFD H₂ was selected, and the basis for the evaluation followed the “Hydrogen Infrastructure Report” produced by Directed Technologies and Ford for the DOE [1]. The costs of hydrogen compression, storage and dispensing were included in this analysis. In addition, economic evaluation of the preliminary ITM Syngas process confirmed the potential for >33% capital cost savings compared with conventional technology based on an ATR and ASU [8-11].

In an evaluation of advanced process concepts, the ITM H₂ process was scaled up to a large hydrogen production plant with CO₂ removal. The process produced 760 MMSCFD of fuel-grade hydrogen at 100 bar and 14,000 tonne/day of CO₂ at 80 bar for sequestration. For this

application, the ITM H2 process was compared to a conventional oxygen-blown autothermal reformer (ATR) with a cryogenic air separation unit (ASU) to supply oxygen, as shown in Figure 3. Economic evaluation of the ITM H2 process showed the potential for over 30% capital cost savings in the syngas generation process area and over 20% capital cost savings for the overall syngas/H₂/CO₂ production process. The ITM H2 process also has a higher thermal efficiency of 74% compared to 71% for the oxygen-blown ATR process. The capital cost and efficiency advantages for ITM H2 are due to the combination of oxygen separation and high temperature syngas production into a single unit operation and the ability to use low-pressure air as the oxidant source.

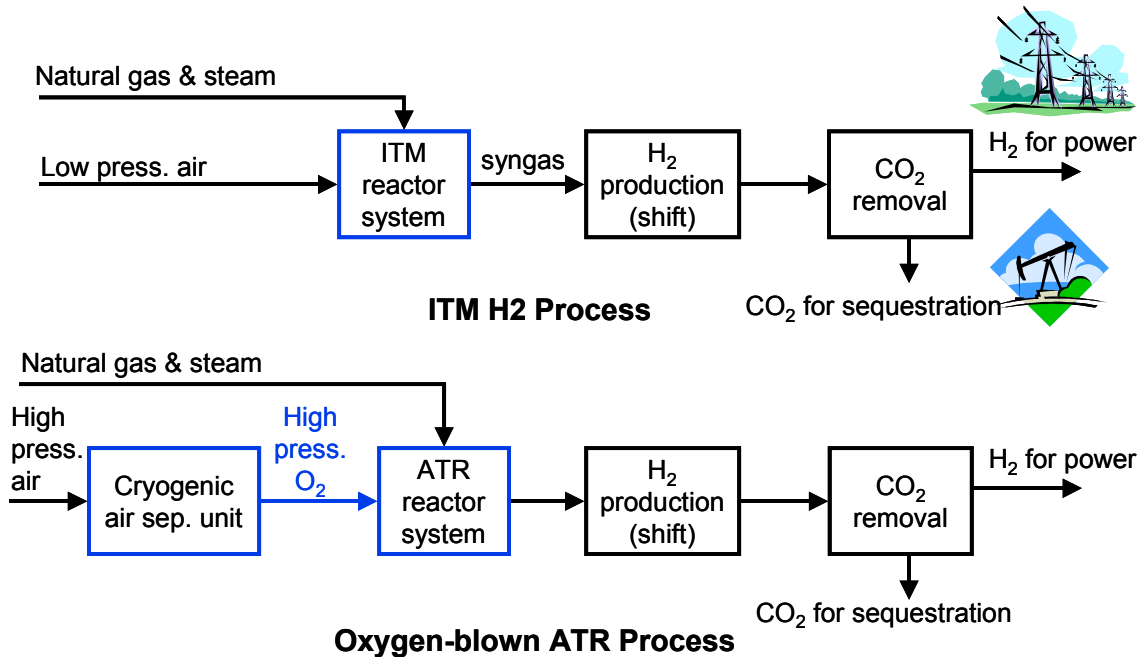


Figure 3 – The ITM H2 Process Compared to Conventional Oxygen-Blown Autothermal Reforming for H₂ Production with CO₂ Removal

Task 2.2 Materials and Seals Development

Air Products and Eltron Research tested tubular membranes and seal assemblies, fabricated by Ceramtec, in high-pressure lab-scale units under ITM Syngas and ITM H2 process conditions. Results of two of these tests are illustrated in Figure 4, which shows oxygen flux measured on the process and air sides of the membrane as a function of time.

In these tests, pre-reformed natural gas mixtures at process pressure were passed over the outer surface of the tubular membrane, while air at atmospheric pressure was fed to the inner surface of the tube. The reaction was monitored by GC analysis of the high-pressure oxidation products and by measuring the oxygen depletion of the exhaust air stream. These tests also evaluated the performance of the seals at high pressure and high temperature. Two tests under continuous ITM H2 conditions at Eltron Research have demonstrated constant oxygen flux for over 4000 hours at 825°C and 250 psig. The results of one of these six-month continuous tests are shown in Figure 4.

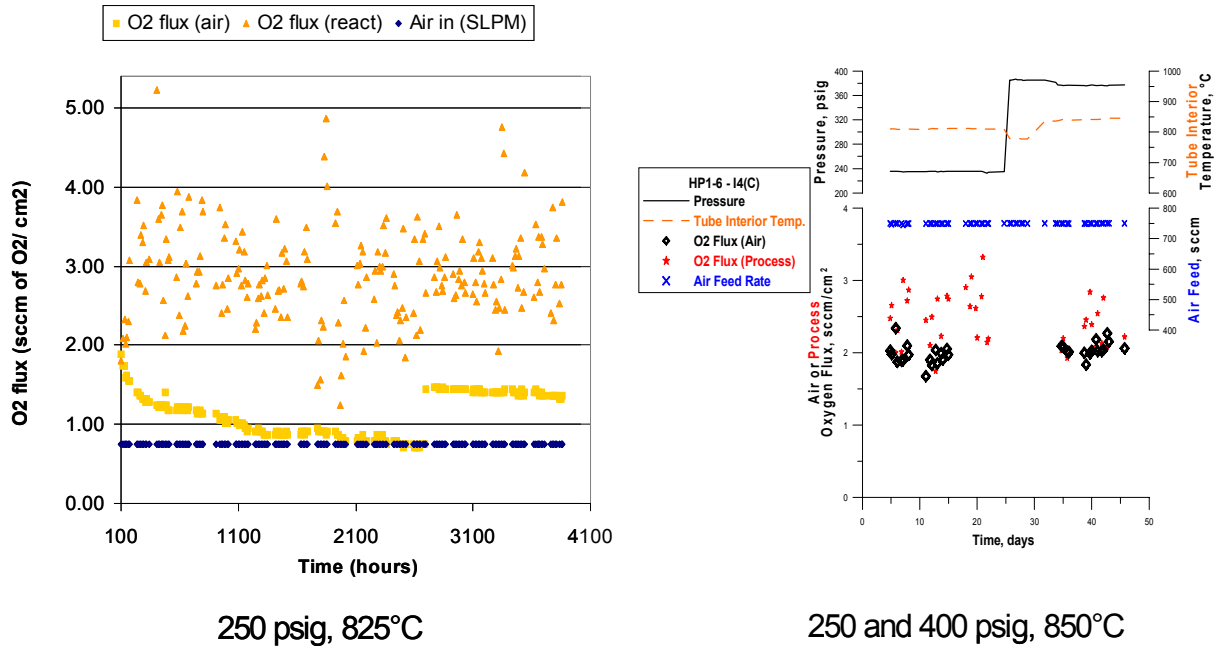


Figure 4 – High Pressure Tests of Tubular Membranes

Eltron Research also tested thin membrane discs, fabricated by Ceramtec, at atmospheric pressure with methane mixtures and air contacted on opposite surfaces of the membrane. Tests were carried out at temperatures around 950°C for periods of up to 1200 hours. Oxygen fluxes in the range 5-10 sccm/cm² were recorded.

A seal assembly was selected for the PDU membrane module, and PDU membrane seal assemblies were fabricated and demonstrated to be leak tight at 425 psi differential pressure and 850°C.

A typical ceramic/metal seal assembly is illustrated in Figure 5, and was developed by Air Products and Ceramtec [12]. A double U-ring assembly is inserted into the annulus formed between a Haynes 230 sleeve and the outer diameter of the ceramic tube. The double U-ring assembly is oriented such that the open section of each U-ring is toward the higher-pressure syngas side. This activates the seal by pressing the side walls of the seal element apart and against the inner and outer surfaces of the annulus. Because each U-ring is compliant, it can accommodate differences in thermal expansion between the Haynes 230 and the tubular I4 membrane without transmitting undue stress.

Task 2.3 ITM Syngas Membrane and Module Design and Fabrication

After extensive thermo-mechanical analysis by McDermott and Ceramatec, a planar sub-scale PDU membrane module design was selected. The advantages of the planar membrane design, compared to the alternative shell-and-tube configuration, include a reduction in the number of ceramic/metal seals per unit active surface area of membrane.

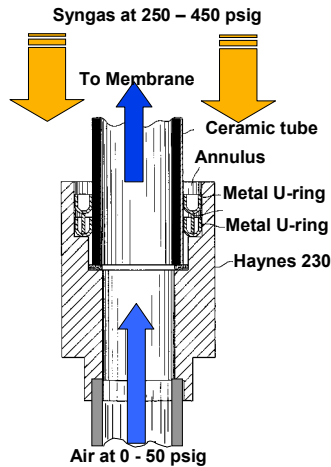


Figure 5 – Ceramic/ Metal Seal Assembly

Ceramatec successfully fabricated complete sub-scale PDU membrane modules. An illustration of the planar membrane module concept is shown in Figure 6 [13]. Air at low pressure is passed through the inner support passages constructed within the planar membrane, while the pre-reformed methane mixture is passed at high pressure over the outer surfaces of the membrane module where partial oxidation takes place to produce syngas.

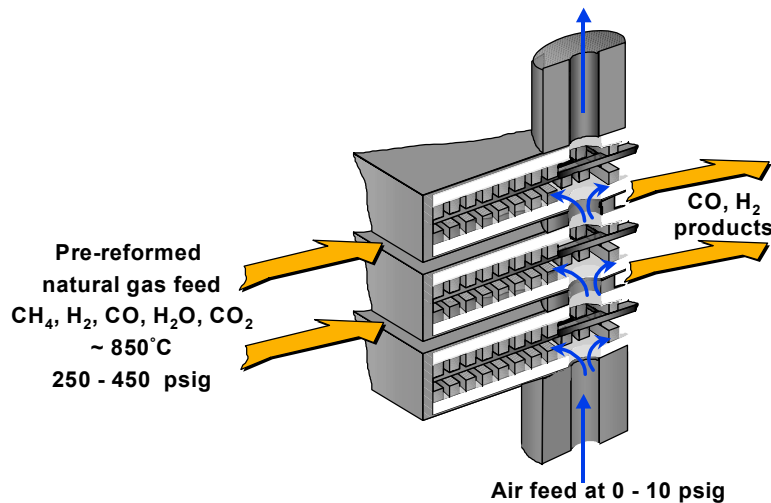


Figure 6 – Conceptual Design for the Planar PDU Membrane Module

Task 2.4 Nominal 24 MSCFD ITM Syngas/ITM H2 PDU

The complete PDU system has been constructed and installed, and is ready for shakedown. The PDU will integrate the various components of the ITM reactor design, and will be used to confirm the performance of the planar membrane modules and seals under commercial process conditions.

The PDU will be able to access the full range of ITM Syngas and ITM H2 process conditions, and will simulate sections of the full-scale non-isothermal ITM Syngas reactor. A process flow diagram of the PDU and an illustration of the reactor vessel are shown in Figure 7. The low-pressure air feed can be blended with additional nitrogen and carbon dioxide to simulate a hot air feed stream produced by partial combustion [8-11].

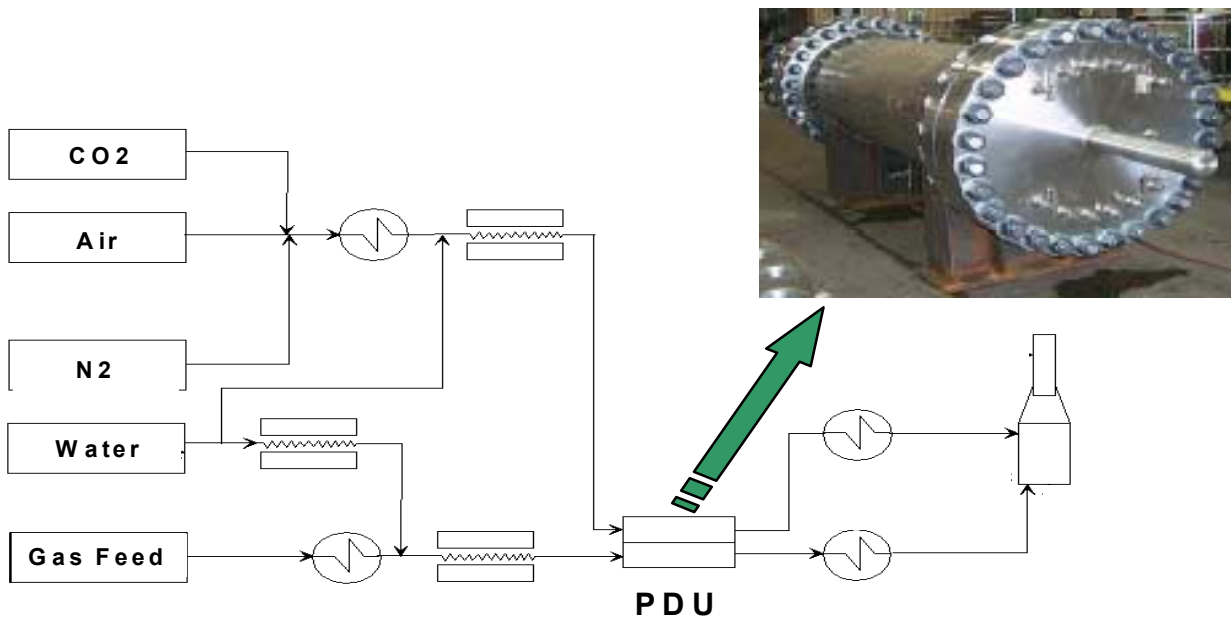


Figure 7 – PDU Process Flow Diagram

Plans for Future Work

The Phase 2 objectives for the next year include the following:

- Completion of more long-term tests of tubular membranes and seals at high pressure
- Demonstration of the performance of sub-scale membrane modules in the PDU
- Evaluation of the ITM H2/ITM Syngas processes using PDU data
- Commissioning the PDF and developing the fabrication of membranes for the SEP
- Design of the SEP reactor and fabrication of the SEP vessel

Conclusions

All of the initial milestones of Phase 2 have been achieved, and the nominal 24 MSCFD PDU has been constructed. Substantial technical hurdles remain to be overcome in the demonstration of the performance of sub-scale membrane modules in the PDU, and in the further scale-up and demonstration planned for the nominal 500 MSCFD SEP.

Technical success will lead to a potential step-change in the costs of distributed hydrogen and syngas required to produce low cost liquid transportation fuels from natural gas. Both of these goals, lower cost distributed hydrogen and lower cost liquid transportation fuels from natural gas are important to the United States economy and energy supply with environmental quality. The collaboration between industry, academia, and the government present in the ITM Syngas/ITM H₂ program is critical for the aggressive development of ITM membranes for these important applications.

References

1. DE-AC02-94CE50389, July 1997, "Hydrogen Infrastructure Report" by Directed Technologies Inc. for The Ford Motor Company and US DOE.
2. P.N. Dyer, R.E. Richards and S.L. Russek, American Ceramic Soc. Ann. Meeting, Indianapolis, April 1999, "ITM Technology for Oxygen Separation and Syngas Production."
3. P.N. Dyer and C.M. Chen, US DOE H₂ R&D Program Review, Denver, May 1999, "Engineering Development of Ceramic Membrane reactor Systems for Converting Natural Gas to H₂ and Syngas for Liquid Transportation Fuels."
4. C.M. Chen and P.N. Dyer, US DOE Alaska GTL Review, Anchorage, May 1999, "Engineering Development of Ceramic Membrane reactor Systems for Converting Natural Gas to H₂ and Syngas for Liquid Transportation Fuels."
5. Solid State Ionics, 134, 21 (2000), P.N. Dyer, R.E. Richards, S.L. Russek and D.M. Taylor, "ITM technology for oxygen separation and syngas production."
6. P.N. Dyer and C.M. Chen, US DOE H₂ R&D Program Review, San Ramon, May 2000, "Engineering Development of Ceramic Membrane Reactor Systems for Converting Natural Gas to Hydrogen and Synthesis Gas for Liquid Transportation Fuels."
7. Gas-to-Liquids Conference, IBC, London, February 2000, P.N. Dyer and C.M. Chen, "ITM Technology for GTL Processing."
8. US Patent 6048472, April 2000, S. Nataraj, R.B. Moore and S.L. Russek, "Production of Synthesis Gas by Mixed Conducting Membranes."

9. US Patent 6077323, June 2000, S. Nataraj, S.L. Russek, "Synthesis gas production by ion transport membranes."
10. US Patent 6110979, August 2000, S. Nataraj, S.L. Russek, "Utilization of synthesis gas produced by mixed conducting membranes."
11. US Patent 6114400, September 2000, P.N. Dyer, S. Nataraj, S.L. Russek, "Syngas production by mixed conducting membranes with integrated conversion into liquid products."
12. European Patent Application 1067320 A2, January 2001, E. Minford, S.W. Rynders, D.M. Taylor, R.E. Tressler.
13. US Patent 5681373, October 1997, D.M. Taylor, J.D. Bright, M.F. Carolan, R.A. Cutler, P.N. Dyer, E. Minford, D.W. Prouse, R.E. Richards, S.L. Russek, M.A. Wilson, "Planar solid state membrane module."

TECHNOECONOMIC FEASIBILITY ANALYSIS OF HYDROGEN PRODUCTION BY INTEGRATED CERAMIC MEMBRANE SYSTEM

**Minish M. Shah and Raymond F. Drnevich
Praxair, Inc.
Tonawanda, NY 14150**

**U. Balachandran, S. E. Dorris, and T. H. Lee
Argonne National Laboratory
Argonne, IL 60439**

Abstract

Praxair, with Argonne National Laboratory as a subcontractor, has initiated a program to develop a small-scale hydrogen production system based on ceramic oxygen transport membrane (OTM) and hydrogen transport membrane (HTM). This system has a potential to significantly reduce the cost of hydrogen for use in the transportation sector for fuel cell vehicle fueling stations and in the industrial sector as a small, on-site hydrogen supply. This paper summarizes the results obtained from a techno-economic feasibility evaluation, as well as the associated HTM performance.

Based on the preliminary economic evaluation, the projected hydrogen cost from a 5,000 scfh plant will be in the range of \$11 to \$14/MMBtu, depending on the number of plants built each year. A significant membrane development program will be required to achieve this cost. To meet the Department of Energy (DOE) target of \$6 to \$8/MMBtu, an additional development program will also be required to reduce the cost of the balance of the plant equipment.

Introduction

Hydrogen is expected to play a vital role in the transportation sector for fuel cell vehicles (FCVs) and in the distributed power generation market for stationary fuel cells. One of the crucial factors for successful introduction of FCVs on U.S. roadways is a low-cost supply of hydrogen. The demand for hydrogen at fueling stations for FCVs is projected to be less than 10,000 scfh. Currently, liquid is the preferred mode of supply for such low-volume requirements. However, the cost of liquid hydrogen is very high at \$29 - \$45/MMBtu depending on volume, location, and length of contract (Chemical Marketing Reporter 2001). To be competitive with cars running on gasoline, the cost of hydrogen delivered to a vehicle must be below \$20/MMBtu. A small on-site plant can eliminate the costs associated with liquefaction and distribution. A key challenge for the on-site plant is to reduce capital costs. The approach taken in this program is to reduce capital costs by reducing the complexity of the process and thus reduce the equipment needed to generate hydrogen.

Praxair has defined a process concept that integrates various processing steps in a single reactor. A schematic diagram of the integrated-membrane reactor separator is shown in Figure 1. The reactor is divided into three compartments by integrating both OTM and HTM into a single unit.

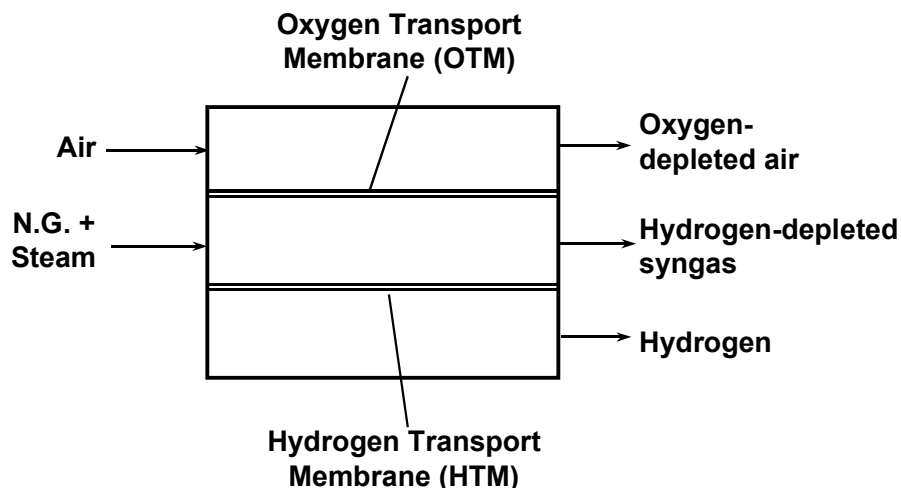
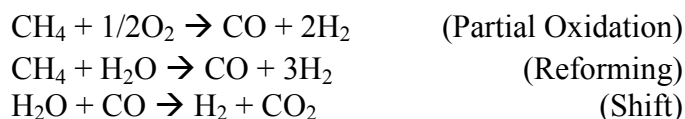


Figure 1. Integrated Membrane Reactor Separator

Air at low pressure (~25 psia) is passed to the retentate side of the OTM and compressed natural gas (200 - 300 psia) and water/steam are passed to the permeate side of the OTM. Oxygen is transported across the OTM to the permeate side, where it reacts with natural gas to form syngas. A portion of natural gas also reacts with steam to form syngas. Additional hydrogen is formed by the water-gas shift reaction:



A catalyst is incorporated in the reactor to promote the reactions. The syngas is also exposed to the retentate side of the HTM. Hydrogen is transported to the permeate side of the HTM by the partial pressure difference driving force. Due to removal of hydrogen from the reaction zone, more hydrogen is formed by the reforming and shift reactions.

As much hydrogen as possible is recovered from the reaction zone by transport through the HTM to the permeate side. Eventually, a partial pressure pinch between the reaction zone and the permeate side is reached, limiting the amount of hydrogen that can be recovered.

Technical Feasibility Analysis

Product Slate

A small volume of hydrogen is required by customers in the fats and oils, float glass, utilities, chemicals, electronics, and metals industries. A majority of these customers are supplied with liquid hydrogen. However, most of them need hydrogen in gaseous form. Therefore, significant number of opportunities are available, if a small on-site plant can supply hydrogen to these customers at a cost that is lower than the cost of liquid.

In the transportation sector, fueling facilities for FCVs will require small on-site hydrogen plants. A typical gas station fuels 200 cars per day or supports 1800 cars over a nine-day refilling cycle for a typical passenger car. A small plant producing 1000-5000 scfh of hydrogen will be able to refuel 11-55 cars per day (or support 100-500 cars over a complete refueling cycle). For the average gas station, this range will represent 5-25% of the total automotive traffic.

Most of the industrial customers require a minimum purity of 99.99%. For a hydrogen FCV, CO can be detrimental to the fuel cell. Although other impurities do not poison the fuel cell, overall hydrogen purity must be high so the fuel cell can be operated at a high hydrogen utilization rate. Therefore, an overall purity of about 99%, with less than 10 ppm CO, is acceptable for fuel cell applications.

The pressure requirements for majority of industrial customers is below 200 psia. In the transportation sector, the required pressure will depend on whether hydrogen is stored as high-pressure gas or as a low-pressure alternative such as a metal hydride. For on-board storage of 5,000 psia of hydrogen, a fueling station may have to store hydrogen at ~7,500 psia for quick filling.

The present analysis is limited to hydrogen production at the pressure attained from the membrane reactor, 15 psia. Three production capacities were selected for economic feasibility analysis: 1,000, 2,000, and 5,000 scfh.

Process and System Design

Various process options, based on the integrated OTM-HTM reactor, separate OTM and HTM reactors, and an air POX reactor integrated with a HTM were reviewed. Based on the

preliminary assessment, the process with integrated OTM-HTM reactor was selected because of its potential for compact plant design and high efficiency. Based on an initial feasibility assessment, it was determined that there are no technical issues that will prevent the development of the integrated OTM-HTM reactor. A process model was developed for an integrated OTM-HTM reactor. The production capacity of 1,000 scfh of hydrogen was used for performance assessment.

A flowsheet for a process based on the integrated OTM-HTM reactor was developed. The pressure on the reaction side was selected to be 250 psia and the pressure on the permeate side was selected to be 20 psia. Heat and mass balances were established. The following simplifying assumptions were made:

- Plug flow exists in various compartments of the reactor (i.e., no radial concentration gradients)
- There were no heat transfer limitation

A kinetic model from the literature was used for the reforming and shift reactions (Xu 1989). Average oxygen flux was assumed for the OTM, based on the values reported in the literature (Shao 2001). For the HTM, a partial pressure pinch of 5 psi was used, i.e., hydrogen partial pressure in the reaction zone is always 5 psi higher than the pressure on the permeate side. Based on initial flux data, it was determined that the average flux through the HTM under the reactor operating conditions would be 1.5 cm³/cm²/min.

The overall efficiency of the plant is defined as follows:

$$\text{H}_2 \text{ Efficiency} = \frac{\text{Energy Recovered in H}_2 \text{ (HHV)} \times 100}{\text{Energy Input in Natural Gas (HHV)}}$$

Based on this definition, the H₂ efficiency of the process is 75.8% (HHV or higher heating value). In comparison, large steam methane reforming (SMR) plants achieve 68% H₂ efficiency (HHV). Including the energy recovered in exported steam, large SMR plants achieve overall thermal efficiency of 80 – 85%, depending on the scale of production. In the case of the OTM-HTM process, there is no steam export. Therefore, the overall thermal efficiency is the same as the H₂ efficiency. The main reason for the lower efficiency of the OTM-HTM process is higher heat losses from the small reactor on a percentage basis. Another reason for the high efficiency of large-scale SMR plants is co-production of steam for export. Table 1 summarizes utility consumption.

Table 1. Consumption of Utilities

Hydrogen capacity, scfh	1,000
N.G., scfh	424
Power, kW	4.6
Water, gpm	1.1
H ₂ Efficiency, %(HHV)	75.8 %

Feasibility Assessment

The feasibility assessment was carried out to identify the technical issues and to determine if any technical issues will prevent the integration of OTM and HTM into one reactor. The assessment was based on the current knowledge of OTM and HTM performance characteristics. The progress made to date in Praxair's syngas alliance program indicates that all of the components associated with the OTM reactor will be available before this program is completed. Detailed design of the OTM-HTM reactor was prepared and important design issues were assessed. The issues that require further development to improve economics were defined in this phase and they form the basis for the development needs of the next phase.

The HTM is the critical undeveloped component. Based on discussions with Argonne National Laboratory (ANL) and the work performed by others developing hydrogen membranes, we anticipate that a cost-effective HTM can be developed. The following issues have been assessed in this phase of the program.

Operating Temperature

For the integrated OTM-HTM reactor, the operating temperature should be such that both OTM and HTM can provide high flux. The work done so far indicates that the preferred temperature for the HTM is between 500 and 900°C and flux is found to increase with temperature up to 900°C. Based on previous work done at Praxair, the OTM can operate at temperatures between 850°C and 1100°C. Since it is feasible to operate both the OTM and the HTM in the temperature range of 850 - 900°C, the actual operating temperature will be fixed by economic optimization. For current analysis, the operating temperature of 900°C was selected.

Membrane Selectivity

It is known that some proton conductors exhibit oxygen permeation in addition to hydrogen. This phenomenon can result in loss of hydrogen. In the reaction zone, there is oxygen activity due to presence of H₂O, CO and CO₂. The decomposition of any of these compounds on the HTM's surface can produce oxygen ions, which can pass through the HTM and react with hydrogen on the permeate side to produce steam. In the experiments carried out by ANL so far, there is no evidence of moisture in the permeate, which indicates there is no oxygen transport across the HTM.

Effect of Syngas Components on HTM

Some of the ceramic membrane materials decompose in the presence of CO₂ and H₂O. Initial tests conducted at ANL in the presence of simulated syngas mixtures indicate that the ceramic material used in this CRADA (cooperative research and development agreement) decomposes in the presence of a large concentration (30%) of CO₂. Finding suitable membrane material that can survive in the syngas environment will be a critical element of the future development program. The research at ANL shows that it is feasible to develop such materials.

Other technical issues for using ceramic membranes are identified below. The work done so far lead to the conclusion that these issues can be adequately addressed by further development. The next phases of the development program will begin addressing the issues of operating pressure, compatibility of catalysts with the OTM and the HTM, long-term stability and reliability, seals, diffusion limitation, heat transfer, reactor design, and tolerance to thermal cycling.

Experimental Studies for HTM

The ANL-2 membrane (the ANL's proprietary material) was used throughout this study. This membrane consists of a proton-conducting material (yttrium-doped BaCeO₃) with metal additive to provide high electronic conductivity and enhance the hydrogen flux. The membrane disks, with varying thickness (200 - 1200 microns), were prepared by conventional ceramic pressing, sintering, and polishing.

Hydrogen Flux

The experiments were carried out to study the effects of hydrogen partial pressure, membrane thickness, and temperature. Gas mixtures consisting of hydrogen and helium were used as feed gases. Both dry as well as wet (containing 3% moisture) feed mixtures were used. The presence of moisture was found to enhance the hydrogen flux by 30 to 50%. Since the syngas mixture in the reactor will contain steam, only experimental results with wet feed mixtures are presented below.

Effect of Hydrogen Partial Pressure

The hydrogen flux through purely mixed conducting ceramic membranes is reported to be proportional to $\ln(p_2/p_1)$, where p_2 and p_1 are partial pressures of hydrogen on feed and permeate sides, respectively. Initial experiments were planned to see if ANL-2 exhibits flux characteristics that are similar to those of other proton conductors. Two sets of experiments (with 1 and 4% hydrogen in the feed) were carried out by varying sweep gas flow to achieve different p_2/p_1 ratios. When flux was plotted against $\ln(p_2/p_1)$, the results were not conclusive. Due to low hydrogen concentration in the feed, absolute flux values were also low, and the likelihood of measurement error was high. Therefore, another set of experiments was conducted at 900°C using ~0.45mm thick membrane with the hydrogen concentration in the feed from 1 to 100%. The hydrogen concentration in the permeate was kept below 1%. The results from these experiments clearly demonstrated that for the ANL-2 membrane, flux was not proportional to $\ln(p_2/p_1)$. It was found that the hydrogen flux is proportional to $(p_2^n - p_1^n)$ (Figure 2). This type of correlation is observed for metal membranes, where a solution diffusion mechanism is responsible for hydrogen transport. It appears that the metal additive in the ANL-2 membrane is a major contributor to the observed hydrogen flux.

Effect of Temperature and Membrane Thickness

The flux measurements were made at temperatures between 600 and 900°C and for membrane thickness between 0.28 and 1.2 mm. Hydrogen concentration in the feed gas was held constant at 77.6% (with 3% moisture and balance being helium). The sweep gas on the permeate side

was nitrogen with 92 ppm hydrogen in it. The sweep flow was adjusted to achieve constant hydrogen concentration (~0.8%) in the permeate. Figure 3 shows the results from this study.

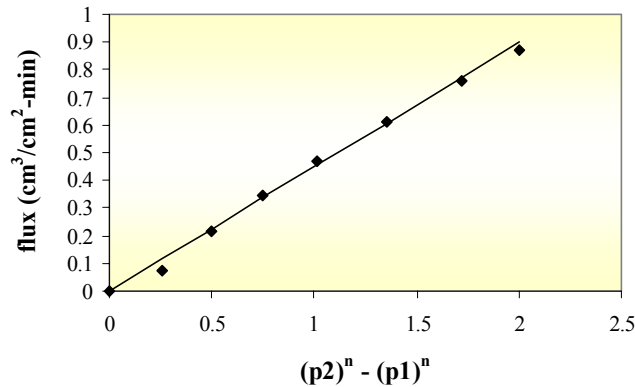


Figure 2. Effect of Hydrogen Partial Pressure on Flux

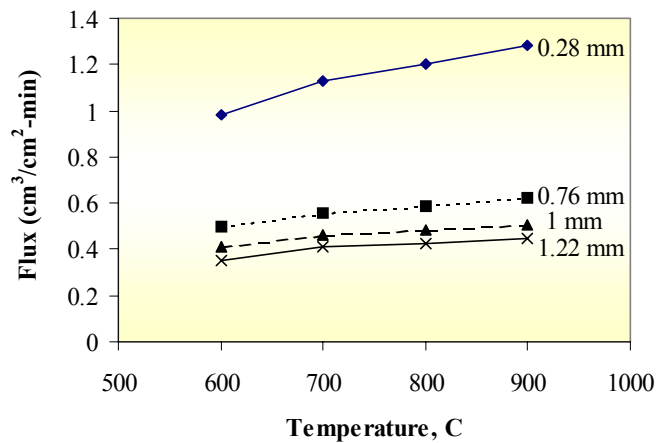


Figure 3. Effect of Temperature on Flux through Membranes of Various Thickness

The flux was found to increase only slightly with temperature. Again, this behavior is more typical of a metal membrane than of a proton conductor. This finding further strengthens the supposition that the metal additive in ANL-2 is the major factor that affects hydrogen transport, and that the contribution from the proton conductor is small.

As membrane thickness decreases the resistance due to bulk transport decreases. However, other mass transport resistances, such as diffusion through the boundary layer and surface exchange reactions, remain constant. It has been reported in the literature that for very thin membranes, surface exchange reactions exerts a dominant effect on flux. To gauge the magnitude of these resistances, $1/\text{flux}$ vs. thickness was plotted (Figure 4).

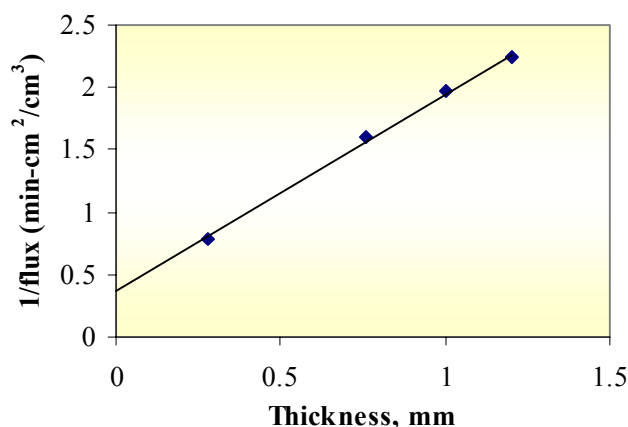


Figure 4. Plot of 1/flux vs. membrane thickness

The intercept on the y-axis represents other mass transport resistances. Thus, for a hypothetical thickness of zero, the limiting flux for a given set of process conditions is $\sim 2.5 \text{ cm}^3/\text{cm}^2/\text{min}$. Based on these results, a flux equation was proposed to predict flux in the reactor and to estimate the membrane area in the reactor. The average flux in the reactor was estimated to be $1.5 \text{ cm}^3/\text{cm}^2/\text{min}$. A preliminary cost estimate indicated that the reactor cost will be more than 75% of the total equipment costs. A literature review indicates that flux as high as $40 \text{ cm}^3/\text{cm}^2/\text{min}$ is reported with certain composite metal membranes (Peachey 1998). Consequently, the process economics were developed based on the fluxes that are expected to be achieved as opposed to the fluxes that were measured in this program.

Flux with Syngas Mixtures

The results of experiments with syngas mixtures are shown in Figure 5. Three syngas compositions were tested. These compositions represent conditions at the entrance and exit of different reactor configurations. Solid lines on the graph are values predicted by the flux equation and the markers are measured flux values. For Mixtures 1 and 2, the flux remained steady for the duration of the test (4 to 6 hours). Also, the predicted values agreed well with experimental values. With Mixture 3, which represented conditions at the exit of the reactor, the flux values declined rapidly. Mixture 3 contained 30% CO_2 (by vol.) and a high level of CO_2 may have caused degradation of the membrane surface.

Economic Feasibility Analysis

A process that uses the integrated OTM-HTM reactor was selected for the economic analysis. For the transportation sector, a production capacity of 1,000 scfh will be desirable. The demand in the industrial sector varies widely between 200 and 35,000 scfh (Heydorn 1998). Plants with the production rates in the range between 1,000 and 5,000 scfh could serve majority of customers in this sector. The hydrogen plant capacity was fixed at 1,000 scfh for the cost estimation. The capital costs for 2,000 and 5,000 scfh were estimated by using appropriate scale-up factors. For each capacity, costs were estimated for 10, 100, and 1,000 plants built/year. The product costs

were estimated and compared with two competing supply options: liquid hydrogen and electrolysis. Market projections were made for the industrial and transportation sectors. Estimation of preliminary development costs and a business case analysis will be performed by May 2001.

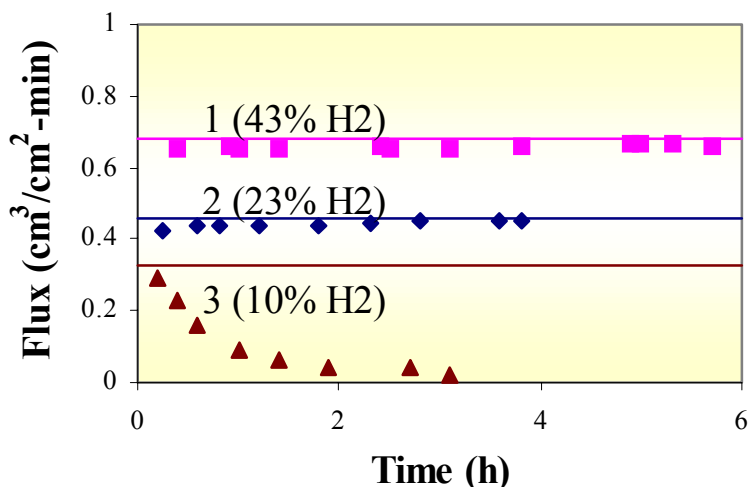


Figure 5. Hydrogen Flux with Syngas Mixtures

Overall Product Costs

The cost to manufacture the membrane reactor was developed based on the reactor design and costing techniques for similar systems under development at Praxair. The cost of the balance of the plant equipment (natural gas compressor, water treatment system, air compressor, heat exchangers, steam generator, and desulfurization unit) was based on purchasing major components from qualified suppliers. The quotes were obtained for multiple-unit purchases (in quantities of 10, 100 and 1,000) when available. Where quantity discount data were unavailable, reasonable cost reduction was assumed based on our experience. A P&ID (process and instrumentation diagram) was developed for controls and instrumentation that are necessary for safe operation, safe startup, and shutdown procedures. The cost of control valves and instruments were estimated based on volume pricing available to Praxair.

A three-dimensional plant layout, with details of piping, skids, and assembly was developed. Based on this layout, the cost of complete assembly was developed including the costs of piping, insulation, equipment, and instrument mounts, electrical, and metal enclosure. Finally, the costs of engineering and design, shipping, installation, and startup costs were estimated. All of these costs were included in the estimate of total capital investment.

The product costs were estimated by adding annual operating, M&R (maintenance and replacement), and capital recovery costs. To estimate capital recovery costs, the method

described in the Hydrogen Infrastructure Report (Thomas 1997) was used. The report has suggested the financial parameters listed in Table 2.

Table 2. Financial Parameters

10% after-tax rate of return
26% corporate tax rate
15-year plant life
2.7% inflation rate

These parameters lead to capital-related charges of 18.5% of capital investment/year. In addition, the assumptions listed in Table 3 were made.

Table 3. Cost Estimation Assumptions

Natural gas	\$3/MMBtu (HHV)
Power	\$0.05/kWh
Water	\$0.1/1000 gal.
M & R	3% of capital investment/year
Capacity Utilization	80%

Figures 6 and 7 show capital and product costs for various cases. As seen from Figure 7, a significant reduction in capital costs will be required to achieve the DOE target of \$8/MMBtu. At 1,000 scfh, it is highly unlikely that we can achieve the necessary cost reduction. At a 5,000 scfh capacity and a production rate of 100-1000 units per year, a capital cost reduction of 50-65% will be required. To achieve this level of cost reduction, the flux target will have to be set at a much higher level than the value assumed for the cost estimation. However, improvement in membrane performance alone will not be sufficient to achieve a 50-65% reduction in total capital. Thus, a development program that focuses on reducing the cost of the balance of the plant and assembly costs will be required in addition to membrane reactor development. We are currently assessing the potential impact of cost reduction areas to estimate the probability of meeting the DOE targets.

The projected costs of hydrogen from OTM/HTM technology are lower than the costs of liquid hydrogen and electrolytically produced hydrogen. Liquid hydrogen costs \$30-\$45/MMBtu, depending on the consumed volume, location and contract length (Chemical Marketing Reporter 2001). The projected capital and M&R costs for mass produced electrolysis equipment (Thomas 1997) and power costs assumed in this study results in the cost of electrolytically produced hydrogen to be \$25/MMBtu for a 5,000 scfh plant.

Market Assessment

The potential market in the industrial sector was assessed based on Praxair's internal information and based on the SRI report (Heydorn 1998). According to the SRI report, 19 billion scf of hydrogen was used as gas by small-volume customers in 1996. These customers are currently supplied by liquid hydrogen and they represent conversion opportunities for on-site plants. It

was assumed that a fraction of the liquid volume will be replaced by on-site plants and that additional customers currently served by ammonia dissociation and electrolysis will also become available for on-site OTM/HTM plants. Furthermore, an average long-term growth rate of 3% was assumed for the small-scale industrial market. Based on these assumptions it was estimated that Praxair will have the opportunity to build 15-50 plants per year, depending on the plant size that is manufactured.

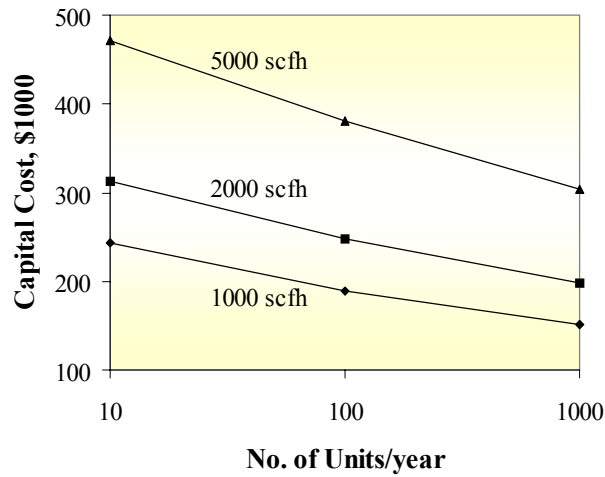


Figure 6. Capital Costs at Various Production Capacities

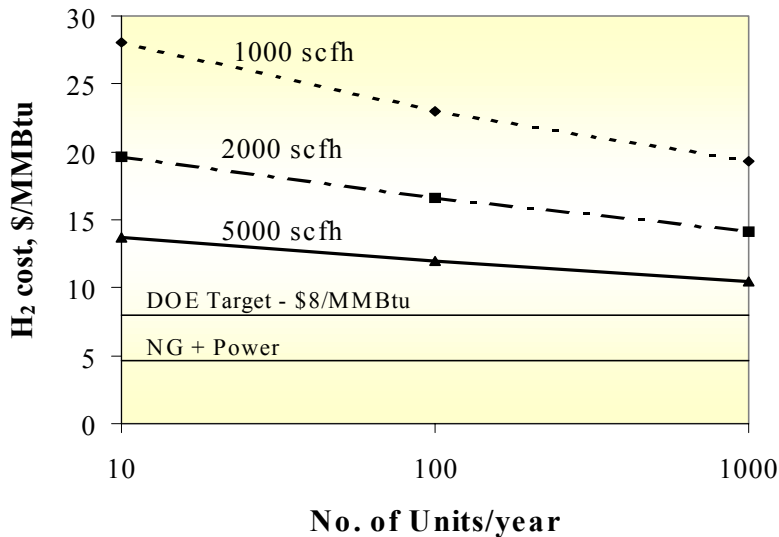


Figure 7. Hydrogen Costs at Various Production Capacities

The estimation for passenger cars powered by fuel cells was based on a modification of the California Air Resources Board (CARB) mandate released in January 2001 on their web site (CARB 2001) for zero emission vehicles (ZEVs). Table 4 lists the assumptions that were made for passenger cars.

Table 4. Assumptions for Fuel Cell Cars Market

No. of cars sold in California in 2003	1.5MM	
Percentage share of large/intermediate volume manufacturer	65%	
Annual car sales growth	1.5%	
Average H ₂ consumption by car (this implies 12000 miles driven/yr and 65 mpgge (miles per gallon of gasoline equivalent) efficiency (HHV) or 5.84 scf H ₂ /mile)	8 scfh	
Market Parameters for Fuel Cell Cars:	Conservative	Optimistic
ZEVs as % of total vehicles sold by large/intermediate manufacturer in 2003	0.5%	0.5%
ZEVs as % of total vehicles sold by large/intermediate manufacturer in 2020	5%	10%
% of ZEVs that are based on H ₂ fuel cells in 2003	10%	10%
% of ZEVs that are based on H ₂ fuel cells in 2020	80%	100%
Ratio of no. of new H ₂ FCVs in US/California in 2003	1	1
Ratio of no. of new H ₂ FCVs in US/California in 2020	5	10

Figure 8 shows the potential number of hydrogen fuel cell cars to be sold in the U.S. per year, based on the optimistic scenario. New hydrogen production capacity required every year was estimated based on the total FCVs (cars only) sold every year and the assumptions for hydrogen mileage and miles driven per year listed in Table 4. With the assumption of 80% capacity utilization, the number of hydrogen plants required at the three capacities (1,000, 2,000, or 5,000 scfh) was estimated. If all plants have a 1,000-scfh capacity, more gas stations can be equipped with a hydrogen supply than with a 5,000-scfh plant. Figure 9 shows the projected percent of gas stations that will be equipped with a hydrogen supply for the optimistic scenario.

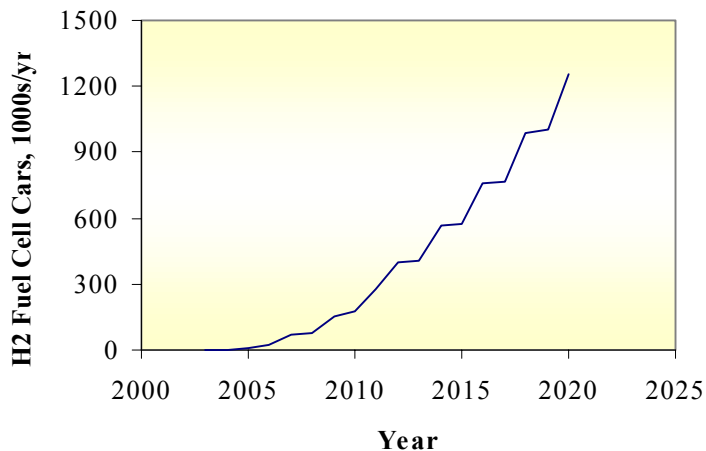


Figure 8. Optimistic Projections for Hydrogen Fuel Cell Cars in the U.S.

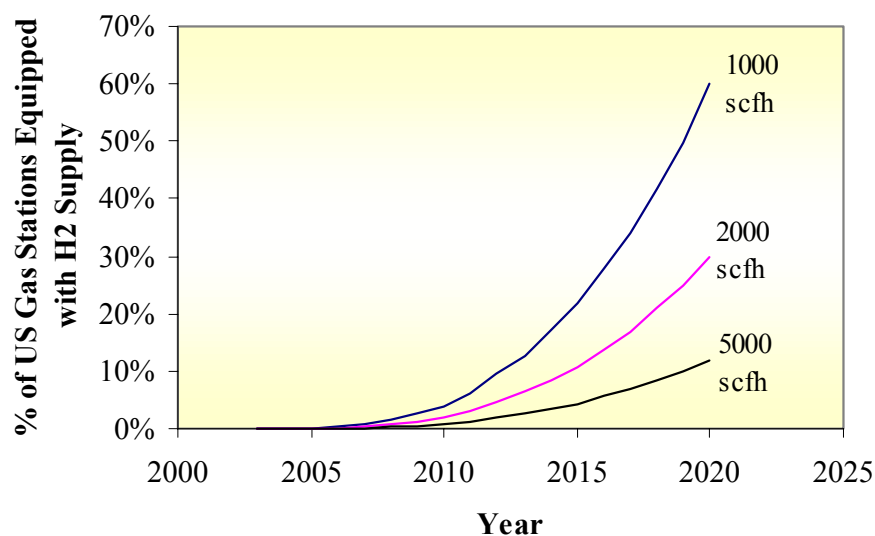


Figure 9. Gas Stations Equipped with Hydrogen Supply at the Three Plant Capacities for Optimistic Projections

Based on the economic analysis, the 5,000-scfh plant has the best chance to offer low-cost hydrogen. However, if gas stations are equipped with 5,000-scfh plants, the percentage of gas stations with hydrogen fueling capabilities will reach only 12% according to optimistic scenario. The larger plants will also likely experience lower utilization, which will drive up the cost of hydrogen. The average consumer would ideally like to see 1/2-2/3 of the gas stations with a hydrogen supply. Smaller plants (such as 1000-scfh) will result in a higher percentage of gas stations with hydrogen fueling capabilities, but the cost of hydrogen from these stations will be high. Thus, there are significant challenges that must be met if the transportation sector market is to materialize. A more aggressive conversion to FCVs may be necessary to satisfy the need of the consumers to reduce the cost of the vehicle and the fuel and increase fuel availability.

Conclusions

Integration of the OTM and the HTM in one reactor is technically feasible. The process based on the integrated reactor will be able to achieve an efficiency that is comparable to the conventional steam methane reformer process. The projected hydrogen costs are lower than the competing supply options, such as electrolysis and liquid hydrogen. Current projections indicate that to achieve an \$8/MMBtu target, the capital cost must be reduced by 50-65%. A multi-pronged development program will be required to achieve such cost reductions. The primary focus will be to develop a low-cost membrane with high hydrogen flux and tolerance for syngas components. Additional efforts must be directed toward reducing the balance of the plant costs.

Acknowledgments

Part of the work at Praxair was supported by the U.S. Department of Energy (DOE) under contract number DE-FC36-00GO10534. The work at Argonne was supported by DOE, Office of Energy Efficiency and Renewable Energy, under contract W-31-109-Eng-38.

References

- California Air Resources Board (CARB) 2001.
<http://www.arb.ca.gov/msprog/zevprog/2001rule/propmods.pdf>
- Chemical Marketing Reporter, January 29, 2001, p. 37.
- Heydorn, B. and Zuanich, J. 1998. Market Assessment Small Scale Hydrogen Generation, prepared by SRI Consulting for Gas Research Institute, GRI-97/0395.
- Peachey, N. M., Dye, R. C., Snow, R. C., and Birdsell, S. A. 1998. "Composite Metal Membrane", U.S. Patent 5,738,708.
- Shao, Z., Dong, H., Xiong, G, Cong, Y., and Yang, W. 2001. "Performance of a Mixed-Conducting Ceramic Membrane Reactor with High Oxygen Permeability for Methane Conversion," J. of Membrane Science, 183:181-192.
- Thomas, C. E., James, B. D., Kuhn, I. F. Jr., Lomax, F. D., and Baum, G. N. 1997. Hydrogen Infrastructure Report, DOE Report No. 47-2-R31148.
- Xu, J. and Froment, G. F. 1989. "Methane Steam Reforming, Methanation and Water-Gas Shift: I. Intrinsic Kinetics," AIChE Journal, 35(1):88-95.

PRODUCTION OF HYDROBROMIC ACID FROM BROMINE AND METHANE FOR HYDROGEN PRODUCTION

**R. W. Bradshaw
Materials Chemistry Dept. 8722**

**R. S. Larson
Chemical & Materials Process Modeling Dept. 8728**

**Sandia National Laboratories
Livermore, CA
94551-0969**

Abstract

A cooperative program between Sandia National Laboratories (SNL) and the SRT Group was recently begun to advance the development of a chemical process to produce hydrobromic acid from bromine and methane. The purpose of the SNL program is to provide fundamental reaction kinetics information that will constitute the basis for system engineering by SRT. The SNL activities consist of computational chemistry and laboratory experimentation. Preliminary calculations of chemical equilibrium behavior and reaction kinetics were performed using the CHEMKIN computer program and its associated thermodynamic and kinetic databases. Calculations were performed for reactions involving the bromine-methane and bromine-methane-steam systems. The equilibrium conversion of bromine to HBr in the two processes is excellent, especially at temperatures below 900K. If equilibrium is achieved in the bromine-methane process, then the other principal product is solid carbon in some form, e.g., coke or soot. If solid carbon is not produced, then the reactor effluent may contain significant amounts of brominated hydrocarbons. From a purely thermodynamic point of view, the bromine-methane-steam process appears to be more attractive because the carbon in methane is converted almost completely into carbon dioxide.

Introduction

A hydrogen production process that requires the formation of hydrobromic acid as one of the primary steps has been proposed by the SRT Group, Inc., Miami, FL. SRT has described the process and preliminary development studies in detail elsewhere, so only the basic features are given here [Schleif 1997, SRT Group 1998]. The initial step in the process is the formation of hydrobromic acid from bromine and a hydrocarbon, e.g., methane. This reaction is conducted at elevated temperature, as high as 800°C. An alternative reaction scheme includes steam among the reactants to convert the carbon in the feedstock to carbon dioxide rather than solid carbon. The HBr generated in the reactor is collected with water to produce a concentrated solution of HBr that is electrolyzed in a separate process step, yielding hydrogen and bromine. The latter constituent is recycled to the reactor to perpetuate the HBr production cycle. The hydrogen is available for generating energy by various means. Alternatively, both constituents may be used to produce electrical power via a regenerative hydrogen-bromine fuel cell of a proprietary design.

A cooperative program between Sandia National Laboratories (SNL) and the SRT Group was recently begun to advance the development of the chemical process to produce hydrobromic acid. The purpose of the SNL participation is to determine fundamental reaction rate equations that will constitute the basis for reactor engineering by SRT. The SNL work consists of several activities. The primary SNL activity in the initial phase of this project is to employ computer modeling of chemical reaction kinetics to determine the reaction rate equations. Computation will be used to evaluate the equilibria of the various reactions studied in order to predict the extent of the desired reaction and the formation of by-products. Another activity is to conduct laboratory experiments to determine the fundamental characteristics of a number of chemical reactions that produce hydrobromic acid from hydrocarbon precursors.

Calculations of both chemical equilibrium behavior and reaction kinetics are required to interpret the laboratory reactor data. These calculations will be performed using the CHEMKIN computer program and its associated thermodynamic and kinetic databases. Additional information may need to be input to complete the database for computations. The results of the laboratory experiments will be compared with the predictions of the computations to refine the reaction rate equations. The equilibrium calculations will enable the experimental apparatus to be designed with full regard for all of the reaction products that may be formed. Such calculations also provide useful information regarding the energetics of the reactions which is useful for engineering design.

This report summarizes the status of the Sandia National Laboratories segment of this project during the startup period of February 2001 through April 2001. The planned future work is also discussed.

Computational Chemistry of Bromine-Methane Reactions

This section summarizes the calculations that have been carried out to determine the feasibility of producing hydrogen bromide from bromine, methane, and (optionally) steam. As is customary in such investigations, the process is first examined from a thermodynamic point of view to determine if it is viable. If it is, then kinetic simulations are carried out to estimate whether the time scales are reasonable. It must be emphasized that the results presented here are tentative

because the chemical mechanisms are almost certainly incomplete, some of the data are of uncertain accuracy, and a detailed parameter study has not been performed at this stage of the project. The results presented here are useful mainly as a guide for companion experiments that are to be conducted at SNL in the upcoming months. The results of these experiments should allow the models to be refined to the point that they can be used with confidence in detailed reactor simulations.

Data Collection

Two primary sources were used to assemble the gas-phase mechanism and data needed for the calculations. The species and reactions involved in methane pyrolysis and combustion were taken from GRI-Mech Version 1.2, and the corresponding thermodynamic data file was used as the default. Reactions and thermodynamic data for bromine-containing species were obtained from a NIST Web site [NIST 2001]. Several reactions tabulated by Babushok [1996] but not included in the NIST website (perhaps because of uncertain accuracy) were added to our compilation. About a dozen miscellaneous reactions from various sources were also added, partly to provide a pathway for complete bromination of methane. Thermodynamic data for all bromomethanes and bromomethyl radicals were obtained by fitting the values reported by Paddison and Tschuikow-Roux [1998] to complement the NIST database. An approximate entry for carbonyl bromide (COBr_2) was constructed by using handbook values of the enthalpy, entropy, and heat capacity at 298K [Dean 1973]. This value was used only for the equilibrium calculations, as a means of demonstrating that this species would not be present in significant amounts. Thus, a more accurate entry was not required.

Equilibrium Calculations

The first step is to perform a purely thermodynamic analysis to determine the species present in the system at equilibrium. The results are a function of the prevailing temperature and pressure, which is taken to be 1 atm. The computations have been carried out using the Sandia EQUIL code, which is basically a CHEMKIN interface to the well-known STANJAN code. The results have been checked against a spreadsheet-based calculation at 298K and the predictions of the online solver EQUILIB-Web [Ecole Polytechnique Montreal 2001]. Both STANJAN and EQUILIB-Web have certain advantages: the latter automatically, and almost effortlessly, gives the global equilibrium composition by including every species in its database, while the former allows one to perform partial equilibrium calculations by including only those species that are of interest. We have used STANJAN here in order to take advantage of its flexibility.

For the system in which bromine and methane are the reactants, the primary reaction is



where C(s) is solid carbon (graphite). This stoichiometry was input to STANJAN, and the results are shown in Figure 1. Note that the ordinate is the *overall* mole fraction, on a logarithmic scale, with both gaseous and solid constituents included. Clearly, the conversion of methane to carbon is essentially complete; the formation of HBr is also nearly complete at low temperatures, but at higher temperatures HBr begins to dissociate into H_2 and Br_2 , and eventually Br_2 itself begins to dissociate. No brominated hydrocarbons are formed under these circumstances.

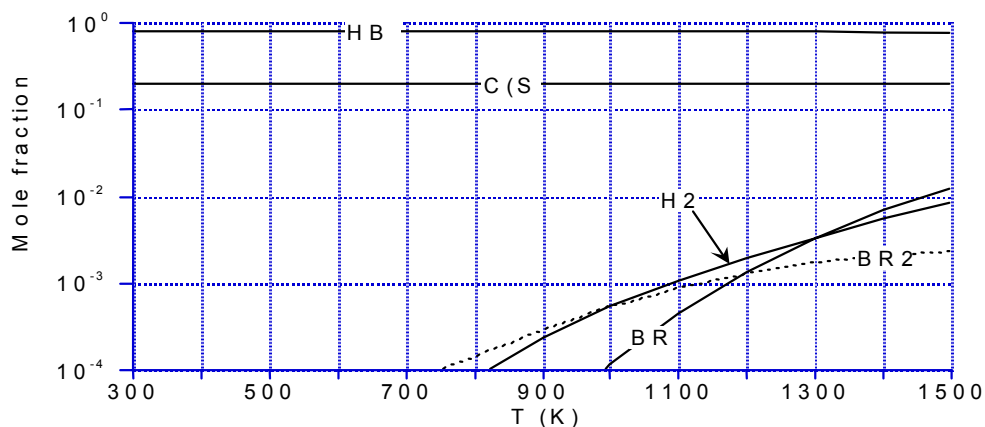


Fig 1. Equilibrium composition $\text{CH}_4 + 2 \text{BR}_2$ from STANJAN

The rate of formation of solid carbon must depend on the surface-to-volume ratio in the reactor, where the surface may include more than just the reactor walls. Therefore, it is possible that carbon deposition may not actually occur to a significant extent under some conditions of practical interest. Because of this, it is useful to carry out partial equilibrium calculations in which solid carbon has been deleted. Performing this calculation, using the list of species involved in the mechanism described above, yields the results shown in Figure 2. Obviously, the situation is now far more complicated. HBr is still the dominant species in the gas, but there is a significant amount of free Br_2 , even at relatively low temperatures, and the carbon is distributed among a wide variety of bromocarbons and hydrocarbons. For kinetic simulations in which solid carbon is not included, we might well expect these same gaseous species to appear. However, it must be emphasized that partial equilibrium calculations must be interpreted cautiously because the results are entirely dependent on the list of species that one chooses to include.

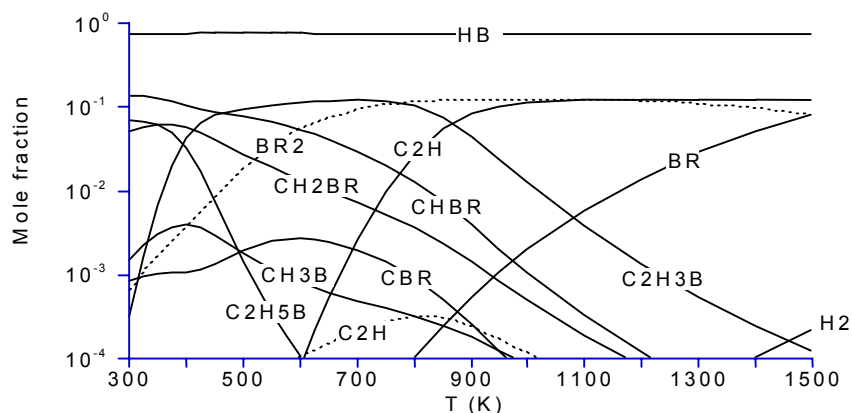


Fig 2. Equilibrium composition for $\text{CH}_4 + 2\text{BR}_2$ from STANJAN (solid carbon not included)

For the system in which H₂O is a reactant, the ideal reaction would be



This stoichiometry was used in additional equilibrium calculations, and the unconstrained results are shown in Figure 3. As before, the ideal product mix is obtained at low temperatures, but significant amounts of by-products begin to appear as T increases. In this case, however, solid carbon is basically absent, so it will not be necessary to deal with the complications involved with heterogeneous reactions. It should also be noted that carbonyl bromide, COBr₂, a highly hazardous substance, is not predicted to form in significant quantities, at least at equilibrium.

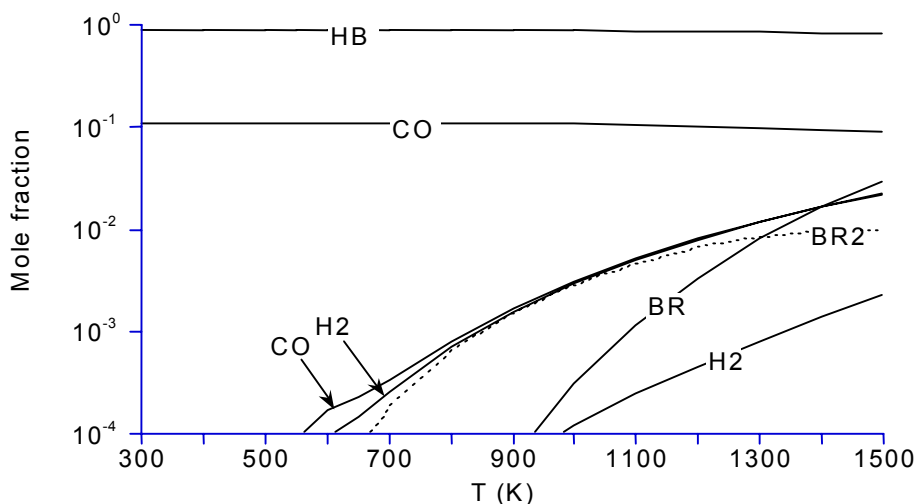


Fig 3. Equilibrium composition for CH₄ + 4BR₂ + 2H₂O from STANJAN

Kinetic Calculations

In order to determine whether the equilibrium compositions computed above can actually be achieved, time-dependent reactor simulations were carried out using the full kinetic mechanism described above. At this point there is nothing to be gained by choosing any particular reactor configuration, so we used the Sandia plug-flow reactor code PLUG; the batch-reactor code SENKIN would almost certainly give very similar results. PLUG is a steady-state code, but the residence time in the reactor assumes the role of the actual time in a transient code. For each set of reactants, the simulation has been carried out for only one or two sets of conditions, so the results are obviously only suggestive.

As mentioned previously, the chemical mechanism does not yet include deposition of solid carbon from the various possible gas-phase precursors. If it did, then the surface-to-volume ratio would become a key parameter. In principle this is easy to remedy, but it is unlikely that the reactive sticking coefficients for most of the gas-phase species have been measured, and the reaction products themselves are probably not known. If experiments show that carbon is

deposited in significant amounts, then the mechanism will obviously have to be augmented. In the meantime, simulations have been carried out for the gas phase alone. With regard to this issue, we note that laboratory tests by SRT resulted in formation of solid carbon for reactions of the bromine-methane-steam system when bromine and steam were present in stoichiometric excess [SRT Group 1998].

A sample set of kinetic results for the bromine-methane system is shown in Figure 4. In this figure, the concentrations of various species are plotted vs. a logarithmic time scale. The initial temperature is specified as 873K, but the reactor is adiabatic, so the temperature will vary as a function of time. The resulting temperature profile is as shown in Figure 5. From Figure 4 it can be concluded that the dominant overall reaction in the first phase of the process is formation of dibromomethane,



This is obviously very exothermic and is essentially complete within 0.01 s. Some CH_3Br is formed as well. At longer times, the CH_2Br_2 is replaced to some extent first by CHBr_3 and then by the unsaturated compounds $\text{C}_2\text{H}_3\text{Br}$ and C_2H_2 , formed endothermically. However, it is clear that the process has not reached equilibrium even after 10^4 s, so the final composition does not quite match that given in Figure 2 for the final temperature of 945K. In any case, the large concentration of brominated hydrocarbons is a cause for concern, and it will be crucial to determine whether deposition of solid carbon can prevent the formation of these compounds.

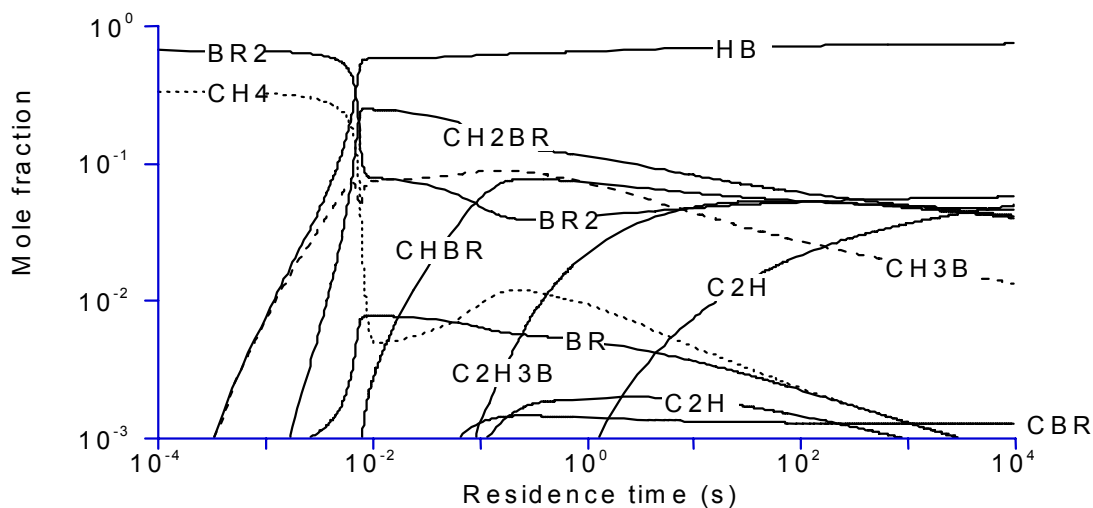


Fig 4. Kinetics for $\text{CH}_4 + 2\text{Br}_2$ (Adiabatic, initial T = 873 K, no solid carbon)

Representative kinetic results for the bromine-methane-steam system are shown in Figures 6 and 7. In this case the initial temperature is somewhat higher (1000K), but the reactor is again adiabatic. The process now appears to take place in three distinct stages. At about 0.001 s, Reaction (3) noted above goes to completion, thereby consuming all of the CH_4 and half of the available Br_2 . This step is significantly exothermic and leaves a mixture containing equal

amounts of Br_2 , H_2O , and HBr , and half this amount of CH_2Br_2 . At times on the order of 1 s, CH_2Br_2 is largely replaced by the more heavily brominated species CHBr_3 , and some CBr_4 . This reaction consumes additional Br_2 and releases hydrogen to form more HBr . It can be seen that the associated heat effect is only slight. However, a true combustion process finally ignites at about 300 s, rapidly pushing the temperature to its final value of 1534K. All of the hydrocarbons (brominated or otherwise) are destroyed to yield CO_2 and CO , and the final composition is just as predicted by Figure 3.

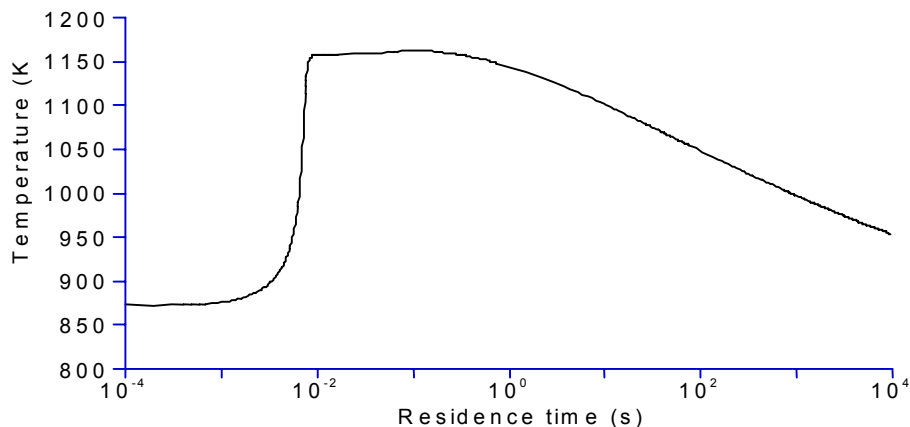


Fig 5. Temperature history for $\text{CH}_4 + 2\text{BR}_2$ (Adiabatic, initial $T = 873 \text{ K}$, no solid carbon)

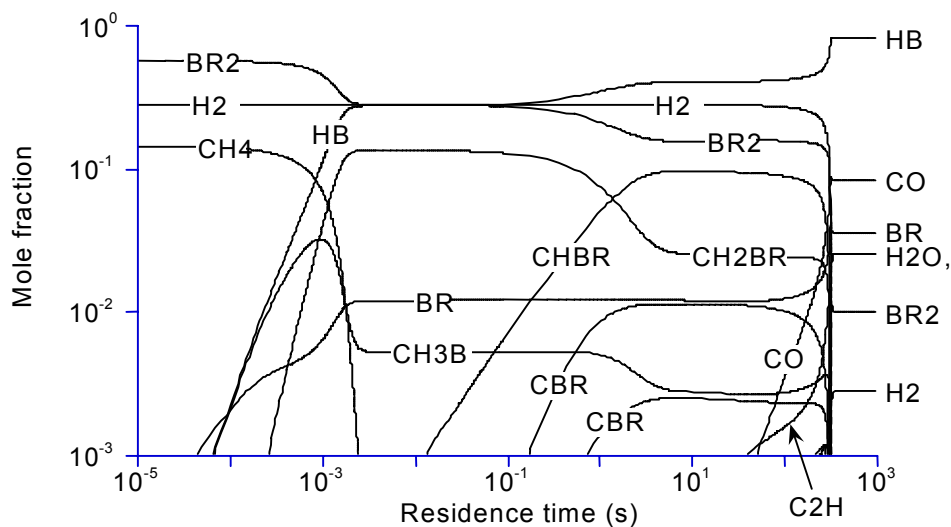
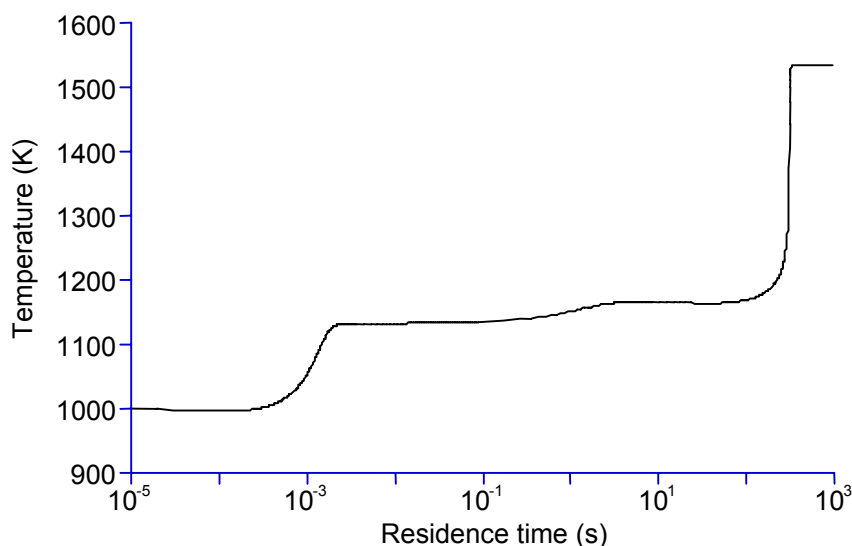


Fig 6. Kinetics for $\text{CH}_4 + 4\text{BR}_2 + 2\text{H}_2\text{O}$ (Adiabatic, initial $T = 1000 \text{ K}$, no solid carbon)



**Fig 7. Temperature history for $\text{CH}_4 + 4 \text{BR}_2 + 2 \text{H}_2\text{O}$
(Adiabatic, initial T = 1000 K, no solid carbon)**

Conclusions

The equilibrium conversion of Br_2 to HBr in the two processes is excellent, especially at low temperatures. If equilibrium is achieved in the bromine-methane process, then the other principal product is solid carbon in some form, e.g., coke or soot. If solid carbon is not produced, then the effluent gas will almost certainly contain significant amounts of brominated hydrocarbons. Not only do these toxic substances present a disposal problem, but they represent a loss of bromine from the system and an incomplete use of the hydrogen introduced in methane. From a purely thermodynamic point of view, the steam process appears to be more attractive, as the carbon in methane is converted almost completely into easily handled CO_2 . However, the kinetics for the steam process are not very encouraging. The residence time required for complete combustion of the carbon is about 350 sec., which would seem to be impracticably long. Of course, the process could be accelerated by using a higher initial temperature.

Future Work

Laboratory experiments will be conducted to provide data that can be used to develop the chemical kinetics equation, rather than demonstrate the process as it might be used in production. An experimental reactor will be designed and constructed to allow a broad envelope of reaction conditions to be evaluated. The most important variables that define this envelope are the reactor temperature, the ratios of the reactants in the feedstock, and the residence time in the reactor. The laboratory reactor will be configured to investigate the reactions of methane with bromine initially and to progress to a study of the reactions that occur when water vapor is present. The extent and rate of the reactions will be determined by analysis of both gaseous and condensed products from the reactor effluent. Analytical techniques will be employed that are suitable for

quantification of the range of brominated hydrocarbons which may form. These techniques include both on-line gas chromatography and off-line analysis. Condensed products will be analyzed by chemical titration and infrared spectroscopy. Other analytical methods will be used as necessary to obtain definitive data.

As part of the continuing computational chemistry effort, the addition of carbon deposition reactions to the mechanism for the bromine-methane process and, possibly, the bromine-methane-steam process is the most significant step that could be taken to obtain a more complete picture of the options for HBr production. However, it is probably not worth pursuing this activity until experiments show that solid carbon forms under conditions of practical interest. It should also be acknowledged that there are several other sources of uncertainty in the calculations, even for the bromine-methane-steam process. First, there is no doubt that the gas-phase reaction mechanism as it stands is incomplete, in part because it has been assembled largely from two independently constructed sub-mechanisms, bromocarbon chemistry and hydrocarbon combustion. It is possible that there are reaction steps for direct bromocarbon combustion that could alter the overall kinetics. In addition, many of the reactions involving bromocarbons have been investigated from the point of view of atmospheric chemistry, so their rates have not been measured at the elevated temperatures of interest for process development. Arrhenius extrapolation of these rates to much higher temperatures is somewhat uncertain, but in the present case there is no alternative. For all of these reasons, the experiments being planned at SNL should provide extremely useful information for model development and refinement.

References

Babushok, V., T. Noto, D. R. Burgess, A. Hamins, and W. Tsang, 1996, *Combust. Flame* **107**, 351.

Dean, J. A. (ed.), 1973, *Lange's Handbook of Chemistry*, 11th edition. McGraw-Hill, New York.

École Polytechnique de Montréal, 2001, <http://www.crct.polymtl.ca/fact/web/equiweb.htm> .

N.I.S.T., 2001, <http://www.cstl.nist.gov/div836/ckmech/nistbfc.html> .

Paddison, S. J. and E. Tschuikow-Roux, 1998, *J. Phys. Chem. A* **102**, 6191.

Schlieff, R. A., M. A. Stoy, H. L. Heaton, and R. J. Hanrahan, 1997, "Production of HBr from the Bromine-Steam and Bromine-Steam-Methane Reactions for Electrolytic Hydrogen Production", SRT Group, Inc., Miami, FL.

SRT Group, Inc., 1998, "Production of Hydrobromic Acid from Bromine, Methane and Steam for Hydrogen Production", Miami, FL.

Acknowledgement

Sandia National Laboratories is a multi-program laboratory operated by Sandia Corporation, a Lockheed Martin company, for the United States Department of Energy under contract DE-AC04-94AL85000.

SOLAR PHOTOCATALYTIC H₂ PRODUCTION FROM WATER USING A DUAL BED PHOTOSYSTEM

**Clovis A. Linkous
Darlene K. Slattery
Florida Solar Energy Center
Cocoa, FL 32922**

Abstract

Organic pigments, surface-modified with catalytic metals, are being employed in various dual modular configurations so as to effect the solar-driven decomposition of water to its constituent elements, particularly hydrogen. Utilizing a UV-filtered Xe lamp, various perylene diimides and indantrones have been observed to preferentially oxidize water to evolve O₂ in alkaline IO₃⁻/I⁻ solution, while phthalocyanine and quinacridones reduced water to evolve H₂. Voltammetric study of Ir, Pt, and Ni co-catalyst materials provided a means of comparing their ability to use the iodine species as electron donors and acceptors. Iodate reduction on Ir appeared to be much faster than iodide oxidation, possibly explaining why Ir is a better co-catalyst for O₂ evolution under these conditions. Interdigitated Ni wire arrays were used as electrochemical equivalents of the dual bed cell in a simulation scheme. It was demonstrated that H₂ and O₂ could proceed at the 10's of mA/cm² level using a redox mediator, in this case ferro/ferricyanide, as the electron donor/acceptor. It was also shown that the rate of gas evolution was strongly tied to the Ox/Red ratio in the working fluid, suggesting that it may be necessary to connect the two modules through an electrolytic concentration cell to sustain vigorous gas evolution.

Introduction

Semiconducting compounds in particulate form are being employed in various dual modular configurations so as to effect the solar-driven decomposition of water to its constituent elements, particularly hydrogen. The goal is to develop a module with low manufacturing cost, safe evolution of H₂ and O₂ in separate compartments, and efficient use of the solar spectrum.

The objective of the current effort is to perform R&D tasks that will enable engineering and economic analysis of the technology. Our preliminary determination, based on materials costs, is that the dual bed could produce H₂ at \$13/mBtu if the solar-to-H₂ energy conversion efficiency of the system is 8% (Block 1998). Having determined a number of molecular structures that make active photocatalysts (Slattery 2000, 2001), our intent is to design, synthesize, and test a number of compounds that would appear to have optimum characteristics.

A schematic of the dual bed concept is shown below in Figure 1. Two pairs of photocatalytic reactions occur. In one container, water is reduced to H₂; the electron equivalents for the reaction come from a redox mediator, M. In the second container, water is oxidized to evolve O₂; here the oxidized form of the mediator acts as electron acceptor. By circulating the mediator in an aqueous solution between the beds, the transfer of charge equivalents between the two water decomposition half-cell reactions is accomplished. While the maximum quantum efficiency for water-splitting is automatically cut in half, one is now able to utilize lower energy photons to perform less energetically demanding chemical steps, and so achieve better utilization of the solar spectrum.

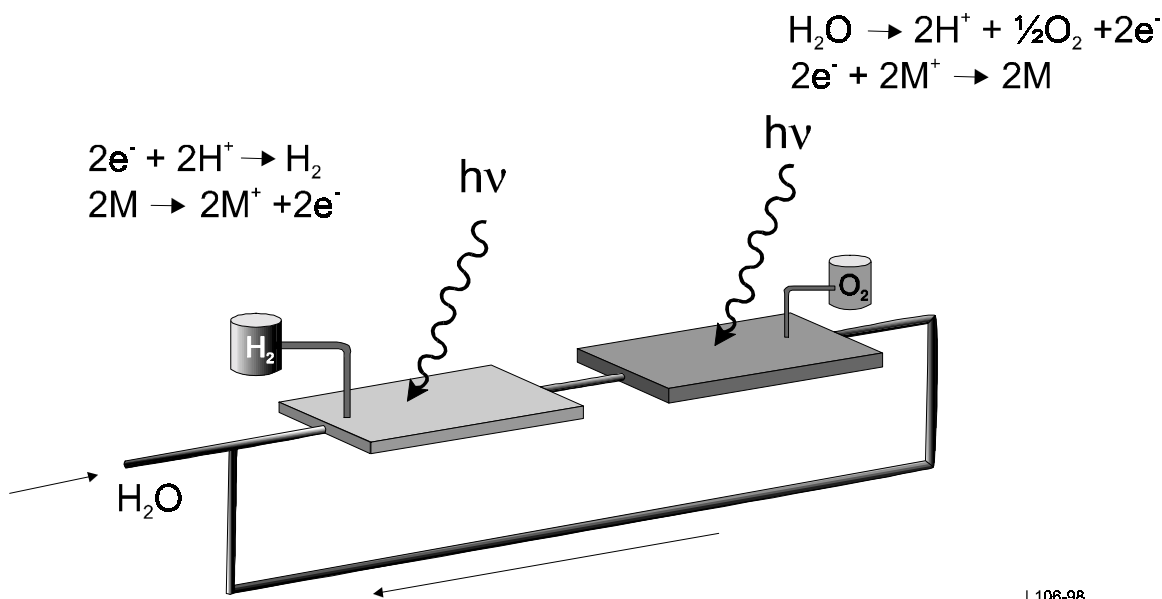


Figure 1. Schematic of a dual bed photocatalytic water-splitting system.

Results and Discussion

Our objective is to perform R&D tasks that will enable engineering and economic analysis of the technology. With that end in mind, our research efforts have gone along two basic directions: 1) photocatalyst development; and 2) systems development.

Photocatalyst Development

Our first task was to revisit many of the photocatalyst/electrolyte systems that we had investigated in the previous contract period, except that now we employed a 400 nm (UV cut-off) filter. This eliminated interfering gas evolution reactions from alkaline iodate solution (UV photochemical disproportionation) and polymer substrate light absorption. The gas evolution levels went down (in 6 h trials, we obtained 32 μl O_2 for the ditridecyl perylene diimide system and 19 μl for indanthrone; 8 μl H_2 for quinacridone and 7 μl for copper phthalocyanine), but nevertheless we still achieved our Phase 1 objective, namely, observation of H_2 and O_2 evolution from respective photocatalysts with the same redox electrolyte (1:1 I^-/IO_3^-). Production efficiencies for the two gases are now at similar levels. In retrospect, as will be discussed in the modeling section of the report, the use of 1:1 Ox/Red likely constituted a substantial limitation on performance.

While a lengthy evaluation process in the search for effective photocatalysts has already been traversed, we nevertheless maintained a modest effort in the synthesis and evaluation of new organic pigment candidates for H_2 and O_2 evolution. For H_2 evolution, we examined representatives of merocyanine family. The band edges looked promising and it has achieved the best performance in solid state organic PV cells (Sayama 2000). However, when we examined it in our aqueous alkaline photocatalytic system, it was found to be photochemically unstable—not just in water, but even in dry air. Thus the transition from solid state to solution can often lead to new decomposition mechanisms.

In the area of O_2 evolution, the companion reaction to H_2 derived from water, we synthesized perfluoroalkyl chain derivatized perylene diimides. We had tested short chain alkyl derivative before with no real improvement over the base compound. However, recent reports have suggested that perfluoroalkyl side chains can afford up to an order of magnitude improvement in photoconductivity. This was an intriguing idea, as it would be thought that long chain substituents would tend to decrease crystalline order, and in so doing shorten charge carrier diffusion length and ultimately quantum efficiency.

As indicated above, we chose to make the perfluoroditridecyl derivative. This is done by heating a solution of the perfluorooctyl iodide in the presence of the base diimide. While work-up and characterization continues, thus far an increase in photocatalytic performance over the base perylene diimide has not been observed.

Co-catalyst Voltammetry

The ability of catalytic substances to work in synergy with the light-absorbing material to accelerate the reaction of interest is well known. One mechanism by which this occurs would be enhanced

rates of charge transfer with the redox mediator, or in our case, I/IO_3^- . We sought to investigate this idea via cyclic voltammetry using the co-catalyst as bulk electrode material. The electrolyte is alkaline iodate/iodide solution, just as in the dual bed system. As shown in Figure 2, the iodine couple does not exhibit reversible behavior, i.e., the voltammetric waves for oxidations and reductions do not occur within a narrow (a few 100 millivolts) range of each other. The iodine species are apparently adsorbed to the electrode surface throughout the electrochemical cycle.

The noble metal co-catalysts nevertheless continue to demonstrate their important role in facilitating the water-splitting process. Ir only exhibited two waves in the cathodic region (2a): one is IO_3^- reduction, while the other is due to O_2 that was generated during the anodic voltage excursion. There was no voltammetric activity that could be ascribed to iodide oxidation. Therefore, one might conclude that the reason Ir is a better co-catalyst than Pt for photocatalytic O_2 evolution is that it is resistance toward the back reaction, i.e., I^- oxidation.

The pair of waves in the Pt voltammogram (2b) correspond to I^- oxidation and IO_3^- reduction. With only I^- or only IO_3^- initially present, essentially the same voltammogram was obtained, although the proportional size of the two peaks was altered somewhat. In the absence of iodine species, the voltammogram was featureless out to the solvent limits. The hysteresis or current crossover effect seen in the negative potential regime, plus the steepness of the current decay for the oxidative wave once again indicates that iodine species are strongly adsorbed to the electrode surface throughout the applied potential range. The peak potentials are nearly 1.0 V apart, demonstrating rather poor reversibility for the iodine couple.

The Ni wire voltammogram (2c) showed most of its activity in the anodic region. In the absence of iodine species, a nearly reversible oxide formation and reduction wave was observed in the +250 mV potential region (SCE ref). Adding IO_3^- had little effect; however, I^- substantially interfered with the oxide formation reaction and subsequent O_2 evolution. Iodine species had little effect in the negative voltage region. The intent is that Ni may be a cheap co-catalyst substitute for Pt in the H_2 -evolving module.

The activity series for O_2 evolution continues to be $\text{Ir} > \text{Pt} > \text{Ni}$, as was derived for M/TiO_2 systems. While iodine adsorption bodes poorly in terms of electrolyte recirculation, it may have catalytic effect for O_2 evolution. Ultimately, it was found that the ferro/ferricyanide couple, $\text{K}_4[\text{Fe}(\text{CN})_6]/\text{K}_3[\text{Fe}(\text{CN})_6]$, exhibited considerable more reversibility on the co-catalyst materials tested, and so was used in the systems development work described below.

Systems Development

While identification of effective photocatalysts and co-catalysts is an ongoing task, it is also intended that we deduce the optimized configuration of the various components. In the current contract period, we wanted to simulate a dual bed system under mass transport limitation conditions, i.e., a system where the rate of reaction on the photoparticle surface is so great that the redox mediator is depleted as it passes through each module. This question has an impact on what the ultimate solar energy conversion efficiency of the apparatus will be.

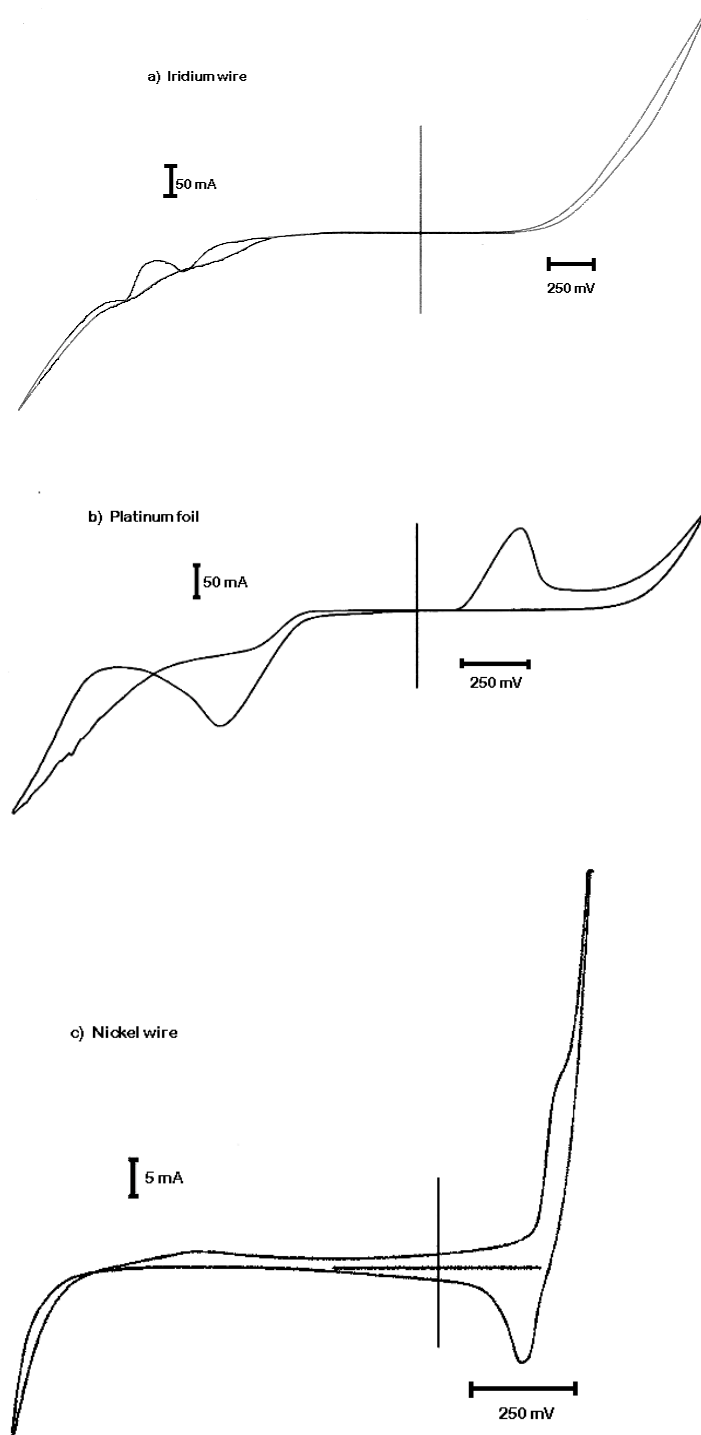


Figure 2. Cyclic voltammograms of co-catalyst materials in iodide/iodate alkaline electrolyte. 1.0 M NaOH, $[KIO_3] = [KI] = 0.1$ M, 50 mV/s, Ar purged solution, SCE reference.

Consequently, we constructed an electrochemical equivalent of a dual bed cell. The idea was to have microelectrode arrays in close proximity to each other that would perform their respective electrode reactions: either O_2 evolution and mediator reduction, or H_2 evolution and mediator oxidation. This was done by stringing Ni wire back and forth across a piece of “perf board” between the holes in such a way that alternate parallel wires belonged to an electrically isolated system. The result was an “interdigitated” array of Ni metal wire that would function as an electrochemical equivalent of a dual bed cell.

A photograph of the electrochemical set-up is shown in Figure 3. A pair of Ni wire arrays were placed into respective modules and sealed. A dual channel power supply was utilized to independently vary the applied voltage (or simulated photopotential) to each cell. A pump circulated an alkaline solution of ferro/ferricyanide ion. The headspace above the working fluid in each compartment was connected to a gas volume measurement apparatus (inverted graduated cylinders). Adding this feature created some difficulty in maintaining a constant solution volume inside each module, however.



Figure 3. Electrochemical equivalent of dual bed cell using interdigitated arrays.

Using an analytical concentration of 0.1 M Fe complex ($[Fe(CN)_6]^{3-} + [Fe(CN)_6]^{4-} = 0.1$), we found that we could sustain the respective gas evolution reaction at the 5-10 mA/cm^2 level. Observing the electrode arrays under an optical microscope, one could observe gas evolution off of alternate wires as shown in Figure 4. If we attempted to further increase the current density of the system, the power supply, operating in the current limiting mode, would raise the voltage into the 1.5 V+ range, whereupon we would observe gas evolution from all the wires in the array, i.e., regular water electrolysis.

If the initial mediator concentration was either all Ox or all Red, mediator-driven gas evolution was easily observed. If, however, we operated the cells under nearly equal concentrations of Ox

and Red, the effect was quite difficult to achieve. This means that as gas evolution proceeds across the module in the direction of fluid flow, Ox is being converted to Red, or vice versa. The product of the mediator conversion reaction builds up, until the back reaction rate nulls out the forward one. Consequently, it may be necessary to include a redox flow cell between the modules with a voltage assist that will condition the mediator concentration for its respective module. With a mediator as reversible as ferro/ferricyanide, an external voltage of only a couple tenths of a volt may be all that is necessary to sustain the net photochemical water-splitting reaction.

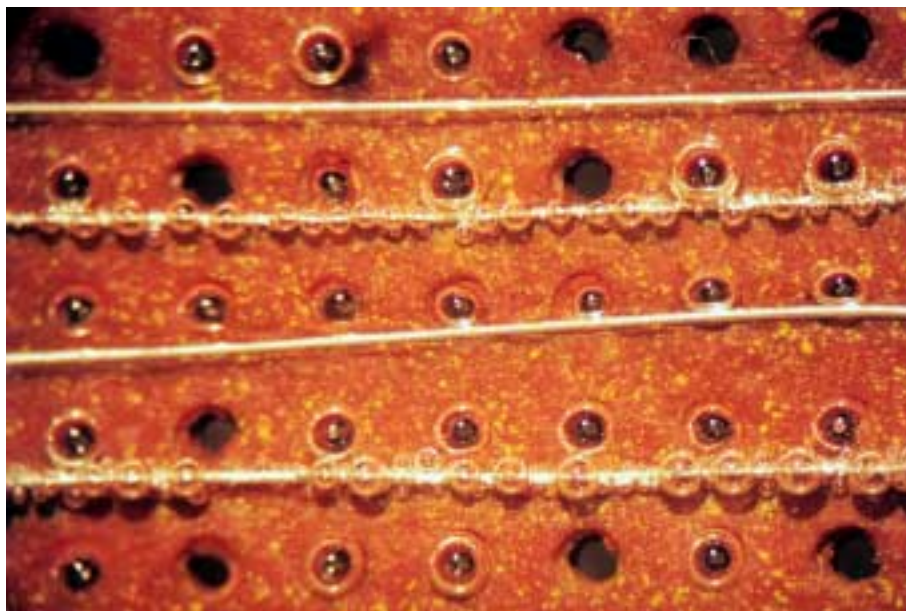


Figure 4. Microscope image of H₂ evolution from cathode array.

Future Work

In terms of photocatalyst development, it is important to understand mechanisms of excitonic charge carrier production. The organic pigments are doing a good job in terms of absorbing large amounts of solar photons, but their conversion into charge carriers that can perform oxidations or reductions needs work. In the area of systems studies, we intend on building and demonstrating a mediator regeneration cell in conjunction with photochemical modules. We will also develop mathematical models that will lay out mediator concentration gradients and gas evolution rates, which can be related to conversion efficiency. As efficiencies improve, we will construct and demonstrate larger photocatalytic modules. We are currently at the 6" square size; we see no limitations in building up to the 48" square size. Whether it makes sense to ever build a module larger than that (at least for the shorter dimension) is open to debate, since that would take it into the custom building materials realm where nonstandard sizes substantially increase module cost.

References

Block, D.L. 1998. "Comparative Costs of Hydrogen Produced from Photovoltaic Electrolysis and from Photoelectrochemical Processes." In *Hydrogen Energy Progress XII. Proceedings of the 12th World Hydrogen Energy Conference, vol 1*, 185-194, Buenos Aires, Argentina.

Sayama, K., K. Hara, N. Mori, M. Satsuki, S. Suga, S. Tsukagoshi, Y. Abe, H. Sugihara, and H. Arakawa. 2000. "Photosensitization of a Porous TiO₂ Electrode with Merocyanine Dyes Containing a Carboxyl Group and a Long Alkyl Chain." *Chemical Communications*, 1173-1174.

Slattery, D.K., C.A. Linkous, and N.E. Gruhn. 2000. "Organic Pigments as Photocatalytic Agents in a Solar Water-Splitting Scheme." In *Hydrogen Energy Progress XIII. Proceedings of the 13th World Hydrogen Energy Conference*, 390-395. Beijing, China.

Slattery, D.K., C.A. Linkous, N.E. Gruhn, and J.C. Baum. 2001. "Semiempirical MO and Voltammetric Estimation of Ionization Potentials of Organic Pigments. Comparison to Gas Phase Ultraviolet Photoelectron Spectroscopy." *Dyes and Pigments*, 49: 21-27.

PHOTOELECTROCHEMICAL SYSTEMS FOR HYDROGEN PRODUCTION

A. Bansal, Todd Deutsch, Jennifer E. Leisch, Scott Warren and J. A. Turner
National Renewable Energy Laboratory
1617 Cole Boulevard, Golden, Colorado 80401

A.M. Fernández
Departamento de Materiales Solares, CIE-UNAM
Temixco, Morelos, 62580, Mexico.

Abstract

This report summarizes the work from two of the main research areas (surface modification and new materials) that are part of NREL's effort towards a photoelectrochemical-based direct water splitting system. In the area of surface modification for control of band edge energetics, p-GaInP₂ surfaces were modified with phthalocyanins, porphyrins and other organic molecules with the aim of moving band edge positions and catalyzing interfacial charge transfer for photoelectrochemical hydrogen generation. The molecules were adsorbed either by drop coating method or by in-situ deposition. Mott-Schottky measurements in the dark showed that the molecules exhibited varying amount of shifts in the band edge positions. Tetraphenyl porphine Cobalt (II) (CoTPP) showed the largest positive shift (+0.27 V) which is very close to the ~0.3 V shift required to create an unassisted water splitting system. Mott-Schottky measurements of CoTPP modified electrodes under illumination showed that the surface modification led to decreased charge transfer ability and hence greater band edge migration as compared to an unmodified surface. In the area of new materials, ternary semiconductor films based on compositions of Cu-Sb-Se were grown on 304 stainless steel/Cr and ITO-glass using a combination of electrodeposition and chemical bath techniques. The samples were annealed in N₂ atmosphere at various temperatures. Photoelectrochemical studies were used to establish the bandgap, the flat-band potential and the doping density of the material, with an eye towards determining the applicability of the CuSbSe system for the photoelectrochemical decomposition of water.

Introduction

Photoelectrochemical systems being developed for the conversion of solar energy into hydrogen consist of a semiconductor electrode in contact with an aqueous electrolyte. When the semiconductor is irradiated with light greater than its bandgap, photoinduced charge separation occurs in the electrode resulting in a photocurrent in the cell. This photocurrent splits water into hydrogen and oxygen at separate electrode surfaces. For the direct photoelectrochemical decomposition of water to occur, several key criteria of the semiconductor must be met. The semiconductor's band gap must be sufficiently large to split water and yet not too large as to prevent efficient absorption of the solar spectrum (the ideal range then is 1.8-2.2 eV), the band edges of the semiconductor must overlap the hydrogen and oxygen redox potentials, and the charge transfer across the semiconductor/liquid interface must be fast enough to prevent corrosion and band edge migration. Our approach then has been to look for new semiconductor materials with bandgaps in the ideal range and then attempt to catalyze their surface and engineer their bandedges if necessary.

In the area of new materials, we have prepared thin polycrystalline films of Cu-Sb-Se using a combination of electrodeposition and chemical bath technique. X-ray analysis indicates that the films mainly have the Cu_3SbSe_3 phase. The optical and photocurrent measurements show that the band gap is around 1.61-1.68 eV. In this report, we discuss the synthesis and characterization of these films.

Gallium indium phosphide, has a band gap of 1.8-1.9 eV, thus meets the criteria of band gap energy. Its band edges are, however, 0.2-0.4 V too negative to achieve the band edge overlap criteria and they are pH sensitive [1]. The electrode also accumulates photogenerated charges at its surface, thus contributing to surface corrosion and band edge migration away from the desired electrode energetics.

Chemical modifications of the semiconductor electrode surface can help the system ameliorate both these problems. By performing different chemical treatments at the semiconductor surface, the band edges can be shifted to appropriate energetic positions and the interfacial charge-transfer can be catalyzed. We have shown that adsorption of organic and inorganic molecules at p-type GaInP_2 can shift the band edges of the semiconductor positive or negative [2]. In particular, we showed that modification of p- GaInP_2 surface with 8-quinolinol shifted the semiconductor band edges positive by as much as 0.3 V. On the other hand, we have also shown that transition metals can minimize band edge migration by catalyzing charge transfer across the p- GaInP_2 /water interface [3].

In this section we combine two surface modification approaches mentioned above by investigating the effects of adsorption of organometallic compounds to simultaneously affect band edge shift as well as act as an electrocatalyst for the p- GaInP_2 /water interface. Unmetallated and metallated porphyrins as well as phthalocyanins were used in this study to modify the electrochemical properties of the p- GaInP_2 electrodes. In addition we also report modifications of p- GaInP_2 surfaces with ethylenediammine tetraacetate (EDTA), 3,4,9,10-perylene tetracarboxylic Anhydride (PTCDA) and poly(diallyldimethyl ammonium) chloride (PDDA) as these molecules have also been reported in the literature to affect the band edge positions of

semiconductors. Although phthalocyanins and porphyrins have been widely studied in the literature as photosensitive elements and as catalysts, to the best of our knowledge, this is the first study that explores the effect of these molecules on the photoelectrochemical properties of a semiconductor/liquid junction.

Dark Mott-Schottky Characteristics of p-GaInP₂ Surfaces Modified with Porphyrins - Figure 1 shows the flatband potentials of unmodified and porphyrin-modified p-GaInP₂ surfaces in pH 7 solution. The solid circles represent surfaces modified by a ‘drop-coating’ method and the squares represent surfaces modified by an ‘in-situ’ method. The solid diamond on the left represents the mean value and standard deviation of the flatband potentials measured for an untreated surface in pH 7 buffer solution. The solid black line represents the H₂O/O₂ redox potential. The valence band edge of the semiconductor is ~0.15 V positive of the V_{fb} values shown.

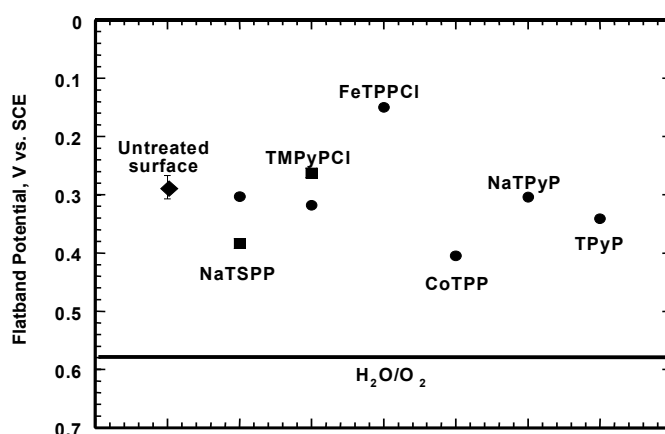


Figure 1: Flatband potentials (V_{fb}) observed for untreated and porphyrin-modified p-GaInP₂ surfaces in pH=7 (phosphate) buffer solution. The solid circles represent surfaces modified by the ‘drop-coating’ method and the squares represent surfaces modified by the ‘in-situ’ method. The solid diamond represents the mean value of the flatband potentials measured for an untreated surface in pH 7 buffer solution. The error bars represent the standard deviation. The solid black line represents the H₂O/O₂ redox potential. The valence band edge of the semiconductor is ~0.15 V positive of the V_{fb} values shown.

In order for the cell to split water without any external voltage assistance, the measured flatband potential of the semiconductor must be below (more positive of) the H₂O/O₂ redox potential. Figure 1 shows that only three cases show a statistically significant shift in the flatband potential. As compared to an untreated surface in pH 7 solution, the average shift shown by FeTPP-treated surface prepared by the drop coating method is –0.14 V, the shift shown by an etched surface run in a pH 7 solution of NaTSPP is +0.10 V and the shift shown by CoTPP-treated surface prepared by the drop coating method is +0.12 V.

Dark Mott-Schottky Characteristics of p-GaInP₂ Surfaces Modified with Pthalocyanins - Figure 2 shows the flatband potentials of unmodified and phthalocyanin-modified p-GaInP₂ surfaces in pH 7 solution. The symbols used here are the same as those used in figure 1. Of all the phthalocyanins used in this study, only two exhibited marginally significant shifts in the flatband potentials. The ZnPc-modified surface prepared by the drop coating method shifted the V_{fb} by – 0.07 V and the etched surface run in AlPcCl(Sulf)₄ solution showed a band edge shift of –0.06 V.

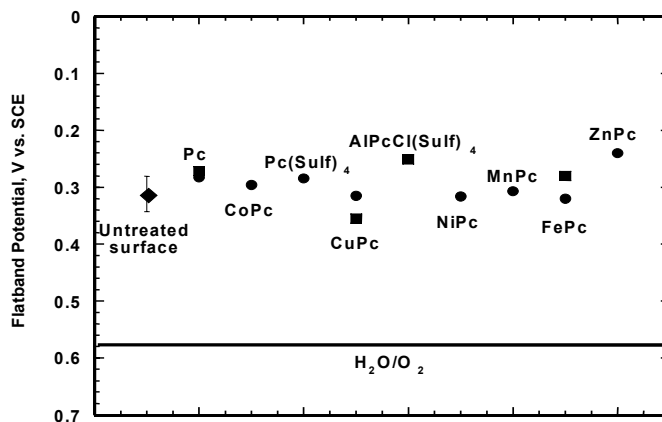


Figure 2: Flatband potentials (V_{fb}) observed for untreated and phthalocyanin-modified p-GaInP₂ surfaces in pH=7 (phosphate) buffer solution. The symbols used here are the same as those used in Figure 1. The solid black line represents the H₂O/O₂ redox potential. The valence band edge of the semiconductor is ~0.15 V positive of the V_{fb} values shown.

pH dependence of Flatband Potentials of Modified p-GaInP₂ Surfaces in the Dark – Figure 3 shows the flatband potential values measured for untreated and modified p-GaInP₂ surfaces in solutions of various pH. The only derivatizations that showed statistically significant shifts were Pc tetrasulfonate at pH 0 (-0.09 V), CuPc at pH 0 (-0.09 V), PTCDA at pH 0 (-0.10 V) and CoTPP at pH 4 (0.27 V). Of these, the CoTPP modification in pH 4 solution is of particular interest as the flatband potentials shifted positive by a significant amount and the band edges now overlap the hydrogen and oxygen redox potentials (Figure 3 inset).

Ability of CoTPP to Catalyze Charge Transfer at the p-GaInP₂/Water Interface – Figure 4 shows the flatband potential values measured for an untreated and a CoTPP-modified surface in pH 4 solution, in the dark and under various levels of illumination. As the level of illumination increases the band edges are observed to migrate negative on both surfaces, indicating accumulation of photogenerated charges at the interface. The V_{fb} values for CoTPP-modified surface are observed to have shifted more negative than for the untreated surfaces for a corresponding level of photocurrent density.

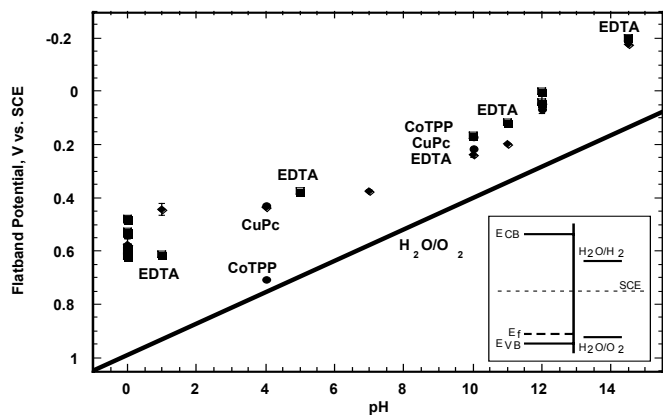


Figure 3: Flatband potentials (V_{fb}) observed for untreated and modified p-GaInP₂ surfaces in solutions of various pH. The symbols used here are the same as those used in Figure 1. The solid black line represents the H₂O/O₂ redox potential. The valence band edge of the semiconductor is ~0.15 V positive of the V_{fb} values shown. Inset: Band edge and Fermi level positions of p-GaInP₂ with respect to oxygen and hydrogen redox potentials in the liquid phase.

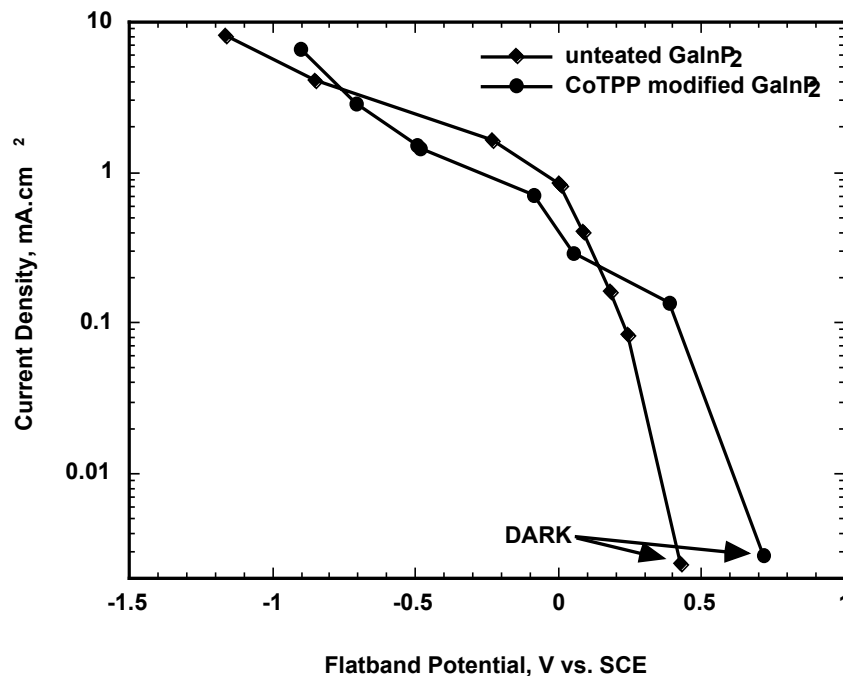


Figure 4: Flatband potentials (V_{fb}) observed for untreated and CoTPP-modified p-GaInP₂ surfaces in pH 4 solution, in the dark and under various levels of illumination.

Discussion

Of all the porphyrins, phthalocyanins and other organic molecules evaluated in this study (Figure 3), only a few showed significant band edge shifts. At pH 7, the significant ones were FeTPPCl (−0.14 V), NaTSPP (+0.10 V), CoTPP (+0.12 V), ZnPc (−0.07 V) and AlPcCl(Sulf)₄ (−0.06 V). None shifted the band edges positive enough to take it past the water/oxygen redox potential. Measurements made at other pH values also showed shifts of less than 0.10 V, with one exception. p-GaInP₂ surfaces modified with drop coated CoTPP exhibited a flatband potential shift of 0.27 V. This was the largest positive flatband shift observed in this study and was significantly within the 0.2-0.4 V range desired for creating a water splitting system.

The CoTPP-treated surface was, therefore, subjected to a more detailed study. It is known that the unmodified p-GaInP₂ surface is pH sensitive. To evaluate how the band edges of the modified surface shifted as a function of pH, the CoTPP-treated surface was immersed in solutions of various pH. Figure 5 shows that the CoTPP modified surface is also pH sensitive, albeit to a different extent. It is seen that for pH < 10, the shift in the flatband potential of a CoTPP-modified surface is greater than that for the unmodified surface and this shift increases with decreasing pH. It is advantageous to have a large positive shift as one can expect that part of it would be negated by band edge migration under illumination.

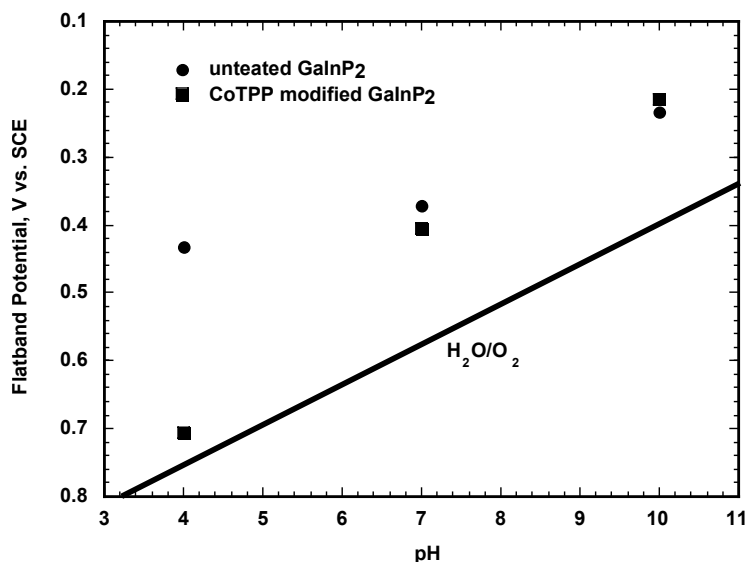


Figure 5: pH sensitivity of band edges for untreated and CoTPP-modified p-GaInP₂ surfaces.

Both band edge shift and enhanced charge transfer ability are necessary to realize a viable water splitting system. Therefore, having observed the ability to shift the p-GaInP₂ band edges positive, the CoTPP-modified surface was evaluated for enhanced or decreased ability to transfer charge across the p-GaInP₂/water interface as compared to the unmodified surface. The migration of the measured flatband potential values towards negative potential in Figure 4 shows that the modified surface continues to have less than optimal interfacial charge transfer rate. When the V_{fb} values under illumination for both the surfaces are normalized to their respective

V_{fb} values in the dark, it becomes clear that the CoTPP modification slightly impedes charge transfer. Furthermore, the advantage of positive band edge shift is lost as the illumination level is increased beyond that corresponding to a photocurrent density of approximately 0.2 mA/cm^2 (Figure 4), which is much less than what is required for a working device.

An additional observation from the testing of a variety of organometallic molecules is that the band edge shifting characteristics of a molecule does not depend solely on the organic body of that molecule. Testing of FeTPPCL and CoTPPCL, which have the same organic structure, showed a remarkably different band edge shift characteristics. While FeTPPCL shifted band edge by -0.14 V in the negative direction, CoTPP shifted the band edges positive by $+0.12 \text{ V}$. Based on this, it is apparent that the metal ion complexed at the center of the organometallic moiety can play a significant role in determining the extent of the band edge shift

Band Edge Engineering Summary

This section showed that ‘band edge engineering’ of the p-GaInP₂/water interface could be performed by suitable surface treatments of the semiconductor surface. Organometallic molecules such as porphyrins and phthalocyanins can be adsorbed to the semiconductor surface to shift its band edges positive or negative to various extents. The CoTPP-modified p-GaInP₂ surface showed a band edge shift of $+0.27 \text{ V}$, but the modification reduced the charge transfer efficiency, resulting in increased band edge migration under illumination for the modified surface. It is clear that additional catalysis of charge transfer will be needed to make this system work. Work in this area is currently under progress.

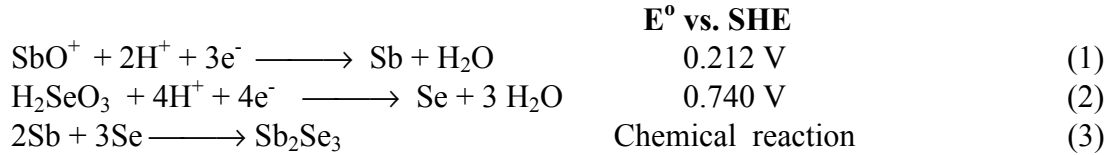
Characterization of Cu-Sb-Se Films Prepared by Chemical-Electrochemical Deposition

Ternary alloy semiconducting materials resulting from alloying of binary semiconducting (having well defined physical properties) usually result in ternary materials whose bandgaps vary between the limits bound by the binary constituents. The three known copper selenoantimonate compounds, CuSbSe₂ [4], Cu₃SbSe₃ [5] and Cu₂SbSe₄ [6] have bandgap values between Sb₂Se₃ and Cu₂Se. It is anticipated that, ternary materials resulting from the intermixing of the Sb₂Se₃ with Cu₂Se would have their bandgap varying between 1.55 eV [7] to 2.2 eV [8], the ideal range for water splitting. Single crystals of the these ternary alloys, which in normal course would be the preference for device applications, may not to be possible over an extended composition range due to the limited solid solubility of Sb₂Se₃ in Cu₂Se. However, the known relaxation of solid solubility limits during thin film growth, coupled with appropriate growth conditions could result in thin films of copper antimony selenide materials.

Considering these aspects, copper antimony selenide films were prepared using a combination electrodeposition and chemical bath technique. In this section, we report on the optical characteristics, the structure, and the atomic composition. Electrochemical measurements in various aqueous electrolyte solutions were done to determinate flat-band potential and photoresponse.

Discussion

The electrodeposition of Sb_2Se_3 is most likely due to the combination of electrochemical and chemical reactions as follows:



The mechanism for the formation of the copper selenide has not been established, however, it may be considered as being formed by the following step:



According with the c-T diagram [9] the formation of CuSbSe_2 may proceed by the following solid solution reaction:



Figure 6 shows the growth curve for electrodeposited Sb-Se films and chemically deposited Cu-Se films on 304 stainless steel/Cr substrate. The applied potential is varied for the preparation of the Sb-Se films. In all cases, the Cu-Se films were deposited with the same chemical bath for the same period (six hours). We observed a gradual increase in film thickness with the duration of the Sb-Se film deposition until the film reached the final thickness. Also, it is possible to observe an increment in the rate of deposition when the applied potential increases.

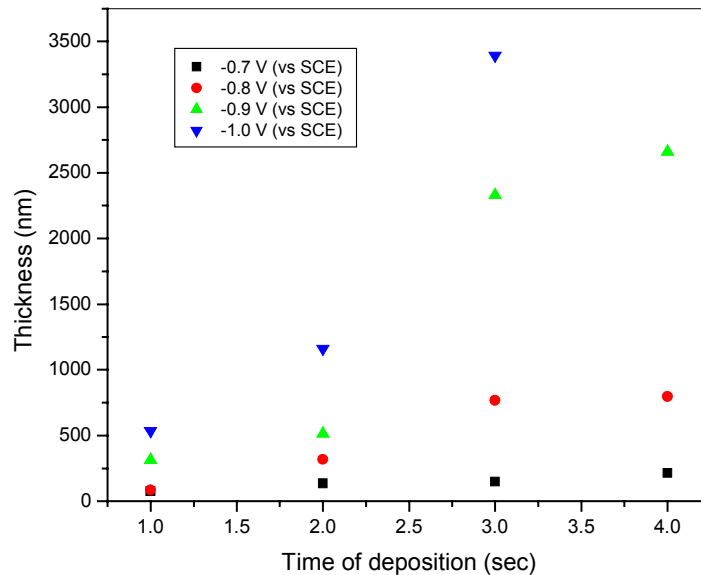


Figure 6: Cu-Sb-Se film thickness as a function of the deposition time of Sb-Se films, at different applied potential of Sb-Se films.

Table 1 lists the atomic ratio of the Cu-Sb-Se films for three different applied potentials. As we observed in the table, after annealing the samples at 400°C, the atomic composition changes drastically, likely due to possible phase changes, from Cu₃SbSe₄ to Cu₃SbSe₃. This effect also shows in the XRD patterns. XRD peaks for annealed samples at 300°C and 400°C in nitrogen atmosphere showed that for the samples annealed at 300°C the major phase corresponded to Cu₃SbSe₄ with a Sb₂Se₃ phase also observed. However, when the samples were annealed at 400°C, the Cu₃SbSe₃ phase was the major phase. This transformation may be possible due to the average Sb-Se distance [8] being almost the same for both compounds as well as the distance between the Cu atoms in the structure.

Table 1: Atomic ratios for three different applied potentials

Sample Number	Applied Potential for Sb-Se electrodepos. (V vs. SCE)	Atomic composition Annealed at 300°C			Atomic composition Annealed at 400°C		
		Cu (at.%)	Sb (at.%)	Se (at.%)	Cu (at.%)	Sb (at.%)	Se (at.%)
A	-0.7	35.956	16.106	47.936	45.727	10.060	44.212
B	-0.8	38.811	11.035	50.153	46.353	9.494	44.152
C	-0.9	39.290	13.070	47.639	44.354	12.785	42.859
D	-1.0	33.189	18.174	48.635	44.058	12.949	42.991

The EPMA results for annealed samples of Cu-Sb-Se on 304 stainless steel/Cr substrates. The duration of the time for the deposition of Sb-Se was 45 min., and the duration of time for the deposition of Cu-Se was six hours. The chemical composition for both baths was described above.

The optical transition was obtained for these films, using the dependence of α on $h\nu$, according to the following relation:

$$\alpha \propto (h\nu - E_g)^n \quad (6)$$

where α is the absorbance, ν the frequency of wavelength, h the Planck constant and E_g the optical bandgap. Table 2 shows the variation of the bandgap after annealing at 300°C and 400°C.

Table 2: Variation of the bandgap after annealing

Sample number	Optical Bandgap E_g (eV)	
	Annealed temperature, in N ₂ atmosphere	
	300°C	400°C
A	1.85	1.58
B	1.78	1.70
C	1.83	1.67
D	1.80	1.65

The bandgap values (E_g) for annealed samples of Cu-Sb-Se on ITO-glass. The experimental conditions for the preparation of the samples were described above.

The current-voltage curves showed a low cathodic current density below open-circuit voltage down to about -1.0 V, indicating that the samples are p-type. When the samples were exposed to the light the reverse current increased as expected.

Figure 7 shows a typical Mott-Schottky (M-S) plot ($1/C^2$ vs V) for sample D (see Table 1). The plot is fairly linear. Very little hysteresis was seen in all of the samples tested. The slope of the linear portion was slightly frequency-dependent, and showed no variation with pH. Inserting the value of this slope into the Mott-Schottky relationship:

$$\Delta(C^{-2})/\Delta V = 8\pi/\epsilon q N_D$$

where the ϵ is the dielectric constant of the semiconductor, N_D is the donor density and q is the absolute value of the elemental charge, a value of $N_D \cong 1.1 \times 10^{20} \text{ cm}^{-3}$ was found. The intersections of the extrapolated linear portion with V-axis give the flat-band potential. The following values were found: $V_{fb} = 0.622, -0.5071, -0.3765,$ and -0.2773 V at pH = 3, 5, 7 and 10, respectively. The results demonstrate that the flat-band potential V_{fb} shifts towards positive voltages with increasing pH. The variation of V_{fb} versus pH, yielding a straight line with a slope of 0.0528 V per pH unit.

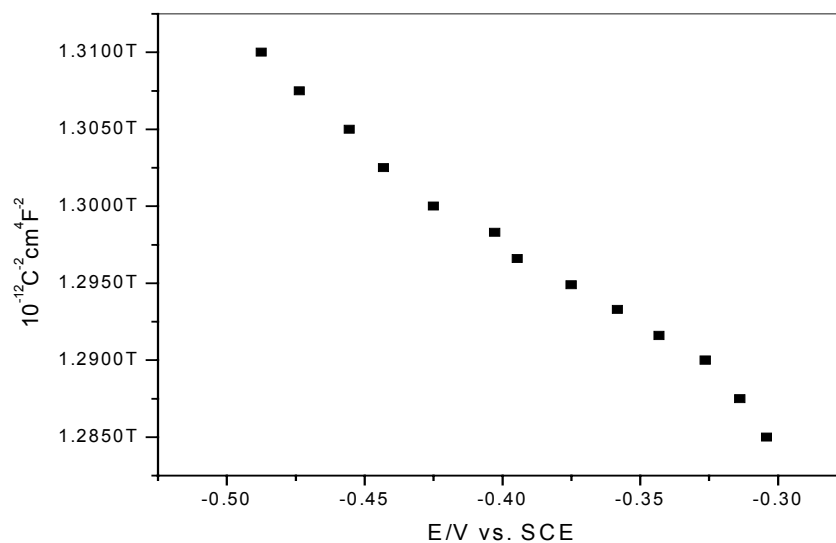


Figure 7: Mott-Schottky plot ($f = 10$ kHz) for Cu_3SbSe_3 in aqueous electrolyte of pH 3.

Figure 8 shows a plot of photocurrent versus wavelength for a sample D under reverse bias. By plotting a function of the current versus the energy of incident light, and extrapolating to zero, the direct band gap was found to about 1.61 eV. This value is very close to the previous value obtained by optical measurement.

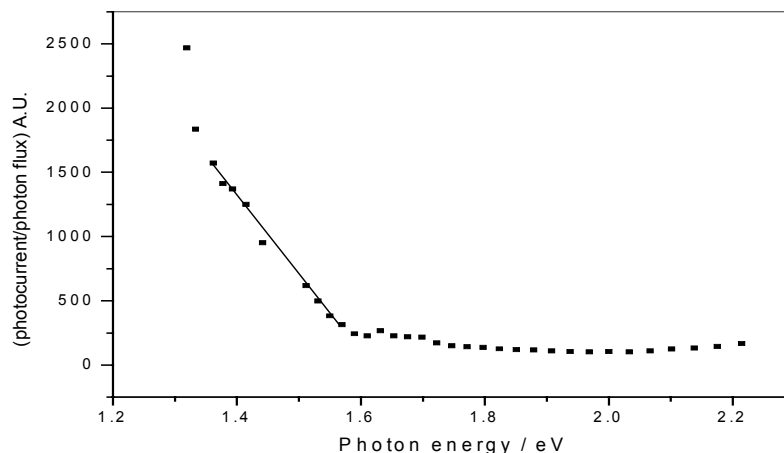


Figure 8: Band gap analysis of Cu_3SbSe_3 for direct (I^2) gap. The graph shows that the bandgap is 1.61eV.

New Material Summary

We reported the preparation of Cu-Sb-Se films using a combined electrodeposition and chemical bath technique. After annealing, the films were polycrystalline with expected atomic composition. The EPMA and XRD analysis indicated that the films mainly have the Cu_3SbSe_3 phase. The optical and photocurrent measurements show that the band gap is around 1.61-1.68 eV. The flat-band potential values and a doping density of about $1.1 \times 10^{20} \text{ cm}^{-3}$ were observed. The shift in the flat-band potential with the pH is linear, with slope of about 53 mV per unit pH. This material will now be studied for possible water splitting activity.

Acknowledgements

We thank Dr. Brian A. Gregg of NREL for providing us the various phthalocyanins, porphyrins, PTCDA and PDDA. SW, JL and TD thank Linda Lung and acknowledge funding from the summer ERULF program.

This work was supported by the Hydrogen Program of the U.S. Department of Energy.

References

1. S. S. Kocha, J. A. Turner, and A. J. Nozik, *J. Electroanal. Chem.* **1994**, 367, 27.
2. S. Kocha, J. A. Turner, *Journal of The Electrochemical Society*, **142**, 2625, (1995)
3. A. Bansal, and J. A. Turner, *J. Phys. Chem. B*, 104, p 6591, (2000).

4. R.M. Imamov, Z.G. Pinsker, and A.I. Ivchenko. *Soviet Physics-Crystallography*, **9** (1965) 721.
5. A. Pfitzner, *Z. anorg. Allg. Chem.*, **621** (1995) 685.
6. A. Pfitzner, *Zeitschrift für Kristallographie*, **209** (1994) 685.
7. A.P. Torane, K.Y. Rajpure, C.H. Bhosale, *Materials Chemistry and Physics*, **61** (1999) 219.
8. V.M. García, P.K. Nair, M.T.S. Nair, *Journal of Crystal Growth*, **203** (1999) 113.
9. G.B. Gather, R. Blachnik, *Journal of the Less-Common Metals*, **48**(1976) 205
10. J. Li, Z. Chen, R-J Wang, D.M. Proserpio, *Coodination Chemistry Reviews*, 190-192 (1999) 707.

PHOTOELECTROCHEMICAL HYDROGEN PRODUCTION

**Eric Miller and Richard Rocheleau
Hawaii Natural Energy Institute
School of Ocean and Earth Science and Technology
University of Hawaii at Manoa
Honolulu, Hawaii 96822, USA**

Abstract

At the University of Hawaii (UH), the approach to developing high-efficiency, low-cost photoelectrochemical (PEC) processes for the direct production of hydrogen has included the use of integrated electrochemical/optical models to design photoelectrodes based on multijunction thin-film technology; materials research to identify critical issues on photoelectrode efficiency and stability; and the fabrication and testing of photoelectrodes for optimization and life-testing. In recent years, we designed photoelectrodes using monolithically stacked triple-junctions of amorphous silicon (a-Si) and mechanically interconnected side-by-side copper-indium-gallium-diselenide (CIGS). This year, significant progress was made in optimizing constituent films for these photoelectrode designs. Photoelectrodes using both a-Si and CIGS were fabricated and tested. Both types of photoelectrodes were fabricated using optimized NiMo, Fe:NiOx, ITO (indium-tin-oxide), and polymer-encapsulation films deposited at the University of Hawaii. The a-Si solar cells used in these studies were deposited by the University of Toledo using a process that yielded electrical efficiencies as high as 12.7%. The 13% efficient CIGS cells were provided under subcontract by the University of Delaware. Based on the electrical efficiency of the cells and prior experiments using these catalytic coatings, solar-to-hydrogen efficiencies of 6% to 8% were expected for the a-Si based photoelectrodes. However, peak efficiencies of only 2.5% were measured in outdoor tests. The discrepancy has been attributed to handling-induced degradation in the a-Si triple-junction performance. Severe degradation also occurred in CIGS diodes when cut for photoelectrode fabrication. Open-circuit voltage in the CIGS triple-stacks was reduced from 1.8 V to below 1 V, making water-splitting impossible, despite predicted solar-to-hydrogen efficiencies in excess of 10%. Planned future work includes development of improved handling techniques to demonstrate the true hydrogen production potential in the photoelectrodes, with greater emphasis on the higher-efficiency CIGS devices. Plans also include continued development of the hybrid solid-state/PEC photoelectrode described at the FY 2001 Annual Review Meeting. This design combines a double-junction amorphous silicon cell with a dye-sensitized TiO₂ or WO₃ photoelectrochemical junction.

Introduction

Under the sponsorship of the U.S. Department of Energy, research at the Hawaii Natural Energy Institute of the University of Hawaii has aimed at developing high-efficiency, potentially low-cost, photoelectrochemical (PEC) systems to produce hydrogen directly from water using sunlight as the energy source. The main thrust of the work has been the development of integrated multijunction photoelectrodes, comprising semiconductor, catalytic, and protective thin-films deposited on low-cost substrates (such as stainless steel), for solar hydrogen production (Rocheleau et al. 1998). In the illustration of a generic hydrogen photoelectrode shown in Figure 1, sunlight shining on photoactive regions of the electrode produces electric current to drive the hydrogen and oxygen evolution reactions (HER, OER) at opposite surfaces. Hydrogen photoelectrode operation represents a complex interaction of photovoltaic, optical, and electrochemical effects, and an important part of the UH research has been the development of integrated models combining these effects (Rocheleau and Vierthaler 1994). Figure 2 shows a schematic of the model used in the analysis of a triple-junction photoelectrode.

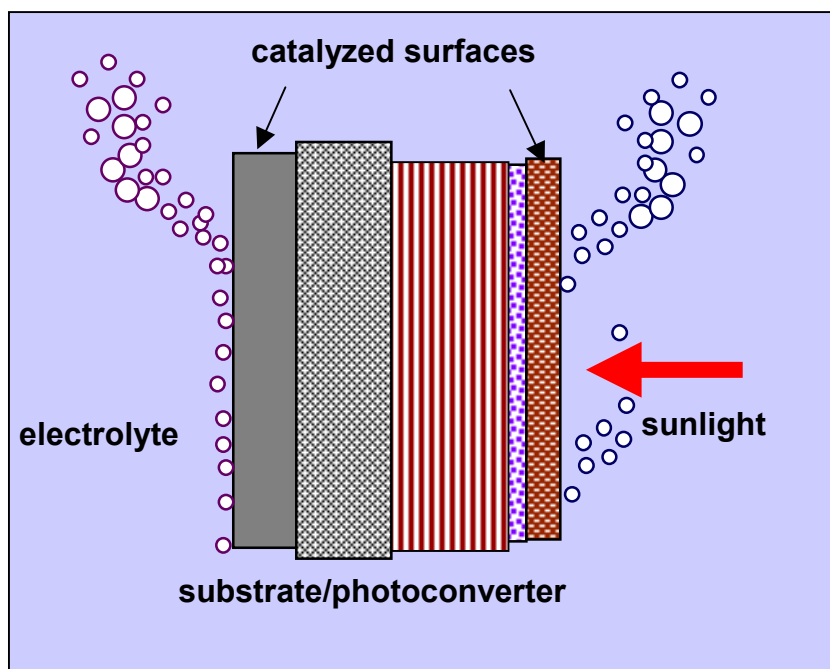


Figure 1. Photoelectrochemical hydrogen production

In order to meet DOE goals, a PEC system must be low-cost, operate at solar-to-chemical conversion efficiencies greater than 10%, and have long operating lifetimes. Numerous approaches involving a variety of semiconductors have been explored since the early 1980s, but none have successfully satisfied both the efficiency and stability criteria. The high voltage required to dissociate water and the corrosiveness of the aqueous electrolytes have been major hurdles. Based on results from numerous modeling and proof-of-concept experiments conducted at UH over the course of the PEC research, our approach has been to develop photoelectrodes incorporating multijunction thin-film photoconvertors (for high voltage) and thin-film catalyst and protective layers (for stability).

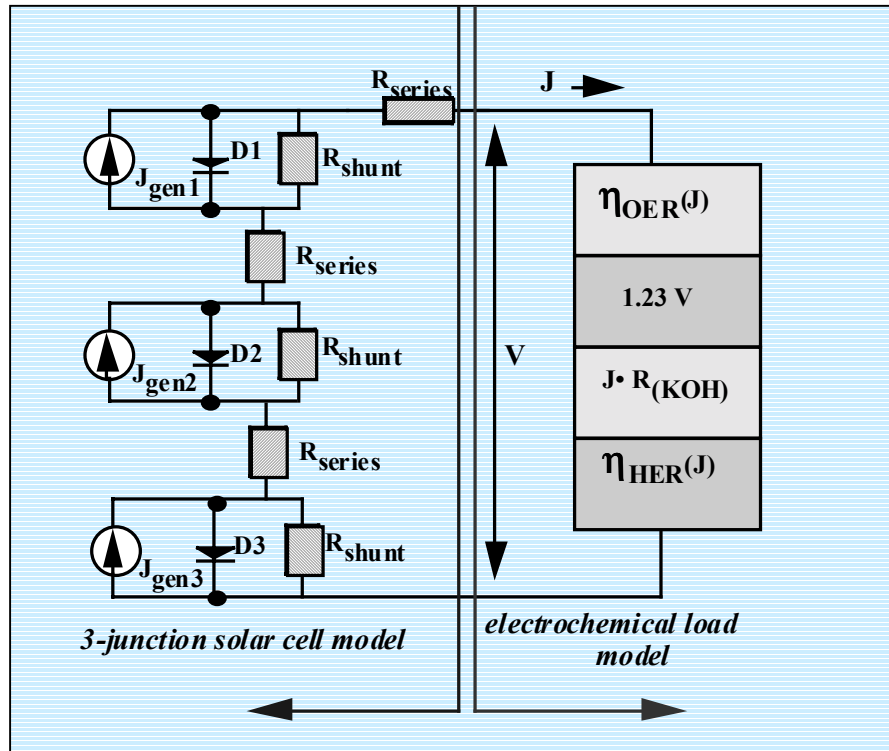


Figure 2. Model of triple-junction photoelectrode

Specifically, our work has provided strong evidence that direct solar-to-hydrogen conversion efficiency of up to 10% can be expected using photoelectrodes fabricated from low-cost, multijunction amorphous silicon (a-Si) (Rocheleau and Miller 1997), while conversion efficiencies approaching 15% are possible using advanced photoelectrode designs based on multijunction copper-indium-gallium-diselenide (CIGS) cells stacked in a side-by-side configuration (Miller and Rocheleau 2000). Both the a-Si and CIGS photoelectrode systems have the potential for low cost based on the very thin semiconductor layers involved and on compatibility with high-throughput manufacturing processes.

Over this past year, we have modified the basic integrated photoelectrode to allow both a-Si and CIGS structures to be used. Schematics of the most recent designs are shown in Figures 3a and 3b for a-Si and CIGS devices, respectively. Using high-efficiency a-Si triple-junction solar cells deposited by the University of Toledo, and high-efficiency CIGS/CdS cells deposited by the Institute for Energy Conversion (IEC) at the University of Delaware, we fabricated simple proof-of-concept test structures for both these photoelectrode designs. Fabrication of the test structures, as described in detail in following sections, was completed at UH using the thin-film catalyst and protective layers developed through our PEC research (Miller and Rocheleau 1999; Miller and Rocheleau 2000).

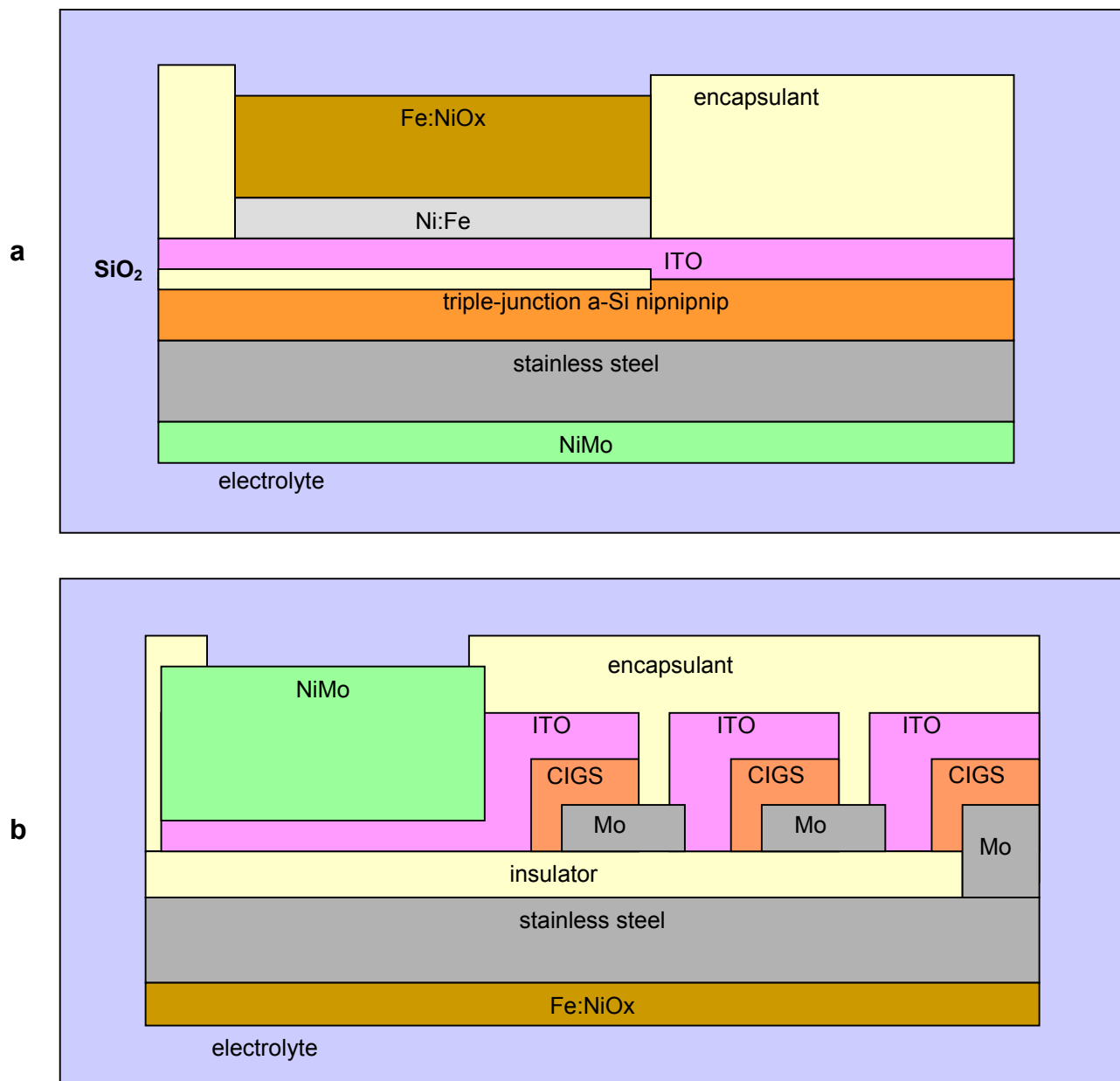


Figure 3. Structure of photoelectrode test devices

Under current funding, in addition to the proof-of-concept photoelectrode fabrications, we developed the conceptual design for a “hybrid” multijunction photoelectrode, incorporating current-matched solid-state and electrochemical photojunctions. This structure, as illustrated in Figure 4, is most easily implemented using a double-junction a-Si device deposited on stainless steel foil. In the configuration shown, the back surface of the foil substrate is treated with a thin-film HER catalyst, and the front surface of the solid-state solar cell component is coated with a thick photoactive material, such as dye-sensitized TiO₂ or WO₃, which replaces the top junction in the original triple-junction a-Si design.

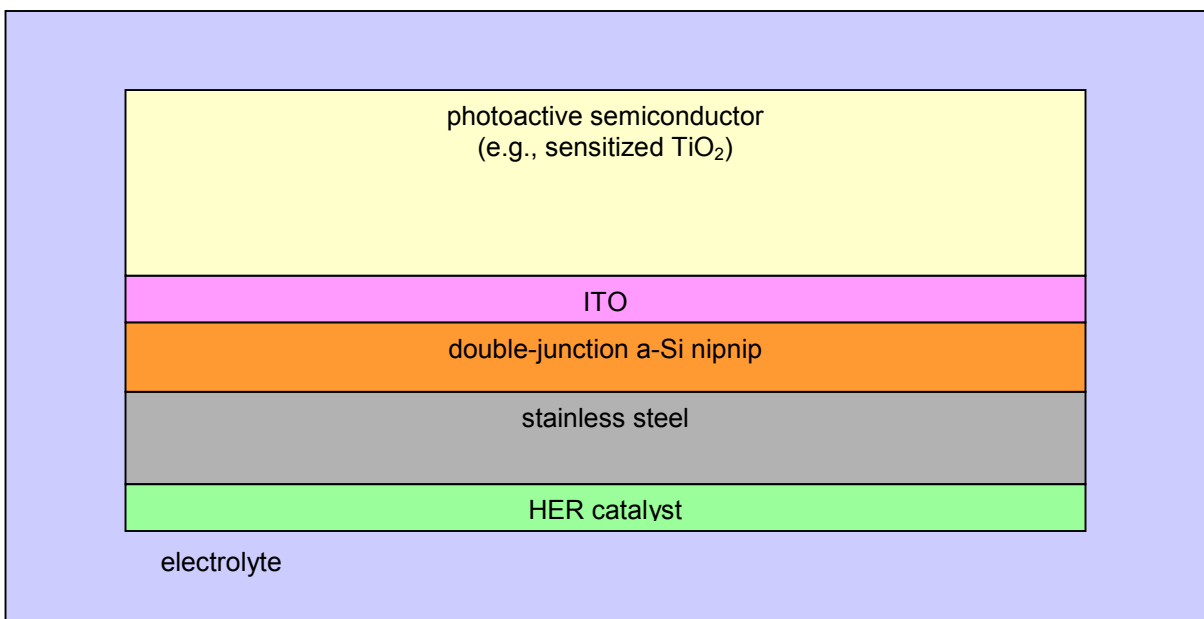


Figure 4. Basic structure of the hybrid photoelectrode

Potential advantages of the hybrid design include simplified fabrication, greater stability, and lower cost. In addition, elimination of lateral current collection loss and reduction of front-surface OER overpotential loss could lead to improved photoelectrode performance. A more detailed description of this new design and its features is presented in later sections.

Goals and Objectives

The ultimate goal of this research has been the development of a high-efficiency, low-cost photoelectrochemical process for the direct production of hydrogen. Over the course of our PEC development work, we have developed integrated electrochemical/optical models to identify materials and multijunction electrode designs with potential for high efficiency, and have fabricated and tested photoelectrodes engineered to maximize efficiency and stability for given material properties.

The primary goals for this past year have included:

- The development and evaluation of multijunction a-Si based photoelectrodes based on the design illustrated in Figure 3a, optimized for operation in KOH.
- The development and evaluation of mechanically interconnected, high-efficiency, CIGS-based photoelectrodes, based on the design depicted in Figure 3b.
- The design of advanced photoelectrode designs using new materials or configurations (such as the hybrid photoelectrode shown in Figure 4) to obtain enhanced stability and efficiency, and to minimize cost.

Progress in achieving these goals is described in the Progress Status section below.

Progress Status

Under previous contracts at UH, the efforts focused on demonstrating the feasibility of the photoelectrochemical approach using thin-film solar cell materials. Optimizing the optoelectronic performance and chemical stability of each of the thin-film components of the photoelectrode, including semiconductor layers, the hydrogen and oxygen catalysts, and transparent contact and protective films, was a significant part of the effort. After the successful demonstration of the proof-of-concept using separated anode/cathode configurations (Rocheleau et al. 1998), the primary goal became the development of photoelectrodes configurations based on planar fabrication of thin-films onto inexpensive substrates without external interconnects. In this report, photoelectrodes without anode/cathode interconnects are referred to as “integrated photoelectrodes.”

Activities during Phase I of this contract have focused on fabricating and testing proof-of-concept photoelectrodes using both a-Si and CIGS thin-film solar cells, and the development of the conceptual design for a new hybrid configuration in which the outermost junction is a true electrochemical junction. Specific tasks have included:

- 1) Model Development: Continued upgrade of the integrated electrical/optical model for PEC analysis.
- 2) Materials Research: Continued optimization of the catalyst and protective coatings for use in the a-Si and CIGS integrated photoelectrodes.
- 3) Amorphous Silicon Photoelectrodes: Fabrication and outdoor testing of triple-junction a-Si photoelectrode structures based on the design shown in Figure 3a.
- 4) CIS/CIGS Photoelectrodes: Construction of a mechanically interconnected CIGS photoelectrode device approximating the more complex structure of Figure 3b.
- 5) Advanced Photoelectrodes: Formulation of the new hybrid design, as shown in Figure 4, with a specific implementation incorporating a-Si solid-state junctions and an outer layer of a material such as dye-sensitized TiO₂ or WO₃ to form the PEC junction.

The progress status of tasks 1 through 5 is discussed below.

Integrated Model Development

For several years, we have been developing electrical and optical models for design and optimization of hydrogen photoelectrodes. The electrical model, based on an equivalent circuit model, was developed at UH to simulate solid-state junction performance in conjunction with electrochemical loads (Rocheleau and Miller 1997). The optical model, based on the commercially available analysis package, *Essential Macleod*, is used to derive the absorption profiles in the multijunction structures of interest. To date, the electrical and optical components

are independently operational, but not fully integrated into a single user-friendly package. Integrating the models, as well as upgrading them to analyze the advanced hybrid photoelectrode design, are efforts that are currently underway.

Materials Research

This year, we continued research to optimize component films necessary to the integrated photoelectrode structures under investigation. Significant progress was made in developing improved catalyst films, in the deposition of high-efficiency a-Si and CIGS cells onto metallic substrates (IEC at the University of Delaware and University of Toledo, respectively), in the optimization of indium-tin oxide (ITO) films for transparent contact layers, and in the use of a highly transparent and stable polymer adhesive as a photoelectrode encapsulant.

In recent years, we have relied on cobalt-molybdenum (CoMo) thin-films sputter-deposited from an alloy target as the HER catalyst in our photoelectrode structures. These films have demonstrated good HER activity and excellent long-term stability over a three-year continuous operation test (Rocheleau et al. 1998). One major drawback has been the difficulty obtaining hot-pressed CoMo alloy targets from the vendors. This year, we spent considerable effort investigating alternative mixed-metal films as the HER catalyst, including nickel-molybdenum (NiMo), nickel-iron (NiFe), and cobalt-nickel (CoNi). Each of these materials was sputter-deposited from alloy targets. Target compositions of 50:50 for the NiMo and CoNi, and 81:19 for the NiFe permalloy were evaluated.

Figure 5 shows voltammetry scans of the three new catalyst materials, with traces for Ni and CoMo included for reference. It is clear that all the alloy films exhibit lower hydrogen overpotentials compared to the plain nickel substrate. Of the materials tested, the NiMo films exhibited the lowest hydrogen overpotentials, slightly outperforming CoMo. Figure 6 shows SEM scans of as-deposited CoMo, NiMo, CoNi, and NiFe films taken at a magnification of 80,000x. Clear differences in the surface morphologies of the four films are evident. In comparison to the CoNi and NiFe films, CoMo and NiMo exhibit a finer grain structure, which is possibly a factor in the lower overpotentials in these materials. Based on results from these experiments, the NiMo alloy films were selected as a lower-cost replacement for CoMo in our photoelectrode designs. Long-term stability tests are in progress to further assess the applicability of these films.

In addition to the HER catalyst development, we also made further improvements to the reactively sputtered Fe:NiOx films developed at UH as an OER catalyst (Miller and Rocheleau 1997). Specifically, the effects of oxygen partial pressure in the reactive sputter gas on OER activity were explored. Figure 7 shows current-overpotential curves for three films sputtered from the same NiFe permalloy target, but with slightly different oxygen partial pressures in the argon-oxygen sputtering ambient. Film 2 (with 14% oxygen content) exhibits a clear improvement in OER activity compared to Film 1 (previous standard conditions, with 21% oxygen) and Film 3 (17.5% oxygen), indicating the existence of a local maxima for catalytic activity as a function of oxygen partial pressure in the processing environment. Further investigation of this observed effect is in progress.

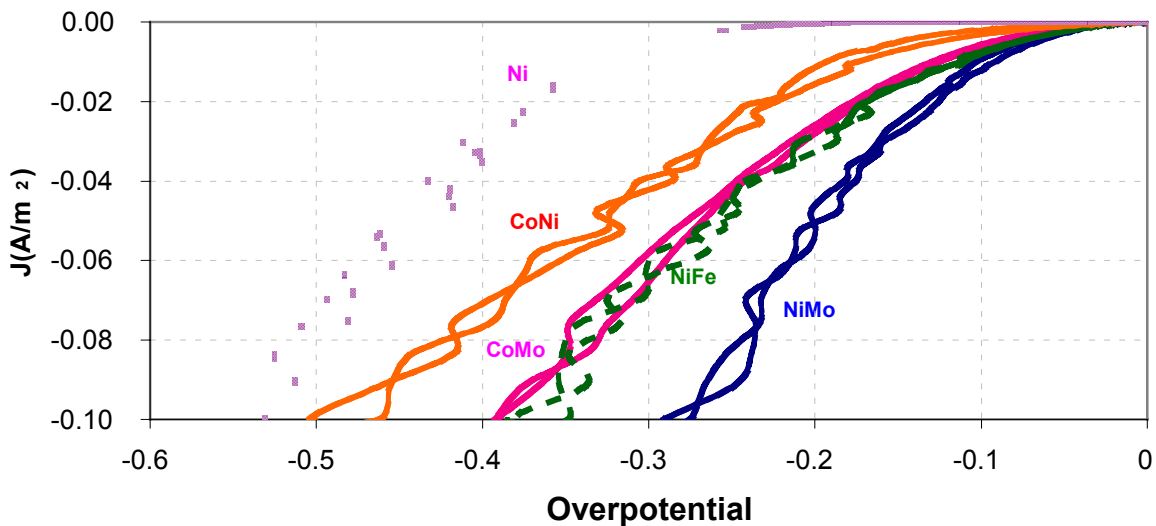


Figure 5. Comparison of HER catalyst film activities

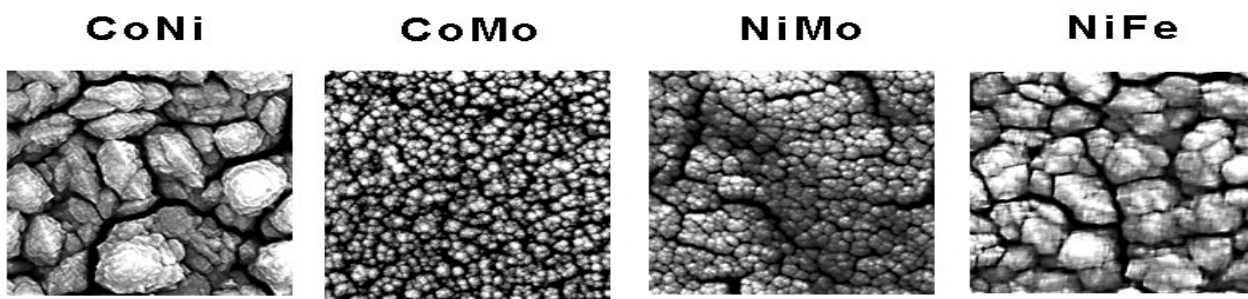


Figure 6. Surface morphology of HER catalyst films

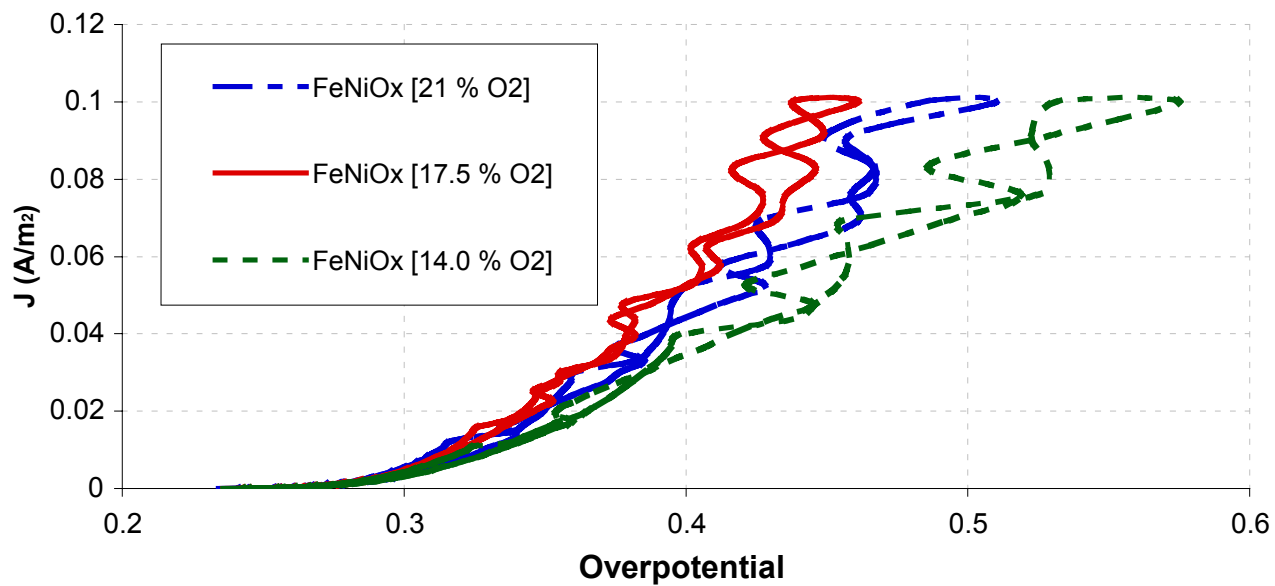


Figure 7. Comparison of Fe:NiOx catalyst film activities

Last year, we reported efforts to fabricate integrated photoelectrodes using triple-junction amorphous silicon cells. These structures used sputter-deposited ITO (top contact layer), CoMo (HER catalyst), Fe:NiOx (OER catalyst), and TiO₂ (encapsulant). Apparent shorting at device edges and at TiO₂ surfaces was observed in these devices. This year, we modified the a-Si photoelectrode design to eliminate this problem. The TiO₂ was replaced with a highly stable transparent polymer as the encapsulant. Other changes included improved a-Si cells, use of CoMo in place of NiMo, and improved chemical resistance of the ITO.

The high-efficiency, triple-junction, amorphous silicon solar cells used in this work have been provided by Xunming Deng of the University of Toledo. This year, Toledo researchers successfully demonstrated photovoltaic efficiencies up to 12.7% in their triple-junction cells deposited onto stainless steel (SS) foil. This is the highest efficiency to date for their laboratory (Wang et al. 2001). The quantum efficiency characterization for one of these devices is shown in Figure 8.

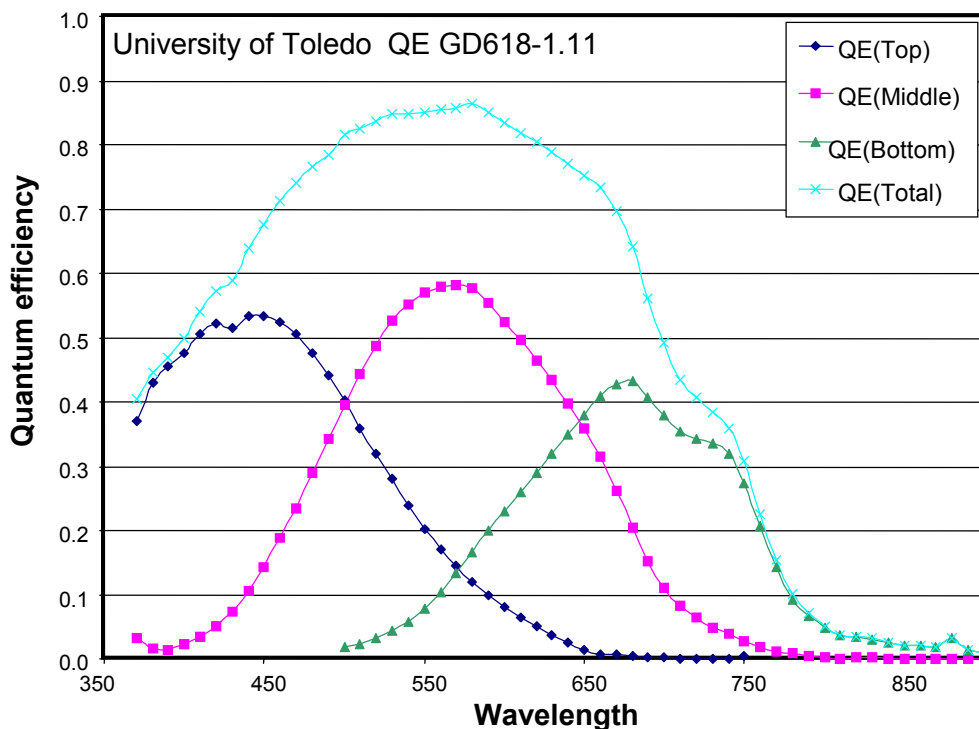


Figure 8. Quantum efficiency of high-performance a-Si triple-junction

For photoelectrode applications, the University of Toledo researchers deposited their new high-efficiency cells onto stainless steel foil pre-coated on the reverse side with NiMo HER catalyst. We subsequently completed the devices with ITO, Fe:NiOx OER catalyst, and encapsulant.

Corrosion-resistant ITO films deposited under process conditions that also yielded high conductivity and transparency were reported last year (Chin 2000). These ITO films were specifically developed for photoelectrode applications. Figure 9 shows the measured percentage

weight loss of ITO films deposited under various conditions (on stainless steel 302) as a function of time immersed in 1N KOH. A substantial fraction of the film mass was removed in the samples deposited at 100°C, while little to no change was observed in the films deposited at 200°C. This past year, we completed an analytical correlation between film structure and the observed ITO film properties. Figure 10 summarizes the measured the X-ray diffraction (XRD) parameters, normalized counts per second, and grain size at primary crystal orientations, for the different deposition conditions. Of these samples, film sample 2 (deposited at 200°C and with 0.125% oxygen in the sputtering ambient) was the most resistant to corrosion, but also exhibited the best transparency and conductivity. The optimization of these three properties is well-correlated with enhanced film grain-size and preferred <222> orientation.

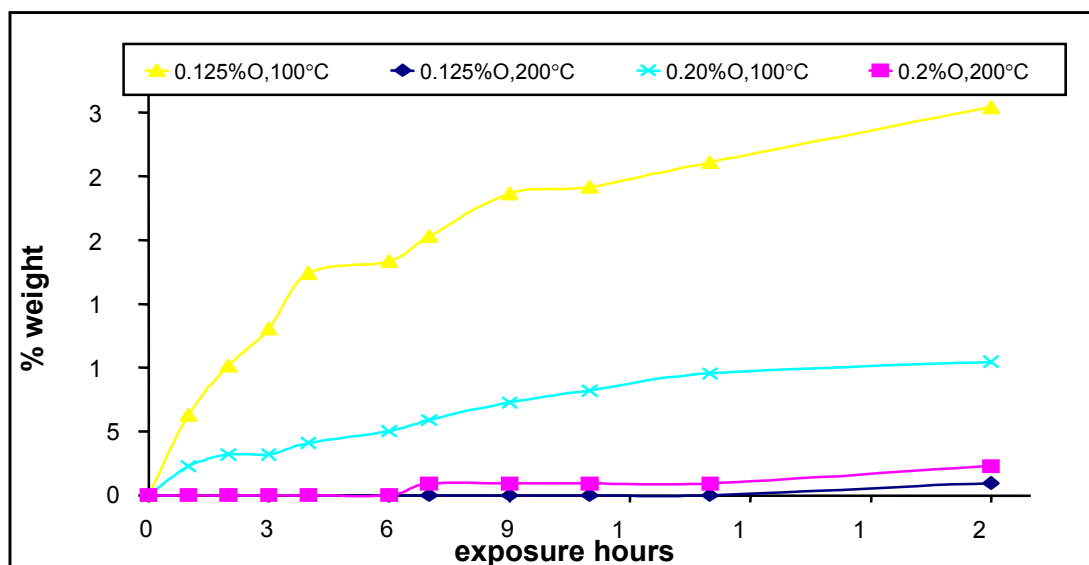


Figure 9. Comparison of ITO film stability in 1N KOH

Results of initial efforts to develop a chemically stable integrated photoelectrode were reported at the FY 2000 Program Review Meeting (Miller and Rocheleau 2000). These devices were fabricated using sputter-deposited TiO₂ as the transparent encapsulant, selected based on its reported compatibility in KOH and results from initial stability experiments. During testing, however, it was evident the TiO₂ surfaces were being driven to potential levels sufficient to drive oxygen evolution and other active corrosion reactions. This year, we conducted a thorough search to find a replacement for TiO₂ as the protective window layer. Of several materials tested, the best results were obtained using the Mater Bond polymer system EP39-2, a transparent epoxy polymer, designed specifically for potting optoelectronic devices. This material was found to have excellent optical properties, as shown in the transmission and reflectance plots in Figure 11, and good stability in KOH. In addition, the material was compatible with traditional screen-printing techniques, which could be readily applied to the planar photoelectrode structure.

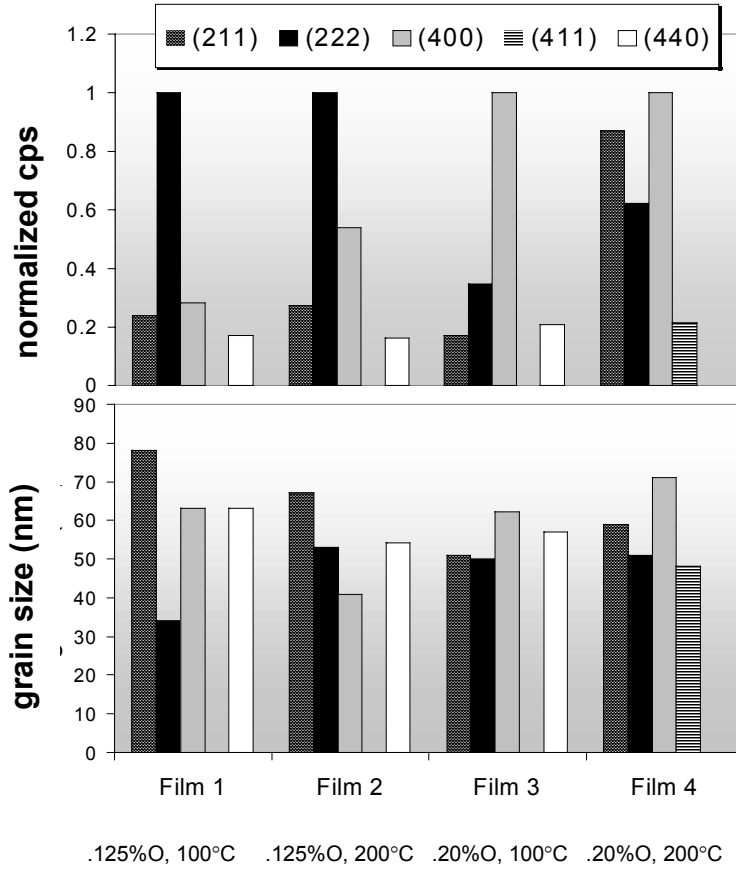


Figure 10. Crystallography of ITO films

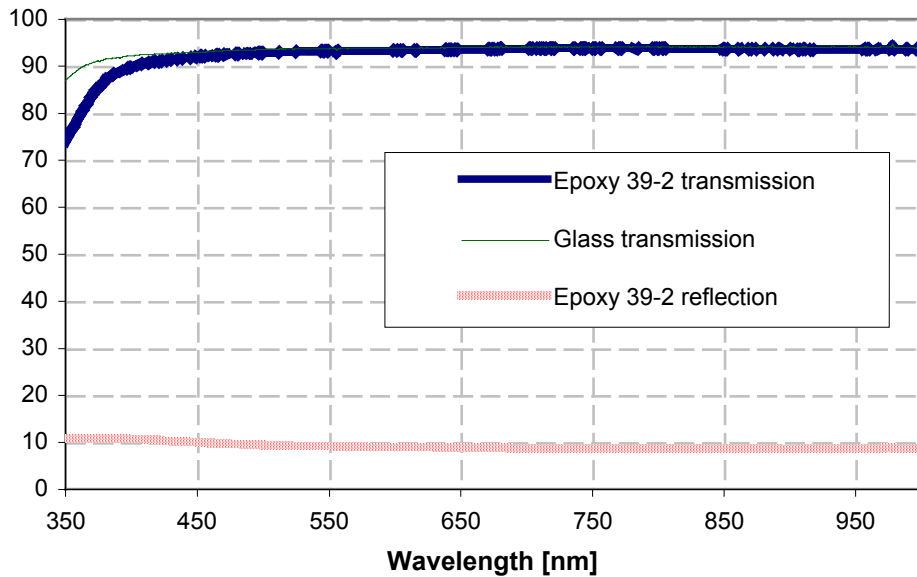


Figure 11. Optical properties of polymer encapsulation film

Amorphous Silicon Photoelectrode Development

A key milestone for this past year was the fabrication and testing of integrated amorphous silicon photoelectrodes. The a-Si photoelectrode structure was modified from last year's design to incorporate the University of Toledo's high-efficiency cells, NiMo (instead of CoMo) catalyst, and EP39-2 polymer (instead of TiO₂) encapsulant. The processing sequence for fabricating these devices, the status of a prototype reactor for photoelectrode testing, and results from preliminary testing of the fabricated photoelectrode structures are discussed below.

Photoelectrode Fabrication

The triple-junction amorphous silicon photoelectrode structure shown schematically in Figure 3a was fabricated onto 1" x 1" stainless steel squares using the following procedure:

- 1) Sputter-deposit a NiMo film (about 1 μ m thick) on back of cleaned stainless steel (SS) substrate.
- 2) Deposit triple-junction a-Si nipnip (by PECVD at University of Toledo) on front SS surface.
- 3) Sputter-deposit a thin SiO₂ insulation layer (about 500 \AA thick) through mask over approximately half the Si area.
- 4) Sputter-deposit the ITO top contact film (about 1200 \AA thick) through a shadow mask over entire active area.
- 5) Sputter-deposit a NiFe/Fe:NiOx film (about 1 μ m thick) through mask on front in-line with the SiO₂ insulator.
- 6) Screen-print polymer encapsulant (about 3 μ m thick) over uncatalyzed portion of the active Si.

The devices were cleaned using methanol and DI (deionized) water between processing steps. In total, 36 photoelectrodes were fabricated using a-Si cells from four separate PECVD runs (nine substrates per run). Completed devices are shown in Figure 12.

Small-Scale Reactor

At the FY 2000 Program Review, we reported the design of a small-scale hydrogen photoreactor with gas collection and solar-tracking features intended for photoelectrode testing. This year, we completed the construction of the reactor, shown in Figure 13. The calibrated burettes mounted at the top of the reactor are connected to gas collection ports for hydrogen and oxygen collection. The gases are generated at opposite sides of the photoelectrodes. The reactor body is mounted onto the tripod using an equatorial-mount to facilitate solar tracking during outdoor tests.

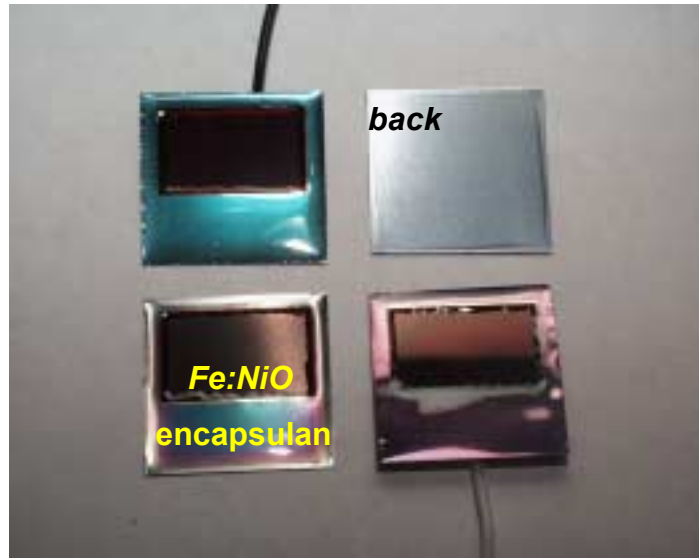


Figure 12. Completed a-Si test photoelectrode



Figure 13. Hydrogen photoreactor for photoelectrode tests

Initial testing was performed using the small-scale reactor; however, characterization of the solar-to-hydrogen efficiency using gas evolution measurements was limited by incomplete gas collection. At the relatively low rates achieved in these tests, bubbles became trapped in the narrow pathway leading to the burettes. Hydrogen efficiencies were obtained by modifying some of the fabricated photoelectrodes, as described below, to allow direct measurement of the current passing between the anode and cathode. Plans have been developed to modify the reactor to allow more efficient gas collection.

Photoelectrode Testing

The a-Si photoelectrodes were modified, as shown in Figure 14, by attaching electrical leads between the anode and cathode sides of the electrode. The electrical leads were attached at the back HER surface, which was then potted over with an insulating polymer layer to prevent any hydrogen evolution from the surface. This lead was then connected through an ammeter to a secondary HER electrode placed behind the photoelectrode. This allowed measurement of hydrogen photocurrent for calculation of hydrogen efficiency.

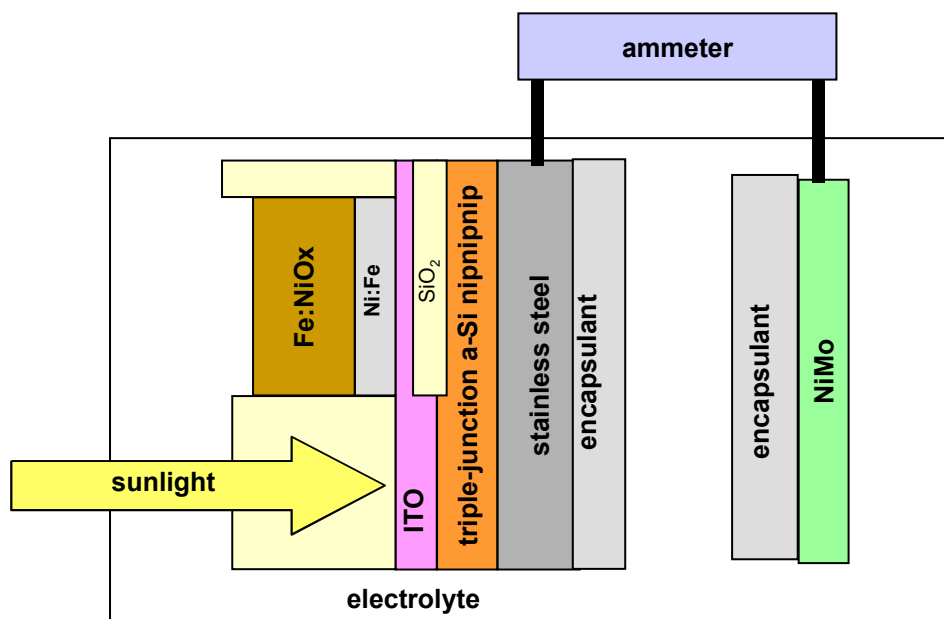


Figure 14. Photoelectrode structure modified for efficiency measurements

Of the 36 photoelectrodes that were fabricated, 12 were modified per Figure 14 for efficiency measurements. These 12 were tested in 1N KOH under simulated solar illumination (ELH lamps) and outdoors under sunlight. In all 12 devices, gas bubbles were observed evolving from the catalyst surfaces. Figure 15 is a photograph of one of the photoelectrodes under test. Unfortunately, significant shortcomings in both efficiency and stability were observed over the course of these tests.

The triple-junction a-Si cells fabricated at the University of Toledo exhibited as-deposited photovoltaic efficiencies up to 12.7% and open-circuit voltages up to 2.3 V. Based on these parameters, our models indicated solar-to-hydrogen efficiencies ranging from 6% to 8% were expected. The loss from the electrical efficiency and range is based on lost area and estimated ranges for optical, electrical, and electrochemical losses. However, only 3 of the 12 devices tested under outdoor conditions demonstrated hydrogen efficiencies exceeding 1%, and the highest observed efficiency was 2.5%. This disappointing result was later traced to degradation in the solar cell performance as a result of the processing steps used in photoelectrode fabrication.

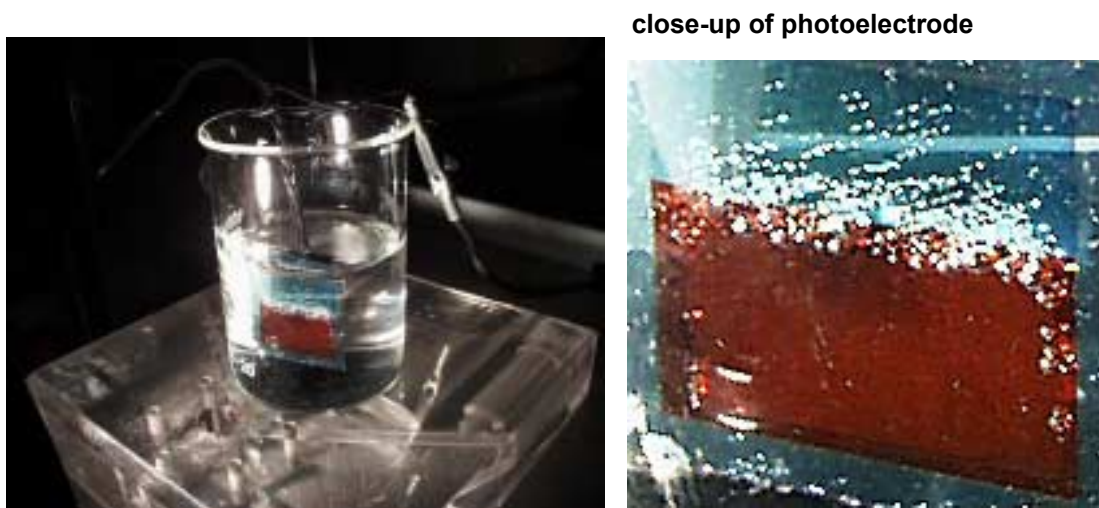


Figure 15. Gas evolution at a-Si photoelectrode surface

When the photoelectrodes were tested as solar cells in air, the open-circuit voltage in all devices was found to have degraded to less than 1.5 V (from initial values around 2.2 V to 2.3 V). In a few cases, voltages as low as 0.3 V were measured. This level of degradation in the photovoltaic performance provided sufficient explanation for the low solar-to-hydrogen efficiencies. After in-depth discussions with the University of Toledo, we concluded that the triple-junction cells were being damaged over the course of fabricating them into photoelectrodes, despite the fact that standard planar fabrication techniques were being employed. Our experiments in previous years to modify solar cells into photoelectrodes did not result in such severe solar cell degradation. There is evidence that the processing procedures used to produce the high-efficiency 12.7% solar cells also result in devices that were more susceptible to handling damage. The tradeoff between efficiency and yield is not uncommon in solid-state device research. It was agreed that near-term follow-up work to fabricate hydrogen photoelectrodes from a-Si cells should utilize more established triple-junction recipes giving slightly lower PV efficiencies (10-11%) but higher yield.

In addition to the lower than expected efficiencies, an unanticipated mode of instability was observed in some of the photoelectrodes during testing. In half of the modified photoelectrodes tested in KOH under outdoor conditions, the OER catalyst layer on the front surface separated from the underlying layers after approximately 30 minutes of operation. Although the catalyst films did not appear to have dissolved or be completely removed, the appearance of “wrinkles” in the OER catalyst film surfaces and a corresponding drop in performance made it clear that they were no longer effectively connected with the rest of the device. This effect did not appear in the remaining 6 test devices, even after 4 hours of testing.

Film separation in planar devices is often an indication of adherence problems due to inadequate surface preparation prior to deposition. The separation effect was not observed in the long-term stability tests in KOH of the Fe:NiOx catalyst material deposited on nickel foil (Rocheleau et al. 1998). The nickel foil substrates, however, were thoroughly cleaned and etched in HCl before deposition of the oxide film, whereas only methanol/DI water rinses were used between

layering steps in the photoelectrodes. The acid etch was not included to avoid damaging underlying photoelectrode component layers. Clearly, an improved method of surface preparation for the Fe:NiOx sputtering step needs to be devised to eliminate the film adhesion problem. One effective approach that has been employed with success in other labs (Inal 1997), but would require some hardware modifications to our sputtering system at UH, involves sputter-etching the surface in a low-vacuum argon ambient immediately prior to film deposition.

CIS/CIGS Photoelectrode Development

Another key milestone for this year was completion of our preliminary investigation of CIGS photoelectrodes, including corrosion testing of CIS/CIGS materials, and fabrication of a mechanically interconnected test structure simulating the side-by-side series connected configuration. Results in these areas are discussed below.

Corrosion Tests

The basic structure of a CIS or CIGS photoelectrode in the side-by-side series connected configuration was shown in Figure 3b. Although the CIS or CIGS material in this arrangement is completely encapsulated and has no direct contact with the electrolyte, long life in a commercial unit is expected to be enhanced by corrosion resistance in all constituent films. Preliminary testing of CIS films deposited on molybdenum foil indicated reasonably good corrosion resistance in KOH electrolyte. Figure 16 shows SEM images of the CIS surface taken before and after 48 hours of immersion in 1N KOH. Although sparsely scattered vacancies appear in the film grain structure after KOH exposure, the basic surface morphology remains unchanged.

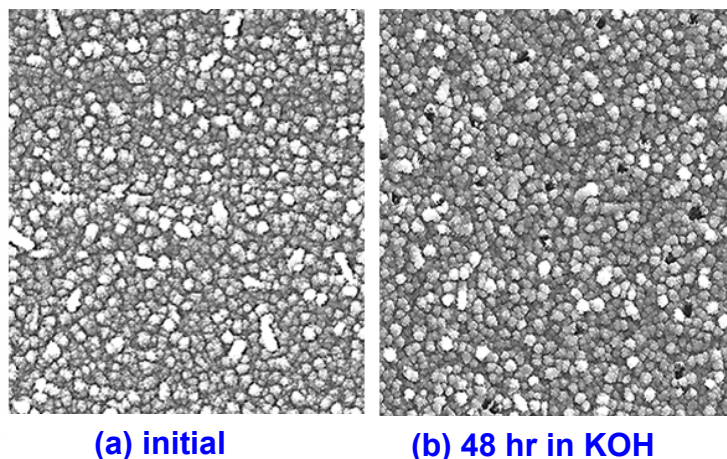


Figure 16. SEM images of CIS films before and after 48-hour KOH exposure

Completed CIGS diodes deposited on molybdenum-coated glass substrates were fabricated by the Institute for Energy Conversion (IEC) at the University of Delaware for evaluation in our photoelectrode development program. Attempts to evaluate the stability of these devices in

KOH were hampered by tendencies of the films to separate from the substrates, an effect similar to that seen in the OER catalyst films in the a-Si photoelectrodes. The CIGS diodes tended to peel away from the substrates after several minutes immersed in 1N KOH, but did not appear to be dissolved. The substrate adhesion problem needs to be addressed before the corrosion resistance of the diodes can be properly evaluated.

Photoelectrode Fabrication

The integrated multijunction CIGS photoelectrode in the side-by-side configuration of Figure 3b is clearly more complex than the corresponding monolithic structure in Figure 3a for the a-Si devices. Despite the complexity, industrial processes have been developed for production of similar structures for PV modules (Gay 1998). A commercially available PV module produced by Siemens Solar Industries that is so configured is shown in Figure 17.

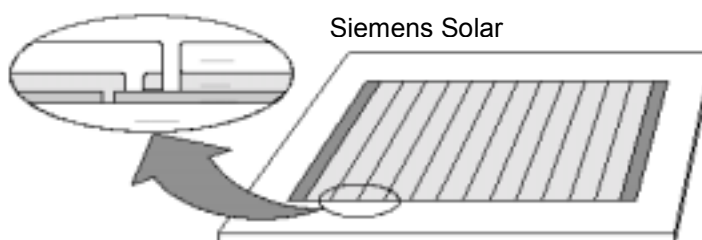


Figure 17. PV module with side-by-side CIS cells

Since the techniques for side-by-side cell fabrication are currently beyond the scope of our laboratory capabilities at UH, our initial attempts to explore the CIGS photoelectrode used mechanically interconnected CIGS devices as shown in Figure 18.

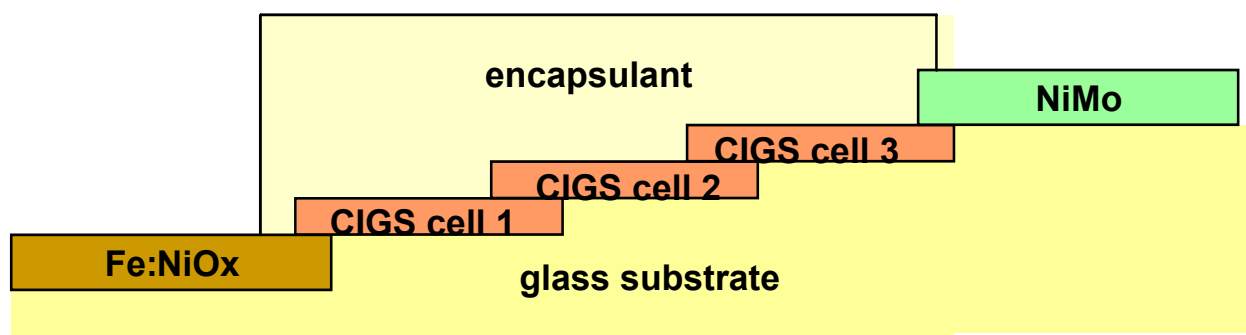


Figure 18. Mechanically stacked configuration for CIGS test photoelectrode

CIGS diodes with as-deposited PV efficiencies of 13% and open-circuit voltages of 0.6 V were deposited onto 1” square molybdenum foil substrates by the IEC in Delaware. These samples were cut and stacked along with NiMo and Fe:NiOx coated nickel foil pieces in the configuration shown in Figure 18. Conductive epoxy was used to interconnect front-to-back of successive layers, and the EP39-2 polymer was used as the transparent encapsulant over the photoactive region. The resulting test device is pictured in Figure 19.

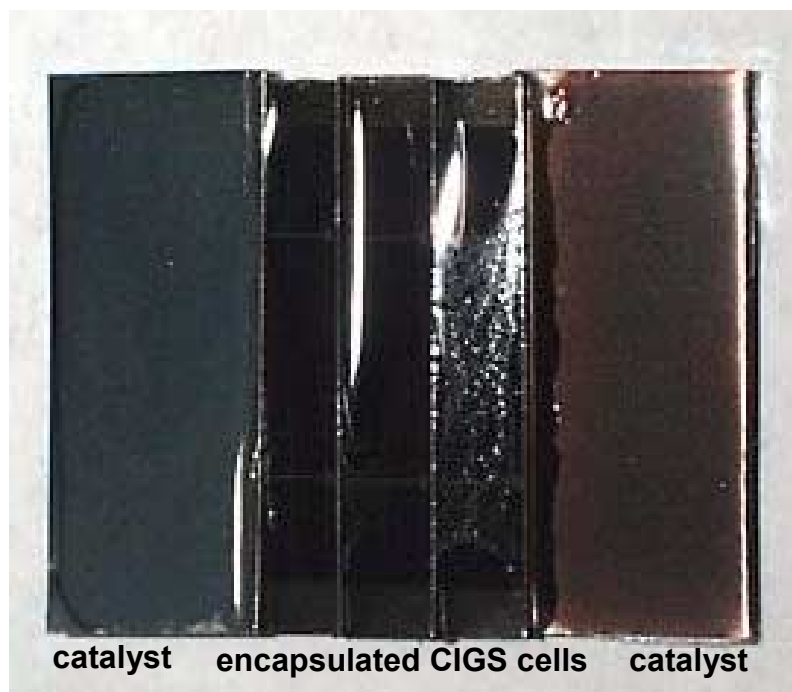


Figure 19. Mechanically stacked CIGS test device

Prior to testing in KOH, the assembled CIGS device was tested for PV properties under sunlight. It was found that the expected open-circuit voltage of 1.8 V for the triple-junction had been reduced to below 0.9 V after photoelectrode assembly. Further investigation revealed that the process of mechanically cutting the devices degraded the open-circuit voltages by about a factor of 2, consistent with the observed result in the triple-junction. Since the voltage had dropped below the levels necessary for water-splitting, the device was not tested as a photoelectrode. Alternate methods of fabricating CIGS photoelectrode test devices that do not compromise the CIGS diodes are being explored.

Advanced Photoelectrode Designs

A third key milestone this year was the conceptual design development for the hybrid solid-state/PEC photoelectrode shown in Figure 4. This design was motivated both by recent advances in semiconductor materials (such as dye-sensitized TiO_2 and WO_3) for photoelectrochemical applications (Graetzel 2000; Swiss Federal Institute of Technology 1996), and by our models. In the high-efficiency, triple-junction, amorphous silicon solar cells deposited by the University of Toledo for our photoelectrode research this year, the top “nip” junction was designed to absorb most strongly in the 350-500 nm range, as was shown in the quantum efficiency curves in Figure 8. In principle, this top cell could be replaced by a PEC junction with strong absorption in a similar range to form a water-splitting photoelectrode for hydrogen production. As was shown in Figure 4, this hybrid photoelectrode could be fabricated on SS with the back surface catalyzed for the hydrogen evolution reaction (HER), and the front surface deposited with a double-junction “nipnip” topped with an ITO/photoactive-semiconductor layer. The semiconductor top

layer forms a PEC junction in electrolyte, and must have appropriate conduction band alignment for the oxygen evolution reaction (OER). In addition, the PEC junction must be strongly absorbing in the 350-500 nm region for current matching to the underlying solid-state junctions. Research advances in dye-sensitized TiO₂ and tungsten trioxide (WO₃) indicate that these may be suitable candidate materials for the hybrid photoelectrode. For example, Figure 20 shows the quantum efficiencies of TiO₂ PEC junctions as a function of sensitizing dye (Swiss Federal Institute of Technology 1996). The junction sensitized with the RuL₃ dye exhibits peak absorption near 500 nm, consistent with the requirements for the hybrid photoelectrode.

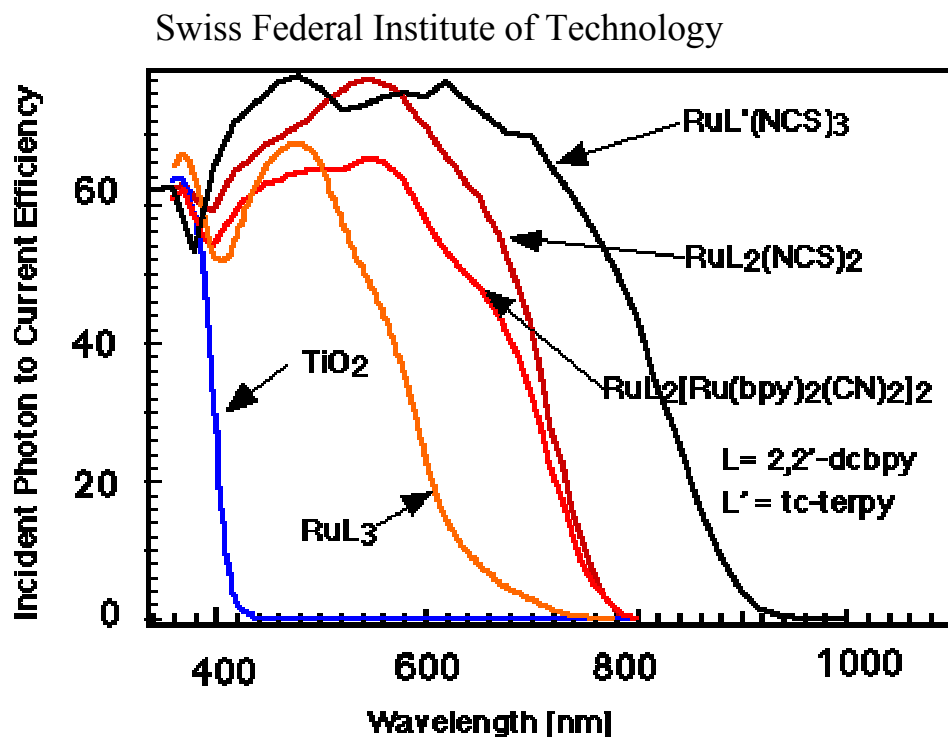


Figure 20. Quantum efficiencies of dye-sensitized TiO₂ PEC junctions

Important issues in development of the hybrid photoelectrode design include the voltage and current-matching requirements in the solid-state and electrochemical junctions. Once updated with material properties of the TiO₂/WO₃, our integrated models incorporating electrical, electrochemical, and optical analyses will be a powerful tool in this development effort. Material optimization and electrolyte selection for stable and efficient PEC interfaces are also critical to the hybrid photoelectrode design.

Summary

This year, we made significant progress in three areas of research: 1) the optimization of constituent films for integrated multijunction photoelectrodes based on amorphous silicon and CIGS semiconductors; 2) the fabrication of test devices for the a-Si and CIGS integrated photoelectrode configurations; and 3) the design of a hybrid solid-state/PEC photoelectrode design.

Progress in materials optimization was made on several fronts. High-efficiency a-Si triple-junction devices (12.7%) were successfully deposited by the University of Toledo on stainless steel foil precoated with HER catalysts. CIGS devices with efficiencies exceeding 13% were deposited by the IEC, University of Delaware, on molybdenum foil, also compatible with photoelectrode designs. At UH, high-activity NiMo and Fe:NiOx film catalysts were developed to maximize solar-to-hydrogen efficiencies in the photoelectrode configurations. Indium-tin-oxide (ITO) used as transparent contact films in all designs was further optimized for corrosion resistance. Several candidate materials for photoelectrode encapsulation were evaluated for transparency, adhesion, and chemical stability, with the EP39-2 polymer adhesive demonstrating the best overall performance.

Using results from the material optimization effort, proof-of-concept test devices were fabricated for both a-Si and CIGS integrated multijunction photoelectrodes. Test devices for the amorphous silicon, monolithically stacked, integrated photoelectrode incorporated the high-efficiency a-Si material from Toledo, and test devices for the CIGS side-by-side integrated photoelectrode used the high-efficiency CIGS material from Delaware.

Unfortunately, there was limited success in test results using the integrated photoelectrodes. Although 6% to 8% solar-to-hydrogen efficiencies were expected for the a-Si photoelectrodes, the peak efficiency measured in outdoor tests was only 2.5%. We attribute the difference to severe degradation in the triple-junction a-Si PV cells as a result of handling and further processing steps for photoelectrode fabrication. Fe:NiOx film separation from the underlying layers was also observed in about half the a-Si photoelectrodes tested. We attribute this problem to inadequate cleaning between processing steps. As with the a-Si test devices, manual cutting of the CIGS diodes deposited on molybdenum foil also resulted in severe degradation in PV performance. In the CIGS photoelectrodes, the open-circuit diode voltages were reduced below the point where water-splitting is possible. Alternative methods for forming the side-by-side junctions for successful demonstration of the CIGS photoelectrode concept are being investigated.

Based on reported advances in photoactive semiconductor materials, we applied our integrated electronic/optical/electrochemical models in developing the conceptual design for a hybrid solid-state/PEC photoelectrode. The initial design incorporates a double-junction a-Si solid-state device coated with a thick protective transparent material such as dye-sensitized TiO₂ or WO₃, which also forms a third junction, an electrochemical junction with the electrolyte. With proper design of voltage and current characteristics, the hybrid triple-junction is expected to split water with good efficiency and improved stability.

Conclusions and Plans

As a result of this year's work, we have arrived at some fundamental conclusions regarding the relative advantages and disadvantages of the various integrated photoelectrode configurations under consideration. Based on these conclusions, we have reprioritized our efforts and formulated specific plans for future work, emphasizing the CIGS side-by-side configuration and the hybrid configuration.

The integrated solid-state, triple-junction photoelectrode designs, either with amorphous silicon or CIGS, offer promising efficiency and stability, but there are also inherent disadvantages. First, electronic losses due to the lateral collection of current through the front-surface ITO are inevitable. Second, the lateral design with separated photoactive and catalyzed areas on the front surface complicates commercial-scale manufacture and increases the potential for long-term degradation along material seams exposed to electrolyte. In the a-Si version, an additional loss term is the high effective OER overpotential due to the limited Fe:NiO_x area on the front surface. The integrated triple-junction a-Si photoelectrode, using state-of-the-art a-Si processing to obtain PV efficiencies around 13%, is expected to split water with solar-to-hydrogen efficiencies between 6% and 8%, based on integrated models including all losses.

On the other hand, CIGS diodes using state-of-the-art processing can have PV efficiencies exceeding 18% (Tuttle et al. 1995). In addition, the catalyst at the front surface is the HER catalyst, which, although still limited by area, has inherently lower overpotential. Solar-to-hydrogen efficiencies exceeding 10% are readily achievable using the CIGS devices. There are added complexities in the fabrication of the side-by-side CIGS photoelectrodes, which require further development. However, large-scale manufacturing processes for such a configuration are already in place in the PV industry (Gay 1998). The disadvantages in complexity are outweighed by the potential for higher efficiency in the integrated CIGS photoelectrodes. We have therefore decided to emphasize development of these devices over the triple-junction a-Si counterparts.

The advanced hybrid photoelectrode offers advantages over both the a-Si and CIGS solid-state designs. The lateral current collection loss is eliminated, the front surface overpotential loss is reduced, and the geometry is greatly simplified, easing fabrication. In addition, greater long-term stability is expected, a result of the thick uniform outer layer of TiO₂ or WO₃. The simplified fabrication and inherently low cost of the oxide junction could significantly lower system cost. We have therefore concluded that the primary emphasis needs to be placed on developing the hybrid photoelectrode design to take advantage of the inherent benefits.

Based on our conclusions, we propose the following plan for future work in photoelectrode development:

- 1) Triple-junction amorphous silicon integrated photoelectrodes:
 - Complete testing of photoelectrodes in process for publication.
- 2) Triple-junction CIGS integrated photoelectrodes:
 - Continue development and optimization of the side-by-side design.
 - Identify potential partners to produce side-by-side CIGS test structures.
 - Fabricate and test photoelectrodes based on industry partner's structures.

3) Hybrid solid-state/PEC photoelectrodes:

- Establish partnerships with research organizations developing dye-sensitized TiO₂ and WO₃ for photoelectrochemical applications.
- Obtain current optical and electrochemical data for sensitized TiO₂ and WO₃.
- Adapt integrated model to design hybrid systems with optimized efficiencies.
- Fabricate test devices using a-Si solid-state double-junction and a dye-sensitized TiO₂ or WO₃ PEC junction (with ITO interconnect layer).

We plan to continue our cooperative partnerships with the University of Toledo and the IEC of the University of Delaware to obtain high-efficiency a-Si and CIGS devices. Additional partnerships will be sought in both academia and industry for the fabrication of side-by-side CIGS junctions, and for the development of sensitized TiO₂ and WO₃. Through participation this year in the 2000 IEA meeting of Annex 14 on Photoelectrochemical Hydrogen Production, we have already established important contacts with members of the Swiss-Federal Institute of Technology and with the Centro de Investigacion en Energia in Mexico.

Acknowledgments

We wish to thank the U.S. Department of Energy for support of this work under Grant DE-FG04-94AL85804. We also thank Xunming Deng of the University of Toledo for fabrication of amorphous silicon samples, and Bill Shafarman of the Institute for Energy Conversion at the University of Delaware for fabrication of CIGS samples.

References

- Chin, G. P. 2000. "Characterization and Optimization of Indium-Tin-Oxide (ITO) for Hydrogen Photoelectrodes." University of Hawaii Master's Thesis in Electrical Engineering.
- Gay, R. R. 1998. "Status and Prospects for CIS-Based Photovoltaics." Siemens Solar Industries White Paper <<http://www.siemenssolar.com/cis.pdf>>.
- Graetzel, M. 1999. "The Artificial Leaf, Bio-Mimetic Photocatalysis." *Catech*, 3(1):4-16.
- Inal, O. 1997. "Plasma-Assisted Processing of Materials." In *Proceedings of Ninth International Metallurgy and Materials Congress*, 377-382, Istanbul, Turkey.
- Miller, E. L., and R. E. Rocheleau. 1997. "Electrochemical Behavior of Reactively Sputtered Iron-doped Nickel Oxide." *Journal of the Electrochemical Society*, 144(9):3072-3077.
- Miller, E. L., and R. E. Rocheleau. 1997. "Electrochemical and Electrochromic Behavior of Reactively Sputtered Nickel Oxide." *Journal of the Electrochemical Society*, 144(6):1995-2003.

Miller, E. L. 1996. "A Study of the Electrochemical Behavior and Optical Properties of Reactively Sputtered Nickel Oxide and Nickel-Iron Oxide." University of Hawaii Ph.D. Dissertation in Electrical Engineering.

Miller, E. L., and R. E. Rocheleau. 1999. "Photoelectrochemical Hydrogen Production." In *Proceedings of the 1999 U.S. Department of Energy Hydrogen Program Annual Review Meeting*, Lakewood, CO: U.S. Department of Energy.

Miller, E. L., and R. E. Rocheleau. 2000. "Photoelectrochemical Hydrogen Production." In *Proceedings of the 2000 U.S. Department of Energy Hydrogen Program Annual Review Meeting*, San Ramon, CA: U.S. Department of Energy.

Rocheleau, R. E., and E. L. Miller. 1997. "Photoelectrochemical Production of Hydrogen: Engineering Loss Analysis." *International Journal of Hydrogen Energy*, 22(8):771-782.

Rocheleau, R. E., E. L. Miller, and A. Misra. 1997. "Photoelectrochemical Hydrogen Production." In *Proceedings of the 1997 U.S. Department of Energy Hydrogen Program Annual Review Meeting*, 345-358, Miami, FL: U.S. Department of Energy.

Rocheleau, R. E., E. L. Miller, and A. Misra. 1998. "High-Efficiency Photoelectrochemical Hydrogen Production Using Multijunction Amorphous Silicon Photoelectrodes." *Energy and Fuels* 12:3-10.

Rocheleau, R. E., and M. Vierthaler. 1994. "Optimization of Multijunction a-Si:H Solar Cells Using an Integrated Optical/Electrical Model." In *Proceedings of the 21st World Conference on Photovoltaic Energy Conversion*, 567-570. Honolulu HI: Institute for Electrical and Electronics Engineers.

Swiss Federal Institute of Technology. 1996. "Dye-Sensitized Solar Cells Based on Nanocrystalline Oxide Semiconductor Films." <<http://dcwww.evl.ch/icp/ICP-2/solarcellE.html>>.

Tuttle, J., et al. 1995. "Thin-Film Cu(In,Ga)Se₂ Materials and Devices: A Versatile Material for Flat Plate and Concentrator Photovoltaic Applications." *Society of Photo-Optical Instrumentation Engineers*, 2531:194-200.

Wang, W., X. B. Liao, S. Han, H. Povolny, X. B. Xiang, W. Du, and X. Deng. 2001. "Triple-Junction a-Si-Based Solar Cells with All Absorber Layers Deposited at the Edge of a-Si to μ -Si Transition." <<http://www.physics.utoledo.edu/~dengx/ref3.pdf>>.

HYDROGEN PRODUCTION THROUGH ELECTROLYSIS

**Robert J. Friedland
A. John Speranza
Proton Energy Systems, Inc.
Rocky Hill, CT 06067
May 2001**

Abstract

This paper describes the progress of cost reduction activities on a PEM electrolytic hydrogen generator series at Proton Energy Systems, Inc. (Proton) under cooperative agreement DE-FC36-98GO10341 with the Golden Field Office of the Department of Energy (DOE).

Proton's goal is to reduce the cost of our hydrogen generator family 50% by the end of 2002 and show evidence of further dramatic reductions in the years beyond. We will do this by focusing cost reduction efforts on three key elements of the electrolyzer: the electrolysis cell stack, the power conditioning and renewable interface, and the electrical controls and software. We will implement these reductions on our smaller (HOGEN[®] 40) electrolyzer first and expand those improvements to the larger electrolyzer towards the end of the program. All of the improvements undertaken on this program will benefit the full line of electrolyzers so that the cost of large and small energy storage applications will be reduced.

Proton has made significant progress in the last year on reducing the cost of many of the items in the hydrogen generator. As shown in Figure 1, cost reduction efforts are ahead of the schedule shown last year at the 2000 Annual Review. This is due to specific accomplishments on the program plus advances in other areas not covered in the program such as cost reductions in sheet metal and system assembly labor. It should be noted that all cost reduction projections from 2002 through 2005 are based on 500 units per year, and cost reduction projections beyond 2005 are based on 5000 units per year. These numbers are certainly not mass production numbers, but represent our projections of realistic numbers of units being sold into various markets. If one were to increase the numbers by a factor of ten or one hundred, then additional cost savings would certainly follow.

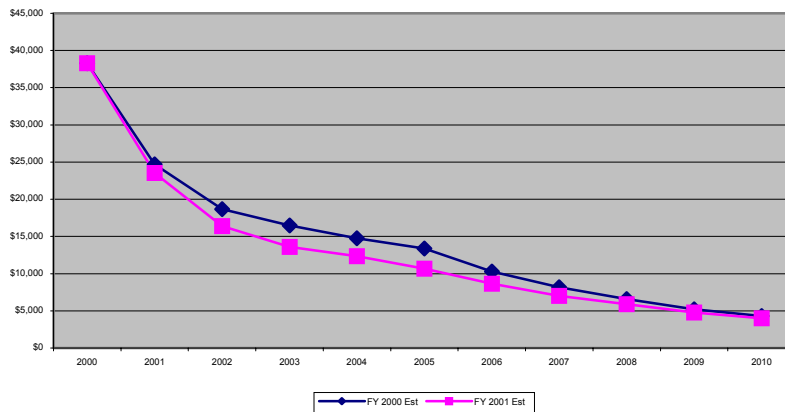


Figure 1 – HOGEN 40 (6kW) Ten Year Cost Projection

Background

Since the inception of the program on April 15, 1998, Proton has successfully demonstrated a fully functioning integrated renewable hydrogen utility system in conjunction with STM Power at Arizona Public Service (APS) in Tempe, AZ. This system coupled a solar concentrating dish, an external combustion engine and a Proton HOGEN[®] 300 hydrogen generator. The system was installed and operating from May of 1999 through the end of the Phase I program in December of 1999. A description of the technical performance of the system and a market assessment is detailed in the Final Technical Report¹.

The Phase I demonstration efforts and market evaluation showed that a hydrogen generator coupled with some form of renewable power and some form of energy conversion device has a distinct advantage over a battery system backing up the same renewable application. Proton cannot determine which renewable technology will win out in the end, nor predict which energy conversion device will be the most cost effective. However, it is clear that the link to these alternatives lies in the ability to convert excess renewable power into hydrogen and have the hydrogen available for conversion back to power, on demand.

To that end, Proton proposed a Phase II that moved away from the solar concentrating dish effort and focused on cost reduction efforts aimed at the hydrogen generator family. The HOGEN[®] 40 was chosen as the model for these cost reduction efforts even though the HOGEN[®] 300 series generator was used in the Phase I of the program. This was done for two reasons. First, the smaller size of the HOGEN[®] 40 generator made cost reduction activities and hardware purchases less costly, and thus enable a larger scope of effort and impact on return. Second, advances are scalable. In other words, improvements and cost reductions made on the HOGEN[®] 40 can be scaled to the larger HOGEN[®] 300 series generators rather easily and with less financial and programmatic risk. The specifics of this proposal were outlined in the Technical Paper submitted for last year's annual review².

Long Term Goals

All of Proton's cost reduction goals are focused on the long term markets associated with sustainable power. However, there are three other markets where the hydrogen generator technology fits well and where products can move into commercial applications while the renewable technologies mature, come down in cost and become more commercially available.

These markets, shown in Figure 2, all have unique attributes that require different cost structures and pricing to compete effectively. Based on these markets and Proton's internal projections for numbers of units, market share and earnings, a detailed cost reduction plan was developed. The plan, as it pertains to hydrogen generators, focused on the HOGEN[®] 40 and the HOGEN[®] 380 sized units with the near term emphasis on the HOGEN[®] 40.

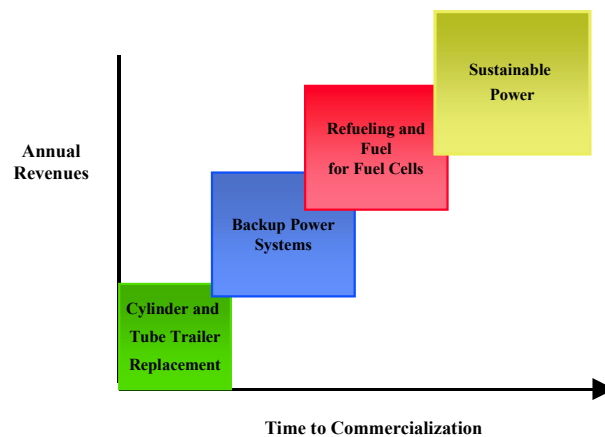


Figure 2 – Market Scope and Timing

The hydrogen program has a goal of hydrogen production at the lowest possible cost. To that end, Proton has established a cost goal of \$1000 per kW in the near term and \$500 per kW within ten years. The goal of \$1000 per kW is achieved rather quickly on the larger generator, but requires a few more years on the HOGEN[®] 40. This is not unexpected, as the economies of scale on the larger unit are much more favorable than on the smaller unit. Regardless, both units project costs that are comfortably under \$1000 per kW by 2010. The following sections will discuss in further detail the areas of cost reduction under the current agreement.

Technology and Product Impact of Program

The breadth of this program and the impact it has on the commercial rollout potential of PEM electrolysis is worth spending a little time discussing. All of the products and technology that Proton develops are born from PEM electrolysis. Advances in the core of that technology cross from one product to the next and impact all areas of our business. All of Proton's cost reduction goals are focused on the long term markets associated with sustainable power. However, there are other markets where the hydrogen generator technology fits well and where products can move into commercial applications while the renewable technologies mature, come down in cost and become more commercially available.

These markets all have unique attributes that require different cost structures and pricing to compete effectively. Based on these markets and Proton's internal projections for numbers of units, market share and earnings, a detailed cost reduction plan was developed. The plan, as it pertains to hydrogen generators, focused on the HOGEN[®] 40 and the HOGEN[®] 380 sized units with the near term emphasis on the HOGEN[®] 40. The cell stack sizes and system integration cost reduction tasks that are core to those products all transfer with minimal or no modifications to the other products.

When looking at the electrolysis cell stack, any changes to the cell materials of construction, the various catalyst loadings, or the stack embodiment, must be thoroughly tested to verify product integrity, safety and reliability. This type of testing can only be achieved through long duration testing of multiple configurations and designs. Regardless of the size of the cell itself, the improvements, or often more importantly the lessons learned, provide extremely valuable data and insight into possible cost reduction ideas. This program begins to move down that pathway with efforts targeted at catalyst loadings, materials substitution and improvements in manufacturing processing. These items have and will continue to be developed and put on test throughout this fiscal year up to the end of the program. Cost reduction projections assume at least one year of full testing before any changes are made on customer deliverable hardware. This conservative approach is vital to maintaining quality hardware and satisfied customers.

Often overlooked in the PEM fuel cell and electrolyzer product area is the importance of focus on system cost and integration issues. These areas encompass, at a minimum, fluids management, gas pressure, gas purity, manufacturability and all of the safety requirements in the various countries. Add to this the complexities in packaging and shipping hardware through different environments and over varying road infrastructures, and the pathway to delivering a fully commercial product gets even more complex. Proton has made significant advances in commercializing industrial hydrogen generators. This has included significant efforts in obtaining domestic and international marks such as CE, NTRL and CSA. This program has augmented these efforts by focusing on specific systems areas for cost reduction. These include the electronic control section, use of welded tube assemblies and exploration of various power conditioning options. As stated earlier, all of these cost reduction advances provide the building blocks for our other product areas and enable us to get real time commercial experience by applying these cost reductions to our industrial product lines.

Specific Accomplishments to Date

The following sections will discuss the specific areas targeted on this program, the milestones and objectives of each of those items and the status of progress to date.

Control Board Development

The current control system on the HOGEN[®] 40 generators has over 30 components, a significant amount of point to point wiring and discrete power modules. This task is aimed at integrating as many of these components as practicable into a dedicated control board. The task is a design effort, which utilizes a control board that was previously developed for our laboratory scale

hydrogen generator (Figure 3) as a platform from which the functionality can be increased to encompass the necessary controls for the HOGEN[®] 40. An additional benefit of the board is the ability to utilize a digital operator interface and replace two analog gauges on the front panel (Figure 4.) This interface will allow for more detailed diagnostics and system monitoring by the operator/technician. The milestone for this item was to complete development testing of the prototype board by May of 2001. Prototype hardware testing is scheduled to conclude prior to May 31 with firmware testing to follow prior to June 15, 2001.



Figure 3– Current Control System



Figure 4 – Prototype Control Board

Efforts on the board have exceeded expectations. Testing has been very successful and has verified the hardware design and functionality. Some additional modifications and improvements are planned for the board beyond the prototype phase, which include integrating a few more components and reducing the overall production cost. The control board design, and associated validation testing, will be completed by the end of this calendar year. The cost reductions associated with this effort are impressive. The current material cost for the discrete components in the control system is approximately \$1,600 and takes about 40 hours of labor to assemble. The board cost is projected to be approximately \$300 and the labor will be reduced to less than one hour.

Power Supply

This task was intended to accomplish a full investigation of the landscape for power supplies that would be viable for the HOGEN[®] 40 series product. It was also intended to look for a universal interface that would be capable of taking input from various renewable sources.

The current design uses a switch mode power supply, which is very compact, power factor corrected, and efficient. However, the cost of the power supply is approximately \$3,500 (\$.35/watt) and the technology does not readily lend itself to cost reduction. Investigation of several alternatives led us to Sustainable Energy Technologies (SET) who developed a prototype

9kW power supply (Figure 5) that has a price of \$1,500 (\$.16/watt) at a quantity of 500 units. Our goal is to develop a power conditioning module that represents a technically equivalent alternative to the current power conditioning module at less than \$.15/watt. The successful testing of the prototype unit provided by SET (Figure 6) has led us to believe that this is a goal well within reach.



Figure 5 – Prototype Power Conditioner

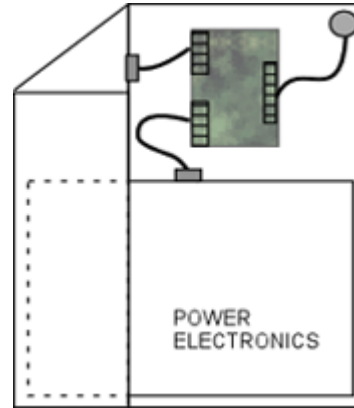


Figure 6 – Next Generation Concept

The only drawback to this prototype is the overall size, which is significantly larger than the envelope of the switch mode supplies. Further development activity will continue with SET to work on envelope versus cost. Another factor is that the success of the board activity has opened up potential volume in the current package that may be of adequate size to allow for a larger power supply. This analysis will continue throughout the remainder of this year.

Component Cost Reductions

The milestone on this task is to design and verify cost reductions on castings, manifolds, drying and fluid control components by September 2001. The idea is to take a significant look at fabrication methods, component count and technology being employed to reduce the overall cost of the fluid side of the system.

This item has shown very encouraging results. Reviewing fluid plumbing runs, simplifying them and replacing expensive tube fittings (Figure 7) with welded tubes (Figure 8) has reduced the overall fitting count by over 50%. This has had a major impact not only on the cost of the fittings and the assembly time associated with making up tube fittings, but the overall elimination of numerous leak paths has increased the robustness and integrity of the entire unit.

The development efforts on gas drying have enabled the development of a low cost pressure swing absorption dryer (Figure 9) that can be manufactured in low quantities for under \$2,000 compared to the previous palladium membrane type of dryer being used for approximately \$7,500. In higher volumes the cost of this dryer will be well under \$1,000.

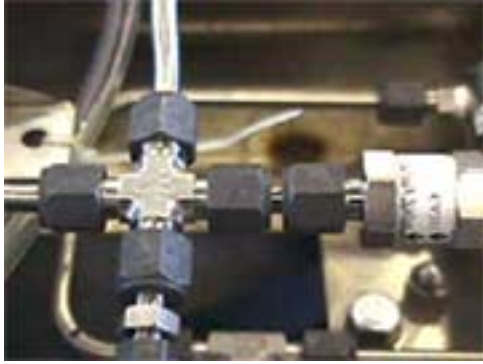


Figure 7 – Typical Fitting Connection



Figure 8 – Welded Tube Assemblies



Figure 9 – Pressure Swing Adsorption Dryer

Manufacture a Cost Reduced Prototype

The milestone for this task was to complete a prototype system to use as a test bed (Figure 10) for all of the cost reduction items by January 2001. The unit was completed in January and has been used for the testing of the control board as well as the development of the gas dryer and the new plumbing runs. It is our intention to build in all of the validated cost reduction ideas into this unit as a means of validating how they all relate and function as a system.



Figure 10 – Prototype System w/ Digital Interface

Alternate Energy Inputs

This milestone was designed as an investigation and understanding task. Numerous developers overlook, or fail to fully understand, the difficulty in interfacing different types of renewable technology with PEM products. As mentioned earlier in the Power Supply task, Proton has been working with SET to develop a universal interface. In addition, Proton has been working with Illinois Institute of Technology (IIT) on an overall system integration task combining a HOGEN[®] 40 (which they purchased), with a photovoltaic array and a fuel cell. This full-scale demonstration will provide valuable real world data on a complete system architecture. The renewable interface designed by SET will take a 5kW PV or Wind input with a wide input voltage range and utilizing full maximum power point tracking algorithms deliver a current controlled output to the electrolyzer for hydrogen production and storage. A HOGEN[®] 40 electrolyzer has been shipped to IIT and is scheduled to be fully functional on grid power by June 15, 2001. The SET renewable interface will be delivered to Proton on June 30, 2001 and following some initial testing will be shipped to IIT for integration and testing with a 2.6 kW PV system. Figure 11 below illustrates a typical renewable power system that might be utilized for small village or remote telecommunications applications. Demonstrations like IIT's help to make clear that the only long-term viable path to sustaining a renewable grid is through electrolysis and high-pressure hydrogen storage. The data and integration insight gained from this collaborative project will be invaluable to understanding the issues associated with designing, deploying, and maintaining renewable systems for a variety of applications.

Cell Stack

This milestone encompasses various tasks including catalyst loading reduction, process cost reduction for catalyst deposition and materials processing, design and analysis of cast stack components, and internal flow field material characterization. Completion dates are spread out through much of this calendar year. Due to the highly proprietary nature of these activities a full discussion of the specifics of this task will not be described in this paper.

In general, some of the detailed efforts are slightly behind schedule, but many significant advances are being made. Testing of many of these cost reductions are beginning and will require at least six months to one year of testing prior to being evaluated for possible implementation into a commercial product. Cost reduction assumptions have built in a two-year lag on improvement implementation.

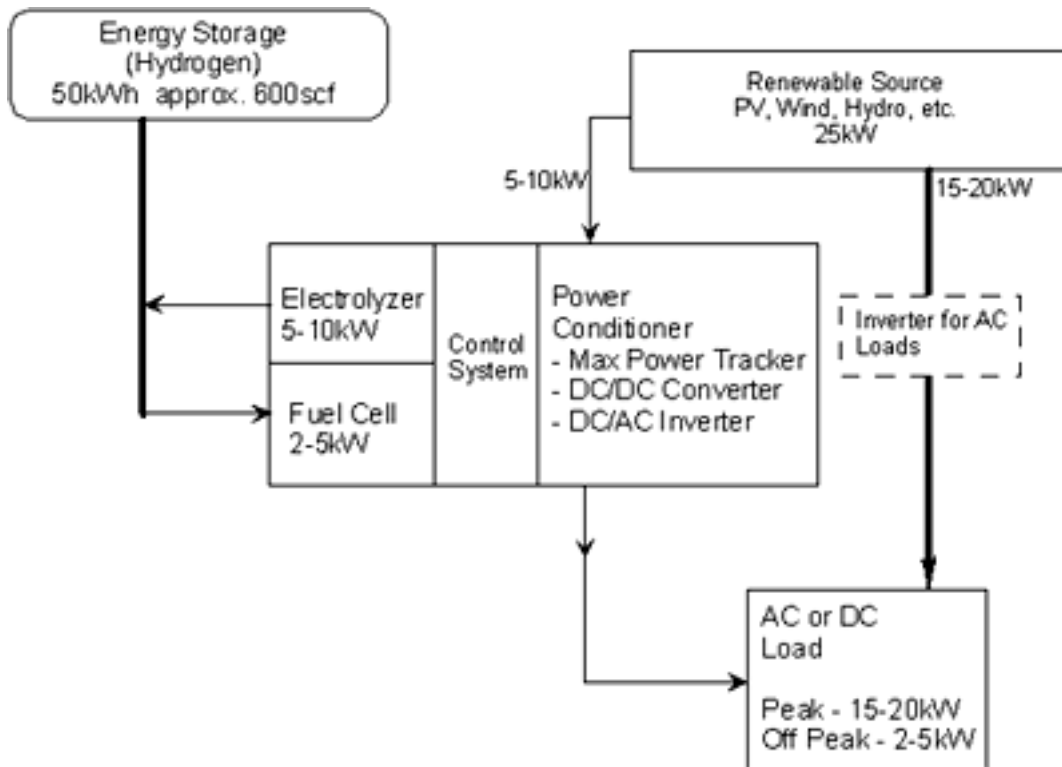


Figure 11 – Renewable Interface Concept

Plans for Future Work

The plans for future work revolve around completing work on the HOGEN[®] 40 efforts and beginning to advance them towards the HOGEN[®] 380 series generators. The first task is to fully validate and implement the cost reductions on the HOGEN[®] 40 product. Much of the verification testing is complete, but additional efforts remain on the control board to fully validate the design and implement production level cost reductions. The control board and some of the fluids components need to undergo further testing in order to achieve a confidence level high enough to integrate them into production. The second task is to continue testing and research on the cell stack efforts. Due to the time requirements of testing these items, the more advances we can make and get on test, the better our chances of achieving nearer term cost reductions.

Finally, on the HOGEN[®] 380 series generators, we will initiate design efforts on a control board based on the one designed for the HOGEN[®] 40. The essential functionality of the board is the same, but some of the on-board diagnostics and aspects of the system will differ to some extent. We will also look into power supply options on this unit. The various power supply options are somewhat different given the much higher power levels and larger package size.

References

1. Friedland, R., Smith, W., Speranza, A., January 2000. *Integrated Renewable Hydrogen Utility System*, Phase I Final Technical Report and Market Assessment PES-T-99014.
2. Friedland, R., May 2000. *Integrated Renewable Hydrogen Utility System*, Phase II Technical Paper for Annual Technical Peer Review.

RENEWABLE HYDROGEN SYSTEMS INTEGRATION AND PERFORMANCE MODELING

**Roger Jacobson, Richard Purcell, Daniel Wermers
Desert Research Institute
Reno, NV 89512**

**Byard Wood, Denis Donovan, Denise Lane, Michael Matheus
University of Nevada, Reno
Reno, NV 89557**

Abstract

This project has developed and tested a renewable energy fuel cell (REF) system for off-grid or supplemental power application. The system is composed of solar panels (2 kW), wind turbines (3 kW), inverter (4 kW), electrolyzer (5 kW), batteries, hydrogen tank, fuel cell (2 kW), load cell (5 kW), computer system, and miscellaneous sensors and electronic components (Snyder 2000). The operation of the REF system is controlled by the computer and is designed to provide the power required by the load bank utilizing power from the solar panels, wind turbines and/or the fuel cell. A major emphasis of this project was to develop a computer system to evaluate inputs from approximately 25 sensors and utilize this information to control the entire system, including the fuel cell. The basic logic is that the electrolyzer generates hydrogen during times when excess solar and wind energy is available and then the fuel cell utilizes this hydrogen to produce electricity when there is insufficient solar and wind energy. The REF system functions very well in the Reno, Nevada, environment, which has a good balance of solar and wind energy throughout the year.

Introduction

Fuel cell systems utilizing renewable energy are attracting increasing interest. This attention is perhaps related to energy costs, reliability of energy and a need to feel in control of one's energy future. If individuals are planning to purchase a system based on logic and not because they just want one, at least three major conditions should be met for a system such as described above: competitive energy costs, reliable system and ease of use. The major focus of this project was the last component, ease of use, because without a system that was self-managed and controlled, most users will avoid use because of the complexity and time required to operate this system. The system needs to appear seamless to the user so that the exact source of energy at any particular time is not known and no system adjustments are required if power consumption increases or decreases.

The basic operating philosophy of the REF system is to carefully monitor all of the component sensors to determine system conditions and then to have the computer control the operation to match the power demand and optimize the system function. All electrical components are connected to a 24 VDC busbar (Figure 1), which allows power to be managed between power input, energy storage and power consumption devices. The busbar voltage is also a major parameter that is monitored to determine the REF system function and health. There are several REF system logic controls, such as not permitting the electrolyzer and the fuel cell to operate at the same time because the electrolyzer is only to operate when excess power is available. Another reason to not operate the fuel cell when sufficient wind and solar energy are available is to maximize system efficiency. When power is used to operate the electrolyzer and the hydrogen is then used to produce electricity from a fuel cell, the efficiencies of both the fuel cell and electrolyzer (both much less than 100%) need to be combined to get the overall system efficiency (20-30% depending on conditions).

The logic control for the REF system was a challenge because the sensor data needed to be collected every few seconds for real time system control and the same computer needed to be sending out device control signals on a real time basis. This control is particularly critical when operating the fuel cell under changing power conditions. The situation is only possible because there is a small battery pack in the REF system that helps "buffer" the system and allow the fuel cell a few seconds to change power output and match power demands.

Discussion

System Configuration

As discussed previously, the REF system is complex but is comprised, primarily, of commercially available components that are configured to produce power from renewable non-polluting sources and provide reliable power that will require a minimum attention by the user. The basic components are shown in Figure 1. The details of the fuel cell system are shown in Figure 2 with both the computer inputs and commands shown as well as the control of the hydrogen and airflow. The computer first determines if power from the fuel cell is required. If so, then it starts the fuel cell and monitors its performance until power is no longer needed from

the fuel cell. At that time the computer performs a shutdown procedure. There are also two ARGGA hydrogen detectors, one by the electrolyzer and the second near the fuel cell, that are constantly monitored and if any hydrogen is detected the system closes the valve from the hydrogen tank and stops the electrolyzer.

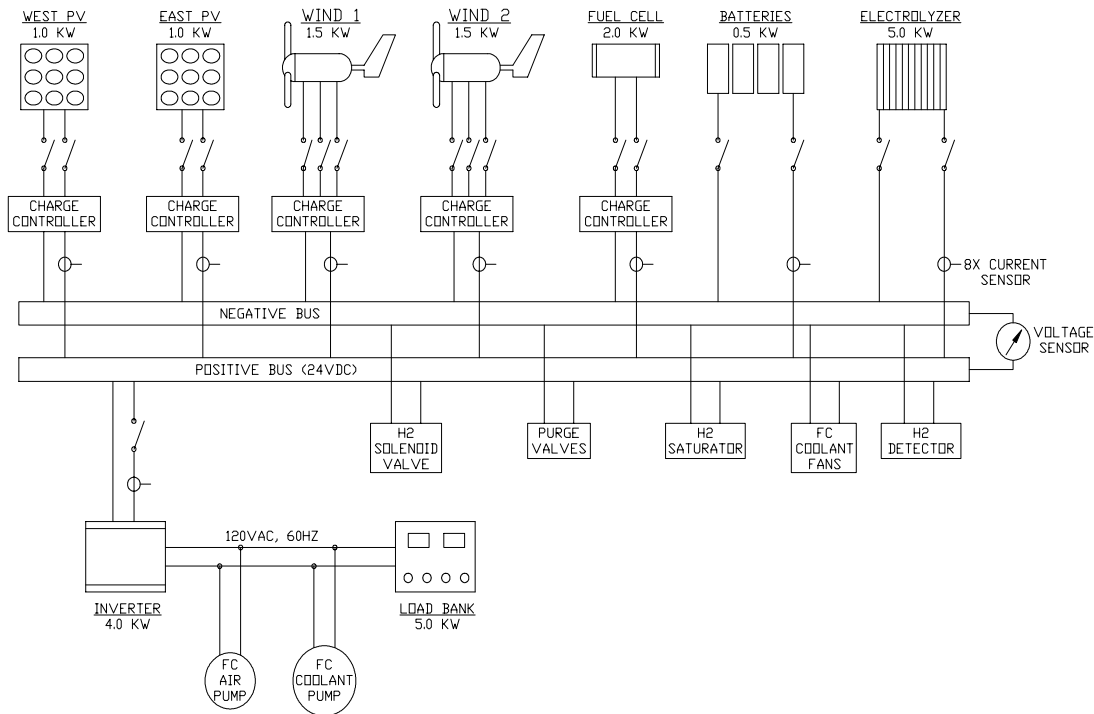


Figure 1. Connections to a Common Electrical Bus

Energy for the system is provided by two Siemen solar panels, each producing 1 kW, mounted on Zomeworks trackers. Two Bergey 1.5 kW wind turbines mounted on individual sixty-foot towers also provide additional power. This power is converted to 24 VDC by Trace and Bergey charge controllers and fed onto a common 24 VDC electrical bus. Current from the busbar keeps a small battery pack charged, feeds power to the load bank via a Trace inverter and also supplies power to the electrolyzer. The load bank is a series of resistors that can be programmed to simulate any type of electrical load profile.

The electrolyzer is a major piece of equipment, representing nearly half of the total cost of the REF system. It was purchased from Stuart Energy and delivered as a completed system in its own cargo box. The hydrogen is compressed to approximately 100 psi and stored in an 80 cubic foot tank. The hydrogen pressure is dropped to approximately 5 psi before being introduced into the fuel cell. Air is introduced into the fuel cell by the use of a Gast linear air pump (blower) and is also controlled by the computer so that air flow can match hydrogen flow and produce variable power outputs. The fuel cell has a maximum output of approximately 2 kW and was manufactured by Dais-Analytic. Most of the remaining components (e.g. the cooling system, charge controller and multiplexer) shown on Figure 2 were fabricated by DRI after purchasing

Sensor Array

Sensors are critical for the proper functioning of the entire REF system because they measure total system performance and feed these data to the computer for decision making. A summary of the sensors is shown in Figure 3, with several of the sensors listed actually having several measured parameters associated with them. One example is wind energy, which is generated by two wind turbines and is comprised of five sensors: 2 anemometers, wind direction and 2 that measure amperes. At the present time, the REF system has 27 sensors but the number changes as the system evolves. Also several of the sensors are redundant. There are also several sensors that provide secondary information and need not be sampled every 0.1 - 5 seconds but rather every few minutes.

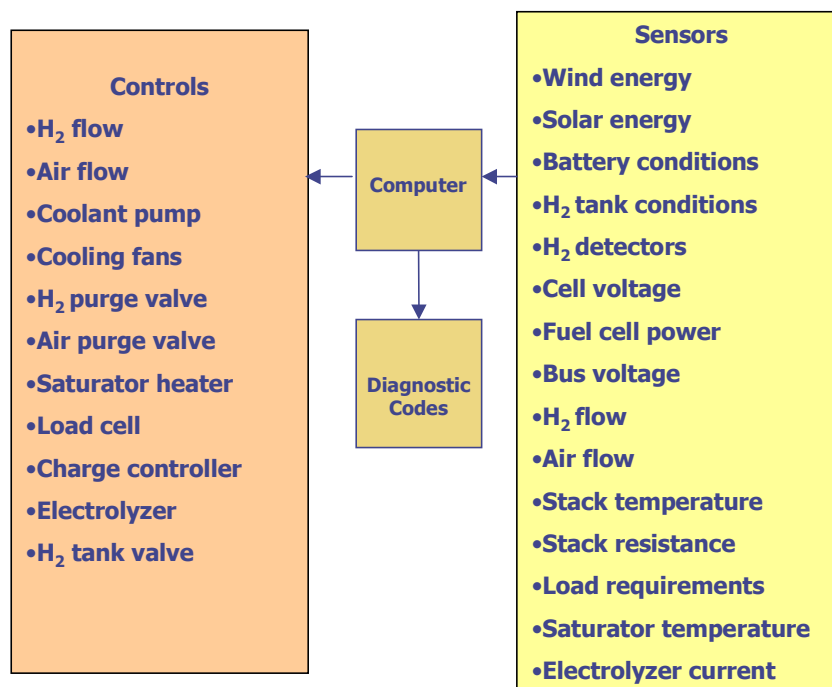


Figure 3 – Logic Control Diagram

Both the solar and wind energy are intermittent sources of energy as is demonstrated in Figures 4 and 5. Even during daylight hours the solar resource is variable because of changes in cloud cover. This is demonstrated by the solar energy variability as seen in Figure 4. The wind energy is an even less reliable resource. It is also one that is more difficult to predict when sufficient wind will be available to generate power. The data demonstrate that the wind needs to blow approximately 10 mph before any power is generated. Until the wind approaches 20 mph, minimal power is generated. Wind energy utilization is one of the more difficult problems for which to develop logic control because the duration and strength of the wind resource, which is unknown, is critical. The wind energy is used in one of three ways: 1) to keep the batteries charged, which is easy to program and requires little power because the battery pack is small; 2) to provide power to the load bank; and 3) to generate hydrogen by powering the electrolyzer. The last is most difficult because there is some startup time required before hydrogen production

begins and substantial power is consumed before hydrogen can be produced, compressed and stored. The electrolyzer is also the largest energy sink in the REF system. It cannot be throttled, so it acts as a nominal 1-2 kW load that is either on or off. If the wind runs for short time intervals and then stops, it is not prudent to start the electrolyzer and therefore the program must consider many factors when determining if the electrolyzer should be started. This problem is more acute at night when no solar energy is available. The use of wind energy to power the load cell is relatively straightforward but there is a problem of power switching under certain circumstances. One example is at night when operating on the fuel cell at a relatively low load and then the wind starts blowing and producing enough power to power the load cell and also the electrolyzer. The question is at what point is the fuel cell shut off and the electrolyzer started, because it has been determined that the wind will continue to blow for some minimum time.

Busbar voltage is monitored as an indicator of the overall system condition. All power goes through this component and therefore it is the best single measurement of whether or not power is being supplied at rates that are sustainable. Figure 6 illustrates the changes in voltage on the busbar when the REF system has the electrolyzer operating (2/27 and 2/28) versus days when the electrolyzer is not functioning (2/24 and 2/25).

The voltage and flow of current to and from the batteries (Figure 7) are also carefully monitored to insure that the batteries are functioning normally and that they are not placed in a condition where they can be damaged. The battery pack is essential to the function of the REF system because it provides a buffering of current in the system, especially during changes in power consumption of devices, such as the electrolyzer and load cell. Current flow from batteries is also carefully monitored when increasing the power of the fuel cell to meet the load cell demand. The power from the fuel cell is increased until the current flow from the batteries is zero.

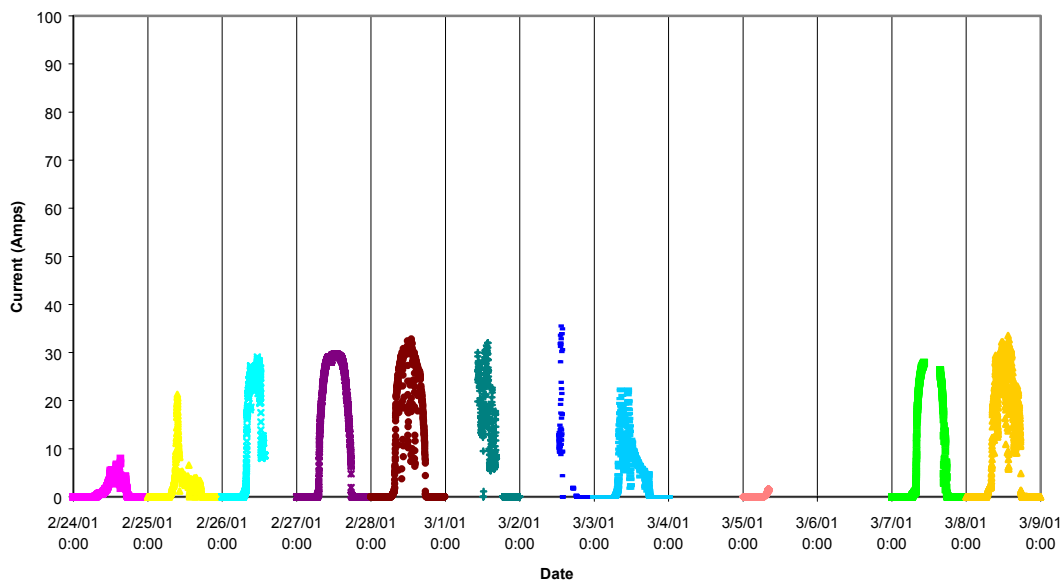


Figure 4 – Solar Energy Production

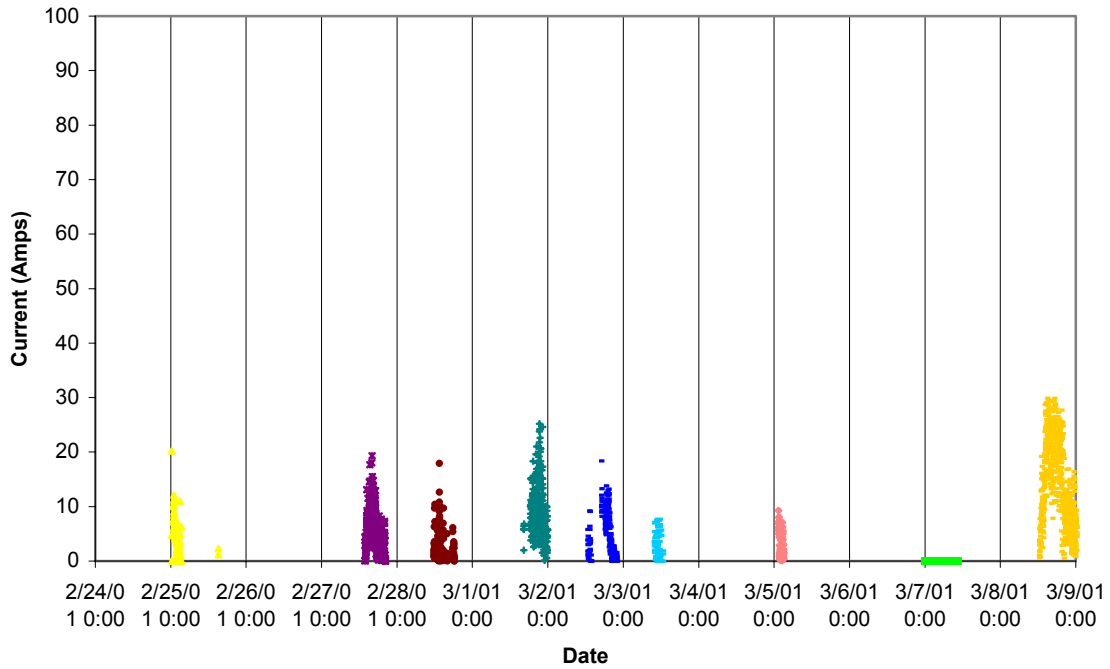
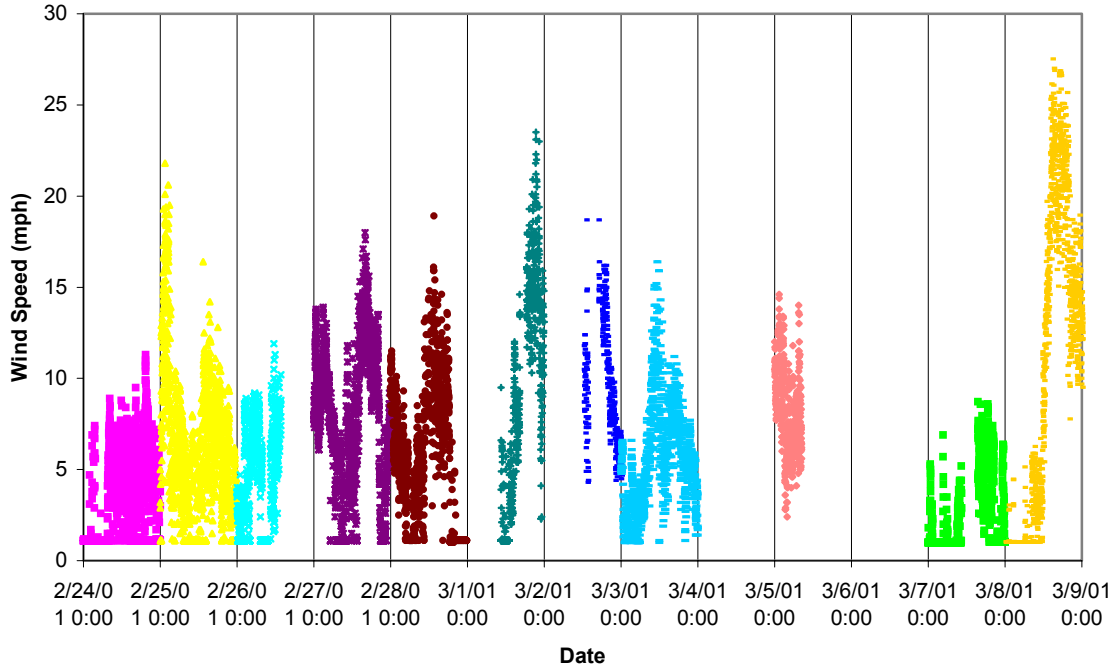


Figure 5 – Wind Velocity and Energy Production

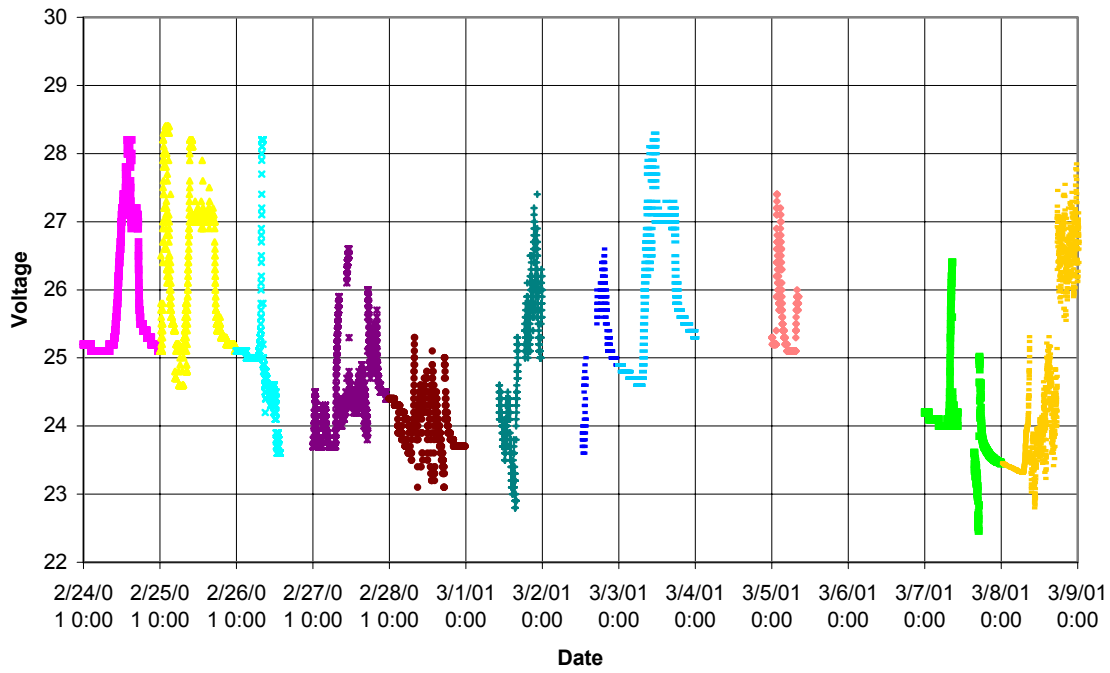


Figure 6 – Busbar Voltage

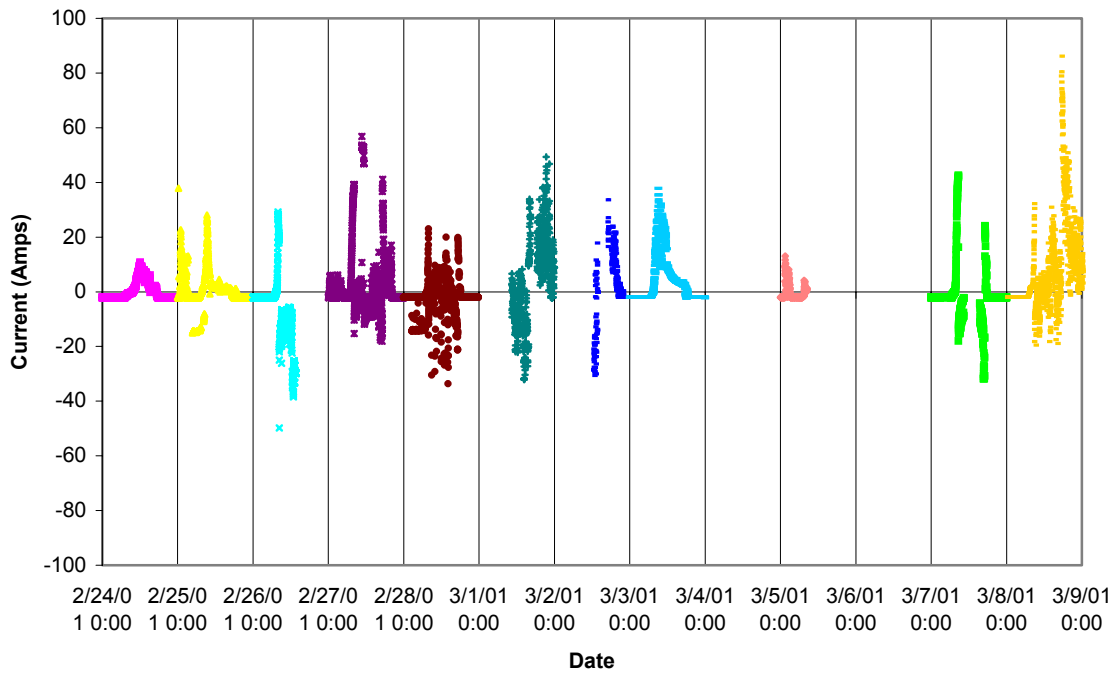


Figure 7 – Battery Current Flow

The REF system control was undertaken as a two-step process in order to clearly separate the component control from the logic control programming. The first step was to establish a computer control for all of the individual components shown in Figure 3 and to carefully test to ensure that the control worked under a wide variety of conditions. Some of the controls were a simple on/off application, such as the coolant pump, cooling fans, and the purge valves. Other controls (hydrogen and air flow, etc.) were more complex and required the ability to operate under different settings. There also needed to be a calibration curve established between the computer settings and the amount of hydrogen or air delivered per unit time. The system was designed using LabView software and is flexible so that additional components may be added in the future.

System Control Design

The most complicated system control application was to develop a fully automated system that can take sensor information and establish a set of system controls that will operate the entire system in a “hands off” mode. Version 1 was designed to handle most of the anticipated conditions that the REF system was expected to confront in normal operation. The general power consumption on a 24-hour basis needed to be established (Figure 8) so that the load cell could be programmed. This information was obtained by estimating the total energy available, on a daily basis, in both the winter and summer and then assuming as a first approximation that one half of the power produced by solar and wind energy would be used to produce hydrogen for utilization in the fuel cell (Figure 9). These values need to be refined as more data become available and the calculations should be done on a monthly basis. The daily load profile shown in Figure 8 was constructed to represent a low nighttime load followed in the winter by an increased load from 6 to 8 AM and then an intermediate load during the day. There is also an evening peak until 10 PM and then a low nighttime load. Summer power differs in that there is a mid-day high caused by air conditioning but otherwise the two profiles are similar. This profile is approximately what a residential load will represent in Western states but there will not be a constant load during any time interval. Also the changes in power consumption will not be represented as a step function. These were established as initial operating conditions in an attempt to bracket the fuel cell power output and generally determine how much solar and wind power will be required for hydrogen production.

The programming logic has three basic decision criteria: 1) is power from the fuel cell required to match load bank demand; 2) is there enough excess power to run the electrolyzer and 3) does an unsafe condition exist? There are dozens of other decisions that also need to be made during daily operation. System operation and control can perhaps be best described by analyzing the general operation during a typical day (Figure 8). Starting at midnight, the power consumption is low and totally supplied by the fuel cell using hydrogen stored from previous days. If there is a small amount of wind energy then it supplies the demand and the fuel cell is off. If there is substantial wind then it will supply the low base load and also operate the electrolyzer and produce hydrogen. This will occur only until the hydrogen tank is full. This entire operation with the required decisions and control is made by the computer obtaining information from an array of sensors. At 6:00 AM the power demand increases and on a typical day the fuel cell output will increase to meet this new demand. There generally is not sufficient solar energy to

supply power but if wind energy is available it will be utilized to offset the load and possibly to produce hydrogen. In the winter the power demand decreases at 8:00 AM as people leave the house and the load for the next nine hours is supplied by a combination of wind, solar and fuel cell power. Again if sufficient solar and wind energy are available hydrogen will be generated for future use in the fuel cell. This is the period of time when most of the hydrogen is produced and stored. At 5:00 PM the power demand increases and generally the power will be supplied by the fuel cell unless there is wind power available. In an attempt to maximize REF system efficiency, solar and wind power are utilized directly rather than producing hydrogen and operating the fuel cell. The power is reduced at 10:00 PM and the load is generally carried by the fuel cell unless there is sufficient wind energy. During this entire time several sensors are checking for unsafe conditions, such as a hydrogen leak, and if any are detected the REF system is shut down in a safe manner and an error code displayed.

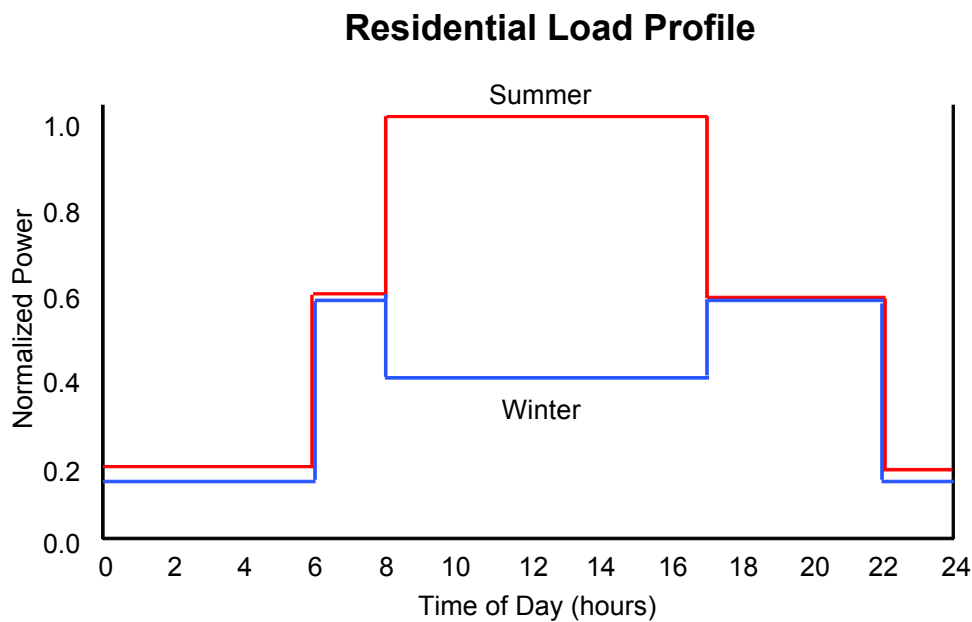


Figure 8 – Residential Load Profile

The above description is generally how the system behaves but there are a series of decisions made based on sensor input. Some of the more common operations can be described as a series of if-then statements:

- Busbar voltage < 26 VDC, then assess power requirements
 - are batteries charging or discharging?
 - if charging then fuel cell off; if discharging, is electrolyzer on?
 - if electrolyzer on, turn off and re-assess power requirements
 - if still discharging, initiate sequence to bring fuel cell online
- Busbar voltage > 26 VDC, then fuel cell off
 - is the hydrogen tank full?
 - if yes, don't activate electrolyzer
 - if no, then are wind or solar power available?
 - if no, don't activate electrolyzer; if yes, then activate

Energy Production

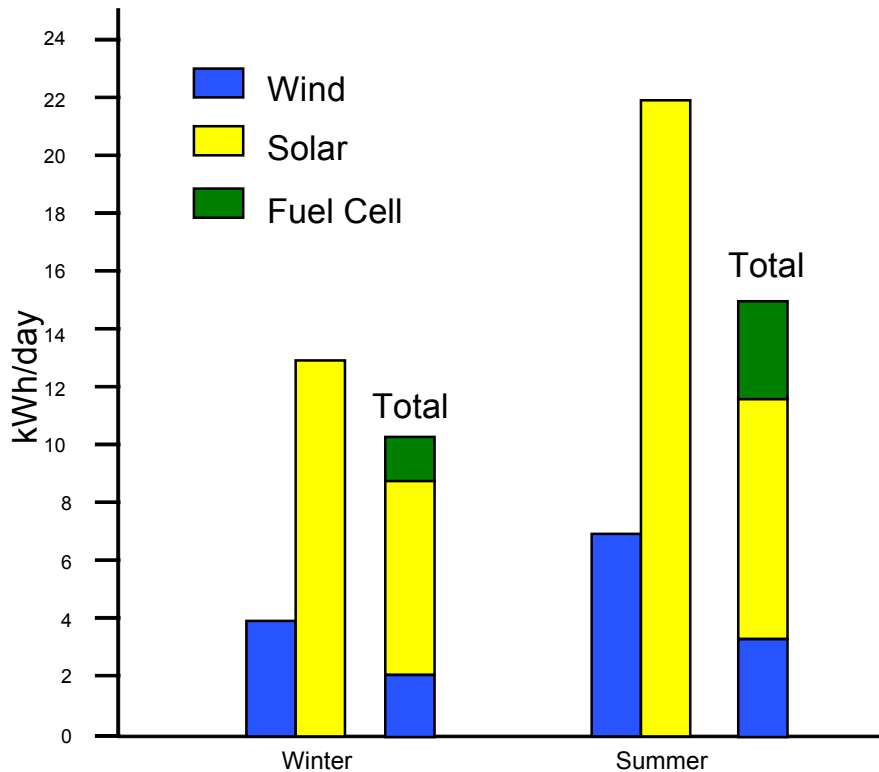


Figure 9 – Energy Production from the REF System

These are some examples of the type of decisions that are made continuously during any day of operation. The goal is to keep the batteries at a near full charge and only allow them to be discharged for a short period of time and then recharged. This allows the batteries to act as a buffer for the REF system when components such as the electrolyzer or load bank are suddenly turned on or up.

Conclusion

The REF system is viable for numerous applications, provided component costs can be reduced. It can be made reliable and the entire system can operate seamlessly and with a minimum of user time. The basic REF system configuration is sound, with the common 24 VDC busbar being essential to the overall system. Several of the components could have been sized differently but they were available at the beginning of the project. Integrating sensor data into the system worked well using LabView software and Fieldpoint hardware and also provides great flexibility for changes and additions. Establishing computer control of individual components before attempting to have the entire REF system run by the computer was very prudent. Several issues were solved quickly because it was possible to readily separate component functions and isolate problems. Version 1.0 of the software REF system control has been completed, which provides the ability to collect real time data and utilize this information to control numerous components

to provide seamless power to a load bank. The software will be tested with increasingly complex conditions and modified as required to continue to provide the power required at the load bank and also operate in a safe manner.

Future Work

The next research phase will focus on: 1) developing advanced software; 2) evaluating how to make the existing system more functional and cost-effective; 3) collecting performance data under various load profiles (farm/ranch, business, etc.); and 4) exploring ways to optimize the system and increase efficiency. Advanced software development will focus on handling more complex real world conditions that occur during sustained operation. This will include the failure of various components, as well as, major changes in power consumption coupled with a dramatic decrease in solar or wind energy. Version 1.0 of the software makes decisions strictly based on current conditions with no capability to forecast future energy supply over the next few days. The next version will explore various options to incorporate forecast information into conditioning the control logic to manage power in the REF system. Optimal performance by having the computer fine-tune the system is important to obtain maximum efficiency. One way this will be accomplished is by making small changes in the flow of hydrogen and air and carefully monitor fuel cell power output to achieve the best power to input ratio.

Adding capacity to various components will be evaluated in order to obtain a system that is sized properly for the expected conditions. At the present time several components appear to be undersized but with more operating information it will be possible to make a definitive evaluation and reconfigure the system. Collecting data utilizing other load profiles will greatly increase the utility of the REF system and allow for the refinement of the software system. Other simulations should include the farm/ranch and small business applications. Another key component of future work needs to focus on increasing system efficiency by reducing parasitic losses and other operating inefficiencies. A major focus of this activity is to refine the operating conditions of the 5 kW electrolyzer, which is either off or on. In the on condition, the power consumption is high and not able to be controlled. A better system would have a charge controller on the electrolyzer so that small amounts of excess solar or wind energy could be used to generate hydrogen.

Acknowledgments

The REF system development is funded by the U.S. Department of Energy, Office of Power Technologies through the Hydrogen Program. Assistance on electrolyzer operation was provided by Stuart Energy and DIAS-Analytic helped with the fuel cell setup. Los Alamos National Laboratory provided valuable assistance on defining fuel cell operating conditions. The Desert Research Institute provided financial assistance and help from facilities was invaluable in getting the sensors to work properly.

References

Snyder, J.D. 2000. An Integrated Renewable Hydrogen Energy System. Unpublished Master's Thesis, University of Nevada, Reno, 198 p.

OVONIC METAL HYDRIDE BASED HYDROGEN ICE SCOOTER

**Krishna Sapru, Subramanian Ramachandran,
Zhaosheng Tan and Eugene Kurlonko
Energy Conversion Devices, Inc.
1675 West Maple Road, Troy, MI 48084**

Abstract

Metal hydrides are solid-state, compact, and reversible means of hydrogen storage at low pressure; ideal for on-board hydrogen storage on two- and three-wheelers. Of the nearly 200 million gasoline ICE two-wheelers on the streets of the world, most of them are in the developing nations like India and China. Major cities in these countries have air pollution that has reached alarming levels. The merits of hydrogen as the ultimate clean fuel is well-accepted. Even as various means of hydrogen production and distribution are being debated, it is crucial to promote hydrogen-fuelled vehicle and metal hydride technology that can help achieve this goal. We report on the use of ECD's metal hydride storage modules for ICE scooter applications and also on the work undertaken by ECD to convert a gasoline ICE scooter to run on hydrogen.

Introduction

Globally two-wheelers create as much air pollution as the passenger cars over their lifetime. There are approximately 200 million two-wheelers on the streets of the world. This has resulted in extremely poor air quality in many of the cities in Asia. New Delhi has one of the worst air qualities in the world and hence stricter emission controls were mandated. Commendable measures are being undertaken to convert all public transport vehicles (buses, taxis and three-wheelers) to CNG. As a result the air quality has improved in a relatively short time. However,

this is not a long-term solution since CNG is a limited resource. For a long-term solution non-depletable and sustainable energy sources are being considered [1,2].

As a part of the program partially funded by the U.S. DOE Hydrogen Energy Program, ECD is involved in converting a gasoline ICE scooter to run on hydrogen, in addition to developing metal hydrides and on-board metal hydride storage system for the scooter and determining the cost and availability of renewable hydrogen.

This paper will report some of the properties of ECD's low-temperature metal hydrides and hydrogen storage modules. Preliminary results on the conversion of a Honda Elite 80 gasoline scooter will also be discussed.

Metal Hydride Storage Systems for H-ICE Scooters

ECD has developed metal hydrides with suitable thermodynamic and kinetic properties for use in the H-ICE scooters [3]. The cycle life (hydriding – dehydriding) of the alloys in the presence of pure hydrogen and in the presence of hydrogen with trace contaminants (CO and moisture) was determined. The alloy that was chosen for use in the storage system has 1.5 wt% reversible storage capacity at 30°C, above 1 atm pressure. The alloy was cycled 1080 times in pure hydrogen without any measurable loss in reversible storage capacity. The alloy has good cycle life in hydrogen containing 0.1 vol% CO (over 320 cycles), and slightly modified alloy composition shows improved moisture resistance, as indicated by a test of 532 cycles with hydrogen containing 100 ppmv moisture. Large quantity of the alloy was manufactured in ECD's production facility by induction melting. The material is reduced in size and packaged to optimize the heat and mass transfer characteristics. An ideal metal hydride (MH) storage module design for hydrogen ICE scooter will depend on the several considerations such as:

1. Desired driving range
2. Drive cycle
3. Thermodynamic and kinetic properties of the alloy
4. Geometrical considerations

Two types of MH modules were tested their hydrogen charge/discharge characteristics. They are air heat exchange modules (OAC) and liquid heat exchange (OTP) modules, as shown in Figure 1. The air heat exchange modules are suitable for smaller scooters like Honda Elite 80, which has an air-cooled engine. The liquid heat exchange modules could be conveniently integrated into larger scooters such as Honda Helix, which are equipped with liquid-cooled ICE engine. Their technical specifications are summarized and listed in Table 1.

Hydrogen discharge characteristic from OAC-1 are shown in Figure 2. In the ambient air, OAC-1 module delivers hydrogen up to 30 minutes at a constant rate of 25 SLM (standard liter per minute), the estimated rate of hydrogen consumption by Honda Elite. No sophisticated thermal management is necessary for achieving a good reversible desorption of the stored hydrogen.



Figure 1: Ovonic prototype OAC-1 and OTP-1 metal hydride hydrogen storage modules.

Table 1: Specifications of OAC-1 and OTP-1 storage modules

Modules	Total Weight (kg)	Foot Print (in ³)	Charging Pressure (psig)	Charging Duration (hour)	Hydrogen Stored (gram)
OAC-1	20	5×18×12	150	1.5	120
OTP-1	35	5×18×9	150	3.5	300

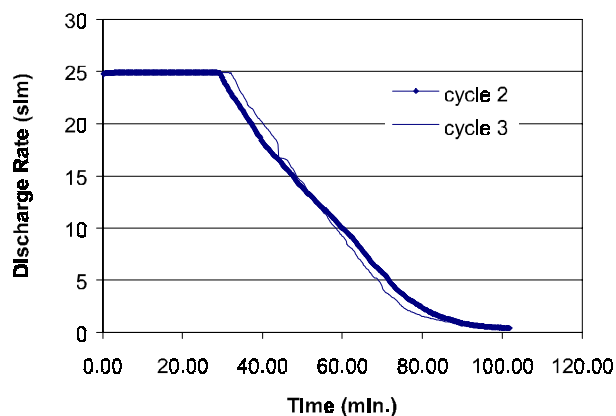


Figure 2: Hydrogen discharge rate of OAC-1 storage module in ambient air

Metal Hydride – Electrolyzer System

Availability of hydrogen to meet the refueling needs of the H-ICE two-wheelers is very important for the long-term field testing and evaluation of the hydrogen ICE with on-board metal hydride. The hydrogen produced in the short-term may be derived from fossil fuel but would

ultimately be derived from renewable sources and processes. ECD is addressing renewable means to produce hydrogen via water electrolysis using either PV power or using bagasse cogeneration power. The cost comparison of these two approaches is being evaluated.

ECD has negotiated an agreement to integrate metal hydride storage systems with an alkaline electrolyzer (IMET[®] 10) manufactured by Hydrogen Systems (Montreal, Quebec, Canada). The electrolyzer delivers hydrogen at a rate of 180 slpm at 150 psig. The moisture and oxygen from the product hydrogen will be removed using an external dryer and deoxygenation system. The pressure and purity of the product electrolytic hydrogen has been found suitable to charge the metal hydride. Estimates show that the IMET[®] 10 can feed hydrogen to either 50 OTP storage systems or to 120 OAC storage systems.

Specifications and Performance of Gasoline Scooter Engine

Scooter engine specification/vehicle description

The Honda Elite CH 80, 2000-year model, four-stroke scooter with a 79 cc engine, was screened for oil control and was found to be satisfactory. Good oil control minimizes the problem of unwanted combustion by the carbon residual deposits from the oil.

Some of the salient features are given below, and with more details in the scooter manual [4].

The engine is an air-cooled, 4 –stroke single cylinder engine with overhead cam.

Bore x stroke	49.5x41.4mm
Displacement	79.7 cc
Compression ratio	9.3:1
Cylinder compression	199 psig
Intake valve	Opens 0 deg BTDC (before top dead center) at 1mm lift
	Closes 20 deg ABDC (after bottom dead center) at 1 mm lift
Exhaust valve	Opens -2.5 deg BBDC (before bottom dead center) at 1 mm lift
	Closes 30 deg ATDC (after top dead center) at 1 mm lift
Idle speed	1800 +/- 100 rpm
Ignition timing	18 deg BTDC at 1800 rpm (idle), advance starts at 2400 rpm and full advance to 27 deg at 3000 rpm.
Vehicle capacity load	152 Kg
Transmission	V-belt drive, CVT
Gear ratio	2.8 – 1.08
Final reduction	8.382:1
Carburetion	16 mm venturi diameter

Instrumentation and data acquisition

A magnetic pick-up is located on the stator assembly (mounted on the crank shaft) that provides the pulse that triggers the spark plug. The spark plug is fired twice in an engine cycle; once during the power stroke and once during the exhaust stroke. The vehicle was fitted with an on-

board data acquisition unit (Advantage Motor Sports, Flemington, New Jersey). Initially the unit was configured to measure the engine RPM and the front wheel speed. Later the cylinder head temperature (CHT, type J or type K) and the exhaust gas temperature (EGT, type K) were included. The CHT is measured at the spark plug. The data can be exported into an Excel spreadsheet.

Baseline performance with gasoline

The performance of the scooter with gasoline was studied. A water brake engine dynamometer (Go Power Corp, Palo Alto, California) was mounted to the crankshaft of the engine. A 50 lb load cell (model LC101-50, Omegadyne) was connected to a 6" load-arm to read the load. The load value could be directly read from a display/power supply unit – Omega DP-25 S. Additionally, the DC voltage output from the load cell could be measured with a voltmeter and the load value determined from a calibration chart. RPM was measured with an inductively coupled pick-up that was part of the Advantage Motorsports' data acquisition unit. The transmission between the crankshaft and the rear wheel was decoupled.

With the engine idling, the exhaust temperature, the temperature of the air around the engine, the engine body and the exhaust skin temperatures were measured with a type K thermocouple after warming the engine for approximately 10 –15 minutes. The readings are listed below:

Engine body	200 –225 F
Exhaust	170 F
Air around the engine	135 F – 150 F
Exhaust skin	225 F (measured at the end of the exhaust tail pipe)

A digital tachometer (MHT 96 meter, Track Master, Inc, Taylor, Michigan) that works on the principle of inductive pick-up was included to get a direct display of the engine rpm.

The baseline performance of gasoline powered Elite was determined. Load is applied at WOT by controlling the water inlet valve to the dynamometer. A constant rpm was maintained for 2 minutes before moving to the next data point and measurements were done in the rpm range of 2000-6000. A plot of power, and torque versus rpm is shown in Figure 3. We see that the engine is capable of producing 3.8 hp at 6000 rpm and the torque changes by 28 %, from 3.5 N-m to 4.5 N-m as the rpm changes from 2000 – 6000. The exhaust temperature ranged between 380 – 600 deg C.

Conversion to Run on Hydrogen

Three different methods were adopted to introduce hydrogen to the engine, viz:

- a. Modify the carburetor, admit hydrogen continuously at the throat of the carburetor
- b. Admit hydrogen continuously into the intake manifold
- c. Timed-fuel injection into the intake manifold

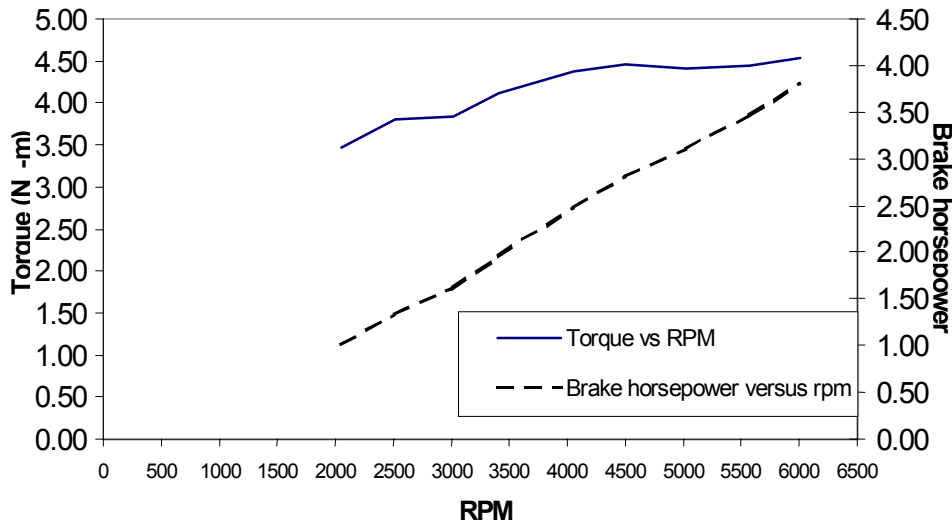


Figure 3: Torque and EGT versus rpm for a gasoline Honda Elite 80 cc scooter engine, ignition at 18 deg BTDC.

Instrumentation

For preliminary testing, hydrogen was supplied from a compressed gas cylinder (UHP grade, AGA size 049, 2400 psig pressure) regulated to operating pressure of 20 psig or lower. Hydrogen flow was measured using a correlated rotameter (Porter Instruments), 150 mm in length with a 1/4" stainless steel float (density: 8.03 gm/cc, 1.063 grams). Correlation charts and correction factors for pressure and temperature were obtained from the manufacturer. An orifice plate (Lambda Square, Inc, Bay shore, New York) will be used to determine the hydrogen flow rate. The upstream pressure (Omega PX 176), the differential pressure drop (Sensotec, Columbus, Ohio) across the orifice plate and the gas temperature (type K thermocouple) will be required to calculate the hydrogen flow rate. In addition to the Advantage Motorsports' D/A unit, a portable data logger from Omega (Omega 3000) was used to log up to three voltage and three temperature readings. A double barrier flash arrester (Kemp, Florida) was installed close to the carburetor/intake manifold to prevent the flame from reaching the hydrogen source. A 5-gas exhaust emission analyzer (TIF, Florida) was used to measure and log the concentration of oxygen and NOx in the exhaust gas. A portable hydrogen leak analyzer (A Ti technologies, Pennsylvania) was also used to measure the hydrogen concentration in the exhaust and to detect hydrogen leaks elsewhere in the test station.

Ignition system modification

The spark plug was triggered off the cam rather than the crankshaft. This eliminates the spark in the exhaust stroke and minimizes the possibility of backfiring. The spark trigger from the cam was used in all the runs with hydrogen gas.

Carburetor modifications and hydrogen induction into carburetor

Hydrogen was delivered into the throat of the carburetor at 8 – 10 psig. Stock timing (18° BTDC) was used. The measured load, hydrogen flow and RPM are given below in Table 2. The modifications carried out are as follows:

- Removed the float bowl chamber, closed the float chamber with a flat aluminum plate with a 1/8” NPT port to admit hydrogen
- Opened up the metering (main) jet from 0.032” to 0.04” to allow more hydrogen flow.

Table 2: Performance characteristics of Elite 80 with hydrogen into carburetor

Run #	Avg RPM	Engine Temperature (deg C)				EGT deg C	Torque (N-m)	Power (hP)	H ₂ flow rate (l/min @ Pr. psig)
		T1	T2	T3	Avg. CHT				
1	2317	56		67	95	235	1.36	0.44	17.6 @ 6 psi
2	2417	62	66		103	232	1.56	0.55	18.5 @ 8 psi
3	2822	61	64	74	128	224	1.39	0.59	36.9 @ 8 psi
4	3269	67	72	89	144	277	1.19	0.55	23 @ 8 psi
5	3891	74			133	270	1.02	0.56	23 @ 8 psi
6	4258	76	79		144	318	0.92	0.54	21.2 @ 8 psi
7	3720	84	92		157	294	1.36	0.67	23 @ 8 psi

Figure 4 shows the torque and power curve versus rpm for the run described above. The exhaust gas temperature ranges between 200 – 350 deg C and increases with engine speed. The peak torque of 1.5 N-m is generated at ~ 2400 rpm and the peak power of 0.7 hP at 3700 rpm. The NO_x and oxygen concentration in the exhaust were monitored and the NO_x level was low (less than 10 ppm) when the engine was running lean ($\lambda > 4$). However, on occasions when more load was applied on the dynamometer, the rpm decreased and to keep the rpm high, more hydrogen

was admitted. This resulted in the NOx level increasing steadily from 200 ppm ($\lambda = 3$) to as high as 3000 ppm ($\lambda=1$). The engine quits running when the mix got rich. The engine was backfiring. The spark plug (NGK, 10 mm) shows grayish blue appearance suggestive of very high temperature at the spark plug and may promote preignition. It was felt that the constant presence of hydrogen-oxygen (air) mix in the carburetor was a probable cause for unwanted combustion. Hence it was decided to admit the hydrogen into the inlet manifold. It should also be noted that the fuel-air mix is lean and that may partially explain the low power output.

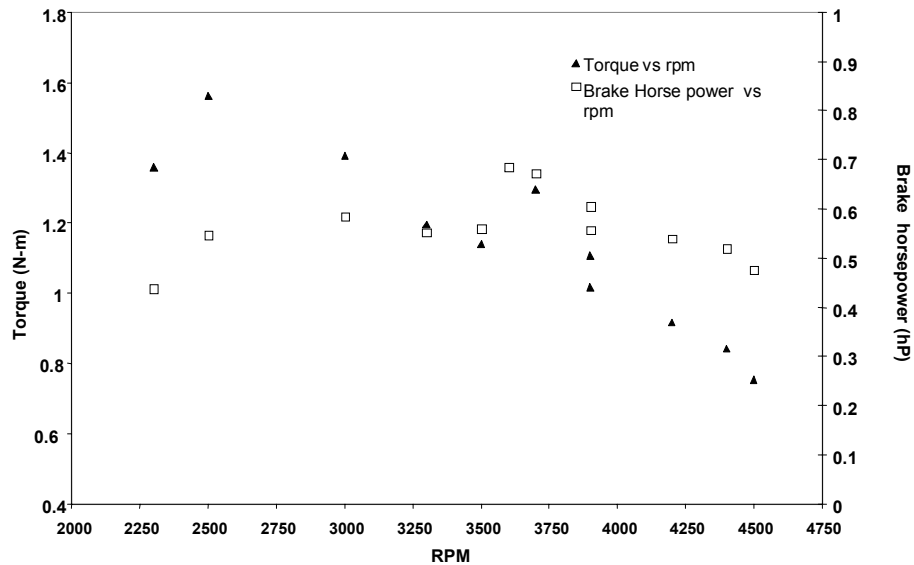


Figure 4: Torque and power versus rpm for hydrogen ICE Honda Elite 80 cc scooter at WOT (wide open throttle), lambda = 3 - 5

Hydrogen induction into the inlet manifold

The NGK spark plug was replaced with a BOSCH surface gap spark plug (10mm) that is known to run cooler. The hydrogen port in the carburetor was closed and instead hydrogen was fed into the inlet manifold, downstream of the carburetor. The carburetor was otherwise intact and the throttle valve was still being used to control the airflow. Several experiments were conducted by varying the spark timing to the following values:

The ignition was timed to occur at 45°, 21° and 18° BTDC. The spark occurs at 18° BTDC (at < 2400 rpm) and the CDI advances it to 27° BTDC at 3000 rpm. A type K thermocouple was used to measure the CHT at the spark plug. The scooter engine attained temperature of 138 deg C (280 F) after 40 min. A maximum torque of 1.3 N-m was generated at 3600 rpm. At higher RPM increasing the load on the engine resulted in the engine stalling. Compared to the other runs, the engine temperature did not rise sharply. With the spark timing fixed at 18 deg BTDC, the scooter was tested once again to determine the torque and power curve versus rpm (Figure 5).

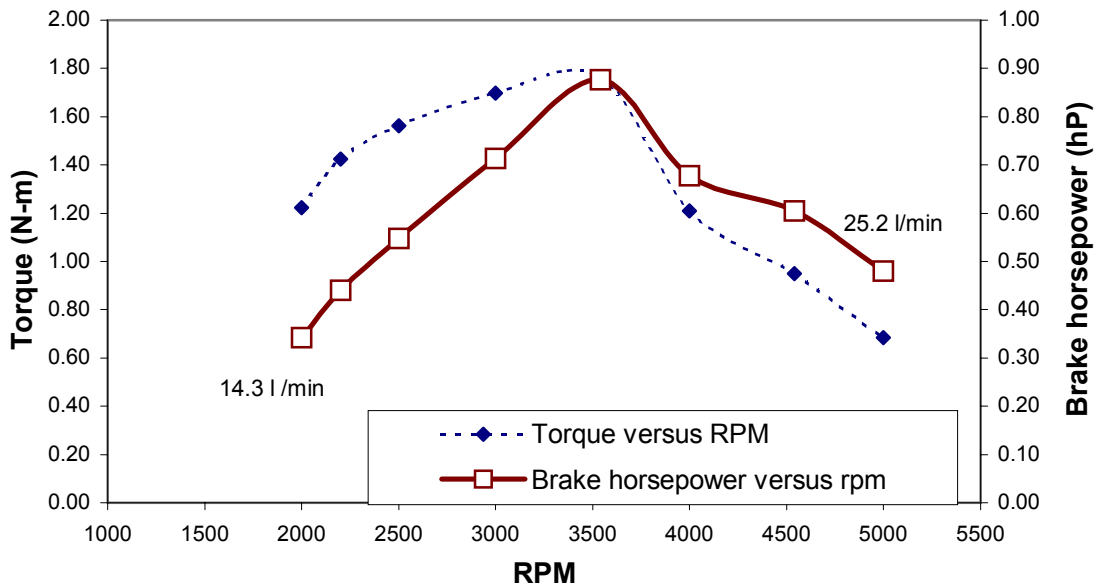


Figure 5: Performance characteristics of a Honda Elite 80 cc, hydrogen admitted into intake manifold at WOT, $\lambda = 2$

We see that the engine develops peak torque of 1.8 N-m at 3500 rpm and falls rather rapidly at higher speeds. The ignition timing undergoes an advance to 27° BTDC at 3000 rpm. This may be a reason why the torque drops very sharply at higher speed.

Timed manifold induction of hydrogen

Continuous hydrogen induction into the intake manifold still results in frequent back-firing of the engine. In order to minimize this, fuel injection was timed using an ECU (Electronics Control Unit, Velcam Consulting, Detroit, MI). The ECU uses for input the signals from a Manifold Absolute Pressure (MAP) sensor, a Throttle Position Sensor (TPS) and the Top Dead Center (TDC) signal from a Variable Reluctance sensor. The fuel injector pulse width is determined based on these input and varies between 3 ms and 10 ms depending on the MAP and throttle position. Two fuel injectors were used to obtain high enough flow at low supply pressure (10 psig or lower) so that lambda values close to 2 or lower could be achieved at Wide Open Throttle (WOT.) The fuel injectors open after the exhaust valve has closed during the intake stroke following the valve overlap period. This is likely to help in two ways,

- dilute and cool the exhaust gas in the residual volume
- minimize back-firing by not mixing hydrogen with hot exhaust gas

No significant gain in power was observed by using timed injection of hydrogen; however there was significant reduction in backfiring as lambda values approached 2 or lower.

Having succeeded in minimizing the occurrence of backfiring using Timed-Manifold Injection, it was decided to use hydrogen from a metal hydride instead of a compressed gas cylinder.

The objective of the next run was to establish the driving range of the scooter with on-board metal hydride. OAC-1 was used for on-board hydrogen storage and exchanged heat passively with the hot exhaust. The storage system was placed in close contact with the hot-exhaust tubing and the heat-exchange between the storage system and the exhaust tube was realized using natural convection or forced convection of ambient air. The RPM was fixed around 3000 –3200 rpm where the peak power is produced. The parameters and the performance results are summarized below:

On-board hydrogen storage	120 grams
Total duration of the run	77 minutes
RPM range	2990-3200
Brake Horsepower	0.3 – 0.6 hP
Estimated vehicle speed at 3000 rpm	16 mph (26 kph, at high gear)
Range	22 miles (33 km)
Approximate hydrogen consumption	3.6 grams/km (120 grams of H ₂ was used)

Table 3 below shows the performance in a different run at WOT with hydrogen supplied from a metal hydride pack (OAC -1) with 120 grams of reversible hydrogen storage capacity.

Table 3: Performance of Honda Elite 80 supplied with hydrogen from metal hydride pack

RPM	EGT (°C)	Lambda	Torque (N-m)	Power (hP)	H ₂ flow (L/min)	H ₂ pressure (psig)
2500	124	3	1.8	0.62	23.7	14
3000	201	2.4	1.6	0.66	24	8
3500	221	2.3	1.4	0.67	27.9	10

Discussion

Conversion of a gasoline ICE to hydrogen ICE is on-going at ECD. We have converted a Honda Elite 80 cc scooter to run on hydrogen. Due to the wide flammability range of hydrogen and the low ignition energy required, the problem of back-firing is common. The ignition timing that results in the maximum torque with hydrogen has to be determined. For most of the tests spark timing of 18° BTDC (up to 2400 rpm) was used. The stock CDI (capacitive discharge unit) progressively advances the timing to 27° BTDC at 3000 rpm. The present spark trigger

configuration allows changing the spark timing only on the advanced side. In fact, retarded ignition is recommended for hydrogen since it burns faster than gasoline.

Preliminary tests have been carried out with on-board hydrogen storage in a metal hydride. Hydrogen desorption is an endothermic reaction and the metal hydride exchanges heat with the exhaust gas passively. The equilibrium plateau pressure increases with increase in temperature at a given hydrogen concentration in the alloy. It is important to have a good exchange of heat so that the supply pressure is high enough at the injector to allow for sufficient hydrogen injection. Rapidly dropping hydrogen supply pressure due to insufficient heat exchange appears to affect the hydrogen flow. This results in a fuel-air ratio that progressively becomes leaner and the power output decreases at a given throttle position.

An orifice plate is being used to measure the hydrogen flow rate, in addition to a rotameter. If this is found to be acceptable (in terms of accuracy and repeatability) it will be considered for on-board fuel measurement. A 'fuel gauge' built around this orifice plate would determine the state of charge of the metal hydride bed.

Conclusions

In this paper, we have evaluated the suitability of an Ovonic Metal Hydride for on-board hydrogen storage for a near-term application of hydrogen technology, namely hydrogen ICE scooter. The metal hydride storage system used (OAC -1) stores 120 grams of hydrogen (reversible capacity). The storage system supplied hydrogen for 77 min to the engine that is unoptimized. This translates to a range of approx 33 km at a speed of 26 kph.

Future Work

Tests are on-going with hydrogen induction timed into the intake manifold with an electronic fuel injection controller. An electronic spark ignition system purchased from MSD Ignition would enable us to change the spark ignition timing to obtain the maximum torque. In addition to engine dynamometer testing, chassis dyno testing under typical driving cycles will be carried out to evaluate the performance of the scooter. In addition to completing the tests on Honda Elite 80, we will also convert a Honda Helix, which has a 250-cc, water-cooled, four-stroke engine. Further alloy development and storage system development work will be carried out to improve the driving range of the vehicle and to reduce the system weight.

Acknowledgement

We acknowledge the U.S. DOE (Hydrogen Program) for partially funding this program under contract DE-FC36-97GO10212.

References

1. Sapru K. 2000. "Strategies for Introducing Renewable Hydrogen for Transportation and Cooking in Developing Countries" in *Proceedings of the 13th World Hydrogen Energy Conference*, 168-172. Beijing, China
2. Sapru K. 2001. in the *International Conference and Exposition on Sustainable Development of Alternate Energy Driven Vehicle Program*, 17-18 April 2001, NewDelhi, India
3. Sapru K. et.al, 2001. in the *Proceedings of the 12th Annual U.S. Hydrogen Meeting*, 189-201. Washington D.C., USA
4. Honda Service Manual of CH80 Elite, Honda Motor Co., LTD. Tokyo, Japan, September, 1988

RESEARCH AND DEVELOPMENT OF A PEM FUEL CELL, HYDROGEN REFORMER, AND VEHICLE REFUELING FACILITY

Cooperative Agreement NO:DE-FC08-99NV13578

**Venki Raman
Air Products and Chemicals Inc.
Allentown, PA 18195**

Abstract

Air Products and Chemicals, Inc. has teamed with Plug Power Inc., of Latham, NY, and the City of Las Vegas, Nevada, to develop, design, procure, install, and operate an on-site hydrogen generation system, an alternative vehicle refueling station, and a stationary hydrogen fuel cell power plant, to be located in Las Vegas, Nevada.

This proposed facility will become the benchmark for validating new natural gas based hydrogen production systems, PEM fuel cell power generation systems, and numerous new technologies for the safe and reliable delivery of hydrogen as a fuel to vehicles. Most importantly, this facility will serve as a commercial demonstration of hydrogen as a safe and clean energy alternative.

Significant progress was achieved in the current year in all aspects of the project development including the H₂ generator, fuel station, and stationary fuel cell. The following sections report on this progress and the future plans and milestones in the next year.

Project Overview

A team of three organizations, Air Products and Chemicals Inc., Plug Power Inc., and the City of Las Vegas, has come together to develop, design, procure, install, and operate an alternative vehicle refueling station, and a stationary hydrogen fuel cell power plant, to be located in Las Vegas, Nevada. The objective of this project is to advance the technology and validate the commercial viability of an alternative refueling station for dispensing H₂/CNG blends and pure H₂ to vehicles, and which includes a stationary fuel cell. This co-production of hydrogen fuel and electric power is referred to, as an “Energy Station.” Air Products is the prime contractor to DOE for this technology validation project. Figure 1 is a block diagram of the proposed refueling facility. This refueling station will include onsite hydrogen generation equipment supplied by Air Products and a stationary fuel cell powered electric generator, to be supplied by Plug Power under a subcontract to Air Products. The City of Las Vegas (CLV) is also a team member, providing the site location and the operating and maintenance staffing for the refueling station. The DOE cooperative agreement covers a five-year nominal period for development, design, installation, startup, and up to 4 years operation of the refueling station.

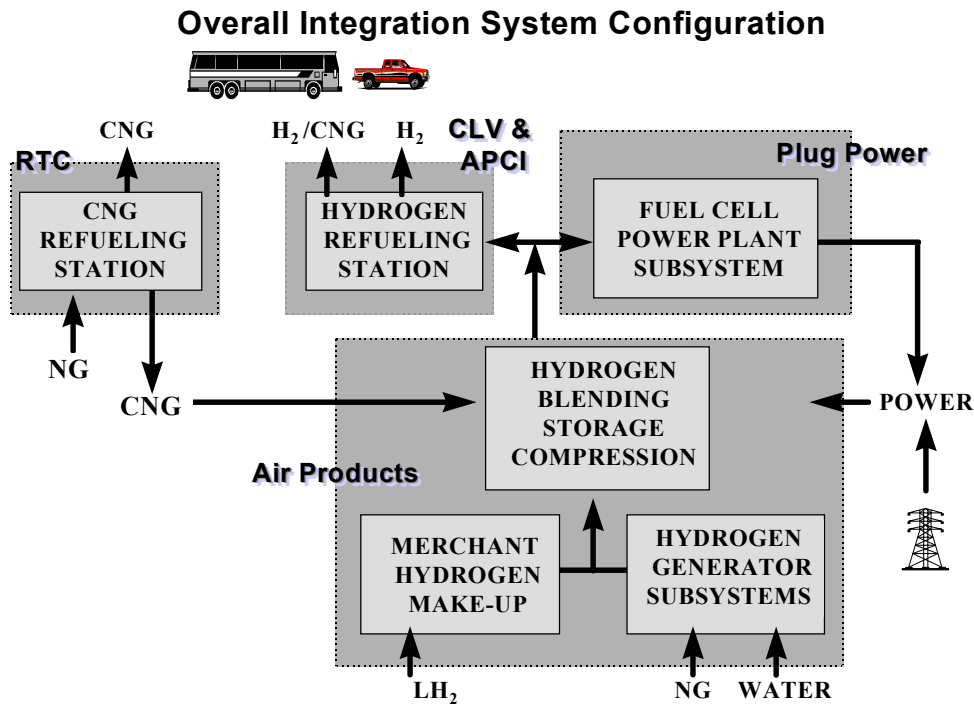


Figure 1

In Phase 1 a standard merchant liquid hydrogen supply system (liquid hydrogen storage tank and vaporizers) will be installed to satisfy initial demand of hydrogen at the refueling station. A blending system will be installed that will mix hydrogen with compressed natural gas (CNG) in a pre-determined blend to be dispensed to the alternative fuel vehicles. The station will also be able to dispense pure hydrogen to vehicles. The hydrogen compression, storage, blending and

dispensing systems will be installed nominally in July 2001 to make the station operational to meet initial refueling requirements. It is expected that there will initially be two Light Duty Vehicles (LDVs) and one para-transit bus fueled with the CNG/H₂ blend. There will also be one H₂ Hybrid Electric bus (operating at low pressure with metal hydride storage) fueled with the pure hydrogen.

CLV will be receiving six new CNG fueled buses in July 2001. Upon successful testing/operation of the first CNG/H₂-fueled para-transit bus, CLV will proceed to convert their six new buses, beginning in August 2001, to CNG/H₂-blended fuel operation. They expect to have all six buses converted over a six-month period, nominally one bus per month through January 2002. H₂ demand growth is expected to continue as additional buses and light duty vehicles are converted to the alternative fuels over the remaining three years of the demonstration project.

To meet this increasing demand, natural gas-based onsite hydrogen generation equipment will be installed and operated at the refueling station in the second phase of the project. In addition, a Fuel Cell Power Plant, that will use hydrogen feed to generate electric power for the refueling station will be completed for installation at the refueling station. The fuel cell will be operated to balance the hydrogen demand on the hydrogen generator for vehicle refueling. For system reliability, the onsite hydrogen generation system will continue to be backed up or supplemented by the liquid hydrogen supply system.

Should the alternative vehicle refueling demonstration station prove to be successful, it is anticipated that vehicle fleets would continue to grow. Plans are included in the project to expand hydrogen generation capacity early in 2002 to meet this additional demand and improve station reliability.

Process Description of the Facility

The overall integrated system configuration and the general areas of responsibility of each member are illustrated in Figure 1. The following section is a general description of the scope of the facility to be installed.

A hydrogen supply system with capacity to meet the nominal projected hydrogen requirements and provides additional capacity to allow growth of the station to serve fleets of commercial vehicles in the future. This hydrogen supply system will consist of natural gas-based hydrogen generation subsystem and a liquid hydrogen make-up backup supply subsystem.

A compressed natural gas (CNG) system that will be installed at the proposed CLV site as part of a separate program would be used to supply the CNG. Tie-ins for the CNG supply would be made on the outlet of the CLV fueling station storage tubes and routed to the hydrogen/CNG blend fuel station that will be designed and constructed by Air Products. This system includes hydrogen compression, storage and blending subsystems that will supply the H₂-and CNG/H₂, blended fuels to the metering and dispensing units.

A Fuel Cell Power Plant being supplied by Plug Power will help to test, and demonstrate the technical and economic viability of integrating baseload fuel cell power generation with on-site hydrogen production for vehicle refueling. The fuel cell power plant will be connected to the fuel station, and to the local power grid.

Project Objectives

The technical objectives of the project include the following:

1. Resolve design issues and demonstrate small, on-site H₂ production for fuel cells and H₂ fuel stations
2. Design, construct, and operate a multipurpose refueling station
3. Dispense CNG, H₂/CNG blends, and pure H₂ to up to 27 vehicles
4. Design, construct, and operate a 50kW fuel cell on pure H₂
5. Evaluate operability, reliability, and economic feasibility, of integrated power generation and vehicle refueling designs
6. Maintain safety as a top priority in the refueling station and fuel cell design and operation
7. Obtain adequate operational data on fuel station to provide basis of future commercial fueling station designs. Develop appropriate “standard” designs for commercial applications
8. Expand the current facility to serve as the first commercial facility when sufficient hydrogen demand develops. Ultimately serve as a link in a national H₂ corridor.

Project Status

Significant progress was made in the development of this project in the current year as described below:

H₂ Generator

We completed construction of a fully integrated auto thermal (ATR)-based prototype H₂ generator, and successfully tested it at the Air Products laboratories in Allentown, PA to demonstrate technical viability of the technology. Several operational issues around heat and waste gas management were resolved as part of meeting this major milestone.

We completed an internally-funded study on the competitiveness of various reformer technologies, and concluded that steam methane reformer (SMR) technology was more economical than ATR technology at this size range (50-100kW), to generate pure H₂. An SMR technology vendor was identified and procurement was initiated for the next generation unit at a nominal 100 kW size.

Fuel Station

Air Products has completed the fuel station design, and various equipment components such as the compressor, storage tubes, blender, and dispenser have been fabricated.

Process and design hazards and operability (HAZOP) reviews have been completed for the prototype H₂ generator, fuel station and fuel cell.

Electrical supply design for the project site has been completed by the City of Las Vegas for the project site at the CLV West Service Center.

Fuel Cell

Plug Power recommended a change in the fuel cell design basis from the originally proposed automotive system that was being developed under a separate DOE initiative, to one based on their commercial residential fuel cell system and stack design to minimize technical, schedule, field support and cost risk. This recommendation was approved, and the design of the 50 kW Fuel Cell System has been completed.

Testing of the various parts of the system has been completed, including: air and hydrogen humidification components, mass flow meters, blower, inverter/power conditioner, motor controls, and the stack voltage monitoring card. The 50 kW fuel cell stack system comprised of eight 7.5 kW stack modules was also tested in parallel/series configuration. The fuel cell is now in the final assembly process.

Nevada Power approved the grid interface including the design of interconnection of the fuel cell with the grid at the project site.

Future Work and Milestones

The planned work and milestones for the upcoming year are as follows:

H₂ Generator

We plan to install and operate the prototype ATR H₂ generator at the Las Vegas facility in August 2001. The next generation SMR H₂ generator 100 kW (3000 SCFH H₂) will be constructed and tested at the vendor's facility in Summer 2001. This unit will be installed in Las Vegas by January 2002.

Opportunities to integrate and test a metal hydride "thermal" compressor will be evaluated with the scale-up SMR H₂ generator. This system is intended to take advantage of the waste heat from the reformer to compress the H₂ for the fuel station.

Comprehensive system testing and analysis will be completed in the summer of 2002.

Fuel Station

The multi purpose fuel station is expected to be operational in July 2001 starting with a fuel source of delivered liquid hydrogen.

The fuel station will be tied-in to on-site sources of H₂ with future installations of the prototype ATR (Aug 2001), and later the SMR H₂ generator (January 2002).

Fuel Cell

The fully assembled 50kW Fuel Cell System will undergo operational testing at Plug Power's facilities in Latham, NY in May 2001. The unit will be shipped to Las Vegas in June for installation and start up in July 2001.

Performance data will be monitored and recorded daily during operations at Las Vegas. The fuel cell unit will be upgraded as required to increase its reliability, availability and performance in the field.

Shown below is a photo of the assembled 50kW fuel cell power plant.



Figure 2
Plug Power Fuel Cell Power Plant

Leadership-Cooperative Efforts

Venki Raman gave technical presentations on Hydrogen Fuel Infrastructure at the following conferences:

1. Energy Frontiers International, Marcos Island, FL, February 1-2, 2000
2. 11th Annual NHA Conference, Tyson's Corner, VA, March 1-2, 2000

3. IQPC Fuel Cells 2000 Conference, Palm Springs, CA, May 24-25, 2000
4. Florida's Hydrogen Summit, Tallahassee, FL, October 24-25, 2000

Outreach efforts have been made to auto participants of the California Fuel Cell Partnership with a view to promote the Las Vegas site as a link in a California-Nevada H₂ corridor.

Acknowledgments

The invaluable contributions made by the following individuals in achieving the progress reported here is gratefully acknowledged:

Mr. James Gast – Program Manager, Mr. Edward Kiczek, Mr. Todd Carlson, Mr. Richard Colwell, Mr. Keith Schultz, Mr. Gerald Lewis (H₂ Generator)

Mr. David Farese, Mr. David Imler, Mr. Joseph Cohen, Mr. James Hansel, Mr. John Fischl (H₂ Fuel Station) all of Air Products.

Mr. Scott Wilshire, and Mr. David Parry (Fuel Cell), Plug Power Inc.

Mr. Dan Hyde, and Mr. Jianzhong Jiang (Fuel Station Siting), City of Las Vegas.

THE RURAL AREA POWER PROGRAM DIESEL REFORMER EVALUATION

**Dennis Witmer
Thomas Johnson
Ronald Johnson
University of Alaska Fairbanks
Fairbanks, AK 99775**

**Jay Keller
Andy Lutz
Sandia National Laboratories
Livermore, CA**

Abstract

The Remote Area Power Program was created to evaluate the possibility of using PEM fuel cells with diesel reformers for residential power in remote areas. This technology was advertised as being clean, efficient, reliable, and cost-effective, and business plans were presented that showed major commercial deployment by 2001 or 2002. The industry also claimed that diesel reformers would be available in the near future, which would make this technology very attractive for remote areas like rural Alaska. Based on these claims, a technology validation program was started in the summer of 1998 to verify these claims.

The program has evaluated a total of five PEM fuel cell stacks, and diesel reformers from two sources. However, we have been unable to obtain an integrated reformer/fuel cell system from an industrial source, and are experiencing some difficulties with the small-scale diesel reformers delivered to the program. Furthermore, our work to date has been unable to verify some of the more attractive claims of this technology with hardware delivered to the program, including the efficiency and reliability necessary for successful commercial deployment.

Background

In order for PEM fuel cell systems to obtain a significant market, they must successfully compete with existing technologies, and prove significantly better than these technologies in some way. For the case of rural Alaska, the existing conventional technology is the Diesel Electric Generator (DEG). Current electrical generation costs in remote villages vary from 20 to 80 cents per kilowatt hour, indicating the possible presence of a profitable niche market for competing technologies.

The PEM fuel cell suppliers claimed that their systems would provide electricity at an efficiency of 40% net electrical (LHV), be reliable with a lifetime of 40,000 hours (5 years), and have a capital cost of about \$3,500 per 5kW unit, where heat produced by the unit could be recovered for residential use. Furthermore, there were significant claims with regards to the environmental benefits, with some web sites claiming that the only emissions would be water vapor (how a hydrocarbon can be reformed without the production of CO₂ was not addressed). The goal of this program was to evaluate these claims, and to demonstrate this technology in the field.

Methods and Results

The first major goal of this program was to measure the thermodynamic efficiencies of the PEM systems. Since the efficiency depends on the system boundary, our choice of boundaries was to make this system as directly comparable to conventional technology as possible. We elected to use the same system boundary that Alaskan utilities use for evaluating the efficiency of their operation, i.e., the AC electrical energy out divided by the diesel fuel in (LHV).

A PEM fuel cell system requires three subsystems in order to meet the diesel in/AC out boundary: a reformer, to convert the hydrocarbon fuel into usable hydrogen, a PEM fuel cell stack to convert the hydrogen into DC electricity, and an inverter to convert the DC electricity in to AC usable by the residence. There are also significant balance-of-plant issues, including air supplies for both the reformer and the fuel cell stack, and water supplies for both the fuel cell and the reformer. These balance-of-plant needs require blowers and pumps, which act as parasites on the system. In addition, if the unit is to be operated in a grid-independent mode, some of the energy must be stored in a battery bank, which reduces the overall system efficiency.

In order to make these measurements, several test benches were built, carefully calibrated, and used to evaluate the fuel cell performance. During the first two years of this program, the systems efficiencies were measured for five fuel cell stack systems operating on pure hydrogen. Our findings, which were consistent between stacks, indicated that current technology can deliver nearly 50% net electrical efficiency based on the LHV of hydrogen when the stacks are operated at 2.5 kW DC out. This is a system number for a stack operated at atmospheric pressure with a blower, and includes all parasites and a hydrogen purge resulting in some fuel loss.

The program then moved on to the more difficult issue of the diesel reformer. It soon became apparent that there were some outstanding issues associated with reforming in general, and some

issues very specific to the reforming of diesel and other heavy hydrocarbons. One important issue is simply that as reformers get smaller, the surface-to-volume increases, resulting in higher heat losses from the smaller devices. This, in turn, leads to problems in maintaining even temperature distributions in these small devices, which can lead to operational issues. Furthermore, the additional heat loss must result in a lower reformer efficiency, as compared with the efficiencies achievable in larger systems.

It also became apparent that there are many ways of defining an efficiency of a reformer. For catalyst evaluations, some sources report a fuel conversion rate as an efficiency, as this does indicate how well the catalyst is at converting a feed stock into hydrogen. However, for steam reforming, heat must be supplied to drive the exothermic reaction forward, and this heat must be supplied in one form or another from the incoming fuel. For this reason, we elected to use an efficiency based on the fuel value of the usable hydrogen delivered from the reformer to the fuel cell divided by the fuel value of the incoming fuel. Electrical parasitics required by the reformer also were measured, and subtracted from the electrical output of the fuel cell system.

The Northwest Power Steam Reformer

The first reformer evaluated was supplied to the program from Northwest Power Systems of Bend, Oregon (currently Idatech). Northwest Power is developing residential power systems based on methanol as a feedstock, and the kerosene/diesel reformer represented a first attempt to expand the fuel options used by their technology. This reformer was a steam reformer with a membrane to purify the hydrogen, with only small amounts of water vapor and methane as impurities. The high quality of this product gas has been verified by gas analysis, which indicated that there is less than 1ppm CO in the product gas.

The NPS steam reformer was successfully used in a demonstration, using desulfurized kerosene as a fuel, providing hydrogen to a 3kW fuel cell stack, which powered an inverter, and was used to run the laboratory lights during a public demonstration.

However, there were several drawbacks to the NPS diesel reformer. When the unit was operated in a self-sustained mode, the overall efficiency as defined above was at best about 35%. Measurement of the energy balance indicated that significant energy was lost through the combustion exhaust. Our runs with this unit were also frequently interrupted by coking events, which were explainable in part by control system problems. However, other issues were likely involved, and it was not clear that these issues could be addressed within the scope of this program.

The Autothermal Integrated System

There are two different technologies for PEM fuel cell systems operating on hydrocarbon fuels. The first, described above, is to create a reformer that provides pure hydrogen to a PEM stack designed to run on this gas. However, the purification of the reformer product gas is done using a membrane, and the membrane needs a significant partial pressure drop in order to work. But

once the pure gas is provided, the PEM stack issues are much simpler, as the pure gas is much easier to handle in the stack.

The second alternative is to use a reformer that provides a hydrogen-rich gas stream to the fuel cell. This strategy is used in the phosphoric acid and solid oxide fuel cell systems, and has the advantage that the reformer can operate at near atmospheric pressure. However, PEM technology is significantly different than the other fuel cell technologies in that it is sensitive to much lower levels of CO in the gas stream, and so the clean-up stages must provide adequate removal of this CO from the product stream.

One of the major advantages of this scheme is that an autothermal reformer can be used, similar to those in other fuel cell systems, but with a more robust CO removal system. Autothermal reforming includes a partial oxidation reaction (POX) followed by a steam reforming reaction. Since the partial oxidation reaction is exothermic (it is a fuel-rich combustion reaction, which produces both hydrogen and heat) and the steam reforming reaction is endothermic, the net result is a reaction that produces a hydrogen-rich stream without heat transfer across a heat exchanger wall. A disadvantage of this system is that the gas that is fed to the fuel cell is not pure hydrogen, but rather a mixture of carbon dioxide, water vapor, methane, nitrogen, and hydrogen. Therefore the fuel cell anode sees a lower partial pressure of hydrogen, and produces a somewhat lower electrical potential than would a pure hydrogen fuel cell stack.

In order to test this system, the RAPP Program solicited bids for an integrated autothermal PEM system using diesel or kerosene. This bid was awarded to Dais Analytic, and required delivery of a diesel reformer by May 2000, and delivery of an integrated system suitable for residential power by August 2000. The diesel reformer to be delivered in May was part of an existing program between Argonne NL and Dais, and was to be first shipped there for preliminary evaluation before being sent to Alaska.

However, the shipment of the diesel reformer did not occur in May 2000, and by late August, some concern was raised. At this time, the DOE project officer decided that something needed to be done to motivate Dais, and arranged a training meeting at Dais in late August. Representatives from Sandia NL Livermore, Argonne, and the UAF Energy Center went to the Dais Analytic site in Woburn, MA for a week-long training session.

There were two significant things that did not occur during the week. The first was that the reformer did not run, due largely to the non-performance of an auxiliary burner. The second item was that the management of Dais-Analytic failed to provide a suitable revised timetable for delivery of the integrated system within the specifications of the contract, and instead tried to renegotiate the terms and conditions of the agreement, for a significantly increased amount. These discussions eventually ended with a termination of the contract for the integrated system for non-performance of the contract.

The Dais Analytic diesel reformer was eventually delivered to Argonne NL on October 31, 2000, precisely one year after the original date specified in the contract with Argonne. The unit was shipped to the UAF Energy Center, and arrived shortly before the end of the year.

It quickly became evident that the Dais diesel reformer is a laboratory device, and a significant distance away from being a commercially viable unit. The performance of the auxiliary burner continued to be an issue for two reasons: the low fuel flow rate caused problems with the nozzle in the burner, and the glow plugs used to ignite the fuel-air mixture frequently failed. The second issue led to some additional problems, when a short in the glow plug led to 120 volt current jumping a relay and damaging the electronics in the control board, causing a delay in the testing program. Eventually, however, these issues were solved at least to the level where the reformer could be operated for experiments.

In spite of the difficulties experienced, the Dais diesel reformer proved to perform well in the laboratory. The control system supplied with the unit functioned quite well, as start-up and operation required very minimal operator interaction. The materials used in the construction of the reformer were quite robust, as the high temperature heat exchangers and reactor vessels were made of Inconel. The design was well-integrated, especially with respect to heat recovery from the reactors and flow streams, as the majority of the heat released was recovered for preheating reactant feed stocks. During operation, the unit operated in a very stable fashion, and no evidence of coking was experienced, even during a 30-hour run.

One of the major advantages of the Dais reformer is its ability to operate with fuels containing substantial sulfur contents. This is due to the sulfur tolerant catalyst in the autothermal reactor. However, the water-gas shift reaction catalyst is sensitive to the presence of sulfur, so that sulfur still must be removed before the gas stream reaches that catalyst. However, this can be accomplished by scrubbing the H_2S from the gas stream downstream from the autothermal reactor, a much more convenient point in the process to extract this sulfur.

The goal of our operation of the reformer has been to operate a PEM fuel cell stack on the hydrogen-rich stream provided by the reformer. To date, however, we have been unable to get the gas clean-up stages to work properly, and have not been able to complete this task. We are hoping to accomplish this task in early summer 2001.

In lieu of this experiment, we have attempted to estimate the system performance, from diesel in to the system to AC out. This calculation is necessary to compare the efficiency of the PEM system to that of conventional technology currently in use in remote areas, namely, the diesel electric generator, with an efficiency of about 33% (with today's technology) and rising to close to 40% in the near future.

Our estimates for the autothermal system are as follows: the reformer operates at a conversion efficiency of 80% (Hydrogen energy out to Diesel energy in), 80% of the hydrogen fuel is utilized by the fuel cell, the stack operates at 90% of the pure hydrogen voltage due to the dilution of the gas, the fuel cell efficiency is about 53%, and the inverter efficiency is 90%, giving a resulting efficiency of about 26%. However, there are possibly significant efficiency hits in the system that are not accounted for in this calculation, such as the electrical energy needed to run the blower for the reformer, the possible use of batteries for storage and peaking loads (a necessity in a grid-independent system). These will affect the system efficiency in a negative way. At this point in time, it seems likely that the system efficiency based on current technology will be somewhere in the low 20's.

There are also significant open issues with regards to the PEM stack, especially with regards to stack lifetime. While the industry has projected costs based on stack lifetimes of 40,000 hours, the best results so far are only at 10,000 hours for some single-cell experiments, and a lifetime of only several thousand hours for stacks. While these numbers may be adequate for transportation applications or backup power, they are inadequate for residential power systems, where the fuel cell must operate continuously.

Conclusions

Despite the considerable excitement with regards to PEM residential power systems for distributed generation, evaluation of hardware delivered to the RAPP program indicates that this technology in its present state of development does not present clear advantages for power generation in remote areas. Efficiencies measured are lower than those of conventional power systems, and significant reliability issues remain to be solved. Diesel reforming remains a difficult issue, although the autothermal reformer may be more suited to this fuel than steam reforming. While cost projections based on mass manufacturing indicate that this technology may be economically viable in the future, current prices for PEM systems remain high.

Bibliography

Cleghorn, Simon, "Production of a Qualified Polymer Electrolyte Fuel Cell Membrane Electrode Assembly for Emerging Commercial Applications," 2000 Fuel Cell Seminar Abstracts, pg. 35-39

Gulzow, Erich, H. Sander, N. Wagner, M. Lorenz, A. Schneider, M. Schulze, "Degradation of PEFC Components," 2000 Fuel Cell Seminar Abstracts, pg. 156-159

Kreutz, Thomas G., and Joan Ogden, "Technical and Economic Assessment of Natural Gas-Fuelled PEMFC Cogeneration Systems for Residential Applications," 2000 Fuel Cell Seminar Abstracts, pg. 436-439

Shindo, K., T. Ouki, A. Fujii, O. Tajima, N. Nishizawa, T. Susai, "Development of a PEFC Co-Generation System for Residential Use," 2000 Fuel Cell Seminar Abstracts, pg. 492-495

Edlund, D. J., W. A. Pledger, and A. Dickman, "Field Testing Residential Fuel Cell Systems," 2000 Fuel Cell Seminar Abstracts, pg. 496-498

Krumpelt, M., J. D. Carter, R. Wilkenhoener, S. H. D. Le, J-M. Bae, and S. Ahmed, "Catalytic Autothermal Reforming for Fuel Cell Systems," 2000 Fuel Cell Seminar Abstracts, pg. 542-545.

“FILLING UP WITH HYDROGEN 2000”

**Matthew J. Fairlie, Paul B. Scott
Stuart Energy, USA
Van Nuys, CA 91406**

Abstract

The purpose of Stuart Energy’s prototype deployment program “Filling Up with Hydrogen 2000” is to build on-site electrolytic hydrogen generators for refuelling gaseous hydrogen vehicles. The general objective of this prototype deployment program is to demonstrate that electrolysis based hydrogen generators can meet market cost and performance targets. The program is in year 3 of Phase 2.

In Phase 2 of the Stuart/DOE program Stuart Energy will deploy two types of appliances called Fleet Fuel Appliances and Personal Fuel Appliances. The Fleet Fuel Appliance is intended for use with buses, trucks and other centrally fuelled fleet vehicles where fuel production rates in excess of 400 SCFH (10 Nm³/h) are required. The Personal Fuel Appliance is designed for use with consumer vehicles at the home or office, and can be sustained by the utility infrastructure of the typical North American home. The production rate of these units is in the range of 50 SCFH (1.5 Nm³/h). Both types of appliances will be capable of delivering gaseous hydrogen at high pressure (up to 5000 psig) to the vehicle. The goals of the program are to demonstrate the performance and cost objectives projected in the Phase 1 commercialization plan while accomplishing a safe and convenient refuelling process.

Introduction

The objectives of the past year were to demonstrate operation of Stuart's new CST electrolytic cell stack technology in large-scale application as part of a hydrogen bus refuelling station at SunLine Transit in 1000 Palms, California, build and test two smaller fleet fuel appliances using a different but related cell stack technology, and on a smaller scale through the prototyping program for the personal fuel appliance deliver a fuel appliance to a major automaker for evaluation. The key to achieving the cost targets in both product lines is the CST cell stack. The knowledge gained from the demonstrations will provide an experience base for the cell stack technology for later commercialization, and is a cost effective approach to equipment testing being that the user picks up the operating costs.

Stuart's prototype development plan not only includes the testing of the cell technology, but also provides public exposure to the fuel appliance concept; introducing customers to the idea of distributed on-site hydrogen production as well as providing valuable precedents for the development of codes and standards and hydrogen project risk assessment. The operation of the bus fuel appliance (P3-1A) at SunLine Transit provides public access to the technology through SunLine. The low-pressure fueler (P3-1B LP) provides a demonstration of a system, which can refuel metal hydrides. The high-pressure fueler (P3-1B HP) demonstrates the concept of a distributed "community fueler". The prototyping of the personal fuel appliance (PFA P1 Model 25) at major automakers will provide the auto industry the opportunity to assess and evaluate the concept of a small onsite hydrogen generator and potential home based fuelling appliance.

While the design and manufacture of the P3 prototypes provides a proving ground for component technology, primarily the cell stack, the design emphasis in the next 12 months will be development of the P4 systems. The P4 prototypes will realize a projected 50% reduction in appliance footprint and will be the basis for achieving manufacturing cost targets.

Discussion

Stuart Fleet Fuel Appliance Program

The Fleet Fuel Appliance is directed at the refuelling needs of hydrogen buses, trucks and other centrally fuelled fleet vehicles. Conceived to be a scalable product, 1 to over 30 vehicles can be supported with one appliance. The progress and development of Fleet Fuel Appliance prototypes follows a four-phase product development program, which is now in its third phase. The 17.7 million-dollar program will be completed by 2003. The ultimate cost goal for the fleet fuel appliance is \$3000 per SCFM hydrogen production/refuelling capacity. Relationships with bus operators and hydrogen bus companies will be developed during the prototype deployment period from 1999-2002. Commercialization will occur from 2002 to 2004 and will probably be led by fuel cell urban buses. Table 1 shows the deployment schedule for fleet fuel appliance prototypes and prototyping partners identified at this time.

Table 1. Schedule for Fleet Fuel Appliance Prototypes

PROTOTYPE	PROTOTYPING PARTNER	DELIVERY DATE
<u>Fleet Fuel Appliance</u>		
P3-1A	SunLine Transit	Q1 2000
P3-1B (High Pressure)	Powertech Labs	Q1 2001
	California Fuel Cell Partnership	Q3 2001
P3-1B (Low Pressure)	Fuel Cell Propulsion Institute*	Q4 2001
P4-1	TBA	Q3 2001
P4-10	TBA	Q2 2002
<u>Personal Fuel Appliance</u>		
PFA-P1-99	Ford Motor Company	Q1 2001

* Proposal under consideration

P3 Fleet Fuel Appliance Progress

Prototype P3-1A

P3-1A demonstrates Stuart’s new MW-CST or multi-stack electrolyzer cell technology and is intended for use with bus fleets and large retail outlets. The appliance is capable of producing up to 1490 SCFH at full current (12000 amps). The unit has been operating at SunLine Transit in 1000 Palms, CA and is being used to fuel a fleet of buses including two Hythane buses and a Ballard fuel cell bus. A Ballard Fuel Cell Bus being fuelled is shown in Figure 1.



Figure 1 – Ballard Fuel Cell Bus being fuelled at SunLine.

The unit is connected to a high-pressure storage system (approx. 100,000 SCF) and an external dispenser, which is part of a public access hydrogen fuelling station, the first of its kind in North America. The dispenser was designed by Stuart and built by Fuelling Technologies Inc. High-pressure hydrogen is distributed through one hose and high pressure Hythane, a mixture of 20% by volume hydrogen in natural gas, from the other. General operating characteristics of the cell are summarized in Table 2.

Table 2. General Operating Characteristics of the Cell

OPERATING CHARACTERISTIC	SPECIFICATION
Maximum Output	1490 SCFH
Maximum pressure	4000 psig
Cell Voltage efficiency @ 70 C & 95% maximum output	83% wrt HHV
Gas purity (ex. moisture)	99.65%

Over the period from mid-July 2000 to March 31, 2001 the unit operated for 960 hours (cells and compressor) producing 1,200,000 SCF of hydrogen fuel. The demonstration is planned to continue until March 31, 2003. The P3-1A Fleet Fuel Appliance at SunLine Transit is shown in Figure 2.



Figure 2 – The P3-1A Fleet Fuel Appliance at SunLine

Prototype P3-1B LP

The low-pressure Fleet Fuel Appliance, P3-1B LP, delivers a rated hydrogen output of 400 SCFH at 200 psig. In May 2000, P3-1B successfully completed 3000 hours of in-house testing. In the upcoming year, hydrogen generated from the prototype will be used to demonstrate refuelling hydrogen vehicles in underground mining applications. The unit (a solid model shown in Figure 3) uses two single-stack H-CST electrolyzers and two compressors (one duty and one stand-by).

Prototype P3-1B HP

P3-1B HP Fleet Fuel Appliance successfully passed factory tests (750 hours) and has been delivered to Powertech Laboratories in Vancouver BC. Based on the same platform as P3-1B LP the unit uses H-CST single stack electrolyzer technology.

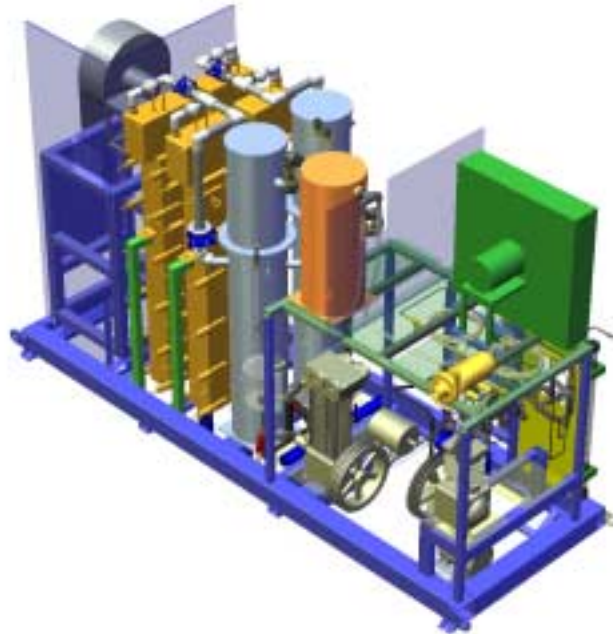


Figure 3 – Model of P3-1B (LP)

The unit incorporates the power conditioning system, two cells and two compressors in a linear designed platform that can be readily scaled to large sizes, up to six cells. The unit has both a catalytic purifier as well as high performance dryer, which is, installed inter-stage. The hydrogen production rate is rated at 400 SCFH at a maximum pressure of 5000 psig with plans to increase pressure to 6000 psig. Since arriving at the site the unit has run over 300 hours. The unit is being used to test and certify storage tanks for hydrogen vehicles. A photograph of the unit at Powertech is shown in Figure 4.



Figure 4 – The P3-1B (HP) at Powertech Labs, Surrey, BC

A summary of the operating characteristics of the high and low-pressure units is summarized in Table 3.

Table 3: Operating characteristics of P3-1B Prototypes

OPERATING CHARACTERISTIC	P3-1B (HP) SPECIFICATION	P3-1B (LP) SPECIFICATION
Production Rate (max)	450 SCFH	400 SCFH
Pressure	5000 psig	200 psig
Hydrogen Purity	99.993%	99.994%
Moisture (dew point temperature)	-65 C	-70 C

Prototype P3-5 Cell Stack Assembly

The P3-5 fuel appliance, capable of fuelling 5 buses or approximately 10000 SCFH was taken to the design stage of the cell stack assembly only. The cell stack assembly is designed to be assembled in 2- block cell platforms, with each block consisting of 6 stacks. The modules are aligned in a row to form a “U” shaped bank, which can be assembled inside an enclosure. The cell stack assembly design will be used in future bus fueler prototypes. A 3-D model of the P3-5 Cell Module is shown in Figure 5.

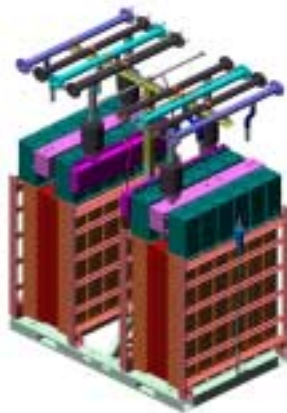


Figure 5 – 3-D Model of P3-5 Cell Module

The modules as assembled stand approximately 12 feet tall, 8 feet wide, by 6 feet long and weigh 13,000 lb. Installed the entire cell battery, with gas and feedwater headers connected, will be 14 feet high, 8 feet wide and 30 feet long. The unit will be capable of generating 10,000 SCFH.

Although a number of proposals for supplying bus filling stations have been made to Europe, California and Brazil, there have been no confirmed projects. As a consequence the plan for this prototype has been modified to include only the design and construction of the prototype. A photograph of the P3-5 Cell Prototype is shown in Figure 6.

Light/Medium-Duty Fleet Applications

**Kirk Collier
NRG Tech
Reno, NV 89502**

Abstract

NRG Tech has developed and implemented a retrofit strategy for light and medium-duty vehicles to convert them to operate on mixtures of hydrogen and natural gas (called HCNG). The vehicles achieve equal vehicle range and reduced exhaust emissions, and are more powerful than the same vehicle operating on natural gas alone. The retrofit strategy uses mixtures of hydrogen and natural gas containing at least 30 mole % hydrogen, incorporates exhaust gas recirculation for charge dilution, utilizes three-way catalyst for emissions control, and includes a supercharger for superior performance. One light-duty and one medium-duty vehicle are being retrofitted. The light-duty vehicle is a Ford F-150 dedicated natural gas truck, and the medium-duty vehicle is a 23-passenger Eldorado paratransit bus. The bus has been in service as a natural gas retrofit. Preliminary testing has shown equivalent vehicle range (about 200 miles), reduced NO_x and CO emissions, and a 28% increase in horsepower for the OEM Ford F-150. Conversion of the Eldorado bus is expected to be completed before the end of this fiscal year.

Introduction

The project is designed to bring hydrogen fuels to the marketplace in the short term. Because of the current high cost of hydrogen and the high purity hydrogen requirements of current fuel cell technology, the successful commercial implementation of hydrogen as a fuel is very much in the future. Because of this situation, a strategy is needed for earlier commercial implementation of hydrogen as a fuel. That strategy is to supplement natural gas with hydrogen for use in internal combustion engines. The rate of supplementation ranges between 30 and 50% by volume hydrogen. This range allows for enough hydrogen to significantly enhance the combustion of natural gas while remaining within an operational window that does not require extensive engine modifications.

Goals and Objectives

The goals and objectives for the project are:

- To exceed California 2002 SULEV emissions
- To enhance vehicle performance
- To develop a commercialization strategy for economic growth for the state of Nevada

NRG Tech has developed and implemented a retrofit strategy for light and medium-duty vehicles to convert them to operate on mixtures of hydrogen and natural gas. The vehicles achieve equal vehicle range and reduced exhaust emissions, and are more powerful than the same vehicle operating on natural gas alone. The retrofit strategy uses mixtures of hydrogen and natural gas containing at least 30 mole % hydrogen, incorporates exhaust gas recirculation (EGR) for charge dilution, utilizes three-way catalyst for emissions control, and includes a supercharger for superior performance. One light-duty and one medium-duty vehicle are being retrofitted. The light-duty vehicle is a Ford F-150 dedicated natural gas truck, and the medium-duty vehicle is a 23 passenger ElDorado paratransit bus. The bus has been in service as a natural gas retrofit.

Our project partners are the City of Las Vegas, who will refuel the vehicles; Bechtel Nevada, who is the project manager; and the Regional Transit Commission, who will operate the paratransit bus.

Retrofit Strategy

The retrofit strategy uses mixtures of hydrogen and natural gas containing at least 30 mole % hydrogen, incorporates exhaust gas recirculation (EGR) for charge dilution, utilizes three-way catalyst for emissions control, and includes a supercharger for superior performance. This deviates from our original strategy of using lean burn as the charge dilution mechanism. The reasons for this change are as follows:

- **Improved Power**
Lean burn created a problem with acceleration from a complete stop. Once the supercharger created boost, the driveability was excellent. However, off-idle acceleration was poor. The solution to this problem was to change the stall characteristics (the “K” factor) of the torque converter. This is a labor and capital expense burden. Also, because the amount of EGR can be varied without proportionally affecting the vehicle-out NO_x emissions, the supercharger can be designed to improve vehicle performance superior to that achieved by the same

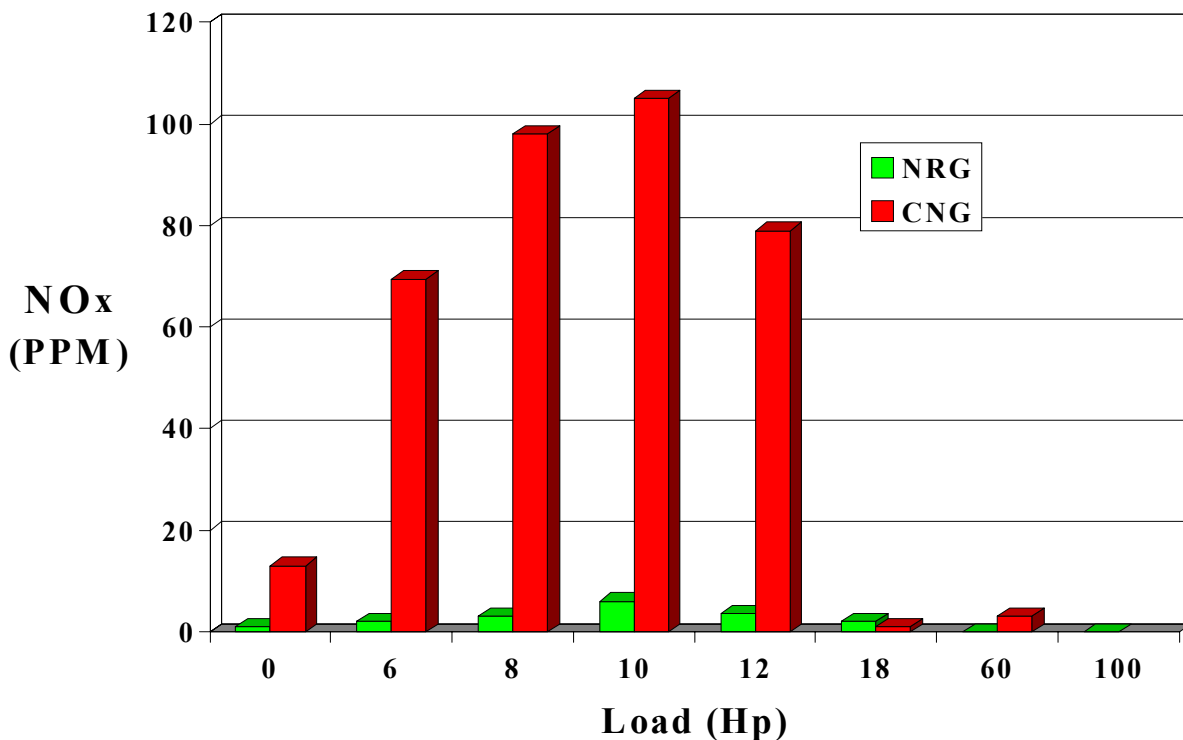
- vehicle operating on gasoline.
- Uses Existing Engine Computer
With the lean burn strategy, an aftermarket engine control computer was required to control air-fuel ratio and ignition timing. By using NRG's EGR strategy, the factory computer is retained.
- Uses Existing Oxygen Sensor
For lean burn, a special oxygen sensor, called a UEGO sensor, had to be incorporated to control air-fuel ratio with 10% exhaust gas oxygen. These sensors and associated electronics are very expensive and prone to failure. With the EGR system, the standard oxygen sensors are used.
- Uses Existing Feedback Control System
For a three-way catalyst system to operate at maximum efficiency, a very precise, complex feedback control strategy must be used. By using EGR charge dilution, the factory oxygen control strategy is applicable to HCNG fuel.

The bottom line to these advantages is that the current retrofit using HCNG with EGR for charge dilution become a much more cost-effective retrofit.

Current Results

Figure 1 shows the NO_x emissions results for chassis dynamometer testing of the Ford F-150. Of note is the ambient temperature and vehicle testing methodology for these results. Dynamometer cell temperature for these tests was approximately 42°F and air was forced underneath the vehicle chassis to simulate actual driving conditions in a cold climate.

**Figure 1. Ford F150 NO_x Emissions - CNG Vs. NRG
HCNG Technology**



Notice that the NOx emissions results are very dependent upon catalyst temperature for natural gas operation. By reducing engine out NOx emissions by a factor of from nine to four, the catalyst system using HCNG and NRG's implementation technology does not have to produce high effectiveness to eliminate NOx emissions. Once the catalyst comes up to temperature at higher loads, the factory natural gas system will perform effectively.

Preliminary testing has also shown equivalent vehicle range (about 200 miles for the F-150), reduced NOx and CO emissions, and a 28% increase in horsepower for the OEM Ford F-150.

Conclusions

NRG Tech has developed a low-cost retrofit package for light-to-medium duty vehicles that will incorporate up to 50% hydrogen in the fuel. This package will improve performance and exhaust emissions over the unconverted vehicle at a cost that can make it marketable in the current business climate.

HYDROGEN-BASED UTILITY ENERGY STORAGE SYSTEM

**Robin Parker
SRT Group, Inc.
P.O. Box 330985
Miami, FL 33233
and
William L. Clapper, Jr.
SunLine Services Group
32-505 Harry Oliver Trail
Thousand Palms, California 92276**

Abstract

SRT Group, Inc. (SRT), a leader in innovative energy processes involving halogens, has developed and patented an innovative electrical energy storage and hydrogen production system. The SRT system stores off-peak electricity and produces hydrogen via a novel natural gas/steam thermo-electrochemical process. The following economic analysis indicates that the system can provide on-peak electrical power competitive with natural gas-fueled peaking-turbines and can co-produce hydrogen at costs considerably below that of delivered merchant hydrogen. Preliminary market estimates indicate a \$250 million U.S. and \$400 million world annual market potential for the SRT system. Competitiveness is achieved due to: (1) the cost for the SRT system is allocated between two products and revenue sources, namely hydrogen and electric energy storage; (2) a very high 89% utilization factor; (3) reducing high-cost electrical needs with low-cost natural gas; and (4) low capital investment. Based on the promise of SRT's early investigations and analysis, the U.S. Department of Energy (DOE) agreed to cost-share 50% of the cost to develop the processes under the auspices of an SRT/DOE Cooperative Agreement. The SRT/DOE program has been in place since 1995 and is culminating with a planned integrated system demonstration in Palm Desert, California and Laramie, Wyoming. The proposed demonstrations will convert intermittent wind energy to provide uninterrupted and reliable electrical energy to the electric grid and produce merchant hydrogen.

Introduction

SRT is a small technology-oriented firm with a business focus on developing and licensing renewable energy technologies. It supports its R&D activities through internal resources, as well as grants and contracts from the federal government. Currently, SRT is developing an electrical energy storage and hydrogen production concept through cost-shared programs with the DOE. This concept requires the integration of two sub-systems or components.

The first is a hydrogen/bromine regenerative electrochemical cell that is well-suited for energy storage applications such as peak shaving, load management and other emerging distributed utility applications. A regenerative hydrogen/bromine cell facilitates electrical energy storage by consuming electricity in electrolyzing hydrogen bromide into hydrogen and bromine reactants as stored chemical energy. The hydrogen and bromine are later reacted electrochemically in the cell to produce electrical energy. Hence, the cell is regenerative (reversible), in that it can efficiently operate as an electrolysis cell producing reactants and consuming electricity or as a fuel cell consuming reactants and producing electricity. In effect, the cell operates as a battery, exchanging electrical and chemical energy, with one difference: the reactants are stored outside of the cell as opposed to a battery where the reactants are inside. Therefore, to increase capacity (kWh) it is only necessary to add more reactants rather than more batteries.

This electrochemical cell technology was originally developed in 1979 by General Electric Co. and was later demonstrated by United Technologies Corporation under DOE and DOD programs. DOE interest in the technology was in response to the 1970's Arab embargo for providing energy storage to reduce the nation's dependence on oil-fueled power generation. The DOD's interest in the 1980's was to provide an electrochemical break, or division between the electric grid and missile silos to prevent EMF damage. Innogy Technologies has developed an industrial-scale, bromine-based regenerative cell for electric utility energy storage. The Innogy cell has been designed for high-volume, low-cost manufacturing and will be adapted for service in the SRT system.

The second component is a chemical reactor that thermochemically produces hydrogen bromide (HBr) and carbon dioxide (CO₂) from water (H₂O), natural gas (CH₄) and bromine (Br₂). The regenerative cell and chemical reactor integrated in a system produces hydrogen and stores electrical energy.

Discussion

In the SRT system, the hydrogen/bromine regenerative cell is used both as a fuel cell to generate electricity and as an electrolyzer to produce marketable hydrogen. Due to its reversible operation, it is used in an energy storage system, storing and dispatching electricity during off-peak and on-peak periods. Off-peak periods are those times of the day (typically at night) when the utility has excess generating capacity and electricity energy is inexpensive due to oversupply. On-peak energy is the opposite; the generating capacity is fully used and electricity is expensive. Thus, utilities have a 'time-of-day-rate' for industrial customers, which reflects the cost difference between on-peak and off-peak energy. Generally off-peak periods are much longer than on-peak periods. This difference between length of periods provides an opportunity to

produce more hydrogen than what is required for its fuel cell (on-peak discharging) mode providing excess or supplemental hydrogen bromide electrolyte is available during the electrolysis (off-peak charging) mode.

The technology under development by SRT is a thermo-electrochemical process whereby hydrogen bromide electrolyte is produced from natural gas, water and bromine. The integration of this chemical reactor with the regenerative cell provides a dual-functional system designed to serve both as an electricity load-leveling device and as a hydrogen producer. The block diagram below illustrates the integrated dual-function system.

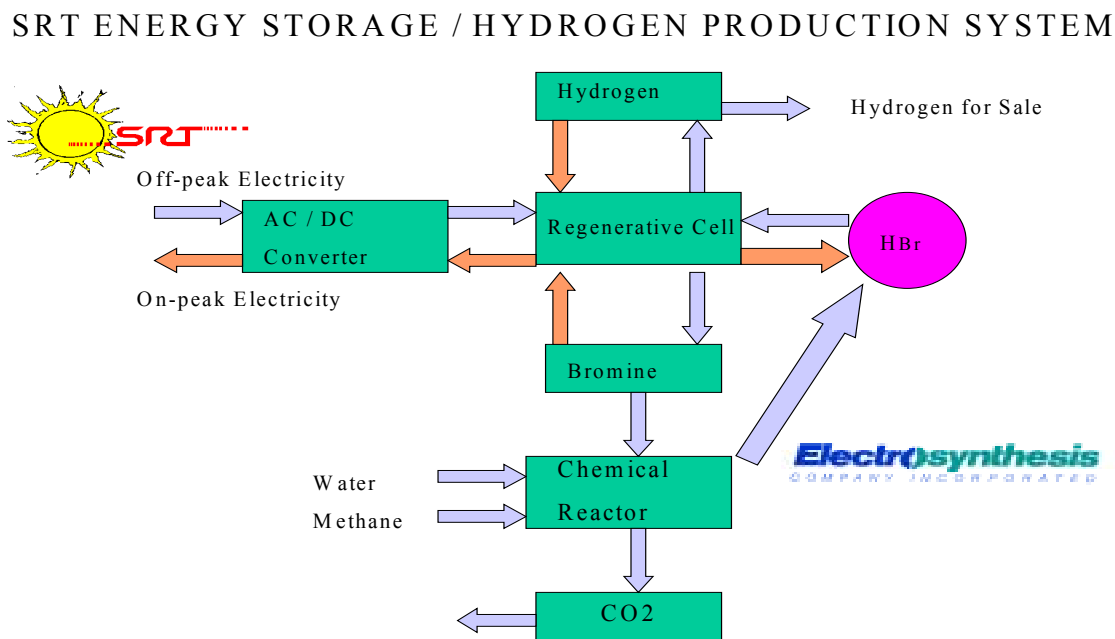


Figure 1: Block Flow Diagram of the SRT Energy Storage/Hydrogen Production System

Technical Background

Electrolysis is currently the most practical method for producing small and moderate quantities of hydrogen (< 1 million scfd). Electrolysis also produces the purest hydrogen. However, hydrogen produced from water electrolysis is relatively expensive. This is due to the high capital cost of the electrolysis cells and electrical energy requirements. Electricity is an expensive, high-value source of energy when compared to other sources such as coal, natural gas or gasoline. Hence, a process that reduces the amount of electrical power required to produce a given amount of hydrogen is very advantageous. How a reduction in electrical energy costs translates into a reduction in hydrogen production costs becomes apparent by comparing the differences in theoretical or ideal cell voltages needed to electrolyze HBr vs. H₂O.

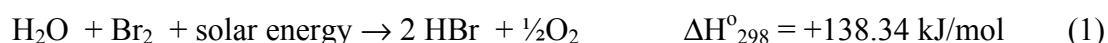
The theoretical cell voltage of HBr is 0.555 Volts and that of H₂O is 1.229 Volts. Actual voltage for commercial electrolysis (which includes inefficiencies and parasitic losses) generally range from 0.9 - 1.0 Volts and 1.8-2.2 Volts for HBr and H₂O, respectively. One Volt is the equivalent of 12.06 kWh/lb of hydrogen. Thus, the electrolysis of HBr requires from 9.65 - 10.85 kWh/lb of hydrogen produced. Water, in comparison, requires 21.71-26.53 kWh/lb. Accordingly, electrolyzing HBr instead of water can reduce electrical energy requirements by over 50 percent. Work by Rockwell International has demonstrated HBr electrolysis at about 0.6 Volts; this is less than one-third the voltage required for water electrolysis using current technology.

Thus, by forming HBr as an intermediate hydrogen carrier from water and bromine, the energy cost, which is the largest cost element of electrolytic hydrogen, is significantly reduced. As an example, if electricity costs \$.02/kWh and natural gas costs \$2/MBtu, the SRT process substitutes roughly \$6.00 of high-value electrical energy with \$2.00 worth of lower-value natural gas. Electrical power requirements are a major expense factor that conspires against widespread electrolytic hydrogen production.

Additionally, when recombining hydrogen and bromine in a fuel cell, up to 90% of the chemical energy stored in the reactants can be recaptured as electricity, versus only about 50% for state-of-the-art hydrogen/air fuel cells. This leads to an electric-to-electric efficiency approaching 80% for the system versus 40% for hydrogen/air and 35% for most fossil fuel-fired power generators. In fact, the electrical characteristics of the hydrogen/bromine fuel cell can be compared to a battery in terms of response time, with the major difference that it is only necessary to increase the amount of chemical reactant to increase capacity (kWh). Other benefits afforded by hydrogen bromine are reduced capital and O&M costs.

Technical Concept

Under the auspices of the DOE Hydrogen Program, SRT has over the last five years investigated extensively the photochemical reaction between bromine, steam and solar energy at elevated temperatures for the production of HBr:



The HBr is subsequently electrolyzed into H₂ and Br₂, in a regenerative cell:



The hydrogen is stored for sale or power generation, while bromine is either stored or returned to the reactor for further HBr production.

Solar energy is not always available (at night, during cloudy weather or at high latitudes) and where it is available, the hardware to collect it is expensive. SRT found that the capital costs and intermittent nature of solar energy made the process uneconomical with today's economic conditions of low-cost fossil fuels. In an effort to reduce the capital cost and siting limitations

inherent in using solar energy, SRT investigated an alternative reaction for producing HBr. This reaction adds methane to equation 1:



Thus the chemical energy available from methane can substitute for solar energy. This also has the effect of simplifying the process and making it economically attractive. Thermodynamic calculations performed by researchers at Sandia National Laboratory, California confirmed that this would be a useful avenue of investigation. SRT personnel built and tested a laboratory-sized bromine/steam/methane reactor. Preliminary results showed that HBr could be produced from bromine, steam and methane at a conversion rate of 95% at 750°C without a catalyst.

An alternate reaction to produce HBr without co-producing the greenhouse gas CO₂, is to react bromine with methane to produce HBr and solid carbon. The carbon can be sequestered as a marketable product. This reaction as shown in equation 4, is also being investigated in the SRT/DOE Sandia program.



Based on these investigations, SRT has integrated its new hydrogen production processes utilizing the bromine-methane reactions with regenerative HBr cells incorporated in its energy storage approach.

Hydrogen/Bromine Energy Storage

The possibility of using a reversible hydrogen/halogen cell for electric energy storage was first suggested in 1964. The proposed system includes a solid polymer electrolyte (SPE) cell, power conditioner and storage for hydrogen, bromine and hydrogen bromide.

The hydrogen/bromine energy storage system has definite advantages over other battery systems:

- (1) the hydrogen and bromine electrodes are fully reversible allowing very high electric-to-electric efficiencies;
- (2) the same electrodes can be used as electrocatalysts for both chemical and electricity generation and therefore, the same cell can be used for both functions;
- (3) the cell is capable of operating at a high current and high power density in both modes, resulting in lower capital costs;
- (4) reactants for chemical and electricity generation are stored separately from the cell which makes it cost effective for both peaking and load leveling (weekly cycle) and low-cost capacity (kWh) increases;
- (5) also, the components are low cost (plastics and composites).

The major disadvantage of the hydrogen/bromine energy storage system is its use of bromine. Bromine, the only liquid non-metal element known, is a dark red, fuming liquid. It is reactive and corrosive and has a substantial vapor pressure at room temperatures. However, bromination is an essential chemical process with related industrial safety, material and operating standards

well known. Because of bromine's toxicity the proposed system draws on the vast experience available from the related chlor-alkali industry.

Design safety features of the hydrogen/bromine energy storage system include:

- 1) selection of highly reliable equipment, only tried and tested equipment;
- 2) high safety factor, 50% (rather the usual 10%), minimal use of valves and flanges;
- 3) all purges and vents discharge through neutralizing and disposal systems;
- 4) complete modularization of the system with computer monitoring of all operations;
- 5) enclosure with a slight negative pressure, with air discharge through a neutralizing wash;
- 6) incorporation of monitors to detect incipient failure and interlocking systems to stand-down a faulty module while the remainder of the plant operates;

and finally, in the event of an undetected chemical leak, passive neutralization systems are employed. This is achieved by using crushed limestone beds to neutralize bromine and hydrobromic acid into benign salts.

Users of the SRT system will have to fully identify its economic strengths and siting limitations before determining its market niche. A review of the earlier (1970-79) development work concluded that there are three primary siting opportunities: 1) industrial; 2) utility; and 3) remote sites. The requirements for each application are indicated in Table 1 below.

Table 1 Comparison of Siting Requirements for the HBr Energy Storage System			
Environment	Safety	Utilities available to site	On-site required utilities
Industrial site, factories all around & proximity of other workers at other plants	Highest degree of safety required with every type of safety device available; independently contained modular systems.	Treated water, electric power, fuel oil and natural gas.	Soften water, fire-fighting water, effluent storage and treatment, electric power network.
Utility site, proximity of workers at other plants.	Same as industrial site.	Cooling water, soften water, steam, compressed air, electric power, fuel oil, and natural gas.	Same as industrial site.
Remote site, deserted area, no facilities or workers nearby.	Low degree of safety required, equipment might be in open air.	Raw water, electric power.	Same as industrial site.

Conclusions

1. The hydrogen produced by the SRT system can be used as a chemical feedstock or as an energy carrier.
2. The concurrent R&D program has been successful on the 10 kw program.
3. Phase 1 of the demonstration project is fully funded.
4. The partnership of Department of Energy, SRT Group, State of Wyoming, Wyoming Business Council, Western Research Institute, Innogy Technologies, Electrosynthesis Corporation, SunLine Transit Agency, and SunLine Services Group is a major cooperative with multi-state implications.
5. The 50 kw unit is in evaluation.
6. The testing facility is completed and test drawings are in progress.

Future Work

1. Completion of test stand plans and specifications.
2. Test Stand fabrication.
3. Procurement of test equipment.
4. Installation and checkout of the 50 kW unit.
5. Test and Evaluation of the 50 kW Unit.
6. Preparation of commercialization plan.

References

Analysis of the Merchant Electrical Energy Storage/Hydrogen Production system under Development by SRT Group, Inc. January 2000. A report prepared for the U.S. Department of Energy by the SRT Group, Inc.

SunLine Transit Agency: Hydrogen Commercialization for the 21st Century

William L. Clapper, Jr.
SunLine Transit Agency
32-505 Harry Oliver Trail
Thousand Palms, CA 92276

Abstract

Hydrogen technology will one day help solve pollution and resource consumption problems. It offers a clean, safe, reliable and locally produced source of fuel. Hydrogen fuel cell vehicles can replace those powered by hydrocarbon-based internal combustion engines (which emit greenhouse and smog-producing gases). Further environmental benefits can be realized when the hydrogen is generated using renewable resources, such as solar and wind. The result is a clean, renewably produced fuel that can be used to supply public and private transportation vehicles that emit only water.

To establish hydrogen as a commercial transportation fuel, refueling infrastructure and hydrogen vehicles must be designed, built, operated and maintained. Training and support services must be established and, above all, safety must be considered throughout. Successful projects build confidence in hydrogen systems and facilitate the transition of hydrogen technologies into the market place.

SunLine Transit Agency is leading one of the world's most complex integrated hydrogen demonstration projects. Both renewable- and fossil-based hydrogen production technologies are being evaluated, along with compressed gas storage. The hydrogen produced on site powers buildings and fuels a variety of transportation vehicles. The ongoing testing will pave the way for the complete transition of California's Coachella Valley public transit system to hydrogen fuel cell vehicles. The SunLine facility is truly today's model of tomorrow's world.

Introduction

In 1994, the SunLine Transit Agency, whose mission is to provide and expand the Coachella Valley's public transit service, became the first public transit fleet in the nation to park all of its diesel buses and switch overnight to a fleet operated 100 percent by compressed natural gas (CNG). Working with such manufacturers as Cummins Engine Company, Detroit Diesel, Engelhard Corporation and John Deere, SunLine has become a continuous beta test site for clean air equipment innovations.

Because of its experience with alternative fuel technology, SunLine was tapped by the U.S. Department of Energy to coordinate several projects designed to advance the commercialization of hydrogen as a transportation fuel. As part of this effort, SunLine was tasked with disassembling, relocating and integrating projects by Clean Air Now and the Schatz Energy Research Center at Humboldt State University into its transit fleet at the Thousand Palms headquarters. This mammoth undertaking culminated in the April 2000 grand opening of the world's first hydrogen generation/storage/fueling facility built by a public transit agency. The facility boasts two Hythane[®] buses (which use 80% CNG/20% hydrogen), the country's only XCELLSIS ZE-bus (zero-emission fuel cell bus), the nation's first street-legal hydrogen fuel cell mini-car (SunBug), three hydrogen fuel cell powered golf carts and a hydrogen powered internal combustion engine pickup. Since November 2000, SunLine has used hydrogen generated onsite to fill the vehicles, which are run regularly on Coachella Valley roads. SunLine is operating this "lab on wheels" to determine the supportability, reliability, maintainability and operability of a fleet of hydrogen-powered vehicles. Of particular interest are the public transit vehicles – the two Hythane[®] and the XCELLSIS ZE busses.

Background

SunLine is the umbrella organization for two joint power authorities, SunLine Transit Agency and SunLine Services Group, and a non-profit 501(c)3, Community Partnership of the Desert. All three entities serve the nine desert resort cities that comprise the Coachella Valley in California, including Palm Springs and areas of unincorporated Riverside County. All share a common board of directors, comprised of an elected official from each jurisdiction.

In 1992, the board members took a bold step and unanimously voted to replace SunLine's fleet with one powered exclusively by an alternative fuel as a major step towards preserving one of the desert's primary assets, its blue skies. They also included a resolution stating that all vehicles purchased in the future would be powered by alternative fuels.

SunLine staff researched alternative fuel technology and decided that compressed natural gas would be the short-term fuel choice, providing immediate air quality benefits and serving as a bridge to the longer-term target - hydrogen. Working with colleges and university to devise training curriculum, natural gas utility to build the infrastructure, government agencies to address policy and permitting issues, and manufacturers to procure the necessary equipment, in 1994 SunLine made the swift, successful transition to their fleet of CNG vehicles.

Hydrogen Headquarters

The first steps towards realizing a fleet of hydrogen-powered vehicles began in 1999. At the request of the U.S. Department of Energy and the Federal Transit Administration, the projects from Clean Air Now and Schatz Energy Research Center at Humboldt State University were disassembled, relocated and integrated into SunLine's facilities. This massive task began with SunLine being assured that no one in the region had the expertise to do what was needed. Like many other myths surrounding hydrogen, this proved to be untrue. With a good set of plans and close supervision, local contractors were able to complete the job and the facility was officially christened in April 2000.

On-site hydrogen production began in November 2000 using two electrolyzers and a Hydrogen Burner Technology (HBT) natural gas reformer. The first electrolyzer, a Teledyne Brown unit, not only has the task of producing 40 standard cubic feet of hydrogen per hour, it is also testing the viability of using solar power. The hydrogen is separated from water, piped and then compressed into mobile low-pressure storage tanks, then used to fill the golf carts and SunBug. These vehicles, built by Schatz Energy Research Center, and jointly owned by SunLine and the City of Palm Desert, require a total of 360 standard cubic feet of hydrogen per day.

The Teledyne Brown electrolyzer requires 7.5 kilowatts of electricity to produce the hydrogen. This power is supplied by 480 feet of raised photovoltaic panels and 200 Siemens solar panels. Combined, the panels have the capacity to produce 37 kilowatts of electricity. When available, the excess electricity is used to support the second electrolyzer, the on-site Zweig Education Center and the Schatz Hydrogen Generation Building (houses the Teledyne Brown electrolyzer and a visual education display on electrolysis). On cloudy days, the electrolyzer may use power from the grid. Hydrogen production by this electrolyzer is shown in Figure 1, for an 8-month period beginning in June 2000. The solar panel power production for 4 months in 2001 is shown in Figure 2.

The second electrolyzer is a self-contained Phase 3 (P3) Stuart Energy unit that produces and compresses 1,400 standard cubic feet of hydrogen per hour. The hydrogen production by this electrolyzer for 9 months, also beginning in July 2001, is shown in Figure 3. The hydrogen is piped to a high-volume high-pressure storage facility. The FIBA Technologies storage system is comprised of a 16-tube Department of Transportation (DOT) storage trailer and two high-pressure ASME tube tanks. The DOT trailer can store up to 104,000 standard cubic feet of hydrogen at 3130 psi. The ASME tube tanks can store an additional 12,500 standard cubic feet at 4000 psi. These tanks are attached to a cascade control panel used to fill hydrogen buses and pickups at the public fueling island, located across from SunLine's on-site compressed natural gas station in Thousand Palms.

The public access fueling island was incorporated from the Clean Air Now project. The station utilizes equipment from Stuart Energy and Fueling Technology and features two hose dispensers, one for pure hydrogen and one for Hythane[®]. The Hythane[®] dispenser was specially designed to allow the hydrogen and natural gas to be mixed as they are being pumped. The station currently provides fuel for the two Hythane[®] buses, the XCELLSIS ZE-bus, the hydrogen pickup and a hydrogen-powered Shelby Cobra racing car that is privately owned by an engineer from the

University of California, Riverside College of Engineering-Center for Environmental Research Technology (CE-CERT). Data related to fuel usage and miles driven by the Hythane[®] buses are shown in Figure 4.

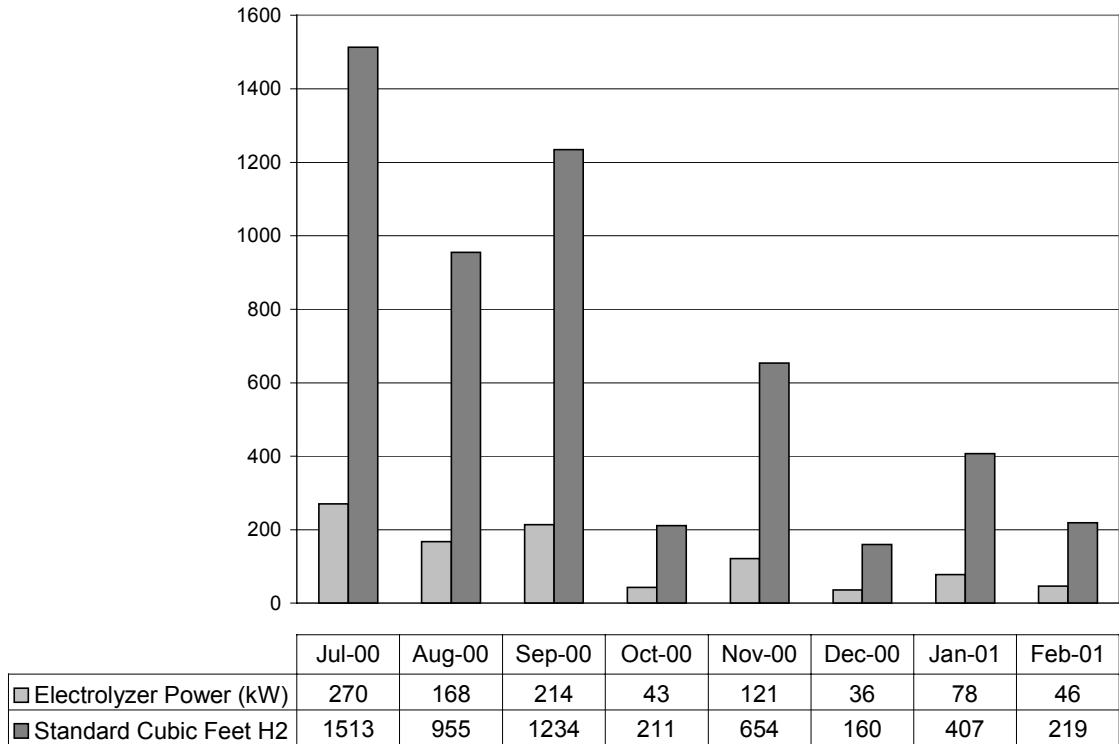


Figure 1: Teledyne Energy Systems electrolyzer power usage and hydrogen production.

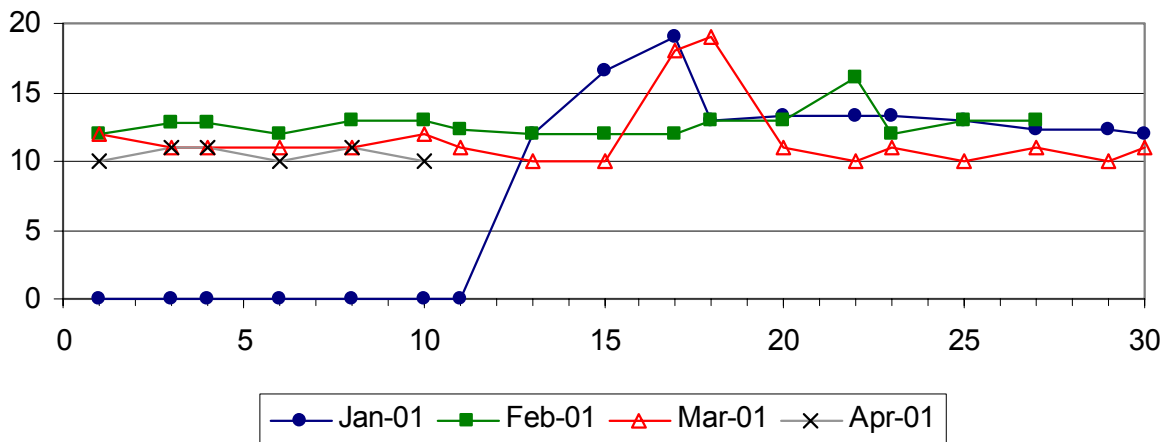


Figure 2: Solar power profile at SunLine.

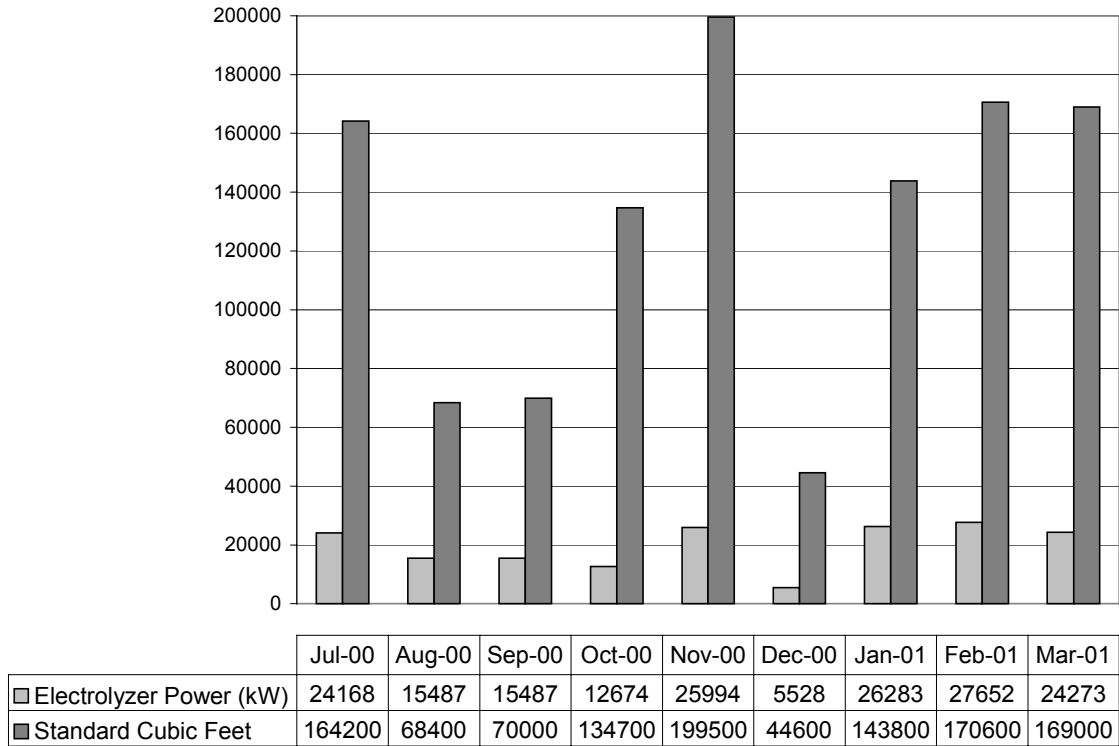


Figure 3: Hydrogen produced using Stuart Energy Systems P3 Unit.

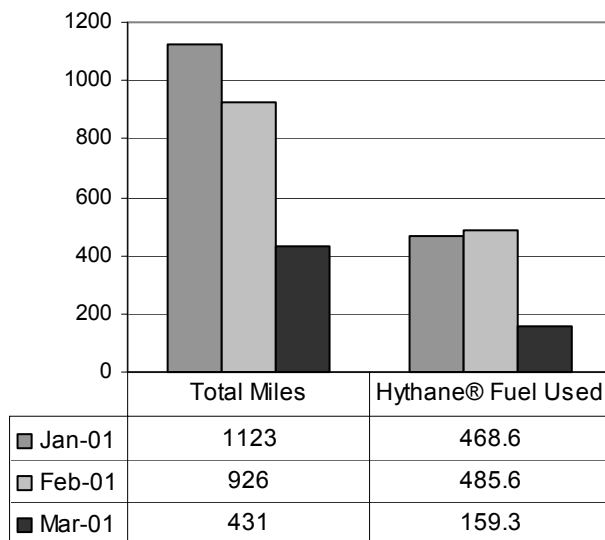


Figure 4: Hythane® Bus Miles Driven and Hythane® Usage.

In addition to the two electrolyzers, SunLine is reforming hydrogen from natural gas. The HBT stationary reformer utilizes under-oxidized burner (UOB™) technology and a QuestAir purification system to produce 4,200 standard cubic feet of hydrogen per hour. The hydrogen is 99.999% pure and is enough to fuel five buses a day. Currently, the project generates more hydrogen than it can store or utilize in its existing fleet, so the hydrogen from the HBT reformer is temporarily being flared. However, SunLine is investigating additional storage options and potential customers for the excess hydrogen.

SunLine is poised to begin testing Hythane® in an unmodified CNG engine. If the testing proves successful, the CNG fleet will be converted to Hythane®. Plans also continue towards the long-term goal of replacing the entire fleet (buses, trucks and passenger vehicles) with zero emission fuel cell vehicles. The first installment of fuel cell vehicles is scheduled for 2003. If all goes according to plan, SunLine and AC Transit in Northern California will each receive 10 fuel cell buses as part of the California Fuel Cell Partnership Bus Demonstration Project.

Outreach

An important aspect of any hydrogen demonstration project is outreach. SunLine is committed to educating the public on the benefits of clean fuels technology and mass transportation. Since SunLine is currently the only site in the world where hydrogen generated on site from solar energy is used to power buildings and Hythane® and zero-emission fuel cell vehicles, and will, in the near future, demonstrate hydrogen generation from wind power, it is ideally positioned to educate as it demonstrates.

SunLine built and operates the world's first Clean Fuels Mall where compressed natural gas, liquefied natural gas, hydrogen and Hythane® are available to the public 24 hours a day. Additionally, global shoppers for electrolyzers, reformers and other equipment that generates, stores and dispenses alternative fuels can visit SunLine to see prototype and product-development units in operation. SunLine has worked with the equipment manufacturers to develop educational displays and kiosks located throughout its facilities.

SunLine has produced an educational video series entitled "Energy Matters." Thirteen, two-minute videos are available on the Web at www.sunline.com and cover such topics as alternative fuels, electricity and the grid, fuel cells, microturbines and new car technologies. The videos are also available to teachers and administrators for use in classrooms. SunLine is also working with local schools to develop activity books and workbooks for third to sixth graders that will correspond to the video series.

When SunLine converted its bus fleet to CNG they partnered with the College of the Desert, the local community college, to devise training curriculum. College of the Desert, located in Palm Desert, California, now offers a unique Advanced Transportation Technologies program that teaches students about clean fuel vehicles, electronics and systems that will run the vehicles of the future. Students who complete the 2-year program earn an Automotive Technologies Associate of Arts Degree and acquire in-demand job skills repairing and maintaining clean fuel vehicles.

Finally, representatives of SunLine are traveling throughout the region and around the world to share its experiences and the opportunities of clean fuel vehicles. Audiences include the technical hydrogen community, policy makers, financial officers, community groups and schools.

Summary

The Coachella Valley of California has become the world's leading test bed for alternative fuels technologies. Environmental stewardship, leadership, technology advancement, strategic thinking and partnership development are the fundamentals on which the Coachella Valley public transit system has been built. Now with seven years of experience in CNG vehicle technology and the knowledge gained in hydrogen production, storage and utilization, SunLine Transit Agency is poised to begin transitioning the Coachella public transit fleet to zero-emission hydrogen fuel cell vehicles.

In the coming years, SunLine will continue testing its Hythane[®] and hydrogen vehicles. Once feasibility has been established, the entire fleet of CNG vehicles will be converted to Hythane[®]. SunLine will also continue to produce hydrogen on-site and will incorporate wind into its power supply infrastructure. As early as 2003, conversion of the transit fleet to hydrogen fuel cell vehicles will begin. SunLine will work with its partners to incorporate the latest technology developments and to publicize the opportunities hydrogen technologies present. By continually demonstrating the safety and reliability of hydrogen technologies, SunLine will help lead the way to our hydrogen future. SunLine is truly today's model for tomorrow's world.

SEPARATION USING ENCAPSULATED METAL HYDRIDE

L. K. Heung
Westinghouse Savannah River Technology
773A, Savannah River Site, Aiken, SC 29808

Abstract

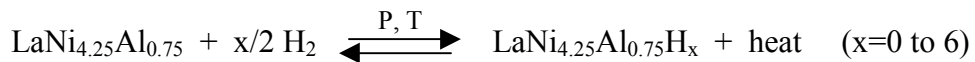
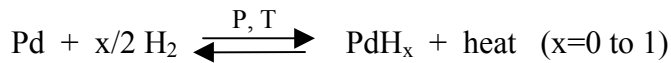
Metal hydride particles were encapsulated in a porous silica matrix. The encapsulation process successfully converted the small metal hydride particles into large granules suitable for packing gas separation columns. The granules absorbed hydrogen readily and withstood many hydrogen absorption cycles without producing fines. The porosity of the silica matrix was optimized so that the pores were large enough to allow hydrogen to easily move within the matrix and react with the metal hydride particles, but small enough to act as a filter to prevent passage of larger molecules including harmful impurities. An experimental apparatus has been installed to test the granules for hydrogen separation from other gases using a thermal absorption process.

Introduction

Metal hydrides can absorb hydrogen selectively and reversibly. They are ideal for use in hydrogen separation if not for some practical problems. Metal hydrides can be “poisoned” by reactive impurities such as carbon monoxide and thereby become inactive. Their particles break up to fines after repeated reaction with hydrogen. The fines can plug up columns and stop gas flow. Therefore, before they can be used for hydrogen separation applications, the above problems must be solved. In this work, a sol-gel encapsulation method was developed that can overcome these two problems. The plan is to produce encapsulated metal hydride material for packing experimental columns. The columns will be tested for hydrogen separation with synthetic gas feeds using a temperature swing absorption process. The goal is to develop an efficient hydrogen separation process for hydrogen production, and for hydrogen recovery from waste streams.

Metal Hydride Basics

A special group of metals and metal alloys can react with hydrogen reversibly under moderate conditions, like room temperature and atmospheric hydrogen pressure. The reaction product is a metal hydride. The term metal hydride has been used loosely to mean both the metal and the product. Examples are palladium and La-Ni-Al alloys. Their reactions may be expressed as follows:



These metal hydrides can be used for hydrogen storage and for hydrogen separation.

Metal Hydride for Hydrogen Separation

For hydrogen separation, metal hydrides can be applied in a temperature swing absorption (TSA) process. In a typical TSA process, the metal hydride is packed in a jacketed column. The jacket can be heated and cooled to swing the column temperature. During the absorption phase of a cycle, the column is cooled and the mixture to be separated is fed into one end of the column. Hydrogen in the mixture is absorbed by the metal hydride. The other gases simply pass through the column and can be discharged as waste. When the metal hydride in the column is saturated with hydrogen, the feed is stopped, and the column is heated to discharge the hydrogen. High purity hydrogen can be produced. Cooling and heating can be achieved with low quality or waste heat sources. A low cost separation process can be developed. Figure 1 illustrates the schematic of a separation column.

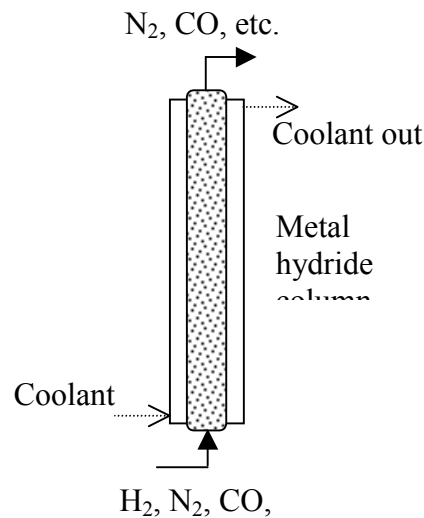


Figure 1. Hydrogen separation column

However, before we can put such a process into practical use, we must overcome two technical problems. First, metal hydride particles break up to fines in micron size. The fines can compact themselves and plug up gas flow paths. Second, reactive impurities, such as carbon monoxide, can “poison” the surface of the metal hydride particles and render them inactive to hydrogen. The metal hydride fines must be converted to stable granules, and must be protected from active impurities.

Sol-Gel Encapsulation of Metal Hydrides

It is well known that highly porous silica gels can be made via the sol-gel process (Thomas 1988). The pore size of the dried gels can be varied from less than 30 Å to larger than 100 Å (0.01 micron) depending on fabrication conditions. It is also known that similar highly porous silica material can also be produced from fumed silica products. The pores in this type of porous silica can be 10 or more times smaller than the smallest metal hydride particles. It appears that silica gel is an excellent porous matrix to encapsulate and trap the metal hydride fines. The high porosity of these gels provides many paths for hydrogen gas to reach the encapsulated metal hydride particles. The pore size can also be controlled to screen out impurities other than hydrogen. These possibilities have been studied in an earlier project. Findings of that work have been published (Heung, 1999). The steps to produce encapsulated metal hydride are described below.

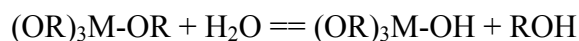
Preparing metal hydride powders

Commercially produced $\text{LaNi}_{4.25}\text{Al}_{0.75}$ in the form of millimeter size particles is first activated by exposing to 5 atm hydrogen gas at room temperature, and then subjected to repeated hydriding and dehydriding. After about 20 cycles, most of the particles will break up to powders small enough to go through a 45 micron sieve. These fresh metal powders must not be exposed to air in a single step because air exposure will cause too much oxidation, rendering the material useless. They must be exposed to air gradually over several days, so that a thin layer of oxide can slowly form on the surface of the metal particles. This thin oxide layer protects the metal particle from further oxidation. The particles are then stable and can be handled in open air. After being sieved through a 45-micron sieve, the metal hydride powders are saved for encapsulation.

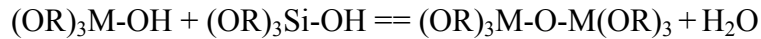
Porous Silica Formation

Porous silica may be produced using a sol-gel process. The process starts with the hydrolysis of an organo metallic compound. The hydrolyzed compound is polymerized via water and alcohol condensation. A dry product is produced after the water and alcohol are removed. Thermal treatment following the drying step is sometimes used to further modify the structure of the final product. The reactions involved are described as follows:

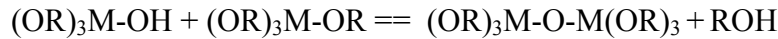
Hydrolysis:



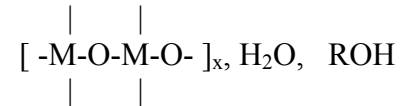
Water condensation:



Alcohol condensation:



Final products:



where M is an element such as Si, Al and Ti, and R is an alkyl group ($-C_xH_{(2x+1)}$).

In addition to the above sol-gel approach, porous silica can also be produced using fumed silica. Commercially available fumed silica is produced by the hydrolysis of silicon tetrachloride vapor in a flame of hydrogen and oxygen. In the combustion process, molten spheres of silica are formed. The diameters of these spheres are in the order of nanometers. They collide and fuse with one another to form branched, three-dimensional, chain-like aggregates. Fumed silica can polymerize via the hydrolysis process when blended with water, to form a highly porous product.

Encapsulating metal hydride

Metal hydride powders are encapsulated in a porous silica matrix by using two different methods. The first uses a sol-gel to produce the matrix and the second uses fumed silica. Both methods can encapsulate metal hydride particles at ambient or low temperatures, which have no adverse effect on the integrity or properties of the particles.

Sol-Gel Method

The sol-gel method to encapsulate the metal hydride particles involves the following steps. Solution A is prepared by adding ethanol to water while stirring. The ethanol to water ratio is two to five parts water to one part water. The acidity of the solution is adjusted by adding HCl until the pH value is in the range of 1 to 2.5. Solution B is prepared by mixing ethanol into tetraethyl orthosilicate (TEOS) in the ratio of one part ethanol to two parts TEOS. Solution A is added to solution B slowly while stirring continuously to form a sol. To the sol a measured amount of the metal hydride powders prepared earlier is added. The mixture is stirred to keep the metal hydride particles dispersed uniformly throughout the sol. The mixing is maintained until the sol turns into gel and the metal hydride particles become suspended in the gel. The gel is then allowed to mature for several days. When the polymerization is complete, the gel becomes a solid phase submerged in the liquid water and ethanol. The liquid is evaporated at room temperature, followed by evacuation at temperature of up to about 600 °C. After drying, large pieces of silica encapsulated metal hydride are formed. The large pieces are mechanically broken up into granules of 1-5 mm size for testing. Refer to Figure 2 for encapsulation steps.

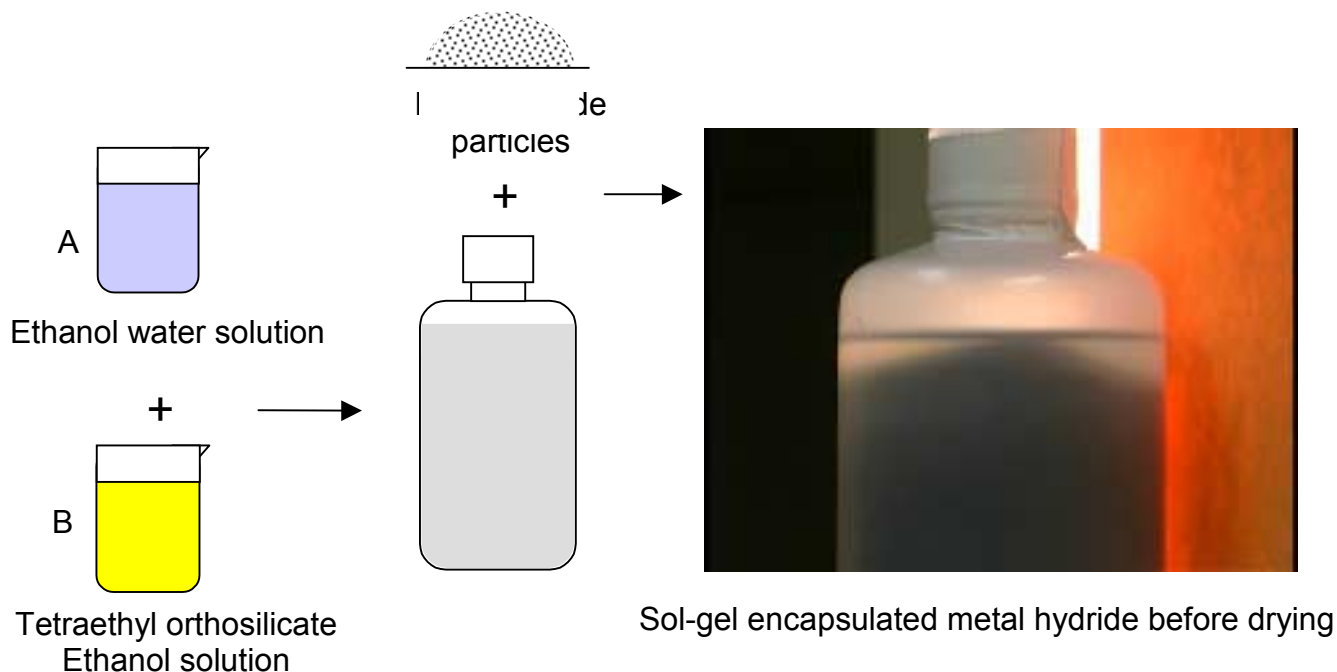


Figure 2. Encapsulation process

Fumed Silica Method

In this method, commercially available CAB-O-SIL[®] fumed silica from Cabot Corporation is used to embed the metal hydride particles. The fumed silica, in the form of a light and fluffy powder, is added and blended into water a little at a time. A water-like sol is formed. The mole ratio of water to fumed silica is between 10 to 30. While stirring continuously, a measured amount of metal hydride powders is added, also in small steps. In the end, a uniform, thick, watery mixture is formed. The mixture is poured quickly into a tray and spread out to solidify. The solid is dried in air and then broken into granules of 1-5 mm size for testing.

Hydrogen Separation Test

The encapsulated metal hydride as shown in Figure 3 will be tested for hydrogen separation from synthetic gas mixtures in a small laboratory scale.

A small test column and a gas manifold have been fabricated and installed for the testing. The column is a U-shape stainless steel tube, 3/4" diameter and 6" long. The manifold is built from 1/8" stainless steel tubing to minimize the gas holdup of the system. The feed mixture will be synthesized by metering the component gas with mass flow controllers. The gas mixture, after passing through the column, will be sampled with thermal conductivity device. See Figures 4 and 5. A breakthrough in hydrogen concentration will be detected when the column is saturated with hydrogen. The synthetic feeds planned for the tests include mixtures of hydrogen, nitrogen, methane, carbon monoxide and moisture. The performance of the material will be evaluated on the amount of hydrogen it can remove in each cycle under different conditions that include feed

composition, flow rate and number of cycles. Initial test is expected to begin in about two months.



Figure 3. Silica encapsulated metal hydride



Figure 4. Separation test column



Figure 5. Separation test manifold

Acknowledgments

The Hydrogen Program of the U.S. Department of Energy funded this work.

References

L. K. Heung, G. G. Wicks, "Silica embedded metal hydrides", *Journal of Alloys and Compounds* 293-295 (1999) 446-451.

I. M. Thomas in *Sol-gel technology for thin films, fibers, preforms, electronics, and specialty shapes*, L. C. Klein (editor), 1988, p2.

DEFECT-FREE THIN FILM MEMBRANES FOR H₂ SEPARATION AND ISOLATION

Tina M. Nenoff
Sandia National Laboratories
PO Box 5800, MS 0755
Albuquerque, NM 87185-0755

Abstract

Our long-term goal is to synthesize defect-free thin film membranes with crystalline inorganic molecular sieves (zeolites) for use in hydrogen production technologies. Current hydrogen separation membranes are based on Pd alloys or on chemically and mechanically unstable organic polymer membranes. The use of molecular sieves brings a stable inorganic matrix to the membrane. The crystalline frameworks have “tunable” pores that are capable of size exclusion separations. The frameworks are made of inorganic oxides (e.g., zinc oxide, gallium oxide, alumino silicates, silico titanates) and result in materials with thermal stability up to 600°C. The pore sizes and shapes are defined crystallographically (<1Å deviation) which allows for size exclusion of very similarly sized molecules. In comparison, organic polymer membranes are successful based on diffusion separations, not size exclusion.

Introduction

This project is focused on the research and development of crystalline, inorganic, molecular sieve (zeolite) thin film membranes for light gas molecule separations. In particular, we are interested in separating and isolating H₂ from CH₄, CO, CO₂ and N₂ gases. Current hydrogen separation membranes are based on Pd alloys or on chemically and mechanically unstable organic polymer membranes. The use of molecular sieves brings a stable (chemically and

mechanically stable) inorganic matrix to the membrane. The crystalline frameworks have “tunable” pores that are capable of size exclusion separations. We envision impact of positive results from this program in the near term with hydrocarbon fuels, and long term with biomass fuels.

During this reporting period, we focused our research on the synthesis of various classes of microporous phosphate-based, aluminosilicate and silico titanate phases, both as bulk and thin film materials. Within this arena, we have begun to explore the gallium/phosphate phase space; five new phases have been synthesized. Furthermore, we have focused our efforts on the membranes synthesis and diffusion studies of different silicate-based zeolite membranes. These membranes have been successfully synthesized as defect-free membranes with separation abilities of key gas molecules. We continue our collaboration with New Mexico State University in the area of molecular dynamics modeling, transition state theory and simulations of light gas molecules diffusing through our membrane materials.

Discussion

This year, we have focused on the synthesis of novel Ga/F/P based microporous materials. In this area, we have worked on synthesizing phases with specific pore sizes for light gas molecule sieving and separation. Furthermore, we have attempted to synthesize the new phases as thin film membranes.

First, $\text{Ga}_4(\text{PO}_4)_4\text{F}\cdot\text{N}_2\text{C}_7\text{H}_{11}\cdot 0.5\text{H}_2\text{O}$, a new microporous 3D framework material was synthesized as a bulk crystalline powder, fully characterized and in press (Bonhomme, 2001). Its three dimensional framework (Figure 1) is composed of novel distorted “bowl-shaped” octameric double four-ring units, which are built up by corner-sharing PO_4 and GaO_4 tetrahedra and GaO_4F trigonal bipyramids. The structure consists of a pseudo-hexagonal array of cylindrical twelve-member pores running parallel to the *c* axis hosting the protonated 4-dimethylaminopyridine (4-DMAP) molecules. These pores are interconnected along the *b* axis through double eight-ring windows. The framework remains stable up to 300°C under oxygen. However, attempts to remove the organic molecule from the pores has been unsuccessful to date (both by calcination and solvent extraction, i.e., HCl/EtOH wash). Pore sizes are in the range for light gas separations.

Second, a new 3D open-framework fluorogallophosphate, $\text{Ga}_5(\text{PO}_4)_5\text{F}_4 \cdot 2[\text{N}_2\text{C}_4\text{H}_{12}]$, was synthesized solvothermally using either 1,4-diazabicyclo[2.2.2]octane (DABCO) or piperazine as a templating agent (Bonhomme, 2001). The 3D framework is built-up by corner linked PO_4 tetrahedra, GaO_4F trigonal bipyramids and GaO_4F_2 octahedra (see figure 2). The building block of the structure is an hexameric unit of composition $[\text{Ga}(\text{PO}_4)]_5\text{F}_4$. The organic template molecules reside in cavities formed by the intersection of 8 member channels running along [100] and irregular pores parallel to [001]. The crystalline framework remains stable up to 350°C under oxygen. Pore sizes are in the range for light gas separations.

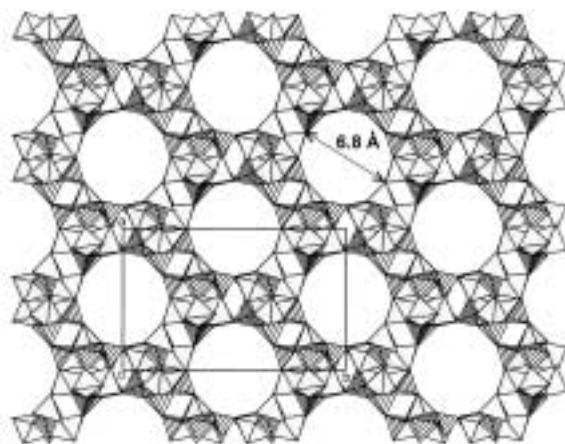


Figure 1: 3D framework of $\text{Ga}_4(\text{PO}_4)_4\text{F}\cdot\text{N}_2\text{C}_7\text{H}_{11}\cdot 0.5\text{H}_2\text{O}$; pore residing H_2O and 4-DMAP molecules not shown, for clarity.

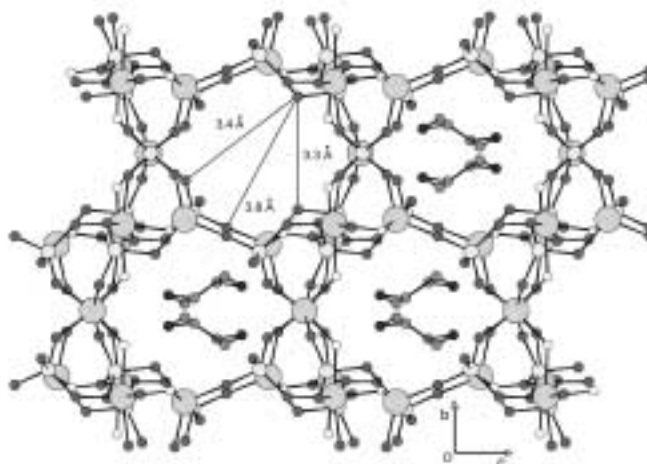


Figure 2: $\text{Ga}_5(\text{PO}_4)_5\text{F}_4 \cdot 2[\text{N}_2\text{C}_4\text{H}_{12}]$, view down 8-ring channels that contain the occluded piperazine molecules.

Initial Ga/P and F-based microporous thin film materials' growth studies have been tried on Ga_2O_3 substrates. To date, it appears that the Ga_2O_3 substrates are resistant to film growth, yet the phases do grow as unsupported bulk. Therefore the Ga_2O_3 substrate is not interfering with the syntheses. Attempts to physically attach the bulk phases to the substrate are ongoing. Initial alumina studies on Al_2O_3 did show selectivity of $\text{N}_2/\text{He} > 20$. Experiments are continuing.

This year we have also focused on silicate-based thin film membranes that are able to separate the light gases of choice. One area of interest is in the aluminosilicates. We have been focusing on making defect-free Al/Si films for three reasons: (1) they are easily grown on alumina substrates and allow us to perfect the methodology for making the larger-pored, commercially available zeolites, (2) literature reports show that various metal doped zeolites show light gas

separation ability, and (3) the methodology for Al/Si films will be similar for Ti/Si films (more difficult phases due to high pH requirements).

We have started working with commercially available and well-studied ZSM-5 porous zeolites. These zeolites are valuable for hydrocarbon separations. Because we can make these defect-free with our seeding methods, we will extend our experience to other zeolites.

For the ZSM-5 films, the as-synthesized membranes have zero permeation, due to Na cations and occluded H₂O molecules. Then, the film is heat-treated and has selectivity for certain light gases. In Figure 3, the SEM shows that crystals grow deep into the substrate pores, and only small and on surface not continuous layers.

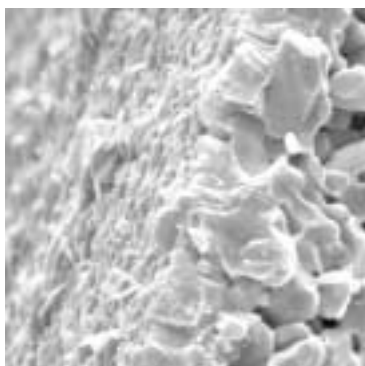


Figure 3: Cross section of alpha alumina disk/pellets with a 1 micron thick defect-free thin film of Zeolite ZSM-5 (right side is substrate with larger pores, center and left side is the film).

We are now able to synthesize defect-free thin film membranes that show no SF₆ or CO₂ permeance. Because crystals are grown on both sides of the support, the flux through the membrane is still low. However initial studies do show preferential movement of smaller, nonpolar gas molecules (ie. H₂) as compared to the larger, nonpolar (ie. CO₂) ones. One example of flux studies on pure gases, through a Na-ZSM-5 dehydrated membrane (at RT, flux sccm; permeance $\approx 10^{-6}$ mole/m² Pa sec), with crystals on both sides of membrane: H₂/N₂ ≥ 61 , He/N₂ ≥ 7 , H₂/CH₄ =7, H₂/CO₂ ≥ 80 , H₂/O₂ ≥ 11 .

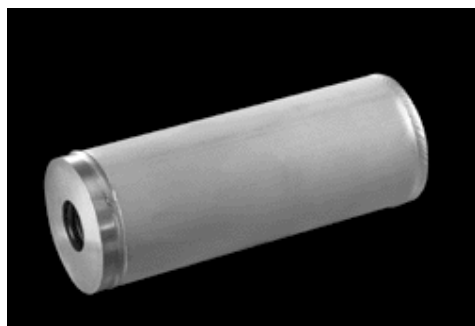
This compares well to literature values of pure gas volume detection methods for ZSM-5 films (Lai, 2000; Nobel, 1999; Nobel, 2000) which show a low permeance $\approx 10^{-7}$ mole/m² Pa sec, and selectivity of H₂/N₂ ≥ 3.91 , He/N₂ ≥ 3.22 , N₂/CO₂ = 0.625, H₂/N₂ =100 (only at elevated temperature of 150°C and low permeance of 10⁻¹⁰).

However there are crystals grown on both sides of the disk. One side is cleared of crystals by mechanical means. When one side is cleared, flux is increased 3 fold. The synthesis method involves mechanical application of colloid-based seeding of about 0.1micron size powdered crystals. Multiple layers of differing thicknesses and concentrations are applied to fill in defect

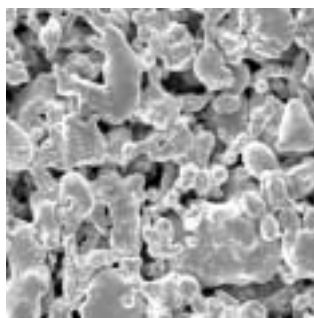
sites. Permeation values on this membrane and membranes with one crystal side removed are still being collected.

We have also begun research into various silico titanates phases for thin film membranes. Work to date has shown that due to high pH and long reaction times and temperatures, the alumina substrate dissolves. Work continues into reaction modifications for thin film growth.

Industry is interested in working with membranes on sturdy supports; supports need to be compatible with plant conditions. In an effort to keep in line with industry values, we have begun research into thin film growth on stainless steel supports. We have had discussions with Pall Corporation (a separations membrane manufacturing company, East Hills, NY), as a possible future commercialization partner of defect-free membranes for gas and chemical separations. On a fact-finding visit to their facilities (2/9/01), we were supplied with a sample of porous stainless steel (316, 316L) metal substrate, shown in Figure 4. Initial attempts to synthesize a crystalline film only produced an amorphous gel. We are now attempting seeding techniques to promote film growth.



a.



b. $\bar{\quad} \approx 10$ microns

Figure 4: (a) porous metal filter cartridges are made with Pall PSS s-series (b) SEM, top view, of Pall PSS s-series support only.

Though commercialization of these materials is still in the future, some early investigations show that membrane technology continues to grow in importance on the world market. Some economic estimates of membrane commercialization show that worldwide sales of synthetic membranes is greater than \$2B, with an annual growth of 12-15% expected. Furthermore, 75% of the market belongs to the U.S., Japan, and Western Europe. For gas separation membranes in particular, economic estimates from 1996 predict that by 2000, the membrane gas separation business would grow to about \$500M (Puri, 1996).

Conclusion

This program is focused on the synthesis, modeling, validation and testing of defect-free thin film membranes for the separation and isolation of H_2 gas. These robust thin films are made of chemically and mechanically stable crystalline inorganic molecular sieves (zeolites). Successes

from this program will have direct effects on national concerns such as hydrocarbon fuels and biomass energy. The membranes are molecular sieve/zeolite crystalline phases that are capable of molecular sieving small gas molecules, thereby allowing for H₂ purification.

This year we have accomplished our milestones and have made in-roads into developing industrial partnerships necessary for future commercialization of our membranes. We continue our collaboration with NMSU for modeling and simulation with focus on silicates and silicotitanates. We have synthesized one of the phases as a thin film membrane, tested for permeation and separations, and have shown excellent separation values for various light gases of interest. Work continues on improving our silicate-based defect-free thin film membranes.

Future Work

Future work plans for next year include the continuation of our work on synthesis, modeling and thin film growth of novel microporous phases for light gas separations, including novel alumino silicates and silico titanate phases. Furthermore, we plan to explore the thin film growth of alumino silicates zeolites doped with other elements for maximized adsorption and selectivity of H₂ over other light gases of interest. The permeation work will focus on the study of pure and mixed gas systems, both at room temperature and 80°C. We will continue to attempt thin film syntheses on stainless steel and alumina supports. Again we plan to tie this research with the modeling and simulation efforts of this past year, with collaborators at New Mexico State University (Dr. Martha Mitchell, Dept. of Chemical Engineering). Our focus will be on the silico titanates and how they compare to known silicate-based zeolites. We will continue to build interactions and collaborations with outside industries for potential future collaborations and commercialization partnerships.

Acknowledgements

This work was supported by the United States Department of Energy under contract DE-AC04-94AL85000. Sandia is a multi-program laboratory operated by Sandia Corporation, a Lockheed Martin Company, for the United States Department of Energy.

I would like to thank my co-workers who also participated in this program: Dr. Francois Bonhomme, Mr. Steven G. Thoma and Mr. Daniel Trudell of SNL, and Dr. Martha Mitchell (NMSU).

References

Bonhomme, F., S. G. Thoma, M. A. Rodriguez, T. M. Nenoff. 2001. "Ga₄(PO₄)₄F·N₂C₇H₁₁·0.5H₂O" A 3D Open Framework with 12-member Pores and "bowl-shaped" Building Units." *Chem. Mater.*, in press.

Bonhomme, F., S. G. Thoma, M. A. Rodriguez, T. M. Nenoff. 2001. "Piperazine templated 3D fluoroaluminum phosphate: Synthesis and characterization of $\text{Ga}_5(\text{PO}_4)_5\text{F}_4 \cdot 2[\text{N}_2\text{C}_4\text{H}_{12}]$." *Microporous and Mesoporous Materials*, in press.

Lai, R., G. R. Gavalas. 2000. *Microporous and Mesoporous Materials*, 38:239-245.

Noble, R., et.al., 1999. "Alkali-Free ZSM-5 Membranes: Preparation Conditions and Separation Performance." *Ind.Eng.Chem. Res.*, 38:3635-3646.

Nobel, R., et.al., 2000. *J. Mater. Chem.*, 10:1131-1137.

Puri, P. S. 1996. Chemical Industry Digest, 4th Quarter.; Technology Information Forecasting and Assessment Council, 2001.

FEASIBILITY OF FULLERENE HYDRIDE AS A HIGH CAPACITY HYDROGEN STORAGE MATERIAL

R.O. Loutfy and E.M. Wexler
Materials and Electrochemical Research (MER) Corporation
Tucson, AZ 85706

Abstract

The results of recent investigation of fullerene–fullerene hydride system as a potential high capacity hydrogen storage option are presented. Theoretically, C_{60} fullerenes can reversibly store up to 7.7 wt.% hydrogen by forming fullerene hydride $C_{60}H_x$. However, high temperature and pressure are currently required to enable hydrogen exchange in this system. For example, direct hydrogenation of fullerenes in the presence of gaseous hydrogen at $\sim 450^\circ\text{C}$ and ~ 3 MPa yields fullerene hydride with ~ 6.1 wt.% hydrogen content. Over the past years, MER has been searching for practical ways to facilitate hydrogen storage on fullerenes at milder conditions. The main focus of the research was concentrated on optimizing catalytic system including transition-metal liquid state catalysts, as well as modifying electronic structure of fullerenes by doping them with electron-donating elements (for example, alkali metals). As a result of this investigation, certain progress was made in lowering the temperature and pressure required for hydrogenation. However, dehydrogenation parameters still remain to be optimized.

Introduction

Hydrogen is a convenient, safe, versatile fuel source that easily converts to a desired form of energy, without releasing harmful emissions. One of the major applications of hydrogen as a fuel source is for the fuel cell-based energy sources, both for military and commercial use due to recent developmental advances in fuel cell technology. Currently, there are four major approaches

to hydrogen storage. They include physical storage via compression or liquefaction; chemical storage in hydrogen carriers (e.g. methanol, ammonia); metal hydrides; and gas-on-solid adsorption (physical and chemical). Although each storage method possesses desirable attributes, no approach satisfies all of the efficiency, size, weight, cost and safety requirements for transportation or utility use.

Among other options, carbon-based hydrogen adsorption materials hold particular promise for meeting and exceeding the hydrogen storage energy density targets.

Fullerenes, a new form of carbon with a closed-caged molecular structure first detected by Smalley [Kroto and Smalley, 1985], were selected for investigating as a potential hydrogen storage material based on their ability to react with hydrogen via hydrogenation of carbon-carbon double bonds. The theory predicts that maximum of 60 hydrogen atoms can be attached both to the inside (endohedrally) and outside (exohedrally) of the fullerene spherical surface and that a stable $C_{60}H_{60}$ isomer can be formed loaded with ~7.7 wt.% hydrogen. Since many of the fullerene reactions appear to be reversible, if a 100% conversion of $C_{60}H_{60}$ is achieved, 30 moles of H_2 gas would be liberated from each mole of fullerene hydride:



Since 1 mole of H_2 gas can produce 67.25 W·hr of electric power, 30 moles of H_2 generated by 1 mole of $C_{60}H_{60}$ should produce 2017.5 W·hr of electricity resulting in 2.6 kW·hr/kg or 4.4 MWh/m³ power density (density of $C_{60}H_{60}$ is ~1700 kg/m³).

During our previous studies, it was shown that thermodynamically both hydrogenation and dehydrogenation reactions can occur at moderate conditions, however, practical realization poses a real challenge.

This paper summarizes and discusses results of the past year research activities aimed at optimization of hydrogenation and dehydrogenation reactions in fullerene-fullerene hydride system with the objective of increasing the weight percentage of reversible hydrogen at mild reaction conditions.

Background

The process of hydrogenation of fullerenes involves formation of C-H bonds as a result of breakage of C=C double bonds of fullerenes and H-H bonds of molecular hydrogen to form hydrogen atoms. Although the hydrogenation reaction is exothermic (the heat is released as a result of reaction), additional energy is required to break these bonds. Besides the thermodynamics involved into this process, a certain energy barrier has to be overcome for the reaction to occur. From our experimental results of solid state hydrogenation of fullerenes in gaseous hydrogen atmosphere at temperature ranging between 400 – 450°C and pressure ranging between 60 – 80 MPa, the activation energy for the hydrogenation was estimated to be 100 kJ/mole (1.0 eV/ H_2). Considering the dehydrogenation process, the potential barrier, associated with the breakage of C-H bonds, re-establishing C=C double bonds and forming molecular hydrogen, is even higher - about 160 kJ/mole (1.6 eV/ H_2). The conceptual model for hydrogenation and dehydrogenation is schematically illustrated in Fig. 1.

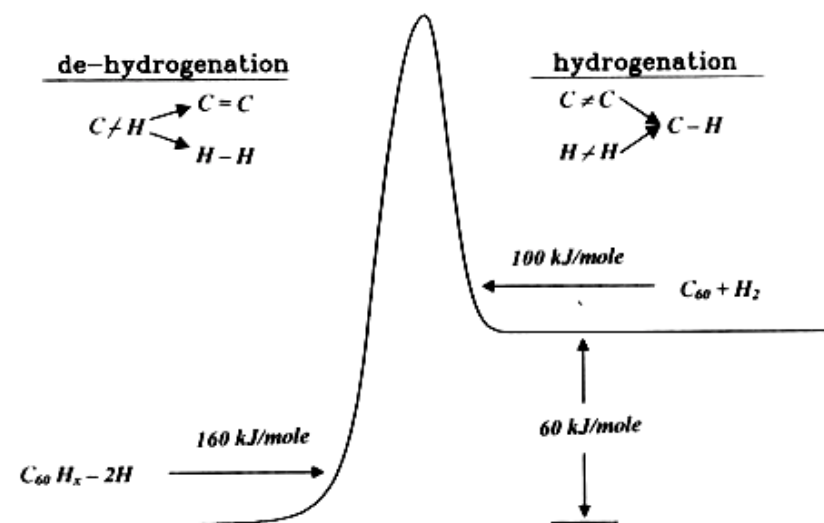


Figure 1. Activation Energy of $C_{60}H_x \rightleftharpoons C_{60}$ Transformation

Typically, high reaction temperature and pressure are required to overcome these barriers. That is why selection of the proper catalyst is crucial for facilitating the reactions at milder conditions.

During the course of investigation, MER has explored various options to improve reversible hydrogen storage on fullerenes under moderate reaction conditions including a number of novel approaches, such as using liquid catalysts, molten salts, changing electronic structure of fullerenes, etc. As a result, significant progress was made in carrying out hydrogenation and dehydrogenation reactions at temperatures below 200°C and moderate pressures. Although the percentage of reversibly exchangeable hydrogen in these systems still remains below the level required for efficient practical applications, the conducted research has produced an invaluable amount of unique knowledge and resulted in better understanding of the processes and mechanisms involved in hydrogen related-chemistry of fullerenes.

This paper discusses the most interesting results, both theoretical and experimental, obtained during the course of the investigation, which create the basis for further research aimed at more complete realization of the hydrogen storage potential offered by fullerenes.

Technical Approach and Summary of Past Work

MER has been investigating hydrogenation of fullerenes for nearly a decade. The motivation was based on the theoretical capacity of $C_{60}H_{60}$ hydride to store ~7.7 wt.% hydrogen. Initial attempts to produce hydrogenated fullerenes by direct hydrogenation in gaseous hydrogen atmosphere at elevated temperature and pressure (400 – 450°C, 60 – 80 MPa) resulted in $C_{60}H_x$ compounds with hydrogen content up to 6.1 wt.% (Fig. 2).

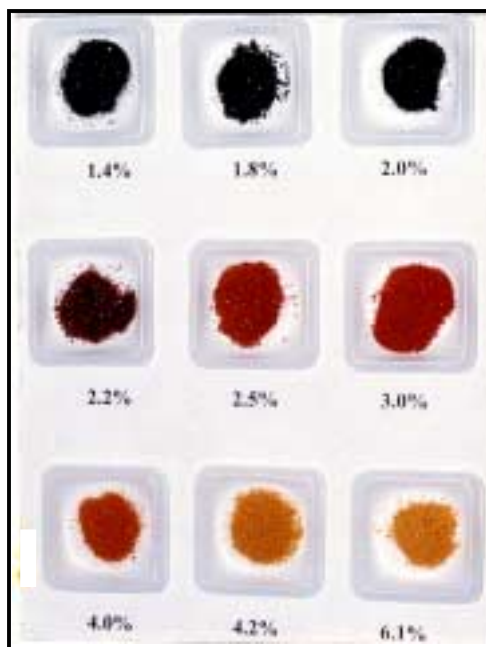


Figure 2. Samples of hydrogenated fullerenes

Introduction of the catalyst (supported precious metals, for example, Pt/C) allowed us to somewhat decrease the temperature and pressure required for the reaction, although not significantly due to insufficient contact area between the two solids. Further introduction of the liquid phase in the form of a solvent resulted in a dramatic decrease in temperature and pressure of hydrogenation (180°C and 12 MPa). However, the weight percentage of stored hydrogen also dropped due to the additional weight of the solvent.

These results confirmed the later findings based on thermodynamical analysis conducted on hydrogen storage in fullerenes [Loutfy, 2001], which suggested that both reactions of hydrogenation of fullerenes and dehydrogenation of fullerene hydrides are thermodynamically favorable at reasonably low temperatures; it is just a matter of overcoming corresponding energy barriers. Also, the analytic results showed that in order to increase the amount of reversible hydrogen, fullerenes shall be hydrogenated to as high levels as possible (practically 6% or better) because of varying stability of fullerene hydrides ($C_{60}H_{36}$ appears to be the most stable form of fullerene hydrides since it has the lowest enthalpy of formation).

Thus, in order to lower the activation energy responsible for high temperature and pressure conditions of the reactions involved in hydrogen storage on fullerenes, the following approaches should be considered:

- Selecting and optimizing the catalytic system,
- Conducting reactions in the liquid phase,
- Modifying the electronic structure of fullerenes.

Experimental Results and Discussion

In order to realize the approaches listed above, the enhancement of fullerene-based hydrogen storage systems were studied using liquid phase transition metal catalysts which would provide catalytic activity along with liquid phase for the reaction, and fullerene doping with alkali metals to facilitate charge transfer by modifying their electronic structure.

Liquid Phase Catalytic System

The following transition metal-based liquid state catalysts were used for evaluation: $\text{Ti}(\text{OPr}^i)_4$, $\text{Ti}(\text{O}i\text{Bu})_4$, $\text{Zr}(\text{O}i\text{Bu})_4$, $\text{VO}(\text{OC}_3\text{H}_7)$, $\text{Ta}(\text{OC}_2\text{H}_5)_5$, and $\text{Nb}(\text{OC}_2\text{H}_5)_5$. Implementation of these catalytic materials enables a liquid-state introduction of Ti, Zr, V, Nb, Ta ions to the fullerene solid, resulting in promoting fullerene hydrogenation and dehydrogenation due to a much higher contact surface area. Similar materials, namely $\text{Ti}(\text{O}i\text{Bu})_4$ were also reported to be capable of catalyzing the reaction of dehydrogenation of NaAlH_4 and Na_3AlH_6 [Jensen, 1999].

As a result of conducting a series of experiments, it was shown that reversible hydrogenation of fullerenes and dehydrogenation of fullerene hydrides can be achieved in the temperature range of 180–250°C in the presence of liquid transition metal catalysts. However, the amount of rechargeable hydrogen was still too low. Figure 3 illustrates the results of dehydrogenation run performed using fullerene hydride C_{60}H_x ($x \approx 28$) mixed with $\text{Ti}(\text{OPr}^i)_4$ at 250°C.

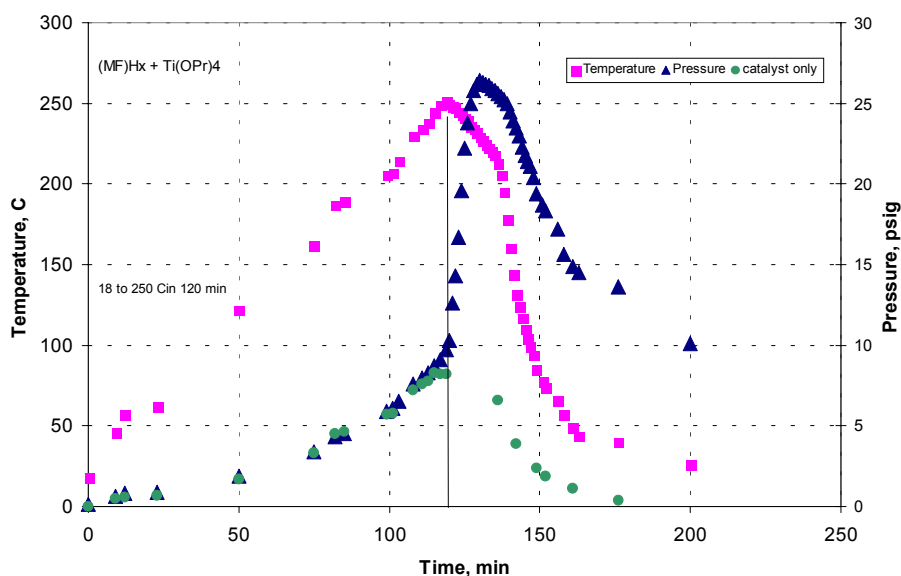


Figure 3. Dehydrogenation of C_{60}H_x in presence of $\text{Ti}(\text{OPr}^i)_4$

The data presented on the graph show the change in pressure in the reactor containing fullerene hydride mixed with the catalyst versus time as the temperature reaches 250°C and then drops. For comparison purposes, similar data obtained for the catalyst only are plotted. As one can see from the graph, the pressure in the reactor increases with temperature up to ~27 psi in case of C_{60}H_x + catalyst, as opposed to only ~8 psi in case of catalyst alone. When the system was cooled down,

the residual pressure in the reactor with fullerene hydride was ~ 0 psi, which was first interpreted as caused by evolved hydrogen. However, the gas chromatography analysis of the gas phase in question revealed only ~ .5% of hydrogen present the gas mixture with, the rest of it being saturated hydrocarbons. In addition, when the reactor was opened, it appeared that the initial slurry composed of fullerene hydride and liquid catalyst was converted to a solid compound. This suggests that fullerene hydrides actually react with $\text{Ti}(\text{OPr}^i)_4$ causing this conversion. Similar results were obtained with other catalysts. In fact, rest of the catalysts appeared to be even less thermally stable than $\text{Ti}(\text{OPr}^i)_4$. The effect of heating on catalyst conversion in the presence of pressurized hydrogen gas can be clearly seen from the data presented in Table 1.

Table 1. State change of the liquid metal alkoxide catalysts as a function of temperature and hydrogen pressure

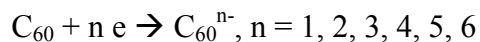
Catalyst	RT → 150°C Vacuum	RT → 200°C 18-25 psi, 6 h	150°C 500-550 psi, 6 h	200°C 500-550 psi, 6 h
$\text{Ti}(\text{OPr}^i)_4$	Liquid	Liquid	Liquid	Slurry
$\text{Zr}(\text{O}i\text{Bu})_4$	Liquid	Liquid	Slurry	White solid
$\text{VO}(\text{OPr}^i)_3$	Liquid (turned purple)	Suspension (purple)	Dark solid	N/a

As it can be seen from the Table 1, the catalysts survive the temperature of 200°C at low hydrogen pressure, but start converting to a solid under higher pressure. As a result, maximum hydrogen discharge can be obtained only during the first run, when the liquid phase is still present. When attempting repeated cycling, performance declines due to loss of the liquid phase in the process of hydrogenation, when elevated hydrogen pressure is required.

Hence, transition metal-based liquid catalysts do enhance hydrogen exchange in fullerene–fullerene hydride system, but the benefit is insufficient due to their limited stability and added weight.

Modifying Electronic Structure of Fullerenes

Another approach utilized in this work was based on changing the electronic structure of fullerenes by doping with alkali metals (Na, K, Li). When reacting with fullerenes, alkali metals donate their electrons to fullerenes causing charge transfer and resulting in formation of *fulleride anions* [Goldshleger, 1997; Cioslowski, 1995]:



The process of intercalation was conducted by placing weighed stoichiometric amounts of fullerene powder and alkali metal (Na, K, Li) into a closed container, heating to 400°C for about 10-12 hours and then cooling down. As a result, metal vapors precipitated on the fullerene powder to produce intercalated compounds of the following composition: Na_3C_{60} , Na_6C_{60} , K_3C_{60} , Li_6C_{60} and Li_3C_{60} .

Resulting alkali metals–fullerene compounds appeared to be more reactive with hydrogen under mild conditions without requiring additional catalyst. The experimental results of hydrogenation of alkali metal-doped fullerenes are shown in the Table 2.

Table 2. Hydrogen Storage Capacity of Na, K, Li - Doped Fullerenes at 200°C

Starting Material	Process parameters		Final Product	Wt.% Hydrogen
	Pressure, psi (MPa)	Time, hr		
1. Na ₃ C ₆₀	600 (~ 4)	6	Na ₃ C ₆₀ H ₁₉	2.30
2. Na ₃ C ₆₀	1500 (~ 10)	6	Na ₃ C ₆₀ H ₂₃	2.74
3. Na ₃ C ₆₀	2000 (~ 14)	6	Na ₃ C ₆₀ H ₂₆	3.19
4. Na ₃ C ₆₀	2000 (~ 14)	24	Na ₃ C ₆₀ H ₃₃	3.91
5. Na ₆ C ₆₀	1500 (~ 10)	24	Na ₆ C ₆₀ H ₃₆	3.99
6. K ₃ C ₆₀	600 (~ 4)	2	K ₃ C ₆₀ H ₅	0.58
7. K ₃ C ₆₀	1500 (~ 10)	2	K ₃ C ₆₀ H ₁₀	1.10
8. K ₃ C ₆₀	1500 (~ 10)	24	K ₃ C ₆₀ H ₂₉	< 3.0
9. Li ₃ C ₆₀	1500 (~ 10)	6	Li ₃ C ₆₀ H ₁₀	1.30
10. Li ₃ C ₆₀	1500 (~ 10)	24	Li ₃ C ₆₀ H ₂₄	< 3.0
11. Li ₆ C ₆₀	600 (~ 4)	2	Li ₆ C ₆₀ H _{7.5}	0.95
12. Li ₆ C ₆₀	1500 (~ 10)	6	Li ₆ C ₆₀ H ₁₇	2.17
13. Li ₂₀ C ₆₀	1500 (~ 10)	24	Li ₂₀ C ₆₀ H ₂₇	< 3.0

As it can be seen from this Table, the increase in pressure and time leads to higher weight percent hydrogen storage in fullerenes at 200°C. For example, hydrogenation of Na₃C₆₀ under 2000 psi for 24 hr results in 3.91% hydrogen storage without usage of any additional catalyst. The growth in hydrogen storage can also be observed if the concentration of alkali metal increases. Thus, switching to Na₆C₆₀ with higher content of sodium allows to reach 3.99% hydrogen storage at 1500 psi hydrogen pressure at the same duration of hydrogenation process. On the other hand, one can see that the hydrogen storage capability of K- and Li-doped fullerenes is considerably less than that of Na-doped fullerenes under similar conditions. As a result of this investigation, we can conclude that Na - doped fullerenes are more efficient in hydrogen storage than K and Li ones.

To verify the relationship between the level of hydrogenation and the alkali metal content, an attempt was made to produce highly intercalated fullerene compound with high concentration of alkali metal. According to Nalimova (1998) and Sklovsky (1998), the highest alkali metal content in fullerenes can be achieved using Li metal (Li₁₂₋₂₀C₆₀), although similar compounds with Na (for example, Na₁₆C₆₀) were also reported. Based on the high-pressure intercalation procedure described in these sources, a Li₂₀C₆₀ compound was produced by applying ~800,000 psi (5.5 GPa) pressure to the anvil cell containing stoichiometric amounts of fullerenes and Li, at 280°C. The produced compound was characterized by XRD, IR and ⁷Li NMR to confirm that no excessive Li was left after intercalation, and then tested for hydrogen storage. As a result of 24-hour exposure of this compound to hydrogen under 200°C at 1500 psi (~ 10 MPa), the level of hydrogenation did not exceed 3 wt.%, which is similar to the results obtained using Li₃C₆₀. This fact can be a result of Li clusters formation on the available C₆₀ sites, which means that not all the charge brought in

via Li atoms is transferred to fullerene cage, or can be attributed to the phase transition, which C_{60} undergoes at high pressures [Bashkin, 1994; Rao, 1997]. These findings suggest that an optimum concentration of the alkali metal might exist to allow maximum level of hydrogenation of Li_xC_{60} compounds. This possibility along with Na_xC_{60} compounds with $x > 6$, will be studied during the future work.

As it can be seen from the described results, modification of electronic structure of fullerenes by doping them with alkali metals does improve hydrogenation process at lower temperature and pressure. However, the dehydrogenation of the produced hydrides still remains a problem. According to the experimental data, only about 1.1 wt.% of hydrogen was released by heating a hydrogenated sample of $Na_3C_{60}H_{33}$ to $200^\circ C$ in vacuum for 6 hours. During the future research effort, the effect of a catalyst on dehydrogenation of such compounds will be studied.

In addition, an attempt was made to intercalate fullerenes with Cesium in order to facilitate charge transfer. It is realized, however, that in order to compensate for the weight increase due to the higher molecular weight of Cs, such systems will have to be able to achieve higher hydrogen storage capacity. Cs_3C_{60} was prepared by reaction of C_{60} with Cs in liquid ammonia, followed by heating at $150^\circ C$ [Palstra, 1995]. This route circumvents formation of the energetically more stable Cs_1C_{60} and Cs_4C_{60} phases. According to the procedure described in this source, Cs metal and C_{60} powder in a stoichiometric ratio of 3:1 were cooled in an evacuated container by a dry-ice/isopropanol slush. Anhydrous NH_3 was condensed onto Cs/ C_{60} mixture through a vacuum line. The C_{60} powder completely dissolved in the liquid NH_3 , indicating charge transfer from Cs to C_{60} (pristine C_{60} is insoluble in liquid NH_3). After about half an hour, NH_3 was evaporated from the solution by heating up the container to $150^\circ C$ under vacuum, conditions sufficient to remove NH_3 from $NH_3Cs_3C_{60}$. Heating was stopped when no more NH_3 evolved from the container. The produced compound was exposed to hydrogen gas at 1500 psi (~ 10 MPa) at $200^\circ C$ for 6 hours resulting in ~ 3.3 wt% hydrogen storage based on preliminary data. These data will also be verified during future activities on the project.

Physical Adsorption of Hydrogen on Fullerenes

Enhancement of physical adsorption on fullerenes can be achieved by structural fragmentation resulting in opening of fullerene cage. According to the activation procedure developed at MER, fullerenes undergo oxygen treatment followed by CO_2 activation, which results in a dramatic increase in surface area (from ~ 4 m^2/g to almost $3,000$ m^2/g) while maintaining a narrow pore size distribution between 2 to 20 \AA . The bulk density of so treated fullerenes varies between 0.9 and 1.2 g/cc. These characteristics perfectly agree with requirements for ideal hydrogen adsorbent derived by Chahine (1996).

The hydrogen storage capacity of activated fullerenes was measured using an original computer-controlled experimental setup, which allows precise measurement of adsorption isotherms in wide range of temperatures and pressures. The comparative hydrogen adsorption isotherms obtained using activated and untreated fullerenes are shown in Fig. 4.

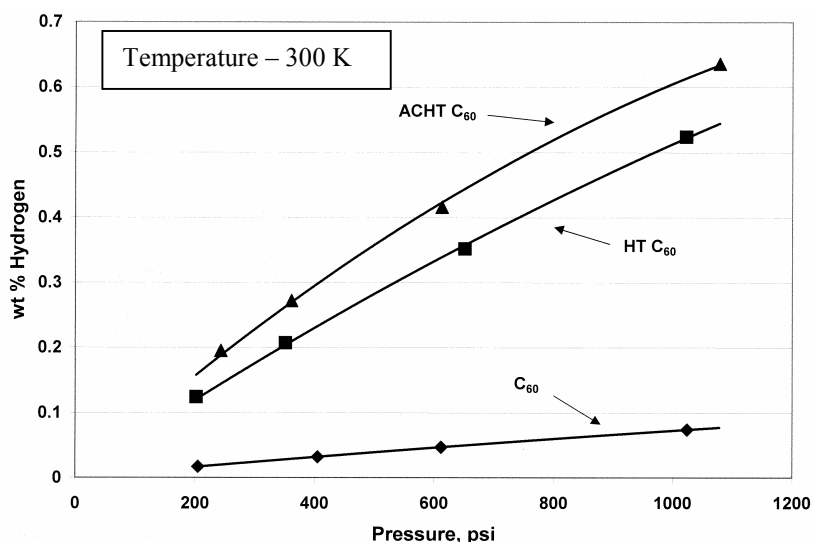


Figure 4. Physical Adsorption of Hydrogen on Fullerenes

As it can be seen from the graph, about 0.64 wt.% hydrogen storage was achieved on oxygen and CO₂ activated fullerenes (ACHT C₆₀) at ~1000 psi and ambient temperature as opposed to 0.51 wt.% on just oxygen-treated fullerenes (HT C₆₀) and 0.08 wt.% on untreated fullerenes (C₆₀) respectively. Considering the density of ACHT C₆₀ of 0.9 g/cc and HT C₆₀ of 1.2 g/cc, the volumetric hydrogen storage capacity of these materials translates into 5.8 g/l and 6.2 g/l respectively.

The obvious advantage of fullerenes is their ability to be pelletized without any binder. In this case, the packing density may reach 1.5 g/cc or higher, increasing the volumetric capacity to about 9.5 g/l. In combination with moderate heat of adsorption (~10 kJ/mol), this makes fullerenes very attractive candidates for physical hydrogen adsorbents.

In some way, the mechanism of hydrogen adsorption using structurally modified fullerenes is similar to that on single-wall nanotubes (SWNT). Structural optimization of SWNT calls for open-ended short-length nanotubes, which are supposed to facilitate hydrogen access to the internal cavities. However, similar structure is achieved by utilizing fragmentation of fullerenes. This may suggest that the hydrogen storage capacity of both materials at the same conditions should also be similar, which is below 1 wt% so far.

Conclusions and Future Work

Based on the performed work, MER has developed a great deal of new knowledge about the physics and chemistry of fullerenes, and their potential use as advanced hydrogen storage materials. It is clear that the major problem preventing the required level of reversible hydrogenation at moderate conditions is associated with dehydrogenation of fullerene hydrides characterized by high level of activation energy as well as high thermal stability caused by low enthalpy of formation. The latter can be dealt with by increasing the levels of initial hydrogenation of fullerenes. To lower the activation energy barrier, the optimization of the catalytic system as well as electronic structure of fullerenes is required. Based on the results achieved earlier, the following activities are planned for the future research.

1. MER will continue optimizing charge transfer using alkali metal-doped fullerenes by altering dopants and varying their content. In addition, the catalytic approach will be applied to facilitate hydrogen exchange in such compounds. One of the options will be using Na_xC_{60} in conjunction with TiCl_3 , which is similar to the approach undertaken in recent studies of NaAlH_4 and Na_3AlH_6 .
2. MER will further investigate and evaluate Cs-doped fullerenes to establish Cs effect on hydrogen exchange at moderate temperatures in this system.
3. MER will continue to study physical adsorption on activated fullerenes to establish the practicality of using this method in commercial systems.
4. MER will perform cost analysis to estimate the projected cost of the fullerene-based hydrogen storage option.

In terms of commercialization, MER has moved far forward in attempting price reduction of fullerenes by establishing *Fullerene International Corporation* (www.fullereneinternational.com), a joint venture with Mitsubishi Corporation and RCT. As a result of this joint effort in optimizing process parameters and scaling up the production, the price of fullerenes and fullerene-related materials is expected to drop significantly (\$30 – 60 per 1 kg over the next 3 years), which will make them practically available worldwide.

Acknowledgments

Current research project is being sponsored by US DOE Hydrogen Program, Contract DE-FC36-00G010532.

References

- Bashkin, I.O. et al. 1994. *J. Phys.: Condensed Matter*, 6: 7491.
- Chahine, R. and Bose, T.K. 1996. "Characterization and Optimization of Adsorbents for Hydrogen Storage". In *Proceedings of the 11th World Hydrogen Energy Conference*, 2: 1259-1261. Stuttgart, Germany, 23-28 June.
- Cioslowski, J. 1995. *Electronic Structure Calculations on Fullerenes and their Derivatives*. Oxford University Press.
- Goldshleger, N.F. and Moravsky, A.P. 1997. "Fullerene Hydrides: Synthesis, Properties, and structure." *Russian Chemical Reviews*, 66 (4): 323 – 342.
- Jensen, C.M. et al. 1999. "Advanced titanium Doping of sodium Aluminum Hydride: Segue to a Practical Hydrogen Storage Material?" *Int. J. of Hydrogen Energy*, 24: 461-465.
- Kroto, H.W. and Smalley, R.E. 1985. *Nature*, 318: 162-163.

Loutfy, R.O. and Wexler, E.M. 2001. "Investigation of Hydrogen Storage in Fullerene Hydrides." In *Metal Hydrides and Carbon for Hydrogen Storage* (Final Report for IEA Task 12) <http://www.eren.doe.gov/hydrogen/iea>

Nalimova, V.A. 1998. "High Pressure For Synthesis and Study of Superdense Alkali Metal – Carbon Compounds." *Mol. Cryst. Liq. Cryst.*, 310: 5-17.

Palstra, T.T.M, et al. 1995. "Superconductivity at 40K in Cesium Doped C₆₀". In *Proceedings of Material Research Society Symposium*, 359: 285-288.

Rao, A.M., et al. 1997. *Appl. Physics A*, 64: 231.

Sklovsky, D.E., et al. "High Pressure Lithium Intercalation Into Catalytic Carbon Nanotubes." *Mol. Cryst. Liq. Cryst.*, 310: 165-171.

CARBON NANOTUBE MATERIALS FOR HYDROGEN STORAGE

**A.C. Dillon, K.E.H. Gilbert, J. L. Alleman, T. Gennett, K.M. Jones, P.A. Parilla,
and M.J. Heben
National Renewable Energy Laboratory
Golden, CO 80401-3393**

Abstract

Carbon single-wall nanotubes (SWNTs) are capable of adsorbing hydrogen quickly, to high density, at ambient temperatures and pressures. Last year, we presented the details of a new SWNT cutting procedure that enabled hydrogen storage densities up to 7 wt% to be achieved as measured by temperature programmed desorption (TPD). We also acquired a new Alexandrite laser and performed initial synthesis experiments which resulted in materials that were ~ 40 - 50 wt% pure SWNTs, in contrast to the 20 - 30 wt% SWNTs typically found in the materials generated with the older laser. Hydrogen storage in carbon single-wall nanotubes is recently becoming the focus of numerous research groups outside of NREL. However, no one has yet achieved the high hydrogen capacities that we have reported. We have therefore this year taken great care to confirm our TPD calibration. We have shown good agreement between our TPD system and our volumetric Sievert's apparatus for three different hydride standards, including Pd, Ti and Ca. In all three cases we observed agreement between the two systems within $\pm 3\%$ as well as good precision for the expected hydrogen content for each of the samples. Unfortunately, this year we have also found that materials generated with our new Alexandrite laser do not have the high hydrogen storage capacities we reported last year even when all of the same sample purification, cutting and activation steps are taken. Typical hydrogen storage capacities on these new materials range from 2 - 4 wt%. Fortunately however, we have set up our new two color Raman spectroscopy lab which enables us to distinguish between different

types of nanotubes. We have found that our old laser materials were a heterogeneous mixture of both semi-conducting and metallic nanotubes while our new materials contain predominantly metallic tubes. We therefore believe that the semi-conducting tubes may be better suited for hydrogen storage applications. We have performed a very detailed laser-synthesis study of the production of nanotubes versus changing peak pulse power. We have established that semi-conducting tubes are produced at much higher density for very high peak powers. We have also increased our ability to produce tubes with specific diameters. This knowledge will enable us to re-optimize our hydrogen storage capacities on our new materials. Finally, this year we have developed a rapid method for evaluating the purity of a given SWNT material employing Raman spectroscopy at 488 nm.

Statement of the Problem / Relevance of the Work

Background

With the 1990 Clean Air Act and the 1992 Energy Policy Act, the United States recognized the need for a long-term transition strategy to cleaner transportation fuels¹. This realization comes while the U.S. continues to increase petroleum imports beyond 50% of total oil consumption; with nearly 50% of the total oil consumed being used in the transportation sector². Because of the potential for tremendous adverse environmental, economic, and national security impacts, fossil fuels must be replaced with pollution-free fuels derived from renewable resources. Hydrogen is an ideal candidate as it is available from domestic renewable resources, and usable without pollution. It could therefore provide the long-term solution to the problems created by the Nation's dependence on fossil fuel.

Interest in hydrogen as a fuel has grown dramatically since 1990, and many advances in hydrogen production and utilization technologies have been made. However, hydrogen storage technology must be significantly advanced in performance and cost effectiveness if the U.S. is to establish a hydrogen-based transportation system.

Hydrogen provides more energy than either gasoline or natural gas on a weight basis. It is only when the weight, volume, and round-trip energy costs of the entire fuel storage system and charging/discharging cycle are considered that hydrogen's drawbacks become apparent. New approaches enabling more compact, lightweight, and energy-efficient hydrogen storage are required in order for the wide-spread use of hydrogen powered vehicles to become a reality.

Research and development geared towards implementation of a national hydrogen energy economy has many indirect economic benefits. With almost 600 million vehicles in the world in 1992 - double the number in 1973 - the conflict between energy requirements, power generation, and environmental concerns is felt on a worldwide basis³. Thus, in addition to providing domestic energy alternatives, investment in hydrogen energy research will result in opportunities for U.S. technologies in overseas markets.

Currently Available Hydrogen Storage Technologies

Hydrogen can be made available onboard vehicles in containers of compressed or liquefied H₂,

in metal hydrides, or by gas-on-solid adsorption. Hydrogen can also be generated on-board by reaction or decomposition of a hydrogen containing molecular species⁴. Although each method possesses desirable characteristics, no approach satisfies all of the efficiency, size, weight, cost and safety requirements for transportation or utility use. The DOE energy density goals for vehicular hydrogen storage call for systems with 6.5 wt% H₂ and 62 kg H₂/m³.

Gas-on-solid adsorption is an inherently safe and potentially high energy density hydrogen storage method that should be more energy efficient than either chemical or metal hydrides, and compressed gas storage. Consequently, the hydrogen storage properties of high surface area "activated" carbons have been extensively studied⁵⁻⁷. However, activated carbons are ineffective in hydrogen storage systems because only a small fraction of the pores in the typically wide pore-size distribution are small enough to interact strongly with gas-phase hydrogen molecules.

The first measurements of hydrogen adsorption on carbon single-wall nanotubes (SWNTs) were performed here at NREL with highly impure samples. The room-temperature stabilization that was demonstrated at atmospheric pressures suggested the possibility of 5-10 wt % hydrogen storage in SWNT-based systems⁸. Contradictory results from purified SWNTs indicated that such high storage densities could only be achieved with cryogenic temperatures (80 K) and high pressures (158 atm)⁹, consistent with theoretical consideration of van der Waals interactions between H₂ and SWNTs¹⁰⁻¹². However, we showed two years ago that SWNTs can adsorb between 3.5 and 4.5 wt% at room temperature and room pressure when un-optimized preparation procedures were employed, and large-diameter SWNTs were also shown to adsorb 4.2 wt% hydrogen at room temperature and ~100 atm¹³. Last year we showed that hydrogen storage densities can be optimized to values as high as 7 wt%, and presented results from experiments designed to elucidate the mechanisms responsible for the unique hydrogen adsorption properties. There have been various reports of highly different values for SWNT hydrogen storage capacities in the last year from multiple different groups around the world. This "hydrogen storage controversy" was highlighted in a recent report in *Nature* in which our program was cast as leading the field¹⁴. Due to this extreme controversy, we have taken very careful steps to confirm our measurement calibration this year, and we hope that others in the field will take the same precautions. We have also now believe that semi-conducting single-wall carbon nanotubes have a greater hydrogen storage capacity than metallic tubes. The fact that the types of nanotubes occurring in various materials vary dramatically may account for some of the controversy within the field. Other factors which influence SWNT hydrogen storage capacities of course include sample purity and activation conditions. This year we have developed a laser synthesis method for the production of predominantly semi-conducting tubes and have improved our ability to tailor SWNT diameter distributions. These efforts will enable us to optimize the hydrogen storage properties of the Alexandrite laser materials. We have also developed a method for the rapid determination of whether a given nanotube material is highly pure.

Technical Approach and Summary of Past Work

We have been working on the idea that aligned and self-assembled single wall carbon nanotubes could serve as ideal hydrogen adsorbents since 1993. The concept was motivated by theoretical calculations¹⁵ that suggested that adsorption forces for polarizable molecules within SWNTs would be stronger than for adsorption on ordinary graphite. Thus, high H₂ storage capacities

could be achieved at relatively high temperatures and low pressures as compared to adsorption on activated carbons.

In the Proceedings of the 1994 Hydrogen Program Review, we presented microbalance data that demonstrated gravimetric hydrogen storage densities of up to 8.4 wt% at 82 K and 570 torr on samples containing carbon nanotubes. This substantial uptake at low hydrogen pressures demonstrated the strong interaction between hydrogen and these materials, consistent with higher heats of adsorption than can be found with activated carbons.

In the 1995 Hydrogen Program Review Proceedings, we presented the results of our temperature programmed desorption (TPD) studies that showed significant H₂ adsorption near room temperatures. The adsorption energies on nanotube materials were estimated to be a factor of 2-3 times higher than the maximum that has been observed for hydrogen adsorption on conventional activated carbons. These were the first results which demonstrated the existence of stable adsorbed hydrogen on any type of carbon at temperatures in excess of 285 K. We also analyzed the nanotube production yields versus rod translation rate in the electric arc.

In 1996, we performed a detailed comparative investigation of the hydrogen adsorption properties of SWNT materials, activated carbon, and exfoliated graphite. We also determined that the cobalt nanoparticles present in the arc-generated soots do not play a role in the observed hydrogen uptake. We determined the amount of hydrogen that is stable at near room temperatures on a SWNT basis is between 5 and 10 wt%, and found that an initial heating in vacuum is essential for producing high temperature hydrogen adsorption. Further experiments suggested that SWNTs are selectively opened by oxidation during this heating, and that H₂O is more selective in oxidation than O₂ due to hydrogen termination of dangling bonds at the edges of opened nanotubes. Purposeful oxidation in H₂O resulted in hydrogen storage capacities which were improved by more than a factor of three. We also correlated the measured nanotube densities produced by specific synthesis rod translation rates during arc-discharge with hydrogen storage capacities determined by TPD. Finally, we utilized NREL's High Flux Solar Furnace to form nanotubes by a new and potentially less expensive route for the first time.

In 1997, the desorption of hydrogen was found to fit 1st order kinetics as expected for physisorbed H₂, and the activation energy for desorption was measured to be 19.6 kJ/mol. This value is approximately five times higher than the value expected for desorption of H₂ from planar graphite and demonstrates that SWNT soots can provide very stable environments for H₂ binding. We also employed diffuse reflectance Fourier transform infrared (DRFTIR) spectroscopy to determine the concentrations and identities of chemisorbed species bound to the carbon surface as a function of temperature, and determined that "self-oxidation" allows high-temperature adsorption of hydrogen to occur in the arc-generated SWNT materials. We also began synthesizing SWNT materials in much higher yield than is currently possible with arc-discharge by using a laser vaporization process. We determined that the very long SWNTs made by this method could not be activated towards high-temperature H₂ physisorption by the same oxidative methods that were found to be effective for tubes produced by arc-discharge.

In 1998, we made significant advances in synthesis and characterization of SWNT materials so that we could prepare gram quantities of SWNT samples and measure and control the diameter

distribution of the tubes by varying key parameters during synthesis. By comparing continuous wave (c.w.) and pulsed laser techniques, we learned that it is critical to stay in a vaporization regime in order to generate SWNTs at high yield. We also developed methods that somewhat purified the nanotubes and cut them into shorter segments. We performed temperature programmed desorption spectroscopy on high purity carbon nanotube material obtained from our collaborator Prof. Patrick Bernier, and finished construction of a high precision Sievert's apparatus that allows the hydrogen pressure-temperature-composition phase diagrams to be evaluated for SWNT materials.

In 1999, we improved our laser-based method so that material containing between 20 - 30 wt% SWNTs could be generated at a rate of ~ 150 mg/hr or ~ 1.5 g/day. A simple 3-step purification technique was developed that resulted in single walled carbon nanotubes of greater than 98 wt% purity. A thermal gravimetric analysis (TGA) method was developed to allow the accurate determination of nanotube wt% contents in carbon soots. We also established a process for reproducibly cutting purified laser-generated materials. This advance was necessary since laser-produced tubes were found to be unresponsive to the oxidation methods that successfully opened arc-generated tubes. TPD spectroscopy demonstrated that purified cut SWNTs adsorbed between 3.5 – 4.5 wt% hydrogen under ambient conditions in several minutes and that the adsorbed hydrogen was effectively "capped" by CO_2 .

Last year we presented the details of a new cutting procedure and showed that, when optimized, hydrogen storage densities up to 7 wt% can be achieved. Infrared absorption spectroscopy measurements on pristine and H_2 -charged samples indicated that no C-H bonds are formed in the hydrogen adsorption process. These experiments are in agreement with an earlier temperature programmed desorption analysis which showed that hydrogen molecules are not dissociated when bound to the SWNT surfaces⁸. This conclusion is further supported by first neutron scattering measurements of hydrogen adsorbed onto SWNTs that were performed through collaboration with researchers at NIST and the University of Pennsylvania¹⁶. We also developed methods to tune SWNT diameters during synthesis so that mechanistic aspects of H_2 storage could be probed¹⁷, and learned how to de-tangle and organize individual tubes to form "superbundles" that will afford high volumetric storage densities¹⁸. Finally, we performed the first synthesis experiments with a newly acquired Alexandrite laser. Raman spectroscopy indicated that the as-produced materials were ~ 50 wt% pure SWNTs, in contrast to the 20 to 30 wt% usually seen with the previous laser.

This year we have shown good agreement between our TPD system and our volumetric Sievert's apparatus for three different hydride standards, including Pd, Ti and Ca. In all three cases we observed agreement between the two systems within $\pm 3\%$ as well as good precision for the expected hydrogen content for each of the samples. Unfortunately, this year we have also found that materials generated with our new Alexandrite laser do not have the high hydrogen storage capacities we reported last year even when all of the same sample purification, cutting and activation steps are taken. Typical hydrogen storage capacities on these new materials range from 2 – 4 wt%. Fortunately, however, we have set up our new two-color Raman spectroscopy lab that enables us to distinguish between different types of nanotubes. We have found that our old laser materials contained a heterogeneous mixture of semi-conducting and metallic nanotubes while our new materials contain predominantly metallic tubes. We have therefore

concluded that the semi-conducting tubes may be better suited for hydrogen storage applications. We have also performed a very detailed laser-synthesis study of the production of nanotubes versus changing peak pulse power. We have established that semi-conducting tubes are produced at much higher density for very high peak powers and increased our ability to produce SWNTs with specific diameters. This knowledge will enable us to re-optimize our hydrogen storage capacities on our new materials. Finally, this year we have developed a rapid method for evaluating the purity of a given SWNT material employing Raman spectroscopy at 488 nm.

Experimental

Pulsed Laser Synthesis of SWNTs

This year the SWNT materials were produced exclusively with our new Alexandrite laser (755 nm). Targets are made by pressing graphite powder doped with 0.6 at% each of Co and Ni in a 1/8" inch dye at 20,000 psi. Laser syntheses are performed at 1200 °C with 500 Torr Ar flowing at 100 sccm. The laser may be operated in a free-running mode with average powers varying from ~20 - 500 W/cm². The free running mode consists of ~ 1 ns pulses that are ≤ 1 ns apart and are produced in packets of ~ 1 μs inside a 100 μs train repeated at 10 Hz. The effective pulse width is ~1 μs. For free running laser vaporization, crude soots may be produced at rates of 10-200 mg/hr depending on the laser power density. The Alexandrite laser may also be operated at 10 Hz and a constant average power while the laser pulse width is precisely tuned to a value between 100 ns and 2.5 μs. This capability enables the effect of peak pulse power on SWNT size and type to be unambiguously determined and controlled.

Purification of Laser-generated SWNTs

Approximately 80 mg of the above laser-generated crude is refluxed in 60 ml of 3M HNO₃ for 16 h at 120 °C. The solids are collected on a 0.2 μm polypropylene filter in the form of a mat and rinsed with deionized water. After drying, an ~ 82 wt% yield is obtained. The weight lost is consistent with the digestion of the metal and an additional ~ 12 wt% of the carbon impurities. The carbon mat is then oxidized in stagnant air at 550 °C for 10 min., leaving behind pure SWNTs. When care is taken to remain in a vaporization regime during synthesis, materials that are > 98 wt% pure may be obtained as determined by thermal gravimetric analysis (TGA). Also, TGA reveals that since the laser-generated tubes are not highly defective, none of the SWNTs are destroyed in the purification process.

Cutting of Laser-generated SWNTs

Purified 1-3 mg samples are sonicated in 20 ml of 4M HNO₃ with a high-energy probe for 10 minutes to 24 hrs at powers ranging from 25 – 250 W/cm². The very long nanotube ropes found after purification¹⁹ are cut and re-assembled. This large-scale cutting observed is consistent with the generation of cuts and defects that have been observed by others²⁰⁻²². We find that cutting with a high-energy probe in HNO₃ is necessary to achieve high-capacity ambient H₂ adsorption.⁹ Also the cutting process incorporates metal particles ranging in size from several nanometers to several microns in the SWNT samples. X-ray patterns of the particles in the cut samples are consistent with an alloy of nominal composition TiAl_{0.1}V_{0.04} as expected for disintegration of the

ultrasonic probe. We believe that this alloy mediates the hydrogen adsorption process and is necessary to observe high hydrogen storage capacities.

Temperature Programmed Desorption

Details of the ultra high vacuum (UHV) chamber employed for the TPD studies have been reported previously^{4,8}. Briefly, carbon samples weighing ~1 mg are placed in a packet formed from 25 μm thick platinum foil and mounted at the bottom of a liquid nitrogen cooled cryostat. The packet is resistively heated with a programmable power supply. Pinholes in the foil enable gas diffusion into and out of the packet. An ion gauge and capacitance manometer are employed to monitor pressure. Gas exposures are controlled with a variable conductance leak valve. Isolation gate valves separate the sample compartment during high-pressure gas exposures. A mass spectrometer measures species with an m/e up to 300 a.m.u. and insures that only hydrogen is involved in adsorption/desorption cycles. The instrument is easily calibrated²³ by thermally decomposing known amounts of CaH_2 . The amount of evolved hydrogen is linear with the weight of decomposed CaH_2 , and the calibrations were performed with amounts of CaH_2 that yield a TPD signal similar to the SWNT samples. The TPD system has also been calibrated with hydrogen desorption studies of Pd and Ti hydrides. All three hydrogen calibration methods have been confirmed with our Sievert's volumetric technique within $\pm 3\%$. Prior to hydrogen adsorption studies SWNT samples are initially degassed by heating in a vacuum of $\sim 10^{-7}$ torr to 823 - 973 K at 1 K/s. The sample temperature is measured with a thin thermocouple spot-welded to the platinum packet. Room temperature H_2 exposures for ~ 1 minute at pressures between 10–500 torr saturate the hydrogen adsorption. Capacity determinations in the TPD are done by cooling the sample to 130 K prior to evacuation of the chamber.

Raman Spectroscopy

Raman spectroscopy is performed using ~ 7 mW of the 488 nm line of an Ar ion laser or ~ 9 mW of the 632.8 nm line of a HeNe laser. The scattered light is analyzed with a Jobin Yvon 270M spectrometer equipped with a liquid-nitrogen cooled Spectrum One CCD and a holographic notch filter. A 2400 grooves/mm grating is employed at 488 nm. However, it is necessary to employ a 1200 grooves/mm grating at 632.8 nm in order to observe the entire spectral range of interest. A Nikon 55 mm camera lens is employed both to focus the beam on the sample to a $\sim 0.25 \text{ mm}^2$ spot and to collect the Raman scattered light. At 488 nm a resolution of $2\text{-}4 \text{ cm}^{-1}$ was measured across the entire range with Oriel spectral calibration lamps. The resolution is decreased by approximately a factor of two for the spectra obtained at 632.8 nm. Averaging three 30 s scans is sufficient to obtain high intensity, well-resolved Raman spectra. Raman spectra are normalized for the different laser powers.

Sievert's Apparatus

The schematic diagram of the volumetric (Sievert's) apparatus is shown in Figure 1. The amount of H_2 gas adsorbed in a test sample is determined by measuring the pressure of a known number of gas moles introduced into a calibrated volume at known temperature as a function of time. Helium gas is used to calibrate the sample volume including the dead space of the sample itself. The total amount of hydrogen adsorbed can also be measured through desorption.

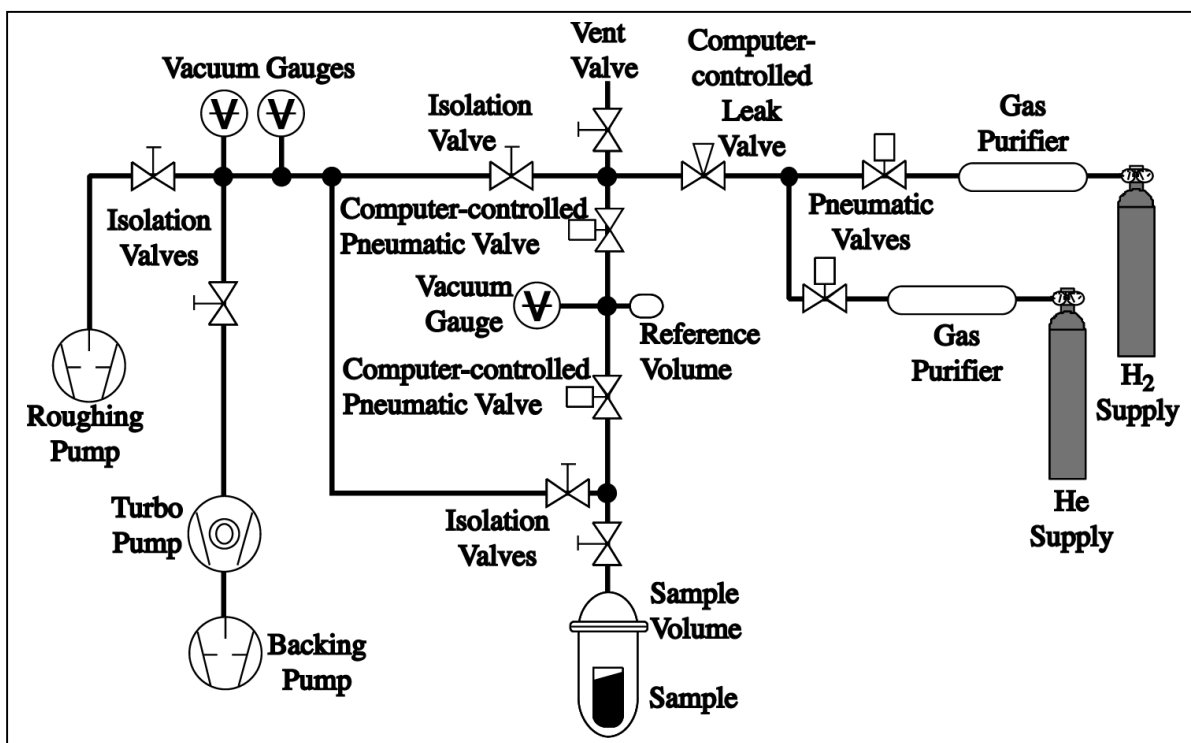


Figure 1: Schematic diagram of the Seivert's volumetric apparatus.

Results and Discussion

Rigorous Calibration of TPD Apparatus

Figure 2 displays temperature programmed desorption curves for the three standards employed to calibrate the TPD system including a) calcium hydride, b) palladium hydride and c) titanium hydride. Several separate spectra were obtained following the same sample preparation technique for a given hydride, and very good agreement is obtained in each case. The CaH_2 was employed to establish the initial sensitivity of the TPD mass spectrometer. It was assumed that the 95 wt% pure Aldrich CaH_2 supplies a standard which is 4.5 wt% hydrogen, a value similar to the capacities observed for our SWNT samples. This type of approach has been used successfully by others to achieve good accuracy calibrating systems for CO_2 desorption²³. We have also directly measured the hydrogen desorption for a CaH_2 sample that has been completely decomposed in our Seivert's apparatus to correspond to a value of 4.35 wt%.

In an effort to further solidify our TPD calibration, we endeavored to find a standard that could be charged *in situ* with identical pressure/temperature cycling and analyzed by both the TPD and Seivert's methods. Ideally, we would be able to perform the calibration with a pressure/temperature cycle which was similar to that used for charging SWNT samples. Palladium powder was chosen since fast hydrogen adsorption/desorption kinetics can be obtained at relatively low temperatures, and well-defined capacities of hydrogen can be repeatedly prepared. We first obtained adsorption isotherms from a Pd sample with the Seivert's

apparatus. Figure 3 shows an adsorption isotherm obtained from a Pd sample at 28 °C. The curve is in good agreement with adsorption isotherms published in the literature²⁴, showing a knee in the curve at 0.65 H/M. To evaluate the H/M value at lower temperatures, the Pd was charged with 20 torr H₂ at room temperature and then cooled with liquid nitrogen. While the sample was cooled, the head-space gas was evacuated. The sample was then heated to 300 °C and the trapped hydrogen was desorbed into the closed system. The number of moles of gas evolved was determined by measuring the pressure rise in the closed system after accounting for the fact that a small portion of the system volume was at 300 °C (the remainder being at 28 °C). Separate experiments confirmed that additional hydrogen uptake did occur while the sample was cooled from room temperature, and that the kinetics of hydrogen adsorption/desorption were "frozen-out" at ~120 K. The H/M value for the Pd after this P-T cycle was found to be 0.77 to 0.79 as expected from the literature²⁵. Palladium samples were then loaded into the TPD apparatus, and the same P-T charging cycle was performed. Following temperature programmed desorption, the integrated area of the TPD curve indicated an amount of hydrogen equal to 0.78 H/M using the calibration value determined from the CaH₂ decomposition experiments. Thus, good agreement was found between the TPD and Seivert's systems when cross-calibration was performed using a well-behaved standard charged under identical conditions.

As a final calibration test we monitored the hydrogen desorption from a TiH₂ standard obtained from our CRADA partners, Honda R & D Americas, Inc.. The titanium hydride was assumed to be charged to the maximum capacity of 4 wt% hydrogen. A value of exactly 4.0 wt% was measured for this

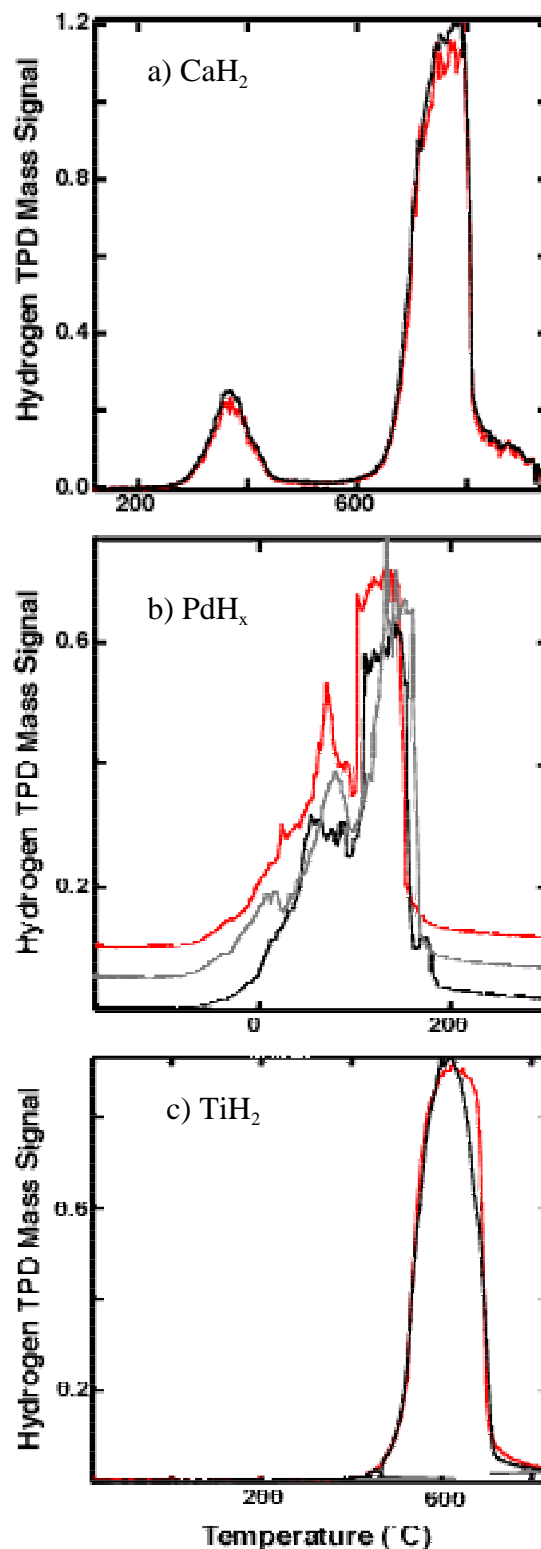


Figure 2: Hydrogen TPD spectra for three different calibration standards: a) CaH₂, b) PdH₂ and c) TiH₂.

standard with our volumetric technique, and employing the TPD technique a value of 3.9 wt% was obtained. Following these very careful calibration efforts, we are supremely confident in all of our reported SWNT hydrogen storage capacities. Since the development of a high capacity hydrogen storage system is so extremely important to the utility of hydrogen as a renewable energy source, we hope that all of the research groups working in the area will also take great care in reporting very accurate hydrogen adsorption measurements.

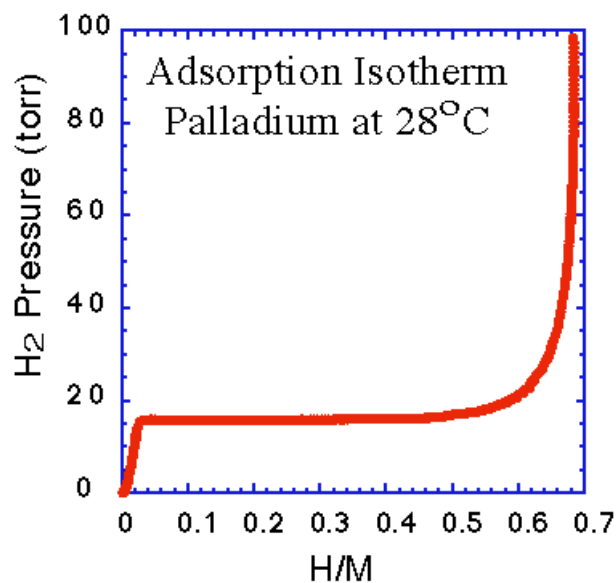


Figure 3: Adsorption isotherm from Pd sample at 28 °C, showing a knee in the curve at 0.65 H/M.

Decreased Hydrogen Adsorption on Alexandrite Laser Materials

By the end of the last fiscal year, the Molelectron Nd:YAG laser that was in use to produce our SWNT materials had been failing more and more regularly. Additionally problematic was the fact that the laser spot itself was very inhomogeneous and irreproducible after required flash lamp changes. We therefore replaced the Molelectron with a new Light Age, Inc., Alexandrite laser. Raman spectroscopy indicated that the as-produced materials were ~ 40 to 50 wt% pure SWNTs, in contrast to the 20 to 30 wt% usually seen with the Molelectron laser. However, following our standard purification, cutting and activation techniques, we found that the hydrogen storage capacities of the Alexandrite laser generated materials were typically between 2.0 – 4.0 wt%. Figure 4a displays a typical TPD spectrum of an Alexandrite laser generated material. This particular sample capacity was measured at 3.5 wt%. As observed previously hydrogen desorption occurs from at least two desorption sites with TPD peaks at ~410 and ~613 K. Figure 4b displays the desorption isotherm obtained with our Seivert's apparatus for the same sample. Here a value of only 2.5 wt% hydrogen was measured.

In general we have found the hydrogen adsorption capacities of SWNT materials measured with our Seivert's apparatus to be ~40-50 wt% lower than the values obtained with our TPD apparatus. We believe that the lower hydrogen capacities are measured for SWNT samples in the Seivert's system because there is an inherent difference in the way samples are degassed. In the Seivert's apparatus the dimensions of the tubing are small, as is the case for most volumetric systems. It is therefore impossible to degas the sample as efficiently as in the TPD system which has very high conductance. This failure to fully degas the sample results in a reduced hydrogen storage capacity. It is also apparent that the hydrogen storage capacities for the Alexandrite materials have decreased significantly from the values of 6-7 wt% reported last year for the Nd:YAG materials. These results suggest that the type of SWNT employed for various adsorption materials may be very critical to the optimization of hydrogen storage capacities. Thus, since we have shown that both SWNT type and subsequent processing are critical to

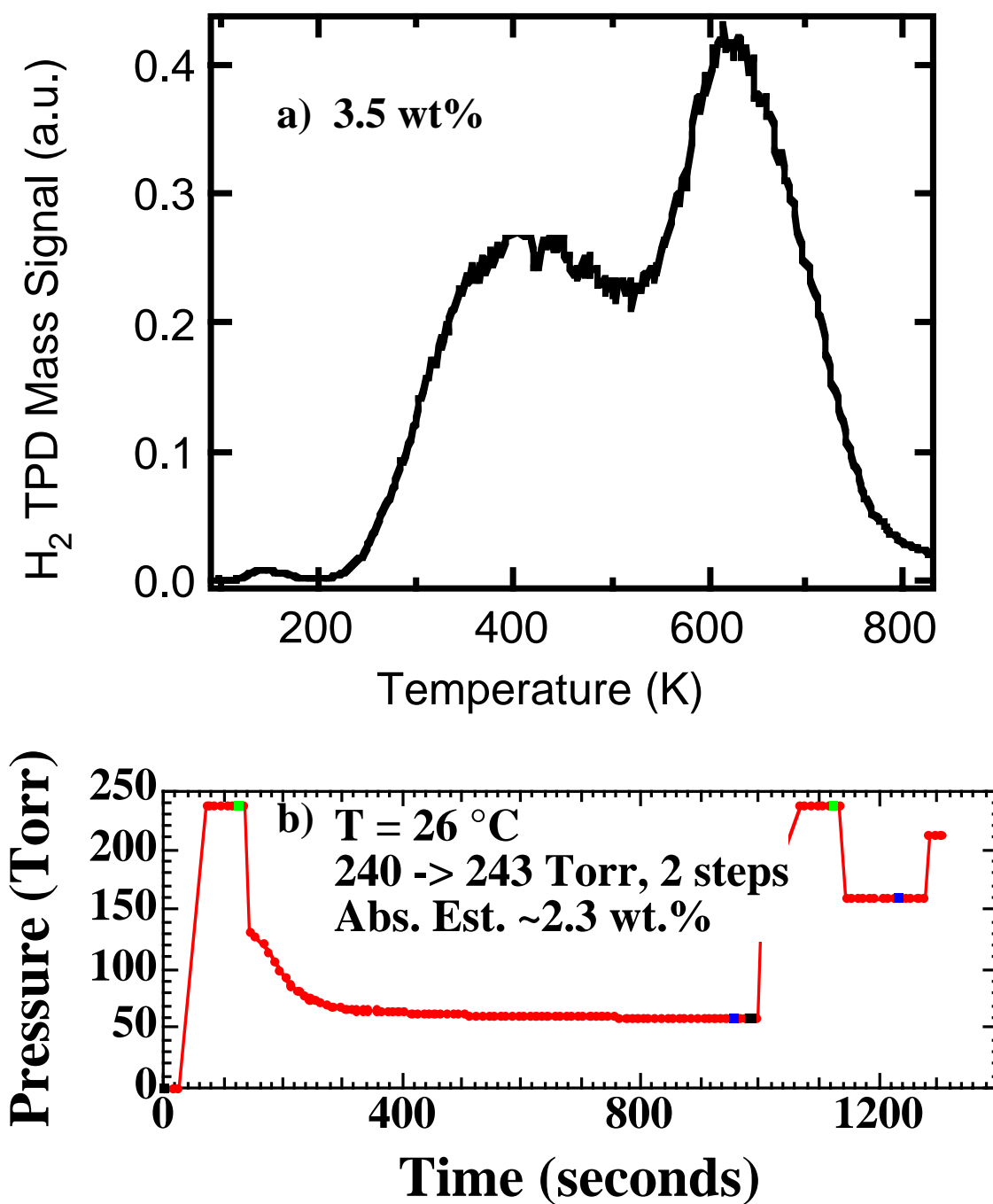


Figure 4: Hydrogen desorption from an Alexandrite laser generated material as probed by a) temperature programmed desorption and b) the Seivert's volumetric apparatus. The measured hydrogen capacities were 3.5 wt% and 2.5 wt%, respectively. The lower value measured by the Seivert's apparatus is attributed to difficulty in degassing the sample efficiently in the volumetric apparatus.

optimizing hydrogen storage properties, the large discrepancies reported for hydrogen storage on various carbon nanotube materials are perhaps not unanticipated.

Optimal Nanotubes for Hydrogen Storage and Their Controlled Laser Production

We have recently acquired a He:Ne (632.8 nm) laser for our Raman spectroscopy set-up. Previously the system relied upon a single Ar ion laser (488 nm). The Raman modes of SWNTs are resonantly enhanced with different tubes being at resonance for different wavelengths of excitation. At 488 nm only semi-conducting SWNTs are at resonance resulting in a Raman signal that is essentially due to resonant semi-conducting tubes. At 632.8 nm both metallic and semi-conducting nanotubes may be at resonance²⁶. However, the dominant peaks of the Raman tangential bands for semi-conducting SWNTs occur at 1563 and 1591 cm^{-1} while those for the metallic tubes occur at 1540 and 1581 cm^{-1} ²⁶. Figure 5 displays the Raman spectra in the radial breathing mode region of a) Nd:YAG and b) Alexandrite laser-generated crude materials for excitations at 488 and 632.8 nm. The frequencies observed for the SWNT radial breathing modes are strongly diameter-dependent with the smaller tubes appearing at higher frequency²⁷. For both of these materials the tangential bands observed for 632.8 nm were not significantly shifted from the values reported for the dominant peaks of the metallic tubes. It may therefore be assumed that predominantly metallic SWNTs are being probed for these laser-generated materials²⁸.

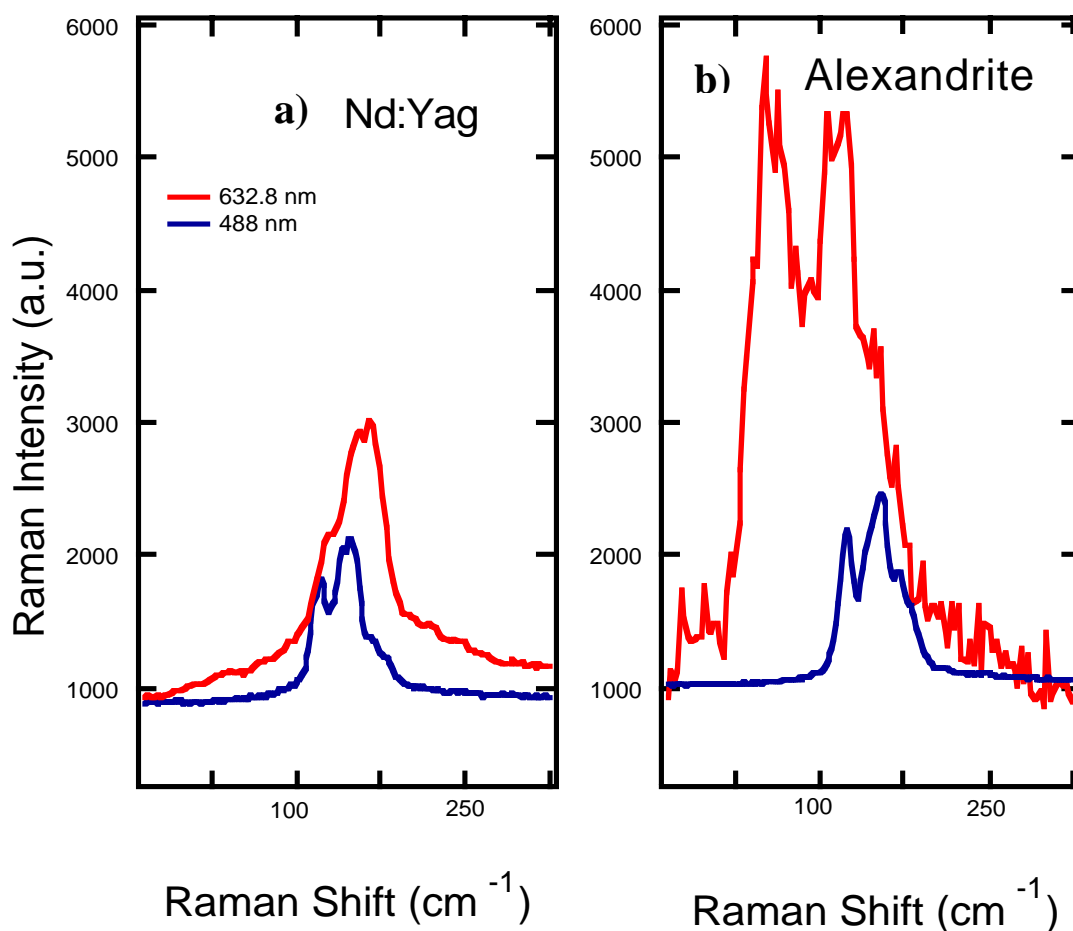


Figure 5: Raman spectra of the radial breathing modes for excitations at 488 and 632.8 nm of laser generated materials generated with a) the Nd:YAG and b) the Alexandrite.

The spectra of the radial breath modes for the Nd:YAG and Alexandrite materials appear quite different. The most striking feature is that the intensity of the spectrum observed at 632.8 nm in Fig 5b is much stronger relative to that observed at 488 nm implying a much larger concentration of metallic tubes in the Alexandrite materials. Since the hydrogen storage capacities for the Alexandrite materials have decreased from 6-7 wt% (Nd:YAG) to 2-4 wt%, the Raman results also suggest that semi-conducting single-wall carbon nanotubes are more efficient for the optimization of hydrogen storage capacity. We have therefore conducted a very detailed study of the production of specific sizes and types of SWNTs versus laser peak pulse power employing the Alexandrite laser²⁸. We have found that at a constant synthesis temperature of 1200 °C, the diameter distributions of both the semi-conducting and the metallic SWNTs may be tailored through variation in laser peak pulse power. In each case smaller diameter nanotubes are produced with increasing peak pulse power. It is also possible to regulate the fractions of the semi-conducting or metallic tubes by varying the synthesis peak pulse power. In this case, higher peak powers result in the production of semi-conducting SWNTs at a much higher density. It is possible that not only the ratio of the semi-conducting to metallic SWNTs is important for the optimization of hydrogen storage properties but also that the production of the specific diameters observed in Fig. 5a is critical for optimal hydrogen adsorption. In either case we are well poised to tailor the nanotube contents of our Alexandrite materials and obtain an optimal hydrogen storage capacity that equals or exceeds that observed for the Nd:YAG materials.

A Simple Method to Determine if SWNT Materials Contain Carbon Impurities

In 1999, we developed a rigorous method for the determination of SWNT contents in various materials employing thermal gravimetric analysis (TGA) and inductively coupled plasma spectroscopy¹⁹. It is often desirable though to obtain a more rapid estimate of whether a given nanotube material is high quality. However, we have found that employing other commonly used analytical tools to estimate SWNT contents in various materials can sometimes be misleading. For example Fig. 6a displays a scanning electron microscope (SEM) image of crude laser-generated material. In the SEM image it is very difficult to discern any non-nanotube fractions in the material either carbon or metal. The SEM image therefore suggests that this crude laser-generated material is perhaps greater than 90 wt.% SWNTs. Figure 6b, however, is a TEM image of the same nanotube crude. In this image the single-wall carbon nanotubes are still readily apparent, but amorphous carbon and/or nano-crystalline graphite as well as metal nanoparticles are also easily observed. Although TGA analysis of this material following a nitric acid reflux showed this material to be high quality, containing ~35wt.% SWNTs, it is obviously not nearly as pure as the SEM image of Fig. 6a suggests. Figure 6 indicates that transmission electron microscopy is a more powerful technique for determining SWNT purity levels than scanning electron microscopy. However, employing TEM to estimate SWNT purity levels is still not sufficient. The most obvious reason is simply that TEM is a highly localized technique. While one section on a TEM grid may appear to contain only carbon nanotubes, another could depict micron sized particles of graphite. In addition, it is very difficult to tell from a TEM image of nanotube bundles whether the tubes are surrounded by an impurity coating. Such a coating could easily constitute as much as 50 wt.% of the material.

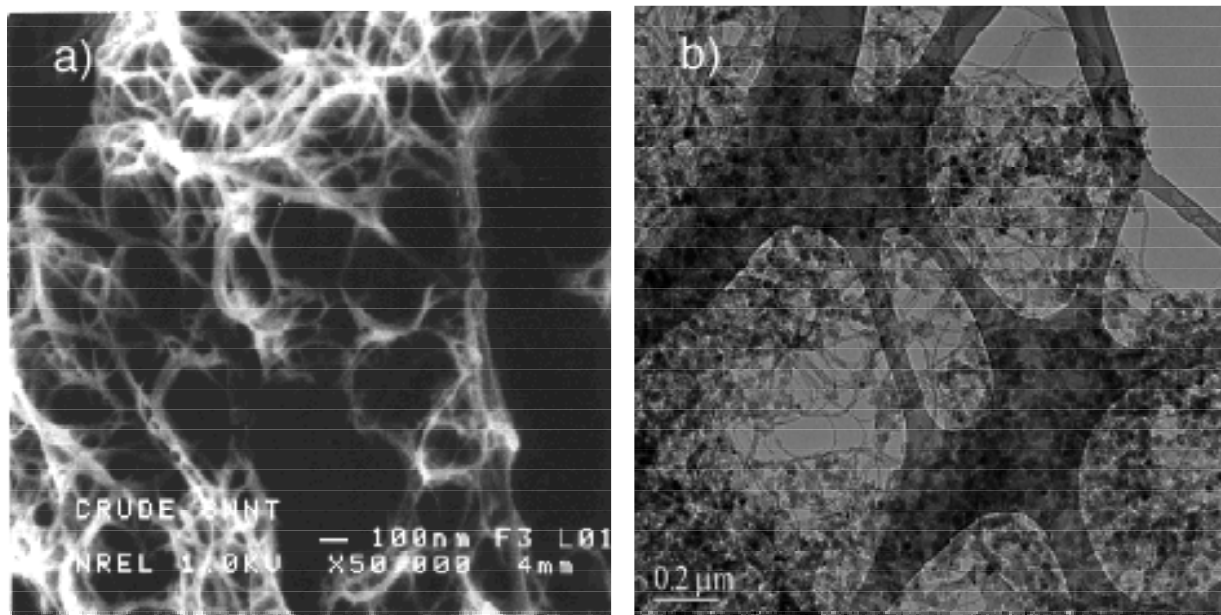


Figure 6: a) SEM image of laser generated SWNT crude and b) TEM image of the same material. Although this material contains only ~35 wt.% SWNTs, the SEM image is similar to SEM images observed for materials that contain > 90 wt.% SWNTs.

We have established a method using Raman spectroscopy to determine whether the non-nanotube carbon fractions have been removed during purification²⁹. Figure 7a displays Raman spectra of the tangential modes of a laser-generated crude and of the same material following purification. As expected the intensity of the spectrum of the purified material is greater than that of the spectrum of the impure sample. However, it is not possible to correlate Raman intensity to absolute purity of the SWNT samples as the intensities of fully purified materials vary dramatically. This is likely simply due to the presence of different concentrations of SWNTs that are resonantly enhanced at the particular excitation wavelength²⁷. A blow-up of the Raman spectra of the crude and purified materials is shown in Fig. 7b. Here the SWNT Raman band at 1350 cm^{-1} is clearly observed. It is striking that the band for the purified material is much narrower than the band for the crude. This is because the band of the crude material is also comprised of the much broader D-band of nanocrystalline graphite impurities. We have found that for purified SWNT samples that are free of non-nanotube carbon, the ratios of the SWNT band at 1593 cm^{-1} to the band at 1350 cm^{-1} are constant for both the heights and the full-widths-at-half-maximums. The ratio of the area of the band at 1350 cm^{-1} to the area of all three²⁷ of the tangential bands is also constant. If all three of these conditions are met, Raman spectroscopy identifies the SWNT samples as being free of non-nanotube carbon impurities. Unfortunately Raman spectroscopy is blind to the presence of residual metal catalyst particles. TGA and ICP allow this fraction to be quantified. Also the values of the ratios may not be extrapolated to estimate SWNT contents in impure materials as the widths of the impurity D-bands vary as a function of the particle size. However, this ability to rapidly determine whether a given single-wall carbon nanotube sample is free from carbon impurities should facilitate the wide array of SWNT research efforts including the development of a carbon nanotube based vehicular hydrogen storage system.

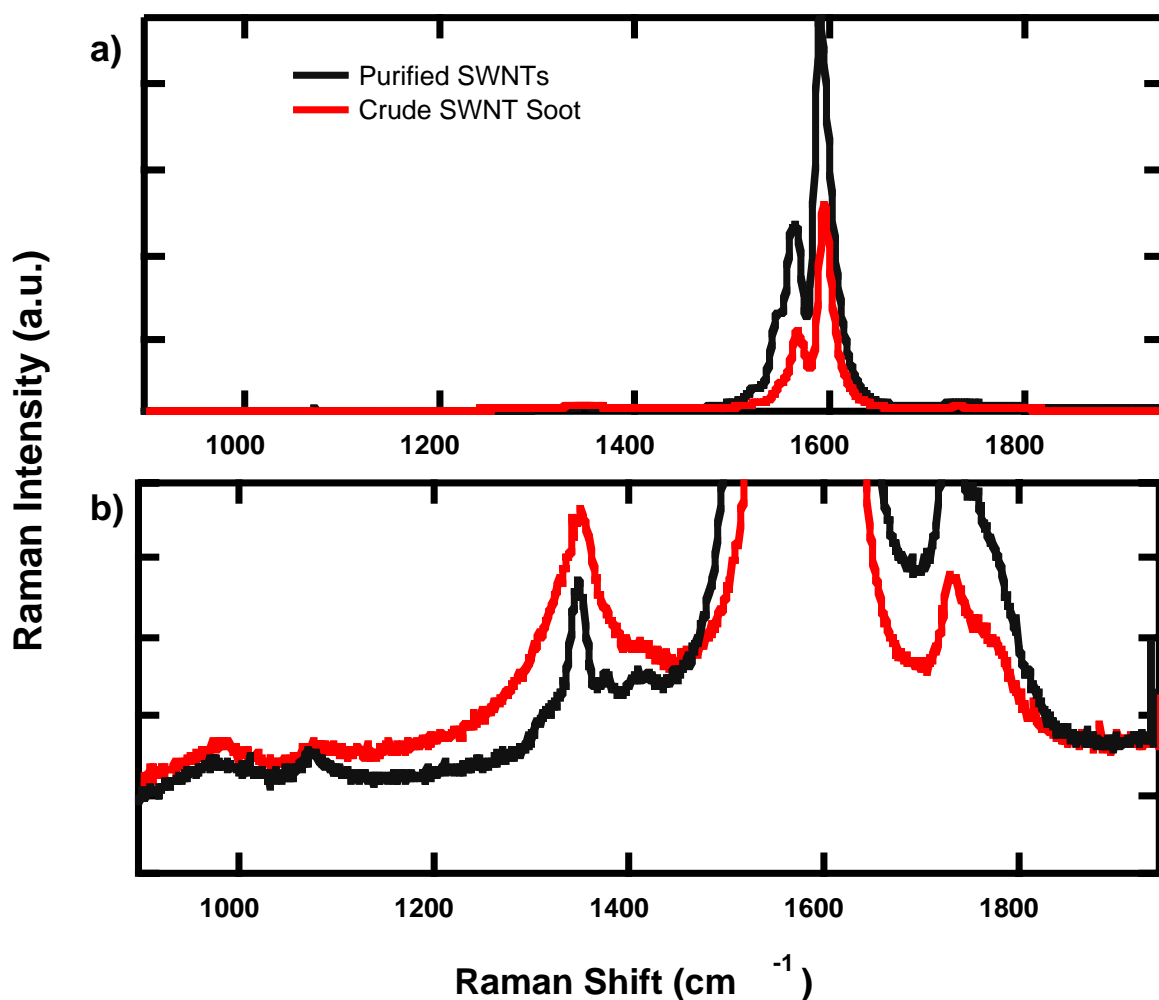


Figure 7 : Raman spectra of **a)** crude and purified laser-generated SWNTs between 1000-1800 cm^{-1} and **b)** a blow-up of the same spectra to magnify the band at 1350 cm^{-1} .

Conclusions/Future Work

Hydrogen storage in carbon single-wall nanotubes is recently becoming the focus of numerous research groups outside of NREL. In fact we were recently highlighted as the field leaders in a *Nature* article focusing on the wide scope of reported hydrogen storage capacities in carbon single-wall nanotube materials¹⁴. Because a such a wide-range of SWNT hydrogen storage capacities has been reported, we have taken great care to confirm our TPD calibration. We have shown good agreement between our TPD system and our volumetric Sievert's apparatus for three different hydride standards, including Pd, Ti and Ca. In all three cases we observed agreement between the two systems within $\pm 3\%$ as well as good precision for the expected hydrogen content for each of the samples. We therefore have utmost confidence in all of the hydrogen storage numbers that we report. We hope that other groups will take care to ensure the accuracy of their measurements as well.

Unfortunately, this year we have also found that materials generated with our new Alexandrite laser do not have the high hydrogen storage capacities we reported last year even when all of the same sample purification, cutting and activation steps are taken. Typical hydrogen storage capacities on these new materials range from 2 – 4 wt%. Fortunately however, we have set up our new two color Raman spectroscopy lab that enables us to distinguish between different types of nanotubes. We have found that our old laser materials were a heterogeneous mixture of both semi-conducting and metallic nanotubes while our new materials contain predominantly metallic tubes. We therefore believe that the semi-conducting tubes may be more optimal for hydrogen storage applications.

We have performed a very detailed laser-synthesis study with our new Alexandrite laser on the production of nanotubes versus changing peak pulse power. We have found that at a constant synthesis temperature of 1200 °C, the diameter distributions of both the semi-conducting and the metallic SWNTs may be tailored through variation in laser peak power. In each case smaller diameter nanotubes are produced with increasing peak pulse power. It is also possible to regulate the fractions of the semi-conducting or metallic tubes by varying the synthesis peak pulse power. Here, higher peak powers result in the production of semi-conducting SWNTs at a much higher density.

Finally we have developed a simple method employing Raman spectroscopy at 488 nm to determine the presence of carbon impurities in SWNT materials. This process enables us to quickly identify high purity SWNT samples. The new capability will greatly facilitate our hydrogen storage research efforts.

The fact that we have increased our synthesis capabilities to produce SWNTs with both specific sizes and types should enable us to fully optimize a SWNT hydrogen storage system. Our discovery this year that the Alexandrite laser generated materials have reduced storage capacities and also contain predominantly metallic SWNTs suggests that semi-conducting SWNTs are more effective for hydrogen storage applications. It may also be possible that hydrogen storage is only optimized for a very specific and narrow diameter range of SWNTs. In the upcoming year we will continue to evaluate the most optimal tube composition for hydrogen storage applications. We will then employ our new Alexandrite controlled production methods to produce these refined materials. Our current state of the art production and purification techniques provide gram quantities of high quality material per day. We will of course continue to focus on up-scaling the production and purification of SWNT adsorbent materials.

Acknowledgements

T. Gennett worked at NREL while under a sub-contract to Rochester Institute of Technology. We wish to thank Leonid Grigorian from Honda R&D Americas for many helpful conversations.

References

- 1 J. S. Cannon, *Harnessing Hydrogen* (INFORM, Inc., New York, 1995).
- 2 National Energy Strategy (1991/1992).

- 3 C. Flavin and N. Lessen, *Power Surge* (W.W. Norton & Co., New York, 1994).
- 4 A. C. Dillon, T. A. Bekkedahl, A. F. Cahill, K. M. Jones, and M. J. Heben, in *Carbon Nanotube Materials for Hydrogen Storage*, Coral Gables, FL, 1995, p. 521-542.
- 5 C. Carpetis and W. Peschka, *Int. J. Hydrogen Energy* **5**, 539-554 (1980).
- 6 J. A. Schwarz, in *Modification Assisted Cold Storage (MACS)*.
- 7 J. A. Schwarz, in *Activated Carbon Based Storage System*, Honolulu, HI., 1992, p. 271-278.
- 8 A. C. Dillon, K. M. Jones, T. A. Bekkedahl, C. H. Kiang, D. S. Bethune, and M. J. Heben, *Nature* **386**, 377-379 (1997).
- 9 Y. Ye, C. C. Ahn, C. Witham, B. Fultz, J. Liu, A. G. Rinzler, D. Colbert, K. A. Smith, and R. E. Smalley, *Applied Physics Letters* **74**, 2307 (1999).
- 10 Q. Wang and J. K. Johnson, *J. Phys. Chem. B* **103**, 4809-4813 (1999).
- 11 Q. Wang and J. K. Johnson, *J. Chem Phys. B* **110**, 577-586 (1999).
- 12 M. Rzepka, P. Lamp, and M. A. d. I. Casa-Lillo, *J. Phys. Chem* **102**, 10894-10898 (1998).
- 13 C. Liu, Y. Y. Fan, M. Liu, H. T. Cong, H. M. Cheng, and M. S. Dresselhaus, *Science* **286**, 1127 (1999).
- 14 C. Zandonella, *Nature* **410**, 734-5 (2001).
- 15 M. R. Pederson and J. Q. Broughton, *Physical Review Letters* **69**, 2689 (1992).
- 16 C. M. Brown, T. Yildirim, D. A. Neuman, M. J. Heben, T. Gennett, A. C. Dillon, J. L. Alleman, and J. E. Fischer, *Chem. Phys. Lett.* **329**, 311-316 (2000).
- 17 A. C. Dillon, P. A. Parilla, J. L. Alleman, J. D. Perkins, and M. J. Heben, *Chem. Phys. Lett.* **316**, 13-18 (2000).
- 18 T. Gennett, A. C. Dillon, J. L. Alleman, F. S. Hassoon, K. M. Jones, and M. J. Heben, *Chem. of Mat.* **12**, 599-601 (2000).
- 19 A. C. Dillon, T. Gennett, K. M. Jones, J. L. Alleman, P. A. Parilla, and M. J. Heben, *Advanced Materials* **11**, 1354-1358 (1999).
- 20 K. B. Shelimov, R. O. Esenaliev, A. G. Rinzler, C. B. Huffman, and R. E. Smalley, *Chem. Phys. Lett.* **282**, 429-34 (1998).
- 21 J. Liu, A. G. Rinzler, H. Dai, J. H. Hafner, K. R. Bradley, P. J. Boul, A. Lu, T. Iverson, K. Shelimov, C. B. Huffman, F. Roderiguez-Macias, Y.-S. Shon, T. R. Lee, D. T. Colbert, and R. E. Smalley, *Science* **280**, 1253-56 (1998).
- 22 K. L. Lu, R. M. Lago, Y. K. Chen, M. L. H. Green, P. J. F. Harris, and S. C. Tsang, *Carbon* **34**, 814-16 (1996).
- 23 J. Wang and B. McEnaney, *Thermochimica Acta.* **190**, 143-153 (1991).
- 24 H. Frieske, E. Wicke, and B. Bunsenge, *Physik Chem* **77**, 50 (1973).
- 25 Schirber and Northrup, *Phys. Rev. B* **10**, 3818 (1974).
- 26 P. Pimenta, M. Marucci, S. D. M. Brown, M. J. Matthews, A. M. Rao, P. C. Eklund, R. E. Smalley, G. Dresselhaus, and M. S. Dresselhaus, *Journal of Materials Research* **13**, 2396-2403 (1998).
- 27 A. M. Rao, E. Richter, S. Bandow, B. Chase, P. C. Eklund, K. A. Williams, S. Fang, K. R. Subbaswamy, M. Menon, A. Thess, R. E. Smalley, G. Dresselhaus, and M. S. Dresselhaus, *Science* **275**, 187-191 (1997).
- 28 A. C. Dillon, J. L. Alleman, T. Gennett†, K. M. Jones, P. Parilla, K. E. H. Gilbert, and M. J. Heben, (submitted to *J. Phys. Chem.*).
- 29 A. C. Dillon, T. Gennett, J. L. Alleman, K. M. Jones, P. Parilla, and M. J. Heben, (submitted to *Appl. Phys. Lett.*).

Doped Carbon Nanotubes for Hydrogen Storage

Ragaiy Zidan
Savannah River Technology Center
Savannah River Site
Aiken, SC 29808

Abstract

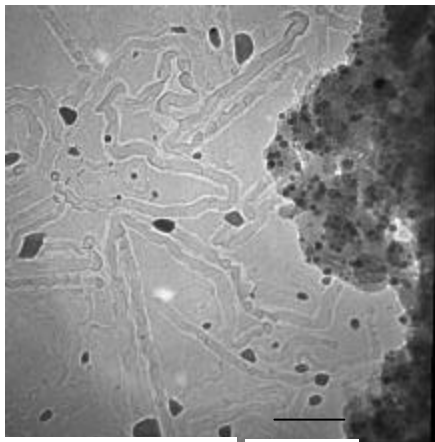
The ultimate goals of this research are to develop and demonstrate a low-cost hydrogen storage material that has a hydrogen capacity greater than 5.5 wt%, is stable with hydrogen cycling, and possesses favorable thermodynamic and kinetic characteristics suitable for transportation and portable devices applications. The approach to achieve these goals is to combine different solid-state hydrogen storage technologies and produce a superior hydrogen storage system. Carbon nanotube technology represents a new direction for solid hydrogen storage especially if these materials can be altered to store large amounts of hydrogen at room temperature. Modification of carbon nanotubes systems is expected to enhance and tune the hydrogen storage capabilities of the nanotubes. Carbon nanotubes were produced using different methods. Purification and high yield were achieved. Samples have been doped and spectroscopic characterization was conducted. Introducing transition metals and hydrogen bonding clusters inside these tubes can facilitate the uptake and release of hydrogen by and from the carbon nanotubes, at practical temperatures and pressures. These impeded clusters should be capable of bonding large amounts of hydrogen with favorable thermodynamics and enhanced kinetics while the transition metals catalyze the hydrogen to react with the clusters/nanotubes system.

Introduction

A major difficulty of utilizing hydrogen as fuel or energy carrier has been the absence of a practical means for hydrogen storage. Developing a high-density hydrogen storage system, above 5 weight percent, that can release hydrogen at a temperature lower than 100°C, has been the focus and the goal of researchers for years. Current approaches of hydrogen storage are compressed gas, liquid, or in the form of solid hydrogen. A solid hydrogen storage system is reliable, simple to engineer, and tremendously safer. Examples of solid hydrogen storage are metal hydrides, carbon (nanotubes, Fullerenes and activated carbon) or glass microspheres. In 1991, Sumio Iijima produced nanotubes by vaporizing carbon graphite, using an electric arc under an inert atmosphere [1]. The discovery has generated much interest and created extensive research activity into the properties and application of the nanometer-scale cylindrical carbon tubes. At first, the nanotubes were multi-layered, made up of 2 to 50 concentric cylindrical shells with outer diameters of few tens of nanometers and lengths on the order of few μm . Further research activities led by two independent efforts resulted in the development of single wall carbon nanotubes (SWNT) in macroscopic quantities. [2, 3]. It has been reported that large-diameter single wall nanotubes can be an ideal media for hydrogen storage because of their high gravimetric energy density [4]. Several research institutes and companies in the U.S. and elsewhere are exploring the use of carbon nanotubes for hydrogen storage. Single wall nanotubes technology represents a new direction for solid hydrogen storage especially if these materials can store larger amounts of hydrogen at room temperature than does graphite alone. Our objective has been to utilize the physisorption effect and generate a chemisorption effect by introducing transition metals and hydrogen bonding clusters inside the tubes. Controlling the type and size of the clusters is expected to allow us to tune the material for hydrogen sorption at desired temperatures and pressures.

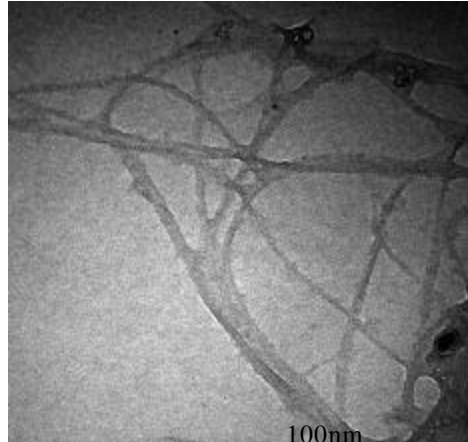
Results and Discussion

It has been argued that contamination during sample preparation or during experimental measurements can produce unreliable results [5]. Precautions were taken to avoid errors or misleading data that can lead to incorrect conclusion regarding the hydrogen uptake and release by and from the carbon nanotubes. The sample preparation system, the thermodynamic characterization system, and the hydrogen uptake and release quantification system were all confined in an argon gas atmosphere glovebox connected to sensors and computer interface for control and data monitoring. Hence, the nanotubes samples can be purified, degassed, opened and doped under inert atmosphere. The samples can be then hydrided/dehydrided using a thermogravimetric analyzer (TGA) and the heat of reaction can be measured using a scanning calorimeter (DSC) without the risk of exposing the samples to contamination. SWNT samples provided by Dr. Ching-Hwa at UCLA were prepared by carbon evaporation in the presence of metal catalysts [6,7]. Samples were purified and characterized by SEM. Several purification schemes were applied to remove impurities from SWNT. For example, SWNT samples were exposed to oxidative environment. Samples were washed out in acid to remove metal particles. See Fig 1a., 1b.



100nm

Fig 1.a SWNT sample as received



100nm

Fig1.b SWNT sample after purification

In collaboration with Dr. Apparao M. Rao at Clemson University (SC), other samples were prepared using CVD methods. The metal particle and nanotubes were created in a uniform configuration that can be controlled. These types of samples can be prepared in large quantities. See Fig. 2.

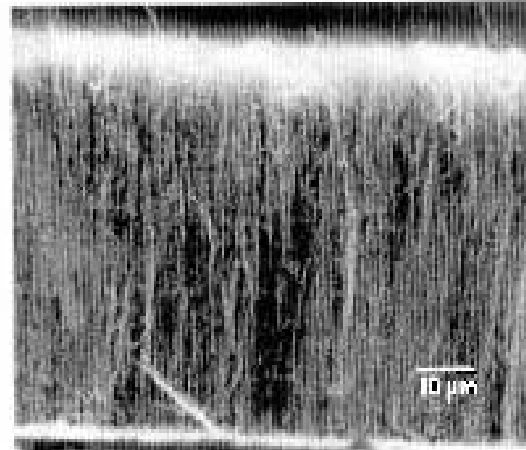
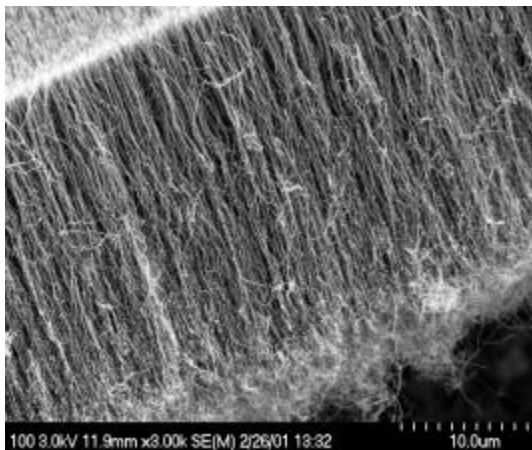


Fig. 2 Samples prepared by CVD methods showing the metal particles at the top of the nanotubes

The samples were characterized using (TEM) microscopy to determine the size of the tubes and the impeded metal particles. See Fig. 3 [8].

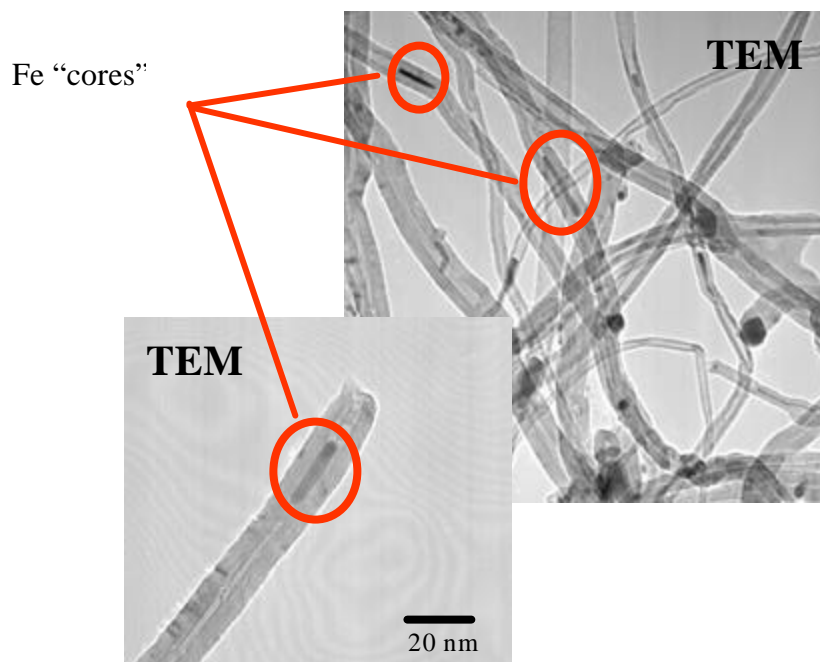


Fig. 3 TEM Images of Nanotubes grown from ferrocene saturated xylene-ferrocene mixtures [8]

Conclusions

Our immediate plan was to establish a state of the art capability for synthesizing, modifying and doping carbon nanotubes for hydrogen storage as well as to establish reliable means for characterizing these materials. The characterization effort involved material characterization using spectroscopic measurements (SEM, TEM, and EDS). Hydrogen sorption characterization systems (e.g. TGA, TVA, and DSC) were enclosed in an inert atmosphere to avoid the possibility of contamination. Our objective was aimed at producing large quantities of pure carbon nanotubes that represent a practical sample of material. We felt that large quantities of consistent structures, that can be modified as needed, were required to avoid discrepancy in the data. Consequently, through different means of synthesis, high purity samples were obtained. The samples were doped with metals as planned.

Future Work

In order to determine the hydrogen sorption performance of these carbon nanotubes preliminary Thermal Desorption Spectrum (TPD) measurements will be performed on samples, using thermovolumetric and thermogravimetric systems. The rate of hydriding and dehydrating will be obtained at fixed temperatures and pressures. The stability of the doped SWNT with cycling will be determined. The thermodynamic characteristics of samples will be obtained. The type and size of nanotubes and clusters that result in a reversible high hydrogen capacity will be

identified. The effect of contaminants on the performance of hydrogen uptake and release and the capacity of hydrogen will be investigated

References

- 1- S. Iijima, Nature, 354 (1991) 56
- 2- S. Iijima and T. Ichihashi Nature, 363 (1993) 603
- 3- D. S. Bethune, C.H. Kiang, M. S. de Vries, G. Gorman, R. Savoy, J. Vazquez and R. Beyers, Nature, 363 (1993) 605
- 4- A. C. Dillon, K. M. Jones, T. A. Bekkedahl, C.H. Kiang, D. S. Bethune and M.J. Heben Nature, 386 (1997). 377
- 5- R. T. Yang, Carbon 38 (2000) 623
- 6- D. S Bethune, C. H. Kiang, M.S. de Vries, G. Gorman, R. Savoy, J. Vazquez and R. Beyers Nature 363 (1993) 605
- 7- C. H. Kiang, W. A. Goddard, R. Beyers J. R. Salem and D. S. Bethune phys. Chem. 98(1994) 6612
- 8- J.Liu, R. Czerw, D.L. Carroll and A.M. Rao, (in preparation)

CATALYTICALLY ENHANCED SYSTEMS FOR HYDROGEN STORAGE

Craig M. Jensen, Dalin Sun, Brad Lewandowski, Kristin K. Kumashiro,
Walter P. Niemczura, David Morales-Morales, and Zhouhui Wang
Department of Chemistry
University of Hawaii
Honolulu, HI 96822

Abstract

The effects of two classes of dopants on the rates of the dehydriding of doped NaAlH_4 to Na_3AlH_6 and Al have been studied under the practical relevant conditions of 100°C and a constant pressure of 1 atm. Aluminum-transition metal alloys were found to have little or no effect while doping with transition metal-aluminum hydride complexes resulted in only modest kinetic enhancement. The dehydriding rates of hydride doped with 2 mol % $\text{Ti}(\text{O}^n\text{Bu})_4$ or $\beta\text{-TiCl}_3$ are adequate to meet the demands of a fuel cell operating under practical conditions. Mixtures of NaH and Al doped with 2 mol% $\text{Zr}(\text{O}^n\text{Pr})_4$ will undergo hydriding to NaAlH_4 in 15 minutes under 120 atm of hydrogen at 120°C . Methods have been developed whereby the different species that are present during the dehydriding of the doped hydrides can be directly observed and quantified by solid state ^{27}Al , and ^{23}Na NMR spectroscopy. Solid state ^1H NMR spectroscopy has allowed the unexpected observations that $\sim 25\%$ of the hydrogen in NaAlH_4 is highly mobile at even ambient temperature and that titanium doping results in a significant increase in the proportion of mobile hydrogen in the **bulk** material. ^{27}Al and ^{23}Na NMR studies indicate that the mobility of hydrogen results from the breaking of Na-H rather than Al-H bonds. The arsino pincer complex, $\text{IrH}_2\{\text{C}_6\text{H}_3\text{-}2,6\text{-(CH}_2\text{AsBu}^t\text{)}_2\}_2$ has been synthesized and found to catalyze the dehydrogenation of methylcyclohexane to toluene. The $>20\%$ conversion obtained using this catalyst is much greater than the 10% conversion obtained with $\text{IrH}_2\{\text{C}_6\text{H}_3\text{-}2,6\text{-(CH}_2\text{P}^t\text{Bu}^t\text{)}_2\}_2$ but far short of practically significant mark of $>90\%$.

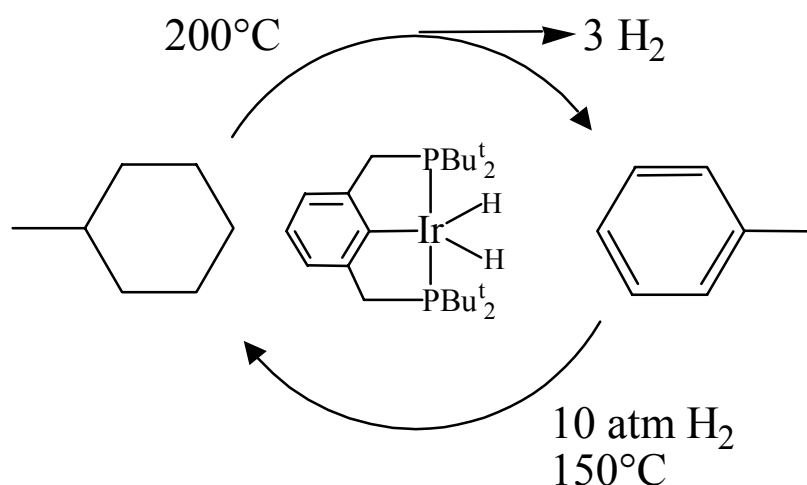
Introduction

A major obstacle to the conversion of the world to a “hydrogen economy” is the problem of onboard hydrogen storage. Despite decades of extensive effort no material has been found that has the combination of a high gravimetric hydrogen density, adequate hydrogen dissociation energetics, long-term cyclability, and low cost required for commercial vehicular application. A priori, sodium aluminum hydride (NaAlH_4) would seem to be viable candidate for application as a practical onboard hydrogen storage material. It has a high weight percent available hydrogen content (5.6%), low cost (\$50/metric ton), and is readily available in bulk. However, thermal-activated evolution of hydrogen from NaAlH_4 occurs at appreciable rates only at temperatures well above its melting point of 183°C . Additionally, this process can be reversed only under severe conditions. Thus, until recently, complex aluminum hydrides were not considered as rechargeable hydrogen carriers. This situation was changed by recent studies that have shown that upon doping with selected transition metals, the dehydriding of anionic aluminum hydrides could be kinetically enhanced and rendered reversible under moderate conditions in the solid state (Bogdanovic and Schwickardi, 1997; Jensen et al., 1999; Zidan et al., 1999; Bogdanovic et al., 2000; Jensen and Gross, 2001). We have developed methods of doping NaAlH_4 with titanium, zirconium and other catalysts such that: 1) rapid dehydriding occurs at temperatures as low as 100°C ; 2) rehydriding can be accomplished in only 15 minutes; and 3) 5.0 weight percent hydrogen can be repeatedly cycled through dehydriding/rehydriding. It now appears that it is not unreasonable to think that catalytically enhanced complex aluminum hydrides could be developed as a means of practical storage of hydrogen for an onboard PEM fuel cell.

We have also been investigating hydrogen storage through the reversible dehydrogenation of cycloalkanes to arenes. Cycloalkanes are cheap and abundant. The dehydrogenation of cycloalkanes to arenes releases approximately 7 weight percent hydrogen. Such a storage system also meets criteria of low cost and high hydrogen density required for practical applications. However, it is generally considered to be impractical as their dehydrogenation occurs at adequate rates only in the presence of high loadings of heterogeneous, precious metal catalysts at temperatures in excess of 300°C .

The PCP pincer complex, $\text{IrH}_2\{\text{C}_6\text{H}_3\text{-}2,6\text{-(CH}_2\text{P}^t\text{Bu)}_2\}$ (**1**) is a uniquely active and robust catalyst for aliphatic dehydrogenations (Gupta et al., 1996; Gupta, Hagen et al., 1997; Gupta, Kaska et al., 1997; Xu et al., 1997; Liu et al., 1999; Jensen, 2000). In contrast to most catalysts that have been reported thermochemical dehydrogenation of alkanes, the pincer catalyst does not require a sacrificial hydrogen acceptor. Thus in the presence of the pincer catalyst, alkanes are efficiently dehydrogenated to alkenes with the direct evolution of H_2 (Gupta, Hagen et al., 1997; Jensen, 2000). The pincer catalyst is also the first reported homogeneous catalyst for the dehydrogenation of cycloalkanes to arenes (Gupta, Hagen et al., 1997). Unlike the heterogeneous catalysts that are known for this reaction, it shows appreciable activity at temperatures as low as 100°C and very low catalyst loadings (Gupta, Hagen et al., 1997; Jensen, 2000). We have also found that the pincer complex also catalyzes the hydrogenation of arenes to cycloalkanes under moderate (10 atm) pressures of hydrogen. The two-way, hydrogenation/dehydrogenation activity of the catalyst suggests its application in a hydrogen storage system based on the reversible dehydrogenation of a cycloalkane to its arene analog, such as the methylcyclohexane/toluene system seen in Scheme 1.

Scheme 1



Temperatures in excess of 200°C are thermodynamically required to achieve a usable pressure of hydrogen from the dehydrogenation of alkanes. However, unlike solid hydrogen storage materials, liquid cycloalkanes can be easily transported within a system. Thus a small portion can be continuously feed into a small hot tube at a rate that insures an adequate supply of hydrogen for the onboard application. This system is also attractive since it is compatible with the existing gasoline infrastructure. The major drawback to homogenous, pincer complex catalyzed systems is that pronounced product inhibition occurs after dehydrogenation of about 10% of the cycloalkane to arene. The dissociation of product from the catalyst is apparently reversible and, at high concentrations, arenes effectively compete with alkanes for coordination to complex. In an attempt to eliminate this problem, we have synthesized a novel iridium complex containing a pincer ligand in which the phosphorous donor atoms are substituted by arsenic atoms. It is our premise that this adjustment will alter the electronic environment at the metal center and improve the alkane/arene binding selectivity. We have found that significantly improved levels of conversion of methylcyclohexane to toluene can be achieved with the arsino complex.

Results

Task 1. Testing of Aluminum-Transition Metal Catalysts for the Reversible Dehydrogenation of NaAlH₄. The aluminum-transition metal alloys (TiAl, Ti₃Al, Zr₃Al, and Ni₃Al) and the transition metal-aluminum hydrido complexes: $\{[(C_5H_5)_2ZrH(\mu-H)_2AlH_2(NMe_3)]\}$ and $\{(C_5H_5)_2Ti(\mu-H)_2AlH_2(THF)\}$ were studied as catalysts for the reversible dehydrogenation of NaAlH₄. The complexes were synthesized through methods that have been reported in the literature (Khan et al., 1997; Fryzuk et al., 1997) while the alloys were purchased from Alfa Aesar. Small amounts (~2 mole%) of the alloys and complexes were introduced into the bulk NaAlH₄ through ball milling techniques under an inert atmosphere. The dehydrogenation behavior of the doped hydrides were screened by thermal programmed desorption and isothermal

desorption studies using a modified Sievert's type apparatus. Little or no kinetic enhancement was observed in all of the samples doped with aluminum alloys. Hydrogen desorption was accelerated in the samples doped with the transition metal-aluminum hydride complexes. However, the desorption rates were much lower than those observed for samples doped with $\text{Ti}(\text{O}^n\text{Bu})_4$ or $\text{Zr}(\text{O}^n\text{Pr})_4$.

In order to obtain a meaningful comparison of the relative catalytic enhancement produced by the various dopants, we conducted isothermal desorption studies of samples of the hydrides under the practical relevant conditions of 100°C while maintaining a constant pressure of 1 atm. During the initial dehydriding reaction



we observed the hydrogen flow rates seen in Table 1.

Table 1. Rates of dehydriding of NaAlH_4 containing 2 mole % dopant at 100°C , against a constant pressure of 1 atm.

Catalyst Precursor	Rate of desorption (wt %/hr)
$\text{Ti}(\text{O}^n\text{Bu})_4$	1.8
$\beta\text{-TiCl}_3$	1.8
TiCl_4	1.8
$\text{Zr}(\text{O}^n\text{Pr})_4$	0.6
$\{(\text{C}_5\text{H}_5)_2\text{ZrH}(\mu\text{-H})_2\text{AlH}_2(\text{NMe}_3)\}$	0.2
$\{(\text{C}_5\text{H}_5)_2\text{Ti}(\mu\text{-H})_2\text{AlH}_2(\text{THF})\}$	0.2

We were surprised to find that the rates observed for hydride doped with either $\text{Ti}(\text{O}^n\text{Bu})_4$ or $\beta\text{-TiCl}_3$ are adequate to meet the demands of a fuel cell operating under practical conditions.

We have also found that NaH and Al doped with 2 mole percent $\text{Zr}(\text{O}^n\text{Pr})_4$ will undergo the reverse of the dehydriding reactions seen in equations 1 and 2 (below) more rapidly and under milder conditions than had been previously appreciated.



Absorption of 4.4 weight percent hydrogen was seen to occur within 15 minutes at 120°C under a pressure of 125 atm of hydrogen. Thus our benchmarking of the previously reported catalysts revealed that the only remaining kinetic barrier to the practical utilization of NaAlH_4 is the development of an improved catalyst for the "second" dehydriding reaction seen in equation 2.

Task 2. Solid State Nuclear Magnetic Resonance Spectroscopic Studies of the Reversible Dehydriding of NaAlH_4 and Active Catalyst. In collaboration with Prof. K. Kumashiro and Dr. W. Niemczura of the UH Department of Chemistry, we developed methods whereby we have directly observe and quantify the different species that are present during the dehydriding of the doped hydrides by solid state ^{27}Al , and ^{23}Na NMR spectroscopy. Additionally, as seen in Figure 1, wideline ^1H NMR spectra show that, contrary to the accepted model of the bonding in

Group 13 complex hydrides, ~25% of hydrogen in NaAlH₄ is highly mobile at even ambient temperature.

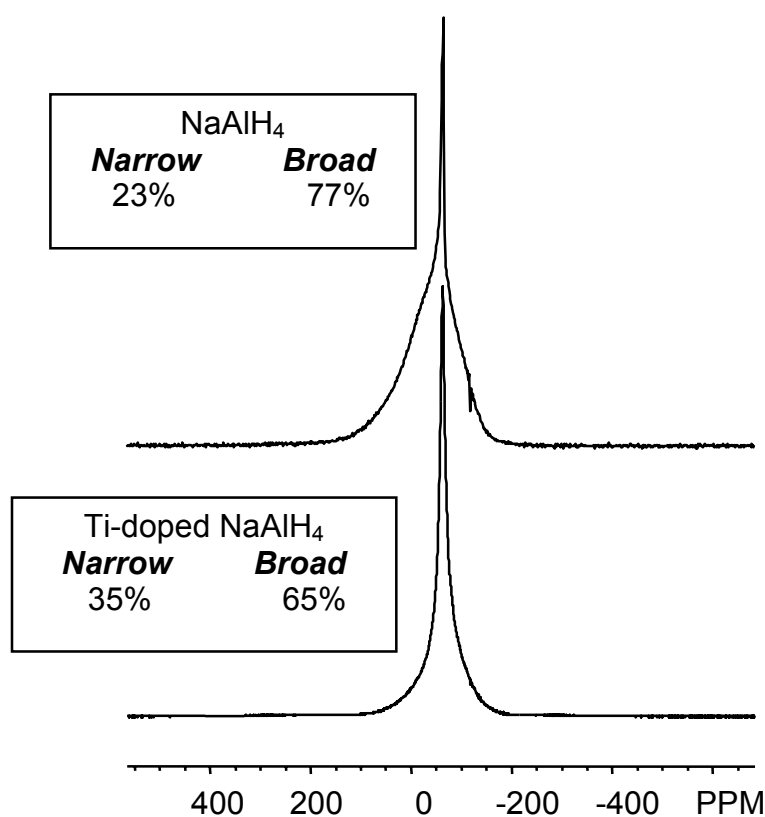


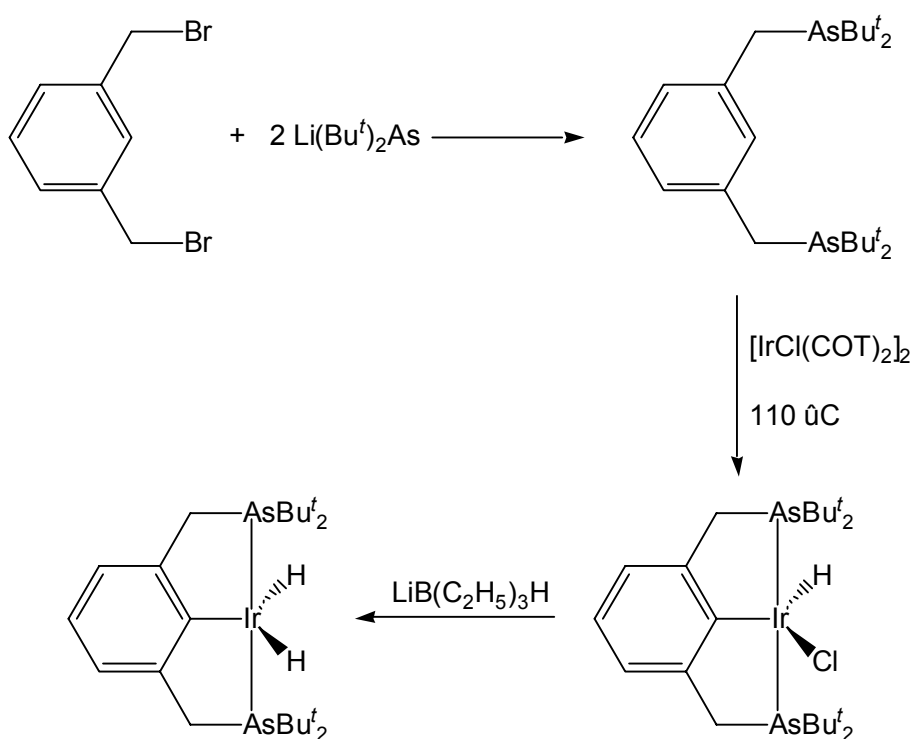
Figure 1. Solid state ¹H NMR spectra of NaAlH₄ with and without doping with 2 mol% Ti(OⁿBu)₄.

Surprisingly, the ²⁷Al, and ²³Na NMR studies indicate that the mobility of hydrogen results from the breaking of Na-H rather than Al-H bonds. We have observed (Figure 1) that samples of the hydride that are doped with titanium have a significant increase in the proportion of mobile hydrogen in the **bulk** material. Therefore, we can directly observe the lowering of the energetic barrier to the activation of hydrogen in the hydride and thus quantify the fundamental catalytic effect of the dopant. We are now beginning studies in which the populations of mobile hydrogen in undoped, titanium-doped, and zirconium-doped hydrides are quantified at temperatures ranging from 20-150°C. The activation parameters for the fundamental hydrogen activation process will be calculated from the variable temperature data.

Task 3. Synthesis and Testing of an Arsino Pincer Catalyst for Reversible Alkane Dehydrogenation. We successfully synthesized the arsino pincer complex, IrH₂{C₆H₃-2,6-(CH₂AsBu^t₂)₂} as seen in Scheme 2. Reaction of α,α'-dibromoxylene with two equivalents of lithium di-*t*-butylarsinide gave α,α'-bis(arsino)xylene in >90% yield. The hydrido chloride iridium complex, IrHCl{C₆H₃-2,6-(CH₂AsBu^t₂)₂} was then synthesized by refluxing the α,α'-bis(arsino)xylene with [Ir(COE)(μ-Cl)]₂ in toluene for 24 h. Subsequent reaction of the hydrido chloride complex with LiBEt₃H under an atmosphere of H₂ gave the target dihydride complex

that was characterized by ^1H , ^{13}C , and ^{31}P NMR spectroscopy. The catalytic activity of the arsino pincer complex for the dehydrogenation of toluene to methylcyclohexane at 200°C was quantified by gas chromatography. We have observed that the catalytic dehydrogenation of methylcyclohexane to toluene proceeds to $>20\%$ compared to the only 10% conversion that was obtained with the phosphino catalyst. This result verifies our hypothesis that the σ -donor strength of the ligand greatly influences the attainable conversion level in the catalytic system. Unfortunately, the conversion level is still far short of the practically significant mark of $>90\%$ and it seems unlikely that we will be able to adjust the catalytic system such that we can attain such high levels of conversion.

Scheme 2. Synthesis of $\text{IrH}_2\{\text{C}_6\text{H}_3\text{-2,6-(CH}_2\text{AsBu}^t\text{)}_2\}$.



Conclusions

We have examined the effects of two classes of dopants on the rates of the dehydriding of doped NaAlH_4 to Na_3AlH_6 and Al under the practical relevant conditions of 100°C and a constant pressure of 1 atm. Aluminum-transition metal alloys were found to have little or no effect while doping with transition metal-aluminum hydride complexes resulted in only modest kinetic enhancement. However, benchmarking the dehydriding rates of hydride doped with $\text{Ti}(\text{O}^i\text{Bu})_4$ and $\beta\text{-TiCl}_3$ has revealed that these materials undergo dehydriding at rates adequate to meet the

demands of a fuel cell operating under practical conditions. We have also found that NaH and Al doped with 2 mole percent $\text{Zr}(\text{O}^n\text{Pr})_4$ will undergo hydriding to NaAlH_4 more rapidly and under milder conditions that had been previously appreciated. Thus, three key practical kinetic parameters have now been established for NaAlH_4 at acceptable doping levels: 1) dehydriding of NaAlH_4 to Na_3AlH_6 and Al at the rate of 1.8 wt% per hour at 100°C under 1 atm; 2) rehydriding of 4.4 wt% can be accomplished in only 15 minutes; and 3) 5.0 wt% hydrogen can be repeatedly cycled through dehydriding/rehydriding. Thus these materials hold great promise as hydrogen carriers for onboard fuel cells. However, further catalyst development is required in order for these materials to achieve commercial viability.

We have developed methods whereby the different species that are present during the dehydriding of the doped hydrides can be directly observed and quantified by solid state ^{27}Al , and ^{23}Na NMR spectroscopy. Additionally, solid state ^1H NMR spectra has allowed the unexpected observations that ~25% of the hydrogen in NaAlH_4 is highly mobile at even ambient temperature and that titanium doping results in a significant increase in the proportion of mobile hydrogen in the **bulk** material. Furthermore, ^{27}Al , and ^{23}Na NMR studies indicate that the mobility of hydrogen results from the breaking of Na-H rather than Al-H bonds. Thus we can directly observe the lowering of the energetic barrier to the activation of hydrogen in the hydride and therefore quantify the fundamental catalytic effect of the dopant. Extensions of these studies should elucidate the mechanism of the catalyzed dehydriding reactions and lead to the characterization the enigmatic active catalyst in the doped hydrides.

We have successfully synthesized the arsino pincer complex, $\text{IrH}_2\{\text{C}_6\text{H}_3\text{-2,6-(CH}_2\text{AsBu}^t_2)_2\}$ and to found it to catalyze the dehydrogenation of methylcyclohexane to toluene. The >20% conversion obtained using this catalyst is much greater than the 10% conversion that was obtained with the phosphino catalyst. This result verifies our hypothesis that the σ -donor strength of the ligand greatly influences the attainable conversion level in the catalytic system. Unfortunately, the conversion level is still far short of the practically significant mark of >90% and it seems unlikely that we will be able to adjust the catalytic system such that we can attain such high levels of conversion.

Future Work

Despite progress in maximizing the catalytic enhancement of both the dehydriding and rehydriding process, it has not yet been demonstrated that >5 wt% hydrogen can be reversibly released from these materials under conditions that are required for the practical operation of an onboard fuel cell. Our studies also indicate that the titanium and zirconium catalysts can act in concert to yield a material with adequately enhanced kinetic performance over the course of the complete dehydriding reaction sequence and its reverse (Zidan et al., 1999). However, the requirement of dual catalysts significantly affects the cyclable hydrogen weight percentage of the hydride. Therefore, the contribution of the transition metal dopant to the weight of the material must be minimized. During the next year of this project, we plan to determine the minimum levels of titanium and zirconium loadings that are required to adequately enhance the kinetics of NaAlH_4 under the practically relevant conditions. Dehydriding studies will be carried out under

positive pressures (1-2 atm) of hydrogen and rehydriding will be carried out at pressure of less than 100 atm and temperatures of less than 100°C.

As discussed above, we have found that solid state ^1H NMR spectroscopy allows us to directly observe the lowering of the energetic barrier to the activation of hydrogen in the hydride. Therefore we plan to quantify the fundamental catalytic effect of the titanium and zirconium dopants. We are now beginning studies in which the populations of mobile hydrogen in undoped and doped hydrides are quantified at temperatures ranging from 20-150°C. The activation parameters for the fundamental hydrogen activation process will be calculated from the variable temperature data. We also plan to prepare bulk quantities of the catalytically active species through the stoichiometric reaction of NaAlH_4 with catalyst precursors. We will then characterize the materials that are produced through solid state ^1H , ^{27}Al , and/or ^{23}Na NMR spectroscopy. We hope to then determine the identity of the active catalyst through comparison of these spectra to those of samples of titanium and aluminum compounds that are considered to be likely catalyst candidates.

Finally, before abandoning our efforts with the arsino pincer catalyst, we plan to conduct wrap-up studies in which we will examine the dehydrogenation of other cycloalkanes including decalin and dicyclohexyl. It is conceivable that the increased steric bulk of the corresponding products, naphthalene and biphenyl will result in reduction of the bond strengths to the iridium center and therefore allow higher conversion levels to be attained.

References

- Bogdanovic, B. and M. Schwickardi. 1997. *J. Alloys and Comp.*, 1-9:253.
- Bogdanovic, B., R.A. Brand, A. Marjanovic, M. Schwickardi, J. Tölle. 2000. *J. Alloys and Comp.*, 302:36.
- Fryzuk, M.D., G.K.B. Clentsmith, S. J. Rettig. 1997. *Inorg. Chem. Acta*, 259:51.
- Gupta, M., C. Hagen, W.C. Kaska, R. Flesher, and C.M. Jensen. 1996. *J. Chem. Soc. Chem. Commun.*, 2083.
- Gupta, M., C. Hagen, W.C. Kaska, R.E. Cramer, C.M. Jensen. 1997. *J. Am. Chem. Soc.*, 119: 840.
- Gupta, M., W.C. Kaska, and C.M. Jensen. 1997. *J. Chem. Soc., Chem. Commun.*, 461.
- Jensen, C.M., R. Zidan, N. Mariels, A. Hee, C. Hagen. 1999. *Int. J. Hydrogen Energy*, 24:461.
- Jensen, C.M. 1999. *J. Chem. Soc., Chem. Commun.*, 2443.
- Jensen, C.M., K.J. Gross. 2001. *Appl. Phys. A*, 72:213.

Khan, K., C.L. Raston, J.E. McGrady, B.W. Skelton, A.H. White. 1997. *Organometallics*, 16:3252.

Liu, F., E.B. Pak, B. Singh, C.M. Jensen, and A.S. Goldman. 1999. *J. Am. Chem. Soc.*, 121:4086.

Xu, X., G.P. Rosini, M. Gupta, C.M. Jensen, W.C. Kaska, K. Krough-Jespersen, and A.S. Goldman. 1997. *J. Chem. Soc. Chem. Commun.*, 2273.

Zidan, R.A., S. Takara, A.G. Hee, C.M. Jensen, 1999. *J. Alloys and Comp.*, 285:119.

LIGHT-WEIGHT HYDRIDE DEVELOPMENT

K. J. Gross, G. J. Thomas, E. Majzoub and G. Sandrock
Sandia National Laboratories
Livermore, CA 94550

Abstract

The discovery that hydrogen can be reversibly absorbed and desorbed from complex hydrides (the alanates) by the addition of catalysts has created an entirely new prospect for lightweight hydrogen storage. These materials offer the possibility to achieve our program goal, which is to develop lightweight materials for onboard hydrogen storage in PEM fuel cell vehicles. Previous work concentrated on identifying both the positive and negative aspects of using catalyzed alanates as a practical means of storing hydrogen. We began by investigating the hydrogen storage properties of NaAlH₄ mechanically doped with 2 mol% each of the liquid alkoxides Ti(OBuⁿ)₄ + Zr(OPr)₄ catalysts (Generation I). On the positive side, these materials have nearly ideal equilibrium thermodynamics, good packing densities, moderate volume expansion and useful sintering properties. Negative aspects that were found include slow kinetics, less-than-theoretical reversible capacities, and impurities in the released hydrogen gas stream. Our current research has focused on developing solutions to these barriers. Two new generations of materials have been investigated. These are Generation II which utilizes solid TiCl₃ to catalyze NaAlH₄ and Generation III which involves the direct synthesis of catalyzed NaAlH₄ from NaH, Al and catalyst precursors.

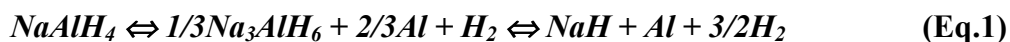
In-depth rate studies and material analysis were performed on the Generation II materials leading to a comprehensive understanding of the interaction of TiCl₃ with NaAlH₄ and ultimately the trade-off between improved kinetics and lower hydrogen capacities. These materials also demonstrated better capacities and rates than the earlier Generation I materials. Arrhenius analysis of the rate data made clear that the activation energy is lowered with even low levels of catalyst doping. This clearly points to a catalyst-induced change in hydride decomposition (and probably reformation) mechanisms.

Generation III materials show hydrogen absorption and desorption rates well over an order of magnitude faster than Generation II alanates. In addition, the alanate purification step has been eliminated leading to a radically simplified processing method. This in hand will lead to significantly lower production costs. The direct synthesis technique also eliminates all traces of hydrocarbon impurities in the product hydrogen gas stream. This year's work represents a number of significant advances in the development of practical and inexpensive light-weight hydrogen storage materials.

Introduction

The alkali metal alanates are compounds belonging to the larger class of complex hydrides. In the past, they were known to liberate copious amounts of hydrogen either by direct thermal decomposition or by one-time hydrolysis. However, they were generally considered too irreversible for practical hydrogen storage applications. This was until Bogdanovic et al (Bogdanovic' 1997) demonstrated that the alanate, NaAlH_4 , would reversibly desorb and absorb hydrogen under relatively mild conditions when doped with Ti-based catalyst. Since that time there has been a growing body of work in characterizing catalyzed alanates, as well as the development of new catalysts and methods of preparation (Bogdanovic' 2000, 2001, Jensen 1999, 2001, Zidan 1999, Zaluska 2000, 2001, Gross 1999, Thomas 1999).

Unlike the interstitial intermetallic hydrides, the alanates release hydrogen through a series of decomposition/recombination reactions:



The two combined reactions give a theoretical reversible hydrogen storage capacity of 5.6 wt.%. Previous studies showed that the first reaction will release 1 atm of H_2 at 33°C and the second reaction releases 1 atm of H_2 at 126°C (Bogdanovic' 2000, Gross 2000).

Two areas of progress have been identified as being necessary to develop catalyzed-alanates into a practical material for hydrogen storage for PEM fuel cell vehicle applications:

- A) The optimization of the catalyst as to (a) type, (b) doping process and (c) mechanistic understanding.
- B) Engineering development and determination of practical properties.

We have employed a parallel approach to address these two areas by working concurrently on the following topics:

- Innovating methods to synthesize the alanates and improve the catalyst doping process to improve both rates and capacity,
- Characterizing relevant material properties of each new generation of material to aid in developing the next generation and to gain a fundamental understanding of the hydrogen absorption and desorption processes,
- Evaluating the behavior of our materials on an engineering scale to ensure that they are on track for eventual commercialization.

The primary goal of this current years work was to resolve potential problems identified last year that would preclude using the alanates for fuel-cell vehicle applications. Previous cycling tests indicated a much lower than expected capacity after the first desorption. Besides this, the use of alkoxide-based Ti and Zr catalysts introduces oxygen and hydrocarbon impurities into the sample which were still present after several cycles. Such impurities could cause irreversible damage to PEM fuel cell catalysts. For this reason we began to investigate a second-generation material which used the inorganic catalyst TiCl_3 as well as a purely dry doping process. However, GC-MS analysis indicated that even without using alkoxide-based catalysts the alanate itself contained measurable quantities of residual THF. This residual THF comes from the purification process in which NaAlH_4 is dissolved in THF, decanted and then vacuum precipitated. The drawbacks of using solvent-prepared NaAlH_4 as the starting material were clear and led us to develop third generation material that employs a direct-dry-synthesis/doping technique. This approach is also being pursued in other laboratories (Bogdanovic' 2001, Zaluska 2001).

Experimental Basics

Crystalline NaAlH_4 was made by cryopumping THF from a 1.0M solution of NaAlH_4 in THF (Aldrich Chemical No. 40,424-1), followed by vacuum drying with a mechanical and/or turbomolecular pump. Mixtures of NaAlH_4 and solid TiCl_3 (99.999% Aldrich Chemical No. 51,438-1) were weighed in a purified argon glovebox in the levels of 0.9, 2, 4, 6 and 9 mol% TiCl_3 . These mixtures were then ball-milled in argon for 3 hours, using a high-energy SPEX® mill and WC balls and milling vial. The powder-to-ball weight ratio was approximately 1:12. Samples were transferred from the milling pot to the reactor vessel in the Ar glovebox. X-ray diffraction (using special airless sample holders) was done before and after milling; in all cases the complete conversion of TiCl_3 to NaCl during milling was confirmed.

Dehydriding and hydriding rates and capacities were obtained volumetrically using a Sieverts' apparatus and a cylindrical 316 SS reactor (1.3 cm outer diameter by 0.12 cm wall thickness and length of 12cm) containing about 1.5 g of catalyzed samples. A thermocouple well, in the center of the vessel, allows for accurate temperature measurements during cycling. The reactor was heated externally by an electrical heating tape. Absorption pressure changes were quantified with a calibrated 200 atma pressure transducer and desorption pressures with a 1000 Torr (1.3 atma) Baratron® capacitance manometer. Data were recorded via computer and measurements lasted from minutes to several days, depending on the TiCl_3 level and test pressure and temperature conditions.

Hydrogen capacity and rates were measured during the second absorption and desorption half-cycles at 125°C. During absorption, the applied H_2 pressure was generally in the 80-90 atm range well above the 30-40 atm plateau pressure for NaAlH_4 at 125°C. For the desorption experiments, the back-pressure during NaAlH_4 decomposition was kept below 1 atma and during Na_3AlH_6 decomposition below 0.25 atma well below the Na_3AlH_6 plateau pressure of about 2 atma. Hydrogen capacity data are presented as weight % with respect to the total sample weight including the catalyst.

Isothermal Arrhenius analyses were performed as follows: Measurements were started after several hydriding/dehydriding cycles with samples in the fully hydrided condition and cooled to room temperature. The pressure rise from desorption into a known volume, at a given temperature, was measured. The temperature was then increased. The desorption rates were determined at each temperature from the slope of the essentially linear increase in pressure with time. This procedure was continued up to 150°C. The sample was held at this temperature until the NaAlH₄ decomposition step (Eq.1) was finished. The sample was then quickly cooled to 40-60°C and the Na₃AlH₆ rates determined by the same procedure. The rate data are presented as weight % with respect to the starting alanate weight before doping.

Experimental Results – Generation II Alanates

Our initial studies focused on what we now refer to as Generation I materials (Gross 2000, 2001a, Sandrock 2001a). These consisted of NaAlH₄ mechanical mixed with 2 mol% each of liquid Ti(OBuⁿ)₄ and Zr(OPr)₄. The use of this formula was based on the observation that combined Ti- and Zr-doping resulted in maximum desorption kinetics for both steps of Eq.1 (Zidan, 1999). Because decomposition of the alkoxides produced organic impurities in the desorbed hydrogen, we redirected activities toward the inorganic catalyst precursor TiCl₃. This last year much of our work was performed on Generation II materials (Sandrock 2001b). These were prepared by ball milling solid TiCl₃ with solid NaAlH₄ (vacuum dried from THF solutions).

Interaction of TiCl₃ with NaAlH₄

The interaction between NaAlH₄ and TiCl₃ was investigated by XRD (X-ray Diffraction) (Gross 2001b). Two samples were prepared by ball-milling solid NaAlH₄ in argon for 3 hours. One sample was milled together with 9 mol% solid TiCl₃. The other was milled without any catalyst. The XRD measurements of these two samples are compared in Figure 1. TiCl₃ was not observed. However, NaCl is clearly present. Thus, NaAlH₄ and TiCl₃ react during the milling process to form NaCl. This result is significant in that it points to the catalyst being composed of a TiCl₃ decomposition product probably in the form of Ti metal or an alloy.

Another important observation is that NaAlH₄ decomposes to a considerable degree during mechanical milling when TiCl₃ is added. This can be seen in the greatly reduced intensities of the NaAlH₄ peaks and the presence of reflections from Na₃AlH₆ and Al. This means that the catalytic processes leading to desorption of the NaAlH₄, occur even at the relatively low temperatures reached during ball milling.

Capacity Loss with Increasing Catalyst Content

The XRD results showing that NaAlH₄ and TiCl₃ react during the milling process to form NaCl also explains much of the previously observed capacity loss. The amount of NaAlH₄ that is rendered inactive by decomposition into NaCl and Al is proportional to the quantity of added TiCl₃. The total reversible hydrogen capacity loss increases with increasing catalyst content (Figure 2). The origin of an additional capacity loss on the order of about 10% below the theoretical level is still not fully understood.

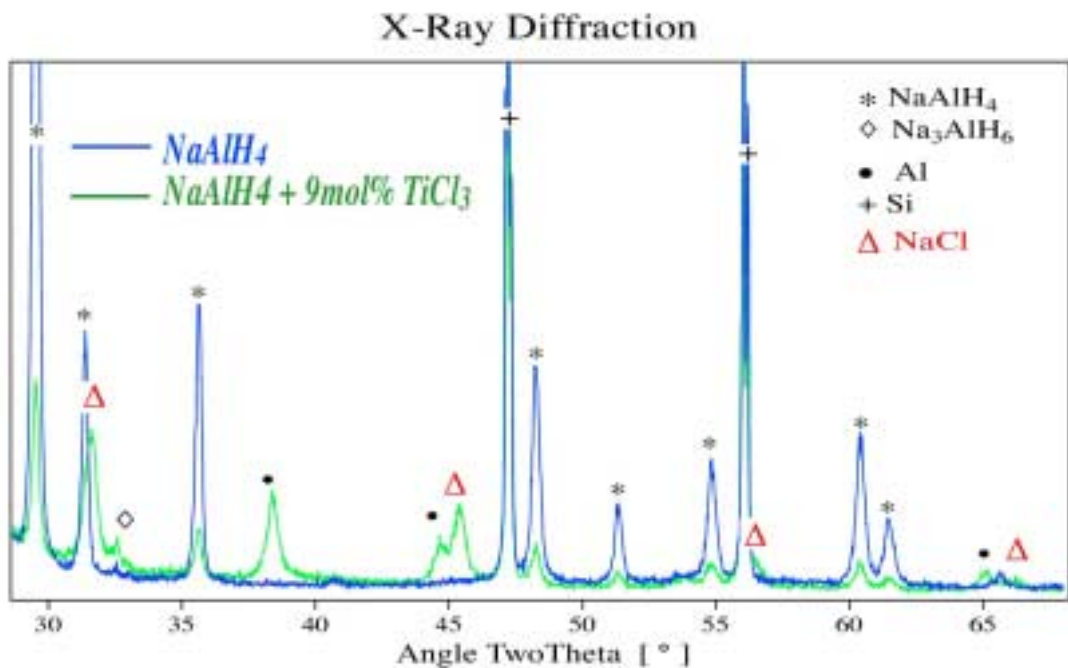


Figure 1 – X-ray diffraction patterns of NaAlH_4 after ball milling (green/gray) with TiCl_3 catalyst and (blue/black) without catalyst.

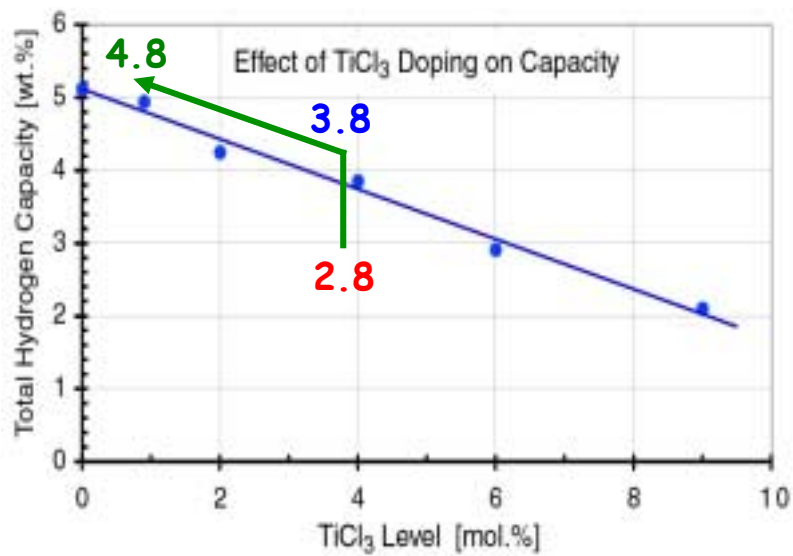


Figure 2 – Reversible hydrogen capacity as a function of TiCl_3 content.

Improved Kinetics with Increasing Catalyst Content

Contrary to the generally held view, the rates of hydrogen absorption and desorption are strongly dependent on the level of catalyst doping. Desorption kinetics were measured at different temperatures for NaAlH_4 samples doped with 0.9, 2, 4, 6 and 9 mol% TiCl_3 . An Arrhenius analysis was very effectively applied to the results (next section). The effect of catalyst doping is made clear when the hydrogen desorption rates are plotted versus catalyst content. This is shown in Figure 3 for 125°C , which is a temperature which will provide hydrogen at greater than atmospheric pressures, as may be required for fuel cell applications. In this case, the desorption rates were calculated from rate constants obtained from the Arrhenius analysis (note, the 9% TiCl_3 points were not calculated but rather taken directly from a quasi-isothermal desorption curve). Such an analysis provides a practical way to determine the catalyst doping level required to reach specified desorption rates. Comparing Figures 2 and 3, it is clear that improvements in kinetics with increasing Ti-catalyst-level must ultimately be weighed against the loss of reversible hydrogen capacity. These studies provide the practical tools necessary to choose a reasonable balance between kinetics and capacity.

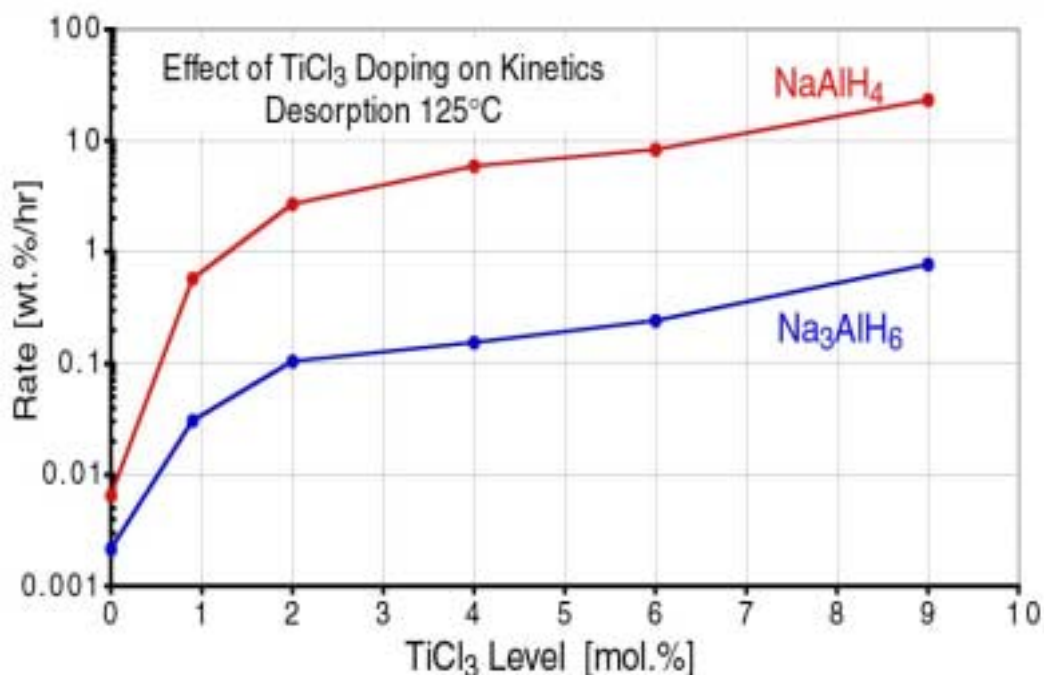


Figure 3 – Rates of hydrogen desorption as a function of TiCl_3 content for the decompositions of NaAlH_4 and Na_3AlH_6 .

Isothermal Kinetic Measurements and Arrhenius Analysis

During the last year we performed isothermal Arrhenius analyses on both the NaAlH_4 and Na_3AlH_6 decomposition reactions for the 0, 0.9, 2, 4, and 6 mol% TiCl_3 samples. The Arrhenius equation to describe thermally activated chemical process is given by

$$\text{Rate} = k \exp (-Q/RT) \quad (\text{Eq.2})$$

where k is the pre-exponential rate constant, Q is the thermal activation energy, R is the gas constant and T is absolute temperature. Thus, an Arrhenius plot consists of plotting $\ln(\text{rate})$ vs. $1/T$, with the slope of the plot representing the activation energy Q and the $1/T=0$ intercept representing the rate constant k . The resultant Arrhenius plots for 0 to 6% TiCl_3 are shown in Figures 4 and 5 for NaAlH_4 and Na_3AlH_6 decompositions, respectively. All of the data can be represented quite well with an exponential equation of the form Equation 2. These fits have important engineering value by conveniently allowing one to calculate true isothermal kinetics at any temperature and also model non-isothermal operation of hydrogen storage tanks or other commercial processes.

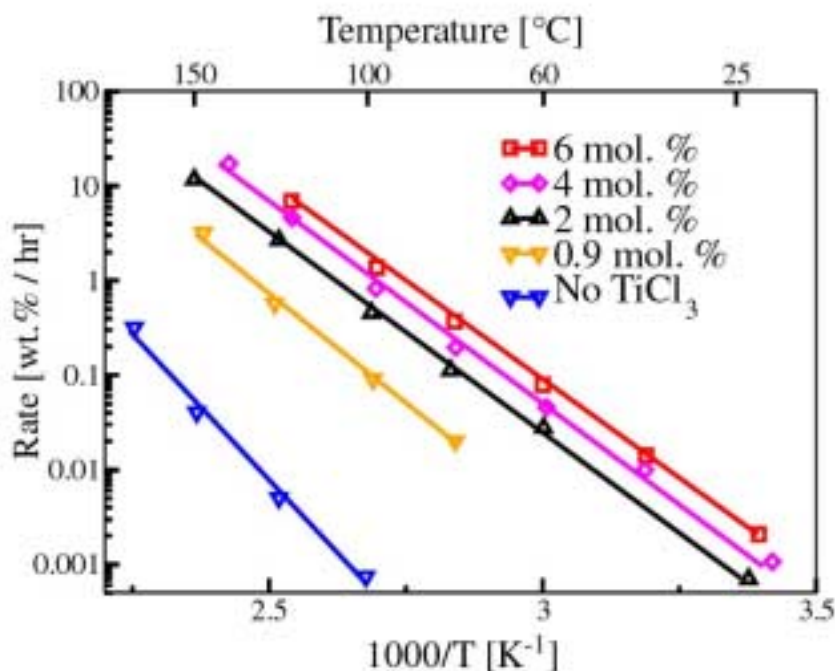


Figure 4 – Arrhenius plot of the hydrogen desorption rates vs. $1/T$ for the decomposition of NaAlH_4 .

The effects of catalyst level on the Arrhenius plots are quite dramatic. Note the multiple order of magnitude rate shifts for both the NaAlH_4 and Na_3AlH_6 lines as TiCl_3 levels are increased (or equivalently the substantial shifts in temperatures for given rates). Let us explore these remarkable differences by examining the Arrhenius parameters Q and k for all the samples evaluated. Q and k are plotted versus TiCl_3 level in Figures 6 and 7, respectively. As can be seen in Figure 6, the Q 's are nearly equal for the decompositions of both the NaAlH_4 and Na_3AlH_6 with 0% TiCl_3 , but drop to much lower and different levels when even a small amount of catalyst is added (0.9%). This indicates a substantial easing of the thermally activated mechanism. Q then remains virtually constant with TiCl_3 level above 0.9%, suggesting no further change in fundamental mechanism after the first small Ti-addition. Figure 7 shows similar decreases of k , including NaAlH_4 - Na_3AlH_6 differentiation starting with the first small Ti-addition. Unlike Q , however, k increases monotonically with further increases in TiCl_3 addition,

and is therefore alone responsible for all the further increases in kinetics above the first 0.9% Ti-addition.

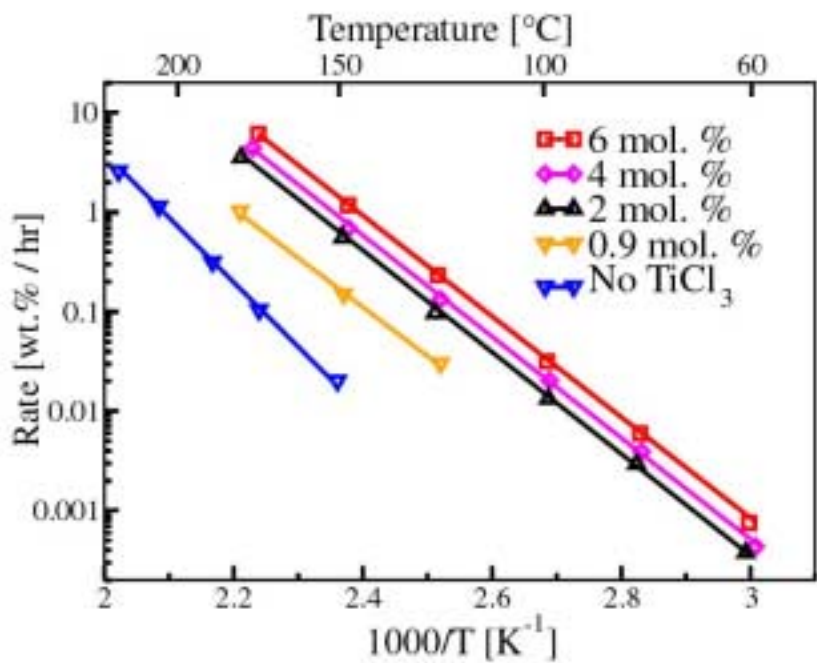


Figure 5 – Arrhenius plot of the hydrogen desorption rates vs. $1/T$ for the decomposition of Na_3AlH_6 .

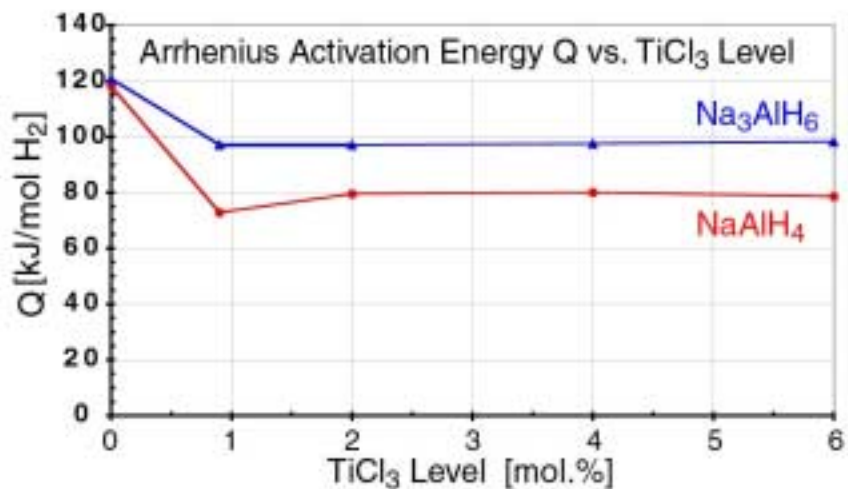


Figure 6 – Activation energy Q as a function of TiCl_3 content for the decompositions of NaAlH_4 and Na_3AlH_6 .

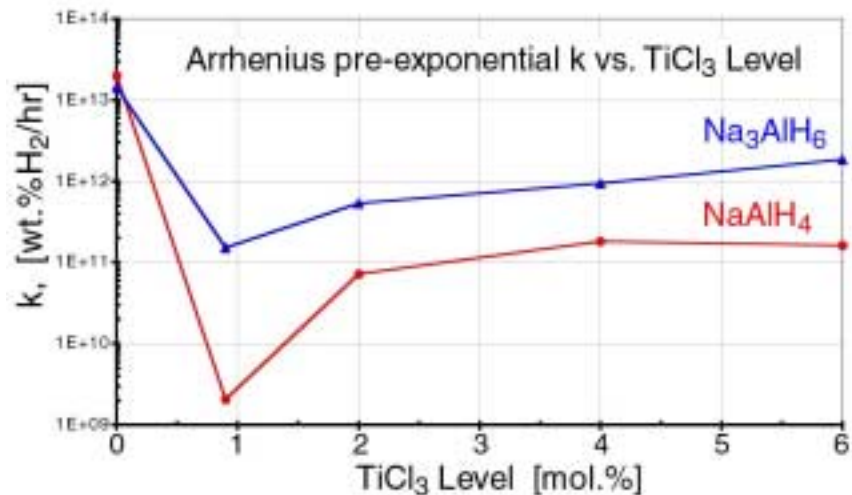


Figure 7 – Pre-exponential factor k as a function of TiCl_3 content for the decompositions of NaAlH_4 and Na_3AlH_6 .

Scaleup Test Bed-2

As a continuation of the engineering activities we reported last year (Gross 2000), a second scaleup test bed was constructed, loaded with 72 g of 4 mol% TiCl_3 catalyzed NaAlH_4 and evaluated over four complete discharge/charge cycles. This second bed consisted of a 24.5 cm long stainless steel tube 3.17 cm diameter by 0.21 cm wall thickness (Figure 8). These dimensions are perhaps typical of one element one might find in practical vehicular-sized storage system. The intent was to study rate behavior and to model same from combined kinetic and heat transfer points of view. For that reason, two axial thermocouple wells were included (one centerline and one at the half-radius). Thermocouples were placed at top, middle and bottom in each well, and also at equivalent places on the outside diameter (total of nine measuring thermocouples). The instrumented reactor, wrapped with electrical heating tape, was evaluated on a new apparatus built for that purpose (Figure 8). It was designed for isobaric charging, followed by non-isobaric discharging into a large calibrated volume. All data was logged via computer for subsequent analysis.

Charging runs were done at 125°C at 60, 75 and 90 atm applied hydrogen pressure. For comparison purposes, an additional charging run was done at 100°C and 90 atm. Discharging runs were performed at 80, 100, 125 and 150°C. As only one example, the 100°C discharge curve is shown in Figure 9. About 2.2 wt.% H_2 is released in 3 hours, representing decomposition of the NaAlH_4 phase (first step). The decomposition of the Na_3AlH_6 then begins sequentially, but that is a much slower process. The temperature was then increased to 150°C to complete the Na_3AlH_6 decomposition. A large amount of such data was generated as is now being analyzed. The marks placed on the reactor (Figure 8) were used as reference points to determine if any expansion deformation took place during the cycling. No measurable deformation was found.

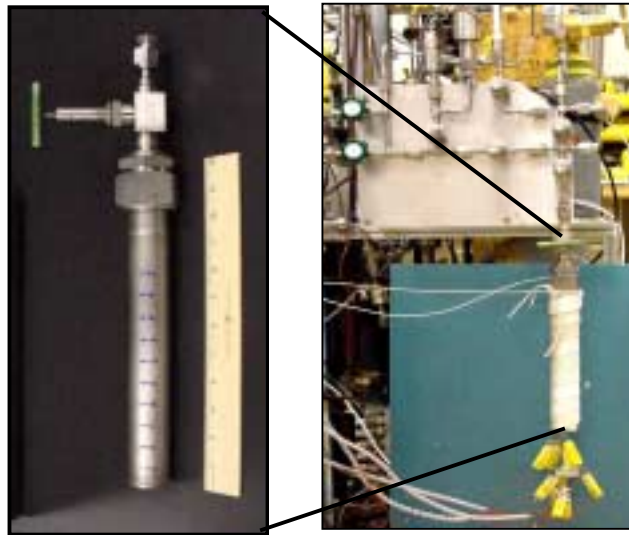


Figure 8 – Scaled-up Bed-2 and test stand showing control manifold, tape heater and axial thermocouples.

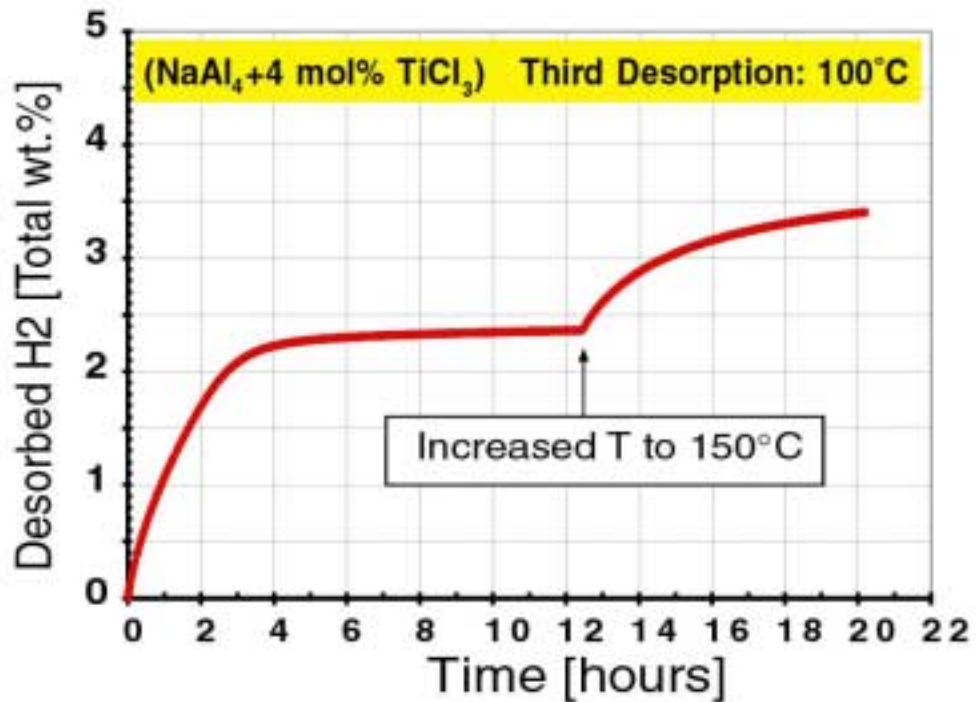


Figure 9 – Third hydrogen desorption from scaled-up test Bed-2.

The capacity (3.4 total wt.% H₂ in Figure 9) was somewhat disappointing, but an expected result of the inherent losses that result from the Generation II catalyzing reaction (reaction of the TiCl₃ catalyst precursor with some of the NaAlH₄ to form NaCl). During the evaluation of Bed-2 an

improved catalysis process (Generation III) was developed that may reduce this problem (see Figures 11 and 12 and discussion which follows). Therefore no more work will be done on Bed-2 and a new scaled-up reactor Bed-3 will be evaluated with Generation III catalyzed alanate.

Experimental Results – Generation III Alanates

While residual gas analysis (Figure 10) of the Generation II materials showed significantly reduced levels of hydrocarbon contaminant compared to the Generation I alanates, trace levels of impurities remained. These were identified by GC/MS analyses as residual THF (and pentane if used for precipitation) remaining from the NaAlH_4 purification process. This and the lower than desired reversible capacities lead to the development of a direct synthesis/catalyst doping technique that is now used to produce Generation III alanates. These materials are prepared directly from the decomposition products and catalyst. No solvents whatsoever are used in this process. As a result the desorbed hydrogen shows no hydrocarbon contaminants (Figure 10). Only trace levels of H_2O and CO from the vacuum system are observed. Perhaps the most significant impact of these results is the fact that catalyzed alanates can now be produced under relatively mild conditions without solvents, thus substantially reducing raw material and production costs.

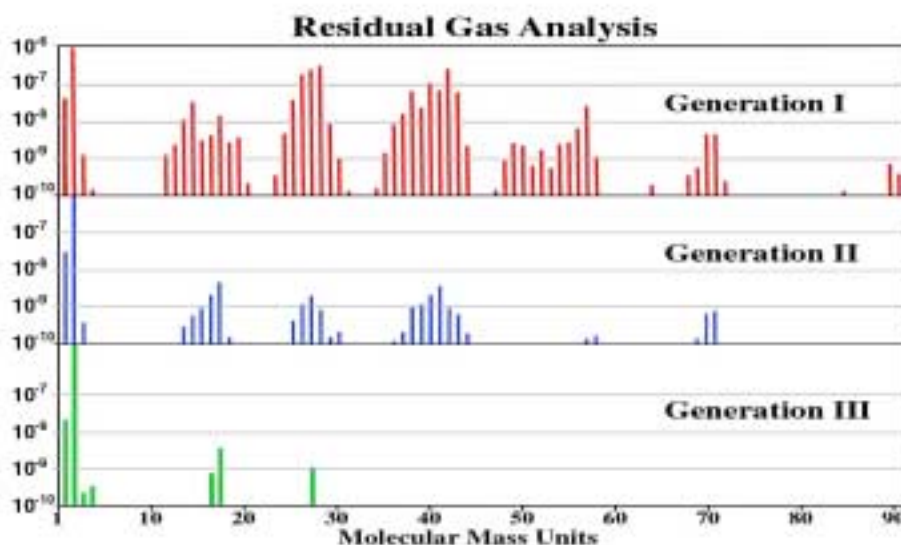


Figure 10 – Residual desorbed gas spectra from samples of Generation I, II and III materials.

An added benefit is that the starting composition of these Generation III materials can be tailored to reduce inactive by-products (namely Al) of the catalyst doping process. Depending on the level of catalyst employed this can significantly improve the reversible hydrogen capacity.

In addition to these remarkable improvements, the Generation III materials also surprised us by having astonishingly rapid kinetics. The absorption and desorption kinetics of the Generation III alanates are compared with Generation II materials in Figures 11 and 12 respectively. The

absorption rates are some 20 times faster for the Generation III alanates and they are about 10 times better in desorption.

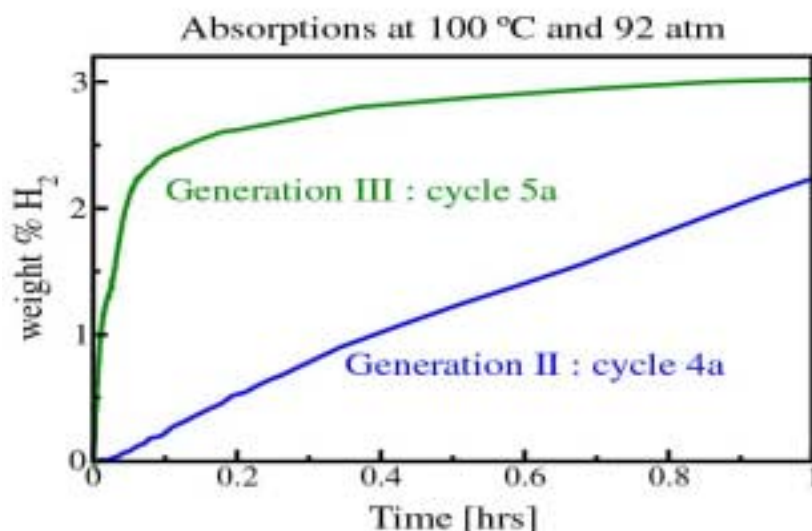


Figure 11 – A comparison of hydrogen absorption by samples of Generation II and III materials (both 4 mol% catalyst).

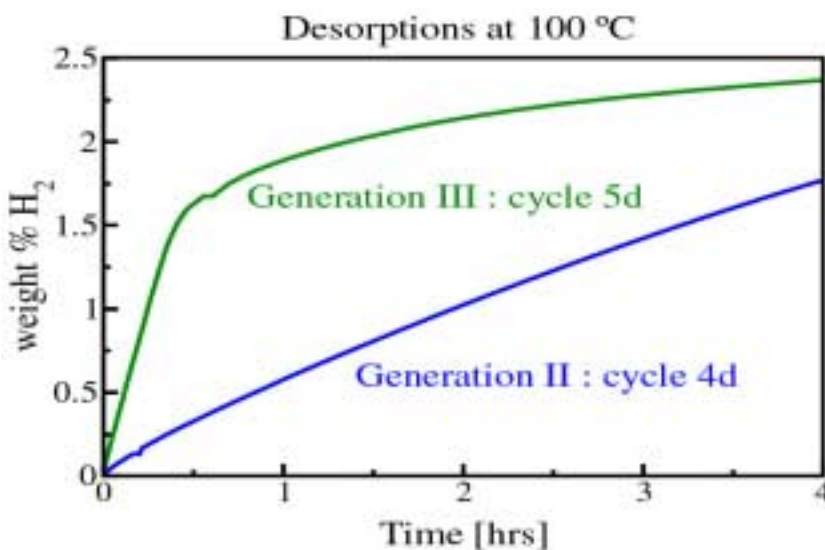


Figure 12 – A comparison of hydrogen desorption from samples of Generation II and III materials (both 4 mol% catalyst).

An important effect, which was not observed in previous generations of materials, is that the kinetics improved dramatically with the first couple of cycles. This is somehow an activation process that is likely a result of the catalyst's initial interaction with the alanate and particle size reduction. Figure 13 shows the first two hydrogen absorption cycles (100 atm H₂) for Generation III alanate doped with 1 mol% catalyst. The absorption rate in the 2nd cycle is significantly better than even the 4 mol% TiCl₃ doped Generation II materials and the same is true for desorption. This is significant because high rates may now be achieved with much lower catalyst loading.

This, in turn, means that higher reversible capacities can now be obtained. In this case the sample reversibly absorbed and desorbed 4.8 wt.% hydrogen.

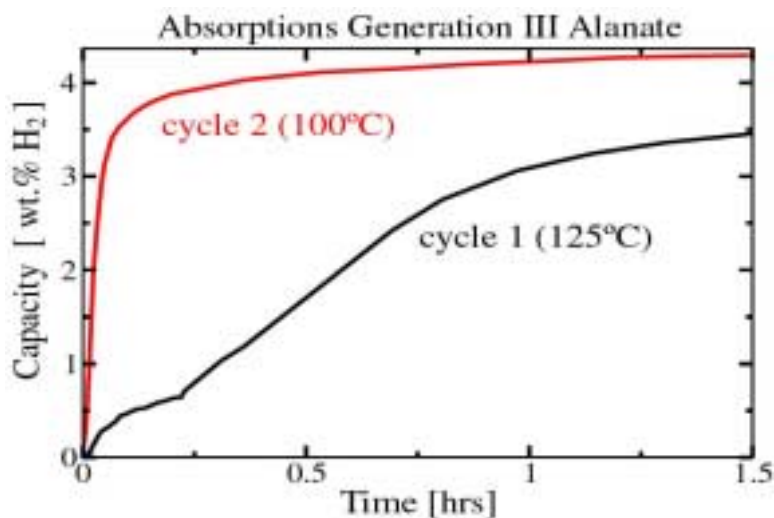


Figure 13 – Activation effect of first two cycles on Generation III materials (1 mol% catalyst).

Conclusion

The advances that have been achieved thus far can be appreciated by revisiting Figure 2. Generation I materials had relatively low true capacities (2.8 wt.% H₂) due in large part to the excess weight of the alkoxide catalyst precursors (22 wt.% for 4 mol% catalyst). Initial improvements (3.8 wt.% H₂) were accomplished by switching to the inorganic solid catalyst TiCl₃. Using Generation II alanates, we demonstrated that the reaction between TiCl₃ and the alanate leads to a trade-off between increased kinetics and loss of capacity as the catalyst level is increased. On moving from Generation II to Generation III materials the capacity was improved to 4.8 wt.% H₂ simply by reducing the level of catalyst loading required to achieve the same hydrogen sorption rates. In summary, the latest generation of catalyzed alanates has resolved the issue of hydrogen gas contamination and offer rapid kinetics and high capacities in a material that should be substantially less costly and complicated to produce than previous generations.

Future work

Our future work is now focused on further improving the capacity and kinetics of the Generation III alanates. These materials will be examined through extensive cycle-life and scale-up studies. We are also expanding the new synthesis and catalyst doping techniques to other complex hydrides. This includes investigating Mg-based complex hydrides in collaboration with the University of Geneva.

An important observation was made during recent studies. Millimeter-size aluminum flakes were completely consumed by the alanates during absorption. This is an area of safety concerns

that many researchers and commercial entities may not have considered. There is a strong possibility that cycling the alanates in aluminum-based vessels will cause erosion of the vessel walls and ultimately lead to vessel failure. We are currently investigating the interaction of the catalyzed alanates with various containment vessel materials.

Acknowledgements

We wish to acknowledge the valuable collaboration of C. Jensen of the University of Hawaii. We thank D. Meeker of SNL for his expert technical help in all aspects of the experimental measurements and Ken Stewart of SNL for all of his contributions in developing our experimental equipment.

Funding is provided by the U.S. Department of Energy, Office of Power Technologies, Hydrogen Program Office under contract DE-AC36-83CH10093. Sandia is a multi-program laboratory operated by Sandia Corporation, a Lockheed Martin Company, for the U.S. Department of Energy under contract DE-AC04-94-AL85000.

References

- Bogdanovic', B. and Schwickardi, M. 1997. "Ti-doped alkali metal aluminum hydrides as potential novel reversible hydrogen storage materials," *J. Alloys and Compounds*, **253**:1.
- Bogdanovic', B., Brand, R.A., Marjanovic', A., Schwikardi, M., and Tölle, J. 2000. "Metal-doped sodium aluminum hydrides as potential new hydrogen storage materials," *J. Alloys and Compounds*, **302**:36.
- Bogdanovic B., Schwickardi M. 2001. "Ti-doped NaAlH₄ as a hydrogen-storage material – preparation by Ti-catalyzed hydrogenation of aluminum powder in conjunction with sodium hydride," *Applied Physics A*, 72 (#2):221.
- Gross, K.J., Guthrie, S.E., Takara, S., and Thomas, G.J. 1999. "In situ X-ray diffraction study of the decomposition of NaAlH₄," *J. Alloys and Compounds*, **297**:270.
- Gross, K.J., Thomas, G.J., and Sandrock, G., 2000. "Hydride development for hydrogen storage," in *Proceedings U.S. DOE Hydrogen Program Review*, NREL/CP-570-26938,452. San Ramon, CA.
- Gross, K.J., Thomas, G.J., and Jensen, C.M., 2001a. "Catalyzed Alanates for Hydrogen Storage," In *Proceedings of the International Symposium on Metal Hydrogen Systems*, Noosa, Australia, Oct. 2000.
- Gross, K.J., Sandrock, G., and Thomas, G.J. 2001b. "Dynamic In Situ X-ray Diffraction of Catalyzed Alanates," In *Proceedings of the International Symposium on Metal Hydrogen Systems*, Noosa, Australia, Oct. 2000.

- Jensen, C.M., Zidan, R.A., Mariels, N., Hee, A.G., and Hagen, C. 1999. "Advanced titanium doping of sodium aluminum hydride: segue to a practical hydrogen storage material?," *Int. J. Hydrogen Energy*, **24**:461.
- Jensen C.M., Gross K.J. 2001. "Development of Catalytically Enhanced Sodium Aluminum Hydride as Hydrogen Storage Material," *Applied Physics A*, 72(#2):221.
- Sandrock, G., Gross, K., Thomas, G., Jensen, C., Meeker, D. and Takara, S. 2001a. "Engineering considerations in the use of catalyzed sodium alanates for hydrogen storage," In *Proceedings of the International Symposium on Metal Hydrogen Systems*, Noosa, Australia, Oct. 2000.
- Sandrock, G., Gross, K., Thomas, G. 2001b. "Effect of Ti-catalyst content on the reversible hydrogen storage properties of the sodium alanates," submitted *J. Alloys and Compounds*.
- Thomas, G.J., Guthrie, S.E., and Gross, K. 1999. "Hydride development for hydrogen storage," in *Proceedings U.S. DOE Hydrogen Program Review*, NREL/CP-570-26938,452. Denver CO.
- Zaluska, A., Zaluski, L., and Ström-Olsen, J.O. 2000. "Sodium alanates for reversible hydrogen storage," *J. Alloys and Compounds*, **298**:125.
- Zaluska A., Zaluski L., Strom-Olsen J.O. 2001. "Structure, catalysis and atomic reactions on the nano-scale: a systematic approach to metal hydrides for hydrogen storage", *Applied Physics A*, 72(#2):157.
- Zidan, R.A., Takara, S., Hee, A.G., and Jensen, C.M. 1999. "Hydrogen Cycling Behavior of Zirconium and Titanium-Zirconium Doped Sodium aluminum Hydride", *J. Alloys and Compounds*, **285**:119.

HYDROGEN STORAGE IN POLYMER-DISPERSED METAL HYDRIDES (PDMH)

**Wayde R. Schmidt
United Technologies Research Center
East Hartford, CT 06108**

Abstract

Metal hydrides, dispersed in a polymeric matrix, are under investigation as unique hydrogen storage media. It is proposed that the relatively low gravimetric capacity of metal hydrides can be significantly enhanced by incorporating a low-density polymer that can both interact with the hydride on a molecular level, and store additional hydrogen within the polymer structure. An extensive series of polymers, varying in chemical structure, composition and thermal stability, were processed thermally, mechanically or by plasma spray techniques and evaluated for hydrogen storage capacity. Select combinations of polymer and processing method are undergoing further evaluation for hydrogen storage capacity when combined with specific metal hydrides. In this manner, the experimental design space of polymer/process/metal hydride can be explored to better understand the benefits provided by polymer-dispersed metal hydrides (PDMH). In addition to conventional pressure composition isotherm (PCI) measurements, PDMH samples are characterized by thermal analysis, electron microscopy and electron paramagnetic resonance techniques. The last method is particularly important for probing the creation of free radicals that may result from processing the polymers. It is likely that free radicals play a critical role in the mechanisms of hydrogen storage in PDMH – possibly facilitating hydrogen dissociation and enhancing molecular interactions with the metal hydride.

Introduction

Hydrogen storage has been extensively studied in recent history and yet no single technology currently meets automotive goals of 5.5 wt% gravimetric capacity and 60 kg/m³ volumetric capacity. Although many hydrogen storage methods are under consideration, including, but not limited to, carbon nanotubes, liquid hydrogen, compressed gas, and metal hydrides, United Technologies Research Center has focused on a novel approach by dispersing metal hydrides in polymer support phases. The primary advantages of metal hydrides are the relatively high volumetric capacity and the inherent safety of such systems – applied heat is required to release hydrogen. The intent of this contract activity is to explore the preparation of ‘Polymer Dispersed Metal Hydrides,’ or PDMH, and assess their value as a unique storage medium for hydrogen. The goal is to advantageously combine the volumetric storage capacity of metal hydrides, with the low density of polymeric materials, in an effort to improve the gravimetric storage capacity by factors of 2-5 relative to non-dispersed metal hydrides. In addition, it is conceivable that dehydrating temperatures may be reduced, potentially enabling automotive waste heat to effectively dissociate the hydride. Dispersion of the metal hydride in a polymer support phase may also increase the stability of the metal hydride, possibly through reduction of hydride decrepitation (Meinzer 1994).

Prior to this effort, little experimental data existed on the hydrogen storage capacity of PDMH systems, although arguments were made supporting the expected increase in PDMH gravimetric capacity over the metal hydride alone, based solely on relative density (Jarvi 1999; Meinzer 1994). Preliminary work at UTRC measured hydrogen weight loss, as a function of temperature, for several metal hydrides and polymers containing these metal hydrides. Figure 1 summarizes these data. Comparing results for TiH₂ alone, and Polymer 3 plus 5% TiH₂, the data indicate that the combination of TiH₂ and Polymer 3 provides a factor of 15 increase in the weight of hydrogen released, at constant temperature. Specifically, this sample was a plasma-sprayed blend of Kapton polyimide and TiH₂. By extending this 15X performance increase to magnesium hydride or other high capacity hydrides, it was envisioned that the DOE goal of 5.5 wt% gravimetric capacity could be readily achieved. Moreover, the successful demonstration of such high storage capacity could lead to an economical weight/volume ratio for a fuel tank sized for current gasoline fueled automobiles (DeLuchi 1992; Dillon, *et al.* 1997).

Unfortunately, metal hydrides exhibiting higher gravimetric capacities also tend to exhibit poor dehydrating kinetics and generally require higher temperatures to access the maximum amount of hydrogen (e.g. MgH₂). Table 1 provides a list of metal hydrides and corresponding properties as adopted from <http://hydpark.ca.sandia.gov/>. Temperature limitations must be considered carefully during the selection and processing of metal hydrides within a polymer support matrix. Nevertheless, hydrogen storage in metal hydrides remains an active area of research because of their potential use as simple, compact, robust and potentially inexpensive storage devices.

The prime objective of UTRC’s innovative research program in PDMH is to characterize the performance and mechanism(s) of hydrogen storage in these materials, while pursuing DOE goals. Initial efforts focused on determining the hydrogen storage capacities of the polymers separately from those of the well-established metal hydrides. PDHM samples demonstrating suitable performance enhancement over baseline metal hydrides would be prepared in larger

quantities to examine scale-up effects. Based on the optimum performance obtained in this program, a brief system assessment would be performed in view of the DOE capacity goals. The assessment would provide preliminary cost estimates for a hydrogen storage bed and an analysis of the thermal requirements for hydrogen delivery, for an appropriately sized system.

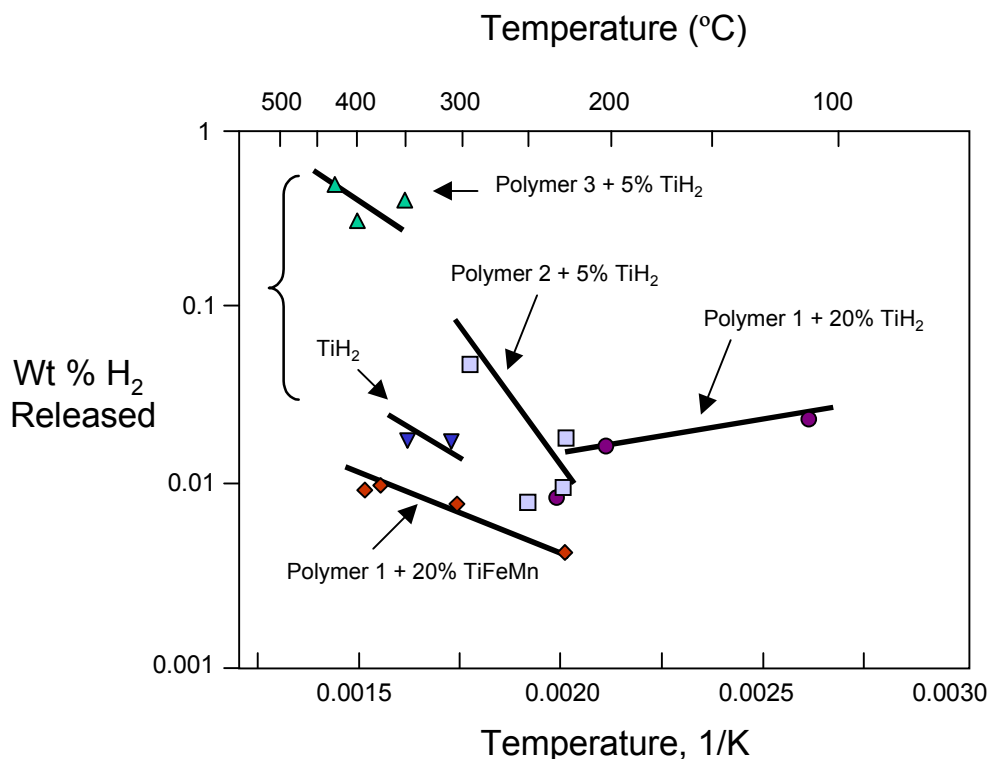


Figure 1. Early UTRC Measurements of Hydrogen Released from Various PDMH

Table 1. Representative Metal Hydrides Considered in this Study

Material Selection - Metal Hydrides

Metal Hydride	T(C@1atm)	wt.% H ₂ stored	commercial source
Ti(Fe _{0.9} Mn _{0.1})	3	1.90	Ergenics Hy-Stor 102
LaNi ₅	12	1.49	Ergenics Hy-Stor 205
CaNi ₅	43	1.87	Ergenics Hy-Stor 201
LaNi _{4.7} Al _{0.3}	45	1.44	Ergenics Hy-Stor 207
Ti(Fe _{0.8} Ni _{0.2})	73	1.30	Ergenics Hy-Stor 103
Mg ₂ Ni	255	3.60	Ergenics Hy-Stor 301
Mg	279	7.66	
Ti	643	3.98	

Experimental Methods

The general experimental approach for this study is shown pictorially in Figure 2. The approach is designed to probe polymer/processing method/metal hydride design space, but initially focuses on the effect of processing on polymer structure. In this manner, the hydrogen storage capacity of the polymer phase can be independently examined from that of the metal hydride in a PDMH.

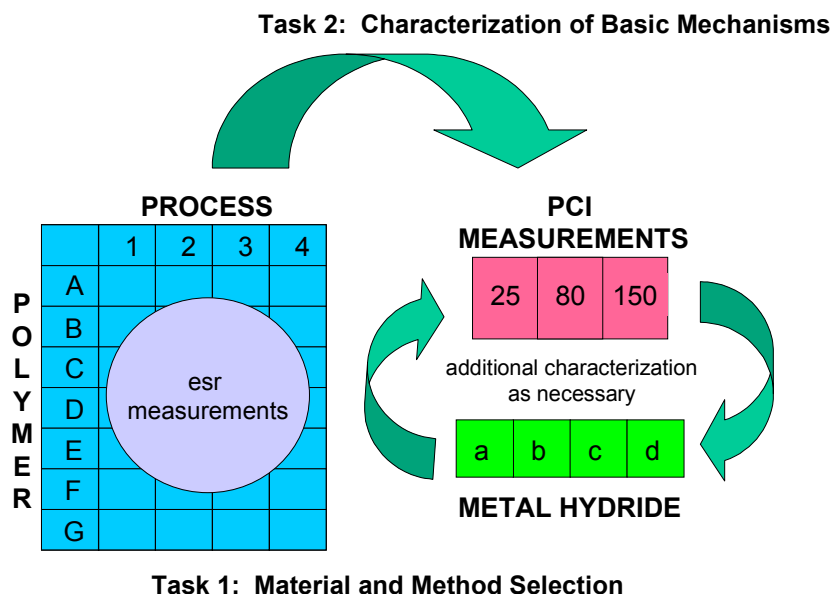


Figure 2. Experimental Approach for PDMH, Showing Relationship of Tasks

Generically speaking, polymers (A-G) undergo various processing methods (1-4) and are characterized following sample preparation. One method to characterize structural changes of polymers is electron spin resonance (ESR) or electron paramagnetic resonance (EPR) spectroscopy, in which microwave radiation induces transitions between magnetic energy levels of electrons with unpaired spins. Unpaired electrons are relatively unusual in occurrence, but are present in free radicals, triplet electronic states and transition metal ions. Unpaired electrons of free radicals are generally left following homolytic fission of a covalent bond – *i.e.* polymer chain scission (Willard, *et al.* 1981). Thus, EPR provides a means to probe the concentration of free radicals in a polymer sample.

Polymers were selected to cover a wide range of chemistries and level of thermal stability. All polymers were obtained as samples or purchased from commercial vendors and used as-received. Nafion NR-50 superacid catalyst was obtained from Engelhard (Seneca, SC). Polyaniline powder was purchased from Ormecon Chemie (Ammersbek, Germany). Polytetrafluoroethylene (PTFE), polyamide (Nylon 6), polyetheretherketone (PEEK) and polypropylene (PP) powders were purchased from Goodfellow (Berwyn, PA). Polyvinylidene (PVDF) powder was purchased from Aldrich (Milwaukee, WI). A very limited quantity of ground Kapton polyimide was obtained from DuPont (Wilmington, DE) – a surrogate polyimide, LaRC-SI, was obtained from Imitec, Inc. (Schenectady, NY).

Polymer samples were processed using four methods - no additional processing (as-received), thermally, mechanically, or by plasma spray. The relative thermal stability of each polymer was studied using thermogravimetric analysis (TGA). These experiments were performed using a TA Instruments TGA 2950 (New Castle, DE), in both argon and air, with a heating rate of 5°C per minute from room temperature to 800°C. Based on the TGA results, bulk portions of each polymer were subjected to thermal processing in flowing argon to 80°C, 150°C or 400°C in a conventional tube furnace. Additional portions of polymer samples were mechanically milled for 0.5 or 2 hours in an 8000D SPEX CertiPrep Dual Mixer/Mill[®] (Metuchen, NJ) with hardened steel vials and steel balls. Polymer samples were arc plasma-sprayed at ZatorskiCo (East Hampton, CT) using parameters suitable for delivering powder-based coatings of engineered plastics. Most powders were sprayed using a standard Metco 3MB plasma spray gun, a GP or GH nozzle, a customized Sultzzer-Metco Twin 10C powder feeder, primary gas flow rates of 150 SCFH, an applied voltage of 60V and a current of approximately 300A. The spray gun was mounted in a custom capture vessel, which reduced the velocity of the expanding gas through expanding cross-section, allowed convenient capture of the sprayed powder, and provided for gas venting.

The hydrogen storage capacity of each processed polymer sample was measured. Hydrogen absorption/desorption measurements were performed at Advanced Materials Corporation (Pittsburgh, PA) and UTRC using a computer-controlled, gas reaction controller pressure-composition isotherm (PCI) measurement system from Advanced Materials Corporation. The PCI unit was equipped to operate over a pressure range of 0.01 to 50 atmospheres of hydrogen and a temperature range of 25°C to 500°C. Samples for PCI measurements were prepared and loaded under controlled atmosphere conditions in a drybox. A sample size of one gram was typically used for PCI measurements. Blank absorption/desorption experiments were run each day with an empty sample chamber at the temperatures of interest (25°C, 80°C, 150°C, and 400°C) and used to correct subsequent measurements.

Metal hydride samples were purchased from Ergenics (Ringwood, NJ) and used following activation procedures recommended by the vendor. The experimental plan combines specific metal hydrides with combinations of polymer/processing method that show encouraging hydrogen storage results, in an iterative manner. Materials characterization is provided at intermediate steps in the process (Figure 2). For example, if plasma-sprayed LaRC-SI demonstrates measurable hydrogen storage, a metal hydride such as LaNi₅ will be combined with LaRC-SI, and the resulting blend processed by plasma spraying prior to additional PCI measurements.

Electron paramagnetic resonance (EPR) measurements were performed at 9.5-9.6 GHz (X-band) at room temperature using a Bruker ESP300E spectrometer. Powdered polymer samples were placed in quartz tubes (4 mm o.d., 3.2 mm i.d., 178 cm length). To ensure reliable intensity measurements, all tubes were filled to a constant height (~ 8 cm) such that the sample height was greater than the resonance cavity, a rectangular TE(102) cavity. A Bruker weak pitch sample (with dimensions identical to that of the samples) with a spin density of $1.13 \times 10^{13} \pm 5\%$ spins per centimeter was used as a standard for intensity measurements. Spectra in a set of samples were recorded using the same measurement parameters (microwave power, modulation

amplitude, receiver gain, conversion time, etc.). Double integration of the EPR spectra were carried out using the Bruker data analysis package after baseline correction.

Results and Discussion

Materials Characterization

Thermal analysis of the polymer samples showed similar results for both argon and air atmospheres. In general, the polymers showed minimal weight loss until a critical temperature was reached – above this temperature, a significant weight loss occurred. Figure 3 displays four representative TGA data sets for polyaniline, polypropylene, polytetrafluoroethylene, and LaRC-SI polyimide. From these plots, insight can be gained on the relative thermal stability of the materials, particularly when application temperatures are considered. It would be impractical to design a hydrogen storage system that operates at temperatures significantly above the critical temperature of a given polymer. For example, the polyaniline sample loses approximately 5% of its initial weight by 100°C, followed by an additional 50% loss beginning near 200°C. Above 400°C, the polymer gradually loses weight at a rate of nearly 0.025% per 100°C to 800°C. Polypropylene and polytetrafluoroethylene undergo single, yet catastrophic, weight losses. These materials lose all of their sample weight by approximately 450°C and 600°C, respectively. The LaRC-SI sample exhibits the highest thermal stability of these examples, with a nominal 2% loss to 500°C, followed by an additional 35-40% weight loss by 800°C. Thus, the relative thermal stability of these polymers is found to be polyaniline < polypropylene < polytetrafluoroethylene < LaRC-SI. While this result is useful from a systems design perspective, it also suggests other processing influences. For example, bulk thermal processing at 400°C is likely to modify the LaRC-SI polymer structure significantly less than the polyaniline material, because their decomposition behavior is noticeably different.

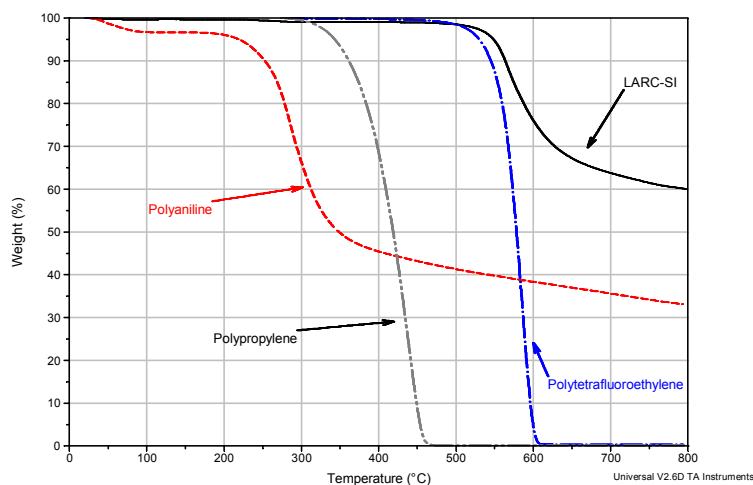
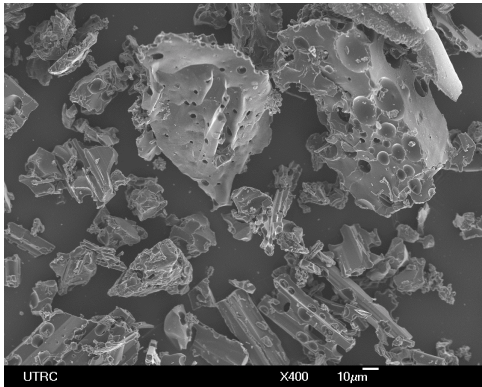


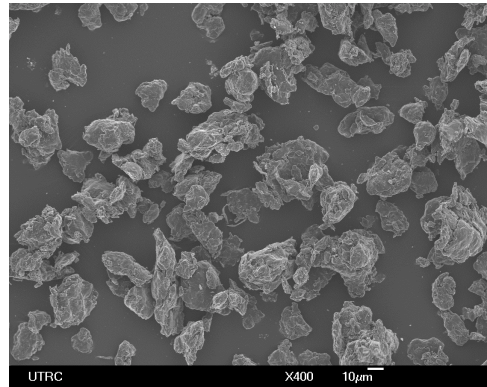
Figure 3. Representative Thermal Analysis Data for Several Polymer Samples

Changes to the polymer powder morphology are also of interest, whether induced by the processing method or by the cyclic absorption/desorption of hydrogen during the PCI

experiments. Metal hydrides typically undergo decrepitation during such cycles, but the effect of cycling on polymers is unknown. One example of morphological change induced by processing method is shown in Figure 4. Scanning electron microscopic (SEM) images of LaRC-SI powders were taken of the as-received polymer (Figure 4, left hand image) and after ball milling the polymer for two hours (Figure 4, right hand image). At least two interesting observations can be made from these images. First, the as-received powder consists of irregularly sized angular particles, many with residual bubbles on the surface. Second, the ball milling process generally reduces the particle size of the polymer and creates a more homogeneous distribution of particles.



**LaRC-SI polyimide
as received**



**LaRC-SI polyimide
milled 2 hours in Ar**

Figure 4. Representative SEM Micrographs of LaRC-SI Polymer Powders

The plasma spray process is a particularly interesting method to impart high energy into a material. Figure 5 shows a sample of LaRC-SI and 5 wt% TiH₂ undergoing the plasma spray process – the intense energetics of the process are readily apparent, and small, glowing particles can be seen at the end of the particle stream. A close-up view of the nozzle is also shown.



Figure 5. Plasma Spraying of LaRC-SI/5% TiH₂; Nozzle Geometry Shown in Inset

Although thermal, mechanical and plasma-spray processing offer unique means to combine polymers and metal hydride powders, the actual nature of the interactions between the phases, as

well as the location of each phase, is unclear. For example, in a PDMH consisting of LaRC-SI and TiH_2 , it would be beneficial to determine the location of each phase within the composite, as well as any differences imparted by the various processing methods. To examine this issue, a blended powder containing 95 wt% LaRC-SI and 5 wt% TiH_2 was prepared. This sample was plasma sprayed and examined by conventional SEM and using backscattered electrons (BSE). Figure 6 shows the results of this analysis. The left hand image of Figure 6 shows a typical SEM micrograph of the plasma sprayed sample. In comparison to the image in Figure 4 of the as-received polymer, the plasma sprayed sample contains more rounded particles – suggesting that the particles have partially deformed, perhaps by melting, in the plasma. The right hand image of Figure 6 is a back scattered image of the same sample region, and distinguishes atomic weight differences. Specifically, particles containing the heavier Ti appear brighter in the image. It is apparent that a larger particle containing Ti is not in close proximity to a polymer particle (right side of right hand image), while a smaller Ti-containing particle is embedded within a polymer particle. The relationship between polymer and metal hydride interparticle spacing and hydrogen storage is not known at this time, but certainly worthy of further study.

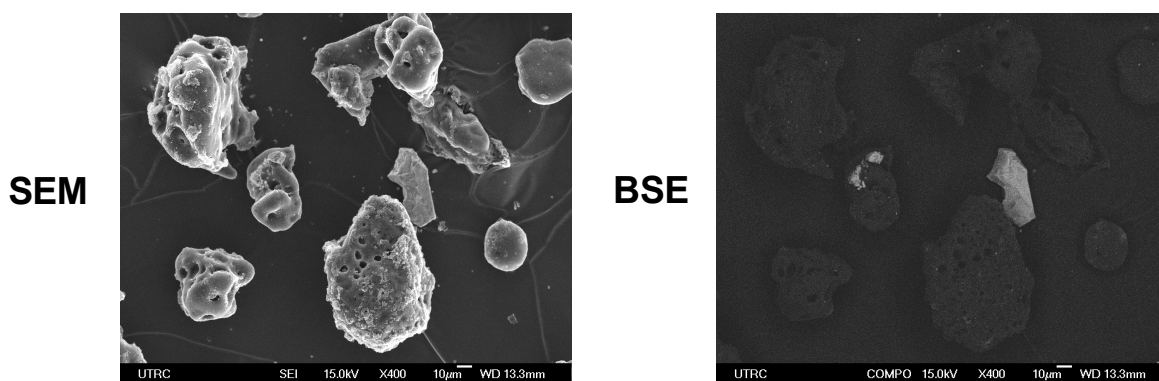


Figure 6. Representative SEM Micrographs of Plasma Sprayed LaRC-SI/5% TiH_2

Hydrogen Storage Measurements

Preliminary PCI measurements on plasma-sprayed blends of LaRC-SI and 5 wt% TiH_2 were performed at Advanced Materials Corporation at 300°C and 400°C. These relatively high temperatures were chosen in attempts to reproduce data shown in Figure 1 (TiH_2 and Polymer 3 + TiH_2). Although these temperatures are required to achieve significant hydrogen absorption in TiH_2 , they are unsuitable for use in PEM-based fuel cells, which typically require application temperatures of 80°C to 120°C. The data presented in Figure 7 summarize two absorption/desorptions cycles at 400°C and one cycle at 300°C. Note that the maximum stored hydrogen content is about 0.36 wt%, which nicely confirms the data in Figure 1, but which falls far short of the DOE goal of 5.5 wt%. Hysteresis is also noticeable between the absorption and desorption stages of the cycle, becoming smaller with increased cycling and lower temperatures. One possible explanation for the observed hysteresis is a thermally-induced structural change in the polymer or the metal hydride phase.

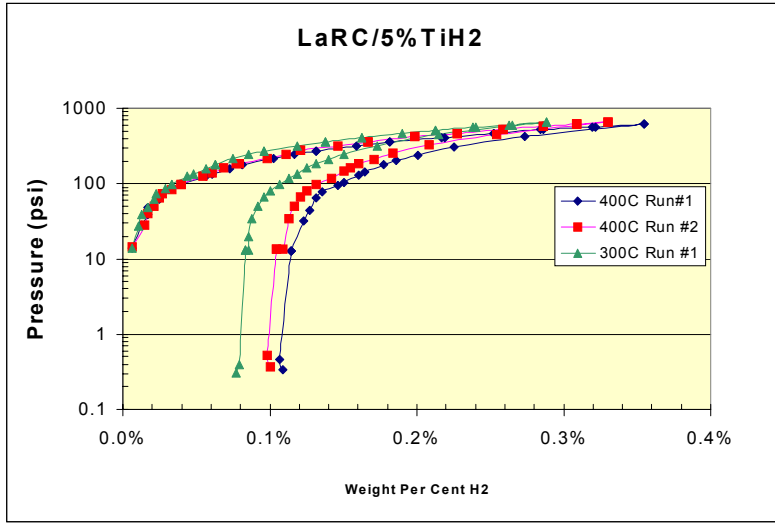


Figure 7. Initial PCI Data for Plasma Sprayed LaRC-SI/5% TiH₂

Over 50 additional PCI measurements (absorption and desorption cycles) were performed at UTRC since these initial data were acquired. Specifically, PCI data were obtained for as-received polymers at 25°C, 80°C, 150°C, and 400°C; for 2 hour ball milled samples at 25°C and 150°C; for 400°C processed polymers at 25°C; and for several plasma sprayed polymers at 25°C. To date, within experimental error and reproducibility limits, no processed polymer sample has shown measurable hydrogen storage capacity that differs significantly from the blank sample holder. As examples, Figure 8 shows two PCI curves of a blank sample holder and plasma-sprayed Nylon 6 polyamide sample. Both data sets were acquired at UTRC at room temperature. Note that the Y-axis displays pressure of applied hydrogen gas, in atmospheres, and the X-axis reflects the amount of hydrogen ab/desorbed, in weight percent. There is virtually no difference between the data sets. Similar results have been achieved with essentially all of the polymer samples in the absence of metal hydride.

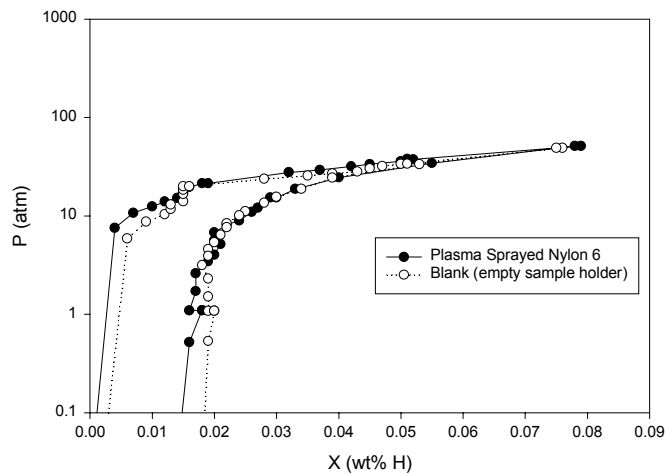


Figure 8. Typical UTRC PCI Data

Electron Paramagnetic Resonance (EPR) Measurements

Preliminary EPR measurements (not shown) on as-received and plasma-sprayed LaRC-SI indicated that the as-received material had a relatively low signal intensity compared to the plasma-sprayed material. Qualitatively, these measurements implied that the plasma spray process altered the polymer structure and created a population of free radical sites through bond scission. Additional work was performed in an effort to quantify the density of free radicals created by the various processing methods. Quantitative experiments were performed on as-received and several processed LaRC-SI samples, although under different conditions. Figure 9 summarizes these experiments. The series of curves shows relative intensity versus magnetic field for the processed samples. The integrated intensity of the signal increased in this order: as received (2.82×10^{15} spins/gram) < 150°C sample (3.49×10^{15} spins/gram) < 2 hour ball milled sample (2.44×10^{16} spins/gram). Note that the LaRC-SI sample shows little thermal degradation by 400°C (Figure 3), suggesting that loss of hydrogen atoms may not be a significant source of free radicals. To date, the EPR spectrum of the plasma sprayed sample has not been acquired, but it is expected to show significantly higher free radical concentration than the other samples due to the high energy of the plasma spray process.

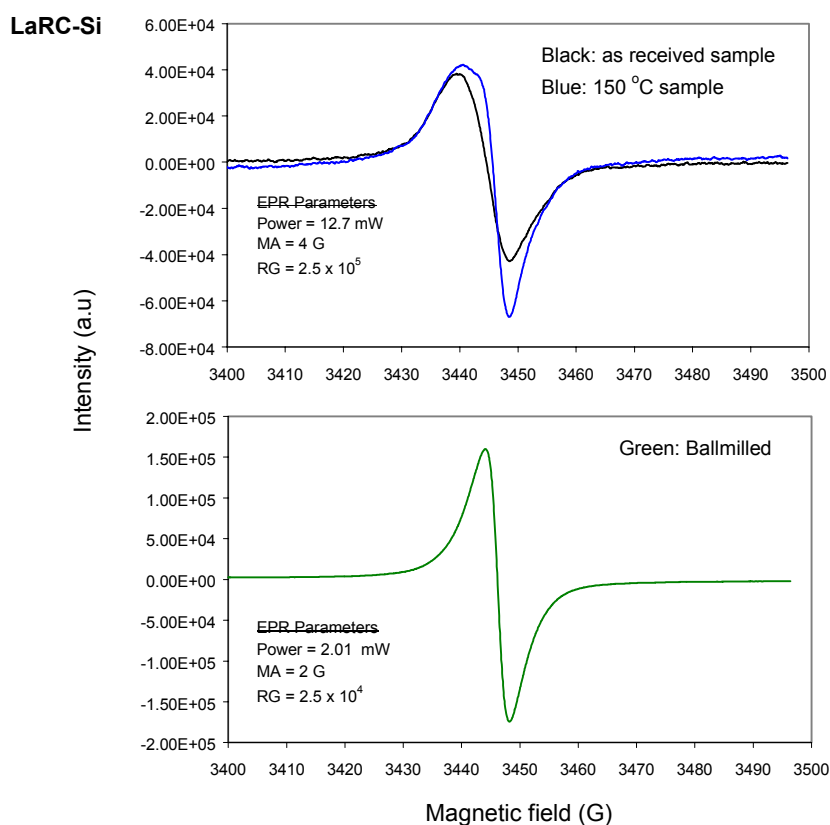


Figure 9. Representative EPR Data for Processed LaRC-SI Polyimide Samples

Figure 10 summarizes a similar experimental study for Kapton, and does not include quantified plasma spray data. The as-received sample and a sample processed at 150°C show similar spin densities of 1.24×10^{16} spins/gram of sample. Kapton thermally processed at 400°C or ball-

milled for 2 hours, shows measurably higher spin densities of 4.83×10^{16} spins/gram and 8.01×10^{16} spins/gram, respectively. In general, the measured spin densities of the Kapton samples were significantly higher than the LaRC-SI samples, suggesting differences in structural robustness between the two polymers.

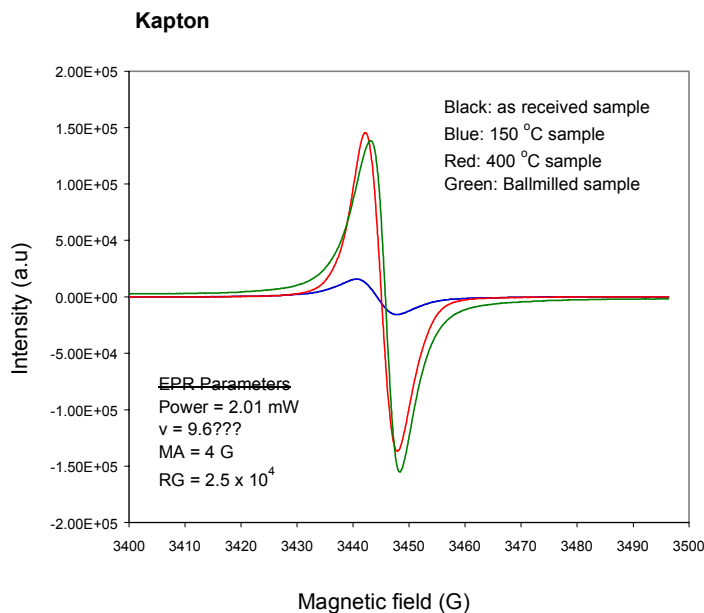


Figure 10. Representative EPR Data for Processed Kapton Polyimide Samples

While it is evident that choice of processing method can influence the resulting chemical structure of the polymer, the relationship with a polymer's initial or modified structure, and its ability to store hydrogen or interact with the metal hydride, is not clear at this time. These topics will comprise the focus of future efforts.

Hydrogen Storage Mechanisms in Polymers

The exact role, if any, that a polymer plays in modifying the hydrogen storage capacity of a metal hydride is unknown at this time. While no significant evidence for storage enhancement has been found to date, it is plausible that a polymer structure could interact with molecular hydrogen. Given that each polymer sample contains a high concentration of hydrogen covalently bonded to the polymer structure, it is conceivable that hydrogen species could interact on a molecular level. For example, depending on the charge of the hydrogen species, a combination of covalent, ionic, metallic, H-bonding and van der Waals interactions could exist within and between the polymer chains and/or with the metal hydride. Free radicals present within the polymer structure could further participate in hydrogen movement through the polymer network. Figure 11 provides a schematic diagram hypothesizing the role of the polymer. With Kapton polyimide as the polymer example, this study has shown that plasma spray processing introduces a significant free radical population into the sample. Although the exact location of the free radical sites has yet to be determined (but can be specifically assigned based on the EPR spectral

characteristics), they can be represented as dangling bonds, denoted in red in Figure 11. As a hydrogen molecule diffuses near a dangling bond, it can dissociate into two hydrogen atoms, which can further interact with the polymer free radical to form a covalent bond, or diffuse into the metal hydride lattice. Of course, the actual surface chemistry of the metal hydride must be considered in this example. The yellow inset box implies that the metal surface is populated by various oxide, hydroxide, water, or adsorbed diatomic hydrogen species – each will influence the incorporation of hydrogen atoms into the structure. The reversibility and thermodynamic stability of the covalent bond, newly created between hydrogen atom and the polymer, must also be considered. Nevertheless, Figure 11 presents one possible scenario for the role of polymers.

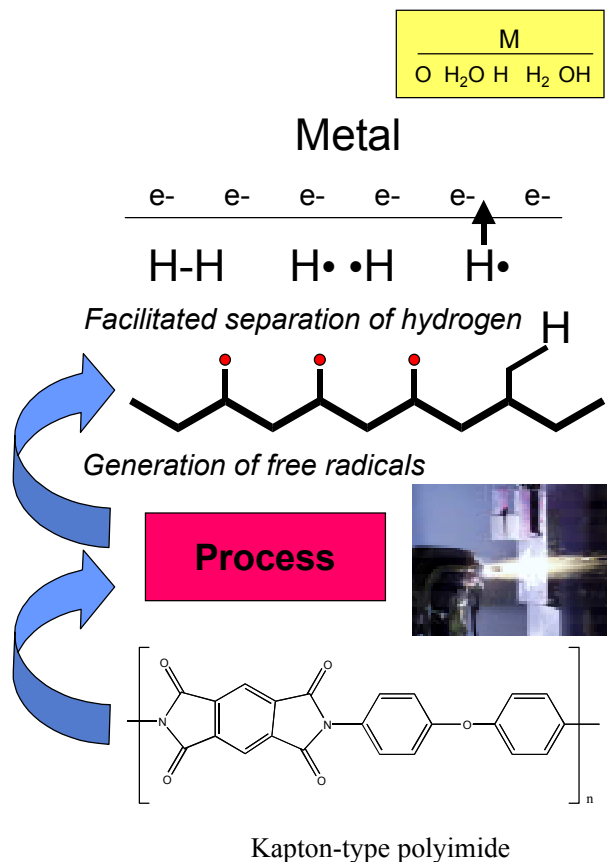


Figure 11. Possible Relationship Between Free Radicals and Hydrogen in PDMH

Conclusions

Dispersion of metal hydrides into low-density polymers, capable of storing hydrogen, is a unique approach to meeting the energy storage requirements of fuel cell powered automobiles. UTRC has begun to explore materials and processing design space to elucidate mechanisms of hydrogen storage in PDMH systems. To date, there is little experimental evidence to support the notion that polymers alone provide significant hydrogen storage capacity. Work continues to examine the inter-relationship between the dispersed metal hydride and the polymer support phase, and the resulting hydrogen storage behavior of the composite. In particular, the microstructural

distribution of metal hydride and polymer phases, and the effect of homogeneity on performance at a given temperature, must be determined.

EPR spectroscopic techniques have proven valuable in confirming and quantifying the amount of free radicals in processed polymer samples. The role free radicals play in hydrogen storage remains unclear, however, but reinforces the need to better understand the molecular interactions between metal hydride and polymer phases. The thermal stability of the polymer phase, relative to the operation temperature of the fuel cell, is also a critical consideration when designing a PDMH-based hydrogen storage system.

Future Work

Ongoing efforts are focused towards completing the EPR spectral measurements on all plasma-sprayed polymer samples. Additional PCI experiments, at various temperatures, are similarly planned for the plasma-sprayed polymers. Following assessment of the ‘best’ combination of processing method and polymer, select mixtures of polymer and LaNi₅ and Mg₂Ni will be prepared and processed accordingly. The hydrogen storage capacity of these optimized composite samples will be measured between room temperature and 150°C. The effects of varying the polymer/metal hydride composition ratio will also be investigated.

Assuming that sufficient hydrogen storage capacity is measured for the optimized samples, a qualitative systems design will be developed to account for weight, volume, cost and thermal requirements of a commercial PDMH approach.

Acknowledgments

Polymer Dispersed Metal Hydride program efforts were performed under DOE contract DE-FC36-00G010535 to United Technologies Research Center. Mr. Ronald Brown at UTRC is recognized for performing sample preparation and hydrogen storage measurements. Mr. Ray Zatorski at ZatorskiCo performed all plasma spraying of polymer and polymer/metal hydride samples. Drs. Donald Anton, Thomas Jarvi and Richard Meinzer at UTRC provided valuable discussions relating to experimental design and hydrogen storage. Dr. Wendy Shaw at PNNL performed preliminary EPR measurements on initial plasma-sprayed polymer samples. Dr. Ravi K. Kukkadapu carried out the majority of EPR measurements at the W. R. Wiley Environmental Molecular Sciences Laboratory (EMSL), a national scientific user facility sponsored by the U. S. Department of Energy’s Office of Biological and Environmental Research and located at Pacific Northwest National Laboratory (PNNL), Richland, WA. Dr. Kukkadapu was supported by EMSL operating budget. PNNL is operated for the Department of Energy by Battelle Memorial Institute under contract DE-AC06-76RLO1830. Dr. John Darab at PNNL provided additional insight into the induced structural changes of the polymer samples.

References

DeLuchi, M. A., 1992. In: *Hydrogen Fuel-Cell Vehicles*, Institute of Transportation Studies, UC Davis.

Dillon, A. C., Jones, K. M., Bekkedahl, T. A., Kiang, C. H., Bethune, D. S., and Heben, M. J. 1997 *Nature*, 386:377.

Jarvi, T. D., Dec. 15, 1999. *Hydrogen Storage in Polymer Dispersed Metal Hydrides*, UTRC Proposal P.300.0024 in response to U. S. DOE Solicitation DE-PS36-00GO10482.

Meinzer, R. A., U. S. Patent 5,360,461 Nov. 1, 1994. *Polymeric Storage Bed for Hydrogen*.

Willard, H. H., Merritt, L.L., Dean, J. A., and Settle, F. A. 1981. *Instrumental Methods of Analysis, Sixth Edition (Chapter 12)*. Stamford; Wadsworth Publishing Co.

NEXT GENERATION HYDROGEN TANKAGE

**Andrew Weisberg
Lawrence Livermore National Laboratory
Livermore, CA 94551**

Abstract

Efforts to continue research on advanced hydrogen vehicular tank technologies have been focused on a strategy that allows an affordable return to frontier experimentation, can sort out the mechanism responsible for premature failure in the record-setting tanks built in 2000, has a plausible path to adoption by industry, enables new classes of small hydrogen powered vehicles, supplies examples for regulatory reform initiatives, and demonstrates the effectiveness of innovations expected to reduce hydrogen vehicular tank cost (in mass production) by roughly a factor of two over the current state of the art.

Beside the overall strategy, two subtasks are detailed and some of the related efforts performed by LLNL's tankage research team are described briefly. Monitoring technical progress on DOE's ongoing contract with Quantum, learning from Sandia's destructive test program, and attempting to troubleshoot the multiple-organization vehicle integration efforts on two demonstration programs (the FutureTruck Competition and the Nevada Bus Project) are discussed briefly as sources of learning and opportunities to assist related efforts. The rationales for initiatives that LLNL has pursued in advocating technical reforms to current hydrogen tank safety regulations are also dissected.

Strategic Crossroads

The team at LLNL that set the percent-by-weight-hydrogen record in the year 2000 has to solve the inevitable strategic problem – what to do next.

This central problem had several disparate subproblems. Understanding of what happened at the limits of manufacturable tank weight performance was incomplete. A mysterious failure mechanism remains unidentified, and resources were clearly inadequate to return to the same experimental conditions. Many sorts of high leverage tankage innovations have come to light that were simply not affordable to investigate. Nearly commercial spinoffs of LLNL tankage innovations proven across the past three years were already heading for vehicle integrations demonstration projects, in which the LLNL team had a coordinating role. The expertise required to contribute to those demonstrations would soak up most of the DOE-funded staff hours at LLNL in FY01. The lessons learned from the contract and demonstration roles turned out to be relevant for the bigger strategic problem.

Related Activities

Arduous participation in demonstration vehicle projects will be sketched in a section (Demonstration Projects) below. That participation may appear tangential to the research conclusions that form the backbone of this Annual Report. In two different ways, those efforts resulted in learning that come in early enough to determine strategy. A relevant failure mode was observed in prequalification testing conducted by IMPCO (now Quantum), the winning bidder now under contract with DOE to develop lightweight hydrogen tanks. LLNL team members acting as technical monitors on that contract were able to debrief IMPCO on results that would otherwise have escaped notice. Another relevant failure mode was encountered several months later at Sandia in extreme penetration testing.

These failures that LLNL learned of and inquired further about came to LLNL's attention because participation in DOE demonstration and development projects paid for large (>\$100K) human interface costs. These failures were relevant because their shrapnel morphology appeared similar to the mysterious failure mechanism that cost LLNL's record-setting tanks a consistent 7% in weight performance.

The other connection or spinoff of LLNL tankage 'diplomacy' came through LLNL's assumed responsibility to contribute expertise into the tankage regulatory process. It had become clear to LLNL tankage innovation advocates over the past ~3 years that safety regulations derived from the NGV2 standards for compressed natural gas tanks were seriously flawed. LLNL's first recommendations were contributed in haste to the ISO regulatory process in 1999. Another round of recommendations had accumulated from LLNL's participation in the IMPCO development contract over year 2000. Now year 2001 has delivered some lessons vital to new recommendations that counter deeper conceptual flaws in proposed regulations. Besides penalizing innovation and testing the wrong objectives, draft regulations now before the ISO are already posing barriers to adoption of hydrogen fueled vehicles by robbing obvious safety innovations of the ability to be certified safe.

Strategic Choice

If the LLNL tankage team chooses the right direction for its investigations, all of these partially related problems can be tacked with research results. Instead of ‘diplomacy’ and exponentiating manpower costs that must be sunk into regulatory ‘outreach’ programs, new experiments with actual hydrogen tanks could directly alter future regulations and development possibilities. No arm twisting will be required to get manufacturers to adopt the new technology LLNL has selected. The routes to adoption available for previous generations of LLNL hydrogen tankage innovation were closing down as some of the fruits of LLNL labors in previous years approach commercialization. Thiokol, which made the bridge between state-of-the-art aerospace composite fabrication expertise and LLNL new technology initiatives in tankage, is effectively out of this business (due to management decisions and ownership changes). No strategy that threatens the market positions of current tankage manufacturers is likely to prosper. Therefore it makes sense to move LLNL’s tankage research focus 3-5 years into the future, away from its previous 1-2 year aims.

This strategic choice was well aligned with the suggestions of Sigmund Gronich, in charge of DOE’s Hydrogen Program. In a tankage research planning session (August 2000), he suggested moving LLNL’s focus from weight to economic performance. Economic performance was also an imperative to be able to afford any experiments that might return to conditions similar to the mysterious failure mode on the weight frontier. The Hydrogen Program insisted on economic analysis in every years reporting prior to this year, and the 500,000 cars/year quantities used as the basis for those required cost projections allowed for several next generations of tankage technology. What innovations would be advanced enough not to threaten current commercialization market positions but could still pay their own way and sell themselves by reducing the cost of hydrogen tankage?

Experimental Program Rationale

This strategy of pursuing the next generations of vehicular hydrogen tankage does more than supply a plausible path to market adoption. It would be worthless without an understanding of what techniques to investigate and why. Without models validated by testing actual hardware, economic performance projections based on technologies that may not work would be moot. When this fiscal year began, the burst failure mechanism that limited tank weight performance wasn’t understood, and appeared unlikely to be sorted out without an effort our industrial partners (Thiokol and IMPCO) call a “Science Experiment.” Why might it be worthwhile to conduct those experiments? Without the understanding that such experiments should bring, the proponents of advanced technology would be promoters, not experts. Economic performance and plausible adoption paths provide the why for selecting among innovations, as long as near-term economics can afford the experiments to prove the innovations will perform as advocated.

The LLNL tankage research strategy that has emerged is quite detailed. Test articles suitable for motorcycles, scooters, lawnmowers, wheelchairs, leaf blowers, etc. go a long way to solving the experiment affordability problem. End dome contours are currently being computationally designed by a LLNL subcontractor to complete the specifications for a liner mold. A reasonable fabrication price is likely to be bid that could deliver copies of an integrated tank test article for

<\$500, using less than \$15 of T700S (the most economic composite fiber type available for the next few years).

The economic performance projected for the next generation tanks that LLNL advocates is not the same as the economic affordability of research experiments. Those experiments are designed to understand the technical issues that separate the current state of the art from one that is projected to cost approximately half as much to do the same job. Performing research, not necessarily mass production, at a smaller tank scale has many other advantages besides affordability of experiments. It threatens no hydrogen tank commercialization efforts now underway, and postpones the prohibitively high cost of tooling up to manufacture tanks big enough for automobiles or trucks to ambitious firms, who can pay for it when the production volumes in a next generation industry can afford it.

Technologies Selected

Figure 1 shows LLNL’s most recent cost projections as a function of the total quantity of automotive scale tanks produced. These projections are based on component and assembly costs of a 5,000 psi tank that holds 3.6 kilograms of hydrogen. These projections extend results that have already been confirmed by LLNL’s collaborators in industry (for low volume, near-term commercial production) to later generations of mass production. They forecast a switch to next generation technologies advocated below at quantities that can afford to sink their significant development costs, somewhere between 20,000 and 1,000,000 units produced.

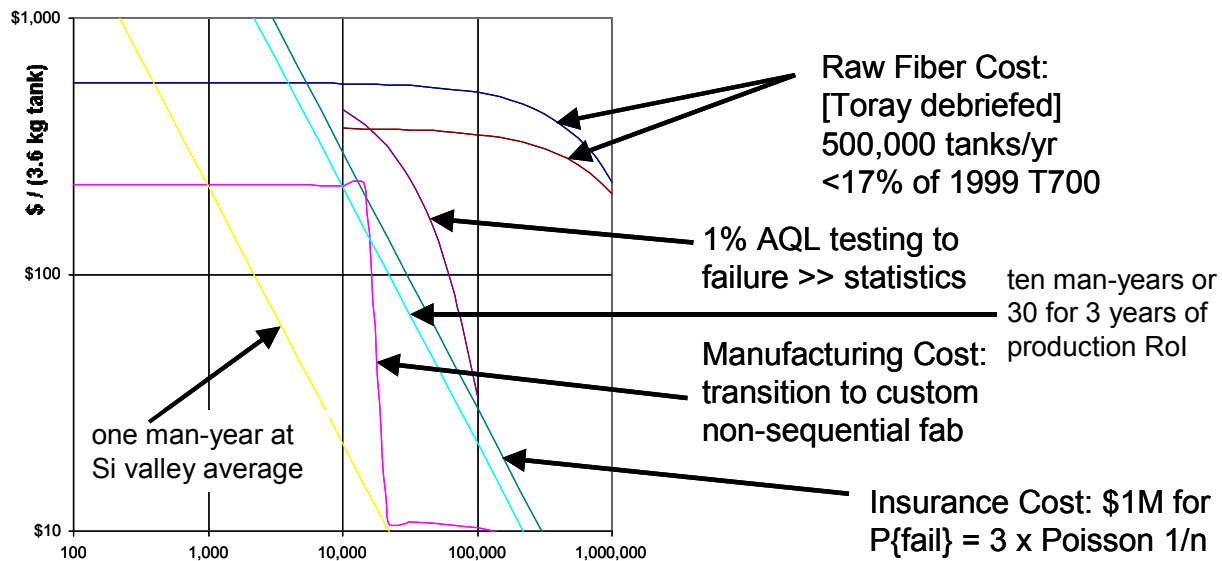


Figure 1 – Cost Projections vs. Quantity Manufactured

What advanced technologies can pay for their own development and still save costs in hydrogen tankage? A preliminary understanding of the design options and process parameters required to specify today’s best hydrogen tanks was forming over the last two years as LLNL collaborated

with Thiokol, ATL, and IMPCO to build record-setting tanks. That understanding was inadequate to chart the possible frontiers for innovation. Several experts were added to the LLNL team's roster of consultants, and a mini-forum was held between the entire LLNL team, its consultants, and likely subcontractors in Salt Lake City early in 2001. A very truncated list of innovations emerged from that meeting that combine to save a projected 50% in tank cost. These projections are based on detailed estimates of the improvements possible in the various component costs of the detailed production economics models that industry has already agreed with at low volumes, they rely on an understanding of how various innovations would change components of the tanks themselves, not on hand-waving. These projected savings depend on recognition by the regulatory consensus that difficult testing programs will allow manufacture of safer, lighter, more compact, as well as less expensive tanks.

For the purposes of proving that a tank technology is manufacturable and safe, statistical quantities of tanks must be tested to failure. Smaller research test articles make statistical testing affordable for LLNL tank research efforts, while sufficient production volumes of larger tanks can afford this cost by allocating ~0.5 to a few percent of each production run to a form of self-insurance. Most of tank cost in large scale production is proportional to composite materials mass. This cost component includes the expensive fiber, as well as machine time to process fibers into overwraps. If fiber material and production processes are unchanged, lighter tanks will be proportionally cheaper tanks. Roughly 35% of the LLNL projected tank cost savings of 50% comes from weight reduction. All of these analyses assume the same economical winner of the competition among composite materials for lowest cost per unit strength (Toray's T700S), but LLNL's analyses forecast the substitution of much higher production rate processes (fiber placement of performs in molds) for the conventional fiber winding process. Weight reduction that is correlated with cost reduction can be advantageously traded for higher density to simplify packing enough hydrogen to drive long ranges aboard more conventional vehicle designs, at the cost of about 17% for 10,000 psi operation than the current 5,000 psi technology.

Blow Molding

The rest of LLNL's projected cost savings come from lower component and manufacturing operations counts. The quasi-instantaneous (generally below 2 seconds per molding cycle) provides access to a much wider list of plastic liner materials than the state of the art rotational molding plastics that LLNL has explored exhaustively in previous years. This process is capable of producing the thinnest liners possible without etching (a costly process that is difficult to control, used in exotic aerospace aluminum and titanium tank liners). Thinner liners have a slight but significant effect on saving weight, increasing overall density, and reducing cost. Tooling for blow molding cost so much for an automotive scale tank that this process must wait for at least 10,000 units to be produced to be economically advantageous. For near-term experiments, a preliminary quotation (January 2001, from a contractor recommended via Kirtland AFB tank researchers) for tooling and 200 liners from the first mold run was \$20,000 for a mold just 10" long and 5" across.

Blow molding provides a cost-effective substrate for several coating-in-the-round processes LLNL hopes to investigate in 2002. Although cost savings from the high-volume blow molding

process are barely significant for the entire tank, the new liner materials this process can form into liners are very significant because they facilitate low-cost, high-throughput, and structure mass saving innovations. Blow molding can produce liners so thin that the best coatings can account for most of an advanced liner, so soluble that etching them out to manufacture 'linerless' designs could produce cheaper tanks by removing failure initiation sites on the liner-composite interface. Some blow-moldable liner materials are strong enough to allow prestressed coatings and very high winding tension to be applied onto pressurized liners before they are reinforced with cured composite overwrapping. Integrated tank leak/permeation testing will provide the first valid data on permeation aging and statistics. Thin liners combined with minimum weight composite overwrapping should also be ideal for recreating the mysterious failure mode whose elimination could save 7% in costly fiber mass.

Process Research

Burst testing of statistical quantities of small tanks can provide direct evidence that 33% of the 35% savings projected due to weight reduction is feasible. Dropping safety factors from 2.25 (burst pressure over maximum expected operating pressure) to the vicinity of 1.5 (where many aerospace systems are routinely engineered with great attention to performance variation) will depend on plenty of burst data statistics to recruit a consensus of safety 'experts.' One of the process variables that statistical process research should explore directly influences variability in burst pressures for at least one failure mode: bending in the transition region between end dome and cylindrical sections of a tank. This variable is also a design variable, and will be constrained by the shape of molded liners' end domes unless very advanced forms of composite fabrication (fiber placement that can preclude lateral tow slip and depart from geodesic fiber trajectories) are employed instead of winding. Ultimately those advanced processes may be economically justified at high volumes, but they will be difficult to include in near term variation of parameter studies. These sorts of studies are the staple of Silicon Valley semiconductor process research, and make sense to conduct whenever it is possible to gather enough statistics.

The other two process parameters that are affordable and important enough to investigate on a one-year timescale are wind tension and curing cycle temperature. The parameter list for manufacturing next generation composite tanks can get much longer, but twenty five produced and burst test articles barely suffice to begin exploring statistical performance. Five burst pressure measurements are required for reasonable confidence in estimating variance, so five tanks with identical manufacturing process parameters must be built to determine the performance and manufacture controllability of each point one might advocate exploring in process parameter space. Wind tension is the process parameter anecdotally known to greatly influence burst pressure. The mysterious failure mode of the record setting tanks was encountered on tanks that were wound with unusually low tension. Micro buckling of the wound composite before it was cured, or alteration of HDPE thin liners curing a cure just degrees below HDPE's flow temperature are two strong hypotheses that might explain consistent, measured 7% low strain at failure (compared to Thiokol's large data base of measurements on the same composite materials and TCR matrix impregnation and winding machines, but cured on sand mandrels).

Experimental Equipment

Experimental plans have been developed in even greater detail than the previous consideration of which process variables to vary might suggest. Two test sites have been considered, and are accessible for burst testing, while both manufacturers LLNL has worked with in the past (Thiokol and IMPCO) have an incentive to perform at least one or two burst tests to cross check their own burst testing procedures. Two related instrumentation systems, one at LLNL, another at a likely testing subcontractor, are being built up to allow safe burst testing in bunkers. Percent hydrogen by weight performance also relies on accurate measurements of tank volumes at elevated pressure, which can be made by at least three techniques. Both test rigs should be capable of making volume vs. pressure measurements by the most accurate technique, weighing the water that is pumped into the tank under test during a preliminary run up to proof pressure.

The LLNL field test rig has been designed for subsequent augmentation to allow it to take data at video rates. This feature will allow trials of non-imaging sensors (e.g. fiber proximity sensors, laser beam occlusion, piezo accelerometers) with sufficient bandwidth to resolve the mechanism responsible for “turn to dust” failures. This new failure mechanism has likely been observed in three related series of tank-destroying tests, including LLNL’s mysterious discrepancy between 12% design and 11.3% tested-to-failure percent-by-weight-hydrogen result. It has anecdotally been observed many times in impacting testing of military composite subassemblies like missile casings, but not reported because subsequent design modifications ‘fixed’ it.

Benign Failure Possibility

The ability to observe “turn to dust” failures as they happen has pure scientific value as well as potentially vital safety benefits for compressed hydrogen storage. The lack of large shrapnel (except for the end domes in Sandia’s experiments, which were shielded from the failure onset site by massive clamping straps) in the ~7 related failures suggests that the lightest tank technologies could be designed to burst with unprecedented safety, producing shrapnel but not shrapnel hazards. Expertise at Thiokol familiar with very many failure analyses has argued persuasively that the lack of large shrapnel precludes these failures being localized. If one part of a tank fails first, it always kicks portions of the opposite side away intact.

The conclusion that this failure mode is not localized, plus the speed of the tanks self-destruction recorded on fast-framing cameras by Thiokol and Sandia (which proved this phenomena happens in less than 250 microseconds) endorse the most likely hypothesis: this is a new class of instability. This unproven mechanisms is analogous to turbulence in fluids, where orderly motions becomes disorderly, except that it results in fracture on a characteristic small scale. Similar to snow avalanches, which discharge gravitational potential energy already stored in a medium, this hypothetical mechanism would discharge stored strain energy. Unlike avalanches, or detonation waves which release available chemical energy already stored in their media, this mechanism partakes of fundamentally tensor mechanics due to stress waves in partially ordered, anisotropic, two phase media. No mathematical models capable of handling this hypothesis have yet been found in the literature of physical instabilities.

Fiber dust shrapnel is potentially benign shrapnel. A bit of sheet metal is sufficient to stop a five micron rod of fiber from puncturing people, or even nearby equipment. The creation of this shrapnel should soak up a lot of free energy creating fresh surfaces, like the Velcro tape detachment 'ripcords' now providing dissipation in safety harnesses. The energetics of free surface creation energies in composites also appears to be a neglected topic in the literature of composite materials testing or modeling. Sharpie impact testing (which measures toughness by measuring energy lost in propagating a crack through a bar) might be followed by SEM-based estimates of free surface are creation to estimate the amount of energy shrapnel creation might be consuming. Such quantitative estimates might agree with the 1-2 megajoules of stored strain energy LLNL has calculated were present at burst in the record setting tanks. Combined with another safety initiative (that takes advantage of hydrogen flame speed to vent the ~ half gigajoule of chemical energy stored in a Smart Tank), the development of benign shrapnel would render next generation compressed hydrogen tanks much safer than any other chemical energy storage system.

Safety Considerations

Rather than attempt to dissect the demonstration projects that the LLNL tankage team was involved in from the research plans sketched above, their inherent cross fertilization can be seen if the order of exposition follows regulatory issues into the demonstration projects with their wealth of vehicle+infrastructure integration requirements. LLNL entered the hydrogen tankage regulatory arena in order to enable the adoption of thin, rotationally molded plastic tank liners (whose performance was a key to weight minimization). Metal lined tanks continue to lose the weight and cost performance competition with plastic liners, whenever the competition is performed on a level playing field. Yet the about-to-be-adopted hydrogen vehicle tankage safety regulations contain many leftovers from the era of metal tanks' impermeability, as well as a few bad assumptions from the natural gas tank safety (NGV2) regulations.

Unless the allowable permeation specifications are rewritten, the only plastic-lined hydrogen pressure vessels (Type IV tanks) that will be considered safe have liners almost as thick as their composite overwraps. Fortunately, analyses being performed to contribute to new building codes are bearing out the excessive, 1-2 orders of magnitude in excessive conservatism grandfathered into the ISO TC197 (hydrogen vehicular tanks safety standard), which the LLNL tankage team discovered was based on assumption errors in 1999.

Thin liners enable relatively lightweight tanks, but their relatively insignificant cost savings (2-4% in LLNL projections) are almost irrelevant compared to the benefits likely to accrue from their ~5-fold larger range of available materials. The testing of permeation phenomena for a variety of new liner materials pointed out the advantages of integrated pressure vessel permeation testing compared to single material coupon testing. Thiokol and IMPCO found a factor of two independently in pre-NGV2 qualification test programs that consistently measured vessel permeation below what the coupon permeation tests predicted. This in not good news, since nobody has studied cyclic and environmental degradation of permeation resistance. By testing permeation at beginning of life (even when the required test sequence makes end of life test articles available), excess liner thickness is being required to preserve an untested, ad hoc

safety factor that even meager statistical test could drastically reduce while actual safety would be improved by knowledge of how permeability degrades.

Consideration of the safety implications of hydrogen permeation leads to the conclusion that key current regulations are based on flawed assumptions. Catalytic safety components inside a tank’s envelope aren’t rewarded, since hydrogen leaving the tank interior is circumscribed instead of hydrogen escaping to the tank exterior where it could contribute to flammable gas mixtures. Since advanced tanks require “shoulder pads” to pass the currently required drop test, components exterior to the pressure containment envelope are clearly part of the item being safety certified. The only harm done by regulations that ignore the possibility of turning permeated hydrogen into water vapor is that thin liner innovations are erroneously assumed to be unsafe.

Smart Tanks

Other safety recommendations appear in Table 1. LLNL staff still has the expertise to contribute constructively to the strife that advocating these recommendations would entail, but not the support sufficient to see that strife through to victory. Several of the highest leverage suggestions derived from Sigmund Gronich’s suggestion that LLNL follow up on the Smart Tank efforts funded by DOE some years ago. Like the diplomacy required to advocate regulatory initiatives, debriefing of the now reassigned experts in industry who performed the Smart Tank work was abandoned for lack of resources. But Before Task 1 of LLNL AOP for tankage in FY01 was concluded, it turned out that Bluetooth (a trademark held by a consortium) Wireless technology is destined to make earlier work obsolete. At <\$10 per chip, with a proven wireless range of 15 feet, this technology already has a manufacturer base, a customer base in luggage and hospital equipment and truck tires, a software community, dozens of venture funded new applications, and production volumes growing rapidly somewhere beyond 2 million chips per year.

Table 1- Recommendations for Regulatory Improvements

Redefine permeation to allow water from catalytic vent devices
Set permeation specification 1,000X too conservative, not 10,000X Worst-case garage ventilation rates and statistics are known, stay < LEL
Test permeation at end of cycle life (test article already in NGV2) Current test at beginning of life fails to screen for barriers that degrade Current tests may give false optimism to some barrier technologies Counterproductive waste of safety margin on permeation for degradation
Measure worst-case temperature rise allowable for fast fill rates Filling stations need to know what inlet temperatures are safe for liners
Allow orderly migration to advanced standards as quantities rise Standard practice in Electrical Engineering standards (e.g. ethernet) Advances 'unsafe' without such provisions for revision every few years
Wireless “Smart Tank” features phased in to avoid filling mistakes Earliest software prevents tanks from being used beyond tested cycle life Later prevent tanks from being re-used after mishandling and accidents
Allow statistical qualification to trade cost and mass for more testing
Allow nondestructive testing to trade cost and mass for more testing
Collect real crash data to establish crash-worthiness of mountings
Reward tougher designs by requiring adequate self-insurance plans

A vehicle or portable appliance with a Smart Tank can be a lot safer. Fire risks can be mitigated by remote control. DTI claimed (in a phone conversation) that 5% of auto accidents include fire. Firefighters can easily communicate with Bluetooth enabled ‘smarts’ to specify when and how hydrogen that is still in the fire hazard vicinity can be safely vented. Certainly dropped tanks, filling to excessive pressure levels, tanks resold after collisions, and tanks sold beyond their cycle life can all be prevented by ‘smarts’ that implement a fuel ‘level’ sensor. This avenue of innovation may not need government sponsorship, but its insertion into the contentious safety regulatory arena will consume lots of “people skills” that industry has little incentive invest until ‘smarts’ are deemed safe.

Demonstration Projects

The demonstration projects LLNL participated in were very instructive, as well as sources of intense frustration for their remaining participants. DOE solicited advanced weight performance tanks based on LLNL’s research in FY98 and FY99 from industry in March of 2000. LLNL tankage research team members acted as technical monitors assisting the DOE Golden contracting office/officer to write the solicitation and keep the winning bidder on track toward likely success in the upcoming vehicle demonstrations. What to deliver has changed twice in the course of this contract. Two sorts of demonstration vehicles are to receive tanks supplied by this contract. Figure 2 presents a quick sample of the LLNL’s teams’ original design for the first of these two projects, the FutureTruck SUV competition.

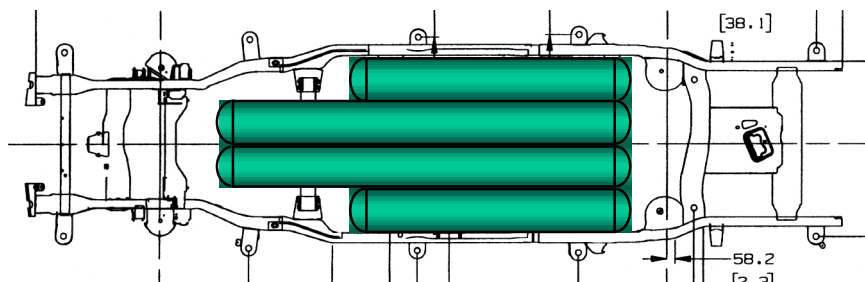


Figure 2 – Original tank layout fit in frame of GM Suburban SUV

The Nevada Bus project presented a plethora of issues (“who’ll do what?”) that needed resolution before solicitations could be written for vehicle integration contractors who would install DOE-supplied tanks, modify the bus, train its operators, etc. Many staff hours were spent at LLNL figuring out what needed to be installed or tested, who was capable of doing it, and who would be responsible for what. Ultimately LLNL’s planning effort for this project was captured in a 24-page suggestion document delivered to the OE Contracts office in Golden, Colorado, which is currently overseeing the ongoing tank development contract. Although LLNL learned how to build and safety certify compressed hydrogen filling facilities, it seems best to clone and employ the costly implementation currently deemed safe in Palm Desert, California.

In advocating a division of labor for the Nevada Bus project, LLNL investigated how to develop a fueling infrastructure and what is needed to modify a vehicle for crashworthy roof-mounted tanks. Oral and written reports of these lessons learned helped convince DOE Hydrogen Program management to let industry “carry the ball” on hydrogen vehicle demonstrations from now on. Liability considerations provided a major justification for this decision. This decision made sense to the LLNL team, but it also effectively severed LLNL participation in the FutureTruck competition (two university teams, Texas Tech and Virginia Tech, are installing DOE supplied tanks on GM SUV’s as this report is being written), as well as in the Nevada efforts. Safety arrangements on these projects are likely to be made by GM in Michigan and Air Products in Nevada. These arrangements will doubtless contribute to the several proprietary fueling implementations that are currently deemed safe in the absence of applicable regulations and even in the absence of disinterested qualification testing.

Acknowledgments

Management of LLNL’s internally-funded EyeGlass LDRD Strategic Initiative has allowed the author to pursue tankage research at some cost to their project’s own probability of success. Other projects at LLNL (sponsored by DARPA, NASA, AFRL, and internal funding) have contributed sufficient support to related research on this leading edge of Joules-per-kilogram.

References

Technical report (not referenced in text above, but prepared at DOE request)

Myers, B., 2001. *Bromine Safety*, UCRL (Research Letter) number to be determined, Livermore, CA: Lawrence Livermore National Laboratory.

PERFORMANCE AND CERTIFICATION TESTING OF INSULATED PRESSURE VESSELS FOR VEHICULAR HYDROGEN STORAGE

**S. M. Aceves and J. Martinez-Frias
Lawrence Livermore National Laboratory
7000 East Ave., L-644
Livermore, CA 94551, USA**

**O. Garcia-Villazana and F. Espinosa-Loza
FIMEE, Universidad de Guanajuato
Salamanca, Gto. Mexico**

Abstract

Insulated pressure vessels are cryogenic-capable pressure vessels that can be fueled with liquid hydrogen (LH₂) or ambient-temperature compressed hydrogen (CH₂). Insulated pressure vessels offer the advantages of liquid hydrogen tanks (low weight and volume), with reduced disadvantages (fuel flexibility, lower energy requirement for hydrogen liquefaction and reduced evaporative losses). The work described here is directed at verifying that commercially available pressure vessels can be safely used to store liquid hydrogen. The use of commercially available pressure vessels significantly reduces the cost and complexity of the insulated pressure vessel development effort. This paper describes a series of tests that have been done with aluminum-lined, fiber-wrapped vessels to evaluate the damage caused by low temperature operation. All analysis and experiments to date indicate that no significant damage has resulted. Required future tests are described that will prove that no technical barriers exist to the safe use of aluminum-fiber vessels at cryogenic temperatures. Future activities also include a demonstration project in which the insulated pressure vessels will be installed and tested on two vehicles. A draft standard will also be generated for obtaining certification for insulated pressure vessels.

Introduction

Hydrogen-fueled vehicles present features that make them serious candidates as alternatives to today's petroleum-powered vehicles. Hydrogen vehicles can use the advanced technology of electric vehicles to improve environmental quality and energy security, while providing the range, performance, and utility of today's gasoline vehicles.

Probably the most significant hurdle for hydrogen vehicles is storing sufficient hydrogen on board. Hydrogen storage choices can determine the refueling time, cost, and infrastructure requirements, as well as indirectly influence energy efficiency, vehicle fuel economy, performance, and utility. There are at least three viable technologies for storing hydrogen fuel on cars. These are compressed hydrogen gas (CH_2), metal hydride adsorption, and cryogenic liquid hydrogen (LH_2). Each of these has significant disadvantages.

Storage of 5 kg of hydrogen (equivalent in terms of energy to 19 liters; 5 gallons of gasoline) is considered necessary for a general-purpose vehicle, since it provides a 640 km (400 mile) range in a 34 km/liter (80 mpg) hybrid vehicle or fuel cell vehicle. Storing this hydrogen as CH_2 requires a volume so big that it is difficult to package in light-duty cars (Pentastar Electronics, 1997). The external volume for a pressure vessel storing 5 kg of hydrogen at 24.8 MPa (3600 psi) is 320 liters (85 gal). Hydrides are heavy (300 kg for 5 kg of hydrogen, Michel et al., 1996), resulting in a substantial reduction in vehicle fuel economy and performance.

Low-pressure LH_2 storage is light and compact, and has received significant attention due to its advantages for packaging (Braess and Strobl, 1996). Significant recent developments have resulted in improved safety (Pehr, 1996a, 1996b), and fueling infrastructure (Hettinger et al., 1996). Disadvantages of low-pressure LH_2 storage are the substantial amount of electricity required for liquefying the hydrogen (Peschka, 1992); the evaporation losses that may occur during fueling low-pressure LH_2 tanks (Wetzel, 1996); and the evaporative losses that occur during periods of inactivity, due to heat transfer from the environment.

An alternative is to store hydrogen in an insulated pressure vessel that has the capacity to operate at LH_2 temperature (20 K), and at high pressure (24.8 MPa; 3600 psi). This vessel has the flexibility of accepting LH_2 or CH_2 as a fuel. Filling the vessel with ambient-temperature CH_2 reduces the amount of hydrogen stored (and therefore the vehicle range) to about a third of its value with LH_2 .

The fueling flexibility of the insulated pressure vessels results in significant advantages. Insulated pressure vessels have similar packaging characteristics as liquid hydrogen tanks (low weight and volume), with reduced energy consumption for liquefaction. Energy requirements for hydrogen liquefaction are lower than for liquid hydrogen tanks because a car with an insulated pressure vessel can use, but does not require, cryogenic hydrogen fuel. A hybrid or fuel cell vehicle with 34 km/l (80 mpg) gasoline-equivalent fuel economy could be refueled with ambient-temperature CH_2 at 24.8 MPa (3600 psi) and still achieve a 200 km range, suitable for the majority of trips. The additional energy, cost, and technological effort for cryogenic refueling need only be undertaken (and paid for) when the additional range is required for longer trips. With an insulated pressure vessel, vehicles can refuel most of the time with ambient-temperature

hydrogen, using less energy, and most likely at lower ultimate cost than LH₂, but with the capability of having 3 times the range of room-temperature storage systems. Use of compressed hydrogen in all trips under 200 km (which represent 85% of all the distance traveled in the USA, (Klinger and Kuzmyak, 1984) reduces the total energy consumption by 16% over the energy consumed by a vehicle that is always filled with LH₂.

Insulated pressure vessels also have much reduced evaporative losses compared to LH₂ tanks. This has been demonstrated in a previous work (Aceves and Berry, 1998), which presents a thorough analysis of evaporative losses in cryogenic pressure vessels based on the first law of thermodynamics. Figure 1 illustrates some of the main results. This figure shows hydrogen losses during vehicle operation. The figure assumes that two vehicles are fitted with cryogenic hydrogen storage tanks with the same capacity (5 kg). One vehicle has a low-pressure (0.5 MPa; 70 psia maximum) conventional liquid hydrogen tank, and the other has an insulated pressure vessel. The vehicles are identical in every respect, except for the tanks. The vessels are filled to full capacity with liquid hydrogen, and then the vehicles are driven a fixed distance every day. When the fuel runs out, the amount of fuel burned by the engine and the amount of fuel lost to evaporation are calculated, and the results are shown in Figure 1. The figure shows total cumulative evaporative hydrogen losses out of a full tank as a function of the daily driving distance, for a high-efficiency vehicle (34 km/l or 80 mpg gasoline equivalent fuel economy). As expected, evaporative losses increase as the daily driving distance is reduced, because less driving results in a longer time for hydrogen evaporation. The figure shows that a low-pressure LH₂ tank loses hydrogen even when driven 100 km per day. Losses from a LH₂ tank grow rapidly as the daily driving distance drops. A vehicle driven 50 km per day (the average for the USA, Aceves and Berry, 1998) loses almost 1 kg (20%) of the fuel to evaporation. On the other hand, insulated pressure vessels lose hydrogen only for very short daily driving distances (less than 5 km/day). Most vehicles are driven considerably more than this distance, so that most vehicles equipped with an insulated pressure vessel would never lose any hydrogen to evaporation.

The low losses in insulated pressure vessels are the result of the flow work (work required to extract the hydrogen from the vessel, VanWylen and Sonntag, 1978). The hydrogen stored in the vessel does work as the hydrogen is being extracted, cooling down in the process. This effect is very significant for hydrogen, due to its low molecular weight.

From an engineering and economic perspective, insulated pressure vessels strike a versatile balance between the cost and bulk of ambient-temperature CH₂ storage, and the energy efficiency, thermal insulation and evaporative losses of LH₂ storage.

Considering all the potential benefits of insulated pressure vessels, it is important to determine what type of pressure vessel could be operated at both high pressure and cryogenic temperature. Of the available pressure vessel technologies commonly used for vehicular storage of natural gas (Institute of Gas Technology, 1996), it appears that aluminum-lined, composite-wrapped vessels have the most desirable combination of properties for this application (low weight and affordable price). However, commercially available aluminum-composite pressure vessels are not designed for low temperature applications.

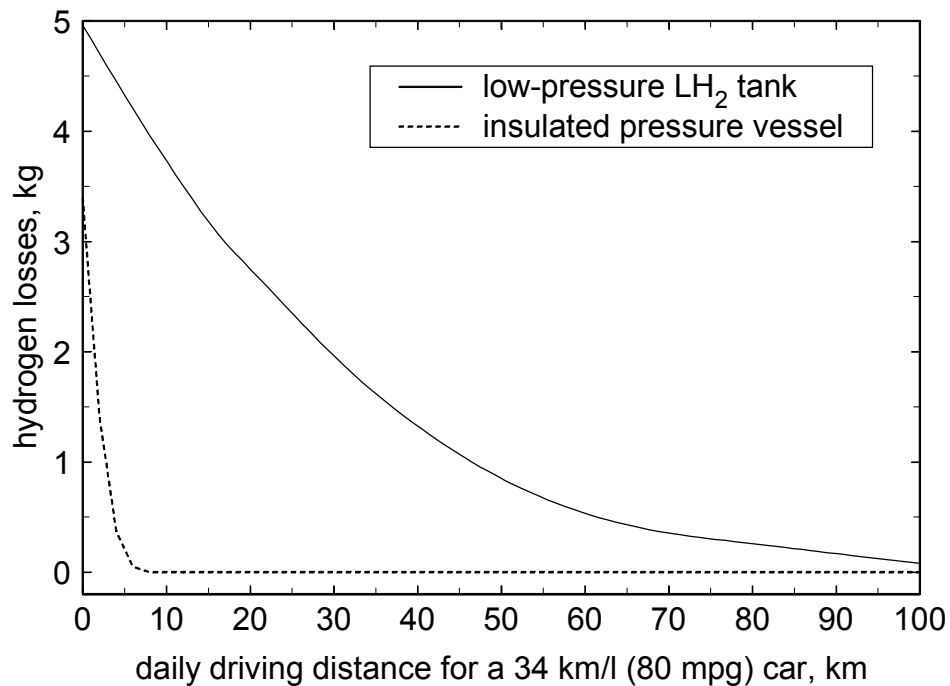


Figure 1. Cumulative hydrogen losses in kg as a function of daily driving distance, for vehicles with 17 km/liter (40 mpg); or 34 km/l (80 mpg) fuel economy, for two cryogenic hydrogen storage vessels.

This paper describes work in progress directed at evaluating the possibility of using commercially available aluminum-fiber pressure vessels at cryogenic temperatures and high pressures, as would be required for vehicular hydrogen storage in insulated pressure vessels. The paper gives a description of previous and ongoing tests, followed by future tests. The purpose of these tests is to demonstrate that no technical barriers exist that prevent the use of aluminum-fiber pressure vessels at cryogenic temperatures. As a future task, we are planning to generate a draft for a certification standard which will be submitted to the relevant administrative bodies (DOT, ISO) for their consideration and approval. Another planned activity is a demonstration project in which insulated pressure vessels will be installed and tested on two vehicles.

Completed Tests

Pressure and Temperature Cycling

Pressure vessels have been cycled through 900 high-pressure cycles and 100 low-temperature cycles. The cycles are alternated, running 9 pressure cycles followed by a temperature cycle, and

repeating this sequence 100 times. This test is expected to replicate what would happen if these vessels were used in a hydrogen-fueled car. Liquid nitrogen is used for low-temperature cycling and gaseous helium for high-pressure cycling. To accomplish the required testing, an experimental setup has been built inside a high-pressure cell. A schematic is shown in Figure 2. The valves shown in the schematic are controlled by computer, which allows the system to run with no supervision, resulting in fast cycling. An aramid-aluminum and a carbon fiber-aluminum pressure vessel have been cycled. The characteristics of these are listed in Table 1.

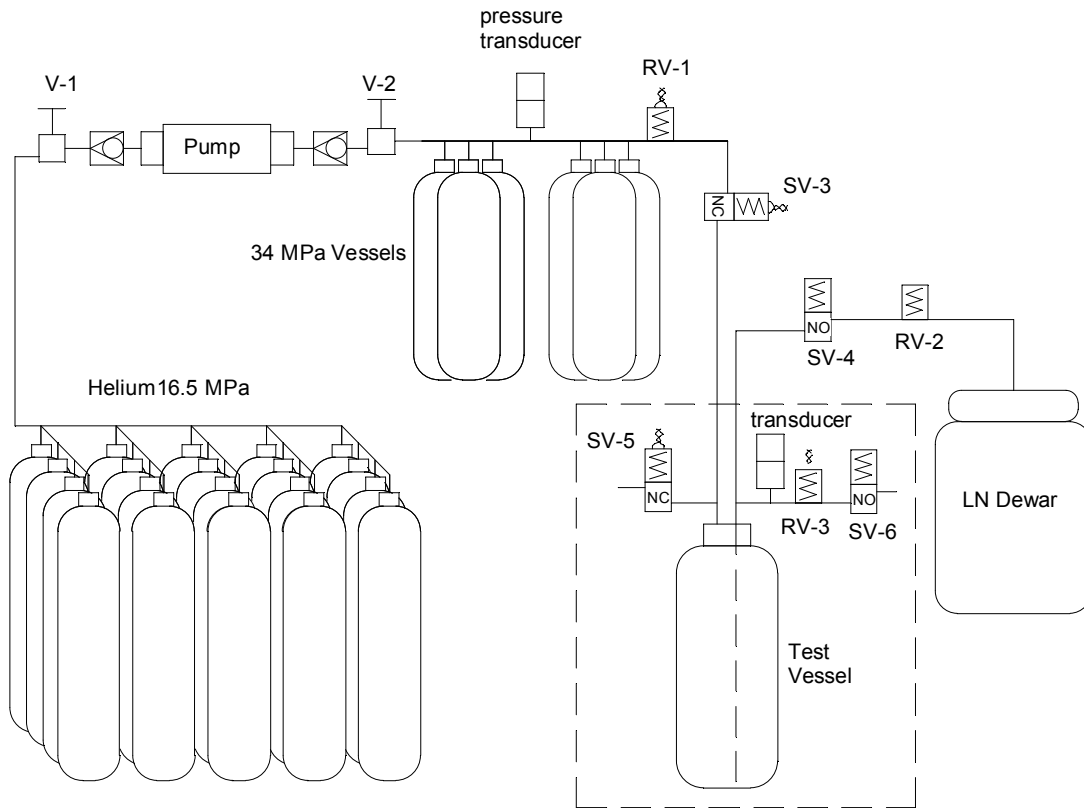


Figure 2. Schematic of the experimental setup for temperature and pressure cycling of pressure vessels.

Two cyclic tests have been completed, one on an aramid-aluminum pressure vessel and other on a carbon fiber-aluminum pressure vessel. The vessels have not failed during the test, and they have not shown superficial evidence of damage under observation. The carbon fiber-aluminum vessel was instrumented with strain gages in addition to the thermocouples and pressure sensor. Results from the strain gages will be used for validating the finite element analysis.

Burst Test

The aramid-aluminum and the carbon fiber-aluminum pressure vessels were burst-tested after being cycled and ultrasound-tested. The burst test was conducted according to the Code of Federal Regulations-Department of Transportation standards for pressure vessel certification

(CFR-DOT, 1996a). Figure 3 shows the variation of pressure as a function of time for the aramid-aluminum vessel. Failure occurred by hoop mid cylinder separation, which is the preferred mode of failure. The burst pressure was 94.2 MPa (13.7 ksi), which is substantially higher than the minimum burst pressure of 72.4 MPa (10.5 ksi). The very high value of the burst pressure compared to the minimum burst pressure may be due in part to work hardening that took place during the cold cycling of the vessel. The carbon fiber-aluminum also failed at a pressure higher than the minimum required.

Table 1. Characteristics of the Tested Hydrogen Vessels and Their Planned Insulation

	Aramid-Aluminum	Carbon Fiber-Aluminum
Mass of hydrogen stored, kg	1.13	0.44
Vessel weight, kg	10	4.1
Internal volume, liters	17.6	6.8
Internal diameter, m	0.2	0.17
Internal surface area, m ²	0.48	0.25
Design pressure, MPa (psi)	24.1 (3500)	31 (4500)
Performance factor ¹ , m (10 ⁶ in)	13000 (0.5)	13115 (0.51)
Safety factor	3.0	2.5

¹ defined as burst pressure*volume/weight.

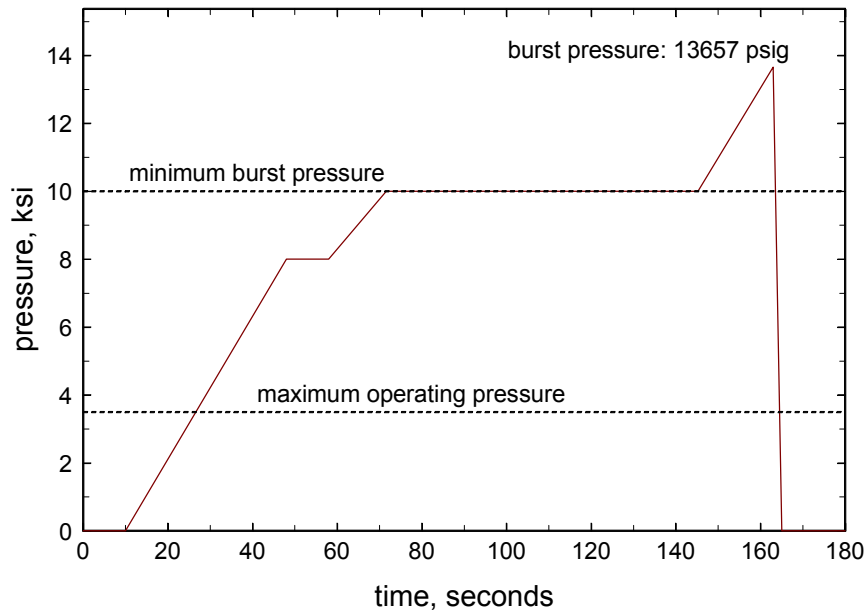


Figure 3. Pressure as a function of time during the burst test of the aluminum-lined, aramid-wrapped vessel. The burst pressure was 94.17 MPa (13657 psig).

Finite Element Analysis

Cyclic and burst testing of the pressure vessels has been complemented with a finite element analysis. The finite element analysis is done to determine whether low temperature operation can result in damage to the pressure vessel. Finite element analysis has been conducted with a commercial finite element package (ANSYS, Inc., 1999). A mesh has been developed. This is an axisymmetric mesh with 1195 elements. Sensitivity of the results to mesh resolution was tested by building a second mesh with 4234 elements. Little difference was observed between the Von Mises stresses obtained with the two grids. Physical properties of fiber-epoxy laminae were obtained from available literature at ambient and cryogenic temperatures (Reed and Golda, 1994, Morgan and Allred, 1989). Lamina properties are then converted into properties of the composite matrix. This is done by using a computer program (Hull and Clyne, 1996). This program assumes that the matrix is a homogeneous, orthotropic material. The properties of the matrix are then used in the finite element thermal and stress analysis.

Finite element analysis of the pressure vessel includes the manufacture of the pressure vessel, starting from the curing process and continuing with the autofrettage cycle. The autofrettage is a process in which the vessel is subjected to a high internal pressure (45.5 Mpa, 6600 psi, in this case) to introduce a level of plastic deformation and pre-stress. After the autofrettage, the vessel is subjected to a series of low temperature and high-pressure cycles. These are identical to the sequence used for the cyclic test of the pressure vessel, consisting of a cryogenic cycle, down to liquid nitrogen temperature and followed by nine pressure cycles up to the design pressure.

Figure 4 shows the results of the analysis for plastic deformation in the aluminum at two points. These points are located at the center of the cylindrical part of the tank. The figure shows that the autofrettage cycle introduces a high level of plastic deformation. The first few cryogenic cycles also introduce some plastic deformation in the liner. However, successive cryogenic cycles introduce less and less plastic deformation, until the plastic deformation asymptotes to a value slightly higher than 4%. Further cycles do not increase the level of plastic deformation, and therefore the pressure vessel is not expected to fail due to repeated cryogenic cycles. This is in agreement with the cryogenic cyclic tests, in which the vessels were subjected to 100 cryogenic cycles with no damage or failure.

Insulation Design and Insulated Pressure Vessel Construction

Insulated pressure vessels have been designed to operate with multilayer vacuum superinsulation (MLVSI). MLVSI has a good thermal performance only under a high vacuum, at a pressure lower than 0.01 Pa (7.5×10^{-5} mm Hg; Kaganer, 1969). Therefore, the use of MLVSI requires that an outer jacket be built around the vessel. Two designs for the insulation have been built: a first-generation design and a second-generation design. The first-generation vessel is a 1/5-scale vessel that stores about 1 kg of liquid hydrogen, and it is shown in Figure 5. This design has been built for cyclic testing and for DOT certification tests. The insulation design includes access for instrumentation for pressure, temperature and level, as well as safety devices to avoid a catastrophic failure in case the hydrogen leaks into the vacuum space. Five pressure vessels have been built according to the first-generation pressure vessel design. These vessels have been tested or will be soon tested for compliance with DOT/ISO certification standards.

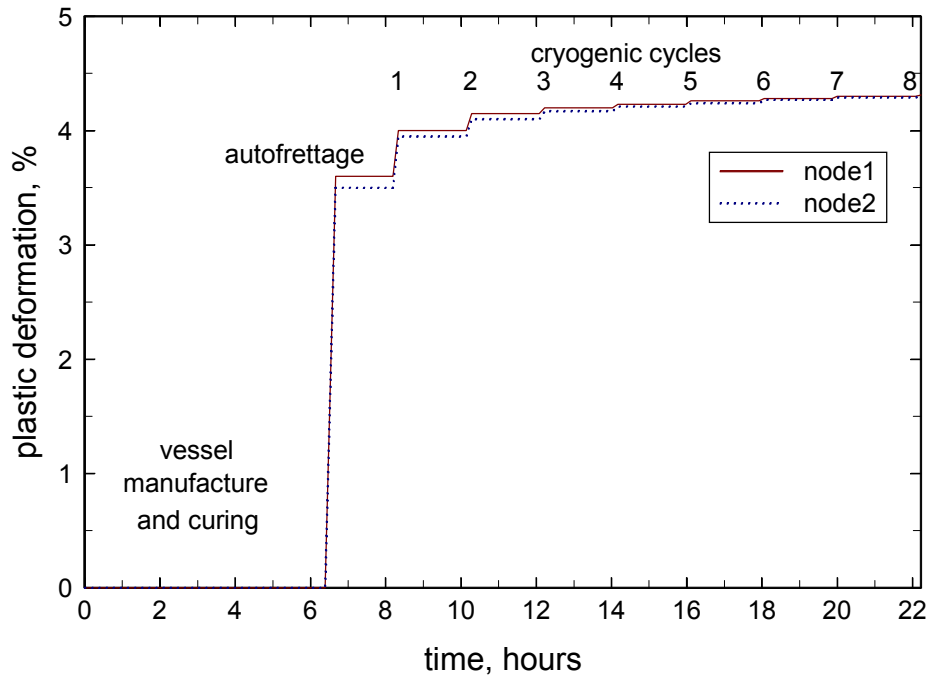


Figure 4. Plastic deformation obtained from the finite element analysis for two points in the aluminum liner. Nodes 1 and 2 are located at the center of the cylindrical part of the tank.

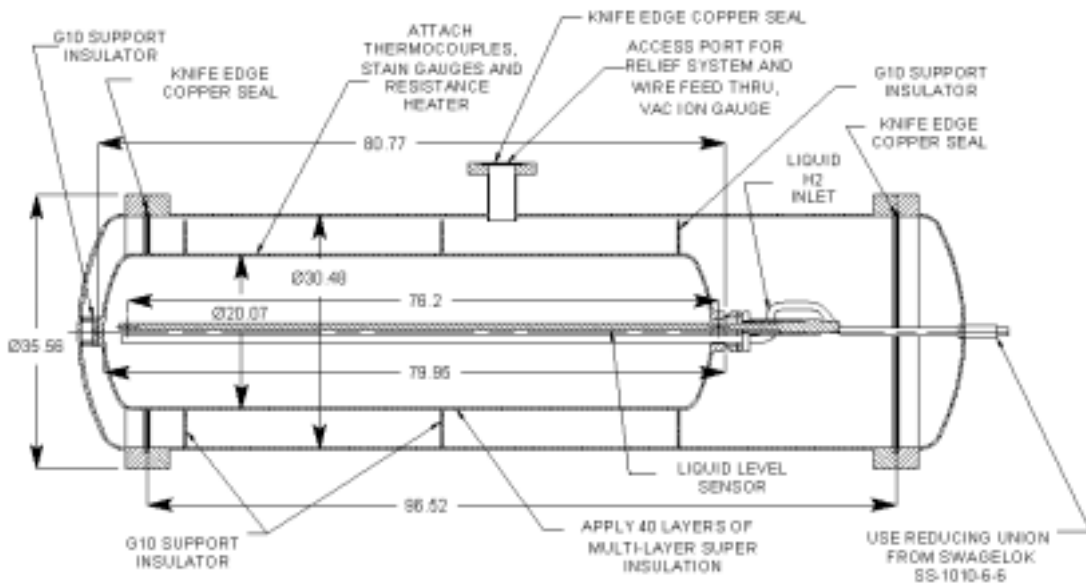


Figure 5. Insulation design for first-generation pressure vessel. The figure shows a vacuum space, for obtaining high thermal performance from the multilayer insulation, and instrumentation for pressure, temperature and level. Dimensions are given in cm.

The second-generation pressure vessel design is shown in Figure 6. This vessel can store about 6 kg of liquid hydrogen. This design includes a vapor shield to reduce evaporative losses in addition to the instrumentation and safety devices that exist in the first generation vessel. These vessels are currently being built. The second generation of pressure vessels will be used for DOT and SAE tests, and for incorporation into demonstration vehicles.

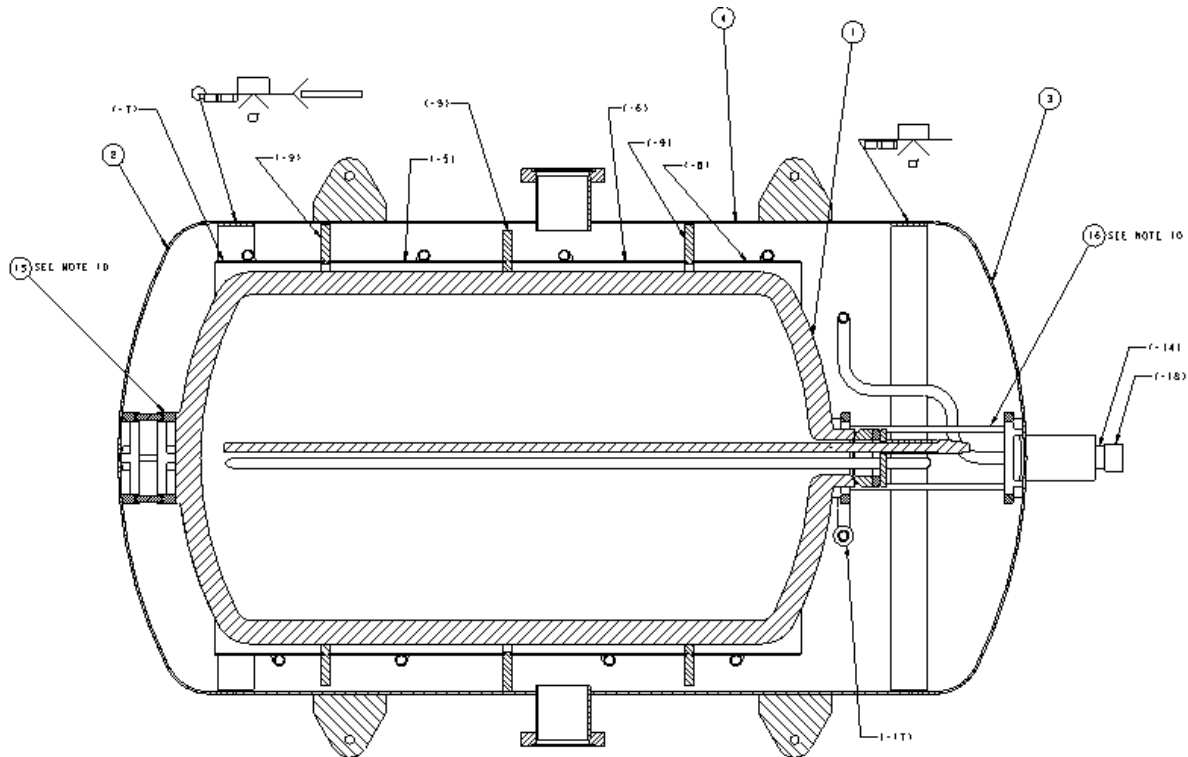


Figure 6. Insulation design for second-generation pressure vessel. The figure shows a vacuum space, for obtaining high thermal performance from the multilayer insulation, instrumentation for pressure, temperature and level, and a vapor shield for reducing hydrogen evaporative losses.

Cyclic Testing of Insulated Pressure Vessels

The insulated pressure vessels of the first generation (Figure 5) have been cycle tested. This is done to verify that the pressure vessel or the outer jacket does not develop leaks during repeated stresses that occur during cycling. One of these first-generation pressure vessels has been subjected to 1000 cycles, following the same procedure as previously used for the pressure vessels with no insulation (see “Pressure and Temperature Cycling” above). The remaining four first-generation pressure vessels have been subjected to a cold shock and pressure test before being subjected to DOT testing. The experimental setup for this test is the same as previously used for cyclic testing (Figure 2). The test procedure is as follows: The vessel is pressurized with

compressed helium to 1.2 times the Maximum Allowable Working Pressure (MAWP). The pressure is held for a minimum of 30 minutes. Then, the pressure vessel is shock conditioned by cycling it 3 times to low temperature with liquid nitrogen. Finally, The vessel is leak tested with helium to 0.25 times the MAWP. Any leakage detected with a mass spectrometer leak detector is unacceptable. The same shock conditioning test procedure will be used for the second-generation, full-size pressure vessel before being tested according to the DOT and the SAE standards.

Liquid and Gaseous Hydrogen Testing

A first-generation insulated pressure vessel has been tested with liquid and gaseous hydrogen. The vessel was first shock-tested and leak-tested. The insulated pressure vessel was then transported to a remote facility for testing with liquid hydrogen. Testing involved filling the vessel with LH₂ to study the insulation performance, the performance of the sensors, and the problems involved with pumping the LH₂ into the vessel. This test is expected to replicate what would happen to the vessel during fueling and operation in an LH₂-fueled car. The test was conducted successfully. There was no damage to the vessel due to the low temperature operation, all the instrumentation operated properly at the low temperature, and there was no hydrogen ignition or explosions.

DOT, ISO and SAE Certification Tests

Along with the cryogenic cyclic tests and the finite element analysis, the insulated pressure vessels are being subjected to certification tests according to the standards set by the Department of Transportation (DOT), the International Standards Organization (ISO) and the Society of Automotive Engineers (SAE). A list of the tests that may be relevant to insulated pressure vessels has been generated, and so far five of the certification tests have been successfully completed with first-generation insulated pressure vessels (shown in Figure 5). The selected tests are listed next. The list also describes which tests have been completed and which are in progress.

- Cycling, ambient temperature. 10000 cycles from less than 10% of the service pressure to the service pressure, 10 cycles per minute maximum (CFR-DOT, Title 49, 1996a). Each test cylinder must withstand the cycling pressurization test without any evidence of visually observable damage, distortion, or leakage. This test has been successfully completed.
- Cycling, environmental. 10 cycles per minute maximum. 1) 5000 cycles from zero to service pressure with tank at 60°C (140°F) and air at ambient temperature and 95% humidity, 2) 5000 cycles from zero to service pressure with tank at -51.1°C (-60°F) and air at ambient temperature, 3) 30 cycles from zero to service pressure, ambient conditions 4) burst test the cycled vessel (CFR-DOT, Title 49, 1996a). Each test cylinder must withstand the cycling pressurization test without any evidence of visually observable damage, distortion, or leakage. This test has been successfully completed.

- Cycling, Thermal. 10 cycles per minute maximum. 1) 10 000 cycles from zero to service pressure at ambient temperature, 2) 20 thermal cycles with tank temperature varying from 93.3°C (200°F) to -51.1°C (-60°F) at service pressure, 3) burst test the cycled vessel (CFR-DOT, Title 49, 1996a). Each test cylinder must withstand the cycling pressurization test without any evidence of visually observable damage, distortion, or leakage. This test has been successfully completed.
- Gunfire. Pressurize vessel with air or nitrogen to service pressure, and impact the vessel with a 0.30 caliber armor-piercing projectile with a speed of 853 m/s (2800 ft/s). The cylinder is positioned in such a way that the impact point is in the cylinder side wall at a 45° angle with respect to the longitudinal axis of the cylinder. The distance from the firing location to the cylinder may not exceed 45.7 meters (150 feet) (CFR-DOT, Title 49, 1996a). The cylinder shall not fail by fragmentation. This test has been successfully completed.
- Bonfire. Pressurize cylinder with air or nitrogen to service pressure. Set pressure relief devices to discharge at 83% of the cylinder test pressure. The cylinder shall be exposed to fire until the gas is fully vented. The temperature measured on the surface tank exposed to the fire has to be between 850 and 900°C (CFR-DOT, Title 49, 1996a; ISO, 1999). The venting of the gas must be predominantly through the pressure relief device.
- Drop Test from 3 m (10 ft). 1) The cylinder is dropped vertically onto the end, 2) the cylinder is dropped horizontally onto the side wall, 3) the cylinder is dropped onto a 3.8 x 0.48 cm (1 ½ x 3/16 inch) piece of angle iron, 4) after the drops, the vessel is cycled over 1000 pressure cycles from 10% of service pressure to the service pressure, at 10 cycles per minute (CFR-DOT, Title 49, 1996; ISO, 1999). The cylinder then has to be burst tested; the burst pressure of this vessel has to be at least 90 % of the minimum burst pressure.
- Drop tests from 10 m and 3 m. 1) Drop from 10 m. The drop test subjects a full-size vehicle fuel tank to a free-fall impact onto an unyielding surface from a height of 10 m. The fuel tank is released by firing one or more explosive cable cutters simultaneously. The fuel tank impacts the outer shell on the critical area as determined by the manufacturer. The fuel tank is filled with an equivalent full weight of liquid nitrogen saturated to at least 50% of the maximum allowable working pressure of the fuel tank. 2) Drop from 3 m. The drop test subjects a full-size vehicle fuel tank to a free-fall impact onto an unyielding surface from a height of 3 m. The fuel tank is released by firing one or more explosive cable cutters simultaneously. The fuel tank impacts the outer shell on the critical area as determined by the manufacturer. The fuel tank is filled with an equivalent full weight of liquid nitrogen saturated to at least 50% of the maximum allowable working pressure of the fuel tank (SAE J2343, 1997). There shall be no loss of product for a period of 1 hour after the drop other than relief valve operation and loss of vapor between the filler neck and the secondary relief valve in the case of a test involving the filler neck. Loss of vacuum, denting of the vessel, piping and piping protection, and damage to the support system are acceptable.

- Flame test. The tank should contain an equivalent full level of liquid nitrogen saturated at one half the maximum allowable working pressure (MAWP). The tank should be inverted and subjected to an external temperature of 538°C (1000°F) for 20 minutes without the vessel reaching relief pressure (SAE J2343, 1997).

Additional plans include the installation of insulated pressure vessels into demonstration hydrogen-powered vehicles. For this application, the NFPA (NFPA 57, 1996; NFPA 52, 1998), and CFR-DOT (Title 49, 1996) standards will be reviewed to prepare the required tests to guarantee the safety of the operation. Future work will also focus on developing a testing procedure for achieving certification of insulated pressure vessels.

Conclusions

Insulated pressure vessels are being developed as an alternative technology for storage of hydrogen in light-duty vehicles. Insulated pressure vessels can be fueled with either liquid hydrogen or compressed hydrogen. This flexibility results in advantages compared to conventional hydrogen storage technologies. Insulated pressure vessels are lighter than hydrides, more compact than ambient-temperature pressure vessels, and require less energy for liquefaction and have less evaporative losses than liquid hydrogen tanks.

For reduced cost and complexity it is desirable to use commercially available aluminum-fiber pressure vessels for insulated pressure vessels. However, commercially available pressure vessels are not designed for operation at cryogenic temperature. A series of tests has been carried out to verify that commercially available pressure vessels can be operated at cryogenic temperature with no performance losses. All analysis and experiments to date indicate that no significant damage has resulted. Future activities also include a demonstration project in which the insulated pressure vessels will be installed and tested on two vehicles. A draft standard will also be generated for obtaining certification for insulated pressure vessels.

Acknowledgments

This project is funded by the DOE Hydrogen Program, Sig Gronich and Neil Rossmeisl, Program Managers. Work performed under the auspices of the U.S. Department of Energy by University of California Lawrence Livermore National Laboratory under Contract W-7405-ENG-48.

References

Aceves, S. M., Berry, G.D., 1998, "Thermodynamics of Insulated Pressure Vessels for Vehicular Hydrogen Storage," ASME Journal of Energy Resources Technology, June, Vol. 120, pp. 137-142.

ANSYS, Inc., 1999, "ANSYS Version 5.6 Technical Handbook," Canonsburg, PA.

Baur L., 1995, "Composite Pressure Vessel with Metal Liner for Compressed Hydrogen Storage," Proceedings of the 1st IEA Workshop on Fuel Processing for Polymer Electrolyte Fuel Cells, Paul Scherrer Institut, Villigen, Switzerland, International Energy Agency, Swiss Federal Office of Energy, September 25-27, 1995, p. 45-69.

Braess, H.H., and Strobl, W., 1996, "Hydrogen as a Fuel for Road Transport of the Future: Possibilities and Prerequisites," Proceedings of the 11th World Hydrogen Energy Conference, Stuttgart, Germany.

Code of Federal Regulations, Department of Transportation (CFR-DOT), 1996a, "Basic Requirements for Fully Wrapped Fiber Reinforced Aluminum Lined Cylinders," Title 49, CFR 107.105 Standard.

Hettinger, W. Michel, F., Ott, P., and Theissen, F., 1996, "Refueling Equipment for Liquid Hydrogen Vehicles," Proceedings of the 11th World Hydrogen Energy Conference, Stuttgart, Germany, pp. 1135-1143.

Hull, D., and Clyne, T.W., 1996, "An Introduction to Composite Materials," Cambridge University Press, Cambridge, Great Britain.

Institute of Gas Technology, 1996, "Compressed Natural Gas Storage Optimization for Natural Gas Vehicles," Gas Research Institute Report GRI-96/0364, Des Plaines, IL.

International Standards Organization (ISO), 1999, "Gas Cylinders – High Pressure Cylinders for the on-Board Storage of Natural Gas as a Fuel for Automotive Vehicles," ISO Standard ISO/FDIS 11439:ccyy(E).

Kaganer, M.G., 1969, "Thermal Insulation in Cryogenic Engineering," Israel Program for Scientific Translation Ltd., Jerusalem, Israel.

Klinger, D., Kuzmyak JR., 1984, "Personal Travel in the United States," Vol. 1, 1983-1984, Nationwide Personal Transportation Study, Report PB89-235378, prepared for the US Department of Transportation, Office of Highway Information Management, Washington, DC.

Michel, F., Fieseler, H., Meyer, G., and Theissen, F., 1996, "Onboard Equipment for Liquid Hydrogen Vehicles," Proceedings of the 11th World Hydrogen Energy Conference, Stuttgart, Germany, pp. 1063-1077.

Morgan, R.J. and Allred, R.E., 1989, "Aramid fiber reinforcements," in "Reference Book for Composite Technology," Edited by Lee, S.M., pp. 143-166, Technomic Publishing, Lancaster, PA.

National Fire Protection Association (NFPA), 1998, "NFPA 52: Compressed Natural Gas (CNG) Vehicular Fuel System Code," Quincy, MA.

National Fire Protection Association (NFPA), 1996, "NFPA 57: Liquefied Natural Gas (LNG) Vehicular Fuel System Code," Quincy, MA.

Pehr, K., 1996a, "Experimental Examinations on the Worst Case Behavior of LH₂/LNG Tanks for Passenger Cars," Proceedings of the 11th World Hydrogen Energy Conference, Stuttgart, Germany.

Pehr, K., 1996b, "Aspects of Safety and Acceptance of LH₂ Tank Systems in Passenger Cars," International Journal of Hydrogen Energy, Vol. 21, pp. 387-395.

Pentastar Electronics, 1997, "Direct-Hydrogen-Fueled Proton-Exchange-Membrane Fuel Cell System for Transportation Applications, Conceptual Design Report," Report DOE/CE/50390-9,

prepared for U.S. Department of Energy, Office of Transportation Technologies, under contract DE-AC02-94CE50390.

Peschka, W., 1992, "Liquid Hydrogen, Fuel of the Future," Springer-Verlag, Vienna, Austria.

Reed, R.P., and Golda, M., 1994, "Cryogenic Properties of Unidirectional Composites," *Cryogenics*, Vol. 34, No. 11, pp. 909-928.

Society of Automotive Engineers (SAE), 1997, "Recommended Practices for LNG Powered Heavy-Duty Trucks," SAE.J2343.

Wetzel, F.J., 1996, "Handling of Liquid Hydrogen at Filling Stations," Proceedings of the 11th World Hydrogen Energy Conference, Stuttgart, Germany, pp. 1123-1134.

ADVANCED THERMAL HYDROGEN COMPRESSION

**Mark Golben
David H. DaCosta
Ergenics, Inc.
247 Margaret King Avenue
Ringwood, NJ 07456**

Abstract

Ergenics, Inc. is developing a novel thermal hydrogen compressor that operates in conjunction with advanced hydrogen production technologies and improves the efficiency and economics of the compression and hydrogen utilization process. The thermal compressor is an absorption-based system that uses the properties of reversible metal hydride alloys to silently and cleanly compress hydrogen; hydrogen is absorbed into an alloy bed at ambient temperature and, subsequently, is released at elevated pressure when the bed is heated with hot water. Compression energy can be supplied by waste heat or solar hot water. Two recent innovations strongly suggest that thermal compressors can be used for non-pure hydrogen streams likely to result from advanced production methods. The first involves a combination of processes that permit the absorption of impure hydrogen streams by hydride alloys. It may be possible to employ these processes to remove contaminants that may damage fuel cells or advanced storage materials located downstream from the compressor. The second innovation is a modular alloy bed design that permits rapid hydrogen absorption kinetics, enabling a reduction in compressor size with an associated reduction in capital cost. The results of an investigation into the feasibility of integrating purification processes with thermal compression is presented in this paper, along with engineering design considerations for miniature modular hydride heat exchangers. Preliminary data from thermal compressor tests at 5,000 psig outlet pressure are included.

Introduction

Ergenics is investigating the application of its novel thermal hydrogen compression process to hydrogen produced from renewable resources. Thermal hydrogen compressors have offered significant operational and economic advantages over traditional mechanical compressors when the hydrogen is pure and flow rates are relatively low. However, hydrogen produced from renewable resources can contain impurities that might damage a thermal compressor and, if thermal compressors are to play a major role as hydrogen becomes an increasingly important part of America's energy supply, increased flow rate capabilities must be economical. In addition, new storage systems require hydrogen pressures of 5,000 to 10,000 psig, much higher than the current industrial practice of 3,600 psig.

The thermal compressor is an absorption-based system that uses reversible metal hydride alloys to silently and cleanly increase hydrogen pressure. Previously, reversible metal hydride alloys would sustain damage from hydrogen impurities at low levels of <50 ppm. Ergenics has developed three processes that may permit hydride alloy beds to tolerate higher levels of impurities, in some cases up to 10,000 ppm or more. Passive Purification is used for water vapor and oxygen, Elevated Temperature Desorption is used for CO and CO₂, and Automatic Venting can clear inert gas blanketing caused by N₂ and CH₄. Employing these processes in a thermal compressor may assure long operational life.

A secondary benefit could be realized if the purification processes would not only protect the compressor from contaminant-caused damage, but also remove contaminants that damage or degrade performance of downstream equipment. For example, carbon monoxide can damage electrode catalyst in PEM fuel cells. Combining compression with purification can potentially increase fuel cell performance and extend fuel cell electrode life. There is even the potential to use compression with purification to resolve system-level issues that may be encountered with new, high energy density hydrogen storage materials currently under development. Some of these new materials must be charged at elevated pressure and may be sensitive to impurities.

In work reported last year (DaCosta 2000), Ergenics accomplished the following tasks:

- we classified the hydrogen composition and operating conditions expected to result from various advanced production techniques to determine which processes would be good candidates for thermal compression;
- we identified the three techniques that can mitigate the effect that impurities have on thermal compressor operation; and
- we prepared a preliminary design for a 3,600 psig, 2,000 scfh refueling station thermal compressor, compared the thermal compressor with a mechanical compressor and performed a hazardous operation analysis.

Subsequent investigation focused on using a thermal compressor to provide the dual function of compression and purification to mitigate fuel cell degradation from CO. We developed a correlation for CO removal that can be used to optimize hydrogen compressor/fuel cell systems.

Thermal hydrogen compressors have been limited to applications with relatively low flow rates (<400 scfh) due to heat transfer limitations associated with large alloy beds. In order to permit economical scale-up to production-sized units competitively superior to mechanical compressors, Ergenics has developed and patented an advanced hydride bed design with rapid heat transfer capabilities. The hydride bed is essentially a miniature high surface area hydride heat exchanger, which permits the construction of large compressors of small size and cost. The small hydride beds can be thermally cycled at a rapid rate (≈ 2 minutes) in order to process high hydrogen flow rates. The unique hydride heat exchanger design is modular and lends itself to high-volume, low-cost production.

The emerging need to compress hydrogen beyond the current industrial practice of 3,600 psig provides additional incentive to develop thermal compression, in order to obviate increased maintenance associated with mechanical compressors operating at such high pressures. Alloy development and tests to verify the ability of hydride alloys to function in the 5,000 psia range and beyond have commenced.

Thermal Compressor Purification Processes

Impurity Effects on Hydride Alloys

Gaseous impurities expected to appear in hydrogen produced from renewable resources include the “usual subjects” - water vapor, air (including oxygen, nitrogen, and argon), carbon monoxide, carbon dioxide, and methane (DaCosta 2000). Impurities interact with hydride alloys with varying effects (Sandrock 1984), as follows:

- *Poisoning* results in a rapid decrease in hydrogen capacity with cycling. Damage from poisoning tends to be localized on the alloy particle surface, so it is often possible to restore performance with little, if any, loss in capacity. Oxygen and CO are impurities that poison alloys.
- *Retardation* is manifested by a reduction in absorption kinetics without loss in ultimate capacity. With enough time, full capacity can be achieved. Retardation is often a result of impure species forming weak bonds on the alloy surface that impede hydrogen absorption. Carbon monoxide and water vapor retard hydriding.
- *Reaction* causes irreversible capacity loss through bulk corrosion of the alloy. Reaction results in the formation of very stable chemical compositions that do not reversibly hydride and cannot be easily returned to their original state. Active sulfur compounds such as SO₂ cause irreversible damage due to the reaction mechanism.
- *Innocuous Blanketing* results from impure gas species congregating on the alloy surface and forming a blanket that reduces the rate of hydrogen absorption. Gases that cause blanketing, such as nitrogen and methane, are easily removed by venting.

Purification Processes for Use With a Thermal Compressor

Ergenics has developed three processes, summarized in Table 1, that permit hydride alloy beds to tolerate higher levels of impurities.

Table 1. Thermal Compressor Purification Processes

Impurity	Process	Comments
H ₂ O, O ₂	Passive Purification	Hydride Heat Exchanger in-situ process prevents retardation and poisoning. Removes O ₂ from hydrogen.
CO, CO ₂	Elevated Temperature Desorption	115°C desorption removes CO impurities from alloy surface.
N ₂ , Ar, CH ₄	Automatic Venting	Clears inert gas blanketing and removes impurity from hydrogen.

Water Vapor and Oxygen

Water vapor is the most common contaminant in hydrogen. It affects hydride alloys through the mechanisms of retardation followed by poisoning. When hydrogen absorption begins, water vapor is carried towards the alloy surface by the hydrogen. The water molecules gather and become concentrated on the alloy surface, slowing the passage of hydrogen to the alloy (retardation).

Hydride alloys contain nickel, which normally acts as a dissociation catalyst for hydrogen molecules prior to absorption. The nickel can also act as a weak catalyst for dissociating water molecules. As water molecules are dissociated at the surface of the alloy particles, the resulting hydrogen would be absorbed into the alloy, but oxygen tends to react with the rare earth element (lanthanum or mischmetal), forming a stable oxide that is no longer available to hold hydrogen. Hydrogen absorption capacity decreases (poisoning).

Nickel-metal hydride battery alloy development by Ergenics and others stimulated a large body of research into the corrosion of hydride electrodes immersed in electrolytes. A number of corrosion inhibiting additives, such as cobalt and tin, have been identified for immersed alloys, and we have found these to have positive impact on preventing poisoning in gaseous systems as well.

Ergenics has developed a method of removing water vapor and oxygen from hydrogen within a hydride alloy bed (Golben 1999). This in situ purification process permits the alloy to operate as if it was absorbing clean, dry hydrogen. Named “Passive Purification,” the process includes catalytic recombination of oxygen impurities, physical water removal and the use of corrosion inhibitors in the alloy formulation. During desorption of dry hydrogen from the alloy, water that was removed during the absorption process is evaporated into the hydrogen as it exits the bed. The Passive Purification process successfully permits cycling hydride alloys with hydrogen that is saturated with water vapor and contains some oxygen.

Carbon Monoxide and Carbon Dioxide

It has been suggested that a single monolayer of CO and, to a lesser degree, CO₂ prevents hydrogen absorption into hydride alloys, probably by forming Ni-carbonyl bonds on the alloy surface that deactivate the dissociative properties of the nickel (Sandrock 1997). Figure 1 shows the effect of cycling LaNi₅ alloy in hydrogen contaminated with CO. Interestingly, there is

almost no degradation of performance cycling at a temperature of 115°C. This suggests that an elevated temperature desorption can remove the CO molecule from the alloy to restore full performance. More importantly, the CO can be vented during this desorption process and removed from the hydrogen stream. CO removal may prolong the life of catalysts used in fuel cells or other downstream equipment.

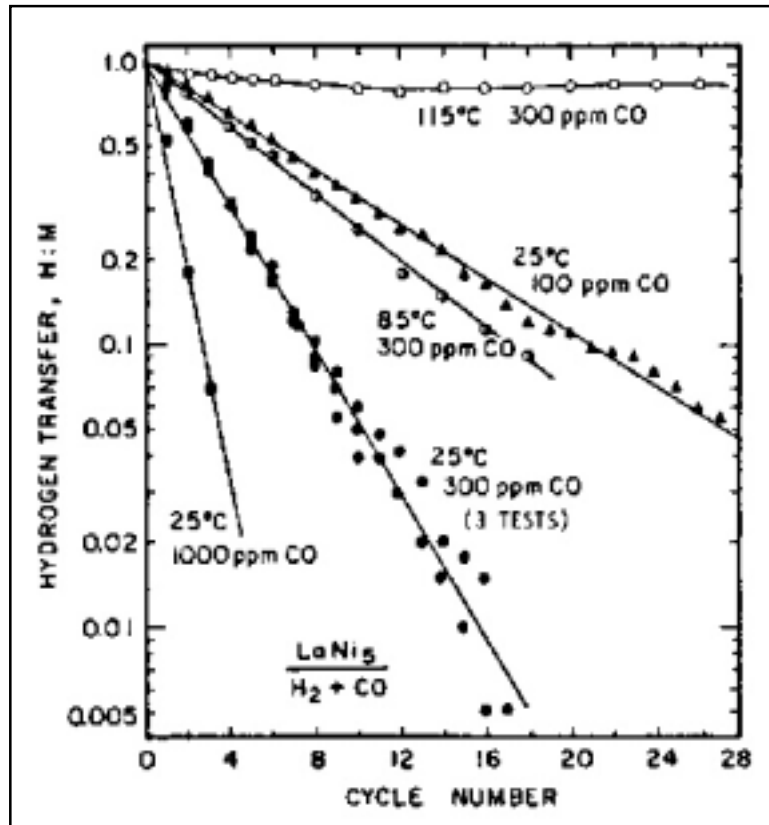


Figure 1: Elevated temperature desorption removes CO from LaNi₅ hydride alloy. (Eisenberg 1983)

When CO is vented, the hydrogen required to sweep it away will be lost. Ergenics has calculated a relationship between the CO inlet concentration, the CO outlet concentration and the quantity of hydrogen that will be vented in the process. A curve that shows this relationship for an outlet hydrogen purity of 99.999% (10 ppm CO) appears in Figure 2. From this data, it will be possible to predict optimal conditions for a compressor/fuel cell system. The thermal compressor venting process can be fine-tuned to remove enough CO to prolong fuel cell catalyst life, but prevent excessive venting of hydrogen fuel.

Nitrogen and Methane

Nitrogen, methane, noble gases, and ammonia do not react with hydride alloys, but if present in enough quantity, can form an innocuous blanket, that reduces the rate of the hydrogen absorption to a crawl. During a desorption cycle, hydrogen can be used to sweep away impurities that cause innocuous blanketing. In a similar fashion to elevated temperature desorption suggested for CO

removal, these gases can be either removed from the hydrogen stream by an automatic venting process or be allowed to pass through the compressor.

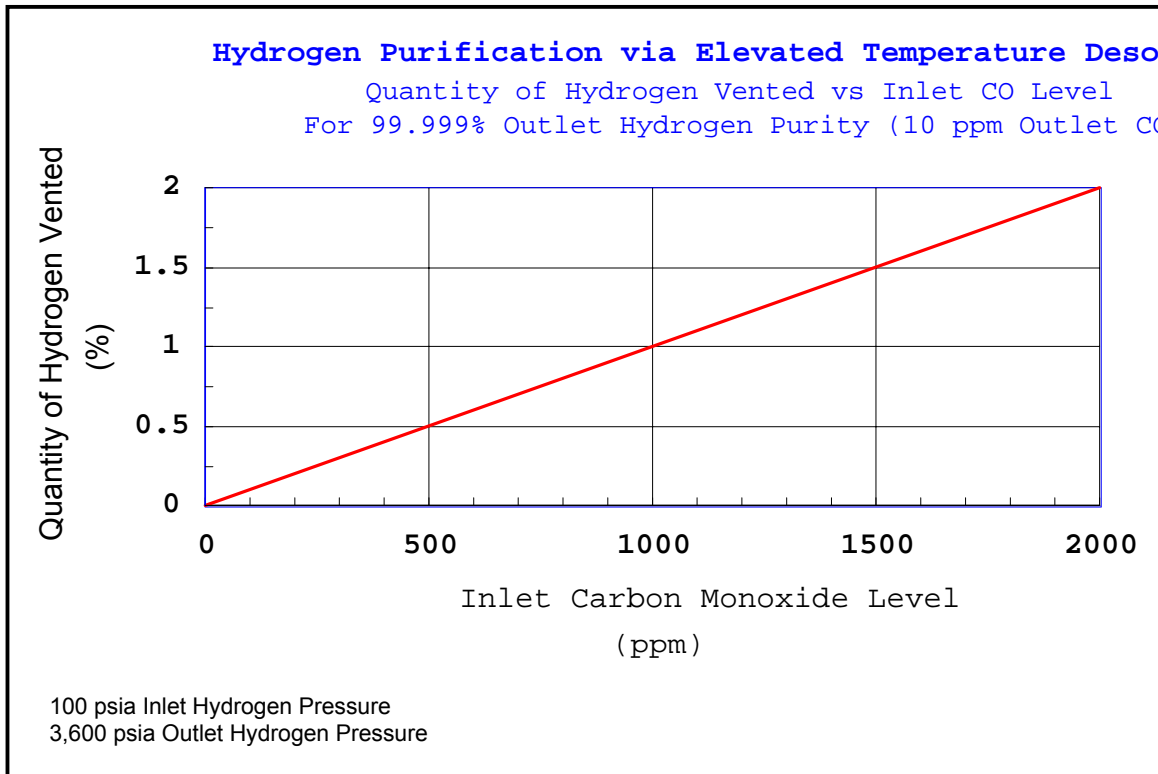


Figure 2: Thermal compressors can remove CO from hydrogen to protect fuel cell catalyst.

Miniature Modular Hydride Heat Exchangers

In order to process the higher flow rates of hydrogen expected from advanced production processes, Ergenics has developed and patented an advanced hydride bed design with rapid heat transfer capabilities. The hydride bed is essentially a miniature high surface area hydride heat exchanger, which permits the construction of large compressors of small size and cost. The small hydride beds can be thermally cycled at a rapid rate (≈ 2 minutes) in order to process high hydrogen flow rates.

Two miniature heat exchanger configurations have been developed. The first resembles a conventional shell and tube heat exchanger with hydrogen and hydride alloy contained within stainless steel tubes and a water-ethylene glycol mix on the shell side (Figure 3). The shell is constructed of 2-inch diameter copper tubing with an expander at one end that mates with a 3-inch diameter stainless tube sheet. The heat exchanger contains approximately one hundred (100) 0.125-inch diameter, Type 304L stainless steel tubes. The hydrogen process boundary is

of all-welded construction. This configuration was selected for the initial thermal compressor design.

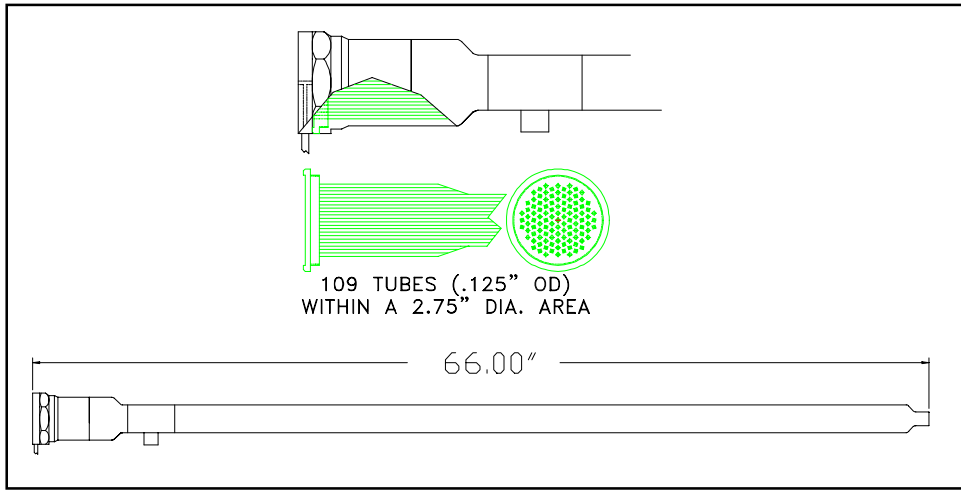


Figure 3: All-welded miniature hydride heat exchanger reduces compressor size and cost.

The second heat exchanger configuration employs Ergenics' ring manifold design, which permits a higher density tube arrangement for reduced size and weight (Figure 4). The tubes are joined to the central manifold via brazing. The ring manifold heat exchanger is the key to smaller and more cost effective compressors when production volumes increase.

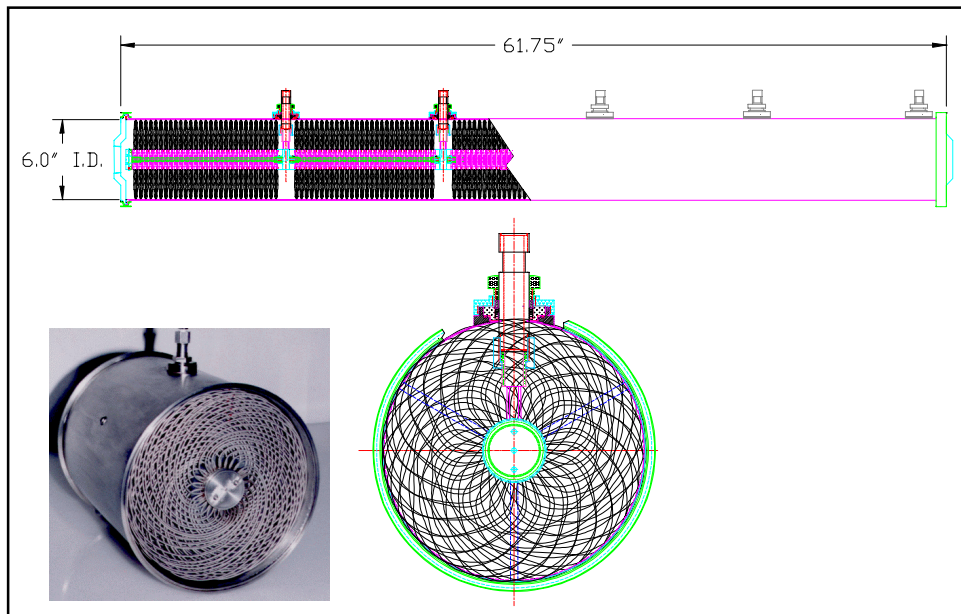


Figure 4: Compact ring manifold hydride bed showing five stages in a single shell will further reduce size and cost. Inset shows a typical ring manifold heat exchanger.

Operation to 5,000 psig

In a privately-funded project, Ergenics built a single-stage, electrically-heated compressor with the following performance characteristics:

Inlet P - 300 psig
Outlet P - 5,000 psig
Inlet Flow - 5.5 std. l/m continuous
Outlet Flow- 5.5 std. l/m average

The compressor employs a miniature hydride heat exchanger measuring 4 inches in diameter by 10 inches long depicted in Figure 5. Hydride alloy is contained within 0.125-inch diameter Inconel tubes. The heat exchanger is placed within an electrically heated furnace, which is cooled with ambient temperature air from a fan during absorption and periodically heated to 400°C to compress and release hydrogen. The hydride alloy was extensively tested after “soaking” at high pressure and temperature, with no disproportionation detected. (Disproportionation occurs when the elemental constituents of an alloy diffuse together and form stable, non-reversible hydrides.) Cycle time for absorption and desorption is relatively long at 16 minutes, because of heat transfer inefficiencies associated with air heating and cooling (rather than water).



Figure 5: Miniature Hydride Heat Exchanger for 5,000 psig Operation

A metal hydride inlet accumulator vessel accepts a continuous flow of inlet hydrogen at 300 psig. Periodically, hydrogen flows from the accumulator to the hydride heat exchanger during the absorption cycle.

Figure 6 plots furnace temperature, hydrogen pressure and outlet flow rate vs time for four thermal cycles. Outlet pressure was regulated by a valve. After each heating cycle, pressure was manually vented to 300 psig, accounting for the flow rate spikes at 1200, 2100, 3000 and 4000 seconds. During one test, pressure was increased to 6,000 psig. Testing of the electrically heated thermal compressor proved that hydrogen outlet pressures of over 5,000 psig are achievable with this technology. Achieving very high pressures in a multi-stage thermal compressor that uses only hot water as the energy source is a goal of our future work.

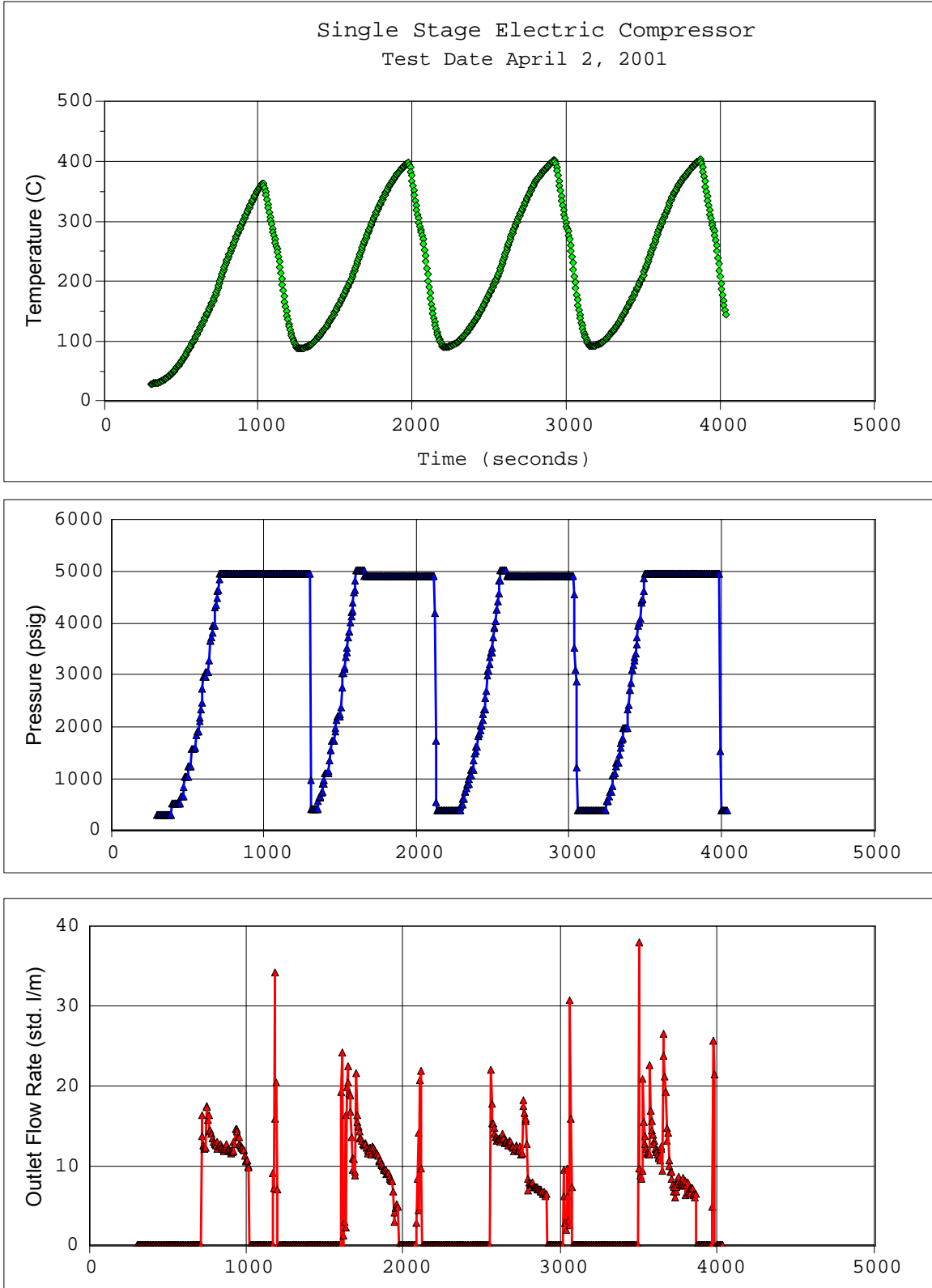


Figure 6: Thermal Compressor Operation at 5,000 psig

Future Work

Removing or Tolerating Impure Gas Species

In order to validate the conclusions reached to date, we plan to construct and demonstrate a single-stage thermal compressor that employs a miniature hydride heat exchanger and an associated test apparatus that will verify thermal compressor performance while processing hydrogen with impure gas species. The test apparatus will be flexible enough to vary inlet impurity levels to determine threshold contamination levels (levels at which compressor performance is affected). Three purification technologies will be demonstrated: passive purification for oxygen and water, inert gas purification, and elevated temperature desorption for CO and CO₂.

Compression with Purification

For impurities that can adversely affect fuel cell operation (e.g. nitrogen, CO), outlet hydrogen purity will be monitored to verify the degree to which a thermal compressor can perform the dual function of compressing and purifying hydrogen. This will allow the evaluation of trade-offs between hydrogen purity and compressor and fuel cell operating efficiencies necessary for the design and integration of full-scale systems.

Operation over 5,000 psig in a multi-stage, hot-water-powered compressor

For high pressure operation over 5,000 psig, a suitable last-stage hydride alloy must be engineered and tested for long-term stability in the very high pressure environment. While anticipated operating temperatures of 90 to 110°C are modest for typical alloys, long term “soak” tests at pressures over 5,000 psig are warranted to assure alloy disproportionation is not encountered.

Process Validation

The entire thermal compression process will be validated in a pilot-scale system that includes both the single stage (first stage) used for purification studies and subsequent stages needed to boost hydrogen pressure to over 5,000 psig. The flow rate capability of the pilot-scale system will be similar to that required for overnight refueling of a hydrogen fuel cell automobile.

Acknowledgement

This material is based on work partially funded by the United States Department Of Energy’s Hydrogen Program under Cooperative Agreement No. DE-FC36-99GO10448.

References

DaCosta, David H. 2000. “Advanced Thermal Hydrogen Compression.” In *Proceedings of the 2000 U.S. DOE Hydrogen Program Review*, 720-727. San Ramon, CA: NREL/CP-570-28890.

Eisenberg, F.G., Goodell, P.D. 1983. "Cyclic Response Of Reversible Hydriding Alloys In Hydrogen Containing Carbon Monoxide." *Journal of Less-Common Metals* 89: 55-62.

Golben, M., DaCosta, D.H. 1999. "Advanced Thermal Hydrogen Compression." In *Proceedings of the 34th Intersociety Energy Conversion Engineering Conference*. Warrendale, PA: SAE International.

Sandrock, G.D. 1997. "State of the Art Review of Hydrogen Storage in Reversible Metal Hydrides for Military Fuel Cell Applications," Office of Naval Research. Ringwood NJ: SunaTech, Inc.

Sandrock, G.D.; Goodell, P.D. 1984. "Cyclic Life of Metal Hydrides with Impure Hydrogen: Overview and Engineering Considerations." *Journal of Less-Common Metals* 104, 159-173.

SMALL BATTERY – FUEL CELL ALTERNATIVE TECHNOLOGY DEVELOPMENT

**Mahlon S. Wilson, Christine Zawodzinski,
Materials Science and Technology Division, MS D429
Los Alamos National Laboratory, Los Alamos, NM 87545**

**Mark Daugherty
Enable Fuel Cell Corp. (DCH Technology, Inc.; www.dcht.com)
2120 W. Greenview Dr. #1, Middleton, WI 53562**

Abstract

Fuel cells are currently attracting significant publicity and attention for applications as diverse as transportation and cellular phones, yet they are probably still some years away from any sort of meaningful commercial utilization. In the effort described here, two general postulates are being followed in an attempt to increase the speed and probability of commercial success for fuel cells. The first axiom is that fuel cells need to be as simple as possible to compete against well-established and entrenched technologies. With simplicity comes reliability and low costs. To a large degree then, simplicity is more important than the absolute top performance that can be attained. The second premise is that the most vulnerable market for fuel cell penetration is the one occupied by batteries for relatively low power applications such as personal electronics, etc. While conventional batteries currently have a lock on such applications, they are expensive (often thousands of dollars per kilowatt – hour), have low energy densities and frequently contain environmentally suspect materials. With these issues in mind, for the past two years we have been developing “Air-Breather” fuel cells, which are exceedingly simple and most effective for small battery types of power levels. This year, in addition to further development and testing of air-breather fuel cell stacks and systems, we are also exploring approaches that address the fuel storage issues that may be the primary obstacles to commercialization.

Introduction

Depending upon the fuel storage technology, portable fuel cell systems can provide substantially higher energy densities than similar-sized battery packs and are typically much more environmentally benign. Correspondingly, interest in fuel cells for portable power applications is rapidly increasing and, in all likelihood, the first widespread consumer applications of hydrogen technologies will be in such portable fuel cells. Previously, the challenges introduced with fuel cell water management and/or fuel storage issues invariably resulted in discouragingly complex portable power systems. Where we thus primarily differ from most other portable power efforts is our emphasis that success will require the development of extremely simple fuel cells and systems. Simplicity beneficially influences cost, durability and reliability. A particularly simple and effective fuel cell system, the “air-breather,” was the basis for a Cooperative Research and Development Agreement (CRADA) between Los Alamos National Laboratory (LANL) and DCH Technology/Enable Fuel Cell Corporation covering the first two years of this project. The air-breather is a unique low-power portable fuel cell and system that can be sufficiently inexpensive and is reliable enough to eventually compete head-to-head with batteries in electronics-type applications. The advantage of this fuel cell system over previous fuel cell designs is that it is inherently stable and self-regulating without the need for peripherals such as cooling or reactant flow fans. It can operate effectively with no active humidification, no active cooling, and no pressurization or forced flow of the cathode air (Wilson 1996). More details on some of the systems under development and testing by Enable FCC over this past year will be presented below.

Now that the air-breather is at a relatively advanced stage of development, the CRADA has been extended for a third year (FY'01) to allow LANL to primarily address fuel issues and continue to assist Enable FCC in their product development. While a number of storage options exist for hydrogen fuel cells (e.g., metal hydrides, chemical hydrides, pressurized, etc.), none are particularly amenable for consumer applications at this point. Ideally, the fuel storage subsystem would be symbiotically integrated with the fuel cell side such that consumer-friendly, inexpensive and reliable overall systems can be realized. While the requirements of portability and simplicity render many complex fuel-side approaches impractical that would otherwise be viable for, say, transportation, it is conversely possible to consider approaches for the portable applications that would not be feasible or tolerable for large scale systems. For example, high costs per kWh of capacity or low system efficiencies that would not be attractive for most (larger) applications may possibly provide costs and/or energy densities that are still very attractive when compared to batteries.

Discussion

Fuel Issues

Some perspective on the hydrogen storage possibilities can be gained from a comparison of generic hydrogen storage technologies as shown in Figure 1. This figure depicts the theoretical hydrogen energy densities of various potential hydrogen sources such as methanol (MeOH), low temperature metal hydrides (Metal-H), high-pressure hydrogen gas (20kpsi H₂) and chemical hydrides, such as sodium borohydride (NaBH₄). Also shown for the methanol and sodium

borohydride cases are the differences if the water for the $\text{CH}_3\text{OH} + \text{H}_2\text{O}$ and $\text{NaBH}_4 + 2 \text{H}_2\text{O}$ reactions is supplied from water carried along with the system or supplied with product water from the fuel cell. It should be stressed that these are ideal numbers, the inclusion of factors such as void fractions, containment vessels and conversion efficiencies significantly decrease the actual values attainable. The point is, however, that despite the attention paid to methanol (i.e., direct methanol fuel cells) and chemical hydrides because of their significant gravimetric hydrogen storage densities, even lowly metal hydrides, of only about 1.5% hydrogen by weight, are most likely superior when considered on a volumetric basis. Particularly as systems become smaller, a smaller size is more important than a lighter weight. In such cases, integrating a metal hydride into a fuel cell system is much simpler for portable applications than the other options where water and/or the chemical reactions need to be managed in some manner. As such, one of the specific tasks that LANL is addressing this year is how a portable hydride/fuel cell system based on otherwise well established storage materials can be made robust and user-friendly and its use “transparent” to the consumer. The particular approach LANL is pursuing hinges on technologies previously developed elsewhere within the laboratory.

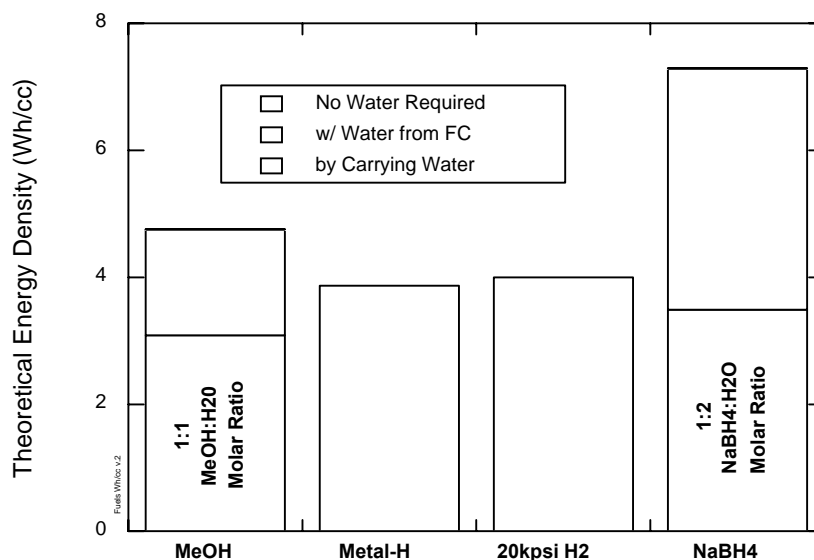


Figure 1 – Theoretical Energy Densities for Various Fuel Options.

The second approach initiated this year at LANL brings the “simplicity” theme, as described in the introduction, to the fuel side as well as the fuel cell. For portable power applications, this can be accomplished in ways that would not be practical or possible in larger systems. Research is progressing on combining the fuel and fuel cell symbiotically such that the net package is extremely simple, e.g., no moving parts, etc. On the other hand, a considerably larger fraction of the theoretical energy densities (as shown in Figure 1) needs to be sacrificed due to the approach. However, the remainder is still quite compelling when compared to conventional batteries and the inefficiencies and complexities inherent in more conventional fuel cell systems are avoided. As such, the net result may be that the systems are not so very different overall. The simpler system would then conceivably prevail in the commercial arena because it would correspondingly be more robust and less expensive than more conventional systems.

While advances have been made in the two fuel approaches being pursued by LANL this year, the efforts are still very much in their infancy and more explicit details can not be provided at this point. While this year's LANL portion of the CRADA has primarily focussed on addressing fuel issues, Enable FCC has continued to develop and test air-breather fuel cell stacks as well as develop new packages and systems for general and specific applications.

Air-Breather Stack and System Development and Testing

Figure 2 provides a photograph and specifications of the first air-breather fuel cell commercial product, the Enable™ 12 Watt PFC (Personal Fuel Cell). The assembly is protected by a shroud with elongated openings that allow air to freely convect over the stack to provide cooling. Although pictured in a recumbent position, the PFC can also be mounted vertically and affixed atop the hydrogen supply in a tower configuration that is then suitable for supporting, for example, a camping lantern.



Figure 2 – Photograph and specifications of the Enable™ 12 Watt PFC.

To compete with batteries, fuel cells will need to be able to function at least as well under environmental extremes as the technologies they are trying to replace. Enable FCC subjected a damaged 20-cell stack to a variety of temperature and humidity conditions in an environmental test room at the University of Wisconsin. Figure 3 depicts a family of polarization curves for the stack. As can be seen, the curves are rather tightly clustered ranging from slightly below freezing (-1°C or 30°F) to a rather aggressive 42°C (107°F). The single curve outside the cluster is for -16°C operation (ca. 3°F). The already sub-par performance of the damaged stack probably lessens the severity of the high temperature situation (i.e., less power, less heat to eliminate). However, the low temperature performance should be exacerbated (less heat to sustain itself) and it is quite impressive that it does as well as shown under the sub-freezing conditions. Curiously, one of the possible advantages of the air-breather in this case is that it is a relatively dry system. Thus damage due to water freezing in flow-fields or other passages is avoided, and the water in the membrane is less likely to freeze because the freezing point is suppressed as the water content drops. As suggested by the one higher temperature curve that deviates from the rest, the relative humidity also has somewhat of an effect in the most extreme cases. Since it appears to be mostly a mass transport limitation effect, perhaps the slight increase in water vapor content is sufficient to unduly limit oxygen access, but this is only speculation at this point.

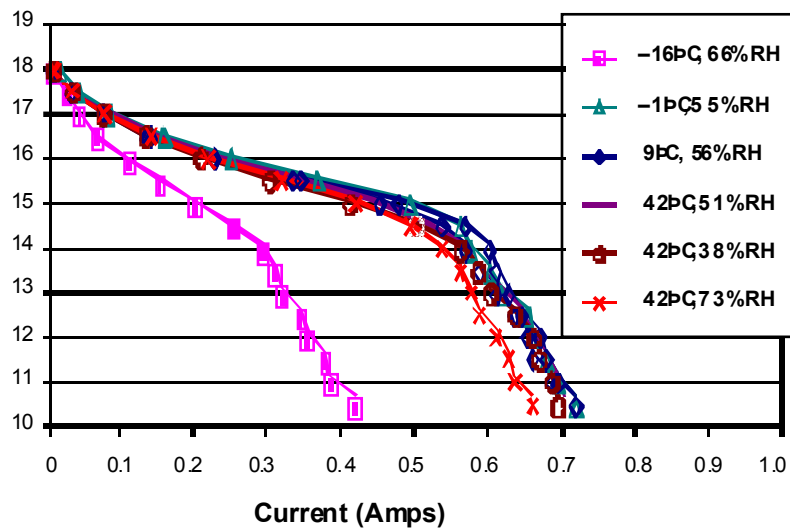


Figure 3 – Polarization curves of a passive air-breather fuel cell stack obtained in an environmental chamber.

For cost considerations, it is naturally desirable for the fuel cell to provide all of the necessary power without requiring a battery in the system for start-up or surge. In such cases, the fuel cell stack will need to offer quick start-up and load following as well as stability. Figure 4 depicts start-up and load following for an off-the-shelf 3-cell Enable™ stack. As can be seen, it comes up quickly and also responds rapidly and stably as the load is varied.

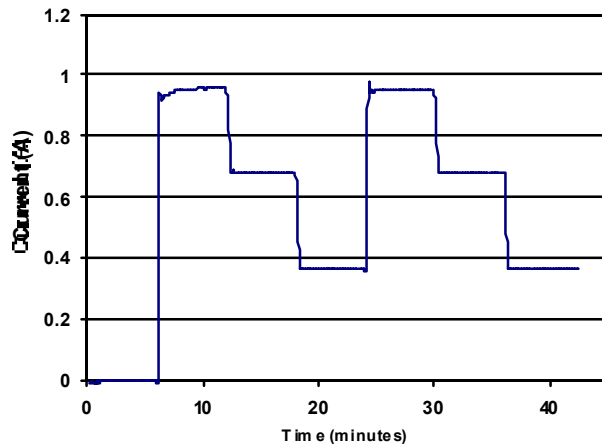


Figure 4 – Startup and passive load following for a 20-Cell PFC stack.

Enable FCC is performing substantial materials testing to assure the longevity and performance of the fuel cell stack components. Most of this testing is performed on 3-cell stacks, and one such test is shown in Figure 5. Aside from occasional performance losses due to hydrogen

supply difficulties, the stack performance was quite stable for the roughly 1500 h shown. The stack has operated an additional 500 hours since this plot was compiled with virtually identical results. To some extent, the stable performance may also be partially attributable to an inherently dry system, as many degradation mechanisms such as catalyst ripening (particle growth) and corrosion are dependant upon the amount of water present.

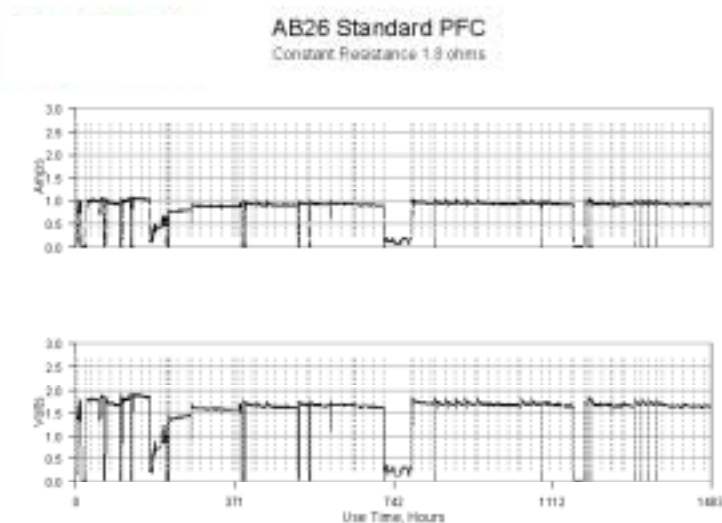


Figure 5 – Life test of a 3-Cell stack.

On the right side of Figure 6 are shown the 12-watt PFC alongside a 70 standard liter metal hydride canister. As the canister is exhausted, it can be replaced with a new one and later refilled for reuse. On the other hand, the entire device may possibly be returned for recharging. In this case, the metal hydride would be an integral part of the package. One such example of this packaging approach is shown on the left side of Figure 6. Here, a roughly 6 volt (i.e., shorter) version of the PFC stack is packaged in a commercial lantern battery housing along with a tailor-made 24 standard liter metal hydride canister as well as the pressure regulator, shut-off valve and other requisite fittings. Since the package provides 6 volts, it can serve as a drop-in alternative to a conventional lantern battery, although provision must be made to allow air access to the slots around the base.

The stack next to the lantern battery is a 3-cell test stack for a smaller diameter version of the PFC stack that has a footprint roughly the size of a D-cell battery. The active area per unit cell of these “D-cell” series of stacks of about 4 cm² is less than a third that of the PFC stack, yet it provides roughly half the current of the larger stack. Higher current densities can usually be attained in the smaller stacks because diffusion and heat transfer path lengths are shorter and the higher surface area to volume ratios that are attained with smaller devices further facilitates cooling.

One of the applications for a 14-cell version of the “D-cell” size stacks is shown in Figure 7. Here, a fuel cell version of a heavy-duty flashlight is shown alongside the alkaline batteries that are replaced by the fuel cell system. The specifications of the two systems are provided in Table 1. While the fuel cell light is somewhat heavier, it burns brighter, lasts another 50% longer, and

is rechargeable (the comparison would be even more favorable against rechargeable batteries). The fuel cell stack is very similar in overall size to a D-cell and is partially visible through the air slots in the neck of the flashlight. The metal hydride canister is the bulge at the base of the flashlight.



Figure 6 – A 6V Lantern Battery fuel cell package, a 3-cell “D-Cell” stack, a 12-watt PFC and its metal hydride canister.



Figure 7 – Fuel Cell Light and Comparable Batteries.

Table 1 – Specifications of the Fuel Cell Light and Comparable Alkaline Batteries.

	<u>Average</u> Voltage	<u>Energy</u> Watt-hrs	<u>Duration</u> hours	<u>Volume</u> in ³	<u>Weight</u> lbs	<u>Energy Density</u> Wh/in ³	<u>Density</u> Wh/lb
<i>Conventional alkaline 6 D-cell battery basis</i>	6.75	49	14	20	1.88	2.4	26.1
<i>PFC 70 liter hydride</i>	7.5	81	20	20.4	1.9	3.36	35.8
<i>PRC D-cell</i>				<u>3.68</u> 24	<u>0.36</u> 2.26		

Figure 8 portrays the internal components of the fuel cell light. As shown in the figure, at least 10 cm (4 in) of the length is taken up by the quick-connect, alignment flange and pressure regulator. Ultimately, more compact elements can be introduced and the metal hydride tank could be streamlined such that the fuel cell package would have the same profile as the battery light with the same hydride capacity as before. Alternatively, the original size canister could still be used and the entire package significantly shortened.



Figure 8 – Flashlight housing, fittings and hydride.

Because of the higher voltage of the fuel cell over the battery shown in Table 1, about 15% more power is provided to the bulb than with the batteries and it is correspondingly brighter. Figure 9 provides the voltage/current curves for the flashlight bulb and the 14-cell fuel cell stack. Conversely, using a bulb with a slightly higher bulb impedance that provides the same brightness as the battery system would then yield a 15% longer use time.

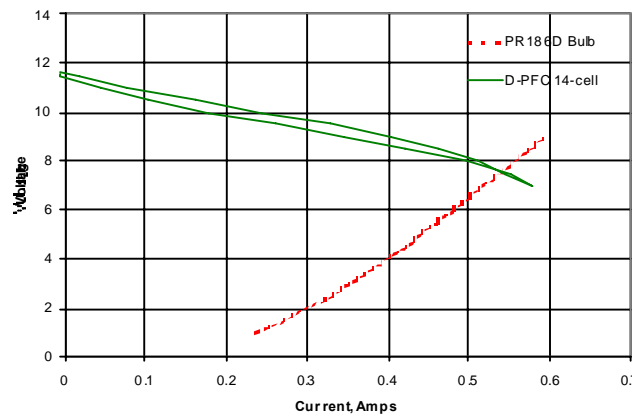


Figure 9 – Characteristic V/I curves of the flashlight fuel cell and bulb.

Conclusions

The air-breather design has demonstrated its versatility and adaptability for a number of packaging options developed by Enable FCC. In testing, the particular attributes of the air-breather have shown it to be surprisingly tolerant to a wide range of environmental conditions and display the operating characteristics that will be needed to be competitive for commercial applications. The only real missing aspects are cost-effective and “transparent” fuel storage systems and their integration into the overall fuel cell system as it would appear in the hands of a consumer. LANL is developing two separate approaches to help address these needs.

References

Wilson, M. S., 1996. “Annular Feed Air Breathing Fuel Cell Stack.” *U. S. Patent No. 5,514,486*.

LOW COST, HIGH EFFICIENCY REVERSIBLE FUEL CELL (AND ELECTROLYZER) SYSTEMS

**Technology Management Inc.
9718 Lake Shore Boulevard
Cleveland, Ohio 44108
216-541-1000
tmi@stratos.net**

Abstract

A reversible solid-oxide fuel cell (SOFC)/electrolyzer system capable of storing electrical energy generated from renewable sources at projected round-trip efficiencies over 80% and providing backup power generated from propane at efficiencies over 60% (LHV) was studied. The systems perform all electrochemical functions using a single stack assembly with a unique systems design that stores both gases and thermal energy. Total system capital and operating costs are projected to be lower than an equivalent lead-acid battery with a backup generator system. This work was a follow-on to experimental work funded under NASA SBIR Phase I and II programs.

Introduction

Grid-independent electric power systems using renewable power sources (such as solar, wind, and water) can potentially drastically reduce CO₂ emissions while offering siting flexibility and economic advantages. Cost is the major barrier to the practical use of systems of this type. Because power is generated intermittently and is variable -- the nature of renewable generation -- such systems typically require both a large energy storage capacity and a backup generator. Practical choices to meet these requirements are deep-cycle lead acid batteries for storage plus an engine generator. While batteries can achieve high energy storage efficiencies near 80%, the

battery/generator combination is quite expensive (first cost plus maintenance costs). In addition, current generators using internal combustion technology are highly polluting, noisy, and have low fuel efficiencies.

Fuel cell technologies are described in the 2001 DOE Hydrogen Program Annual Operating Plan as "cost effective, highly efficient, and critical for overall success in the Hydrogen Program Strategic Plan." As shown in Figure 1, fuel cells serve as both a transitional technology -- as the world moves away from fossil fuels, and as an end point technology -- for the efficient production and utilization of hydrogen.

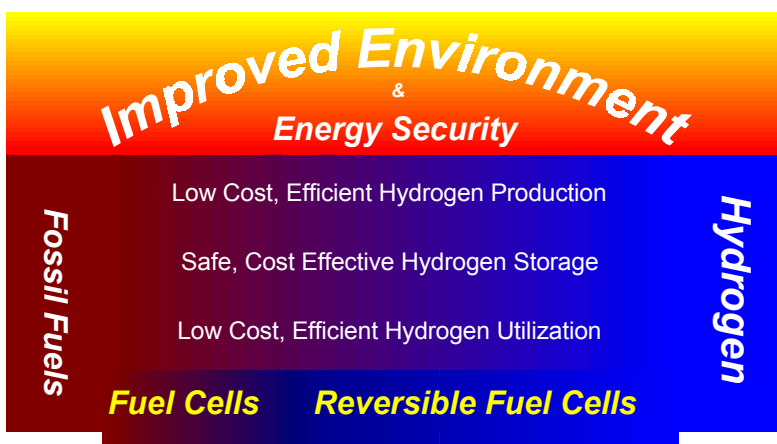


Figure 1. Fuel Cells as a Transition Technology as Described in the DOE Hydrogen Program Strategic Plan.

The Reversible TMI Solid Oxide Fuel Cell (SOFC) Systems

The TMI reversible system employs a high-temperature, solid oxide-based electrochemical process to produce electricity from common hydrocarbon fuels (e.g., natural gas, propane and bio-derived fuel) as well as hydrogen. Operated in electrolyzer mode, the TMI reversible system uses electricity and thermal energy to convert pure water into fuel (hydrogen and oxygen). Heat is a byproduct of all high temperature fuel cells. However, compared to other fuel cells that operate at low temperature (e.g., proton exchange membrane (PEM)), the TMI reversible system can use the waste thermal energy produced during electricity generation mode to achieve high systems efficiency in electrolyzer mode, ultimately lowering product life cycle costs for the combined system. Low cost is a stated goal of the DOE Hydrogen Program.

Specific potential advantages of high temperature SOFC systems over lower temperature systems include:

1. Higher potential "round trip" energy storage efficiency (80% vs. 65%)
2. High fuel-to-electricity efficiency using common fuels instead of hydrogen

3. Lower costs due to reduced part count and increased efficiency.
4. Higher reliability because of modular scalable designs.

At the cell level, the SOFC uses the high operating temperatures (~800°C) of SOFCs to improve electrode kinetics, making low electrode polarization voltages possible. By using steam rather than liquid water for electrolysis, a smaller Gibbs Free Energy change is required, resulting in higher overall system efficiency. Key to this is the capture of heat during fuel cell operation and retention for use later to offset the total energy required by the electrolysis process. Additionally, the high quality exhaust heat can be used to pre-process carbonaceous fuels, adding to overall efficiency if and when these fuels are used.

Scope of Work

The scope of the “Low Cost, High Efficiency Reversible Fuel Cell Systems” project focused on the economic impact of a small scale reversible TMI fuel cell system module in a wind-coupled, grid independent, residential power application. This focus also included comparisons with other varieties of renewable systems in the same configuration, since most economic analyses in the literature are derived from larger size configurations that benefit from economies of scale. The work also included some laboratory tests to demonstrate cell performance characteristics consistent with extensive experimental work performed previously by TMI under NASA SBIR Phase I and II studies in 1998-99. This previously funded work demonstrated actual operation of the reversible TMI cell design and provided data showing the feasibility of very high system efficiencies.

Results

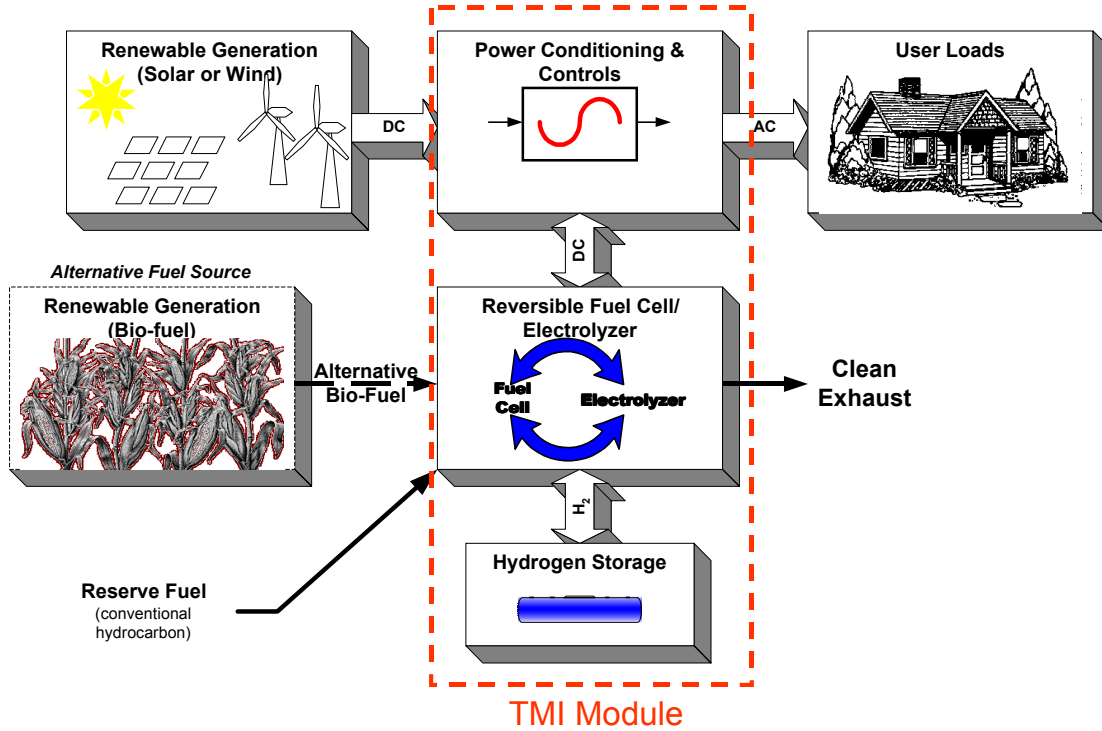
Engineering Cost Study

For this study, TMI performed the conceptual design and simulations of a configuration based on the TMI reversible solid oxide fuel cell/electrolyzer system using hydrogen for energy storage and backup power generation from propane and ambient air. The main system components included an electrolyzer (for generation/storage of H₂), a fuel cell (for conversion of stored H₂ back into electricity), and a back-up generator producing electricity from propane. Figure 2 shows how this design concept can be retrofitted to use existing wind-based technology.

Design Considerations

The analysis assumed hydrogen is stored as a gas at near-ambient temperature, an energy storage efficiency (electrical energy out/electrical energy in) near 80% (similar to lead acid batteries), and a system efficiency near 60% (LHV) when using propane, with negligible air pollutant emissions. All thermal, electrical, and chemical energies were considered and it was assumed that thermal energy spontaneously flows only from higher to lower temperature. All electrochemical and thermal processes are performed under conditions as close to equilibrium as practical. Based on prior experimental work by TMI, electrochemical H₂/O₂/H₂O cells were assumed to operate with only small differences between electrolysis and fuel cell voltages.

(a) Reversible Fuel Cell/Electrolyzer



(b) Traditional System

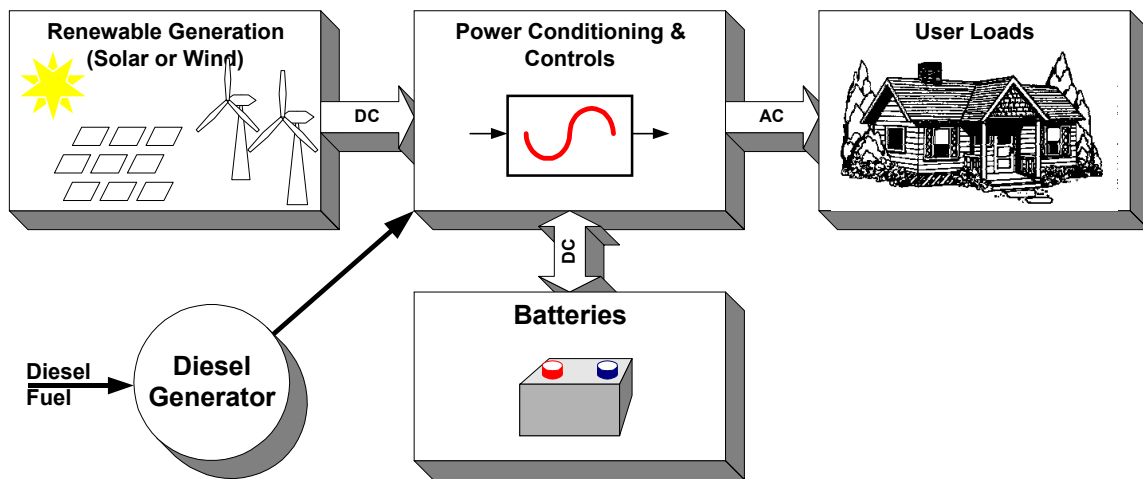


Figure 2. Reversible Fuel Cell System Compared to Existing Designs

Example Requirements Summary

This case study is based on a hypothetical residence of 2500 square feet at a remote site near Boulder, Colorado. The assumed power requirements are limited to 120 volts AC, 60 Hertz, single phase with good power quality needed (true sine wave with low total harmonic distortion, good voltage and frequency regulation) for computers, home entertainment, noise minimization, and other reasons. A high degree of reliability was also deemed to be essential (system outages being very infrequent and brief). The residence was assumed to use propane fuel for all significant heating needs: space heating, cooking, hot water, and clothes dryer. The residence has no air conditioning, but does use cooling fans (and possibly evaporative coolers) and most types of small kitchen and household appliances. The maximum instantaneous peak AC demand (to handle motor starting, etc.) is 3000 Watts and 4000 Volt-Amperes (VA).

The assumed average daily AC net power usage (averaged over 365 days) was 15,360 Watt-hours/24 hr (an average of 640 Watts and a total of 5606 kWh/year). This average usage is about 85% of the assumed worst case day. Dividing 640 Watts by the specified system peak capacity of 3000 Watts is an annual load factor of 21.3%. This value is typical for residences without air conditioning.

The assumed average cost of propane fuel is \$1.00 per gallon delivered, including tank rental charges for propane (also called liquefied petroleum gas or LPG). Its lower heating value (LHV) is assumed to be 84,300 BTU/gallon. This calculation equals a cost of \$11.86 per million BTU. In comparison, if diesel fuel is assumed to cost \$1.50 per gallon delivered with a LHV of 128,000 BTU/gal., an equivalent dollar cost per million BTU is \$11.72 (1999 price estimates).

Reversible Fuel Cell/Electrolyzer Assumptions

The proposed reversible system for the above case provides both energy storage (using H₂) and backup generation from propane fuel. The system utilizes four (4) identical reversible fuel cell/electrolyzer modules having preliminary specifications as described in Table 1.

Each module contains the following components:

- solid oxide stack
- hydrogen gas storage system
- liquid water storage system
- multifunction power conditioning circuit
- small lead-acid battery (for instantaneous load following)
- balance of system components, including compact heat exchangers, pump, blowers, valves, insulation, startup heater, control system, sensors, enclosure, etc.

Comparisons

Five cases were considered in detail (using estimated 2009 selling prices for the new-technology systems) and are summarized in Figure 3. The installed costs in the table were computed using a system peak power requirement of 3.0 kW, an average annual power requirement of 640 W/day,

and rounding to the nearest \$100. Although the example application used in this report is based upon a moderate-sized residence, most of the considerations cited also apply to smaller and larger systems having average power requirements anywhere from about 500 to at least 5000 Watts. New technologies recommended are applicable to both new installations and upgrades of existing systems.

Table 1. Module Specifications

Parameter	Value	Units
Nominal Output Power	1000	Watts
Maximum Surge Power	4800	VA
Nominal Energy Storage	6500	Wh
Output AC Voltage (60 Hz)	120	Volts rms
Typical Net Propane Efficiency	62%	LHV
Typical Energy Storage Efficiency	81%	Wh
Noise @ 1 meter	< 50	DbA
Retail Price (est. 2009)	\$3400.	
Average Annual Maintenance	\$170.	

Each case had advantages and disadvantages depending on the objectives. For maximum reduction in pollution, the renewable wind and wind-hybrid systems (both with and without reversible fuel cells) offer the lowest CO₂ emissions. The diesel generator system is available ‘today’ but when factors such as load leveling and maintenance are included, this system appears to be poorly suited for year round off-grid applications.

Reversible Fuel Cell Experiments

The main advantage of the SOFC is its potential for high reversible efficiency. However, this assumes the capability to store and recycle thermal energy. Thus, reversible cell operation in a single device requires completion of a key development to enable electrochemical processes to occur at similar temperatures, and thereby mitigate thermodynamically undesirable steps.

As part of this program, TMI performed experimental work that demonstrated reversible operation of single cells under conditions that represented the average predicted environment and gas composition in a reversible system. A sketch of the cell design for a reversible cell is shown in Figure 4. This work included design modifications tailored for reversible cell operation, preliminary sealing technology to prevent gas mixing, and modified gas distribution manifolds.

The cell area specific resistance (ASR) was about 10% higher for reversible cell designs compared to state-of-the-art TMI SOFC designs but was acceptable for early development. The best cells were operated in steady state (non-cycling) conditions for up to 2000 hours. This work is being actively extended to include the full range of predicted operation conditions in cells and in small stacks.

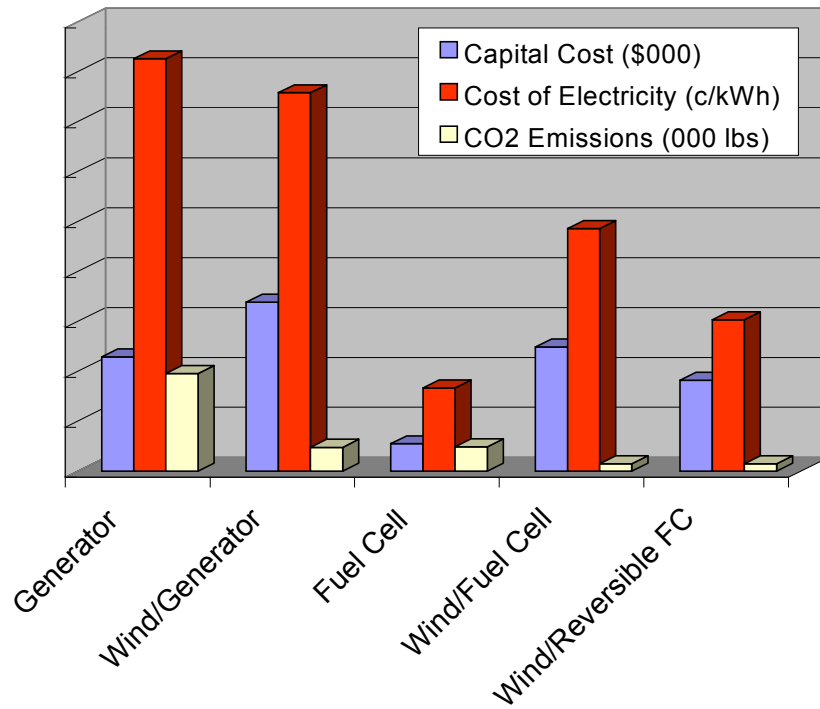


Figure 3. Costs and CO₂ Emission for Several Configurations

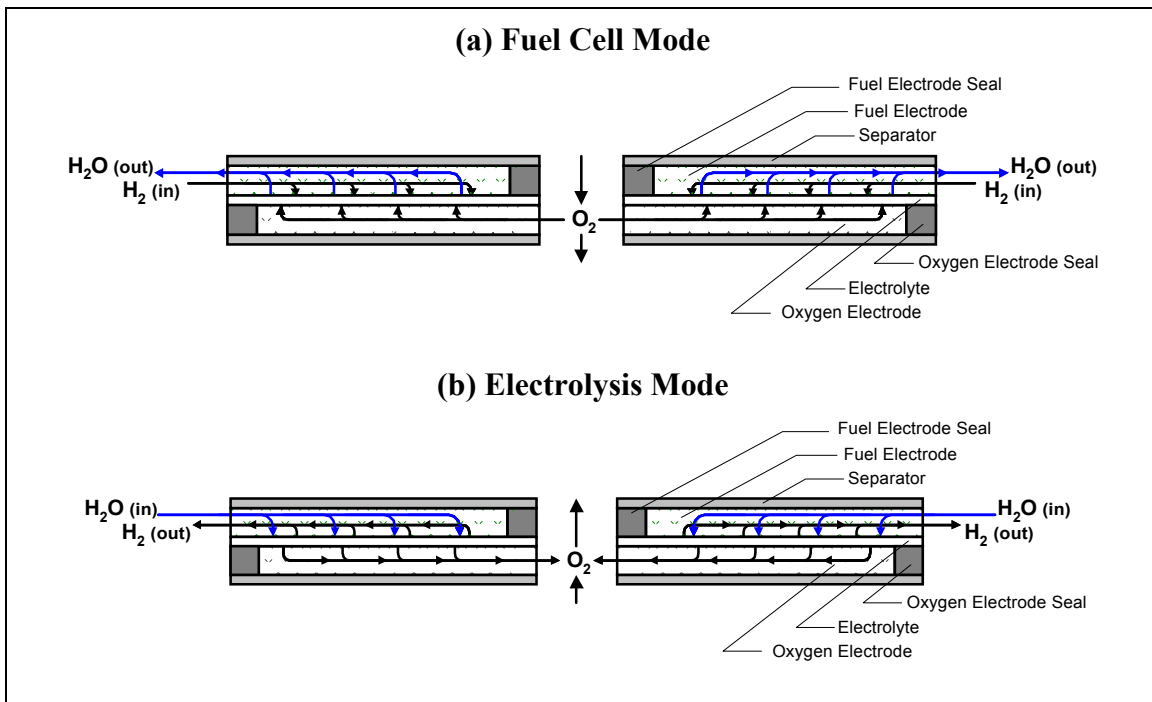


Figure 4. TMI Reversible Cell Flow Diagram

Conclusions and Recommendations

- The TMI reversible solid-oxide system is environmentally and economically attractive for renewable applications.
- TMI's high efficiency fuel cell systems has the potential for low costs and is a transitional technology en route to renewable-based systems.
- Additional experimentation is required to validate model assumptions.

On-going Work

This study is not complete. Three principal areas are being actively pursued: (1) reversible/high-efficiency small stack development and demonstration, (2) life and gas cycling experiments, and (3) updated cost and efficiency calculations.

Acknowledgements

TMI would like to acknowledge the Department of Energy's Golden Field Office for their support during this project.

HIGH-EFFICIENCY STEAM ELECTROLYZER

**Ai-Quoc Pham
Lawrence Livermore National Laboratory
7000 East Avenue, L-350, Livermore, CA 94550**

Abstract

We are developing a novel high-efficiency, high-temperature steam electrolyzer. Although water or steam electrolysis is well known to be one of the cleanest ways to produce hydrogen, widespread utilization is hindered by high operational costs because of high electricity consumption. To decrease the electrical power input requirements in electrolysis, our approach uses natural gas as an anode depolarizer. This approach essentially replaces one unit of electricity with one equivalent-energy unit of natural gas at much lower cost. The direct use of natural gas on the electrolyzer enables very high system efficiency with respect to primary energy. Experiments performed on single cells have shown a voltage reduction as much as 1 V when compared to conventional electrolyzers. System efficiency has been estimated to be 50 to 80%, depending on the electrolytic current. A 200-W prototype unit is being developed.

Introduction

Currently, most hydrogen demand is met by hydrogen production from fossil fuels, i.e., by steam reforming of natural gas and by coal gasification. However, most of these central plants are located in remote areas. The hydrogen produced must then be delivered to the users either by truck or via hydrogen pipelines. Because of the inherently low energy density of hydrogen, transportation by truck is not a viable option. Hydrogen delivery using pipelines is not cost-effective either because of the high cost of the pipelines (about \$1 million/mile). Therefore, hydrogen production for a future hydrogen economy is likely to be accomplished using a distributed system where hydrogen is produced close to where it is consumed. A distributed hydrogen production system using small conventional steam-reforming reactors is not feasible

because of the very high cost of the reactors at small scales. More interesting approaches, such as autothermal reforming as well as partial oxidation processes, are currently being pursued. However, these approaches are fairly complex, involving several additional steps, such as high-temperature shift, low-temperature shift, and preferential oxidation or hydrogen gas separation.

Hydrogen can be produced from water or steam electrolysis using much simpler technology. Because of the modularity of the electrolyzer, electrolysis can be done at a large central plant, at a refueling station, or even at home. In addition, electrolysis using renewable electricity offers the possibility of producing hydrogen without any greenhouse gas emissions. However, water electrolysis has not had a significant commercial impact because it has not been cost-effective.

The main drawback of conventional electrolyzers is the high electricity consumption. Electricity from the typical grid is known to be by far the most expensive form of energy. As a result, electrolytic hydrogen is more expensive than the steam-reformed hydrogen by a factor of at least two to three (Donitz 1980, Donitz 1985, Donitz 1990). Moreover, electricity is not a primary energy but must be produced using fossil fuels, nuclear fuels, or renewable energy. Considering the fact that production of electricity has an average efficiency of less than 40% with respect to primary energy, the overall efficiency of the electrolyzer in general is below 40% (Donitz 1990). In addition, less than 20% of the overall electricity production in the United States uses renewable energy. As a consequence, electrolysis using electricity from the grid is not a carbon-free process but actually involves the production and release of large amounts of greenhouse gases. From this viewpoint, conventional electrolysis is probably the worst hydrogen production technology in terms of greenhouse gas emissions. On the other hand, electrolysis using exclusively renewable energy would have limited applications because it must be linked directly to a renewable energy source.

Recently, we have developed a new approach to reduce the electricity consumption in electrolyzers (Pham 2000). Reduced electricity consumption was achieved by using natural gas to reduce the chemical potential difference across the electrolyzer cell. The concept is called Natural-Gas-Assisted Steam Electrolysis (NGASE). Although NGASE still involves carbon emissions because of the use of natural gas, the high efficiency and the simplicity of the system make it attractive as a hydrogen production technology for the transitional phase toward the hydrogen economy.

The goal of this project is to develop a prototype 1-kW-equivalent NGASE system for technology validation in 2006.

Concept

In conventional steam electrolyzers, the gas supplied to the cathode side (where water is decomposed) is usually a mixture of steam and hydrogen, while the gas supplied to the anode side is usually air. At zero current, the system has an open-circuit voltage of 0.8 to 0.9 V, depending on the hydrogen/steam ratio and on the operating temperature. In order to electrolyze water, a voltage that opposes and is larger in magnitude than the open-circuit voltage must be applied to pump oxygen from the steam side to the air side. Clearly, much of the electricity

used, 60 to 70% of the total electrical power, is “wasted” by forcing the electrolyzer to operate against the high chemical potential gradient for oxygen.

To lower the open-circuit voltage, and thereby the electricity consumption, our approach is to replace the air in the anode side with natural gas. The reducing character of natural gas helps to lower the chemical potential difference between the two sides of the electrolyzer. One can distinguish two different modes of operation: total oxidation or partial oxidation of natural gas. In the first case, natural gas is used in the anode side of the electrolyzer to burn out the oxygen resulting from the electrolysis, thus reducing or eliminating the potential difference across the electrolyzer membrane. The products of the reaction will be CO₂ and steam. High fuel utilization is required. The role of natural gas is just to lower the chemical potential gradient, and therefore the electricity consumption. This mode replaces one unit of electrical energy by one equivalent-energy unit of natural gas at one-fourth the cost. Thermodynamics limits the operational temperature for the total oxidation mode to temperatures lower than 800°C. Above 800°C, carbon monoxide becomes more stable and total oxidation is not possible.

In the second operational mode, an appropriate catalyst on the anode side promotes the partial oxidation of natural gas to CO and hydrogen. The resulting gas mixture, also called syngas, can be used in important industrial processes such as the synthesis of methanol and liquid fuels. Most importantly, CO can also be shifted to CO₂ to yield additional hydrogen. In this process, hydrogen is produced at both sides of the steam electrolyzer. The overall reaction is equivalent to the steam reforming of natural gas. In contrast to steam-reforming reactors, the modular characteristics of the electrolyzer, together with the absence of the extensive heat exchangers, make it economically feasible to make small-scale hydrogen production units. However, the partial oxidation approach is much more complex than the total oxidation mode because it involves several additional reactor units, as described above for the steam-reforming process.

In both cases, the key point of the approach is to use natural gas directly in the electrolyzer instead of using natural gas to make electricity at the central plant. The efficiency will be higher, and the carbon emissions will be lower than in conventional electrolysis.

Summary of Previous Accomplishments

We have demonstrated the proof-of-concept of the NGASE approach using single disks. A voltage reduction of 1 V was observed when methane was used in the anode side. The electricity consumption was estimated to be about one order of magnitude smaller than in conventional electrolyzers. Using thin film and novel catalyst materials, we demonstrated very high performance, up to 1 A/cm² at only 0.5 V at 700°C. At 800°C, cell current was as high as 2.4 A/cm². For electrolyzer stack development, we selected the tubular approach since tubular structure has good mechanical integrity while enabling operation at high pressures. A tube fabrication process has been developed.

Accomplishments

Tube Fabrication

Making electrolyzer tubes is the single most important effort in the whole fabrication process of the NGASE stack. Since we have demonstrated the feasibility of the NGASE concept for small disk samples, the technical success of the project now depends largely on the scale-up, i.e. the fabrication of the electrolyzer tubes. During FY00, we developed a laboratory-scale fabrication process to make tubes. However, the thin-film coating turned out to be extremely challenging. Indeed, although it is reasonably easy to fabricate defect-free thin films on small samples, the risk of having defects on large-size samples multiplies linearly with increasing area. The most detrimental defect is short-circuiting through the electrolyte coating because of the presence of pinholes. Even just one pinhole that causes short-circuiting in the electrolyzer renders the whole tube useless. The defects typically come from fabrication of the tube or from the coating itself. Figure 1 shows an example of a defect caused by the tube fabrication. A large hole can be seen on the surface of the tube. The presence of the hole causes disruption in the electrolyte coating. When the cathode is subsequently deposited (not shown in the picture), the cathode material can penetrate inside the coating and be in contact with the anode, causing short-circuiting. At first, we had a coating yield of less than 10% for 3-inch tubes.

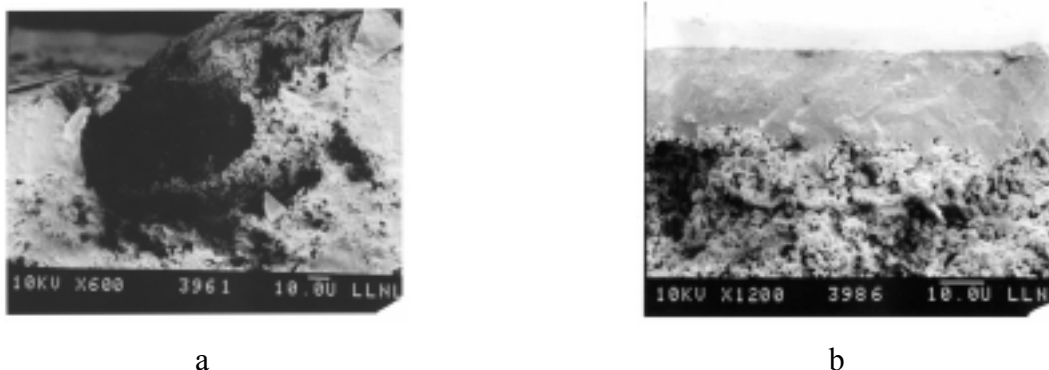


Figure 1: Cross section views of: a) pinhole defect on the tube surface; b) thin film electrolyte coating without defect even though there is a pinhole on the tube surface.

We have improved both the fabrication process to have less defects on the tube surface, and the coating process itself to make it less sensitive to tube defects. Figure 1b shows an example of a tube that has a surface pinhole. Using the improved coating process, we could deposit a defect-free electrolyte film that actually covered the tube pinhole. The new process has a yield of 80%. We are working to further improve the yield rate. The short-circuiting problem was a major hurdle in the development of the prototype electrolyzer stack. This problem is now overcome.

Using the improved fabrication process, we have been able to make longer tubes, up to 6 inches in length. Figure 2 shows an example tubes at different steps in the fabrication process.



Figure 2: Pictures of tubes at different steps in the tube fabrication process

Performance Characterization

The electrolyzer tubes were submitted to several tests to evaluate the mechanical and electrochemical performances. Pressure tests indicated that the tubes survived up to 200 psi at room temperature and 85 psi at 700°C. The test at room temperature was limited to 200 psi because of the testing apparatus, not because of the tubes themselves. The test at 700°C was stopped at 85 psi because of leakage through the high temperature seals, which prevented further pressurization. With better seals, we expect to demonstrate tube survival above 150 psi at temperatures.

The tubes were also submitted to repeated temperature cyclings with ramp rate up to 20 °C/min. No degradation was observed.

Figure 3 shows the electrochemical performance of a single tube. Each tube produced about 30 and 70 sccm hydrogen from the cathode side (steam side) at 700 and 800°C respectively. In the partial oxidation mode where hydrogen is produced on both sides, the total hydrogen produced was 280 sccm. Tube performance is still only 30% of disk data. Efforts to improved tube performance are planned for 2002.

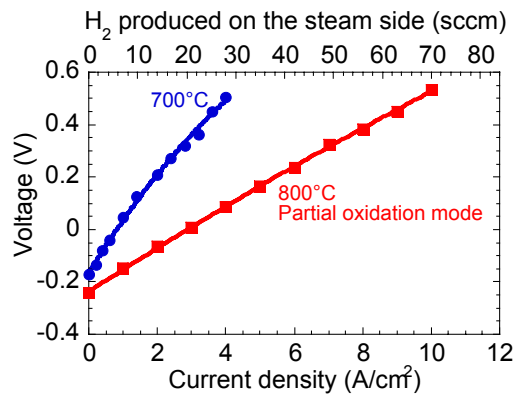


Figure 3: Electrochemical performance of single tube

Electrolyzer Stack Development

In FY2000, we selected the tubular configuration approach for the NGASE stack. The tubular stack design enables us to electrochemically compress hydrogen in the steam side while having natural gas at ambient pressure only inside the tube. This eliminates the need for a natural gas compressor. This year, we continued the development of the stack. In particular, the effort was focused on:

Seal Development

Due to the operation at high pressure-differential, conventional high-temperature ceramic and glass-ceramic seals barely meet the requirements. We thus selected the metal-to-ceramic brazing as sealant approach. Various brazing alloys were tested for their compatibility with the tube as well as with the alloy serving as interconnect. The best seal tested so far survived pressures up to 85 psi; beyond this threshold, seal leakage occurred. By further optimizing the thermal expansion matching between the different components, better seals can be developed. In a parallel effort, we are developing an engineering design that will eliminate the need for high temperature sealant.

Tube-To-Tube Series Connections

Each electrolyzer tube operates at high current, up to 70 A, and at a voltage lower than 1 V. In order to increase the voltage, we developed the tube-to-tube series connection approach. This approach is similar to the segmented-in-series originally developed for Solid Oxide Fuel Cells for similar purpose. However, due to the favorable environment in the electrolyzer case, as compared to the fuel cell case, metallic interconnect can be used to electrically connect tubes together. Figure 4 shows a picture of three tubes that are connected in series via the metal interconnects that were brazed to the tubes.



Figure 4: Three tubes with series connection

200 W Stack Development

We are currently working on the 200 W electrolyzer stack. Figure 5 shows the initial model of twelve tubes connected in series and in parallel; together with the metal vessel that will enable the operation at pressures up to 150 psi. Pressurization test of the bench scale reactor was accomplished.

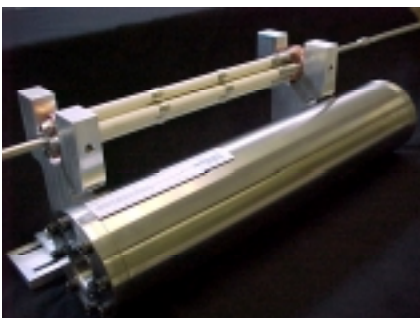


Figure 5: NGASE stack model with 12 tubes

System Analysis

Preliminary system design of the NGASE was completed for this phase. The result of the system analysis is illustrated in Figure 6. The single cell data was used for analysis. Using an average efficiency of 40% for the grid, it is shown that, when properly designed, the electrolyzer efficiency is between 50 to 85% with respect to primary energy. Several factors, including the natural gas fuel utilization at the anode and the electrolytic current density, have strong influence on the system efficiency. The efficiency increases dramatically with decreasing electrolytic current. At a high current density of 1 A/cm^2 , the efficiency would be 53% (80% fuel utilization, LHV) while at 0.4 A/cm^2 , it is as high as 76%. However, capital cost consideration would impose a limit in how low the current density can be. The efficiency also increases with increasing consumption of natural gas in the anode. However, it will be difficult in practice to

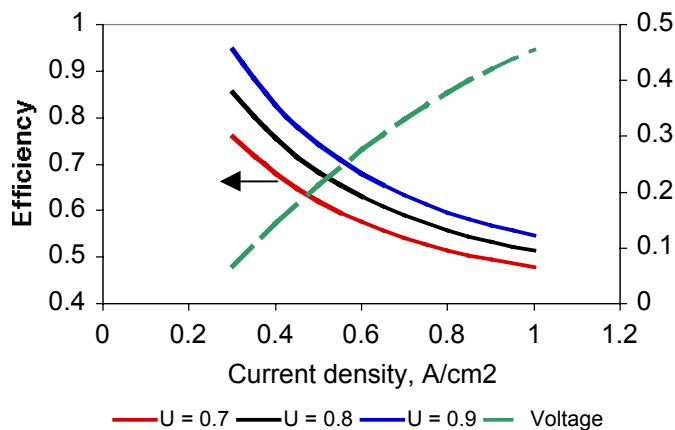


Figure 6: Efficiency as a function of current density at different fuel utilizations U

have a natural-gas utilization higher than 85%. Nevertheless, the analysis indicates that the NGASE can have much higher efficiency with respect to primary than the conventional electrolyzers, for which the efficiency is typically less than 40% (Donitz 1990). Compared to other reformer approaches, the NGASE has more operational flexibility since the efficiency and hydrogen production rate can be easily adjusted depending on the requirements.

Conclusion and Future Work

We have advanced considerably the development of the NGASE. The scale-up to larger size samples has encountered some difficulties that are typical in most scale-up efforts. The coating problem has been overcome. The groundwork for stack development was accomplished. Preliminary system analysis indicates high efficiency, up to 80% can be achieved.

We will further improve the tube fabrication process in order to have tube performance close to that of single disks. Long-term stability will be evaluated. We will continue the system and process engineering to develop NGASE stacks. Our goal is to fully develop a NGASE prototype for technology validation in 2006. American Fuel Cell LLC (AFC), a private start-up company, has recently negotiated exclusive licensing of our technology. AFC will work with us through a CRADA to bring this technology to commercialization. In particular, AFC will provide the manufacturing support that is much needed for the fabrication of kW size systems.

References

- Donitz, W., Schmidberger, R., Steinheil, E., Streicher, R., *Int. J. Hydrogen Energy*, **5**, 55 (1980).
- Donitz, W., and E. Erdle, *Int. J. Hydrogen Energy*, **10**, 291 (1985).
- Donitz, W., Erdle, E., Streicher, R., 1990. *Electrochemical Hydrogen Technologies.*, Wendt, H., Editor. Elsevier. p 213.
- Pham, A.Q., H. Wallman, R.S. Glass, US patent n°6051125 (April 2000).

GALLIUM NITRIDE INTEGRATED GAS/TEMPERATURE SENSORS FOR FUEL CELL SYSTEM MONITORING FOR HYDROGEN AND CARBON MONOXIDE

**Stephen C. Pyke
Peterson Ridge, LLC
PO Box 1257
Sisters, OR 97759**

**Larry Sadwick
Department of Electrical Engineering
University of Utah
Salt Lake City, UT 84104**

Abstract

Experimental results indicate the Pt-GaN-based FET (field effect transistor) gas sensors has the required sensitivity to measure the CO concentration in the 0-500 ppm range in H₂ and that the array concept for analyzing complex mixtures is more sensitive with increasing temperature >100 °C. The work leverages significant contributions in the literature on FET-based sensors on silicon and gallium nitride device electronics to extend the performance envelope for the FET-based gas sensor technology to high temperature. Results for the Pt and Rh catalytic gates at temperatures at and above 150 °C suggest a complex interaction of CO (51-1,014 ppm) and oxygen (0-5,000 ppm) and no saturation by hydrogen at 35vol%. The results are discussed in terms of the models currently used to describe the FET sensing mechanism.

Introduction

Gas sensing and analysis based on gas adsorption on a catalytic metal surface has been extensively explored using chemically sensitive semiconductor devices (Lundstrom 1989 and Spetz 1992). Recent work on field effect devices using catalytic metal gates on silicon carbide substrates has been reviewed (Spetz 1997 and Tobias 1997) and suggests the promising application of the field effect technology for high temperature gas monitoring. The limited use of large bandgap semiconductors for volume electronic applications has resulted in limited sources for devices for sensor applications. It is reasonable therefore to examine other high bandgap semiconductors as potential sources for high temperature sensors. Other materials in the III-V group of compound semiconductors are a potential source.

The field effect technology using catalytic metal electrodes on a semiconductor exploits chemisorption which is often dissociative (bond-breaking). The effect of hydrogen was reported first by Lundstrom (Lundstrom 1975) on a palladium gate field effect transistor (FET) on silicon. Later work demonstrated sensitivity to ethylene and carbon monoxide (Poteat 1983), hydrogen sulfide, propylene oxide, ethylene, formic acid, carbon monoxide and NO₂ (Hughes 1987). More recently, hydrogen, carbon monoxide, ethylene and acetylene effects have been observed on metal-insulator-semiconductor (MIS) capacitors with electrodes of pure platinum and platinum and palladium compositions with small amounts (ca. 5-10%) of transition metals such as copper, silver, and chromium (Feinstein 1997 and Pyke 1993).

There are two well-known hypotheses for how hydrogen and other gases are sensed by catalytically-active metal electrodes on FET sensors. Both hypotheses concur the change in work function alters the population distribution of carriers in the semiconductor under the metal by changing the surface potential of the semiconductor. In the first model, molecular hydrogen dissociates on the catalytic metal forming two adsorbed hydrogen atoms. Depending on their solubility and diffusivity, hydrogen atoms penetrate the metal to reach the metal-insulator or metal-semiconductor interface. In this model, only hydrogen alters the surface potential of the semiconductor covered with a solid electrode. The steady-state concentration of adsorbed hydrogen is mediated by reaction with other gases adsorbed on the surface, affecting the hydrogen concentration at the metal-insulator or metal-semiconductor interface. Thus, gases impacting the concentration of hydrogen on a catalytic surface can be measured only indirectly through the effect they have on hydrogen concentration at the metal-insulator or metal-semiconductor interface. In the second model, a perforated or porous solid electrode adsorbs gas as in the first model, however it is proposed the dipole field-produced hydrogen changes the surface potential of the semiconductor without diffusion into the metal (Dobos 1990, Hedborg 1994 and Lundstrom 1996). The dipole field is proposed to result from adsorbates at the edges of the perforations or pores. A similar but more aggressive design to expose more of the metal surface facing the semiconductor used a suspended metal electrode (Cassidy 1986). By etching away a sacrificial metal layer deposited between the dielectric and the catalytic metal, a cavity is produced which is accessible to gas. Perforations in the suspended metal allow any gas to penetrate to the cavity and adsorb on the metal facing the semiconductor. In principle, nearly the total underside surface is available for any gas to adsorb and produce the dipole field and so influence the surface potential of the semiconductor.

GaN High Temperature Electronics

Owing to their wide bandgap, the III-V nitrides are attractive for high-temperature, high-power electronics applications. Forming low contact resistivity, thermally stable and uniform ohmic contacts constitutes a major obstacle for wide band gap materials such as GaN. With a band gap about 3.4 eV, Ga-N is therefore, receiving increased attention. GaN-based devices and circuits have the potential to operate at 600°C or higher temperatures. For GaN and other highly ionic semiconductors, evidence has suggested that the Schottky barrier height of metal to III-nitride contacts strongly depend on the difference between the work function of the metal and the electron affinity of the semiconductors. It is fairly easy for metals with lower work functions to form ohmic contacts on n-GaN. This explains why Ti, Al, W, and Cr are chosen as ohmic contacts on n-GaN. Similarly, metals with higher work functions, such as Pt, Rh and PdAg, are expected to form good Schottky barriers (necessary for high impedance contact and low leakage current) to n-GaN.

As with other semiconductor systems, especially compound semiconductor systems, the formation of an alloyed semiconductor/contact is usually the most straightforward method to achieve “ohmic” behavior. This is most certainly true for other group III-V semiconductors such as the well-studied and characterized GaAs semiconductor. Almost all known, successful contacts to III-V semiconductors consist of bi-level to multi-level metallization schemes. The interface between the semiconductor and the first metallization layer is the most important, for it controls the transport mechanism(s). Usually, chemical or thermal reactions, solid-state diffusion and interdiffusion, and/or other methods produce mixing, due possibly to material damage (i.e., ion mixing and ion implantation). The key is to find some species, usually an element, that reacts with the respective substitutional dopant and either the group III or group V element to form an alloy of variable composition such that transitions occur from semiconducting to semimetallic to metallic. This type of contact, essentially, forms a tunneling ohmic contact with linear I-V characteristics. An example of this is the Au-Ge-Ni ohmic contact to n-type GaAs.

Among the several metals studied for ohmic contacts on n-GaN, Pd/Al and Ti/Al were found to have the lowest specific contact resistances. The formation of Pd/Al on n-GaN has been reported (Ping 1996), whose specific contact resistance was found to be 1.2×10^{-5} ohm-cm² upon annealing at 650°C for 30 seconds. A significant improvement with Ti/Al on n-GaN was obtained (Lin 1994), who employed a Ti/Al bilayer deposited by e-beam evaporation followed by rapid thermal annealing (RTA) at 900°C for 30 sec in N₂ ambient. A specific contact resistance of 8×10^{-6} ohm-cm² was reported. One recently proposed ohmic metallization scheme involved Ti/Al-based composites, namely Ti/Al/Ni/Au (150•/2200•/400•/500•) preceded by a reactive ion etching (RIE) process that most likely rendered the surface highly n-type (Fan 1996). After annealing at 900°C for 30s, specific contact resistance of 1×10^{-7} ohm cm² for a doping level of 4×10^{17} cm⁻³ was obtained. Unfortunately, Au reacted with GaN during the annealing.

Lin et al. found specific contact resistance of Ti/Al metallization suffered from Ga outdiffusion and subsequent reaction with Al rendering the surface metal discontinuous and increasing its resistance. A second sequence of Ti/Al was added (Wu 1995) following the annealing step, to

minimize the high resistivity problem. Ohmic-specific contact resistance was lowered to $\sim 3 \times 10^{-6}$ ohm cm^2 .

Pt, Rh and PdAg as Catalytic Gate Materials

Platinum and palladium were selected because each has shown sensitivity in the ppm range for ethylene, acetylene and carbon monoxide. Both metals are also PROX catalyst candidates, and both metals have been used as Schottky junctions on GaN. PdAg was selected, because the mechanical integrity is better than pure Pd at these hydrogen concentrations. Rhodium was selected, because of its PROX catalytic activity and to help resolve the effects of the multiple gases in combination with platinum and PdAg. Each of these metals is expected to adsorb CO preferentially in the fuel stream just as in the PROX catalyst. It was surmised the reaction of CO and hydrogen with oxygen on the surface of the catalyst produces a steady-state surface composition that can be detected through the work function change of the catalyst. The higher affinity for CO in preferential catalysis also suggests the three metals should show sensitivity for carbon monoxide even in the presence of a great excess of hydrogen.

Experimental

Fabrication

We have successfully fabricated Schottky contacts using platinum, palladium/silver and rhodium. We used process technology that has resulted in contacts that only a few of which have survived without delamination. The gate metals were applied to a variant of the MESFET called a MODFET for modulation-doping-field-effect-transistor. The architecture is shown in Figure 1. The gates are the two strips at the centers of the two FETs on the left. Each gate is bounded by a source and drain ohmic contact.

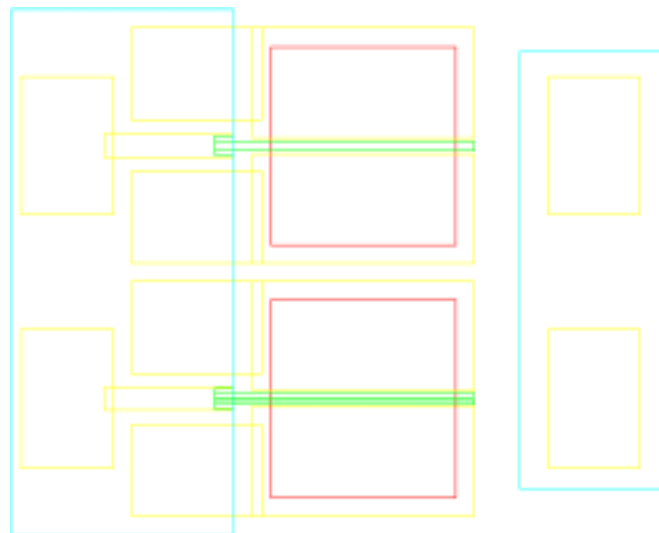


Figure 1: FET Sensor Architecture showing two FETs. The right-hand feature is a set of bonding pads for thermocouples.

Two gate designs (single and dual strips) were fabricated. The collocation of the single and dual gate on the wafer makes for the closest match in electrical properties for the most accurate comparison of the gas effect.

The design dimensions and the actual dimensions are shown in Table 1 below.

Table 1: Dimensions of FET Sensors

	Single Gate		Dual Gate		No Gate
	Design	Actual	Design	Actual	Design
Gate Length	200 • m				
Ohmic Contacts	20000 • m ²		20000 • m ²		20000 • m ²
Gate Metal Width	10 • m	8.6 • m	2x5 • m	2x4.25 • m	n/a
Gate Metal Area	2000 • m ²	1920 • m ²	2000 • m ²	1900 • m ²	n/a
Drain-Gate	3~4 • m	5 • m	2 • m	3.5 • m, 3.7 • m	n/a
Drain-Source	17 • m	18.7 • m	17 • m	18.7 • m	17 • m
Intergate spacing	n/a		3 • m	3.1 • m	n/a
Gate Area Exposed	1400 • m ²	2030 • m ²	1400 • m ²	2050 • m ²	3400 • m ²
Ratio of Gate Exposed to Covered	0.7	1.06	0.7	1.08	n/a
Ratio of Gate Edge to Area	0.2 • m ⁻¹	0.21 • m ⁻¹	0.4 • m ⁻¹	0.42 • m ⁻¹	

The actual dimensions were determined from the transmission electron microscope (TEM) micrograph shown in Figure 2 below and the scanning electron microscope (SEM) micrograph of the single gate in Figure 3.

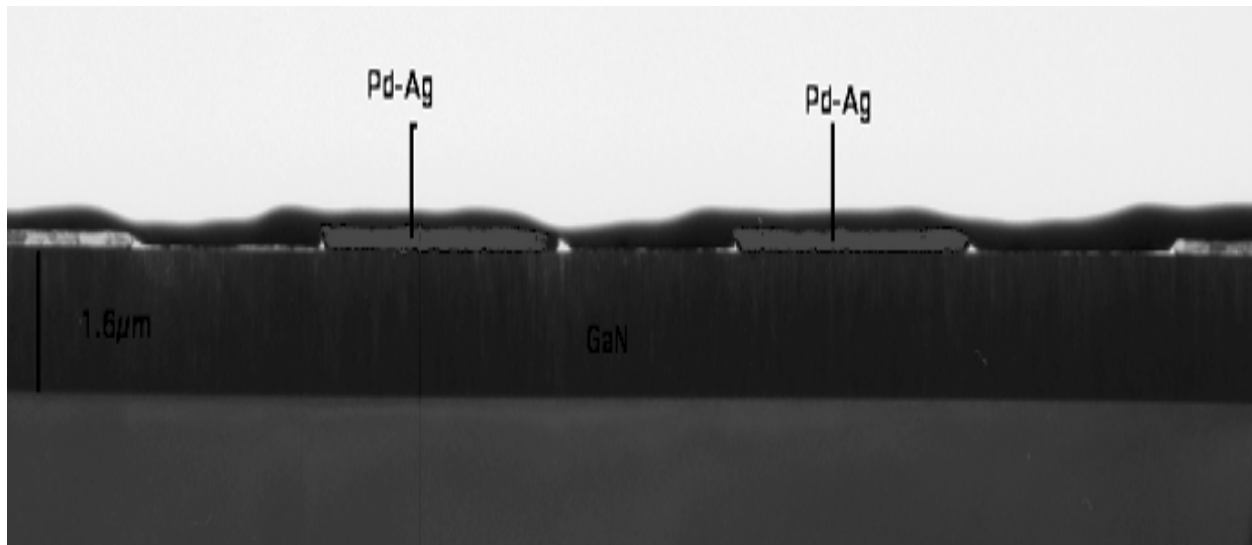


Figure 2: TEM photomicrograph of the cross-section of the dual gate device.

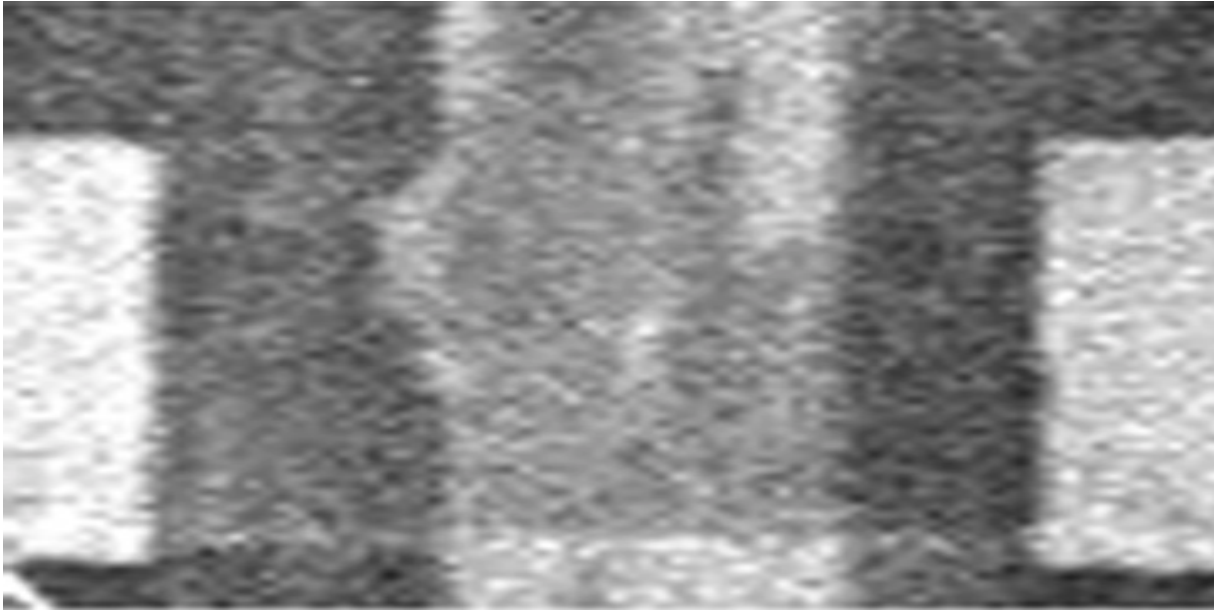


Figure 3: SEM micrograph of a representative single metal gate.

The metal thickness for PdAg was measured in the TEM image shown in Figure 4. The film thickness proposed (ca. 50-100 nm) was expected to be an island type film (e.g. where the films become discontinuous). There is no evidence of porosity or pinholes. The film is continuous and appears densely packed.

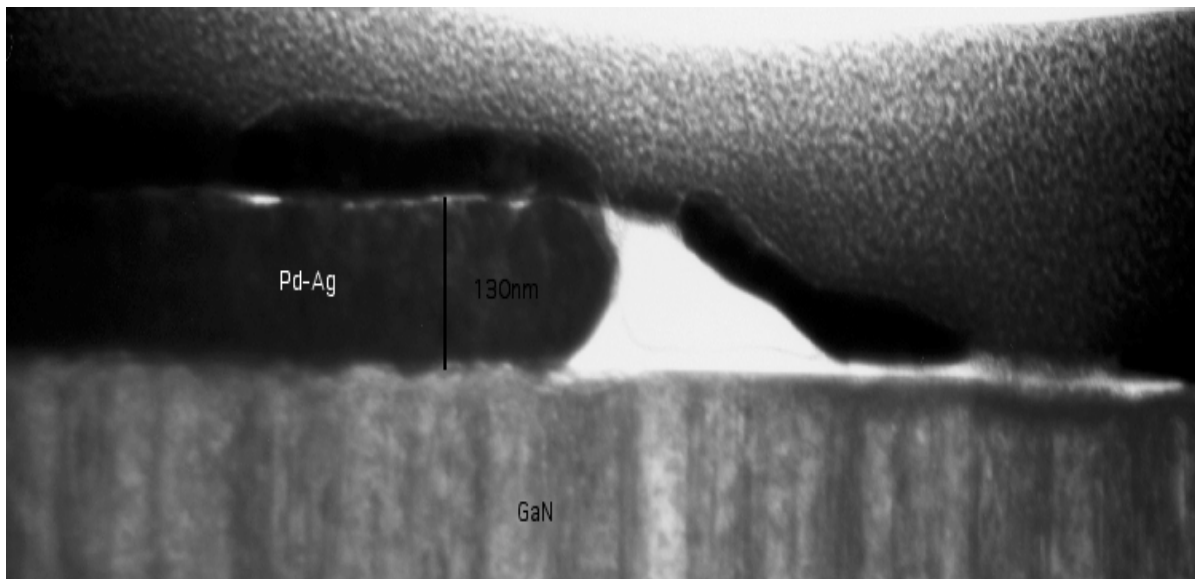


Figure 4: TEM micrograph of the PdAg with film thickness of 130 nm.

All of the metallization was carried out at the University of Utah. All metals were deposited by e-beam evaporation at the Hedco Laboratory at the University of Utah. Following the deposition, all sensors were subjected to annealing at 600°C for 5 minutes in the vacuum chamber. All three gate metals exhibited poor adhesion (Figure 5.) Only four working PdAg sensors were fabricated – all of these on one test article.

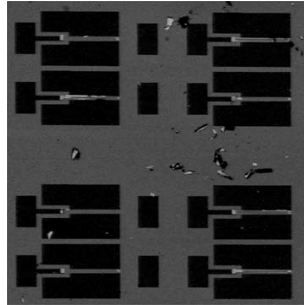


Figure 5: Rhodium sensor showing catastrophic delamination of the gate metal typical of the first fabrication run of these devices.

The sensors supplied by U. Utah include five with no gate (for reference), four with PdAg, eight with Rh and six with Pt. The pad assignments and electrical characteristics are shown in Figure 6.

Sample : No - Gate
Gate :

Device #	Drain or Source Pad #	Gate Pad #	$I_{d,max}$ @ $V_{ds} = 20$ V	Single or Dual Gate
1	7,8		23.88 mA	Un-gated
2	9,10		24.37 mA	Un-gated
3	11,12		25.56 mA	Un-gated
4	16,17		23.30 mA	Un-gated
5	18,19		21.42 mA	Un-gated
6				

Sample : Rh Up
Gate : Rhodium

Device #	Drain or Source Pad #	Gate Pad #	$I_{d,max}$ @ $V_G = +1.5$ V @ $V_{ds} = 15$ V	Single or Dual Gate
1	5,7	4	34 μ A	D
2	8,9	24	492 μ A	S
3	10,11	14	366 μ A	S
4	15,21	20	31.4 μ A	D
5				
6				

Sample : Pd - Ag Up
Gate : PdAg

Device #	Drain or Source Pad #	Gate Pad #	$I_{d,max}$ @ $V_G = +1.5$ V @ $V_{ds} = 15$ V	Single or Dual Gate
1	12,16	13	1.29 mA	D
2	17,18	10	2.1 mA	S
3	21,22	8	1.93 mA	S
4	23,24	7	1.29 mA	D
5				
6				

Sample : Rh DWN
Gate : Rhodium

Device #	Drain or Source Pad #	Gate Pad #	$I_{d,max}$ @ $V_G = +1.5$ V @ $V_{ds} = 15$ V	Single or Dual Gate
1	6,7	5	40.5 μ A	S
2	3,16	2	28.8 μ A	D
3	8,9	10	189.5 μ A	S
4	11,12	14	40.6 μ A	D
5				
6				

Sample : Pt - Right
Gate : Platinum

Device #	Drain or Source Pad #	Gate Pad #	$I_{d,max}$ @ $V_G = +1.5$ V @ $V_{ds} = 15$ V	Single or Dual Gate
1	11,12	14	1.50 mA	D
2	7,9	10	3.92 mA	D
3	18,20	19	2.40 mA	D
4	21,23	22	4.72 mA	S
5				
6				

Sample : Pt - Left
Gate : Platinum

Device #	Drain or Source Pad #	Gate Pad #	$I_{d,max}$ @ $V_G = +1.5$ V @ $V_{ds} = 15$ V	Single or Dual Gate
1	11,18	17	5.24 mA	S
2	9,10	8	4.52 mA	D
3				
4				
5				
6				

PAD ASSIGNMENT

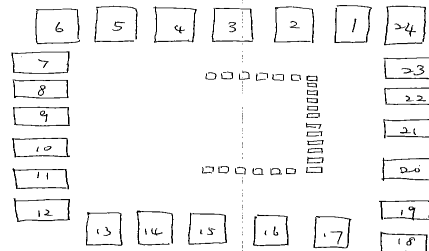


Figure 6: Listing of the pad assignments and device electrical characteristics of each of the devices

Sensor Electronics

Sensor electronics were designed to operate FET sensors at a constant source drain current. As changes in the gate voltage due to gas exposure change the source drain current, a feedback voltage equal and opposite to the gas effect is applied to the gate. The field gradient between the gate metal and the GaN can cause migration of charged species that result in long-term changes in the baseline electrical properties of the device. The potential for long term changes (drift) is reduced if the field remains constant. The circuit elements are shown in Figure 7.

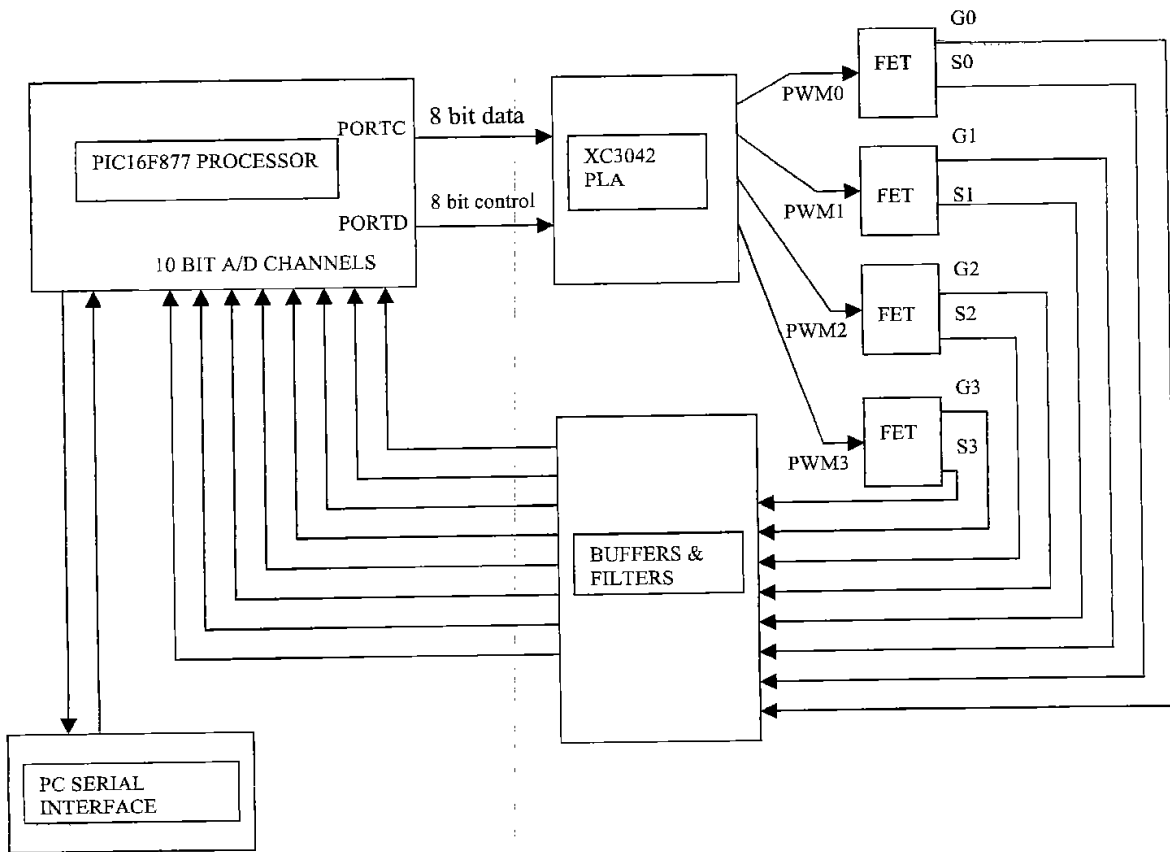


Figure 7: Block diagram of the constant current constant voltage sensor drive circuit.

The system consists of a MicroChip PIC 16F877 RISC controller, XYLINX XC3042 PLA, and unity gain buffers for the A/D interface used to maintain constant source current with up to four MODFETs or MESFETs. The PIC contains eight 10-bit A/D channels. Four channels are used to monitor FET source current (1 per FET). The other 4 channels are used to monitor FET gate voltage. The XC3042 is programmed to contain four 12-bit pulse width modulators (PWMs) that are used to control gate voltage. The PWMs are buffered using Analog Devices AD823 OP-AMPS. The PWMs are filtered using 2 pole R/C pi filters that have a pole frequency of 1 Hz.

The circuit is programmed through an RS232 connection with a terminal program (Hyperterminal on the data PC). The drain source voltage is a constant 12V. The unit searches

for the gate voltage to achieve the target source drain current. When the unit finds this gate voltage, it locks each sensor so that only external changes to the gate voltage or source drain current cause the output voltage to the gate metal to change.

Sensor Test Design

Testing in gas was done with the sensor in a quartz chamber (shown in Figure 8) heated by infrared radiation from quartz halogen lamps.



Figure 8: Sensor chamber showing exhaust tube at the right.

An aluminum plate with a Buna rubber gasket was clamped to the flange. Sensor wires, gas and thermocouple connections were made through penetrations in the aluminum plate and sealed with high-temperature RTV.

Data were obtained by polling four sensor gate voltages and four source voltages using a CIO-DAS16/Jr data acquisition board for the PC from Computerboards, Middleboro, MA. Data were logged by a program called vlogger and stored as a time-tagged text file. The text files were imported into Microsoft Excel and charted. We used two standard charts for data analysis. The first was an x-y plot of gate voltage versus time. The second chart was a 3-D surface chart with the x-axis showing CO concentration, the y-axis showing O₂ concentration and the z-axis showing the measured gate voltage.

Results

Surface and Interface Chemical and Structural Analysis

Focused ion beam trenching and TEM and X-ray analysis scanning across freshly exposed interfaces were performed. The data suggest little interdiffusion as close to the interface as 125 •. An unexpected result was that the Pd/Ag atomic ratios suggest substantial surface segregation of Ag. Both the lower surface near the GaN and the upper surface show

approximately 50-60% decrease in the Pd/Ag atomic ratio in the bulk from about 2:1 Pd:Ag to about 1:1 Pd:Ag at the surface. This is surprising in that both surfaces show similar effects suggesting little if any chemical or mechanical effect of the different interfaces. The surface energy and resulting reorganization in the annealing process is more consistent with the observation of a weak bond with the GaN and little or no Pd or Ag in the GaN quite near the interface.

The TEM and X-ray results show little or no interdiffusion of Rh with GaN. The rhodium material is thinner than the PdAg and shows evidence of less than theoretical density (see Figure 9).

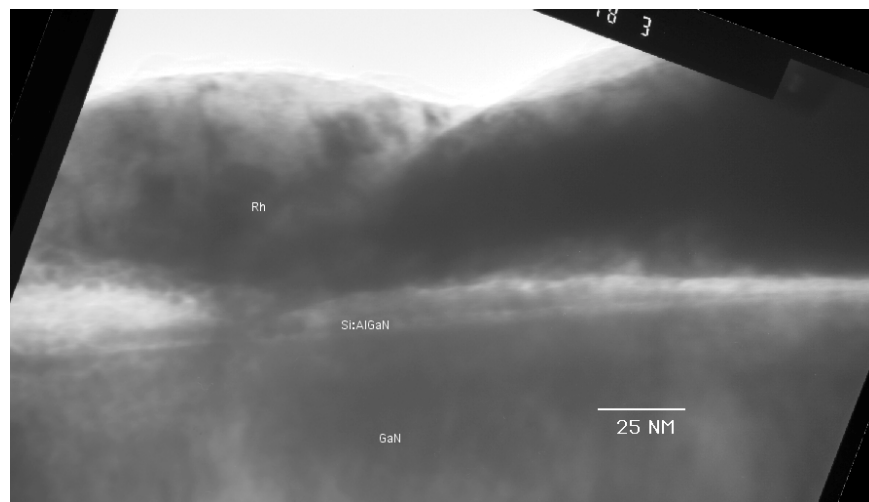


Figure 9: TEM of Rhodium film.

The Rh showed no interdiffusion with GaN within the resolution limit of the analysis (ca. 125 Å). The annealing treatment during fabrication was at a temperature much higher than that seen by any of the sensors during gas testing.

Gas Testing

Sensors were fabricated on sapphire substrates and dye attached to glass for easier electrical connection and are shown in Figure 10.

Gas exposure experiments were run at temperatures $T = 125^\circ\text{C}$. The gas concentration was varied by adjusting the duty cycles of a system of valves connected to a mixing manifold and controlled by a PC (See Table 2). The O_2 , CO and balance gases were all 35.0 ± 0.1% (vol) hydrogen. The O_2 standard was 2.0 ± 0.1% (vol) O_2 and the CO standard was 2010 ± 10 ppm. All gases were analyzed and certified by Scott Specialty Gas.

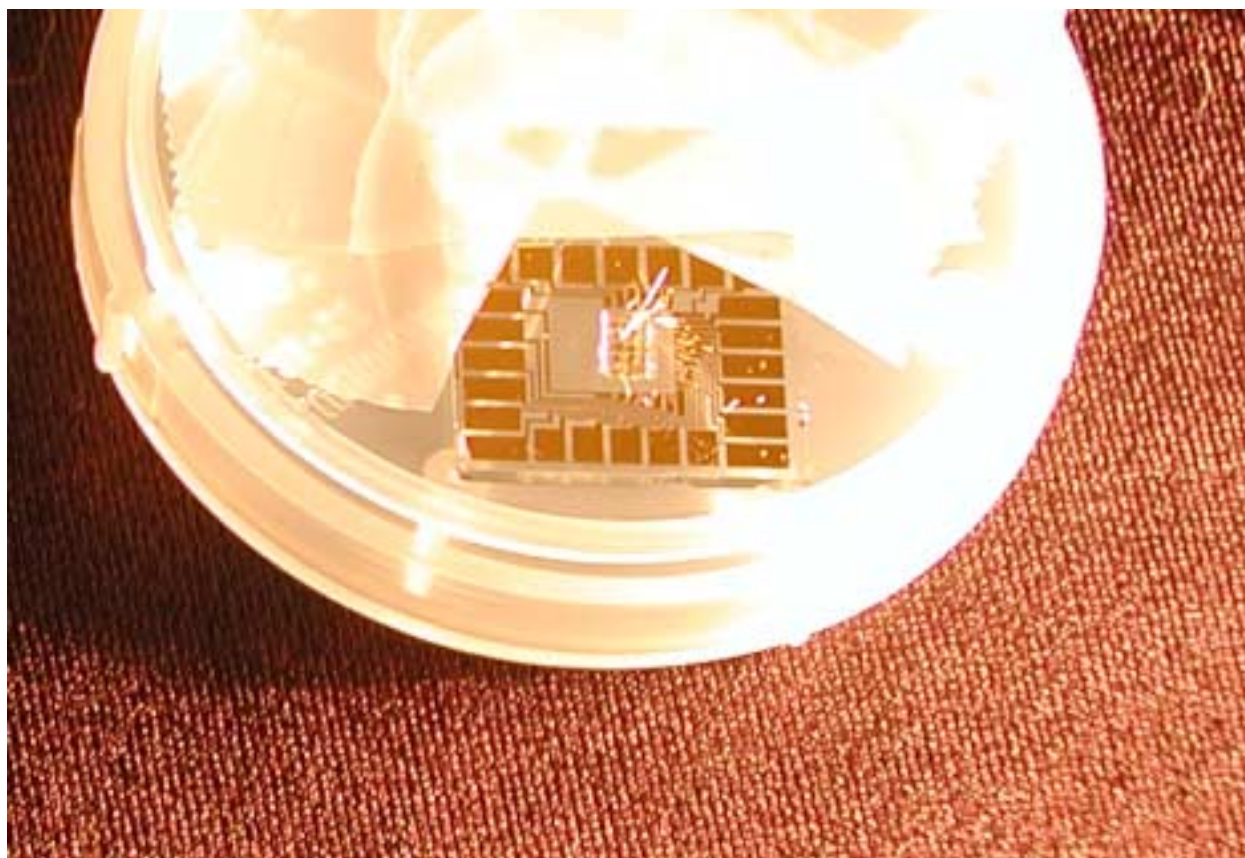


Figure 10: Sensor packaging.

Table 2: Order of experiments.

Total Flow (SCCM)	O ₂ (SCCM)	CO (SCCM)	Balance (SCCM)	[O ₂]ppm	[CO]ppm	p
600	300	15	285	5000	51	
600	300	300	0	5000	1015	
600	300	150	150	5000	507	
600	50	150	400	833	507	
600	50	300	250	833	1015	
600	50	15	535	833	51	
600	0	300	300	0	1015	
600	0	150	450	0	507	
600	0	15	585	0	51	

The flow rates of gases in Table 2 are in standard cubic centimeters per second.

Gate Voltage Versus Time

Initial experiments were performed on the PdAg sensor with each of the standard gas blends. Temperature was controlled by switching two 500-W quartz halogen lamps located above and

below the sensor chamber. Switching was accomplished by a CN4800 temperature controller and SSRDUAL240DC40 solid-state relay, Omega, Stamford, CT. A thermocouple (J-type) was bonded to the bottom of the glass sensor package. The thermocouple voltage was input to the CN4800 controller to maintain a constant temperature. Temperature fluctuations at the set point were less than $\pm 1^\circ\text{C}$. Voltage changes were in the range of 20 mV for PdAg for all exposures shown in Table 2 up to 125°C . There was typically greater sensitivity to the target gases with an increase in temperature for the Rh and Pt sensors. Unfortunately, the PdAg wire bonds were damaged prior to testing above 125°C . The highest temperature attained with the experimental test equipment was 200°C for the Rh results shown in Figure 11.

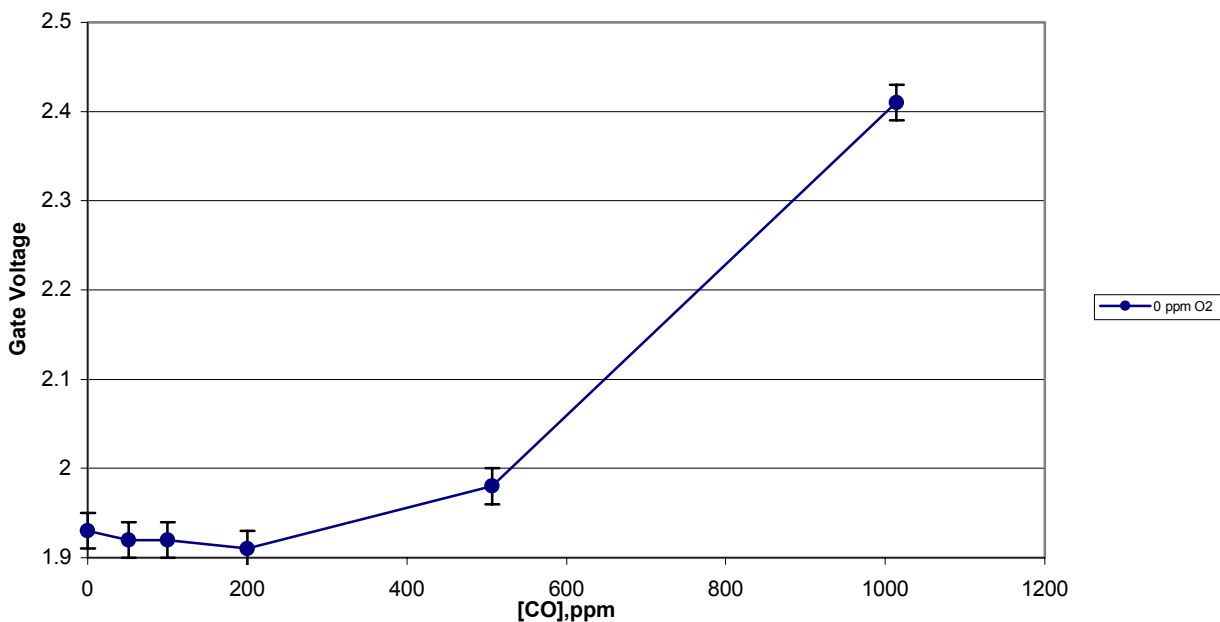


Figure 11: Rh sensor response to CO at zero ppm O₂ and 200°C

The data for Rh show substantially more sensitivity at 50°C on the dual gate sensors. By 150°C , all of the Rh sensors were showing the same response pattern with a maximum of 0.2V change in gate voltage compared with 0.3V change for Pt at 1014 ppm CO. At 200°C , the Rh sensor response increases significantly.

Experimental Results in CO and O₂

We constructed surface plots for results on Pt sensors showing the main effects of the two concentration variables on the gate voltage at 50°C , 100°C and 150°C (Figures 12, 13 and 14, respectively). We can also qualitatively assess the interaction effects of one concentration variable on the other. These results are shown below.

Both the single and dual gate responded in a similar pattern, with the dual gate more sensitive at low levels of CO (ca. <500 ppm) at 150°C . Neither has CO sensitivity in the target region of

low levels (ca. <500 ppm) until 150°C. At 100°C, the sensitivity to CO at 5,000 ppm O₂ changes sign compared to 0 ppm O₂.

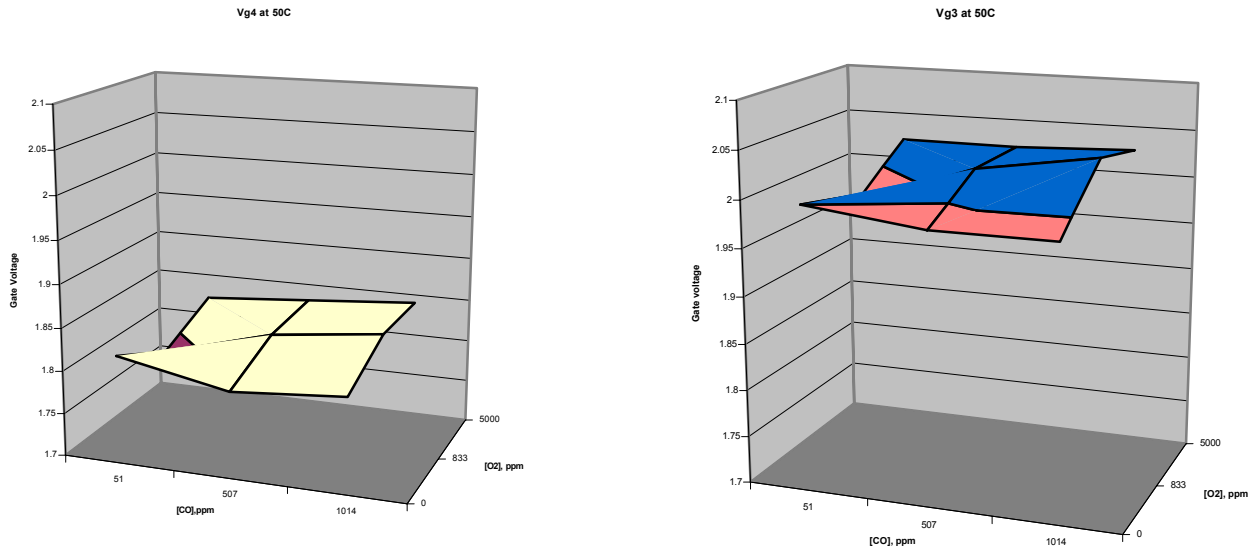


Figure 12: Single gate response on left. Dual gate response right. Both at 50°C.

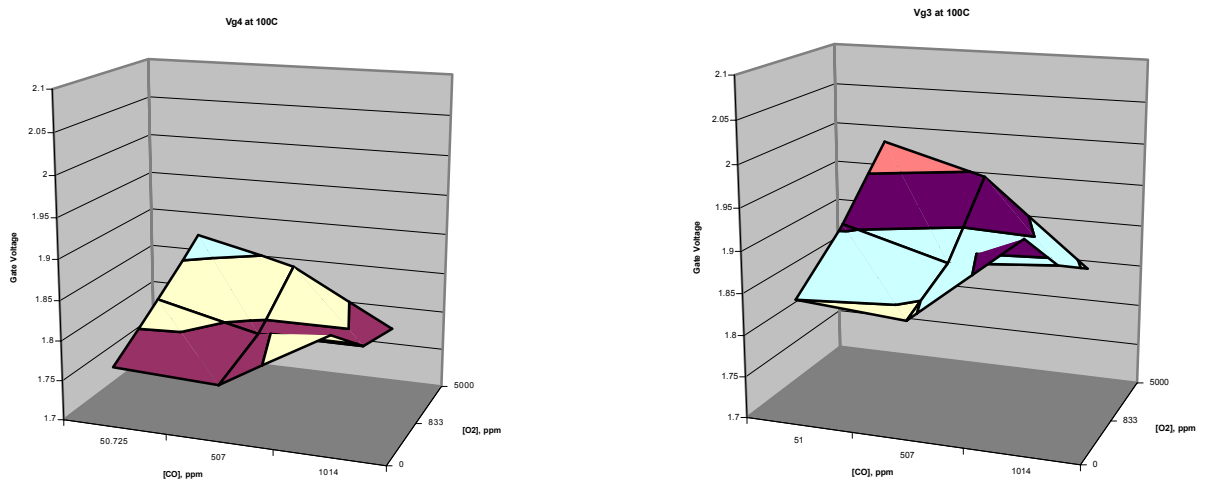


Figure 13: Single gate response on left. Dual gate response right. Both at 100°C.

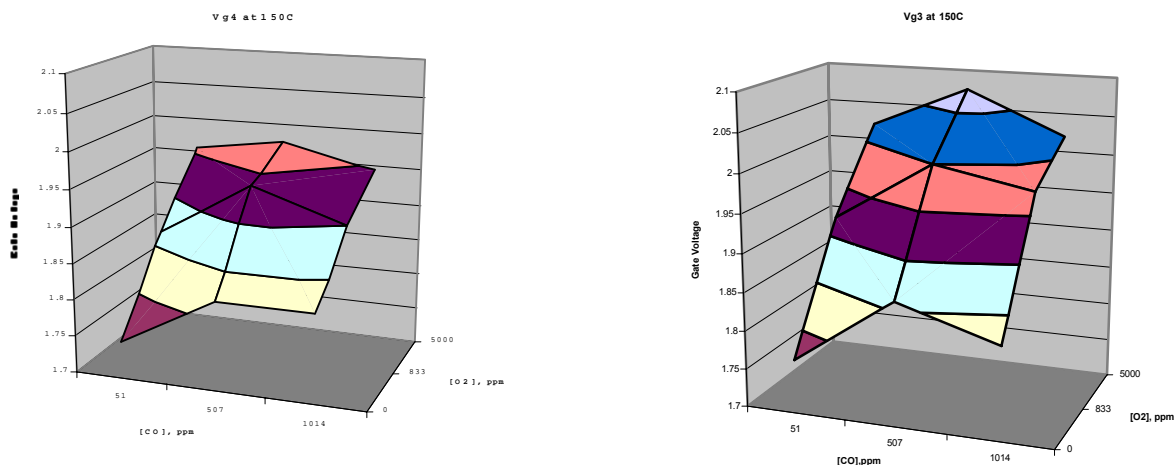


Figure 14: Single gate response on left. Dual gate response on right. Both at 150°C

Discussion and Conclusions

The strongest conclusions we can draw are: 1.) the gate Pt and Rh do not mix with the GaN up to 600 •C (5 minutes in vacuum), and mixing would not be a likely source of long-term drift in performance; 2.) little intermixing means poor adhesion and a poor manufacturing yield; 3.) high hydrogen concentration (35vol%) does not poison the sensor to ppm levels of CO; 4.) the O₂ sensitivity is comparable to the sensitivity to CO; 5.) the dual gate design shows greater sensitivity to CO and O₂ at temperatures >100•C; and 6.) the potential exists for sensing CO below 500 ppm in pure H₂ using catalytic gate FET sensors (i.e. with a separate sensor selective for CO or O₂, the CO and O₂ concentrations can be resolved assuming a simple mixture of H₂ and CO with only O₂ as an interferent). Since other contaminants are likely in H₂ fuel from carbon based-fuel sources, additional testing with other potential interferents is necessary and at higher temperatures in order to determine the performance of a sensor array based on the GaN FET sensor.

A tentative conclusion can be drawn that the improved sensitivity is the result of the dual gate over the single gate design. There is a twofold greater edge length of the dual gate over the single gate designs and is consistent with the model that more than hydrogen can adsorb and cause a direct change in the device performance. How the adsorption alters the field inside the semiconductor is an issue that begs further study.

Acknowledgments

The authors would like to acknowledge the support provided by the DOE Hydrogen Program through contract no. G010453. The authors are also grateful for the design and fabrication assistance of Howard Chern at the University of Utah, Randy Sindelar for electronics design and Jack McCarthy at OGI for microscopy.

References

- Cassidy, J., S. Pons and J. Janata. 1986 *Anal. Chem.*, 58:1757.
- Dobos, A.K., et al. 1990. *Sensors and Actuators*, B1:25
- Fan, Z., S.N. Mohammad, W. Kim, O. Aktas, A.E. Botchkarev, K. Suzue, and H. Morkoc. 1996. *J. Electronic. Materials*, 25:1703.
- Feinstein, D.I., C. Renn, M. Scharff and S.C. Pyke. 1997 "Metal-Insulator-Semiconductor (MIS) Gas Sensor Array for Gas Analysis and Diagnosing Faults in Oil-Filled Power Transformers," 191st Meeting of the Electrochemical Society, Montreal, Quebec, Canada.
- Hedborg, E., F. Winqvist, and I. Lundstrom. 1994. *Appl. Phys. Lett.*, 64(4):420.
- Hughes, R.C., W.K. Schubert, T.E. Zipperian, J.L. Rodriguez and T.A. Plut. 1987. *J. Appl. Phys.*, 62:1074.
- Lin, M.E., Z. Ma, F.Y. Huang, Z.F. Fang, L.H. Allen, and H. Morkoc. 1994. *Appl. Phys. Lett.*, 64:1003.
- Lundstrom, I., M.S. Shivaraman, C. Svensson, and L. Lundqvist. 1975. *J. Appl. Phys.*, 26:55.
- Lundstrom, I., M. Armgarth and L.-G. Petersson. 1989. *CRC Critical Reviews in Solid State and Materials Sciences*, 15:201-278.
- Lundstrom, I., and L.G. Petersson. 1996. *J. Vac. Sci. Technol.*, A, 14(3):1539.
- Niessen, A.K., and A.R. Miedema. 1983. *Ber. Bunsenges. Phys. Chem.*, 87:717 and references therein.
- Ping, A.T., M. Asif Khan and I. Adesida. 1996. *J. Electronic. Materials*, 25:819.
- Poteat, T.L., B. Lalevic, B. Kuliyeve, M. Yousef and M. Chem. 1983. *J. Electron. Mater.*, 12:181.
- Pyke, S.C. 1993. "Transformer Fault Gas Analyzer," (invited paper) First Annual EPRI Substation Equipment Diagnostic Conference, Palo Alto, CA.
- Spetz, A.L., F. Winqvist, H. Sundgren and I. Lundstrom. 1992. "Field Effect Gas Sensors," in G. Sberveglieri (ed.), *Gas Sensors*, Kluwer, Dordrecht, 219-279.
- Spetz, A.L., A. Baranzahi, P. Tobias and I. Lundstrom. 1997. *Phys Stat. Sol. (a)* 162:493-511.
- Tobias, A. Baransahi, A. Lloyd-Spez, O. Kordina, E. Janzen and I. Lundstrom. 1997. *IEEE Electron Device Letters*, 18:287-289.
- Wu, Y., W. Jiang, B. Keller, S. Keller, D. Kapolnek, S. DenBarrs and U. Mishra. 1995. *Topical Workshop on III-V Nitrides*, Nagoya, Japan.

DESIGN AND DEVELOPMENT OF NEW NANO-ENGINEERED GLASS-CERAMIC PROTON CONDUCTING MEMBRANES

Steve W. Martin*, Renaud C. Belin and Jacob T. Sutherland
Department of Materials Science & Engineering
Iowa State University, Ames, IA 50011

Abstract

New high-temperature, anhydrous fast proton conducting (FPC) membranes for use in new high-performance fuel cells are being developed. These new nanoengineered glass-ceramic proton conducting membranes (GCPCMs) are expected to yield high proton conductivities between 100 and 300°C, excellent thermal stability, up to 300°C, superior electrochemical and chemical stability, and zero fuel cross-over diffusion. These high-performance GCPCMs are expected to solve many if not all of the critical problems currently seen in the proton conducting membrane-of-choice, NafionTM, used in polymer electrolyte membrane (PEM) fuel cells.

In this effort, sulfide-based materials have been studied. These materials doped with H₂S are stable in air and water, which is an obvious requirement of a H₂-O₂ fuel cell. Glassy and crystalline sulfide-based materials have been synthesized and high-pressure protonating experiments performed. Using such a method, these experiments resulted in protonated amorphous materials. Structural characterization of the obtained protonated materials has been carried out using IR and Raman spectroscopies and x-ray diffraction.

* Author to whom correspondence should be directed

Introduction

Fuel cells, based upon hydrogen as the fuel and air as the oxidizer, are known to hold great promise as portable energy sources to replace the internal combustion engine as well as some battery technologies (Colombian 1999). While there are many different configurations of such fuel cells (e.g., Blomen 1993), polymer electrolyte membrane (PEM) fuel cells are among the most promising for a number of different reasons (Colombian 1999, pp.63 and 493). They offer a lower operation temperature, simplified cell configuration, relatively quick and efficient start-up, inexpensive cell design, and relatively high power densities. Much research has been done to move the PEM fuel cell from design into the production stage (e.g., Gottesfeld 1997).

However, PEM fuel cells are not without many critical problems and unresolved design issues. Low-temperature operation is required to protect the fragile polymer membrane and to keep it hydrated so as to maintain its high proton conductivity. Because the polymer membrane is hydrated, many fuels such as methanol rapidly diffuse across the membrane to the cathode and dramatically degrade the performance of the fuel cell (e.g., ONR-DOE 1999). The relatively low operation temperature also limits the catalytic efficiency of non-platinum catalysts.

For these reasons, higher temperature, anhydrous, solid, high-proton conductivity membranes are critically needed. By operating above the steam point of water, the by-product water is produced as a more easily managed gas, less expensive catalysts with good performance at elevated temperatures can be used, and, due to their solid structure, would have zero cross-over of fuels such as methanol.

In this project, new anhydrous, glass-ceramic proton conducting membranes (GCPCMs) are being designed and developed. Such membranes are expected to have proton conductivities in excess of $10^{-1}(\Omega^{-1}\text{cm}^{-1})$ above 100°C (see Figure 1), and zero electronic conductivities combined with superior thermal, mechanical, chemical, and electrochemical stabilities. Their solid and anhydrous structure will obviously limit fuel crossover as well. By using carefully controlled glass-ceramic processing, the anisotropy and texture of the nanostructures of the GCPCMs can be tailored to the perpendicular direction of the thin film and thereby optimizing the conductivity. The mechanical properties will also be optimized through the generation of a two-phase glass-ceramic with a carefully controlled and fine-grained nanostructure. Finally, because of their inherent increased thermal-mechanical stability, the thermal and electrochemical stability of the GCPCMs will be far superior to that of NafionTM and Nafion-like polymer membranes. Thin film processing of glass-ceramic materials is a well-known area of materials processing and will be used to process thin films of the GCPCMs.

Chalcogenide fast ion conducting (FIC) glasses proved unsuitable for use in rechargeable lithium batteries because of the volume changes that occur in the cells during both discharge and recharge cycles of the cells (Julien 1994). However, such volume changes do not occur in hydrogen-oxygen fuel cells because both reactants and products are brought to and carried away from the electrodes as liquids and/or gases. Hence, mechanical strain in the fuel cell during operation is not an issue and as such, the mechanical strength of the GCPCMs combined with their high proton conductivity, and high chemical and electrochemical stabilities gives them tremendous advantages over polymer membranes. For these reasons, GCPCMs become an

exciting and new alternative technology for solving many if not all of the problems associated with PEM fuel cells.

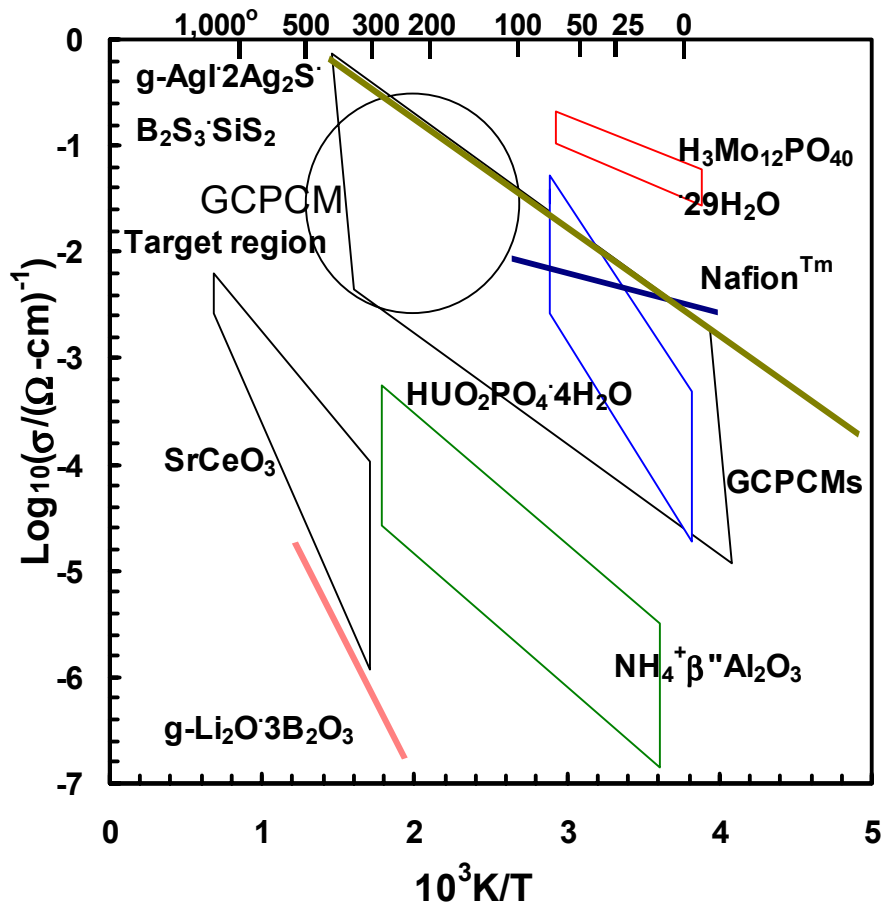


Figure 1: Arrhenius plots of the conductivity for different proton conducting solids (Colombian, P. 1999, Martin, S. W. 1991, Kincs, J. 1996). FIC glasses, $g\text{-Li}_2\text{O}\cdot 3\text{B}_2\text{O}_3$ and $g\text{-AgI}\cdot 2\text{Ag}_2\text{S}\cdot 2\text{B}_2\text{S}_3\cdot \text{SiS}_2$, are included to show the level of conductivity increase that can be achieved when oxide chemistries are replaced by optimized sulfide chemistries.

Inorganic glassy FICs have been known for a long time and much success has been achieved at increasing their ionic conductivity through systematic manipulation of the glass chemistry (Martin 1991). Oxide glasses, like oxide ceramic proton conductors, exhibit ion conduction, but it is very limited due to the strong coulombic interaction between alkali and oxygen anions (Martin 1986). Proton conducting oxide glasses are likewise known and exhibit similar low conductivity values (Abe 1993). Higher values can be obtained by using heavily hydrated oxide glasses, but these glasses, like their hydrated salt and polymer analogs, suffer from low operating temperatures (Abe 1982) due to the boil-off of water.

Recently, chalcogenide-based glasses, those based on the elements S, Se, and Te, have been found to exhibit many orders of magnitude increase in the alkali ion conductivity over their oxide analogues (Angell 1992). For example, see the comparison of two such glasses on Figure

1, cf. $g\text{-Li}_2\text{O}+3\text{B}_2\text{O}_3$ and $g\text{-AgI}+2\text{Ag}_2\text{S}+\text{B}_2\text{S}_3+\text{SiS}_2$. Conductivities as high as $10^{-2}(\Omega\text{cm})^{-1}$ at room temperature have been observed for these chalcogenide glasses (Kincs 1996) and it naturally becomes a question of whether an attempt has been made to develop similar FPC chalcogenide glasses. After a very thorough search of both the open and patent literature, no record has been found of the attempt to synthesize a proton conducting chalcogenide glass that would determine whether the 1,000- to 1,000,000-fold increase in conductivity for alkali ion conducting sulfide glasses over that of the oxide glasses is also observed for proton conducting sulfide glasses. In fact, no record can be found of a proton-containing sulfide glass, independent of whether the glass was used a fast ion conductor or not.

Our research group has studied chalcogenide-based glass former systems extensively and has developed synthetic procedures to easily prepare these materials in large quantities (Cho 1995). The system that we have explored is based on strongly glass-forming sulfide compounds. Our base material is known to be relatively stable in air and water. H_2S has been added to this base material by gaseous reaction between H_2S and the base glass heated above their vaporization temperature.

Experimental Section

Preparation of the Base Materials

To prepare the sulfide-based material, the corresponding elements, mixed in stoichiometric amounts, were sealed under vacuum in a silica tube and heated at 900°C in a rotating furnace for eight hours. Slow cooling in the furnace leads to crystallization while water quenching leads to a glassy material. A glove box ($<4\text{ppm O}_2$ and H_2O) was used for all handling of starting and final materials.

Preparation of the Protonated Materials

H₂S Flow Protonation Experiment

A carbon crucible was loaded with the starting material and placed in a silica tube. This is accomplished in a glove box with an inert He atmosphere. The material was heated under a H_2S gas flow for 1 hour at temperatures higher than its sublimation temperature, which allows the reaction between gaseous starting material and H_2S . The product of the reaction is deposited in the cold part of the tube outside the furnace. It appears as a light brown powder and is the same whether the starting material crystalline or glassy.

High Pressure Protonation Experiments

In order to facilitate the reaction between H_2S and the base material, a high-pressure system, shown in Figure 2, was constructed. This system allows the reaction at pressures higher than atmospheric pressure, outside of the glove box. It is composed of a reaction vessel made of alumina surrounded by a stainless steel 310 sheath connected to two gas cylinders (H_2S and N_2). After the reactor is placed in a furnace, connected to the system and put under vacuum, it is filled with H_2S gas. A water-cooling collar is placed around the top part of the reactor.

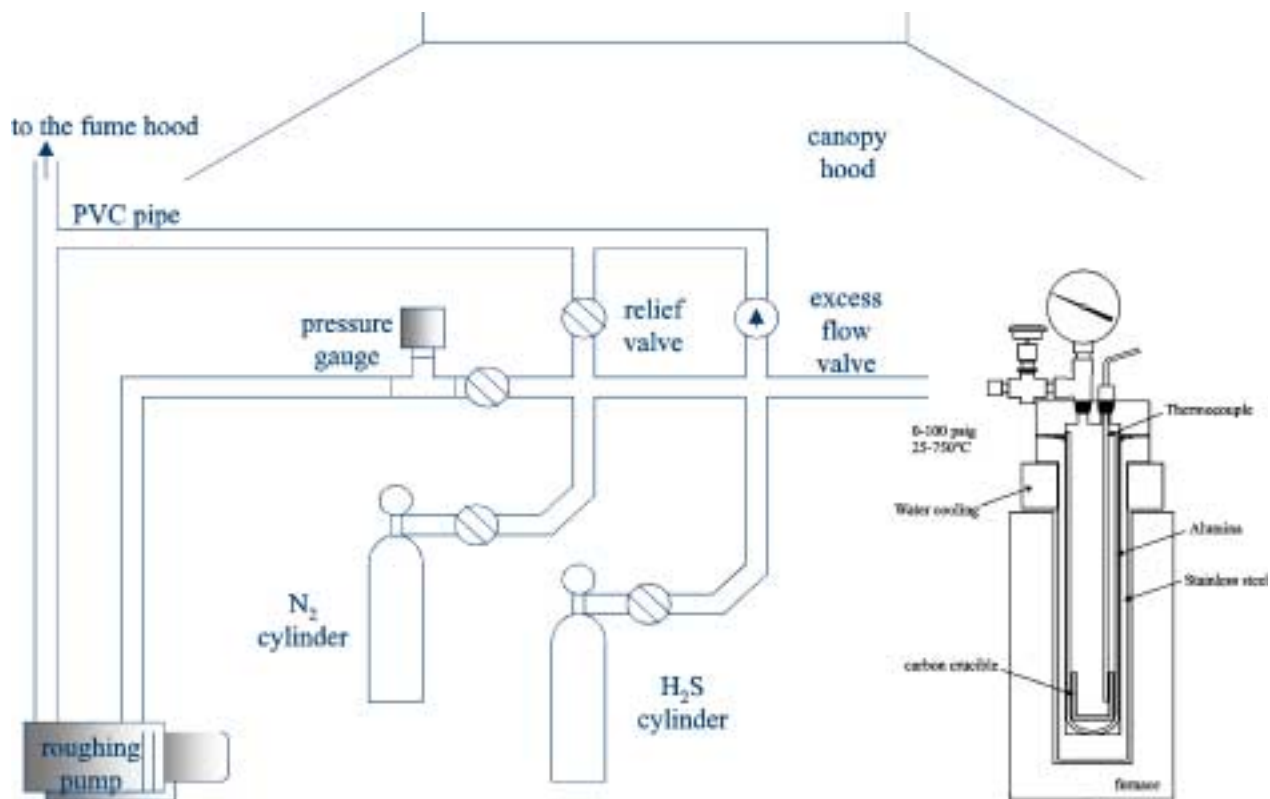


Figure 2: High-pressure synthesis system.

This device meets all the necessary safety requirements for handling and using H_2S gas: it is surrounded by polycarbonate protective sheets and is situated under the canopy hood. All the exhaust parts are linked to the main fume hood pipe through PVC pipes. A H_2S leak detector has been installed near the system and safety procedures have been developed for the use of H_2S in the laboratory.

High Pressure Protonation Experiments

Successful protonation experiments were conducted using the previously described system. The starting material was placed in a carbon crucible inside of the reactor then held for a few hours at high temperature under a high pressure of H_2S . After all the material was sublimated, a very thin brown powder was collected in the cold top part of the reactor.

Results and Discussion

Characterization of the Base Material

The Raman spectra of crystalline starting material are represented in Figure 3A ($100\text{-}500\text{ cm}^{-1}$) and Figure 3B ($100\text{-}4000\text{ cm}^{-1}$). These spectra are in good agreement with spectra reported earlier for tetrahedral sulfide-based materials (Kawamoto 1982, Boolchand 1986). It can be explained

in terms of vibrations of isolated tetrahedral units, even though the units are connected together. The four vibrational modes are Raman active. The more intense Raman peak at $\sim 360\text{ cm}^{-1}$ is assigned to the ν_1 (A_1) mode, while the ν_2 (E), ν_3 (F2), and ν_4 (F2) modes are observed at frequencies around 120, 424, and 157 cm^{-1} respectively (Kawamoto 1982). The X-ray diffractogram of the material shown in Figure 5 confirms its crystallinity.

The mid-IR spectrum, Figure 4, shows two bands around $3,400$ and $2,900\text{ cm}^{-1}$. They correspond to O-H and C-H impurities in the material. Such bands were observable in one the commercial starting elements. By examining the Raman spectra in a larger frequency range, shown in Figure 3B, it is clear that these bands have a very low intensity compared to the main vibrations bands, showing that the amount of impurities is quite small.

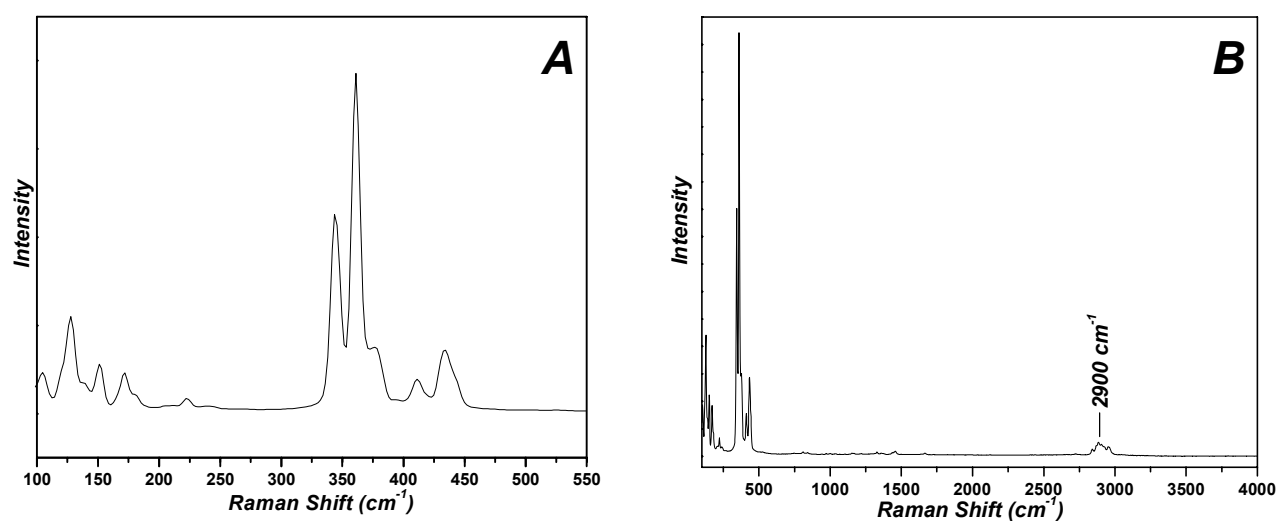


Figure 3: Raman spectra of the sulfide starting material, low frequency range (A) and full frequency range (B).

Characterization of the Protonated Materials

H₂S Flow Protonated Materials

Figure 4 shows the infrared spectra of the obtained material by using a flow of H_2S over the starting material compared to the starting material. If the material incorporated H_2S , an infrared band for the S-H vibration should be observable around 2500 cm^{-1} . Unfortunately, this is not the case, as the S-H band is as small as in the starting material itself.

High Pressure Protonated material

In order to characterize the nature of this material, x-ray diffraction, and IR and Raman spectroscopy have been carried out.

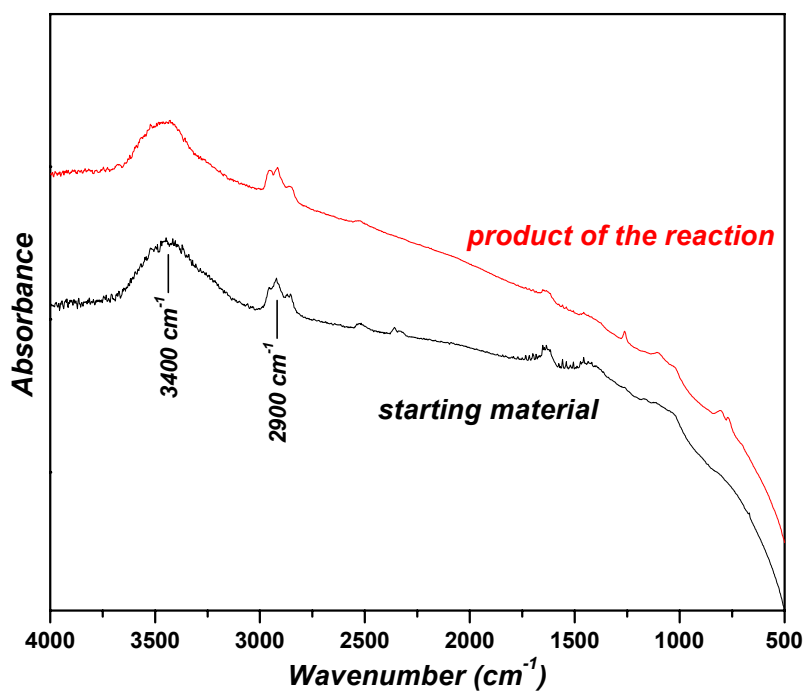


Figure 4: IR spectra of the starting material and of the obtained material.

The x-ray diffractogram on Figure 5 shows that this material is amorphous, as no diffraction peaks are observed. For comparison, the XRD pattern for the crystalline starting material is shown. The IR spectrum of Figure 6A shows a comparison between the glassy starting material and the protonated material. While the slight O-H and C-H contamination is still present, the S-H vibration band at 2500 cm^{-1} is now clearly observable, indicating the protonation of the material. The Raman spectra on Figure 6B shows that the structure of the protonated GeS₂-based material is very close to that of normal glassy material as the four tetrahedral bands ν_1 (A₁), ν_2 (E), ν_3 (F₂) and ν_4 (F₂) are still observable at 342, 115, 368 and 150 cm^{-1} . However, there is a main difference: the presence of a band at 415 cm^{-1} could account for a partial change of symmetry in the structure from T_d to C_{3v} and C_{2v} as the network is depolymerized and H₂S incorporated in the material. Kamitsos et al. have observed the same features in silver thiogermanates system (Kamitsos 1994).

The stability in air and water of the protonated material has been tested where samples have been kept in air and water for several days. Raman and infrared spectra were recorded after this. There were no noticeable differences between the original protonated material and the samples obtained after such a treatment, showing that this material is relatively stable to moisture, which is really promising for fuel cells applications.

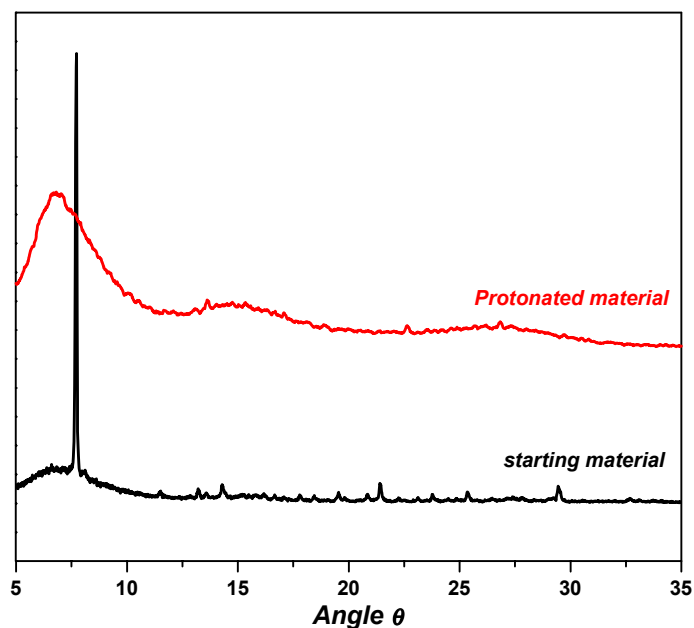


Figure 5: X-ray diffractogram of the starting material and of the protonated material.

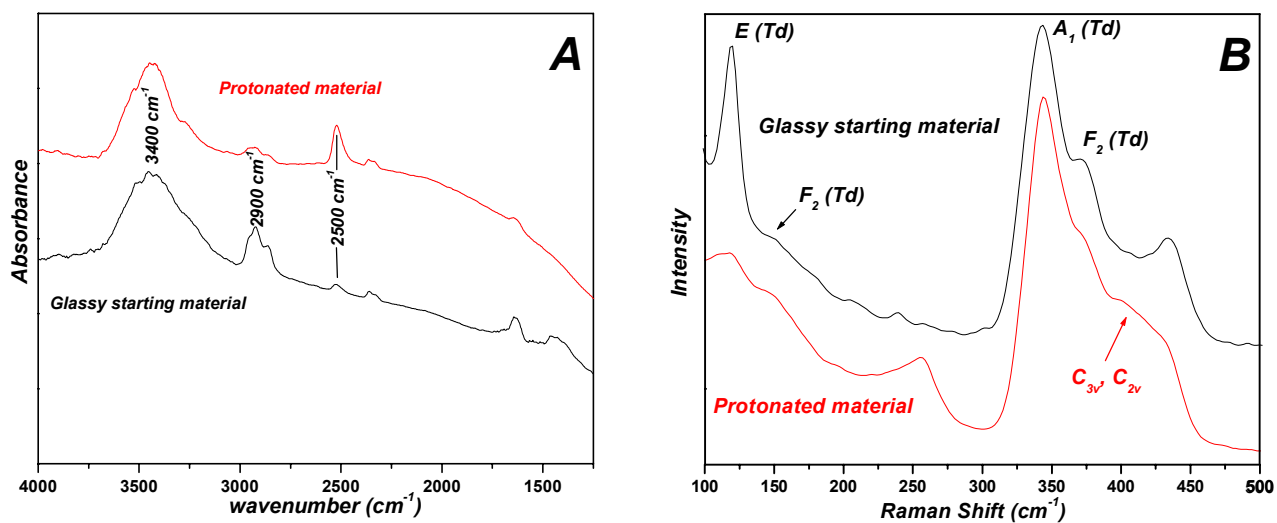


Figure 6: IR (A) and Raman (B) spectra of the protonated material and of the glassy starting material.

Future Work

Glass-ceraming these materials prior to use and optimizing the nanostructure and properties of the resulting glass-ceramic is expected to produce membranes with higher performance than the base-materials alone. The glass-ceramic will not only have a higher thermal stability since it is already crystallized it will be expected to have improved chemical and electrochemical stabilities as well. By controlling the nucleation and growth kinetics during the glass-ceramic processing, careful control will be achieved over the resulting physical properties of the GCPCMs. Multi-dimensional glass-ceramic processing “maps” will be developed by varying the processing conditions; nucleation temperature; nucleation time; growth temperature; growth time; and nucleating agent through predetermined ranges. Careful analysis of the resulting nanostructures will be determined using SEM, the physical properties of the GCPCMs will be carefully characterized. Proton conductivity will be determined using impedance spectroscopy. Electrochemical stability, chemical stability, thermal stability limit thermal expansion coefficient and mechanical strength will also be determined. ^1H NMR spectroscopy will be used to characterize proton conduction dynamics in GCPCMs.

References

- Abe, Y., Shimakawa, H., Hench, L. L. 1982. *J. Non-Cryst. Solids*, 51:357.
- Abe, Y., Hosono, H., Lee, W. H., Kasuga, T. 1993. *Phys. Rev. B*, 48(15):621.
- Angell, C. A. 1992. *Annu. Rev. Phys. Chem.*, 43:693.
- Belin, R. 2000. PhD thesis. Université Montpellier II, France.
- Blomen, L., Mugerwa, M. 1993. *Fuel Cell Systems*. New York, Plenum Press.
- Boolchand, P., Grothaus, J., Tenhover M., Hazle, M. A. 1986. *Phys. Rev. B*, 33:5421.
- Cho, J., Martin, S. W. 1995. *Phys. Chem. Glasses*, 36(6):239-43.
- Colombian, P. 1999 *Fuel Cells: Green Power*. Publication number, LA-UR-99-3231, Los Alamos National Laboratory, J. Millikan, ed.
- Julien, C., Nazri, A. 1994. *Solid State Batteries: Materials Design and Optimization*. Boston, Kluwer Academic Publishers.
- Kamitsos, E. I., Kapoutsis, J. A., Kryssikos, G. D., Pradel, A., Ribes, M. 1994. *J. Solid State Chem.*, 112(2):255-61.
- Kawamoto, Y., Kawashima, C. 1982. *Mat. Res. Bull.*, 17:1511-16.
- Martin, S. W. 1986. *J. Non-Cryst. Solids*, 83:185.

Martin, S. W., Bloyer, D. R. 1990. *J. Am. Ceram. Soc.*, 73:3481.

Martin, S. W. 1991. *J. Am. Ceram. Soc.*, 74:1767.

Kincs, J., Martin, S. W. 1996. *Phys. Rev. Lett.*, 76:70.

ONR-DOE. 1999. *Proceedings of the Workshop on Polymer Electrolyte Fuel Cells*. Baltimore, MD, Oct. 6-8.

Thomas, D., Tridot, G. 1964. *Hebd. Seances Acad. Sci.*, 259:3559.

INTERFACIAL STABILITY OF THIN FILM HYDROGEN SENSORS

**Roland Pitts, Ping Liu, Se-Hee Lee, Ed Tracy
National Renewable Energy Laboratory
Golden, CO 80401**

**R. Davis Smith, Carlton Salter
DCH Technology
Valencia, CA 91355**

Abstract

The goal of this research is to make available the technology to produce low-cost, lightweight, reliable hydrogen sensors for use as safety monitors wherever hydrogen is used, stored, or produced. Prior work has identified thin films that can be used as hydrogen detectors by measuring physical properties of those films and monitoring those characteristics that change in the presence of hydrogen. In all of the thin film sensors investigated to date, long-term changes in the response to hydrogen after exposure to ambient air, or short-term changes in response after exposure to pollutants have been noted. The specific objective of this work is to study those mechanisms affecting the stability of the films with respect to these environmental factors and to use the knowledge gained from these studies to craft methods of mitigating those mechanisms. We have worked primarily with thin films that can be coated on the end of a fiber optic cable. This configuration meets the qualifications of being lightweight, potentially very inexpensive, and inherently safe, since no electrical leads are employed in the monitored space. We have concentrated on studying the stability of the palladium surface with respect to the dissociation of hydrogen, since the use of palladium as either the primary sensor material or as a catalyst layer over the sensor materials appears to constitute the method of choice for such low-cost hydrogen sensors.

Introduction

Public perception of the hazards of hydrogen fuel use, its production, and storage as well as governmental regulation will require extensive safety precautions and codes to be in place before hydrogen can be incorporated into the energy infrastructure in a meaningful way. Currently, commercial hydrogen detectors are not useful for widespread use, particularly in transportation, because they are too bulky, expensive, and dangerous. Work sponsored by the DOE Hydrogen Program has developed promising technologies for satisfying the future demands. Sensors that exhibit physical changes when exposed to hydrogen have been fabricated and tested, and promise to provide inexpensive hydrogen detection. For example, there are thick film and thin film metallic sensors that exhibit conductivity changes when hydrogen adsorbs on the surface and is incorporated into the lattice. There are thin film sensors that are deposited as a part of a field-effect transistor, where accumulation of atomic hydrogen at the metal/insulator interface results in a change of response from the circuit. Finally, there are chemochromic sensors, where reaction of thin films with hydrogen gas results in an optical change that can be sensed by a probe beam of light. All of these sensors have the potential for degradation in their performance over time due either to mechanisms that are inherent in their construction, a result of their cyclic interaction with hydrogen, or contamination from impurities in the environments in which they will be used. Prior research to study those issues has ranked their importance to the various sensor concepts and has at least suggested the relevant mechanisms, which point to methods of mitigating these factors. The research reported here addresses those issues and will be directed toward substantially extending the lifetime and utility of these sensors, especially in the configuration that is based upon the optical response of the sensor materials. This concept appears to offer the greatest safety by design, and would appear to meet cost goals.

Background on Optical Sensors

The fiber-optic sensor consists of coatings at the end of an optical fiber that sense the presence of hydrogen in air. When the coating reacts with the hydrogen, its optical properties are changed. Light from a central electro-optic control unit is projected down the optical fiber where it is either reflected from the sensor coating back to central optical detector, or is transmitted to another fiber leading to the central optical detector. A change in the reflected or transmitted intensity indicates the presence of hydrogen. The fiber-optic detector offers inherent safety by removing all electrical power from the test sites and reduces signal-processing problems by minimizing electromagnetic interference. Critical detector performance requirements (for all four configurations) include high selectivity, response speed, and durability as well as potential for low-cost fabrication.

Fiber-optic sensors have been made in a variety of configurations, most using one or more thin films at the end of the cable. Butler (1991, 1994) suggested using a thin film of Pd as a mirror on the end of a fiber optic cable. Garcia (1996) and Mandelis (1998) describe a more sensitive (and much more complex) method of sensing hydrogen optically. They use a diode laser and beam splitters to illuminate reference flats in a gas flow chamber. One flat is coated with Pd, while the other is coated with Al. Reaction of hydrogen at concentrations above 0.2% in nitrogen is registered by the optical changes of the Pd film.

Ito (1984) originally proposed using the palladium-catalyzed reaction of amorphous tungsten oxide with hydrogen in a fiber-optic hydrogen detector. The reaction causes partial reduction of the tungsten oxide and introduces a strong optical-absorption band near 800 nm. The increase in absorption reduces the intensity of the light beam reflected by the coated optical fiber. We found this sensor design to be adequately sensitive, but too slow for the intended use.

A different sensor design using a surface-plasmon resonance (SPR) configuration was also evaluated (Raether, 1988 and Chadwick, 1993). Chemochromic materials, such as tungsten oxide and certain Lanthanide hydrides (Griessen, 1997) were used in thin film stacks on a sensor head at the end of an optical fiber (Benson, 1998). A layer of silver was deposited first, in which the surface plasmon was generated. The chemochromic layer was deposited upon the silver, followed by a thin layer of palladium, which acted as the hydrogen dissociation catalyst. When hydrogen comes in contact with the sensor head, small amounts of atomic hydrogen change the optical properties of the chemochromic layer. The SPR shifts in response to very subtle changes in the refractive index of the coating and is detected as a change in intensity of the reflected beam of light. This shift can be monitored to provide a faster response than was evident in the first tungsten oxide sensors.

Yet another variation of this sensor design uses Pd deposits on the sides of the fiber optic cable, after the jacketing material in a section of the fiber is removed (Tabib-Azar, 1999). In this configuration the Pd interacts with the evanescent field as the light beam propagates down the fiber via total internal reflection. When exposed to hydrogen, the complex index of refraction of the Pd film changes, affecting the transmission of light down the fiber. Detection of variations of light intensity at the end of the fiber signals changes in the Pd film due to the incorporation of hydrogen. This construction allows multiple sensors to be deposited along a single strand of fiber-optic cable. However, to allow this concept to identify the sensing station that has detected hydrogen, fiber optic Bragg gratings (FBGs) must be etched into the fiber at each station (Sutapun, 1999). The individual gratings are tuned to specific wavelengths. Then, they are coated with Pd. Hydrogen incorporated into the Pd causes an expansion of the film that results in a stretch of the fiber and an alteration in the spacing of the FBG. The FBG acts as a strain gage and shows a linear response in the shift in Bragg wavelength with hydrogen concentration over a range from 0.3% to 1.8% hydrogen in nitrogen. Thus, multiplexed hydrogen sensors may be fabricated on a single fiber.

We have extended the concepts of Benson, et al. (1998), and have improved upon the chemochromic materials used as the sensing material under the Pd layer (Liu, et al., 2001). Materials are now available that can be tailored in sensitivity and response to hydrogen. There is hope that they can be made at least semi-quantitative in the measurement of the partial pressure of hydrogen over useful ranges up to 100 % hydrogen.

Key Issues

There are four key issues to be met by any hydrogen detector, if it is to gain wide acceptance for use within the hydrogen infrastructure (production, storage, transportation, and utilization).

- **Performance** – sensors must respond to the presence of hydrogen well before the explosive limit (4% H₂ in air) is reached. This requirement dictates that a premium is placed on detecting small quantities of hydrogen in the ambient atmosphere (prefer detection limit of 0.5% or better). The sensor must also respond quickly (prefer response time of 1 second or less), so that corrective action or evacuation can occur before the explosive limit is reached. Fast response times are also desired for diagnostic study of hydrogen transportation systems (vehicles, electrolyzers, storage containers, etc.).
- **Lifetime** – sensors must have a usable lifetime consistent with the application for which it is intended. For transportation applications that must be at least the time between scheduled maintenance (minimum 6 months, prefer 1 year or more). In this respect the sensor must be operational with no active effort for a minimum of that period, while exposed to ambient conditions.
- **Reliability** – sensors must indicate the presence of hydrogen reliably. That is, they must perform to some specification, each and every time they are exposed to hydrogen over the lifetime of the sensor. Response must not drift outside acceptable limits over that lifetime. Functionality of the sensors should be easily verifiable, but there will be a low tolerance for false alarms. Sensors should be able to survive multiple excursions to hydrogen concentrations above the explosive limit without damage.
- **Cost** – sensors and their controllers must be reasonably priced, so that their inclusion within the hydrogen infrastructure can be ubiquitous. A worthy goal is \$5 per sensor and \$30 per controller. As long as performance, lifetime and reliability are not compromised, less expensive is better.

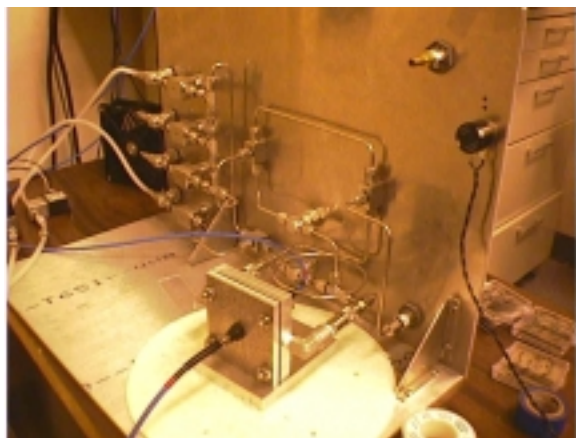
The common link in all of the hydrogen sensor concepts is that they all use Pd as a catalyst, because of its superior properties among the noble and semi-noble metals for dissociating and transporting hydrogen. Molecular hydrogen dissociates on the Pd surface, and atomic hydrogen diffuses rapidly through the film. Physical or optical changes in the Pd film itself, or in adjacent films or interfaces, are used to detect the presence of hydrogen. All of the current sensor concepts share Pd as the catalyst. Therefore, we have chosen to focus on stability issues related to ambient exposure of Pd and cyclic exposure of Pd to hydrogen. Additional work reported here has focused upon the interface between the Pd layer and the optically active layers used for fiber optic sensors.

Experimental

Thin films of the active layers of the optical sensors were fabricated by standard techniques of vacuum deposition. Thermal evaporation was carried out on a Varian Model 3118 evaporator. Sputtered films were prepared on a Leybold magnetron sputter coater, and plasma enhanced chemical vapor deposition was done on a Plasma Technology system. Performance testing of the completed articles was carried out at the National Renewable Energy Laboratory (NREL). Analytical investigations of failed articles were carried out in the Device Characterization Laboratory at NREL.

The fiber-optic sensor test station consisted of a gas flow manifold that could be switched automatically from gas mixtures containing hydrogen to air. Switching was controlled by the

same computer used to acquire optical spectra. The manifold delivered the test gas stream into a test chamber, constructed so that the dead volume was minimal (0.1 cm^3). In addition the chamber was constructed so that we could measure either spectral transmittance or reflectance. The spectrometer used for the optical measurements was an Ocean Optics S2000 spectrometer, measuring flux from 300 nm to 800 nm. Either fiber-optic tips or small glass slides coated with the active layers could be used as test articles. Glass slides were often used to simplify deposition and analysis after testing. The details of this measurement system appear in Fig. 1 and Fig. 2.

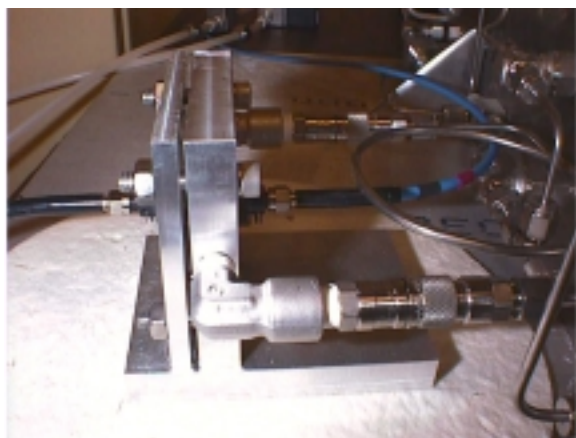


Manifold and Test Station



Test Chamber

Figure 1. Fiber-Optic Sensor Test Station



Test Chamber, Transmission Mode



Gas Manifold

Figure 2. Transmission Mode and Gas Manifold Details

Analytical work on functional and failed specimens was carried out with an array of tools available in the Characterization Laboratories at NREL. These included optical microscopy with Nomarski phase contrast (Neophot 21), electron microscopy (JEOL JSM-5800 and JSM-6320), Auger electron spectroscopy (Physical Electronics 670 Auger Nanoprobe), and X-ray photoelectron spectroscopy (Physical Electronics 5600 ESCA System).

Results

The major issues focused upon during the experimental work for FY 2001 were protection of the palladium (Pd) catalyst films from airborne contaminants and characterization of the metal oxide-palladium interface.

Protection of Pd Catalyst Layer

Several different strategies were investigated for extending the sensor lifetime by inhibition of Pd catalyst poisoning. These strategies included addition of alloying elements and deposition of various protective coatings.

Addition of Alloying Elements to Pd Catalyst

Experimental work on hydrogen separation membranes (Bryden, 1998) suggested that the use of Pd-Fe alloys might inhibit poisoning of the catalyst surface in ambient air. In addition, the Robust Hydrogen Sensor manufactured by DCH Technology makes use of a Pd-Ni alloy maintained above ambient temperature. For these reasons it was decided to fabricate sensors using the above-mentioned alloys in place of pure palladium and compare their response to sensors made with the original catalyst composition.

The sensor alloy films were prepared by vacuum co-evaporation. Compositions of the alloys were varied from approximately 5 to 20 percent Fe or Ni. The sensors were deposited on microscope slides and tested in the custom-made gas manifold using a 0.1% hydrogen/nitrogen mixture. The sensors using alloyed Pd films did not display additional resistance to poisoning at ambient temperature as compared with pure Pd at any of the alloy compositions used. Consequently, the work was discontinued in favor of an approach using protective coatings.

Protective Coatings for Inhibition of Pd Catalyst Poisoning

Several organic and inorganic coatings were tested for their ability to inhibit poisoning of the Pd catalyst.

Organic Coatings

Organic coatings investigated included colloidal Teflon and Nafion, as well as a dense, amorphous organic film. These coatings tended to deactivate the catalyst immediately upon deposition due to their organic nature or that of their precursors. They may occupy or block a significant portion of the Pd surface sites that would otherwise be available for the dissociation

of hydrogen. Another type of film was therefore developed based on a mesostructured Pd. This film created a nanoporous structure that prevented subsequent films from blocking active sites on the evaporated Pd. Sensors with this nanoporous coating overcoated with the dense, amorphous protective layer have shown increased resistance to poisoning for a period of over a month, as illustrated in Fig. 3.

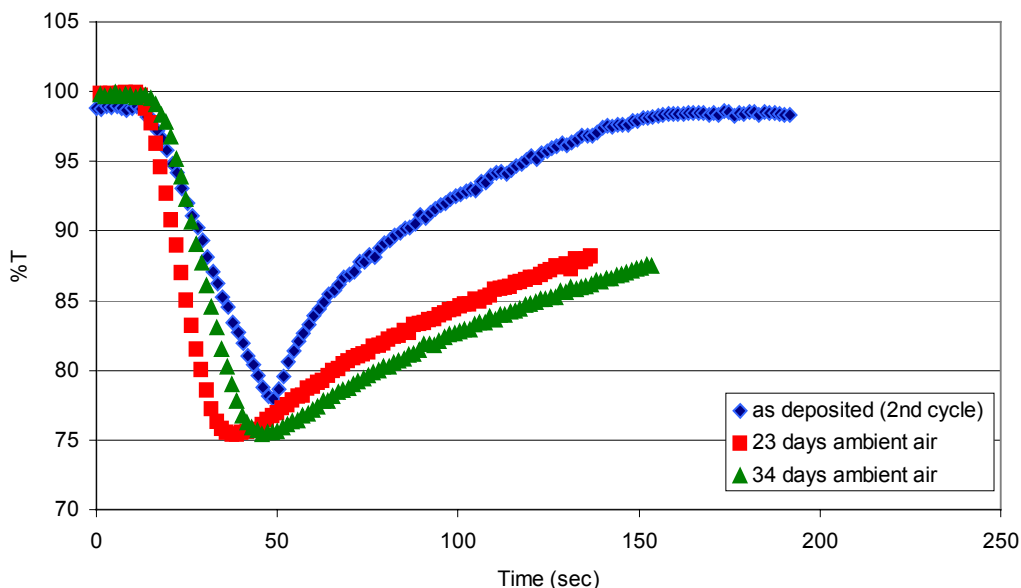


Figure 3. High sensitivity sensor response to 0.5% hydrogen after 34 days with “dense” protective coating

Inorganic Coatings

The study of inorganic coatings was focused mainly on the deposition of colloidal metal oxide films. Films of varying thickness were deposited by spin coating on freshly made and aged sensors. Sensors with the coating were functional for a period of approximately two weeks then started to degrade. Fresh sensors with activated coatings were still functional for periods exceeding one month, whereas a duplicate sensor with no protective coating degraded within a few days as shown in Figures 4 and 5. High durability sensors were completely degraded after periods exceeding 1 month. When coated with an activated metal oxide layer, the same sensors were partially rejuvenated. Figure 6 shows data for one of these sensors.

A possible theory for the observed behavior is that the relatively large pore size of the coating does not provide complete protection against airborne contaminants. However, the activated coating serves as a powerful catalyst to remove gaseous hydrocarbon species. The main source of contamination on the Pd active sites may be due to the formation of a chemisorbed methyl-Pd species (Albers, 1995). The activated coating removes the gaseous precursors before they can reach these sites. Previously contaminated sensors may be rejuvenated due to the migration of atoms on the Pd surface. When a methyl group migrates to the protective layer it is subsequently

removed. After a certain time enough active sites on the Pd are again free to catalyze the hydrogen dissociation reaction.

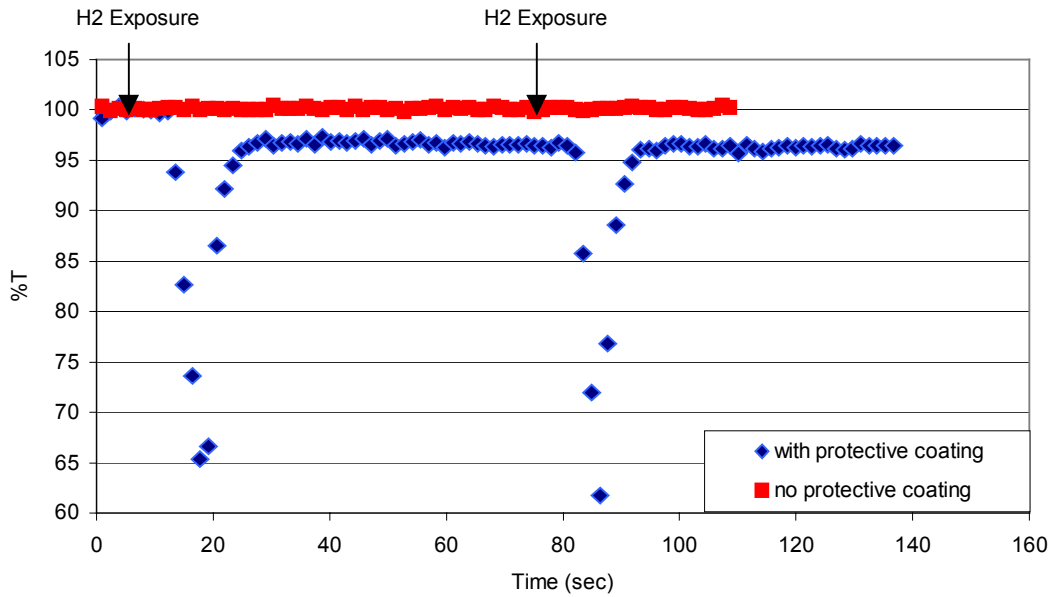


Figure 4. High sensitivity sensor response to 0.1% hydrogen after 10 Days with and without protective coating

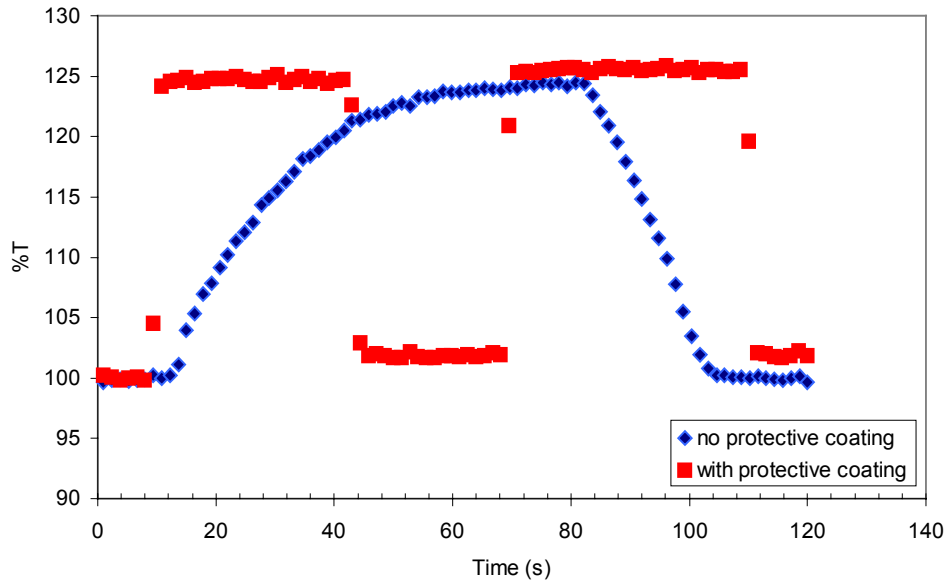


Figure 5. High durability sensor response to 4% hydrogen with/without protective coating (after 5 days ambient air exposure)

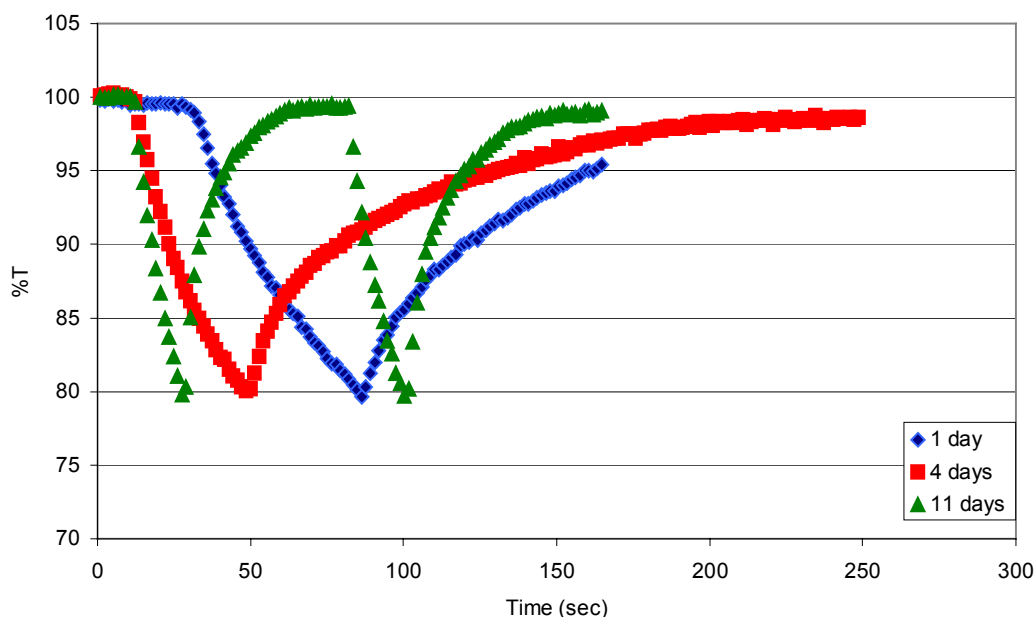


Figure 6. Regeneration of high sensitivity sensor exposed to 0.1% hydrogen: protective coating applied after 44 days

Characterization of the Metal Oxide/Pd Interface

Tests performed on aged sensors led to the conclusion that contamination of the catalyst active sites is primarily responsible for the observed degradation. In most cases once enough active sites are free on the Pd film the underlying metal oxide behaves normally even after a period of one year. To confirm this behavior further experiments were conducted on sensor films using AC impedance spectroscopy. A variety of sensor structures were developed that allowed us to examine the charge transfer process across the interface. In the simplest case, a sandwich structure of Pd/WO₃/ITO-glass (Indium Tin Oxide) was fabricated. Two different WO₃ layers were employed, with one of them showing improved response time to hydrogen. Preliminary data demonstrated that the faster sensor had a much smaller charge transfer resistance. This result indicated that for pristine sensors with a very active Pd catalytic layer the interface charge transfer process could be the rate-determining step during hydrogen insertion. Further measurements were performed on the two sensors to record their stability during storage. It was found that the charge transfer resistance became similar, while their chemochromic performance remained very different. One possibility is that the diffusion rate of proton in the tungsten oxide layer could be responsible for the difference. Efforts were then made to measure the diffusion coefficient of protons using AC impedance spectroscopy. At very low frequencies the impedance usually corresponded to the solid-state diffusion. Unfortunately, such a diffusion process was not observed with the sandwich structure employed in this study due to the apparent shorting of the device. The shorting was consistent with the fact that tungsten oxide is a semiconductor, which behaves like a conductor at very low frequencies. We attempted to insert

a proton conductor between WO_3 and ITO to address this issue. However, the proton conductors investigated so far all have limited conductivities at room temperature. Consequently, the impedance spectra were dominated by the contribution from the proton electrolytes. We will continue to search for a suitable proton conductor that will allow us to determine the proton diffusion coefficient in tungsten oxide.

Summary and Conclusions

We have researched the issues regarding the interfacial stability of thin film, fiber-optic sensors. We have determined that the new chemochromic materials developed last year are extraordinarily stable and undergo no measurable changes in performance when stored in air over periods in excess of one year. This result implies that the interface between these materials and the Pd catalyst overlayer remains stable, and the fouling of the Pd surface itself is the primary mode of degradation of these sensors. Fouling of the active sites on the surface of the catalyst occurs rapidly (1 to 5 minutes) with deliberate exposure to contaminants like CO, CH_4 , and H_2S . It occurs more slowly (1 to 2 weeks) in ambient air.

Codeposition of getter materials with the Pd was not successful in extending the lifetime of the sensor in air, although some protection to H_2S was noted. Assembling multi-layered thin films to provide protection to the active hydrogen dissociation sites by inhibiting access of pollutants to the Pd surface does offer a good measure of protection. We have sensors in test with these coatings that have been exposed to ambient air in excess of 1 month and still function as well as pristine, just-made sensors. These coating strategies appear to offer some protection from pollutants such as the H_2S as well.

Future Work

Research this year has established that we have developed stable chemochromic materials and that we have effective means of protecting the Pd catalyst from contamination in ambient air. There are a number of issues that remain to be resolved in the future.

- How long can the hydrogen dissociation catalyst be protected from trace contaminants in the air and from common pollutants found in the transportation environment?
- What is the response of these fiber-optic sensors over a useful range of temperatures (40°C to -40°C)?
- What is the response of these sensors to concentrations of H_2 above the explosive limit, and can they be made quantitative?
- What is the optimum thickness for all of the individual layers in these multi-layered, thin film devices?

Work will continue to understand the behavior of the optical films and catalyst and resolve these issues.

Acknowledgements

The authors want to thank the DOE Hydrogen Program for financially supporting this work under Contract No. DE-AC36-99GO10337 and DCH Technology for its significant contribution under a Cooperative Research and Development Agreement (CRD-96-046).

References

- Albers, P., H. Angert, G. Prescher, K. Seibold and S. F. Parker. 1999. "Catalyst Poisoning by Methyl Groups." *Chem. Commun.* :1619-1620.
- Benson, D. K., C. E. Tracy, G. A. Hishmeh, P. A. Ciszek, Se-Hee Lee, and D. P. Haberman. 1998. "Low-cost, fiber-optic hydrogen gas detector using guided-wave, surface-plasmon resonance in chemochromic thin films," Proceedings of the SPIE International Symposium on Industrial and Environmental Monitors and Biosensors, Boston, MA, November 2-5.
- Bryden, K. J. and J. Y. Ying. 1998. "Pulsed Electrodeposition Synthesis and Hydrogen Absorption Properties of Nanostructured Palladium-Iron Alloy Films." *J. Electrochem. Soc.*, 145(10): 3339-3346.
- Butler, M. A. 1991. "Fiber Optic Sensor for Hydrogen Concentrations near the Explosive Limit," *J. Electrochem. Soc.* 138, L46.
- Butler, M. A. 1994. "Micromirror optical-fiber hydrogen sensor," *Sensors and Actuators B* 22, 155.
- Chadwick, B., and M. Gal. 1993. "Enhanced optical detection of hydrogen using the excitation of surface plasmons in palladium," *Applied Surface Science* 68, 135.
- Garcia, J. A., and A. Mandelis. 1996. "Study of the thin-film palladium/hydrogen system by an optical transmittance method," *Rev. Sci. Instrum.* 67 (11), 3981.
- Griessen R., et al. 1997. "Yttrium and Lanthanum Hydride Films with Switchable Optical Properties," *J. Alloys and Compounds*, 253-254:44-50.
- Huang, W., R. Zhai, and X. Bao. 1999. "Direct observation of subsurface oxygen on the defects of Pd(100)," *Surf. Sci. Lett.* 439, L803.
- Ito, K., and T. Kubo. 1984. "Gas Detection by Hydrochromism," In *Proceedings of the 4th Sensor Symposium, Tsukuba, Japan, Dec. 1984*, pp. 153-156.
- Liu, P., Se-Hee Lee, C. E. Tracy, J. R. Pitts, and R. D. Smith. 2001. "Metal Oxide Stabilized Palladium Sensor For Hydrogen Detection," in the *Electrochemical Society PV series*, in press.

Mandelis, A., and J. A. Garcia. 1998. "Pd/PVDF thin film hydrogen sensor based on laser-amplitude-modulated optical-transmittance: dependence on H₂ concentration and device physics," *Sensors and Actuators B* 49, 258.

Raether, H. 1988. *Surface Plasmons on Smooth and Rough Surfaces and on Gratings*, Springer-Verlag, Berlin, p. 21.

Smith II, R. D., D. L. Olson, T. R. Wildeman, and D. K. Benson. 2000. "Fiber Optic Sensor for Diffusible Hydrogen Determination in High Strength Steel," *Proceedings from Phonics West 2000 Conference*, Jan. 25-28, 2000, SPIE, San Jose, CA.

Sutapun, B., M. Tabib-Azar, and A. Kazemi. 1999. "Pd-coated elastooptic fiber optic Bragg grating sensors for multiplexed hydrogen sensing," *Sensors and Actuators B* 60, 27.

Tabib-Azar, M., B. Sutapun, R. Petrick, and A. Kazemi. 1999. "Highly sensitive hydrogen sensors using palladium coated fiber optics with exposed cores and evanescent field interactions," *Sensors and Actuators B* 56, 158.

Codes and Standards Analysis

**Dr. Michael R. Swain
Eric Grilliot
Patrick Filoso
Dr. Matthew N. Swain
University of Miami
Coral Gables, FL 33124**

Abstract

The following report contains work on three separate tasks. They are as follows:

Task A -- Safety Analysis of California Fuel Cell Partnership Building
Task B -- Development of Method to Determine Hydrogen Sensor Placement
Task C -- Safety Analysis of Home Refueling Systems

The work in Task A is an analysis of the existing system and procedures that deal with hydrogen leakage from hydrogen fuel vehicles. The work in Task B is the construction of a computer model of a 5000-square foot building. The model is to be used while developing a method for using helium-filled bubbles to determine hydrogen sensor placement. The work in Task C was divided into three additional areas:

- Area 1 - Computer modeling of hydrogen leakage to assist in writing International Mechanical Code for ventilation and setbacks.
- Area 2 - Determination of minimum hydrogen leakage rate that can support a flame.
- Area 3 - Analysis of hydrogen flame impingement on gypsum board.

Introduction

The goals and objectives of this work effort were set by anticipating the needs of various projects and authors of codes and standards. The work effort had to be altered slightly in July 2000 and March 2001 to take into account information not known previously. Task A was changed from modeling of an underground garage to modeling of the California Fuel Cell Partnership building in Sacramento. Task B was postponed to allow for additional work in Task A and Task C.

Task A – CaFCP Building Safety Analysis

Task A addresses six questions concerning the CaFCP building in Sacramento CA. They are as follows:

1. Is the present ventilation adequate?
2. When should high ventilation flow rate be used?
3. Can a burnable mixture of hydrogen be drawn into the A/C system?
4. Should the garage door be opened in conjunction with high flow rate ventilation?
5. How will the present system handle PRD activation?
6. Is exhaust inlet placement optimized?

Six computer models have been run to analyze six accident scenarios. These six accident scenarios will be presented in the following seven figures. The conclusions reached about each of the six questions above will be addressed figure by figure.

The leakage rate was set at 80 SCFM hydrogen. This was chosen because it represents a reasonable maximum flow rate above which the excess flow valve would be activated. In addition, multiple safety systems would have to fail to produce an 80 SCFM hydrogen leak. At a leakage rate of 80 SCFM, the excess flow valve mounted in the tank would shut off hydrogen flow from the tank.

The air ventilation rates for the bay, without any forced ventilation, were measured as 371 SCFM. It would require a procedural error for a vehicle to be in the building under these conditions. If a vehicle is in the building, a ventilation rate of 2100 SCFM should be present. Figure A1 shows how large a combustible cloud would be produced for a leakage rate of 80 SCFM with a ventilation rate of 371 SCFM. The cloud surface mesh in red shows the boundaries of a 4.1% hydrogen concentration cloud, while the cloud surface mesh in blue shows the boundaries of a 0.82% hydrogen concentration cloud. 4.1% hydrogen is the leanest burnable mixture of hydrogen and air. The hydrogen leakage rate of 80 SCFM empties the fuel tank in 20 minutes. It can be seen that after five minutes of leakage a column of burnable mixture rises to the ceiling and begins to spread across the ceiling. After 20 minutes, a layer of burnable gas from 3.4 to 5.0 feet thick rests on the ceiling. It will take an additional 47 minutes for this cloud to completely disappear. The bay was receiving 0.265 air exchanges per hour; 0.208 air exchanges were required to remove all burnable gas mixtures.

The baseline ventilation rate of the bay is 2100 SCFM whenever a vehicle is present in the bay. This is depicted in Figure A2. If the system functions properly, this ventilation rate would increase to 6300 SCFM if a concentration of 0.82% hydrogen were detected 18 inches below the ceiling. If the system fails the ventilation rate would remain at 2100 SCFM as depicted in Figure A2. Once again the cloud surface mesh in red depicts 4.1% hydrogen concentration and the cloud surface mesh in blue depicts 0.82% hydrogen concentration. It can be seen the baseline ventilation rate of 2100 SCFM almost eliminates the accumulation of burnable hydrogen air mixtures at the ceiling. The bay would be emptied of burnable mixture two minutes after the fuel tank is empty (20 minutes). The bay was receiving 1.5 air exchanges per hour; 0.050 air exchanges were required to remove all burnable gas mixtures.

If the ventilation system functions properly the ventilation increases to 6300 SCFM when hydrogen is sensed. This is depicted in Figure A3. The red cloud surface mesh shows 4.1% hydrogen concentration. It can be seen that 6300 SCFM ventilation prevents the burnable column of hydrogen from reaching the ceiling. At 20 minutes, the column has not reached the ceiling and will disappear ten seconds after the vehicle runs out of hydrogen (at 20 minutes.) The bay was receiving 4.5 air exchanges per hour; 0.013 air exchanges were required to empty the bay of burnable mixture. To be adequate, the ventilation rate must prevent the accumulation of hydrogen concentrations greater than 4.1% on the ceiling of the building. 6300 SCFM is capable of this for leakage rates of 80 SCFM hydrogen. Therefore, a 6300 SCFM ventilation rate is needed.

Figure A4 shows the effects of moving the vehicle. Placing a vehicle as shown in Figure A4 creates the largest distances between the hydrogen leak and the exhaust vents. This does place the leak in close proximity to the air conditioning inlet. In this case, the ventilation rate began at 2100 SCFM and increased to 6300 SCFM after 38 seconds of leakage. This is the time when the first sensor detects 0.82% hydrogen concentration. That sensor reached 0.41% hydrogen concentration after 27 seconds of leakage. If the sensor were raised 12 inches (to 6 inches below the ceiling) it would have reached 0.82% hydrogen concentration after 31 seconds. It can be seen that the ventilation system also prevents the burnable cloud of hydrogen from reaching the ceiling with a vehicle in this position. Once again the burnable cloud disappears within ten seconds of the vehicle running out of hydrogen (20 minutes). 6300 SCFM is capable of preventing hydrogen concentrations of 4.1% on the ceiling. A 6300-SCFM ventilation rate is needed.

The questions raised by the previous accident scenario are: does burnable hydrogen enter the air conditioning inlet in the upper corner of the bay, and what effect does opening the bay garage door have on the results? Figure A5 shows the bay with 4400 SCFM of air conditioning circulation included. The first sensor reaches 0.82% hydrogen after 60 seconds of leakage. This initiated the higher exhaust flow rate (6300 SCFM) and the opening of the garage door. It reaches 0.41% hydrogen after 37 seconds of leakage and would have reached 0.82% hydrogen after 42 seconds if located six inches from the ceiling instead of 18 inches. The garage door requires 23 seconds to open. Figure A5 shows the two accident scenarios (closed door, open door) after five minutes of leakage. It can be seen that opening the garage door has reduced the fresh air makeup flow through the air conditioning system, thereby increasing the hydrogen concentration in the air conditioning system to values above 0.82%.

Figure A6 shows the two accident scenarios after ten minutes of leakage. The hydrogen air mixtures exiting the air conditioning system, in the bay with the open garage door, were greater than 0.82% but less than 4.1%. The hydrogen-air mixture exiting the air conditioning system, in the bay with a closed garage door, was less than 0.82% hydrogen.

Figure A7 shows the two accident scenarios after 20 minutes of leakage. The ventilation systems in both bays have prevented the burnable column of hydrogen air mixture from reaching the ceiling. In both cases, the bays will contain no burnable hydrogen within ten seconds. The bay with the closed garage door will require 1721 seconds to empty below 0.82% hydrogen concentration. The bay with the open garage door will require 1706 seconds. The burnable hydrogen (4.1% by volume) does not enter the air conditioning system. Opening the garage door does not appreciably assist in removing hydrogen from building. However, raising the floor exhaust inlet vent to the ceiling would aid in the removal of hydrogen from the building.

Task B - Development of Method to Determine Hydrogen Sensor Placement

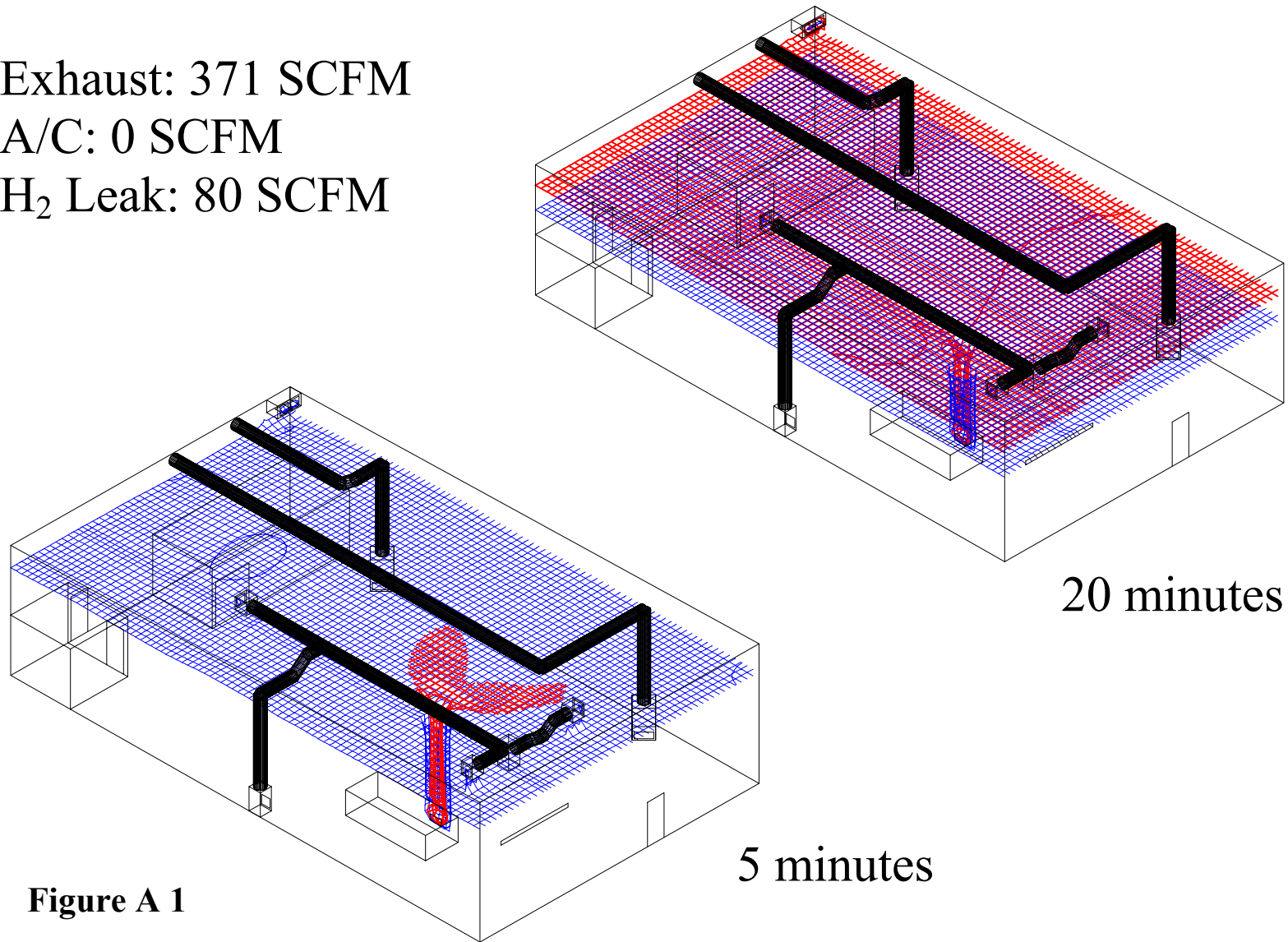
Task B, which was discontinued in March 2001, was the development of a method to determine hydrogen sensor placement. The procedure used to develop the method was to produce an experimentally-verified computer model of a 5000-square foot building with helium leakage. The model was then tested with hydrogen releases. The model will be used to test the accuracy of determining hydrogen sensor location with a method to be developed in the coming year. The development and testing of the computer model will be discussed herein.

Figures B1 and B2 show the 5000-square foot warehouse with the flow field generated by the 8900 SCFM exhaust fans. Office space exists at either end of the warehouse accounting for the missing volumes on the first floor level at each end of the warehouse. It can be seen that the flow on the office wall at the near-end of the warehouse is complicated. A circulation is created with the flow moving to the left, high on the wall, and to the right near the floor. The gas motion created by the circulation is clearly visible in Figures B3 and B4. Hydrogen is leaking from the wall at 20 SCFM. The plot of 0.8% hydrogen at 10 and 30 seconds shows the top of the gas cloud moving to the left and the bottom to the right. The gas leak was positioned on the office wall for verification of the model.

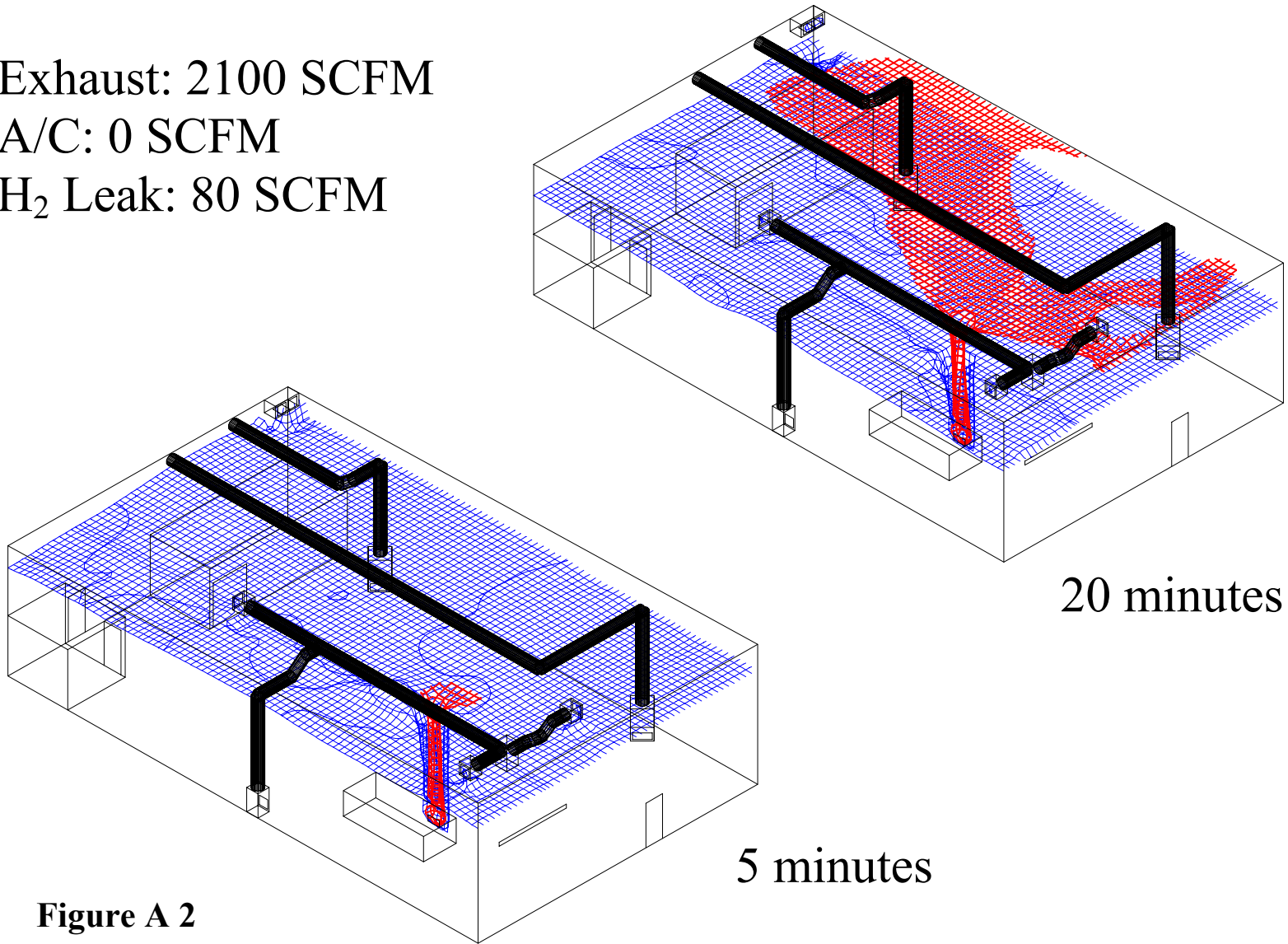
Figure B5 shows the boundaries of 0.8% hydrogen concentration after 60 seconds of leakage. The experimental verification was ended after 60 seconds. Figure B6 shows the boundaries of 0.8% helium concentration after 60 seconds of leakage. The clouds formed by helium were very similar to the clouds formed by hydrogen.

Instantaneous gas releases were performed in the center of the bay at the floor. The instantaneous gas releases were performed with no circulating airflow (exhaust fans were off.) Instantaneous releases were performed experimentally by constructing a breakaway clamshell plastic bag with measured nylon lines attached at multiple locations along the seam. The nylon lines allowed the bag to be snapped open. The bags were filled with a measured amount of helium or hydrogen.

Exhaust: 371 SCFM
A/C: 0 SCFM
H₂ Leak: 80 SCFM



Exhaust: 2100 SCFM
A/C: 0 SCFM
H₂ Leak: 80 SCFM



Exhaust: 3600 SCFM
A/C: 0 SCFM
H₂ Leak: 80 SCFM

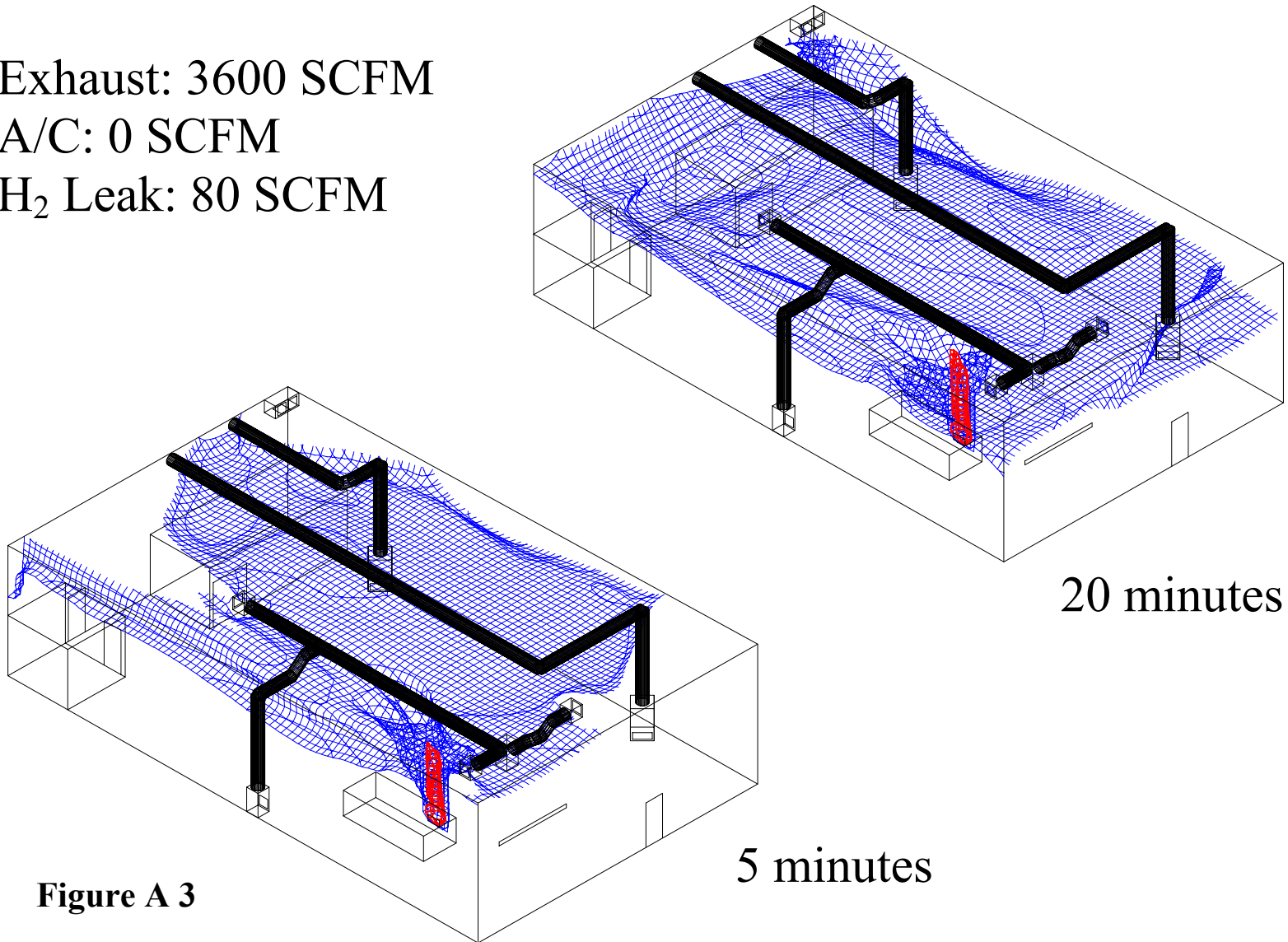


Figure A 3

Exhaust: 2100/6300 SCFM
A/C: 0 SCFM
H₂ Leak: 80 SCFM

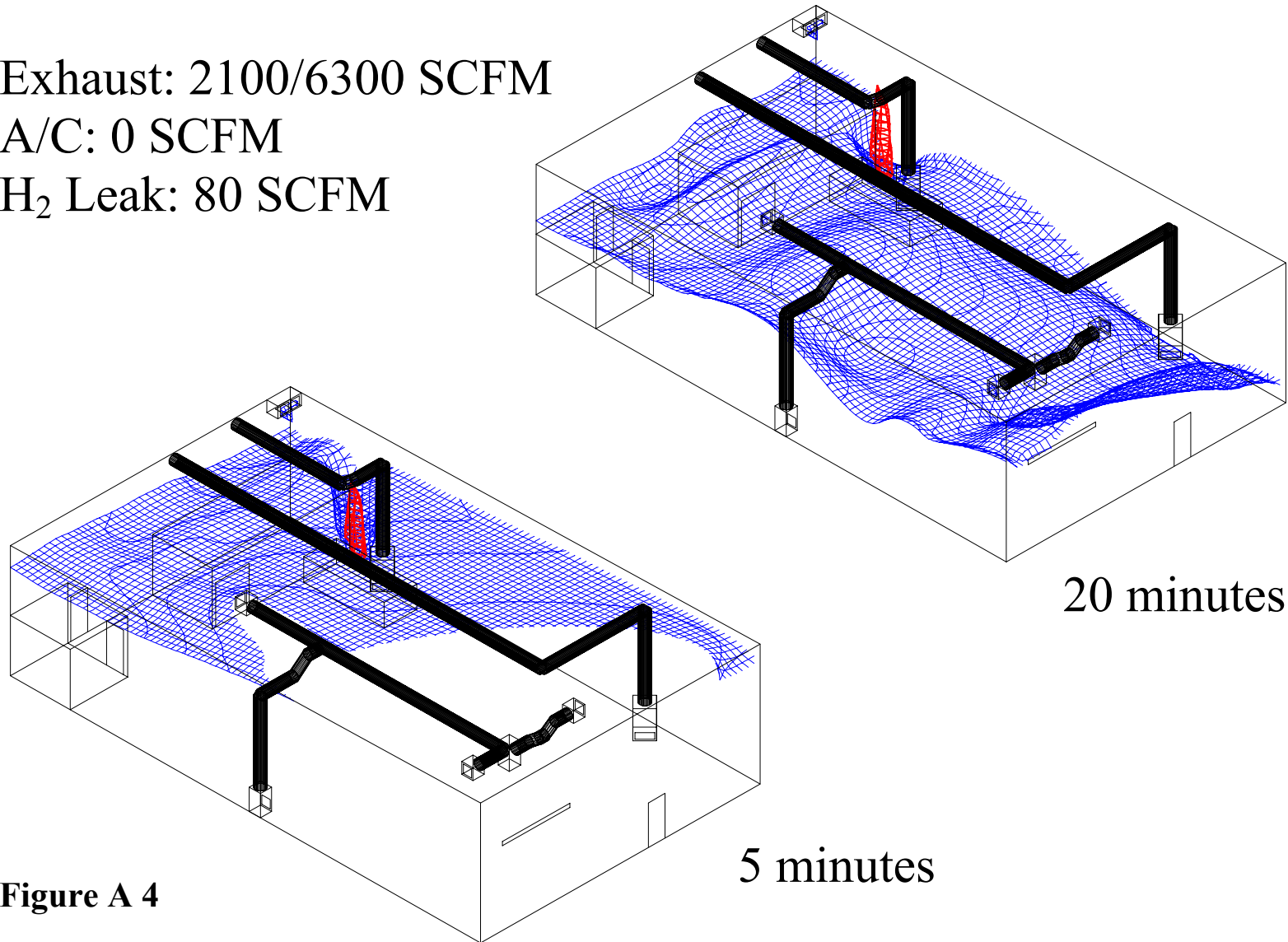


Figure A 4

Exhaust: 2100/6300 SCFM
A/C: 4400 SCFM
H2 Leak: 80 SCFM
5 minutes

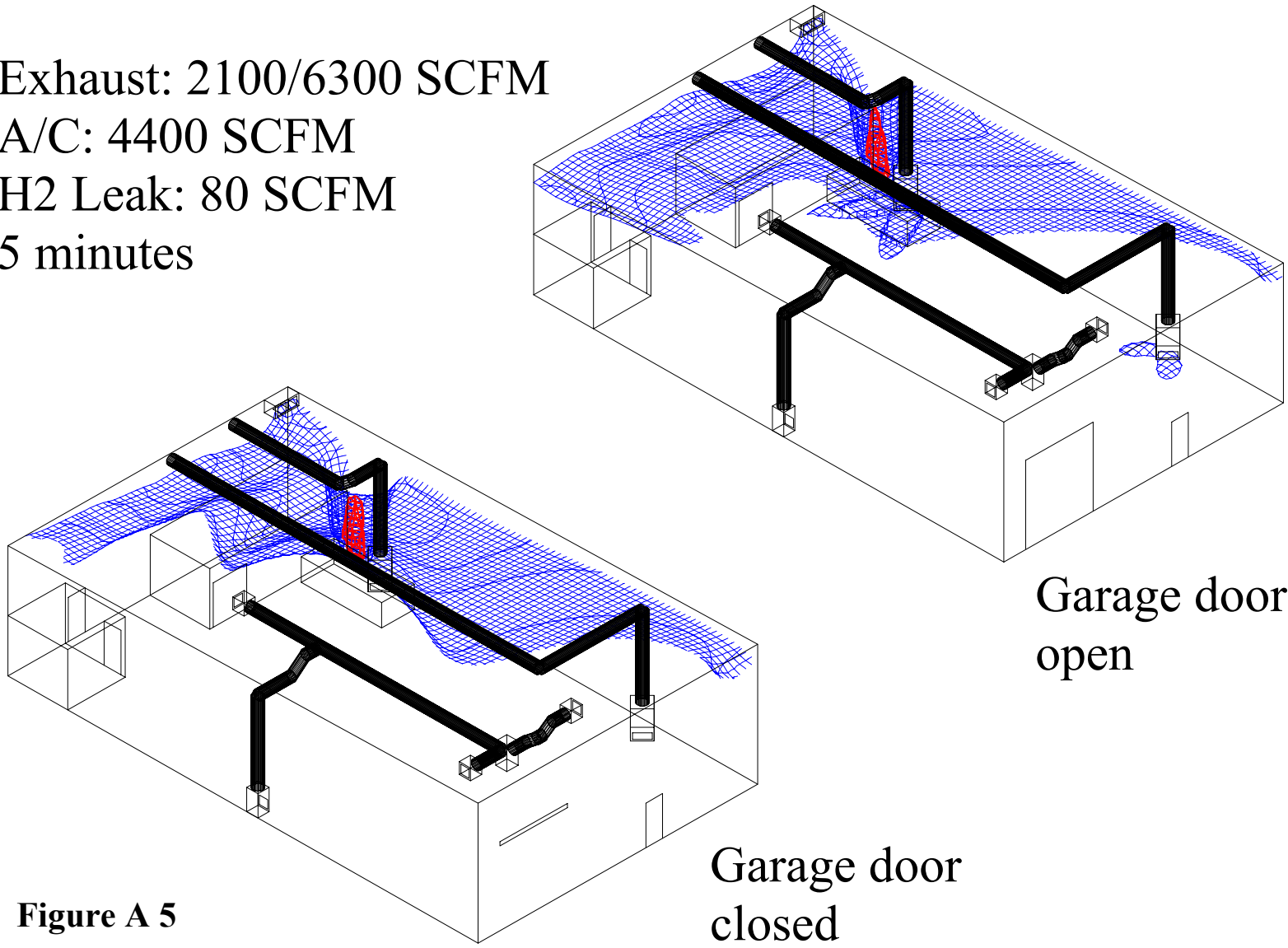


Figure A 5

Exhaust: 2100/6300 SCFM
A/C: 4400 SCFM
H2 Leak: 80 SCFM
10 minutes

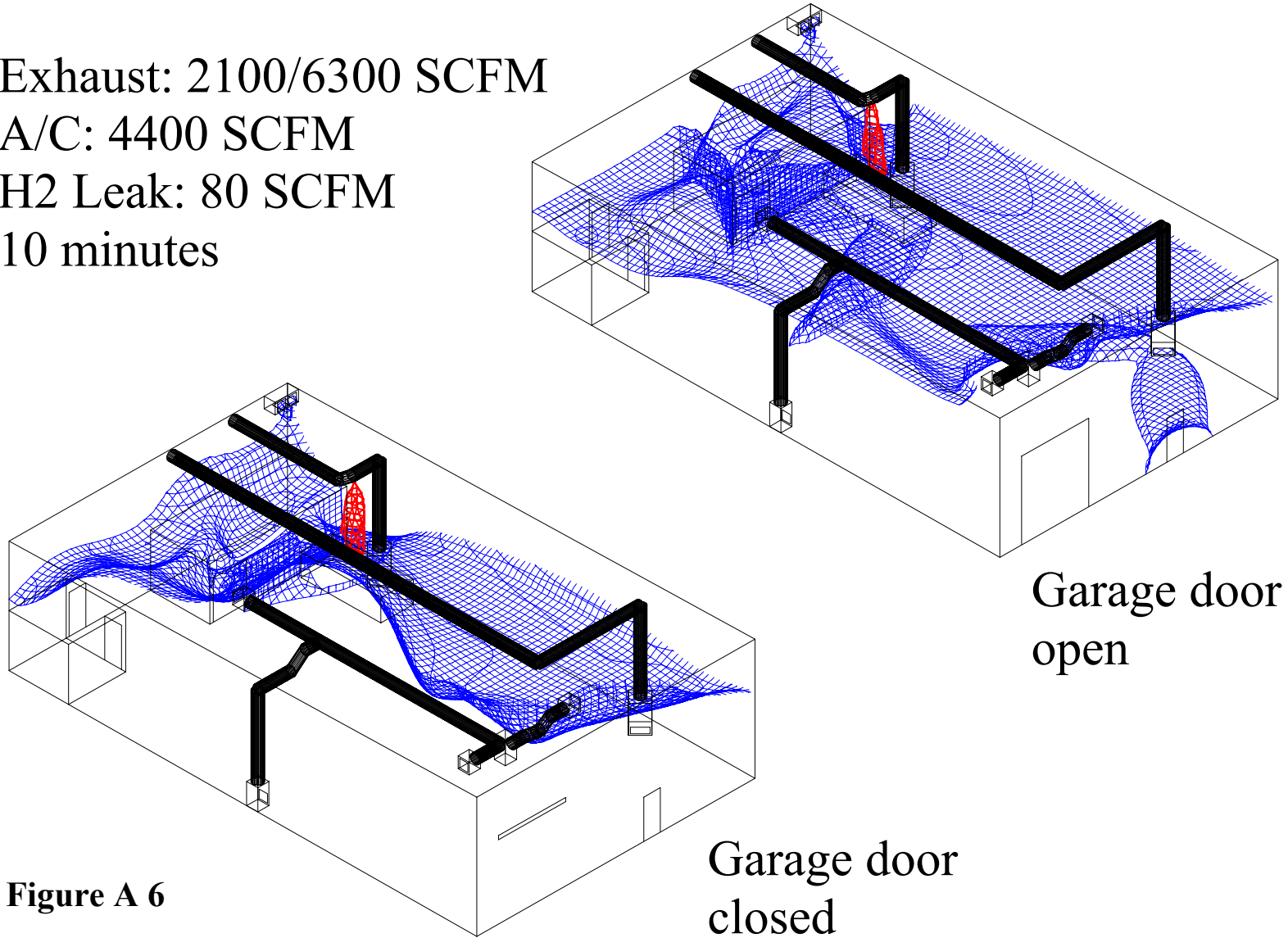


Figure A 6

Exhaust: 2100/6300 SCFM

A/C: 4400 SCFM

H2 Leak: 80 SCFM

20 minutes

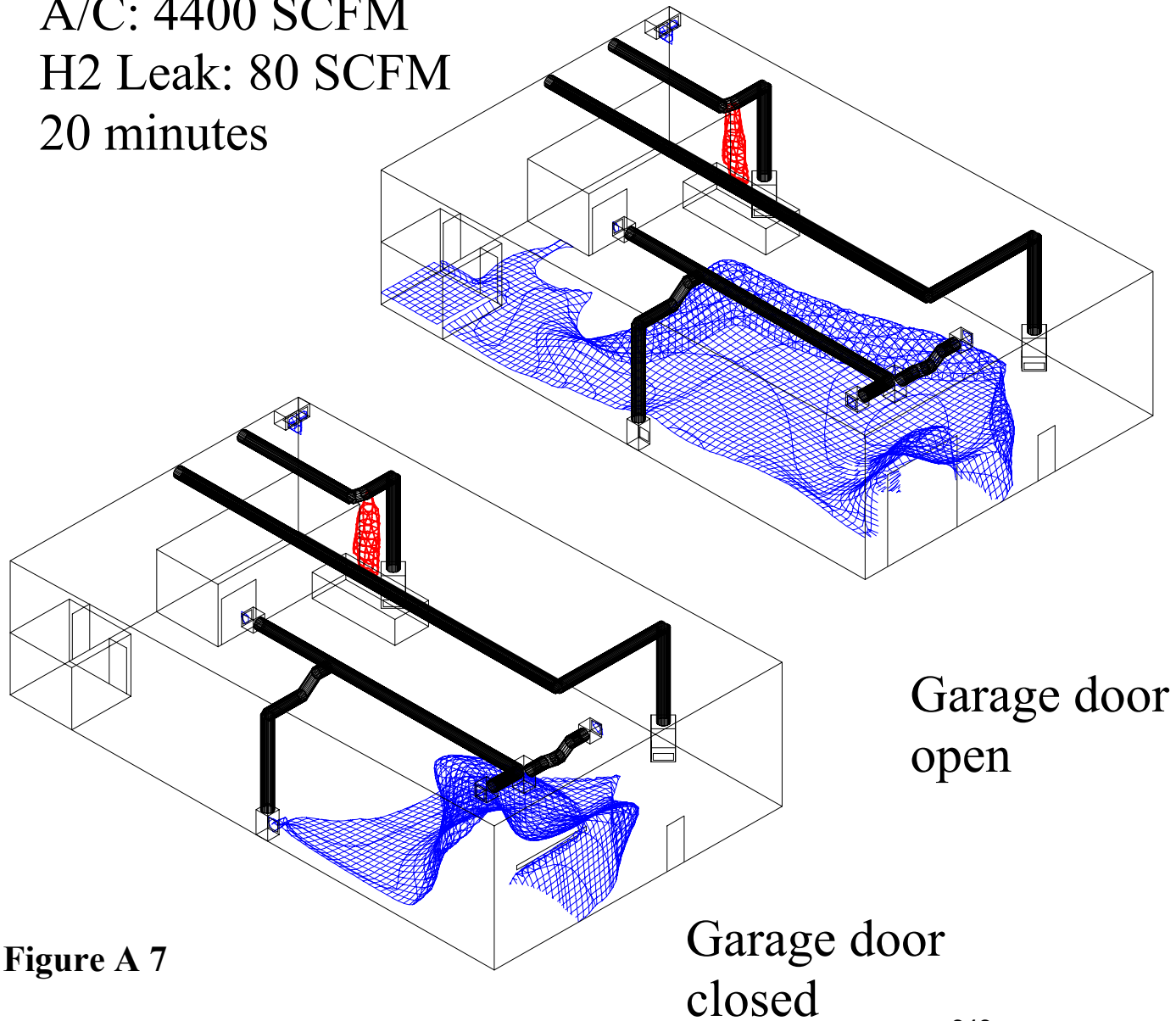


Figure A 7

Figure B7 and B8 show the position of hydrogen at 1.0% and 4.1% concentration one second after an instantaneous release of 8 cubic feet. The clouds are similar in size because there has been little diffusion in the first second.

Figures B9 and B10 show the same release at 2 seconds. Figures B11 and B12 show the same release at 3 seconds. The 4.1% hydrogen concentration cloud has risen off the floor, and is decreasing in size as it rises. Both the 1% concentration cloud (Figure B13) and the 4.1% concentration cloud (Figure B14) have reached the ceiling at four seconds. By ten seconds, the 1% concentration cloud (Figure B15) has spread over the ceiling. By seven seconds, the 4.1% concentration cloud (Figure B16) vanishes and there is no longer any burnable mixture of hydrogen and air in the enclosure.

The computer model of the 5000-square foot warehouse is finished and experimentally verified with helium and hydrogen. The next step is to determine if a method utilizing helium bubbles can be developed to show the proper locations for hydrogen sensors.

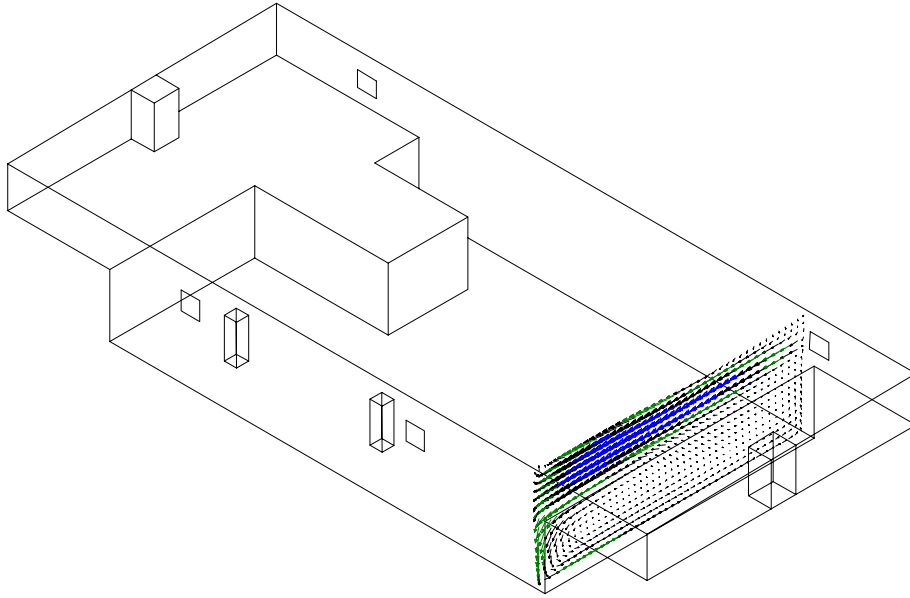


Figure B 1 - Flow field produced by 8900 SCFM exhaust fans

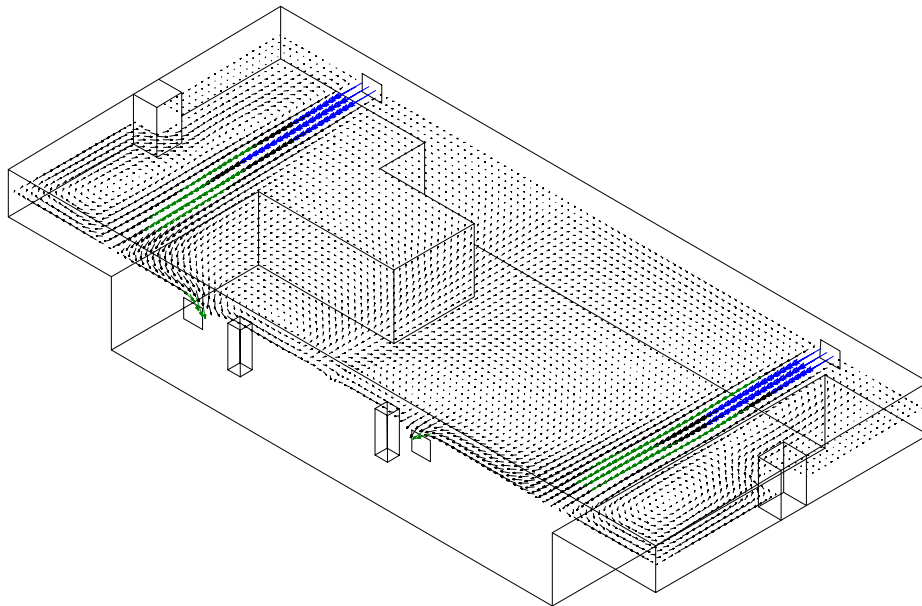


Figure B 2 - Flow field produced by 8900 SCFM exhaust fans

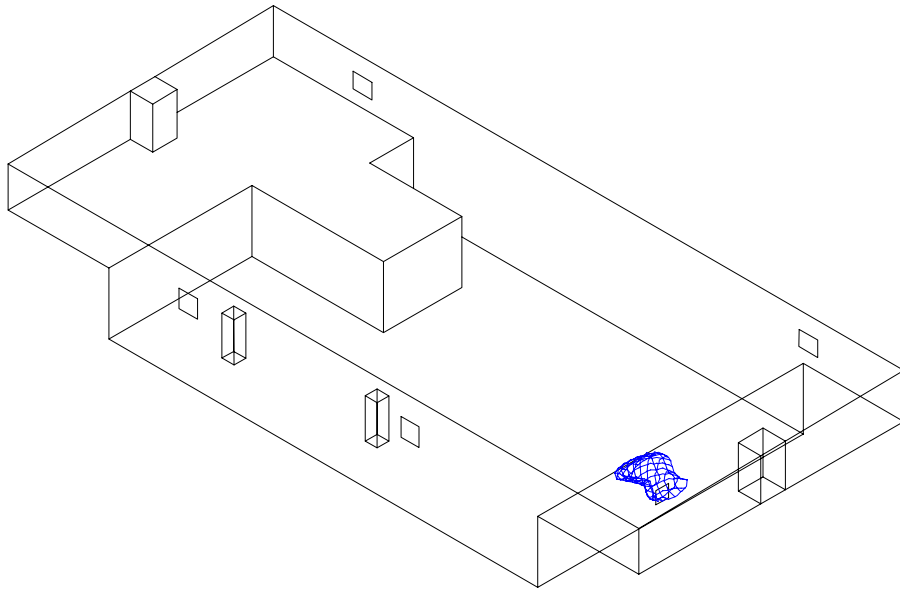


Figure B 3 - 20 SCFM hydrogen leakage after 10 seconds

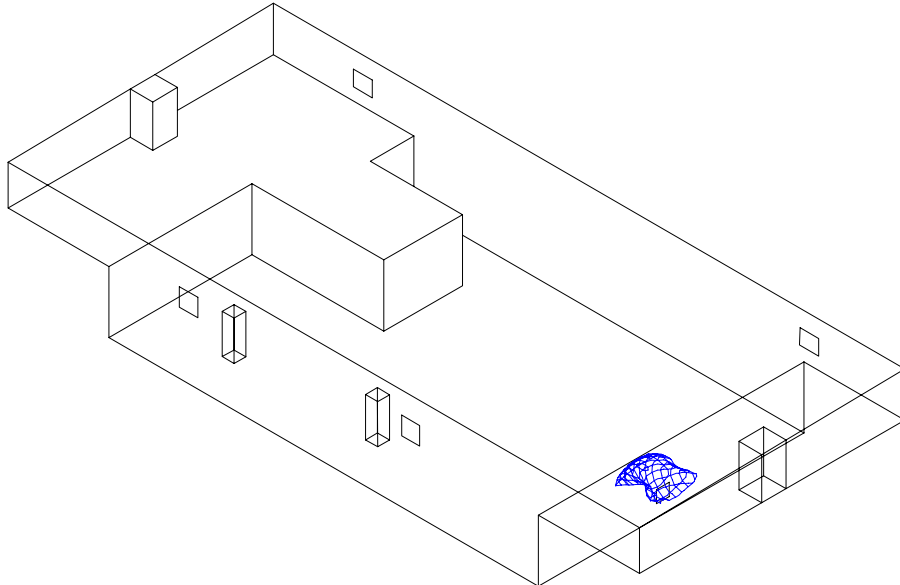


Figure B 4 - 20 SCFM hydrogen leakage after 30 seconds

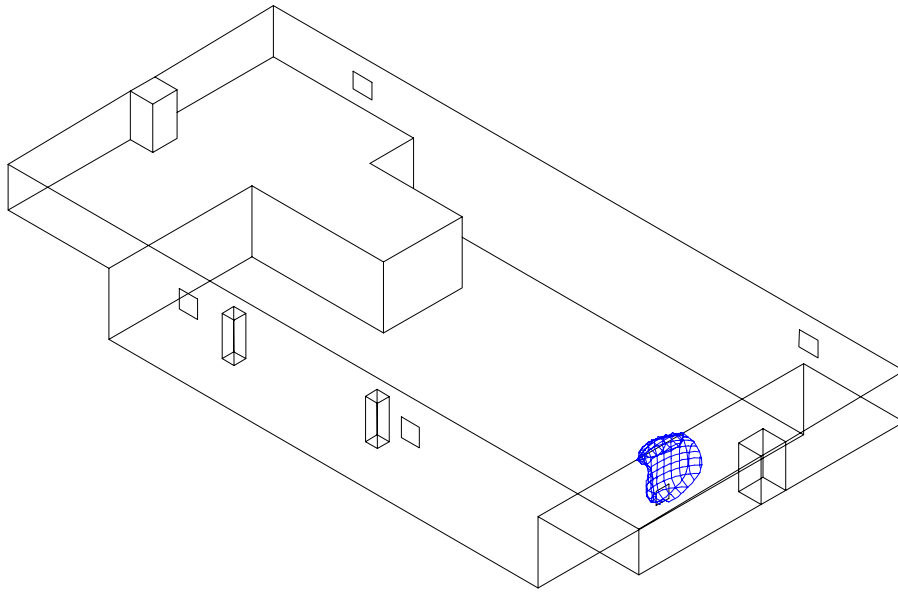


Figure B 5 - 20 SCFM hydrogen leak after 60 seconds

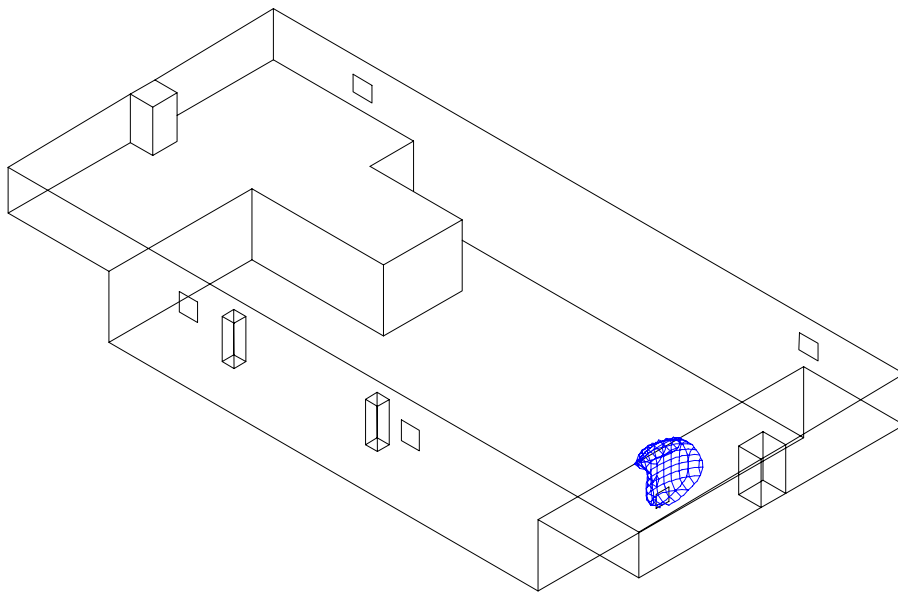


Figure B 6 - 20 SCFM helium leak after 60 seconds

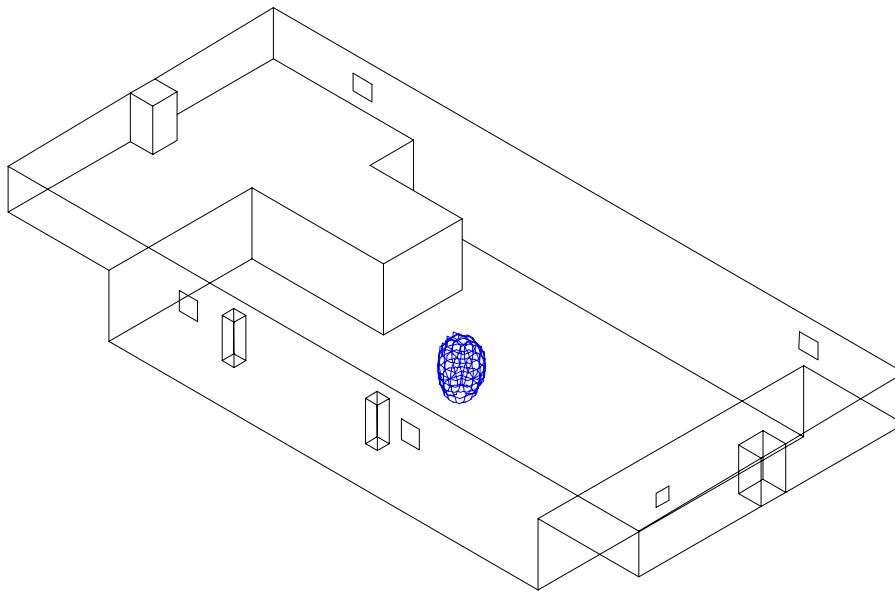


Figure B 7 - Instantaneous release, 8 cubic feet of hydrogen, 1% concentration after 1 second

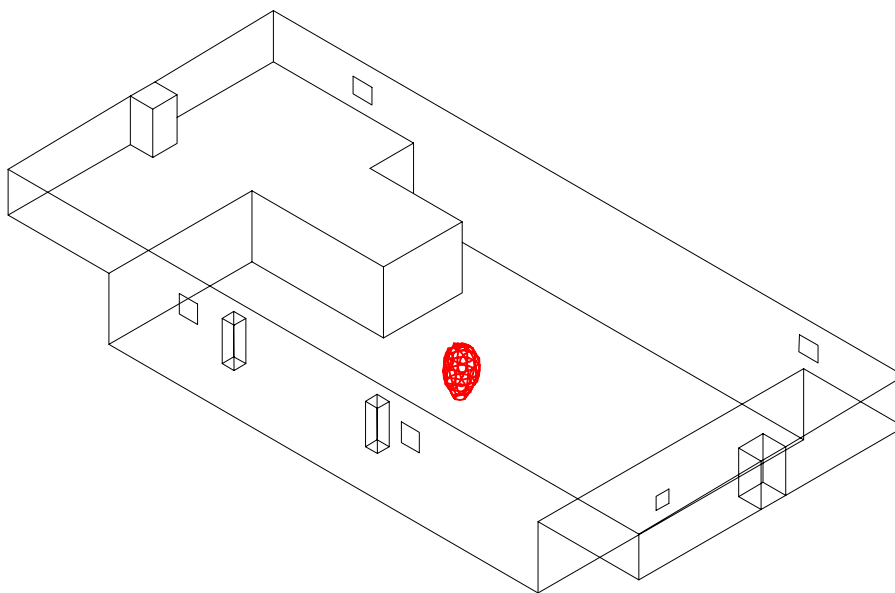


Figure B 8 - Instantaneous release, 8 cubic feet of hydrogen, 4.1% concentration after 1 second

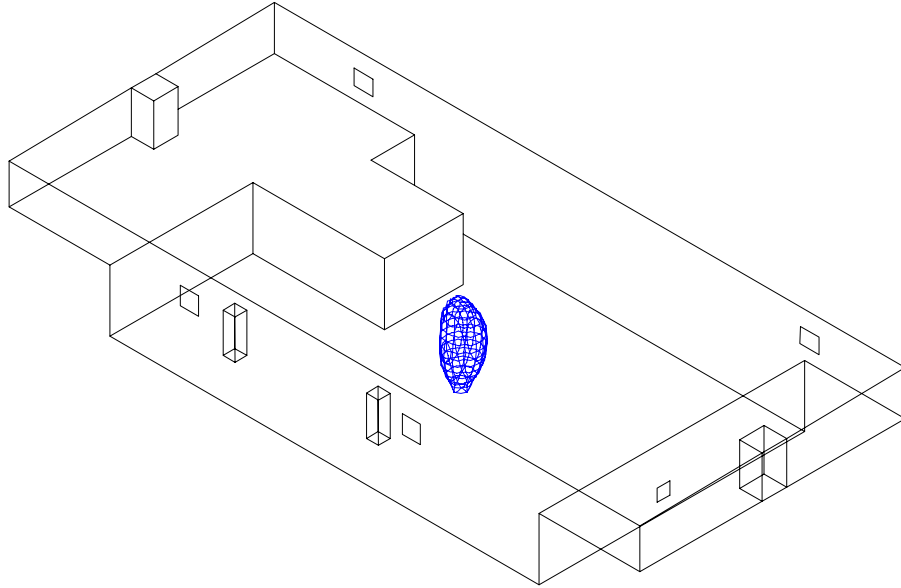


Figure B 9 - Instantaneous release, 8 cubic feet of hydrogen, 1% concentration after 2 seconds

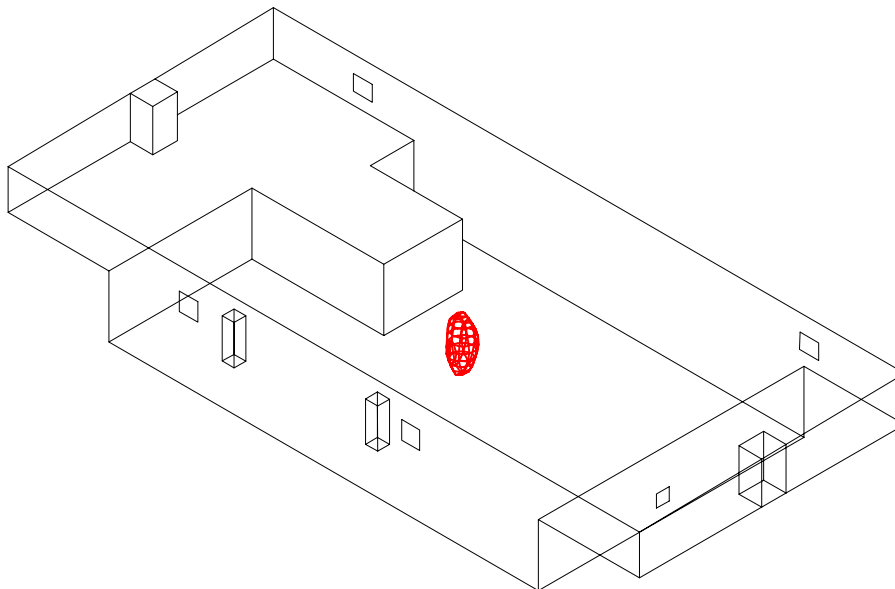


Figure B 10 - Instantaneous release, 8 cubic feet of hydrogen, 4.1% concentration after 2 seconds

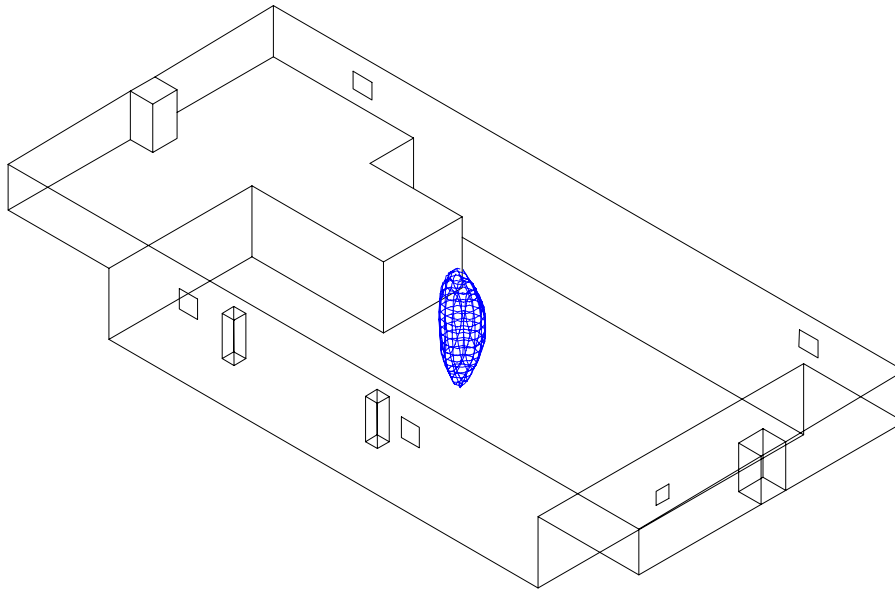


Figure B 11 - Instantaneous release, 8 cubic feet of hydrogen, 1% concentration after 3 seconds

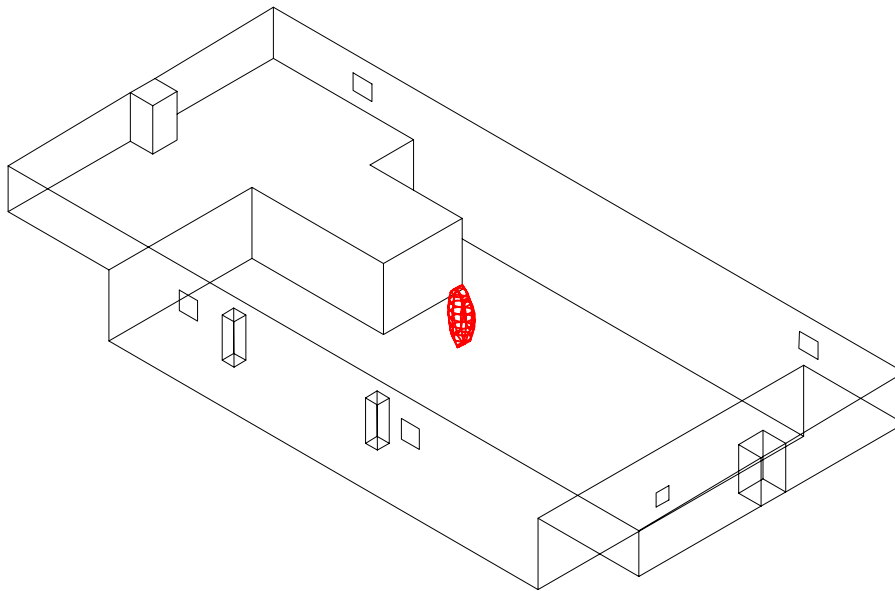


Figure B 12 - Instantaneous release, 8 cubic feet of hydrogen, 4.1% concentration after 3 seconds

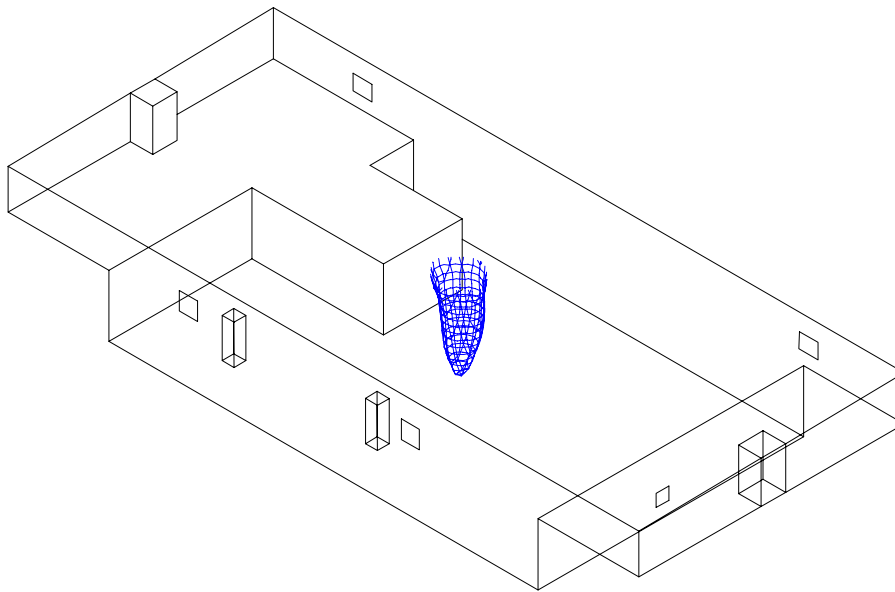


Figure B 13 - Instantaneous release, 8 cubic feet of hydrogen, 1% concentration after 4 seconds

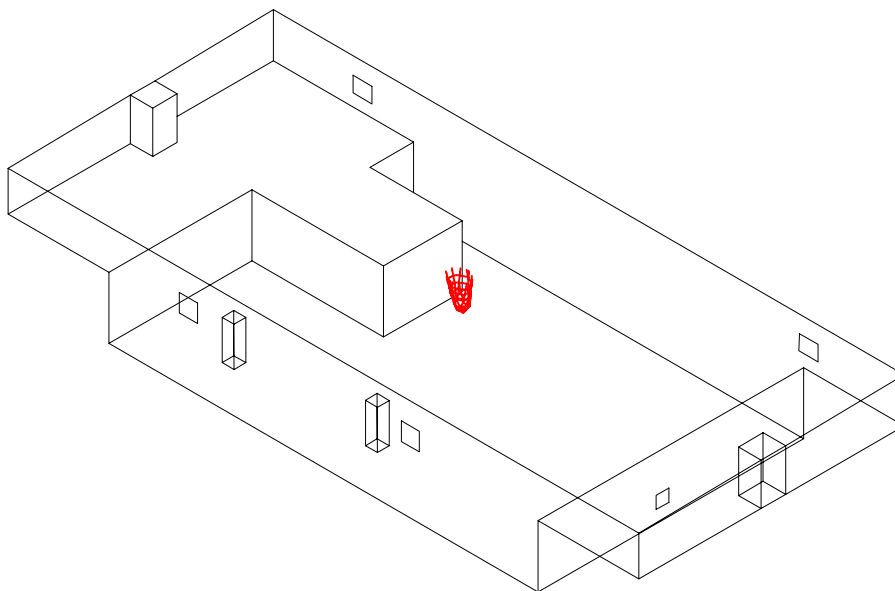


Figure B 14 - Instantaneous release, 8 cubic feet of hydrogen, 4.1% concentration after 4 seconds

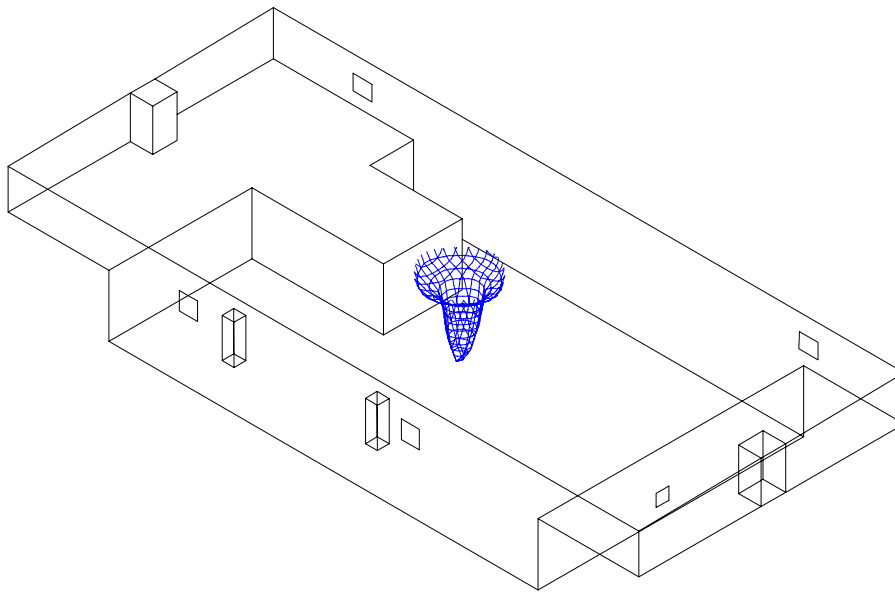


Figure B 15 - Instantaneous release, 8 cubic feet of hydrogen, 1% concentration after 5 seconds

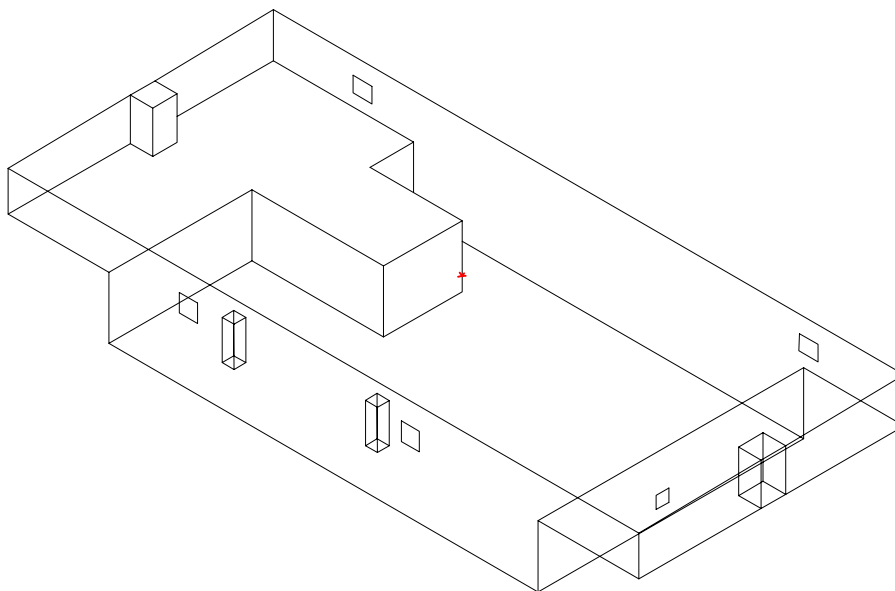


Figure B 16 - Instantaneous release, 8 cubic feet of hydrogen, 4.1% concentration after 5 seconds

Task C – Home Refueling System Safety Analysis

Task C addresses three questions concerning the writing of ICC building codes:

1. Are existing codes adequate for the use of home refueling systems in residential garages?
2. Is there a minimum safe hydrogen leakage rate?
3. What damage is done to gypsum board after hydrogen flame impingement?

The Use of Existing Codes for Home Refueling Systems

Task C was initiated with a survey of potential home refueling systems. Thirteen companies were identified as suppliers of hydrogen production equipment. They are as follows:

Electrolysis devices:

Bhabha Atomic Research Centre [BARC]
Trombay Bombay 400 085, India

Electrolyser Corporation, Ltd.
210-290 North Queen Street
Toronto, Canada, M9C 5L2

Hydrogen Systems NV
Brugstraat 45/1, B-2300 Turnhout
Belgium

Norsk Hydro ASA
N-0240 Oslo
Norway

Proton Energy Systems (PEM Electrolyzers)
50 Inwood Road
Rocky Hill, Connecticut 06067

Stuart Energy Systems
122 The West Mall
Toronto, Ontario
M9C 1B9 Canada

Teledyne Energy Systems
10707 Gilroy Road
Hunt Valley, MD 21031-1311

Fuel processors:

Dais-Analytic Corporation
11552 Prosperous Drive
Odessa, FL 33556

General Electric Company
3135 Easton Turnpike
Fairfield, CT 06431

Harvest Energy Technologies
9253 Glenoaks Boulevard
Sun Valley, California 91352

Hydrogen Burner Technology
1310 Logan Avenue, Suite E
Costa Mesa, California 92626

IdaTech, aka - Northwest Power Systems
924 S.E. Wilson Ave. Suite F
Bend, Oregon 97702

Wellman CJB Limited
Airport Service Road
Portsmouth, Hampshire, PO3 5PG
United Kingdom

Leakage rate for the hydrogen home refueling accident scenario was determined by the ICC. The hydrogen leakage rate was determined as 0.67 SCFM and was the result of a request by one of the above-mentioned suppliers. The proposal was made that the present codes would prevent hydrogen from accumulating above 0.8% hydrogen concentration.

The ICC International Mechanical Code requires either 100 CFM ventilation per car for a separate garage or 1.5 CFM/ft² floor area for multiple garages. The first accident scenario for a residential garage was a single wall fan that pulled in 100 CFM of fresh air through the middle of the wall (Figure C1). Gases go out at the bottom of the garage door near the home refueling unit. Figure C1 shows the gases of 0.8% hydrogen concentration after five minutes of leakage as they rise from the home refueling unit and reached the ceiling. Figure C2 shows that after 30 minutes the upper half of the garage contains a hydrogen concentration greater than 0.8%.

Figure C3 shows a garage in which 100 CFM of ventilation enters the single-car garage through an open door. After one hour of leakage, the upper 3/4 of the garage contains hydrogen concentrations greater than 0.8%.

Figure C4 shows a garage in which an exhaust fan produces 100 CFM of ventilation out of the wall opposite the home refueling system. Figure C4 shows the upper half of the garage contains hydrogen and a concentration greater than 0.8% after one hour of leakage.

Figure C5 shows the effects of removing 100 CFM of air from a slot 1/2 foot tall and 9 feet wide in the far end of the garage. Figure C5 shows the upper 2/3 of the garage is filled with hydrogen gases greater than 4.1% hydrogen after one hour and 45 minutes of leakage.

The present code allows garages using CBS construction to use partial blocks at the floor level to provide natural ventilation. Figure C6 shows the effects of the addition of a 100 CFM exhaust fan to one of those locations. It can be seen slightly more than the upper half of the garage is filled with a mixture greater than 4.1% hydrogen concentration after one hour and 45 minutes of leakage.

Figure C7 shows the effect of increasing the ventilation rate to 283.5 CFM (189 ft² floor area * 1.5 CFM/ft² = 283.5 CFM). It can be seen that the upper 2/3 of the garage is filled with gases that are more than 4.1% hydrogen.

It is concluded that the present code cannot assure the concentration of hydrogen remains below 0.8%, or even below 4.1% (burnable mixture of hydrogen and air.)

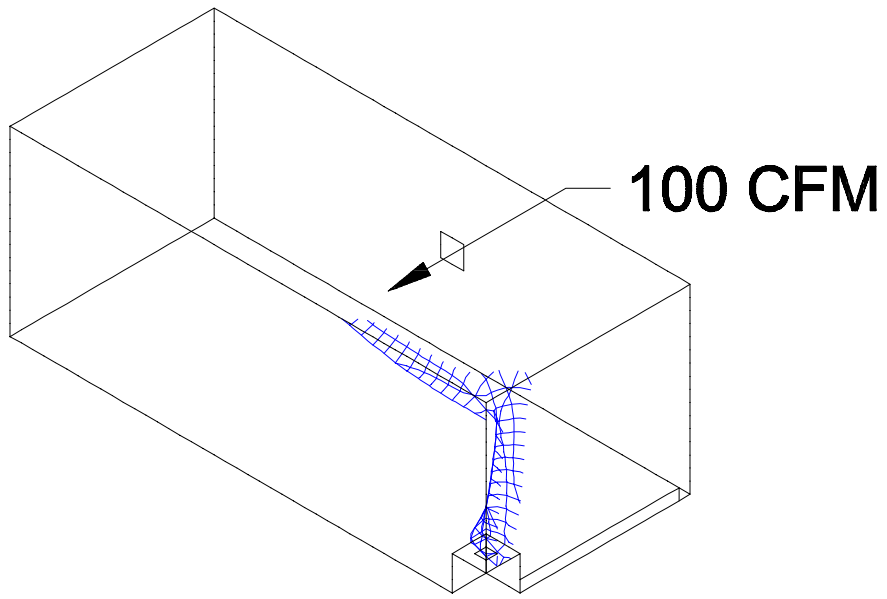


Figure C 1 - Residential garage 0.8% hydrogen at 5 minutes

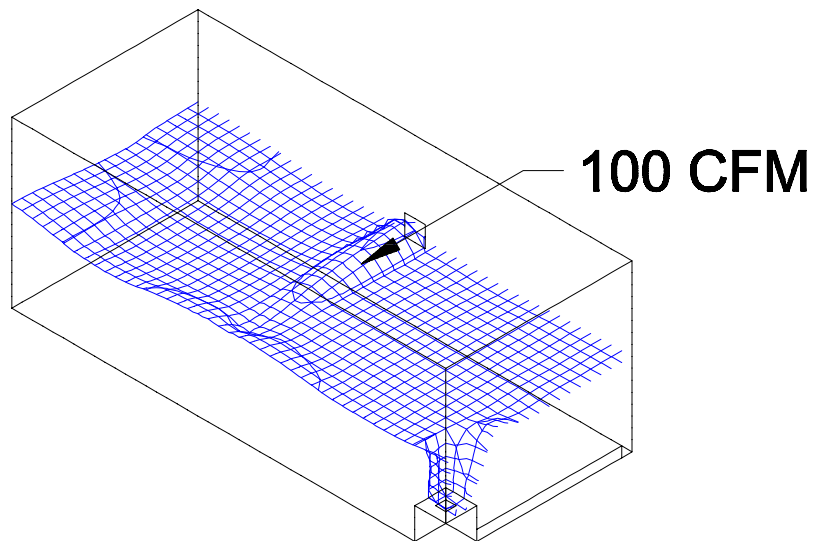


Figure C 2 - Residential garage 0.8% hydrogen at 30 minutes

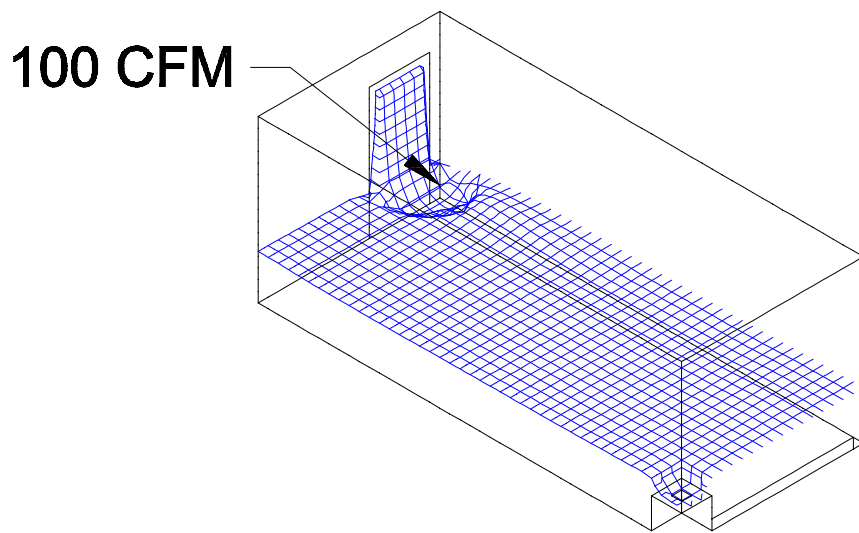


Figure C 3 - Residential garage 0.8% hydrogen 60 minutes

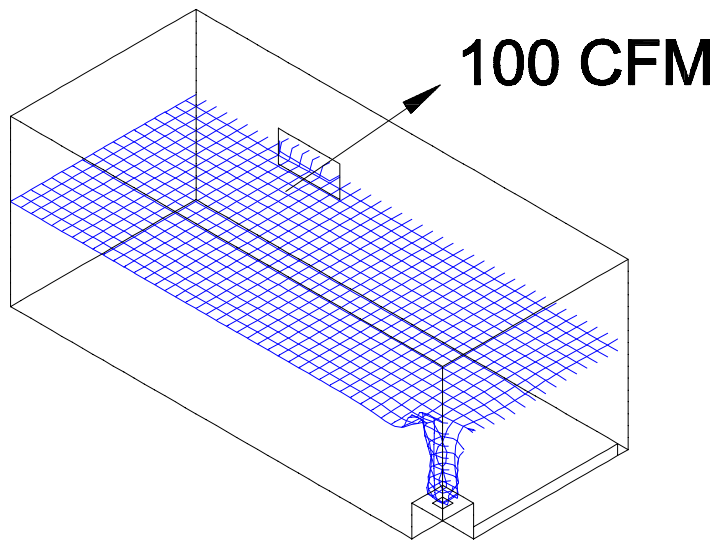


Figure C 4 - Residential garage 0.8% hydrogen 60 minutes

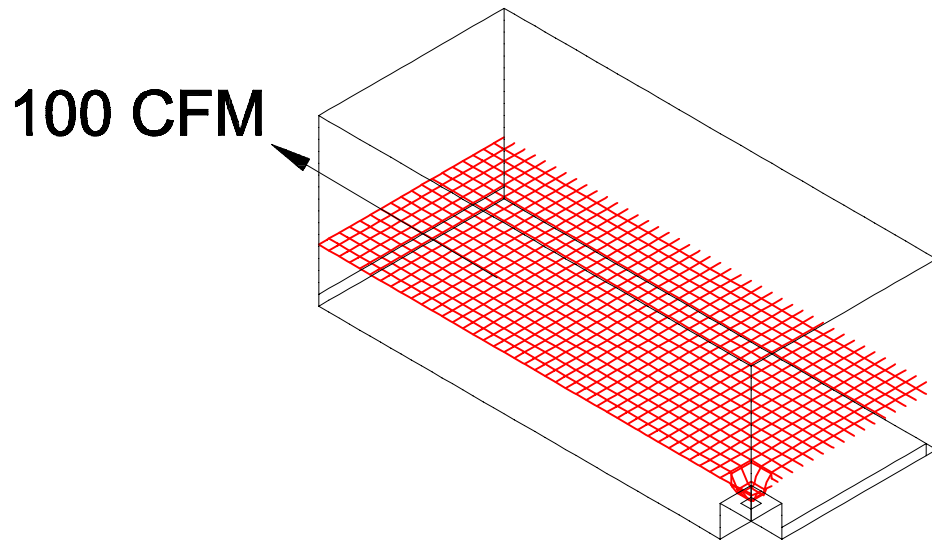


Figure C 5 - Residential garage 4.1% hydrogen 105 minutes

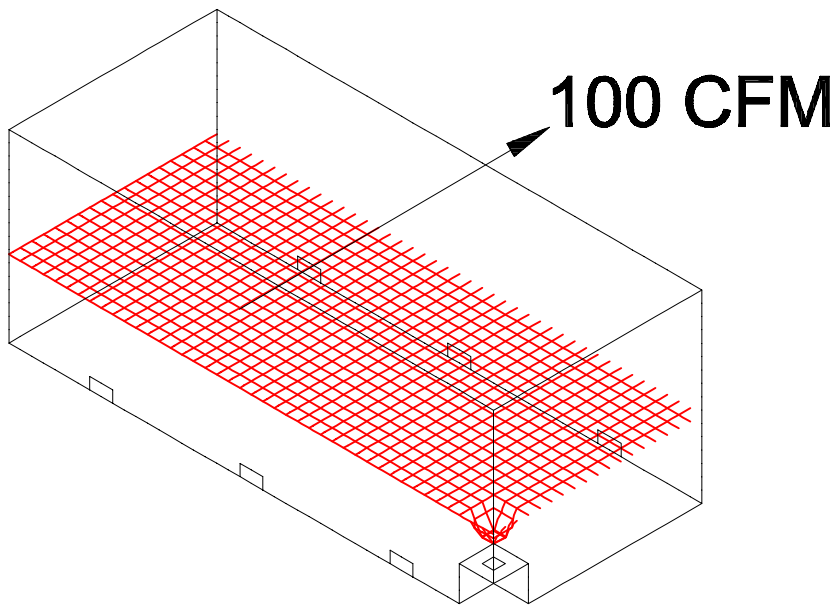


Figure C 6 - Residential garage 4.1% hydrogen 105 minutes

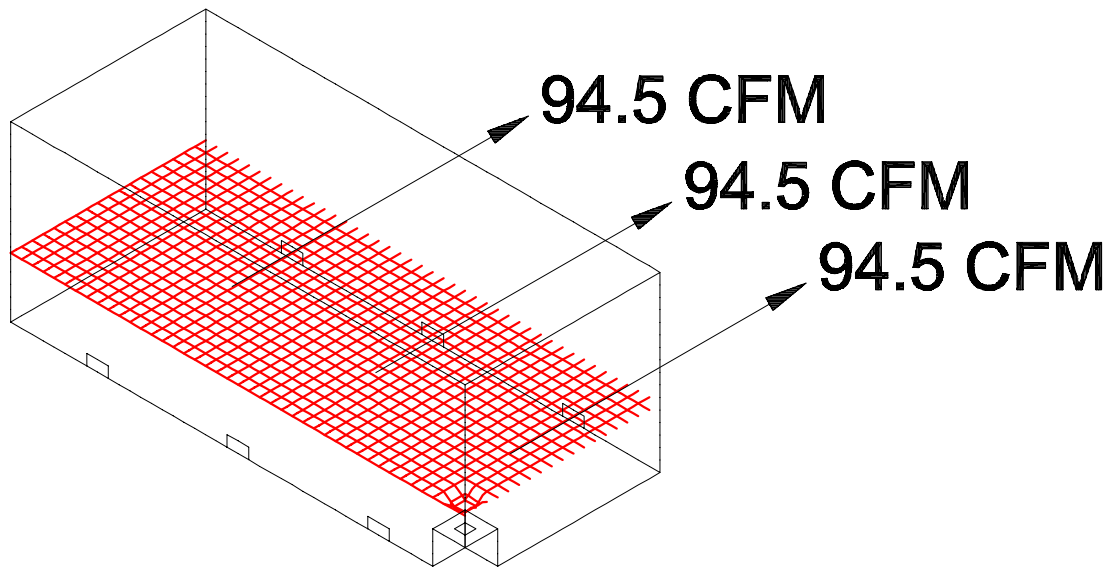


Figure C 7 - Residential garage 4.1% hydrogen at 165 minutes

Minimum Hydrogen Leakage Rate for Standing Flames

The risk incurred by the leakage of hydrogen into unconfined or large enclosures decreases as the flow rate decreases. At low leakage rates, the ability to sustain a flame, and therefore an ignition site, decreases and eventually becomes zero. Experiments were conducted to begin to determine what a minimum burnable flow rate of hydrogen would be. The experimental procedure was as follows:

1. A 3-inch long, 3-inch diameter cylindrical block of brass was machined to have exit holes of the following diameters (Note: the diameters are drill bit diameters):

Hole Number	Hole Diameter (cm)
1	0.061
2	0.089
3	0.127
4	0.175
5	0.203
6	0.262
7	0.323
8	0.419
9	0.513

2. Brass was chosen because of its high heat capacity (370 Joules/kg K).
3. Swagelock fittings were attached to the opposite side of the block in order to feed the hydrogen through the holes.
4. Hydrogen was allowed to flow through each hole, individually, and the flow rate was adjusted to 6 cc per minute. This flow rate was found to sustain a hydrogen flame at each hole.
5. The hydrogen flowing through each hole was ignited using a common match.
6. The flow rate was then reduced until a hydrogen flame was no longer present. The hydrogen flame was detected by measuring the temperature above the flame with a thermocouple. Since the brass block remained at constant temperature (26.1°C), temperatures recorded above 100°C at the flame location, were assumed to indicate the presence of a flame.
7. Steps 4, 5, and 6 were repeated for each hole.

No hole was able to support a hydrogen flame at less than 3.5 cc/min. The smaller holes were self-extinguishing, within five to ten seconds, due to water condensation.

Hydrogen Flame Impingement

The use of hydrogen fuel vehicles inside wood frame structures may result in hydrogen flame impingement on interior walls. The gypsum board that covers the wood frame can be installed in a variety of ways dependent on code requirements. Tests were run to determine the amount of damage done by hydrogen flame impingement on gypsum board mounted on two-by-four wood frames. The test utilized 1.7 pounds of hydrogen vented in 100 seconds beginning at a flow rate of 1000 SCFM. The jet was placed 2.5 feet away from the gypsum board as this distance was found to produce the maximum heat transfer in previous tests. Five tests were performed (See Table C1). Figure C8 – C10 show photos of the testing.

Table C1

Gypsum board thickness	Distance between two by fours	Maximum temperature rise at back of gypsum board
1/2 inch sheet	Twenty-four inches	144 degrees F.
1/2 inch sheet	Sixteen inches	142 degrees F.
5/8 inch sheet	Twenty-four inches	126 degrees F.
Two 5/8 inch sheets	Twenty-four inches	4 degrees F.
5/8 inch sheet with seam	Twenty-four inches	138 degrees F.

It can be seen that the use of two 5/8 inch sheets of Fire Code Type X gypsum board reduced heat transfer through the boards to nearly zero. This same test conducted with automobile door sheet metal produces a temperature rise on the order of 1400 degrees F.



Figure C 8 – Hydrogen flame impingement on gypsum wallboard seam

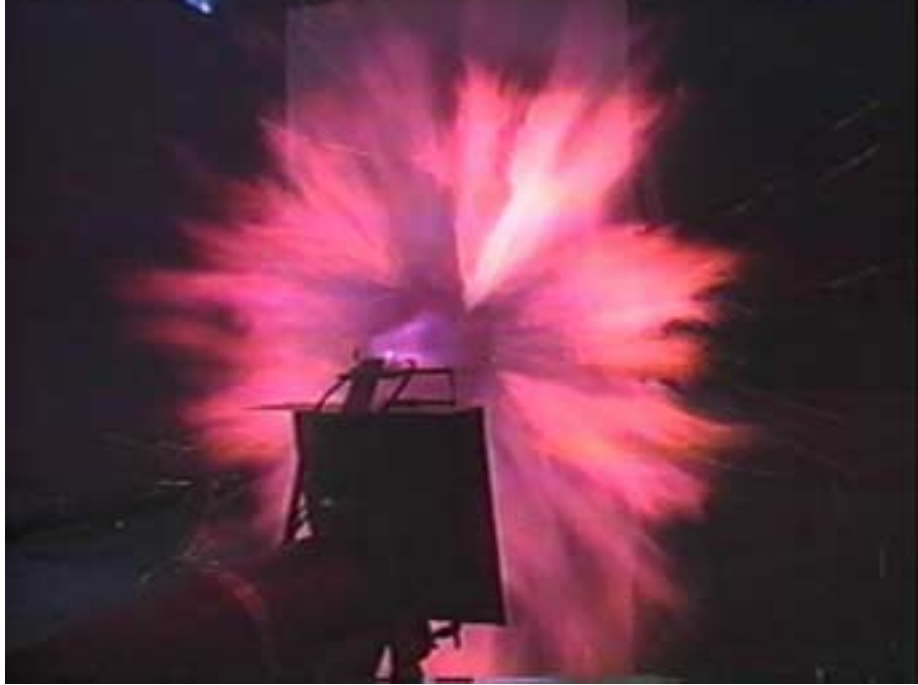


Figure C 9 - Hydrogen flame impingement, early in burn



Figure C 10 - Hydrogen flame impingement on gypsum wallboard (paper cover burning)

TESTING OF HIGH PRESSURE HYDROGEN COMPOSITE TANKS

**Ben C. Odegard, Jr. and George J. Thomas
Sandia National Laboratories
Livermore, California, USA**

Abstract

The goals of this project were (a) to provide data to manufacturers, regulatory agencies and the public that are beyond the scope of certification tests to help in demonstrating the viability of onboard compressed gas hydrogen storage, and (b) to provide quantitative information on tank failure and hydrogen release that can be used in the development of improved materials and environmental models. The project consisted of two phases. The first phase focused on tank properties, while the second phase characterized the properties of the ignited hydrogen plume venting from a high-pressure tank. Our results in the first phase indicate that the energy for penetration and a critical flaw size can be quantitatively determined for a specific tank design. The second phase results show that under realistic penetration conditions, ignition of the gas does not produce severe shock wave or temperature conditions to the surrounding environment. Furthermore, the polymer liners in Type IV tanks reduced release rates in some cases.

Introduction

The certification of lightweight composite-based high-pressure tanks for use in onboard hydrogen storage applications generally follows tests and procedures developed for compressed natural gas vessels^{1,2,3,4}. These tests generally consider the long-term integrity of the vessels (e.g., cycling fatigue, abrasion) and environmental factors, such as corrosion. Such testing is a necessary condition for the tanks to be accepted by end users and are generally performed by the tank manufacturer. However, there are additional data to be gained from catastrophic testing of high-pressure tanks that can increase our knowledge of the properties of composite tanks. A greater understanding of the failure modes and the properties of hydrogen gas plumes vented from high pressure tanks could aid in enhancing the acceptance of hydrogen for vehicular use as well as increasing the confidence of regulatory agencies, manufacturers and the public in the use of high pressure tanks as hydrogen storage devices. Furthermore, this additional information could be applied to extending current models to fully understand failure mechanisms beyond a uniform burst test condition. This project was aimed at these issues, with the intention of providing experimental data not generally obtained during the certification procedure.

Briefly, the goals of this project can be summarized as follows:

- (a) to provide data to manufacturers, regulatory agencies and the public that are beyond the scope of certification tests to help in demonstrating the viability of onboard compressed gas hydrogen storage, and
- (b) to provide quantitative information on tank failure and hydrogen release that can be used in the development of improved materials and environmental models.

Initially, our plans were to conduct a comparative study between hydrogen and other fuels, such as gasoline, natural gas, and propane. The data were to be documented and distributed both in written form and in video/film through a collaborative effort with the H2000 project. The project was to be reviewed and approved by an oversight committee of experts coming from both industry and federal agencies. However, the program plan was significantly modified from the original plan in response to criticisms from the reviewers in the FY00 Hydrogen Program Review, using input from the oversight committee members as well as other consultants. The scope of the project was also greatly reduced and focused specifically on quantitative tank penetration tests.

The final project, now completed, consisted of two phases. In Phase I, tests were aimed at generating data on the properties of the tank containing high-pressure gas. The energy required to penetrate the filament-wound composite vessel was determined and examined with current modeling predictions on composite vessels. Phase II of the project addressed the effects of a hydrogen release from a high-pressure tank and the impact of an ignition of the escaping gas plume. The results of Phase I demonstrated that there is a critical flaw size for these vessels above which catastrophic failure will occur. The results also showed a linear dependence of penetration energy on the penetrating rod diameter and thus a relationship with the shear strength of the composite vessel lay-up. The results of Phase II show that ignition of a hydrogen gas release from a high-pressure tank, with a credible release rate, is no worse than other fuels, such as gasoline or propane, and may be less damaging to nearby personnel and equipment.

Test Program Description

Composite Pressure Tanks

State-of-the-art composite vessels were manufactured by a commercial vendor for these tests. They were purchased commercially through a competitive bidding process and certified for use at 34.5 MPa (5000 psi) hydrogen. The polymeric-lined, graphite/glass-reinforced epoxy vessels (Type IV) were tested by the manufacturer to 96 MPa without visible damage. The internal volume is 24 liters with an outside diameter of 23 cm and a total outside length of 35 cm. When filled to 34.5 MPa, they have a storage density of 5-wt.% hydrogen. These vessels are compatible for both hydrogen and natural gas containment. A photograph of the general features of the cylinder is shown in Figure 1. Vessel features include a steel (4340 HSLA) single collar with an attached valve. An integrated pressure relief device is generally used, but was not included for these tests. A small number of similarly constructed vessels (Type IV) were purchased from another vendor. However, the modified test matrix did not include these vessels.



Figure 1. Photograph showing general features of the tests cylinders.

The structural lay-up consisted of a 5 mm thick fiberglass composite outer wrap over an 8 mm thick graphite fiber inner wrap. The liner was a 7 mm thick high-density polymeric liner (Note: these thickness values are approximate). A high strength, low alloy steel collar at one end of the cylinder joined the liner material to the cylinder valve. A schematic of the cylinder lay-up is shown in Figure 2.

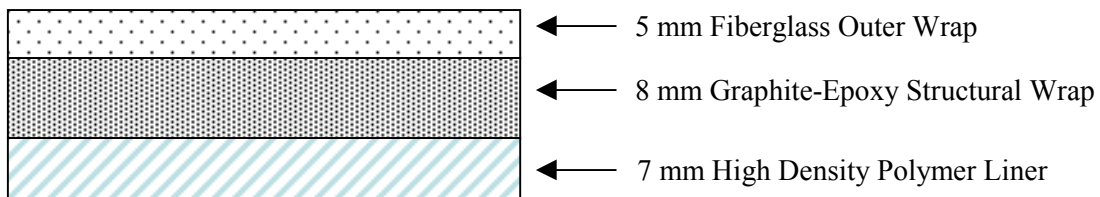


Figure 2. Schematic of composite lay-up.

Test Procedure

Only penetration tests were made in the modified test matrix and two different test sites were used. In Phase I, tests were conducted at a drop tower facility which allowed better video diagnostic capability. However, a large cylindrical shield was employed to protect adjacent buildings and personnel from the potential debris. All Phase I tests were made on tanks filled with nitrogen. In Phase II, a remote facility was used to allow measurements on the hydrogen plume ignition. Overall views of the sites are shown in Figure 3a and 3b. A continuous spark igniter system was used to assure ignition during the hydrogen tests. This simply consisted of a high-performance vehicular spark plug transformer supplying high voltage to spark plug wires positioned at the edge of the expected release plume. More details are given later in this report.



Figure 3a showing drop tower used for nitrogen tests (Tests 1-9)



Figure 3b showing remote cable site used for the hydrogen tests (Tests 10-14)

Extensive diagnostics were employed at both sites. Standard speed (30 fps) videos were used to record the overall test area and to observe close-in to the penetrator impact region on the tank. High-speed video (1000 fps) and film (4000-5000 fps) were used to examine the details of the penetration, tank response and gas release. The internal gas pressure was also recorded throughout the test procedure to determine the gas release rate. Additionally, during Phase II tests, an infrared camera was employed to record the temperature profiles of the ignited gas plumes and pressure transducers were positioned near the target area to determine pressure wave propagation. Post-test examination of the tanks was also conducted, particularly in the fracture regions, to yield information on the failure characteristics of the materials used in the fabrication of the vessels.

In each of the tests, a blunt, cylindrical, weighted rod was dropped onto a rigidly mounted tank. The rod was cable-guided to strike approximately in the center of the cylindrical portion of the tanks. Three different rod diameters were used: 12.7, 25 and 50 mm. The energy of the rod was controlled by adjusting the height and the weight of the rod assembly. Accurate determinations of the impact energy and the energy loss in penetrating the tank could be made directly through velocity measurements taken from the high-speed film and video recordings. A total of 14 tests were conducted, 9 in Phase I and 5 in Phase II. An overall summary of the test conditions is given in Table I.

Table I: Test parameters and observations from the Phase I and Phase II testing

Test #	Rod Dia. (cm)	Cylinder Pressure [MPa]	Drop Height [m]	Rod Weight [kg]	Rod Velocity [m/s]	Rod Energy [kJ]	Remarks
Nitrogen Tests							
1	5.08	24.8	12.1	18.14	13.7	1.7	No visible damage No gas release
2	5.08	24.8	15.2	18.14	18.0	2.9	No visible damage No gas release
3	5.08	24.8	28.0	18.14	22.25	4.52	Visible surface damage No gas release
4	5.08	24.8	26.8	49.0	20.7	10.58	Penetration Gas Release Gas release in 0.2 sec.
5	5.08	34.5	26.8	49.0	20.7	10.58	Penetration Tank Failure
6	5.08	34.5	15.2	49.0	16.8	6.92	Penetration Tank Failure
7	2.54	34.5	15.2	49.0	16.8	6.92	Penetration Gas Release Gas release in 0.2 sec.
8	1.27	34.5	30.5	12.3	22.9	3.2	Penetration Gas Release Blocked
9	1.27	34.5	30.5	12.3	22.9	3.2	2" Longer spike Penetration Gas Release Blocked
Hydrogen Tests							
10	1.27	34.5	30.5	12.2	22.9	3.2	Penetration Gas release w/ignition Partially blocked Gas release in 6 sec.
11	1.27	24.8	30.5	12.2	22.9	3.2	Penetration Gas release w/ignition Partially blocked Gas release in 60 sec.
12	1.27	34.5	30.48	12.2	22.9	3.2	Penetration Gas Release, no ignition Partially Blocked Daylight Test
13	2.54	34.5	34.4	12.2	24.4	4.3	Penetration Gas release w/ignition Release rate <1 sec
14	1.27	24.8	30.5	12.2	22.9	3.2	Penetration Gas Release w/ignition Blocked

Phase I Results and Discussion

Energy required for penetration

There is little information available in the literature on penetration energies, or on scaling effects for the diameter, wall thickness, etc., in composite tanks. Consequently, we based our initial penetrator energy value on a bullet penetration test conducted by the tank manufacturer. Based on their information, a 50-caliber, 163-grain (10.6 gm) bullet with a muzzle velocity of 850 m/s will penetrate both sides of the tank. The kinetic energy of the bullet is calculated at 3.6 kJ. Hence, an upper estimate of the energy required to penetrate one wall is about 1.8 kJ. Since the bullet had velocity after exiting the second wall, the actual energy imparted to the tank was somewhat lower. We chose this value as a starting point to determine the minimum energy for penetration. However, our initial test was conducted with a larger diameter rod, 50 mm, or approximately 4-5 times greater than the bullet.

The first three tests, summarized in Table I, were conducted on the same tank since the first two drops did not induce any visible surface damage to the tank. The tank was rotated between tests to change the impact point on the surface. In the third test, conducted at an initial energy of 4.5 kJ, the tank surface was damaged, but not penetrated. The initial energy was more than doubled in Test 4, using a new tank, and the penetrator rod easily penetrated the tank at an energy just over 10 kJ. Measurements on a frame-by-frame basis from the high-speed photometrics determined that the 50 mm rod required an energy of 6 kJ to penetrate one side of the tank. The first four tests were conducted with a nitrogen fill pressure of 24.8 MPa (3600 psi). Test 5 was conducted at a higher fill pressure, 34.5 MPa (5000 psi), and with an initial energy just above 10 kJ. For Test 6 the penetration energy was decreased to approximately 7 kJ with all other test parameters similar to Test 5. This test verified the energy value for penetration. Variations in penetration energy for the different fill pressures were within the experimental uncertainty of the measurements.

Additional tests were then conducted with different diameter rods and the penetration energy determined as a function of rod diameter. These results are plotted in Figure 4. One can see that the energy is a linear function of diameter that suggests shear strength dependence as shown in the following equation:

$$\text{Penetration energy} = E_p = \tau \pi d t \delta x$$

Where τ is the shear strength of the composite, d is the diameter of the rod, t is the shell thickness and δx is the distance required to shear the lay-up. Thus, the effective shear area is defined by the circumference of the penetrating rod and the wall thickness over which the rod acts. Examination of the tank penetration shows a cylindrical hole of nearly the same diameter as the rod that is consistent with the above interpretation. Further, high-speed video observations during one of the tests showed an intact disc of the tank shell being ejected from the penetrated region, nearly the same diameter as the rod, again, consistent with the above interpretation.

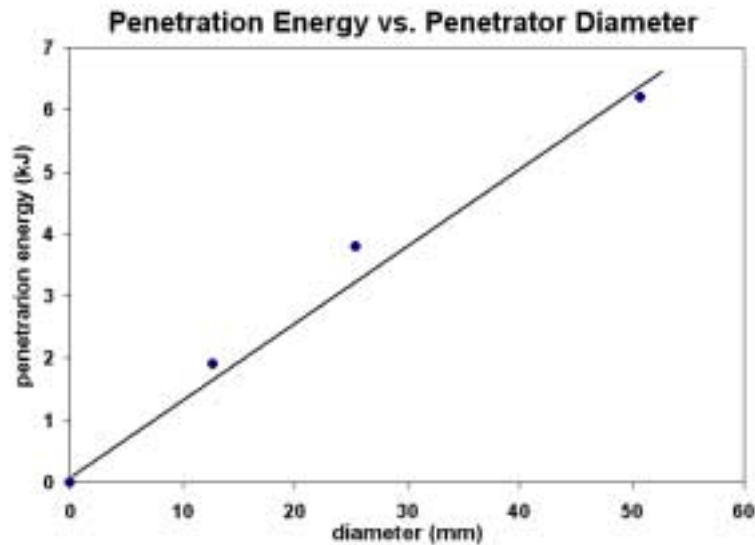


Figure 4. A plot of the measured penetration energy as a function of rod diameter.

Critical penetration size

Overall, the tanks exhibited very robust behavior and, as reported above, required significant energies to penetrate the vessel walls. Furthermore, the penetration is relatively benign and exhibits little collateral damage; that is, (a) the puncture size is of the order of the penetrating rod, (b) the puncture does not grow significantly beyond the rod dimensions, (c) there is little fragmentation produced and, (d) the gas is vented out the hole with the tank remaining intact. The release rate of the gas from the puncture can be dramatically reduced by partial sealing of the exit hole by the organic liner. This will be further discussed later in this report.

There are limitations to any container design, however, and our tests purposely extended beyond credible accident scenarios to determine the limits in the current pressure vessels. We determined that there is a critical penetration size above which the tanks will not contain the design pressure and the tanks will fail catastrophically. Referring to Table I, Tests 4, 5, 6 and 7 span the test conditions over which the tank will fail or not fail. It was found that at a fill pressure of 34.5 MPa, a 50 mm diameter penetration (Test 5) resulted in a circumferential tank failure initiating at the edge of the hole. Test 6 was a repetition of Test 5 to verify that the observed failure was not unique to the particular tank used in the test. This pressure and rod diameter was the only condition found to produce a tank failure. All other rod diameter-fill pressure conditions resulted simply in venting of the fill gas with no further structural failure. A simple calculation of the stress induced in the region of the vessel based on penetration size indicates a shear strength range for the fiber wrap to be 150 - 200 MPa.

Phase II Results and Discussion

The previous tests were conducted using nitrogen as the fill gas to avoid ignition issues and focused on the properties of the high-pressure composite tanks. During the second phase, tests were conducted using hydrogen as the fill gas and were aimed at examining the characteristics of ignited gas plumes vented from punctured high-pressure tanks. Two additional diagnostics, as well as those employed in Phase I, were included for these tests. First of all, an infrared (IR) camera operating at 30 fps was used to observe flame evolution within the gas plume. The camera was temperature-calibrated to provide an approximate temperature gradient within the gas plume. Secondly, pressure transducers were placed at different distances from the tank penetration point to quantify the pressure pulse induced in the surrounding region by ignition of the venting gas. In all, five additional penetration tests were conducted during this phase of the program, with all but one test made with a 12.7 mm diameter rod. Gas ignition was assured through a set of 10 continuous spark igniters placed on a line 15° from vertical from the rod impact point, spaced at 10 cm intervals and at 90° positions around the hole. These positions attempted to provide a spark source at the edge of the gas plume where the hydrogen/air mixture was within the ignition range for hydrogen. The authors are indebted to Michael Swain and Matthew Swain of the University of Miami for sharing their insight and experience in positioning the igniters.

Infrared observations

Figure 5 shows a false color infrared image of the ignited gas plume 133 ms after puncture and ignition during Test 10. In this test, the tank was filled with hydrogen to 34.5 MPa and a 12.7 mm diameter rod was used. The hole in the outer composite wrap was measured after the test and found to be about 25% larger than the rod diameter. The color variation in the figure corresponds to temperature gradients (as indicated on the color bar at the bottom of the figure). This image is one of a series of images that show the evolution of the gas plume with time and was chosen to show the maximum temperature reached during the test. The peak temperature of about 1100°C was reached when the ignition center had risen to almost 6 meters above the test platform. Note that the plume has expanded to almost 3 meters width at this height, consistent with a half angle of 15° assumed in placing the igniters. After 300 ms, the maximum temperature in the plume had dropped to about 800°C. This example was typical of all of the tests and shows that the very high buoyancy of hydrogen rapidly elevates the flame front away from the surrounding area. These results are consistent with those of Swain et. al. ^{5, 6, 7, 8}, in which a continuous gas source was used to form an ignited hydrogen plume. The present results show that with rapid depressurization of a punctured tank, the gas plume both decreases and rises with time. More extensive IR images are shown in the final report of this project to be published.

Pressure impulse measurements

As mentioned previously, pressure transducers were placed at different distances from the pressure vessel to obtain information on the magnitude of the pressure pulse near ground level induced by ignition of the escaping gas. Since the transducers had a limited pressure range, 3 transducers were used in each test, placed at 0.75, 1.5, and 3 meters from the point of impact.

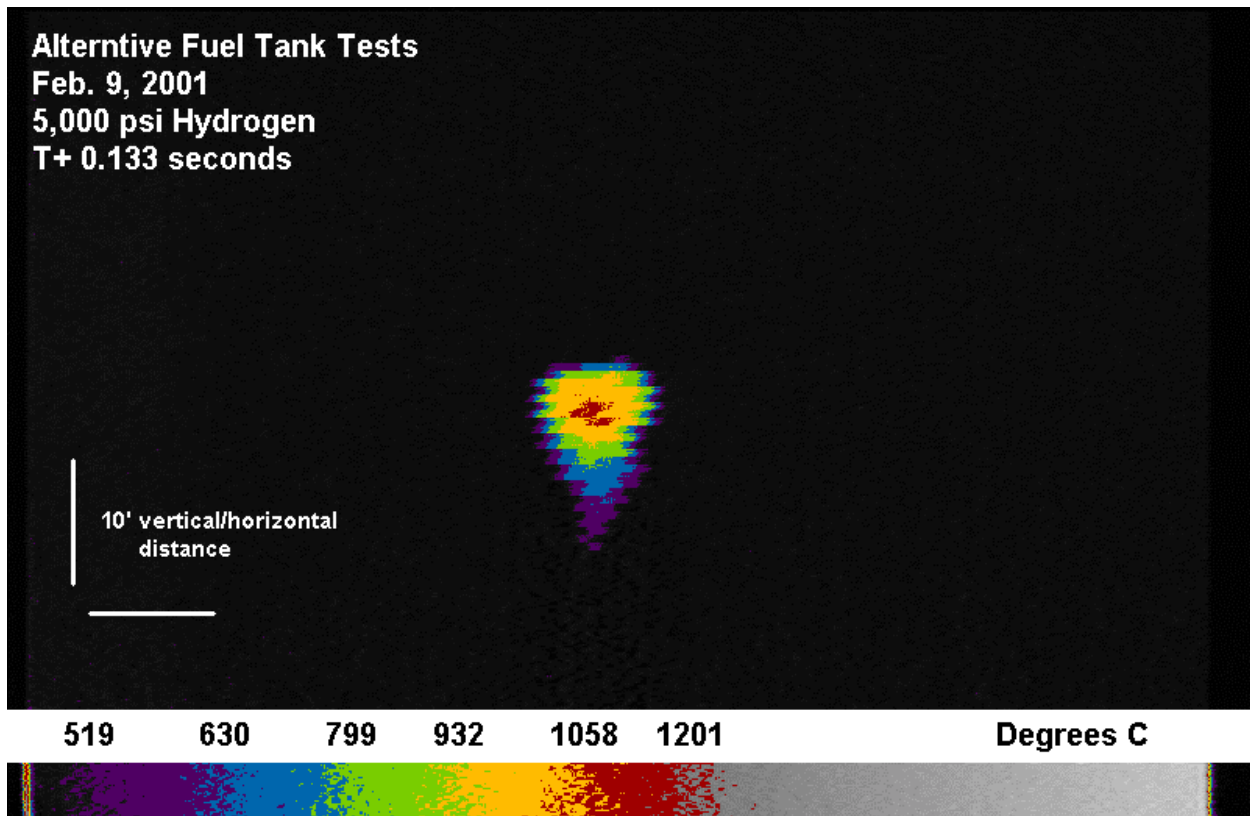


Figure 5. A false color infrared image of an ignited gas plume 133 ms after puncture and ignition of the hydrogen-filled vessel. This image shows the maximum temperature reached during the event. The color bar at the bottom gives the corresponding temperatures and colors.

The transducers were approximately 1 meter off the ground. Figure 6 is a plot of a transducer output approximately 1.5 meters from the ignition source during Test 10 (12.7 mm rod, 34.5 MPa fill pressure). The peak pressure of 0.01 MPa (1.4 psi) above ambient was of very short duration and coincided with ignition of the gas. There is a slight under-pressure developed about 100 ms later that is expected from a pressure wave where the high pressure pulse sweeps air away from the immediate region of the event. At 3 meters from the point of ignition, the peak pulse pressure was only 0.001 MPa (0.14 psi), consistent with a spherical ($1/r^2$) drop-off in pressure with distance. Overall, this is a relatively modest pulse that, we believe, would not lead to serious injuries or damage. As discussed in the next section, Test 10 produced a clean venting of the gas and a relatively large hole for the gas to be vented. We believe that this size of hole, which is larger than typical tubing diameters used in plumbing high pressure tanks, is a reasonable maximum credible failure for a tank of this design. Hence, the present results suggest that the risks associated with storing high-pressure hydrogen are no greater, and perhaps less than, other fuels, such as gasoline or propane.

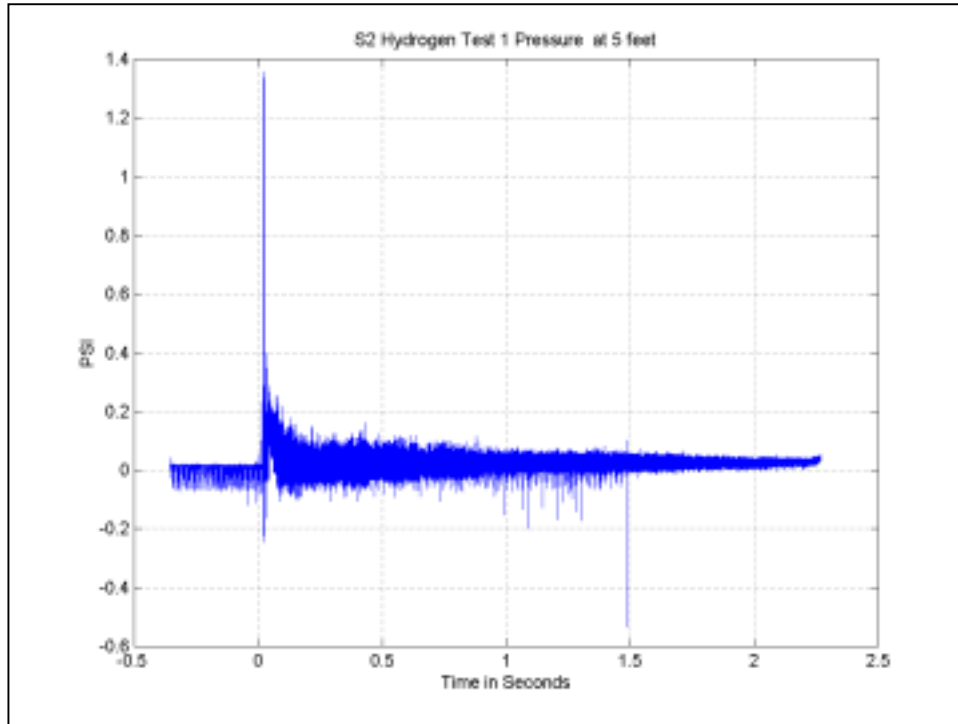


Figure 6. A plot of the overpressure induced by ignition of the venting gas during Test 10 at a distance of 1.5 meters from the tank.

Following the tests, the pressure vessels were disassembled and photographed in order to gain additional information on the test results. This was particularly important with the 12.7 mm diameter penetrator tests because of rod bounce, liner resealing and their effect on the gas venting behavior. The tank pressure as a function of time following rod penetration for Tests 10, 11 and 12 is plotted in Figure 7. Photographs of the tank liners in the region of the punctures are also included in the figure. One can see from the plot that in Test 10 the gas pressure rapidly and smoothly decreased, with the tank emptying after about 5 seconds. In contrast, the gas venting in the other two tests was discontinuous. The discontinuities are related to the rod and polymer liner interaction. It was observed on the video data that after penetration, the rod was always pushed out of the puncture hole by the internal gas pressure, climbed to about a third of the drop height, then fell back to the same region of the tank. The characteristic time for this to occur was about 2.6 seconds in all cases. However, the rod did not always produce the same result when striking the tank on the second time. In Test 10, the photograph of the liner shows that the rod fell a short distance from the original hole (the black circular region), but did not penetrate the liner (the white circular region). In Tests 11 and 12, the gas vented more slowly than in Test 10 and one can see the reason for this in the associated photographs of the liners. In Test 11, the liner was cut open, but a hole was not punched out. Since the puncture was smaller in area, the release of gas was much slower than in the previous test. Interestingly, when the rod fell back, it re-entered the same hole and effectively sealed the tank, preventing further gas release even at an internal pressure of over 14 MPa. Test 12, with a lower fill pressure (24.8 MPa) showed different behavior from the previous two tests. In this case, gas release was extremely slow after

the first penetration, consistent with the small liner cut shown in the photograph. When the rod fell the second time, however, the liner hole was opened somewhat further and the gas release rate increased. These tests, we believe, are a further indication that the tank design is robust and the liner characteristics mitigate some of the potential impact of tank penetrations.

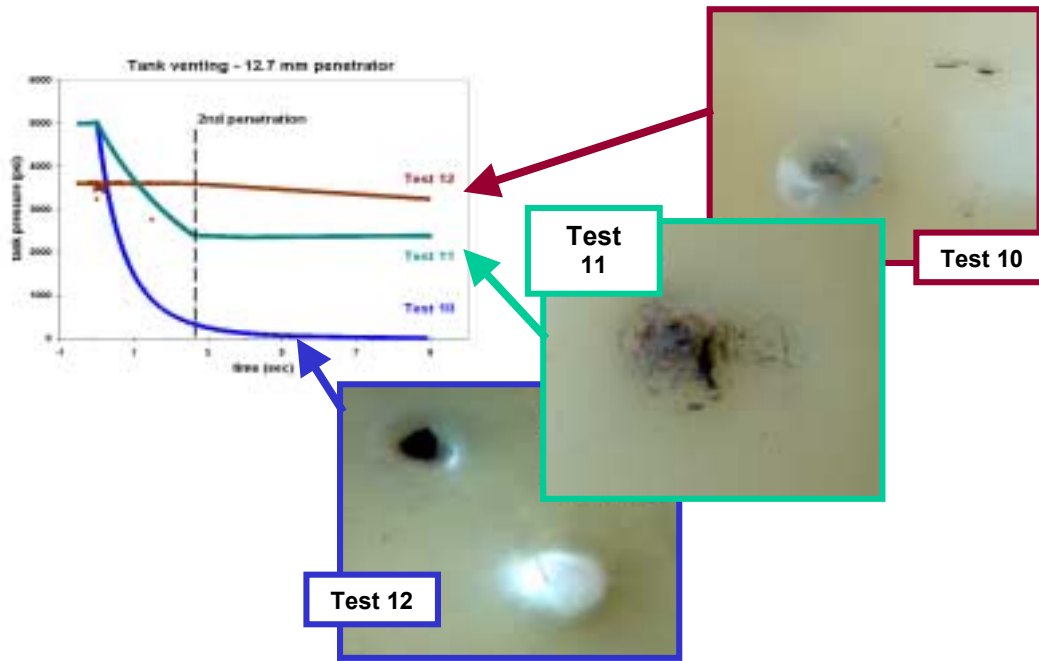


Figure 7. A composite of the measured cylinder pressures during Tests 10-12 with photographs of the corresponding liners obtained after the tests.

Summary

The results of the Phase I measurements suggest that (a) there is a pressure-dependent critical flaw size for composite tanks and, (b) there is a shear energy per unit length required to penetrate the composite wrap and liner that can be quantitatively determined. The values of these parameters are dependent on the specific tank materials and wrap design. The results also suggest that such measurements could be of value in developing composite tank models and in extrapolating tank response beyond the limited range of certification tests.

There are at least three independent modeling efforts that could utilize the data generated in Phase II of this project. First of all, the tank penetration and response results could be used to develop better, more detailed models of material behavior and failure characteristics for Type IV pressure vessels. Secondly, the measured blow-down rates can be compared to predictions based on classical models of supersonic flow through ideal orifices in order to more closely couple such calculations to real-life conditions. Thirdly, the flame propagation measurements can provide useful information for modeling hydrogen burn conditions resulting from high-pressure gas venting into the atmosphere.

One additional result generated by the tests is the overpressure produced by the shock wave of venting and burning. This information should be of value to regulatory agencies, insurance companies, etc.

The objectives of this project were to determine the response of high-pressure hydrogen vessels to extreme conditions, quantify the results and document them for public awareness. It is hoped that the results will aid in fostering acceptance of hydrogen as an alternative to hydrocarbon fuels.

Acknowledgements

We would like to acknowledge the efforts of Timothy Brown and Jeff Cherry with the Sandia National Laboratories test site department. Tim Brown was responsible for directing the nitrogen tests at the drop tower. Jeff Cherry was responsible for directing the hydrogen tests at the remote cable site. Also, Jeff Cherry and his staff have been invaluable in offering suggestions on test details and processing the data collected during these tests. Michael Swain and Matthew Swain of the University of Miami provided valuable information in the test lay out for the hydrogen tests. We would also like to acknowledge the assistance of the Oversight Committee members in monitoring the overall test matrix and for providing valuable insight and guidance during the course of this program. The Oversight Committee consisted of Robert Mauro (NHA), George Schmauch (Air Products, HTAP), Mahendra Rana (Praxair), Robert Zalosh (Worcester Polytech). William Hoagland and Geoff Holland from the Project 2000 staff were very helpful during the initial planning stages of this project. A special thanks is given to John Smith (NIST) for his assistance in obtaining valuable documents germane to this project. Karen Campbell (Air Products) was instrumental in obtaining high-pressure hydrogen for the tank fills.

The U.S. Department of Energy funded this work. The authors wish to express a special acknowledgement to N. Rossmeissl for his continued support and direction during the course of this project.

Sandia is a multi-program laboratory operated by Sandia Corporation, a Lockheed Martin Company for the United States Department of Energy under contract DE-AC04-94-AL85000.

References

1. CGA Docket 77-8, 1982, "Cylinder Specification Subcommittee Report on Basic Considerations for Composite Vessels."
2. DOT-CFFC, 1996, "Basic Requirements for Fully Wrapped Carbon-Fiber Reinforced Aluminum Lined Vessels."
3. DOT FRP-1 Standard, 1981, "Basic Requirements for FRP Type 3FC Vessels."

4. NGV2, 1992, "Basic Requirements for Compressed Natural Gas Vehicle (NGV) Containers," NSSN.
5. Swain, M. R. 1995, "Safety Analysis of High Pressure Gaseous Fuel Container Punctures," In *Proceedings from DOE Hydrogen Program Review*.
6. Swain, M. R. and M. N. Swain, 1996, "Task D: Hydrogen Safety Analysis," In *Proceedings from DOE Hydrogen Program Review*.
7. Swain, M. R, E. S. Grilliot, and M. N. Swain, 1997, "Risks Incurred by Hydrogen Escaping from Containers and Conduits," In *Proceedings from DOE Hydrogen Program Review*.
8. Swain, M. R., J. Shriber, and M. N. Swain, 1998, "Comparison of Hydrogen, Natural Gas, Liquefied Petroleum Gas, and Gasoline Leakage in a Residential Garage," *Energy and Fuels*, 12: 83-89.

Fuel Leak Simulation

**Dr. Michael R. Swain
University of Miami
Coral Gables, FL 33124**

Abstract

This work effort was conducted to serve two purposes. The first was to produce a video comparing the severity of a hydrogen and gasoline fuel leak and ignition. The second was to determine why the hydrogen flames videotaped were so easily visible. The videotape was completed and lasted approximately 3.5 minutes. The flame visibility was due to naturally-occurring particulate matter in the air. The particulate matter contained sodium, which enhances flame visibility.

Introduction

This work has been conducted to fulfill two objectives. They are:

1. Produce a 3.5 minute video comparing the severity of ignition of single failure mode fuel leaks from a hydrogen or gasoline fueled vehicle.
2. Determine why the hydrogen flames videotaped in previous experiments are so easily visible.

Previous experiments on the combustion of a hydrogen leak from a hydrogen-powered automobile have shown that the hydrogen diffusion flame has a yellow color. This is not consistent with a hydrogen diffusion flame entraining a relatively pure nitrogen/oxygen mixture and suggests the presence of an unknown impurity or impurities. The chemistry associated with a turbulent hydrogen/oxygen/nitrogen diffusion flame is well characterized, producing super-equilibrium concentration levels of the hydroxyl radical, together with hydrogen atoms in rich parts of the flame and oxygen atoms in lean areas. None of these species produces an emission signature in the visible portion of the spectrum. The object of this work was the characterization of the spectral content of the emission from such a diffusion flame.

Video of Fuel Leakage and Ignition

The video was completed on schedule and was shown publicly March 5, 2001 at the NHA meeting in Washington. Eight frames from the video are included in the Appendix. At the NHA meeting, an oral narration was given with the video. The video simply depicts the single failure mode leakage and ignition of fuel from the two vehicles but, as of yet, has no narrative. It is felt a narrative describing in detail the accident scenarios for the two vehicles and perhaps some additional video footage of hydrogen fuel line leakage should be added before the video is presented to the public.

The gasoline and hydrogen single failure mode accident scenarios were as follows:

Gasoline leakage: the fuel line of a gasoline fueled vehicle was punctured with 1/16 inch diameter hole and gasoline leaks out of the fuel line under the middle of the car. During the 3.5 minutes of videotaping, the vehicle leaks five pints of gasoline (approximately 70,000 BTU). Several events of interest occur including a deflagration of gases inside the vehicle interior and trunk, ruptures of the vehicle's tires, and an unrestrained release of coolant from the air conditioner. These should be described in the narration.

Hydrogen leakage: the hydrogen-fueled vehicle was designed consistent with existing manufacturer specifications. They include sensors for hydrogen that activate shut-off solenoids in the hydrogen tank, and computer programming to shut off fuel supply if fuel flow exceeds that used by the fuel cell, or fuel flow delivered drops by a predetermined amount. In light of the additional safety precautions designed into hydrogen-fueled vehicles the most severe single failure mode accident scenario is that of hydrogen leakage at the tank pressure release device (PRD) causing a standing flame, which in turn causes the PRD to allow all the hydrogen in the tank to escape in 100 seconds. During the video, the hydrogen vehicle leaks 3.4 pounds of hydrogen (approximately 175,000 BTU).

For hydrogen to leak under a hydrogen-powered vehicle in amounts that would produce a severe accident four failures, must occur. They are:

1. Fuel line or component sealing failure.
2. The hydrogen sensor system that detects hydrogen and shuts off hydrogen flow must fail.
3. The tank mounted excess flow valve required by manufacturers specifications must fail.
4. Flow sensing computer programs, that compare hydrogen flow to hydrogen consumption of the fuel cell, must fail.

Other failures could disable some of the above-mentioned systems but no single failure mode could produce a severe hydrogen leak under the vehicle.

Conclusions Concerning Video

The damage to the gasoline-powered vehicle was severe. The hydrogen-powered vehicle was undamaged. The maximum surface temperatures measured on the hydrogen-powered vehicle

were 117°F on the rear window glass and 67°F at the rear tray (between the rear window and rear seat).

The 3.5-minute video of the accidental leakage and ignition of a hydrogen- or gasoline-powered vehicle should have a narration added to describe their respective accident scenarios and events occurring in the video. Additionally short (5-second) video segments should be added to show the diminished severity of hydrogen leakage and ignition when interrupted by one of the onboard safety systems.

Spectral Analysis of Hydrogen Flames

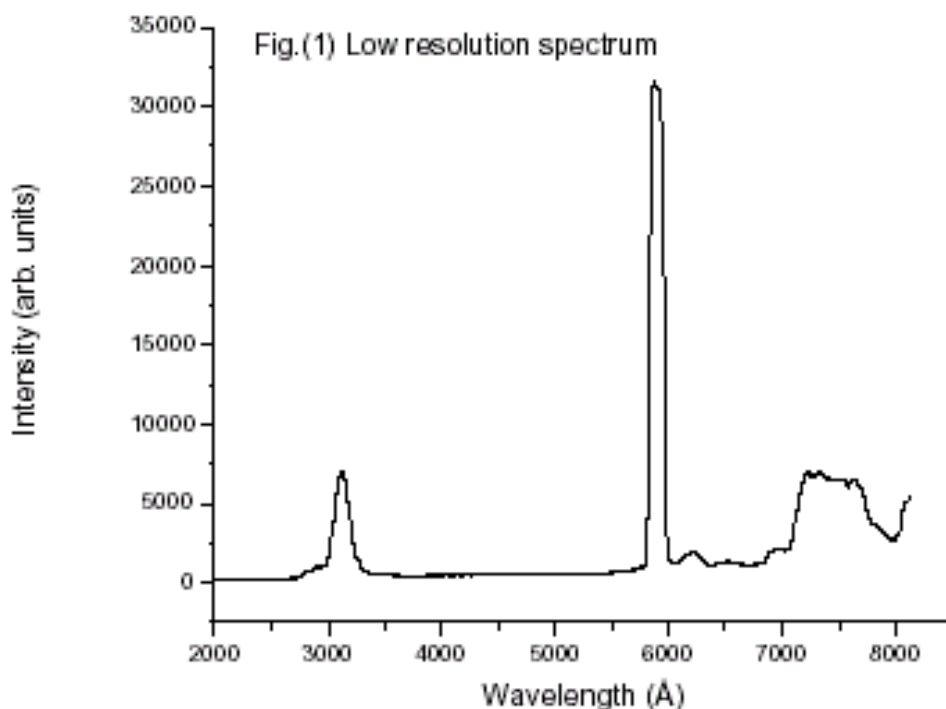
The hydrogen flames were subjected to spectral analysis to investigate flame visibility. The cause of enhanced hydrogen flame visibility was found to be naturally-occurring particulate matter, containing sodium, which was entrained into the flame. This has occurred during all the tests conducted over the last 30 years. The following is a description of the spectral analysis.

The experimental setup consisted of two optical multichannel analyzers (OMA) based on 1024 element diode arrays that were mounted on spectrographs. In a conventional single element detector/spectrometer system, one obtains a spectrum by tuning a diffraction grating and observing the light intensity at the detector as a function of wavelength. In an OMA system, the diffraction grating is fixed and the diode array is placed in the output focal plane of the spectrograph. Hence the OMA collects an instantaneous snapshot of a complete spectrum. In these experiments two EG&G OMA's were used. The unintensified array was mounted on a 1/4 m spectrograph that contained a 150 grooves/mm grating. This low-resolution system had a spectral width of approximately 6000 Å allowing it to cover the ultraviolet, visible and near infrared. The intensified array was mounted on 3/4 m spectrograph containing a 2400 grooves/mm grating. This system had a spectral width of approximately 160 Å with a resolution of 0.6 Å. Fused silica lenses were placed in front of the entrance slits to attempt to image a relatively narrow portion of the hydrogen diffusion flame. The lenses and spectrographs were placed approximately 1 meter from the flame. The lenses and spectrographs were adjusted by focusing onto a small calibration lamp to ensure that both systems were imaging the same region of the flame. Spectra were obtained simultaneously using both systems.

Results and Discussion

Figure (1) shows a typical low-resolution spectrum of the flame and is not corrected for the spectral response of the spectrograph and diode array. It is clear however, that three features dominate the spectrum:

- 1) a broad peak in the ultraviolet at ~ 3000 Å.
- 2) a narrow peak at ~ 5890 Å.
- 3) a broad peak in the near infrared between 7000-8000 Å.

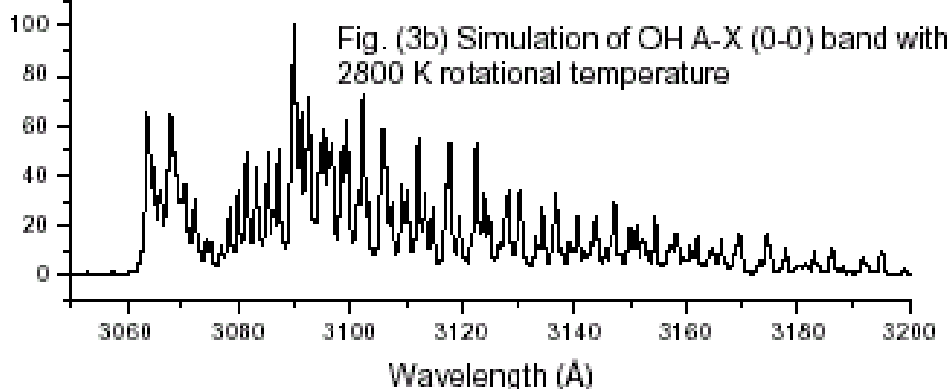
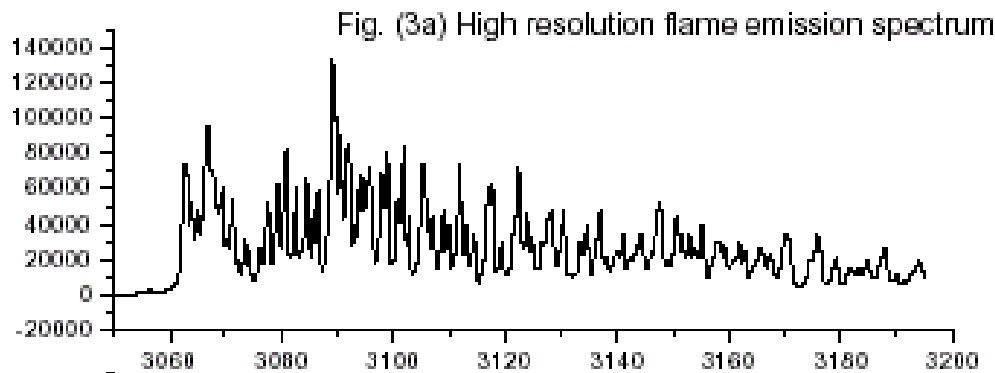
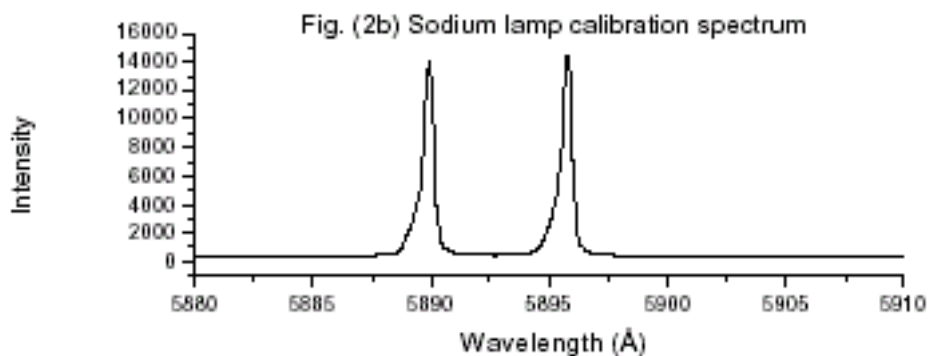
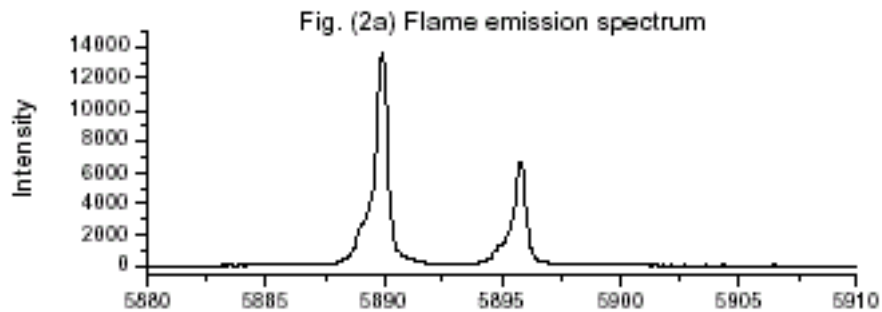


There is an additional signal that lies above the background noise. Its integrated intensity is small compared with the main features and no clear spectral signature can be identified at this spectral resolution.

Figure (2a) shows a high-resolution spectrum of the 5890 Å feature taken with the 3/4 m spectrograph. Figure (2b) shows the spectrum of a high-pressure sodium lamp taken under identical conditions with the lamp in place of the flame. The high-resolution spectrum demonstrates unequivocally that the dominant flame emission is due to sodium D line emission. The characteristic D line doublet is due to emission from the excited 2P state and consists of the D1 line due to the ($^2P_{1/2} - ^2S_{1/2}$) transition at 5895.93 Å and the D2 ($^2P_{3/2} - ^2S_{1/2}$) transition at 5889.96 Å.

Figure (3a) shows a high-resolution spectrum of a portion of the 3000 Å feature. It can be seen that, in contrast to the sodium D lines we have a complex multi-line spectrum. This is characteristic of the spectrum of a simple diatomic or polyatomic molecule and the relatively open structure suggests a hydride. The strong emission spectrum of the OH A $^2\Sigma - X^2D$ (0-0) band lies in this region. This emission is characteristic of H_2/O_2 flames and has been extensively observed and characterized. A quantitative identification requires a computer simulation of the spectrum. Figure (3b) shows a simulation of the OH A-X (0-0) emission spectrum assuming a rotational temperature of 2800 K and a spectral resolution of 0.6 Å. The simulation clearly identifies the experimental feature as being due to OH. We have not attempted to identify the broad infrared spectral feature. Several sets of high and low-resolution spectra were obtained and this involved relighting the flame several times. It is an extremely turbulent diffusion flame

but nevertheless the degree of reproducibility of both the low and high-resolution spectra was remarkable.



These results demonstrate that the dominant spectral feature in the visible region of the spectrum is due to sodium D line emission. This is due to particulate matter containing sodium that is entrained into the flame. The results also demonstrate that we can obtain high-resolution spectra of the OH radical, which may serve as an important flame diagnostic particularly of flame temperature. If the sodium emission is due primarily to thermal excitation, then the brightness of the sodium D line emission will depend on the diffusion flame temperature.

Conclusions Concerning Spectral Analysis

The cause of enhanced hydrogen flame visibility was entrained particulate matter that contained sodium that was naturally occurring in the air.

Appendix (Frames From Video)



Photo 1 - Time: 0 min, 0 sec - Hydrogen powered vehicle on the left. Gasoline powered vehicle on the right.



Photo 2 - Time 0 min, 3 seconds - Ignition of both fuels occur. Hydrogen flow rate 2100 SCFM. Gasoline flow rate 680 cc/min.



Photo 3 - Time: 1 min, 0 sec - Hydrogen flow is subsiding, view of gasoline vehicle begins to enlarge



Photo 4 - Time: 1 min, 30 sec - Hydrogen flow almost finished. View of gasoline powered vehicle has been expanded to nearly full screen



Photo 5 - Time: 2 min, 20 sec - Frame prior to interior deflagration.



Photo 6 - Time: 2 min, 20 sec - Deflagration in the interior, following frame shows flames exiting around edges of trunk lid.



Photo 7 - Time: 2 min, 40 sec - Frame prior to driver's side rear tire rupture.



Photo 8 - Time: 2 min, 40 sec - Driver's side rear tire rupture sends debris out the passenger side of the vehicle.

ADVANCED INTERNAL COMBUSTION ELECTRICAL GENERATOR

**Peter Van Blarigan
Sandia National Laboratories
Livermore, CA 94550**

Abstract

In this paper, research on hydrogen internal combustion engines is discussed. The objective of this project is to provide a high-efficiency means of renewable hydrogen-based fuel utilization. The development of a high-efficiency, low-emissions electrical generator will lead to establishing a path for renewable hydrogen-based fuel utilization. A full-scale prototype will be produced in collaboration with industrial partners.

The electrical generator is based on developed internal combustion reciprocating engine technology. It is able to operate on many hydrogen-containing fuels. The efficiency and emissions are comparable to fuel cells (50% fuel to electricity, ~ 0 NO_x). This electrical generator is applicable to both stationary power and hybrid vehicles. It also allows specific markets to utilize hydrogen economically.

Introduction

Two motivators for the use of hydrogen as an energy carrier today are 1) to provide a transition strategy from hydrocarbon fuels to a carbonless society, and 2) to enable renewable energy sources. The first motivation requires a little discussion while the second one is self-evident. The most common and cost-effective way to produce hydrogen today is the reformation of hydrocarbon fuels specifically natural gas. Robert Williams discusses the cost and viability of

natural gas reformation with CO₂ sequestration as a cost-effective way to reduce our annual CO₂ emission levels. He argues that if a hydrogen economy was in place then the additional cost of natural gas reformation and subsequent CO₂ sequestration is minimal (Williams 1996). Decarbonization of fossil fuels with subsequent CO₂ sequestration to reduce or eliminate our CO₂ atmospheric emissions provides a transition strategy to a renewable, sustainable, carbonless society. However, this requires hydrogen as an energy carrier.

The objectives of this program for the year 2001 are to continue to design, build, and test the advanced electrical generator components, research hydrogen-based renewable fuels, and develop industrial partnerships. The rationale behind the continuation of designing, building, and testing generator components is to produce a research prototype for demonstration in three years. Similarly, researching hydrogen-based renewable fuels will provide utilization components for the largest possible application. Finally, developing industrial partnerships can lead to the transfer of technology to the commercial sector as rapidly as possible.

This year work is being done on the linear alternator; two-stroke cycle scavenging system, electromagnetic/combustion/dynamic modeling, and fuel research. The Sandia alternator design and prototype will be finished, and the Magnequench design will be tested. Work on the scavenging system consists of using KIVA-3V to investigate loop and uniflow configurations. Ron Moses of Los Alamos National Laboratories is conducting the modeling; modeling of the alternator is being performed. Hydrogen-based renewables, such as biogas and ammonia, are the fuels being researched. Outside of modeling and research, an industrial collaboration has been made with Caterpillar, Unique Mobility and Magnequench International, a major supplier of rare earth permanent magnet materials.

Background

Electrical generators capable of high conversion efficiencies and extremely low exhaust emissions will no doubt power advanced hybrid vehicles and stationary power systems. Fuel cells are generally considered to be ideal devices for these applications where hydrogen or methane is used as fuel. However, the extensive development of the IC engine, and the existence of repair and maintenance industries associated with piston engines provide strong incentives to remain with this technology until fuel cells are proven reliable and cost-competitive. In addition, while the fuel cell enjoys high public relations appeal, it seems possible that it may not offer significant efficiency advantages relative to an optimized combustion system. In light of these factors, the capabilities of internal combustion engines have been reviewed.

In regards to thermodynamic efficiency, the Otto cycle theoretically represents the best option for an IC engine cycle. This is due to the fact that the fuel energy is converted to heat at constant volume when the working fluid is at maximum compression. This combustion condition leads to the highest possible peak temperatures, and thus the highest possible thermal efficiencies.

Edson (1964) analytically investigated the efficiency potential of the ideal Otto cycle using compression ratios (CR) up to 300:1, where the effects of chemical dissociation, working fluid thermodynamic properties, and chemical species concentration were included. He found that

even as the compression ratio is increased to 300:1, the thermal efficiency still increases for all of the fuels investigated. At this extreme operating for instance, the cycle efficiency for iso-octane fuel at stoichiometric ratio is over 80%.

Indeed it appears that no fundamental limit exists to achieving high efficiency from an internal combustion engine cycle. However, many engineering challenges are involved in approaching ideal Otto cycle performance in real systems, especially where high compression ratios are utilized.

Caris and Nelson (1959) investigated the use of high compression ratios for improving the thermal efficiency of a production V8 spark ignition engine. They found that operation at compression ratios above about 17:1 did not continue to improve the thermal efficiency in their configuration. They concluded that this was due to the problem of non-constant volume combustion, as time is required to propagate the spark-ignited flame.

In addition to the problem of burn duration, other barriers exist. These include the transfer of heat energy from the combustion gases to the cylinder walls, as well as the operating difficulties associated with increased pressure levels for engines configured to compression ratios above 25:1 (Overington and Thring 1981, Muranaka and Ishida 1987). Still, finite burn duration remains the fundamental challenge to using high compression ratios.

The goal of emissions compliance further restricts the design possibilities for an optimized IC engine. For example, in order to eliminate the production of nitrogen oxides (NO_x), the fuel/air mixture must be homogeneous and very lean at the time of combustion (Das 1990, Van Blarigan 1995). (It is subsequently possible to use oxidation catalyst technologies to sufficiently control other regulated emissions such as HC and CO.) Homogeneous operation precludes diesel-type combustion, and spark-ignition operation on premixed charges tends to limit the operating compression ratio due to uncontrolled autoignition, or knock. As well, very lean fuel/air mixtures are difficult, or impossible, to spark-ignite.

On the other hand, lean charges have more favorable specific heat ratios relative to stoichiometric mixtures, and this leads to improved cycle thermal efficiencies. Equivalence ratio is no longer required to be precisely controlled, as is required in conventional stoichiometric operation when utilizing three way catalysts. Equivalence ratio is defined here as the ratio of the actual fuel/air ratio to the stoichiometric ratio.

Combustion Approach

Homogeneous charge compression ignition combustion (HCCI) could be used to solve the problems of burn duration and allow ideal Otto cycle operation to be more closely approached. In this combustion process a homogeneous charge of fuel and air is compression heated to the point of autoignition. Numerous ignition points throughout the mixture can ensure very rapid combustion (Onishi et al 1979). Very low equivalence ratios ($\phi \sim 0.3$) can be used since no flame propagation is required. Further, the useful compression ratio can be increased, as higher temperatures are required to autoignite weak mixtures (Karim and Watson 1971).

HCCI operation is unconventional, but is not new. As early as 1957 Alperstein et al. (1958) experimented with premixed charges of hexane and air, and n-heptane and air in a Diesel engine. They found that under certain operating conditions their single-cylinder engine would run quite well in a premixed mode with no fuel injection whatsoever.

In general, HCCI combustion has been shown to be faster than spark ignition (SI) or compression ignition combustion. And much leaner operation is possible than in SI engines, while lower NO_x emissions result.

Most of the HCCI studies to date however, have concentrated on achieving smooth releases of energy under conventional compression condition (CR ~ 9:1). Crankshaft-driven pistons have been utilized in all of these previous investigations. Because of these operating parameters, successful HCCI operation has required extensive exhaust gas recirculation (EGR) and/or intake air preheating. Conventional pressure profiles have resulted (Thring 1989, Najt and Foster 1983).

In order to maximize the efficiency potential of HCCI operation, much higher compression ratios must be used and a very rapid combustion event must be achieved. Recent work with higher compression ratios (~21:1) has demonstrated the high efficiency potential of the HCCI process (Christensen et al 1998, Christensen et al 1997).

In Figure 1, the amount of work attained from a modern 4-stroke heavy-duty diesel engine is shown at a 16.25:1 compression ratio. The results show that under ideal Otto cycle conditions (constant volume combustion), 56% more work is still available. This extreme case of non-ideal Otto cycle behavior serves to emphasize how much can be gained by approaching constant volume combustion.

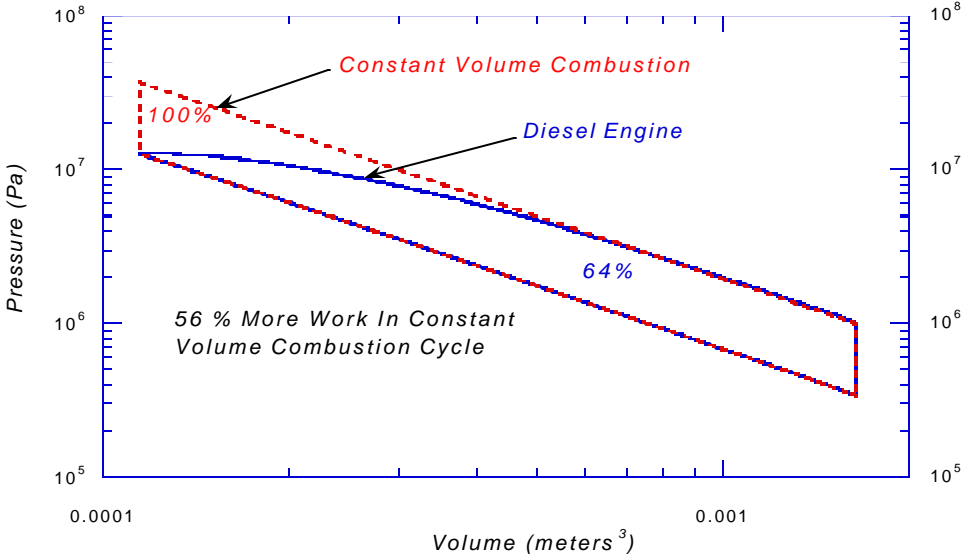


Figure 1 – Modern 4-Stroke Heavy Duty Diesel Engine

Engineering Configuration

The free piston linear alternator illustrated in Figure 2 has been designed in hopes of approaching ideal Otto cycle performance through HCCI operation. In this configuration, high compression ratios can be used and rapid combustion can be achieved.

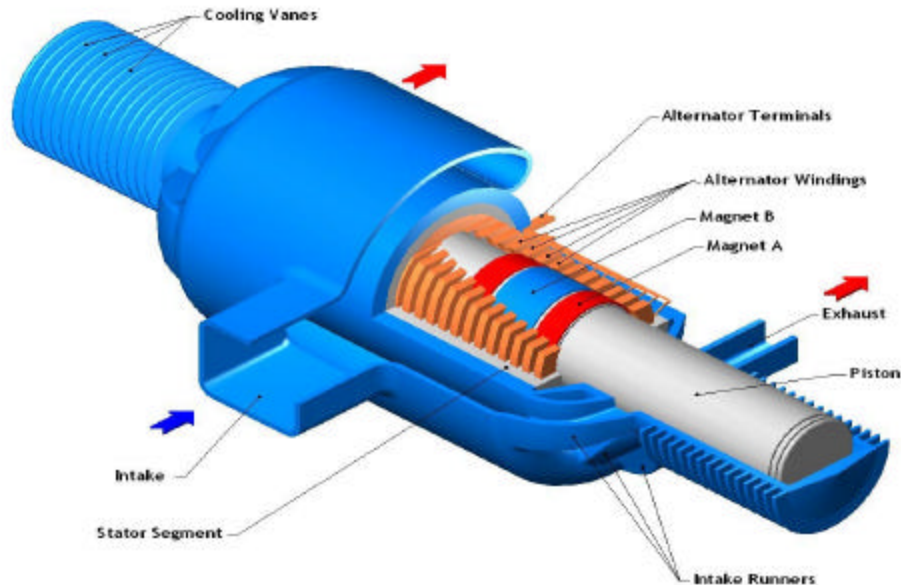


Figure 2 – Free piston linear alternator

The linear generator is designed such that electricity is generated directly from the piston's oscillating motion, as rare earth permanent magnets fixed to the piston are driven back and forth through the alternator's coils. Combustion occurs alternately at each end of the piston and a modern two-stroke cycle scavenging process is used. The alternator component controls the piston's motion, and thus the extent of cylinder gas compression, by efficiently managing the piston's kinetic energy through each stroke. Compression of the fuel/air mixture is achieved inertially and as a result, a mechanically simple, variable compression ratio design is possible with sophisticated electronic control.

The use of free pistons in internal combustion engines has been investigated for quite some time. In the 1950's, experiments were conducted with free piston engines in automotive applications. In these early designs, the engine was used as a gasifier for a single stage turbine (Underwood 1957, Klotsch 1959). More recent developments have integrated hydraulic pumps into the engine's design (Baruah 1988, Achten 1994).

Several advantages have been noted for free piston IC engines. First, the compression ratio of the engine is variable; this is dependent mainly on the engine's operating conditions (e.g., fuel type, equivalence ratio, temperature, etc.). As a result, the desired compression ratio can be achieved through modification of the operating parameters, as opposed to changes in the engine's hardware.

An additional benefit is that the mechanical friction can be reduced relative to crankshaft-driven geometries since there is only one moving engine part and no piston side loads. Also, combustion seems to be faster than in conventional slider-crank configurations. Further, the unique piston dynamics (characteristically non-sinusoidal) seem to improve the engine's fuel economy and NO_x emissions by limiting the time that the combustion gases spend at top dead center (TDC) (thereby reducing engine heat transfer and limiting the NO_x kinetics). Finally, one researcher (Braun 1973) reports that the cylinder/piston/ring wear characteristics are superior to slider/crank configurations by a factor of 4.

The combination of the HCCI combustion process and the free piston geometry is expected to result in significant improvements in the engine's thermal efficiency and its exhaust emissions. The following advantages should be found:

1. For a given maximum piston velocity, the free piston arrangement is capable of achieving a desired compression ratio more quickly than a crankshaft-driven piston configuration. This point is illustrated in Figure 3 where the piston position profiles of both configurations are plotted. The reduced compression time should result in higher compression of the premixed charge before the onset of autoignition.

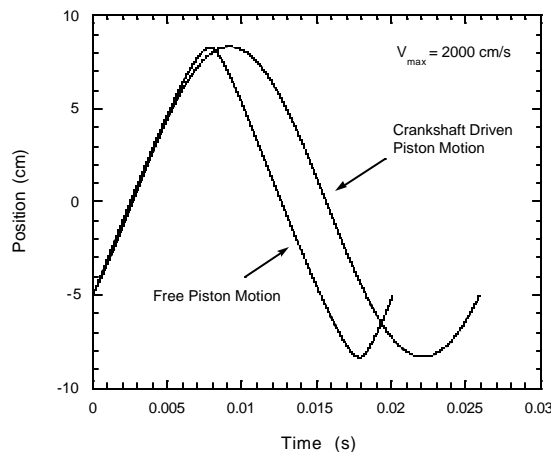


Figure 3 – Piston position vs. time

2. High compression ratio operation is better suited to the free piston engine since the piston develops compression inertially, and as such there are no bearings or kinematic constraints that must survive high cylinder pressures or the high rates of pressure increase (shock). The use of low equivalence ratios in the HCCI application should further reduce the possibility of combustion chamber surface destruction (Lee and Schaefer 1983, Maly et al 1990).
3. The free piston design is more capable of supporting the low indicated mean effective pressure (IMEP) levels inherent in low equivalence ratio operation due to the reduction in mechanical friction.

Integration of the linear alternator into the free piston geometry provides further benefits to the generator design. In this arrangement mechanical losses in the system are dramatically reduced since there is essentially one moving part, and this allows engine operation at a more or less constant piston speed. These points aid in the generator design, and further improve the fuel-to-electricity generation efficiency of the device.

The linear alternator itself is based on technology developed for brushless DC motors. High efficiency and high power density, typically 96% efficiency and 1 hp per pound density characterize this class of motors. Put simply, the rotary configuration is unrolled until flat, then rolled back up perpendicular to the first unrolling to arrive at the linear configuration. Relative to the rotary geometry, the linear device is approximately 30% heavier due to not all of the coils being driven at the same time. Efficiency will be comparable.

2-Stroke Cycle

Inherent in the configuration selected is the need to scavenge the exhaust gases out of the cylinder and replace them with fresh fuel/air charge while the piston is down at the bottom of the cylinder. This requirement is due to the need to have trapped gases in the cylinder to act as a spring, as well as to provide the next combustion event.

Conventional 2-stroke cycle engines have developed a reputation for low fuel efficiency and high hydrocarbon emissions due to short-circuiting of the inlet fuel/air mixture directly to the exhaust port. The typical 2-stroke application stresses power density over efficiency and emissions – chain saws, weed whackers, marine outboard motors. These devices must operate over a wide speed and power range.

In this case the requirements are quite different. The speed of the free piston oscillation is essentially fixed. Power is varied by modification of the equivalence ratio, not the quantity of gas delivered. Power density is not a driving requirement. As a result, the design of this system can be optimized within tight constraints utilizing computational fluid dynamics and experimental gas dynamics techniques.

Experimental Results - FY 2001

Figure 4 shows the results of experimental combustion studies completed with hydrogen. In this investigation, a single-stroke rapid compression-expansion machine has been used to compression-ignite hydrogen. Hydrogen is the fastest burning fuel out of all the fuels tested. The high rate of combustion does approach constant volume combustion. Figure 3 shows a typical logarithmic P/V diagram for hydrogen combustion at top dead center at 33:1 compression ratio. The piston has, for all practical purposes, not moved during the combustion event. In the free piston configuration, high pressure-rise rates can be handled without difficulty since there are no load bearing linkages, as in crankshaft-driven engines. Additionally, operation at equivalence ratios less than 0.5 reduces the need to consider piston erosion, or other physical damage (Maly et al. 1990).

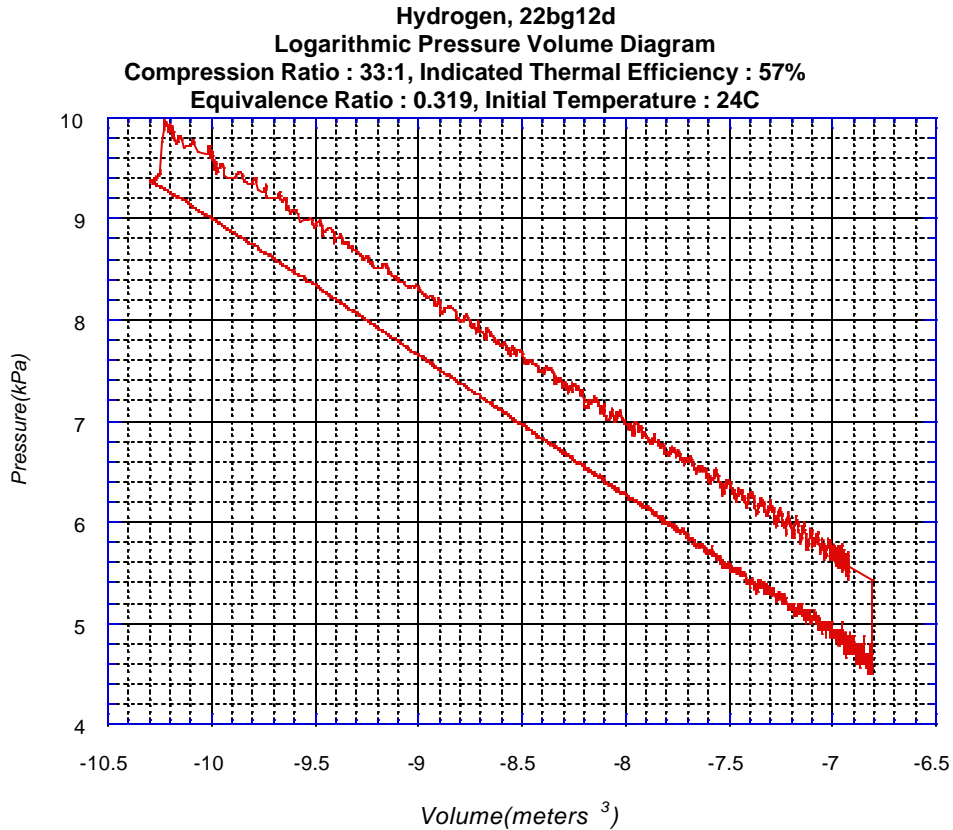


Figure 4 - Hydrogen Combustion

Figure 5 shows the free piston generator again. The overall length of the generator is 76 centimeters, its specific power is 800 watts per kilogram, and it has a power density of 800 watts per liter. Hydrogen based renewable fuels such as biogas (low BTU producer gas H_2-CH_4-CO); ammonia (NH_3), methanol (CH_4O), and/or hydrogen (H_2) can be used directly.

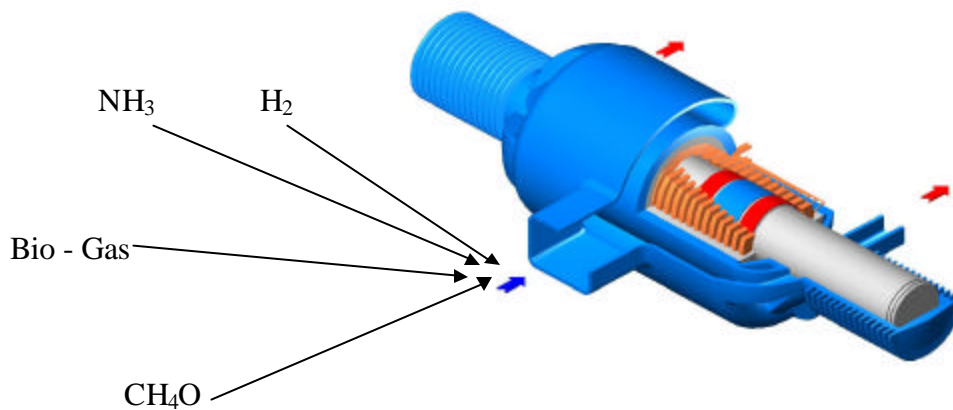


Figure 5 – Free Piston Generator

The alternator consists of moving rare earth permanent magnets and stationary output coils and stator laminations. The design is similar to a conventional rotary brushless DC generator.

Figure 6 shows the magnetic flux path for the linear alternator. It can be seen that the flux through the coils changes direction as the permanent magnet assembly moves down the alternator core. This changing flux induces current in the coils.

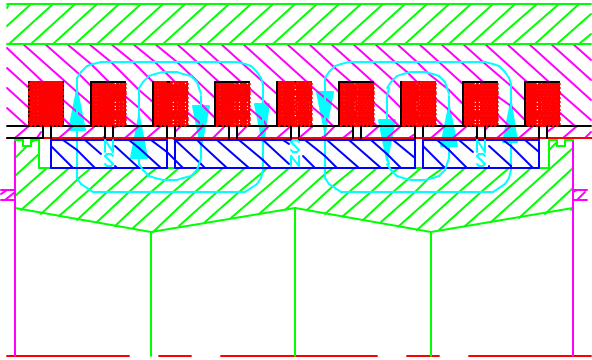


Figure 6 – Alternator Design

Two parallel paths are being pursued to develop the linear alternator. An alternator is being built and tested in-house. As a design tool, we are utilizing a two-dimensional finite element computer code to solve Maxwell’s equations of electromagnetism. MagSoft Corporation produces the code, called FLUX2D. We have investigated various design configurations, and have optimized a design with respect to maximizing efficiency and minimizing size. In parallel, Magnequench, a commercial development partner, is also designing and fabricating an alternator. Both alternator designs are being fabricated and will be tested under full design output conditions on a Sandia designed-Caterpillar engine based tester. The tester will measure both power output and mechanical to electrical conversion efficiency.

Magnequench has delivered three stator assemblies to Sandia, one of which is shown in Figure 7. Also shown in Figure 7 are a short and a long magnet ring. These magnets are pressed from neodymium-iron-boron rare earth material and magnetized in the radial direction. Sandia will assemble the Magnequench supplied magnets to the moving part back iron and provide linear bearing supports. One assembly will then be returned to Magnequench for their own testing.

Figure 8 shows a cut away of the Sandia alternator design. The power output of the linear alternator is 40 kW, and has an efficiency of 96%. The Magnequench design is very similar; the differences are primarily in the coil configuration, magnet fabrication and stator material. The Sandia magnet assembly is fabricated from 10-degree arc magnet segments, which are magnetized in a linear direction

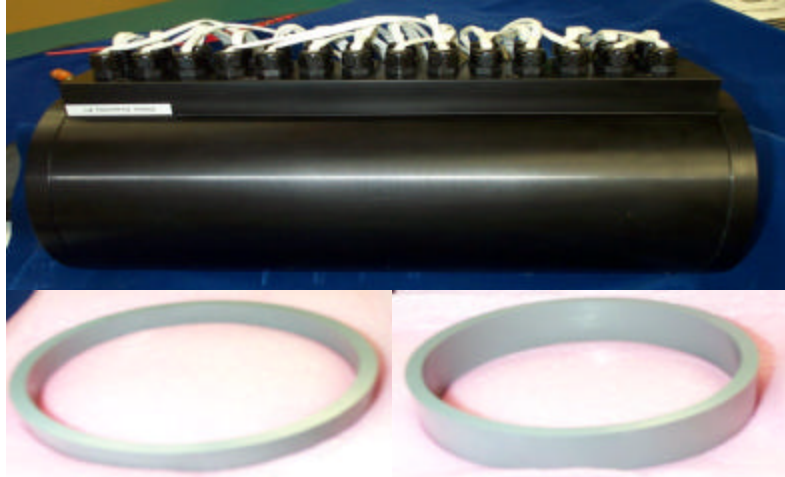


Figure 7 – Magnequench Linear Alternator Stator Assembly

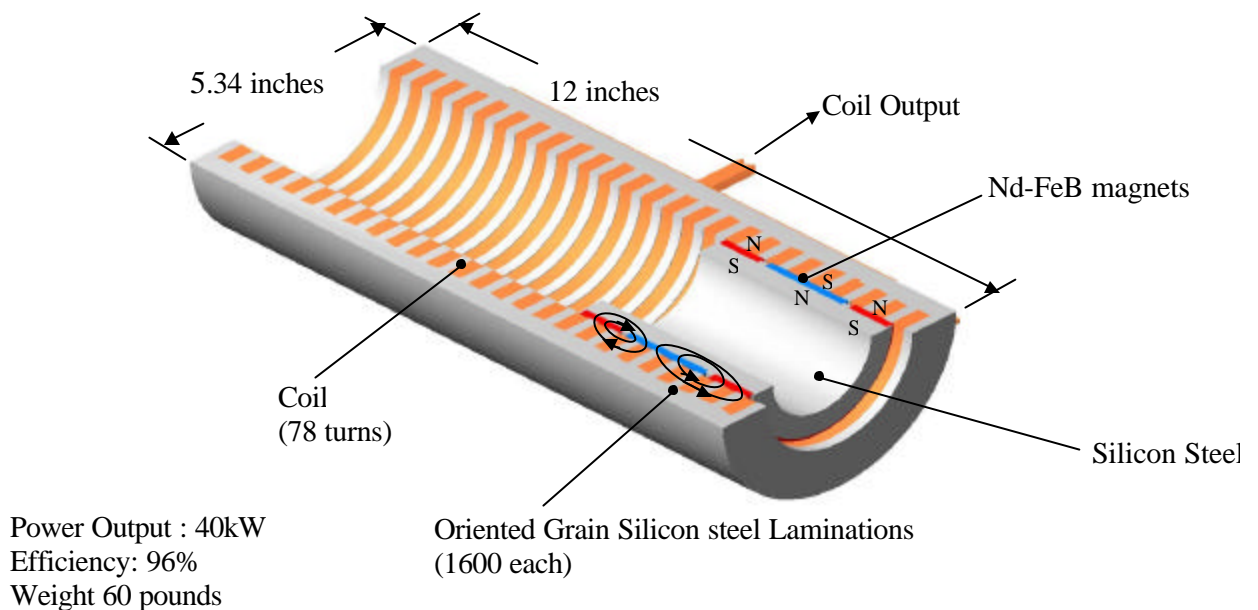


Figure 8 – Sandia Linear Alternator Design

The Sandia stator is an assembly of 1600 laminations punched from anisotropic oriented grain silicon steel. Each lamination has a small angle ground so the assembly stacks into a cylinder. The Magnequench stator material is pressed iron powder in an adhesive matrix.

The Magnequench coils consist of a single row winding of flat wire. The Sandia coils contain 78 turns of square cross section wire. The Magnequench coils must be connected in moving groups of five as the magnet assembly moves in the stator to generate sufficient voltage for efficient power conditioning. The Sandia design has sufficient voltage generation from a single coil and does not require coil switching.

During initial assembly of the Sandia stator laminations to the coils some electrical shorting of the coils to the stator was discovered. Investigation revealed that the wire insulation was being cut by the sharp stator laminations and that the 0.003-inch thick kapton insulation on the coil sides was not robust enough to withstand assembly handling. As a result we are currently modeling larger coil spaces in the stator pieces and smaller coils to determine the effect on alternator performance. Based on these analyses we will choose which part, the coil or the stator lamination, to modify.

Due to the difficulty of the Sandia design assembly, the Magnequench alternator will be the first to be tested on our full-power alternator tester. A mounting fixture, which supports the stator assembly on load cells, has been built and assembly procedures to align and zero the load cells are ongoing. As part of the mounting design the magnet assembly is being developed to be useful for assembly of the prototype engine generator. This assembly requires the development of an inertial weld between the aluminum pistons and the magnet backiron section, which is 1018 steel. Both 6061 and 7075 aluminum are being investigated for the piston material. To date sample welds of both materials have been completed and tooling to tensile test the welds is being fabricated. Some of the components and fabrication tools for the Sandia linear alternator are shown in Figure 9.

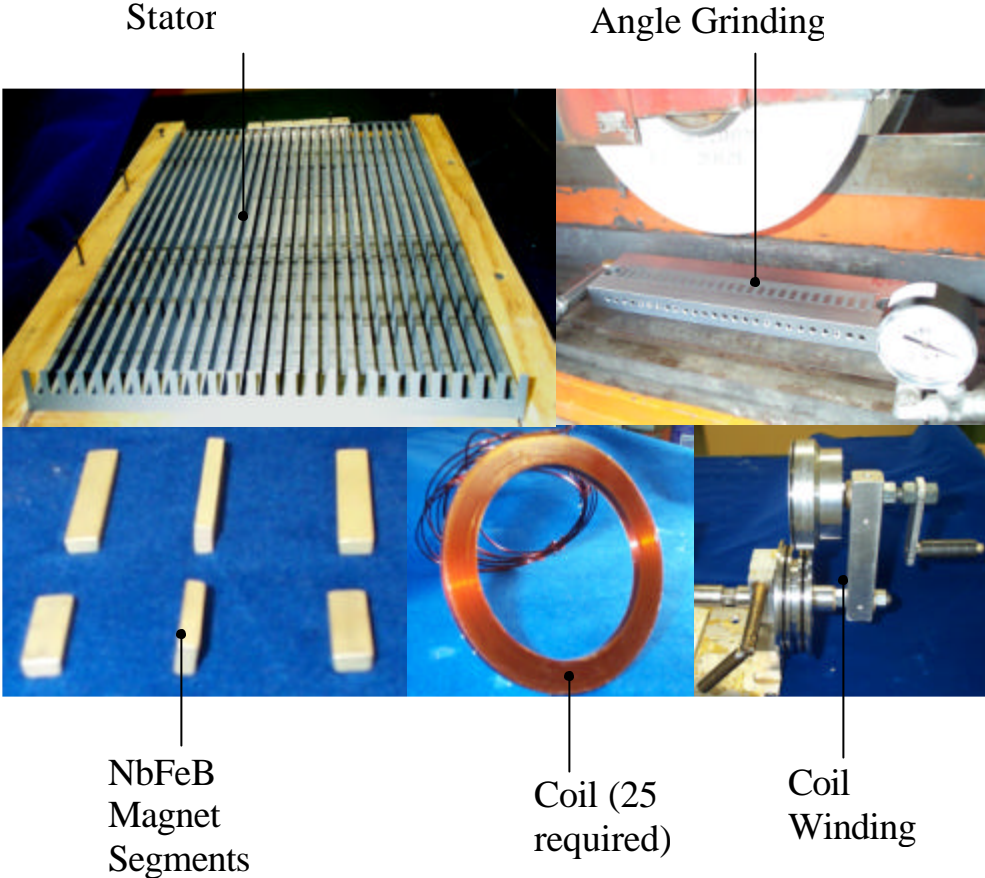


Figure 9 – Linear Alternator Design Components

Alternator Modeling

In preparation for designing the generator control algorithms, a comprehensive mathematical model of the entire physical system is required. One of the challenging aspects of the system model is the electromagnetic performance of the linear alternator. The finite element model (FLUX2D) utilized in the design process is too slow for use in a real-time system model.

To circumvent this situation, we have contracted with Ron Moses of Los Alamos National Laboratory to derive a simplified alternator model. Ron is an expert in electromagnetic systems and excited to be part of our project team. We intend to have Ron develop, with our input, a total system model capable of predicting control system response.

Two Stroke-Cycle Scavenging System Design

Conventional two-stroke cycle engines are designed to maximize power density at the expense of efficiency and emissions. They also must operate over a wide speed and power range.

Our design intent is to maximize efficiency while minimizing emissions at a narrow power output operating condition. As a result, the configuration of the scavenging ports and operating pressures is likely to be unique to this design.

Our approach is to utilize KIVA-3V to design the scavenging system and to validate the KIVA-3V predictions at selected conditions. Towards this goal we have designed an add-on scavenging experiment for our free piston combustion test facility. Figure 10 shows the scavenging experiment on the upper left side connected to the existing combustion experiment on the lower right side. The experiment will reproduce combustion cylinder pressure and temperature conditions immediately prior to scavenging port opening and replicate piston motion during one scavenging cycle. By measuring gases in the cylinder and in the exhaust collector we will be able to discern trapping efficiency and scavenging efficiency during realistic operating conditions.

Figure 11 shows the KIVA-3V modeling results for one particular configuration being investigated. We are striving to design a loop scavenged flow system due to the simplicity it possesses. This year we have analyzed two loop scavenged systems. The first system, shown above, is a conventional design with the exhaust port higher in the cylinder wall than the inlet ports. In this geometry the exhaust port opens first, with a significant quantity of exhaust gases blowing down before the inlet ports open. As the inlet ports open, flow is directed up and away from the exhaust port in an attempt to loop up into the cylinder and flush more exhaust out.

Parameters that were varied include inlet driving pressure, port placement and lead angles, and reciprocating speed. Briefly, the end results were that to avoid short circuiting more than 1% of the inlet flow to the exhaust, only about 50% of the exhaust gases can be removed. A major contributor to this situation was thought to be the placement of the inlet ports below the exhaust port.

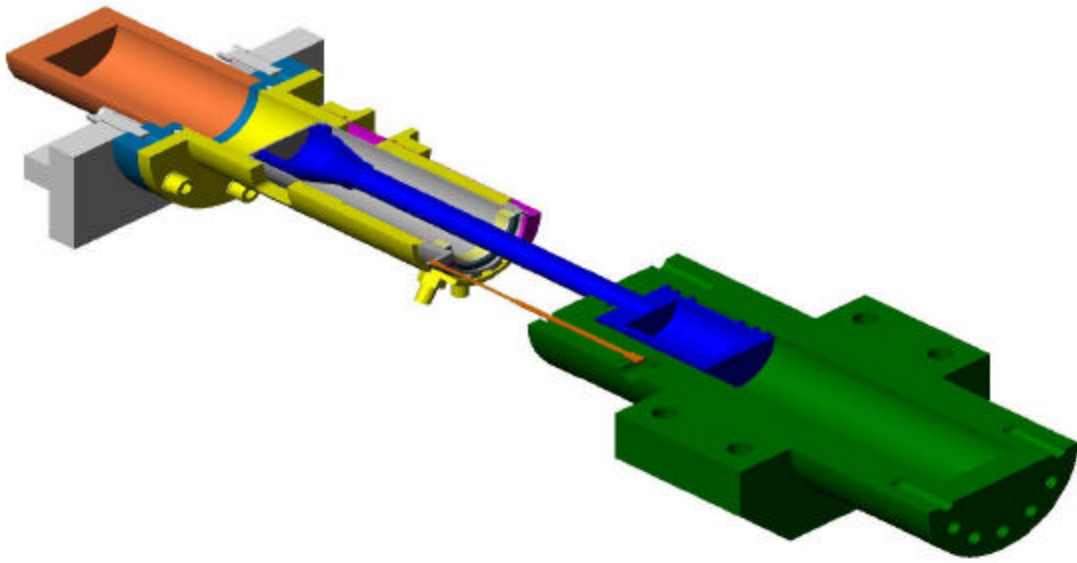


Figure 10 – Scavenging Experiment

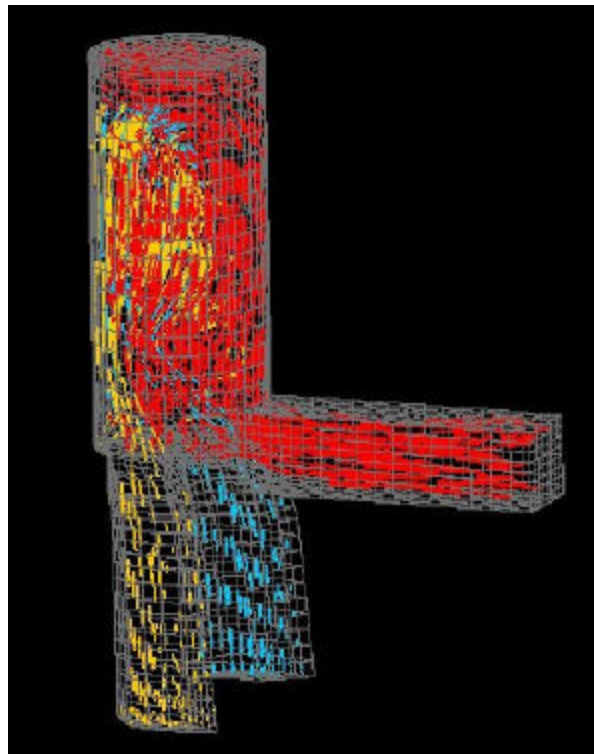


Figure 11 – KIVA-3V flow pictorial - loop

As a result a model was generated with the inlet ports above the exhaust port. Figure 12 shows this configuration. The goal was to generate a fluid motion that would sweep the exhaust gases up the outside of the cylinder and then flow down the center and out the exhaust ports.

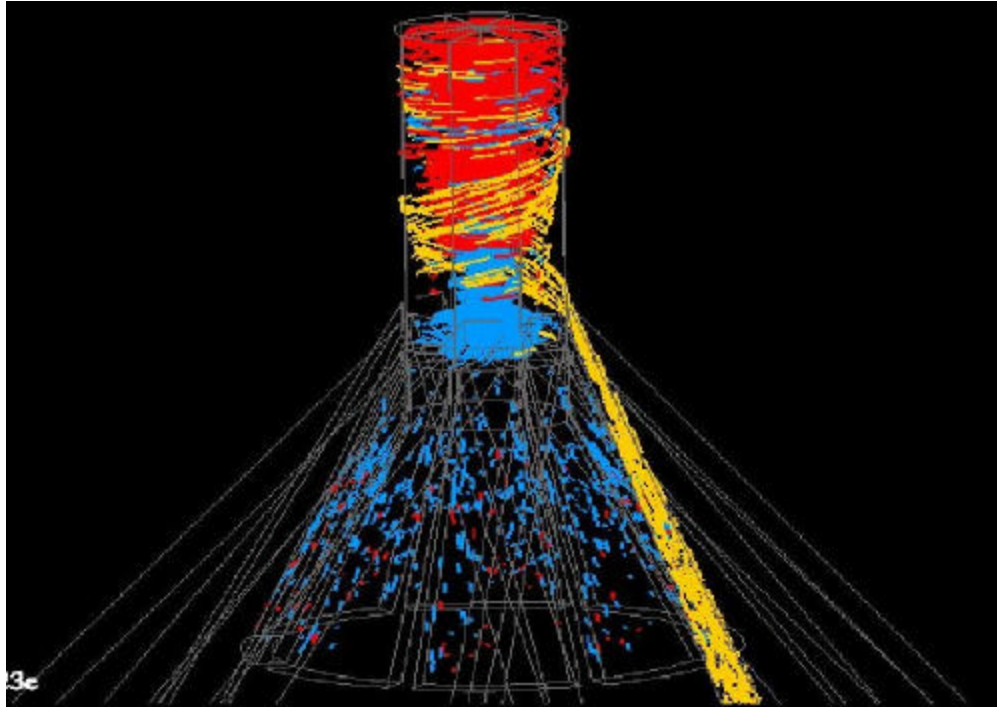


Figure 12 – KIVA-3V flow pictorial – inverted loop

KIVA calculations show the flow sweeping up the outside, but stagnating at the top of the cylinder and not flushing down the center. Part of the difficulty is the high stroke to bore ratio necessary to minimize heat losses and insure adequate compression space at high compression ratio. The results of the calculation show similar performance to the more conventional loop scavenged design.

We are currently designing a uniflow system with 4 exhaust valves in the cylinder head. Variation of the inlet flow geometry/driving pressure has resulted in a more acceptable 80% removal of the exhaust gases with less than 1% short-circuiting of the inlet flow. This configuration, shown in Figure 13 also allows variation of the exhaust port timing since these valves are controlled independently of the piston position. We have been able to consider overexpanded strokes and exhaust residual left at the cylinder head and on top of the piston. This can have the beneficial result of insulating the metal engine parts from the combustible mixture, thus minimizing heat losses and wall quenching.

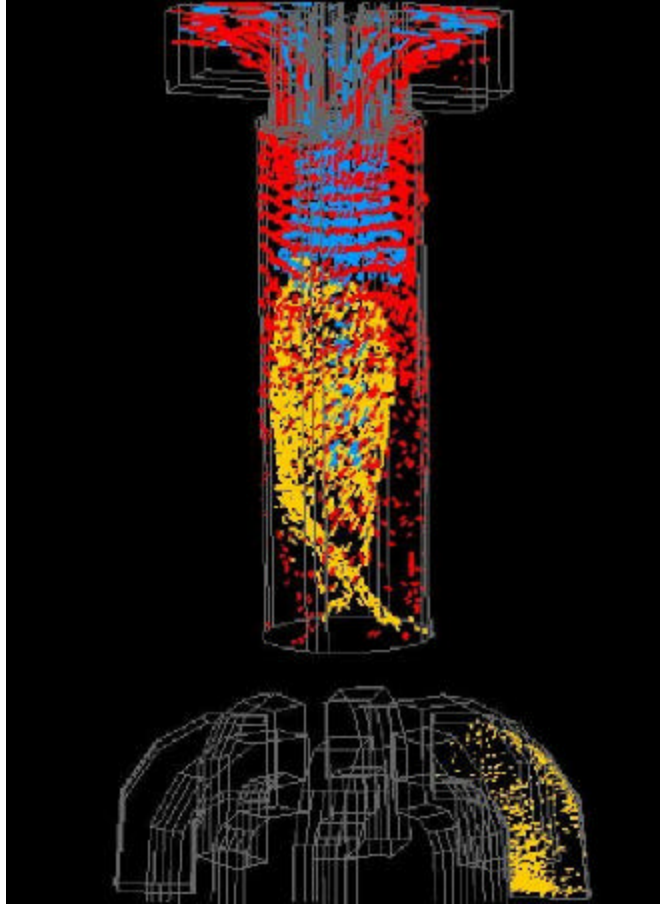


Figure 13 – KIVA-3V flow pictorial – uniflow

Currently the analytical scavenging investigation is centered on maximizing thermal efficiency considering scavenging blower work, overexpanded cycles and friction losses. Both constant pressure and piston motion driven type blowers are considered. Following this investigation the scavenging experiment will be fabricated and key-operating predictions verified.

Hydrogen Based Renewable Fuels

Bio-gas

One of the unique characteristics of HCCI combustion with a free piston is the ability to combust extremely lean mixtures. In the field of gasification of biomass, the simplest approach is to combust the material in an oxygen-starved environment. The resultant gas is a mixture of hydrogen, carbon monoxide, carbon dioxide, methane, and nitrogen. The mixture is too lean for utilization in spark-ignition engines and requires a pilot diesel fuel injection when fumigated into a diesel engine.

Figure 14 shows the results of combustion of a typical low BTU producer gas as would be produced from a crude gasifier as would be found in a developing country. The formulation was kindly supplied by William Hauserman of Hauserman Associates. The results indicate excellent performance in the free piston experiment. In fact, this lean mixture is ideal for achieving the NO_x control upon which our concept is based

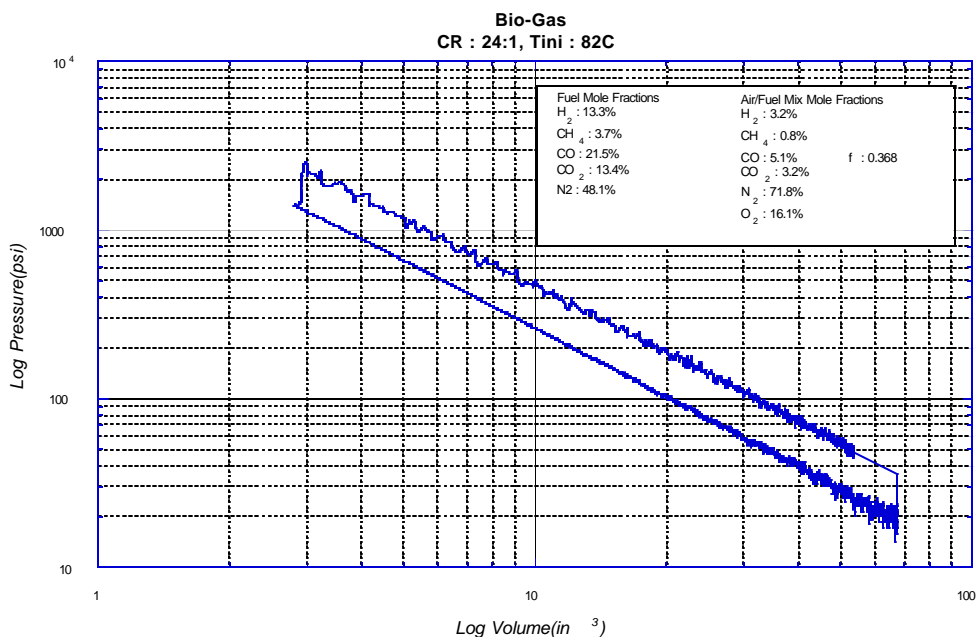


Figure 14 – Biogas Ideal Otto Cycle Performance

The two most challenging aspects of widespread hydrogen application are the storage of hydrogen for mobile applications and the distribution infrastructure. In the United States, approximately one million farms have access to anhydrous ammonia. The distribution infrastructure already exists to deliver approximately 8 billion pounds of anhydrous ammonia to these farms for direct use as a nitrogen soil supplement. The farmers are already handling anhydrous ammonia and could easily use it as a fuel for their farm equipment if an efficient utilization device were available.

In Figure 15, the combustion of ammonia exhibits ideal Otto cycle performance in our free piston combustion experiment, and produces conversion efficiencies comparable to hydrogen (see Figure 16). Ammonia is ideal hydrogen based renewable fuel to use in our free piston generator for several reasons. Ammonia is widely available. 35 trillion pounds of anhydrous ammonia are produced in the United States per year. Ammonia contains no carbon, and can be easily made from hydrogen or natural gas.

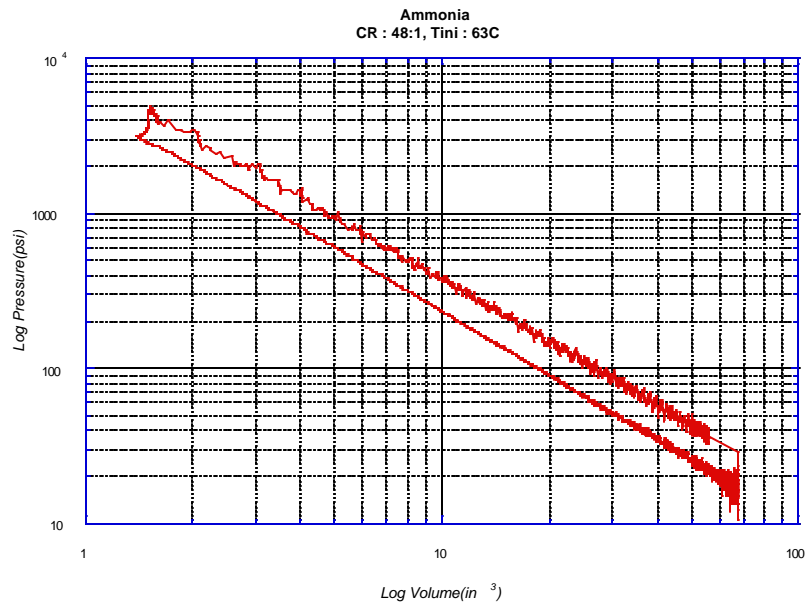


Figure 15 – Ammonia Ideal Otto Cycle Performance

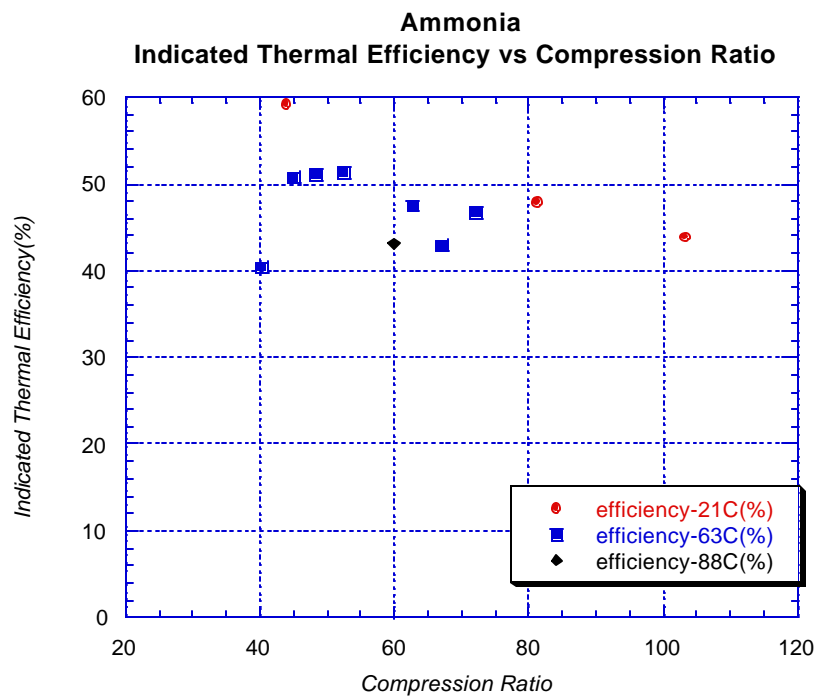
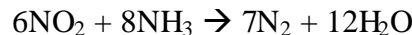
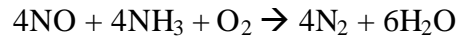


Figure 16 – Ammonia Combustion

Anhydrous ammonia is stored in the same manner as propane, as a liquid under approximately 100-psi vapor pressure at room temperature. If released into the atmosphere, ammonia's density is lighter than that of air and thus dissipates rapidly. In addition, because of its characteristic smell the nose easily detects it in concentrations as low as 5 ppm. Finally, ammonia has such a narrow flammability range that it is generally considered non-flammable when transported.

Ammonia is comparable to gasoline as a fuel for combustion engines. Three gallons of ammonia is equivalent to one gallon of gasoline in energy content. In other terms, 2.35 pounds of ammonia is equivalent to one pound of gasoline in energy content. Cost wise in 1998, bulk ammonia was \$1.13 per gallon gasoline equivalent.

In using ammonia as a fuel, ammonia and air would enter the free piston generator through the intake port. After combustion, any generated NO_x emissions can be readily reduced by reaction with ammonia over a zeolite according to one of the following two reactions:



Measurement of the ammonia and NO_x emissions from typical operating conditions have shown approximately equal quantities (400ppm) of both ammonia and NO. Thus ammonia addition to the exhaust stream may not be required.

Industrial Collaboration

As previously discussed Magnequench International, Incorporated has supplied two linear alternators at no cost in order to develop new applications for rare earth permanent magnets. In addition, Caterpillar Corporation is entering into an information-sharing agreement with our group. The purpose of the collaboration is for CAT to share their free piston lubrication and sealing technology with Sandia while in return applying our linear alternator technology to their free piston hydraulic pump program.

This year Unique Mobility Inc. has expressed interest in collaborating in this program. Their specialty is in the area of permanent magnet motors and power electronics. Both areas of expertise will be of great value to this program.

All three of these collaborations will ease the transfer of this exciting new technology to the industrial sector.

Future Work

Plans for the 2002 fiscal year include completing the two-stroke scavenging system design, developing a comprehensive system model, designing a prototype starting system and quantifying performance of both alternator designs. The principal objectives are to select a

prototype scavenging system, obtain a predictive model of electrical and mechanical components, select a starting system, and collaborate with industrial partners in pursuing other funding.

References

- Achten, P. A. J. 1994. "A Review of Free Piston Engine Concepts," SAE Paper 941776.
- Alperstein, M., Swim, W. B. and Schweitzer, P. H. 1958. "Fumigation Kills Smoke – Improves Diesel Performance," SAE Transactions, vol. 66, pp.574 – 588.
- Baruah, P. C. 1988. "A Free Piston Engine Hydraulic Pump for an Automotive Propulsion System," SAE Paper 880658.
- Braun, A. T. and Schweitzer, P. H. 1973. "The Braun Linear Engine," SAE Paper 730185.
- Caris, D. F. and Nelson, E. E. 1959. "A New Look at High Compression Engines," SAE Transactions, vol. 67, pp. 112-124.
- Christensen, M., Johansson, B. and Einewall, P. 1997. "Homogeneous Charge Compression Ignition (HCCI) Using Isooctane, Ethanol, and Natural Gas – A Comparison With Spark Ignition Operation," SAE Paper 972874.
- Christensen, M., Johansson, B., Amneus, P. and Mauss, F. 1998. "Supercharged Homogeneous Charge Compression Ignition," SAE Paper 980787.
- Das, L. M. 1990. "Hydrogen Engines: A View of the Past and a Look Into the Future," International Journal of Hydrogen Energy, vol. 15, no. 6, pp. 425 – 443.
- Edson, M. H. 1964. "The Influence of Compression Ratio and Dissociation on Ideal Otto Cycle Engine Thermal Efficiency,'Digital Calculations of Engine Cycles, SAE Prog. in Technology, vol. 7, pp. 49-64.
- Karim, G.A. and Watson, H.C. 1971. "Experimental and Computational Considerations of the Compression Ignition of Homogeneous Fuel-Oxidant Mixtures," SAE Paper 710133.
- Klotsch, P. 1959. "Ford Free-Piston Engine Development," SAE Paper 590045.
- Lee, W. and Schaefer, H. J. 1983. "Analysis of Local Pressures, Surface Temperatures and Engine Damages under Knock Conditions," SAE Transactions, vol. 92, section 2, pp. 511 – 523.
- Maly, R. R., Klein, R., Peters, N. and Konig, G. 1990. "Theoretical and Experimental Investigation of Knock Induced Surface Destruction," SAE Transactions, vol. 99, section 3, pp. 99 – 137.

Muranaka, Y. T. and Ishida, T. 1987. "Factors Limiting the Improvement in Thermal Efficiency of S.I. Engine at Higher Compression Ratio," SAE Transactions, vol. 96, section 4, pp. 526 – 536.

Najt, P. M. and Foster, D. E. 1983. "Compression – Ignited Homogeneous Charge Combustion," SAE Paper 830264

Onishi, S., Jo, S. H., Shoda, K., Jo, P. D. and Kato, S. 1979. "Active Thermo– Atmospheric Combustion (ATAC) – A New Combustion Process for Internal Combustion Engines," SAE Paper 790501.

Overington, M. T. and Thring, R. H. 1981. "Gasoline Engine Combustion – Turbulence and the Combustion Chamber," SAE Paper 810017.

Thring, R. H. 1989. "Homogeneous-Charge Compression-Ignition Engines," SAE Paper 892068.

Underwood, A. F. 1957. "The GMR 4-4 'Hyprex' Engine – A Concept of the Free-Piston Engine for Automotive Use," SAE Paper 570032.

Van Blarigan, P., and Green R. 1995. "NO_x Emission Data Verified in a Hydrogen Fueled Engine," Combustion Research Facility News," vol.17, no.4, January/February.

Williams, Robert. January 1996. "Fuel Decarbonization for Fuel Cell Applications and Sequestration of the Separated CO₂," PU/CEES Report No. 295.

COMBUSTION OF HYDROGEN-ENRICHED METHANE IN A LEAN PREMIXED SWIRL BURNER

**R. W. Schefer
Combustion Research Facility
Sandia National Laboratories
Livermore, CA 94551-0969**

Abstract

The stability characteristics of a premixed, swirl-stabilized flame were studied to determine the effects of hydrogen addition on flame stability under fuel-lean conditions. The burner configuration consisted of a centerbody with an annular, premixed methane/air jet. Swirl was introduced to the flow using 45-degree swirl vanes. The combustion occurred within an air-cooled quartz chamber at atmospheric pressure. The results, using methane/hydrogen fuel mixtures, showed that the addition of up to 41% hydrogen significantly extended the lean burning limit. Planar Laser-Induced Fluorescence (PLIF) measurements of the OH radical were applied to study the behavior of the OH mole fraction near the lean stability limit. The results showed that as the lean stability limit was approached the overall OH mole fraction decreased, the flame width decreased and length increased, and the high OH region took on a more intermittent, shredded appearance. For operating conditions near the lean stability limit, the addition of a moderate amount of hydrogen to the methane/air mixture resulted in a significant increase in the OH concentration and a more robust appearing flame.

Introduction

The development of advanced combustion capabilities for gaseous hydrogen and hydrogen-blended hydrocarbon fuels in gas turbine applications is an area of much current interest. Driving this interest are several current needs. One need is the cost-effective utilization of alternative fuels with a wide range of heating values. For example, low and medium heating value fuels containing hydrogen are often produced as a by-product in Coal-Gasification Combined Cycle and Fluidized Bed Combustion installations. These product gases could provide a significant source of cost-effective fuels for gas turbines. A second need is related to the recognition that ultra-lean premixed combustion is an effective approach to NO_x emissions reduction from gas turbine engines. Hydrogen blended with traditional hydrocarbon fuels significantly improves flame stability during lean combustion and allows stable combustion at the low temperatures needed to minimize NO_x production. A longer-term need is the desire to minimize and, eventually, eliminate UHC and CO₂ emissions. The use of hydrogen-blended fuels provides both a solution to the immediate need for NO_x reduction, and also provides a transition strategy to a carbon-free energy system in the future.

Changes in fuel composition, particularly the addition of hydrogen to hydrocarbon fuels, affect both the chemical and physical processes occurring in flames. These changes affect flame stability, combustor acoustics, pollutant emissions, combustor efficiency and other important quantities. Few of these issues are clearly understood. A primary goal of this research is to investigate issues surrounding pure hydrogen and hydrogen-enriched hydrocarbon fuel use. Surprisingly few studies in the literature have been directed toward the effects of hydrogen addition on hydrocarbon flame chemistry and stability, and on pollutant formation under very fuel lean conditions. Relevant studies exist in the areas of spark ignition engines and gas turbine combustors. Studies in spark ignition engines clearly show the benefits of hydrogen addition. For example, Larson and Wallace (1997) showed that spark ignition engines operated on a blend of natural gas and hydrogen produced lower exhaust emissions. Meyers and Kubesh (1997) further showed that hydrogen addition to natural gas extended the lean engine operating limit.

Results in large-scale gas turbine combustors also indicate advantages to hydrogen addition. Clayton (1976) carried out an early study of the effect of hydrogen addition on aircraft gas turbines. Up to 15% hydrogen addition to JP-5 or JP-6 produced leaner blowout limits and corresponding reductions in NO_x (less than 10 ppm @ 15% O₂) while maintaining acceptable CO and HC emissions levels. Tests conducted in a single combustor test stand at full pressure and temperature at the GE Corporate Research and Development Center and in the field in a natural gas-fired cogeneration plant at Terneuzen, The Netherlands, demonstrated improved flame stability with hydrogen addition to natural gas fuel (Morris et al., 1998). Blends of up to 10% hydrogen by volume showed reduced CO emissions under lean conditions, and lower NO_x emissions for a given CO level. The combustion of low BTU gasified fuels with up to 35% hydrogen content has also been demonstrated in an existing, low emission gas turbine with minimal modification (Ali and Parks, 1998).

Experimental System

A schematic of the test apparatus, including the premixer and combustion chamber, is shown in Fig. 1. The inside diameter of the premixer tube is 4.1 cm and the outer diameter of the fuel

centerbody is 2.5 cm. The flame is stabilized on a centerbody with seven 45-degree swirler vanes, located at the end of the mixing chamber. The combustion chamber is a 30.5 cm long quartz tube of 8.3-cm inside diameter. Combustion air is provided by an air compressor and metered upstream of the burner using mass flow meters. The air is dried and filtered to remove particles by suitable in-line filters. The fuels, methane and hydrogen, are metered using mass flow meters. The mass flow meters are calibrated using laminar flow elements to an estimated accuracy of 2%.

A frequency-doubled, Nd:YAG-pumped dye laser provided the ultraviolet laser radiation for excitation of the OH molecule. The beam (8-ns pulse duration, 0.3-cm^{-1} line width) was used to pump the Q₁(8) line of the (1,0) band of the OH A²Σ - X²Π electronic transition at 283.556 nm. Excitation from the N''=8 level was selected to minimize the temperature sensitivity of the fractional population within the absorbing level. The laser-pumped Q₁(8) line has a population fraction that varies by only 10 percent over the temperature range 1000 K to 2300 K. The collimated laser sheet for the OH fluorescence was formed by a cylindrical/spherical lens combination. The OH fluorescence signal was collected using a 105-mm focal length, f/4.5 UV Nikkor lens, passed through a colored glass filter, and focused onto an intensified CCD camera. The intensifier was gated for 400 ns, encompassing the 8-ns laser pulse, to minimize the effects of flame luminescence and background light. The camera was operated in a 512 x 512-pixel format, which provides a field-of-view of 81.9 mm x 81.9 mm with a spatial resolution of 160 μm/pixel.

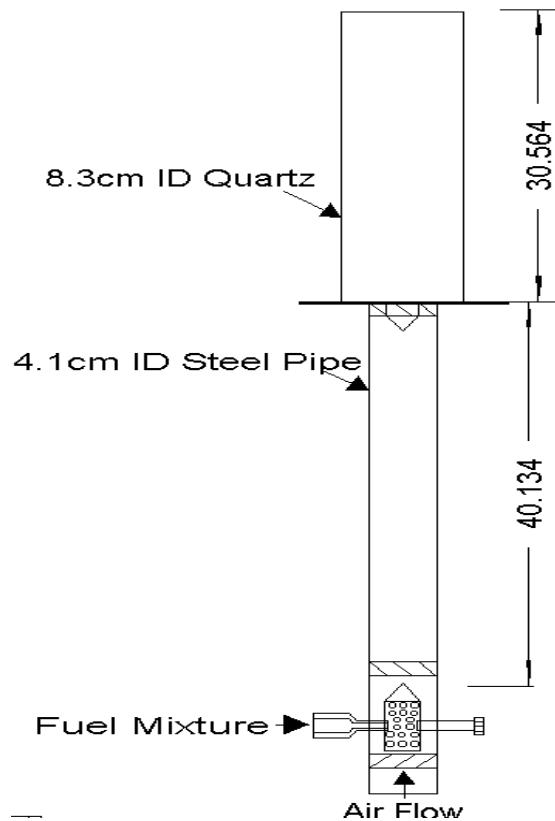
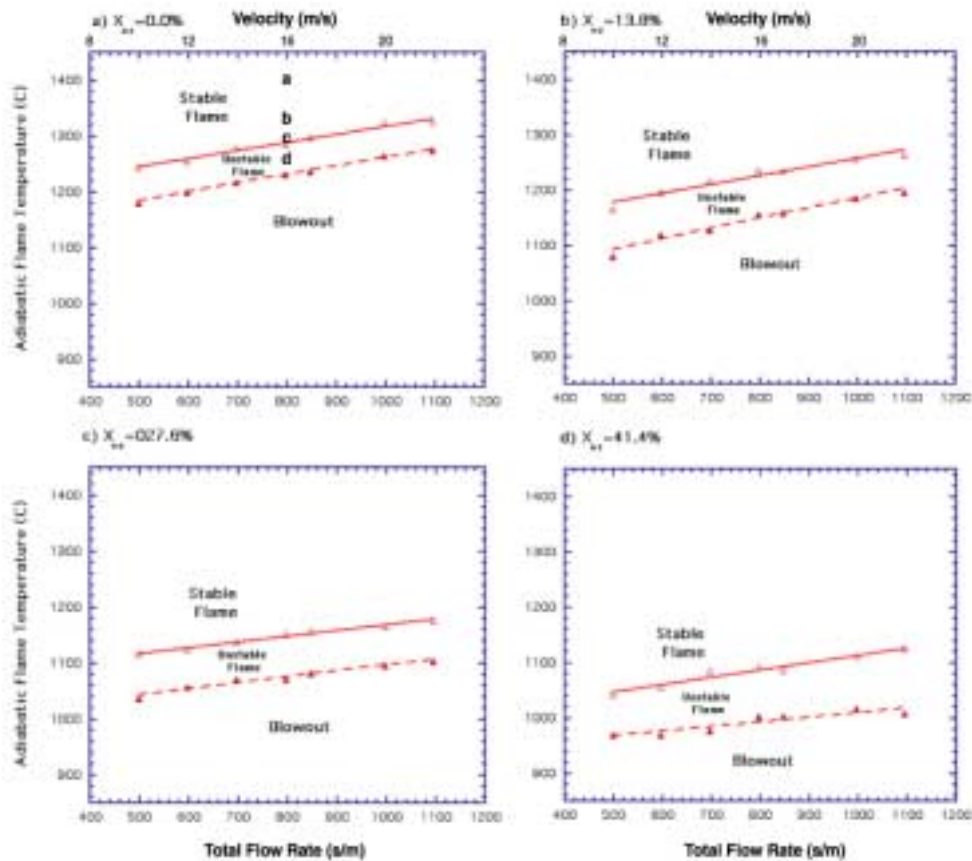


Figure 1. Schematic of experimental swirl burner and premixer.

Results

Flame Stability

The flame stability characteristics were determined for the burner over a range of operating conditions. The resulting lean stability map is shown in Fig. 2a for methane-air flames with no hydrogen addition. The measurements in Fig. 2 were obtained by maintaining a constant total volumetric flow rate and incrementally decreasing the adiabatic flame temperature by reducing the fuel/air ratio. The adiabatic flame temperature, T_{ad} , rather than the more conventional fuel/air ratio was used as the vertical axis in Fig. 2 since burner NO_x emissions are more directly correlated with flame temperature. Note, however, that under fuel-lean conditions both T_{ad} and the fuel/air ratio increase in the same direction along the axis. Generally, the flame blew out at lower flow rates as T_{ad} was decreased, or the fuel/air ratio became leaner. The points in Fig. 2a denoted flames a through d correspond to the flame photograph sequence in Fig. 3 where the total flow rate is maintained constant while T_{ad} is decreased.



03:30:20 R8

Figure 2. Swirl-burner flame regime and blowout map for premixed $\text{CH}_4/\text{H}_2/\text{air}$. a) $X_{H_2}=0.0\%$, b) $X_{H_2}=13.8\%$, c) $X_{H_2}=27.6\%$, d) $X_{H_2}=41.4\%$.

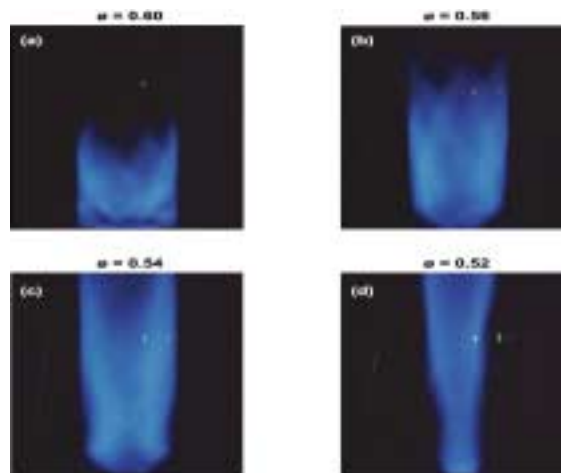


Figure 3. Direct flame luminosity photographs. $u=14$ m/s, $X_{O_2}=0.0$. a) $T_{ad} = 1385C$; b) $T_{ad} = 1311C$; c) $T_{ad} = 1274C$; d) $T_{ad} = 1237C$

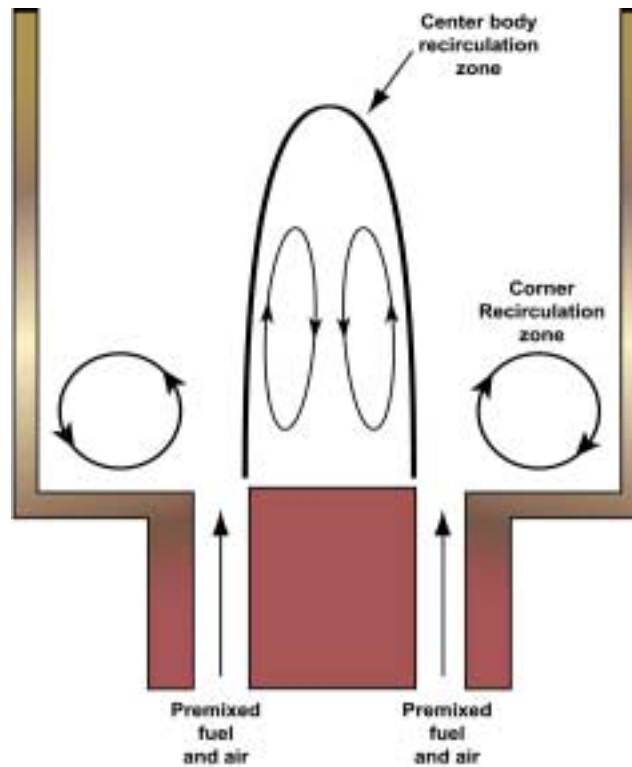


Figure 4. Schematic of flow field in swirl-stabilized combustor.

A discussion of the flame behavior seen in Fig. 3 is facilitated by considering the flow field associated with this burner configuration. Figure 4 shows schematically the likely flow field based on other observations in the present flame. As shown, the flow downstream of the inlet consists of two recirculation zones. One, located downstream of the centerbody, is consistent with velocity measurements in bluff-body stabilized flows (Schefer et. al, 1987). The second is associated with the quartz confinement tube and is located in the outer corner region where the vertical confinement tube walls intersect the horizontal inlet plate. This is typically referred to as the corner recirculation zone. At the highest flame temperature of 1385C (flame a in Fig. 3a), the flame is short and blue and fills the entire quartz confinement tube in the upstream region. Note also with this flame, combustion in the corner recirculation zone is clearly indicated by the continuous flame emission originating there. Decreasing T_{ad} , visible emission from the corner zone becomes increasingly intermittent until, at $T_{ad} = 1311C$ (flame b) there is no visible flame in the corner recirculation zone. The diameter of the flame decreases as the flame moves away from the confinement tube walls and length of the flame increases as T_{ad} is decreased until, for $T_{ad} = 1274C$ (flame c), the flame extends past the downstream end of the quartz tube. Finally, further reductions in T_{ad} cause the flame to become unstable, oscillating between a larger-diameter flame that extends across much of the confinement tube (similar to flame c), to a much narrower flame that can best be described as a narrow cylinder extending along the center of the enclosure. Flame d at $T_{ad} = 1237C$ is typical of this condition. The flame remains like this until, at sufficiently lean conditions, the flame becomes paler blue and eventually is extinguished. This corresponds to the flame lean blowout condition.

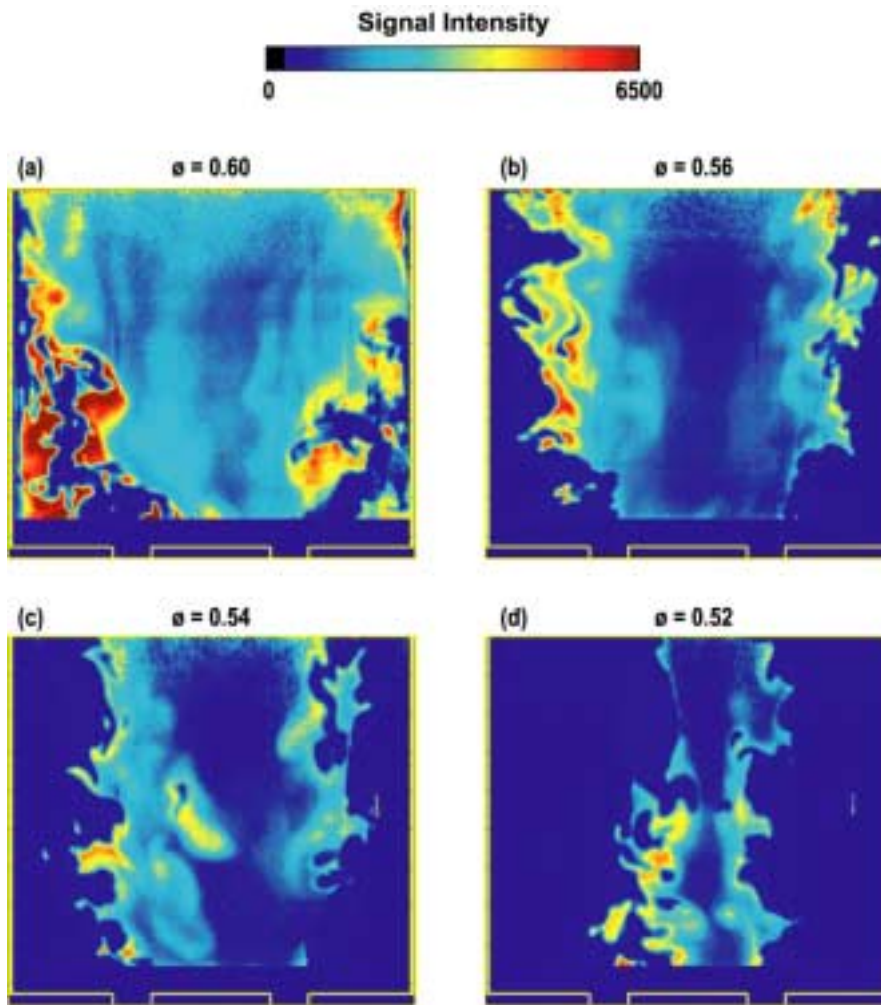
The OH PLIF images corresponding to flames a through d are shown in Fig. 5. For all equivalence ratios the outer edge of the high OH region is very irregular and probably reflects variations in the local velocity, which contort the flame surface. The OH is uniform throughout much of the flame, with locally high concentration regions forming thin filaments that typically extend along the irregular interface located between unburned reactants and combustion products.

Effects of Hydrogen Addition on Lean Flame Stability

A major question in this study is the effect of hydrogen addition on flame stability under lean operating conditions. To characterize the effect of hydrogen addition on lean burner stability, various amounts of hydrogen were added to the methane/air mixture and the flame stability measurements were repeated. Also shown in Fig. 2 are the resulting lean blowout curves for 13.8%, 27.6% and 41.4% hydrogen dilution. It can be seen that hydrogen addition significantly extends the lean stability limits. For example, at a velocity of 10 m/s, the methane flame blows out at $T_{ad} = 1170C$. The addition of 41.4% of hydrogen extends the stable flame regime to $T_{ad} = 1058C$. This change represents a 10.6% reduction in T_{ad} at the lean flame stability limit.

Of particular interest is the effect of hydrogen addition on the OH concentration near the lean flame stability limit. Phillips and Roby (1999) proposed that the enhanced reaction rates with hydrogen are due to an increase in the radical pool. For example, H radicals are important to flame stability because of their role in the important chain branching reaction $H + O_2 \leftrightarrow OH + O$. Furthermore, the reduction in CO emissions with hydrogen addition was attributed to the increased radical pool. Higher OH concentrations are likely to promote completion of CO oxidation to CO_2 via the OH radical. OH PLIF images near the lean blowout limit are shown in

Fig. 6. Figures 6a and 6b show two images taken on different laser shots at $T_{ad} = 1237\text{C}$ and an inlet velocity of 17 m/s with no hydrogen addition. This velocity is just below the blowout velocity of 18 m/s for this T_{ad} . Comparison of the two images shows the time-varying nature of the flame. Figures 6c and 6d show results for the same velocity and nearly the same $T_{ad} = 1241\text{C}$, but with 13.8% hydrogen addition. Comparison of these images shows that the size of the high OH region increases considerably, that the OH region is more continuous and that the peak OH levels along the outer edges of the flame are higher. Similar to the behavior with no hydrogen addition, further increases in the velocity with hydrogen added result in a narrower, elongated, and more shredded flame as blowout is approached.



031301.08 RS

Figure 5. Single-shot, OH PLIF images in swirl-stabilized flame. Same flame sequence as photographs in Fig. 4. The false color map indicates OH mole fraction. Burner inlet nozzle location is indicated at the bottom of the image.

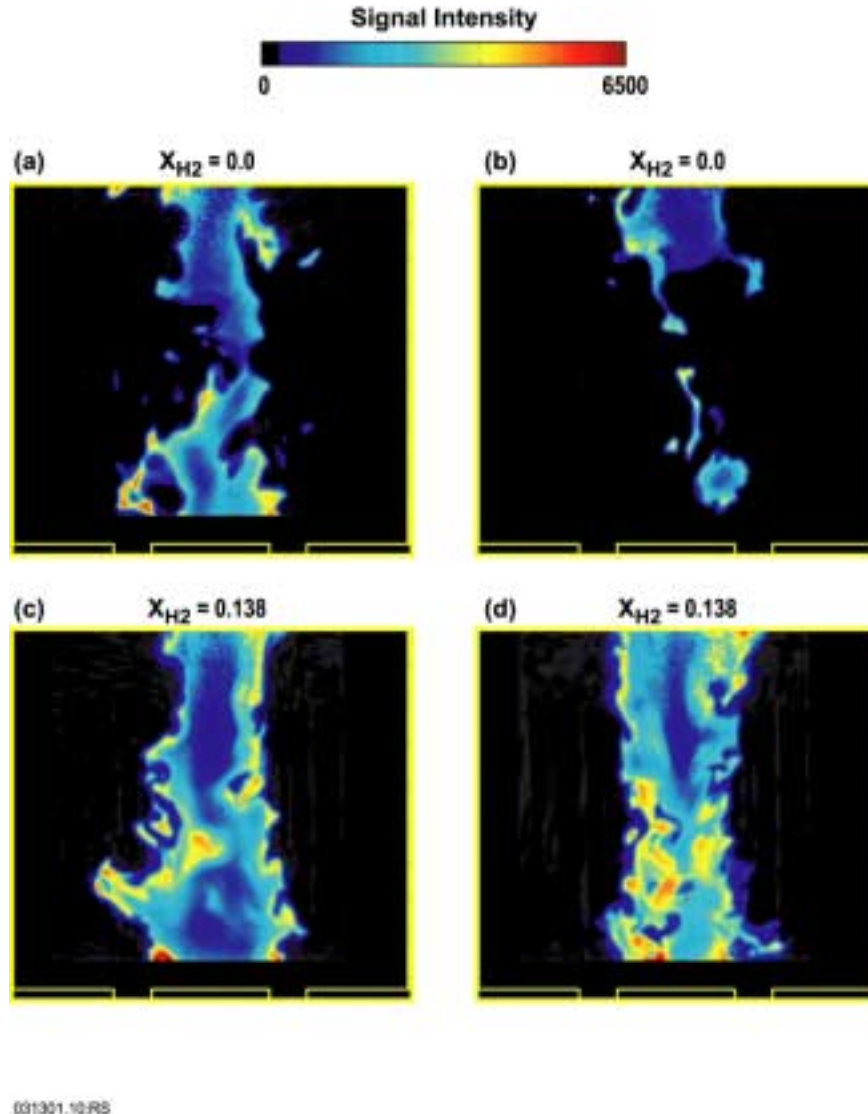


Figure 6. Single-shot, OH PLIF images in swirl-stabilized flame. $u=17$ m/s. a), b) $X_{H_2}=0.0$, $T_{ad} = 1237C$; c), d) $X_{H_2}=0.138$, $T_{ad} = 1241C$.

Time-Averaged OH Distributions

The above results emphasize the instantaneous OH distributions. Also of interest are the time-averaged OH distributions. The time-averaged OH distributions for $X_{H_2}=0.0$, 0.138 and 0.414 are shown in Fig. 7. At these flow conditions, for no hydrogen addition there is no flame in the corner recirculation zone. With the addition of hydrogen the OH extends upstream into the corner recirculation zone along a layer adjacent to the inner wall of the quartz tube. Increasing the hydrogen addition from 0.138 to 0.414 results in the OH concentration extending across a slightly wider fraction of the corner recirculation zone.

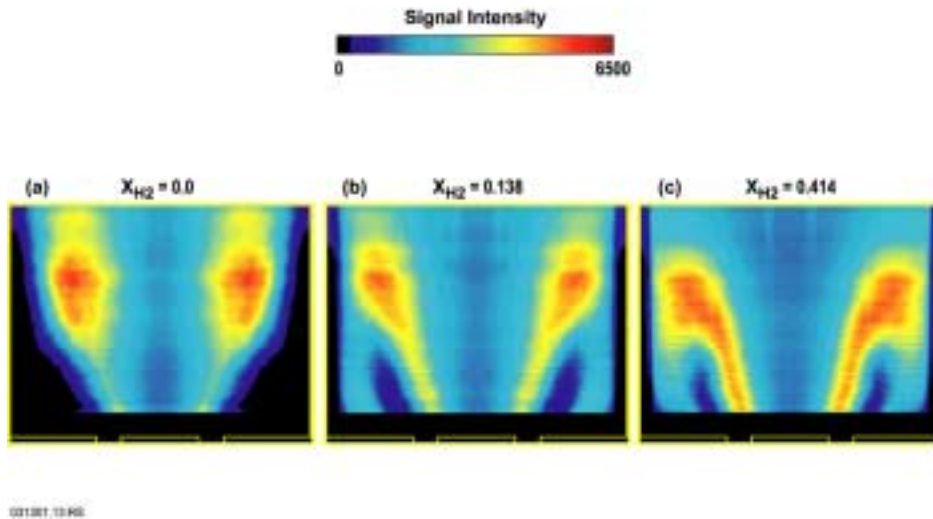


Fig. 7. Time-averaged OH PLIF images in swirl-stabilized flame. $u=14$ m/s. a) $X_{H_2}=0.0$, $T_{ad} = 1274C$; b) $X_{H_2}=0.138$, $T_{ad} = 1280C$; c) $X_{H_2}=0.414$, $T_{ad} = 1303C$.

As with the three flames shown in Fig. 7, the effect of hydrogen addition considerably alters the global flame characteristics and makes direct comparisons of the OH levels difficult. To minimize this problem, flow conditions were determined where the hydrogen addition could be varied while maintaining the same global flame characteristics. It was found that for $u=14$ m/s and $T_{ad} \approx 1250C$, hydrogen addition could be increased from 0% to 13.8% while maintaining a flame similar to that shown in Fig. 7 a). That is, no flame in the corner recirculation zone and a flame that has moved away from the quartz walls. Time-averaged radial profiles corresponding to these conditions are presented in Fig. 8. They show that an increase in the hydrogen from 0% to 13.8% causes nearly a 44% increase in the maximum OH. Other data shows that a subsequent increase from 13.8% to 41.4% hydrogen results in a much smaller 4% increase in the maximum OH.

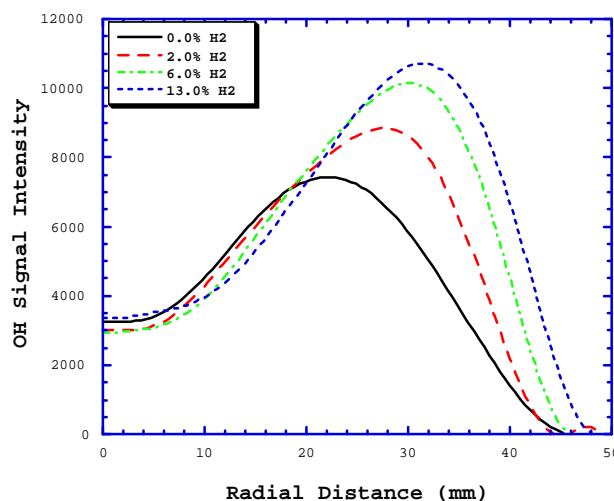


Figure 8. Radial profiles of OH intensity for different hydrogen addition at $y=40$ mm. $u=14$ m/s, $T_{ad} = 1250C$.

Conclusions

PLIF measurements of the OH radical were made to understand the effects of hydrogen enrichment on methane flames near lean blow out. Both instantaneous and time-averaged data were measured. The lean stability limit was lowered by the addition of hydrogen to the fuel, as expected. This improved stability with hydrogen enrichment is postulated to be a direct result of increasing the H, O, OH radical concentrations, which increases several key reaction rates. Results showed that moderate amounts of hydrogen enrichment led to significant increases in the OH radical concentrations. Specifically, the addition of up to 13.8% hydrogen causes a 44% increase in the maximum OH concentration, while further increases result in only marginally higher radical concentrations for the conditions tested.

Acknowledgments

This research was supported by the U. S. Department of Energy Hydrogen Program.

References

- Ali, S. A. and Parks, W. P. 1998. "Renewable Fuels Turbine Project." ASME Paper 98-GT-295.
- Clayton, R. M. 1976. "Reduction of Gaseous Pollutant Emissions from Gas Turbine Combustors using Hydrogen-Enriched Jet Fuel—A Progress Report." NASA TM 33-790.
- Larsen, J. F. and Wallace, J. S. 1997. *J. Engineering for Gas Turbines and Power*, 119: 218-226.
- Meyers, D. P. and Kubesh, J. T. 1997. *J. Engineering for Gas Turbines and Power*, 119: 243-249.
- Morris, J. D., Symonds, R. A., Ballard, F. L. and Banti, A. 1998. "Combustion Aspects of Application of Hydrogen and Natural Gas Fuel Mixtures to MS9001E DLN-1 Gas Turbines at Elsta Plant, Terneuzen, The Netherlands." ASME Paper 98-GT-359.
- Phillips, J. N. and Roby, R. J. 1999. "Enhanced Gas Turbine Combustor Performance Using H₂-Enriched Natural Gas." ASME Paper 99-GT-115.
- Schefer, R. W., Namazian, M. and Kelly, J. 1987. "Velocity Measurements in a turbulent Nonpremixed Bluff-Body Stabilized Flame." *Combust. Sci. Technol.*, 56: 101-138.

Hydrogen/Natural Gas Blends for Heavy-Duty Applications

**Kirk Collier
NRG Tech
Reno, NV 89502**

Abstract

NRG Tech is developing engine technology that is applicable for use in heavy-duty vehicle applications. This technology deals specifically with the use of mixtures of hydrogen and natural gas (called HCNG). This application of HCNG technology is unique for two reasons. One is the very high brake mean effective pressures (BMEPs) required by the engines. The other is the very large reductions in regulated exhaust emissions that can be achieved relative to both diesel and natural gas alternatives. The design strategy uses mixtures of hydrogen and natural gas containing at least 30% molar hydrogen, incorporates lean burn and possibly some exhaust gas recirculation for charge dilution to control NO_x. CO and NMHC emissions will be controlled by an oxidizing catalyst. At this stage in the project, NRG has developed three candidate engine platforms, ranging from 7.4 to 8.4 liters displacement, of its own for evaluation. Testing on one of the platforms has shown NO_x levels of 0.22 g/hp-hr using a weighted eight-mode steady state test with CO emissions essentially eliminated.

Introduction

The project is designed to bring hydrogen fuels to the marketplace in the short term. Because of the current high cost of hydrogen and the high purity hydrogen requirements of current fuel cell technology, the successful commercial implementation of hydrogen as a fuel is very much in the future. Because of this situation, a strategy is needed for earlier commercial implementation of hydrogen as a fuel. That strategy is to supplement natural gas with hydrogen for use in internal combustion engines. The rate of supplementation ranges between 30 and 50% by volume hydrogen. This range allows for enough hydrogen to significantly enhance the combustion of natural gas while remaining within an operational window that does not require extensive engine modifications.

Goals and Objectives

The goals and objectives for the project are:

- Develop a critical database to determine criteria for achieving ultra-low exhaust emissions with internal combustion piston engines for applications that now use diesel engines.
- Develop engine configurations that can replace existing diesel engines utilizing HCNG fuel achieving equivalent power relative to: 4.0 g/hp-hr NO_x, 15.5 g/hp-hr CO, and 1.2 g/hp-hr NMHC.

NRG Tech has investigated the following design variables:

- Compression ratio
- Combustion chamber design
- Ignition system
- Exhaust gas recirculation (EGR)-to-lean burn ratio
- Exhaust catalysts
- Water injection

Current Results

Tests on engine compression ratio ranged from 9.1 to 15.0 to 1. The desirable range for this technology range between 12 and 15 to 1. The optimum combustion chamber shape appears to be one that minimizes the surface to volume ratio. However, care must be taken to avoid engine knock. This can require non-optimal designs for emissions, but will allow knock-free operation.

An important result of our work has been the development of the proper fueling system for the engine. Table 1 shows the emissions results of testing two different fueling system designs. At low engine rpms, each system appears equal in performance. However, at higher engine rpms, one system is clearly superior to the other. Incorporating the proper fueling system and fueling strategy is crucial to the successful implementation of HCNG technology.

Table 1. Effect of Fueling System Design

System Type	RPM	Equiv. Ratio	BMEP (psi)	NO _x (g/hp-hr)
Design 1	1700	0.51	101	0.06
Design 2	1700	0.52	103	0.05
Design 1	3000	0.55	105	0.08
Design 2	3000	0.55	101	0.92

Testing the effect of ignition systems, spark plug location, and number of spark plugs yield mixed results. If the combustion chamber and the fueling system are not optimized, high-energy ignition systems and multiple spark plugs show improved performance. However, when the combustion chamber and fueling system are engineered properly, high-energy ignition systems and multiple spark plugs show minimal positive effects.

Table 2 shows the emissions results for a 7.4L V8 engine developed by NRG Tech. The two engine rpms chosen represent maximum engine torque and maximum engine horsepower. Various fractions of each power level for each rpm including idle make up the test. The emissions from each point are multiplied by a weighting factor (shown in the table) and added together to result in an overall value of emissions that represent a typical heavy-duty driving application. The design goal of this engine is to replace an existing 5.9L, 200 hp engine currently used in heavy-duty applications.

Additional tests were performed on a supercharged 4.6L engine where 0.11 g/hp-hr of NO_x was achieved at 120 psi BMEP.

Equivalence ratios ranging from 0.48 to 0.56 were used to achieve these emissions results. The electronic controls developed in the project were used to set the proper air-fuel ratio depending upon operating conditions and the allowable tradeoffs with NMHC emissions.

Table 2. 8 Mode Steady State Emissions Summary
200 hp Platform
 NRG Hydrogen-Enriched Natural Gas Bus Engine

Individual Modes	NOx g/hp-hr	THC g/hp-hr	NMHC (g/hp-hr)	CO g/hp-hr	Weighting Factor
1800 rpm - 100% Load	0.37	3.70	0.07	0.00	0.15
- 75% Load	0.20	5.80	0.10	0.00	0.15
- 50% Load	0.10	5.48	0.10	0.00	0.15
- 10% Load	0.25	5.10	0.10	0.00	0.10
2800 rpm - 100% Load	0.10	5.63	0.26	0.00	0.10
- 75% Load	0.09	4.71	0.19	0.00	0.10
- 50% Load	0.11	6.01	0.26	0.00	0.10
- Idle	0.40	17.44	0.36	0.00	0.15
Weighted 8 Mode (g/hp-hr)	0.22	7.00	0.18	0.00	
Weighted 8 Mode (g/kw-hr)	0.29	9.38	0.24	0.00	

Conclusions

NRG Tech has determined the proper configuration and allowable design deviations of the crucial engine parameters required to make HCNG fuel a viable commercial success. Emissions results show that NOx emissions compatible with proposed future emissions standards for heavy-duty vehicles are achievable with this fuel, but only if properly implemented.

PROCESS ANALYSIS WORK FOR THE DOE HYDROGEN PROGRAM - 2000

**Wade A. Amos, Margaret K. Mann, Pamela L. Spath, Janice M. Lane
National Renewable Energy Laboratory
Golden, CO 80401**

Abstract

In 2000, process analysis work conducted at the National Renewable Energy Laboratory for the Department of Energy's Hydrogen Program included cost analyses on both long-term basic research concepts and nearer-term fossil-based technologies. Additionally, a life cycle assessment on wind/electrolysis was performed for comparison of the environmental impacts of hydrogen production with those from steam methane reforming. The goal of this work is to provide direction, focus, and support to the development and introduction of hydrogen through evaluation of the technical, economic, and environmental aspects of hydrogen production and storage technologies. The advantages of performing analyses of this type within a research environment are several-fold. First, the economic competitiveness of a project can be assessed by evaluating the costs of a given process compared to the current technology. These analyses can therefore be useful in determining which projects have the highest potential for near-, mid-, and long-term success. Second, the results of a technoeconomic analysis are useful in directing research toward areas in which improvements will result in the largest cost reductions. Finally, as the economics of a process are evaluated throughout the life of the project, advancement toward the final goal of commercialization can be measured. Life cycle assessment (LCA) is used to identify and evaluate the environmental impacts of emissions and resource depletion associated with a specific process. When such an assessment is performed in conjunction with a technoeconomic feasibility study, the total economic and environmental benefits and drawbacks of a process can be quantified. Material and energy balances are used to quantify the emissions, resource depletion, and energy consumption of all processes required to operate the process of interest, including raw material extraction, transportation, processing, and final disposal of

products and by-products. The results of this inventory are then used to evaluate the environmental impacts of the process so that efforts can be focused on mitigating negative effects.

The studies that were conducted this year are summarized below. The actual milestone report for each study is available from the authors. Analyses were conducted on the following:

- Assessment of wind energy coupled with a reversible fuel cell
- Analysis of the production of hydrogen from Air Products' SER and ITM reactors
- Evaluation of the cost of hydrogen production via photobiological algal systems
- Life cycle assessment of wind/electrolysis, compared to SMR
- Assessment of thermocatalytic hydrogen production from natural gas decomposition
- Summary and map of analysis work funded by the U.S. DOE Hydrogen Program

The analyses conducted by NREL's process analysis task for the Hydrogen Program in 2000 served to refine our understanding of the economic feasibility of many research projects, as well as to quantify the environmental impacts of two methods of hydrogen production. Overall, process analysis at NREL helps the Hydrogen Program to methodically assess the applied research portfolio, in order to focus on those projects that have the potential to significantly contribute to the adoption of clean hydrogen systems. Results from the economic studies help researchers concentrate their efforts on those areas that have the greatest impact on cost, such that novel technologies can be commercialized more quickly. Hand-in-hand with cost analysis, LCA studies help the Program and the hydrogen community quantify the environmental status of various hydrogen technologies. Finally, process analysis helps streamline the transition to the hydrogen economy, balancing environmental requirements and economic constraints.

Assessment of Wind Energy Coupled with a Reversible Fuel Cell

This study examined the economic advantages that could be gained by storing off-peak wind power for sale during peak periods of the day. The report examined a number of different scenarios. In one case, it was assumed that a hydrogen bromide (HBr) fuel cell was used at the wind farm site for storing off-peak power for sale during on-peak periods of the day. In a second scenario, it was assumed that power transmission lines from the wind farm to the metropolitan area where it would be consumed were constrained. Power was therefore transmitted at night and during other off-peak times and stored using the HBr reversible fuel cell system for sale during peak periods of the day. Both of these cases were compared to systems without storage, operating under the same limitations.

There is a major difference between the scenarios mentioned above. With the constrained power transmission lines, no power can be sold directly from the wind turbines to the grid during peak times. In the case with unconstrained power, the system can supply wind power directly to the grid (the most efficient mode of operation) or use stored hydrogen in the HBr system to supply electricity using the HBr fuel cell. Excess power during peak periods could also be stored using the HBr system, but for the highest electricity sales revenue, it was assumed that all the wind power produced during peak periods went directly to the grid.

Although the HBr system was clearly able to increase the electricity selling price, using the HBr storage system for electricity storage results in a 36% loss in power compared to supplying the electricity directly to the grid (i.e., 64% round-trip storage efficiency). In the case of constrained transmission lines, all the off-peak power produced by the wind turbine went through storage and no on-peak power from the turbines could be sold. These factors resulted in a lower volume of electricity sales in all cases and lower overall electricity revenue, despite the higher selling price. The economics of this system naturally looked worse once the capital costs were factored in.

This analysis used Minot, North Dakota, wind turbine performance data for an Atlantic Orient Corporation 15/50 wind turbine and power demand and cost data from the New England Power Pool. These were the data available at the time of the analysis, but another analysis is planned using one of NREL's advanced turbine designs with a more complete wind data set and power data from the Chicago and Denver power markets. The results are not expected to change significantly.

Analysis of the Production of Hydrogen from SER and ITM Reactors

Sorption-Enhanced Reactor

Air Products is developing the sorption-enhanced reactor (SER) to reduce capital costs by operating at a lower temperature and lower pressure, and achieving a higher conversion of methane to hydrogen in the reforming reactor, eliminating the need for subsequent shift reactors. This is accomplished by mixing materials with the reforming catalyst that will adsorb carbon dioxide, shifting the equilibrium in the reactor toward higher hydrogen concentrations.

While the SER process is simpler and has lower capital costs than a conventional steam methane reforming process, the need for purge steam to desorb the carbon dioxide captured by the sorbent results in poor heat integration and additional natural gas consumption. The overall hydrogen yield is therefore lower and results in a hydrogen selling price of \$12-\$17/GJ (HHV basis). This price may be competitive for customers far from a centralized hydrogen production facility, but would not be directly competitive with large-scale steam methane reforming. Improvements in the economics of the process would depend upon changes in either the reforming catalyst to allow a different purge gas, or changes in the sorbent to allow a higher-pressure purge and improved heat recovery.

The hydrogen selling price for a 2.5 million scfd (246 kg/h) plant was estimated at \$16.80/GJ of hydrogen, including a 15% internal rate of return. For a 10 million scfd (984 kg/h) plant, the hydrogen selling price dropped to \$12.60/GJ due to economies of scale and proportionally lower labor costs. These prices were based upon the reactor conditions reported by Air Products at the 1999 Hydrogen Program Review. While these selling prices are higher than the \$5-\$8/GJ estimated price for hydrogen from steam methane reforming, a small-scale SER process might be more economical for onsite generation compared to conventional steam reforming for supplying liquid hydrogen to a remote location, which can cost \$20/GJ or more.

Ion Transport Membrane Reactor

Air Products is developing the ion transport membrane (ITM) reactor to reduce the cost of producing hydrogen. The ITM reactor would eliminate the oxygen plant required for conventional partial oxidation hydrogen production, thereby reducing the capital and/or operating costs.

An analysis of the ITM production process resulted in a hydrogen selling price of \$21.60/GJ of hydrogen for a 2.5 million scfd (246 kg/h) plant, including a 15% internal rate of return. For a 10 million scfd (984 kg/h) plant, the hydrogen selling price dropped to \$18.40/GJ due to economies of scale and proportionally lower labor costs. Some credit was taken for excess electricity produced using an off-gas combustion turbine. While these selling prices are again higher than the \$5-\$8/GJ estimated price for hydrogen from steam methane reforming, a small-scale ITM process might be economical for onsite generation compared to supplying liquid hydrogen to a remote location from a centralized steam reforming plant. The cost estimates in this study are preliminary because of limited data on the ITM membrane. Information on the cost of the ceramic ITM membrane and its performance characteristics would be needed to make a final comparison with steam methane reforming or other technologies.

These projected hydrogen costs are very dependent upon the cost of the ceramic material used in the ITM reactor. The cost of the ceramic was estimated using information for hydrogen transport membranes, but because the ceramic is a large contributor to the overall plant cost, further information is required from Air Products to better estimate the true capital costs of a full-scale plant. The key to the process is the development of an ion transport membrane capable of efficiently removing oxygen from air to supply a partial oxidation reaction. This membrane would replace the high-cost oxygen generation plant that would normally be required for such a process. If the ITM reactor could be constructed for half the cost, the hydrogen selling price would drop to \$15/GJ for the 10 million scfd (984 kg/h) plant size.

Evaluation of the Cost of Hydrogen Production via Photobiological Algal Systems

It was recently discovered that *Chlamydomonas reinhardtii* (green algae), under sulfur-deficient, anaerobic conditions, will spontaneously produce hydrogen gas at measurable rates without any special equipment and without genetic or mutation modification. These results have been verified, but whether photobiological hydrogen production with green algae is economically viable is another, separate question. The purpose of this study was to estimate what the hydrogen production costs might be using the current system, to determine what cost reductions might result from expected improvements, and to identify what design variables have the most importance on the process economics.

The current procedures used in the lab do not resemble what a full scale process might look like, however, the methods used are effective for data collection to model the full-scale system. Using current laboratory conditions, the hydrogen selling price would be estimated at over \$5,000/GJ

for a system large enough to supply hydrogen to 100 cars per day (300 kg/d). This cost drops to \$1,000/GJ with an improved process design, taking into account verified improvements over the current lab procedures. If the current areas of research are successful in meeting their targets, this cost would most likely drop another factor of ten to \$100/GJ. Then assuming some breakthroughs in materials and biological function—yet not exceeding what is theoretically possible—the cost could drop another order of magnitude to \$10-\$20/GJ with a highly simplified production system.

As expected, the analysis results show significant effects from varying the algae concentration, the specific hydrogen yield, the amount of transmitted light and the pond depth. Changing the daily hydrogen production rate showed very high costs at low production rates, but at larger plant sizes, there is very little economy of scale and so there is only a slight increase in profits for facilities larger than 300 kg/d.

The results from varying the algae concentration show that there is an optimum concentration: if the algae concentration is too low, the capital cost for larger tanks and the operating cost for handling more water increase the hydrogen selling price. If the concentration is too high, poor light penetration results, requiring extra production capacity. This optimum concentration is based on economic factors, in addition to light absorbance and kinetic factors.

The specific hydrogen yield had the largest effect on the economics, partly because there are no adverse effects from increasing the yield—the higher the yield, the lower the costs. Likewise an increase in light transmittance due to decreasing the algae antennae size will always result in lower costs. However, if genetically engineered organisms are required to accomplish this, there may be additional regulatory requirements and/or higher design and operating costs associated with maintaining pure strains and preventing contamination.

Another important factor is reducing the recovery time. If any daylight hours are lost to recovery and transition instead of production, this represents a direct loss in production capacity and requires extra pond capacity. Eliminating the recovery step helps reduce the cost a little more, but more importantly allows for a simpler process design.

By varying the pond depth, it was shown that after a certain point, creating a deeper pond results in no added benefit only increased capital costs. This is because the algae are so efficient at absorbing light, the algae more than a few centimeters below the surface see almost no light. Adding more algae capacity below this depth just results in a more costly tank and more material to handle, but because the light intensity is so low, the additional algae are producing very little, if any, extra hydrogen.

Naturally the average hours of sunlight affected the economics. What might be important is whether the hydrogen production rate remains high at low light levels. If this is the case, hydrogen production may still be adequate on rainy or cloudy days.

The cost of the transparent material for constructing the bioreactor is an important consideration. Material costs range over several orders of magnitude going from expensive glass to very thin,

cheap sheets of polyethylene plastic. An important consideration includes the hydrogen permeability of the material. For example, the permeability of hydrogen through PVC is several hundred times less than the permeability through polyethylene, but PVC costs almost 100 times more.

Some factors that were shown to be less important were the settled solids density, the wasting rate, the mixing requirements, the pumping requirements, and many of the balance of plant costs. These items may make the difference between prices of \$50/GJ and \$15/GJ of hydrogen, but other improvements must be made before things like power consumption become a real concern.

The most important conclusions from this study are:

- The current experimental conditions and procedures do not represent what the design criteria would be for a full-scale process.
- No *one* improvement in the cyclic process would result in enough of a cost reduction to make the process economical—work is required on several fronts.
- Successful research and development in multiple areas might result in a hydrogen selling price close to the current program goal of \$15/GJ for hydrogen from renewable sources.
- The success of this process will require higher specific hydrogen production rates, increased light transmittance through the algae, shortening of the recovery period and a bioreactor with low material costs that could be designed with a shallow pond depth.

Life Cycle Assessment of Wind/Electrolysis Compared to SMR

Although hydrogen is generally considered to be a clean fuel, it is important to recognize that the steps involved in producing it may have negative impacts on the environment. Examining the resource consumption, energy requirements, and emissions from a life cycle point of view gives a complete picture of the environmental burdens associated with hydrogen production. Life cycle assessment (LCA) is a systematic analytical method that helps identify and evaluate the environmental impacts of a specific process or competing processes. Life cycle assessments were conducted on two hydrogen production systems: steam methane reforming (SMR) and wind/electrolysis. Each LCA was performed in a cradle-to-grave manner. For the SMR system, this included plant construction and decommissioning, natural gas production and distribution, upstream processes required for plant operation such as electricity generation and distribution, the recycling of materials, and the disposal of wastes. Natural gas lost to the atmosphere during production and distribution is also taken into account. Wind/electrolysis is unique in that the resources required, energy consumed, pollutants emitted, and waste generated mostly occur during construction, with almost no emissions resulting from its operation. In contrast, the majority of the environmental stressors in the SMR system are a result of natural gas production and distribution.

In terms of total air emissions, CO₂ is emitted in the greatest quantity, accounting for more than 95 weight percent of the total air emissions for both systems. For the SMR system, the vast majority of the CO₂ (84%) is released at the hydrogen plant. Very few non-CO₂ emissions come from the operation of the SMR plant itself. For wind/electrolysis, 77% of the system's CO₂ is a

result of producing concrete and steel for the wind turbines and hydrogen storage. For the wind/electrolysis system, the second highest air emission is particulates. These come primarily from quarrying the sand and limestone needed for concrete production.

The greenhouse gas emissions from these systems are CO₂, CH₄, and N₂O, and can be normalized to describe the systems' total global warming potential (GWP). Normalization factors for CO₂, CH₄, and N₂O are 1, 21, and 310, respectively. The global warming potential (GWP) of the SMR system is 12 times higher than that for the wind/electrolysis system. Table 1 summarizes the total greenhouse gas emissions from each system.

Table 1 - Global Warming Potential

System	GWP g CO ₂ eq. per kg H ₂	% contribution to GWP		
		CO ₂	CH ₄	N ₂ O
SMR	11,888	89.3	10.6	0.1
Wind/electrolysis	970	97.9	0.6	1.5

The energy balance of these systems can be represented as the net energy ratio, which is the total amount of energy contained in the product hydrogen divided by the total energy consumed by the system that produces the hydrogen. This ratio was calculated to be 0.66 for SMR and 13.2 for wind/electrolysis. Because the SMR system is based on consumption of a non-renewable resource, the amount of energy in the product is less than the amount of energy consumed by the system. In contrast, the wind/electrolysis system delivers more energy than it consumes.

These two studies are the first in a series of assessments to compare the environmental benefits and drawbacks of hydrogen production via different technologies. Future work will involve using these studies to assess integrated systems for the following three hydrogen applications: transportation, remote communities, and residential. These studies can also be compared to hydrogen production via other routes such as biomass and photovoltaics. Additionally, longer-term technologies (e.g., photobiological and photoelectrochemical hydrogen production) can be examined using life cycle assessment to explore opportunities for reducing environmental consequences.

Assessment of Thermocatalytic Hydrogen Production from Natural Gas Decomposition

A technical and economic analysis was performed to examine two process designs for producing hydrogen via thermocatalytic decomposition of natural gas. Research for this process is being conducted by Dr. Nazim Muradov of the Florida Solar Energy Center (FSEC). The first design uses partial oxidation of some of the natural gas and carbon within the reactor to produce heat for the decomposition reaction. The second design uses combustion of natural gas to heat the carbon in a separate vessel. The hot carbon is then recycled back to the reactor. Both methods use

pressure swing adsorption (PSA) to purify the product hydrogen, with the PSA off-gas recycled to the reactor to improve hydrogen production efficiency. A pure carbon byproduct, free of sulfur and ash impurities, is assumed to be sold.

Due to the recent volatility in the natural gas market, hydrogen selling price results were presented as a function of natural gas cost. Depending on the size of the plant and natural gas cost, the results of a sensitivity analysis predict the plant gate hydrogen selling price to be \$11-\$31/GJ for the partial oxidation system, with an expected cost of \$19.53/GJ for a 20 million scfd plant and a year 2000 natural gas cost of \$3.72/GJ of natural gas. For the three-vessel system, the predicted price range was \$7-\$21/GJ of hydrogen, with an expected price of \$10.71/GJ. These selling prices assume a carbon byproduct selling price of \$0.30/kg and a 15% internal rate of return. The following three plant sizes were evaluated: 6, 20, and 60 million scfd (591, 1969 and 5906 kg/h) of hydrogen, with the largest plant size having the lowest hydrogen selling price. Hydrogen storage and transportation contribute an additional \$0.10-\$13.00/GJ depending on the customer location and delivery method.

Results from the sensitivity analysis determined the contribution of 25 assumption variables to uncertainty in the hydrogen selling price. Those variables that have the greatest influence on hydrogen selling price are yield of carbon, hydrogen production factor, operating capacity factor, and carbon selling price. In addition to varying carbon selling price with other variables in the Monte Carlo analysis, the carbon price was also varied independently to determine the dependence of hydrogen selling price on carbon selling price alone. If the carbon cannot be sold as a byproduct, the hydrogen selling price increases by \$8/GJ from the base case in the partial oxidation system and by \$5/GJ in the three-vessel system.

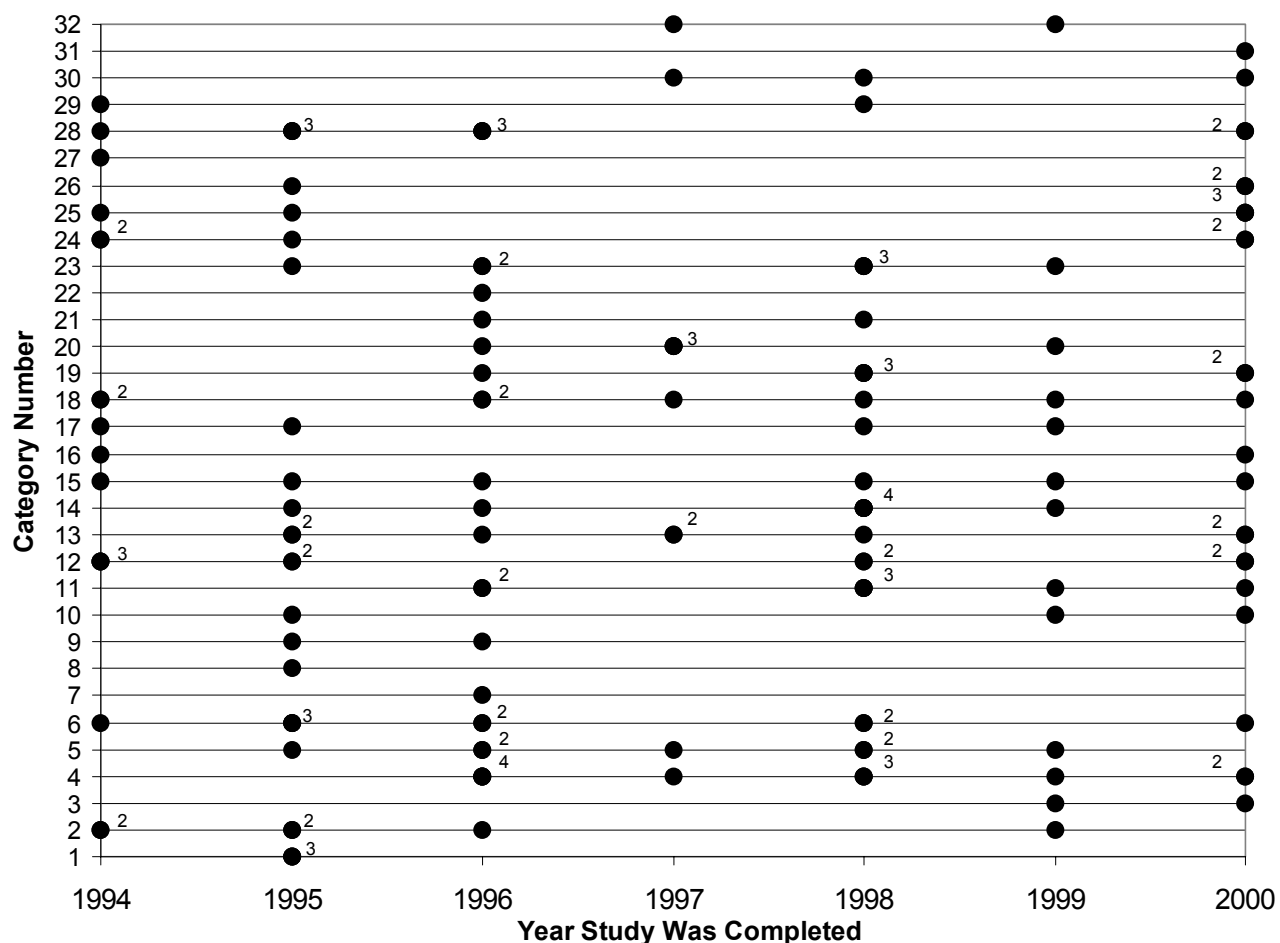
To accurately compare the greenhouse gas emissions from these two processes with those from steam methane reforming (SMR), a life-cycle approach was taken and emissions from the hydrogen production plant, upstream natural gas production, natural gas distribution, and avoided carbon black production were included. Emissions from these sources were reduced by 59% for the partial oxidation system compared to SMR and were reduced 33% for the three-vessel system.

Results of the sensitivity analysis yielded several research recommendations. Current data from Dr. Muradov are based on a single-pass reactor setup. Experimental trials with a carbon recycle to the reactor will give a better understanding of how the carbon's catalytic activity changes over time. Also, the carbon selling price has a large influence on the hydrogen selling price, so in-depth testing of the carbon quality and purity will allow a more accurate determination of the carbon selling price.

Summary and Map of Analysis Work Funded by the U.S. DOE Hydrogen Program

A visual map of hydrogen analysis studies funded by DOE in the past six years was constructed and is shown in Figure 1.

Figure 1 - Map of Hydrogen Analysis Summaries



Note: Numbers indicate how many studies were conducted in each category each year. Only one study was conducted if there is no number.

Some preliminary conclusions from this map are:

- Many studies have been done for hydrogen production and hydrogen distribution, however, few studies have been completed concerning newer developing hydrogen technologies and niche markets.
- Many transportation studies have been completed.
- Very few studies are shown in the areas of safety and environmental concerns.

The purpose of this work is to determine areas of focus for future analyses and also to provide a quick reference for finding studies already completed. A total of 76 studies were summarized and sorted into the following categories shown in Table 2.

Table 2: Categories for Analysis Map

H₂ Production

1. Grid electrolysis
2. Natural gas
3. Coal
4. Sunlight
5. Wind
6. Biomass
7. Hydroelectric
8. Geothermal
9. MSW
10. Comparison studies

H₂ Distribution

11. Stationary storage
12. Infrastructure - H₂ transmission
13. Infrastructure - refueling stations

Electricity Generation

14. Renewables
15. Stationary FCs

Market Analysis

16. Transportation
17. Distributed power

Transportation

18. Onboard storage
19. Fuels
20. Fuel cell vehicles
21. Hybrid electric vehicles
22. Internal combustion engine vehicles
23. Comparison studies

Outreach

24. Industry
25. Education

Safety

26. Codes and standards
27. Ventilation systems

Analysis Methodology

28. Project evaluation
29. Modeling

Environmental Concerns

30. CO₂ sequestration
31. Vehicle emissions
32. Life cycle assessment

Outreach

The reports summarized came primarily from the Hydrogen Program Reviews (1994-1999). In addition, articles by subcontractors of the Program were included. Only those efforts supported by the Program were included, while undertakings outside of the Program were not reviewed. The articles reviewed should not be considered exhaustive. Because there is no listing of all projects/publications funded by the Hydrogen Program, it was impossible to ensure that all efforts had been reviewed. However, since all of the Program Reviews were covered, it is likely that the most important efforts have been addressed.

In some cases, the analyses occurred over several years, with progress reports occurring in different Program Review Proceedings and the author list changing. In these cases, only a single entry is noted in the figure. Reports that encompassed more than one analysis area were listed in all applicable analyses areas. The map and categories will be periodically updated as new studies are published and as feedback is received from the authors and Program stakeholders.

Summary

This year's analyses examined several new or developing technologies for hydrogen production. Besides providing an estimated hydrogen selling price for each process, the analyses identified the major contributors to the selling price so efforts can be made to improve the economics. Sensitivity analyses and Monte Carlo help supply insight into the likelihood that certain changes will improve the economics of a process, or whether there are limiting factors that cannot be overcome. Without conducting these periodic assessments of economic potential, a project could be funded for several years without concentrating research efforts in the right areas to achieve the most benefit for the money spent.

Likewise, LCAs provide insight into the environmental aspects of a process. LCAs can be used to study a single process or to compare alternatives. Through a systematic cradle-to-grave investigation, an understanding of the benefits or drawbacks is possible. What may look like a good idea initially, may have far reaching impacts that are not immediately obvious. The next step will be to take the quantitative information on resource depletion, emissions, waste production and energy consumption to evaluate the overall impact of competing technologies on the environment.

Lastly, because it is important to use systems analysis studies to guide the future course of the Hydrogen Program, the mapping and associated database of prior analyses will help identify sources of information already available and show where further work must be done.

U.S DEPARTMENT OF ENERGY HYDROGEN PROGRAM INFRASTRUCTURE ACTIVITIES

Carol J. Hammel and Russ Hewett
National Renewable Energy Laboratory
Golden, Colorado

Abstract

In fiscal year 2000, the National Renewable Energy Laboratory (NREL) undertook two primary activities to support the assessment and development of infrastructure for the use of hydrogen in buildings and transportation applications. Those activities include: (1) the Blueprint; a government-industry effort to facilitate the development of adequate infrastructure in the next five years for hydrogen technologies; and (2) codes and standards activities, designed to incorporate hydrogen safety issues into existing and proposed national and international codes.

This paper will review both activities with respect to: (1) background issues; (2) goals and objectives; (3) status of progress; (4) milestones; (5) proposed future work; (6) leadership and cooperative efforts; and (7) methodology.

Background

Hydrogen is already being used as an energy resource in modest amounts in the United States and other industrialized countries. But more importantly, hydrogen is one of our “fuels of the future” for buildings, transportation, and portable applications.

The United States Department of Energy (DOE) has established a goal for hydrogen to supply 10 percent of the nation’s demand for energy by 2025. It is anticipated that hydrogen technologies in the transportation sector will be coming online in the next five to ten years. To assess the key issues associated with developing supporting infrastructure, the Blueprint government-industry

effort is focusing on four main technical areas: (1) refueling stations; (2) hydrogen storage systems; (3) hydrogen safety issues; and (4) codes and standards. The Blueprint is also geared at developing government-industry action plans for each of these technical areas.

With respect to codes and standards, existing safety rules, regulations, and consensus standards relating to the transporting and utilization of hydrogen are adequate for today's small markets. However, in the case of widespread usage of hydrogen for future emerging applications, today's safety rules, consensus standards and codes will not be adequate. Systematic efforts are required at the local, state, and federal government levels, as well as by producers and users of hydrogen products, (e.g., automotive industry) to: (1) identify safety-related issues; and (2) develop, update and validate regulations and codes and standards relating to the safe production, transportation, use, and servicing of hydrogen-fueled systems.

Goals and Objectives

Blueprint

The goal of the Blueprint effort is to outline a five-year action plan to develop a hydrogen fuel infrastructure for both heavy-duty and light-duty vehicles. The Blueprint is based on the assumption that hydrogen-fueled vehicles, in both fuel cell and hydrogen internal combustion engine (ICE) applications, will fulfill a portion of the zero emission vehicle (ZEV) requirement in California and other states that have adopted the ZEV program. The Blueprint's goal is to work closely with facilities instituting hydrogen systems, and to facilitate the assessment of additional infrastructure requirements and deployment activities.

The primary objective of the Blueprint is to propose a strategy to develop a fuel infrastructure to meet near-term needs for hydrogen systems. This strategy will closely reflect on-going activities, and reference key engineering and institutional issues. A cooperative government-industry process will be outlined, utilizing current experience to craft future activities.

Codes and Standards

The goal of the codes and standards effort is to incorporate hydrogen safety issues into existing and proposed national and international codes in order to facilitate market acceptance and deployment. The objective is the development of codes and standards for the following applications:

- transportation (fuel cells and internal combustion engines)
- buildings (fuel cells)
- portable appliances (fuel cells).

For these three applications, codes and standards are being developed relating to producing, transporting, storing, dispensing and using hydrogen.

Status of Progress

Blueprint

The Blueprint Roadmap Meeting, held in September 2000 produced consensus on the most important and pressing issues to be considered in hydrogen infrastructure development and deployment. The issues are organized according to four technical areas, listed below.

Refueling Stations

- A master rollout plan is critical, focusing on commercialization requirements as well as technical issues. The rollout plan will include a deployment plan, and will identify markets.
- An economic assessment is needed that will examine subsidies, incentive programs, and cost targets.
- Accurate and affordable metering is a top priority. Equipment R&D, and customer interface are two key areas.
- Gas purity/composition standards are also central. Technology improvement is needed in the hydrogen gas cleanup system.
- Design optimization for refueling stations can be realized through expandable and upgradeable station designs.
- Training and education is key, particularly emergency response training.

Hydrogen Storage

- 5000 psi technology, including a focus on components, leakage and permeation, and standards.
- 10,000 psi technology, placing an emphasis on container optimization, components, and in and out efficiency.
- Liquid technology, focusing on container optimization, components, and infrastructure.
- Low-pressure adsorption was considered in the discussions but the issues were not prioritized because of the long-term implications of the storage medium.

Codes and Standards

- Coordination and synchronization of codes and standards on the national and international level is critical.
- Currently, a lack of suitable installation, product, and storage standards exists, therefore complicating, if not precluding, commercial project development.
- A technical basis is needed for codes and standards development.
- Education of codes and standards officials is vital.

Hydrogen Safety

- A great need exists for a comprehensive database that will serve as a knowledge center, and as a living web site technical tool.

- Increased detection and verification facilities are needed to accommodate a variety of hydrogen development and demonstration activities.
- A verification facility is needed to execute integrated system design. The verification facility would provide the opportunity to design, build, and verify integrated systems.
- Operations, maintenance, and training are key. A verification facility could be used to determine procedures and to train personnel.
- Education of John and Jane Q. Public is critical. An everyday device or “toy” is needed to familiarize the public with the use of hydrogen.

As a result of the Blueprint meeting, the DOE Hydrogen Program expanded its 2001 work effort to include safety database development, increased solicitations for onboard and off-board refueling and storage, and field verification activities.

The Blueprint effort is receiving support from the National Hydrogen Association, industry, the South Coast Air Quality Management District, and other agencies. In addition, efforts are ongoing to ensure active participation from the natural gas industry, and to integrate applicable “lessons learned” into the development of hydrogen infrastructure.

Codes and Standards

International Code Council (ICC) Hydrogen Ad Hoc Committee

Between regularly scheduled meetings, the International Code Council (ICC) Hydrogen Ad Hoc Committee is continuing its efforts through six working groups:

- Working Group 1: Residential Garages
- Working Group 2: Commercial Garages (open and enclosed)
- Working Group 3: Fuel Dispensing/Refueling Stations
- Working Group 4: Portable Fuel Cell Appliances
- Working Group 5: Hydrogen Gas Generation Appliances
- Working group 6: Identification of Standards Deficiencies and Needs

The Ad Hoc Committee has completed initial rough drafts of code changes proposed for incorporation into the International Fire Code and the International Fuel Gas Code. The goal is to complete recommended changes so that they can be presented for approval at the ICC 2002 code development/hearing cycle. The next meetings of the full Ad Hoc Committee meeting will be held on June 4-5, 2001 at NREL.

The National Fire Protection Association (NFPA)

The National Fire Protection Association (NFPA) has made the decision to develop its own new building code called *NFPA 5000* independently of the ICC. The NFPA 5000 will address hydrogen in the code.

NREL initiated working with NFPA to coordinate efforts. In addition, NREL is working towards becoming a representative on one of the *NFPA 5000* code development committees.

NFPA recently made the decision to participate in the NREL technology transfer/marketing research targeted at building code and fire safety official officials. This includes participating in the focus group program to (1) generate feedback regarding the usefulness of the hydrogen safety handbook; (2) generate feedback regarding the usefulness of the hydrogen safety video; (3) generate input regarding hydrogen safety-related information needs not being addressed in the handbook and/or video; and (4) generate input regarding the best ways and mechanisms for providing needed information.

Fire and Flame Impingement Tests

NREL is monitoring the work and results from the hydrogen fire and flame impingement tests being conducted for the Hydrogen Program by Dr. Michael Swain (Associate Professor of Mechanical Engineering at the University of Miami). The objective of these tests is to assist the ICC Hydrogen Ad Hoc Committee and others in determining what level of fire protection is needed for hydrogen-powered or hydrogen-fuel-cell powered vehicles housed in residential garages. Concerning his results, NREL funded Dr. Swain to present a paper at the NFPA World Fire Safety Congress held in Anaheim, CA in May 2001.

International Standards Organization

NREL is supporting the International Standards Organization's Technical Committee 197 (ISO/TC197) hydrogen standards development efforts. NREL has awarded a subcontract to TISEC, Inc., to address the issue of identifying internationally acceptable criteria for confining hydrogen under pressure. Dr. Robert Hay will be the TISEC principal investigator in this activity.

The subcontract was awarded on April 24, 2001. It will involve conducting a quantitative study of requirements and existing pressure vessel codes and standards to formulate recommendations to ISO/TC-197 that will resolve the current national differences existing among committee members and that are compatible with other existing international codes and regulations

International Electrotechnical Commission

Mr. Algis Vasys (consultant to NREL on hydrogen codes and standards) has been appointed to serve as the DOE/NREL Hydrogen Program's representative on Technical Committee 105 (TC/105) of the International Electrotechnical Commission (IEC). Within TC/105, Mr. Vasys will be serving on WG5, that addresses stationary fuel cell power plant installation standards.

The mission of IEC is to promote, through its members, international cooperation on all questions of electrotechnical standardization and related matters, such as the assessment of the conformity to standards. The technologies coming under the purview of IEC includes: electricity, telecommunications, energy production and distribution, and electronics.

Milestones

Blueprint

Conduct Core Group Meeting. (May 2000)

The Blueprint's Core Group, comprised of Shell Hydrogen, Praxair, Air Products, Ford Th!nk Group, Stuart Energy, and the California Energy Commission met on May 8, 2000. The purpose of the meeting was to develop better coordination and collaboration with the Gas Research Institute's Natural Gas Vehicle Infrastructure Industry Working Group, with the DOE Office of Transportation Technologies' "Fuels for Fuel Cells Plan," and with the California Fuel Cell Partnership. In addition, potential brainstorming exercises were conducted with respect to developing a roadmap for the Blueprint.

Conduct Roadmap Meeting. (September 2000)

A Blueprint roadmap meeting was held on September 21 – 22, 2000 to prioritize critical issues and develop initial action plans. The group divided into focus groups concentrating on four key technical areas: safety, storage, refueling stations, and codes and standards. Focus group findings are reviewed in the previous section.

Conduct Working Group Meeting. (September 2001)

A hands-on meeting is scheduled to include all of the facilities that are currently installing hydrogen infrastructure for transportation application. An inventory of key institutional and technical issues will be developed, highlighting "lessons learned." Technical teams will be formulated to follow up with next steps, including station design, and tank certification. A key element to the working group meeting scheduled for September 2001 will be to identify markets to focus infrastructure efforts. These will focus on a small number of "early adopters" in California, Nevada, Arizona, New York, and Massachusetts. Regional market for penetration profiles will be developed. Retailing stations will be geographically concentrated to fully utilize the infrastructure. The purchase of government fleet vehicles will be carefully coordinated with infrastructure installation. Finally, coordination will be developed between our manufacturers and fuel providers to optimize timing of supply and demand.

Codes and Standards

Draft a professional quality document on codes and standards issues. (July 2001)

NREL initiated a marketing research and technology transfer activity targeted at the nation's building code and fire safety officials. This included disseminating copies of the draft report "*The Hydrogen Handbook for Building Code and Fire Safety Officials*" and the video "*Hydrogen: The Matter of Safety*." The objectives are to: (1) get feedback regarding the usefulness of the handbook; (2) get feedback regarding the usefulness of the video; (3) get input regarding hydrogen safety-related information needs not being addressed in the handbook and/or

video; and (4) get input regarding the best ways and mechanisms for providing needed information. NREL planned and began conducting a series of focus group sessions around the country targeted at building code and fire safety officials to determine information needs and mechanisms. The results from the focus group sessions will be used as the basis for designing the new document and its contents. Sessions are planned with: (1) International Conference of Building Officials; (2) Underwriter Laboratories; (3) Fairfax County, VA building code officials; (4) Southern Building Code Congress; (5) Marietta, GA Fire Department fire safety officials; and (6) National Fire Protection Association.

Participate in ICC meetings and report as necessary. (September 2001)

NREL is participating in the work of the International Code Council (ICC) Hydrogen Ad Hoc Committee. The objectives of the Ad Hoc Committee are to: (1) review current codes and standards relating to hydrogen; (2) identify proposed changes to international codes and work to get them incorporated into the International Residential Mechanical/Plumbing Code (IRM/PC), the International Fire Code (IFC) and the International Fuel Gas Code (IFGC); and (3) identify other standards needs and deficiencies and generate standards for incorporation into model codes.

The Ad Hoc Committee was successful in getting its initial recommended changes into the ICC's IRM/PC, IFC and IFGC at the ICC 2001 Code Development/Public Hearing Cycle on 19 March 2001 held in Portland, OR. In addition, the Committee completed initial rough drafts of standards proposed for incorporation into the IFC and IFGC as part of the ICC 2002 code development cycle.

Proposed Future Work and Milestones

Blueprint

Work for the remainder of fiscal year 2001 will focus on organizing and designing the Blueprint working group meeting, tentatively scheduled for September 2001. In the planning process, coordination will take place with other groups who have initiated hydrogen infrastructure development, such as the California Fuel Cell Partnership in the Sacramento, CA area, and Sunline Transit Agency in Thousand Palms, CA. In addition, technical teams addressing tank certification, refueling station design, and other technical issues will be formulated.

It is anticipated that the Blueprint technical teams will refine action plans as necessary, continuing to meet in fiscal year 2002.

Codes and Standards

The work of the ICC Hydrogen Ad Hoc Committee will continue to develop consensus standards and to incorporate hydrogen-related standards into the IFC, IRM/PC and the IFGC. The focus of these efforts will be: (a) hydrogen flexible connector standard; (b) portable fuel cell appliance standard; (c) need for harmonizing standards regarding the definitions of "stationary," "portable" and "residential" fuel cell power plants; and (d) need for resolving differences between standards

regarding stationary fuel cells available today and anticipated concepts involving new technologies.

The marketing research and technology transfer activities targeted at building code and fire safety officials will continue. The focus will be on continuing to identify their issues and concerns regarding the installation and safe use of hydrogen-powered appliances and addressing these issues and concerns in a credible, professional-quality manner. The emphasis will be on using results of “code and standards validation work” (e.g., testing and evaluation work being conducted by Dr. Michael Swain of the University of Miami).

Since a major promising potential application of hydrogen fuel cells is motor vehicles, the Program will seek to establish a collaborative working relationship with the Society of Automotive Engineers with respect to codes and standards work.

The Program is developing hydrogen technologies for three applications: transportation, buildings and portable applications. For each of those applications, safety issues must be addressed with respect to the production, transportation, storage, dispensing and use of hydrogen. Furthermore, many organizations are involved in developing standards (e.g., NFPA, SAE, ICC, etc.). Consequently, major thrusts in the Program’s codes and standards activity must be to: (a) keep abreast of hydrogen-related codes and standards ongoing in various organizations; (b) work to coordinate efforts and prevent needless duplications of efforts; (c) identify deficiencies and gaps in the work in progress throughout the country; and (d) work to identify the appropriate forums for addressing any critical deficiencies and gaps. These coordination and “codes and standards development management” activities will continue.

Proposed Milestones

- Development of three new proposed draft standards by the ICC Ad Hoc Committee to address deficiencies in the ICC model codes (September 2002)
- Blueprint Technical Team refined action plans (September 2002)

Leadership – Cooperative Efforts with Other Organizations

NREL is an invited member of the Society of Automotive Engineers (SAE) Fuel Cell Recycling Subcommittee. In addition, NREL has been and will continue to work collaboratively with SAE, the International Code Council, the National Hydrogen Association and the International Standards Organization.

Methodology

The methodology for both infrastructure tasks is to optimize the Blueprint and codes and standards activities through coordination and joint work projects with ongoing hydrogen infrastructure efforts. In particular, coordination will take place with the National Fire Protection Association, Natural Gas Institute, International Standards Organization, International Electric Technical Commission, Society of Automotive Engineers, and numerous hydrogen fueling facilities in California, Nevada, and Michigan.

DISTRIBUTED HYDROGEN FUELING SYSTEMS ANALYSIS

**C. E. (Sandy) Thomas, John P. Reardon, Franklin D. Lomax, Jr.,
Jennifer Pinyan & Ira F. Kuhn, Jr.**

**Directed Technologies Inc.
3601 Wilson Boulevard, Suite 650
Arlington, Virginia 22201**

Abstract

Directed Technologies Inc. has analyzed the costs and other attributes of three fuel infrastructure systems to support fuel cell vehicles: hydrogen, methanol and gasoline. This work compliments previous DTI analyses of onboard fuel system costs for these three fuels B onboard hydrogen storage systems in the case of hydrogen, and onboard fuel processors for methanol and for gasoline. The results of our fuel infrastructure cost analyses contradict the conventional wisdom that a hydrogen fueling infrastructure would be very expensive. In fact, we estimate that the total costs to society of providing a hydrogen infrastructure for fuel cell vehicles via steam methane reforming of natural gas at the local fueling station would be up to two times less costly than maintaining the existing gasoline infrastructure. Both hydrogen and methanol fuel infrastructures based on natural gas would be less expensive than the crude oil-to-gasoline path used to power cars today.

We also analyzed several other aspects of the three fuel systems. For gasoline, we evaluated the likely costs of producing a low-sulfur, fuel cell-grade gasoline. For methanol, we estimated likely future fuel costs, assuming that millions of fuel cell vehicles required new methanol production capacity. For hydrogen, we completed several older analyses such as comparing booster-compression vs. cascade-filling of tanks, producing hydrogen on-site from trucked-in methanol, evaluating the greenhouse gas effects of electrolyzing water in various countries around the world, and evaluating the economic benefits of producing electrical peak power shaving utilizing hydrogen made off-peak at the local fueling station in a stationary fuel cell system.

Executive Summary

Directed Technologies, Inc. has analyzed the costs of the infrastructure to supply hydrogen, methanol and gasoline to fuel cell vehicles. In previous studies we evaluated primarily the impact of these three fuels on the vehicle, and we also evaluated the costs of producing hydrogen by steam reforming of natural gas and by electrolysis of water. In this study we analyzed and compared the likely costs to provide and maintain a gasoline infrastructure, a methanol infrastructure and a direct hydrogen infrastructure to support fuel cell vehicles.

Our primary conclusion from this analysis is that the costs of maintaining the existing gasoline infrastructure per vehicle supported are up to two times more expensive than the estimated costs of building and maintaining either a methanol or a hydrogen fuel infrastructure. This result may be surprising to many who subscribe to the notion that providing a hydrogen infrastructure is exorbitantly expensive. This might be true for the case of hydrogen produced at a large a central plant combined with a national hydrogen pipeline system. But we assume a less costly option: the hydrogen is produced and dispensed locally by reforming natural gas, utilizing the existing natural gas infrastructure.

Specifically, we estimate the following infrastructure costs for the three fuel options:

- Gasoline: maintaining the current gasoline infrastructure systems requires annual capital investments of approximately \$1,230 for each new conventional vehicle sold.
- Hydrogen: maintaining the existing natural gas infrastructure and producing and installing small-scale steam methane reformers to produce hydrogen at the local fueling station requires annual capital investments of between \$600 to \$800 for each new direct hydrogen fuel cell vehicle sold.
- Methanol: installing a local methanol infrastructure requires about \$75 for each fuel cell vehicle sold initially, based on current excess methanol production capacity that could support up to six million fuel cell vehicles; once this level is reached, we estimate methanol capital expenditure costs of \$525 to \$700 for each new methanol fuel cell vehicle sold, assuming that the methanol is produced from stranded natural gas. If the natural gas field must be developed to supply the methanol plant, then the methanol infrastructure costs would increase to between \$830 and \$1,000 per new methanol fuel cell vehicle, or still less than maintaining the current gasoline infrastructure for conventional cars.

In addition, the capital expenditure estimates for methanol and hydrogen may be high, in the sense that we have effectively assumed that the hydrogen and methanol production equipment is replaced every 13 years when the FCV is scrapped. To the degree that this equipment has longer lifetime, the effective infrastructure cost per new FCV sold would be less. This is not true of the gasoline infrastructure annual capital investment estimates made in this report, where we have good historical capital expenditure data from a well-established global oil industry.

Primary conclusion: society could reduce the total annual investments in light duty vehicle fuel infrastructure by half if we switched from gasoline-powered internal combustion engines to either hydrogen- or methanol-powered fuel cell vehicles.

We have previously estimated the incremental vehicle costs for producing direct hydrogen, methanol and gasoline fuel cell vehicles. The following table combines our estimates of fuel infrastructure and incremental vehicle costs for each fuel:

Table 1. Estimated incremental cost for fuel infrastructure and fuel cell vehicles in mass production

	Direct Hydrogen Fuel Cell Vehicle	Methanol Fuel Cell Vehicle	Gasoline Fuel Cell Vehicle
Incremental Vehicle cost	\$1,800	\$2,300 to \$3,400	\$3,400 to \$6,300
Infrastructure cost/vehicle	\$600 to \$800	\$75 to \$700	\$1,230
Total incremental cost	\$2,400 to \$2,600	\$2,375 to \$4,100	\$4,630 to \$7,530

Based on total fuel infrastructure cost, both on and off the fuel cell vehicle, we conclude hydrogen is the least costly option, followed by methanol and then gasoline as the most expensive option.

Other secondary findings from this year's analysis work include:

For the gasoline option, we looked at the likely costs for reducing sulfur content below 1 ppm in gasoline, a requirement to protect the onboard fuel processor and the fuel cell anode. At least two options are feasible, neither of which would add significant cost to gasoline for use in FCVs:

- Sulfur could be reduced from 30 ppm, the likely mandated levels in gasoline by 2004, with an onboard sulfur absorber costing less than \$50 that would last the life of the car.
- Oil companies could supply a low octane, fuel cell-grade of gasoline with less than 1 ppm sulfur at a cost equal to or less than the cost of current high octane gasoline; however, the oil companies would risk losing revenues at stations initially that provided a low octane fuel that could only be used by fuel cell vehicles.

For the methanol option, we concluded that:

- Methanol priced at the historical average of 59¢/gallon at the U.S. Gulf could be delivered to a FCV owner at 78¢/gallon; at this price methanol in a FCV would be competitive per mile driven with wholesale gasoline at 90¢/gallon in an ICEV.
- Methanol from a new dedicated production plant using cheap \$0.50/MBTU natural gas could be delivered to the Gulf for approximately 33¢/gallon and to the pump at 52¢/gallon, which would provide a 30% cost reduction over 90¢/gallon wholesale gasoline in an ICEV.
- However, oil companies have three other options to monetize stranded natural gas, each of which requires lower capital cost by some estimates than methanol production: LNG (liquid natural gas) capital costs are less than methanol by some estimates, gas-to-liquids are potentially less costly, and natural gas hydrates, if developed as planned, may be the least costly method of transporting stranded natural gas to the market.

For the hydrogen options, we investigated four separate topics and came to these conclusions:

- Installing a 200-kWe stationary fuel cell electrical generator at a hydrogen fueling station can improve the project economics over selling hydrogen alone and, more importantly, can provide needed revenue in the early days of FCV market penetration while FCVs are still scarce. In California, a 500-FCV station with a 200-kWe fuel cell generator could sell electricity during six peak hours for 6¢/kWh and hydrogen at \$1/gallon gasoline-equivalent. In Alaska, with lower natural gas prices, on-peak electricity could be sold at 6¢/kWh and hydrogen at 60¢/gallon of gasoline-equivalent and still make 10% real, after-tax return on investment. Even if only 200 FCVs were available in the region (at a station built with a 500-FCV fueling capacity), the Alaskan fuel supplier could sell electricity for 6¢/kWh and hydrogen at 90¢/gallon of gasoline-equivalent.
- Producing hydrogen by electrolyzing water in most nations of the world would increase greenhouse gas emissions, since much of the world's electricity is produced by coal or natural gas. Electrolytic hydrogen from grid electricity in the U.S. will create a net increase in greenhouse gases for at least the next two to three decades. Electrolytic hydrogen consumed in a FCV will reduce greenhouse gases in only five major nations in the world: France (nuclear), and Brazil, Canada, Norway and Sweden (mostly hydroelectric).
- Producing hydrogen on-site from methanol would cost 30% more than reforming natural gas with methanol and natural gas at their historic price levels, or 17% more with natural gas commercial rates at \$8/MBTU (HHV) instead of \$5/MBTU that prevailed up until 2000.
- The booster-compressor hydrogen tank-filling scheme suggested by Tom Halvorson of Praxair in place of the more conventional cascade filling system did not offer significant benefits when low-cost carbon fiber storage tanks are used. With the more expensive steel tanks on site, the booster-compressor option would reduce costs about 22% for a small, 100-FCV fueling system, but savings are minimal for either larger, 900-FCV stations or stations using less expensive composite storage tanks.

Introduction

Directed Technologies, Inc, (DTI) was awarded a 3-year grant in FY 1999 to extend our previous analyses of fuel options for fuel cell vehicles. As part of this grant, we were tasked to investigate the fuel infrastructure necessary to provide hydrogen, methanol and gasoline to fuel cell vehicle (FCV) owners. While the sponsors of this work, the Hydrogen Program Office, are interested in developing hydrogen as an energy carrier, they must also have a credible assessment of the competing fuels for FCVs, primarily gasoline and methanol.

Previous analyses by DTI had concentrated on the effects of fuel choice on the FCV itself (Thomas-1988e, 1988f, 1999a, 1999b, 2000a & 2000b). In particular, we conducted detailed cost assessments on both the fuel cell system as well as partial oxidation fuel processing systems to convert gasoline into hydrogen (James-1997a & 1999c and Lomax-1997). DTI had also previously conducted an assessment of the costs of providing a hydrogen infrastructure under contract to the Ford Motor Company and the U.S. Department of Energy through their multi-year cost-shared contract with Ford to develop a direct hydrogen FCV (Thomas-1997b, 1998a, 1998b & 1998c). However, this work on hydrogen infrastructure identified several key areas that required more detailed analysis to increase the DOE's confidence in our preliminary hydrogen cost and availability projections.

While gasoline is widely available in the industrialized nations, we expect that a new fuel cell grade of gasoline might be required to support fuel cell vehicles should onboard gasoline processors be developed. Therefore the oil industry might have to make new investments to reduce if not eliminate sulfur or other compounds that might damage or impair the performance of fuel processor or fuel cell catalysts. Another option would be to produce a new fuel such as synthetic gasoline, naphtha, diesel fuel or dimethylether (DME) made from natural gas – the “gas-to-liquids” pathway. These synfuels would contain negligible sulfur, and might also be used as a clean diesel substitute for compression ignition engines.

Finally, the methanol industry would have to install a totally new local distribution network to supply neat methanol to local fueling stations.¹ The methanol industry currently has excess production capacity, so that no new methanol production plants would have to be constructed until as many as six million fuel cell vehicles were on the road. Eventually new capacity would be required. We have analyzed the likely cost implications of large new methanol production and distribution facilities

¹Approximately 65 M-85 dispensers (85% methanol and 15% gasoline) were set up in California to support flexible fuel internal combustion engine vehicles, but the gasoline in M-85 would certainly foul the catalysts in a methanol reformer. In addition, many of these M-85 dispensers have been shut down, since few owners of flex fuel vehicles (vehicles that can run on M-85 or gasoline) actually use M-85, opting instead to refuel with the more readily available gasoline.

Hydrogen Infrastructure

During the past year, we evaluated four issues related to hydrogen generation for fuel cell vehicles. Several of these tasks are related to issues raised by DTI and others in previous years, but never analyzed in detail. The four tasks are:

- Cogeneration of electricity at hydrogen fueling stations
- Greenhouse gas impacts of electrolytic hydrogen
- Cost of hydrogen produced on-site from methanol
- Booster compression vs. cascade filling of high pressure hydrogen

Electricity and Hydrogen Cogeneration

In past years we analyzed the economics of coproducing hydrogen and electricity from a stationary fuel cell system (Thomas-1998d, 1999c & 1999d). In this case the stationary fuel cell project was justified primarily by selling electricity to the building owner. Hydrogen made off-peak as a co-product for sale to either industrial customers or to FCV owners was shown to enhance the project economics.

In this task we explore the opposite situation: the project is based on providing hydrogen for fuel cell vehicles from a steam methane reformer. The compressor and storage tanks are already on-site, along with a steam methane reformer. We make the following assumptions:

1. A stationary PEM fuel cell system is added to the hydrogen fueling station to produce electricity.
2. The steam methane reformer is enlarged to produce enough extra hydrogen during off-peak hours to supply the stationary fuel cell during peak electrical demand.
3. No additional hydrogen storage capacity is assumed, since the fuel cell can extract hydrogen from the storage cascade at very low pressure using hydrogen that would otherwise not be used.² We have assumed in the fueling station model that at most 50% of the hydrogen in the cascade filling tanks are never used to fill high pressure car tanks. The fuel cell operating at pressures below 40 psia can effectively use this very low pressure residual hydrogen.
4. Electricity is sold to the utility during peak hours at a price to recover only the capital cost of the fuel cell system plus the incremental cost of the over-sized reformer, plus fuel and operating expenses.
5. The baseline assumptions for this fueling station are listed in Table 2. The cost data for production quantities of 1,100 and 10,000 units are taken from previous DTI studies for the DOE. The hydrogen from this fueling station sized to support 1,000 FCVs (approximately 125 cars refueled each day – an average fueling station) could be sold at a cost competitive to wholesale gasoline in the range between 80 to

²The assumption of no new storage capacity is probably valid for fuel cell systems up to 200-kWe for a fueling station sized to support 1,000 or more FCVs. We assume storage for 80% of one day's FCV consumption, or about 400 kg of hydrogen, which requires 800-kg storage capacity. A 200-kWe fuel cell system operating for 6 hours each day would consume 72 kg of hydrogen, or much less than the 400 kg of spare low pressure storage available in the tank cascade for the FCVs.

90¢/gallon. The electricity could be sold to the utility during peak hours (assumed here to last for 6 hours per day) at 13.5 to 18.4¢/kWh. In all cases the capital recovery rate is set to yield a 10% real, after-tax return on investment.

While the electricity rates of 13.5 to 18.4¢/kWh may seem high, they may be quite reasonable for on-peak prices in many locations. Thus utilities may agree to pay these peak rates in exchange for deferring the construction of new production, transmission and distribution (T&D) facilities.

Table 2. Baseline parameters for 100 kW stationary fuel cell placed on hydrogen fueling station site

	First Unit	100 Quantity	10,000 Quantity
Capital Costs			
SMR (FCV demand)	\$569,800	\$193,600	\$65,750
SMR (Added Electricity demand)	\$39,500	\$13,400	\$4,500
Total SMR Cost	\$609,300	\$207,000	\$70,250
Compressor	\$94,800	\$32,200	\$10,900
Hydrogen Storage	\$350,700	\$220,800	\$157,000
Dispenser	\$75,800	\$25,700	\$8,800
Stationary Fuel Cell	\$75,800	\$46,200	\$28,200
Inverter/controls	\$70,700	\$35,100	\$17,400
Total Capital	\$1,277,100	\$567,000	\$292,550
Allowable Prices for 10% Real, After-Tax Return on Investment			
Peak Electricity Price (¢/kWh)	28.3	18.4	13.5
Hydrogen Price (\$/kg)	2.60	1.93	1.68
Hydrogen Price (\$/MBTU-LHV)	22.9	17.0	14.8
Hydrogen Price (\$/gallon gasoline-eq.)	1.20	0.89	0.77

Other assumptions: California commercial energy prices (natural gas = \$6.21/MBTU; electricity = 8.8¢/kWh); 100 kW fuel cell system; peak electricity sold for 6 hours/day; plant availability = 95%; fueling station supports 1,000 FCVs; FCV fuel economy = 66 mpgge; ICEV fuel economy = 30 mpg; annual miles traveled = 12,000.

The owner of the hydrogen fueling station may also want to trade-off hydrogen prices for electricity prices. The installation of a stationary fuel cell system at the hydrogen fueling station can help to ease the cash flow problem in the early days of FCV market penetration. We have analyzed the following scenario: suppose a fueling station owner installs a hydrogen fueling appliance to support 500 FCVs (which would correspond to about 60 to 65 cars per day filling their compressed hydrogen tanks.) Suppose further that there are very few FCVs utilizing the fueling station initially. We looked at the station economics if the station owner also installed a 200-kWe PEM fuel cell system to produce electricity from the steam methane reformer and hydrogen storage tank system. We further assumed that the local utility grid would buy the electricity generated for six hours per day at a premium price. Presumably this fuel cell electricity could be sold immediately if it would be installed in a region with a highly loaded transmission & distribution system.

The results of this hydrogen and peak electricity co-generation are shown in Figure 1 for four cases in California: 50 FCVs, 100 FCVs, 200 FCVs, and the full design value of 500 FCVs that would fully utilize the hydrogen fueling facilities. In all cases we assume large scale mass production (10,000 stationary fuel cell systems produced). With only 50 FCVs in the neighborhood of the fueling station (10% of the design load), hydrogen would have to be sold at \$2.14/gallon of gasoline equivalent to provide the fueling station owner

with a 10% return on investment on the hydrogen fueling equipment. The stationary fuel cell system (including extra cost for the oversized reformer) would make the goal 10% return if electricity could be sold to the grid at 14.5¢/kWh during six hours per day. If, however, the local utility could pay even more to reduce their peak load, then the cost of hydrogen could be reduced. For example, if the on-peak electricity could be sold for 18.5 ¢/kWh, then the hydrogen could be sold at \$1.25/gallon of gasoline equivalent, as shown by the upper diagonal line in Figure 1.

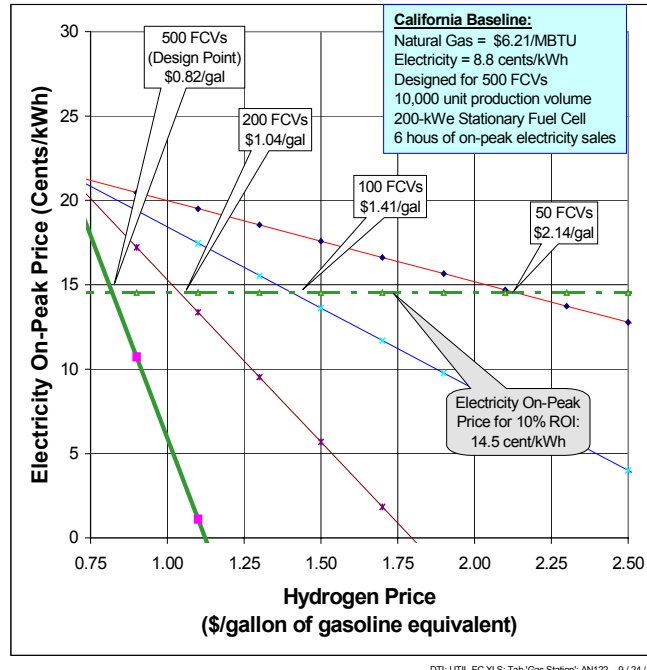


Figure 1. Estimated trade-offs in peak electricity and hydrogen prices for a hydrogen fueling station with a 200-kW on-site stationary fuel cell system.

Once there were over 100 FCVs using the hydrogen fueling station, then the price trade-offs could go the other way: the price of on-peak electricity could be reduced in exchange for increased hydrogen prices. For example, with 200 FCVs utilizing the hydrogen from the 500-FCV station, hydrogen could be sold at \$1.04/gallon equivalent to recover the fueling station equipment costs, which is near the current wholesale price of gasoline without taxes. The station owner could probably increase the price of hydrogen to something like \$1.50/gallon, assuming that it would not be taxed initially to encourage clean fuels. In this case (hydrogen priced at \$1.50/gallon with 200 FCVs), then the electricity could be sold at only 6¢/kWh for six hours on-peak, which might be a bargain for utilities faced with new T&D investments. Of course the owner may be in the enviable position of selling both electricity and hydrogen above their 10% return prices, making a greater return on investment.

When the hydrogen fueling station was fully utilized (500 FCVs), the options become even more attractive. Hydrogen could be sold at \$1.00/gallon, matching current wholesale gasoline with on-peak electricity sold to the grid at 6¢/kWh. In this case both state and federal highway taxes could be added to the hydrogen, as would be required in a mature FCV market.

The previous figure assumed old natural gas commercial rates in California (\$6.21/MBTU-HHV). The situation in Alaska would be much better, since natural gas has previously averaged only \$2.37/MBTU³. As shown in Figure 2, peak electricity could be sold at 10.3¢/kWh, with hydrogen from a fully utilized fueling station (500 FCVs) sold at only \$0.57/gallon equivalent. Even if only 100 FCVs were available, hydrogen could be sold at \$1.50/gallon with on-peak electricity sold at 6.3¢/kWh.

³These natural gas prices are based on 1998 data. Well-head prices for natural gas have escalated sharply in 2001, from roughly \$2/MBTU up to as much as \$10/MBTU before dropping back to the \$5 to \$6/MBTU range in March of 2001. Many analysts expect that the recent resurgence of natural gas drilling will roll back some of these increases, but the commercial rates for natural gas will probably increase more than analysts projected just one year ago.

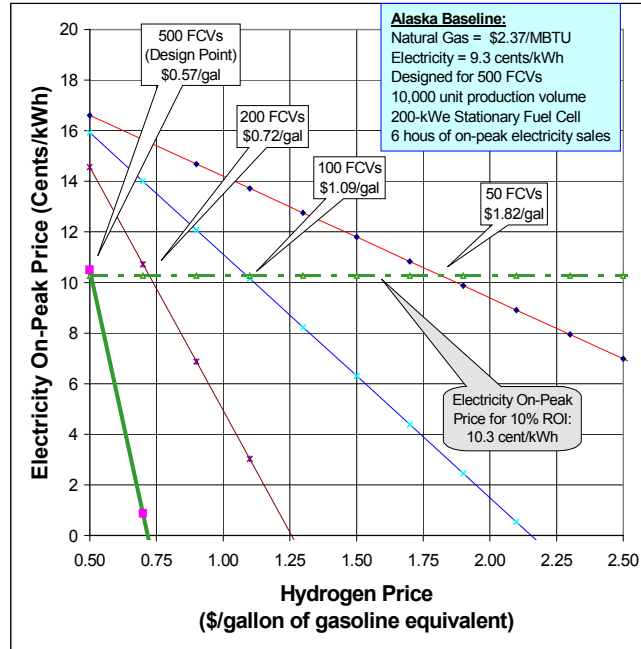


Figure 2. Estimated trade-offs in peak electricity and hydrogen prices in Alaska.

The previous two figures assumed that the utility bought back electricity during six hours of their peak load. Some utilities might be willing to pay more for peak electricity during a shorter period of time. Figure 3 illustrates the trade-off between electricity price and on-peak time for both California and Alaska. Thus a hydrogen fueling station owner in Alaska could make the goal of 10% return on investment by selling electricity at 10.3¢/kWh for six hours or for 20.6¢/kWh for three hours, etc.

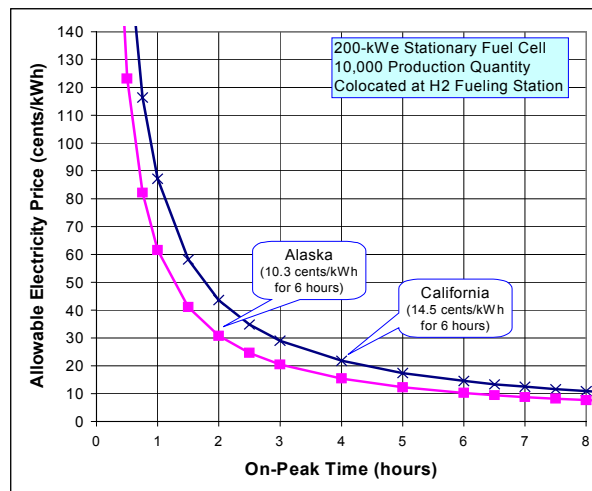


Figure 3. Allowable on-peak electricity price to make 10% real, after-tax return on investment as a function of the number of on-peak hours per day.

Electrolytic Hydrogen Assessment

DTI also previously estimated the cost of hydrogen produced by electrolyzing water using off-peak electricity (Thomas-1998d, 1999c & 1999d). As shown in Figure 4, the cost of hydrogen generated by steam reforming of natural gas is competitive with taxed gasoline for large fueling stations supporting more than 1,000 FCVs (or 125 vehicles refueled per day.) However, the cost of trucking in liquid hydrogen gets prohibitive for stations supporting less than 1,000 FCVs. On-site reforming of natural gas is competitive for stations supporting more than 100 FCVs, assuming the development of factory-built, small-scale steam methane reformers (scaling down existing industrial SMRs would not be competitive.) In fact, hydrogen from these low cost, factory-built SMRs would be competitive with wholesale gasoline per mile driven.⁴ That is, a driver of a conventional vehicle would pay as much for wholesale gasoline (before road taxes) per mile as the driver of a hydrogen-powered FCV.

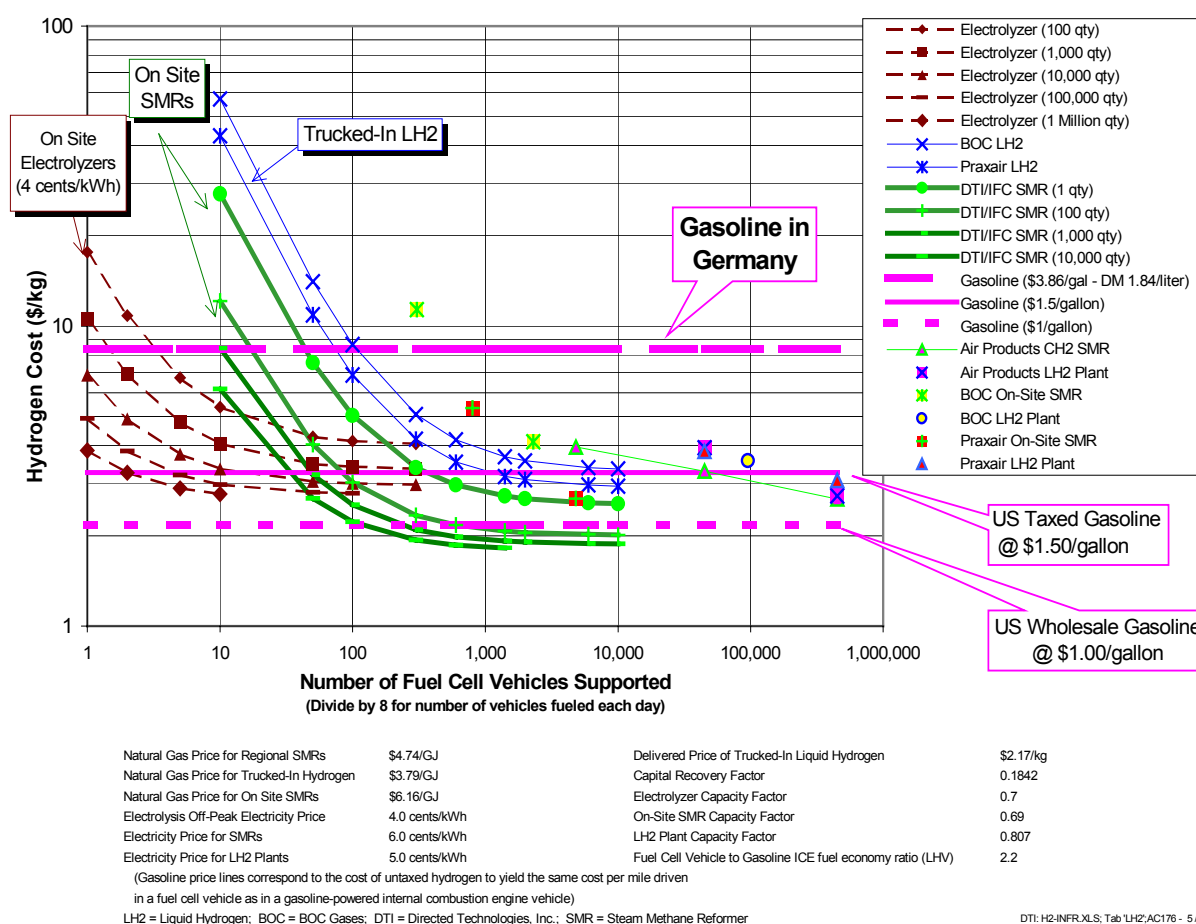


Figure 4. Estimated cost of 5,000 psi compressed hydrogen from various production sources, compared to the equivalent cost of gasoline on a per mile basis.

⁴The data in Figure 4 were updated from our previous reports to reflect increased cost of gasoline, natural gas and electricity.

For fueling stations supporting fewer than 100 FCVs, however, even the on-site SMRs could not compete with wholesale gasoline. In the early days of FCV market penetration, many fleet owners would have fewer than 100 FCVs. For example, a company with 200 vehicles might only convert 5 or 10 vehicles to run on hydrogen initially to test out this new technology. In this case electrolyzers would provide the lowest cost hydrogen as shown on the left side of Figure 4, assuming that off-peak electricity could be purchased for 4 cents/kWh. Thus electrolyzers could provide lower cost hydrogen for small fleets or for public fueling stations during the early phases of FCV market penetration.

However, electrolytic hydrogen has one major barrier in the United States: since over 55% of all U.S. electricity is generated from coal, using electrolytic hydrogen in a FCV in most parts of the U.S. would actually increase total greenhouse gas emissions compared to operating a conventional gasoline ICEV. Based on the average marginal U.S. grid generation mix, total greenhouse gas emissions would more than double for a FCV running on electrolytic hydrogen compared to the standard ICEV.

As the electrical generation grid moves to increased use of renewable electricity and/or nuclear power, the FCV powered by electrolytic hydrogen will eventually be superior to even a FCV running on hydrogen from natural gas. In this task, we analyzed the necessary changes in the utility grid generation mix that would result in greenhouse gas parity for the FCV running on electrolytic hydrogen compared to an ICEV of the same size.

The analysis of greenhouse gases from electrolysis should take into account the marginal utility generation mix. That is, adding a new electrical load such as a group of electrolyzers will require the electric utility to produce additional electricity. In general utilities run their lowest operating cost generators full time (if possible) as baseload. In general, this means turning on hydroelectric and any renewable energy first, followed by nuclear power, then coal, then natural gas, then oil and finally diesel fuel⁵. The marginal mix then depends on the time of day and the generation mix in a given region. Figure 5 illustrates the likely generation mix in Southern California before deregulation, based on the generators owned at that time by Southern California Edison and the Los Angeles Department of Water and Power. Between them, these LA utilities produced 36% of their electricity from natural gas, 32% from coal⁶, 22% from nuclear, and 10% from hydroelectricity. We have arbitrarily assumed that 40% of the natural gas is consumed in high efficiency (50% for air cooled and 54% for steam-cooled) combined cycle turbines, and 60% in single-cycle natural gas aeroderivative turbines at 35% efficiency for small units, to take into account the introduction of higher efficiency combined cycle turbines in the future. We added this distinction to illustrate that even as more combined cycle turbines are added, the older single-cycle turbines are moved to the top of the peak shaving list. As a result, adding new load such as an electrolyzer will necessarily mean more electricity from the older, less efficient plants during peak hours.

⁵This ranking from lowest cost to highest cost is based on operating costs only. On a life-cycle basis including capital recovery, natural gas turbines are less costly than coal-powered generators, while the coal costs less than natural gas per unit energy. Once the equipment is in place, however, the utilities tend to dispatch electricity on the basis of operating cost, not life cycle cost.

⁶Although there are no coal plants in California, these two utilities owned large coal plants in Utah and Nevada.

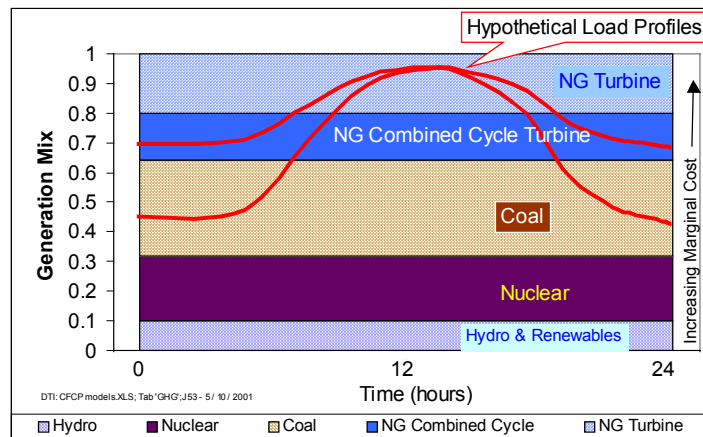


Figure 5. Illustration of likely marginal electronic grid generation mix in the Los Angeles area.

Returning to Figure 5, the two daily load lines illustrate the likely marginal grid mix for electrolyzers (and other new loads) – adding new loads will draw power from the generators just above the load profile at any time of the day. As new loads come on line, the utilities will increase output from the marginal (highest operating cost) generators. With the top load profile in Figure 5, this would imply that all electrolyzer electricity should be attributed to a mix of low efficiency and higher efficiency gas combined cycle turbines. No credit is given for either nuclear, hydroelectric or particularly renewable electricity, which is all baseload, operated 24 hours per day whenever possible. The lower load profile in Figure 5 is even worse. With this profile, the utilities would have to turn on coal generators at night to supply electrolyzers added to the grid. Thus off-peak electricity might be less expensive, but in this case it would produce considerably more greenhouse gases due to the increase in coal generator output.

Advocates of using electrolyzers to produce hydrogen have suggested that new renewable energy such as from wind turbines could be used to reduce greenhouse gases. In this concept, electricity from remote wind turbines would be wheeled to the local fueling station over the utility grid. These green electrons would then be converted to hydrogen for FCVs, which would then reduce GHGs by displacing gasoline-powered ICEVs.

From a societal viewpoint, however, this may not be optimum utilization for these green wind electrons. Another option is simply to displace electricity produced from existing electrical generators, thereby also reducing greenhouse gas emissions. As shown in Figure 5 above, displacing grid electricity even in California which has a high fraction of nuclear and hydroelectric power would cut down GHGs by reducing fuel burned in natural gas or even coal turbines. In fact, displacing grid electricity does reduce GHGs more than making hydrogen for FCVs as shown in Figure 6. Depending on the marginal grid mix, displacing grid electricity with wind power in the LA basin would reduce GHGs by about 600 to 800 grams of CO₂-equivalent for each kWh of wind electricity. This same kWh of wind electricity would produce enough electrolytic hydrogen to cut GHGs by only 300 to 500 grams of CO₂, depending on the type of electrolyzer and the fuel economy of the FCV relative to a gasoline ICEV. We show two types of electrolyzers in Figure 6: a conventional electrolyzer with atmospheric pressure hydrogen output, and an electrolyzer with 300 psia hydrogen output. The higher pressure electrolyzer reduces the compressor load, thereby using less electricity to compress the hydrogen to 7,000 psi for storage. We also show two fuel economy ratios: 1.7 to one and 2.2 to one. The 2.2

fuel economy improvement corresponds to our estimate for a mature FCV. Early FCVs will probably be less efficient, which would reduce the GHG savings from electrolytic hydrogen.

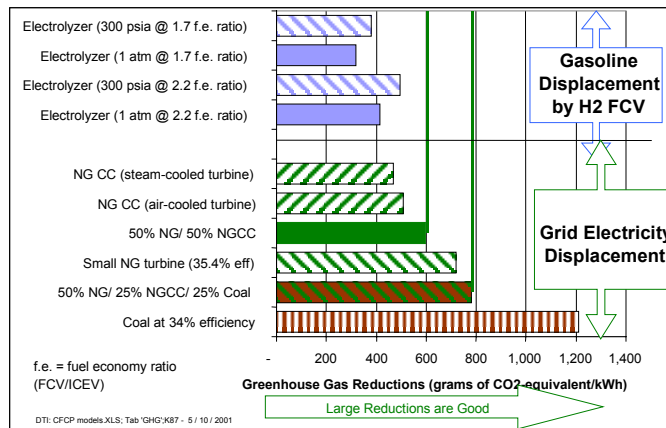


Figure 6. Illustration of greenhouse gas reductions, comparing the use of electrolytic hydrogen in FCVs to displace gasoline in ICEVs (upper four bars), with displacing grid (lower six bars).

Some proponents of electrolyzers have suggested that the grid could not accept wind power at night. If this were the case, then making hydrogen for use in FCVs would be a net reduction in GHGs. However, once a wind turbine is installed, a utility operator will always operate it 24 hours per day (or at least whenever the wind is blowing) as baseload, since it has the lowest operating costs. The operator will therefore turn down virtually any other generator at night to accept the low cost wind energy to minimize overall costs. Therefore wind power will not be rejected until such time that the grid has more wind electricity at night than the night time load. The key question for wind/electrolysis/hydrogen systems is when will wind power grow to equal the minimum utility off-peak load?

Projecting future utility grid mix is difficult, but we can make some general observations:

1. Current coal-based plants which produce over 50% of all U.S. electricity today are under-utilized, despite the fact that they can generate electricity at costs between 1 to 3¢/kWh, less than the cost of electricity produced by a new combined cycle gas turbine system. U.S. coal plant utilization has been averaging around 62%. Thus increased demand caused by electrolyzers could increase coal electricity production, the worst outcome from a GHG perspective.
2. Nuclear power generation was not expected to grow and may even have decreased over the next few decades as plants are retired and not replaced, again placing pressure to use more coal-based electricity. The new Bush administration will attempt to revive the nuclear power industry, but under the best political circumstances no new nuclear plants are likely for at least 15 years. Any reduction in nuclear power production would shift the marginal electricity mix toward more coal during off-peak hours where nuclear power may have dominated previously.
3. Most new generation capacity will be based on very efficient combined cycle gas turbines running on natural gas. Efficiencies up to 48% are feasible today, with projections as high as 54% forecast by some

observers. Gas turbines can also be cycled up and down in power quickly, making them the logical choice to handle peak power loads.

4. Even the most optimistic projections of renewable energy grid penetration do not show significant contributions over the next few decades.

Figure 7 illustrates the electrical generation mix that would be required to reduce greenhouse gases for hydrogen produced by electrolysis. The upper horizontal line indicates that the ICEV would produce about 415 grams/mile of CO₂-equivalent emissions. The lower horizontal line shows that hydrogen produced from natural gas would reduce GHGs by about 40%. The sloped lines project the GHGs for a direct hydrogen FCV running on electrolytic hydrogen from the power grid as function of the fraction of the marginal grid mix consisting of some combination of nuclear and renewables. If we start with the current average grid mix in the U.S. (not the marginal mix), then the fraction of renewables and nuclear would have to increase to about 60% before the FCV greenhouse gas emissions would be reduced to the level of the gasoline ICEV, and to about 74% renewables and nuclear to match the current greenhouse gas emissions of a FCV using natural gas-derived hydrogen.

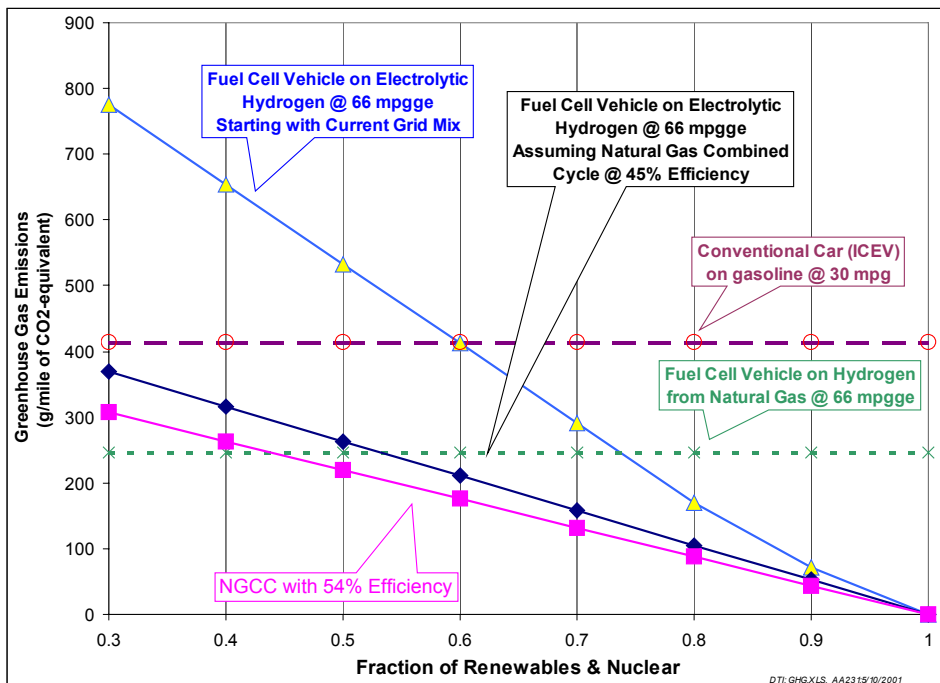


Figure 7. Greenhouse gas emissions from FCVs powered by electrolytic hydrogen, compared to ICEVs (upper horizontal line) and FCVs with hydrogen from natural gas (lower horizontal line)

The two lower sloped lines in Figure 7 correspond to the GHG emissions assuming that all marginal grid electricity came from natural gas combined cycle plants, operating at 45% efficiency (current technology) to 54% efficiency (projected potential with steam-cooled combined cycle natural gas turbines). In this case, renewables and nuclear would need to account for 50% of marginal power to 40% in the case of the 54% efficient combined cycle plants. From this analysis, we need to achieve more than 70% renewables plus

nuclear grid penetration with the existing grid, or some combination of large-scale introduction of natural gas combined cycle plants in conjunction with 40% to 50% renewables plus nuclear.

What is the likelihood of either combination? The standard energy forecasts by groups like the U.S. Department of Energy’s Energy Information Administration do not forecast any significant growth in renewables and nuclear by 2020, the end of their time horizon as illustrated in Table 3. We have also included some forecasts by other groups including the Gas Research Institute, Standard & Poor’s DRI and the WEFA. None of these forecasts show renewables and nuclear above 23% penetration by 2020.

Table 3. Projections of the average U.S. grid mix for 2015 and 2020.

Annual Energy Outlook 2000	Coal	Oil	NG	Nuclear	Renewables (Hydro)	Sum of Renewables & Nuclear
2015 - AEO Reference Case	52.1%	1.0%	25.7%	12.1%	9.1%	21.2%
2015 - AEO Low Economic Growth	52.5%	0.8%	24.5%	12.6%	9.6%	22.2%
2015 - AEO High Economic Growth	52.4%	1.3%	26.0%	11.5%	8.7%	20.2%
2015 - WEFA Group	39.6%	0.6%	41.1%	8.2%	10.5%	18.7%
2015 - Gas Research Institute	56.3%	0.7%	24.1%	9.9%	8.9%	18.9%
2015 - Standard & Poor's DRI	47.6%	2.8%	26.9%	12.9%	9.8%	22.7%
2020 - AEO Reference Case	52.1%	0.8%	28.5%	9.7%	8.9%	18.6%
2020 - AEO Low Economic Growth	52.4%	0.7%	27.1%	10.4%	9.5%	19.8%
2020 - AEO High Economic Growth	54.6%	1.3%	26.5%	9.3%	8.4%	17.7%
2020 - WEFA Group	38.8%	0.5%	43.5%	6.1%	11.1%	17.2%
2020 - Standard & Poor's DRI	46.1%	2.9%	30.3%	11.5%	9.2%	20.7%

One of the most optimistic projections for renewable energy was made by a group of environmental organizations⁷ in 1990. They published a report entitled “America’s Energy Choices,” outlining several scenarios. The most optimistic of these scenarios was their “climate stabilization” plan, which predicted the generation of 1,500 terawatt-hours of electricity from renewables by 2030, which would amount to 61% of all electricity generated in that year (this scenario also assumes a 50% reduction in electricity consumption, requiring far greater energy efficiency improvements than any other projection). However, actual renewables have fallen well below the American’s Energy Choices pathway in the ten years since it was published, as shown in Figure 8. In fact, actual introduction of renewables has been negligible on a national scale compared to total grid energy production. The actual renewable energy (98% hydroelectric) has in fact fallen below the AEC “reference case,” the least optimistic projection for renewables, and is less than half the projected level for the climate stabilization scenario. At the very least, we have lost a decade in pursuing the aggressive climate stabilization pathway, and there is very little to indicate that the U.S. will embark on this pathway anytime soon.

⁷The AEC group included the Alliance to Save Energy, the American Council for an Energy-Efficient Economy, the Natural Resources Defense Council and the Union of Concerned Scientists.

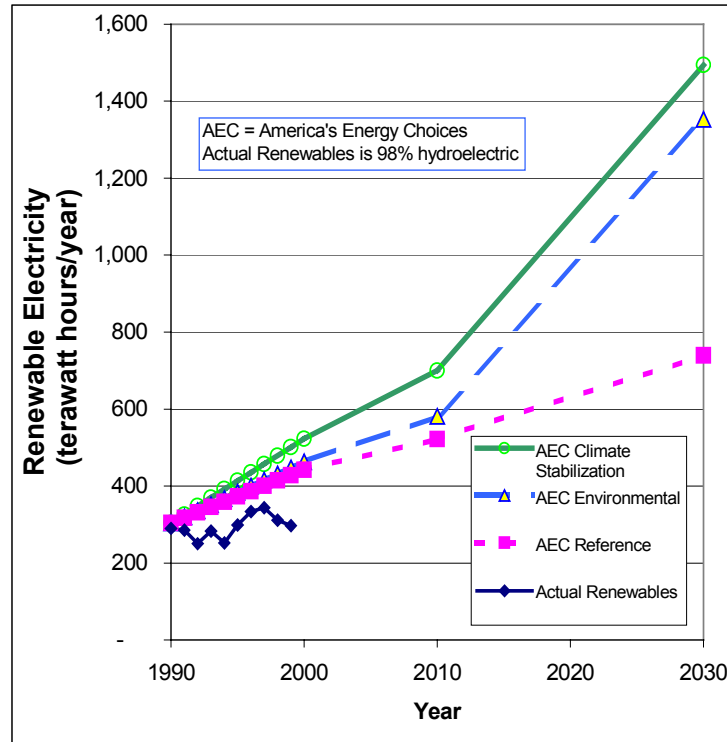


Figure 8. Comparison of the AEC 1990 projections for renewable energy growth with the actual renewable electricity over the last decade.

We also looked at several longer range projections to the year 2050 by two organizations: the World Energy Council (WEC) and the Electric Power Research Institute (EPRI). As shown in Figure 9, only the most optimistic of these scenarios would yield a significant reduction in GHGs from direct hydrogen FCVs using electrolytic hydrogen by the year 2050. And none of these pathways would provide lower GHGs than a FCV using hydrogen from natural gas today. However, this figure is based on the average utility grid mix projected for 2050, not the marginal grid mix. Depending on the circumstances at that time, the marginal grid mix could produce lower GHG emissions.

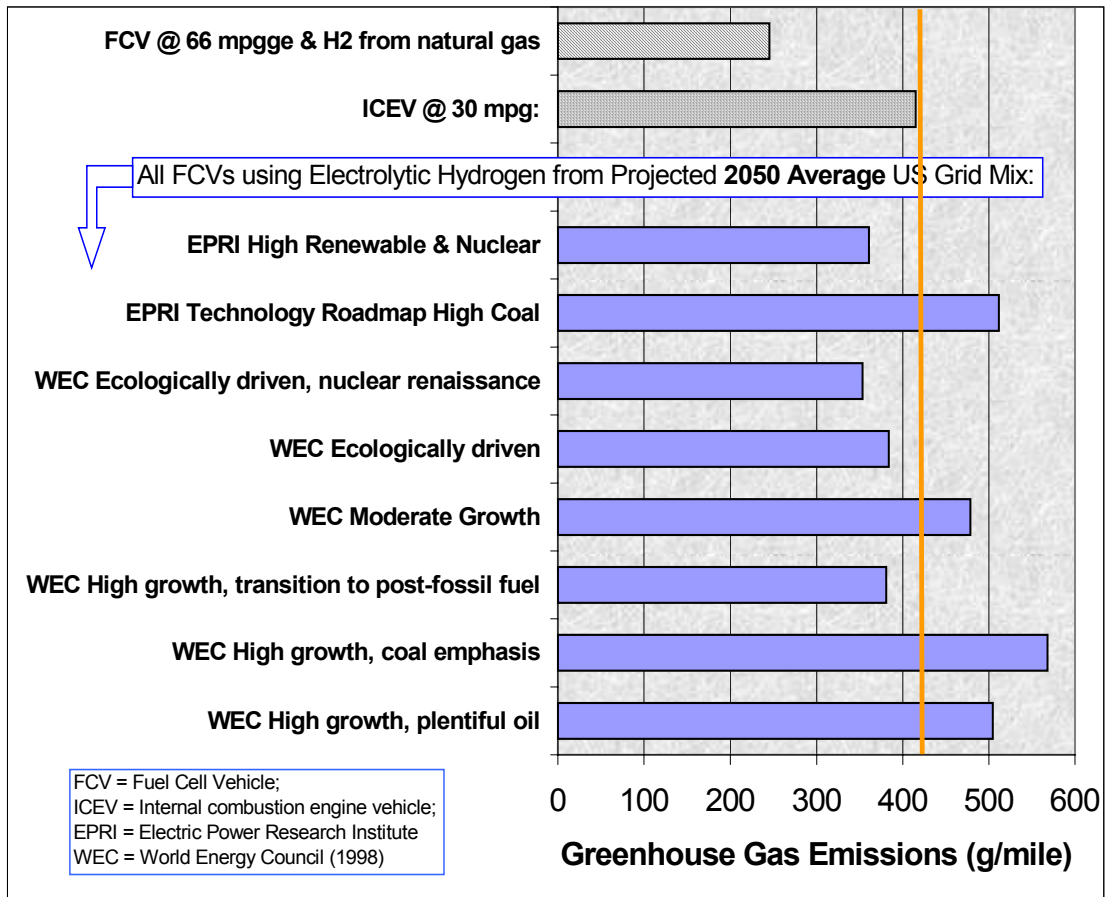


Figure 9. Estimated greenhouse gas emissions from a FVC using electrolytic hydrogen produced from the projected average utility grid mix in 2050, compared to gasoline ICEVs and FCVs powered by hydrogen made from natural gas.

We conclude that electrolytic hydrogen in the U.S. is unlikely to reduce greenhouse gas emissions when consumed by a FCV for at least three decades, and possibly longer, unless the country begins to aggressively invest in renewable energy or nuclear energy. There may also be some regions of the nation such as the Pacific Northwest where the grid is sufficiently “green” to produce a net reduction of greenhouse gases. In addition, off-grid applications such as a wind or PV system connected directly to an electrolyzer would essentially eliminate any greenhouse gas emissions.

The situation is not much better in most parts of the industrialized world. Most of central Europe uses considerable coal in their electrical generation mix. The five major nations with electrical generation capacity favorable to electrolysis are Brazil, Canada, France, Norway and Sweden, as shown in Table 4 below. All other major nations of the world would produce more greenhouse gases with electrolysis than by burning gasoline in current vehicles.

Table 4. Electricity grid mix (percentage) for major nations (consuming over 100 billion kWh) in 1997

	Electricity Production (Billion kWh)	Hydro	Coal	Oil	Gas	Nuclear
Australia	182.6	9.2	80.1	1.3	7.6	-
Brazil	307.3	90.8	1.8	3.2	0.4	1.0
Canada	575	61.1	17.4	2.4	4.1	14.4
China	1,163.4	16.8	74.2	7.2	0.6	1.2
France	498.9	12.5	5.2	1.5	1.0	79.3
India	463	16.1	73.1	2.6	6	2.2
Italy	246	16.9	10	46	24.9	-
Japan	1,029	8.7	19.1	18.2	20.5	31
Korea	244	1.2	37.4	16.8	13	31.6
Mexico	175	15.1	10	54.3	11.5	6
Norway	110	99.4	0.2	-	0.2	-
Poland	141	1.4	96.7	1.4	0.2	-
Russia	833	18.8	16.8	5.3	45.3	13.1
Saudi Arabia	104	-	-	57.5	42.5	-
South Africa	208	1	92.9	-	-	6.1
Spain	186	18.6	34.3	7.2	8.8	29.8
Sweden	149	46.2	1.9	2.1	0.5	46.8
Turkey	103	38.5	32.8	6.9	21.4	-
Ukraine	178	5.5	27.6	4.3	17.9	44.7
UK	344	1.2	34.8	2.3	31.3	28.5
US	3,670	9	53.8	2.9	13.8	18.2

Hydrogen Produced from Methanol On-Site⁸

We explored the economics of using methanol as the hydrogen carrier from remote low-cost natural gas sources to the fueling station⁹. That is, methanol would be reformed at the local fueling station to provide hydrogen for a direct hydrogen FCV. The intent of this option would be to exploit the low cost stranded natural gas from remote sites including sea-based oil platforms. The natural gas that was previously flared for lack of a market would be converted to methanol, shipped by tanker ship to the major nations, and then to the local fueling station where it would be converted to hydrogen for storage on the FCV. We explored two aspects of the methanol route: the cost of the stationary methanol reformer, and the likelihood of oil and gas companies converting stranded natural gas to methanol instead of the other options for monetizing remote natural gas. This particular option might also have benefits should automobile manufacturers build both methanol and hydrogen-powered FCVs.

Capital Cost Estimates for Small-Scale Stationary Methanol Fuel Processors

The chemical conversion of methanol to hydrogen-rich gas mixtures has been studied intensively since the petroleum crisis of the 1970's. Two principal pathways have traditionally been evaluated, steam reforming (SR) of methanol with water and autothermal reforming (ATR) of methanol with air and water. The former has been demonstrated widely, and has well-known operating parameters over the preferred catalysts, mixed oxides of copper and zinc stabilized by alumina. The latter pathway has been demonstrated at Argonne National Laboratory and by Johnson Matthey PLC in Great Britain. These efforts in autothermal reforming have been conducted more recently, and less is known about catalyst durability, a central problem with the copper-based catalysts used in methanol systems, especially at the high temperatures characteristic of autothermal reforming. Whether the conversion is accomplished through SR or ATR, methanol conversion requires a less sophisticated chemical process train operating at lower temperatures than competing hydrogen production techniques based upon other fuels such as natural gas. Lower temperature methanol reformers should have lower capital cost compared to natural gas, naphtha, or gasoline reformers. This study compares the likely manufacturing cost of SR and ATR reformers based on traditional catalyst compositions in combination with commercially available pressure swing adsorption (PSA) gas cleanup equipment.

The reformers are sized such that a packaged system could support a 50-vehicle fleet. Assuming that each vehicle travels 12,000 miles per year, each vehicle would require on average 0.5 kg of hydrogen fuel per day¹⁰. If a capacity factor of 69% is assumed to cover daily and seasonal demand variation, the 50-car station would produce at least 36 kg/day at peak capacity. In previous research conducted by the authors (Thomas-1997a), a small-scale reformer system for natural gas included six reforming modules with a capacity of 8 kg/day each.

⁸Frank Lomax is the primary author of this section

⁹This task was suggested by Dave Nahmias, at the time Chairman of the DOE Hydrogen Technical Advisory Panel (HTAP).

¹⁰This hydrogen consumption assumes a 5-passenger vehicle such as a Ford AIV (aluminum intensive vehicle) operating on a 1.25 times accelerated EPA combined cycle (45% highway and 55% city driving). We estimate a fuel economy of 66 mpgge on this accelerated driving schedule.

This represented a capacity factor of just over 50%, but allowed one entire unit to be removed for service without interrupting operation of the refueling station. Further, the manufacture of identical subassemblies allows higher volume manufacturing techniques than would otherwise be appropriate. In this study, it is assumed that reformers are manufactured to serve 500,000 vehicles that are assumed to be sold over a six-year period. It is assumed that the vehicles are sold at the rate of 83,000 units per year, and that a total of 10,000 50-car refueling stations are required over that same period. For reformers employing six identical subassemblies, 10,000 subassemblies would be produced each year.

The general configuration of the refueling station is shown in Figure 10. The reformer subassemblies produce hydrogen-rich reformat gas at elevated pressure (7 bar – 20 bar). This gas is cooled in an intercooler, condensate is removed in a liquid trap, and the dry, cool gas is delivered to the PSA unit. Here, the impurities are adsorbed onto a high surface area adsorbent, and the clean hydrogen passes through the bed with a nominal pressure loss (< 1 bar). Periodically the pressure on the bed is then reduced, and the impurities are desorbed and returned to the system for subsequent combustion to provide energy to the process. The clean, pressurized hydrogen is then delivered to the compression and storage subsystems for greater pressurization, storage and subsequent delivery to the vehicles during refueling. The hydrogen compressor and storage tank costs were considered in previous research by the authors, and will be used again in this study. The PSA unit assumed here is based on the HyQuestor™ 605 that is manufactured by QuestAir Technologies¹¹. Also included in the refueling system is an electronic controller and a compressed nitrogen supply system for valve operation and safety purging¹². It is assumed here that the reformers are operated continuously at some level in order to maintain the catalyst in the reduced state. If intermittent operation is desired, a hydrogen supply system and feed valves will be required to reduce the catalyst.

¹¹ QuestAir Technologies was formerly named Questor Industries, Inc.

¹² The nitrogen employed will require an oxygen content of about 100 ppm for shutdown purposes, as the reduced copper catalysts are pyrophoric, and must be gradually returned to their stable, oxidized state upon shutdown.

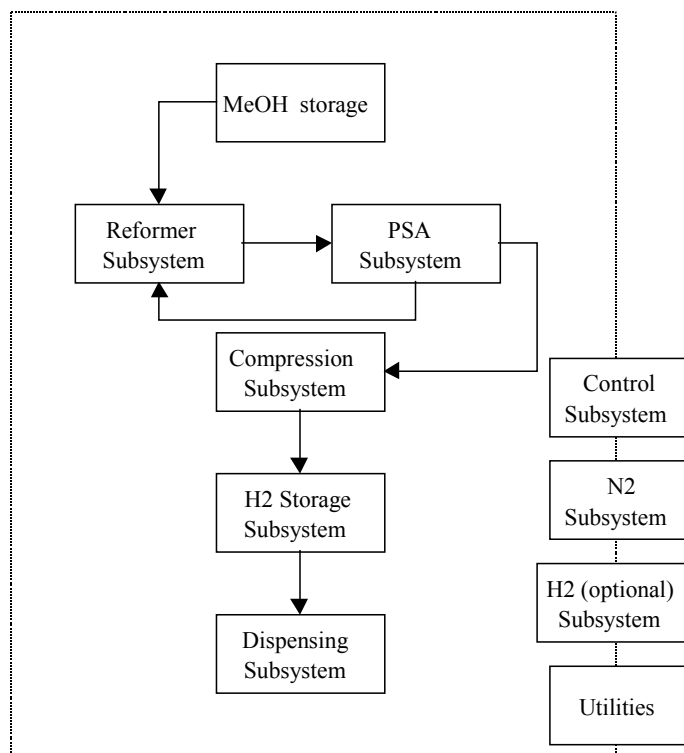


Figure 10. Methanol-based Hydrogen Fueling Station Process Flow

Because the SR and ATR MeOH reformer subsystems are fundamentally different in their design, they will be addressed separately in the following paragraphs. The balance of the refueling system is essentially identical for the two technologies, and is based on previous research conducted by the authors that will be briefly summarized after the detailed discussion of the reformer subsystems.

Methanol Steam Reformer Subsystem

Methanol steam reforming is typically carried out over a “mixed oxide” catalyst containing oxides of copper, zinc and aluminum. The formulation and mechanical form of these catalysts are typically similar to those for water gas shift reactors in high temperature fuel reformer systems such as those employed for the reformation of natural gas or naphtha. Operation in the steam reforming mode on such catalysts is limited at low temperature by the formation of condensate on the catalysts at the dew point for the pressure of operation, and on the high side by sintering of the catalyst, which becomes appreciable above 260°C (Pepley-1997). Because the methanol reforming reaction is endothermic, heat transfer must be accomplished between a high-temperature gas stream and the cooler reactants.

The hot gas is typically produced by combustion of unused hydrogen, carbon monoxide and methanol in the tailgas from the PSA purification system, with oxygen from air. The adiabatic flame temperature of this gas is typically well above the 260°C temperature limit for the mixed oxide catalysts. Further, heat transfer between the gas and the reforming catalyst is difficult to achieve. For these reasons, a number of groups have demonstrated methanol steam reformers that utilize an intermediate heat transfer fluid such as a high-

temperature oil that is heated in a separate heat exchanger by the combustion gas and then passed over tubes containing the reforming catalyst and the reacting steam-methanol mixture.

Thus, a methanol steam reformer system usually comprises the following:

- a heat exchange reactor that allows for rapid heat exchange between a heat transfer fluid and the catalyst zone where reaction occurs
- a separate heat exchanger for heating the heat transfer fluid with hot gases
- a combustor for burning the fuel gas in air prior to heating the heat transfer fluid.
- a vaporizer where the fuel/water mixture is boiled and superheated to the reactor inlet temperature
- an intercooler where the hot reformat gas can be cooled by the incoming combustor air before being sent to the PSA unit
- a condensate trap for removing condensed water and methanol
- an air blower to provide combustion/cooling air
- a water deionization system
- feed and recirculation pumps for the various feedstocks

Additionally, the system requires control thermocouples, pressure relief devices, and appropriate valves to control the process flows. A system of this type is illustrated in Figure 11. Valves and sensors are omitted from this diagram. This proposed system is a hybrid of the high temperature, adiabatic methanol steam reformer patented by Engelhard (Beshty-1990) and the essentially isothermal reformers used by other workers¹³.

¹³ The isothermal approach seems to have been first patented by Hidetake Okada of Nippon sanso Kabshiki Kaisha in Tokyo, Japan. This patent # 4,865,624 is dated Sep. 12, 1989. This design has subsequently been used by Amphlett, *et al* of the Royal Military College of Canada and Daimler Benz Ballard (dbb) in their NECAR 3 system.

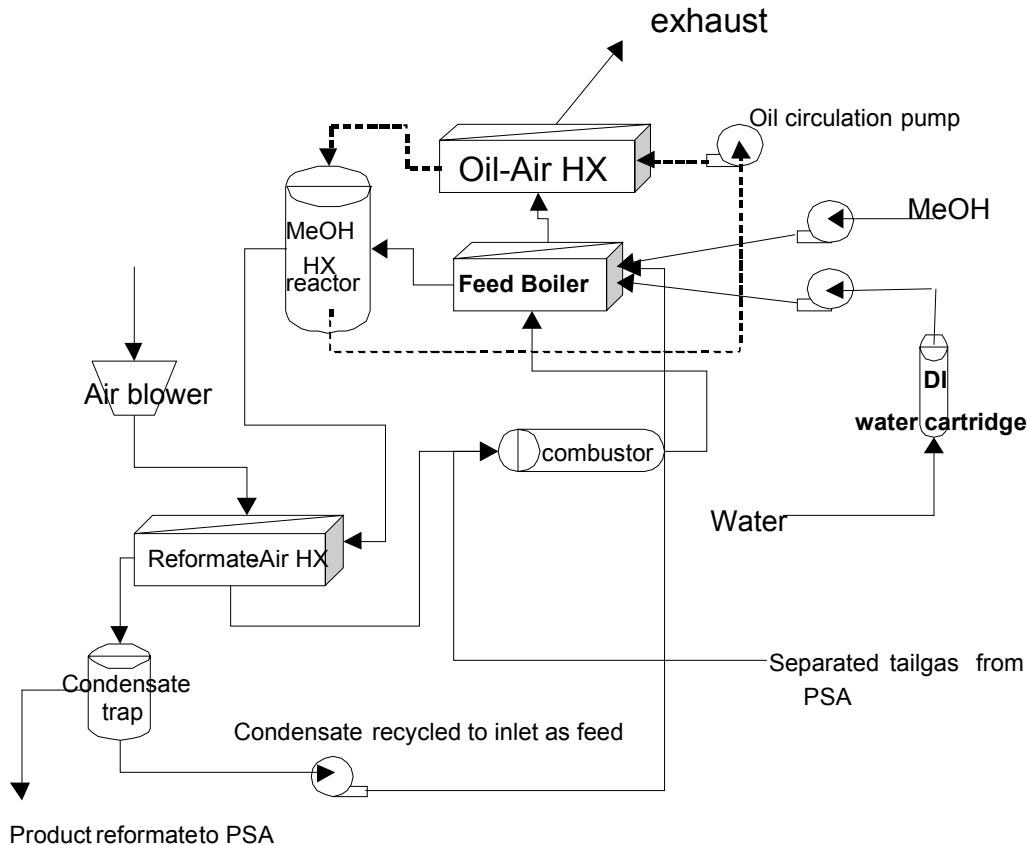


Figure 11. Methanol Steam Reformer System Schematic

Excellent research by Amphlett and Pepley, *et al* (1997) has provided kinetic data for such oil-heated methanol steam reformers. Extrapolation from their data suggests that a methanol steam reformer based on mixed oxide catalysts and operated in a high pressure regime suitable for use with a PSA system (15 – 20 bar) would require roughly 0.2 kg of catalyst per kW thermal of hydrogen produced. This is based upon a reformer utilizing 12.7 mm o.d. reformer tubes. Their data suggest heat transfer limitations, which may make a reactor based upon smaller tubes even more compact. If each subassembly is designed to produce 8 kg of hydrogen per day, and the PSA system recovers 80% of the hydrogen produced (McLean-1997), then each subassembly will require approximately 2.75 kg of catalyst if 12.7 mm reformer tubes are used. Whereas the industrial catalysts typically used in research are nominally 3mm right cylindrical extrudate with a specific gravity of about 1.35, it is assumed here that a finer extrudate is used in the small-scale reformers to facilitate rapid heat transfer, good flow distribution, and easy reactor loading. The specific gravity of such a catalyst is assumed to be approximately 2. No improvements in kinetics are expected, as reactor testing has confirmed that the industrial catalysts have a high effectiveness factor (Amphlett-1988).

Table 5 illustrates the amount of tubing of each size required for each subassembly. These calculations assume that a spiral tube-in-tube geometry is employed. This type of construction requires a minimal number of seals, all of which can be readily and inexpensively accomplished through either manual or automatic gas

tungsten arc welding (GTAW). Spiral tube heat exchangers are often employed in the chemical process industry, but are not usually considered for mobile applications because they are ill suited for operating environments involving mechanical shock as the tubing is not well-supported. In the proposed design, the inner reformer tubes are first inserted into a larger diameter outer tube then the assembly is bent using an automatic tube-bending machine. For the purposes of this study a 3-pass design using 12.7 mm o.d. tubes as the reformer tubes and 38 mm o.d. tubing for the outer tube is assumed. In this configuration, tubing would have to be shipped in 5 m (~15') lengths, which is feasible. The coiled tubing can then be supported in a protective housing formed from 20 cm o.d. tubing. The tubes are supported on stamped frames that support each loop at four points. The supports can be attached to the tube bundle, then riveted to the protective housing. Insulation can also be provided between the tube bundle and the housing wall to minimize heat losses. It is assumed that ceramic felt insulation is employed for that purpose. Figure 12 shows a schematic view of the completed spiral heat exchange methanol steam reformer.

Table 5: Tube geometry for methanol steam reformers

Tube geometry	10 mm (0.375")	12.7 mm (0.5")
volume per length (cc/m)	47	94
catalyst mass per length (g/m)	94	187
total length required for subassembly	21.2	14.7
# of 15 cm diameter loops required, 1 pass	45	31
# of 15 cm diameter loops required, 2 pass	23	16
# of 15 cm diameter loops required, 3 pass	15	10

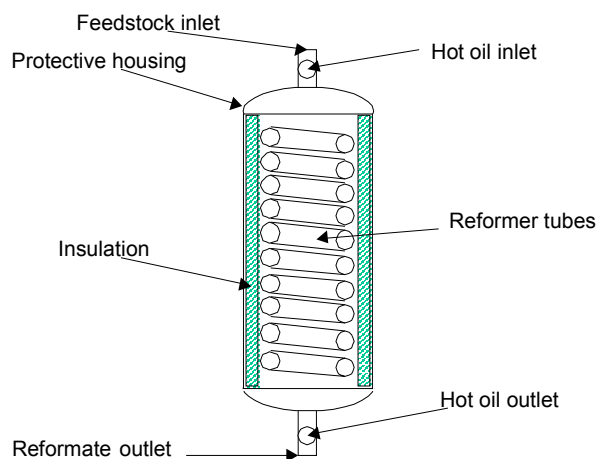


Figure 12. Spiral Methanol Steam Reformer Schematic

Construction of a large number of compact heat exchangers could present a manufacturing cost obstacle, especially if each unit required separate tooling, materials of construction, etc. For the purposes of this study, it is assumed that brazed plate-fin heat exchangers with identical plate dimensions are used for all of the system heat exchangers. The capacity of the individual units is then adjusted by increasing or decreasing the number of plates used. It is assumed that 25 cm by 10 cm plates are used with each “plate” including a 0.5 mm separator plate, a 2.4 mm thick manifolding frame, and a stamped finsheet 23 cm x 7.6 cm by 2.4 mm

high. The heat exchanger fins are assumed to be spaced 22 fins per inch and stamped from 0.1 mm (0.004”) thick stainless steel foil¹⁴. We assume that 409 stainless steel is used, and that the separator plates are clad with nickel brazing alloy. This type of construction has been demonstrated industrially for maximum temperatures up to 550°C. The stamped components are assembled and brazed in a continuous hydrogen belt furnace.

The combustor uses a combustion catalyst to burn the tailgas from the PSA unit to provide process heat for the reformer system and to reduce emissions of pollutants such as carbon monoxide. The combustor is also used during startup to bring the reformer components up to temperature, and must thus have a preheater and a means of delivering unreacted liquid methanol. The combustor comprises the following:

- a catalyzed monolith loaded with a combustion catalyst such as Pd-Pt on -alumina
- a sheet metal housing that contains the catalyst and allows mounting to the structural frame
- a refractory liner to protect the housing and fuel injection system from temperature excursions
- a low pressure fuel injector to deliver atomized liquid methanol
- an electric heating element (automotive glowplug) to bring the combustion catalyst to light-off temperature during startup

The methanol steam reformer requires 18 feed and circulation pumps that deliver reactants, recycle condensate, circulate heating oil, and deliver neat methanol for startup. The oil is circulated with a gear pump, since this type of pump is well-suited to handling high-temperature fluids at moderate pressure head. A gear pump with a fixed-speed, 110 VAC drive is assumed. For recycling condensate and metering methanol and water at high pressure, OEM-style metering pumps like those supplied by FMI are assumed. These pumps will allow a nominal delivery pressure of 10 bar. It is assumed that both the methanol and water feed pumps are driven by a single variable speed 110 VAC drive, as their delivery ratios are fixed. The condensate pump is driven by a fixed-speed 110 VAC drive that is controlled by a float switch. The condensate trap is a simple stainless steel vessel with a float switch.

The system also requires a variety of valves, relief devices and temperature probes. A back-pressure regulator is employed to control delivery of reformat product to the PSA system. A zero back-flow regulator will also act as a check valve to protect the reformer system from over-pressure should a failure occur in the downstream processes. A nitrogen purge solenoid valve is required for safety reasons should an over-temperature or over-pressure situation occur. A hydrogen delivery solenoid valve is also required for system startup. A minimum of two pressure relief valves are required, one for the reactant loop and one for the pressurized heat transfer fluid. For full code compliance, a relief device of some kind must be provided on each high pressure device or one device each for the evaporator, oil heater, reactor, and intercooler. All four of the relief valves can be reseating valves with high-temperature seals such as Kalrez. A minimum of five control thermocouples are necessary: in the combustor, after the combustor, in the air stream after the evaporator, in the hot oil loop after the oil heater, and in the reformat outlet. It is assumed that an automotive ECU-type controller is supplied for each subassembly, and that this controller interacts with the refueling

¹⁴ Fins of this type can be produced using machinery provided by Robinson Fin Machines, Inc. that is capable of stamping 300 fins per minute, or ~35 cm of 23 cm wide fin material per minute.

station control system.

The manufacturing cost of the system is estimated based upon the Design For Manufacture and Assembly (DFMA)¹⁵ techniques pioneered by Boothroyd and Dewhurst and used previously by the authors to estimate manufacturing costs for various systems. The estimated cost and bill of materials for the steam reformer system is shown in Table 6. Surprisingly, this cost is higher than that previously estimated by the authors for a steam methane reformer subassembly that operates at much higher temperature. Analysis of the estimates shows that a significant cost is incurred as a result of pumps for each subassembly, over \$500. This suggests that one pathway to reduce cost would be to implement a centralized pumping concept as applied to the steam methane reformer. Also, the fact that this system is configured to operate with a PSA system instead of a high-temperature metallic membrane leads to the requirement for intercooling, condensate recovery, and condensate recycle. All of this suggests that the totally modular approach that proved appropriate for steam methane reforming using a high-temperature metal membrane may not be appropriate for a steam methanol reforming system.

¹⁵DFMA is a registered trademark of Boothroyd Dewhurst, Inc.

Table 6. Budgetary estimate of the steam methanol reformer subassembly

assembly name	component name	usage	make/buy	material	finished part dimensions (cm)				part characteristics							total unit cost before	marked-up unit cost	total cost w/markups	assembly mfg
					L	W (od)	D (id or t)	s.g.	mass (kg)	volum e (L)	material cost (\$/kg)	part material cost	mfg. Cost						
steam reformer																			
	reformer tube	3	buy	316L	500	1.27	1.09	7.9	1.317	0.167	\$6.60	\$8.69	\$0.50	\$9.19	\$13.22	\$39.65			
	heat exchange jacket	1	buy	316L	498	3.8	3.6	7.9	4.571	0.579	\$6.60	#####	\$0.50	\$30.67	\$44.08	\$44.08			
	end boss fitting	2	make	316L	5	3.8	0	7.9	0.448	0.057	\$3.30	\$1.48	\$5.00	\$6.48	\$8.10	\$16.19			
	outer housing	1	make	316L	57	20	19.8	7.9	2.814	0.356	\$6.60	#####	\$1.00	\$19.57	\$24.46	\$24.46			
	end dome	2	buy	316L	5	20	0.1	7.9	0.496	0.063	\$6.60	\$3.27	\$1.00	\$4.27	\$6.14	\$12.29			
	tube support	4	buy	316L	57	6	0.1	7.9	0.27	0.034	\$6.60	\$1.78	\$0.25	\$2.03	\$2.92	\$11.69			
	insulation blanket	1	make	ceram fiber	57	20	16	0.5	3.222	6.443	10.76/sqm	\$3.85	\$0.02	\$3.87	\$4.84	\$4.84			
	catalyst	1	make	G66B					2.75	1.375	#####	#####		\$37.13	\$46.41	\$46.41		#####	
evaporator assembly																			
	separator plate	11	buy	409	25	10	0.05	7.8	0.099	0.013	\$2.00	\$0.20	\$0.27	\$0.47	\$0.67	\$7.39			
	fin sheet	11	buy	409	23	23.4	0.01	7.8	0.043	0.005	\$4.00	\$0.17	\$0.10	\$0.27	\$0.39	\$4.27			
	manifold frame	11	make	409	25	10	0.24	7.8	0.474	0.06	\$1.50	\$0.71	\$0.10	\$0.81	\$1.01	\$11.15			
	end plate	2	make	409	25	10	0.24	7.8	0.474	0.06	\$1.50	\$0.71	\$0.10	\$0.81	\$1.01	\$2.03		\$6.25	
oil heater assembly																			
	separator plate	11	buy	409	25	10	0.05	7.8	0.099	0.013	\$2.00	\$0.20	\$0.27	\$0.47	\$0.67	\$7.39			
	fin sheet	11	buy	409	23	23.4	0.01	7.8	0.043	0.005	\$4.00	\$0.17	\$0.10	\$0.27	\$0.39	\$4.27			
	manifold frame	11	make	409	25	10	0.24	7.8	0.474	0.06	\$1.50	\$0.71	\$0.10	\$0.81	\$1.01	\$11.15			
	end plate	2	make	409	25	10	0.24	7.8	0.474	0.06	\$1.50	\$0.71	\$0.10	\$0.81	\$1.01	\$2.03		\$6.25	
intercooler assembly																			
	separator plate	21	buy	409	25	10	0.05	7.8	0.099	0.013	\$2.00	\$0.20	\$0.27	\$0.47	\$0.67	\$14.11			
	fin sheet	21	buy	409	23	23.4	0.01	7.8	0.043	0.005	\$4.00	\$0.17	\$0.10	\$0.27	\$0.39	\$8.15			
	manifold frame	21	make	409	25	10	0.24	7.8	0.474	0.06	\$1.50	\$0.71	\$0.10	\$0.81	\$1.01	\$21.29			
	end plate	2	make	409	25	10	0.24	7.8	0.474	0.06	\$1.50	\$0.71	\$0.10	\$0.81	\$1.01	\$2.03		\$8.75	
combustor assembly																			
	bottom housing	1	make	316L	30	10.16	10	7.9	0.6	0.076	\$6.60	\$3.96	\$1.00	\$4.96	\$6.20	\$6.20			
	top housing	1	make	316L	20	10.16	10	7.9	0.4	0.051	\$6.60	\$2.64	\$1.00	\$3.64	\$4.55	\$4.55			
	refractory liner	1	make	fiberfrax	40	10	7.5	1	1.374	1.374	\$3.00	\$4.12	\$1.00	\$5.12	\$6.40	\$6.40			
	Pt-Pd on ZTM	1	buy		20	7.5	0	0.974	0.86	0.883	\$81/L	#####		\$71.53	\$89.42	\$89.42			
	glowplug	1	buy											\$10.00	\$14.38	\$14.38			
	low pressure fuel injector	1	buy											\$5.00	\$7.19	\$7.19		#####	
pumps, valves and misc.																			
	condensate pump and drive	1	buy											\$50.00	\$71.88	\$71.88			
	condensate trap and float	1	buy											\$50.00	\$71.88	\$71.88			
	MeOH & water pump	2	buy											\$35.00	\$50.31	\$100.63			
	variable speed motor	1	buy											\$100.00	\$143.75	\$143.75			
	gear pump and drive	1	buy											\$75.00	\$107.81	\$107.81			
	ASME relief valve	4	buy											\$5.00	\$7.19	\$28.75			
	backpressure regulator	1	buy											\$20.00	\$28.75	\$28.75			
	gas feed solenoid	2	buy											\$20.00	\$28.75	\$57.50			
	k-type thermocouple	5	buy											\$5.00	\$7.19	\$35.94			
	ECU	1	buy											\$240.00	\$345.00	\$345.00			
subtotal																\$1,415	#####		
plumbing allowance																		\$100.00	
total																\$1,567.39			

If the system were modified to a slightly more conventional layout where the combustor, intercooler, oil heater, and vaporizer functions were centralized, several advantages might accrue. First, the number of feed pumps required would be reduced to three per refueling station instead of eighteen. The number of combustor units would be reduced to one from six, and the number of oil feed pumps would be similarly reduced. The reactors, which are readily manufactured using high-volume techniques, would remain modular, and they could either be operated as independent loops through the use of on-off valves in the reactant and coolant loops, or they could be operated at varying space velocity. The provision of valves would be more desirable as it would better facilitate removal of individual units for repair. The economies of scale lost in the heat exchanger production would be essentially negligible, as the unit elements of the heat exchangers would

remain identical, and be produced in similar volumes. The units would likely be batch brazed at higher cost, but the difference is likely to be rather small as the batch furnace would be run semi-continuously as roughly 25 large heat exchangers would have to be produced per working day. This may require two furnaces or more as the cycle times for such components can be several hours. The impact on the cost of the pumps and valves is more difficult to assess, as these components then become essentially low-production, bought components, for which overhead charges become much more substantial. A detailed analysis of the cost of a more traditional system is beyond the scope of the present study, but the evidence suggests that this approach may offer some benefits for a low-temperature methanol steam reformer refueling system operated with PSA cleanup.

Autothermal reformer subsystem

Autothermal reforming of methanol with oxygen from air has been demonstrated by two principal groups. Kumar and Ahmed of Argonne National Laboratory have demonstrated autothermal reforming over mixed oxide catalysts like those used in steam reforming¹⁶, while Jenkins of Johnson Matthey used copper on silica supports with a small amount of palladium on silica for light-off purposes (Jenkins-1988). General Motors later demonstrated a scaled-up version of the Argonne unit as part of their methanol fuel cell vehicle development work. Much less data are available regarding the life-cycle durability and operating characteristics of autothermal methanol reformers than for steam reformers. However, research results suggest that the units demonstrated to date require roughly 0.1 to 0.17 kg catalyst per kW hydrogen production. If we consider the 80% recovery in the PSA system and the fact that sintering in the higher temperature (> 400°C) ATR process may reduce activity, the 2.75 kg per subassembly figure used for the steam reformers seems reasonable. Because there is still significant energy in the tailgas not recovered from the PSA unit, the ATR system is not vastly different from the steam reforming system presented earlier (Figure 13).

¹⁶ Kumar and Ahmed, "Development of a catalytic partial-oxidation reformer for methanol used in fuel cell transportation systems," TOPTEC presentation, Sante Fe, NM, March 28-29, 1995.

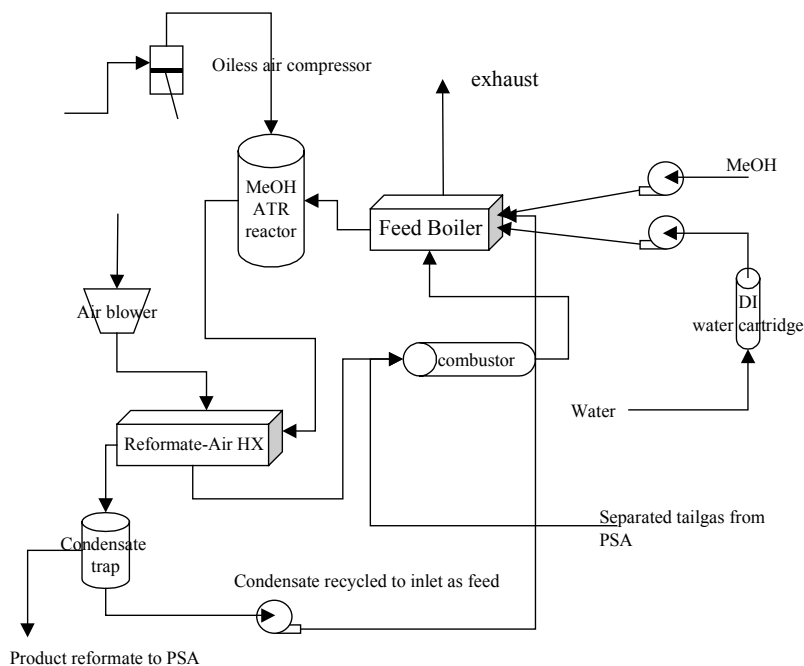


Figure 13. Methanol Autothermal Reformer System Schematic

An oil heater is not required since the system generates heat internally. The heat in the tailgas is used to vaporize and superheat the methanol and water feed, although the degree of superheat is likely larger than in the case of the steam reformer. An oil-free air compressor is added to supply compressed air to the system at elevated pressure (7 to 10 bar). The product intercooler is also likely larger, as the reformat inlet temperature will be higher than in the steam reformer. The combustor is unchanged, as are the methanol and water feed pumps and condensate recycle pumps. A slightly smaller number of relief valves and control thermocouples are required in the simpler ATR system. The major difference between the two systems is the cost and complexity of the reactor itself, which is much less complicated and expensive in the autothermal reformer system.

The autothermal reformer (ATR) is technically a plug flow, adiabatic, packed bed catalytic reactor. The packed catalyst bed is chosen as a cylinder with a 5:1 aspect ratio. A 2-liter bed is then 8 cm in diameter and 40 cm long. For the standard commercial G66 catalyst pellets, such a bed is roughly 25 particle diameters in diameter and 125 particle diameters in length. The figures of merit easily surpass the values of 10 and 20 respectively that are general criteria for minimization of entrance and wall effects in packed bed reactors. The catalyst bed is contained in a thin-gage metallic housing with a 40-mesh screen at the bottom to retain the catalyst charge. This inner housing is subsequently GTAW-welded into a slightly larger outer housing that serves as a pressure vessel made of 3 1/2" schedule 40 alloy 316L stainless steel. The annulus formed between the two housings is used as flow passage for the inlet air that is used to cool the outer structural wall. This is similar to the 5-kW test reactor used at Argonne National Laboratory¹⁷. The superheated methanol and

¹⁷ Personal communication with Shabbir Ahmed, Fall, 1997.

steam are supplied at the top of the bed and the reactor operates in a downflow fashion. The entire reactor can be fabricated from standard, stock material with the addition of three drilled holes and a few rolled flanges. This large reduction in complexity relative to the steam reformer is evidenced in the much-reduced manufacturing cost of the ATR reactor itself.

Table 7 shows, however, that the estimated cost for the entire subassembly is similar to that for the methanol steam reformer since the total cost is dominated by ancillaries such as pumps, and in the case of ATR, by air compressors. As with the SMR, a hybrid of a high rate of manufacture reactor concept with a series of larger heat exchangers would probably be less expensive. Indeed, because of the simplicity of the autothermal reactor, a single reactor may also be less expensive, as it would only require a 12L volume, less than a typical wastebasket. Such a reactor could be constructed from less than a meter length of standard 6” pipe. Appropriate air compressors to supply air to such a system also exist, as do properly-sized pumps. Once again, the use of plate-frame heat exchangers with a fixed geometry greatly reduces the cost of the heat exchange subsystems, as a large number of standardized parts could be produced.

Table 7: Estimated cost for methanol ATR subassembly

assembly name	component name	usage	make/buy	material	finished part dimensions (cm)				part characteristics			material cost (\$/kg unless noted)	part material cost	mfg. Cost	Total unit cost before markups	marked-up unit cost	total cost w/ markups	assembly mfg. Cost
					L	W (od)	D (id or t)	s.g.	mass (kg)	volume (L)								
Autothermal reformer																		
	catalyst housing	1	make	316L	40	8.2	8	7.9	0.8037144	0.101736	\$6.60	\$5.30	\$1.00	\$6.30	\$7.88	\$7.88		
	catalyst support screen	1	make	316L	0.1	8	0	3.5	0.0396896	0.005024	\$15.00	\$0.60	\$0.10	\$0.70	\$0.87	\$0.87		
	outer housing	1	make	316L	40	10.2	9.0	7.9	5.460023336	0.69114219	\$6.60	\$36.04	\$1.00	\$37.04	\$46.30	\$46.30		
	end dome	2	buy	316L	5	10.2	9.0	7.9	0.682502917	0.08639277	\$6.60	\$4.50	\$1.00	\$5.50	\$7.91	\$15.83		
	catalyst	1	make	G66B					2.75	1.375	\$13.50	\$37.13		\$37.13	\$46.41	\$46.41		
																		\$12.50
evaporator assembly																		
	separator plate	15	buy	409	25	10	0.05	7.8	0.09875	0.0125	\$2.00	\$0.20	\$0.27	\$0.47	\$0.67	\$10.08		
	fin sheet	15	buy	409	23	23.4	0.01	7.8	0.0425178	0.005382	\$4.00	\$0.17	\$0.10	\$0.27	\$0.39	\$5.82		
	manifold frame	15	make	409	25	10	0.24	7.8	0.474	0.06	\$1.50	\$0.71	\$0.10	\$0.81	\$1.01	\$15.21		
	end plate	2	make	409	25	10	0.24	7.8	0.474	0.06	\$1.50	\$0.71	\$0.10	\$0.81	\$1.01	\$2.03		
																		\$6.25
intercooler assembly																		
	separator plate	31	buy	409	25	10	0.05	7.8	0.09875	0.0125	\$2.00	\$0.20	\$0.27	\$0.47	\$0.67	\$20.83		
	fin sheet	31	buy	409	23	23.4	0.01	7.8	0.0425178	0.005382	\$4.00	\$0.17	\$0.10	\$0.27	\$0.39	\$12.04		
	manifold frame	31	make	409	25	10	0.24	7.8	0.474	0.06	\$1.50	\$0.71	\$0.10	\$0.81	\$1.01	\$31.43		
	end plate	2	make	409	25	10	0.24	7.8	0.474	0.06	\$1.50	\$0.71	\$0.10	\$0.81	\$1.01	\$2.03		
																		\$8.75
combustor assembly																		
	bottom housing	1	make	316L	30	10.16	10	7.9	0.600106752	0.07596288	\$6.60	\$3.96	\$1.00	\$4.96	\$6.20	\$6.20		
	top housing	1	make	316L	20	10.16	10	7.9	0.400071168	0.05064192	\$6.60	\$2.64	\$1.00	\$3.64	\$4.55	\$4.55		
	refractory liner	1	make	fiberfrax	40	10	7.5	1	1.37375	1.37375	\$3.00	\$4.12	\$1.00	\$5.12	\$6.40	\$6.40		
	Pt-Pd on ZTM	1	buy		20	7.5	0	0.974	0.86016375	0.883125	\$81/L	\$71.53		\$71.53	\$89.42	\$89.42		
	glowplug	1	buy										\$10.00	\$14.38	\$14.38			
	low pressure fuel injector	1	buy										\$5.00	\$7.19	\$7.19			
																		\$12.50
pumps, valves and misc.																		
	condensate pump and drive	1	buy										\$50.00	\$71.88	\$71.88			
	MeOH & water pump	2	buy										\$35.00	\$50.31	\$100.63			
	variable speed motor	1	buy										\$100.00	\$143.75	\$143.75			
	Air compressor	1	buy										\$250.00	\$359.38	\$359.38			
	ASME relief valve	3	buy										\$5.00	\$7.19	\$21.56			
	backpressure regulator	1	buy										\$20.00	\$28.75	\$28.75			
	gas feed solenoid	2	buy										\$20.00	\$28.75	\$57.50			
	k-type thermocouple	3	buy										\$5.00	\$7.19	\$21.56			
	ECU	1	buy										\$240.00	\$345.00	\$345.00			
	subtotal															\$1,486	\$40.00	
	plumbing allowance															\$100.00		
	total															\$1,626.12		

Assessment of Methanol Reformer Impact on Hydrogen Cost

We next compare the capital cost of on-site methanol reformers with on-site natural gas reformers, and the impact of those costs on the price of hydrogen produced by both systems. The cost of hydrogen will depend, of course, on the cost of the two feedstocks: methanol and natural gas, in addition to capital cost. From

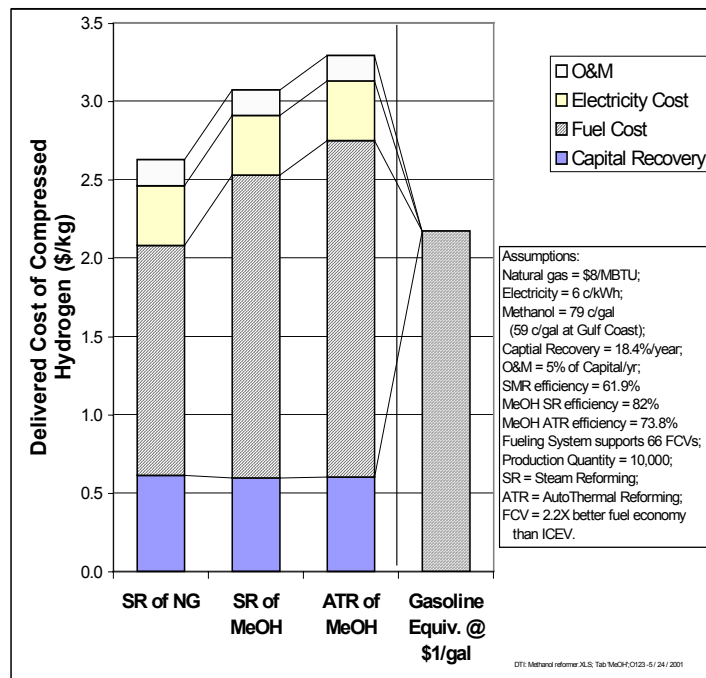
previous sections, we projected that methanol could be delivered to fueling stations at a cost in the range of 79 cents per gallon, which is equivalent to \$13.24/GJ on a lower heating value basis. For comparison, natural gas had been priced in the range of \$2/MBTU (HHV) at the well-head, \$3/MBTU industrial, and \$5/MBTU commercially. However, natural gas well-head prices spiked to as high as \$10/MBTU in early 2001, before falling back to the \$5/MBTU range. Assuming this \$3/MBTU increase in well-head price is passed on to commercial customers, then prices in the range of \$8/MBTU (HHV) would be expected. This corresponds to \$8.4/GJ on a lower heating value basis. Thus natural gas, even with recent price increases, would still be 37% less expensive than methanol per unit energy at the fueling station.

The capital cost estimates for both natural gas and methanol reformers are summarized in Table 8 for six-module systems with a peak capacity of 48 kg of hydrogen per day, enough to support over 66 FCVs assuming a 69% fueling station capacity factor. All capital cost estimates are based on the production of 10,000 fueling appliances. While the ATR system has lower reformer costs, this advantage is countered by a more expensive PSA gas purification system to handle the extra nitrogen in the gas stream, a result of adding air to the reactor combustion process. After adding in the common additional components (PSA, hydrogen compressor, hydrogen storage and dispensing systems) to make a complete fueling appliance, the methanol processors are only 3% less expensive than a natural gas-powered fueling system.

Table 8. Capital Cost Estimates for Natural Gas and Methanol Fuel Processors

	Steam Reforming of Natural Gas	Steam Reforming of Methanol	Autothermal Reforming of Methanol
Single Reformer Module	\$763	\$726	\$605
6-module Reformer system	\$5,036	\$4,792	\$3,993
Pumps & compressors	\$1,584	\$1,012	\$1,380
ECU	\$345	\$345	\$345
Housing	\$1,390	\$1,390	\$1,390
Piping & misc. (10%)	\$504	\$479	\$399
PSA	\$2,670	\$2,670	\$3,500
H2 compressor	\$4,684	\$4,684	\$4,684
Storage	\$9,331	\$9,331	\$9,331
Dispenser	\$4,846	\$4,846	\$4,846
Total capital cost	\$30,389	\$29,548	\$29,868

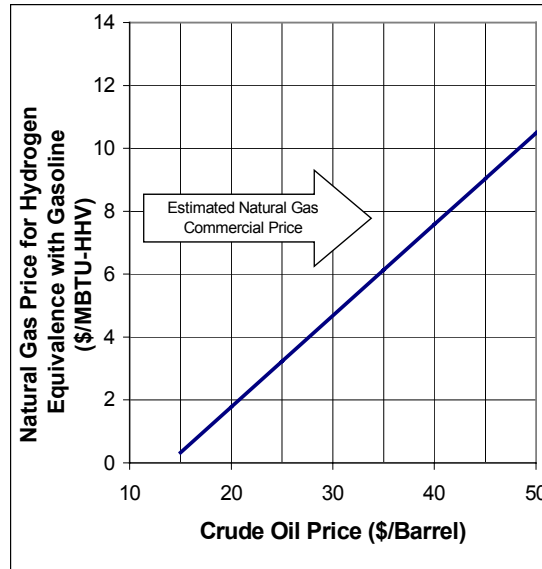
The impact of these capital costs on the price of hydrogen necessary to bring a 10% real, after-tax return on investment is shown in Figure 14. Since capital costs are virtually equal, the cost of fuel dominates the required hydrogen price. Since methanol is projected to cost more per unit energy than natural gas under current circumstances, hydrogen from natural gas is the least expensive option. For reference, the right bar in Figure 14 shows the cost of hydrogen to be equivalent to the price of wholesale gasoline – \$1.00/gallon assuming crude oil at \$32/barrel. Thus hydrogen from natural gas is projected to cost the driver about 18% more per mile traveled than wholesale gasoline. This implies that even if hydrogen were taxed at the same rate per mile as gasoline, it would still be competitive. Hydrogen from methanol would be less competitive under our baseline assumptions.



DTI: Methanol reformer.XLS, Tab 'MeOH', 01/23 - 5 / 24 / 2001

Figure 14. Estimated price of hydrogen to yield a 10% reaxm after-tax return on investment.

We can also invert the calculation, and ask what the price of fuel should be such that the cost of hydrogen per mile in a FCV will be equal to the cost per mile of gasoline in an ICEV. The results are shown in Figure 15 for natural gas and in Figure 16 for both methanol systems (SR and ATR.) For natural gas, the estimated commercial price in the range of \$8/MBTU would required crude oil at \$40/barrel for wholesale gasoline to be competitive with hydrogen from natural gas. For methanol the estimated pump price of 79¢/gallon would only yield cost competitive hydrogen if crude oil prices increased to \$50/barrel. Conversely, methanol cost would have to be reduced to about 35¢/gallon at the pump to make hydrogen competitive with gasoline with crude oil selling at \$30/barrel. Subtracting off the estimated 19¢/gallon cost of regional and local methanol distribution and storage, then the required cost of methanol at the U.S. Gulf would have to be in the vicinity of 16¢/gallon. We conclude that hydrogen made from methanol at the local fueling station will be unlikely to be competitive with natural gas, as long as natural gas is available at costs below \$10/MBTU.



ETH: Methanol reformer V1 © Tai Ma/GE/CMG, LLC / 11 / 2009

Figure 15. Price of natural gas to produce hydrogen costs per mile in a FCV equal to untaxed gasoline in a ICEV from crude oil at the indicated price.

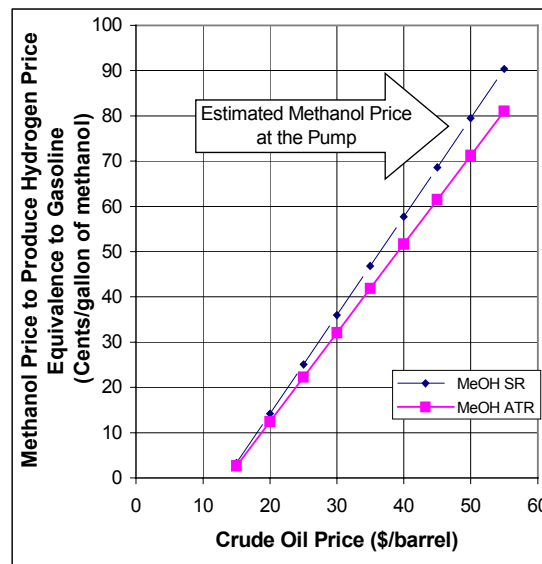


Figure 16. Price of delivered methanol at the pump to produce hydrogen costs per mile equal to untaxed gasoline costs per mile.

Hydrogen Tank Filling Options

During our hydrogen infrastructure contract with Ford and DOE, Tom Halvorson of Praxair suggested a new approach to filling FCV tanks with 5,000 psi compressed hydrogen (Halvorson-1996). With conventional cascade filling, the fueling station storage tanks would need to be pressurized to very high levels, on the order of 7,000 to 8,000 psi to provide rapid filling of 5,000-psi vehicle tanks. Halvorson suggested an alternative

using a booster compressor. The main storage would be at an intermediate pressure, say 3,600 psi. The FCV tank would be partially filled from this 3,600 psi source. The booster compressor would then be used to boost the pressure to 5,000 in each car tank. It was speculated that this booster compressor system might have several potential advantages over the pure cascade filling. The storage tanks would be certified for lower pressure and would cost less. Not all the hydrogen is compressed to the 8,000 psi range, thereby reducing average compression costs. Time did not permit a thorough optimization of this approach on the previous Ford/DOE contract, however, so we analyzed the Halvorson booster compressor filling system under this grant.

This study is concerned with minimizing the costs of a small hydrogen fueling station (50 to 450 kg/day enough to support a fleet of 100 to 900 FCVs or 12 to 110 FCVs fueled each day) by exploring different methods of filling compressed hydrogen tanks on FCVs. The fueling station has a small steam-methane reformer on-site with a serial pressure swing adsorption (PSA) gas purifier, a storage compressor (or booster compressor), a pre-compressor surge-tank reservoir, compressed gas storage cylinders, one or more dispensing posts, and an electronic control system. The reformer, PSA system, dispenser and control system will be the same for either booster compressor dispensing or cascade dispensing for the same average hydrogen production rate with no load following. Cascade dispensing and booster compressor dispensing are compared with various cost parameters to explore their economic merits. For booster compression we consider a trade-study with 3 minute, 5 minute and 7 minute fast-fills of 4 kg hydrogen per fill. Cascade dispensing uses a compressor sized for the average production flow rate. The FCV receiver cylinder is assumed to hold 5 kg total at 5,000 psig and 27°C, and a certain amount of over-pressurization (6200 to 6500 psig) is required to overcome fast-fill tank heating (see following section). The maximum storage pressure is 3,600 psig for the booster compressor case with a minimum of 750 psig in peak season. In contrast, cascade dispensing will consider 6,000, 7,000, and 8,000 psig storage cylinders arrayed in 3 or 4 cascade stages. The parameter study examined both steel and composite storage cylinders. In the following sections we define cascade filling and booster compression filling, review the costs of hydrogen storage, steam methane reformers and hydrogen compression, and then present the comparison costs for several modes of filling compressed hydrogen tanks on FCVs. But first we analyze the pressure necessary to completely fill hydrogen tanks on the vehicles.

Hydrogen Tank Filling Overpressure¹⁸

When high pressure hydrogen is passed into FCV onboard tanks, the gas and the tank will heat up. After the filling operation is complete, the tanks will cool and the pressure will fall lower than the fill pressure. To achieve a 5,000 psig final pressure in the tank, then, the filling pressure must be higher than 5,000 psia. The tanks must be designed to withstand the higher pressure, although the pressure differential is much less than the burst pressure capability of these tanks. Carbon fiber composite tanks must be qualified to survive pressures that are 2.25 times greater than operating pressure or 11,250 psig in the case of 5,000 psig tanks. As shown below, tank heating requires overpressures of at most 6,300 psig.

A simple thermodynamic analysis was performed on the FCV receiver cylinder to understand how much additional pressure might be needed to achieve a complete fill with the associated temperature rise. The

¹⁸John Reardon is the primary author of these sections on tank filling options

energy balance on the control volume assumes that the supply enthalpy crossing the receiver boundary is constant, and the internal energy change of the system is composed of contributions from both the compressed gas and also the container mass.

$$h_{\text{supply}} \Delta m = \Delta U_{\text{gas}} + \Delta U_{\text{tank}} \quad (1)$$

In this equation, h_{supply} is the supply line enthalpy at TS, and m is amount of hydrogen transferred and is equal to the difference between the final mass, m_2 and the initial mass, m_1 of hydrogen in the receiver tank; ΔU_{gas} is the change in internal energy of the gas inside the tank boundary; ΔU_{tank} is the change in internal energy of the tank itself as the temperature rises from the initial state temperature T_1 to the final state temperature T_2 . The heat loss from the tank by natural convection is assumed negligible during the fast-fill process.

Assuming constant specific heats and creating a parameter for the ratio of heat capacity of the tank $(mCv)_{\text{tank}}$ to the total gas heat capacity $(m_2Cv)_{\text{gas}}$, the following expression was derived for the temperature ratio as a function of α and of the ratio of initial to final mass states (m_1/m_2). The tank mass is estimated to be 50 kg for T-700 carbon fibers, and 75 kg for Panex-33 fiber tank, and 800 kg for a steel tank, giving parameters of 0.92, 1.38, and 7.5, respectively. In the Equation 2 below, T_s is the supply line temperature, and T_1 is the initial state temperature of the system.

The limiting case of a tank having zero mass is described by $\alpha = 0$. In this limiting case, the right hand side of Eq. 2 simplifies to the specific heat ratio γ when the tank is initially evacuated ($m_1=0$).

$$\frac{T_2}{T_1} = \frac{T_s}{T_1} \left(\frac{\gamma}{1+\alpha} \right) \left(1 - \frac{m_1}{m_2} \right) + \frac{1}{1+\alpha} \left(\frac{m_1}{m_2} + \alpha \right) \quad (2)$$

Some analysts have ignored the effects of the tank, predicting a 40% rise in temperature for an empty tank as depicted in Figure 17 for the upper line ($\alpha = 0$). The actual rise is much less for steel tanks (lower line in Figure 17) and intermediate for the carbon fiber composite tanks. The calculated absolute temperature rise factor (T_2/T_1) is 1.167 for an initially 20% full T-700 composite tank (1 kg/5 kg H_2) where the initial temperature and supply temperature are equal to 27°C. This would give a final pressure of 6,074 psig for a 203-liter vessel. If the feed temperature were 40°C, for example after the booster compressor final cooler, then the pressure would rise to 6,243 psig with a complete fill. This suggests that a 6,000 psig peak storage pressure cascade array is insufficient to sustain 100% complete fills throughout the dispensing day.

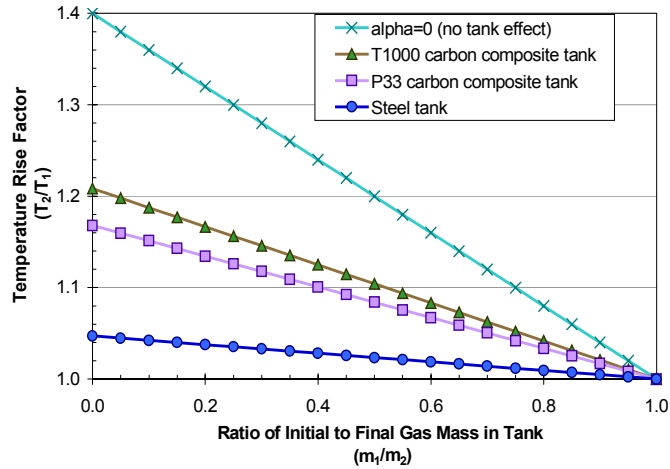


Figure 17. Temperature rise ratio due to fast filling for compressed gas tanks as a function of initial to final gas mass.

Description of Cascade Dispensing

Cascade dispensing is the most common method of achieving a fast-fill of compressed natural gas into natural gas vehicles, whereby dispensing is sequenced from an array of storage cylinders from lowest to highest pressures to fill the vehicle receiver vessel. Figure 18 is a schematic of the compressor, storage and sequencing dispenser configuration considered for the cascade dispensing option. The hydrogen production stream is compressed and fed to a storage array and priority sequenced to recharge the storage vessels from highest to lowest pressure.

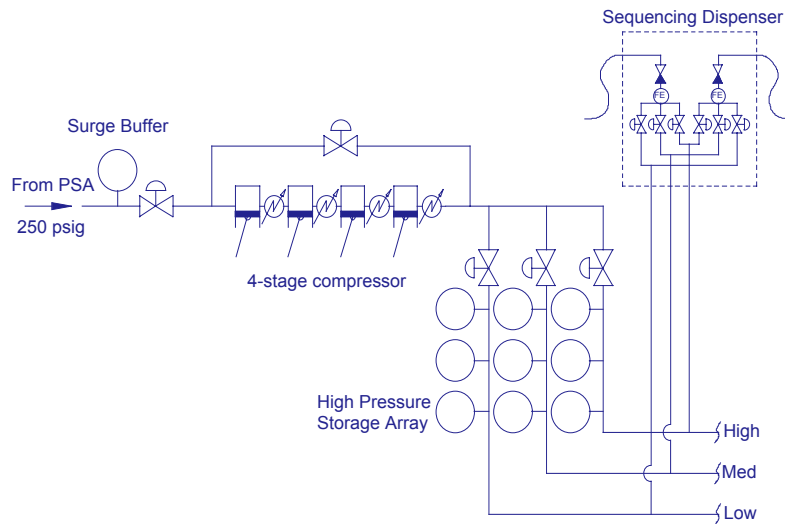


Figure 18. Schematic layout of the cascade dispensing option.

A small surge tank receives the hydrogen production stream from the gas separation PSA unit during the time of a single fuel dispensing if there is one dispensing post. If there are two or more dispensing pumps, then the probability, Φ , of overlapping fuel dispensing from multiple dispensing posts is calculated and used to weight determine the size of the surge tank. The probability of overlap was estimated to be 50% of the relative time for fuel dispensing compared to the total amount of time to fuel (3 minutes, 5 minutes, & 7 minutes) and to pay (3 minutes). The required surge tank volume is then given by:

$$V_{surge}(cascade) = \dot{m}_{production} t_{dispensing} (1 + \phi(N_{dispPost} - 1)) / \rho_{250\text{ psig}} \quad (3)$$

The relationship to fuel dispensing is somewhat arbitrary for the cascade scenario, but it does give a reasonable and consistent basis for sizing the surge tanks for various station sizing parameters. The cost of 250-psig surge tank storage is estimated to be \$7.50/L in production.

The cascade scenario requires a 3- or 4-stage compressor depending on the maximum storage pressure (6,000, 7,000, and 8,000 psig). The suction pressure is always 250 psig from the PSA system in steady state operation. Compressed hydrogen is priority-sequenced to a series of storage tanks according to their current pressure state. The total number of tanks in the cascade array must be a multiple of the number of stages in the cascade, which are either 3 or 4. The tank size is limited to 25 feet with fixed diameters according to the particular design pressure.

Cascade dispensing results in a minimum hydrogen content that is not available for transfer to the vehicle. The amount of useful hydrogen available for dispensing is described by the utilization efficiency, which is a function of storage pressure (above the vehicle receiver pressure) and number pressure stages in the cascade array. A larger number of stages would increase the utilization efficiency, but storage costs also increases with both the amount of storage and the number of tanks required for a given array. The amount of hydrogen storage for the cascade application is equal to the net hydrogen dispensed (H_2 delivery- H_2 production) in a given dispensing period (night time recovery hours excluded) divided by the hydrogen utilization efficiency, U_H , and the capacity factor for the station ($CF=0.69$ accounts for daily, weekly, seasonal and statistical fluctuations).

$$M_{cascade} = \frac{(M_{dispensed} - M_{produced})}{U_H CF} \quad (4)$$

The hydrogen utilization efficiency for cascade dispensing to a 5,000 psig receiver cylinder was calculated for the present study using rational-function curve fits to data provided by T. Halvorson of Praxair based on his MathCAD model (Halvorson-1996). The data and curve-fits are shown in Figure 19. We also explored the option of load-following -- building a larger reformer to permit increased hydrogen production during peak hours while reducing the size of the storage system. But we found that there is no significant cost reduction with load following -- the added reformer and compressor costs more than offset any savings in storage tank costs.

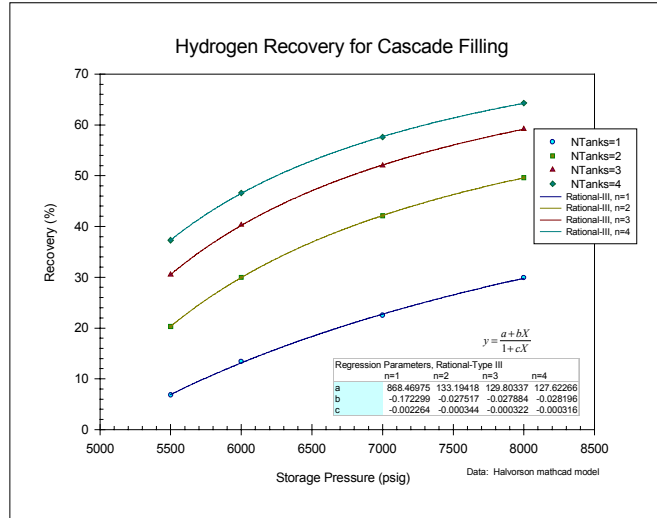


Figure 19. The calculated hydrogen utilization efficiency for a given cascade array as a function of pressure for a 5,000 psig vehicle tank [Ref: Halvorson- 1996]

Description of Booster Compression

The booster-compressor method of fast-filling FCV tanks is shown in Figure 20 as proposed by Tom Halvorson of Praxair. Hydrogen from the SMR system is stored at an intermediate pressure of 3,600 psig. When a FCV tank is connected to the dispenser, it is first filled to the 3,600 psig (or current pressure of the storage tanks). To top off the hydrogen tanks, the booster compressor then raises the pressure in the tank such that the pressure reaches 5,000 psig after the gas and tank cool. A buffer surge tank is provided to store the hydrogen produced by the SMR while any FCVs are refueling.

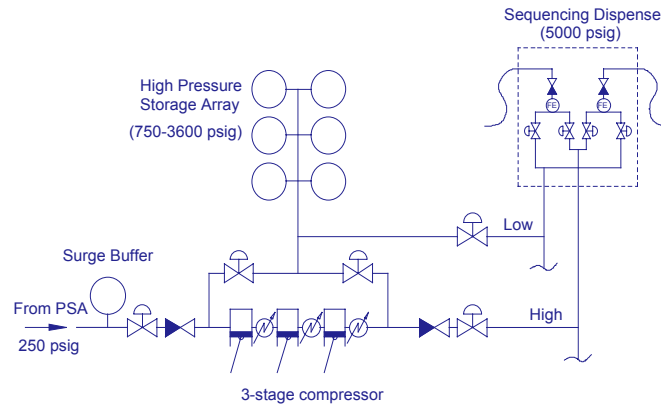


Figure 20. Schematic of the booster-compressor option (A) by Tom Halvorson

The average reformer flow rate for a 100-FCV station is 2.08 kg H₂/hr, while the delivery flow for a 3-minute fast-fill (4 kg H₂) is 80 kg/hr. The booster compressor must meet the design requirements of both hydrogen production and dispensing flow rates at the required outlet pressures. The flexible flow rate is achieved with a density boost and a compressor speed boost, as required to a maximum of 1,500 rpm. The

compression ratio of the compressor is sized for the 3,600 psig storage application, but the flow rate is sized to meet the dispensing demand at peak compressor speed (1,500 rpm). The actual outlet pressure of the compressor at any given time is a function of the backpressure produced by the receiver cylinder. The minimum density boost is 2.83, taking the ratio of densities at 750 and 250 psig respectively. A nominal design flow rate is calculated for compressor sizing according to a reference case of 250 psig suction and 725 rpm. Calculation of the nominal design mass flow rate (Eq. 3) includes the requirement of multiple dispensers with the probability of overlap with multiple dispensing posts. M_{FCV} is on the average 4 kg/ fill.

$$\dot{m}_{nom} = (1 + \phi(N_{disp} - 1)) \left(\frac{M_{FCV}}{t_{disp}} \right) \left(\frac{\rho_{250}}{\rho_{750}} \right) \left(\frac{725rpm}{1500rpm} \right) \quad (5)$$

If the nominal adjusted booster mass flow rate is less than the flow rate required to meet the reformer hydrogen production demand, then the compressor is sized according to the reformer demand, rather than increasing the average compressor speed above the reference 725 rpm to meet the reformer demand. When the compressor is sized according to the booster fast-fill demand, turndown from the nominal compressor speed of 725 rpm is used to adapt to the hydrogen production flow rate. In this way, the majority of compressor operation (meeting hydrogen production demand) is performed at a speed less than or equal to 725 rpm, which lengthens piston ring life.

Since a portion of the FCV fill is accomplished with dispensing directly from hydrogen storage, the relative booster usage time for a given FCV fill ranges from 60 to 82% for an average day, and 60-90% for a peak-dispensing day. The booster mode is used infrequently, approximately 2% of the day for small fueling stations (100 FCV fleet supported, with 1 dispensing post) and only up to 17% for a larger station (900 FCV fleet supported with 4 dispensing lines). A compressor maintenance charge could be assessed as a function of time spent at max speed, but instead a typical annual maintenance fee of 2% of the compressor capital cost was assessed.

The surge tank that is located upstream of the booster compressor is sized with a minimum volume equal to that of the cascade surge tank volume (Eq. 5) plus additional volume for option (A) to accommodate accumulation for a given fill allowing the surge tank to swing in pressure from 100 psig to completely filled at 250 psig. This pressure swing gives a density difference of 0.959 kg/m³. The surge tank volume is calculated with Eq. 6.

$$V_{surge}(booster) = V_{surge}(cascade) + \frac{m_{production} t_{dispensing} (1 + \phi(N_{dispPost} - 1))}{\rho_{250psig} - \rho_{100psig}} \quad (6)$$

The hydrogen production rates for the larger fueling stations require surge tank volumes that are extremely large. For example, a small station supporting a 100-FCV fleet (50 kg H₂/day) would require a 1.7 m³ (water volume) surge tank in the booster compression scenario, but in a larger station supporting 900 FCVs (450 kg H₂/day), the required surge volume approaches 15.4 m³, which may not be practical. Therefore, a second option (B) is proposed whereby a single-stage compressor is used to boost the production stream to the elevated booster suction head, regulated to a fixed 750 psig for this option. A schematic of the modified

booster compressor system option (B) of this study is presented in Figure 21, and the surge tank volume is then calculated in the same way as the cascade surge volume using Eq. 5.

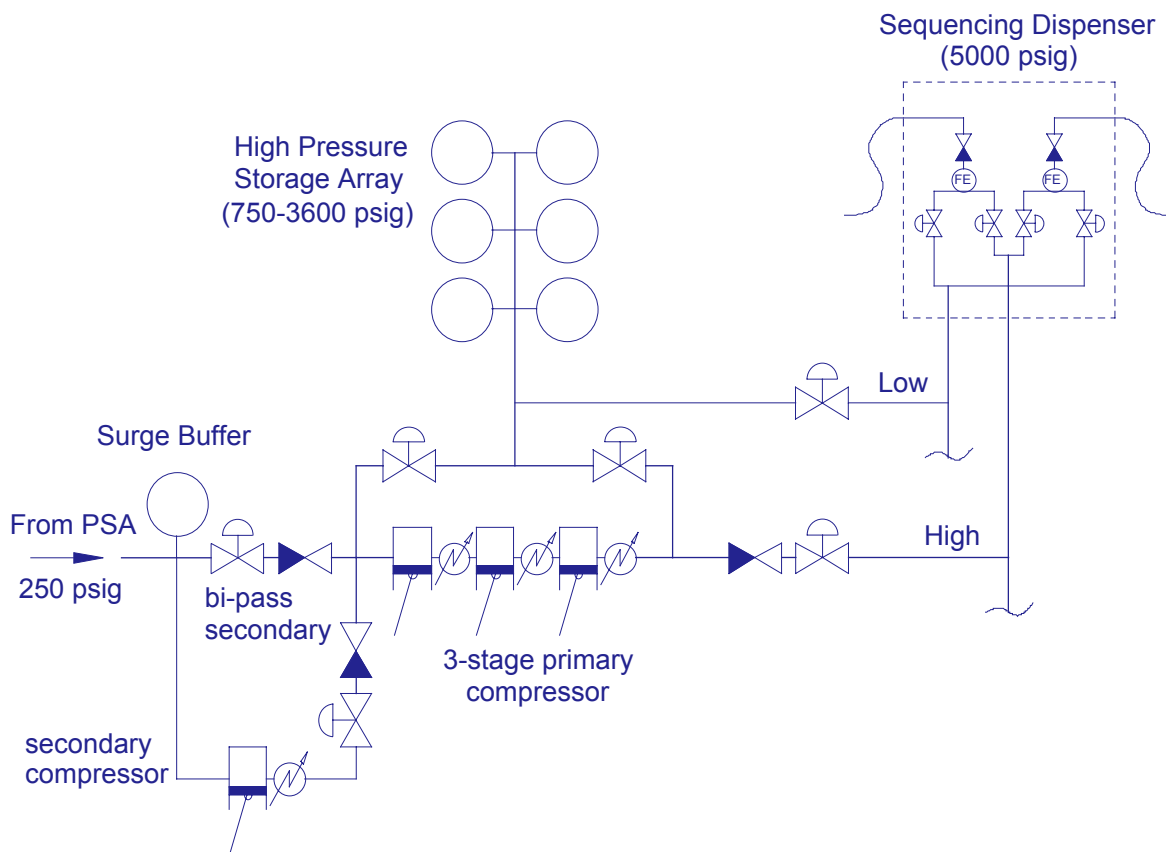


Figure 21. Schematic diagram of the booster compressor system, option (B).

To optimize the cost of the various tank filling options, we must develop a model for the cost of hydrogen storage, hydrogen compression and the steam methane reformer, all as a function of size.

Cost of Hydrogen Storage

Quotations for high pressure tanks were received from a steel tank manufacturer (CP Industries) for currently available storage pressures of 3600, 5000, and 6000 psig. CPI also quoted a special 8000 psig cylinder. A 7000 psi cylinder price was estimated by linear interpolation in volume and price. The cylinder outer diameters were 24, 20, 16, 14, and 12.75" for 3600, 5000, 6000, 7000, and 8000 psig storage, respectively. Mass-produced K-size laboratory cylinders meeting the Department of Transportation specifications DOT3AA3600 and DOT3AA6000 and an ASME 7000 psig accumulator (K-size) were also quoted in 100+ quantities (Norris Cylinder Co.). The DOT3AA6000 holds H₂ and the ASME(K)7000 accumulator holds 1.33 kg H₂/cylinder at room temperature with no over-pressurization. We have also estimated the cost of mass produced T700 carbon fiber composite storage cylinders using a factor of safety of 2.25 (DOT and NGV2 requirement: 2.25 -James-1996) with a loaded fiber cost estimate of \$15/lb. The detailed mass production

cost estimation assumed that the cylinder diameters were the same as the steel tank counterparts for the given pressure. The labor rates were \$1/min, machine rates were \$2/min, and all mark-up factors were 1.5 (James-1999b) As shown in Figure 22, the tank cost of many small K-cylinders is less than cost of larger steel tanks. However, the costs associated with multiple valves and piping to connect these small tanks could offset this cost advantage. The cost of composite storage cylinders could also be reduced by an additional ~30% if the tank fiber cost could be reduced to \$10/lb for the T700 carbon fiber with high production volume.

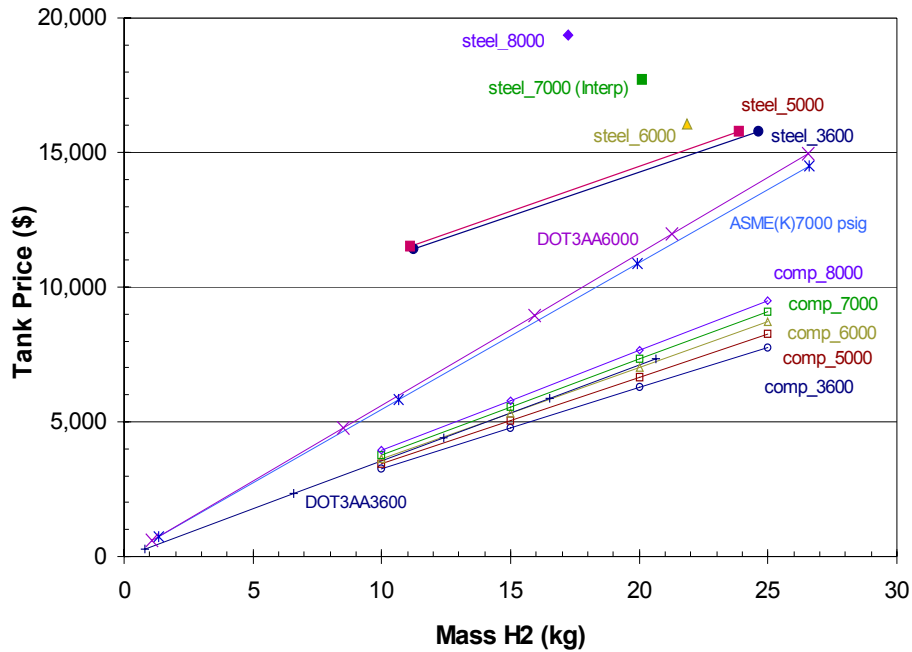


Figure 22. Cost of steel tanks (CPI Industries), DOT3AA K-cylinders, ASME (K-cylinder) 7000, and mass produced T700 carbon fiber composite tanks (2.5 safety factor and \$15/pound fiber cost)

The data in Figure 22 were used to create linear correlations for predicting tank price as a function of stored hydrogen mass (Table 9). In the fueling station cost model the total tank length was limited to 25 ft (wall thicknesses were 1.4 to 1.5 inches), so if the stored mass requirement required a tank longer than 25-ft. then the number of tanks were incremented accordingly and the stored mass per tank was divided evenly. In the cascade filling case, 3 or 4 stage cascades were studied, therefore the number of storage tanks had to be a multiple of either 3 or 4 depending on the number of cascade stages.

Table 9. Storage Tank Cost Correlations used in Parameter Study for Tank Cost =m*(kg H2) + b

Tank Description	m	b
steel 3600 psig	327.8	7709
steel 5000 psig	335.3	7779
steel 6000 psig	373.8	7903
steel 7000 psig	481.7	8038
steel 8000 psig	650.4	8162
T700 Comp. 3600 psig	301.8	228
T700 Comp. 5000 psig	321.2	228
T700 Comp. 6000 psig	338.6	231
T700 Comp. 7000 psig	354.8	232
T700 Comp. 8000 psig	370.4	232
DOT3AA3600	355.3	
DOT3AA6000	632.8	
ASME(K)7000	545.8	

Cost of Hydrogen Compression

Semi-empirical cost correlations for compressors were developed for a given compression ratio as a function of mass flow rate. Quotations for several piston compressors with flow rates in the range of 34 to 550 standard cubic feet per minute (scfm) were obtained from two vendors, RIX Industries and Henderson International Technologies. These compressors were quoted with elevated suction pressures 150 psig to 300 psig with an outlet pressure of 6000 psig. The compressor speeds varied between the two vendors. The three compressor designs are quite different, and may or may not be appropriate for the booster concept. Nevertheless, these manufacturing costs are representative of a given size machine and provide a reference for subsequent correlations. Since the compressors were quoted with flow rates at disparate compressor speeds and suction pressures, the adjusted (nominal) mass flow rate at 725 rpm and 250 psig suction was calculated and used as the independent variable in our cost equations. The reference compressor speed of 725 rpm is used for the sizing flow rate to meet the hydrogen production demands (from the reformer) on the heaviest day of the year; with a 0.69 capacity factor, this gives a compressor speed of 500 rpm to meet the average reformer production demands, and a maximum speed of 1500 rpm to meet the booster delivery flow rate. This essentially limits the maximum boost by compressor speed change to a factor of 2.07 for the heaviest production day of the year. The three-stage compressor can be used to approximate the cost of a 4-stage compressor by assuming that price consists of a 20% base cost with the remaining 80% divided as a cost per stage. Table 10 presents the quotations and the calculated nominal mass flow rate reference compressor speed of 725 rpm at 250 psig suction pressure.

Table 10. Compressor cost quotations as specified with calculated “nominal” hydrogen mass flow rates at the reference condition: 250 psig suction and 725 rpm.

Compressor Vendor	Model	Specifications (outlet/suction/speed)	Mass Flow at 250 psig/725 rpm	Price
RIX Industries	4VX4	6000psig /150 psig 600 rpm/ 4 stages	9.33 kg/hr	75,000
Henderson International	D63-3H	6000psig /300 psig 970 rpm/ 3 stages	48.85 kg/hr	\$146,650
Henderson International	C3T-H	6000psig /150 psig 970 rpm/ 3 stages	58.08 kg/hr	\$183,810

It is assumed that the compressor manufacturer will limit the pressure ratio per stage (PR/Stage) to less than 3 to limit heat dissipation and preserve piston ring life. Therefore, a 3-stage compressor would be used for the 3600, 6000, and 7000 psig outlet pressures, while a 4-stage compressor will be required for the 8000 psig outlet pressure. The PR/stage will vary for the different hydrogen storage applications as shown in Table 11.

Table 11. Compressor selection guide and mass-produced compressor cost correlations.
Maximum PR/stage is 2.99. Cost = m*(kg H₂/hr)+b

Outlet Pressure (264.7 psia suction)	PR/stage (1 stage)	PR/stage (3 stage)	PR/stage (4 stage)	Correlation Parameter (m)	Correlation Parameter (b)
750 psig outlet (booster option B)	2.89			570.4	9940
3600 psig storage		2.39		1172.3	18268
6000 psig storage		2.84		1341.0	20896
7000 psig storage		2.99		1397.8	21781
8000 psig storage			2.35	1473.8	20910

A multiplier based on the difference in PR/Stage was used to produce a cost differential relative to 2.65 (the average PR/stage) for varied PR/stage for each of the various applications. This incremental cost would account for, more or less, heat dissipation and varied mechanical design requirements. In our study an optional single-stage compressor for boosting the hydrogen generation stream to a regulated booster suction head of 750 psig is considered in a trade-off for the booster compression study. The compressor cost correlations used in this study are also presented in Table 11. RIX industries postulated that their compressor cost could be reduced by a factor of 2 for a very large order (1,000 compressors) which is comparable to a calculated cost ratio of 0.522. This factor is used in this study based on the cost of the ten-thousandth unit produced compared to the cost of the first unit for a 0.85 production progress ratio. The resulting estimates of compressor costs in large quantities is shown in Figure 23.

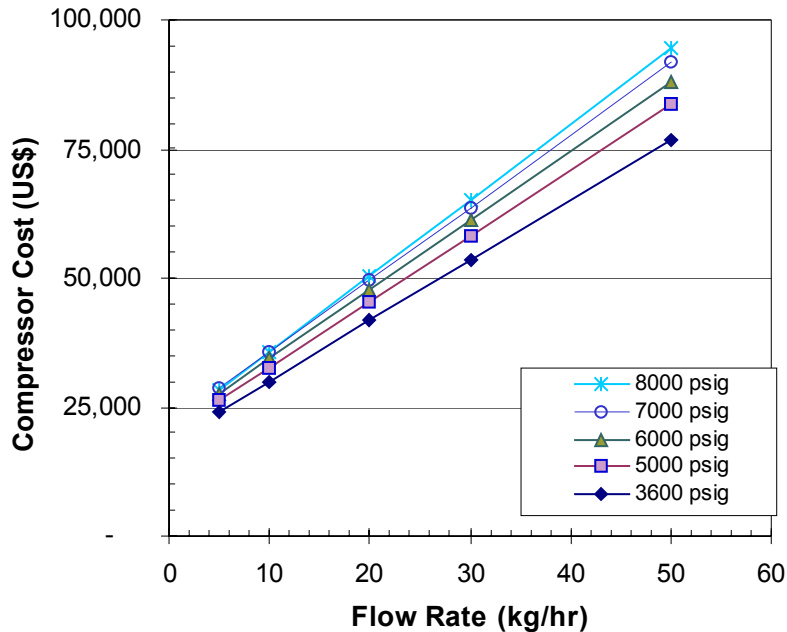


Figure 23. Compressor cost estimates for 1000⁺ unit-production level.

The system cost model must also include the cost of electricity, which depends on the power required to drive the compressor. The power to compress hydrogen in an n -stage compressor is calculated using Eq. 5, where P_0 is the outlet pressure, P_i is the inlet pressure, γ is the specific heat ratio, m is the mass flow rate, R is the universal ideal gas constant, and M is the hydrogen molecular weight.

$$P_{comp} = \frac{\dot{m} RT}{\gamma - 1} \left(\left(\frac{P_0}{P_i} \right)^{\frac{\gamma-1}{n\gamma}} - 1 \right) \quad (7)$$

When the pressure ratio is constant the compression energy is simply equal to power multiplied by time. However, for our case the energy cost to compress hydrogen over a given day's usage for either the booster compressor or the cascade dispensing application will be the time integral of the compression power with a variable pressure ratio, $\theta = P_0/P_i$. The compression power varies during the day for the booster compressor application most since the mass flow rate is boosted during delivery to the FCV. The outlet-to-inlet pressure ratio also changes during a given fill whether the fill is an FCV receiver or the fueling station's storage tanks. The suction pressure of the booster compressor changes as the hydrogen supply (storage) tank is emptied, and the compressor back-pressure changes as the receiver tank is filled. If the supply pressure and receiver tank pressure vary linearly with time, then the outlet-to-inlet pressure ratio can be reasonably represented by a linear expression when the supply pressure is constant (cascade application) or when the supply pressure is much larger than the integral of its rate of change. Equation 8 is used to calculate compression energy E_c over a given time interval t^* . Eq. 8 was derived for a constant mass flow rate with a linearly varying pressure ratio, θ . (The parameter g represents the specific heat ratio expression $\gamma/(\gamma-1)$).

$$E_c = \frac{\dot{m}RT}{M\eta_c} \left(\frac{t^*}{\theta^* - \theta_0} \right) \left(\frac{ng^2}{1+ng} \right) \left[\theta^{*\frac{ng+1}{ng}} - \theta^{\frac{ng+1}{ng}} \right] \quad (8)$$

The compression energy is calculated over discrete time intervals where the mass flow rate is constant and the discrete compression energy contributions are summed over a representative day. The energy cost is converted to dollars with an electricity cost of \$0.08/kWh.

Filling Station Load Profile

The model load profile for the hydrogen fueling station is shown in Figure 24, which is intended to represent the relative dispensing rates for a typical station on an average day. We assume a 0.69 capacity factor to size equipment for accommodating daily, week-end/week-day, statistical and seasonal demand fluctuations. The station is open for 15 hours during the day. The hydrogen production system is operating continuously, and hydrogen reserves are replenished at night. This study considers a trade-off between hydrogen storage costs and compressor and reformer capital and operating costs by comparing the booster compressor options A and B with cascade dispensing options (various storage pressures) for both small stations (50 kg H₂/day) and larger stations (450 kg H₂/day). The small station would support a fleet of 100 FCVs while the larger station would support a fleet of 900 FCV, assuming an 8-day refueling cycle with 4 kg H₂/refill.

Steam Methane Reformer System Cost

The steam methane reformer capital costs, C_{SMR} , were estimated based on an published correlation for a stationary reformer system (Thomas-1997a)

$$C_{smr} = \$5639 + 3096(\dot{m}_{peak}) \quad (9)$$

where m_{peak} is the reformer peak mass flow rate in kg H₂/hr. Dispensers and controls costs are estimated to be \$4,800 and \$5,000 each, electricity costs are billed at \$0.08/kWh, and natural gas feed stocks are assumed to be \$5/1000 scf. This study uses a 0.15 capital recovery factor.

Summary Cost Comparisons of Tank Filling Options

Results for a small fueling station (supporting 100 FCVs with 50 kg H₂/day) using steel storage tanks are presented in Figure 25. The cascade options are sorted and grouped on the left side of the chart while the booster compressor options are sorted and grouped on the right. Booster options (A) and (B) are compared, but the costs of the secondary compressor and surge tank for option (B) are grouped together in the surge tank category. Figure 25 shows that the booster option (A) is less expensive than option (B) for the small station.

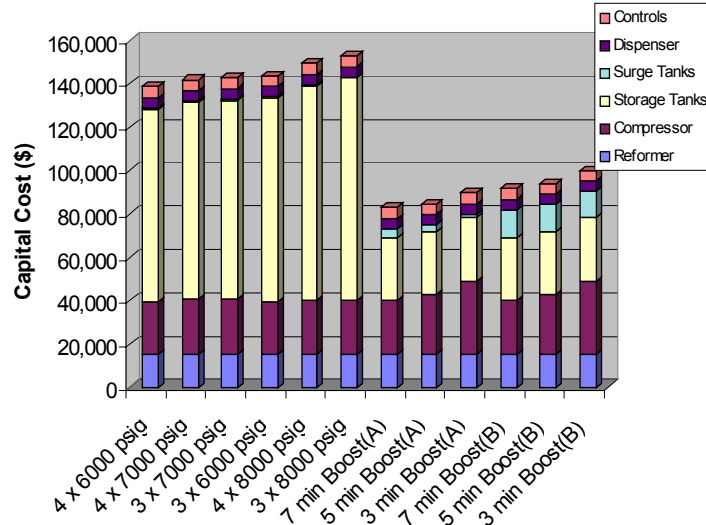


Figure 25. Capital cost estimates for 100-FCV fleet fueling station with steel hydrogen storage tanks

The small station costs less for the booster compressor scenario when steel tanks are used since the storage costs account for 64 to 67% of the capital cost for cascade dispensing but only 30 to 35% of the total capital costs for the booster compressor options. The booster compressor (A) for the 3-minute fast fill is 32% more expensive than the cascade compressor. The 3-minute fast-fill booster would be less expensive than all the cascade options, with booster option (A) (surge tank only) preferred over option (B) (secondary compressor), due to the low hydrogen production rate. The 4-stage cascades are favored over 3-stage cascades, and lower pressure tanks are more cost effective when steel tanks are chosen, probably due to the remarkably high cost differential for steel tanks over 6000 psig. Therefore the additional cost of high pressure tanks supercedes the benefit of hydrogen utilization with higher pressure.

Table 12 below compares the annual operational and amortized capital costs among all the cascade and booster compressor options. The fueling station economics are strongly influenced by capital costs for the small station.

Table 12. Small station (50 kg H₂/day) with steel tanks: annual amortized capital costs in \$U.S. compared to annual electrical energy costs (0.08 \$/kWh) and natural gas feed stock costs \$5/kscf.

	Reformer Electricity	Compressor Energy	Compressor Maintenance	Natural Gas	Amortized Capital	Total	% Capital
Cascade Options							
4 x 6000 psig	228	739	493	16,023	20,692	38,174	54%
4 x 7000 psig	228	925	514	16,023	21,182	38,871	54%
3 x 6000 psig	228	740	493	16,023	21,451	38,935	55%
3 x 7000 psig	228	926	514	16,023	21,328	39,018	55%
4 x 8000 psig	228	933	502	16,023	22,321	40,006	56%
3 x 8000 psig	228	933	502	16,023	22,842	40,528	56%
Booster Compressor Options							
7 min Boost(A)	228	1,201	500	16,023	12,439	30,391	41%
5 min Boost(A)	228	1,215	554	16,023	12,673	30,693	41%
3 min Boost(A)	228	1,228	680	16,023	13,447	31,606	43%
7 min Boost(B)	228	1,201	731	16,023	13,758	31,940	43%
5 min Boost(B)	228	1,215	785	16,023	14,110	32,360	44%
3 min Boost(B)	228	1,228	911	16,023	15,001	33,391	45%

Figure 26 shows the capital cost comparison for a larger station (supporting 900 FCVs with 450 kg H₂/day) using steel tanks. Surprisingly the 3-minute delivery booster compression option is slightly less expensive than the 5- or 7-minute cases. The compressor costs are all the same since the compressor cost has reached its minimum value for the station configuration, so there is no advantage in increasing the fuel delivery time (reducing booster flow rate). This is a special case that occurs with larger fueling stations where the hydrogen production demand is greater than the nominal booster flow rate adjusted for 725 rpm compressor speed and 250 psig suction pressure. (Refer to booster compressor background, compressor sizing). Selecting the larger compressor permits reformer demand to be met with a lower compressor speed. A smaller compressor would require an increase in compressor speed above the reference state (725 rpm) and this could lead to premature piston ring wear or an unknown trade off in capital cost for additional compressor maintenance costs.

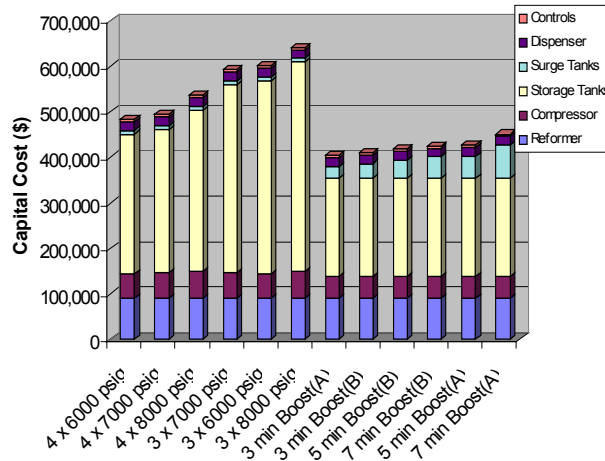


Figure 26. Capital cost estimates for a large 900-FCV fueling station with steel hydrogen storage tanks.

Although booster scenario (A) is the least expensive, its surge tank size is 15,400L. The booster scenario (B) would be more practical with a 3,000L surge tank. Booster scenario (B) could actually be reconfigured to store at a nominal 750 psig pressure with a 2.83 reduction in volume.

The total annual costs for the station (fuel, maintenance and capital recovery) are summarized in Table 13. The amortized costs of the 4-stage 7000 psig cascade system (practical and sufficient pressure) is approaching cost competitiveness with the booster compressor, but the capital cost is still about 20% higher than the 3-minute booster (B). The 3-minute booster compression energy is about 24% higher than the 4-stage 7000 psig cascade option.

Table 13. Large station (450 kg H₂/day) with steel tanks: amortized capital costs, annual electrical energy costs (0.08 \$/kWh) and natural gas feed stock costs \$5/kscf.

	Reformer Electricity	Compressor Energy	Compressor Maintenance	Natural Gas	Amortized Capital	Total	% Capital
Cascade Options							
4 x 6000 psig	2,052	6,642	1,095	144,203	71,289	225,281	32%
4 x 7000 psig	2,052	8,315	1,141	144,203	72,875	228,585	32%
4 x 8000 psig	2,052	8,383	1,175	144,203	79,108	234,919	34%
3 x 6000 psig	2,052	6,651	1,095	144,203	88,947	242,947	37%
3 x 7000 psig	2,052	8,322	1,141	144,203	87,560	243,278	36%
3 x 8000 psig	2,052	8,390	1,175	144,203	94,947	250,766	38%
Booster Compressor Options							
3 min Boost(A)	2,052	10,296	957	144,203	60,708	218,215	28%
3 min Boost(B)	2,052	10,296	1,448	144,203	61,619	219,618	28%
5 min Boost(B)	2,052	9,821	1,448	144,203	62,680	220,203	28%
7 min Boost(B)	2,052	9,363	1,448	144,203	63,796	220,861	29%
5 min Boost(A)	2,052	9,821	957	144,203	64,111	221,143	29%
7 min Boost(A)	2,052	9,363	957	144,203	67,687	224,261	30%

The capital costs for a small 100-FCV station with carbon fiber composite tanks in place of the steel tanks used in the previous two figures are shown in Figure 27. Higher-pressure storage (8000 psig) in 4-stage cascades is preferred among the cascade dispensing options when composite tanks are used. Once again, for the small station, booster option (A) is preferred over option (B). The surge volume for booster option (A) is only 835L for the small station.

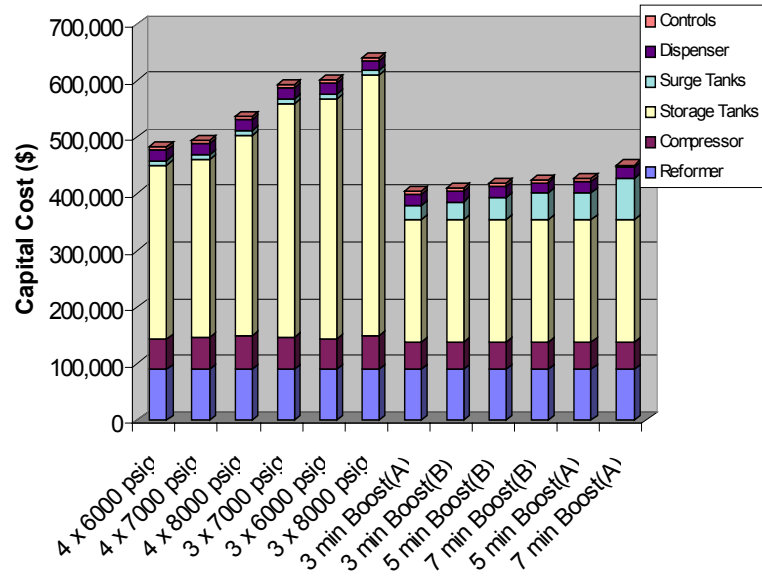


Figure 27. Capital costs for a 100-FCV fleet fueling station with carbon fiber composite hydrogen storage tanks.

The 4-stage 8000 psig cascade configuration has capital costs that are approximately 3% higher than the 3-minute booster (A) counterpart. However, the annual costs (Table 14) show that the cascade option is actually lower in cost, even for the small station when composite tanks are used. Both the 3-stage and the 4-stage 8000 psig cascade option are less expensive than the lowest cost 3-minute booster option. However, the annual cost differences are small and are probably less than the uncertainty in our capital cost estimates. Thus there is no clear-cut advantage to using booster compressor dispensing over cascade dispensing for the small station with composite storage tanks.

Table 14. Small station (50 kg H₂/day) with T700 composite tanks: amortized capital costs, annual electrical energy costs (0.08 \$/kWh) and natural gas feed stock costs \$5/kscf.

	Reformer Electricity	Compressor Energy	Compressor Maintenance	Natural Gas	Amortized Capital	Total	% Capital
Cascade Options							
4 x 8000 psig	228	933	502	16,023	11,297	28,983	39%
3 x 8000 psig	228	933	502	16,023	11,594	29,280	40%
4 x 7000 psig	228	925	514	16,023	11,624	29,314	40%
4 x 6000 psig	228	739	493	16,023	12,168	29,651	41%
3 x 7000 psig	228	926	514	16,023	12,585	30,275	42%
3 x 6000 psig	228	740	493	16,023	12,856	30,339	42%
Booster Compressor Options							
7 min Boost(A)	228	1,201	500	16,023	10,031	27,983	36%
5 min Boost(A)	228	1,215	554	16,023	10,266	28,285	36%
3 min Boost(A)	228	1,228	680	16,023	11,040	29,199	38%
7 min Boost(B)	228	1,201	731	16,023	11,350	29,533	38%
5 min Boost(B)	228	1,215	785	16,023	11,702	29,952	39%
3 min Boost(B)	228	1,228	911	16,023	12,594	30,983	41%

The final comparison is the 450 kg H₂/day station supporting a 900-FCV fleet with composite storage tanks (Figure 28 and Table 15). The capital costs of 4-stage cascades are favored for all these pressures: 6000, 7000, and 8000 psig. The capital costs of the higher-pressure cascade options are lower than the costs of the practical 3-minute booster option (B). The 4-stage 8000-psig cascade option costs \$25K less than the most practical booster option. The amortized cost comparison reveals that every cascade option, with the exception of the impractical 6000 psig, 3-stage cascade system, is less expensive than the most practical 3-minute booster option (B). Once again, when we consider the annual costs, the differences are very small, and selection of the most ideal configuration may depend more on operational preferences than on economic considerations.

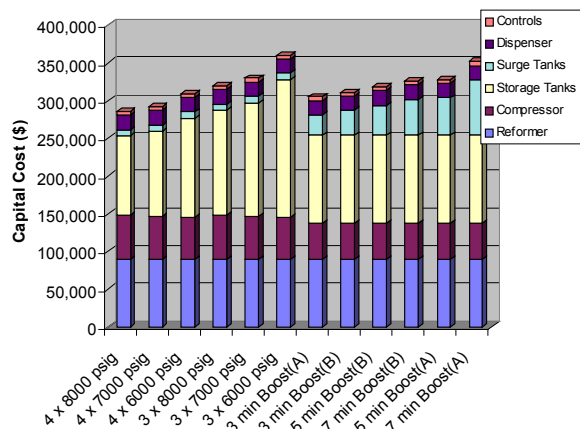


Figure 28. Capital cost for a 900-FCV fleet fueling station with carbon fiber composite hydrogen storage tanks.

Table 15. Large station (450 kg H₂/day) with T700 composite tanks: amortized capital costs, annual electrical energy costs (0.08 \$/kWh) and natural gas feed stock costs \$5/kscf.

	Reformer Electricity	Compressor Energy	Compressor Maintenance	Natural Gas	Amortized Capital	Total	% Capital
Cascade Options							
4 x 8000 psig	2,052	8,383	1,175	144,203	41,633	197,445	21%
4 x 7000 psig	2,052	8,315	1,141	144,203	42,518	198,228	21%
4 x 6000 psig	2,052	6,642	1,095	144,203	45,139	199,130	23%
3 x 8000 psig	2,052	8,390	1,175	144,203	46,680	202,499	23%
3 x 7000 psig	2,052	8,322	1,141	144,203	48,215	203,933	24%
3 x 6000 psig	2,052	6,651	1,095	144,203	52,821	206,821	26%
Booster Compressor Options							
3 min Boost(A)	2,052	10,296	957	144,203	45,773	203,281	23%
3 min Boost(B)	2,052	10,296	1,448	144,203	46,685	204,683	23%
5 min Boost(B)	2,052	9,821	1,448	144,203	47,746	205,269	23%
7 min Boost(B)	2,052	9,363	1,448	144,203	48,861	205,926	24%
5 min Boost(A)	2,052	9,821	957	144,203	49,176	206,208	24%
7 min Boost(A)	2,052	9,363	957	144,203	52,752	209,326	25%

Impact of Booster Compression on Delivered Hydrogen Costs

The use of booster compression did not have a significant impact on hydrogen infrastructure investment costs for carbon fiber tanks, but did reduce the cost when the more expensive steel tanks were used in the smaller

station, as shown in Figure 29. However, for a mature FCV market, each fueling station would typically support over 1,000 FCVs (125 FCVs filling up at the station each day). So the larger 900-FCV station is more representative of the eventual FCV market. For these larger stations, the difference between booster compression and cascade filling is negligible, and in fact the hydrogen cascade filling option is slightly less expensive. We conclude that there is no significant cost advantage in using the booster compression option for larger stations, particularly with the lower cost composite hydrogen tanks.

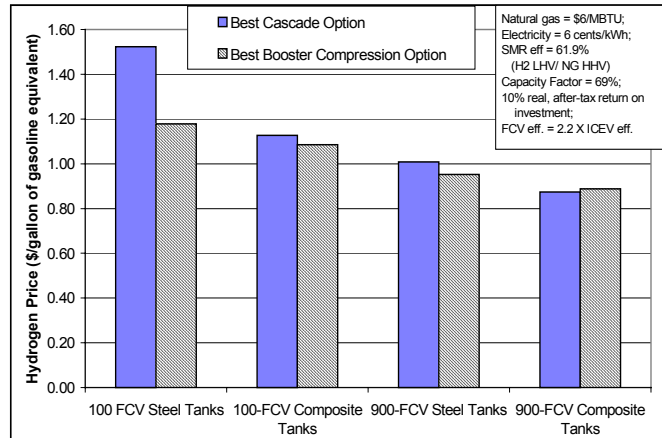


Figure 29. Comparison of hydrogen delivered price for cascade vs. booster compression tank filling for both steel and composite tanks, each for both 100-FCV and 900-FCV fueling stations.

Gasoline Infrastructure Tasks

Annual Gasoline Infrastructure Investments

The global oil industry must make investments each year to maintain the existing gasoline infrastructure. Investments are required for new crude oil exploration and production, crude oil transport to the refinery, refinery maintenance, as well as investments in the actual gasoline delivery system including pipelines, storage facilities, tanker trucks and retail fueling maintenance including the replacement of underground storage tanks. While crude oil is converted into many products other than gasoline, part of these upstream investments are essential to maintain the flow of gasoline to consumers.

Assessment of these oil industry annual investments is desired to compare with the costs of installing a new hydrogen or methanol infrastructure. While gasoline and internal combustion engine vehicles (ICEVs) will be around for many decades, one can postulate a gradual transition to direct hydrogen FCVs. For example, some small fraction of the investment in gasoline infrastructure could be shifted each year to building up a new hydrogen production and delivery system. If the new hydrogen infrastructure costs are approximately equal to or even less than the annual gasoline investments per vehicle supported, then society should be able to accommodate the transition to hydrogen from an economic perspective. Of course oil companies (particularly foreign crude oil suppliers) or other fuel providers may not be willing to make these investments in hydrogen infrastructure, even though our economic analyses show that societal costs would be equal or

lower than current investments. The economic risks of converting from gasoline to hydrogen fueling infrastructure would be larger than continuing the status quo of converting crude oil to gasoline. In the early stages of direct hydrogen FCV introduction, there may be too few FCVs to provide reasonable return on hydrogen infrastructure investment. Nonetheless, an economic evaluation of the relative infrastructure investments for hydrogen and gasoline will help to guide DOE as they plan their research and development portfolio for developing new hydrogen fuel delivery technology. This assessment should also be valuable for other key decision-makers in the auto and fuel industries and in government.

Capital and exploration expenditures of the top 200 refineries in the United States and the top 100 oil companies outside the U.S. are reported in a special issue each September of the *Oil and Gas Journal*. In 1998 the total capital and exploration expenditures by U.S. oil companies were in excess of US\$69 billion with a total annual production of 3,259 million barrels (Mbbbl) of crude oil¹⁹. But we must also consider the investments made by OPEC nations and other foreign companies that provide over half of all U.S. crude oil today. Investments to keep the imported oil flowing to U.S. refineries are necessary to continue supplying gasoline to U.S. drivers. Unfortunately, none of the key Middle East oil producers except Oman report their annual capital expenditures. Furthermore, the reported investments include exploration and production for both crude oil and natural gas extraction. Thus we must estimate both the capital expenditures of key oil-producing states and also the fraction of the annual capital expenditures that affect crude oil compared to natural gas. The estimated split between crude oil and natural gas expenditures is complicated since many fields produce both crude oil and natural gas.

We filled in the gaps of missing capital expenditures by scaling from other similar oil and gas operations in each region, based on the known production levels of crude oil and natural gas for each company. For example, the Saudi Arabian Oil Company does not report their annual capital expenditures, but we do have data from nearby Oman. So we estimated capital expenditures for Saudi Arabia by scaling the Oman expenditures by the ratio of the Saudi production (oil plus natural gas) to Oman's production. In effect we are assuming that the Saudis invested the same percentage of their revenue in capital expenditures as their neighbor. The major companies that required this estimate of capital expenditures are listed in Table 16, along with the surrogate company used for scaling purposes. We had to estimate 29.8% of the global capital expenditures or \$71.2 billion out of \$238 billion total estimated expenditures for 1998.

¹⁹Oil and Gas Journal, September 13, 1999.

Table 16. Oil companies requiring estimation of capital expenditures and total world expenditures.

Non-US companies which did not report Exploration & Capital Expenditure Data	1998 World Wide Oil Production (M bbl)	% World Wide Oil Production	1998 World Wide Gas Production (Bscf)	1998 Total Capital & Expl. Exp. (M\$)	% of World Capital Expenditures	Capital Expenditure Basis
<i>Yacimientos Petroliferos Fiscales Bolivianos</i>	10	0.0%	72	79	0.0%	Brazil, Mexico & Venezuela
<i>Empresa Nacional del Petroleo (Chile)</i>	3	0.0%	54	36	0.0%	" "
<i>Petroleous del Peru SA</i>	42	0.2%	35	232	0.1%	" "
<i>Sonogal (Angola)</i>	268	1.2%	20	1,751	0.7%	Egypt and Algeria
<i>National Oil Corp. (Lybia)</i>	508	2.2%	225	3,401	1.4%	" "
<i>Nigerian National Petroleum Corp.</i>	772	3.3%	135	5,080	2.1%	" "
<i>Enteprise Tunisienne Activities Petrolieres</i>	30	0.1%	12	198	0.1%	" "
<i>Abu Dhabi National Oil Co.</i>	692	3.0%	890	1,939	0.8%	Oman
<i>Bahrain National Oil Co.</i>	38	0.2%	215	134	0.1%	" "
<i>Dubai Petroleum Co.</i>	115	0.5%	67	308	0.1%	" "
<i>National Iranian Oil Co.</i>	1,317	5.7%	1,196	3,604	1.5%	" "
<i>Iraq National Oil Co.</i>	770	3.3%	231	2,028	0.8%	" "
<i>Ministry of Energy & Infrastructure (Israel)</i>	0	0.0%	1	0	0.0%	" "
<i>Kuwait Petroleum Corp.</i>	757	3.3%	207	1,990	0.8%	" "
<i>Qatar General Petroleum Corp.</i>	241	1.0%	684	740	0.3%	" "
<i>Saudi Arabian Oil Co.</i>	3,024	13.0%	1,254	8,019	3.4%	" "
<i>Syrian Petroleum Co.</i>	202	0.9%	141	545	0.2%	" "
<i>Petroleum Unit (Brunei)</i>	51	0.2%	345	1,130	0.5%	Thailand 1997, Australia
<i>China National Petroleum Off-Shore Corp.</i>	120	0.5%	137	1,969	0.8%	" "
<i>China National Petroleum Co.</i>	1,168	5.0%	767	18,593	7.8%	" "
<i>Oil & Natural Gas Corp (India)</i>	240	1.0%	820	4,497	1.9%	" "
<i>Pertamina (Indonesia)</i>	474	2.0%	2,399	9,670	4.1%	" "
<i>Petronas (Malasia)</i>	263	1.1%	847	4,869	2.0%	" "
<i>Oil & Gas Development Co. Ltd (Pakistan)</i>	8	0.0%	61	183	0.1%	" "
<i>Petroleum Authority of Thailand</i>	27	0.1%	577	216	0.1%	Thailand 1997
Sub-Total	11,141	48%	11,392	71,213	29.8%	
US Companies Total World Data - 1998	3,282	14.1%	16,999	61,541	25.8%	
Non-US Compaies Total World Data - 1998	19,914	85.9%	35,683	177,124	74.2%	
World-Wide Totals - 1998	23,196	100.0%	52,682	238,665	100.0%	

A similar procedure for 1997 produced an estimate of \$251 billion total world oil and gas capital expenditures.

The next step is to split these expenditures between crude oil product and natural gas product. We do have reasonably good data on natural gas production and capital expenditures within the U.S. for 1996 and 1997 from the American Gas Association (Wilkinson-1999). Combining all capital expenditures for natural gas exploration, production, storage, transmission and distribution, we estimate that the U.S. natural gas industry annually invests between \$760,000 and \$860,000 per billion cubic feet (bcf) of natural gas delivered to their customers. Since natural gas capital investments have been lagging in recent years, we take the higher estimate as more likely for the 1997-1998 time period considered for the global oil industry capital expenditures. The basis of these estimates is summarized in Table 17 for 1996 and 1997. The AGA lists combined oil and gas dry well costs, so we had to estimate the fraction of dry well costs attributed to natural gas compared to oil wells. We split the dry well costs according to the fraction of expenditures for successful gas wells compared to total successful wells (oil and gas).

Table 17. Estimate of U.S. natural gas industry capital expenditures per unit natural gas consumption

	1996	1997
Capital Expenditures (US\$ billions)		
Natural gas drilling expenditures	5.35	7.84
Natural gas share of dry well expenditures	1.83	2.29
Natural gas transmission & distribution	7.74	6.83
Total Natural gas expenditures (US\$ billions)	14.9	17.0
Disposition of U.S. Natural Gas (billion cubic feet)		
Total U.S. Natural gas consumption	22,560	22,270
Exports from U.S.	+153	+157
Imports to U.S.	-2,937	-2,994
Net US production (bcf)	19,506	19,707
Estimated capital cost per unit production (US\$ millions/bcf)	0.76	0.86

The cost of maintaining the world's gasoline infrastructure relative to the new car population is then determined by scaling the fraction of crude oil going to gasoline and dividing by the total number of new vehicles sold in the world each year. Approximately 40.3% of U.S. refinery product goes to making gasoline in the U.S. (Davis-1999). However, much lower volumes of gasoline are produced in Europe from a barrel of crude oil, since they produce more diesel fuel and other products. The European average for gasoline fraction is only 21.2%, while the average of all OECD²⁰ countries is 29.5% gasoline. We use this value (29.5%) as representative of the world oil refineries, since OECD nations account for about 60% of all oil refining in the world.

The total new light duty vehicle sales in the world reached 54 million vehicles in 1999²¹. However, approximately 25% of new vehicles sold in Europe run on diesel fuel instead of gasoline. We have subtracted off 25% of European light duty vehicle (LDV) sales to estimate total gasoline vehicle sales. As shown in Table 18, we estimate that the oil industry invests about \$1,230 for every new light duty vehicle sold in the world.

At first this estimate might seem high, in the sense that a typical vehicle consumes only 500 gallons of gasoline per year to travel 12,000 miles. Assuming a wholesale price of 80¢/gallon, then the oil company would only receive \$400/year for each car on the road. However, a car typically lasts 13 years, so the total

²⁰Organization for Economic Cooperation and Development includes Australia, Austria, Belgium, Canada, Czech Republic, Denmark, Finland, France, Germany, Greece, Hungary, Iceland, Ireland, Italy, Japan, Luxembourg, Mexico, Netherlands, New Zealand, Norway, Poland, Portugal, South Korea, Spain, Sweden, Switzerland, Turkey, the United Kingdom and the United States.

²¹Ward's Communications, *Ward's Motor Vehicle Facts & Figures 2000*TM, Southfield, Michigan, 2000

oil company revenue over the life of the car is almost \$5,200. Discounted 10% over 13 years, this stream is worth \$2,840. In this context, investing \$1,230 out of \$2,840 discounted revenue is not excessive.

Table 18. Estimate of global oil company capital expenditures per light duty vehicle sold annually

	1997	1998
Global capital expenditures for oil & gas production (US\$ Billions)	252	238
Global Natural gas production (bcf)	52,385	52,682
Estimated capital expenditures for natural gas (US\$ Billions)	45.1	45.3
Net capital expenditures for crude oil (US\$ Billions)	207	193
Capital expenditures attributed to gasoline - 29.5% (US\$ Billions/year)	61.0	56.9
No. of light duty gasoline vehicles sold (millions)	46.9	49.1
Capital expenditures per light duty vehicle (US\$/LDV)	\$1,300	\$1,160

We have also compared this gasoline infrastructure cost per vehicle with the expected cost of providing a hydrogen infrastructure to new direct hydrogen FCVs. We have previously estimated the cost of providing a hydrogen fueling appliance at the local fueling station, based on steam reforming of natural gas (Thomas-1997b & 1998a). But we should also include the annual expenditures to maintain the natural gas infrastructure, just as we did for gasoline.

In the case of natural gas, we can restrict our evaluation to North America, since we do not import any sizeable amounts of natural gas from outside the continent. From Table 2, we estimated the capital expenditures to produce 19,500 bcf of natural gas per year in the U.S. If all this gas had been converted to hydrogen at 62% efficiency (LHV of hydrogen/HHV of natural gas), this gas would have produced 108 million metric tonnes of hydrogen, enough to support a total FCV fleet of 590 million FCVs, or almost three times the total U.S. light duty vehicle fleet of some 201 million vehicles. If we assume that FCVs would have the same turnover rate as ICEVs or about 7.7% per year (13-year average life), then consumers would have to purchase about 45 million FCVs annually in this hypothetical scenario. The annual natural gas investment cost per new FCV sold would then vary between \$328/FCV and \$430/FCV, compared to \$1,230 per gasoline vehicle as summarized in Table 19.

!@#

Table 19. U.S. natural gas capital expenditures & hydrogen infrastructure cost per vehicle

	1996	1997	1998
Natural Gas U.S. Expenditures (US\$ billion)	14.9	17	(20)
Natural Gas U.S. production (bcf)	19,506	19,707	20,000
Potential hydrogen production (metric tonnes)	108	109	110
Total number of FCVs supported by H2 (millions)	590	595	600
New hydrogen FCVs sold per year (millions)	45.4	45.8	46.2
NG infrastructure cost per FCV (US\$/FCV)	\$328	\$370	\$433

Natural gas investments have been growing in the last few years after a long decline, and will undoubtedly increase since the wellhead price of natural gas more than doubled in 2000. We therefore use the higher

estimate of 1998 at \$430/FCV to represent the capital investment to support new natural gas consumption by FCVs. The combined cost of the hydrogen fueling appliances and the natural gas infrastructure costs are summarized in Figure 30 as a function of the number of FCVs supported by the fueling station. This cost will depend on the size of the fueling station and also on the number of hydrogen fueling appliances produced.

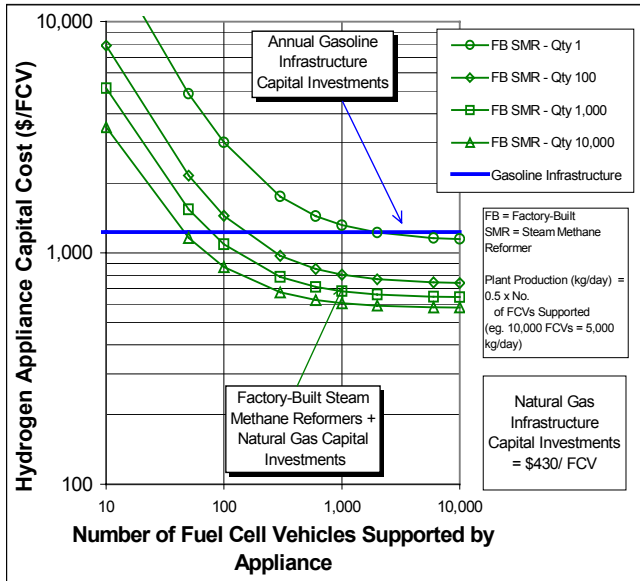


Figure 30. Estimated hydrogen infrastructure capital expenditures (including natural gas infrastructure capital expenditures) per fuel cell vehicle sold, compared to global gasoline infrastructure expenditures per new vehicle sold.

We conclude that the total cost of a distributed hydrogen infrastructure based on small-scale steam methane reformers would cost between \$600 and \$800 per FCV, including the prorated share of the natural gas infrastructure investments, as long as the fueling station supported more than 1,000 FCVs and more than 100 such fueling appliances were built. Therefore total hydrogen infrastructure costs could be up to 50% less than the costs of maintaining the existing gasoline infrastructure system at \$1,230 per new vehicle purchased.

Sulfur Removal²²

Sulfur in gasoline is a major obstacle for fuel cell vehicles with onboard fuel processors. The typical on-board partial oxidation reformer system for a fuel-cell vehicle consists of an auto-thermal steam reformer followed by a high-temperature shift reactor section, a low-temperature shift section and several stages of preferential oxidation. The catalysts of the low-temperature shift (LTS) and preferential oxidation (PROX) reactor sections are poisoned by sulfur at their respective operating temperatures. Their performance is inhibited by even very small concentrations (> 1 ppm S) of hydrogen sulfide in the reformat stream. The on-board POX reformer system will require sulfur removal upstream of the LTS and PROX reactor sections to maintain a

²²Primary author of this section is John Reardon.

reasonable performance over the life of the vehicle.

The EPA has released new Tier II gasoline regulations that require “most refiners and importers to meet a corporate average sulfur standard of 120 ppm and a cap of 300 ppm beginning in 2004. By 2006, the cap will be reduced to 80 ppm and most individual refineries must produce gasoline averaging no more than 30 ppm sulfur” (US EIA-2000). The current national average pool averages 293 ppm for conventional gasoline (CG) and 207 for reformulated gasoline (RFG), but approximately 14 out of 110 U.S. refineries outside of California (o.c.) have gasoline sulfur levels above 500 ppm.

Therefore even the “low sulfur” gasolines proposed by EPA for internal combustion engines would contain too much sulfur for an onboard fuel processor and fuel cell system. This excess sulfur must either be removed at the refinery down to the 1 ppm level, or it must be removed with an onboard sulfur absorber system. We analyzed the cost of these two options, along with a composite approach of partial sulfur reduction at the refinery with a smaller onboard sulfur absorption system. The incremental cost of producing low sulfur gasoline at the refinery is reviewed for 30 ppm and 5 ppm S fuels. We then estimated the cost of installing a mass-manufactured sulfur absorber bed installed onboard a conceptual fuel cell vehicle with an onboard POX reformer. The sulfur absorber is based on ZnO technology achieving less than 0.5 ppm at <350°C in partial oxidation reformat feeds, and is sized for 300 ppm, 30 ppm and 5 ppm gasoline with a 100,000 mile life and 30 mpg assumed fuel economy.

Fuel Cell Vehicle Grade Gasoline

From a vehicle perspective, the best option would be to remove all of the sulfur at the refinery. This would reduce FCV cost and, more importantly, eliminate the need for periodic sulfur absorber replacement over the life of the car. FCV grade gasoline would differ in several respects from a low-sulfur gasoline intended for an internal combustion engine application. First the FCV-grade gasoline would require sulfur content to be less than 1 ppm S if no onboard sulfur absorber were used. Second, the FCV-grade gasoline is essentially a hydrogen carrier destined to be processed in an onboard reformer to produce a hydrogen-rich stream. Therefore there is no need for the fuel to have a high octane number. The oil companies need to identify a refinery gasoline stream that would have low sulfur content, low octane and perhaps little or no additional processing cost to provide a FCV-grade gasoline for an emerging market.

The highest value refinery gasoline streams are the high octane runs. The components of gasoline that promote high octane are aromatic and olefin content, but these molecules have fewer hydrogen atoms per carbon atom, and aromatic compounds in particular would contribute to increased coke formation in the onboard reformer, limiting catalyst life. A typical reformulated gasoline (RFG) has approximately 22% and 28% aromatic content and approximately 300 ppm and 150 ppm S for regular and premium grades respectively. Therefore unprocessed RFG would be undesirable as a fuel for a FCV with an onboard reformer.

Typical low sulfur streams available at the refinery are the reformat stream (< 1ppm S), the isomerate stream (1 to 3 ppm S) and the alkylate run (~10 ppm S). However, these are high-value refinery streams due to their high octane number (~90) and their contribution as premium grade gasoline blend stocks. High gasoline prices have produced a trend away from premium grade gasoline, and if excess capacity were available at the refinery, these low sulfur streams might be useful for very low sulfur FCV-grade gasoline. However, a lower

cost solution is to utilize the strait-run, which is the middle cut of the crude oil distillate. The heavy strait run is typically sent to be desulfurized and reformed to produce a high aromatic content stream. The light strait run has a lower octane number (~70) and contains about 100 to 400 ppm S. This stream is blended into about 4% of the gasoline pool and is considered a low-value blend stock. This stream would however be ideal for an FCV-grade gasoline since it could be purified to 99% conversion with technologies developed for gasoline desulfurization. Indeed, the desulfurization technology restrictions placed to inhibit octane loss (saturation of olefins) are not necessary since the ideal FCV-grade fuel would have fully saturated hydrocarbons.

Since the light strait run is considered a low-value stream, it could perhaps be used to produce batches of FCV-grade fuel with a single desulfurization processing step. The largest component of the regular gasoline pool, FCC gasoline, would require higher processing costs to make FCV-grade gasoline and multiple desulfurization steps. We therefore propose that the FCV-grade fuel could be produced from the low value “light strait run” feed stock at a cost comparable with regular grade gasoline with a single desulfurization step with approximately 99% conversion for sulfur removal.

In summary, it seems reasonable that a low cost FCV specialty grade of gasoline with low octane and low sulfur could be produced in at least batch quantities for an early gasoline FCV market in a cost-effective manner. Therefore, the refinery producing 1 ppm FCV-grade fuel would always be more cost-effective than relying on an onboard sulfur absorber utilizing a fuel with sulfur concentrations above 1 ppm. However, no such fuel is produced and delivered to the retail market at the present time. Furthermore, there are other costs associated with supporting an additional distinct fuel at a given distribution point that should also be considered, but the light strait run would make a good candidate for a cost effective FCV-grade gasoline.

Low Sulfur Regular Grade Gasoline

Next we reviewed the costs of reducing sulfur content at the refinery from current levels of near 300 ppm down to 30 ppm and to 5 ppm to reduce the burden of onboard sulfur removal systems. Sulfur occurs naturally in the higher boiling point fractions of crude oil that contain from .05% (500 ppm) to as much as 3% (30,000 ppm) sulfur. The sulfur is chemically bound as a heteroatom in thiophene and benzothiophene molecules of the heaviest fractions (highest boiling points) of the crude stream. The largest contribution of sulfur to the gasoline pool comes from the fluidized catalytic cracker (FCC) naphtha stream (also known as “cat gas”), since the FCC reactor produces gasoline and diesel from the heavier fractions of the crude oil stream. The FCC naphtha stream accounts for approximately 40% of the gasoline pool but contributes nearly 90% of the sulfur. Deep desulfurization of the FCC feed or product stream alone might be sufficient for current sulfur standards, but other gasoline blend-stocks would have to be further treated to meet a new low sulfur standard. Other sulfur-containing streams such as the light strait run and the coker blend stock contribute less than 5% and ~0.5%, respectively, of the gasoline pool. However, these feed stocks would contribute a total of ~ 30 ppm S by themselves even after dilution with other low sulfur blend stocks. The heavy strait run is typically desulfurized and reformed to improve its octane, so its contribution of sulfur to the gasoline pool is negligible. The alkylate run contributes an insignificant amount of sulfur to gasoline. Its sulfur content is on the order of 10 ppm and constitutes only about 10% of the gasoline pool.

The cost of gasoline processing and sulfur removal is typically higher in the mountain states, Alaska and the

west coast,²³ PADDs 4-5 (outside California, o.c.), than in the east coast, mid west and gulf coast refineries, PADDs 1-3, due to a higher premium paid for octane replenishment and hydrogen usage in the western regions. However, refineries in PADDs 4-5 (o.c.) supply only about 9.5% of the U.S. gasoline production outside of California. Many studies only estimate desulfurization costs for PADDs 1-3, as 14 refineries in PADD 4 will have a geographical exemption or delayed regulator responsibility until 2007, and some refineries serving a large fraction of PADD-4 will also benefit from the same exemption. Notably, there are also 16 small refineries in the U.S. that will have a hardship exemption until 2008 (EPA-1999).

The cost of removing sulfur is refinery-, feed- and technology-dependent. A refiner may choose conventional deep hydrotreating of the FCC feed stream; however, it is well established that in general a less expensive alternative is to desulfurize the FCC product stream (also known as the FCC naphtha run, or “cat-gas”). Conventional hydrodesulfurization (HDS) would reduce the octane number of the product by a large amount (8-12 octane numbers) by saturating the component olefins. The average cost of octane replenishment is 0.7¢/gal-Oct# and is regionally variable from 0.54 to 2.2¢/gal-Oct#. In contrast, many new technologies have been developed to minimize or circumvent octane loss on FCC gasoline desulfurization. This octane loss is only deleterious for internal combustion engines, which is the focus of most discussions in the oil industry regarding desulfurization. While FCVs with onboard reformers do not need high octane, it would be desirable if any FCV-grade gasoline could also be used in an internal combustion engine. In this case both ICEVs and FCVs could use the same gasoline, eliminating the need for a new set of gasoline storage tanks and pumps at each station.

Table 20 presents an example calculation for three “proven” gasoline desulfurization technologies, two “improved” processes and also two “advanced,” low-cost adsorption technologies. In this example, the process parameters from the EPA regulator impact analysis were volume-averaged for PADDs 1-3 and PADDs 4-5. These values assume 95% conversion of sulfur. We have assumed here that 47% of the gasoline pool would be processed to achieve the 30 ppm sulfur standard. This might be represented by a 1,275 ppm feed stream converted to 64 ppm and diluted to 30 ppm. Actual feed stream composition and sulfur removal requirements will vary across the country, and certain technologies may be more favorable with different feed stream compositions, but this calculation is intended only as a single-point cross-technology example. A capital recovery factor of 0.16 is assumed. The EPA assumes a lower profit margin, and other studies have assumed higher values, but the capital recovery is only a small fraction of the total processing costs. Figure 31 presents the process cost breakdown for each technology based on EPA processing parameters and volume averaged costs.

²³ PADD: Petroleum Administrative Districts for Defense (PADD); 1: East Coast, 2: Mid West, 3-Gulf Coast, 4: Mountain States, and 5: West Coast, California excluded.

Table 20. Gasoline Processing Cost (cents/gallon) for 95% Sulfur Conversion where 47% of Final Pool is Processed.

	Proven FCC Gas HDS			Improved FCC-Desulf		Adsorption Technologies	
	Octgain 125	Exxon Scanfining	IFP Prime-G	Octgain 220	CDTech	Black & Veatch (IRVAD)	Phillips S-Zorb
PADD 1-3	2.59	1.75	2.10	2.19	1.62	0.84	1.25
PADD 4-5 o.c.	2.87	2.58	3.19	2.53	2.42	0.86	1.82

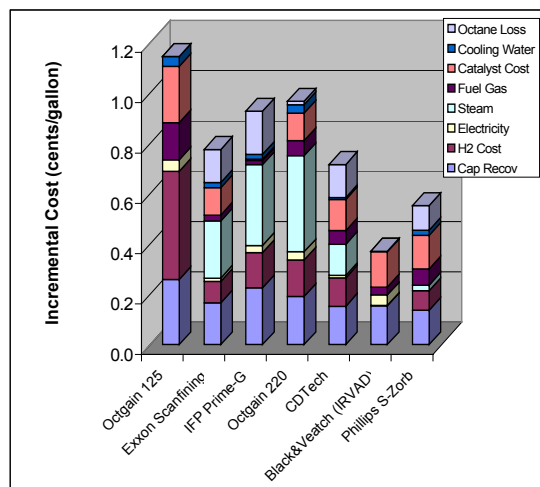


Figure 31. Estimated incremental costs of producing 30 ppm sulfur gasoline compared to conventional 300 ppm gasoline by technology with PADD 1-3 volume-averaged operating costs.

Mobil Octgain 125, Exxon Scanfining, and IFP Prime-G are similar in that they are fixed bed reactor technologies. They differ in approach in that the Octgain 125 process permits saturation of olefins, but recovers octane through isomerization and alkylation reactions within the process reactor, whereas Scanfining and Prime G reduce the severity of temperature and pressure and use catalyst selectivity to minimize octane loss. Where deep desulfurization is required, octane loss would be more extensive with certain of the technologies presented in Figure 31, resulting in higher processing costs than are presented here. The improved Octgain 220 is similar in approach to Octgain 125, but reduces costs by reducing the severity of processing conditions. However, its application is not intended for very high sulfur streams where deep sulfur conversion is required. CD-Tech uses a twin catalytic distillation reactor to proportionate more extensive hydrotreating to the heavier fraction of the FCC naphtha stream. The Black and Veatch adsorption process (IRVAD) uses twin reactor columns with a regenerable alumina adsorbent that is transported circuitously through the adsorber column and the regenerator column. The sulfur heteroatom-containing molecules are scavenged in the adsorber and released in the regenerator in a hydrogen environment. Black and Veatch claim negligible hydrogen consumption with a zero to moderate increase in octane value of the product. It should be noted, however, that the Black and Veatch (IRVAD) adsorption technology produces a ~10,000 ppm S heavy product stream that would also require desulfurization or further processing prior to blending in other product streams. These additional costs were not included, but may be important. In contrast, the Phillips S-Zorb process, which is also a proprietary adsorbent technology, combines desulfurization and adsorption in a single reactor. The adsorbent is regenerated with air and reactivated with hydrogen prior to

recycling back to the adsorbing reactor. There is no high sulfur product stream for S-Zorb.

Mathpro has published two reports estimating the cost of low sulfur gasoline for U.S. refineries in PADDs 1-3. One such study was funded by the American Petroleum Institute (API) estimating the cost of 40 ppm S gasoline based on CDTech and Mobil Octgain 220 used in a notional refinery representing those in PADDs 1-3. (Mathpro-1999a). Their cost estimate for sulfur reduction was 2.25¢/gal for CDTech and 2.6¢/gal for Octgain 220. The EPA reviewed their results adding an incremental cost to achieve 30-ppm standard (2.65¢/gal average) adjusting for 7% ROI before taxes results in 2.2¢/gal. The EPA reviewed several other studies and used the same models to make incremental adjustments for the 30 ppm S standard with updated processing cost numbers and the same capital recovery factors. The studies included the National Petrochemical and Refiners Association (NPRA) funded Mathpro study (Mathpro-1998), the Association of International Automobile Manufacturers (AIAM) funded Mathpro study (Mathpro-1999b), and the Oak Ridge National Laboratories (ORNL) DOE study for mid capacity refinery (Oak Ridge-1999). Finally, Mustang Engineers and Constructors, Inc. published an estimate of ultra low sulfur gasoline (Lamb-2000). The EPA-adjusted desulfurization costs are summarized in Tables 21 and 22 below. The fuel costs to the consumer are calculated based on 12,500 miles per year, with the fuel cost present value assuming 7% discount factor for consumer purchasing.

Table 21. EPA-reviewed processing cost estimates for 30 ppm gasoline by PADD having assumed technology mixes with cost adjustments for 7% ROI before taxes, after tax capital recovery of 0.13. Consumer fuel cost differentials are calculated for 12,500 mi/year and 7% time value of money

30 ppm PADD 1-3 (90.5% US Production)	¢/gal	12.5k mi/yr Fuel Cost \$/yr	8 yr Fuel Cost Present Value (\$ Present Value.)
EPA 2008 Mix Tech, Volume Averaged	1.80	7.5	44.8
API Study, CD Tech, EPA Adj 7% ROI	2.25	9.4	56.0
API Study, Octgain 220, EPA Adj 7% ROI	2.6	10.8	64.7
Mustang Study, mid range	2.75	11.5	68.4
DOE, ORNL mid range, EPA Adj 7%	2.75	11.5	68.4
	average	2.43	10.160.5
30 ppm PADD 4-5 (9.5% US Production)	¢/gal	\$/yr	(\$ Present Value)
EPA 2008 Mix Tech, Volume Averaged	2.83	11.8	70.4
EPA PADD4 Adsorption Tech Only	2.5	10.4	62.2
EPA PADD4 CD Tech Only	3.2	13.3	79.6
NPRA 40 ppm Octgain-125, EPA Adj 7%	3.5	14.6	87.1
AIAM CD-Tech, EPA Adj 7% ROI	2.41	10.0	60.0
	average	2.89	71.9
30 ppm National Average	2.47	10.3	61.5

Table 22. EPA-reviewed processing cost estimates [3,9,10] for 5 ppm gasoline having assumed technology mixes with cost adjustments for 7% ROI before taxes, an after tax capital recovery of 0.13

5 ppm S National Averaged	30 ppm to 5 ppm (¢/gal)	300 ppm to 5 ppm (¢/gal)	Added Fuel Cost (\$/yr)	Fuel Present Value (\$)
EPA CD-Tech (1.4 c/gal) [3]	1.4	3.8	16.1	96.4
EPA CD Hydro/Oct 125 [3]	1.7	4.1	17.4	103.8
EPA FCC Feed HT/CD-Tech [3]	2.1	4.5	19.1	113.8
Mustang Study [9]	1.2	3.6	15.3	91.4
AIAM Study mid range [10]	2.25	4.7	19.7	117.5
average	1.73	4.16	17.5	104.6

The EPA believes that as time progresses a larger portion of refineries will use the lower cost adsorption technologies and that 30-ppm gasoline might cost as low as 1.70¢/gal nationally above regular gasoline. However, the comparative analysis that follows will be using the composite national average of 2.47¢/gal for 30-ppm gasoline, and 4.16¢/gal for 5-ppm gasoline relative to the cost of conventional gasoline having ~300 ppm S. A gross cost estimate for 150-ppm gasoline is 1.12¢/gal based on processing only 21% of the gasoline pool rather than 47% for 30-ppm gasoline. Similarly, 75-ppm gasoline is estimated to be 1.80¢/gallon more expensive. We will use these estimates later to predict the full cost of producing lower sulfur fuel at the refinery plus adding a sulfur absorber on the FCV.

Size and Cost of an Onboard Sulfur Absorber

A sulfur absorber bed for a FCV was sized according to the performance of a typical Zn-O based sulfur absorbent manufactured by Sud-Chemie, G72D consisting of 3/16" diameter pellets with a cost of \$9.89/L in drum quantities. In an automotive application a monolithic absorber bed may be more desirable. Nevertheless, it is assumed that an appropriately-designed absorber will have negligible channeling or internal by-pass. Therefore, the concentration of H₂S exiting the absorber can be determined by equilibrium. The amount of absorbent and operating conditions (flow rate and temperature) determine the sulfur absorption capacity over the life of the unit. The absorption of H₂S from the reformer process gas stream involves a bulk transformation of the ZnO to ZnS with the release of water. Therefore the equilibrium extent of the absorption reaction is inhibited by water vapor concentration.

Absorption capacity is estimated based on H₂S break-through curves at constant temperature and space velocity derived by the absorbent manufacturer. The absorbent capacity increases with temperature and decreases with space velocity. A minimum absorbent bed temperature of 315°C was selected as a preferred design point giving low sulfur concentration after the absorber with a reasonably good absorption capacity. Sud-Chemie supplied absorption capacity data as a function of space velocity (SV) for which the following regression was applied.

$$Uptake \left(\frac{kg}{L} \right) = \frac{a + b(SV)}{1 + c(SV)} \quad (10)$$

The regression parameters for the 315°C data set are (a,b,c)=(0.2472, -9.043e-6, 1.028e-4); the data set encompassed the range of SV from 2000 to 20,000 hr⁻¹. The rational regression had a correlation coefficient of R²=0.999, and the regression was used to interpolate within 2000 to 20000 hr⁻¹ and to extrapolate to ~26,000 hr⁻¹ for this study.

Modeling of a POX reactor system for a fuel cell application (James-1997a) shows that an optimum efficiency is obtained with a reformer exit temperature of 650°C and unity steam-to-carbon ratio (S:C=1). In this case, the water concentration is 16.4 mol%, and the auto-thermal reformer (ATR) would dilute gasoline feed sulfur by a factor of 44.68 after the reactor. Reformate gas would be cooled by a sensible heat exchanger (intercooler or feed water boiler) before contacting the G72D absorber bed at approximately 315°C. Figure 32 shows the equilibrium H₂S concentration in the exhaust from the absorber bed for a given absorber bed exit temperature. The H₂S concentration is 0.09 ppm at 315°C (600 °F) and 0.20 ppm at 343°C (650°F). The absorber should ideally be operated between 315°C and 343°C for maximum absorption capacity (useful life) with low exit sulfur concentrations.

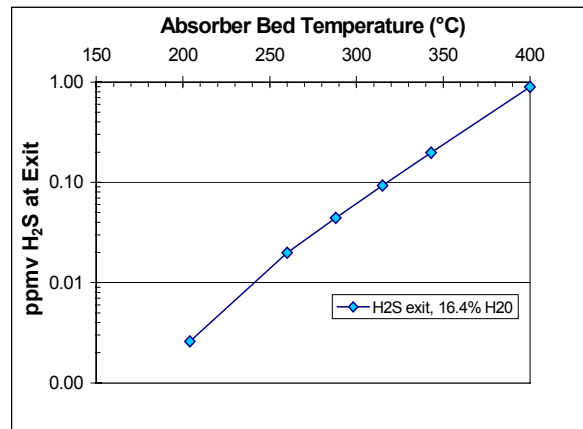


Figure 32. Equilibrium H₂S concentration vs. absorber bed temperature in 16.4% water background.

In this case we size the absorbent for complete sulfur uptake over a 100,000-mile life with an assumed 30-mpg average fuel economy²⁴. For a different fuel economy the absorber may be proportionately sized with respect to the results presented here. Under these assumptions the absorber must have a capacity in excess of 208-g sulfur uptake for a 300 ppm gasoline feed and 20.8-g sulfur uptake for a 30-ppm feed. Figure 33 displays the absorbent volume required to take-up the given amount of sulfur for the various gasoline feeds (fuel

²⁴We have previously estimated that a gasoline-powered FCV would probably have no better fuel economy than an ICEV of the same class. Even in the best case analyzed, the gasoline FCV would have at best 42 mpg fuel economy, compared to 30 mpg for the ICEV.

consumption depending on drive schedule) as a function of space velocity. The absorbent volume must match the volume calculated from the space velocity at the average reformer flow rate.

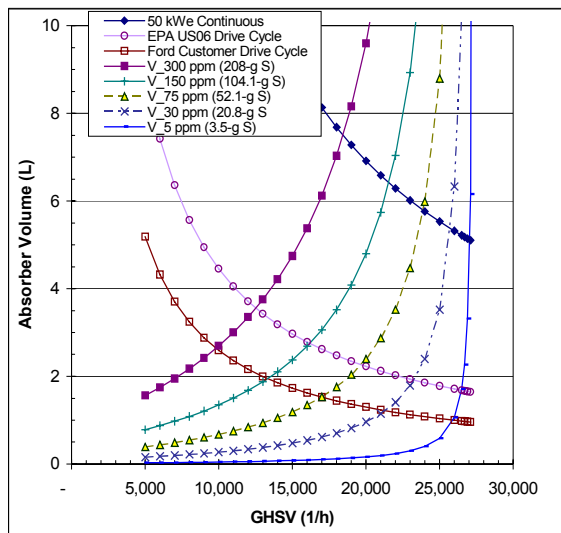


Figure 33. Constant sulfur uptake curves in G72D absorbent vs. space velocity for 100,000 mile vehicle lifetime at 30 mpg with various sulfur levels, along with average flow rates for three different driving profiles.

The average reformer flow rate is estimated to be 432 slpm based on the Ford Customer Drive Cycle (FCDC), (9.38 kWe average fuel cell out put), and 742 slpm based on the EPA’s more aggressive US06 drive cycle (16.1 kWe average). For this study the design space velocity (SV) will be based on the US06 drive cycle. A minimum size selection for 100,000-mile lifetime occurs at the intersection point of the flow rate curve and the uptake curve for the drive cycle and fuel sulfur composition (See Figure 33.) Efficient absorber performance is achieved with $SV < \sim 16,000 \text{ h}^{-1}$, but the automotive application requires low volume which drives the SV above $20,000 \text{ h}^{-1}$ for S compositions $< 75 \text{ ppm}$.

A 2-liter absorber would be sufficient for 100,000-mile installed life for a driver profile equal to the EPA US06 drive cycle (742 slpm average reformer flow rate). The average space velocity is $22,260 \text{ hr}^{-1}$, where the absorption capacity is only 27.9 g/L. Reducing sulfur content in gasoline to 5 ppm yields little advantage, since the absorber size is reduced only slightly, from 2 L to 1.7 L. A more favorable space velocity for absorption capacity can be attained with 2.5-L absorber on the US06 DC ($17,800 \text{ hr}^{-1}$) giving a much improved absorption capacity (76.1 g/L) permitting more than the 100,000 mile expected life even if the fuel contained 75 ppm S on the average. A 3-L absorber would be more cost-effective if the fuel contained 300 ppm S, as the space velocity and consequentially the absorption capacity is much more favorable ($14,840 \text{ hr}^{-1}$, 134 g/L). In this case the vehicle owner would have to change the absorber only every 64,000 miles rather than every 13,000 miles. However, pressure drop could be excessive with increased absorber size, and perhaps a 2.5-liter size would make a good compromise for all fuel compositions.

The absorber cost was estimated using a simplified DFMA²⁵ model. The absorber shell was designed with 10.16 cm nominal OD at 100 psig maximum allowable working pressure (MAWP) and 350°C using ASTM A240-347 stainless steel selected primarily for corrosion life and strength at temperature at a cost of \$6.6/kg. Labor rates of \$60/hr and machine rates of \$120/hr were assumed. The shell cylinder is rolled and seam-welded in large sections then cut to size in one operation. End caps are hot-forged in heated ram and die, then trimmed. There is one sub-assembly where retaining screens are installed into the end-caps. In the final assembly the end-cap is welded to the shell, then a volume of absorbent (G72D, \$9.86/L) is then poured into the container, after which the closing end-cap is installed and welded to the completed unit. The final price was estimated based on 240 units per daily batch, completed in two shifts with production amortization of tool and die costs at a 10,000-unit production level, and with 25% mark-up. The absorber could be integrated into the POX system at a macro-design stage. However, this unit cost estimation enables a comparative analysis for different fuel compositions. Based on this analysis, a 2-L absorber would cost \$40.56, and a 3-L absorber would cost \$56.04. As a point of size reference, the 2-L absorber bed is 24.5 cm long.

$$C_{adsorber} = 15.48 \cdot Vol(L) + \$9.60 \quad (11)$$

Table 23 summarizes the absorber performance and cost analysis. For 100,000 miles at an average fuel economy of 30 mpg, the theoretical FCV would consume 8,706 kg fuel, and the ATR/POX reformer operating at 650°C and S:C=1 would dilute the fuel by a factor of 44.68. The financial calculation for present value fuel costs and absorber replacement costs to the consumer assumes a 7%/year time value of money with an 8-year term (100,000 miles in 8 years). The present value calculation assumes initial installation investment plus the present value sum of replacement costs including a labor and disposal charge of \$50 plus absorber costs.

Finally, the present value of the incremental cost of FCV grade gasoline with 150 ppm, 30 ppm and 5 ppm average sulfur concentrations are compared to conventional gasoline. A 2.5L absorber is used for all cases including replacement costs converted to present value over an 8-year or 100,000-mile life cycle. Figure 33 displays this comparison where the incremental fuel costs are 1.12¢/gal, 1.80¢/gal, 2.47¢/gal and 4.16¢/gal for 150 ppm, 75 ppm, 30 ppm and 5 ppm gasoline, as previously discussed.

Table 23 shows that the 2-liter absorber has the lowest composite cost with an estimated life of ~134,000 miles using 30-ppm FCU gasoline. The combination of fuel and absorber is ~\$102 (present value) for that case. However, Figure 34 shows that the 75-ppm fuel cost with a 2.5-liter absorber has a slightly lower composite cost at \$93, but if the life cycle were increased to 150,000 miles then the 30-ppm fuel combination would be favored again. Refinery gasoline based on absorption technologies would make the gasoline portion even less expensive, yet the lowest cost combination is essentially achieved by the most appropriately-sized absorber (sized closest to 100,000-mile life). Larger absorbers on the order of 2.5 to 3-L are better because they produce a more favorable space velocity (17,800 and 14,800 h⁻¹, respectively) for improved absorption capacity; however, there is likely a trade-off between absorber performance efficiency and pressure drop. The largest contribution to the total life cycle costs is the cost to replace the absorber and the number of replacements required during the vehicle life cycle.

²⁵DFMA a registered trademark of Boothroyd Dewhurst, Inc., refers to “Design for Manufacturing and Assembly” - a methodology for designing low-cost products in mass production (Boothroyd-1994).

Table 23. Absorber cost and present value (P.V.) maintenance cost with 7% ROI on a 8 yr/100k mile life-cycle for various gasoline sulfur compositions. A 30-mpg average fuel economy is assumed.

Gasoline (ppm-S)	100 km S (g)	Units Req'd /100k miles	Filter Change (miles/unit)	Labor & Disposal (\$ P.V.)	Absorber Costs (\$ P.V.)	Total Costs (\$ Present Value)
2-L absorber	24.7 cm long	27.92	g-S/L	Absorber Unit	\$ 40.56	each
300	208.2	7.46	13,409	\$ 373.83	\$ 343.81	\$ 717.64
150	104.1	3.73	26,817	\$ 186.92	\$ 192.19	\$ 379.10
75	52.1	1.86	53,634	\$ 46.73	\$ 78.47	\$ 125.20
30	20.8	0.75	134,085	\$ -	\$ 40.56	\$ 40.56
5	3.5	0.12	804,513	\$ -	\$ 40.56	\$ 40.56
2.5-L absorber	30.8 cm lg	76.1	g-S/L	Absorber Unit	\$ 48.30	each
300	208.2	2.74	36,547	\$ 93.46	\$ 138.58	\$ 232.04
150	104.1	1.37	73,094	\$ 109.88	\$ 84.34	\$ 194.23
75	52.1	0.68	146,188	\$ -	\$ 48.30	\$ 48.30
30	20.8	0.27	365,469	\$ -	\$ 48.30	\$ 48.30
5	3.5	0.05	2,192,816	\$ -	\$ 48.30	\$ 48.30
3-L absorber	37.0 cm lg	134.2	g-S/L	Absorber Unit	\$ 56.04	each
300	208.2	1.55	64,449	\$ 46.73	\$ 108.41	\$ 155.14
150	104.1	0.78	128,899	\$ -	\$ 56.04	\$ 56.04
75	52.1	0.39	257,798	\$ -	\$ 56.04	\$ 56.04
30	20.8	0.16	644,494	\$ -	\$ 56.04	\$ 56.04
5	3.5	0.03	3,866,964	\$ -	\$ 56.04	\$ 56.04

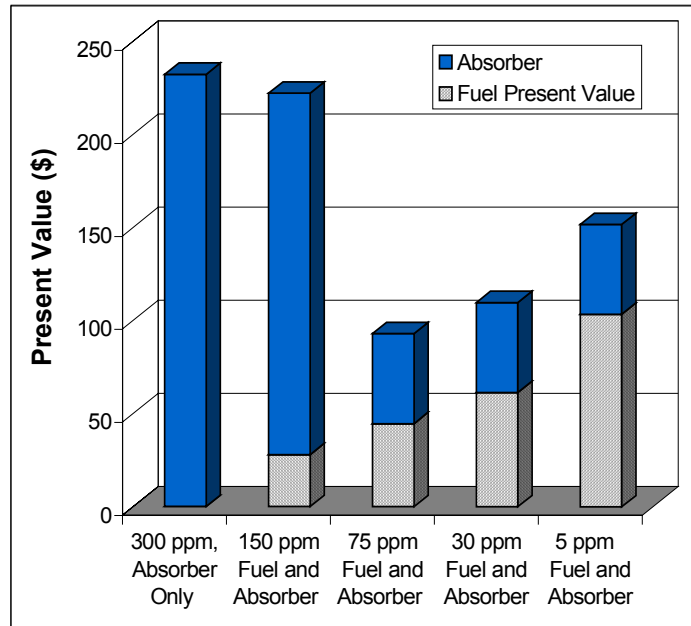


Figure 33. Trade-off between the cost of low-sulfur gasoline (pattern) and ZnO absorbent bed initial and replacement costs (solid).

The packed bed absorber has certain disadvantages in practice for an on-board application including attrition and densification of the bed. But in the absence of data for advanced absorber designs, that would include wash-coated ZnO on monolithic supports and zeolites doped with sulfur specific metal cations, this analysis was performed to consider the cost-effectiveness of refinery gasoline desulfurization compared to on-board sulfur absorbers. Perhaps advanced absorbers, which might occupy a larger, more open-celled geometry, could be utilized to remove sulfur in a cost-effective manner with regular grade gasolines in the range 30-ppm to 75-ppm. This would require further study to confirm. Nevertheless, it does not seem efficient to reduce the level of sulfur in gasoline below 5 ppm at the refinery if an onboard absorber is required since the reduction absorber volume is less than 7% while the incremental fuel cost is nearly 70% more expensive compared to the 30-ppm gasoline. However, it would be preferable to produce an FCV-grade gasoline with <1 ppm S so that no on-board absorber would be required, if such a fuel could be produced at a low cost.

Fuel Cost Comparison Including Sulfur Removal Costs

When we planned this task, we assumed that the cost for removing sulfur would be significant and might impact the fuel choice decision. However, our assessments show that the cost of sulfur removal could be negligible by any of the pathways we investigated. Removing sulfur down to 1 ppm at the refinery for a FCV-grade gasoline could involve no more cost than producing reformulated gasoline (RFG), since there is no requirement to maintain octane rating. In fact, one could argue that a low-octane sulfur-free gasoline could be produced at lower cost than RFG, since less refining would be required. But oil companies would then have to effectively provide another grade of gasoline to their retailers, and they would have to use piping, storage and tanker truck strategies that would prevent sulfur contamination. In this case fuel cell gasoline would incur similar costs to methanol. New tanks and pumps would have to be installed at costs in the range

of \$75,000 to \$100,000 per station. Alternately, gasoline stations would give up one grade of gasoline, which would incur revenue losses until such time as the FCV population increased in the region.

If the oil companies are not willing to invest in producing and marketing a 1-ppm sulfur, low-octane gasoline, then the next best option identified in this study would be to reduce the sulfur level to at least 75 ppm and install an onboard absorber on every FCV. We project fuel cost increase of only 1.8¢/gallon to reduce current sulfur levels from 300 ppm down to 75 ppm. For a FCV traveling 12,000 miles per year, this amounts to an annual increase in fuel expenses of \$8 per year. However, gasoline sulfur content will average only 30 ppm by the time FCVs are introduced according to proposed EPA regulations, so all drivers will pay a few cents per gallon more. The onboard sulfur absorber is projected to cost only \$48 per vehicle to handle 75 ppm sulfur, and only \$40 per vehicle for 30 ppm sulfur. Assuming an 18% capital recovery factor, this would amount to annual costs of less than \$8 per year, which is negligible compared to annual fuel costs of over \$600 per year. We conclude that sulfur removal will not affect the fuel choice between gasoline, methanol and hydrogen.

Methanol Infrastructure

The methanol industry currently has excess production capacity. This excess capacity may increase with the current push by California and other state regulators to curtail the use of MTBE (methyl tertiary butyl ether), the primary oxygenated fuel additive to gasoline mandated by the Clean Air Act Amendments of 1990²⁶. Methanol is the main ingredient (along with isobutylene) used to make MTBE, and the methanol industry was expecting additional MTBE demand to increase the demand for methanol in the future. This may have influenced the decisions leading to the construction of new methanol production plants in the last few years.

One methanol industry analyst (Crocco-1998) estimates that the methanol industry had excess global capacity of almost 8 million metric tonnes per year in 1998. He estimated that this excess capacity would increase to 9.6 million tonnes by 2003, enough to support 5 to 6 million methanol FCVs. Therefore the capital investments to supply methanol to FCVs will be less initially than the investments needed to introduce hydrogen FCVs, and might be comparable to the investments needed by the oil industry to bring a FCV-grade gasoline to the consumer.

Initial Methanol Costs

Given the existing methanol world-wide over capacity, methanol price to the driver will depend on the cost of methanol delivered to the U.S. Gulf coast plus the cost of storage and transportation from the Gulf to the end consumer at the local fueling station.

The cost of methanol delivered to the U.S. Gulf Coast has fluctuated widely over the last decade as shown in Figure 34, reaching an annual average high of over \$1.10/gallon in 1994. This spike was caused by plant outages combined with the implementation of the Clean Air Act Amendments of 1990 that first required the use of oxygenated fuel additives in gasoline. Prices dropped in 1998/1999, but have risen steadily since the spring of 2000. Methanol was selling at over 80 cents/gallon in early 2001 as shown in Figure 35. Over the

²⁶Ethanol is also used as an oxygenate in gasoline, mostly in the farm belt since ethanol is currently made from corn in the US.

last 18 years, the price of methanol at the Gulf has averaged about 59 cents/gallon in constant 2001 US dollars.

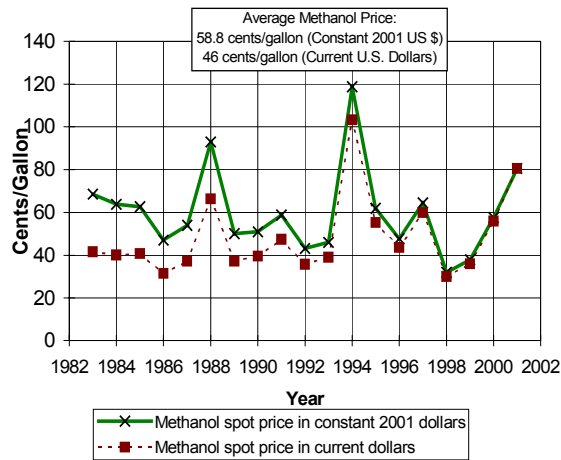


Figure 34. Annual average methanol spot price at the U.S. Gulf Coast

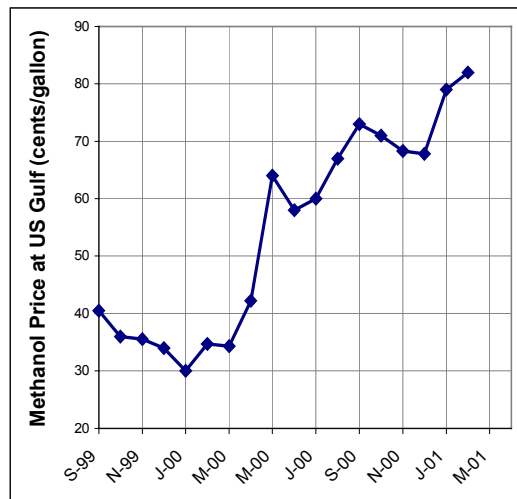


Figure 35. Recent methanol prices at the U.S. Gulf Coast.

The methanol price to the consumer will include the costs of bulk storage at the coast, bulk shipment to regional storage facilities, local distribution to the fueling station, plus retail markup at the station. The retail markup will include capital recovery of the costs of installing methanol tanks, pumps and dispensers plus a margin for the fueling station owner.

The costs to transport methanol should be approximately equal to the costs to ship gasoline. Methanol might cost more to ship initially, since it is more corrosive than gasoline, requiring the avoidance of certain materials in valves, seals, etc. But once proper methanol-compatible materials have been installed, the transportation and storage costs per gallon should be similar for these two liquid fuels.

Long-range and local distribution of gasoline is estimated at 6 cents/gallon. Local service station markup is estimated between 9 to 13¢/gallon (Gray-1989). One article lists the retail markup as 5¢/gallon for employee compensation, 7¢/gallon for rent, pumps and other, and just 1¢/gallon for station profit. The authors of the referenced report speculate that the methanol transportation would cost less than that of gasoline since the methanol would be shipped to ozone non-attainment areas that are typically close to large bodies of water, and hence methanol transportation would be by low-cost barge instead of land tanker trucks as for most gasoline. This assumption does not seem reasonable to us, so we use the estimates for gasoline of 15 to 22¢/gallon total transportation and local distribution costs. Assuming the historical average methanol Gulf price of 59¢/gallon (in constant 2001 US\$), then the consumer would pay between 74 to 81¢/gallon of methanol at the pump (before highway taxes).

If the methanol were used in an internal combustion engine (ICE), then the effective cost of methanol would double, since the energy content per gallon in methanol is about half that of gasoline. However, a methanol FCV will have better fuel economy than the ICEV. The appropriate figure of merit is the cost per mile for each fuel.

We also have to consider highway taxes. Methanol might be given tax breaks initially to encourage its use in clean FCVs. But eventually, if methanol FCVs dominated the marketplace, then state and federal officials would probably adjust the road taxes to collect the same revenue that they do now. The tax should therefore be applied on a per mile basis. If the methanol FCV has twice the energy efficiency as the ICEV, for example, then methanol (with half the specific energy of gasoline) should be taxed the same per gallon as gasoline – the increased fuel economy cancels out the lower volumetric energy content of methanol. We have previously estimated that a methanol FCV would achieve a fuel economy of between 44 to 49 mpgge (miles per gallon of gasoline equivalent on a lower heating value basis), compared to 30 mpg for an equivalent ICEV²⁷, or an improvement factor between 1.47 and 1.63. Under these conditions, then, governments would adjust the methanol road tax to between 54 to 60¢/gallon of methanol used in FCVs to provide the same revenue as gasoline used in ICEVs that is taxed at an average U.S. rate of 44¢/gallon.

With these assumptions, the fuel cost for a methanol FCV would be 3.2 to 3.5¢/mile before taxes. For comparison, the equivalent-sized ICEV would have a fuel economy of 30 mpg. With crude oil selling at \$30/barrel, retail gasoline (before taxes) would cost about \$1.02/gallon. The ICEV fuel cost would then be 3.4¢/mile before taxes. Thus the methanol FCV and the gasoline-powered ICEV would have equivalent fuel costs, if current historically high crude oil prices endured. However, if crude oil returned to previous levels of \$15/barrel, then methanol would cost 50% more per mile than gasoline, as summarized in Table 24.

²⁷All fuel economy estimates are based on an AIV (aluminum intensive vehicle) Sable operating on a 1.25 times accelerated EPA combined cycle (45% highway/55% city driving, with each speed segment in the EPA schedules multiplied by 1.25.)

Table 24. Comparison of methanol FCV and gasoline ICEV fuel costs

	Gasoline ICEV		Methanol Fuel Cell Vehicle
Fuel Economy (mpgge)	30		44 to 49
Fuel Cost at US Gulf	[Crude Oil = \$30/barrel]	[Crude Oil = \$15/barrel]	[Methanol = 59¢/gallon]
Retail Fuel Cost before taxes (¢/gallon)	102	65.5	74 to 81
Consumer Cost per Mile (¢/mile) [Before taxes]	3.4	2.2	3.0 to 3.7

In terms of investment costs, the methanol industry would have to invest in regional storage, transportation and local refueling facilities. The American Methanol Institute estimates a cost of \$50,000 to add one underground tank, pump and dispenser for methanol (Nowell-1998). However, the California Energy Commission reported costs of \$84,300 to \$97,000 to install M-85 (mixture of 15% gasoline and 85% methanol) tanks and dispensers in the early 1990's when the state was encouraging the use of methanol in ICE vehicles. Peter Ward of the CEC estimated that installation alone cost \$40,000 to \$50,000 for an underground tank. We therefore use \$75,000 as a realistic estimate for a single methanol dispenser. A 10,000-gallon methanol tank could support about 1,000 FCVs, assuming that the underground tank was refilled once per week, which implies an investment cost of \$75/FCV. Additional costs would be required for increasing and maintaining the regional methanol storage and transportation system, but we have not attempted to estimate these costs for this assessment.

Long-Term Methanol Investment Costs

Next we estimated the necessary investments and the cost of methanol once new production capacity is required, either due to the introduction of more than a few million methanol FCVs worldwide, or due to increased demand for methanol in the chemical industry, the primary market for methanol today. The primary option for producing low-cost methanol is to convert cheap natural gas into methanol, since transporting methanol over long distances is less costly than shipping compressed natural gas. One option would be to place floating methanol plants on oil platforms that produce natural gas. This associated natural gas might have been flared previously as a nuisance gas, but with increased concern over climate change, there is increased pressure to eliminate most flared gas. Some Scandinavian countries are already imposing a greenhouse gas tax on CO₂ emissions, so flaring of natural gas will have a net cost in the future. The feedstock for methanol in this case would have a negative price, much like the municipal solid waste as a fuel source for making hydrogen. We will explore the costs of producing methanol at distant natural gas sources, transporting that methanol and distributing it to local fueling stations.

The American Methanol Institute estimates that a new methanol plant with a capacity of 10,000 metric tonnes per day would cost approximately \$1 billion (Nowell-1998). Such a plant could support about 2.2 million FCVs, assuming a 45 mpgge²⁸ fuel economy (or 22.5 miles per gallon of methanol), which translates into an investment cost of \$450/FCV.

²⁸miles per gallon of gasoline equivalent (on a lower heating value basis)

Another detailed study (Fox-1993) of potential methanol production plant costs was conducted for the State of California by a group of 10 organizations²⁹ in the late 1980's. This study estimated the capital costs of building a 10,000 metric tonne per day methanol plant in six locations around the world. The results of this study are summarized in Table 25, adjusted to 1999 dollars. Estimates range between \$1.2 billion in Texas to \$2.1 billion in Australia. The cost of natural gas is too high in Texas, and shipping costs might rule out Australia. Trinidad might be a good surrogate for likely costs from methanol produced in South America and the Caribbean with reasonable transportation costs. At \$1.4 billion, the cost per vehicle would then be \$630/FCV. Combining this production plant investment with the local methanol fueling station cost of \$75/FCV yields a total cost estimate of \$700/FCV, or \$525/FCV if the more optimistic AMI methanol plant cost is realized. These costs are less than the \$1,230/ICEV estimated just to maintain the existing gasoline infrastructure. We conclude that installing a complete methanol infrastructure including methanol production plants could be up to 58% less expensive than maintaining the gasoline infrastructure system.

Table 25. Estimated capital costs for a 10,000 metric tonne/day methanol plant

	Capital Cost Estimate (US\$ billions -1999 constant dollars)	Distance from US Gulf (Nautical miles)
Prudhoe Bay, Alaska	2.0	12,000
Alberta, Canada	1.3	9,900
Dampier, Australia	2.1	18,100
Jubail, Saudi Arabia	1.5	13,600
Point Lisas, Trinidad	1.4	4,400
Port Arthur, Texas	1.2	0

This assessment assumes that the methanol is produced from stranded natural gas, such as gas associated with oil production that is too far from a pipeline or end-user to be sold economically. If the methanol has to be produced from a new natural gas source, then additional capital investments would be required to extract and process the natural gas. For example, we estimate that U.S. natural gas exploration and production (excluding transmission and distribution) requires capital investments of \$514,000 per billion cubic feet of natural gas produced each year. One billion cubic feet of natural gas could produce about 11.6 billion gallons of methanol, enough to support 21,700 methanol FCVs with 45 mpgge fuel economy. This size fleet would require 1,670 new FCVs per year, or a net capital expenditure of \$306/FCV. In the case of methanol made from natural gas fields that required development, then, the infrastructure costs would be between \$830/FCV and \$1,000/FCV, still less than the cost of maintaining the current gasoline infrastructure. We conclude that the methanol option must rely on stranded natural gas from oil fields already developed for the crude oil to achieve significant infrastructure savings. But even if the methanol were made from a dedicated natural gas field, the methanol infrastructure expenditures would still be less than those for gasoline.

²⁹Amoco, ARCO, California Energy Commission, Chevron, Canadian Oxygenated Fuels Association, Electric Power REsearch INstitute, Mobil, South Coast Air Quality Management District, Texaco and Union Oil Company of California.

In addition to converting low-cost natural gas to methanol, oil companies also have the option of liquefying natural gas, creating and shipping natural gas hydrates (NGH)³⁰, or converting natural gas to synthetic liquid fuels. Japan now imports considerable LNG from Australia, which provides a competing option to methanol as a means of monetizing otherwise useless natural gas. Gudmundsson et al. (1998) have compared these various options for monetizing stranded natural gas. Figure 36, taken from his paper, shows the cost of bringing energy in natural gas by four options: pipeline, liquefaction (LNG), gas-to-liquids conversion via Fischer-Tropsch processes (Syncrude) and natural gas hydrates (NGH). The natural gas hydrate option appears to be the least costly pathway. In essence the natural gas is stored in artificial ice crystals. These hydrate crystals form naturally in natural gas pipelines at temperatures below 20°C. In this pathway, hydrates would be formed intentionally to act as a carrier for the natural gas. They would then be shipped in containers similar to LNG tankers, but without the need for cryogenic temperatures. The NGH would be transported at temperatures just below zero centigrade, and would require about twice as many tankers as LNG. Nonetheless, the total costs are estimated to be less for NGH than for LNG. The DOE Energy Information Administration states that "it is far safer to create, handle, transport, store and regasify natural gas hydrate than liquefied natural gas."³¹ BG Technology has constructed a prototype hydrate production plant, and is actively seeking partners to capitalize on this method of monetizing stranded natural gas.

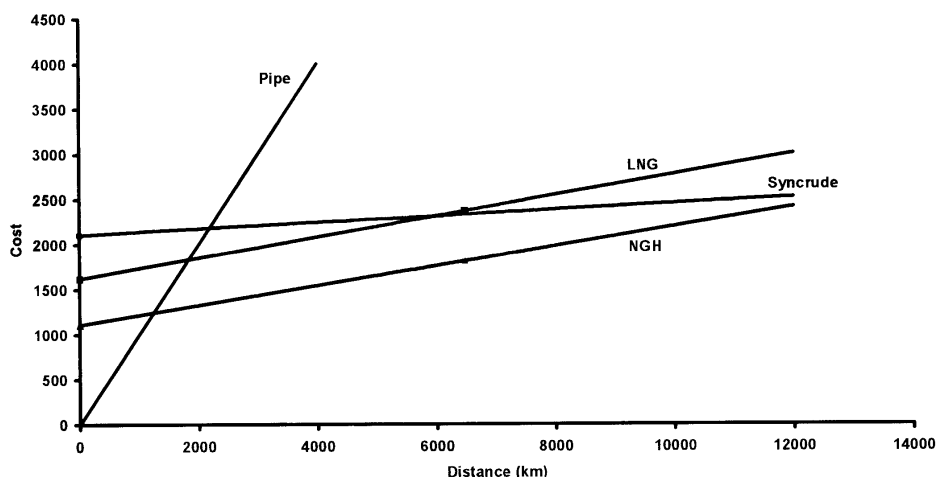


Figure 36. Estimated cost of delivering energy from natural gas by four pathways as a function of distance from the well to the end-user (Gudmundsson-1998)

³⁰Natural gas hydrates are formed by combining natural gas and ice under pressure and can be shipped at low pressures and temperatures just below 0°C, well above the freezing point for methane at -161°C. Note that we are not referring to the naturally occurring natural gas hydrates in the deep ocean that geologists believe contain significantly more stored energy than all other fossil fuels.

³¹*Natural Gas 1998: Issues and Trends*, EIA Office of Oil and Gas, April 1999, p. 81.

Gudmundsson et al. also compared the capital costs of converting natural gas to methanol, syncrude, dimethylether (DME) and NGH. As shown in Figure 37, methanol is the most costly option, although methanol can be produced in very small plants. Of course the NHG pathway requires the most development, and cost projections may not live up to these preliminary projections.

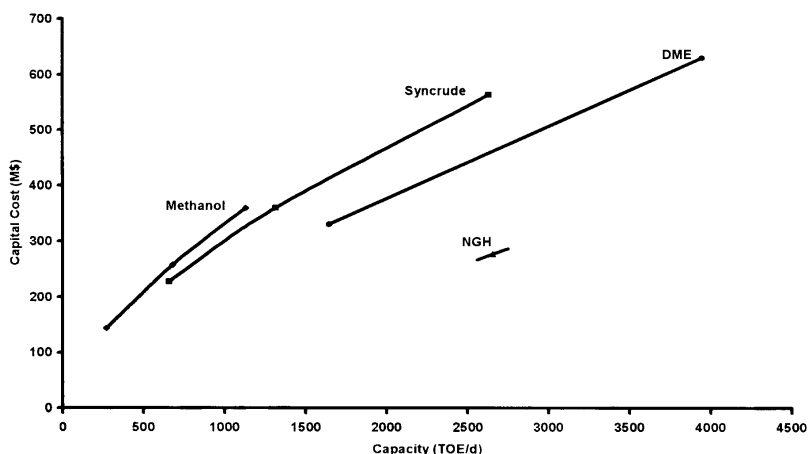


Figure 37. Capital costs for converting natural gas to other fuels for transport to market (Gudmundsson-1998).

Based on the data we have collected, methanol requires more capital investment than the other three options for monetizing natural gas. Synthetic crude production costs slightly less for a given size plant, liquefying natural gas costs less yet, and natural gas hydrate production is the least costly option. From an oil company's perspective, then, natural gas hydrates would appear to be the least costly option for bringing natural gas to the marketplace. Since either hydrates or LNG can be converted to natural gas for the consumer, and since the market for natural gas is well established in the industrialized nations, there would seem to be strong incentive to pursue this option, and, conversely, less motivation to produce methanol which has a much smaller market today.

However, if the FCV market provides a strong economic incentive to convert some stranded natural gas to methanol, then neither LNG nor NGH would be economic for supplying the methanol transportation market, since two fuel conversion steps would be required: one to make the LNG or NGH, and the second in the consumer's country to make the methanol. If methanol is the end goal, then that methanol should be produced at the well head to eliminate the second processing step, since the cost of transporting methanol at room temperature is less than the cost of shipping either LNG or NGH.

We have identified two major companies that are investigating the option of producing methanol adjacent to off-shore oil rigs with associated natural gas capacity: BHP Petroleum has constructed a methanol research plant in Melbourne, Australia to evaluate the floating barge methanol production potential. They estimate capital costs equal to or less than conventional land-based methanol production plant costs. Foster-Wheeler claims 25% to 40% lower methanol production costs with their StarChem Methanol Process (SMP) compared to conventional methanol plants. The SMP uses partial oxidation and membrane separation instead of steam methane reforming.

We conclude that companies with natural gas reserves may have other less costly options than methanol for monetizing stranded natural gas. Thus methanol may have very strong competition in the drive to bring natural gas to market.

Long Term Methanol Delivered Cost

Given the estimate of \$1.4 billion for a 10,000 metric tonne per day methanol plant in the Caribbean, we can estimate the possible cost of methanol delivered to the US Gulf. Assuming an 18% capital recovery factor to provide a 10% real, after-tax return on investment, then the capital recovery cost of the methanol would be 21.8¢/gallon assuming a 95% plant capacity factor. Other costs are summarized in Table 26, assuming operation & maintenance costs equal to 4% of capital costs and natural gas available at only \$0.50/MBTU with a plant efficiency of 75% (LHV). Under these conditions, we estimate that methanol could be delivered to the FCV owner at a cost of 52¢/gallon.

Table 26. Estimated delivered cost of methanol before taxes.

Capital Recovery (18% CRF)	21.8¢/gallon
Operation & Maintenance (4% of capital)	4.8
Natural gas @\$0.5/MBTU (75% efficiency)	3.8
Ocean shipping	3.0
Regional & local transport, storage & dispensing	19
Total	52.4¢/gallon

In the near-term, we estimate that methanol would cost about 79¢/gallon based on the historical average methanol cost at the Gulf of 59¢/gallon in constant 2001 dollars. As discussed earlier, methanol at 79¢/gallon in a FCV would be competitive with wholesale gasoline in an ICEV per mile driven. The projected long term price of 52¢/gallon would therefore give a methanol FCV a 30% fuel cost advantage.

Acknowledgments

The authors would like to thank the U.S. Department of Energy and the Hydrogen Program Office under the leadership of Dr. Sigmund Gronich for supporting this systems analysis work. We would also like to acknowledge the contributions of our colleagues at Directed Technologies, Inc., including Erik Bue, Brian James and Jonathan Ho, as well as the support provided by the Ford Motor Company over the years on related fuel cell and hydrogen projects. We have drawn upon these prior experiences with Ford in many of the tasks reported here.

References

- Amphlett, J.C., *et al*, "Hydrogen production by the catalytic steam reforming of methanol, Part 3: kinetics of methanol decomposition using C18HC catalyst," *The Canadian Journal of Chemical Engineering*, Volume 66, December, 1988, pp. 955.
- Beshty, B. S., *Method of Steam Reforming Methanol to Hydrogen*, U.S. Patent #4,946,667, Aug. 7, 1990.
- Boothroyd, G. (1994), P. Dewhurst and W. Knight, *Product Design for Manufacture and Assembly*, Marcel Dekker, Inc. 1994.
- Crocco, James R. (1998), "Does Methanol Provide a Feasible Alternative for Stranded Natural Gas?" presented to the Monetizing Stranded Natural Gas Reserves conference, San Francisco, December 14-16, 1998.
- Davis, Stacy C. (1999), *Transportation Energy Data Book: Edition 19*, ORNL-6958, Center for Transportation Analysis, Oak Ridge National Laboratory, Oak Ridge, Tennessee.
- EPA (1999), *Tier 2/Sulfur Regulatory Impact Analysis*, Chapter V - Economic Impact, December 1999.
- Fox, Joseph M. (1993), "The Different Catalytic Routes for Methane Valorization: An Assessment of Processes for Liquid Fuels," *Catal. Rev.-Sci. Eng.*, 35(2), 169-212.
- Gray, Charles L. (1989), *Analysis of the Economic and Environmental Effects of Methanol as an Automotive Fuel*, Environmental Protection Agency, Office of Mobile Sources, September 1989.
- Gudmundsson, J.S. (1998), V. Andersson, O.I. Levik and M. Parlaktuna, Norwegian University of Science and Technology, Trondheim, Norway, "Hydrate Concept for Capturing Associated Gas," *1998 SPE European Petroleum Conference*, The Hague, The Netherlands, 20-22 October 1998.
- Halvorson, T. J. (1996), C.E. Terbot, and M.W. Wisz, "Hydrogen Production and Fueling System Infrastructure for PEM Fuel Cell-Powered Vehicles", Praxair Inc., Final Report prepared for The Ford Motor Company, Subcontract No. 47-2-R31157. April 12, 1996.
- James, Brian D. (1996), George N. Baum, Franklin D. Lomax, Jr., C.E. (Sandy) Thomas, and Ira F. Kuhn,

Jr., *Comparison of Onboard Hydrogen Storage for Fuel Cell Vehicles*, Prepared for the Ford Motor Company by Directed Technologies, Inc., Arlington, Virginia, May 1996.

James, Brian D. (1997a), Franklin D. Lomax, Jr., C. E. (Sandy) Thomas, and Whitney G. Colella (DTI), *PEM Fuel Cell Power System Cost Estimates: Sulfur-Free Gasoline Partial Oxidation and Compressed Direct Hydrogen*, October 1997.

James, Brian D. (1997b), C. E. Thomas, George D. Baum, Franklin D. Lomax, Jr., and Ira F. Kuhn, Jr., "Making the Case for Direct Hydrogen Storage in Fuel Cell Vehicles, *Proceedings of the 8th Annual U.S. Hydrogen Meeting*, Alexandria, Virginia, March 11-13, 1997, p. 447

James, Brian D. (1999a), C. E. (Sandy) Thomas, and Franklin D. Lomax, Jr., "Onboard Compressed Hydrogen Storage, *Proceedings of the 9th Canadian Hydrogen Conference*, Vancouver, BC, p. 253-263 February 1999.

James, Brian D. (1999b), and Franklin D. Lomax, Jr. "Mass Production Cost Estimation for Stationary Building Fuel Cell Systems," prepared for the National Renewable Energy Laboratory under Subcontract No. ACG-8-18012-01, June 1999.

James, Brian D. (1999c), Franklin D. Lomax, Jr. and C. E. (Sandy) Thomas, "Manufacturing Cost of Stationary Polymer Electrolyte Membrane (PEM) Fuel Cell Systems," prepared for the National Renewable Energy Laboratory under Subcontract No. ACG-8-18012-01, November 1999.

Jenkins, J.W., *Catalytic Hydrogen Generator for Use With Methanol*, U.S. patent #4,789,540, Dec. 6, 1988.
Lamb, D. G. (2000), "Impact on Future Refinery of Producing Ultra Low Sulfur Gasoline," report by Mustang Engineers and Constructors, Inc.; summary presented at the European Fuels Week in Sicily, April 2000.

Lomax, Franklin D. (1997), and Brian D. James (Directed Technologies, Inc.) and Robert P. Mooradian (Ford Motor Company), "PEM Fuel Cell Cost Minimization Using 'Design for Manufacture and Assembly' Techniques," *Proceedings of the 8th Annual U.S. Hydrogen Meeting*, Alexandria, Virginia, March 11-13, 1997, p. 459.

Mathpro (1998), "Cost of Alternative Sulfur Content Standards for Gasoline in PADD-4", study performed by Mathpro, Inc. for the National Petrochemical and Refiners Association, December, 1998.

Mathpro (1999a), "Costs of Meeting 40 ppm Sulfur Standard for Gasoline in PADDs 1-3 via Mobil and CDTech desulfurization Processes," study performed by Mathpro, Inc. for the American Petroleum Institute, February 26, 1999.

Mathpro (1999b), "Likely Effects on Gasoline Supply in PADD4 of a National Standard for Gasoline Sulfur Content," study prepared by Mathpro, Inc. for the Association of International Automobile Manufacturers, Daimler-Chrysler, and the Ford Motor Company, March 1999.

McLean, C. R., *et al*, *Pressure Swing Adsorption For Small-Scale On-Site Hydrogen Supply*, Questor Industries, Inc., 1997.

Nowell, Gregory P. (1998-State University of New York at Albany), *Looking Beyond the Internal Combustion Engine: The Promise of Methanol Fuel Cell Vehicles*, prepared for the American Methanol Institute, Washington, D.C.

Oak Ridge (1999), "Low Sulfur Impacts on a Mid-Capability Refinery," by Oak Ridge National Laboratory Center for Transportation Analysis for the U.S. Department of Energy Office of Policy, July 1999.

Pepley, B. A. (1997), *et al*, Hydrogen Generation for Fuel-Cell Power Systems by High Pressure Catalytic Methanol-Steam Reforming, Royal Military College of Canada, 1997.

Thomas, C. E. (1997c), *Integrated Analysis of Transportation Demand Pathway Options for Hydrogen Production, Storage and Distribution*, prepared for the National Renewable Energy Laboratory under subcontract No. ACF-4-14266-01, July 1997.

Thomas, C. E. (1997d), Brian D. James, Ira F. Kuhn, Jr., Franklin D. Lomax, Jr., and George N. Baum, *Hydrogen Infrastructure Report*, Prepared for the Ford Motor Company by Directed Technologies, Inc., Arlington, Virginia; Part of the work prepared by the Ford Motor Company for the U.S. Department of Energy, Report No. DOE/CE/50389-504, July 1997.

Thomas, C. E. (1998a), I. F. Kuhn, Jr., B. D. James, F. D. Lomax, Jr. and G. N. Baum, "Affordable Hydrogen Supply Pathways for Fuel Cell Vehicles," *Int. J. Hydrogen Energy*, Vol. 23, No. 6, pp. 507-516.

Thomas, C. E. (1998b), Brian D. James, Franklin D. Lomax, Jr., and Ira F. Kuhn, Jr., *Integrated Analysis of Hydrogen Passenger Vehicle Transportation Pathways*, prepared for the National Renewable Energy Laboratory under contract No. AXE-6-16685-01, March 1998.

Thomas, C. E. (1998c), Brian D. James, Franklin D. Lomax, Jr., and Ira F. Kuhn, Jr., "Integrated Analysis of Hydrogen Passenger Vehicle Transportation Pathways," *Proceedings of the 1998 U.S. DOE Hydrogen Program Review*, Vol. 1, Alexandria, Virginia, April 28-30, 1998, pgs. 233-280.

Thomas, C. E. (1998d) and Brian D. James, "Analysis of Utility Hydrogen Systems," prepared for the National Renewable Energy Laboratory under Subcontract No. ACG-8-18012-01, May 1998.

Thomas, C. E. (1998e), Brian D. James, Franklin D. Lomax, Jr., and Ira F. Kuhn, Jr., "Societal Impacts of Fuel Options for Fuel Cell Vehicles," *International Fall Fuels and Lubricants Meeting and Exposition*, San Francisco, California, 19-22 October, 1998, SAE Paper # 982496.

Thomas, C. E. (1998f), Brian D. James, Franklin D. Lomax, Jr., and Ira F. Kuhn, Jr., "Fuel Options for the Fuel Cell Vehicle: Hydrogen, Methanol or Gasoline?", presented at the Fuel Cell Reformer Conference, South Coast Air Quality Management District, Diamond Bar, California, November 20, 1998.

Thomas, C. E. (1999a), Brian D. James, Franklin D. Lomax, Jr., and Ira F. Kuhn, Jr., "Fuel Infrastructure Costs for Fuel Cell Vehicles," *Proceedings of the 9th Canadian Hydrogen Conference: Hydrogen Power Now*,

Vancouver, BC, Canada, pgs. 452-462, February, 1999.

Thomas, C. E. (1999b), Brian D. James, Franklin D. Lomax, Jr., and Ira F. Kuhn, Jr, "Another Look at the CARB Fuel Cell Technology Advisory Panel Report," *Proceedings of the 9th Canadian Hydrogen Conference: Hydrogen Power Now*, Vancouver, BC, Canada, pgs. 544-552, February, 1999.

Thomas, C. E. (1999e), "Utility Sector Hydrogen System Analysis with Battery Augmentation," Task 4 Final Report prepared for the National Renewable Energy Laboratory under Subcontract No. ACG-8-18012-01, July 1999.

Thomas, C. E. (1999f), Jason P. Barbour, Brian D. James, and Franklin D. Lomax, Jr., "Cost Analysis of Stationary Fuel Cell Systems including Hydrogen Co-Generation," prepared for the National Renewable Energy Laboratory under Subcontract No. ACG-8-18012-01, December 1999.

Thomas, C. E. (2000), Brian D. James, Franklin D. Lomax, Jr., and Ira F. Kuhn, Jr., "Fuel Options for the Fuel Cell Vehicle: Hydrogen, Methanol or Gasoline?" *Int. J. Hydrogen Energy*, Vol. 25, No.6, pp. 551-567, 2000.

Thomas, C. E. (2000b), "On Future Fuels: A Comparison of Options," Chapter 5 of *On Energies-of-Change –The Hydrogen Solution*, Edited by Carl-Jochen Winter, Gerling Akademie Verlag, München, Germany, 2000.

US Energy Information Administration (US EIA-2000), July 2000, http://www.eia.doe.gov/oil_gas/petroleum/special/gasoline_update/market_summary.html

Wilkinson, Paul (1999), David Shin, and Paul Pierson, *1999 Gas Facts (1998 Data)*, the American Gas Association, Washington, D. C. 1999.

**ENHANCING STRATEGIC MANAGEMENT
OF THE HYDROGEN OPTION:
SCENARIO PLANNING BY THE DOE
HYDROGEN TECHNICAL ADVISORY PANEL**

**Jim Ohi
National Renewable Energy Laboratory
Golden, CO 80401**

Abstract

The Secretary of Energy's Hydrogen Technical Advisory Panel (HTAP) conducted two scenario planning workshops. At the first workshop, participants derived preliminary "storylines" that identified and structured the key driving forces and uncertainties from which focused scenarios of hydrogen energy futures can be developed. According to the participants, the key driving forces that will determine the role of hydrogen in plausible energy futures are hydrogen technology development and the interplay between market forces and social concerns. The key uncertainties that will determine how these driving forces play out are the nature and rate of hydrogen technology development and how social concerns about, for example, environmental quality and energy security, affect competitive market forces that determine fuel choice and commercial success of advanced technologies. At the second workshop, participants were asked to build on these storylines by providing more details and exploring implications for hydrogen energy in each quadrant. The Committee has synthesized the insights obtained from the two workshops and prepared more detailed, focused scenarios for hydrogen energy futures that are guided by the HTAP vision. After revision, the scenarios will be adopted by the HTAP and transmitted to DOE. The HTAP will assist DOE in planning and conducting a strategic response workshop in the late summer of 2001 to examine the DOE Hydrogen Program's RD&D portfolio in the context of the HTAP scenarios. The purpose of this workshop will be to draw out more fully the R&D implications of the scenarios and to develop recommendations to the DOE on a strategic context and priorities for its hydrogen RD&D portfolio.

Introduction

In 1992, Congress established the Hydrogen Technical Advisory Panel (HTAP) to advise the Secretary of Energy on the implementation and conduct of the Department of Energy (DOE) Hydrogen Program. The HTAP advises the Secretary on investment strategy and priorities for the research, development, and demonstration (RD&D) of advanced hydrogen energy technologies and on the economic, technical, and environmental consequences of deploying hydrogen energy systems. The Hydrogen Future Act of 1996 further required that the HTAP analyze the effectiveness of the DOE Hydrogen Program and make recommendations to improve the Program for inclusion in a report to Congress by the Secretary. One of the HTAP's recommendations was that the Program conduct scenario planning and analysis to help develop a rationale for a robust, long-term RD&D program. Such a rationale would help to link the HTAP's long-term vision with specific RD&D projects funded by the Program. Scenario planning is a tool that can help the DOE establish a long-term strategic context for its year-to-year investments in hydrogen RD&D. Scenario planning will also help the HTAP articulate a compelling perception of a hydrogen energy future for government leaders and the public.

In 1999, the HTAP established a Scenario Planning Committee to help guide scenario planning and analysis activities conducted by the Hydrogen Program. The Committee is guided by the HTAP's long-term vision for a hydrogen energy future stated below.

Hydrogen will join electricity in the 21st century as a primary energy carrier in the nation's sustainable energy future. Both electricity and hydrogen will ultimately be derived from renewable energy sources, although fossil fuels may serve as a transitional resource. Future hydrogen suppliers will meet a significant portion of America's energy needs for transportation and other applications, thus offering a non-polluting, inexhaustible, efficient, and potentially cost-effective energy system dependent entirely on domestic energy resources.(HTAP 1995)

Scenario Planning Workshops

Workshop 1

At the first HTAP scenario planning workshop, participants derived preliminary “storylines” that identified and structured the key driving forces and uncertainties from which focused scenarios of hydrogen energy futures can be developed. According to the participants, the key driving forces that will determine the role of hydrogen in plausible energy futures are hydrogen technology development and the interplay between market forces and social concerns. The key uncertainties that will determine how these driving forces play out are the nature and rate of hydrogen technology development and how social concerns about, for example, environmental quality and energy security, affect competitive market forces that determine fuel choice and commercial success of advanced technologies. These driving forces and uncertainties were distilled into two “axes” that could be used to create “quadrants” of potential futures that provide labels (“New War, Old Weapons, etc.) and beginning points for storylines as shown in Figure 1.

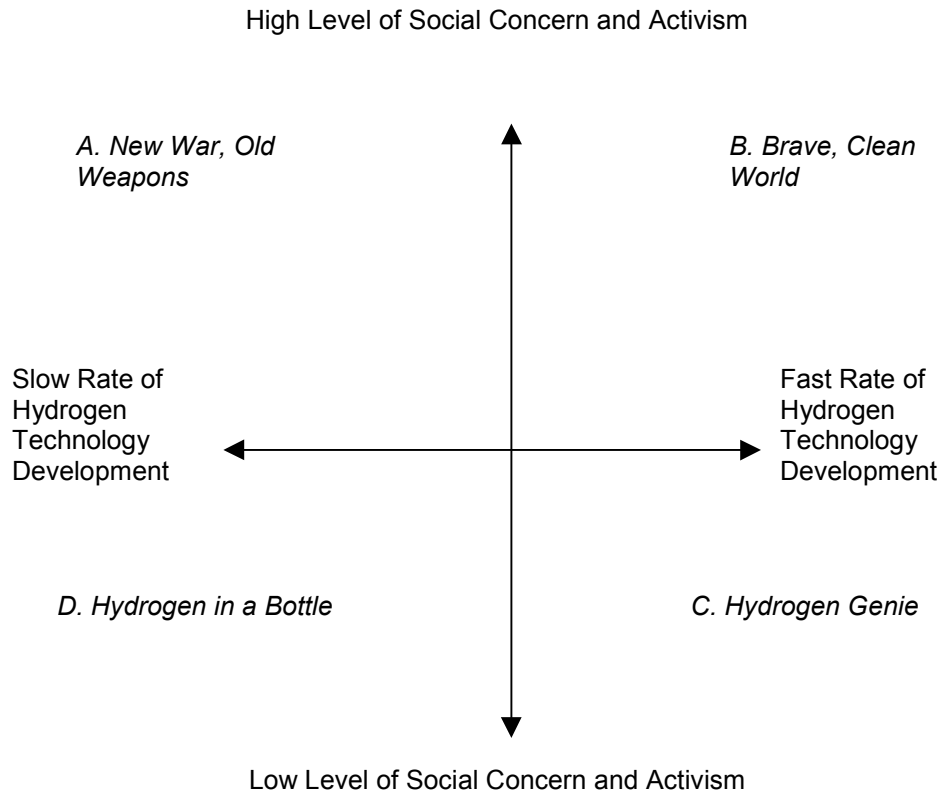


Figure 1. Storylines and Quadrants

Workshop 2

At the second workshop, participants were asked to build on these storylines by providing more details and exploring implications for hydrogen energy in each quadrant. In Workshop 2, four breakout sessions were conducted to draw the social, political, economic, and environmental details needed to prepare “end-state scenarios” for each of the quadrants. In each of the breakout sessions, participants were asked to address three topics listed below.

- Determine the starting point, or where we are today, in terms of the level of social concern and activism and the rate of hydrogen energy technology development.
- Describe the “end-state” of each quadrant implied by the convergence of key driving forces and uncertainties.
- Decide whether the HTAP vision could be attained in the quadrant being addressed. In other words, is there an end-state in the quadrant that incorporates the HTAP vision?

Starting Point

There was near unanimity among the participants of Workshop 2 that the starting point, or current status, lies somewhere in Quadrant D. Some participants from California, which has established the strictest air quality regulations in the nation and zero-emission vehicle mandates, however, felt that the starting point is more accurately located in Quadrant B. Others felt that

even though we are starting from Quadrant D, significant progress has been made in both the rate of hydrogen technology R&D and in the level of social activism and concern over the past five years. Movement from the lower left corner of Quadrant D to the current starting point in the middle of Quadrant D can be an indicator of this progress. In the discussion below on trajectory-based scenarios, the starting point is indicated by “P” in both Figures 2 and 3.

End-state Scenarios

New War, Old Weapons (Quadrant A)

In Quadrant A (Figure 1), the left end of the x-axis implies a negative rate of technology development, where capability is lost through attrition and disrepair of equipment because technology development is not supported financially. The right end of the x-axis implies a level of effort comparable to the Manhattan Project. The bottom of the y-axis indicates a level of social concern where most people don't know that there is a problem and, if there were one, would not care enough to solve it. The top of the y-axis indicates a high level of social concern, where people are motivated to buy clean energy and support tax incentives for hydrogen systems.

Some of the key characteristics of the end-state in Quadrant A are listed below.

- Pure hydrogen from fossil fuels, with sequestration, plus some renewables, ICE (heat engines) and fuel cells
- On-board reforming of fossil fuels
- Hybrid transportation and residential CHP (perhaps offering higher system efficiency and thus lower greenhouse gas emissions)
- Hydrogen enrichment of fossil fuels for stationary applications
- Extension of DOE Office of Fossil Energy's Vision 21: decarbonization of fossil fuels with shift plus CO₂ sequestration and hydrogen utilization leading to production of large volumes of hydrogen that can drive high levels of utilization
- Ground-support vehicles at airports and other fleet vehicles and government vehicles fueled by hydrogen (local air quality is the driver)
- Direct-hydrogen fuel cell vehicles
- Local air quality issues leading to use of compressed natural gas (CNG) as a bridge to hydrogen with final push being reduction of emissions of greenhouse gases

Brave, Clean World (Quadrant B)

The end-state in Quadrant B is characterized by a high degree of social activism, as well as a fast rate of technology development and implementation. Such a society is accustomed to affluence, characterized by 4 to 5 percent annual GNP growth and places a high value on health and food, including acceptance of what is perceived to be superior, genetically modified food sources. Members of this society live longer, with lifespans of 100-105 years, and believe in a balanced lifestyle with telecommuting as a cornerstone. This society adopts concepts of reduction, reuse, recycle, conservation, and dematerialization to minimize consumption of material and energy resources.

The end-state in Quadrant B implies a high level of energy security, including self-contained energy systems with a fuel cell power station in each home; passive solar, hydrogen generated by renewable energy; nuclear, fossil, and fusion power; limited supplies of oil and gas; and methane hydrates as a hydrogen source. Significant advances in nanotube hydrogen storage have taken place. In this Quadrant, the transportation sector enjoys moderate growth, with the emphasis remaining on individual transportation. Each home enjoys a hydrogen-fueled car without compromised drivability. Hydrogen-fueled commercial aviation is the norm. Hydrogen is also used in public transportation, including buses and trains.

In this Quadrant, society has a high level of confidence in its ability to control outcomes. The necessary drivers to reach this end-state include:

- regulatory drivers to protect the public health, such as strict air quality regulations;
- a carbon driver to control climate change, such as a carbon tax or carbon trading mechanism;
- strong economic drivers, including private incentives and public funding to accelerate the R&D cycle;
- public demand and acceptance of new technologies;
- resource availability to enable technological advancement; and
- hydrogen infrastructure readiness.

The HTAP vision can be realized in this Quadrant after a period of adjustment. Short of a monumental technological breakthrough to push the hydrogen economy forward, or the impact of a major energy security crisis, the HTAP vision will be achieved in this Quadrant through the use of regulatory drivers, economic incentives, and public funding targeted at supporting scientific research and developing resource availability. After the HTAP vision is achieved, it could be supported indefinitely in this Quadrant because society would not want to move backwards. A high level of social activism and technological growth will continue even if a rapid rate of technological advances are no longer crucial.

Hydrogen Genie (Quadrant C)

In Quadrant C, the level of social activism and concern is quite low, primarily due to lack of public awareness about hydrogen energy systems. The rate of hydrogen energy technology development, however, is rapid and comparable to the pace of innovation and technological progress in other high-tech industries.

Examples of key parameters that indicate the present status of hydrogen energy and how the “values” of these parameters would change by 2050 given the conditions of Quadrant C are listed in Table 1.

The Hydrogen Genie storyline implies an end-state defined not only by a rapid rate of hydrogen technology development but also by rapid penetration of these technologies into commercial energy markets. Of the four storylines, this storyline is most obviously consonant with the HTAP vision as presently stated. In other words, the “then” values for the parameters in Table 1 help define details of the HTAP vision.

Table 1. Present Status of and Outlook for Key Parameters

Parameter	Now	Then (2050)
Hydrogen Storage	2-5 wt% (mostly in buses)	10 wt% (light-duty vehicles)
Hydrogen Cost	3-10x per energy equivalent of petroleum-based fuels	no more than petroleum-based fuels (w/o taxes)
Hydrogen Safety	good industrial perception, perceived as issue, no codes/standards for retail/public use	non-issue
H ₂ Fueling Infrastructure	H ₂ stations: 3 (US), 1 (Canada), 2 (Germany), ? (Iceland)	100% of service stations have multiple fuel options, incl. H ₂ container swapping
H ₂ fueled mobility	about zero	universal
Propulsion	ICEs on petroleum-based fuels	diverse prime movers on H ₂ , universal regen braking
Electrification	US: 10% renewable	global: 100% renewable
Excise taxes	none on hydrogen	none on non-petroleum-based fuels

Hydrogen in a Bottle (Quadrant D)

The end-state in Quadrant D includes hydrogen as a commodity product, not as an energy carrier. Advances in competing technologies for energy storage (batteries, ultra-capacitors, etc.) are likely to limit the widespread introduction of hydrogen. Alternative fossil fuel sources (methane hydrates, advanced coal, and oil shale), stable prices, and breakthroughs in CO₂ recovery and disposal provide stiff competition for hydrogen technologies. Energy remains cheap, accessible, and convenient. Other ways to address climate change and other environmental issues are developed, obviating the need for hydrogen. The 2050 end-state is further described in three categories, Technology, Market, and Policy, in Table 2.

The HTAP vision could be met, in principle, within Quadrant D. A “functional equivalent” of the HTAP vision that relies on technological and market development trends that will likely continue within the constraints implicit in Quadrant D is possible. The HTAP vision would need to be modified so that the third sentence would read “...future hydrogen suppliers will meet a portion of America’s energy needs for transportation and other applications, thus supporting a non-polluting, inexhaustible, efficient, and potentially cost-effective energy system dependent entirely on domestic energy sources.” The HTAP vision would also need to be modified with the proviso that the transition from natural gas-based systems to renewable-based systems would be in the second half of the 21st century.

Table 2. End-state Characteristics for Quadrant D

Technology	Market	Policy
Light-weight materials	Natural gas and syngas remain relatively cheap	Strong military
Higher efficiency of conversion technologies	Residential/micro generation for CHP + Fuel (NG-fired)	Increased appreciation for global climate change but not a major policy driver
Material limitations on hydrogen storage	Stable energy price/supply	Much more stringent efficiency requirements for appliances, buildings
Modest improvements in hydrogen technologies	Electric vehicles meet performance, efficiency, and convenience targets (independent of storage system)	Policy for incentives rather than regulation
Hydrogen Program goals have been met	Communities convert to CNG/alternative fuels (based on incentives)	Policy to convert to ultra-clean fuels (but how clean is clean enough?)
Production/delivery/availability of hydrogen much improved	Airports convert to LNG (aircraft and support vehicles)	Sunk investments are protected
Advances in gas-to-liquids technologies	LNG infrastructure as bridge to future hydrogen infrastructure	Resistance to, or inertia against, change
Major increase in public/mass transit and use of electromotive drive	Slow turnover of assets	
Electric hybrids	Hydrogen niches: transit buses, portable electric devices, some fleets, localized infrastructure	

Trajectory-based Scenarios

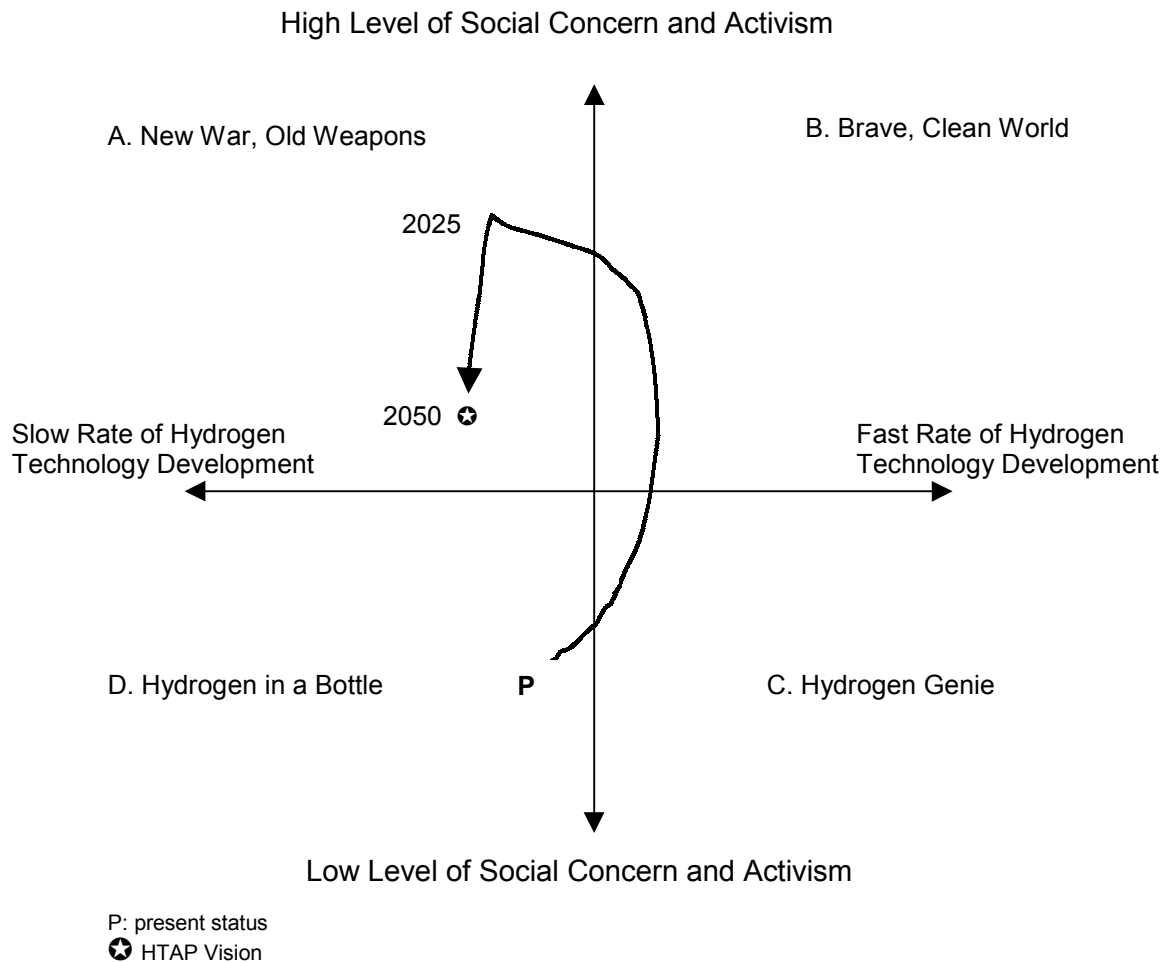
The future, of course, will not unfold according to one storyline and to the exclusion of the others but will in all probability wind and twist its way through all four (and other) storylines. In a second set of breakout sessions, participants in Workshop 2 also examined “trajectories” that involve more than one quadrant and that can lead to a dynamic set of scenarios that cross and weave among the four quadrants. The key question here is whether there is an end-state that is most compatible with the HTAP vision and, if so, what are the most likely trajectories to reach that end-state from the starting points determined earlier. In discussing trajectories, the participants were asked to consider what might happen, or is likely to happen, as well as what one would like to have happen by applying policies involving incentives, mandates, and RD&D. Because of the focus on policies that can help influence movement from the present to future

end-states, trajectory-based scenarios may be particularly relevant and of interest to public sector decision-makers. Three examples of trajectory-based scenarios are described briefly below.

New War, Old Weapons (Quadrant A)

The trajectory is shown in the Figure 2. It begins in Quadrant D and uses a combination of increased social awareness and increased hydrogen technology research. As social concern increases to the point where interest in clean energy and enactment of tax incentives drive greater use of hydrogen, a moderate rate of technological development is maintained. Before about 2025, consumer demand increases rapidly such that a lower rate of technological development is sufficient enough to increase hydrogen usage. Then, between 2025 and 2050, concern about the environment lessens as hydrogen reduces the environmental impact of energy production, conversion, and consumption. Additionally, because hydrogen systems are mass-produced, costs are lowered and tax incentives can be phased out. Note, however, that because technological development is slow and old weapons are assumed in this quadrant, today’s technologies are adapted for hydrogen use, reducing the extent of the positive impact that hydrogen can make.

Figure 2. Trajectory-based Scenario for Quadrant A

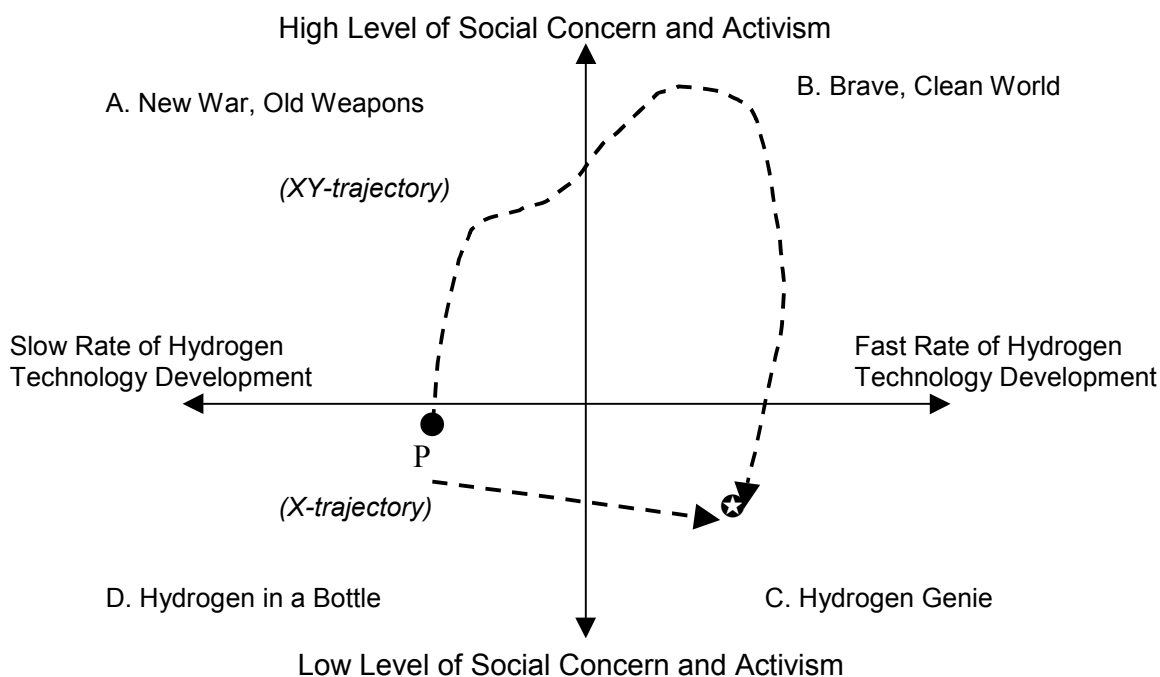


Hydrogen Genie (Quadrant C)

Since there appear to be an infinite number of trajectories to move from the starting point in Quadrant D to an end-state in Quadrant C, the boundaries of the set of possible trajectories should be defined first. These boundaries can be defined by a right angle from the starting point shown in Figure 3. A trajectory parallel to the y-axis (Trajectory Y) would be defined completely by the level of social activism and concern while a trajectory parallel to the x-axis (Trajectory X) would be defined completely by the rate of hydrogen technology development. Trajectories lying between these extreme trajectories (XY trajectories) would be defined by a blend of the two key driving forces.

Strategies based on Trajectory X to reach an end-state defined by the HTAP vision requires an R&D program with a laser-like focus that would hit “home-runs” on all critical R&D needs. Such a pure R&D path to the HTAP vision requires the responsibility to “pick winners,” a role federal R&D programs have traditionally eschewed. This trajectory could also be reinforced by hydrogen R&D programs of other countries, particularly in Europe and Asia. For example, Iceland’s effort to become the world’s first “zero-emission country” could focus and accelerate the federal hydrogen R&D program in the U.S. by emphasizing hydrogen production based on renewable energy resources and the linking of all energy end-use sectors through hydrogen storage and utilization. Trajectory X also requires rapid commercialization of hydrogen technologies. Industry would have to “score” big on R&D home runs “hit” by researchers in national labs, universities, and in the private sector. Some “spill-over” of venture capital pursuing fuel cells investments may be possible for an emerging hydrogen energy market sector. A focused federal hydrogen R&D program could include educating the financial investment community about potential payoffs in an accelerated transition to a hydrogen economy.

Figure 3. Trajectory-based Scenarios for Quadrant C



Strategies based on Trajectory Y to achieve the HTAP vision require long-term national leadership comparable to those asserted by the Eisenhower administration in building the interstate highway system and by the Kennedy-Johnson administration in successfully completing the man-on-the-moon mission. Achieving the HTAP vision would require no less in public leadership at the highest level of the federal government. Realizing the HTAP vision is tantamount to achieving a sustainable energy future, and its realization would have even more impact on the nation and on the world than either of the two examples above has had. As Lester Brown states, “Put simply, the principles of ecological sustainability now require a shift from a carbon-based to a hydrogen-based energy economy”(Brown 2000). With the Cold War ending at the end of the 20th century, a “Green War” is needed to attain a sustainable energy future based on hydrogen and the HTAP vision. A pact between Germany and Japan to launch a political and technological war on CO₂ could help launch a world war on climate change.

Several measures to propel the nation along Trajectory Y are possible. A government-industry consortium, perhaps a Partnership for the Next Generation of Energy (PNGE), may be needed to stimulate and structure public and private sector interest in achieving a hydrogen-based energy economy. Investment credits for business and the R&D community, preferential purchasing incentives, including flexible fleet vehicle purchasing options for the Clean Cities Program, and an excise tax exemption for hydrogen fuel are examples of other Trajectory Y measures.

Both Trajectory X and Trajectory Y are “pure paths” that rely exclusively on accelerating R&D and increasing public activism, respectively. As such, neither is likely to succeed without the other. For example, it will be very difficult to accelerate R&D to the degree required by Trajectory X without heightened public support. Likewise, strong long-term leadership to achieve the vision would be difficult to sustain without significant R&D progress and technology commercialization. Strategies based on XY trajectories that blend policies (mandates and incentives) and targeted R&D investments may be more realistic than those based on X or Y trajectories. These strategies are shown (without priorities implied) in Table 3 as either incentives (Y-type) or R&D needs (X-type), although it is understood that neither type can stand alone and effect rapid movement from Quadrant D to Quadrant C.

Hydrogen in a Bottle (Quadrant D)

With both a low rate of change in hydrogen technology development and a low level of social concern that prevents adoption of policies that would accelerate deployment of hydrogen technologies, Quadrant D scenarios become, more or less, “default” scenarios for hydrogen energy futures. In other words, these scenarios will embody what may happen given the absence of driving forces for hydrogen energy futures. However, the HTAP vision (with some modifications) could be attained in Quadrant D, and robust and flexible scenarios that incorporate most of the HTAP vision are conceivable.

Table 3. Strategies for XY Trajectories

Incentives	R&D Needs
investment tax credits for H ₂ fueling stations and H ₂ vehicles	cost reduction through manufacturability and efficiency of production
agricultural incentives to produce H ₂ feedstocks	use of lower-cost, readily available materials; minimize use of scarce resources
develop, promulgate, and adopt codes and standards for H ₂ use	better sensors
protection and enhancement of public health could lead to stricter mandates on fuels and propulsion devices— incentives would be more effective	increase fuel cell energy density, improve reliability of PEM fuel cells, improve fuel system controls (refueling, pressure control, start-up)
lurking “gasoline liability” issue akin to tobacco liability suits?	high-temperature electrolysis, stationary reformers incorporating C-sequestration
	H ₂ adsorbent systems
	exploit potential H ₂ sources like sewage/solid wastes

The trajectories of these scenarios rely on incremental movement toward hydrogen-based energy futures implicit in current technology development programs and trends, such as those listed below.

- The U.S. space program (NASA) provides a baseline for any hydrogen technology development and deployment path.
- Industry provides a driving force for going beyond the baseline.
- Hydride storage systems and small fuel cells will evolve over the next 50 years.
- Convergence in telecommunications and consumer products markets will provide a base for technology development, mass production, and worldwide exposure of new products.
- Learning curves of manufacturers of small fuel cells will lead to larger fuel cell products.
- Hydrogen-fueled buses will lead to hydrogen cars and fleets of hydrogen vehicles.
- Hybrid vehicles, using fuel cells or internal combustion engines, are options that will be fully explored in commercial markets.
- The cost of fuel cells will be a critical success factor.
- The DOE will develop a hydrogen technology development strategy that leverages other technology development.

These and other factors will provide incremental, stepped trajectories toward the HTAP vision. Attainment of the vision will be almost completely contingent on events and initiatives outside of the DOE Hydrogen Program, especially the commercial success of fuel cell technologies.

Conclusion

The two workshops provided valuable insights and guidance for the HTAP scenario planning and analysis process. The HTAP Scenario Planning Committee will synthesize the insights obtained from the two workshops and prepare more detailed, focused scenarios for hydrogen energy futures that are guided by the HTAP vision. For example, the scenarios could be based on an elaboration of the four end-states and/or one or more trajectories to attain the HTAP vision.

After revision, the scenarios will be adopted by the HTAP and transmitted to DOE. The HTAP will assist DOE in planning and conducting a strategic response workshop in the late summer of 2001 to examine the DOE Hydrogen Program's RD&D portfolio in the context of the HTAP scenarios. The purpose of this workshop will be to draw out more fully the R&D implications of the scenarios and to develop recommendations to the DOE on a strategic context and priorities for its hydrogen RD&D portfolio.

Acknowledgements

The author would like to acknowledge programmatic support provided by Chris Bordeaux, Sig Gronich, and Neil Rossmeissl of the DOE Hydrogen Program and the leadership provided by the current members of the HTAP Scenario Planning Committee: Hank Wedaa and Mounir Kamal (co-chairs), Helena Chum, Mike Hainsselin, David Nahmias, Roberta Nichols, and John O'Sullivan. Merwin Brown, Carol Hammel, Maggie Mann, and Cathy Gregoire Padró of NREL provided technical support and assistance. I would also like to express my appreciation to the participants of both workshops for providing insight and technical expertise to the HTAP scenario planning effort and to the California Energy Commission, California Air Resources Board, and the Sunline Transit Agency for hosting the HTAP scenario planning workshops.

References

Hydrogen Technical Advisory Panel. 1995. *The Green Hydrogen Report*, p.1.

Brown, Lester. 2000. "Challenges of the New Century," *State of the World 2000*, Worldwatch Institute, New York: W.W. Norton and Co., p. 10.

HYDROGEN TECHNICAL ANALYSIS

Project Progress Report

S. Lasher, M. Stratonova, and J. Thijssen
Arthur D. Little, Inc.
Cambridge, MA 02140

Abstract

Arthur D. Little is finalizing an analysis of small-scale purification technologies suitable for hydrogen fueling stations. In this project, Arthur D. Little identified and analyzed three technologies not currently supported by DOE that have some promise as hydrogen purification methods for hydrogen fueling stations. The technologies selected for detailed evaluation in this study were metal membranes without noble metals, dry fluorinated metal hydrides and the application of this fluorinated metal hydride in a slurry.

The detailed study was performed in the context of hydrogen fueling station hydrogen production and storage technologies. The analysis considered the technology R&D status, current and potential performance and cost, and possible development paths. Alternative fueling station scenarios were developed and compared on the basis of cost, performance and overall system efficiency.

Preliminary findings indicate that the use of metal hydride slurries for hydrogen purification and storage shows the highest overall off-board system efficiency of the three. Membranes without noble metals show the potential for the lowest hydrogen selling price for hydrogen production systems utilizing high-pressure steam reformers (hydrogen selling price results not presented here). Both of these, if proven, would represent significant improvements over the current state-of-the-art in hydrogen purification. However, considerable further development will be required to prove the feasibility and optimize the implementation of either of these options.

Introduction

There is increasing interest in the development of small-scale (< 1 million SCFD) hydrogen fueling stations to support direct hydrogen fuel cell vehicles when and if these vehicles capture a significant fraction of the U.S. passenger vehicle fleet. Considerable attention from DOE and others has been focused on small-scale hydrogen generation to minimize the cost of efficient decentralized hydrogen production, thus avoiding the cost of hydrogen transportation from central hydrogen production facilities. However, the critical step of purification and system integration has not received as much attention, although it has considerable impact on the efficiency and cost of hydrogen production. This relatively limited attention to small-scale purification and system integration may eventually result in barriers to broad implementation of hydrogen as a fuel in the future. That is why, though DOE funds the development of some hydrogen purification technologies, DOE wants to better understand what other options may be under development that they are not currently funding.

A hydrogen fueling station with on-site reformer-based production will require hydrogen purification, storage, and dispensing, along with the necessary safety and control components. Small, natural gas-based reformers, being developed for distributed fuel cell power systems, could potentially be used to generate hydrogen rich reformat streams at small-scale fueling stations servicing hydrogen fuel cell vehicles. Purification is an essential step to remove impurities in the reformat that may poison the storage unit or fuel cell, and to remove non-hydrogen species that can dramatically increase the size of the on-site and on-board storage systems.

This paper represents a progress report for this project. Some of the analysis is preliminary and the overall system-level analysis of cost and performance is ongoing. The final analysis will be incorporated into a final report shortly.

Approach

We have reviewed three small-scale purification technologies not being funded by DOE. For the analysis, we considered the integration of these purification technologies for onsite hydrogen production at vehicle refueling stations. Both a larger (300 vehicle per day) and a smaller (30 vehicle per day) refueling station capacity were analyzed. The analysis included assessments of technical maturity and risks, performance, cost, and a comparison to baseline technologies, as well as the identification of key barriers, and an evaluation of possible development paths. For the performance and cost analysis, we developed detailed flowsheet models for each of the options considered, which included steam reformers as well as autothermal reformers. These flowsheet models were used to estimate the conditions, flowrates, power requirements, and heat transfer duties needed for sizing the equipment. Based on the equipment sizes so calculated, we then obtained cost estimates from quotes and from bottom-up cost models developed by Arthur D. Little under other programs.

For the selection of the purification methods to be studied in detail, we first generated a list of potential purification technologies based on literature information and discussions with DOE and others. A rigorous screening was conducted based on the expected applicability of the options to

distributed hydrogen production and on whether DOE already supports the option (options already supported were outside of this scope of the work). The options selected for detailed evaluation were:

- *Non-palladium metal membranes.* Non-palladium metal membranes are a potential low-cost alternative to palladium-based membranes currently in use. Japanese researchers have promising results from amorphous alloy membranes without noble metals (Zr-Ni). Alloys without noble metals may be two orders of magnitude cheaper than palladium-based materials on a weight basis (Hara 2000).
- *Fluorinated metal hydrides (dry).* Fluorinated metal alloys have the potential to simplify system integration by providing purification while storing the hydrogen on-site as a metal hydride. Forming a porous fluoride film on the surface of metal hydride particles is a promising way to protect the metal hydride from poisoning by non-hydrogen species that are less likely to penetrate through the fluoride film than hydrogen molecules (particularly carbon monoxide and water).
- *Metal hydride slurries.* Utilizing fluorinated metal hydrides in slurries could improve system integration even further and possibly allow fast fueling times if the slurry is also carried on the vehicle.

These technologies were also expected to have good potential to reduce cost and improve performance on the system level. On-site production with small-scale pressure swing adsorption (PSA) purification and delivered hydrogen (central production) with on-site dispensing were chosen as the baseline technologies for comparison. In this report, preliminary overall system efficiencies are presented for some scenarios. Hydrogen selling prices for all scenarios are currently being reviewed and are not included in this report. A complete list of scenarios for the final analysis is presented in Table 1.

Overall system efficiencies were determined based on integrated system modeling using thermodynamic software with inputs from developers and prior Arthur D. Little analyses. Optimum system configurations were determined and system models were developed for each scenario. Figure 1 shows the thermodynamic modeling role in determining system efficiency and hydrogen price.

Hydrogen selling prices (not presented here) were determined based on estimated equipment costs, energy costs, and additional conventional economic assumptions. Equipment costs for individual components were estimated based on vendor quotes, bottoms-up manufacturing cost analysis, or prior Arthur D. Little analyses. In some cases, progress ratios were applied to vendor quotes to obtain costs at high manufacturer production volumes. For most equipment, production volumes of 100 units/year were assumed. Higher production volumes were used for estimating low-pressure reformer costs, assuming a synergy between reformers manufactured for distributed fuel cell power systems and those manufactured for hydrogen production. Twenty-four vendors provided input to this analysis to date.

Table 1. Scenarios for Detailed Analysis

On-site Hydrogen Production Scenarios				Delivered Hydrogen Scenarios (Baseline)		
Purification Technology	Reformer	On-site Storage	On-board Storage	Delivered State	On-site Storage	On-board Storage
Pressure Swing Adsorption (Baseline)	Steam	High Pressure	cH ₂ FCV	Liquid Hydrogen	Cryogenic and High Pressure	cH ₂ FCV
	Autothermal	High Pressure	cH ₂ FCV		Cryogenic and Low Pressure	MH FCV
	Steam	Low Pressure	MH FCV	Compressed Hydrogen via Tube Trailer	High Pressure	cH ₂ FCV
	Autothermal	Low Pressure	MH FCV		Low Pressure	MH FCV
Non-Pd Membrane	Steam	High Pressure	cH ₂ FCV	Compressed Hydrogen via Pipeline	None	cH ₂ FCV
	Autothermal	High Pressure	cH ₂ FCV		None	MH FCV
	Steam	Low Pressure	MH FCV			
	Autothermal	Low Pressure	MH FCV			
Fluorinated Metal Hydride (dry)	Steam	Low Pressure	MH FCV			
	Autothermal	Low Pressure	MH FCV			
Fluorinated Metal Hydride Slurry	Steam	Low Pressure	MH Slurry FCV			
	Autothermal	Low Pressure	MH Slurry FCV			

Notes: It was determined that the metal hydride options would not provide benefits for use with compressed hydrogen vehicles.
 cH₂ FCV = Compressed hydrogen fuel cell vehicle utilizing high-pressure on-board storage at 5000 psia.
 MH FCV = Metal hydride fuel cell vehicle utilizing low-pressure metal hydride storage at 100-150 psia.
 MH Slurry FCV = Metal hydride fuel cell vehicle utilizing a low-pressure metal hydride slurry storage (oil plus metal hydride).

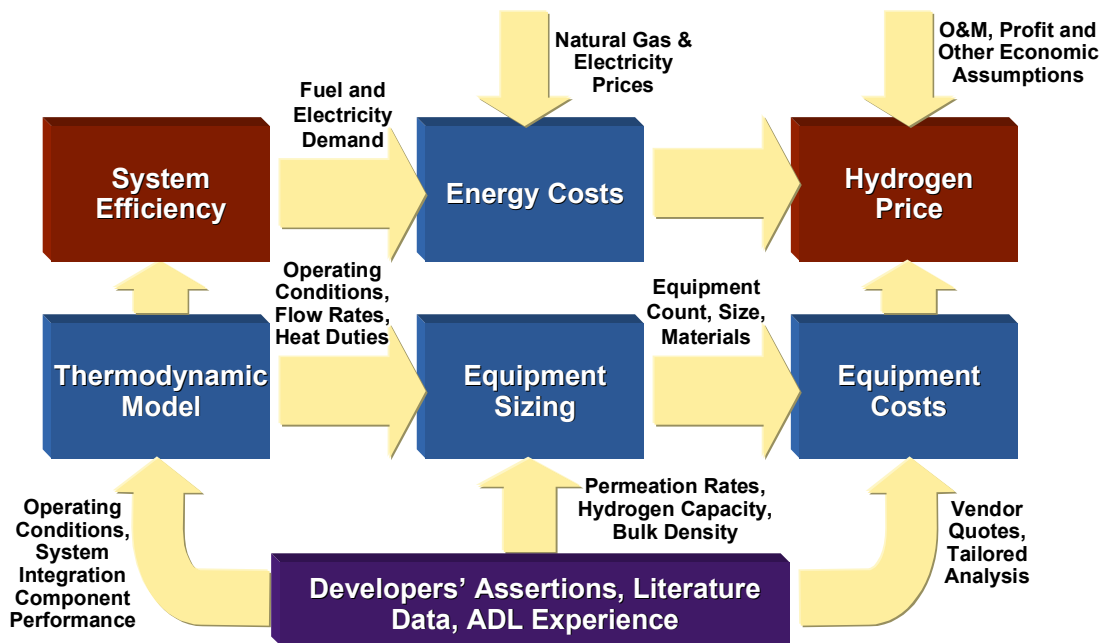


Figure 1. Approach for Determining Efficiency and Price

Discussion

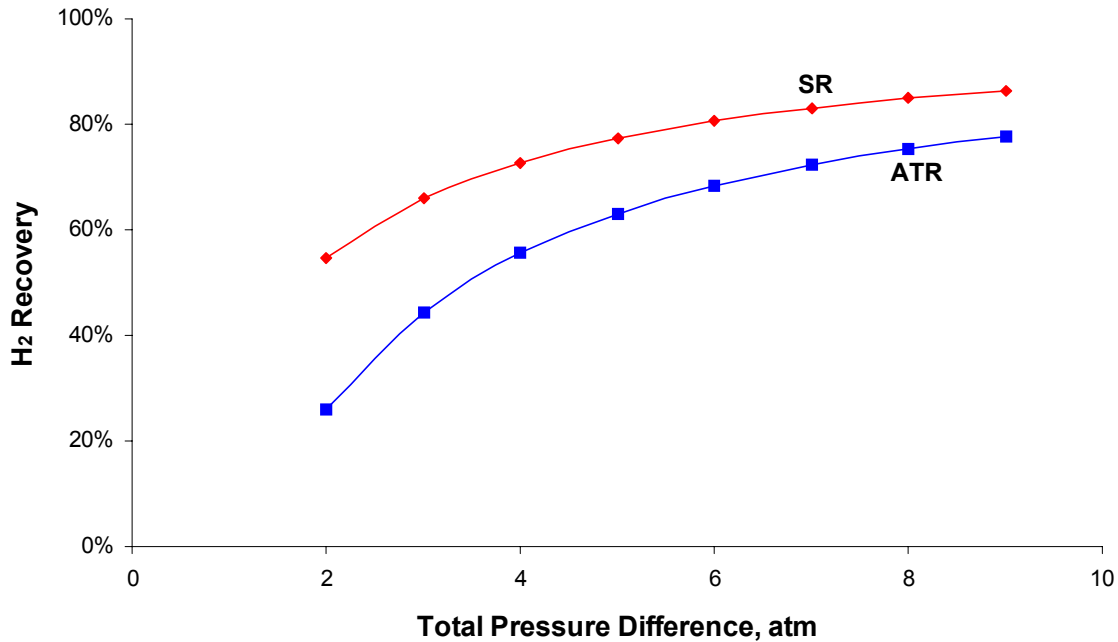
Amorphous Membranes without Noble Metals

Amorphous membranes without noble metals are still in the very early research and development stage (Hara 2000). Japanese researchers were contacted to obtain the current performance of their amorphous $Zr_{36}Ni_{64}$ alloy membrane for hydrogen separation. We developed long-term performance assumptions based on discussions with these developers (personal communication with Pr. S. Hara, National Institute of Materials and Chemical Research, Tsukuba, Japan) and Arthur D. Little comparative analysis. The long-term assumptions were made considering the membranes' intrinsic material properties such as mechanical properties and metal hydride formation conditions. Table 2 shows the current and long-term performance assumptions along with the current performance of a conventional palladium-based membrane.

Table 2. Membrane Performance Assumptions

Key Membrane Design Assumptions		Units	Zr-Ni Current	Zr-Ni Long-Term	Pd-Ag Current (Baseline)
Operating Temperature		°C	350	350	350
Pressure	Feed	atm	3	10	15
	Permeate	atm	1	1	5
Membrane Thickness		μm	30	15	30
Permeability at 350°C		$10^{-9}\text{mol/m s Pa}^{0.5}$	1.2	2.4	15
Permeability Reduction due to CO		%	10	10	5
H₂ Concentration in Permeate		%	100	100	100
Hydrogen Recovery for SR		%	53	86	92

In order to achieve these long-term performance goals, a significant improvement in operating pressure difference across the membrane is necessary (see Figure 2). Note that the hydrogen recovery is also a function of reformat composition. Reformat from steam reforming (SR) natural gas gives higher hydrogen recovery than reformat from autothermal reforming (ATR) natural gas. Such improvements in performance would greatly improve the performance of the membranes, but there is still considerable technology development risk involved in the development and commercialization of purification systems based on these membrane materials (as compared to the risks associated even with palladium-containing metal membranes).



* Maximum achievable membrane hydrogen recovery assuming equilibrium conditions.

Figure 2. Membrane Recovery* as a Function of Pressure

It is believed that operating pressure for Zr-Ni amorphous membranes is limited by crystallization process conditions and not by mechanical properties of the material (Ritchie 2000; Ismail 2001). Amorphous Zr-Ni-based membranes show mechanical properties, such as tensile strength, hardness and Young's modulus, comparable or superior to those of conventional metal-based membrane materials (Davis 1999). The current low operating pressure difference for Zr-Ni membranes is due to crystallization of the membrane material at assumed temperature and pressure. Crystallization of amorphous materials in the presence of hydrogen is caused by metal hydride formation at certain conditions and leads to a dramatic loss in hydrogen permeability. Metal hydride formation conditions strongly depend on the alloy composition and, thus, can be tailored by modifying membrane material composition such as optimizing component ratios and/or adding small amounts of other metals.

Fluorinated Metal Hydrides (Dry)

If successful, the use of metal hydride-based purification technology could significantly reduce the pressure requirements for the raw hydrogen stream, as well as the compression requirements for the purified hydrogen stream. Hydride-based systems could work at low-pressure and possibly even be used to pressurize the hydrogen partially, prior to the final compression stages (Golben 1999; Vanhanen 1999). Conventional purification technologies (PSA, membranes) require high reformat pressures (> 10atm) to obtain acceptable hydrogen recovery at reasonable cost. This high-pressure requirement significantly increases cost and compressor parasitic power; especially if low-pressure reformers, developed and produced for distributed fuel cell power systems, are to be used. Such reformers will likely deliver reformat at between 1-3 atm.

The advantage to using these reformers in a fueling station is that their costs are likely to be much lower due to the relatively high production volumes projected for distributed fuel cell power systems. However, operating low-pressure reformers with conventional purification systems will require very large reformatte compressors, adding significant cost and parasitic power (decreasing system efficiency). For example, a reformatte compressor can use as much as 5% of the hydrogen energy content for electric power to increase reformatte pressure from 3 to 10 atm (assuming reformatte from an ATR and 70% efficient compressor). When typical power plant efficiencies are taken into account, this electric load can significantly reduce overall system efficiency.

If protected from certain impurities, metal hydriding alloys could provide efficient hydrogen purification at low-pressure, permitting the use of potentially low-cost reformers without expensive and power intensive reformatte compressors. Japanese researchers claim that fluorination permits hydriding alloys to tolerate high levels of impurities, and have carried out promising initial feasibility experiments (Liu 1995; Wang 1995). The working hypothesis is that hydrogen molecules could easily penetrate a porous fluoride top layer through microcracks, while larger molecules (impurities) could not. However, the fluoride coating is not infinitely selective to hydrogen, so the hydriding alloy is still poisoned by impurities even if treated. The four basic intermetallic impurity interactions and their effects are listed in Table 3. The quantitative effects on metal hydride performance depends on the impurity nature, fluorination treatment method, and impurity concentration in the bulk gas.

Table 3. Metal Hydride Impurity Interactions

Impurity Interactions	Effect	Compounds
Poisoning	Rapid loss of hydrogen capacity with cycling, caused by impurities strongly or irreversibly adsorbed on the surface active sites	H ₂ S, Organic Sulfur Compounds, CO
Retardation	Reduction in adsorption /desorption kinetics without significant loss in the ultimate capacity, caused by impurities reversibly adsorbed on the surface active sites	CO, CO ₂ , NH ₃
Reaction	Bulk corrosion leading to irreversible capacity loss	O ₂ , H ₂ O
Innocuous	Loss in adsorption kinetics due to surface blanketing	N ₂ , CH ₄

Assuming sufficient sulfur removal prior to reforming, the main impurities of concern in reformatte streams are carbon dioxide (CO₂), carbon monoxide (CO), and water (H₂O). We assumed the levels of these impurities found in reformatte would not significantly affect hydride performance even after thousands of cycles. This assumption is based on developers' claims of

respective impurity tolerances of 20% and 3,000 ppm (dry volume) for carbon dioxide and carbon monoxide, and no effect of water on the fluorinated metal hydride (personal communication with Pr. S Suda, Kogakuin University, Tokyo, Japan; personal communication with K. Kobayashi, Japan Metals and Chemicals Co., Ltd., Japan). No conclusive tests have been carried out to demonstrate that fluorination alone can provide this level of tolerance but no information to the contrary is available either. Table 4 shows the performance assumptions for the metal hydride purification and storage system.

Table 4. Metal Hydride Performance Assumptions

Key FI MH Design Assumptions		Units	LmNi _{4.6} Mn _{0.4}
Absolute H ₂ Capacity		%	1.34
Reversible H ₂ Capacity		%	1.21
Heat of Hydrogenation Reaction		kJ/mol	-39.4
Hysteresis		ln(P _a /P _d)	0.05
Hydrogen Recovery for SR		%	90
Inlet Conditions	Temperature	°C	40
	Pressure	atm	3 and 10 *
Outlet Conditions	Temperature	°C	126
	Pressure	atm	10

Lm is a lanthanum (La) rich mesch metal.

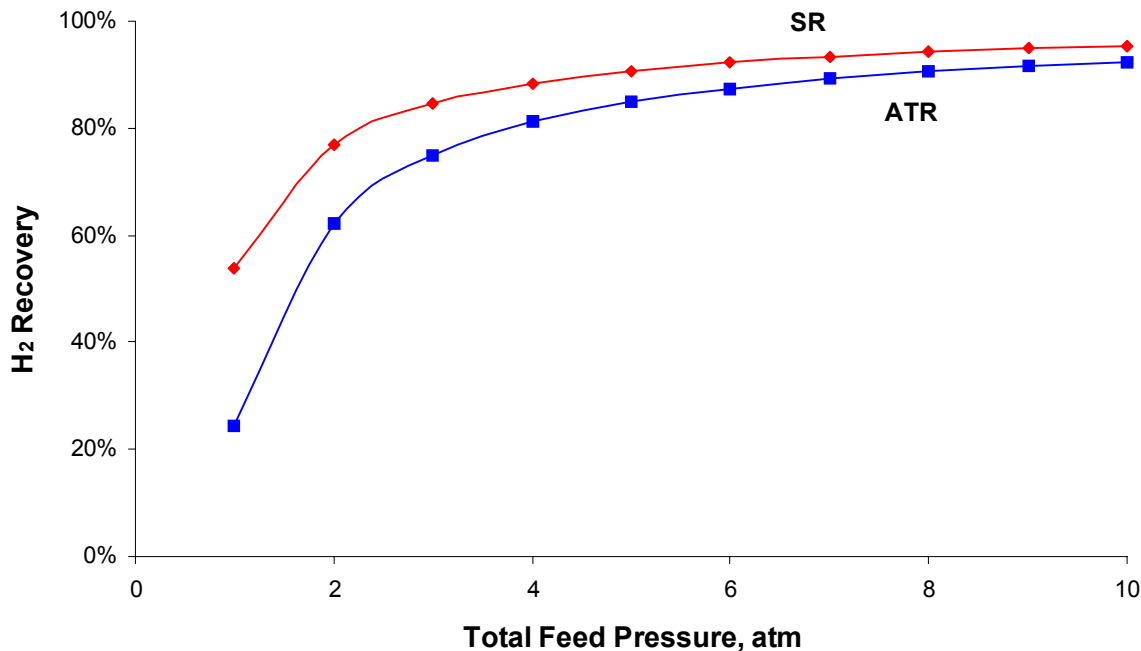
* 3 atm inlet pressure assumes low-pressure reformers, 10 atm assumes high-pressure reformers manufactured specifically for hydrogen production. Hydrogen recovery assumes 10 atm operation.

Metal hydrides are being considered for on-site and on-board storage, due in large part to their potential safety advantage over compressed and liquid hydrogen storage. The disadvantage to metal hydrides is their high cost and low storage density (1-5% wt). Weight is not a major concern for on-site storage, but cost is.

Fluorinating the metal hydrides could provide purification at a relatively small additional cost, making the metal hydride system more cost competitive overall. Japanese academic researchers developed a metal hydride fluorination technique involving metal hydride treatment with fluorine salt in aqueous media (Sun 1999; Liu 1995). A Japanese materials company is developing a fluorination process that does not require use of an aqueous system or, consequently, expensive waste-water treatment system (personal communication with F. Liu, former Kogakuin University, Tokyo, Japan; personal communication with K. Kobayashi, Japan Metals and Chemicals, Japan). The proposed technology employs a fluoro-treatment in the gas phase, similar to other fluorination processes currently employed in the chemical industry.

Combining storage and purification has the additional advantage of long residence times. Innocuous and other non-hydrogen species may significantly reduce the hydrogen absorption

kinetics. However, assuming very long residence times during storage, we have estimated the hydrogen recovery to be limited by system equilibrium only. Figure 3 shows the hydrogen recovery versus system pressure.



* Maximum achievable LaNi_{4.6}Mn_{0.4} hydrogen recovery assuming equilibrium conditions.

Figure 3. Fluorinated Metal Hydride Recovery* as a Function of Pressure

Fluorinated Metal Hydride Slurries

Metal hydride slurries consist of metal hydrides suspended in a liquid material, such as an oil. These slurries can be stored and pumped like a viscous liquid, simplifying and speeding handling and heat transfer. However, slurries suffer from the same high cost as dry metal hydrides and have even lower weight density. Still, with improvements in metal hydride technology, slurries could become a very attractive option, at least for on-site storage.

The performance assumptions for the fluorinated metal hydride slurries are essentially the same as for the dry fluorinated metal hydrides. Experimental and pilot scale work with slurries in the Netherlands has shown that the oil has no noticeable effect on various hydrides (Holstvoogd 1989). As continuous adsorption and desorption processes can be used in this case, higher recoveries are possible with reasonable cost. A higher hydrogen recovery, 94% at 10 atm, was assumed on the basis of a continuous process.

Metal hydride slurry hydrogen purification technology was developed for large-scale applications, such as hydrogen for ammonia plants (Zwart 1989). The technology did not find an industrial application due to high product cost in comparison with large-scale membranes and PSA hydrogen separation. However, metal hydride slurries may present significant advantages

over other processes as it combines hydrogen separation with storage and allows easier and faster vehicle fueling. No fuel cell vehicles have demonstrated this technology for on-board storage. Even if the application for on-board storage would be un-attractive, its use for off-board storage could offer considerable handling, thermal integration, and control benefits over dry hydride systems.

Results

System Efficiency

Individual sub-system performance was determined based on the appropriate integration. For example, purification off-gas (containing un-recovered hydrogen) is recycled for use in the reformer to drive the steam reforming reaction and/or preheat gases. Table 5 shows two examples of the sub-system efficiencies that have been calculated from thermodynamic modeling of high-pressure (~10 atm operating pressure) steam reformer systems.

Table 5. Sub-system Efficiencies Utilizing High-pressure Steam Reformers
Assuming high-pressure storage for compressed H₂ fuel cell vehicles

System Performance, % (LHV)		PSA (baseline)	Non-Pd Membrane*
Gas Efficiency = $\frac{\text{LHV Fuel out}}{\text{LHV Fuel in}}$	Production ¹	100	93
	Purification	76	86
	Storage/Compression	97 ²	97 ²
Parasitic Loss = $\frac{\text{Parasitic Power}^3}{\text{LHV H}_2 \text{ out}}$	Production	1.6	1.5
	Purification	0.6	0.6
	Storage/Compression	7.9 ⁴	12.3 ⁴
System Efficiency including power plant efficiency penalty ⁵		62	59

* Based on long term performance assumptions (see Table 2).

¹ Reformer efficiency calculation does not include the purification and storage recycle gases as fuel inputs (i.e. they are considered “free” inputs). Combined reformer and purification gas efficiencies range from 77-80%.

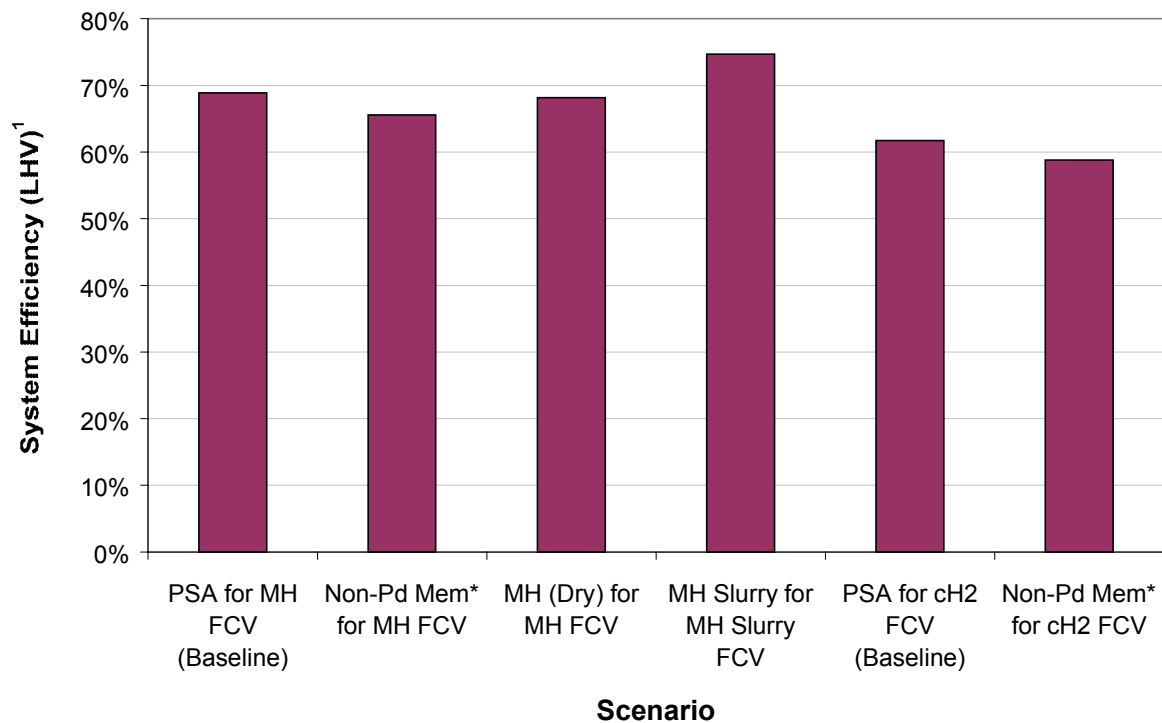
² Includes 3% loss of hydrogen from hydrogen compressors that is recovered and used in the reformer.

³ Includes water pumps, compressors, blowers, and cooling fans.

⁴ Over 90% of this power requirement comes from the compressors required to pressurize the hydrogen to storage pressure (3600 psia) and on-board vehicle pressure (assumed to be 5000 psia).

⁵ Assumes power plant efficiency is 35% LHV based on the average power plant efficiency of a conventional natural gas steam power plant (a combined cycle natural gas power plant average efficiency is 45% LHV).
System Efficiency = (Outlet H₂ LHV)/(Input Natural Gas LHV + Total Parasitic Power/35%).

Overall system efficiencies plotted in Figure 4 show efficiencies are higher for all low-pressure storage options (for MH FCV) versus high-pressure storage options (for CH₂ FCV). This doesn’t take into account the on-board efficiencies that should be lower for the low-pressure storage options due to the increased weight of the on-board metal hydride storage. It is more useful to compare separately the low and high-pressure storage options.



* Based on long term performance assumptions (see Table 2).

¹ Includes a power plant efficiency penalty. Assumes power plant efficiency is 35% LHV based on the average power plant efficiency of a conventional natural gas steam power plant (a combined cycle natural gas power plant average efficiency is 45% LHV). System Efficiency = (Outlet H₂ LHV)/(Input Natural Gas LHV + Total Parasitic Power/35%).

² 10 atm operating pressure

Note: Does not include vehicle fuel efficiency. On-board MH storage options will likely be heavier and have lower fuel economy.

Figure 4. System Efficiencies Utilizing High-pressure² Steam Reformers

The metal hydride slurry option has the highest efficiency due to the high hydrogen recovery for purification and the very low parasitic loads. The metal hydride (dry) is less efficient because the on-site metal hydride storage was assumed to be separate from the on-board storage. This requires the use of an auxiliary burner to generate heat for hydrogen desorption during fueling. While the reformer exhaust provides some heat, most heat is supplied by burning natural gas in the burner (alternatively, additional heat could be supplied by electric heaters). On-site and on-board storage could be combined to increase efficiency, but switching these heavy containers could be unwieldy and would introduce considerable complexity into the fueling and charging process. Slurries, on the other hand, are easily transported from on-site to on-board storage so that on-site hydrogen desorption is not required.

Despite higher assumed hydrogen recovery from purification, the non-palladium metal membrane option has slightly lower efficiency than the pressure swing adsorption baseline. With a steam reformer, not much is gained by increasing purification hydrogen recovery alone because this reformer can efficiently use the un-recovered hydrogen to provide heat for the steam reforming reaction. Results are much different when an autothermal reformer is assumed (results not presented here). The non-palladium option has slightly lower efficiency than the pressure swing adsorption baseline due to additional power required for compressing hydrogen at the membrane exit pressure (~ 1 atm) compared to adsorber exit pressure (~9 atm).

It should be noted that the results presented here are for high-pressure (~10 atm) steam reformer systems only. Modeling low-pressure (~3 atm) steam reformers or autothermal reformers has much different results.

Preliminary Conclusions

Our analysis to date indicates that the use of fluorinated metal hydrides in slurry form could provide significant benefits in terms of off-board system efficiency, especially if the slurry could also be used for on-board storage. Even if only used for purification and on-site storage in decentralized hydrogen production facilities, the use of metal hydride slurries should provide significant efficiency benefits over conventional decentralized hydrogen purification and storage options. However, some technology development will be required to optimize the slurry system, and significant development will be required to develop a stable and effective fluorinated metal hydride that can be produced cost-effectively.

If non-palladium metal membranes could be further developed to operate with reasonable fluxes and at higher pressures, they could provide a very competitive alternative to PSA-based separation and purification systems, though they would not likely yield significant improvements in efficiency.

Based on these results, combined with our ongoing cost analysis, we will make recommendations to DOE regarding the viability of each option, and regarding appropriate R&D activities to further their development.

Acknowledgments

We would like to thank Doug Hooker, Sig Gronich, and the Hydrogen Program Office for their support of this project. We would also like to thank the many developers and vendors who took the time to provide very valuable input.

References

Davis, J.R. 1999. *Metals Handbook*. New York; ASM Intl.

Golben, M. and D. DaCosta. 1999. *Advanced Thermal Hydrogen Compression*, SAE Technical Paper Series 1999-01-2524. Warrendale, PA: the SAE Publication Group.

Hara, S., K. Sakaki, N. Itoh, H.-M. Kimura, K. Asami, and A. Inoue. 2000. "An Amourphos Alloy Membrane without Noble Metals for Gaseous Hydrogen Separation." *Journal of Membrane Science*, 164:289-294.

Holstvoogd, R.D., W.P.M. van Swaakj, G.F. Versteeg, and E.D. Snijder. 1989. "Continuous Absorption of Hydrogen in Metal Hydride Slurries." *Zeitschrift für Physikalische Chemie Neue Folge*, 164:1429-1434.

Ismail, N., A. Gebert, M. Uhlemann, J. Eckert, and L. Schultz. 2001. "Effect of Hydrogen on $Zr_{65}Cu_{17.5}Al_{7.5}Ni_{10}$ Metallic Glass." *Journal of Alloys and Compounds*, 314:170-176.

Liu, F.-J. and S. Suda. 1995. "Properties and Characteristics of Fluorinated Hydriding Alloys." *Journal of Alloys and Compounds*, 231:742-750.

Ritchie, R.O., V. Schroeder, and C.J. Gilbert. 2000. "Fracture, Fatigue and Environmentally-assisted Failure of a Zr-based Bulk Amorphous Metal." *Intermetallics*, 8(5-6):469-475.

Sun, Y.M., X.P. Gao, N. Araya, E. Higuchi, and S. Suda. 1999. "A Duplicated Fluorination Technique for Hydrogen Storage Alloys." *Journal of Alloys and Compounds*, 295:364-368.

Vanhanen, J.P., M.T. Hagström, and P.D. Lund. 1999. "Combined Hydrogen Compressing and Heat Transforming through Metal Hydrides." *International Journal of Hydrogen Energy*, 24:441-448.

Wang, X.-L., K. Iwata, and S. Suda. 1995. "Hydrogen Purification using Fluorinated $LaNi_{4.7}Al_{0.3}$ Alloy." *Journal of Alloys and Compounds*, 231:860-864.

Zwaart, R.L., J.T. Tinge, and W. Meindersma. 1989. "Hydrogen Purification with Metal Hydride Slurries – an Industrial Approach." *Zeitschrift für Physikalische Chemie Neue Folge*, 164:1435-1440.

Commercial Applications for Stationary Fuel Cell Systems

**Dan Stevenson, PE
CTA Energy Solutions
1500 Poly Drive
Billings, MT 59103**

Abstract

The hydrogen fuel cell is arguably the future of power generation for fossil and renewable fuel sources alike. The work reported in this paper focuses on identification, evaluation and development of entry-market stationary fuel cell applications. Previous phases of the Big Sky Fuel Cell Program have focused on researching technology development and appropriate technologies for applications. The present work concentrates on implementing an application research and technology validation program.

There are two major tasks to be completed in this phase of the fuel cell program. The first is the implementation of a proton exchange membrane fuel cell demonstration and evaluation project. This project will install, demonstrate, and evaluate a 4.5 kilowatt PEM fuel cell system installed in a light commercial application. The installation will include innovative cogeneration techniques and an interpretive installation for public education regarding fuel cell technology and related technologies, such as hydrogen production, storage, and use. The demonstration project will be implemented at the West Entrance to Yellowstone National Park and will partially power the Entrance Station complex.

The second task is to identify and evaluate three applications for fuel cell powerplants. The evaluation process began with preliminary identification of target market types, and associated projects. Entry markets identified include Medical Centers, Telecommunication and Data Industries, Banking and Financial Data Processing, and Agricultural Waste to Energy projects.

Many projects were identified initially, and initial narrowing of the projects has been completed. Three projects representative of the identified entry markets for fuel cell technology have been identified, and their evaluation is underway. The projects include a Regional Medical Center, a Data Co-location Center, and a combined beef cattle feeding/processing operation and ethanol plant.

The evaluation of these projects is expected to lead to the development of additional demonstration and evaluation projects in future phases of work. Future work will include the development of the highest potential project as identified by the evaluation of the three projects in this phase.

Introduction

The purpose of the Big Sky Fuel Cell Program (BSFC) is to forward fuel cell technology commercialization through research and implementation of practical and visionary applications of fuel cell technology. The Program's familiarity with the technologies and the benefits that it will produce for the fuel cell industry will aid in technology development, validation, and commercialization. On a local front, economic development within the State of Montana based around the fuel cell industry has been a program mainstay.

The program is presently in its second round of funding. The first round explored the fuel cell technologies that exist, explored projects involving coal gasification to feed a fuel cell power plant, and investigated PEM fuel cell applications. Where the first phase of our program centered on building a general knowledge base about fuel cell technology, the second phase focuses on identifying and implementing actual fuel cell power plant projects.

The BSFC Program is working hard to bring energy alternatives, based on fuel cell focused distributed generation, to the energy industry. The Program's objective for the Phase 2 effort is to demonstrate the viability of fuel cell technology through an actual installation and also identify multiple projects with sound objects and feasibility for additional application research and demonstration of the technology. Work is presently underway on all fronts to make these efforts a resounding success.

Task One – PEM Fuel Cell Demonstration

The proton exchange membrane (PEM) fuel cell powerplant is leading the effort toward commercialization in the 1 to 50 kilowatt market. The commercial applications for distributed cogeneration in this product size range are nearly infinite. The BSFC has identified small, remote, commercial applications as an entry market for this technology, and initiated efforts to identify and evaluate a demonstration project that provides the maximum value possible for the fuel cell industry and the Hydrogen Program.

Project Goals

The goal of the PEM demonstration is to implement a 12-month demonstration of a PEM fuel cell to evaluate its performance in a practical, somewhat harsh environmental, application. The plant will be designed to fully utilize the fuel cell plant's heat production in space heating and domestic water heating cogeneration modes. The potential addition of a small snow-melt system for the fuel cell pad itself is presently being evaluated. The full use of the cogeneration capability is of high priority in this demonstration as maximizing the efficiency of the total plant efficiency is also a goal.

Site Selection

Selection of the demonstration site considered many variables that will affect the outcome of the project. These variables include:

1. The site's ability to allow powerplant installation with minimal risk to the operation of the facility.
2. The site's ability to allow effective powerplant integration electrically and thermally to achieve demonstration project goals.
3. The site's representation of small, remote commercial type loads.
4. The site owners' willingness to site and capacity to monitor the project.
5. The site's potential from the perspective of the fuel cell manufacturing partner. Sites with little public exposure were of little interest.
6. The site's ability to be an effective public education media regarding hydrogen and fuel cell technology.

Several project sites were considered for the demonstration project. These sites included cellular tower installations, small banking outlets, and remote water pumping stations.

The Selected Site

The location that was chosen was the West Entrance Station to Yellowstone National Park. The entrance station, located adjacent to West Yellowstone, Montana is the most traveled entrance to Yellowstone. The site consists of a 600-square foot office building housing the computer and security systems and Ranger offices for the entrance. There are also three entrance kiosks and an ambient air quality monitoring station served from the station's electrical service. The sites electrical service is provided by Fall River Electric Cooperative, a member of the distribution network established by H Power Corporation, a PEM fuel cell plant manufacturer. The facility has a nearly year-round requirement for space heating and also has a minimal domestic water heat requirement, both facilitating optimized cogeneration. The site is staffed by National Park Service staff and NPS electrical and mechanical technicians will be able to access and maintain the plant year-round along with Fall Rivers technicians. All parties involved in the project believe it to be the optimum location for this demonstration for the above technically-related reasons, but also because of the National Park Service's enthusiasm for the project and its public accessibility. The project installation will occur directly inside the Park, past the entrance

station, allowing Park visitors to park and visit the site easily. The demonstration site will be an interpretive installation including permanent media for public education.

The Fuel Cell Powerplant

The fuel cell plant will be provided by H Power Corporation through Fall River Electrical Cooperative, the local H Power distributor. The power plant will be a propane-fueled PEM fuel cell with an average electrical capacity of 4.5 kilowatts. Cogeneration will be accomplished with commercially available equipment.

Task Schedule and Progress

The PEM demonstration is progressing well with the Site Selection and Fuel Cell Manufacturing Partner both completed. A September 1, 2001 delivery on the fuel cell plant is anticipated. Work related to the installation of the fuel cell plant is proceeding and the site is expected to be complete and ready to receive the fuel cell upon delivery. Project completion is expected by September 15, 2001.

Task Two – Commercial Project Identification

Commercialization of fuel cell systems is dependent upon the effective identification of the highest potential entry market segments. The second task in this Phase of work is to identify entry market segments and potential application research/demonstration projects for fuel cell technology. The focus of the BSFC is on near-term technology applications (next 5 years) as well as intermediate-term applications that may be value-added for western region states.

The Market Segments

Many projects were identified and a preliminary round of elimination has taken place. The three projects that were selected for conceptual develop are focused on commercialization of fuel cell technology in the western states region, particularly Montana. The target market segments include:

Regional Medical Centers-

Medical Centers are becoming increasingly sensitive to power quality and reliability. The nature of these facilities also facilitates cogeneration with high temperature fuel cell technologies. The power plant heat rejection rate matches baseline thermal requirements well in this application. The potential of waste-to-energy syn-gas production is also a future consideration with Medical Centers as medical waste is an expensive and hazardous disposal issue. However, the state of the

waste-to-energy processes available are neither economic, nor well-tested in this application. Complication of a first large-scale fuel cell demonstration with one of these technologies would complicate the project to the point of unacceptable risk levels.

Data Centers-

The propagation of Data Centers throughout the Northwest U.S. is a sign of continued growth in the digital age and also a significant burden on the already overtaxed Western grid generation and transmission capacity. The power use density for these facilities can be in excess of 100 watts per square foot resulting in very high electrical demands for a relatively small facility. These same facilities are extremely dependent on premium quality and highly reliability power. The potential for cogeneration at these facilities is low, however the development of the Data Center Campus concept allows cogeneration to be implemented beyond the confines of the Data Center in surrounding process, office, or hospitality related buildings.

Agricultural Waste to Energy

Agriculture in the western U.S. has suffered economically in recent history, spurring a new movement in the area of vertically integrated product production and combined energy and agriculture production facilities. Several developers are working on projects in the Northwest to integrate cattle feeding and processing with ethanol production and other value-added production processes. The process of looking at the entire agricultural and energy production cycles together reveals some exciting synergies that may very well include on-site generation of electric and thermal energy with a fuel cell plant. The environmental and economic benefits of an integrated agricultural and energy plant could revolutionize both industries in Montana.

Project Identification

Projects have been identified and application models, economics and project concepts will be developed for each of the above market segments. Future work in the BSFC program will be focused on implementation of these projects, or the model developed for the market segment.

Based on the evaluations, the projects will be prioritized by potential for fuel cell commercialization and benefits such as economic development and operational improvement in the market segment. Funding for the highest priority project will be pursued for near-term implementation.

Conclusions

The Big Sky Fuel Cell Program's second phase is estimated to be complete in September 2001. With its completion, the second phase will deliver an operating proton exchange membrane hydrogen fuel cell demonstration project. This project will be accessible by over one million visitors to Yellowstone National Park annually and will be designed to maximize public

education about hydrogen and fuel cell technology. In addition to the PEM demonstration, three commercial fuel cell projects will be identified and evaluated as models for fuel cell technology's early market entry. This project identification work and the social and economic benefit that will be identified is the impetus for future work within the BSFC Program.

The BSFC Program is focused on solving present and near-term energy issues as well as assisting long-range project types through implementation. Public education and economic development also remain important objectives of the Program.

Future Work

The future work to be completed by this Program is contingent upon the Technical Advisory Team's review of the work in this phase. Pending review the following are suggested future work items:

Short term work goals:

1. Develop a business plan based on the current state of fuel cell technology and projected development to commercialize stationary systems in the building industry. Develop this business plan in coordination with fuel cell manufacturers by First Quarter 2002.
2. Using the information gathered and project concepts developed in the current phase of our work (Phase Two), implement a minimum of two, preferably four, major (250kW or greater) commercial fuel cell demonstrations by Second Quarter-2003. These projects will be strategically chosen to aid commercialization.
3. Based on the results of project testing programs and monitoring of the above installations, provide critical feedback to fuel cell developers to improve product for the building industry. Have building industry data incorporated into the major manufacturers technology by Third Quarter 2004.

Long term work goals:

1. Execute additional demonstration projects to penetrate additional entry markets. The Vision of our program is to methodically assist in the commercialization and deployment of fuel cell technology. By Fourth Quarter 2005, have fuel cell technology sufficiently demonstrated to entry markets to facilitate commercial deployment of the technology.
2. Develop a deployment team vertically integrated in the energy, equipment sales/service, and building construction industry to smoothly integrate the technology into construction projects. Develop this plan for immediate transition to system commercialization from testing – Early Fourth Quarter 2005.
3. Build on the accumulated experience to make fuel cell technology a reality in the building and construction industries.
4. Develop a waste to energy and hydrogen generation and infrastructure component to our work. A milestone is being determined.

Acknowledgments

The following people and the agencies, or companies that they represent have been of tremendous assistance in this phase of the program. Thank you for your time and assistance:

Public Entities:

Doug Hooker	Department of Energy, Golden Field Office
Mark Williams	Strategic Center for Natural Gas, NETL
Mark Hines	State of Montana-Department of Environmental Quality
Yellowstone District Members	State of Montana-Department of Natural Resources and Conservation
Chancellor Sexton Dr. Barbara Nemecek Brian Gurney	Montana State University-Billings
Dr. Tom Yoder Cheryl Heath	Center for Applied Economic Research
Lynn Weege	Department of Energy, Golden Field Office -Green Energy Parks Program
Tim Hudson Jim Evanoff	National Park Service-Yellowstone National Park
Shad Weber	Natural Resource Conservation Service-USDA

Private Entities:

Don Bottrell Jerry Thomas	Transtech Inc. (Data Center and High Tech Park)
Mitch Goplen	Deaconess Billings Clinic (900ksf Medical Center)
Roger Petersen Dan Gatch Dan Persa	Pennsylvania Power and Light (PPL)
Eric Simpkins	Fuel Cell Energy
Chris Haun Anita LaMendola	H Power

Dave Micheletti

MSE, Inc.

Dave Peterson
Weston Ball

Fall River Electric Cooperative

Ray Armstrong

HKM Engineering

HYDROGEN FUEL CELL BUS EVALUATION

**Leslie Eudy and Richard Parish
National Renewable Energy Laboratory
Golden, CO 80401**

**Jonathan Leonard
Arthur D. Little- Acurex Environmental
Fullerton, CA 92835**

Abstract

Global concern for the environment has been increasing throughout the last decade, and “green” technologies are being emphasized all over the world. Research and development of advanced technologies for the transportation sector has been growing at a rapid pace in an effort to reduce petroleum imports and lower emissions. Developing technologies have recently been incorporated into transit buses because of the additional space and volume that is available for packaging prototype equipment. In the late 1990s, preliminary studies on fuel cell buses were carried out by transit agencies in Chicago, IL; Vancouver, BC, Canada; and Georgetown University in Washington, DC. Although early results were promising, it was clear additional testing and evaluation was necessary before these new technologies could be successfully integrated into a transit fleet. One such evaluation is underway at SunLine Transit Agency in Thousand Palms, California on a bus equipped with a XCELLSiS Phase 4 fuel cell engine. The Department of Energy’s National Renewable Energy Laboratory (NREL) is working with transit agencies and other partners to determine the test and evaluation protocols needed to advance implementation of these new technologies, as well as to document the necessary modifications to the transit agencies’ maintenance and operation infrastructure. By evaluating SunLine, an “early adopter” of the technology, NREL will develop and carry out a test plan for evaluating the fuel cell buses, the hydrogen fueling infrastructure, and maintenance facilities. This paper describes the prototype bus, fueling infrastructure, and maintenance facility at SunLine and begins the process of determining what is needed to evaluate and characterize the bus’ performance in service.

Introduction

Although buses make up less than 1% of the total vehicles operated in the U.S., their concentrated use in the urban environment results in disproportionate public health impacts. Most notably, buses are a major cause of human exposure to emissions of diesel particulate matter, which has been identified by the California Air Resources Board (CARB) as a toxic air contaminant. Transit buses are one of the best applications for alternative fuel or advanced technology vehicles for several reasons: they typically operate in highly urbanized areas where pollution is already a problem; they are centrally located/fueled; they are highly visible; and they are government subsidized. Due to the high visibility and pollution issues, buses have been the focal point for developing zero- and near-zero-emission fuel cell technology for heavy-duty vehicles. Several prototype fuel cell buses have been demonstrated in the U.S. and Canada in the past few years and are expected to be available commercially on a limited basis by 2003. Transit fleets considering advanced technology buses must have information on performance, maintenance, and infrastructure requirements before they can incorporate the buses into their fleet. Therefore, a comprehensive evaluation protocol will have to be developed for testing and evaluating fuel cell buses; and the necessary facility modifications and potential costs will need to be characterized.

California has traditionally led the way in implementing advanced transportation technologies, mainly due to severe air quality problems and the unique charter of CARB to adopt the world's most stringent emissions standards. Zero emission vehicles are a key element in CARB's plan to attain air quality standards, and its recently adopted state-wide urban bus fleet rule requires transit agencies that choose to follow the "diesel path" to begin demonstrations of zero-emission buses by July 2003. In conjunction with CARB and other members of the California Fuel Cell Partnership, a prototype fuel cell bus is currently being demonstrated at SunLine Transit Agency in Thousand Palms, CA. The Zero-Emission Bus, or ZEBus, is equipped with a direct-hydrogen proton exchange membrane fuel cell engine developed by XCELLSiS Fuel Cell Engines Inc. XCELLSiS partnered with SunLine to demonstrate the bus in real-world service. Data gathered from this demonstration will be used to validate the technology and to develop a commercial product. The SunLine demonstration provides an excellent opportunity for researchers to gain an understanding of the prototype bus, its systems, and facility modifications necessary for maintenance and operation. The information being gathered is aiding in the development of procedures for evaluating the next generation of fuel cell buses.

In 2003, AC Transit in Hayward, CA will procure up to 20 fuel cell buses for the California Fuel Cell Partnership's fuel cell bus demonstration program. (SunLine and AC Transit are currently the only two transit agencies that are associate members of the California Fuel Cell Partnership.) The buses from this procurement will be operated by AC Transit, SunLine Transit Agency, and possibly one or two other Bay Area transit properties. NREL plans an evaluation of these buses operating in revenue service.

Background on SunLine Transit Agency

Concerned with poor air quality in the surrounding Coachella Valley of Southern California, in 1992, SunLine's board of directors (all elected officials) mandated a conversion from diesel to alternative fuel buses. Investigation into alternatives to diesel showed that compressed natural gas (CNG) buses offered the lowest-emission commercially available technology available. With help from local partners, such as the Southern California Gas Company, who helped build the fueling infrastructure, and College of the Desert, who developed a training curriculum, SunLine converted its entire fleet to CNG. In May of 1994, SunLine became the first transit district in America to roll out for revenue service with a fleet of 100% CNG buses.

SunLine's management team believes that CNG is the best choice for the present, but also an excellent means to help make the transition to hydrogen as a major transit bus fuel. CNG used as a transportation fuel has storage, dispensing, and handling requirements similar to compressed hydrogen. In addition to the XCELLSiS fuel cell bus, SunLine operates two Hythane® fueled buses. Hythane® is a compressed gas mixture of 20% hydrogen and 80% natural gas (by volume). Adding the small percentage of hydrogen reduces CNG's already low NO_x emissions by over 40%. The use of Hythane® can also help to gradually introduce hydrogen as a commonly used transportation fuel.

Sunline's single fuel cell bus and two Hythane® buses are fueled with hydrogen produced on-site by the transit agency. This paper describes the prototype fuel cell bus, the fueling infrastructure, and maintenance facility at SunLine and discusses some of the issues that need to be resolved for a transit agency to operate and maintain fuel cell buses in real-world revenue service.

Prototype Fuel Cell Bus

XCELLSiS Fuel Cell Engines, jointly owned by DaimlerChrysler, Ford Motor Company, and Ballard Power Systems, is focused on developing, manufacturing, and commercializing fuel cell engines for transportation applications. Their Phase 3 (P3) Test Program included a 2-year demonstration of P3 fuel cell buses at two locations: Chicago, Illinois, and Vancouver, British Columbia. The results from the demonstration were positive and led to many improvements in the Phase 4 (P4) bus design, including the following:

- Engine volume reduction of 50%
- Weight reduction of 3400 lb
- Eight fuel cell stacks (down from 20)
- Number of motors reduced to one (P3 had 12)
- Startup time reduced from 45 to 3 seconds
- Maintenance cost reductions (possibly as much as 90% compared to those of the P3 bus)

The P4 XCELLSiS fuel cell bus currently operated at SunLine is a standard low-floor transit bus purchased from New Flyer and converted by the XCELLSiS/Ballard Power Systems team to fuel

cell power. Table 1 provides an overview of the XCELLSiS fuel cell engine and P4 fuel cell bus. Figure 1 shows a field engineer from XCELLSiS preparing to fuel the bus from the Stuart Energy/Fueling Technologies hydrogen/Hythane® dispenser (described later).

Table 1. Overview of the XCELLSiS fuel cell engine and P4 fuel cell bus

Fuel cell technology	Direct-H ₂ Proton Exchange Membrane
Fuel cell engine make / model	XCELLSiS XCS-HY-205
Fuel cell engine volume / weight	5.32 cubic meters / 2,170 kg (4,774 lbs)
Net shaft power / peak net torque	205 kW @ 2100 rpm / 1,100 Nm @ 800 rpm
Net efficiency	44% to 37% (LHV)
Fuel type	Gaseous hydrogen @ up to 3,600 psig
Fuel storage system / capacity	Std. CNG cylinders / 17,500 SCF of CH ₂ *
Bus range	Approximately 225 miles
Air delivery system / max air flow	Two stage compressor / 600 SCFM
Nominal operating pressure	200 kPa (30 psig)
Cooling system	Water / glycol
Fuel cell operating temperature	70°C to 80°C
System voltage range	600 to 900 VDC
Power conditioning	IGBT inverter, liquid cooled
Electric traction drive	Brushless DC, liquid cooled
Power transmission	Fixed ratio, direct drive
Braking	Dynamic (no regenerative)

* Compressed gaseous hydrogen



Figure 1. XCELLSiS field technician fueling the P4 bus with hydrogen

Currently, XCELLSiS field engineers are handling the day-to-day operations of the P4 fuel cell bus and performing tests to verify and improve its commercial viability. The bus is not yet ready

for revenue service. It is being driven over a similar street route each day, and is equipped with test instrumentation and water-filled tanks on the seats to simulate the curb weight of a loaded bus. Figure 2 shows the interior of the bus during such a test.



Figure 2. Water tanks in the XCELLSiS bus simulate curb weight during testing

Hydrogen Infrastructure

SunLine Transit Agency has adopted a two-pronged approach to its preliminary hydrogen fueling infrastructure. In April of 2000, SunLine opened a hydrogen generation, storage, fueling, and education facility to demonstrate these various approaches to hydrogen production. At the site, hydrogen is produced by solar-powered electrolysis as well as natural gas reforming. In an effort to test the viability of as many renewable sources of hydrogen as possible, SunLine is also interested in producing hydrogen from electrolysis powered by the Coachella Valley's abundant wind resources.

Currently, the hydrogen production, storage, and dispensing infrastructure at SunLine Transit Agency consists of the following main components:

- Three separate systems for onsite hydrogen production (two water electrolysis systems – one which provides fuel for SunLine's fuel cell golf carts and a neighborhood electric vehicle; the other provides fuel for the ZEBus and Hythane® buses; and partial oxidation reforming of natural gas)
- A tube trailer and American Society of Mechanical Engineers (ASME) tanks for storage of approximately 118,000 standard cubic feet (SCF) of compressed hydrogen

- A two-hose fueling station that dispenses compressed hydrogen from one hose and a Hythane® blend from the second hose

Stuart Energy Hydrogen Generator, Storage, and Dispensing System

Currently, all hydrogen used to fuel the XCELLSiS fuel cell bus is produced, stored, and dispensed through a complete system built and packaged by Stuart Energy. Hydrogen production in this system is accomplished by splitting water into hydrogen and oxygen using Stuart Energy’s proprietary electrolysis technology. The resulting hydrogen gas is dried, purified, compressed, and sent to storage, while the oxygen is vented to the atmosphere. Hydrogen fueling of the XCELLSiS P4 fuel cell bus is accomplished with a specially designed dispenser similar to those used by SunLine to fuel its fleet of compressed natural gas buses. Energy to power the electrolyzer is currently provided by the grid with some of that power being offset by SunLine’s photovoltaic arrays (totaling approximately 40 kW) and flat plate arrays.

Specific components of SunLine’s complete “bus fueler” system include the following:

- Stuart Energy Model P3-1A CST multi-stack electrolyzer, with an output of 1400 standard cubic feet per hour (SCFH) of hydrogen
- Stuart Energy hydrogen processing module including a Comp-Air Reavell Model 5000 4-stage hydrogen compressor with an outlet pressure of 5,000 psi
- Modular hydrogen storage consisting of a FIBA tube trailer with 16 DOT tanks holding 104,000 SCF of hydrogen (3,130 psi), and two ASME tanks holding 14,000 SCF of hydrogen (4,000 psi)
- Fueling Technologies, Inc. Model HYDH5210 hydrogen/Hythane® dispenser, with mass flow metering, a separate mixer for Hythane®, and two fast-fill hoses



Figure 3. SunLine’s FIBA tube trailer and ASME tanks for CH₂ storage



Figure 4. Stuart Energy's modular compressed hydrogen station

HbT Natural Gas Reformer

A second source of hydrogen for SunLine's fleet of fuel cell buses will be produced through on-site partial oxidation reforming of natural gas. In mid 2000, the California Air Resources Board approved a grant to HbT (formerly known as Hydrogen Burner Technology) to build and install such a system at SunLine. The HbT system uses HbT's Under-Oxidized Burner (UOB™) technology and a QuestAir purifier to reform pipeline natural gas into high-purity (99.999%) hydrogen. This system, which is currently undergoing checkout testing, will be able to fuel four or five hydrogen buses per day. The system includes the following components:

- Model 4200 NG-A UOB™ reformer/CO shift reactor skid
- Pressure Swing Adsorption (PSA) purification unit
- Integrated automatic Programmable Logic Controller (PLC) controls
- Pressure Dynamics 2-stage hydrogen compressor
- Pressure vessels for hydrogen storage



Figure 5. HbT's Model 4200 NG-A natural gas reformer system at SunLine Transit Agency

As the first U.S. transit agency to build a hydrogen fueling infrastructure, SunLine has broken new ground. Table 2 gives the estimated cost for the infrastructure installed at SunLine. Because this facility is a first of its kind, these costs should be considered preliminary. Some components and systems are essentially pre-commercial, while others are “off-the-shelf.” The cost of adding infrastructure to another transit agency could be different depending on their approach, the specific equipment, the number of buses serviced, and other factors. The costs listed here reflect SunLine Transit Agency’s current experience with providing fuel for its bus fleet.

Table 2. Cost of Hydrogen Fueling Infrastructure Installed at SunLine

Infrastructure Component	System	Manufacturer / Model	Estimated Equipment Cost
H₂ Production, Clean-up, and Compression	Electrolyzer	Stuart Energy P3-1A	Unknown / Proprietary
	Compressor	CompAir Reavell 5000	Included in Stuart Energy package
	Nat. Gas Reformer	Hydrogen Burner Technologies 4200 NG-A	\$450,000
	Compressor	Pressure Dynamics	Included in HBT package
H₂ Storage	Tube Trailer Cylinders (104,000 SCF)	Fiba Technologies	\$104,000
	Stationary Cylinders (14,000 SCF)	Not Available	\$54,000
H₂ / Hythane Dispensing	Hydrogen / Hythane Mixer and Dispenser	Fueling Technologies Inc. HYDH5210	\$32,000

Maintenance Facility for Hydrogen Buses

Currently, SunLine Transit Agency maintains its fleet of CNG buses in a large indoor facility. By contrast, XCELLSiS personnel perform maintenance on the hydrogen fuel cell bus in a separate, smaller facility. As Figures 6 and 7 show, this “outdoor-style” facility consists of an aluminum frame, fireproof canvas, and explosion-proof light fixtures. The “tent” structure is ventilated along the ridgeline to allow hydrogen gas to safely escape if it is inadvertently released from the vehicle. In the near future, hydrogen sensors may be installed along the peak of the structure to alert maintenance staff of a possible leak. This \$95,000 facility is sufficient to maintain the existing XCELLSiS fuel cell bus and possibly up to four additional buses, but it is essentially an interim solution for SunLine Transit Agency. It is also important to note that SunLine’s maintenance facility, while perfect for the agency’s operating climate, would not work

for transit agencies in all climate zones. Eventually, transit districts making a serious commitment to hydrogen fuel cell buses will need to construct state-of-the-art maintenance facilities that meet all applicable safety codes and standards.



Figure 6. Outside of existing maintenance facility for hydrogen buses.



Figure 7. Interior of the hydrogen bus maintenance facility

Issues

The single P4 XCELLSiS bus operated at SunLine Transit Agency is one of a kind and currently the world's most technologically mature on-road fuel cell vehicle. SunLine is among the most progressive transit agencies in America regarding early adoption of advanced low-emission bus technologies and the use of alternative fuels. The existing hydrogen generation, storage, and dispensing systems at SunLine are essentially state-of-the-art for compressed hydrogen use in vehicle applications. Involvement of the California Fuel Cell Partnership will help the program progress to the next stages of deployment when additional buses become available in 2003. Clearly, the right players have been assembled for the SunLine Transit Agency fuel cell bus demonstration, and the program is on track for success.

However, to optimize the program's full potential for success, a number of issues will need to be addressed over the next two years. These include the following:

- Currently, SunLine Transit Agency has a limited role in testing, operating, maintaining, and fueling the fuel cell bus. SunLine provides motor coach operators, preventative maintenance on the bus, and some equipment replacement. At this early stage, XCELLSiS field engineers are performing most other functions on a day-to-day basis. This is necessary in order for XCELLSiS to further the commercial viability of its emerging direct-hydrogen PEMFC technology. However, if fuel cell buses are to be deployed in normal revenue service at

SunLine Transit Agency and other California transit agencies by 2003, it will soon be necessary to increase the hands-on involvement of transit personnel in these processes. A “master plan” for this transition is needed, perhaps through the California Fuel Cell Partnership.

- The existing facilities at SunLine Transit Agency to generate, store, and dispense hydrogen appear sufficient to meet SunLine’s current fuel cell bus program, including plans for modest expansion (~2 or 3 buses). Significantly expanding the fleet beyond a demonstration scale will likely require significant upgrades to key systems, such as expanded fuel storage and an improved maintenance facility. SunLine Transit Agency is already addressing some of these concerns.
- According to SunLine personnel, the biggest barrier to expanding its hydrogen fuel cell bus operations is the current lack of hydrogen-specific regulations addressing safety. Without new codes and standards specifically designed for the unique characteristics of hydrogen, it’s possible that fire-protection and code and safety officials will raise issues that could delay the commercial introduction of hydrogen fuel cell buses by many years.
- There are many logistical issues to be worked out before SunLine Transit Agency can optimize the emerging subsystems in its hydrogen infrastructure. For example, the HbT reformer system produces large volumes of wastewater each day during full operation. This effluent is not hazardous but nonetheless must be disposed of in an efficient, non-disruptive manner. It’s possible that beneficial uses for the effluent can be identified.

Future Work

The goal for the NREL Hydrogen Bus Evaluation Program is to evaluate the performance and operating characteristics of fuel cell buses in revenue service and characterize the maintenance and fueling infrastructure needed to fuel and maintain them. Because fuel cell buses are not commercially available, we will use the prototype fuel cell bus demonstration project at SunLine to understand the technology and plan for the future evaluation. Using the preliminary data collected, NREL plans to:

- Develop and document the procedures necessary to evaluate fuel cell buses
- Perform baseline performance testing of the XCELLSiS fuel cell bus and document the results
- Define and document infrastructure and facility modifications required to add hydrogen fueling and bus maintenance to the AC Transit site
- Evaluate the performance, emissions, cost, and operating characteristics of the Hythane buses

The information collected will be made available on the World Wide Web.

References

Cleaning Up: Zero-Emission Buses in Real-World Use. 2001. A Report on the Phase 3 Fuel Cell Bus Program by XCELLSiS/Ballard Power Systems. http://www.ballard.com/fcb_report.asp

Information provided to NREL and Arthur D. Little by staff from SunLine Transit Agency and XCELLSiS Fuel Cell Engine Company.

INTERNATIONAL ENERGY AGENCY AGREEMENT ON THE PRODUCTION AND UTILIZATION OF HYDROGEN

**Carolyn C. Elam and Catherine E. Gregoire Padró
National Renewable Energy Laboratory
1617 Cole Boulevard
Golden, CO 80401**

Abstract

Although hydrogen systems are recognized as viable, sustainable options for meeting the world's energy requirements, technical and economical barriers must first be overcome before worldwide use of hydrogen is realized. Hydrogen is relevant to all of the energy sectors - transportation, buildings, utilities and industry. It can provide storage options for baseload (geothermal), seasonal (hydroelectric) and intermittent (PV and wind) renewable resources, and, when combined with emerging decarbonization technologies, can reduce the climate impacts of continued fossil fuel utilization. Yet advances must be made in hydrogen production, storage, transport and utilization technologies and in the integration of these components into complete energy systems for hydrogen to become a competitive energy carrier. To expedite the advancement of hydrogen technologies, nations have come together under the auspices of the International Energy Agency's (IEA) Hydrogen Program to collaborate and address the important barriers that impede hydrogen's penetration into the world energy market. Through well-structured, collaborative projects, experts from around the world address many of the technical challenges and long-term research needs that face the hydrogen community. These collaborations have already led to significant advances in renewable hydrogen production and solid storage materials and to the development of tools to evaluate and optimize integrated hydrogen energy systems.

Introduction

The International Energy Agency (IEA) was established in 1974, following the first oil crisis and is managed within the framework of the Organization for Economic Cooperation and Development (OECD). The mission of the IEA is to facilitate collaborations for the economic development, energy security, environmental protection and well-being of its members and of the world as a whole. As part of this effort, the IEA launched the Production and Utilization of Hydrogen Program, known as the Hydrogen Agreement, in 1977 to advance hydrogen production, storage and end-use technologies and to accelerate hydrogen's acceptance and widespread utilization. Currently, Canada, the European Commission, Japan, Lithuania, the Netherlands, Norway, Spain, Sweden, Switzerland, the United States are all active participants in the IEA Hydrogen Agreement.

The IEA Hydrogen Agreement

The members of the IEA Hydrogen Agreement recognize that a long-term research and development effort is required to realize the significant technological potential of hydrogen energy. This effort can help create competitive hydrogen energy production and end-use technologies, and supports development of the infrastructure required for its use. The following have been established as the guiding principles on which the IEA Hydrogen Program is based:

- Hydrogen--now mainly used as a chemical for up-grading fossil-based energy carriers--will in the future increasingly become an energy carrier itself. It is necessary to carry out the analysis, studies, research, development and dissemination that will facilitate a significant role for hydrogen in the future.
- Significant use of hydrogen will contribute to the reduction of energy-linked environmental impacts, including global warming due to anthropogenic carbon emissions, mobile source emissions such as CO, NO_x, SO_x, and NMHC (non-methane hydrocarbons), and particulates.
- Hydrogen is currently used to up grade lower-quality, solid and liquid fossil fuels, such as coal and heavy oils. The use of hydrogen in such applications reduces harmful emissions through more efficient end-use conversion processes and extends the range of applicability. Ultimately, with the addition of hydrogen, carbon dioxide emissions can be used to produce useful chemicals and fuels.
- Hydrogen has the potential for short-, medium- and long-term applications and the steps to realize the potential for applications in appropriate time frames must be understood and implemented.
- All sustainable energy sources require conversion from their original form. Conversion to electricity and/or hydrogen will constitute two prominent, complimentary options in the future.
- Hydrogen can assist in the development of renewable and sustainable energy sources by

providing an effective means of storage, distribution and conversion; moreover, hydrogen can broaden the role of renewables in the supply of clean fuels for transportation and heating.

- Hydrogen can be produced as a storable, clean fuel from the world's sustainable non-fossil primary energy sources - solar energy, wind energy, hydropower, biomass, geothermal, nuclear, or tidal. Hydrogen also has the unique feature that it can upgrade biomass to common liquid and gaseous hydrocarbons, thus providing a flexible, sustainable fuel.
- Hydrogen can be used as a fuel for a wide variety of end-use applications including important uses in the transportation and utility sectors.
- All countries possess some form of sustainable primary energy sources; hence, hydrogen energy technologies offer an important potential alternative to fossil fuel energy supply (in many instances to imported fuels). Utilization of hydrogen technologies can contribute to energy security, diversity and flexibility.
- Barriers, both technical and non-technical, to the introduction of hydrogen are being reduced through advances in renewable energy technologies and hydrogen systems including progress in addressing hydrogen storage and safety concerns.
- Hydrogen energy systems have potential value for locations where a conventional energy supply infrastructure does not exist. The development of hydrogen technologies in niche applications will result in improvements and cost reductions which will lead to broader application in the future.

If the technological potential of hydrogen is realized, it will contribute to the sustainable growth of the world economy by facilitating a stable supply of energy and by helping to reduce future emissions of carbon dioxide. Cooperative efforts among nations can help speed effective progress towards these goals. Inasmuch as hydrogen is in a pre-commercial phase, it is particularly suited to collaboration as there are fewer proprietary issues than in many energy technologies.

Technology Activities

The use of hydrogen as an energy carrier is considered a mid- to long-term goal. Hydrogen production from renewables will likely not be cost-competitive with fossil-based production, at least in the near-term. Likewise, infrastructure barriers, particularly in the storage area, hinder near-term application of hydrogen for transportation applications. Additionally, safety issues, both real and perceived, are concerns for acceptance of hydrogen by the general population. Thus, the Hydrogen Agreement is focused on pursuing technologies that will help overcome some of the infrastructure barriers and/or result in the reduced cost of hydrogen systems.

- To achieve the advantages of a "hydrogen future," namely a reduction in carbon emissions, hydrogen must be able to be cost-effectively produced from renewables. Thus, the Hydrogen Agreement has been pursuing R&D in the solar production area, both biological and

electrochemical. Much must still be learned about photobiological processes before we are able to understand the economic potential of this production technology. The electrochemical approach is, of course, hindered by the fact that photovoltaic technology is not yet cost-effective. Thus, it cannot compete with existing technology, except possibly in small niche markets.

- On-board storage in vehicles is one of the major barriers to the acceptance of hydrogen powered vehicles. Metal hydrides and similar storage medium, such as carbon, are thought to have the greatest potential for the safe, on-board storage of hydrogen. However, work-to-date has not proven cost effective due to the inability of current technology to meet the hydrogen storage percentages required for maintaining vehicle weights within a reasonable range.
- The use of hydrogen in the metals, chemicals, glass, food, electronics, fertilizer, petroleum and space industries is well established. The range of uses has been increasing, as has the consumption by specific application. Historically, hydrogen has had an excellent safety record. The many studies, R&D efforts, and experience base have contributed to the publication of regulations, standards, industrial data sheets and technical reports. Hydrogen safety is an issue of every aspect from production to utilization and continues to be of the utmost importance; not only to those researching, designing and working with it; but to the general public, local authorities, insurance agents, etc., as well.
- Achieving the vast potential benefits of a hydrogen system requires careful integration of production, storage and end-use components with minimized cost and maximized efficiency, and a strong understanding of environmental impacts and opportunities. System models combined with detailed life cycle assessments provide the platform for standardized comparisons of energy systems for specific applications. Individual component models form the framework by which these system designs can be formulated and evaluated.

The Hydrogen Agreement has developed a broad portfolio of collaborative research activities to address the aforementioned challenges for hydrogen penetration into the world energy marketplace.

Renewable Hydrogen Production

As part of the IEA activities, the concept of using solar energy to drive the conversion of water into hydrogen and oxygen has been examined from the standpoints of potential and ideal efficiencies, measurement of solar hydrogen production efficiencies, surveys of the state-of-the-art, and technological assessments of various solar hydrogen options. The analysis demonstrated that the ideal limit of the conversion efficiency for 1-sun irradiance is ~31% for a single photosystem scheme and ~42% for a dual photosystem scheme. However, practical design and material considerations will likely limit conversion efficiencies to less than 16%. Four types of solar photochemical hydrogen systems were identified: photochemical, semiconductor, photobiological and hybrid systems. A survey of the state-of-the-art of these four types was performed and each system (and their respective subsystems) was examined as to efficiency, potential for improvement and long-term functionality [1]. Based on this study, four systems

were selected for collaborative research and development projects:

- Photovoltaic cells plus an electrolyzer
- Photoelectrochemical cells with one or more semiconductor electrodes
- Photobiological systems
- Photodegradation systems

Photoelectrochemical production uses semiconductor technology in a one-step process of splitting water directly upon sunlight illumination by combining a photovoltaic-type cell and electrolysis into a single device. Research efforts are being focused on identifying structures and materials that will meet the high electron voltage (eV) requirements (the optimal absorption threshold for a single photoconverter is at 1.6 eV) to dissociate water, not be susceptible to the corrosiveness of the aqueous electrolytes used in the electrolytic process, and are cost-effective. Amorphous silicon devices are one of the types most favored for such systems, due to their lower cost. These photovoltaic devices have achieved efficiencies of 7-8%. Photovoltaic devices using more expensive materials, have demonstrated efficiencies of over 16% [2]. Researchers are now working to combine the low cost materials and high conversion efficiency materials to achieve a practical application of this promising technology.

An alternative approach to common photovoltaics is to use a tandem device that achieves the direct cleavage of water into hydrogen and oxygen [3]. Such a device is based on the in-series connection of two photosystems. A thin film of nanocrystalline tungsten trioxide (WO_3) absorbs the blue portion of the solar spectrum. The valence band holes (h^+) created by band gap excitation of the WO_3 serve to oxidize water to oxygen, while the conduction band electrons are fed into the second photosystem that consists of dye sensitized nanocrystalline TiO_2 film. The latter is placed directly behind the WO_3 film capturing the green and red portion of the solar spectrum that is transmitted through the top electrode. The photovoltage generated by the second photosystem enables the generation of hydrogen by the conduction band electrons. The overall reaction corresponds to the splitting of water by visible light. 5% overall AM-1.5 solar light to chemical conversion efficiencies have been achieved with this device.

Most photobiological systems use bacteria and green algae to produce hydrogen. These systems hold great promise for long-term sustainable hydrogen production, but face two major barriers for meeting the cost limitations. These barriers are the fairly low solar conversion efficiencies of these systems of around 5-6%, and the fact that nearly all enzymes that evolve hydrogen from water are inhibited in their hydrogen production by the presence of oxygen. To improve solar conversion efficiencies, methods for reducing light-harvesting pigments and antenna length are being developed. In the case of the water-splitting organisms, research efforts are focusing on overcoming oxygen intolerance by developing strains of the green algae, *Chlamydomonas*, which contain oxygen-uptake enzymes, and thus can produce oxygen and hydrogen simultaneously. 5-10% efficiencies have already been achieved with certain strains of the genetically modified water-splitting microorganisms. In the case of fermentative organisms, 60% conversion rates of biomass (acetic acid) to hydrogen, with 2.7% of the light energy absorbed stored as hydrogen, have been reported.

Hydrogen Storage

The use of hydrogen as a vehicle fuel requires a storage means that has inherent safety and both volumetric and gravimetric efficiency. Metal hydrides offer alternatives to the storage of hydrogen in gaseous and liquid form. They store hydrogen in an essentially solid form and offer the potential for volume efficiency, high safety, low pressure containment and ambient temperature operation. Unfortunately, most known hydrides are either heavy in comparison to the hydrogen they carry or require high temperature for hydrogen release. In the past few years, carbon adsorbent materials have also gained attention as a possible, cost-effective storage medium for hydrogen. Whereas carbon was once considered only as a cryo-adsorbent for hydrogen, there is growing evidence that it can store significant quantities of hydrogen at ambient temperature. However, much must still be learned about consistent and high-purity production of these materials and the nature and potential for hydrogen storage [4].

Sixteen metal hydride and four carbon projects were undertaken by the international experts to develop materials with improved gravimetric capacity (5 weight %) and lower temperature (100-150°C) release of hydrogen. Building on the developments from the Max Planck Institute für Kohlenforschung, Germany [5], the international experts undertook several projects to look at catalyzed sodium aluminum hydrides. Through their efforts, a formulation was found that is capable of 5 weight percent reversible hydrogen storage at 120°C. In addition to this significant accomplishment, a great deal of knowledge has been gained on the effects of material formulations and treatments on hydrogen storage capability [6].

To build on the progress made by the completed metal hydride and carbon projects, twenty-two new projects have already been launched. These projects include fundamental investigations of new material formulations, mechanisms of chemical and physical hydrogen storage, and engineering considerations for practical on-board storage. Chemical hydrides will also be added to the array of materials being investigated.

Integrated Systems

Through the IEA Integrated Systems activities, twenty-seven component models have been developed to model hydrogen production, storage, distribution and utilization [7]. Guidelines for a standardized modeling platform have been defined to ensure that the component models can be linked to simulate fully integrated systems [8]. Using the component models, a number of integrated hydrogen energy systems were designed and evaluated [9-16]. Additionally, ten international hydrogen demonstration projects were critically evaluated and compared with regard to system design and performance and safety and regulatory issues [17].

Using the information, tools and methodologies that have been developed, experts are currently evaluating three potential demonstration projects. The first is a “greenfield” community that would be based in the Netherlands where there is an ambitious national plan to require 3% renewables in the power generation mix for new residential districts. Technologies under consideration include PEM and solid oxide fuel cells, heat pumps, and combined heat and power. The second system being evaluated is a hydrogen refueling station for a remote island community in Norway. For this case, a wind park will provide power for the community and for

an electrolysis system to produce hydrogen for a public transportation system. The third case being evaluated is a transportation system. Under consideration are refueling alternatives (gaseous vs. liquid, delivery vs. on-site production), vehicle configuration, drive cycle implications, and cost variations (natural gas vs. electricity). Life cycle impacts and system cost will be key components for evaluating all three cases and their possible configurations.

Research and Development Needs/Future Activities

Many advances were made in the longer-term photoproduction area. However, this work is still at the early development stage. A variety of materials and organisms remain under investigation. System design is also an area that requires a great deal of effort.

Hydrogen use in non-energy processes, such as the chemical, metallurgical, and ceramics industries was identified as an area where a concentrated research effort could facilitate the increased utilization of hydrogen. Annually, these industries account for nearly 50 percent of the world's 500 billion Nm³ hydrogen consumption. Process improvements and novel synthesis approaches could lead to overall efficiency improvements and reduced environmental impacts. Likewise, increased market share for hydrogen in these arenas should lead to expedited infrastructure development, a necessity for facilitating the advancement of the energy-related and renewable-based applications.

Approximately 95% of the hydrogen produced today comes from carbon containing raw material, primarily fossil in origin. The conventional processes convert the carbon to carbon dioxide, the majority of which is discharged to the atmosphere. The growing awareness of the impact of greenhouse gas emissions on global climate change has necessitated a reassessment of the conventional approach. Integrating carbon dioxide sequestration with conventional steam reforming will go a long way towards achieving "clean" hydrogen production. Likewise, improving the robustness of pyrolytic cracking technologies for the conversion of hydrocarbons to hydrogen and pure carbon should not only improve the process economics, but also its applicability to a variety of feeds. Finally, the thermal processing of biomass can yield an economic and carbon-neutral source of hydrogen.

Hydrogen energy system demonstrations continue to be undertaken throughout the world. The experiences gained from these projects need to be compiled and made available to future demonstrators. Public response must be captured and considered when planning any hydrogen demonstration. System efficiency and cost optimization will also remain paramount issues for developing competitive hydrogen-based systems. Thus, utilizing all available information and international expertise and continually refining and expanding modeling tools will be imperative.

Conclusions

As we enter the new millennium, concerns about global climate change and energy security create the forum for mainstream market penetration of hydrogen. Ultimately, hydrogen and electricity, our two major energy carriers, will come from sustainable energy sources, although

fossil fuel will likely remain a significant and transitional resource for many decades. The IEA Hydrogen Program has a vision for a hydrogen future that is one of clean sustainable energy supply of global proportions that plays a key role in all sectors of the economy. This vision will be implemented through advanced technologies including direct solar production systems and low-temperature metal hydrides and room-temperature carbon nanostructures for storage. Hydrogen in the new millennium is synonymous with energy supply and security, climate stewardship, and sustainability.

Acknowledgments

None of the technical progress made in our IEA activities would be possible without the leadership and technical expertise of the Operating Agents (Task Leaders) and the efforts of the international experts and their research teams. The authors would also like to acknowledge the Executive Committee members of the IEA Hydrogen Program: Mr. Neil Rossmeissl, Chair, U.S. Department of Energy; Mr. Nick Beck, Natural Resources Canada; Dr. Giampiero Tartaglia, Joint Research Council, for the European Commission; Mr. Toshiaki Abe, NEDO, Japan; Dr. Jurgis Vilemas, Lithuanian Energy Institute; Dr. Antoon Kipperman, NOVEM, the Netherlands; Mr. Trygve Riss, Research Council of Norway; Dr. Antonio Garcia-Conde, INTA, Spain; Mrs. Karin von Kronhelm, Swedish National Energy Administration; and Dr. Gerhard Schriber, Swiss Federal Office of Energy.

References

1. Bolton, James R., 1996, "Solar Photoproduction of Hydrogen," IEA Technical Report, IEA/H2/TR-96.
2. Khaselev O., Bansal A. and Turner J., 2000, "High-efficiency integrated multi-junction photovoltaic/ electrolysis systems for hydrogen production," Int. J. of Hydrogen Energy.
3. Graetzel, Michael, 1999, "The artificial leaf, bio-mimetic photocatalysis", *Cattech*, Vol. 3, 4-17.
4. Heben, M.J. and A.C. Dillon, "Hydrogen Storage Using Carbon Adsorbants: Past, Present and Future," IEA Agreement on the Production and Utilization of Hydrogen: 1997 Annual Report, Carolyn C. Elam (ed.), 1998.
5. B. Bogdanovic' and M. Schwickardi, 1977, "Ti- Doped Alkali Metal Aluminum Hydrides as Potential Novel Reversible Hydrogen Storage Materials," J. Alloys and Compounds, 253-254, 1-9.
6. Sandrock, Gary (ed.), *in press*, "Task12: Metal Hydrides and Carbon for Hydrogen Storage - Final Task Report," IEA Technical Report.
7. E. Skolnik and V. Putsche, 1999, "Analysis Tools," IEA Technical Report.
8. M. Bracht and E. de Groot, 1999, "Design Evaluation and System Comparison Guidelines," IEA Technical Report.
9. Bracht, M., A. De Groot, C.E. Gregoire Padró, T.H. Schucan, and E. Skolnik, 1998, "Evaluation Tool for Selection and Optimization of Hydrogen Demonstration Projects. Application to a Decentralized Renewable Hydrogen System," Hydrogen Energy Progress XII, J.C. Bolcich and T.N. Veziroglu, eds., 1243-1254.

10. de Groot, A., M. Bracht, C.E. Gregoire Padró, T.H. Schucan, and E. Skolnik, 1998, "Development of Guidelines for the Design of Integrated Hydrogen Systems," Hydrogen Energy Progress XII, J.C. Bolcich and T.N. Veziroglu, eds., 75-86.
11. Schucan, T.H., E. Skolnik, M. Bracht, and C.E. Gregoire Padró, 1998, "Development of Hydrogen Technology Component Models for Systems Integration," Hydrogen Energy Progress XII, J.C. Bolcich and T.N. Veziroglu, eds., 111-120.
12. Gregoire Padró, C.E., V. Putsche, and M. Fairlie, 1998, "Modeling of Hydrogen Energy Systems for Remote Applications," Hydrogen Energy Progress XII, J.C. Bolcich and T.N. Veziroglu, eds., 2247-2262.
13. Gregoire Padró, C.E., 1998, "International Cooperative Development of Design Methodology for Hydrogen Demonstrations," Proceedings of the 9th Annual U.S. Hydrogen Meeting, Vienna, VA, 187-194.
14. Putsche, V, and C.E. Gregoire Padró, 1998, "Systems Modeling of Renewable Hydrogen Production, Storage, and Electricity Generation using ASPEN Plus," Proceedings of the Electrical Energy Storage Systems Applications and Technologies Meeting, Chester, U.K., 95-102.
15. Gregoire Padró, C.E., 1998, "Renewable Hydrogen Energy Systems for Grid-Independent Energy Systems," Proceedings of the 1998 Colorado Renewable Energy Conference.
16. Gregoire Padró, C.E. and M.J. Fairlie, 1998, "Renewable Hydrogen for Rural Electrification," Poster at the Village Power '98 Conference.
17. Schucan, Thomas, 1999, "Case Studies of Integrated Hydrogen Energy Systems," IEA Technical Report.

TECHNOECONOMIC ANALYSIS OF AREA II HYDROGEN PRODUCTION - PART 1

Ali T-Raissi
Florida Solar Energy Center
Cocoa, FL 32922-5703

Abstract

The aim of this analysis is to assess the issues of cost, safety, performance, and environmental impact associated with the production of hydrogen by so-called "Area II" technologies, not presently funded by the U.S. DOE Hydrogen Program. The hydrogen (H₂) rich feedstocks considered are: water, hydrogen sulfide (H₂S) rich sub-quality natural gas (SQNG), and ammonia (NH₃). Three technology areas to be evaluated are:

- 1) Thermochemical H₂S reformation of methane with and without solar interface,
- 2) Thermochemical water-splitting cycles suitable for solar power interface,
- 3) Catalyzed micro-reformers for decomposing ammonia.

This project is a two-year effort with following objectives:

- Analysis of the feasibility of the technology areas 1-3 from technical, economical and environmental viewpoints.
- Evaluation of the cost of hydrogen production by technology areas 1 & 2.
- Feasibility of the technology area 3 as a means of supplying H₂ to fuel cell power plants.

This paper provides the first account of our analysis pertaining to the technoeconomic aspects of H₂S-methane reformation, the magnitude of the H₂S resource and other issues of interest.

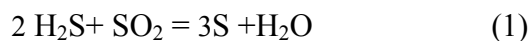
Thermochemical, CO_x-Free, H₂S Reformation of Methane

Background

Approximately one-third of the U.S. natural gas (NG) resource is low or sub-quality gas (SQNG) that does not meet market specifications for pipeline shipment (Hugman et al. 1993). Typical specifications call for gas with no more than 4 percent total carbon dioxide, nitrogen, and other inert gases; and 4 parts per million of hydrogen sulfide (H₂S) gas (Semrau et al. 1995). Some sub-quality gas can be blended with higher quality gas to meet market requirements. However, much of the sub-quality gas is too costly to upgrade and simply shut in.

Hydrogen sulfide concentration in NG varies from traces to 90% by volume. The Smackover zone and a deeper, contiguous zone called the Cotton Valley pinnacle reef in East Texas contain deposits wherein the subterranean gas composition at one location has been measured to contain as high as 87% by volume H₂S gas (Meyer 2000). Elsewhere, other examples of "ultra-sour" gas include: China's Zhaolanzhuang (60-90% H₂S), Canada's Caroline and Bearberry gas fields in West-Central Alberta (70-90% H₂S), Astrakhan gas field by Caspian sea (26% H₂S), and Lacq gas field in France (15% H₂S), to name just few (Kappauf 1985, Ullmann's 1989, Clark 1990).

In natural gas processing, H₂S is viewed as a pollutant requiring treatment and removal. Presently, H₂S is separated from hydrocarbon gases by amine adsorption and regeneration producing acid gas containing 10-90% by volume H₂S. When H₂S concentrations exceed 40%, gas is treated (or "sweetened") in a Claus plant (Cox et al. 1998). In this process, a portion of the H₂S is burned to make SO₂, and then recombined with the main H₂S stream in a catalytic reactor to produce elemental sulfur and steam according to:



Elemental sulfur is sold as a feedstock for sulfuric acid manufacture. In the Claus process, hydrogen in the H₂S is converted to water vapor. Furthermore, since Claus units do not convert all the H₂S to sulfur, tail gas cleanup units are needed to remove traces of SO₂ before the off-gases can be vented to atmosphere (Erekson 1996). It would be advantageous to perform H₂S conversion in a manner so that to recover and recycle its hydrogen content.

Finally, each year, U.S. refineries spend a quarter of billion dollars to produce hydrogen needed for hydrodesulfurization of refinery products (Doctor 1999). This hydrodesulfurization process generated more than 5.5 million tons of hydrogen sulfide waste gas in 1996 (Swain 1999). Furthermore, the review of the historical data on crude oil gravity and sulfur content indicates that generally lower-quality crudes are being processed in the U.S. (Swain 2000). If one could recover the equivalent amount of H₂ from the refineries' waste H₂S stream, it would provide a significant fraction of the hydrogen now used for petroleum refining and upgrading.

Thus, the impetus for this study was to determine the potential for improving the overall economics of the H₂S reformation of natural gas (particularly CH₄) to hydrogen and carbon disulfide (CS₂, instead of CO₂, as in the SMR process). A viable process for H₂S reformation of methane should result in more SQNG being made available for pipeline use as well as additional

onsite H₂ being available for the refinery use. At this point, the main questions that need to be addressed are as follows:

1. What is the magnitude of the resource, *i.e.* how much H₂ can be recovered from H₂S present in the sub-quality natural gas and Claus-type H₂S?
2. Today, the benchmark process for hydrogen production is catalytic reforming of methane (CH₄) with steam. Is there a sulfur analog to steam methane-reforming (SMR) process? In other words, is it technically feasible to reform CH₄ with H₂S (instead of H₂O) yielding H₂ and CS₂ (instead of CO₂)? If so, is the technology available and what are the costs?
3. What are the potential markets and/or outlets for CS₂ product from H₂S/CH₄ reformation?
4. What are the environmental implications of H₂S reformation of natural gas with regard to reduction of greenhouse gases and potential use of solar thermal power?

In the following sections, we present results of our analysis and findings to questions above.

Magnitude of the H₂S Resource

A question is often asked as to the magnitude of H₂S resource. We note that the sub-quality natural gas containing unacceptable levels of H₂S comprises about 14% of the U.S. gas reserves (Dalrymple et al. 1994). Distribution of major H₂S regions in the lower 48 states has been compiled by Hugman et al. (1993). The report identifies about 20 Tcf of H₂S-contaminated sub-quality natural gas reserves. A summary of the more highly contaminated regions/plays is given and in Tables 1 and 2. Based on the measured concentration of hydrogen sulfide (see Tables 1 and 2), an estimate of the magnitude of H₂S resource has been made and given in Table 3. We have also calculated and tabulated the higher heating value of hydrogen produced from H₂S (if all of it were converted to H₂ instead of Claus treatment) via CH₄ reformation. Furthermore, we have given the range of unexplored oil within Alaska's Arctic National Wildlife Refuge (ANWR). We assumed 46.2% yield of gasoline from one barrel of crude oil, see 1998 EIA data (Davis 2000).

The energy potential of the ANWR reserves that can be converted and used to produce gasoline is then calculated to lie between about 3.2 and 36 quads (actually, closer to 3.2 than 36) (King 2000). The data of Table 3 indicate that a potentially comparable amount of energy can be had by efficient conversion of H₂S to clean CO_x-free hydrogen. Therefore, it is worthwhile not to burn H₂S in the process of upgrading the sub-quality natural gas reserves. Note that H₂S in the present SQNG reserves within the lower 48 states can yield hydrogen with energy content comparable to that from ANWR reserves. This resource can be made available where it is needed most (*i.e.*, the lower 48 states) without any threat to the pristine environment of the Alaska's ANWR.

Processes for H₂ Generation from Methane and Hydrogen Sulfide

Steam Methane Reforming (SMR)

The benchmark process for H₂ production is catalytic reforming of NG with steam according to:



Table 1. Range of H₂S content of discovered and undiscovered sub-quality natural gas in the lower 48 United States - *non-associated gas data*[#] (Hugman 1993).

Basin/Formation	H ₂ S (vol%)		Amount of NG (Bcf)			H ₂ S content (Bcf)		
	Mean	Max	a	b	c	a'	b'	c'
Mid Gulf Coast/Smackover	14.957	45.7	254	1289	2201	116.1	589	1006
Mid Gulf Coast/Norphlet	1.867	7.7	165	1844	4403	12.7	142.0	339
Michigan/Niagaran Salina	0.405	5.94	309	22	371	18.4	1.3	22.0
Michigan/Other	0.483	13	8	33	216	1.0	4.3	28.1
Arkla/Smackover	4e-3	0.1	98	864	2913	0.1	0.9	2.9
East Texas/Pettit	0.028	4	342	345	239	13.7	13.8	9.6
East Texas/Cotton Valley	0.187	11.954	2949	734	749	352.5	87.7	89.5
East Texas/Smackover	14.71	47.35	607	303	330	287.4	143.5	156.3
East Texas/Other	0.313	2.927	352	76	669	10.3	2.2	19.6
Louisiana Gulf Coast/Other	1e-3	0.2	5876	11156	19911	11.8	22.3	39.8
Texas Gulf Coast/Miocene	0.054	0.632	143	315	684	0.9	2.0	4.3
Texas Gulf Coast/Frio	4e-3	0.48	1622	3073	6677	7.8	14.8	32.0
Texas Gulf Coast/Vicksburg	0.013	0.1	1082	1851	4026	1.1	1.9	4.0
Texas Gulf Coast/Austin Chalk	0.228	2.194	50	160	348	1.1	3.5	7.6
Texas Gulf Coast/Edwards	1.347	8.222	315	949	2060	25.9	78.0	169.4
Texas Gulf Coast/Other	0.244	2.483	3780	12477	27119	93.9	309.8	673.4
Powder River/Other	1e-3	0.58	41	53	1309	0.2	0.3	7.6
Big Horn/Frontier	0.147	4	125	134	382	5.0	5.4	15.3
Wind River/Cody	4e-3	2.725	371	439	1048	10.1	12.0	28.6
Wind River/Frontier	3.624	4.458	262	360	1916	11.7	16.0	85.4
Wind River/Phosphoria	5.095	14	38	69	165	5.3	9.7	23.1
Wind River/Madison	11	11	0	0	2641	0.0	0.0	290.5
Green River/Frontier	3e-3	0.05	2310	392	4873	1.2	0.2	2.4
Green River/Phosphoria	13.4954	34.9	5	2	25	1.7	0.7	8.7
Green River/Weber	1.031	2.6	376	187	2734	9.8	4.9	71.1
Green River/Madison	2.778	4.6	368	634	8199	16.9	29.2	377.2
Paradox/Mississippian	0.93	1.178	15	9	535	0.2	0.1	6.3
San Juan/Mesaverde	0.016	0.317	6057	849	474	19.2	2.7	1.5
San Juan/Other	0.118	5.9	85	0	409	5.0	0.0	24.1
Overthrust/Weber	21.34	21.34	17	178	2376	3.6	38.0	507.0
Overthrust/Madison	14.838	14.838	782	5543	6311	116.0	822.5	936.4
Overthrust/Sun River	0.1	0.1	5	13	2970	5.0e-3	1.3e-2	3.0
Overthrust/Big Horn	3.858	6.783	54	275	4158	3.7	18.7	282.0
Anadarko/Chase	0.016	0.099	7777	2126	604	7.7	2.1	0.6
Anadarko/Marrow	2e-3	0.016	5124	5665	19183	0.8	0.9	3.1
Anadarko/Chester	1e-3	0.12	751	788	2674	0.9	0.9	3.2
Anadarko/Hunton	0.149	0.763	857	332	314	6.5	2.5	2.4
Anadarko/Other	5e-3	1.028	2868	3140	10630	29.5	32.3	109.3
Permian/Yates	6.7	11.497	168	67	197	19.3	7.7	22.6
Permian/Queen	0.402	4.992	183	67	197	9.1	3.3	9.8
Permian/Grayburg	0.585	1.233	14	58	81	0.2	0.7	1.0
Permian/Clear Fork	0.463	1.421	16	65	94	0.2	0.9	1.3
Permian/Tubb	0.478	1.358	14	44	61	0.2	0.6	0.8
Permian/Wichita Albany	0.458	0.786	53	181	256	0.4	1.4	2.0
Permian/Wolfcamp	0.182	0.652	735	1345	1903	4.8	8.8	12.4
Permian/McKnight	1.396	1.396	16	85	122	0.2	1.2	1.7
Permian/Cisco	0.172	0.485	32	113	158	0.2	0.5	0.8
Permian/Strawn	6e-3	0.434	445	1306	317	1.9	5.7	1.4
Permian/Atoka	7e-3	0.604	315	931	1317	1.9	5.6	8.0
Permian/Morrow	0.035	3.367	781	2345	3318	26.3	79.0	111.7
Permian/Pennsylvania	0.075	0.2	673	1881	2659	1.3	3.8	5.3
Permian/Devonian	0.304	12.5	1482	818	1741	185.3	102.3	217.6
Permian/Silurian	0.238	0.525	101	851	1203	0.5	4.5	6.3
Permian/Fusselman	0.461	1.229	221	204	554	2.7	2.5	6.8
Permian/Montoya	0.199	1.024	15	95	134	0.2	1.0	1.4
Permian/Ellenburger	0.019	0.365	1493	1635	3246	5.4	6.0	11.8
Permian/Other	0.403	3.842	390	1371	1939	15.0	52.7	74.5
Eastern Gulf of Mexico/Norphlet	5.23	5.73	3198	6795	25402	183.2	389.4	1455.5
Gulf of Mexico/Miocene	0	5.5	10329	29053	46797	568.1	1597.9	2573.8

[#] Notes: a,a') current proven reserves; b,b') reserve expected growth in existing fields; and c,c') anticipated new field potential.

Table 2. Range of H₂S content of discovered and undiscovered sub-quality gas in the lower 48 United States - associated & dissolved gas data (Hugman 1993).

Region/Depth (ft)	H ₂ S (vol%)		Current proven	H ₂ S content of the
	Mean	Max	Gas reserves (Bcf)	Associated gas (Bcf)
MAFLA Onshore/10,000-15,000	0.505	1.8	87	1.6
Midwest/5,000-10,000	0.07	7.232	231	16.7
Arkla, East Texas/0-5,000	2e-3	2.755	620	17.1
Arkla, East Texas /5,000-10,000	5e-3	3.8	741	28.2
Arkla, East Texas /10,000-15,000	0.015	5.23	50	2.6
South Texas/0-5,000	0.811	2.194	269	5.9
South Texas /5,000-10,000	0.227	7.091	1776	125.9
South Texas /10,000-15,000	1.079	2.132	74	1.6
Williston/unknown	2.298	11.96	88	10.5
Williston /0-5,000	1.839	3.8	76	2.9
Williston /5,000-10,000	10.608	29	220	63.8
Williston /10,000-15,000	3.006	12	212	25.4
Foreland/unknown	0.132	5	142	7.1
Foreland /0-5,000	2.131	15.976	216	34.5
Foreland /5,000-10,000	0.053	44	770	338.8
Foreland /10,000-15,000	0.368	20	165	33.0
Western Thrust Belt/5,000-10,000	8.337	10.749	113	12.1
Western Thrust Belt /10,000-15,000	0	0.22	315	0.7
Mid-continent/unknown	0.072	0.072	654	0.5
Mid-continent /5,000-10,000	1e-3	0.4	709	2.8
Permian Basin/unknown	0.491	1.36	319	4.3
Permian Basin /0-5,000	0.908	12.5	1592	199.0
Permian Basin /5,000-10,000	3.192	5.8	4135	239.8
Permian Basin /10,000-15,000	0.036	0.7	402	2.8

Table 3. Summary of the sub-quality gas data for combined non-associated and associated/dissolved gas in the lower 48 United States.

Resource	Current proven reserves	Expected growth in existing fields	Anticipated new field potential
Total SQNG, Tcf	80.9	106	238.5
H ₂ S content of SQNG, Tcf	3.4	4.7	9.9
H ₂ Equiv. H ₂ S of SQNG, Tcf	6.3	8.6	18.2
HHV of Equiv. H ₂ from H ₂ S, Quads	2.0	2.8	5.9
ANWR coastal plain, Bbbl/(Quads)	5.7-16/(3.2-36)		

The carbon monoxide (CO) formed during steam reforming reaction above reacts with excess steam, concurrently, to form CO₂ and more H₂ via the exothermic shift reaction:



The net chemical process for steam methane reforming is then given by:



Indirect heating provides the required overall endothermic heat of reaction for the SMR process. In autothermal (or secondary) reformers, the oxidation of methane supplies the necessary energy

and carried out either simultaneously or in advance of the reforming reaction. The equilibrium of the methane steam reaction and the water-gas shift reaction determines the conditions for optimum hydrogen yields. The optimum conditions for H₂ production require: high temperature at the exit of the reforming reactor (800-900°C), high excess of steam (molar steam-to-carbon ratio of S/C= 2.5-3) and relatively low pressures (below 30 atm). Most commercial plants employ supported nickel catalysts to perform the SMR process (Ullmann's 1989).

The steam-methane reforming process described briefly above would be an ideal hydrogen production process if it was not for the fact that large quantities of natural gas (NG), a valuable resource in itself, are required as both feed gas and combustion fuel. For each mole of methane reformed, more than one mole of carbon dioxide is co-produced and discharged into the atmosphere. This is a major disadvantage as it results in the same amount of greenhouse gas emission as would be expected from direct combustion of NG or methane. In other words, production of H₂ as a clean burning fuel via steam reforming of methane and other fossil-based hydrocarbon fuels does not make sense, environmentally, if in the process, carbon oxide gases (CO_x) are generated and released into the atmosphere. Moreover, as the reforming process is not 100% efficient, some of the energy value of the hydrocarbon fuel is lost by conversion to hydrogen but with no tangible environmental benefit, *i.e.* reduction in emission of greenhouse gases. Despite that, the SMR process has the following advantages:

- Produces 4 moles of H₂ for each mole of CH₄ consumed.
- Feedstocks for the process (*i.e.* methane and H₂O) are readily available.
- Can use a wide range of hydrocarbon feedstocks besides methane.
- All process steps are well developed, *e.g.*, desulfurization, hydrocarbon reforming, etc.
- Can operate at temperatures in the range of 800-900°C.
- Operates at low pressures, less than 30 atm.
- Requires low excess steam: S/C ratio of 2.5-3.
- Low reforming input energy required (*i.e.* approximately 17% of the HHV of output H₂).
- Good process energetics, *i.e.* high input energy utilization (reaching 93%).
- Can use catalysts that are stable and resist poisoning.
- Good process kinetics.
- None of the process steps requires expensive materials and/or components.
- No problem with excessive soot formation or carbon lay down.
- No toxic chemicals produced or used.
- Has relatively low capital and operating costs.

Pyrolysis of Natural Gas and Methane

Since natural gas is readily available, relatively cheap resource and composed mainly of CH₄ (with small amounts of other mostly aliphatic hydrocarbons such as ethane, propane and butane), some thermocatalytic processes have sought to decompose NG hydrocarbons, directly (*e.g.* Dahl 2001, Arild 2000, Weimer et al. 2000, Uemura 1999, Muradov 1998, Wammes 1997, Gaudernack 1996, Steinberg 1987) according to:



One of the objectives in these processes is to fix the carbon content of the fuel, to be recovered in a form that is hopefully a salable product (*i.e.* activated carbon, carbon black or other non-graphitic varieties). By far, industrially, the most widely utilized type of carbon is carbon black or furnace black. The carbon black industry is well established and more than 100 years old. Although the list of applications for carbon black is long, about 90% of the production is for a single application, that is as a reinforcing agent and filler for rubber compounds employed in tires and automotive industry.

Carbon black constitutes 20-35% of the mass of automotive tires (Piskorz 1999). Paraffinic hydrocarbons are the best raw material for the production of carbon black. Other feedstocks such as olefins, diolefins, acetylene, and anthracene have also been used (Gallie 1946). There is a complex association between the tire, rubber, and carbon black industries. Markets for carbon black are tight and industry is squeezed between two giants: petroleum and coal industries on the supply side and auto industry on the demand side. In the past, this has historically depressed the price of carbon black. The changing trends in the rubber industry and the future of tire and carbon black producers are discussed by Lebel (1999).

If a hydrocarbon fuel such as NG (mostly methane) is to be used for H₂ production by direct decomposition, then the process that is optimized to yield H₂ may not be suitable for production of high quality carbon black by-product intended for the industrial rubber market. Moreover, based on the data available, to date, it appears that the carbon produced from high-temperature (at 850-950°C) direct thermal decomposition of methane is soot-like material with high tendency for catalyst deactivation (*e.g.* Murata 1997). In other words, if the object of CH₄ decomposition is H₂ production, carbon by-product may not be marketable as high-quality carbon black for rubber and tire applications. Finally, the health and safety issues related to production and use of carbon black is still subject of on-going debate among the occupational and environmental health professionals (Nikula 2000, Brokmann 1998). In the light of the above, it is far from certain that large-scale by-product carbon generated from direct methane/NG decomposition for production of hydrogen fuel will find stable high-value commercial outlets. This is despite the forecasts that there are potentially new and emerging markets for carbon black use in the future (Rusinko 2000, Saraf 1997).

Pyrolysis of Hydrogen Sulfide

Production of hydrogen by direct decomposition of hydrogen sulfide has been studied extensively. There are several good reviews of the subject available (Luinstra 1996, Donini 1996, Zaman 1995, Clark 1990). These reviews provide a detailed description of the H₂S decomposition processes including the use of microwave radiation, electric discharge methods, direct electrolysis, indirect electrolysis, thermal dissociation, thermochemical cycles, photocatalytic, and electron beam irradiation techniques.

Hydrogen sulfide decomposition is a highly endothermic process and equilibrium yields are poor (Clark 1995). At temperatures less than 1500°C, the thermodynamic equilibrium is unfavorable toward hydrogen formation. However, in the presence of catalysts such as platinum-cobalt (at 1000°C), disulfides of Mo or W at 800°C (*e.g.* Kotera 1976), or other transition metal sulfides

supported on alumina (at 500-800°C), H₂S decomposition proceeds rapidly (Kiuchi 1982, Bishara 1987, Al-Shamma 1989, Clark 1990, Megalofonos 1997). In the temperature range of about 800-1500°C, thermolysis of hydrogen sulfide can be treated simply in terms of reaction:



where $x=2$. Outside this temperature range, multiple equilibria involving H₂S, S, HS, H, H₂ and polysulfur species (S_{*x*}, $x=1-8$), and H₂S_{*x*} ($x=2-9$) may be present depending on temperature, pressure, and relative abundance of hydrogen and sulfur (Clark 1990). Kinetics of both catalyzed and uncatalyzed H₂S thermolysis has been extensively investigated (Darwent 1953, Raymont 1975, Al-Shamma 1989, Kaloidas 1989, Shiina 1996, Harvey 1998, Karan 1999, Dowling 1999) and a good review of the subject is provided by Zaman (1995). Above approximately 1000°C, there is a limited advantage to using catalysts since the thermal reaction proceeds to equilibrium very rapidly (Raymont 1974, Noring 1982, Clark 1990). The hydrogen yield can be doubled by preferential removal of either H₂ or sulfur from the reaction environment, thereby shifting the equilibrium. The reaction products must be quenched quickly after leaving the reactor to prevent back reactions (Kappauf 1985, Diver 1985).

Since H₂S decomposition reactions run at relatively high temperatures, this process is a good candidate for interfacing to concentrated solar radiation (Harvey 1998). In fact, extensive work has been conducted over the past twenty years or so to demonstrate the technical and economic viability of hydrogen production via solar thermal pyrolysis of hydrogen sulfide (Kappauf 1989, Lee 1995, Harvey 1998 and references therein).

According to Cox (1998), using an efficient H₂/H₂S separation system, the thermal decomposition of H₂S is able to produce hydrogen at a cost approaching that of the conventional SMR process. The analysis of Cox et al. showed that the most economic route for hydrogen production by direct decomposition of H₂S is one in which CH₄ is burned to supply the decomposition heat and unconverted H₂S is recycled until extinction (see simplified flow diagram of Figure 1). This scheme would produce H₂ at a cost of about \$4.50/10⁶BTU (corrected to 1998 US dollars). This figure compares favorably with \$4.75/10⁶BTU (corrected to 1998 US dollars) for a Claus plant to treat the same amount of H₂S plus a conventional SMR plant to generate an equivalent amount of H₂ gas. In principal, this process can be integrated with a non-polluting heat source (for example, solar) to eliminate emission of greenhouse gases from the combustion furnace. Alternatively, part of the hydrogen gas produced in the process can be rerouted and burned in the furnace as fuel without any emission of greenhouse gases.

Finally, a review of U.S. patent literature revealed that several patents have been granted that describe H₂S decomposition for the purpose of hydrogen production (*e.g.* Wang 1998, Bowman 1991, Elvin 1989, Daley 1984, Norman 1984, Chen 1978, Kotera 1976). These patents provide methods for H₂S splitting via direct thermolytic as well as indirect multi-step thermochemical cycles. Despite all that, no commercial process for the thermal dissociation of hydrogen sulfide exists. In summary, pyrolysis of methane and hydrogen sulfide has been thoroughly investigated. Direct thermal dissociation of methane and H₂S does not generate greenhouse gases. However, compared to SMR process, thermolysis of CH₄ and H₂S generates lesser amounts of hydrogen per mole of methane and hydrogen sulfide reacted. In fact, half as much hydrogen is produced in

the case of methane dissociation and one quarter as much H₂ in the case of H₂S pyrolysis. Unfortunately, SMR plants do emit undesirable greenhouse gases into the atmosphere. An alternative to SMR process that avoids release of greenhouse gases yet generates comparable amount of hydrogen is H₂S reformation of natural gas methane.

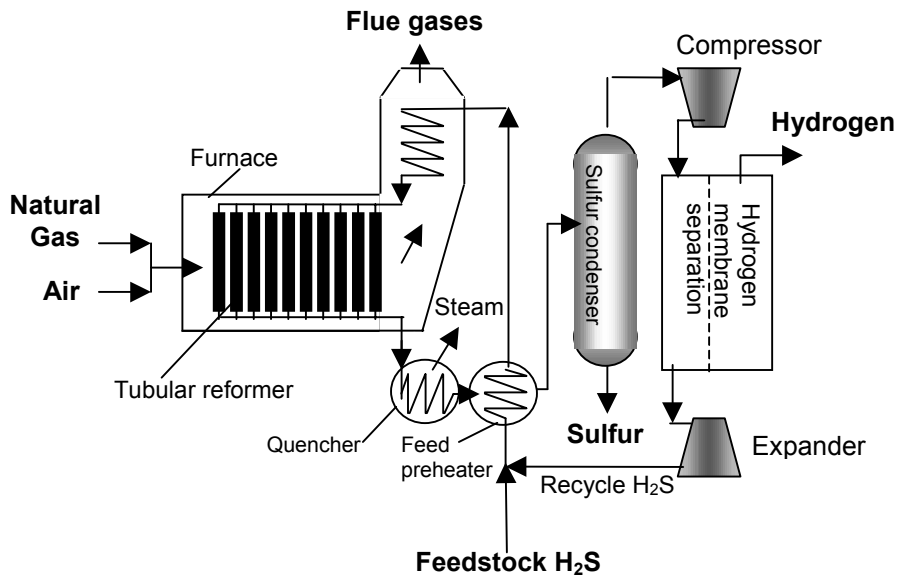


Figure 1- Simplified flow sheet for splitting hydrogen sulfide.

Hydrogen Sulfide Reformation of Natural Gas

The main idea here is to devise a process that combines the virtues of the three basic processes discussed above. They are: steam reforming of natural gas, direct thermolysis of methane and pyrolysis of hydrogen sulfide. Technically, the objective is to conceive a process capable of delivering at least four moles of hydrogen per mole of CH₄ reacted without production of greenhouse gases such as CO₂. The prospective process should be compatible with existing refinery and natural-gas-processing operations and be technically and economically feasible. Due to the availability of sub-quality/sour gas resources and the fact that hydrodesulfurization is a common process in all oil refineries, it made sense to investigate the possibility of H₂S reformation of natural gas. In a way, the reaction of H₂S with methane can be thought of as the sulfur analog of the SMR process. The reactions involved can be expressed in the following simplified forms:



The overall reaction for the H₂S methane reforming process may be written as follows:



The prospective process represented by the overall reaction above will produce carbon disulfide (CS_2) instead of elemental sulfur or carbon black. Unlike elemental sulfur and even carbon black, there are limited outlets for marketing CS_2 as is.

Carbon disulfide is used in the manufacture of xanthate for regenerated cellulosic products such as viscose rayon, cellophane, and non-woven fabrics. The viscose products represent about half of the market for CS_2 . The second major use for carbon disulfide is in the manufacture of carbon tetrachloride (CCl_4) that consumes about quarter of CS_2 production. Other applications include the use of CS_2 as ore floatation agents, rubber accelerators, chain transfer agents for polymerization, and agrochemicals such as fungicides, soil treatment agents, etc. (Ullmann's 1989). The potential market growth for CS_2 has been stymied due to declining rayon market since mid 1960s and phase out of the F-11 and F-12 halocarbons manufactured using CCl_4 .

Annual U.S. production of CS_2 in 1990 was about 114,000 tons (Erekson 1996). This amount of CS_2 required approximately 96,000 tons of elemental sulfur to produce. In 2000, elemental sulfur production in the U.S. was 9.4 million tons, of which 8.4 million tons or about 90% was recovered at petroleum refineries, natural-gas-processing plants, and coking plants (Ober 2001). Clearly, established markets for CS_2 use in the U.S. do not provide an outlet for carbon disulfide produced from sulfur generated at the petroleum refineries and NG-processing plants. In fact, CS_2 production using elemental sulfur recovered at just one 200,000 barrel per day refinery would double current U.S. production of carbon disulfide (Erekson 1996).

A much larger outlet for CS_2 produced from recovered sulfur is for the production of sulfuric acid (H_2SO_4). Already, about 90% of the elemental sulfur produced in the U.S. is used for H_2SO_4 synthesis. In addition, approximately 26% of sulfur consumed in the U.S. in 2000 was provided by imported sulfur and sulfuric acid (Ober 2001). Clearly, huge outlets exist for the CS_2 produced from a prospective process that can convert H_2S from the hydrodesulfurization of petroleum products in refineries and/or sweetening of natural gas. In fact, CS_2 can be a more desirable feedstock for the sulfuric acid plants (Erekson 1996) than elemental sulfur used today. When combusted CS_2 provides more heat than elemental sulfur and CO_2 formed does not affect sulfuric acid solutions and thus would not present any handling problems for the H_2SO_4 plant.

The reaction between CH_4 and sulfur depicted above is the well-known methane process for production of CS_2 . Most commercial CH_4 -sulfur processes employ silica gel/aluminum catalyst for CS_2 production although it is possible for the process to proceed without a catalyst. The reaction of CH_4 with sulfur is thermodynamically favorable for CS_2 formation, and conversion is usually in the range of 90-95% with respect to methane (Ullmann's 1989). The industrial sulfur- CH_4 process operates in the temperature range of 500-650°C and pressure range of 4-7 atm. In the commercial plants, product H_2S is sent to the Claus unit and converted to steam and sulfur.

Conceptually, it should be possible to modify the existing methane-sulfur process and combine it with the H_2S decomposition according to Figure 1. This can be done by combining the product H_2S formed from the reaction of CH_4 with sulfur in the methane-sulfur process with that from the H_2S decomposition process. This approach is depicted in Figure 2. Ideally, both the methane-sulfur and H_2S dissociation reactions are carried out together in one reactor. In that case, the overall process is highly endothermic and requires about 116 kJ/mol of H_2S reacted.

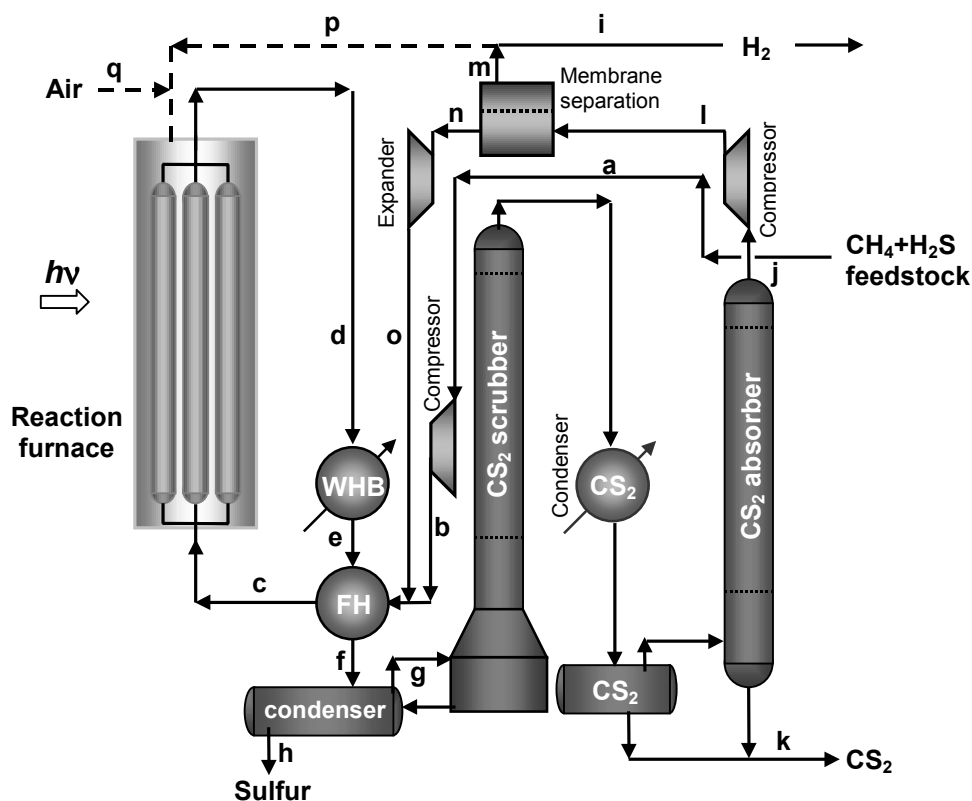


Figure 2- Process for hydrogen and CS₂ production.

With reference to Figure 2, we note that the reaction furnace can be heated by electric power, solar energy or combustion of a portion of the H₂ generated. Harvey (1998) and co-workers have suggested that solar reactors are especially suited to couple to highly endothermic processes such as H₂S splitting because they provide a large energy absorption venue. In fact, several other researchers have also studied the thermochemical decomposition of H₂S using concentrated solar radiation (*e.g.* Bishara 1987, Kappauf 1985). Likewise, solar pyrolysis of methane has also been under investigation (Dahl 2001, Weimer 2000). Notably, H₂S reformation of methane is energetically more endothermic than either H₂S or CH₄ thermolysis. Thus, H₂S reformation of methane should provide an even better process for solar power interface. As far as we know, no experimental work has been carried out to study H₂ production via H₂S reformation of CH₄ under solar-thermal conditions.

The feed stream, a mixture of CH₄ and H₂S represented by stream "a" in Figure 2, is compressed and combined with the recycle H₂S stream "o." The combined stream enters the feed heater (FH) at a pressure of 1.5 atm and 25°C. Stream temperature at the feed heater exit is 552°C. The reforming reactor runs at a pressure of 1.35 atm and a temperature of about 1227°C. The exit stream "d" is rapidly quenched in the waste heat boiler (WHB) to 875°C followed by further cool down (for elemental sulfur collection) to about 390°C.

Most of the residual sulfur is removed at this stage before entering CS₂ scrubber/condenser/absorber train. Finally, a mixture of hydrogen, recycle H₂S and unconverted CH₄ enter membrane hydrogen separation unit at a temperature of about 25°C and a pressure of 10 atm. Typical membrane H₂ separation efficiency of 90% can be assumed. A portion of the recovered H₂ is directed, as necessary, to the reaction furnace and combusted with air to furnish the energy requirement of the reforming reactions during the night or reduced light periods. During the daylight periods, solar energy provides the bulk of the power required for driving the endothermic reforming reactions. In this way, once the reformer reaches steady-state operating condition, its temperature is not affected by the irradiance fluctuations resulting from varying or intermittent solar radiation. The reformer is always kept at optimum and stable temperature and operating state regardless of the changes in the climatic or solar condition.

Chemical Equilibrium Considerations

Calculations involving minimization of the Gibbs free energy were carried out using the F*A*C*T equilibrium code EQUILIB-Web (Pelton 1990) and GASEQ (Morley 2000). We calculated the equilibrium concentration of H₂S-CH₄ reaction products at various temperatures and pressures, and initial H₂S to CH₄ molar concentrations (x). Figures 3 and 4 depict typical results obtained for x values equal to 2, 4 and 6 at 1 atm pressure and reaction temperatures in the range of 500-2000 K.

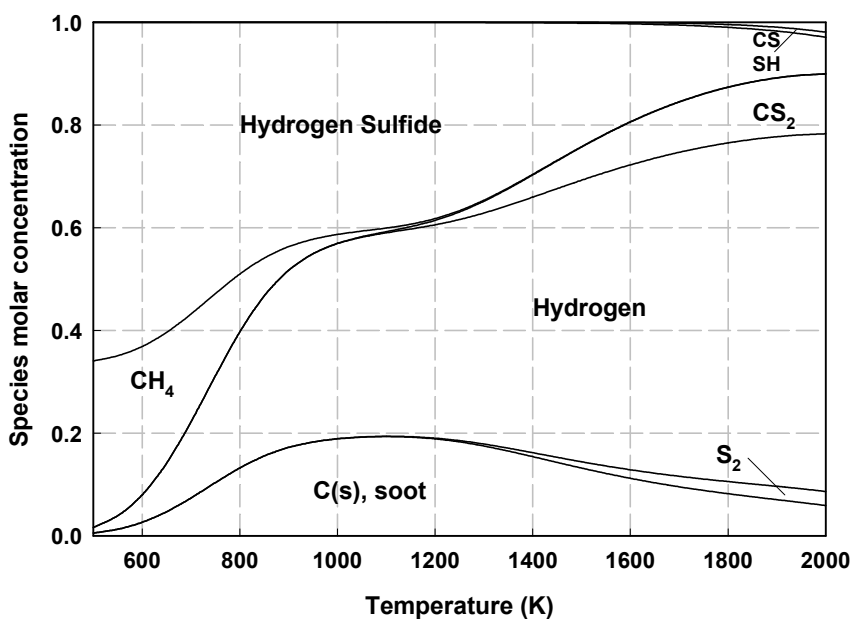


Figure 3- Equilibrium concentration of reaction products of CH₄ + 2 H₂S at 1 atm.

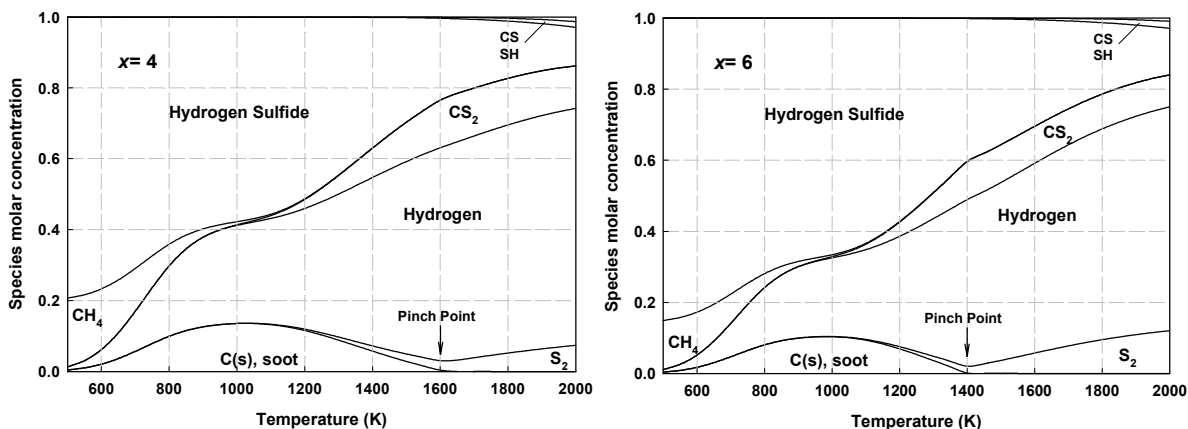


Figure 4- Equilibrium concentration of $\text{CH}_4 + x \text{H}_2\text{S}$ reaction products at twice and three times $x_{\text{stoichiometric}} = 2$.

Several key findings emerge from investigating these results as follows:

- 1- The reaction between sulfur and methane (reaction 7) is the primary CH_4 consuming reaction resulting in the formation of CS_2 .
 - 2- The hydrogen sulfide decomposition reaction (6) does not take effect until about 1000-1100 K (depending upon the H_2S to CH_4 molar feed ratio, x). Generally, the yield of soot/carbon lay-down increases with temperature up to about 1100 K. Above that the yields decrease. Reaction (6) plays a key role in the production of hydrogen and CS_2 from H_2S and CH_4 by providing the required sulfur feedstock for reaction (7) to occur.
 - 3- Hydrogen, CS_2 and S_2 are thermodynamically favored products of H_2S - CH_4 reaction at high temperatures.
 - 4- CS and SH are minor by-products that are thermodynamically favored only at temperatures higher than about 1600 K.
- 1- The temperature span for carbon lay-down for the H_2S - CH_4 reaction system depends primarily on the H_2S to CH_4 molar feed ratio, x . At any given pressure and temperature, there is a specific H_2S to CH_4 molar feed ratio ($x = x_{\text{pinch}}$) for which equilibrium concentration of $\text{C(s)} = 0$, *i.e.* no soot formation is possible. Figure 5 shows the equilibrium products of H_2S - CH_4 reaction system as a function of H_2S to CH_4 molar feed ratios, x , at 1350 K and 1 atm. At $x = x_{\text{pinch}} \approx 6.9$ (about 0.87 on horizontal axes, Figure 5), the combined yield of product carbon and elemental sulfur dips to a minimum. This effect can also be seen in the graphs of Figure 4 that correspond to x values equal to twice and three times the stoichiometric H_2S to CH_4 molar feed ratio of $x_{\text{stoichiometric}} = 2$, respectively. Figure 6 is a plot of $x_{\text{pinch}} / (1 + x_{\text{pinch}})$ vs. temperature depicting the soot-free domain for the H_2S - CH_4 reaction equilibria.
 - 1- The equilibrium yield of the major H_2S - CH_4 reaction by-products are given in Figure 7 for a range of temperatures and H_2S to CH_4 molar feed ratios, x . An examination of these results indicates that, in general, the yield of CS_2 increases with temperature up to a maximum yield that is a function of H_2S to CH_4 molar feed ratio, x . The temperature at which maximum CS_2 yield is obtained corresponds to the no soot formation condition. This temperature is a

function of the H_2S to CH_4 molar feed ratio and lies in the range of about 1100-1300°C, corresponding to x values in the range of approximately 4-6. From a thermodynamics point of view, this range of $x \approx 4-6$ and $T \approx 1100-1300^\circ\text{C}$ seems to provide the optimum conditions needed for performing $\text{H}_2\text{S}-\text{CH}_4$ reformation reactions. This is so because the reaction between H_2S and CH_4 can be conducted at a reasonable temperature range, does not require excessive H_2S recycle, soot formation is nil and production of elemental sulfur by-product can be kept to a minimum.

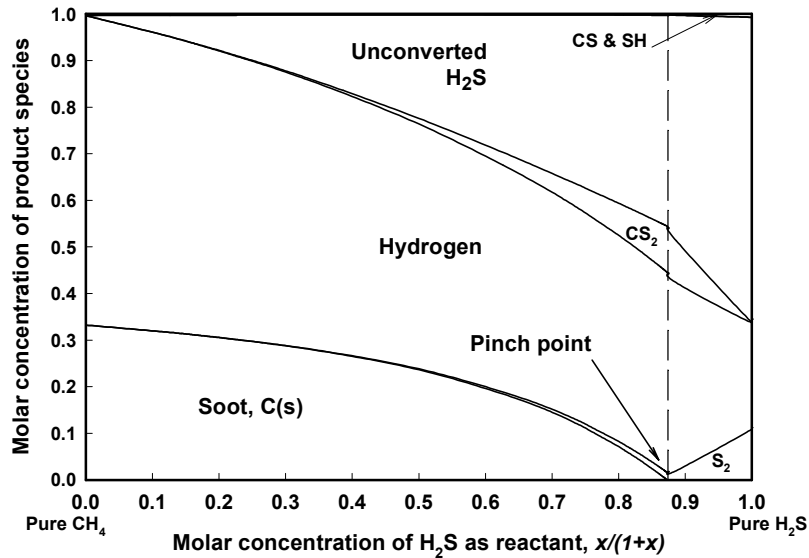


Figure 5- Product slate for reaction $\text{CH}_4 + x \text{H}_2\text{S}$ at 1350 K and 1 atm.

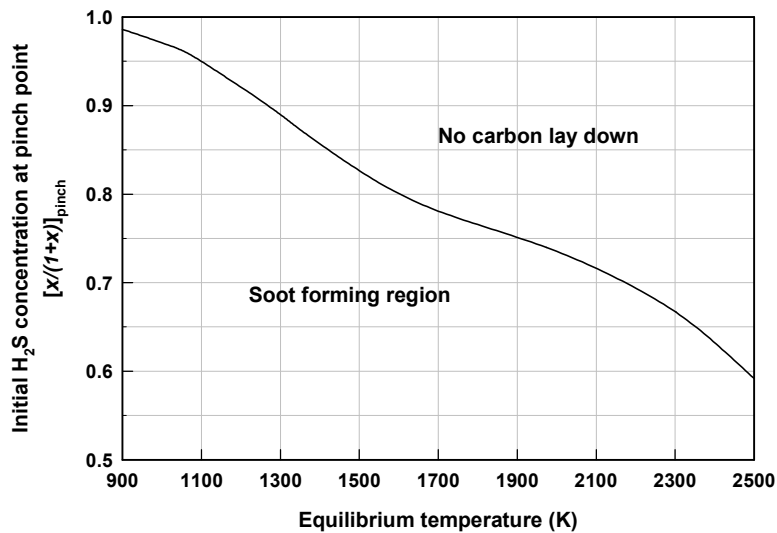


Figure 6- Soot forming region for $\text{CH}_4 + x \text{H}_2\text{S}$ reaction at 1 atm.

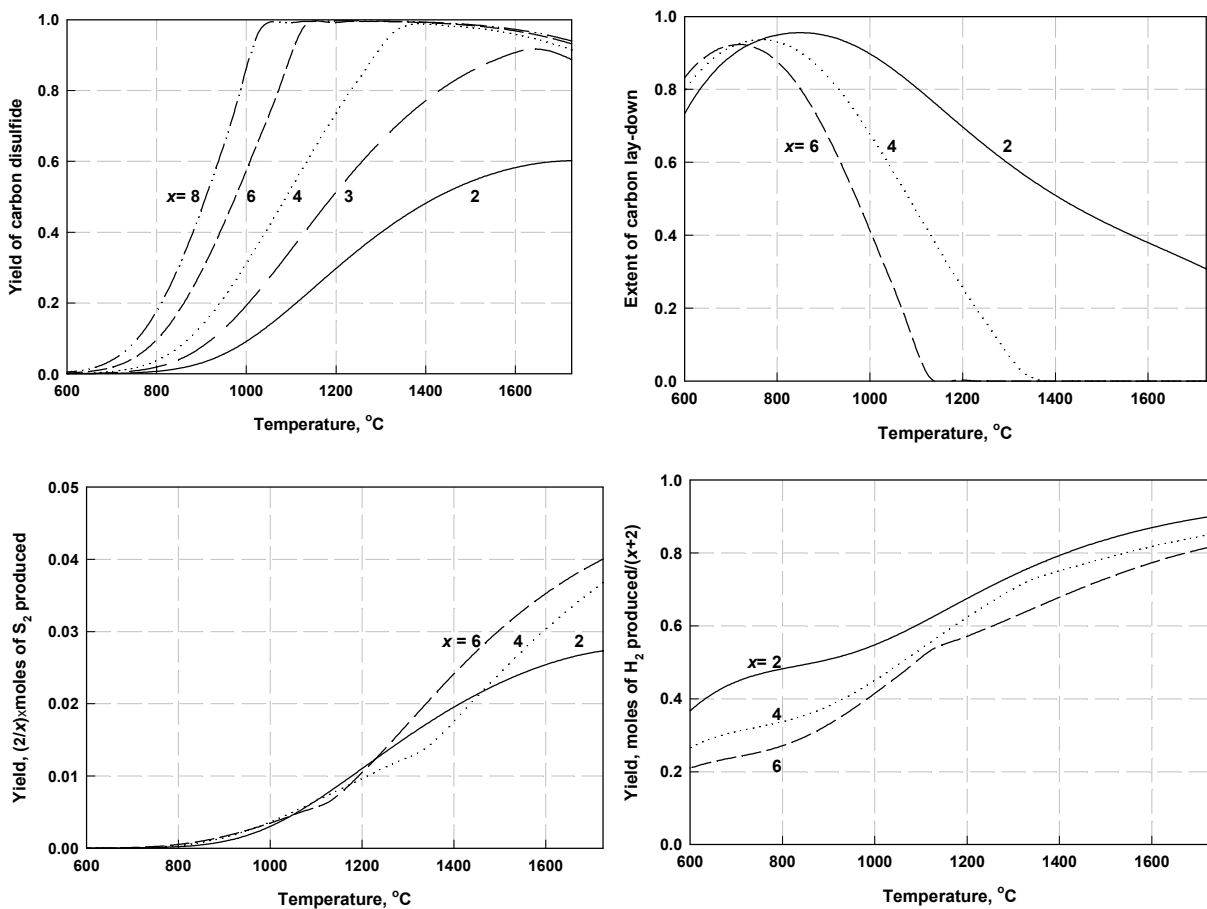


Figure 7- Equilibrium yields of major H₂S-CH₄ reaction products at various H₂S to CH₄ molar feed ratios, x, and 1 atm.

In addition, we calculated the equilibrium concentration of species formed and stream compositions for the H₂S-CH₄ reformation scheme of Figure 2. Results are presented in Table 4 for a H₂ membrane separation efficiency of $\eta_m = 91\%$, reformer temperature of 1350 K and H₂S to CH₄ molar feed ratio of 2.323. In Table 4, if $y = 0$ is allowed (*i.e.* "p" stream in Figure 2 is cut-off and no H₂ gas flows to the burner/reformer), then for every mole of CH₄ reacted, 4.316 moles of hydrogen is produced. In addition, the amount of heat transfer to the reformer is calculated as $\Delta H_{cd} \approx 518.6$ kJ per mole of CH₄ consumed. In the case $y = 0$, ΔH_{cd} must be supplied from an external source such as solar or electric power. ΔH_{cd} is a function of, among others, reformer temperature, pressure and the extent of H₂ recycle. The extent of hydrogen recycle is a function of the membrane efficiency η_m . Table 5 presents ΔH_{cd} values as a function of reformer temperature T_c for the case for which hydrogen recycle is 10%, $T_d = 552^\circ\text{C}$, reformer pressure $P_1 = 1.35$ atm and no carbon lay-down.

The process conditions can be optimized so that the least amount of energy is required for deriving reforming reactions. In general, for CO_x-free operation, ΔH_{cd} can be supplied by one of three methods. One technique is to combust a portion of the H₂ produced (*i.e.* letting $y \neq 0$ in

Table 4). In that case, $y_{max} = 518.6/241.84 \approx 2.14$. In other words, approximately 2.14 moles of hydrogen are required (for each mole of CH₄ consumed) to operate the reformer autothermally. Under these conditions, $100 \cdot (2.14/4.316)$ or about 50% of the hydrogen produced must be burned to derive H₂S-CH₄ reformation reaction (8).

Table 4- Stream compositions for the process scheme of Fig. 2.

Stream No.	T (K)	P (atm)	[CH ₄] (moles)	[H ₂ S] (moles)	[H ₂] (moles)	[CS ₂] (moles)	[S ₂] (moles)	[HS+CS] (moles)	ΔH (kJ/mol)	ΔG ⁰ (kJ/mol)
a	298	1.00	0.98944	2.29853	0	0	0	0	-36.875	-97.91
b	298	1.50	1.0	5.0	0.42235	0	0	0	-27.63	-87.17
c	825	1.45	1.0	5.0	0.42235	0	0	0	-6.785	-204.3
d	1500	1.35	0.01056	2.70147	4.69278	0.98753	0.15382	0.015782	54.84	-295.6
e	875	1.20	0.01056	2.70147	4.69278	0.98753	0.15382	0.015782	29.873	-156.66
f	390	1.10	0.01056	2.70147	4.69278	0.98753	0	0.015782	nc*	nc
g	390	1.09	0.01056	2.70147	4.69278	0.98753	0	0.015782	nc	nc
h	380	1.00	0	0	0	0	0.15382	0.015782	nc	nc
i	298	1.00	0	0	4.27043-y	0	0	0	-1.883E-3	-38.914
j	300	1.00	0.01056	2.70147	4.69278	0	0	0	-7.528	-56.664
k	300	1.00	0	0	0	0.98753	0	0	nc	nc
l	300	10.0	0.01056	2.70147	4.69278	0	0	0	-7.528	-50.92
m	300	1.05	0	0	4.27043	0	0	0	55.865E-3	-39.054
n	300	10.0	0.01056	2.70147	0.42235	0	0	0	-17.861	-71.8613
o	298	1.50	0.01056	2.70147	0.42235	0	0	0	-17.9273	-76.2014
p	298	1.05	0	0	y	0	0	0	nc	nc
q	298	1.00	0	0	0	0	0	0	nc	nc

* Not calculated.

Table 5- Input energy requirement as a function of the reformer temperature.

T _c (°C)	850	950	1050	1160	1227	1727
Input concentration of [H ₂ S] _a (vol%)	69.5	69.4	70.1	70.4	70.6	71.7
ΔH _{cd} (kJ/mol of CH ₄)	663	619.3	589.8	573.65	573.53	649.6

The second method is to use electric heating, if available. The third option may be the use of a concentrating solar furnace. The fact that reaction (6) is highly endothermic makes this option especially attractive. In addition, results of Figures 3-7 indicate the advantages of running H₂S-CH₄ decomposition reaction at high temperatures readily achievable from a typical concentrating solar furnace. We note that solar-only furnaces cannot operate continuously. This has a profound effect on the economics and practicality of solar-only process for providing input power to the H₂S-CH₄ reformation plant. Depending on the particular situation, one, a combination of two, or all three options combined may prove to be the most economical. Plausible scenarios include:

solar-only, combined solar-electric, electric-only, H₂ burning furnace, combined solar and hydrogen combustion furnace, combined electric and H₂ combustion furnace, and combination solar-electric-H₂ combustion furnace. The economics of each approach is affected by the price of natural gas feedstock and electric power used as well as the value of hydrogen and carbon disulfide produced in the process.

Hydrogen and Carbon Disulfide Pricing and Marketing Considerations

As for the value of H₂ produced, no matter what type of process or energy input option is chosen, the H₂S-methane reformation won't be commercially viable unless H₂ production cost is comparable to that from SMR plants. A recent survey of the economics of hydrogen production technologies including SMR process is given by Padró (1999). For large SMR facilities, *i.e.* 50-100 million SCF per day, the hydrogen prices vary between \$5.75 and \$7.90/MMBtu (1998 US dollars). For a small facility having a hydrogen production capacity of 9.5 million SCF per day, a hydrogen price of about \$11.80/MMBtu was given. On average, the price of natural gas feedstock constituted about 60% of the total cost for large SMR plants and approximately 40% for small ones. For these estimates, a natural gas price of \$3.12 per million BTU was assumed.

According to Cox (1998), the supply costs of hydrogen are approximately \$4.20 and \$5.32 (corrected to 1998 US dollars) per million BTU for SMR plant H₂ output of 20 and 5 million SCF per day, respectively. Cox (1998) used a natural gas price of \$1.75 (corrected to 1998 US dollars) per million BTU hydrogen. After correcting for the differences in the feedstock costs, the hydrogen prices from Cox's estimate becomes \$5.72 and \$7.36 per million BTU for H₂ output of 20 and 5 million SCF per day, respectively. This is in general agreement with the figures reported by Padro (1999). We note that at the time of writing this document, the futures contract for natural gas prices (per million BTU) at the New York Mercantile Exchange (NYMEX) for the month of May 2001 varied between \$4.69 and \$3.99.

As for the sulfur recovery part of the H₂S-methane reformation, the by-product credit for CS₂ would lie between the price of recovered sulfur and that commanded by CS₂ in conventional markets (Erekson 1996). The rationale for this is that refineries are already selling the sulfur from Claus operation to the sulfuric acid plants. As noted before, the large outlet for CS₂ is in the production of H₂SO₄. The price of recovered sulfur ranged from \$0.02 to \$0.15/lb depending on purity (Chemical Market Reporter 2000). The price of sulfur corresponds to the lower limit of by-product credit for CS₂. The maximum price that carbon disulfide produced by the H₂S-methane reformation process can fetch is set by its value in the conventional markets that is about \$0.24/lb (Chemical Market Reporter 2000). In short, the by-product CS₂ from H₂S-methane reformation process should command a value in the range of approximately \$0.02 to \$0.20/lb of CS₂ (after correcting for the difference in molar mass between CS₂ and S₂).

Finally, the capital and operating costs of the prospective H₂S-methane reformation plant should be comparable to that of a baseline Claus process that it aims to replace. For example, the capital cost of a modified Claus plant that produces about 600 ton per day (tpd) sulfur is approximately 30 million US dollars (Cox 1998). The total installed cost of a 163 tpd air-based Claus sulfur plant including the tail gas cleanup unit (TGCU) is approximately \$18-20 million (Schendel 1993). We note that TGCUs typically cost as much as the Claus plant itself. A detailed

discussion of the Claus plants, other sulfur recovery and tail gas cleanup processes is given by Leppin (1997). For the large-scale modified Claus units with TGPU, typical, rough, order of magnitude treatment costs are about \$100 per ton of elemental sulfur recovered (Leppin 1997).

Gas Separation and Purification Considerations

As we briefly discussed before, various methods have been devised for the equilibrium displacement and separation of hydrogen from H₂S in hot gas streams. A review of the available techniques has been given by Clark (1990). Examples include the use of polymeric, metallic and ceramic oxide membranes, pressure-swing adsorption (Bandermann 1982) and thermal diffusion through Vycor-type glass or microporous alumina membranes at temperatures as high as 1000°C (Kameyama 1981, Ohashi 1998, Fan 1999, Fan 2000). A good discussion of H₂S/H₂ separation membranes of special interest to this work is given by Cox (1998). A packaged polyimide membrane system can be used to effect hydrogen-H₂S separation if the concentration of H₂S in the mixture does not exceed 10%. Ceramic membranes are not limited by the H₂S concentration, but they yield poor separation factors, typically 2 or lower (Cox 1998). If the separation mechanism is due to Knudsen diffusion as it is for most porous membranes, then the maximum separation factor achieved is 4.1, the square root of the ratio of the molar masses for H₂S and H₂. According to Cox (1998), new membrane separation technologies under development at the Air Products and Chemicals, Inc. (APCI) is poised to change all that. It has been shown that the APCI membrane is not limited by the separation factor 4.1 imposed by Knudsen diffusion separation mechanism.

Catalyst and Kinetics Considerations

One of the main objectives of this effort was to search for processes and catalysts that facilitate the reaction between methane and hydrogen sulfide (reaction 8) to form carbon disulfide and hydrogen. If a suitable catalyst(s) and process can be found, the prospective H₂S-CH₄ reformation process will be able to:

- Eliminate the need for steam-methane reformer for hydrogen production.
- Eliminate the need for Claus plant for treating sulfurous/sour feedstock.
- Yield more than four moles of H₂ for each mole of CH₄ reacted.
- Utilize common feedstocks (*i.e.* CH₄ and H₂S contained in NG and refinery gases).
- Use a range of H₂S to methane molar feed ratios.
- Employ a process with most steps proven at full-scale.
- Operate at a temperature range of 1100-1300°C, ideal for solar interface.
- Operate at low pressures, less than 10 atm.
- Operate with relatively low recycle H₂S, *i.e.*, H₂S/CH₄ ratio of about 4-6.
- Operate with a low dark reforming enthalpy (about half of the output H₂ energy content).
- Function under no soot formation or carbon lay-down condition.
- Simultaneously convert both H₂S and methane to hydrogen gas.
- Operate with no CO_x, acid or greenhouse gases generated or released into the atmosphere.
- Simultaneously fix both C and sulfur in the form of a valuable reagent, *i.e.* CS₂.

As noted before, the H₂S decomposition reaction (6) is an important step in the H₂S-CH₄ conversion process. In addition, we note that effective catalysts such as platinum-cobalt and disulfides of Mo or W supported on alumina are known to considerably hasten H₂S dissociation. On the other hand, reaction (7) is a well-known methane conversion reaction used commercially to produce CS₂. There are also commercial catalysts such as silica gel/aluminum used for CS₂ synthesis reaction (7). Now, the main issue is whether bi-functional catalyst(s) can be found that affect(s) H₂S decomposition reaction (6) while holding activity and stability toward reaction (7). Such catalyst(s) will be able to render the H₂S-CH₄ reformation more efficient and potentially cost effective. The search for such catalysts and processes has been conducted by the Institute of Gas Technology (now Gas Technology Institute, GTI) researchers (Miao 1998, Erekson 1996) and earlier by Schuman (1968). The objective of the work conducted by Miao and Erekson was to develop a two-step thermochemical process. In the first step, a group of catalysts was sought for the direct conversion of methane and hydrogen sulfide to carbon disulfide. In their second step, the CS₂ hydrogenation as to be carried out for the production of gasoline-range hydrocarbon liquids. The first developmental step of their effort has more direct relevance to our own analysis and is summarized briefly below:

1. In a search to find bi-functional catalysts capable of H₂S dissociation while holding activity and stability toward reaction of sulfur and methane, nine catalysts were tested. Experiments were conducted at five different reaction temperatures (*i.e.* 700, 800, 900, 1000, 1100°C), two different residence times (*i.e.* 1 and 5 s), and three distinct H₂S to CH₄ molar feed ratios (*i.e.* $x = 2, 4$ and 8).
2. It was found that the H₂S to CH₄ molar feed ratio, x , had a strong effect on the yield of carbon disulfide. The $x = 2$ (*i.e.* the stoichiometric ratio) did not give the highest CS₂ yield, but the highest yields, >95%, were achieved at $x = 4$ (*i.e.* twice the stoichiometric ratio of 2). In other words, the yields of CS₂ are not as great as when an excess of hydrogen sulfide is in the feed (consistent with the results of Figure 7). This may be at temperatures above 1000°C (1273 K); the conversion of methane nearly reaches completion. At these temperatures dehydrogenated CH₄ or carbon precursors on the surface would be in greater abundance, and with the excess H₂S in the gas phase, CS₂ yield is increased.
3. In general, the CS₂ yield increased with temperature up to 1100°C. Above that the yields decreased - again, consistent with the equilibrium calculations, Figure 7. The highest yields were for catalysts IGT-MS-103 and IGT-MS-105. The designations IGT-MS-103 and IGT-MS-105 refer to Cr₂S₃ and Ce₂S₃ catalysts, respectively.
4. IGT catalysts were tested to determine their propensity and activity toward methane decomposition and surface accumulated carbon regeneration. These tests showed that two catalysts that had most activity for inhibiting carbon formation, as well as for the regeneration after carbon deposition were IGT-MS-103 (Cr₂S₃) and IGT-MS-105 (selenium sulfide) catalysts.
5. Both IGT-MS-103 (Cr₂S₃) and IGT-MS-105 (selenium sulfide) catalysts were active in dissociating H₂S, an essential reaction in the H₂S-CH₄ reformation reaction pathway. In addition, these catalysts were stable above 1000°C (1273 K) and retained most of their original surface area (2-5 m²/g). These catalysts were also the most effective in promoting the reaction of H₂S and the carbon deposits on their surfaces.

In summary, certain transition metal sulfides such as Cr_2S_3 and Ce_2S_3 can work as bi-functional catalysts that are active in dissociating H_2S yet stable at temperatures above 1000°C (1273 K) to allow H_2S reaction with the carbon precursors formed on their surfaces. In general, these catalyst powders are prepared by sulfide conversion, drying, reduction and calcination. In the IGT method, the metal sulfides are precipitated from an aqueous solution of the metal using ammonium hydrosulfide (Miao 1998). There are also commercially prepared metal sulfide catalysts (*e.g.* Cerac 2000). Additional information pertaining to transition metal sulfides, their preparation and properties are given elsewhere (Lacroix 1991, Chivers 1980).

Cost Considerations

As noted above, the highest activity ($>95\%$ at 1100°C toward CS_2 formation) and selectivity among all catalysts tested by IGT belonged to two transition metal sulfide catalysts, particularly Cr_2S_3 . The high yields of CS_2 (and H_2) from the Cr_2S_3 -catalyzed H_2S - CH_4 reformation process were encouraging. A preliminary economic analysis was carried out by IGT to determine the viability of the H_2S - CH_4 process for refinery applications (Erekson 1996). It was assumed that H_2S was available from an acid gas removal unit, H_2S conversion was 100% and hydrogen production was 13 million SCF per day. With these assumptions, the capital and operating costs were estimated without taking credit for elimination of the Claus unit and its associated TGCU. The cost of H_2 was calculated based on a range of by-product credit for CS_2 that was varied from $\$0.04$ to $\$0.23/\text{lb}$ (1995 US\$). The lower limit of the CS_2 price range corresponds to the price of recovered sulfur ($\$0.04$ to $\$0.15/\text{lb}$ depending on purity, 1995 estimate). The upper limit corresponds to the price of CS_2 in the conventional markets. Results of IGT analysis are depicted in Figure 8. Figure 8 shows that as the market value of CS_2 increases, the cost of hydrogen decreases, accordingly. For CS_2 prices higher than about $\$0.10/\text{lb}$, hydrogen cost is negative. In other words, at CS_2 prices above approximately $\$0.10/\text{lb}$, the revenue generated by selling CS_2 would be more than enough to pay for the cost of hydrogen production.

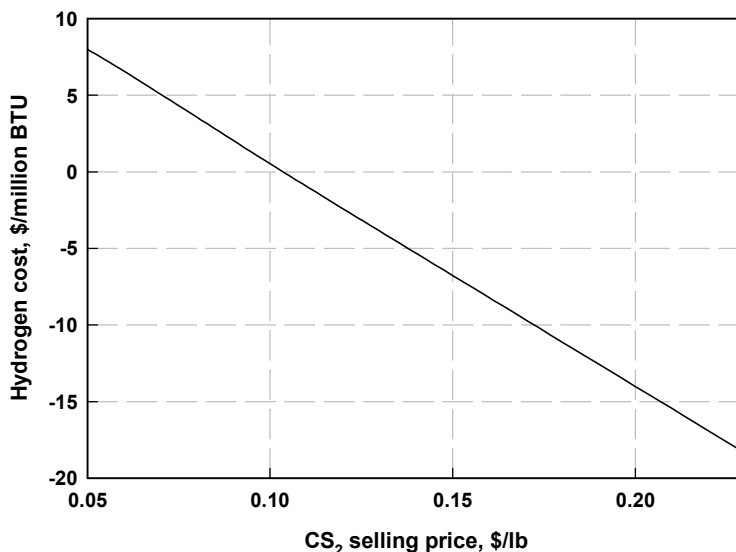


Figure 8- Comparison of CS_2 Selling Price and H_2 Cost (Erekson 1996).

Summary and Recommendations

- The concept of H₂S-methane reformation to produce H₂ and CS₂ was evaluated. In addition, the concept was assessed for its potential for cost-effective production of hydrogen for refinery and other applications.
- An assessment of the magnitude of H₂S resource that can be recovered (in the lower 48 US) from the sub-quality natural gas (SQNG) sweetening and refinery type (hydrodesulfurization) operations was made. It was found that the energy value of the hydrogen extracted from the H₂S-rich feedstocks using H₂S-methane reformation process exceeds 10 quads. The energy potential of the Alaska's Arctic National Wildlife Refuge (ANWR) reserves that can be converted and used to produce gasoline is estimated to lie between about 3.2 and 36 quads. Considering the added energy value of the sweetened SQNG made available by the H₂S-methane process, it appears that an order of magnitude larger untapped energy resource is available within the lower 48 US than there is in the Alaska's ANWR.
- With the state-of-the-technology today, the H₂S-methane reformation process discussed here is technically doable and can be economically viable as well.
- All of the reaction steps for the H₂S-methane reformation process are well-developed and some are already practiced commercially, for many years.
- Viable bi-functional catalysts have been identified and well-developed for the sole purpose of performing H₂S-methane reformation process, efficiently. Among them are several catalysts identified by a recent IGT study aimed at the production of hydrogen and CS₂ from H₂S and CH₄. Cr₂S₃ and Ce₂S₃ catalysts are found to be active in dissociating H₂S and stable at temperatures above 1000°C (1273 K) to allow H₂S reaction with the carbon precursors that reside on their surfaces. All transition metal sulfide catalysts are available commercially.
- A preliminary economic analysis of the H₂S-methane reformation process for H₂ and CS₂ production indicates that the process is a potential replacement for the present day Claus plants and associated Tail Gas Cleanup Units (TGPU). The cost of hydrogen produced depends on the price of the co-produced CS₂ and can conceivably be zero dollars, *i.e.* free.
- Efforts are underway to develop solar-thermal direct decomposition of the methane and H₂S for production of hydrogen. However, despite its potential benefits, no work has been done to show the viability of a solar-driven H₂S-methane reformation process. Considering that close to 50% of the US refinery capacity and considerable SQNG reserves are located in two states that also have considerable solar resource, *i.e.* Oklahoma and Texas, it is worthwhile to begin the development of the solar-driven thermochemical H₂S-methane reformation process

Acknowledgments

The author acknowledges the support of the U.S. Department of Energy Hydrogen Program in funding this work under Grant DE-FC36-00GO10603. Additional thanks to Dr. Sig Gronich and Messrs. Neil Rossmeissl and Douglas Hooker (US DOE), and Dr. David L. Block (FSEC) for providing continued support and guidance for this work.

References

- Al-Shamma, L.M., S.A. Naman. 1989. "Kinetic Study for Thermal Production of Hydrogen from H₂S by Heterogeneous Catalysis of Vanadium Sulfide in a Flow System." *Int. J. Hydrogen Energy*, 14(3): 173-9.
- Arild, V. 2000. "Production of Hydrogen and Carbon with a Carbon Black Catalyst." PCT Int. Appl. No. 0021878.
- Bandermann, F., K.B. Harder. 1982. "Production of H₂ via Thermal Decomposition of H₂S and Separation of H₂ and H₂S by Pressure Swing Adsorption." *Int. J. Hydrogen Energy*, 7(6): 471-5.
- Bishara, A., O.A. Salman, N. Khraishi, A. Marafi. 1987. "Thermochemical Decomposition of Hydrogen Sulfide by Solar Energy." *Int. J. Hydrogen Energy*, 12(10): 679-685.
- Bowman, M.G. 1991. "Thermochemical Cycle for Splitting Hydrogen Sulfide." U.S. Patent No. 4,999,178.
- Brockmann, M., M. Fischer, K. M. Mueller. 1998. "Exposure to Carbon Black. A Cancer Risk?" *Int. Arch. Occup. Environ. Health* 71:85-99.
- Cerac Corporation. 2000. "Technical Publications." Milwaukee, Wisconsin. URL address: <http://www.cerac.com/pubs/proddata/sulfides.htm>.
- Chem. Market Reporter. 2000. "Chemical Prices." *Schnell Publishing Company*, 258(25): 22-41.
- Chen, W-C. 1978. "Process for Recovering Hydrogen and Elemental Sulfur from Hydrogen Sulfide and/or Mercaptants-Containing Gases." U.S. Patent No. 4,066,739.
- Chivers, T., J. B. Hyne, C. Lau. 1980. "The Thermal Decomposition of Hydrogen Sulfide over Transition Metal Sulfides." *Int. J. Hydrogen Energy*, 5(5): 499-506.
- Clark, P.D., N.I. Dowling, J.B. Hyne, D.L. Moon. 1995. "Production of Hydrogen and Sulfur from Hydrogen Sulfide in Refineries and Gas Processing Plants." *Quarterly Bulletin (Alberta Sulphur Research Ltd.)*, 32(1): 11-28.
- Clark, P.D., B. Wassink. 1990. "A Review of Methods for the Conversion of H₂S to Sulphur and Hydrogen." *Alberta Sulphur Res. Quart. Bull.*, 26(2/3/4): 1.
- Cox, B.G., P.F. Clarke, B.B. Pruden. 1998. "Economics of Thermal Dissociation of H₂S to Produce Hydrogen." *Int. J. Hydrogen Energy*, 23(7): 531-544.
- Dahl, J., A. W. Weimer, et al. 2001. "Hydrogen Synthesis by the Solar-Thermal Dissociation of Methane." *Abstr. Pap. - Am. Chem. Soc.* 221: FUEL-008.
- Daley, W.D., R.D. Young. 1984. "Process for Producing Hydrogen and Sulfur from Hydrogen Sulfide." U.S. Patent No. 4,461,755.

Dalrymple, D.A., T.W. Trofe, D. Leppin. May 23, 1994. "Gas Industry Assesses New Ways to Remove Small Amounts of H₂S." *Oil & Gas Journal*, Tulsa.

Darwent, R.de B., R. Roberts. 1953. "The Photochemical and Thermal Decomposition of H₂S." *Proc. Royal Soc. London*, 216: 344-361.

Davis, S.C. Oct. 2000. "Transportation Energy Data Book: Edition 20," *ORNL-6959*.

Diver, R.B., E.A. Fletcher. 1985 "Hydrogen and Sulfur from Hydrogen Sulfide- III. The Economics of a Quench Process." *Energy*, 10(7): 831-842.

Doctor, R.D. 1999. "Recovering Hydrogen and Sulfur from Refinery Wastes." At URL address: <http://www.es.anl.gov/htmls/refinery.wastes.html>.

Donini, J. C. 1996. "Separation and Processing of H₂S in the Fossil Fuel Industry." *Minimum Effluent Mills Symp.*: 357-363.

Dowling, N.I., P.D. Clark. 1999. "Kinetic Modeling of the Reaction between Hydrogen and Sulfur and Opposing H₂S Decomposition at High Temperatures." *Ind. Eng. Chem. Res.*, 38: 1369-1375.

Elvin, F.J. 1989. "Hydrogen Production and Catalyst Demetallization Process." U.S. Patent No. 4,828,684.

Erekson, E.J. 1996. "Gasoline from Natural Gas by Sulfur Processing." *Final Technical Report*, Institute of Gas Technology, DOE/PC/92114--T12. Download the report in PDF format from URL address: <http://kratos.osti.gov:1999/cgi-bin/dexpldcgi?qryAAAYIaWes:19>.

Fan, J., H. Ohashi, H. Ohya, M. Aihara, T. Takeuchi, Y. Negishi, S.I. Semenova. 2000. "Analysis of a Two-Stage Membrane Reactor Integrated with Porous Membrane Having Knudsen Diffusion Characteristics for the Thermal Decomposition of Hydrogen Sulfide." *J. of Membrane Science*, 166: 239-247.

Fan, J., H. Ohya, H. Ohashi, M. Aihara, T. Takeuchi, Y. Negishi, S.I. Semenova. 1999. "Effect of Membrane on Yield of Equilibrium Reaction- Case I: H₂S Δ H₂+1/xS_x with Membrane of Knudsen Diffusion Characteristics." *J. of Membrane Science*, 162: 125-134.

Fletcher, E.A. 1996. "Solar Thermochemical and Electrochemical Research- How They Can Help Reduce the Carbon Oxide Burden," *Energy*, 21(7/8): 739-745.

Gallie, J.F. 1946. "Carbon black manufacture." *Petroleum Processing*, 1: 197-206.

Gaudernack, B. 1996. "Hydrogen from Natural Gas without Release of CO₂ to the Atmosphere." *Hydrogen Energy Prog. XI, Proc. World Hydrogen Energy Conf.*, 11th 1: 511-523.

Harvey, W.S., J.H. Davidson, E.A. Fletcher. 1998. "Thermolysis of Hydrogen Sulfide in the Temperature Range 1350-1600 K." *Ind. Eng. Chem. Res.*, 37: 2323-2332.

Hugman, R.H., E.H. Vidas, P.S. Springer. 1993. "Chemical Composition of Discovered and Undiscovered Natural Gas in the United States- 1993 Update." *GRI-93/0456*.

Kaloidas, V., N. Papayannakos. 1989. "Kinetics of Thermal, Non-Catalytic Decomposition of Hydrogen Sulfide." *Chemical Engineering Science*, 44(11): 2493-2500.

Kameyama, T.M., et al. 1981. "Possibility for Effective Production of Hydrogen from Hydrogen Sulfide by means of a Porous Vycor Glass Membrane." *Ind. Eng. Chem. Fund.*, 20.

Kappauf, T., E.A. Fletcher. 1989. "Hydrogen and Sulfur from Hydrogen Sulfide- VI. Solar Thermolysis." *Energy*, 14(8):443-449.

Kappauf, T., J.P. Murray, R. Palumbo, R.B. Diver, E.A. Fletcher. 1985. "Hydrogen and Sulfur from Hydrogen Sulfide- IV. Quenching the Effluent from a Solar Furnace." *Energy*, 10(10): 1119-1137.

Karan, K., A.K. Mehrotra, L.A. Behie. 1999. "On Reaction Kinetics for the Thermal Decomposition of Hydrogen Sulfide." *J. of AIChE Journal*, 45(2): 383-389.

King, P., S. Begley. July 10, 2000. "An Arctic Battlefield." *Newsweek*, New York, 136(2).

Kiuchi, H., et al. 1982. "Recovery of Hydrogen from Hydrogen Sulfide with Metals and Metal Sulfides." *Int. J. Hydrogen Energy*, 7(6).

Kotera, Y., N. Todo, K. Fukuda. 1976. "Process for Production of Hydrogen and Sulfur from Hydrogen Sulfide as Raw Material." U.S. Patent No. 3,962,409.

Lacroix, M., H. Marrakchi, C. Calais, M. Breysse, C. Forquy. 1991. "Catalytic Properties of Transition Metal Sulfides for the Dehydrogenation of Sulfur-Containing Molecules." *Stud. Surf. Sci. Catal.*, 59 (*Heterog. Catal. Fine Chem.* 2): 277-85.

Lebel, M., V. Vejins, S. Laube. 1999. "Carbon black: Challenges & Opportunities in the Global Tire Market." *Proc., Annu. Gen. Meet. - Int. Inst. Synth. Rubber Prod.* 40th: 59-70.

Lee, C.S., E.A. Fletcher, J.H. Davidson. 1995. "A Reactor-Receiver for Solar Thermolysis of Hydrogen Sulfide." In *Proceedings of Solar '95, The 1995 American Solar Energy Society Annual Conference*, 405-410. Minneapolis, Minnesota.

Leppin, D. 1997. " Gas Research Institute's Program in Small-scale Sulfur Removal and Recovery - 1997 Update." Gas Technology Institute website, paper: <http://www.gri.org/cgi-bin/re?url=http%3A//www.gri.org/pub/oldcontent/tech/e+p/gproc/tu/sulfpaper.html>.

Luinstra, E. 1996. "Hydrogen from H₂S-A Review of the Leading Processes." *Proc. GRI Sulfur Recovery Conf.*, 7th: 149-165.

Megalofonos, S.K., N.G. Papayannakos. 1997. "Kinetics of Catalytic Reaction of Methane and Hydrogen Sulphide over MoS₂." *J. of Applied Catalysis A: General*, 165(1-2): 249-258.

Meyer, H.S. 2000. "Volume and Distribution of Subquality Natural Gas in the United States." *GasTIPS*, GTI website at: <http://www.gri.org/pub/content/feb/20000224/110827/gtwnt00b.html>.

Morley, C. 2000. "Gaseq: A Chemical Equilibrium Program for Windows." website at URL: <http://www.c.morley.ukgateway.net/ver061.htm>.

Miao, F.Q., E.J. Erekson. 1998. "Method for Direct Production of Carbon Disulfide and Hydrogen from Hydrocarbons and Hydrogen Sulfide Feedstock." US patent application 9-018,957. Download the report in PDF format from URL address: <http://kratos.osti.gov:1999/cgi-bin/dexpldcgi?qryJAALdayMW;8>.

Muradov, N.Z. 2000. "Thermocatalytic CO₂-Free Production of Hydrogen from Hydrocarbon Fuels." *Proceedings of the 2000 Hydrogen Program Review*, NREL/CP-570-28890.

Muradov, N.Z. 1998. "CO₂-Free Production of Hydrogen by Catalytic Pyrolysis of Hydrocarbon Fuel." *Energy Fuels*, 12(1): 41-48.

Murata, K., H. Ushijima, K. Fujita. 1997. "Process for Producing Hydrogen from Hydrocarbon." U.S. Patent No. 5,650,132.

Nikula, K. J. 2000. "Rat Lung Tumors Induced by Exposure to Selected Poorly Soluble Nonfibrous Particles." *Inhalation Toxicol.* 12(1-2): 97-119.

Noring, J.E., E.A. Fletcher. 1982. "High Temperature Solar Thermochemical Processing-Hydrogen and Sulfur from Hydrogen Sulfide." *Energy*, 7(8): 651-666.

Norman, J.H. 1984. "Hydrogen Production from In Situ Partial Burning of H₂S." U.S. Patent No. 4,481,181.

Ober, J.A. 2001. "Mineral Commodity Summaries, January 2001." *U.S. Geological Survey*: 160-161.

Ohashi, H., H. Ohya, M. Aihara, Y. Negishi, S.I. Semenova. 1998. "Hydrogen Production from Hydrogen Sulfide Using Membrane Reactor Integrated with Porous Membrane Having Thermal and Corrosion Resistance." *J. of Membrane Science*, 146: 39-52.

Padró, C.E.G., V. Putsche. 1999. "Survey of the Economics of Hydrogen Technologies." Technical Report: NREL/TP-570-27079, National Renewable Energy Laboratory.

Pelton, A.D., W.T. Thompson, C.W. Bale, G. Eriksson. 1990. "F*A*C*T Thermochemical Database for Calculations in Materials Chemistry at High Temperatures." *High Temp. Sci.*, 26: 231-50. Also visit: <http://www.crct.polymtl.ca/fact/web/equiweb.htm>.

Raymont, M.E.D. 1975. "Make Hydrogen from Hydrogen Sulfide." *Hydrocarbon Process*, 54(7): 139-142.

Raymont, M.E.D. 1974. Ph.D. Thesis, University of Calgary, Alberta, Canada.

Rusinko, F., J. L. Morrison. 2000. "Premium Carbon Products from Coal." *Proc. Int. Tech. Conf. Coal Util. Fuel Syst.* 25th: 651-657.

Saraf, S. 1997. "Thermochemical Conversion of Waste Materials to Valuable Products." *Proc., Annu. Meet. - Air Waste Manage. Assoc.* 90th: RP15501/1-RP15501/13.

Semrau, J.T., P. Nagaraju, L.L. Anthony. 1995. "Subquality Natural Gas Sweetening and Dehydration Potential of the Physical Solvent N-Formyl-Morpholine." DOE/MC/28178-95/C0449, Conf-950281--1.

Schendel, R.G. 1993. "SO₂-Generation Process Can Double Refinery Claus Unit Capacity." *Oil & Gas Journal*, Tulsa: September 27 issue.

Schuman, S.C. 1968. "Production of Hydrogen." U.S. Patent No. 3,388,971.

Shiina, H., M. Oya, K. Yamashita, A. Miyoshi, H. Matsui. 1996. "Kinetic Studies on the Pyrolysis of H₂S." *J. of Phys. Chem.*, 100: 2136-2140.

Steinberg, M. 1987. "Clean Carbon and Hydrogen Fuels from Coal and Other Carbonaceous Raw Materials." *Coal Sci. Technol.* 11(Int. Conf. Coal Sci., 1987): 953-7.

Swain, E.J. 2000. "Processed-Crude Quality in US Continues Downward Trend." *Oil & Gas Journal*, Tulsa: March 13 issue.

Swain, E.J. 1999. "U.S. Refinery-Sulfur Production Peaked in 1996." *Oil & Gas Journal*, Tulsa: March 8 issue.

Uemura, Y., H. Ohe, Y. Ohzuno, Y. Hatate. 1999. "Carbon and Hydrogen from Hydrocarbon Pyrolysis." In *Proc. Int. Conf. Solid Waste Technol. Manage.*, 15: 5E/25-5E/30.

Ullmann's. 1989. "Encyclopedia of Industrial Chemistry." A13.

Wamnes, A. N., O. Raanes, et al. 1997. "Carbon Black and Hydrogen Direct from Hydrocarbons." In *Proc. Int. Therm. Plasma Processes Conf.*, 4th: 503-510.

Weimer, A.W., J. Dahl, J. Tamburini, A. Lewandowski, R. Pitts, C. Bingham, G.C. Glatzmaier. 2000. "Thermal Dissociation of Methane Using a Solar Coupled Aerosol Flow Reactor." *Proceedings of the 2000 Hydrogen Program Review*, NREL/CP-570-28890.

Wang, C.S. 1998. "Process for Hydrogen Production from Hydrogen Sulfide Dissociation." U.S. Patent No. 5, 843,395.

Zaman, J., A. Chakma. 1995. "Production of Hydrogen and Sulfur from Hydrogen Sulfide." *Fuel Processing Technology*, 41: 159-198.

IEA HYDROGEN ANNEX 13 TRANSPORTATION APPLICATIONS ANALYSIS

**Susan M. Schoenung
Longitude 122 West, Inc.
Menlo Park, CA 94025**

Abstract

Vehicles and power plants fueled by hydrogen produce virtually no pollutant emissions and are projected to become a serious alternative to hydrocarbon-fueled systems in the future. The transportation sector is already adopting hydrogen in a limited way. Current hydrogen vehicle designs produce power by consuming hydrogen in either a fuel cell or an internal combustion engine (ICE). Hydrogen can be stored on-board as either a compressed gas or a cryogenic liquid. Hydrogen-fueled vehicles need a ready source of fuel for routine use. The infrastructure to provide convenient refueling for passenger vehicles must be put in place in the near future, both in the US and internationally. Options for providing hydrogen fuel include electrolysis of water, reforming of hydrocarbon fuels at the fueling station, and transport of bulk hydrogen. This paper presents results of comparative analysis for passenger vehicle refueling options using either liquid or gaseous hydrogen.

Introduction

The transportation applications project is one of three integrated system activities currently underway as part of IEA Hydrogen Annex 13, "Design and Optimization of Integrated Systems." Two other projects are addressing remote power generation (on a Norwegian island) and residential power and heating (in a Netherlands suburban community).

The goal of these projects is to address specific hydrogen demonstration opportunities, with respect to energy independence, improved domestic economies and reduced emissions. These development activities are selected to provide both specific findings to the immediate region and also generic conclusions to the hydrogen energy community. Rigorous analysis aids both the specific project and can be extended to additional opportunities in participating countries.

The transportation analysis is not as geographically specific as the other two projects. It is, however, based on current U.S. experience with hydrogen fueling infrastructure. It is meant to contribute to the ongoing discussion, both in the U.S. and internationally, on the preferred choice for fueling options and hydrogen distribution alternatives.

Project Scope

The overall scope of the transportation analysis includes a comparison of hydrogen passenger vehicle fueling options, including:

- Refueling alternatives, primarily various sources of gaseous or liquid hydrogen.
- Vehicle configuration alternatives, primarily various hydrogen storage and power plant selections.
- Driving cycle implications.
- Cost variations for electricity, natural gas and hydrogen with conditions and over international boundaries.

Figures of merit for the overall project include:

- Costs, both capital and operating
- Efficiency, both in terms of vehicle fuel economy, and also in terms of overall energy conversion efficiency
- Footprints for refueling station alternatives
- Emissions, for each alternative system

This paper addresses refueling station alternatives, where the primary considerations are:

- Liquid or gas storage on-site
- On-site or off-site hydrogen production
- The utilization factor of the refueling station

The goal is to aid a user's decision with respect to station type and components.

Case Studies

The specific cases analyzed are:

1. Bulk liquid hydrogen from an existing central reformer transported to the refueling station by truck, stored as a cryogenic liquid and dispensed to the vehicle as a liquid.
2. Bulk liquid hydrogen from an existing central reformer transported to the refueling station by truck, stored as a cryogenic liquid and dispensed to the vehicle as a gas.

- Bulk gaseous hydrogen transported to the refueling station by existing pipeline, stored as a compressed gas at 5000 psi and dispensed to the vehicle as a gas. This case is valid only where there is a nearby pipeline. (Pipeline construction costs were not considered.)
- Gaseous hydrogen generated at the refueling station from natural gas by steam methane reforming, stored as a compressed gas at 5000 psi and dispensed to the vehicle as a gas.
- Gaseous hydrogen generated at the refueling station from natural gas by a partial oxidation process, stored as a compressed gas and dispensed to the vehicle as a gas.
- Gaseous hydrogen generated at the refueling station by electrolysis, stored as a compressed gas at 5000 psi and dispensed to the vehicle as a gas. (For the present analysis, grid electricity is assumed to power the electrolyzer. Renewable electricity may be considered later.)

System diagrams for these 6 alternatives are shown in Figure 1.

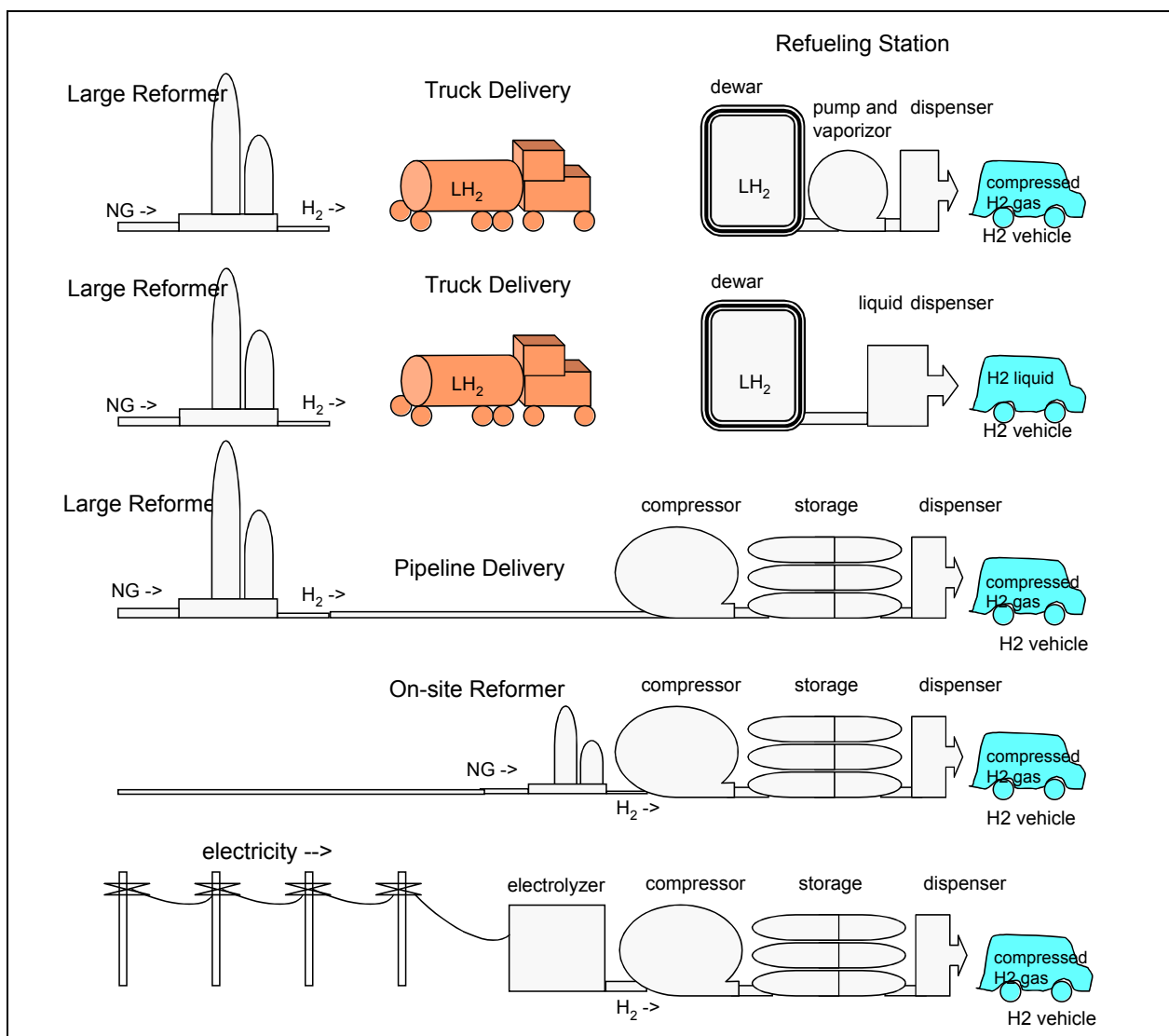


Figure 1. Refueling Station Alternatives

Refueling Station Operation

All refueling station alternatives assume the station is open for business 24 hours per day. Hydrogen is supplied to vehicles from the storage system. The storage is filled intermittently (once per week) in the case of truck delivery. Storage can be refilled continuously in the cases of pipeline gas and on-site production, or scheduled for optimum times, based on the cost of electricity, or other consumables.

The liquid-to-liquid system is assumed to operate similarly to that in the Munich airport, by interconnect to the vehicle and simple pumping of cryogenic liquid into the on-board storage tank. The liquid-to-gas system is also straightforward. It requires a pump and vaporizer, which are available technologies. In the liquid storage case, the dewar maintains a minimum of 30% storage. The gas-to-gas system requires that pressure to the vehicles be maintained at 5000 psi, even though pressure in the storage tank will drop as it is emptied. A boost compressor can provide suitable pressure, as long as the tank pressure remains above about 2000 psi. Thus, the gaseous storage tank must be oversized by about 40%. Figure 2 shows schematically the system diagram for the refueling system.

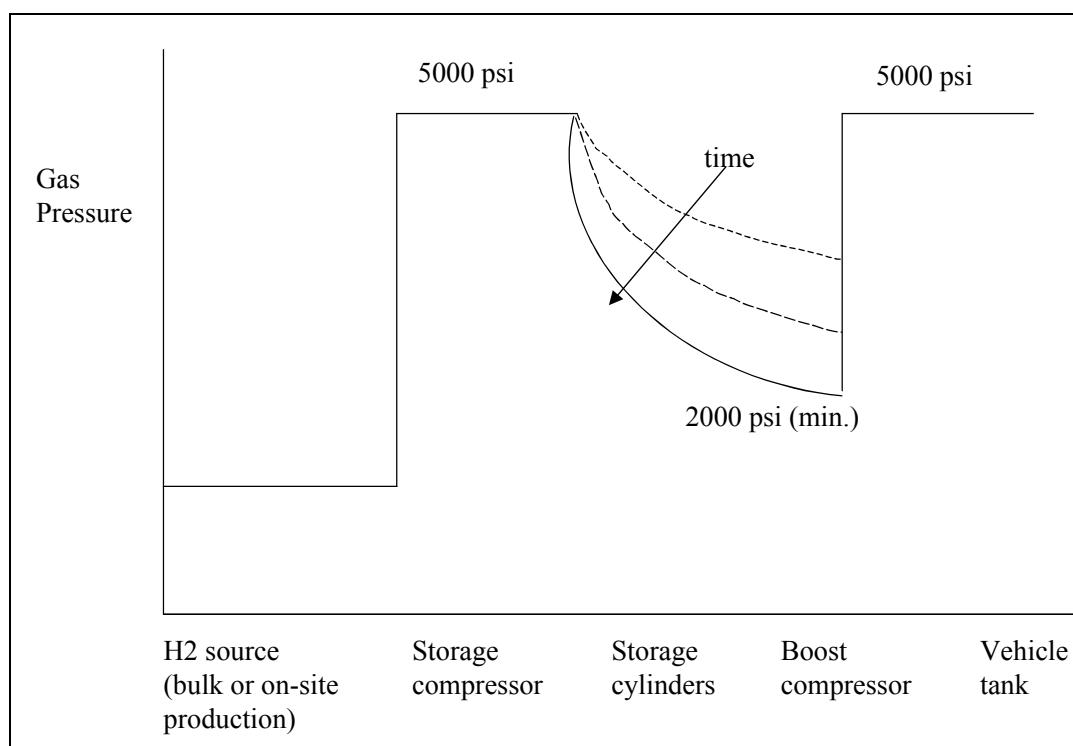


Figure 2. System Diagram for Refueling Analysis for Gaseous Systems

Technology Descriptions

Hydrogen production technologies are current, commercial types. The large reformer is assumed to be existing mature technology, centrally located with existing distribution networks of trucking routes or pipelines. The smaller, on-site generator could be a scaled-down steam methane reformer (SMR), or an autothermal reformer (ATR), or a partial oxidation reformer

(also called an under-oxidized burner, or UOB). For this analysis, both a small SMR and an existing commercial UOB were considered. Although the commercial trend seems to be toward the ATR, no performance, cost or footprint data were available for analysis. Small electrolyzers are commercial products, although improvements in performance and cost are projected with a growing market.

Storage technologies are also assumed to be current, commercial types: a cryogenic liquid dewar for liquid hydrogen, and pressurized tanks for gaseous hydrogen. Other storage types, such as metal hydrides were not considered for bulk on-site storage. Storage compressors are commercial types with suitable flowrate to 5000 psi. A boost compressor is required to dispense at 5000 psi to the vehicle, once gas pressure in the storage tank drops as hydrogen is dispensed. Higher pressure storage would be more compact and require less boost compressor work. Higher pressure tanks are more expensive, however, as are higher pressure storage compressors. The dispensers are still developmental, with limited commercial practice both for gaseous and liquid hydrogen.

Approach

Assumptions

For the transportation infrastructure analysis to proceed, a number of initial assumptions were made regarding operation of the transportation system. These include:

- Only passenger vehicles are currently under consideration.
- The vehicles are assumed to be fueled with hydrogen (either liquid or gas), i.e., fuel processing is NOT done on board. (Later analysis will look at on-board processing.)
- The base case calls for capacity to refuel 100 vehicles per day.
- Each vehicle refueling event requires 4 kg of hydrogen. This is a “consensus” value of multiple other studies and matches the current value for PNGV targets and for the Ford hydrogen ICE vehicle. (Later analysis will look at variations in this requirement based on variations in vehicle weight / configuration, due to storage type and power plant, and to driving cycle assumptions.) As a result, at 100% utilization, 400 kg hydrogen is served per day. Storage is sized to serve the entire anticipated volume of customers, plus a buffer, as described below.
- A refueling station consists of the hydrogen production unit or receiving area, storage and its associated facilities, and the dispensing area with two dispensing units. These are the capital cost components considered in this study.
- Available dispensing hours are 24 hours per day, 365 days per year.
- On-site hydrogen production capacity is sized to fill the required storage once per day. (A trade-off between production capacity or rating and operating hours was considered for the electrolyzer and UOB cases to minimize the combined capital cost and electricity cost.)
- Liquid delivery is scheduled once per week. An average round trip delivery distance of 1500 miles was assumed. The dewar is sized for one week’s service plus 30%, to maintain proper conditions and reduce boil-off in the tank (Richards 2001.)
- Compressed gas storage capacity is oversized by 40% to maintain adequate pressure for dispensing via boost compressor, as indicated previously in Figure 2.
- The pipeline gas case is valid only for locations with existing infrastructure.

Cost Analysis

The cost analysis consists of computing both capital cost and the delivered cost of hydrogen for each alternative station case. The capital cost components include:

- Hydrogen generator (for on-site cases)
- Storage system and auxiliaries
- Storage compressor (for gaseous cases)
- Boost compressor (for gaseous cases)
- Dispensers and auxiliaries

(The central SMR and pipeline are not costed, as they are not part of the station. The cost of delivered hydrogen – liquid or gas – is included in the operation costs.)

For the assumed number of vehicles and mass of hydrogen required for refueling, along with the assumed 5000 psi fill pressure and the requirement to refill the gas storage tank each day, the minimum rating of the storage compressor is determined to be approximately 185 scfm. From the work of Ogden (Ogden 1995), we choose a commercial compressor rated at 254 scfm, for which performance and cost are known. Although this cost could be scaled, it wasn't because an existing product was preferred for the analysis. Likewise, we choose a known boost compressor (100 hp) and a known pump and vaporizer system (20 l/min) that provide 400 scfm to the vehicle tank. The fill time per vehicle is just over 4 minutes.

Table 1 lists the capital cost assumptions for the base cases.

Table 1. Capital Cost Assumptions (Base Case)

Item	Units	Cost	Reference
Pipeline terminus	\$ per each	10,000	(Ogden 1995)
Small SMR	\$/scfd	10	(Ogden 1995), (Keller 2001)
UOB	\$/scfd	4.6	(Hummel 2001)
Electrolyzer	\$/kW H ₂	600	(Fairlie 2000)
Liquid dewar	\$/gal	10	(Richards 2001)
Compressed gas cylinders	\$/scf	2.2	(James 1997), (Amos 1998)
Storage compressors (254 scfm at 5000 psi)	\$ per each	170,000	(Ogden 1995), (Thomas 1998)
Boost compressors (100 psi)	\$ per each	80,000	(Ogden 1995)
Gas dispenser	\$ per each	25,000	(Ogden 1995)
Liquid dispenser	\$ per each	100,000	(BMW/ARAL 2000)
Storage regulator valve	\$ per each	10,000	(Ogden 1995)
Pump and vaporizer	\$ per each	36,000	(Ogden 1995)

Capital costs for the 400 kg/day station are additive:

Total Capital Cost =

Cost of generator + Cost of storage system + Cost of compressors + Cost of dispensers

The operating cost components include:

- Capital charge (cost of money)
- Natural gas (if purchased)
- Hydrogen (if purchased)
- Catalysts or other consumables
- Electricity
- Operations and Maintenance charges (O&M)
- Labor

Table 2 lists the operating cost assumptions for the base cases. The cost of bulk liquid hydrogen is highly dependent on the delivery distance, and almost independent of the amount above a certain value. We assumed an average 1500 mile delivery distance (round trip) and a minimum delivery of 10,000 gal LH2. On-site generation cases assume labor for three full-time persons (one for each of 3 shifts), while delivery cases, which require less on-site attention, assume an equivalent of two full-time persons over a 24-hr operating day.

Table 2. Operating Cost Assumptions (Base Case)

Item	Units	Value	Comments / Reference
Capital charge rate	% of capital cost/yr	15	(Ogden 1995), (Thomas 1998)
Natural gas	\$/MMBTU	6	Base case assumption
Liquid Hydrogen (bulk)	\$/GJ	12	(Richards 2001)
Gaseous Hydrogen (bulk)	\$/GJ	10	(Amos 1998), (Ogden 1999)
Electricity – on peak	¢/kWh	7	(Iannucci 2000)
Electricity – off peak	¢/kWh	2.5	(Iannucci 2000)
O&M	% of capital cost	4	(Ogden 1995)
Labor	\$/yr/person	50,000	(Ogden 1995)
Catalysts	\$/1000 scf H2	.65	(Ogden 1995), (Thomas 1998)

Operating costs are additive for each applicable item in each case, and for the number of vehicles served.

Annual Operating Cost =

$$\text{Capital charge} + \text{Cost of consumables} + \text{Cost of electricity} + \text{O\&M} + \text{Labor}$$

The capital charge, O&M and labor are independent of the number of cars served, whereas the cost of consumables and cost of electricity are proportional to the number of cars served. These assumptions were used in determining the impact of utilization factor on the cost of delivered hydrogen. The cost of served or delivered hydrogen is calculated based on the annual operating costs divided by the amount of hydrogen delivered, in GJ. (The cost per driving cycle will be converted into an equivalent \$/gal gasoline in the next phase of this study).

$$\text{Delivered cost of hydrogen (\$/GJ)} = \text{Annual operating cost} / \text{GJ hydrogen dispensed per year}$$

Each of the station components has an associated efficiency and/or power requirement for operation. Efficiency is applied to the conversion to hydrogen, on a HHV basis. Electricity costs are calculated on the basis of power required during the time of operation. Whether the operation occurs on-peak (6 hours per day) or off-peak (18 hours per day) is also taken into consideration. The values assumed in this analysis are tabulated in Table 3.

Table 3. Operating Performance of Refueling Station Components

Item	Efficiency, %	Power requirement (while operating)	Reference
Small SMR	67	0.6 kWh/1000 scf H ₂	(Ogden 1995), (Edlund 2000)
UOB	69	17.38 kWh/1000 scf H ₂	(Hummel 2001)
Electrolyzer	80		(Fairlie 2000)
Storage compressor (254 scfm at 5000 psi)		82 kW	(Ogden 1995)
Boost compressor (100 hp)		75 kW	(Ogden 1995)
Liquid pump (20 l/min)		1 kW	(Ogden 1995)
Pump and vaporizer (20 l/min)		22.4 kW	(Ogden 1995)

Footprint Analysis

The footprint of the refueling station is of interest for comparing land area requirements for the various alternatives. The footprint was calculated for the following components:

- Hydrogen generator (if applicable)
- Delivery area (if applicable)
- Hydrogen storage and safety keep-out zone
- Compressors and other auxiliary components
- Dispensing area, including driving lane.

Safety codes and standards require a safety keep-out zone or perimeter fencing around hydrogen storage facilities (NFPA 1999, Weinmann 2001). Distances depend on the volume and state of hydrogen (gas or liquid), what other facilities are present and what type of fireproofing is provided. A typical perimeter for gas storage is 15 ft (4.6 m). The requirement for liquid storage can be as great as 50 to 75 ft, according to U.S. codes. Actual practice in the U.S. and Europe is much less as it is determined by local fire officials on the basis of “equivalent” protection (Weinmann 2001, Roby 2001). A base case perimeter value of 15 ft was used for the present analysis.

A representative layout of the site is shown in Figure 3. Footprint assumptions for the various cases are listed in Table 4.

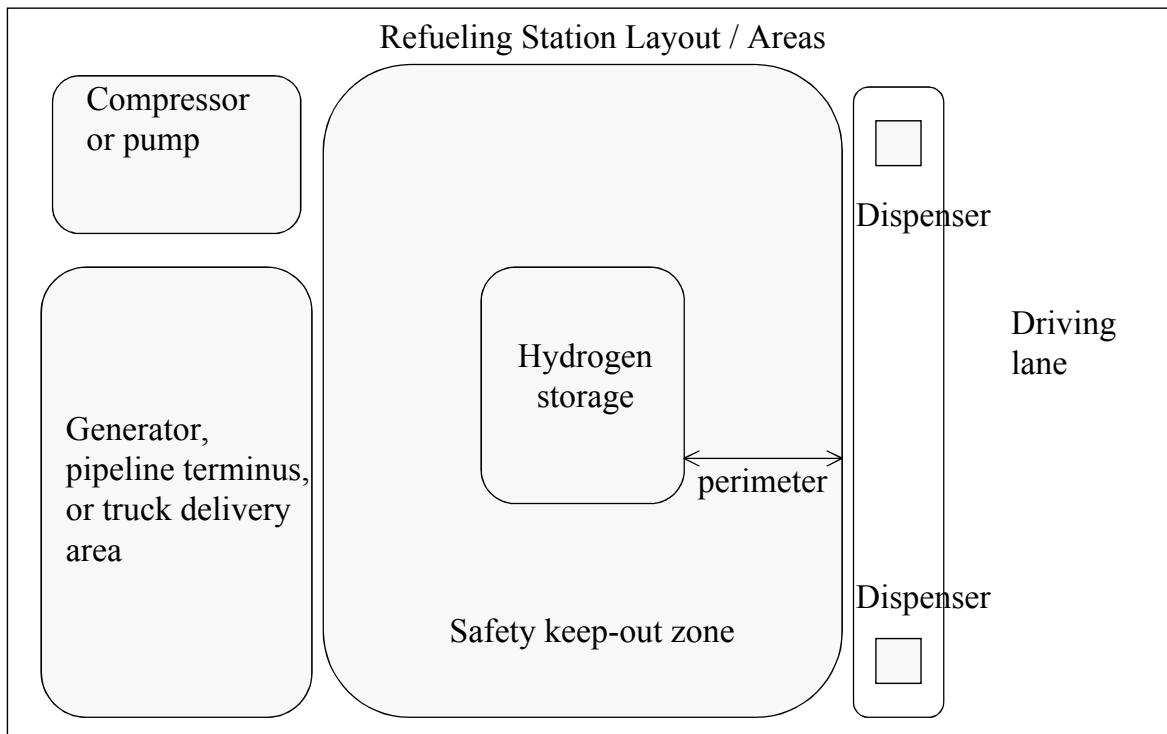


Figure 3. Refueling Station Layout for Footprint Analysis

Table 4. Footprint Areas of Refueling Station Components

Item	Units	Value	Comments / Reference
Truck delivery area	m ² per each	39	Based on a typical service station
Pipeline terminus	m ² per each	20	(Richards 2001)
Liquid dewar	m ² / kg stored	2.75 x 10 ⁻³	(Richards 2001), assumes a standing cylindrical dewar
Pressurized cylinder (5000 psi)	m ² / kg stored	.132	(Abele 2001), based on stacks of horizontal cylinders
Safety zone perimeter	m from storage	5	(Bracha 2001), (Weinmann 2001)
Liquid dispenser area	m ² per each	9	(Thomas 1998)
Liquid pump	m ² per each	negligible	(Richards 2001)
Evaporator and pump	m ² per each	4	(Richards 2001)
Storage compressor	m ² / scfm	.0236	(Hummel 2001)
Boost compressor	m ² / scfm	4	(Ogden 1995)
Small SMR	m ² / scfd	6.4 x 10 ⁻⁴	(Ogden 1995), (Edlund 2000)
UOB Hydrogen generator	m ² / scfd	3.13 x 10 ⁻⁴	(Hummel 2001)
Electrolyzer	m ² / scfd	4.91 x 10 ⁻⁴	(Fairlie 2000)
Gas dispenser area	m ² per each	9	Based on a typical service station
Driving lane	m ² per each	24	Based on a typical service station

Footprints of the individual components for each case are additive.

$$\text{Refueling station footprint area} = \text{Area for hydrogen source} + \text{Storage system area (including safety zone)} + \text{Delivery area} + \text{Dispensing area}$$

Data Sources

An attempt has been made in this analysis to use current or near-term values for costs and equipment sizes. Some vendors and manufacturers were fairly cooperative in providing data; others less so, for competitive reasons. Some information was available from commercial web sites. When necessary, estimates from other studies have been used. The most significant are those of Ogden, Thomas, and various other DOE/national laboratory studies. Broader sources were also sought, and are listed as references within this report.

Results

This section contains results of the study to date, including capital costs, delivered hydrogen costs, sensitivity analyses, and refueling station footprints.

Refueling Station Capital Costs

Figure 4 presents Total Capital Costs for the 6 base cases. The components of those capital costs are shown in Figure 5.

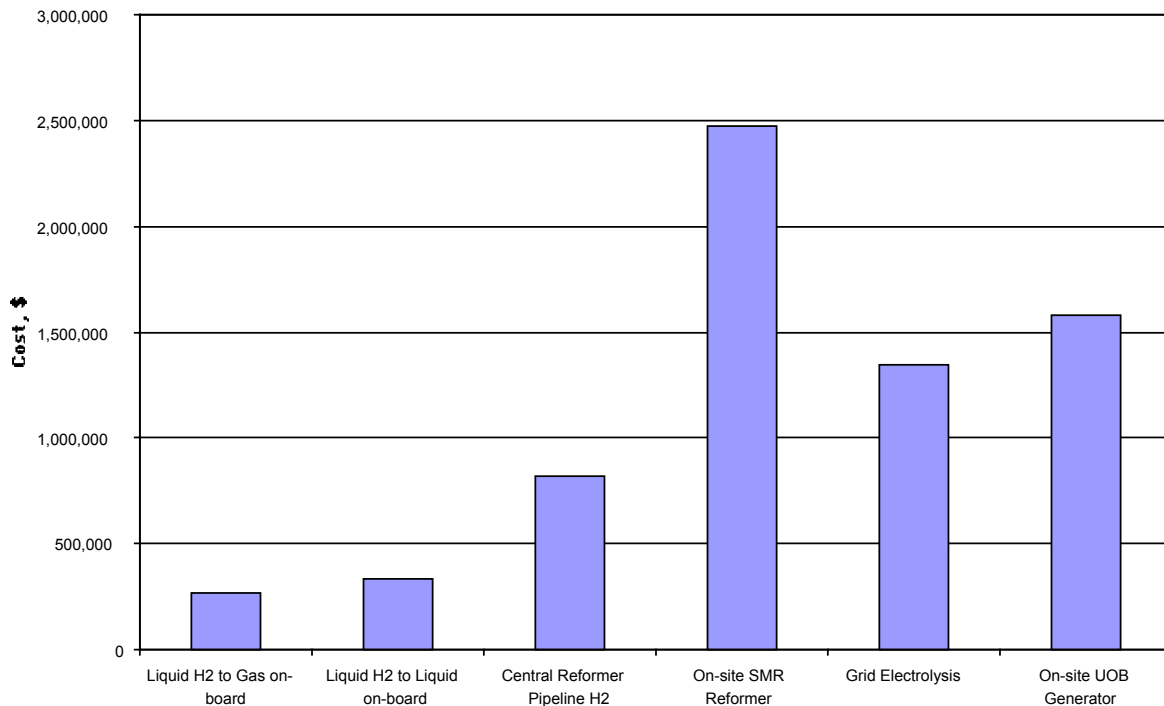


Figure 4. Total Capital Costs for Base Cases: Hydrogen Refueling Station

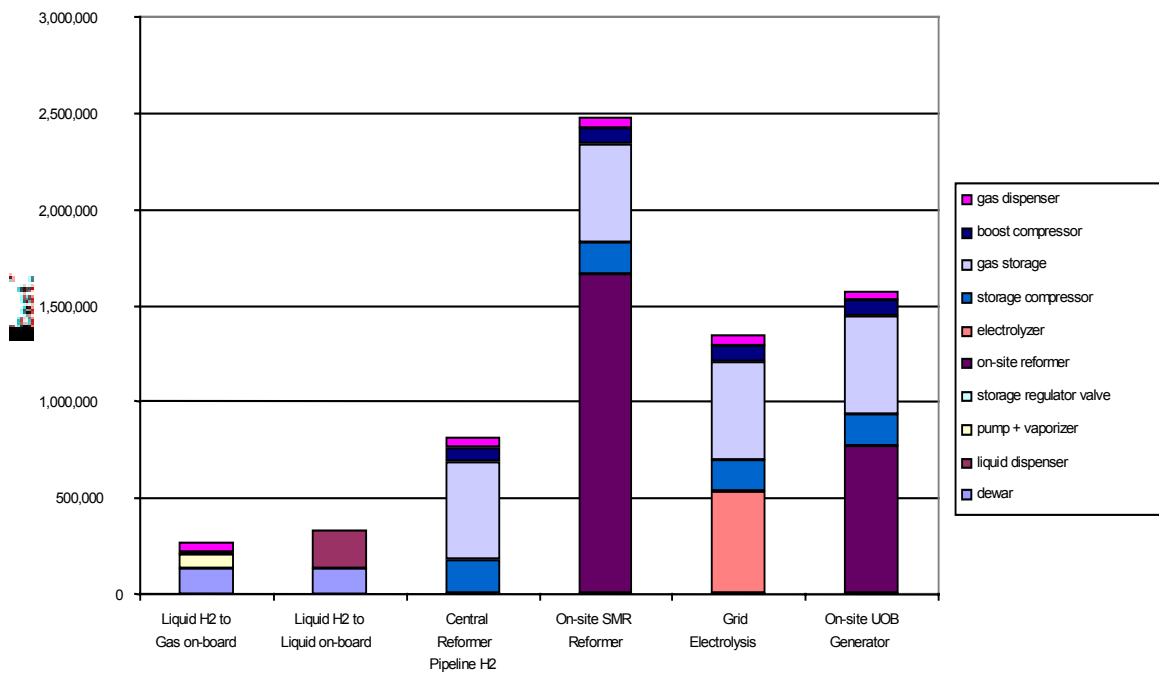


Figure 5. Capital Costs Components for Base Cases: Hydrogen Refueling Station

Cost of Delivered Hydrogen

The cost of hydrogen served or delivered is determined from the annual operating costs divided by the total GJ of hydrogen delivered per year. Figure 6 presents a comparison of delivered cost of hydrogen for the 6 base cases assuming 100% utilization factor for the refueling station, i.e., 100 cars are filled every day. Figure 7 presents the components of the fuel cost for each case.

For the base case, the electrolyzer was sized to produce a full day’s supply of hydrogen during off-peak hours, to avoid on-peak electricity prices. This approach was also considered for the UOB because it also draws a large amount of electricity while operating. For the UOB, however, the increased capital cost for a larger unit was NOT offset by reduced electricity costs, unlike the electrolyzer. Figure 8 presents components of the delivered hydrogen cost for these two generators sized to run either 18 hours or 24 hours per day, thus either using or avoiding on-peak electricity costs. The SMR uses relatively less electricity and the system is optimized to operate 24 hours per day.

Sensitivity Studies

Two sensitivity studies have been completed to this point. First is a look at the impact of under-utilization of the refueling station, as may be the case in the early years of operation. Figure 9 shows a comparison of the cost of delivered hydrogen for 100% and 50% utilization (i.e., 50 cars served per day) for the 6 base cases. Capital charges, O&M and labor are independent of utilization, whereas consumables (i.e. natural gas or bulk hydrogen) and electricity use depend on the number of vehicles served.

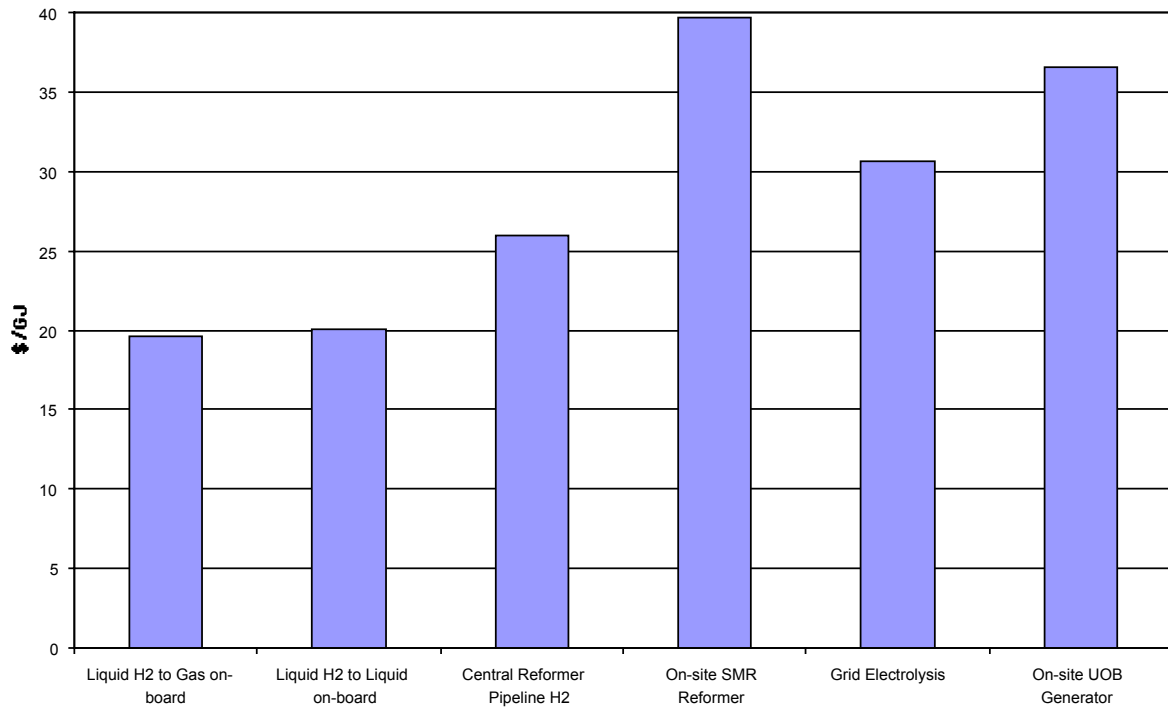


Figure 6. Delivered Cost of Hydrogen (\$/GJ) for Base Cases, 100% Utilization Factor

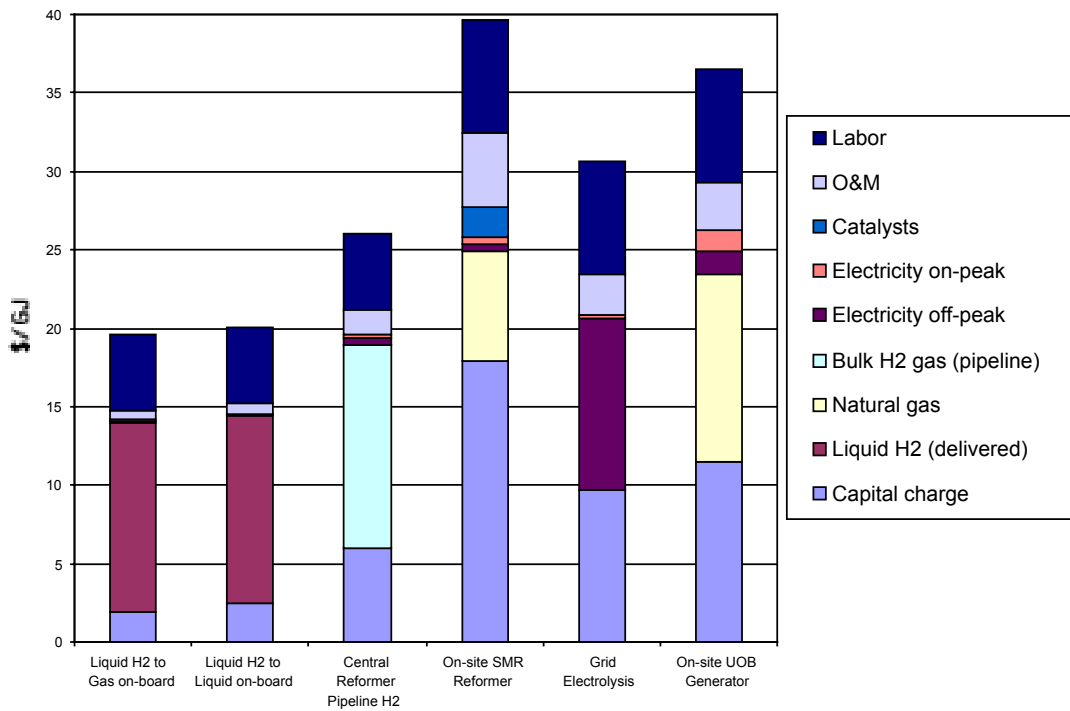


Figure 7. Components of Hydrogen Cost for Base Cases, 100% Utilization Factor

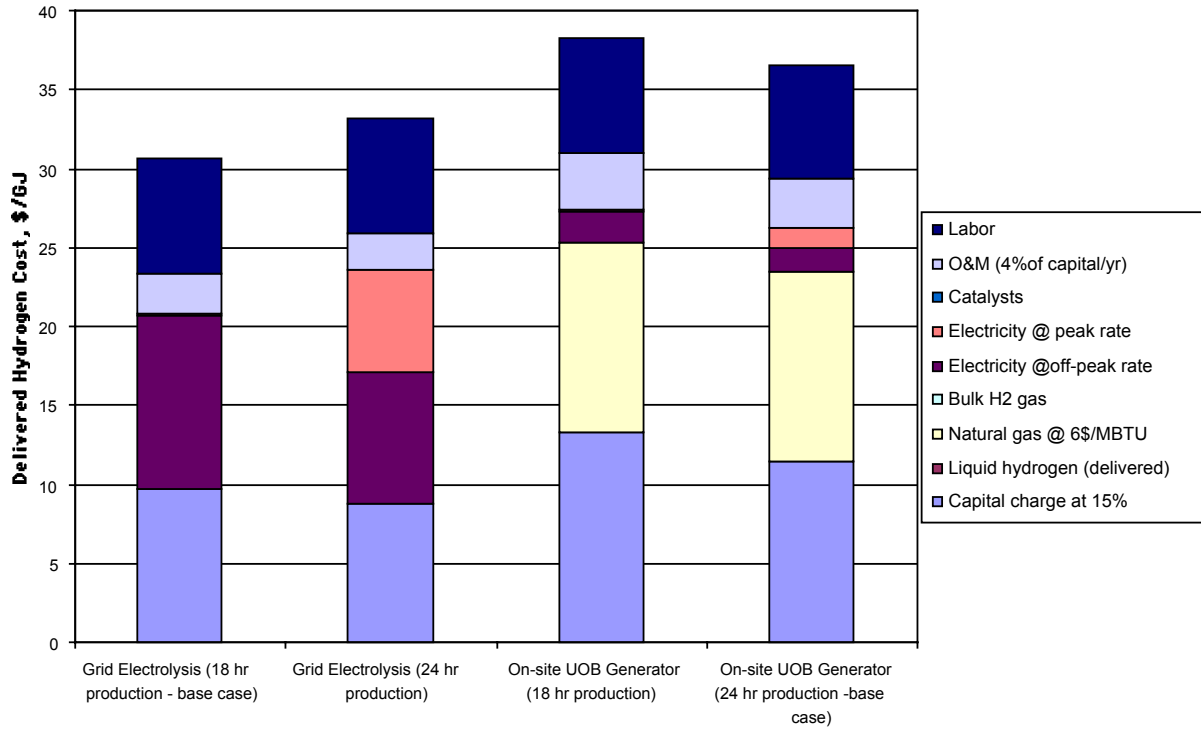


Figure 8. Comparison of Electrolyzer and UOB Generators Sized to Avoid (18-Hr Production) or Use (24-Hr Production) On-Peak Electricity

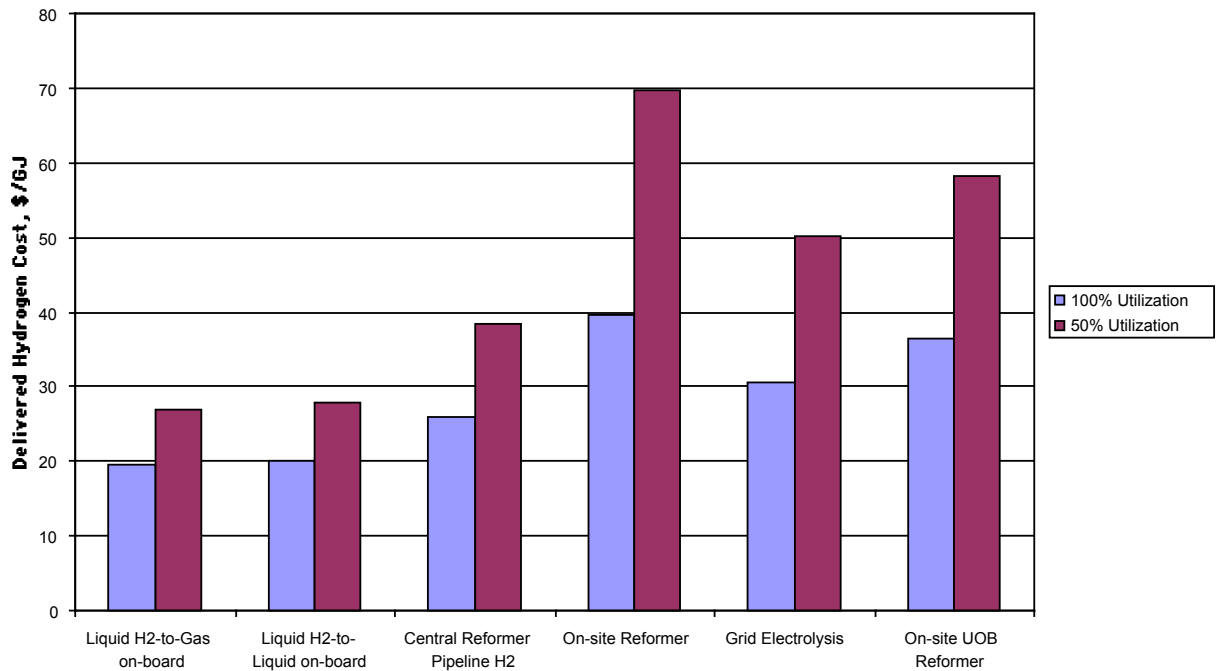


Figure 9. Cost of Delivered Hydrogen for 100% and 50% Utilization Factors

Another sensitivity analysis involves the cost of on-site hydrogen production units, as these make up the largest individual capital cost for those cases. With maturity, costs of these systems are projected to drop from current or near-term costs. Table 4 indicates the two sets of capital costs used in this sensitivity study. Figure 10 presents the capital cost results for these projected cases, in comparison to the other base cases. Figure 11 shows the delivered cost of hydrogen for projected cases; improvements in efficiency have not been projected, however.

Table 5. Capital Costs of On-Site Generators (Base Case and Projected)

System	Base cost	Projected cost	Reference
SMR	10 \$/scfd	5 \$/scdf	(James 1997), (Edlund 2001)
UOB	4.6 \$/scfd	3 \$/scfd	(Hummel 2001)
Electrolyzer	600 \$/kW	300 \$/kW	(Fairlie 2000)

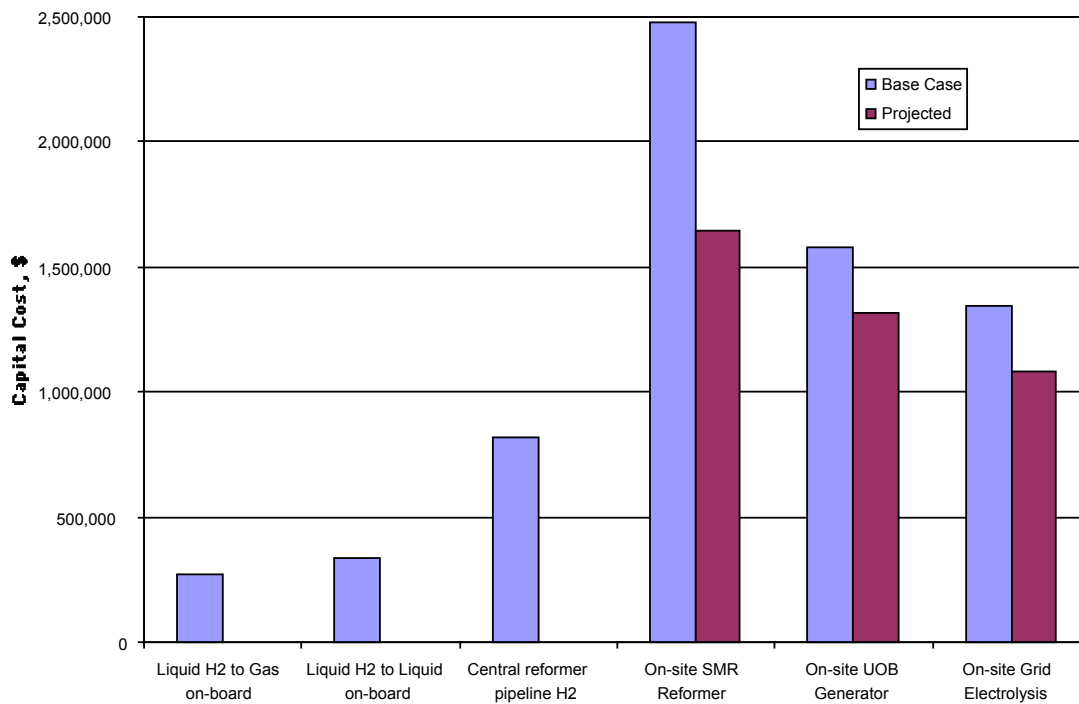


Figure 10. Capital Cost of Alternatives With Projected, Future Costs of On-Site Generators

Footprints

The footprint area results for each of the six base cases are presented in Figure 12. The components of the footprints are presented in Figure 13. Note that the liquid storage results are based on storing one week's mass of liquid hydrogen on-site, whereas only a day's worth of gaseous hydrogen is stored on-site. The footprints are dominated by the safety keep-out zone to a perimeter of 15 ft (5 m).

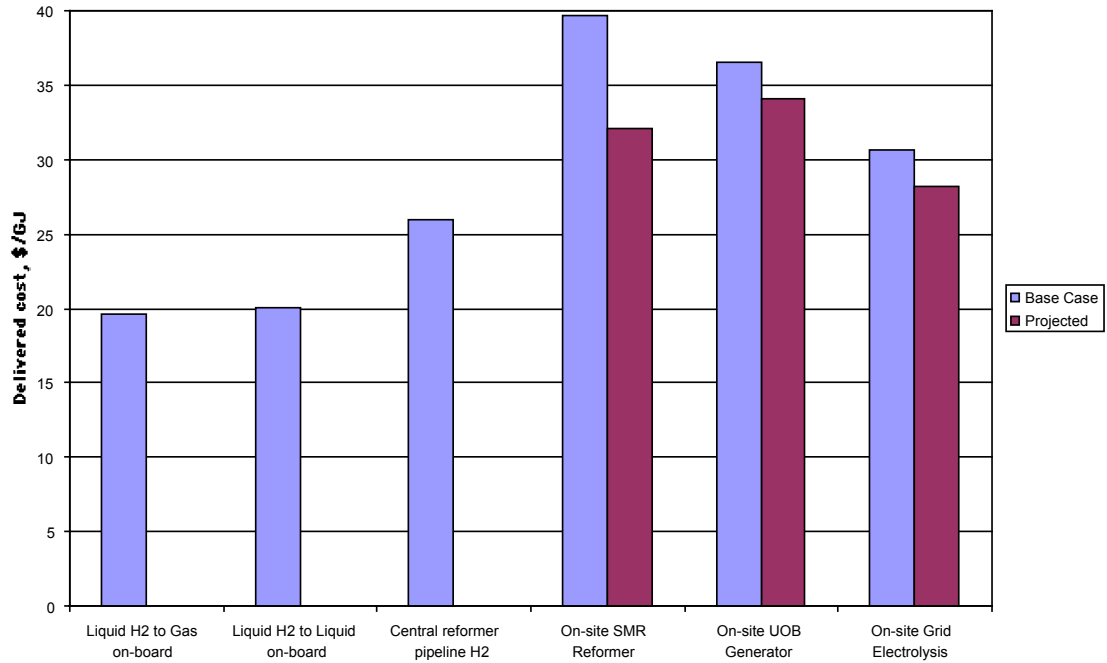


Figure 11. Delivered Hydrogen Cost of Alternatives With Projected, Future Capital Costs for On-Site Generators

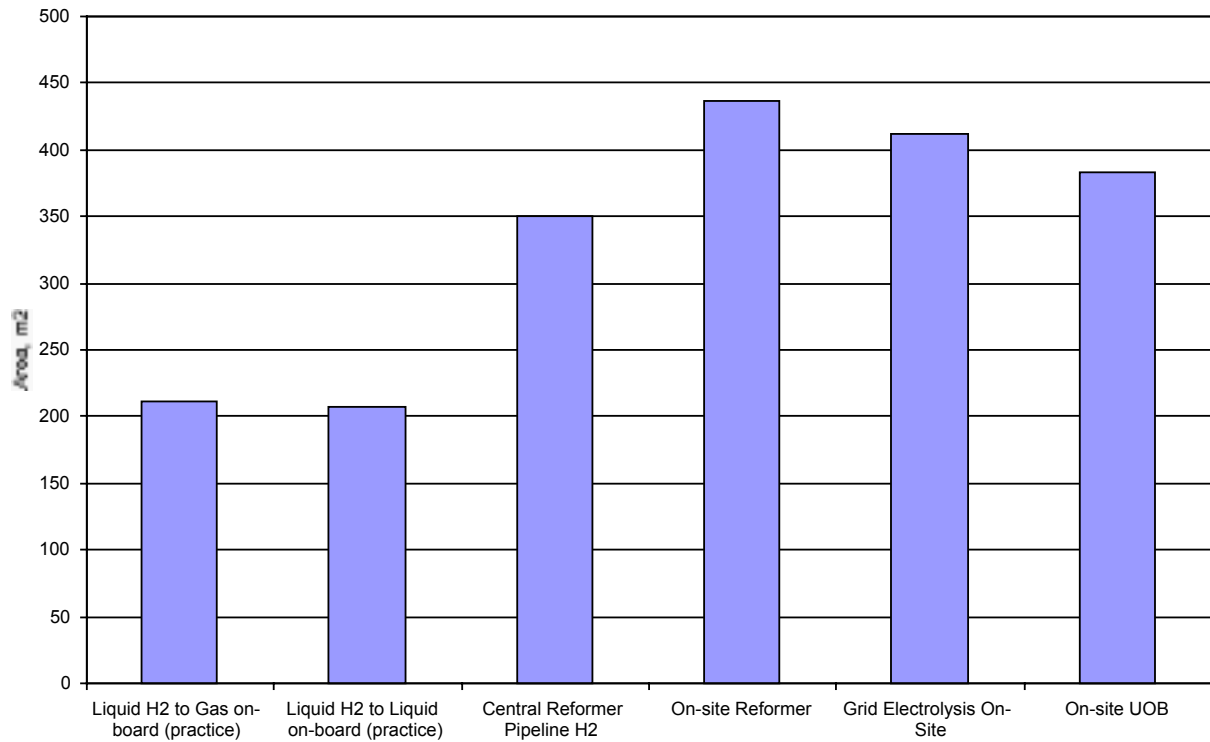


Figure 12. Footprint Areas Required for the 6 Base Cases, 100 Passenger Vehicles Per Day

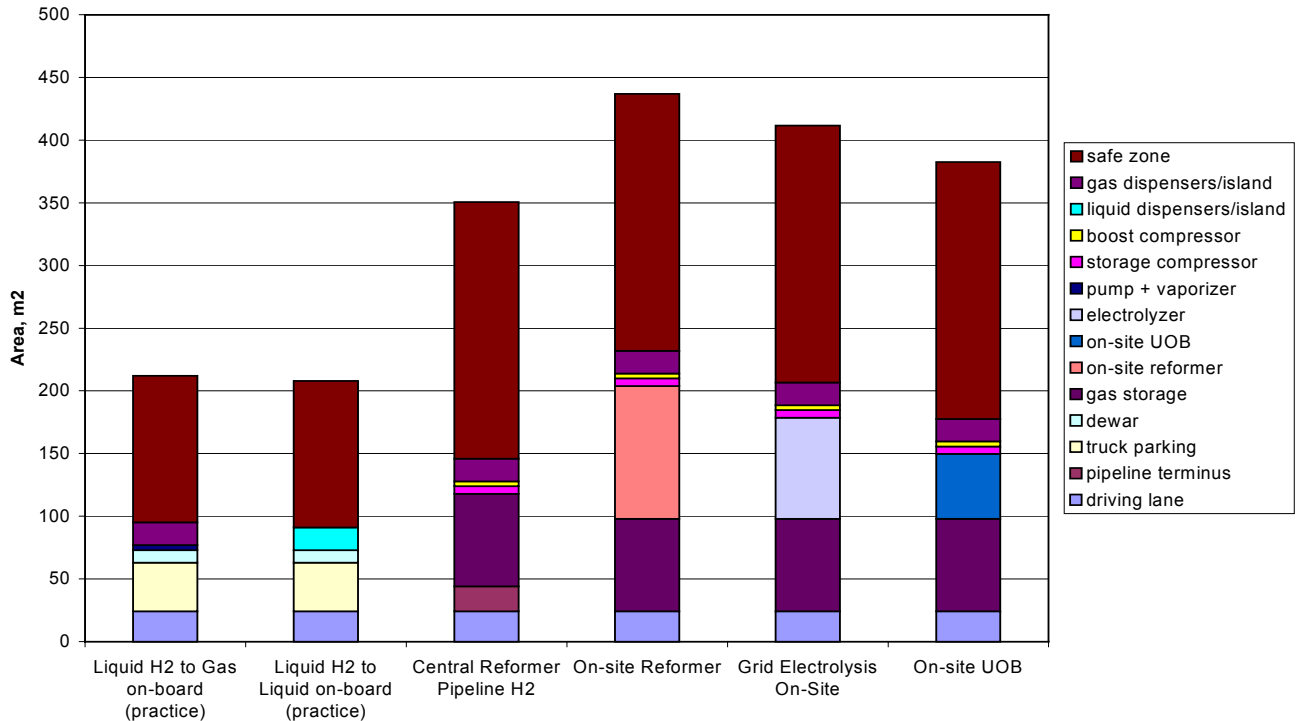


Figure 13. Footprint Components for the 6 Base Cases

Figure 14 shows the same components but includes liquid storage cases with a keep-out zone perimeter of 50 ft (15 m) around the liquid dewar. Although this is the value specified by U.S. fire codes, it is not observed in practice. However, if this perimeter were maintained for neighborhood refueling stations, then liquid storage would be at a severe disadvantage.

From the analysis done to date, the major conclusions are:

- The capital cost of the on-site generation options is greater than bulk delivery of hydrogen to the fueling station. This assumes existing delivery infrastructure. The cost trend for the on-site generation technologies is downward.
- The small steam methane reformer is the most costly option; however there is growing commercial development of this technology.
- The delivered cost of hydrogen is also generally greater for on-site production of hydrogen.
- When the station is underutilized, the delivered cost of hydrogen from all sources is always greater because the capital, O&M, and labor charges are independent of the utilization factor.
- For on-site generation alternatives, where the capital investment is higher, the delivered cost of hydrogen is even higher when the utilization factor is less than 100%.
- Footprint areas for on-site hydrogen generation alternative are somewhat greater than for bulk hydrogen delivered by pipeline.
- Footprint areas for liquid storage options are highly dependent on the safety keep-out zone requirements, and could be prohibitively large if conservative perimeters are maintained.

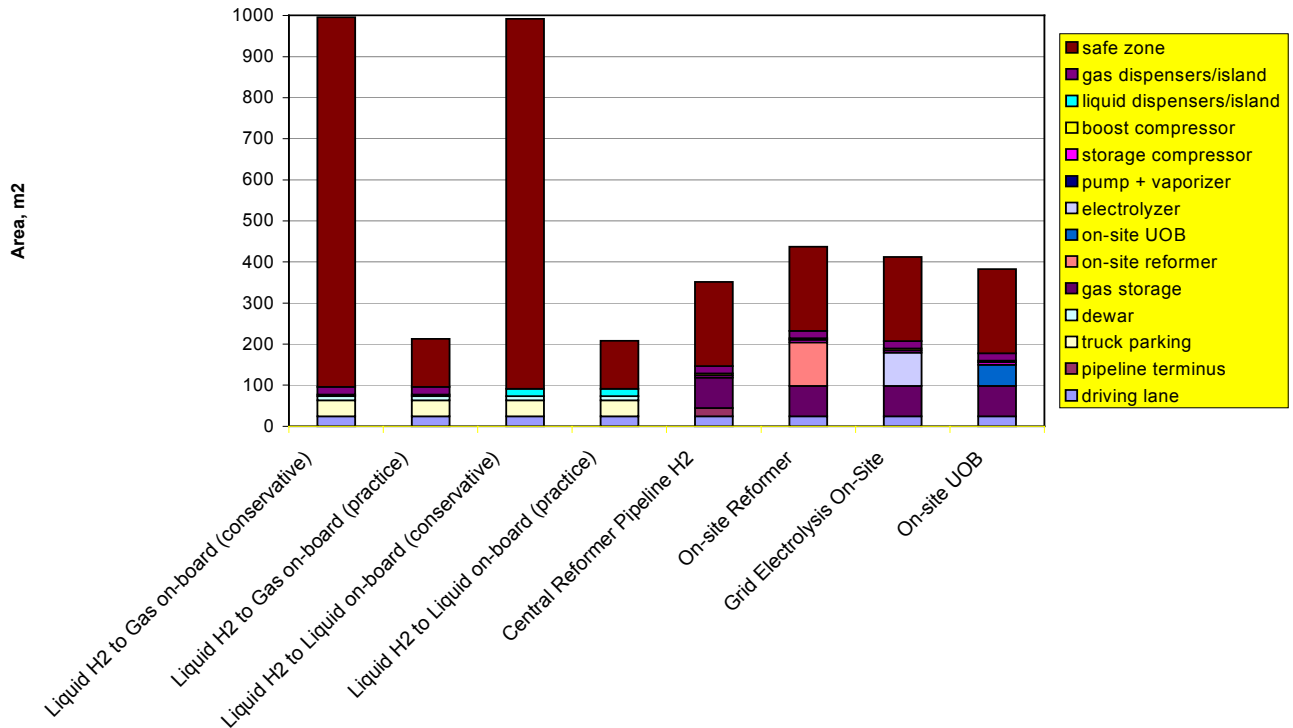


Figure 14. Footprint Components Including Expanded (Conservative) Safety Zone for Liquid Hydrogen

Discussion and Conclusions

This analysis suggests that early stations may be based on the use of delivered hydrogen, with on-site generation coming in as costs of these technologies decrease.

Future Analysis

This project is ongoing; the following analyses are in progress:

- Calculations of fuel economy and system efficiency
- Implications of alternative on-board storage alternatives, especially with regard to weight
- Implications of alternative power plant selections, i.e., fuel cell compared with an internal combustion engine
- Implications of on-board processing, with regard to both weight and cost per driving cycle
- Investigation of global driving cycle variations
- A comparison of overall emissions
- Sensitivity analysis to natural gas and electricity prices
- Consideration of renewable sources of grid electricity
- Analysis and impact of upstream technology developments, especially hydrogen pipelines and large-scale SMR production

All of these analyses are being coordinated with other efforts of the IEA Hydrogen Programme, so that cost and performance assumptions are consistent. The emissions analysis is being undertaken in conjunction with the efforts of the European Union Joint Research Center in Ispra, Italy.

Acknowledgments

The author acknowledges useful input from other members of the Hydrogen Annex 13, especially Arend de Groot of ECN-Netherlands and Jean Dubé of Stuart Energy Systems, Canada.

References

- Abele, A. R. and Niedzwiecki, A. P. 2001. "Quantum's Experience – Leveraging DOE Funding to Accelerate Development and Commercialization of Advanced Hydrogen Storage Technologies." *Proceedings of the 12th Annual U.S. Hydrogen Meeting*. Washington D.C. National Hydrogen Association.
- Amos, W. A. 1998. *Costs of Storing and Transporting Hydrogen*, NREL Report No. NREL/TP-570-25106.
- BMW / ARAL. 2000. Munich Airport Hydrogen Project literature.
- Bracha, M. 2001. Personal communication. Linde-AG (Germany).
- Edlund, D. 2000. "A Versatile, Low-Cost and Compact Fuel Processor for Low Temperature Fuel Cells." IdaTech web site: www.idatech.com.
- Edlund, D. February 2001. Personal communication. IdaTech, Bend, OR.
- Fairlie, M. J. and Scott, P. B. 2000. "Filling Up with Hydrogen 2000." *Proceedings of the 2000 DOE Hydrogen Program Review*. San Ramon, CA. Also, Stuart Electrolyzer Corporation. 2000. Stuart web site: www.electrolyser.com.
- Hummel, G. 2001. Personal communication. Hydrogen Burner Technology, Long Beach, CA. Also, HBT. 2000. Technical specifications. HBT web site: www.hydrogenburner.com.
- Iannucci, J. 2000. Personal communication. Distributed Utility Associates, Livermore, CA.
- James, B. D., Lomax, F. D., and Thomas, C. E. 1997. *Integrated Analysis of Hydrogen Passenger Vehicle Transportation Pathways*. Activity Report, NREL Subcontract No. AXE-6-16685-01.
- Keller, J. February 2001. Personal communication. Sandia National Laboratories, Livermore, CA.
- NFPA. 1999. *Standard 50A: Standard for Gaseous Hydrogen Systems at Consumer Sites and Standard 50B: Standard for Liquified Hydrogen Systems at Consumer Sites*. National Fire Protection Association, Inc.
- Ogden, J. M., et al. 1995. *Hydrogen Energy System Studies*, DOE Report, Contract No. XR-11265-2.

Ogden, J. M. 1999. "Hydrogen Energy System Studies." *Proceedings of the 1999 U. S. DOE Hydrogen Program Review*. Denver, CO.

Richards, J. February 2001. Personal communication. Praxair.

Roby, R. 2001. Personal communication. Combustion Science and Engineering, Inc. Columbia, MD.

Thomas, C. E. and James, B. D. 1998. *Analysis of Utility Hydrogen Systems*, DOE Report, Contract No. ACG-8-18012-01.

Weinmann, O. 2001. Personal communication. HEW Corporation (Germany).

TECHNICAL EVALUATIONS OF DOE PROJECTS AND STORAGE DATABASE

**Edward G. Skolnik, Jennifer Miller, and Christina Y. TerMaath
Energetics, Incorporated
Washington, DC 20024**

Abstract

This paper discusses the methodology and results of a series of nine technical analyses performed by Energetics during the time period April 2000 – April 2001. These site-visit-based analyses of hydrogen technology projects are the latest in a series of over thirty evaluations performed under contract to the DOE Hydrogen Program over the past five years. The results presented in this paper are general in nature; specifics are left to the individual reports on each project.

In addition, this paper discusses the development of a database of hydrogen storage projects. This database is meant to put in one place, information on all hydrogen storage projects, past and present, domestic and international, public and private. In addition, a second database was assembled that identified individuals who would find the storage database of use and interest – hydrogen stakeholders. A total of 112 hydrogen storage projects, and 493 stakeholders were identified in this ongoing process.

Introduction

The work being described here was performed under two different contracts. One involves technical analysis of currently funded DOE/H₂ projects. The second focuses specifically on hydrogen storage technologies. Both of them involve performing on-site technical analyses for the benefit of hydrogen stakeholders. The first contract called for ten site-visit analyses to be performed during the first year of the contract (July 2000-July 2001). The second called for three site visits to storage-related projects, plus the additional development of two databases: one to identify hydrogen stakeholders and a second to identify hydrogen storage projects that have been performed over the last several years in the U.S. and abroad. This paper first discusses the total of nine site visits (six on one contract, three storage visits on the other) completed prior to the Annual Review, and then discusses the databases.

Technical Analyses

Background/Approach

For the past several years, Energetics has been performing site-visit-based technical analyses. The reports based on these analyses have provided hydrogen stakeholders with an in-depth view of research conducted at national laboratories, universities, and industry in support of the U.S. Department of Energy (DOE) Hydrogen Program. The reports have an extra benefit of providing to the Hydrogen Annual Peer Review Panels the type of in-depth, impartial, independent information that cannot be obtained in a 20-30 minute presentation at the Annual Peer Review.

Once a project is chosen for technical assessment, a literature review is performed on the subject. This includes a review of the last two or three years of Annual Operating Plan submittals, monthly reports, the Annual Review paper, reviewers' consensus comments from the past few years, publications in journals by the research group, and journal publications on the same or similar topics by other researchers. The Principal Investigator (PI) is then contacted, and an on-site visit is arranged. A set of topic questions or discussion points is then drawn up and sent to the PI one to two weeks prior to the visit. These questions form the basis for a major part of the discussion during the site visit.

During the site visit a tour is requested, preferably with a demonstration of the experimental process(es) as well as a presentation by the PI on the project and its status. The visit also includes discussions based on the topic questions and any other issues that may result from the tour, demonstration, and presentation. The on-site visit may last from a half-day to over a full day. Following this, Energetics prepares a detailed report, which is made available to the public.

Assessments Performed

By April 2000, Energetics had performed a total of 19 site visits/technical evaluations of hydrogen R&D projects. These projects are shown in Table 1.

Table 1. Technical Assessments Performed Prior to April 2000

Project	Performing Laboratory	Date of Visit
Enzymatic Conversion: Biomass-Derived Glucose to Hydrogen	Oak Ridge National Laboratory	Feb. 1996
Hydrogen from Catalytic Cracking of Natural Gas	Florida Solar Energy Center	Feb. 1996
Hydrogen Manufacture by Plasma Reforming	Massachusetts Institute of Technology	April 1996
Photovoltaic Hydrogen Production	U of Miami	May 1996
Hydrogen Storage in Carbon Nanofibers	Northeastern U	Dec. 1996
Carbon Nanotubes for Hydrogen Storage	National Renewable Energy Laboratory	June 1997
Storage and Purification of Hydrogen Using Ni-coated Mg	Arthur D. Little, Inc.	June 1998
Hydrogen Transmission and Storage with a Metal Hydride Organic Slurry	Thermo Power, Inc.	June 1998
Thermal Management Technology for Hydrogen Storage	Oak Ridge National Laboratory & Materials and Environmental Research, Inc.	August 1998
Improved Metal Hydride Technology	Energy Conversion Devices, Inc.	August 1998
Hydride Development for Hydrogen Storage	Sandia National Laboratories (CA)	Sept. 1998
Biomass to Hydrogen via Fast Pyrolysis and Catalytic Steam Reforming	National Renewable Energy Laboratory	Dec. 1998
Hydrogen Separation Membrane Development	Savannah River Technology Center	March 1999
Hydrogen Production by Photosynthetic Water Splitting	Oak Ridge National Laboratory	March 1999
Bioreactor Project	University of Hawaii	July 1999
Insulated Pressure Vessels for Cryogenic Hydrogen Storage	Lawrence Livermore National Laboratory	September 1999
PEM Fuel Cell Stacks for Power Generation	Los Alamos National Laboratory	January 2000
Hydrogen from Biomass in Supercritical Water	University of Hawaii	March 2000
Hydrogen Storage Tank Liners	Lawrence Livermore National Laboratory	March 2000

During the period between the FY 2000 and FY 2001 Annual Peer Review, Energetics performed a total of nine technical evaluations based on site visits. These are listed in Table 2.

Table 2. Technical Assessments Performed April 2000 – April 2001

Project	Performing Laboratory	Date of Visit	
Hydrogen Storage in Metal Hydride Slurries	Thermo Technologies	August, 2000	S
Conformable Tanks for Hydrogen Storage	Thiokol	September, 2000	S
Solar Photocatalytic Hydrogen Production From Water Using A Dual Bed Photosystem	FSEC	September, 2000	T
Production of Hydrogen Through Electrolysis	Proton Energy	December, 2000	T
Plasma Reforming	MIT	December, 2000	T
Carbon Nanotube Materials for Hydrogen Storage	NREL	February, 2001	T
Hydrogen Composite Tank Program	Quantum (IMPCO)	February, 2001	S
Maximize Photosynthetic Efficiencies and H ₂ Production In Microalgal Cultures	University of California, Berkeley	February, 2001	T
Low-cost Reversible Fuel Cell System	TMI	March, 2001	T

T = Performed under contract DE-FC36-00GO10602 (Technical Analysis of Funded Projects)

S= Performed under contract DE-FG03-00SF22103 (Comprehensive Summary of Hydrogen R&D Technologies—Storage)

Results/Conclusions

A compilation of the individual reports will shortly be made available. For the purpose of this paper, we will make some general observations:

- Many of the laboratory-scale projects are in great need of independent laboratory measurements. This has been true for a long time, especially in cases where product is limited and claims are great. Researchers are sometimes reluctant to provide material to others, citing, among other things, a potential loss of competitive edge to the tester, skepticism in the tester's ability to handle the material properly to get accurate results, or the lack of sufficient material to spare.

Based on what we've seen and heard during the site visits, we believe that we need to overcome these objections and perform independent testing. Lack of sufficient material should not be an excuse. If there is only enough material for one measurement, it should be done by the independent laboratory. If the PI has issues with the independent laboratory, then the PI should be on-site for the test. The mechanism has to be satisfactory to all – but a mechanism is needed.

- Several of the PIs are concerned by what they feel to be inequalities with how their work is viewed. At more than half of the site visits, PIs expressed concern with matters such as: other organizations taking over their projects, being peer reviewed by competitors, and having tests and measurements being run by competitors. The disruption of research due to on-again, off-again funding is another complaint.
- The average researcher in the laboratory still (as last year) does not have a clear concept of: what the DOE Hydrogen Program direction is, who's who in the program and related DOE programs, where the overall hydrogen community stands, etc. (Example: one PI was unaware that the old DOE Office of Utility Technologies (OUT) had become the Office of Power Technologies (OPT) over a year earlier).

This year the researchers were given a rare opportunity. Due to an earlier cancellation, the Hydrogen Technical Advisory Panel (HTAP) Spring Meeting was held immediately before the Hydrogen Annual Peer Review Meeting. As a result, Peer Review attendees who came a day earlier were able to attend the HTAP meeting and get a better understanding of what the hydrogen community is thinking (in last year's Annual Review presentation we had recommended that PIs attend HTAP whenever possible). The HTAP meeting was better attended than ever, but a number of PIs had not gotten the message about the schedule change.

- Pressurized hydrogen storage tanks are a reality. Many of the questions about safety, cycling, and aging – areas that have been of great concern – are being answered. It appears that these pressurized tanks will fulfill at least the near-term requirements for on-board hydrogen storage.
- Progress, albeit slow, is being made on many of the long-term technologies being researched by the Program – the “pure hydrogen” aspect. These are, basically, the photobiological and photoelectrochemical hydrogen production technologies and the carbon nanotube hydrogen production technology (hydride storage is likely in a shorter timeframe).

During the year Energetics had a chance to investigate some of these projects. Put simply, without dwelling on the individual projects, to maximize the chances of success, more needs to be done. There is now a second nanotube project; perhaps there needs to be even more. We are learning that there is much in this area that we did not (and do not) know. In the photobiology area, three laboratories are collaborating (to a degree) on different aspects of using mutants of the alga *Chlamydomonas reinhardtii* to develop water-splitting, hydrogen-producing (on a commercial scale) organisms. Perhaps, a second group could be identified that could go down a different research path.

Regardless, one thing is known. The goal of the hydrogen production from water research must be to make hydrogen; the goal of the hydrogen in nanotubes research must be to store hydrogen. The rest of us must have patience.

- Many of the projects are encouraged to (or obligated to) engage in agreements with non-Federal partners. This has the very positive results of leveraging money, building the technical knowledge base through collaboration, and increasing the overall hydrogen stakeholder base. However, PIs point out the negative aspects as well. It is hard to work for two masters. Partnering often results in a redirection (or even a misdirection) of the intended research.

Databases

Background

DOE has been funding research on various hydrogen storage technologies for many years. The U.S. government, however, is just one of the many entities interested in pursuing these technologies. Many domestic and international corporations, universities, and governments are interested in the advantages hydrogen storage can provide. During FY 2001, Energetics developed a database of the research that has been or is being conducted on hydrogen storage technologies. This database is meant to gather together, all hydrogen storage projects, past and present, domestic and international, public and private. In an effort to identify the hydrogen community to whom this information should be imparted, Energetics also put together a database of hydrogen stakeholders.

Methodology

Two linked Microsoft Access databases were created to store the stakeholder and storage information. The stakeholder database includes the information on hydrogen stakeholders from academia, industry, utilities, project developers, and state and local officials. The information was obtained from attendee lists at such meetings as the Annual Hydrogen Peer Review Meeting, the Annual National Hydrogen Association Meeting, and the semi-annual Hydrogen Technology Advisory Panel Meeting. These were augmented by mailing lists from meetings on related topics such as fuel cells, wind, biomass energy, and photovoltaics as well as Internet searches.

The storage database was created to store the information on hydrogen storage technologies. This database is linked to the stakeholder database to allow for the easy connection of a stakeholder's contact information with details of their research project. The hydrogen storage projects were separated into three types of technologies: carbon structures, hydrides, and physical storage. Information on the storage technologies came from:

- U.S. DOE Hydrogen Program
- Activities from other government agencies
- University and private research (where available)

- International activities as determined from the International Energy Agency (IEA) Hydrogen Implementing Agreement Annexes on storage and on integrated systems
- Internet resources

The stakeholder database contains contact information for 493 domestic and international members of the hydrogen community. These stakeholders can be sorted according to the type of research they are or have been involved in (e.g., production, storage, utilization, validation, analysis and outreach). Each stakeholder has been designated as industry, academia, or government. Other information such as whether the stakeholder is an HTAP member, or former HTAP member is also included. These designations allow for additional sorting options.

A total of 72 research institutions have been identified as conducting studies on hydrogen storage. These institutions are located in 16 different countries (see Table 3) and are responsible for 112 hydrogen storage projects. Just under half of all the hydrogen storage projects that we have identified have been conducted within the U.S. Germany represents the next highest country, accounting for 22% of all research on hydrogen storage technologies. The storage medium being studied the most is hydrides (47%), followed by physical storage devices (30%).

Table 3. Hydrogen Storage Projects by Country and Storage Medium

Country	Carbon Structures	Hydrides	Physical Storage	Total
Australia		1		1
Belgium			1	1
Bulgaria		1		1
Canada		3		3
China	1			1
Denmark			1	1
Finland		2		2
France			2	2
Germany	1	14	10	25
India		1		1
Japan	1	3	2	6
Russia		1		1
Switzerland	1	4		5
UK		1		1
Ukraine		1		1
USA	19	19	11	49
Unknown	2	2	7	11
Total	25	53	34	112

Research on hydrides as a hydrogen storage medium dates back to 1974 when the Public Service Electric Gas Company in Newark, NJ, investigated the possibilities of using hydrogen during

peak demand periods. From then on, research was conducted on hydrides to serve in both stationary and vehicular applications. The stationary applications considered are for utility primary power and peak-shaving applications as well as stand-alone solar and wind power applications. The vehicles range from mining vehicles to buses.

The database includes 25 research projects on carbon structures. The majority of these are directed towards hydrogen adsorption onto carbon nanofibers (see Table 4). For the purposes of this database, fullerene hydrides have been considered as a carbon structure. These projects could also be classified as hydrides, but due to inherent differences between typical hydrides (using metals) and these studies (using carbon) we choose to identify them as carbon structures.

Table 4. Hydrogen Storage Research by Storage Medium and DOE Funding

Storage Type	Total	DOE Funded
Activated carbon	2	1
Fullerene	3	1
Fullerene hydride	2	2
Nanofiber	4	3
Nanotube	12	2
Nanotube & carbon slit pores	1	
Undefined	1	
Metal hydride	52	8
Metal hydride for hydrolysis	1	1
Compressed gas	21	7
Compressed gas – liquid compressed cryogenic.	1	1
Liquid compressed cryogenic	12	
Total	112	26

Physical storage technologies are by far the most developed form of hydrogen storage. As with all types of hydrogen storage, research is currently being done to increase the percent weight and/or volume of hydrogen while lowering the total weight of the system.

Fifteen different organizations, shown in Table 5, have been identified as funding research on hydrogen storage technologies. The U.S. DOE is recognized as supporting just less than one quarter of all the storage projects included in the database. The majority of the funding agencies are international organizations and governments.

The stakeholder and storage databases will shortly be available for stakeholder use.

Table 5. Agencies Funding Hydrogen Storage Research

Domestic	International
Army Research Office	Aventi Res. & Technol
Augusta-Richmond County Public Transportation	AVL LIST GmbH
Honda R&D Americas, Inc	Bavarian State Ministry for Economic Affairs, Transport and Technology (BstMWVT)
National Science Foundation	BRUKER Analytischer Messyechnik GmbH
Petroleum Research Fund of the American Chemical Society	European Commission (EC)
U.S. Department of Energy and its National Laboratories	Free State of Bavaria public funds
	German Federal Ministry for Research and Technology
	MECU/German budget
	Fundacion Antorchas

Acknowledgement

The work presented here is supported by the U.S. Department of Energy under contract numbers DE-FC36-00GO10602 and DE-FG03-00SF22103.

OUTREACH ACTIVITIES

**Laura A. Kervitsky
SENTECH, Inc.
Bethesda, MD 20814**

Abstract

In response to two separate solicitations for Hydrogen Program outreach, SENTECH proposed and was awarded two contracts, a grant through the Oakland Field Office and a cost-shared Cooperative Agreement with the Golden Field Office. Between the two contracts SENTECH has four distinct outreach tasks. These tasks represent both a continuation and extension of on-going outreach activities and newly created activities.

The underlying principal of the outreach activities is to disseminate timely and relevant information on the potential applications of hydrogen energy to as many audiences as possible. The SENTECH outreach activities are designed to reach defined audiences through electronic, written, and oral communications, as determined to be most effective for conveying technical and non-technical information. However, these communications materials are not limited to the audience for which they have been created, thereby enabling the development of a greater portfolio of outreach materials to be used by the Hydrogen Program.

Objectives

The dissemination of information on hydrogen energy is becoming increasingly important as recent technology progress makes hydrogen a realistic energy option. Just five years ago, hydrogen was considered "futuristic." Over the last five years, there have been significant advances in technology development and the formation of strategic partnerships to help bring hydrogen technologies to commercial markets. Further evidence of the real shift in the hydrogen timetable can be found in two recently formed, highly visible international collaborations; the California Fuel Cell Partnership and the Icelandic Hydrogen and Fuel Cell Company Ltd.

These challenges to the notion that hydrogen is a long-term energy option must be accompanied by a more aggressive and comprehensive outreach effort. Recognizing this need for outreach, the Hydrogen Program developed an Outreach and Communication Plan in 1998 based on recommendations of the Hydrogen Technical Advisory Panel. In FY2000, the Hydrogen Program issued two separate solicitations for outreach activities, seeking projects in keeping with the objectives of the Plan.

The outreach activities proposed and now being conducted by SENTECH are designed to complement the research and development work funded by the DOE Hydrogen Program by presenting the technical achievements and validations of hydrogen energy technologies. The activities also raise the visibility of the Hydrogen Program within new audiences, not reached through traditional communication mechanisms and establish communication channels that will enable continued two-way dialog with these audiences in future years. Between the two contract mechanisms, SENTECH has four distinct outreach activities in FY2001.

- Producing two glossy brochures for distribution at two relevant conferences
- Holding ten face-to-face meetings with potential stakeholder organizations not yet involved in the hydrogen community.
- Conducting two educational forums on hydrogen energy for middle school students.
- Designing an Internet database of international hydrogen energy projects.

Current Year Progress

For some of the tasks, SENTECH has picked up where previous work left off, while for other tasks SENTECH has brought new innovative ideas on communication and outreach. In this discussion, a review of the current year progress on each of the four tasks will be presented followed by an overview of future activities within each task area.

All four of the outreach tasks are on track to be successfully completed by the end of the two contract periods.

Communication Documents

SENTECH identified two timely and relevant topics for the production of glossy brochures – the on-site distributed generation and public transit markets for hydrogen energy technologies. These markets represent two near-term applications for hydrogen. The brochures answer the questions of safety, economics and benefits by presenting examples of successful applications of hydrogen in these two markets.

To date, the first brochure on public transit opportunities for hydrogen has been produced (Figure 1) and it was distributed along with other Hydrogen Program materials at the 7th National Clean Cities Conference and Expo in Philadelphia, PA in May 2001. SENTECH's Hydrogen

Power exhibit booth was one of approximately 50 booths on display at the conference. It is estimated that 1000 of the glossy brochures were distributed at the conference.



Figure 1: Inside and Outside of Hydrogen in Public Transit Brochure

The second brochure on the topic of on-site distributed power applications for hydrogen is in production and will be exhibited at the Tri-Service Power Expo to be held in San Diego, CA in June 2001. Again, the brochure and other program materials will be distributed at the Hydrogen Power exhibit booth.

These two particular conferences were identified for a number of reasons. SENTECH exhibited at the Clean Cities Conference and Expo in 1999 and was the only exhibit dedicated to hydrogen. Since 1999, with the completion of two hydrogen bus demonstrations in Chicago, IL and Vancouver, British Columbia (Canada), there was certain to be more coverage of hydrogen energy in transportation applications. The glossy brochure on public transit applications highlights the demonstration projects and presents additional information on the benefits of hydrogen as is appropriate for the Clean Cities audience.

The second conference was not originally identified in the contract. With the late award of the Cooperative Agreement the proposed conference had already taken place and SENTECH was required to find another appropriate conference for the second brochure. The Tri-Service Power Expo, sponsored by the Department of Defense, appeared to be a good candidate because of its specific fuel cell track and overall emphasis on on-site power. It also met the schedule and cost criteria of the contract. Additionally, the conference provides an opportunity for furthering the cooperation and collaboration of the DOD and DOE on hydrogen energy technologies.

While SENTECH researches the brochure content and sketches the initial concept, Vocon Design of Fairfax Station, VA is responsible for the final design, layout and printing.

Industry Meetings

The industry meeting task is a continuation of a highly successful industry outreach project began in 1995. Although the general format was maintained for the 2001 meetings, SENTECH has chosen to target organizations “outside” of the hydrogen community. Three particular industry segments were identified as candidates: architect/engineering firms, renewable energy firms, and industries considered to be “on-the-fence” because they do not see an investment in hydrogen technologies or infrastructure as being of business interest.

In the first round of meetings, five organizations in Portland, OR were brought together for a round table discussion on hydrogen. The participants in the meeting included TriMet, the transit agency serving Portland and the surrounding counties; Northwest Natural Gas, the primary natural gas utility; Lynn & Associates, an economic development consultancy; Portland Energy Conservation Inc., an energy efficiency off-shoot of the Portland Energy Office; and Wexler Associates, an energy project development firm.

The meeting successfully introduced the participants to the potential of hydrogen energy and helped to identify opportunities for niche hydrogen markets in transportation and stationary applications. As expected, there were concerns, particularly in the cost-benefit and long-term deployment of hydrogen energy technologies. Follow-up with the participants included providing additional background materials and contacts with appropriate hydrogen-related organizations.

The second set of industry meetings was held in Honolulu, HI. Three meetings were held Power Light Corporation, the Governor’s Advisor of Technology Development, and Renewable Energy Enterprise LLC. These organizations are exploring the renewable hydrogen energy option for stationary power applications in Hawaii.

Another 3 to 4 meetings will be scheduled over the next few months to complete the ten required meetings. As with the first two sets of meetings, the location and therefore participants in the meetings may be determined in part by SENTECH private sector business in order to fulfill cost-share requirements of the Cooperative Agreement. Trip reports for all industry meetings held will be prepared along with recommendations on follow-up with the participants.

Educational Forums

The educational forum task is also a continuation of a highly successful education outreach project began in 1995 under the expert leadership of Dr. Robert Reeves, Professor Emeritus, Rensselaer Polytechnic Institute. In the ensuing five years, Mary Rose Szoka de Valladares had evolved the educational forums to their current state.

SENTECH has followed the basic recipe of the previous educational forums but has brought in more outside experts to complement the educational content of the forum and has provided more hands-on opportunities for the students. The first forum, held in conjunction with the annual meeting of the National Hydrogen Association in early March 2001, involved seventy-five students from two District of Columbia public middle schools. In addition to the live hydrogen

chemistry show and laboratory, Dr. George Thomas of Sandia National Laboratories made a presentation on the technological challenges of storing hydrogen. A second feature speaker, Jason Samenow of the Environmental Protection Agency's Office of Atmospheric Programs, gave a presentation on the science of global warming and mitigation options.

The last half of the day was spent rotating through the learning center where the students had a chance to get their hands on some energy-related demonstrations; see the hydrogen chemistry laboratory up close; visit the NHA expo hall; and see the hydrogen fueled vehicles on display. The final activity was a career panel featuring Jeff Serfass, Executive Director of the NHA, Josh Pihl a recent college graduate with a chemistry major, and Linda Ulrich of BMW.

The second educational forum is scheduled for May 30 at Warrenton Middle School in Warrenton, VA. On the agenda will be the hydrogen chemistry lecture and laboratory, a presentation by Jim Ohi of the National Renewable Energy Laboratory on renewable energy technologies, and an extensive learning center where the students, usually numbering 100, will have the opportunity to see hydrogen technologies in action, including a DCH fuel cell and sensor, and the SunBug vehicle from SunLine Transit Agency.

As part of SENTECH's collaborative initiative in hydrogen education, the hydrogen chemistry lecture and laboratory was presented to 25 DC area teachers during the Teacher's Sun Day Program as part of the ASES 2001 Solar Energy Forum on April 21, 2001. SENTECH will continue to find opportunities to collaborate with the organizations involved in the Sun Day program including Florida Solar Energy Center, National Energy Education Development Program, NASA, EPA, Alliance to Save Energy, Department of Education, and many others.

For all schools participating in the educational forums and the Sun Day Program, copies of the Mission H₂ CD-ROM and Teacher's Guide were distributed along with information on the other educational materials produced by the Hydrogen Program.

International Hydrogen Project Database

The objective of this task is to create an electronic database for the Internet that provides access to information on domestic and international hydrogen energy research, development and demonstration activities. At present, there is no single source for such information. The International Energy Agency's Centre for the Analysis and Dissemination of Demonstrated Energy Technologies (CADDET) has two energy technology databases, CADDET-EE for energy efficient technologies and CADDET-RE for renewable energy technologies. Hydrogen energy technologies are excluded from these databases because they are not yet commercially available and there is uncertainty as to where hydrogen would fit. However, because several hydrogen energy technologies are on the verge of commercialization and many others are in the later stages of research and development, SENTECH has undertaken the creation of a database modeled on the CADDET databases but specific to hydrogen energy technologies.

SENTECH has partnered with Breakthrough Technologies Institute (BTI) on this project. BTI brings to the project expertise in the development of electronic databases and websites. BTI's role is to create a searchable database using Microsoft Access. SENTECH's role is to research

projects for the database, create the website including securing the website domain, and uploading the database to the website.

SENTECH purchased the website domain name h2world.net and created a website logo (Figure 2). The program ColdFusion was selected as the interface between the database and Internet. SENTECH consulted with David Warner of NREL and David Pegg of AEA Technology (London), both of whom are involved in the CADDET databases for a recommendation on software for the database and upload. The recommendation was for Microsoft Access and ColdFusion. SENTECH has purchased ColdFusion and will be taking a training course the end of May.



Figure 2: Website Logo

SENTECH has developed the website format, incorporating photos and links to other websites to make the database site a one-stop-shop for hydrogen energy information. The launch date for the website will be in July 2001. At that time, SENTECH anticipates having a minimum of 35 international hydrogen energy projects in the database.

Future Plans

It is SENTECH's intent to seek continued funding for further development of the international hydrogen project database. The Cooperative Agreement with Golden Field Office is renewable for up to three years and future work will be proposed if funding is available.

Communication Documents

SENTECH proposes to take the two brochures produced in FY2001 and develop collateral topical workshops and or multi-media products. Additionally, SENTECH proposes to exhibit the Hydrogen Power booth at other relevant conferences to distribute the brochures, Hydrogen Program materials, and other informational materials produced by SENTECH and others.

Industry Meetings

SENTECH proposes continuing to target industries not currently involved in the hydrogen energy community but that have a stake. The ultimate end-point will be to facilitate the formation of teams to implement hydrogen energy projects. Groups not previously involved in the industry meetings are the environmental groups and community advocacy organizations. They represent a valuable and effective vehicle for educating the general public.

Educational Forums

SENTECH proposes to elevate the educational forums to a regional and then national level by utilizing telecommunications technology, particularly the Internet. Future forums may take place in large venues, such as at a college or a university, to take advantage of location and facilities, and to bring in more distinguished speakers. As the forums grow in substance and audience, they will be broadly publicized through appropriate media channels.

International Hydrogen Project Database

SENTECH proposes to further develop the website and update the information contained in the database to keep up with new and evolving projects. Based on initial feedback, modifications will be made as necessary to the search functions, data display, and website features.

SENTECH will also look for opportunities to further collaborate with the IEA and perhaps eventually integrate the hydrogen database with the existing CADDET database at some point in the future.

Acknowledgments

SENTECH would like to acknowledge the individuals who have contributed to the success of this year's outreach activities:

- John Wuilliez, Vocon Design - for artistic contribution to the glossy brochures.
- Robert Reeves, Rensselaer Polytechnic Institute – for consultation on the educational content of the forums.
- George Thomas, Sandia National Laboratories – for an excellent presentation on hydrogen storage at the NHA educational forum.
- Jim Ohi, National Renewable Energy Laboratory – for what is sure to be an excellent presentation on renewable energy at the Warrenton educational forum.
- Mary Rose Szoka de Valladares, DCH Technology – for continued dedication to the educational forums.
- Lara Neer and Tina Schneider, National Hydrogen Association – for invaluable assistance with planning and executing the NHA educational forum.
- Shawn Bennett, Breakthrough Technologies Institute – for making the hydrogen project database a reality.

Inventory and Gap Analysis of Federally Funded Research and Development Activities

**Carolyn C. Elam and Helena L. Chum
National Renewable Energy Laboratory
Golden, CO 80401**

Abstract

Technologies for hydrogen as an energy carrier and fuel have been funded by the U.S. government since the oil embargo of the early 1970's. Hydrogen's potential lies in its ability to serve as an energy carrier that can be consumed at the point of use with little or no pollution. It is not a primary energy source, rather an energy storage medium. When we speak of hydrogen, we are talking about its production, storage, and utilization. It can be produced from renewable or fossil resources. It can be used as a storage medium for intermittent and seasonal renewable technologies and plays an important role in the decarbonization of fossil fuels. It is a fuel for vehicles and propellant for space missions and weaponry. It is used for upgrading chemicals and in many metallurgical processes. The term "Hydrogen R&D" encompasses a broad scope of technologies. The maturity of technologies range from advanced defense and chemical industry applications to fundamental studies of hydrogen-producing microorganisms.

Introduction

Conducting an inventory of federal hydrogen research and development is important for understanding the status of technology development, minimizing duplication of effort and identifying gaps in the federal portfolio. Much effort has been invested in developing future energy scenarios and roadmaps that identify efforts needed to position us to meet future energy requirements. With today's strained R&D budgets, leveraging every available dollar becomes that much more important. Thus, the available interagency portfolio must be well understood and this information used when planning priorities for the coming years.

Methodology

A tiered categorization (taxonomy) is used to summarize those technologies that have been identified as necessary and/or applicable for realizing a hydrogen future. The taxonomy includes a broad range of near-, mid- and long-term technologies that fall under the heading of analysis, production, purification, storage, utilization or infrastructure and was developed in cooperation with the U.S. DOE and its Hydrogen Technical Advisory Panel (HTAP). The taxonomy is a living document that is updated as needs are identified and new technologies emerge. The first three tier levels of the taxonomy are shown in the Appendix.

The Rand Corporation developed (for the Office of Science and Technology Policy) a comprehensive annual database of the ongoing research and development projects sponsored by the twenty-four federal agencies. This Research and Development in the United States (RaDiUS) database compiles information about the efforts of the twenty-seven federal agencies at the project level. Additional database resources include the USDA Current Research Information Search (CRIS) and the DOE Office of Energy Bioscience. These three databases were searched for all research efforts related to hydrogen energy. The taxonomy was used for developing the search criteria. The results of these searches were merged into a single database.

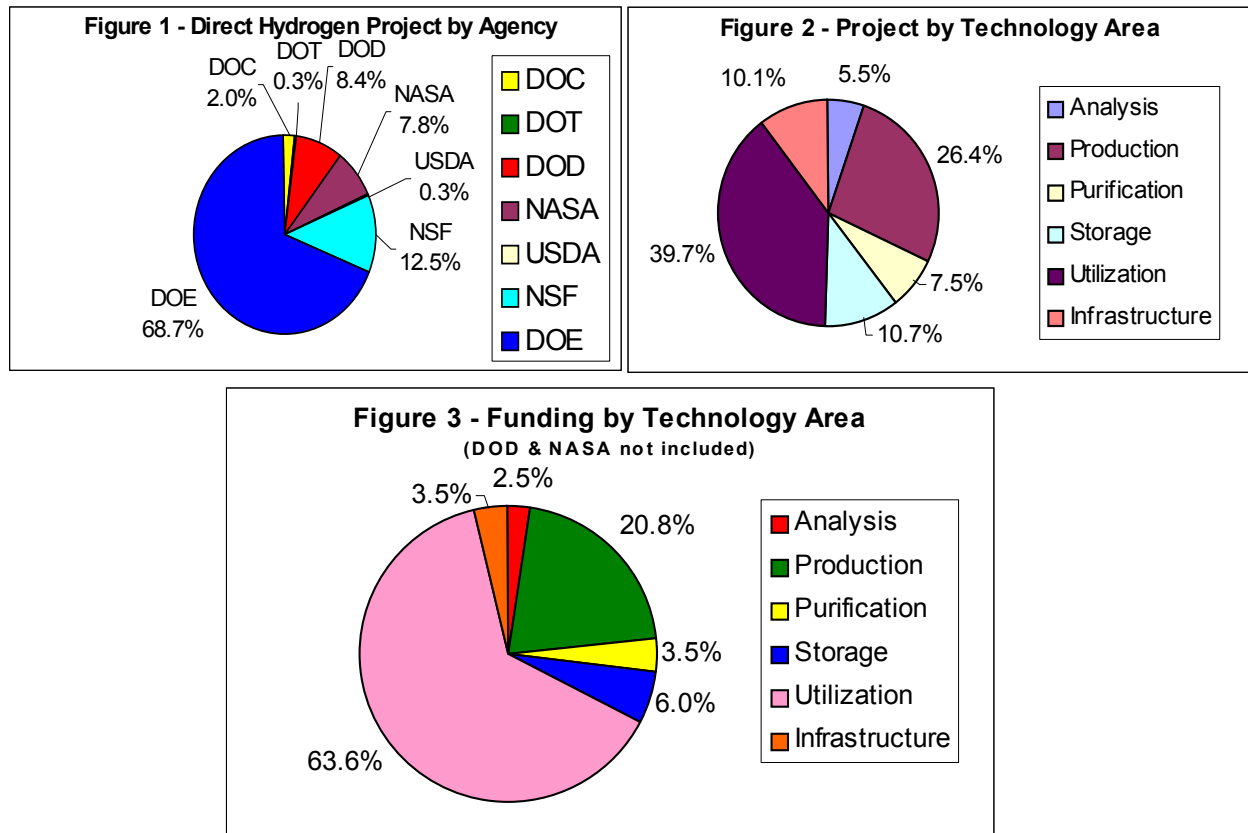
Fiscal year 1999 was selected as the funding year for the inventory, since this was the most recent funding year for which the database information was fairly complete. Even then, there were several records that did not contain FY99 funding information. For these projects, estimates were made based on the period of performance, total project funding and average annual funding. For the DOE, available documentation, including the DOE Office of Power Technologies' Hydrogen Program and NREL Annual Operating Plans, was used to validate project and funding information.

No funding information was available for the DOD and NASA (through the RaDiUS database or other easily accessible resources). This information will need to be obtained from the performer contacts on a project-by-project basis. Thus, DOD and NASA information only rolls up into the project counts for the inventory (they are excluded from the funding analyses).

Results

All records were reviewed and identified as directly related to hydrogen R&D or relevant to the development of hydrogen technologies. The records were then binned by technology area. Up to four tier levels were used to bin the individual records. Seven federal agencies were identified as

providing support for hydrogen R&D projects: Department of Commerce (DOC), Department of Defense (DOD), Department of Energy (DOE), Department of Transportation (DOT), National Aeronautics and Space Administration (NASA), National Science Foundation (NSF) and the U.S. Department of Agriculture (USDA). These agencies combined to fund a total of 426 projects that were identified as directly related (345) or relevant (81) to hydrogen energy R&D. Figure 1 shows the percentages of direct hydrogen projects by agency. The DOE accounted for more than two-thirds of the total funded projects. NSF provided the second greatest number of projects at 12.5%. DOD and NASA contributed similar numbers of projects, accounting for 8.4% and 7.6% of the total federal portfolio, respectively. The remaining agencies account for less than 3% of the total portfolio. By technology area (Figure 3), utilization and production dominate at 39.7% and 26.4%, respectively. Storage and infrastructure are next at around 10% each.



The non-DOD or NASA projects accounted for \$120 million directed towards hydrogen R&D. An additional \$8.9 million supported technologies relevant to hydrogen. The DOE provided nearly 90% of the total funding. The DOT and USDA accounted for less than 0.5% of the total funding, with the remainder nearly evenly split between the DOC and NSF. Nearly two-thirds of the total funding was directed towards utilization technologies, primarily fuel cell development (see Figure 3). Production was the next most supported research area. This trend is very closely mirrored within the DOE, which directed nearly \$70 million towards utilization technologies, compared to \$25

million for production and less than \$5 million each for the remaining areas. As would be expected, the DOC effort was also primarily directed towards utilization technologies. The NSF had a fairly balanced portfolio across all areas, although none received more than \$2.5 million.

Analysis

Analysis projects included development of cost models, technoeconomic assessments of technologies, and evaluation and optimization of integrated hydrogen systems. Feasibility studies and development of business plans for integrated hydrogen energy systems were also included in this area. The DOE is the primary funding source for analysis projects, with nearly \$3 million of effort. The NSF sponsored a small project (\$30K), for the conceptual design phase of a “sustainable homestead.” In all, 19 projects were directed towards analysis of hydrogen technologies/systems.

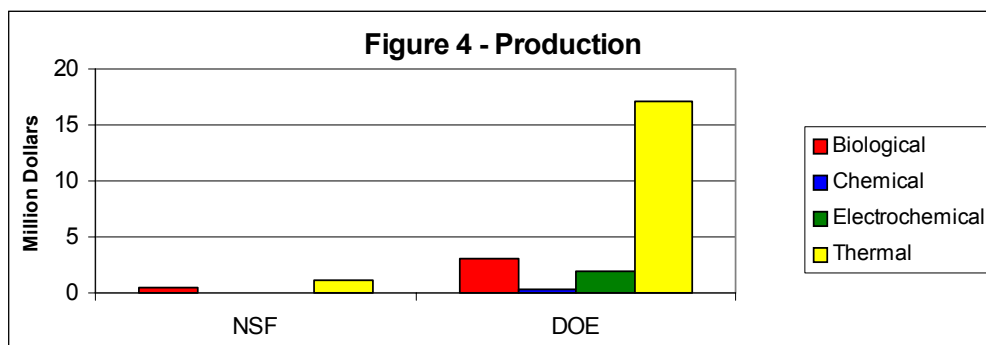
Production

Production routes are divided into four categories: Biological, Chemical, Electrochemical, and Thermal. Of the 91 direct production projects, 24 were biological, 4 chemical, 11 electrochemical and 49 thermal. The thermal routes include both renewable and fossil technologies. The DOD had 2 thermal production projects, one on supercritical water gasification of toxic wastes, the other on plasma reforming. The DOD also had several semiconductor development projects that were identified as relevant to electrochemical hydrogen production. The NSF supported 11 production projects, 5 biological, 5 thermal and 1 chemical (photochemical). Both fermentative and photobiological routes were included. The thermal routes included biomass and fossil gasification, pyrolysis of diesel fuels and reforming technologies. The DOE supported a total of 78 production projects: 19 biological, 3 chemical, 11 electrochemical and 42 thermal. The biological projects included 4 fermentation projects, 13 photobiological studies and 1 bioreactor development. The chemical projects were all photocatalytic work. All four electrochemical routes were supported, with photoelectrochemical and halide electrolysis receiving the greatest support. A total of 13 biomass and fossil gasification projects were supported. Membrane and reforming technologies were included in 9 projects each. Pyrolysis (5), solar thermal (2) and partial oxidation (1) accounted for the remaining projects. Overall, very little work is being done on chemical production routes. Likewise, there was only one partial oxidation project. Hydrogen production by photobiological organisms received a great deal of support, as did hydrogenase-based fermentation. However, there was only a single project dedicated to bioreactor development. Gasification and reforming received the greatest amount of support for the thermal routes, with 14 and 9 projects, respectively.

On a funding basis, thermal technologies received, by far, the greatest amount of support, with more than \$18 million, of which gasification received nearly half (see Figure 4). Biological routes received the next greatest level of support with \$3.5 million, \$2.7 million of which went towards photobiological studies. Again, funding information for the DOD was not available. Total production funding for the NSF and DOE was \$1.6 and \$23.3 million, respectively.

An additional 25 projects, for a total of \$3 million, were found to be relevant to hydrogen production. 15 of these (\$2.4 million) involved genetic modification of microorganisms. These projects generally concerned modification of the photosynthetic pathways of the microorganisms, but were not necessarily specific to the production of hydrogen. Other relevant technologies include

gas filtration technologies for gasification processes, development of semiconductor materials for electrolytic devices, and on-line thermal process monitoring.



Purification

Twenty-six projects and a total of \$4.1 million were directed by three agencies (DOC, NSF and DOE) towards developing purification technologies. Of this, no effort went towards improving the commercially-available absorbent-based technologies, nor in developing new technologies that utilize absorbent materials. One adsorbent project was funded for \$18 K. The remaining went to membrane technologies. Half of the membrane projects and funding went towards ceramic materials. There were an additional 5 metallic membrane projects and 1 polymer membrane project. Funding was split fairly equally between these two technologies. An additional NSF membrane project (\$72K) on zeolite adsorbants was identified that was relevant for hydrogen purification.

Storage

Storage is an area that receives a great deal of attention. It is considered to be one of the main limits for implementation of hydrogen technologies, particularly for mobile applications. The DOC, DOD, NSF and DOE all support the development of storage technologies. The DOC focused their efforts on metal hydrides. The DOD divided their efforts between absorbents, both chemical and metal hydrides; adsorbents, carbon nanotubes; and cryogenic storage, slush hydrogen. The NSF sponsored projects on metal hydrides, carbon nanotubes and zeolites. The broadest scope of projects came from the DOE with efforts in both chemical and metal hydrides, fullerenes, carbon nanotubes, compressors, conformable and composite tanks, cryopressurized storage and cryogenic vessels. More than \$2 million dollars went to support the single DOC metal hydride project. This is nearly 30% of the total storage funding. NSF projects received an average of \$92K each for a total of \$825K. The DOE sponsored \$4.3 million dollars of storage work, which results in a project average of just under \$230K.

An additional 14 projects were found that were relevant to hydrogen storage. Half of these focused on metal hydride material studies. DOD also sponsored a few projects on cryogenic hydrogen that were considered relevant to storage. In all, these projects accounted for just over \$1 million (not including the DOD project).

Utilization

The largest area for support was Utilization, with a total of 137 projects and \$76.3 million. With the exception of NASA, fuel cell development received the greatest amount of support by agency for a total of \$75.1 million. Nearly 90% of the total fuel cell funding support came from the DOE (excluding DOD and NASA for which funding information was not available). As would be expected, NASA's greatest area of emphasis was their combustion-based space propulsion technologies, although they also supported fuel cell development. DOE was the only other agency that sponsored combustion engine development.

No projects were found directed towards development of alkaline fuel cells. Molten carbonate, PEM and solid oxide fuel cells were fairly equally supported at \$27, \$24 and \$22 million, respectively. On a total number of projects basis, PEM fuel cells lead the way with 62 projects. Solid oxide is the next closest with 27, followed by molten carbonate at 9. There were 3 reversible fuel cell projects (2 NASA, 1 DOT) and 2 phosphoric acid projects (DOE). [The 2 phosphoric acid projects appeared to be close-out projects and, although they were active during FY99, they did not receive FY99 funding.] There were also several projects directed towards supporting fuel cell technologies, including material development and fuel processors.

An additional 33 projects and \$4.2 million were found that were relevant to hydrogen utilization. Direct methanol fuel cells made up the majority of these efforts. Other efforts include military applications (explosive devices), emission control and material studies.

Infrastructure

Infrastructure development will be essential for the deployment of hydrogen technologies. This is especially true for mobile applications. Both DOD and NASA sponsor projects on hydrogen safety. Projects cover leak detection, detonation modeling and material integrity. The NSF also supported hydrogen safety work, including detection and modeling and a case study of HBr contributions to ozone depletion. As with the other agencies, safety was the subject of the largest number of projects for the DOE. Projects covered codes and standards, sensors and modeling. Education (interface) was a close second. Projects on hydride slurry transport, refueler development and policy were also supported.

A total of \$4.2 million was spent by NSF and DOE on infrastructure development. Refueling received the greatest amount of funding support, with an average of around \$0.9 million per project. Safety received the next greatest amount of funding with a total of \$1.2 million, or an average of \$100K per project. DOE's hydride slurry transport projects average \$200K a piece for a total of \$600K. The six education projects totaled just over \$400K.

The only transport efforts sponsored by the agencies were hydride slurries. No testing and certification work was identified. Only one case study project was found for safety. For refueling, there were only the two projects sponsored by the DOE. There were no projects on interface standardization, nor on robotics. There was only one policy project and that was support for HTAP.

Eight projects and an additional \$430K were identified that were relevant to infrastructure development. This includes sensor control software, ballistic material embrittlement, modeling and nuclear safety.

Summary

Of the seven agencies that supported hydrogen R&D during FY99, the DOE was the primary non-defense funding source. The DOE's portfolio covered a broad- and fairly-balanced range of technologies. The greatest emphasis was placed on utilization technologies, primarily fuel cells. Production was another area that received a great deal of support. Little work was on-going in the area of purification.

The importance of storage for implementing hydrogen technologies suggests a strong development effort is required in this area. Compared to the single DOC metal hydride project, other agencies only provided moderate funding support to their storage projects. For FY99 the emphasis was primarily directed towards metal hydrides. Most of these materials have not yet shown storage capacities suitable for on-board applications. Thus, the broad portfolio of storage technologies is appropriate.

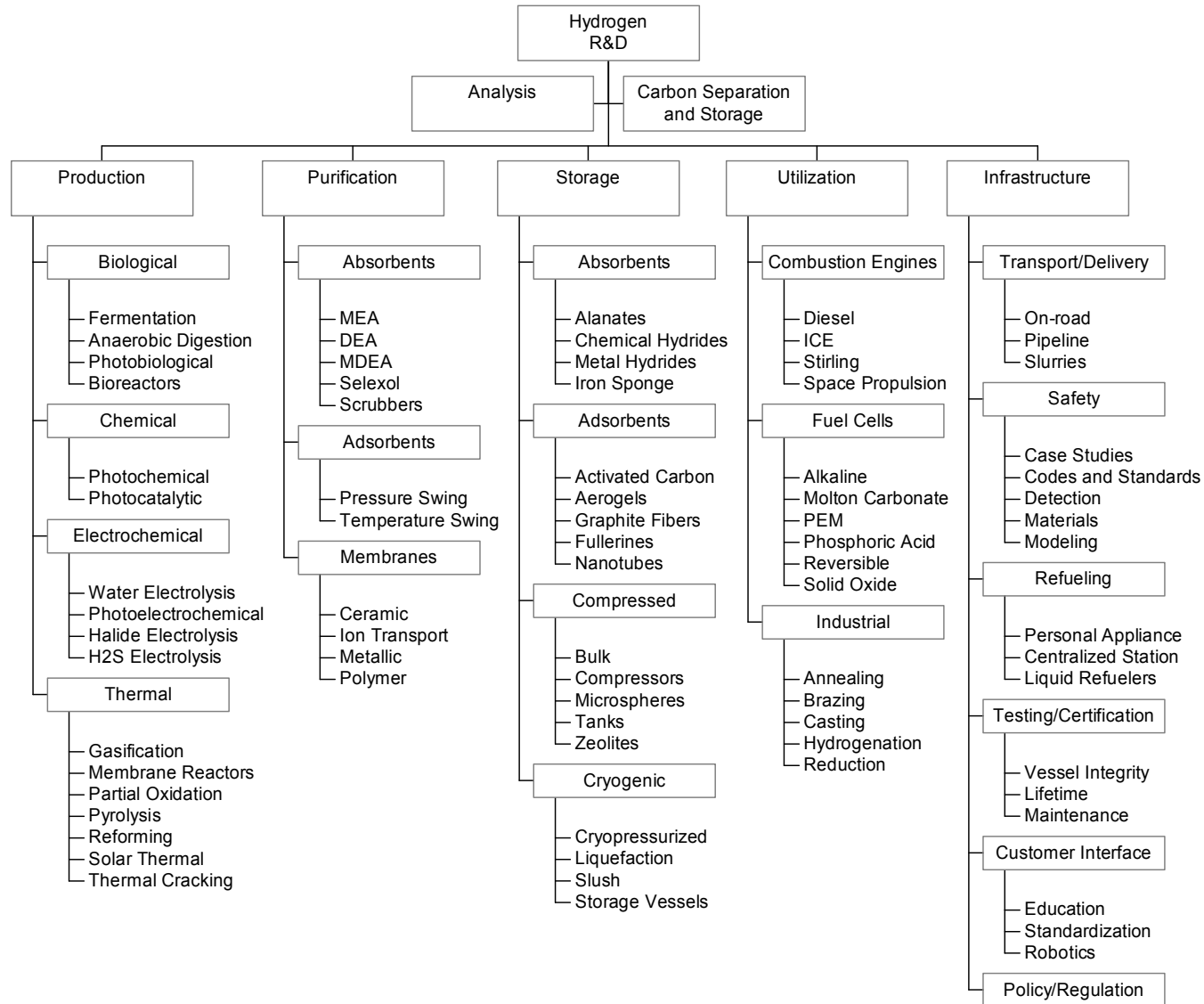
Infrastructure is another enabling area that requires significant emphasis. FY99 efforts were primarily directed towards safety. Although transport of hydrogen is commercially practiced, the existing infrastructure may not be suited to mobile applications. Transportation costs may also restrict segregated production and utilization. Testing and certification is an area that did not receive much attention. As utilization technologies become commercially ready, the testing and certification gap may become significant. Standardization and robotics are other areas for which no effort was being undertaken. For mobile applications in particular, this may inhibit public acceptance and practicality.

On the production side, a lot of effort was put into biological production routes. However, bioreactor development may be a gap for realizing the potential of these technologies. The portfolio was almost evenly distributed between fossil, biomass and direct renewable based production routes.

Still missing from the portfolio are state and local government activities. Many of these involve partnerships for the deployment of fuel cell vehicles. Funding information from the DOD and NASA is also not yet included. Finally, to truly evaluate the hydrogen R&D portfolio, the international picture must be understood, including the private sector investment.

In conclusion, hydrogen energy represents a broad cross-cutting group of technologies that are supported by several federal agencies in the U.S. Effective coordination through information exchange, facilitation of technology transfer, development of national and international collaborations and leveraging of resources can accelerate the path towards a hydrogen future. This coordination is currently hindered by a lack of shared knowledge of hydrogen energy-related R&D programs at both the federal and state/local levels.

Appendix - Hydrogen Taxonomy



NHA HYDROGEN SAFETY CODES AND STANDARDS ACTIVITIES

**Karen Miller
The National Hydrogen Association
Washington, DC 20036-5802**

Abstract

The NHA holds technical conferences with industry, academia, national laboratories, code officials and model building code organizations to bring experts together in a focused activity to develop and write new standards for hydrogen technologies. This includes such items as storage tanks, fueling nozzles, connectors, safety equipment, and other key components and integrated systems needed to move hydrogen into the energy sector.

The NHA supports the development of codes and standards for hydrogen in a variety of applicable organizations. This includes providing experts, technical reports, data and other information needed by the Code Officials to complete the development of these new codes.

Introduction

The NHA has been a catalyst to identify needed codes and standards for the commercialization and deployment of hydrogen energy systems since 1995. Key technical staff, Mr. Bob Mauro and Ms. Karen Miller, have facilitated workshops and working groups, as well as participating on behalf of the hydrogen industry in related standard processes where hydrogen safety expertise is warranted. This work has historically been performed through a partnership of government and industry, using NHA membership dues as cost-share for DOE Hydrogen Program funding. Over the past three years, DOE funding has been reduced, and in some critical areas, eliminated,

putting U.S. manufacturers of hydrogen energy systems and components at risk of competitive disadvantage in a global marketplace.

This paper describes the NHA's Codes and Standards (C&S) activities only. It will show that cooperation, collaboration, and outreach is vital to developing consensus documents. We now have a wealth of information on draft C&S efforts, including identification of needed expertise, which needs to be disseminated to building code officials such as National Fire Protection Association (NFPA), local fire marshals and the public.

Other activities that the NHA performs include an annual meeting and Education and Outreach (E&O) efforts. Because of reduced DOE support, the NHA currently lacks the funding to perform the level of outreach activities necessary to educate code officials on the state of hydrogen technologies, as well as the critical task of preparing the public for hydrogen energy systems.

Mr. Mauro, who has been involved in the NHA since its inception, has recently stepped down from the management of the NHA and has been appointed Technical and Policy Advisor to the NHA Board of Directors. He remains active in the ISO TC-197 portion of the NHA's codes and standards activities. His ongoing role in codes and standards for the NHA is described in this paper.

Discussion

The difference between "Codes" and "Standards" is described here, followed by a description of the role of the National Hydrogen Association in the development of both codes and standards.

Codes

Most jurisdictions have multiple requirements, such as building code, fire code, mechanical code, fuel gas code, local ordinances, and others. Some codes might restrict the use of hydrogen as a fuel through definitions of "Fuel Gas" or other code language. This could prevent the widespread use of hydrogen as a fuel. Several years ago, the NHA identified some suggested work where a cooperative effort between government and industry could pave the way for inclusion of hydrogen energy systems in these requirements. These efforts include:

- Identify key codes and standards affecting hydrogen use
- Evaluate if a change to the document is warranted
- Propose revision to key codes and standards
- Work with codes and standards organizations to implement the changes

The NHA is working with the International Codes Council (ICC) Ad Hoc Committee on Hydrogen. NFPA liaison has recently been established. By working with both organizations,

hydrogen energy systems, including refueling stations, fuel cells, reformers, electrolysers, etc., will be able to be sited, without the need for a cadre of experts to visit each local fire marshal.

Standards

Standards are created to assure consistency in safety and performance of a product or system. The NHA is involved in codes and standards because industry saw a need to assure public confidence in hydrogen energy systems and remove a barrier to commercialization, specifically a lack of consensus codes and standards. The NHA drafts standards where none exist, works with other groups on related standards to provide hydrogen safety expertise, and remains active in both National and International standards development.

Goals and Objectives – Long-Term

The NHA's long-term goals and objectives are:

- To facilitate the development of a hydrogen infrastructure that has the public's confidence in its safety and convenience
- To build an industry consensus on hydrogen safety issues
- To ensure compatibility between various applicable hydrogen codes and standards
- To provide a forum for issues, to present consensus hydrogen energy input domestically, and to furnish a collective U.S. hydrogen industry position at international forums.

Goals and Objectives - This Term

As hydrogen continues to move toward commercialization, the NHA's objective is to continue the process of developing international standards for safety, tanks, connectors, and refueling stations, and identify and begin work on additional draft standards for the safe use of hydrogen. Collaboration with other standards bodies is a key element. NHA's technical goal is to create draft standards for hydrogen systems and components using the expertise of our membership.

Specific objectives for the current C&S effort are to advance work items that the NHA membership started in previous years. These include:

- Conduct a C&S Workshop,
- Take a leadership role in ISO-TC-197,
- Provide hydrogen expertise to IEC-TC-105 U.S. Technical Advisory Group (TAG) on Fuel Cell Technologies, the International Code Council Ad Hoc Committee on Hydrogen, and the Society of Automotive Engineers Fuel Cell Standards Safety Working Group, and

- Facilitate information exchange on hydrogen technologies and infrastructure issues to enable broad consensus building on C&S issues.

Milestones

The following milestones include those activities consistent with the Annual Operating Plan that were actually funded for this period.

Conduct C&S Workshop

The NHA C&S workshop was held on March 5, 2001 in Washington, DC. The proceedings are in preparation, and should be completed by the end of May. One of the highlights of the workshop was a lively discussion between industry, Underwriters Laboratory and the U.S. Department of Transportation on classification of metal hydrides for hydrogen storage.

Take a Leadership Role in ISO-TC-197

Mr. Mauro was elected Chairman of the U.S. TAG for ISO-TC-197. He attended applicable training sessions in February 2001. Courses were: Strengthening the U.S. Voice in International Standardization - The Operating Procedures of ANSI-Accredited TAGs to ISO, and Taking the Secret out of Secretariat: ISO Secretariat Operations. The NHA hopes to conduct regular meetings of U.S. industry prior to ISO-TC-197 plenaries to reach consensus and assure that U.S. interests are considered. A trip report on these courses was submitted to Sandia National Laboratory (SNL) in March and is available on the NHA website.

Update on ISO-TC-197, Hydrogen Technologies Work Item Progress

- WI 15916 Basic Considerations for the Safety of Hydrogen Systems: Final editorial changes have been approved for circulation of the Draft Publicly Available Specification. This document was circulated to the P-members of ISO-TC-197 through May 20, 2001.
- WI 15869 Gaseous Hydrogen and Hydrogen Blends-Land Vehicle Fuel Tanks: To be circulated as a Draft International Standard for a five-month voting period in the next month or two.
- WI 17286 Gaseous Hydrogen-Land Vehicle Filling Connectors: This work item is being advanced, addressing design issues of potential cross-connection. It is still in the working group.
- WI 15866 Gaseous Hydrogen Blends and Hydrogen Fuel-Service Stations: This item is stuck at the working group level. Issues regarding the baseline document and convenor availability are being worked out.

- SAE Documents are a Recommended Practice, but will likely become standards through ISO TC 22/SC21.
- IEC-TC-105 work items are just getting started and are described below.

The NHA developed a draft standard on hydrogen refueling stations for ISO-TC-197. The work item was accepted, but it has not advanced on schedule due to lack of U.S. support for convening this working group.

Provide Hydrogen Expertise to IEC-TC-105 U.S. TAG on Fuel Cell Technologies, the International Code Council Ad Hoc Committee on Hydrogen, and the Society of Automotive Engineers Fuel Cell Standards Safety Working Group

IEC-TC-105

Ms. Miller participated in the first full meeting of the U.S. TAG members of IEC-TC-105 on March 13, 2001, in Lake Buena Vista, Florida. Mr. Kelvin Hecht, formerly of International Fuel Cells, is Chair of the U.S. TAG. Mr. David Conover serves as Deputy Technical Advisor.

New work item proposals discussed are as follows:

- #105/10/NP: Terminology – Fuel Cell Technologies - Project Leader: Mr. Kelvin Hecht, USA - This proposed work item takes the Fuel Cell Glossary developed by the U.S. Fuel Cell Council, adds the Japanese Standards Association Glossary of Terms for Fuel Cell Power Plants, TR C 0001, and builds an international terminology document for future IEC-TC-105 work items.
- #105/11/NP: Fuel Cell Modules - Project Leader: Dr. Gerhard Filip, Germany - The scope of this document is Safety, EMC, quality assurance and environmental aspects of fuel cell modules in all applications.
- #105/9/NP: Stationary Fuel Cell Power Plants – Safety - Project Leader: Mr. Kelvin Hecht, USA - The scope of this proposed work item is performance-based requirements for the design, construction, testing and making of packaged fuel cell power plants. The purpose is to harmonize requirements from EU, Japan and USA using European Directives, MITI requirements and ANSI Z21.83.
- #105/6/NP: Fuel Cell: Testing Methods for Performance of Fuel Cell Power Facility - Project Leader: Mr. Tosiro Terayama, Japan - This standard is intended to cover the test methods for 1) Raw fuel consumption, 2) Temperature and quantity of heat recovered from fuel cell power facilities, 3) Electrical efficiency, 4) Overall thermal energy efficiency, 5) Load following and output power change, 6) Start-up time and shut-down time, 7) Cell stack voltage and current, and 8) Reactive power. The group noted that this scope is significantly beyond the scope of known U.S. standards. U.S. fuel cell manufacturers are encouraged to participate in the development of this standard.

A new work item proposal, not yet numbered, will be submitted to IEC-TC-105 to address Stationary Fuel Cell Power Plants – Installation. The proposed project leader will be Andrew Skok, USA. The group was given the opportunity to sign on to participate in this work item as U.S. experts. Ms. Miller signed on from the perspective of coordination between this activity and the work of the ICC Ad Hoc Hydrogen Committee, which is proposing changes to the U.S. model building codes for installation of fuel cells.

Other new work items are anticipated, but no formal request is yet available. NHA staff indicated a willingness to participate on any item that required a hydrogen-safety review or coordination with other U.S. activities where the NHA is participating.

ICC Ad Hoc Hydrogen Committee

A meeting of the International Code Council Ad Hoc Committee (AHC) on Hydrogen was held in conjunction with the 2001 ICC Code Development Public Hearings March 17-31, 2001, in Portland, Oregon. The ICC hosted this meeting Tuesday, March 20 through Thursday March 22, 2001 at the DoubleTree Hotel-Jantzen Beach.

Ms. Miller attended on behalf of the NHA. Her trip report was provided to SNL, DOE, and National Renewable Energy Laboratory following the meeting. In order to keep the hydrogen community informed, Ms. Miller posts trip reports and any draft codes and standards on the NHA *Members' Only* website. In addition, she publishes the information in an informational article in the NHA's quarterly publication, the *NHA News*.

Guy Tomberlin, AHC Chair, explained that the requested changes to the International Mechanical Code and the International Fuel Gas Code constituted the definitions of stationary fuel cell power system and portable fuel cell power system developed through the AHC meetings. One of the AHC's requested changes to the International Mechanical Code would be heard right away, and experts on hydrogen, as well as anyone who could offer supporting statements for the proposed changes should be prepared to speak.

The AHC's change was first on the agenda. Mr. Tomberlin read a statement of support. There was no opponent to the change. A motion to accept the change as submitted was offered and seconded. The motion passed unanimously.

The AHC's second proposed change to the International Mechanical followed the same format, with no opposition, and passed unanimously. The next step is a public comment period, and a final membership approval in September.

Similar code changes to the International Fuel Gas Code were presented, and Mr. Tomberlin was again the proponent. One of the Committee members questioned a change to the code that said it was important to define Portable Fuel Cell Power Systems, so that it was clear what was portable and what was stationary, as the code did apply to stationary. A motion was made to reject the change. After discussion, the motion to reject the change passed 7-5. The voting members then discussed and voted to file an action in support of the change. This vote passed 86-15.

The final AHC change was presented a short time later. After discussion, it passed.

The next day began with a discussion of progress from working group 3 (WG3) on hydrogen vehicle fuel-dispensing stations. Significant progress was made in identifying references in the codes to allow hydrogen. The work item presently includes gaseous hydrogen only. It was determined that the group would focus on this initially so that the group does not get bogged down in too many details. The group recognized the need to address vehicle service stations, and agreed to do so in the fire code, but not as part of this WG3 effort. It was recommended that the WG3 complete the effort, and make appropriate provisions for hydrogen blends and liquid hydrogen, if necessary.

Society for Automotive Engineers

The Society for Automotive Engineers (SAE) is seeking closer liaison with the NHA in the development of codes and standards of mutual interest. The NHA plans to attend two meetings of this group under this contract. The group meets monthly in Michigan. Ms. Miller attended a meeting in April and plans to attend one in June of this year under the current funding. The NHA does not anticipate attending each monthly meeting, but attendance quarterly is justified.

The Mission Statement of the SAE Fuel Cell Standards Committee is as follows: "Establish standards for vehicle fuel cell systems and its interfaces to the vehicle."

Scope. "The standards will cover the safety aspects of fuel cell systems in vehicles, test procedures to establish the performance of the system/components, and interface requirements."

Efforts Underway:

- Safety Working Group, Recycling Working Group
- Interface Working Group
- Performance Working Group
- Emissions & Fuel Economy
- Terminology
- Reliability

The NHA has taken a role on the Safety and Interface working groups. In many cases, there is no substitute for actually being there to speak on behalf the hydrogen industry. At the April meeting, the convenor of the Safety Working Group was seeking volunteers to address certain elements of the draft standard. The group was determined to use the expertise they had, but if none was available, that element might be excluded from the document. Ms. Miller volunteered to find an expert so that hydrides could be included.

Facilitate Information Exchange on Hydrogen Technologies and Infrastructure Issues to Enable Broad Consensus Building on C&S Issues

Leadership

The NHA's leadership in cooperation with key stakeholders is really what this effort of consensus codes and standards is all about. The NHA participates actively in the development of codes and standards on a national and international basis. The NHA creates draft standards only when our members express a need for the standard in the next 3-5 years, and there are no ongoing efforts to develop the standard. The NHA does not publish standards, so it is imperative that we work with organizations that do. Key staff are active members of the SAE Fuel Cell Standards Committee, the International Codes Council (ICC) Ad Hoc Committee on Hydrogen, and a number of international efforts, including IEC-TC-105 and ISO-TC-197. The NHA presents status of C&S activities at applicable technical conferences and forums, including the DOE Fuel Cell Codes and Standards Summit, NHA C&S Workshops, and other conferences when funding permits. Currently the NHA is participating in an on-line conference for EnergyResource2001 by presenting the NHA's role in C&S activities. Last year the NHA presented these activities at an IQPC conference on Fuel Cell Infrastructure.

The NHA keeps its members informed of progress in the development of hydrogen safety, codes and standards through publication in its quarterly newsletter and by posting information, including draft standards, on the NHA *Members' Only* website. This allows NHA members an opportunity to review the work of other organizations that have requested collaboration with the hydrogen community. The general articles published in the newsletter are made available to the public on the NHA website, and mailed to NHA members. In this way, the information is distributed broadly, and interested parties are given an opportunity to get involved in the standards development process.

The NHA Board is working to develop opportunities to keep up this important work in light of the DOE funding difficulties. It is imperative that additional resources are developed to disseminate the information we are gathering on the draft codes and standards that are being developed, and the issues that impact U.S. manufacturers. In addition, the public must be educated on the benefits and safety of hydrogen energy systems.

Status of Progress - National

NHA Work Items:

- WG1: Connectors
- WG2: Containers
- WG3: Refueling Stations
- WG4: Use of electrolyzers and fuel cells at customer sites, including homes.
- WG5: Safe self-service refueling of vehicles with H₂ (SAE Interface & Safety working groups)
- WG6: Certification program for hydrogen vehicle fuel systems (SAE Coordination)
- WG7: C&S for maritime unique applications of hydrogen (identify unique applications).

The NHA currently supports seven Codes and Standards Working Groups. Connectors and Containers work may continue for higher pressures, if interest and funding allow. Currently the Containers working group is focused on working with the U.S. Department of Transportation on hydride transport.

WG 4-7 began in August 1999. Since that time, funding for the NHA C&S efforts has been intermittent at best. This has impacted the ability to get the work groups together, and conduct outreach with outside experts, in order to advance these items.

There has been some progress, however, particularly on hydrides and maritime. These efforts will be described in the C&S Workshop Proceedings from the March 5 meeting.

The scope of WG 4 is to develop a standard for installation, safety and use of electrolyzer hydrogen generators in end use applications, including the residential, commercial and industrial sectors. Activities will include identifying appropriate group participants in addition to NHA members, assessing the existing relevant codes, establishing parameters and developing a technical envelope for the WG. A code/building and zoning review will also be important to this WG. Finally, the NHA would like to develop a draft standard based on an appropriate template document and scope.

WG 5 will specify design criteria for safe self-service refueling with liquid and gaseous hydrogen. This will include consideration for vehicle grounding, venting of fuel lines and elimination of possible ignition sources. This activity is in conjunction with the SAE Interface and Safety working groups.

The scope of WG 6 is to verify the performance of on-board hydrogen systems. These systems must be safe and perform to specified vehicle standards. The hydrogen system includes storage, generation, distribution, power source, and controls. The NHA is actively working with SAE Fuel Cell Standards Forum C&S safety task force and disseminates the information to WG 6 members.

The scope of WG 7 is to identify maritime-unique applications of hydrogen. This was done in cooperation with the Maritime Hydrogen Technology Development Group as well as other interested standards bodies. The MHTDG has published a massive report on the subject, and provided the NHA with two copies. The group has indicated an interest in taking the maritime work farther, if funding permits.

The NHA is currently working with the ICC to provide technical input and industry support for changes to the model building codes to allow certain hydrogen fuel appliances to be sited. The NFPA has recently developed an interest in hydrogen, and would like to work with the NHA to provide the hydrogen expertise to their working group, which will be similar to the ICC work. The NHA presently is not funded to participate in these activities, but can do it if we are awarded the 3-year contract for C&S activities from DOE. A 3-year contract will significantly improve our ability to plan and conduct workshops, and keep stakeholders, including code officials and the public, informed of the progress.

Status of Progress – International

The NHA has a formal liaison relationship with ISO-TC-197. Mr. Mauro serves as the Chair of the U.S. Technical Advisory Group for 197. His duties include:

- Work with the U.S. TAG Administrator to coordinate U.S. TAG positions
- Coordinate meetings
- Take a lead role in bringing U.S. interests to ISO
- Lead in identifying potential members of the U.S. TAG

Ms. Miller serves on the permanent editing committee, to review draft documents before circulation to ensure that they are in proper English, and do not contain gaps in definitions or data.

Ms. Miller is also a member of IEC-TC-105 and strives to assure the group has liaison with ISO.

IEC-TC-105, when formed, was made up of only fuel cell manufacturers. Participation of other entities, such as NHA and SAE, helps provide the necessary diversity to create a consensus standard.

Although the NHA does not participate on ISO-TC-22/SC 21 work items, automotive members are involved, and the broader NHA involvement occurs in two places - first the SAE work feeds into TC-22/SC 21. Secondly, TC-22/SC 21 has recently agreed to a liaison with ISO-TC-197 on hydrogen issues.

The NHA has been very effective at bringing forward concerns from U.S. members, including the National Labs. We've been able to effect favorable changes in standards brought forward from other countries.

An association, such as the NHA, is able to garner a great deal of consensus. The NHA is especially well-positioned to do this because of the diversity of membership. We are developing standards with input from energy companies, industrial gas suppliers, fuel cell manufacturers, safety equipment and service suppliers, and others.

Proposed Future Work & Milestones

The ICC AHC initial activities are expected to be completed in the 2-3 year timeframe. Building codes are always being revised, and as more hydrogen energy systems become commercial-ready, there is bound to be additional activity required. We do, however, anticipate that the heaviest activity is the current effort, where we are educating building code officials who

recommend changes to the model building codes. NHA support is likely to diminish to special technical or industry support in the outyears.

Very recently, the NFPA has asked for NHA assistance in the development of hydrogen refueling station activities. Some jurisdictions may rely on ICC codes while others rely on NFPA. The NHA will work to ensure these codes are consistent and meet the needs of the industry. In addition, we will strive to broaden the scope beyond refueling stations.

We hope to be able to continue to provide expertise on hydrogen to other C&S efforts, like the SAE, DOE FC C&S Summit, and others, as well as continue providing this support to ISO and IEC. We hope to prepare additional work item proposals on the ongoing work items described earlier, and others that may be needed in the near future, such as 10,000 psi gaseous hydrogen systems, particularly composite storage tanks.

The European Union has adopted a series of hydrogen standards, and is seeking to harmonize those with North America. It will be necessary to work with many manufacturers and organizations to assure that U.S. interests are not overlooked. While European and Canadian companies are receiving significant funding from their governments to develop international standards based on national interests, this is not the case in the United States. The NHA must bridge this gap by assuring that these standards consider U.S. interests. This involves identifying issues and convincing the stakeholders to spend some time looking at the draft standards, and where necessary, participate in the process. Few U.S. hydrogen industry businesses can afford to follow all the activities, let alone participate in them. If someone isn't looking out for them, the international standards that are developed may be unfavorable for U.S. industry.

Conclusions

The National Hydrogen Association has members from automobile companies, fuel cell developers, gas producers, chemical companies, and others. The NHA serves as a catalyst for information exchange and cooperative projects and provides the setting for mutual support among industry, government, and research/academic organizations and provides a national focal point for hydrogen interest and information transfer.

The development of codes and standards allows hydrogen energy systems to be produced, sold, and sited commercially, while increasing public confidence in safety and reliability. U.S. leadership and participation ensures a level playing field that allows equitable distribution of U.S. products globally. Standards could become non-tariff trade barriers. Rules for international trade in hydrogen and hydrogen-related products are being written now. Other industrialized countries have taken initiatives to present their views of the development of rules for hydrogen and hydrogen-related products.

The main barriers to wide-scale use of hydrogen-fueled cars and fleets include lack of infrastructure, public acceptance, coordination and collaboration among potential fleet operators, and applicable codes, standards, and other safety information that can enable siting and ensue the required infrastructure. Removal of these barriers requires that government organizations work

together, and include industry and academia where appropriate to educate the public and prove that fleets of hydrogen-powered vehicles can be operated safely and cost-competitively. The NHA allows a forum for these issues to be discussed and resolved.

European countries, and even Canada, fund their industries to participate actively in the development of C&S that favor their national interest. The U.S. is not doing this and this could result in C&S that favor these countries, to the detriment of U.S. manufacturers. The NHA can bridge this gap by building consensus, looking out for issues that may be unfavorable to U.S. interests, and alert U.S. manufacturers of activities and issues that should be looked at by these companies. The NHA is interested in doing more of this necessary coordination work, particularly now that the European Union is seeking to harmonize their standards with North America.

Acknowledgments

U.S. Department of Energy provided cost-shared funding through Sandia National Laboratory for this effort.

Mr. Mauro and his longstanding efforts in the identification and development of needed codes and standards for hydrogen energy systems, and leadership in establishing an effective NHA C&S program.



Finding words in PDF documents

You can use the Find command to find a complete word or part of a word in the current PDF document. Acrobat looks for the word by reading every word on every page in the file.

To find a word using the Find command:

- 1 Click the Find button , or choose Edit > Find.
- 2 Enter the text to find in the text box.
- 3 Select search options if necessary:
 - Match Whole Word Only finds only occurrences of the complete word you enter in the text box. For example, if you search for the word *stick*, the words *tick* and *sticky* will not be highlighted.
 - Match Case finds only words that contain exactly the same capitalization you enter in the text box.
 - Find Backwards starts the search from the current page and goes backward through the document.
- 4 Click Find. Acrobat finds the next occurrence of the word.

To find the next occurrence of the word:

Do one of the following:

- Choose Edit > Find Again.
- Reopen the Find dialog box, and click Find Again. (The word must already be in the Find text box.)